Springer Series in Materials Science 214

R. G. Sharma

Superconductivity

Basics and Applications to Magnets

Second Edition

Springer

Springer Series in Materials Science

Volume 214

The Springer Series in Materials Science covers the complete spectrum of materials research and technology, including fundamental principles, physical properties, materials theory and design. Recognizing the increasing importance of materials science in future device technologies, the book titles in this series reflect the state-of-the-art in understanding and controlling the structure and properties of all important classes of materials.

More information about this series at http://www.springer.com/series/856

R. G. Sharma

Superconductivity

Basics and Applications to Magnets

Second Edition

Springer

R. G. Sharma
Inter-University Accelerator Centre
New Delhi, India

Formerly at National Physical Laboratory
New Delhi, India

ISSN 0933-033X ISSN 2196-2812 (electronic)
Springer Series in Materials Science
ISBN 978-3-030-75671-0 ISBN 978-3-030-75672-7 (eBook)
https://doi.org/10.1007/978-3-030-75672-7

This Springer imprint is published by the registered company Springer Nature Switzerland AG
The registered company address is: Gewerbestrasse 11, 6330 Cham, Switzerland

Dedicated to

Wife Bimlesh, grand daughters, Oorja, Tanvi and Tavisha

Preface to Second Edition

As an author, I was delighted to see very good response of the readers to the first edition of the book, published in 2015. The unprecedented all-round development that took place in this fascinating field of superconductivity during last 6 years prompted me to bring out the second edition of the book. The book now has the latest updates on all the topics discussed in the first edition. To name a few notable advances made during this period are: (i) REBCO cables have been fabricated carrying current up to 80–100 kA. (ii) A new world record of 45.5 T magnetic field has been established by NHMFL in 2019. (iii) Several accelerator projects such as HL-LHC, HE-LHC and FCC-hh, which may dwarf LHC, have been planned and are being executed. (iv) The latest, electron–ion collider (EIC), launched in May 2020, has been dubbed as the 'Discovery Machine'. (v) The assembly of ITER is in full swing as components from across the globe continue to pour at Cadarache site. (vi) Many countries are building next-generation fusion machines like individual DEMOs for producing power in 2030s. (vi) New record of 1.2 GHz NMR spectrometer has been established by Bruker, and a 1.3 GHz NMR system is nearing completion at FBML, MIT. (vii) Newly designed MRI scanners are now appearing in the market in which a patient can be imagined in sitting, standing or lying positions. (viii) Conduction-cooled 1.5T/3 T MgB_2 magnet MRI scanners might invade market in the near future. All these developments have been adequately discussed, and I am sure the readers will enjoy reading these topics in detail in this new edition of the book.

This edition of the book has 12 chapters in all. Apart from a chapter on the stability of superconductors and practical conventional Nb-Ti, Nb_3Sn, Nb_3Al and V_3Ga superconductors, three separate chapters have been devoted to practical cuprates, MgB_2 and the iron-based superconductors. Emphasis has been given to the recently developed innovative techniques to produce high J_c strands and cables needed for high-field magnets for upcoming accelerators and fusion reactors. The highlight of conductor development has been the techniques invented to produce cables using 2G REBCO tapes in several configurations, like CORC cables by ACT (Advanced Conductor Technologies LLC) and Roebel Bar Cables and CroCos cables by KIT (Karlsruhe Institute of Technology). The ACT-developed CORC-CICC cables are expected to carry a record current of 90–100 kA. Another highlight is the observation of current-blocking bubble formation in isotropic Bi-2212 round wires. This

problem was resolved at NHMFL by using an over-pressure heat treatment (OPHT) technique. A Bi-2212 insert, in fact, produced a field of 33.6 T in a background field of 31 T at NHMFL. Another interesting development has been that the iron based (IBSC) 122 superconductor $(Ba_{0.6}K_{0.4})Fe_2As_2$ with a $T_c = 38$ K has attained a transport J_c as high as 10^5 A/cm^2 (4.2 K, 10 T). This value is more than the threshold set for practical superconductors up to a field of 10 T.

As for the theories, a consensus on the origin of superconductivity in cuprates has not been reached but surprisingly, the BCS theory has been found a perfect fit to superconductivity in MgB_2 ($T_c = 39$ K) and H_3S ($T_c = 203$ K) and is attributed to strong electron–phonon interaction and high-frequency optical phonons. Theorists have now started conjecturing that the BCS theory, one day, may become a unified theory of superconductivity of all the varieties.

Detailed discussion on the successors of LHC, namely the high luminosity LHC (HL-LHC), high energy (28 TeV HE-LHC) and the future circular collider (FCC-hh) with 100 km circumference and 100 TeV collision energy has been given in the book. The magnet systems of ITER have been discussed in greater details. Present status of the assembly of the ITER has been adequately described. The performance of stellarator W7-X operating at MPIPP, Greifswald, Germany, and its upgrade to divertor stage has also been discussed.

The 12th and last chapter titled 'Other Applications of Superconducting Magnets' is about the magnet applications in high-resolution nuclear magnetic resonance (NMR), magnetic resonance imaging (MRI), high-gradient magnetic separators (HGMS) and superconducting magnetic energy storage (SMES) which benefits the society immensely in a variety of ways. NMR spectrometers with a resonance proton frequency of 1.2 GHz ($\equiv$ 28.2 T) from Bruker have set up a new world record in high-resolution NMR spectrometry in 2020. Study of structures and functions of important globular proteins, membrane proteins and protein complexes has become possible first time. The concept of imaging by MRI has gone under sea-change in recent years. Focus has shifted to build MRI machines which are patient centric. The patient need not enter the tubular magnet. Instead, imaging can be done in sitting, standing or in lying position. The second focus is on the conduction-cooled MRI magnets thus doing away with the use of scarce and expensive liquid helium.

The target readership remains the UG/PG students and researchers keen to take a plunge in large-scale international projects on accelerators and fusion reactors. They can find most of the topics in superconductivity, production of practical conductors of all varieties and magnets for applications under one title. I am sure, the readers will find the contents of the book very absorbing and will enjoy reading the book A–Z.

New Delhi, India R. G. Sharma
February 2021

Acknowledgements

The new book contains the recent and most recent developments that have taken place during last 6 years in different areas of superconductivity covered in the book. A significant part of information was obtained from personal contacts who are engaged in large international projects based on magnet applications especially in present and future accelerators and fusion reactors. Quite a few friends went extra mile in requesting their colleagues to provide me with data from their research. Some even prepared copyright-free pictures especially for the book. I express my gratitude and thank them all.

At the outset I would like to thank Lucio Rossi (CERN and now at University of Milano) who helped me tremendously and wrote to his colleagues at CERN to provide me with several pictures of dipoles and quadrupoles to be used in HL-LHC (high-luminosity LHC) and FCC (future circular collider). I place on record my grateful thanks to Ezio Todesco, Frederic Savary, Panagiotis Charitos and Paolo Ferracin of CERN. I am grateful to Yuki Iwasa of FBML (MIT), the best-known person in the fields of NMR and MRI for making quite a few pictures from his research available to me. With great pleasure, I thank my erstwhile colleagues at NRIM (now NIMS) Takao Takeuchi, Shinji Matsumoto, Yoshihiko Takano and Kazumasa Togano for supplying rich data information and several pictures on record superconducting magnets and advance practical superconducting materials. I thank Lubo Kopera and Pavol Kováč, IEE, SAS, Bratislava for supplying good bit of their data plots on a variety of MgB_2wires and cables of different configurations. My special thanks to Lubo Kopera, who prepared picture especially for me from his work.

I am completely overwhelmed by the quick response of many experts during the period of lockdowns and during the period when they were on vacation. I would like to acknowledge the help received from David Larbalestier, Huub Weijners, Renuka Rajput Ghosal T. V. Ramakrishnan (IISc and BHU India), Jung Ho Kim (AIIM, University of Wollongong), Hiroyoshi Sakurai and Hiroki Okumo (RIKEN K-2500 SRC), Takashi Yanagasawa (National Institute of Advanced Industrial Science and Technology), Armando Sarmiento Santos (Universidad Pedagógica y Tecnológica de Colombia) and Takahi Gakuin and Jun Akimitsu (Aoyama Gakuin University) for their help and permission to use pictures. I express my gratitude to Herman ten

Kate (CERN + University of Twente), Wilfried Goldaker and Walter H. Fietz of the KIT, Venkat Selvamanickam (Houston University), for permitted the use of pictures on ultra-high-current 2G REBCO cables.

I also contacted a number of manufacturers of the superconducting wires/cables and magnet-based systems like NMR spectrometers and MRI scanners who readily supplied critical parameters of their products, brochures and pictures for use in my book. For this help, I would like to thank Yifei Zhang and Prateek Dokania of SuperPower, Danko van der Laan of ACT (Advanced Conductor Technologies), David Doll, Peter McIntyre (TAMU), Michael Sumption (Ohio State University) and Mike Tomsic of Hypertech Research, Yuichi Yamada of Sumitomo Electric Industries, Helmut Krauth of Vacuumschmetze, Kuemmerie Rainer of Bruker BioSpin, Craig D. Sergeant of Jeol, Ernst Wolfgang Stautner of GE Global Research, Grasso Gianni and Gazzo of ASG Superconductors, Paramed MRI Unit, Ritta Pietila, Michael Enwal and Karan Mehrotra of MEGIN Oy Finland.

Copyright permissions to use illustrations/figures for the book came fast from Elsevier, Springer Publishing, SpringerNature, Oxford University Press, Cambridge University Press, Nature Publishing Group, American Physical Society, Institute of Physics (IOP), American Chemical Society (ACS) and American Institute of Physics (AIP). I also thank many media/communication centres from several national laboratories in USA for providing high-quality pictures for the book. RightsLink too provided wonderful service for getting copyright permissions from almost all the journals instantaneously.

The book has been written at the Inter-University Accelerator Centre (IUAC), New Delhi, my workplace since 2001. The Director, Prof. Avinash Pandey and the administration of IUAC provided all possible logistic support. I thank them all. Working with stalwarts like M. S. R. Chari of NPL, New Delhi, N. E. Alekseevskii of Kapitza Institute of Physical Problems, Moscow, Kyoji Tachikawa and Hiroshi Maeda of NRIM (NIMS), Tsukuba, O. V. Lounasmaa, Low Temperature Laboratory, Helsinki University of Technology, Helsinki, F. Baumann and Werner Buckel of Karlsruhe University and Shi Ichi Tanuma of ISSP (Tokyo University) impacted me profoundly and shaped my research career. I place on record my deep gratitude to them.

I would like to thank my erstwhile colleagues at NPL Y. Showry Reddy, Manmohan Krishna, Rajan Babu Saxena, Hari Kishan, S V Sharma, Mubeen A. Ansari and Dipten Bhattacharya. I have also referred to the work of some of my Ph.D. students (Sudip R. Jha, Shriram Shukla, Biswanath Sarkar, Renuka Rajput, Saswati Lahiry, Shyam Sunder Dubey, Arvind Pandey and Devraj Mishra at relevant places in the book. I thank them all. I also thank Yogesh C. Saxena, Dipten Bhattacharya, G. Rodrigues and Renuka Rajput for having gone through a chapter each and made valuable suggestions. My own colleagues at IUAC, Rakesh Bhandari, Triptishekar Datta, Anup Choudhury, Rajesh Kumar and P. Konduru helped me in one way or the other. My colleagues Soumen Kar and the young researchers Vijay, Navneet, Sankar and Ajit have been of great help to me. I would like to thank them. I also thank Priyambada Naik, IUAC Library In-charge for her great help in making all the journals accessible from home during the long period of lockdown. This help

was critical for the update on most topics discussed in the book. I also thank Murthi Goirik, graphic designer with long experience in publishing, who prepared several illustrations for the book.

The ambience available at the IUAC has been very conducive for writing the book especially because of my close proximity with my senior colleagues G. K. Mehta and S. C. Pancholi who have authored books earlier.

I thank whole heartedly my son Raghvendra for having gone through some of the chapters of the book and Neeraj, my son-in-law for guiding me during the proof-reading of the typescript of the book. Above all, I thank my wife, Bimlesh, who has been of great strength to me all through my long career. In spite of her health problems, she made it possible for me to sit in front of the laptop for long hours. All other members of my joint family have always been supportive to me for pursuing my academic interests.

Lastly, I thank the readers of the first edition of my book who really were instrumental in motivating me to bring out the second edition.

New Delhi, India R. G. Sharma
February 2021

Contents

About the Author

R. G. Sharma is an emeritus scientist at the Inter-University Accelerator Centre (IUAC) in New Delhi, India. He has been active in the fields of superconducting materials, superconducting magnets and low-temperature physics for 57 years. In 2001, he retired from National Physical Laboratory, New Delhi, as Deputy Director and Head of the Division of Cryogenics and Superconductivity. During the period 2003–2009, he was a visiting professor at the Legnaro National Laboratory (INFN), Padova University, Italy, where he lectured on superconducting materials and mentored Laurea and Ph.D. students.

Dr. Sharma guided ten Ph.D. students on superconducting materials and magnets and has published over 120 research papers in international peer-reviewed journals such as *Physical Review*, *Cryogenics*, *Journal of Low-Temperature Physics*, *Journal of Physics* and *IEEE Transactions.* So far he has delivered about 200 lectures at various national symposia. He has also delivered 168 invited talks and course lectures to masters and PhD students in both India and Italy after his retirement in 2001. He was the Chief Editor *Indian Journal of Cryogenics* from 2014 to 2020. He is the recipient of Indian Cryogenics Council (ICC) Lifetime Achievement Award (2014), the Prof. R. Srinivasan Award for Low Temperature Physics/Cryogenic (2003), the 1996 Materials Research Society of India Medal, the NPL Merit Award (1977) and the A. N. Chatterjee Memorial Award (1977).

Chapter 1
Introduction

Abstract The study of matter at very low temperature is fascinating because the phonon activity dies down at very low temperatures and one can look in to the electronic behaviour minutely. Cryogenic baths of liquefied gases provide excellent medium to cool down samples. Liquefaction of gas is a combination of an isothermal compression followed by an adiabatic expansion. Cascade process were adopted in liquefying oxygen by Cailletet and Pictet independently in 1877. The final cooling stage has always been a Joule-Thomson (J-T) valve. Another important breakthrough came in 1898 when James Dewar succeeded in liquefying hydrogen making a temperature range of 20–14 K accessible. The moment of triumph came in July 1908 when years of hard work by Kamerlingh Onnes at Leiden ultimately resulted in the liquefaction of helium. A temperature range of 4.2–0.8 K, thus, became accessible in the laboratory. A cascade process using L_{air}, LO_2, LN_2 and LH_2 and the J-T expansion valve was employed. Within three years of this discovery came the defining moment of the discovery of superconductivity in April 1911 in pure Hg at just below 4.2 K. Kamerlingh Onnes was awarded Nobel Prize in 2013, and the citation reads *For his investigations on the properties of matter at low temperature which led inter alia, to the production of liquid helium.*

1.1 Why Low Temperature Is so Exciting?

Temperature is one of the most important variable parameters like pressure and magnetic field which can be manipulated to change the phase of the material and thus its mechanical, thermodynamical, chemical, electronic and phonon properties. To carry out studies at low temperatures is particularly interesting. At ambient temperatures, lattice vibrations (which are quantized and are called phonons) in any material are dominant and usually mask its fine properties. As the temperature is lowered, the amplitude of these vibrations is reduced and at very low temperature (close to absolute zero) dies down completely. In other words, the dominant phonon contribution almost disappears, and one can observe the quantum behaviour of matter. Normal laws valid at ordinary temperatures may not hold any more. Some of the properties

R. G. Sharma, *Superconductivity*, Springer Series in Materials Science 214,
https://doi.org/10.1007/978-3-030-75672-7_1

in fact violate all our norms about the matter as to how it ought to behave. Superconductivity and superfluidity are perhaps the most striking phenomena observed at low temperature, which display the quantum behaviour at a macroscopic scale. An electric current can flow persistently in a superconductor (without dissipation) without a voltage, and similarly a superfluid can flow effortlessly (no viscosity) through fine pores, impervious to normal liquid, without a pressure head.

1.2 How to Conduct Experiment at Low Temperatures?

The best way to carry out studies at low temperature is to have a suitable cryogenic bath, which can cover the temperature range of interest. A cryogenic bath is best provided by a liquefied gas. One can pump over the liquid surface to reduce vapour pressure and obtain still lower temperature until it freezes. Thus for example, nitrogen (N_2) gas boils at 77 K (Kelvin) and can be pumped down to 65 K, and hydrogen (H_2) boils at 20 K and can be pumped down to 14 K. Helium (He) is the only stable gas which boils at the lowest temperature, that is, 4.2 K. One can pump liquid helium and can achieve a temperature of 0.8 K. There is a rare isotope of helium with a mass number 3 called ^{3}He. It boils at a temperature of 3.2 K and can be pumped down to 0.3 K. Most interesting thing about these two liquids is that they refuse to freeze even at zero absolute. Both can be solidified only at very high pressure. For their unique and very peculiar properties, they are referred to as Quantum Liquids.

To go to temperature lower than 0.3 K, one can use what we call as ^{3}He/^{4}He dilution refrigerator (DR) and is based upon the finite solubility of ^{3}He (6.4%) in to ^{4}He down to absolute zero. ^{4}He at 1 K is used as a pre-cooling agent. We can use a DR to produce a temperature of a few milli-Kelvin (mK). To go to still lower temperatures, this DR is used as a pre-cooling stage to an adiabatic nuclear demagnetization system and a temperature of a few micro-Kelvin (μK) is achieved. By using a cascade of demagnetization stages, one can go down to nano-Kelvin (nK) and pico-Kelvin (pK). A world record of ultralow temperature ~ 100 pK is held by the Lounasmaa Low Temperature Laboratory of the Helsinki University of Technology, Finland. Whenever the scientific community entered a new regime of low temperature, some discovery or the other of very fundamental importance took place.

1.3 Gas Liquefaction

Broadly speaking, a gas liquefaction is a combination of two thermodynamic processes, an isothermal compression followed by an adiabatic expansion. In the first step, a gas is compressed at high pressure at constant temperature. This is achieved by removing the heat of compression by a suitable cooling mechanism. In the second stage, the compressed gas is allowed to expand under adiabatic conditions, wherein

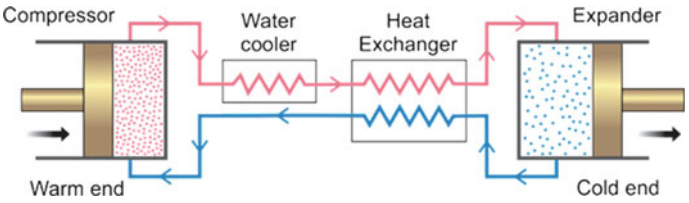

Fig. 1.1 Principle of gas liquefaction

heat is neither allowed to enter nor escape from the system. The temperature, therefore, drops. The process goes on until the gas liquefies. This is schematically shown in Fig. 1.1. The expansion could be of either isenthalpic or isentropic type.

1.3.1 Isenthalpic Process

In isenthalpic expansion one uses an expansion valve or a Joule-Thomson valve through which the high-pressure gas throttles and gets cooled. There is no change in the enthalpy (zero heat transfer and zero work transfer) in this expansion process. This process is sometimes also referred to as the internal work method as it does not remove the energy from the gas. It only moves the molecules apart against the inter-atomic forces. This process is irreversible and therefore not an efficient thermodynamical cycle. Further, the isenthalpic expansion does not always lower the temperature. If the temperature of the gas is above the maximum inversion temperature, it will heat up the gas. The temperature of the compressed gas before expansion should therefore be below its inversion temperature. It is for this reason that gases like helium (45 K), hydrogen (205 K) and neon (250 K) cannot be liquefied using a J-T valve expansion, their inversion temperatures being below the ambient temperature (~ 300 K). These gases have to be pre-cooled to below their inversion temperature before they suffer J-T expansion. A J-T valve is, however, integral to any liquefier and always forms the last stage of cooling since the liquid formation in the expander cannot be sustained. Table 1.1 lists the maximum inversion temperatures (at $P = 0$) of a few permanent gases. The gases, therefore, have to be pre-cooled to below their respective inversion temperature before entering the J-T valve.

1.3.2 Isentropic Process

In the isentropic process, the energy is extracted as external work and always produces cold in contrast to the isenthalpic process. This is also referred to as the external work method. Gas expands in an expander, which can be of reciprocating (piston) engine type or can be a turbine. The process is reversible and thus thermodynamically more

Table 1.1 Maximum inversion temperature of some gases

S. No.	Gas	Max. inversion temperature (K)
1	^{4}Helium	45
2	Hydrogen	205
3	Neon	250
4	Air	603
5	Nitrogen	621
6	Oxygen	761
7	Argon	794
8	Carbon dioxide	1500

efficient. With the same initial temperature of the gas, this process always leads to lower temperature than obtainable with the isenthalpic process. As stated above, the operational problem associated with the expansion of the two-phase mixture (liquid and gas) in an expander makes it mandatory to use a J-T expander as the last stage of the cooling cycle.

1.3.3 The Linde–Hampson Process

Oxygen was first time liquefied by Louis Cailletet of France and Raoul Pictet of Switzerland independently within days of each other in the year 1877. Pictet used a cascade process wherein a pre-cooling stage is cooled by another pre-cooling stage. He used liquid SO_2 and then dry ice (−80 °C, solid CO_2) for pre-cooling. Cailletet used liquid SO_2 for pre-cooling oxygen before it throttles through a J-T valve. A good historical account of the liquefaction processes can be found in 'Cryogenic Engineering' [1]. Von Linde [2] and Hampson [3] perfected the oxygen liquefaction technology by using more reliable ammonia cycle for pre-cooling compressed oxygen and the counter current heat exchangers before the gas expands through a J-T valve. Linde founded Linde Eismaschinen AG in 1879 and later obtained a German Patent in 1895. Basic principle in this process is that air/oxygen is alternatively compressed, pre-cooled and expanded in a J-T valve. This results in reducing the temperature each time until the gas gets liquefied. The pressure used in Linde process is rather high. For example, for air at 300 K, the optimized pressure is about 40 MPa (~ 5880 psi) but the actual machines use a pressure of about 20 MPa. A typical Linde–Hampson cycle is shown in Fig. 1.2.

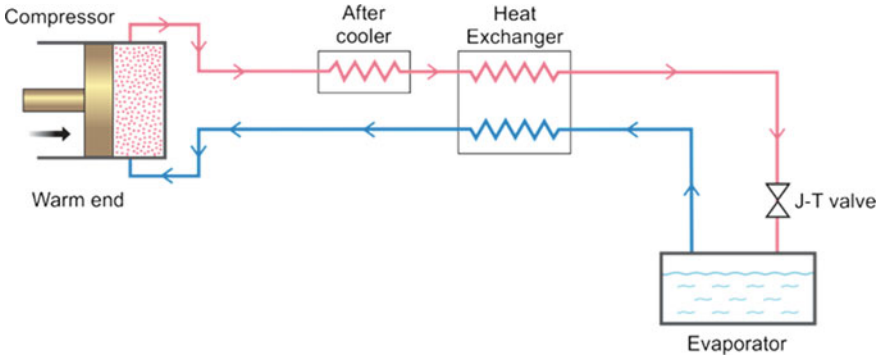

Fig. 1.2 Linde–Hampson liquefaction cycle consisting of a compressor, a counter current heat exchanger and a J-T valve at the final stage

1.3.4 The Claude Process

Claude process [4] is an isentropic process, which is adiabatic, thermodynamically reversible, and therefore more efficient than the isenthalpic process to produce cold. Another added advantage is the lower operating pressure needed for this cycle ~ 1.7 MPa (~ 250 psi). In this process, the gas does an external work in an expansion engine. The engine can either be of reciprocating piston type or of a rotating type. As shown in Fig. 1.3, the gas is compressed to the required pressure and passes through the first heat exchanger. A portion of the gas (60–80%) is then sent to an expander, and the rest continues to move along the mainstream path. The expanded low-pressure cold gas is fed back to the returning gas just after the second heat exchanger. The

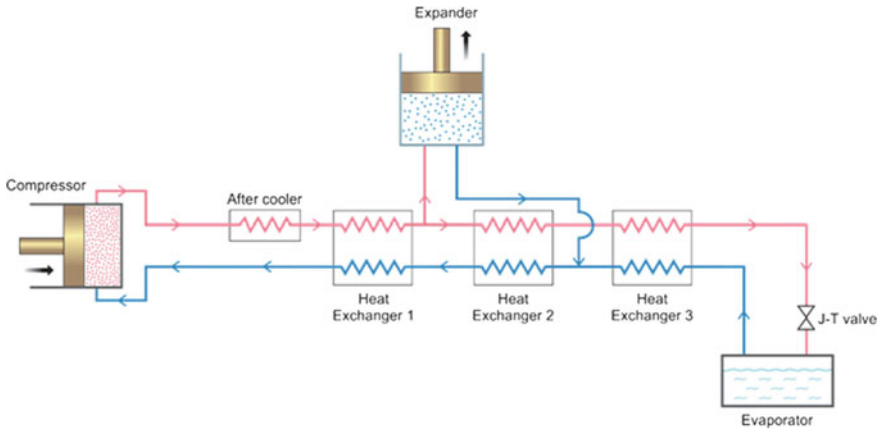

Fig. 1.3 Claude cycle consisting of a compressor, a series of heat exchangers, an expansion engine and a J-T valve in the final stage

return gas cools down the high-pressure incoming gas via the two heat exchangers. Thus, the cold high-pressure gas proceeds via the third heat exchanger, expands in a J-T expander and gets liquefied. The cold vapours from the liquid reservoir return to the compressor via the heat exchangers giving out cold to the incoming high-pressure gas. A J-T expansion valve is still necessary because liquid formation in the cylinder of the expansion engine is not desirable. The stresses caused by the low compressibility of the liquid can damage the cylinder. Rotary turbine expander can, however, tolerate almost 15 wt. % liquid without causing damage to the turbine.

Two great inventions, which took place in the history of gas liquefaction, need to be mentioned here. First in 1892 when James Dewar developed a double-walled vacuum-insulated cryogenic fluid storage vessel (popularly known as Dewar flask). This made it possible to store, transport or pour cryogenic fluid from one vessel to another. Experiments with cryogenic fluids for long duration became possible. Second invention [5, 6] by Dewar was the first time liquefaction of hydrogen in 1898, lowering the temperature range available for studies to 20 K and down to 14 K under reduced pressure. Dewar used the Linde cycle (i.e. high pressure and J-T expansion) using liquid nitrogen as the pre-cooling stage.

A masterpiece treatise on the liquefaction cycles has been written by Barron [7]. Readers are advised to consult this book for details on gas liquefaction and most of the cryogenics topics.

1.3.5 Liquefaction of Helium (1908)

Heike Kamerlingh Onnes at Leiden Institute, The Netherlands, had great fascination for the study of van der Waals equation of corresponding states down to the lowest ever temperatures. Nernst heat theorem and Planck's zero point energy theory further added to his curiosity to achieve the lowest possible temperature. His passion to liquefy helium became all the more stronger. He made use of the Linde technique that is pre-cooling compressed helium to the freezing point of hydrogen (14 K) and subjecting it to J-T expansion. He succeeded in liquefying helium on 10 July 1908. This turned out to be a turning point for the entire condensed matter physics community. This opened the floodgate for getting to lower and lower temperatures. Discoveries one after another followed in quick succession. The first one was, of course, the discovery of superconductivity in 1911 by Kamerlingh Onnes himself. Kamerlingh Onnes got Nobel Prize in 1913 for this work. The Nobel Prize citation dated 10 December 1913 states '*For his investigations on the properties of matter at low temperature which led inter alia, to the production of liquid helium*'. Figure 1.4 shows the schematic diagram of the apparatus used by him for helium liquefaction [8].

As seen in Fig. 1.4, compressed helium gas flows through the liquid air-cooled charcoal Dewar to get rid of moisture, gets cooled through a spiral immersed in pumped hydrogen (15 K), expands through a J-T expansion valve and gets liquefied in the inner most Dewar. The boiling temperature of helium is 4.2 K at atmospheric

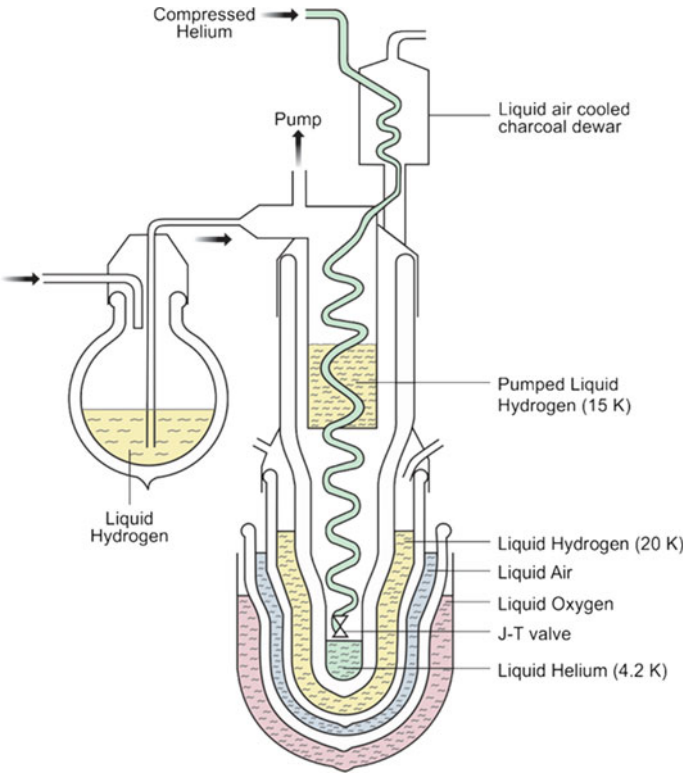

Fig. 1.4 Schematic diagram of the apparatus used by Kamerlingh Onnes for the liquefaction of helium first time. *Courtesy* Peter Kes, Kamerlingh Onnes Laboratorium, Leiden University

pressure. For the next twenty years, the Leiden Laboratory remained a most sought after place for research by the condensed matter physics community from Europe and USA and Kamerlingh Onnes enjoyed complete monopoly.

John Cunningham Mclinnan built the second helium liquefier at the Toronto University in 1923. The design of this machine was borrowed from Kamerlingh Onnes but looked little more elegant. In reality, low-temperature research started flourishing around 1934–35. Four German scientists, namely Franz Simon, Heinrich Kuhn, Nicolas Kurti and Kurt Mendelssohn, joined Clarendon Laboratory at Oxford University at the invitation of Lindemann. Low-temperature research started at Oxford when Simon built a mini He liquefier. Around the same time, Pjotr Kapitza, a collaborator of Lord Rutherford at Cambridge, too built a He liquefier [9] at the Cambridge University. This machine was based upon a rotating expansion engine or the so-called turbine. He made a similar liquefier at the Institute for Physical Problems, Moscow, in 1935. The commercial machine [10] built by Samuel Collins (MIT) and marketed by M/S Arthur D Little of the USA was the beginning of the spread of low-temperature studies using liquid helium the world over. Many countries around

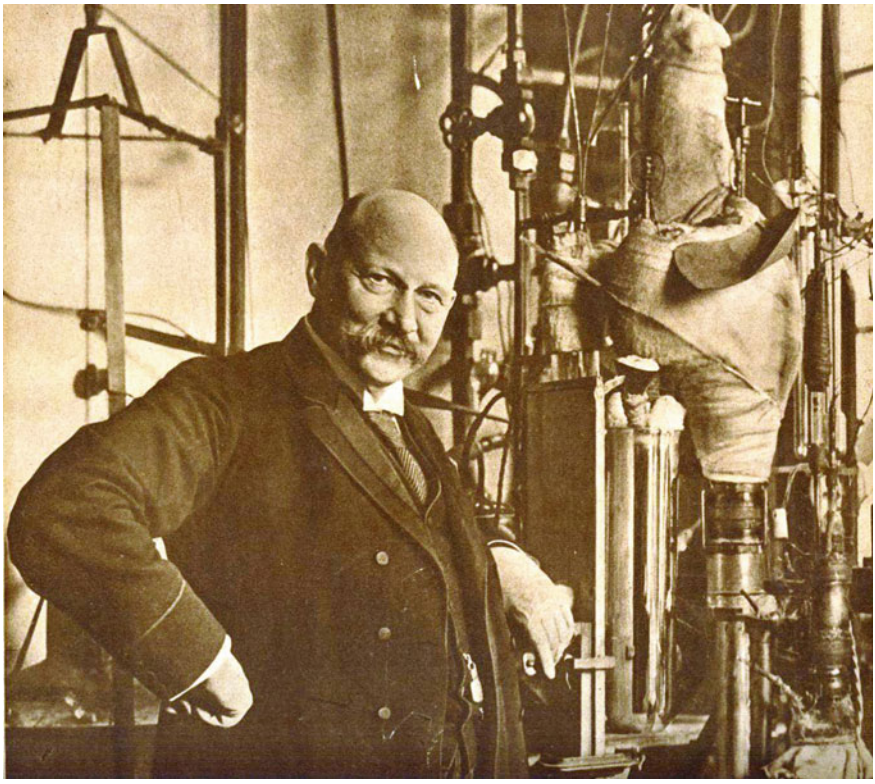

Fig. 1.5 Kamerlingh Onnes in his low-temperature laboratory. *Courtesy* Peter Kes, Kamerlingh Onnes Laboratorium, Leiden University

the globe bought this machine, and the low-temperature research now flourished all around. My earlier place National Physical Laboratory, New Delhi, too acquired Collin's helium liquefier in 1952 and started low-temperature research under the leadership of David Shoenberg. Figure 1.5 shows Kamerlingh Onnes standing near his helium liquefier in his laboratory.

1.3.6 Collins Liquefaction Cycle

The liquefaction cycle used by Collins and shown in Fig. 1.6 is an extension of the Claude cycle (Fig. 1.3). The machine uses three stages of cooling for helium liquefaction, that is, two expansion engines of the reciprocating piston type and a J-T expansion valve as the third stage. Pure helium gas is compressed to about 225 psi pressure, pre-cooled to 77 K and allowed to pass through the first heat exchanger. Thereafter, part of this cold gas expands in the first expander cooling the gas further

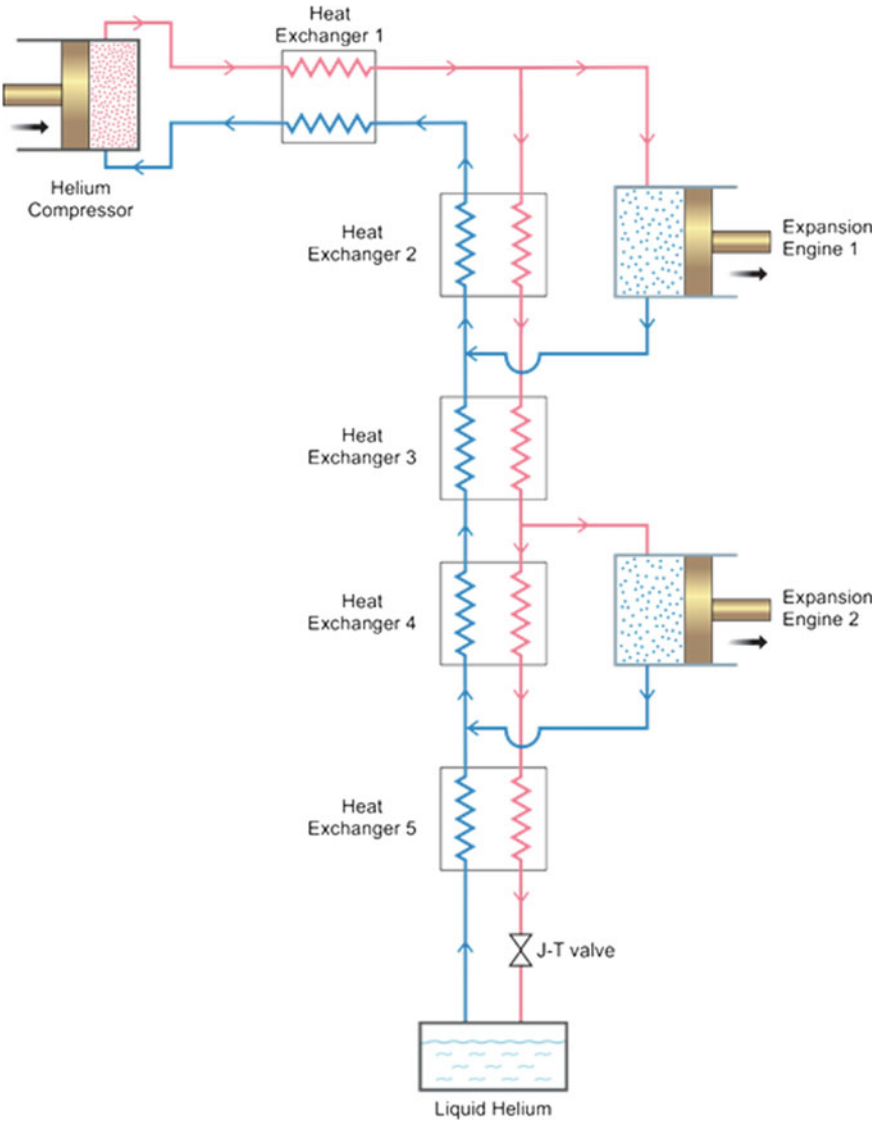

Fig. 1.6 Flow diagram of the Collins helium liquefaction cycle

to about 60 K. This low-pressure gas goes back to the compressor via the second and first heat exchangers cooling in turn the incoming high-pressure gas. Rest of the gas continues to proceed through yet another (third) heat exchanger and again a fraction of the gas expands in the second expander bringing down the temperature of the gas to about 20 K. This temperature is well below the inversion temperature of helium gas. Low-pressure gas again returns to the compressor via the series of

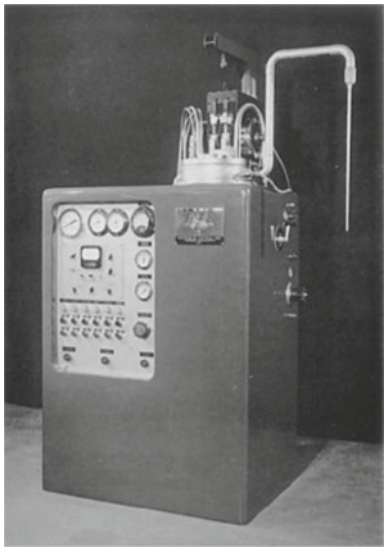

Fig. 1.7 First-generation commercial Collin's helium liquefier ADL make with 4 L/h LHe capacity. This machine functioned for 28 years (1952–1980) at the National Physical Laboratory, New Delhi

the heat exchangers transferring its cold to the incoming high-pressure gas. The cold gas now at 6 K finally throttles through the J-T valve, liquefies and gets collected in the vessel. The liquid helium can be siphoned out of the container for use. The evaporated gas from this container continues to travel to the compressor via the heat exchangers for a continuous operation.

Pre-cooling helium gas with liquid nitrogen though not essential, nevertheless, increases the yield of liquid helium, by almost a factor of two. Figure 1.7 is the photograph of this first-generation Collins liquefier of the ADL make. This machine used to produce 4 L/h liquid with a single compressor. In recent years, reciprocating engines have been replaced by the turbo-expanders which rotate at speeds varying between 250,000 and 300,000 rpm. These machines can produce several hundred litres of liquid helium per hour. Figure 1.8 is a photograph of a modern turbo-cooled helium liquefier custom manufactured and installed by Linde Kryotechnik AG with a refrigeration capacity of 900 W (~ 300 L/h) at our centre, IUAC, in 2012.

1.4 Discovery of Superconductivity—A Fall-Out of Helium Liquefaction

The liquefaction of helium gas in 1908, and just discussed above, was the culmination of a well-designed programme of Kamerlingh Onnes of studying properties of materials at lower and lower temperatures achieved by the successive liquefaction of permanent gases, viz oxygen, air, hydrogen and finally helium. Until this time, there were only conjectures that the electrical resistance of metals will drop to zero as the

Fig. 1.8 Modern-day turbine-based helium liquefier with a refrigeration capacity of 900 W (~ 300 L/h) manufactured by Linde Kryotechnik AG installed at IUAC in 2012. *Photo courtesy* IUAC Delhi

temperature approached absolute zero or will show a minimum and rise again and so on. Kamerlingh carried out electrical resistivity measurements on pure platinum and gold and found that the resistivity attains a temperature-independent constant value below about 10 K. Purer the material, smaller is the value of this residual resistivity. He then took up pure mercury for his studies, as it was possible to obtain mercury in ultra-pure form through multiple distillations. What he found was quite startling and unexpected. The resistance in mercury just close to 4.2 K 'abruptly' dropped to zero (one thousand-millionth part of the normal temperature value) with no potential difference. He, thus, proclaimed that mercury, just below 4.2 K, has entered a new state which he named 'suprageleider' and when translated from Dutch to English became 'supraconductivity' and finally changed to superconductivity [11]. His original resistance versus temperature plot for mercury is shown in Fig. 1.9. Lead and tin were next metals from the periodic table to have shown superconducting transition at 7.2 K and 3.7 K, respectively.

Kamerlingh Onnes also realized soon that this zero potential difference lasts only up to a threshold current in the sample beyond which it rises sharply. Lead, for example, stood superconducting up to a threshold current density of 4.2 A/mm^2 only.

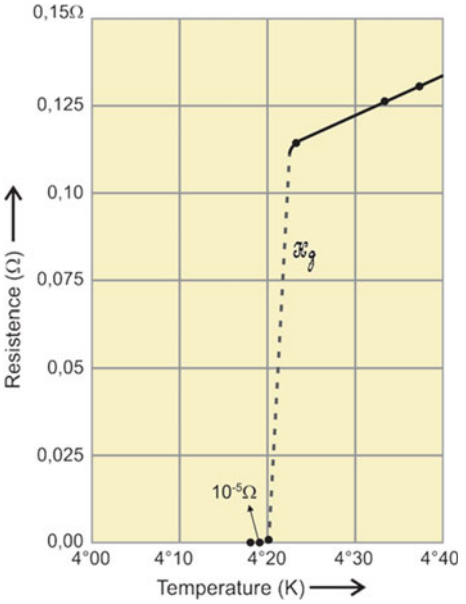

Fig. 1.9 First observation of superconductivity in pure mercury by Kamerlingh Onnes. *Courtesy* Peter Kes, Kamerlingh Onnes Laboratorium, Leiden University

He also observed that superconductivity stays in lead up to a threshold magnetic field of 600 Gauss without a sign of magneto-resistance. Beyond this field, the resistance appears and rises fast with magnetic field. Notwithstanding these limitations, Kamerlingh Onnes did realize that superconducting coils could be used to produce fields in excess of 10,000 Gauss without Joule heating. His dream did come true though 50 years later, and it is all for us to see the great revolution these materials have brought about. How this phenomenon unfolded, understood, different classes of superconductors discovered and put to use in producing high magnetic fields, in accelerators, in fusion reactors and such other applications (NMR, MRI, SMES, levitation, etc.) is discussed in the following chapters.

References

1. K. Timmerhause, R.P. Reed (eds.), in *Cryogenic Engineering, Fifty Years of Progress*. International Cryogenics Monograph Series, Chapter 1 (Springer, New York, 2007)
2. C. Linde, G. Claude, *Liquid Air, Oxygen, and Nitrogen*, trans. by H.E.P. Cotrell (J & A Churchill, London, 1913), p. 75
3. W. Hampson, and G. Claude, *Liquid Air, Oxygen, and Nitrogen*, trans. by H.E.P. Cotrell (J & A Churchill, London, 1913), p. 88
4. G. Claude, C.R. Acad. Sci. Paris. **134**, 1568 (1902)
5. J. Dewar, Preliminary Notes on Liquefaction of Hydrogen and Helium. In: *Proceedings of Chemical Society* No. 158, 12 May 1898
6. J. Dewar, *Collected Papers of Sir James Dewar*, ed. by L. Dewar (Cambridge University Press, Cambridge, 1927), p. 678

7. R.F. Barron, *Cryogenic Systems*, Chapter 3, (Oxford University Press, 1985), pp. 60–150
8. H. Kamerlingh Onnes, Comm. Leiden No. 1206 (1911), Noble Prize Lecture, 11 Dec 1913, http://nobleprize.org/noble_prizes/physics/laureate/1913/ones-lecture-pdf
9. P. Kapitza, Russian J. Phys. (English transl.) **1**, 7 (1939)
10. S.C. Collins, Rev. Sci. Instrum. **18**, 157 (1947)
11. H.K. Kamerlingh Onnes, Commun. Phys. Lab. Univ. Leiden, **29** (1911)

Chapter 2
The Phenomenon of Superconductivity and Type II Superconductors

Abstract A superconductor is not only a perfect conductor ($\rho = 0$) but also a perfect diamagnet ($B = 0$) below T_c. Meissner and Ochsenfeld discovered in 1933 that the magnetic field is expelled out of the body of the superconductor. Field penetrates the material only a small distance, called London's penetration depth, λ which is of the order of 30–60 nm in metal superconductors. These materials also exhibit flux quantization insofar as the field entering a superconducting ring or a cylinder has to be an integral multiple of a flux quantum $\Phi_0 = h/2e$ ($= 2 \times 10^{-15}$ T m^2). The strong evidence of the role of phonons in the occurrence of superconductivity came from the isotope effect. Pippard introduced the concept of long-range coherence among the superelectrons and defined a characteristic length, the coherence length ξ over which the order parameter changes in a superconductor. The coherence length is of the order of 1000 nm much larger than the parameter λ for metal superconductors called type I superconductors. Optical experiments strongly hinted at the existence of an energy gap in the energy spectrum of these materials. All these experimental facts led the three physicists, Bardeen, Cooper and Schrieffer, to formulate the first successful microscopic theory, the BCS theory of superconductivity. Several alloys and compounds were found to be perfect diamagnetic only up to a small field, called lower critical field, B_{c1}. These compounds, however, remained superconducting up to a high magnetic field called the upper critical magnetic field, B_{c2}. Abrikosov explained this behaviour in terms of the formation of negative surface energy at the normal–superconducting interface in these materials called type II superconductors. Beyond B_{c1} field starts entering the material in the form of flux lines each carrying a quantum of flux, $\Phi_0 = h/2e = 2 \times 10^{-15}$ T m^2. At B_{c2} the material turns normal. If a current flows in a superconductor in the mixed state, the flux lines experience Lorentz force, forcing them to move. A voltage appears, and the material turns normal. Flux lines are, however, pinned by impurities or imperfections introduced in the material and the critical current density is increased to desired level. Only type II superconductors are capable of carrying large currents without dissipation in presence of high magnetic field and are of technological importance.

R. G. Sharma, *Superconductivity*, Springer Series in Materials Science 214,
https://doi.org/10.1007/978-3-030-75672-7_2

2.1 Electrical Conduction in Metals

Conduction in materials is a wonderful gift of nature. All materials conduct, but the conductivity can vary from one extreme to another. Pure metals like silver, copper and gold, for example, are the best conductors of electricity. The electrical conductivity in semiconductors, on the other hand, is several orders of magnitude smaller, and other materials do not conduct at all and are perfect insulators. An indication to what extent the conductivity (or the resistivity) varies as one moves away from metals to semiconductors to ionic solids, glasses and finally insulators can be seen from Fig. 2.1. It can vary by about 25 orders of magnitude. According to Drude hypothesis conduction electrons in a metal wander randomly in the background of positively charged ions rigidly fixed to their (ordered) lattice positions. These ions vibrate at quantized frequencies limited to a maximum frequency called the Debye

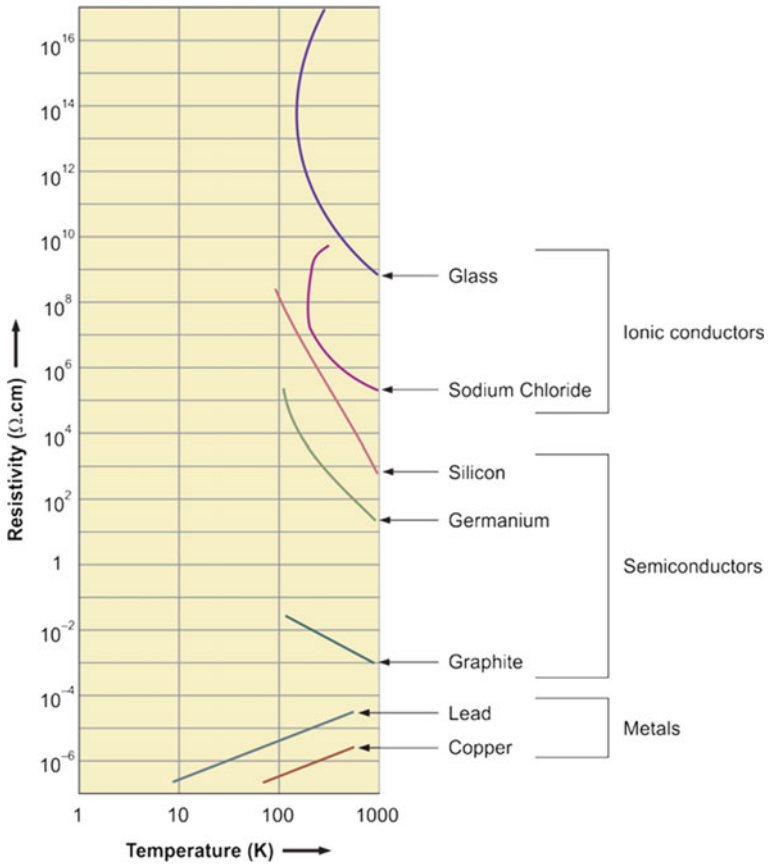

Fig. 2.1 Electrical resistivity in different class of materials varying from very low value for metal to extremely high values for insulators, semiconductors lie somewhere in the middle

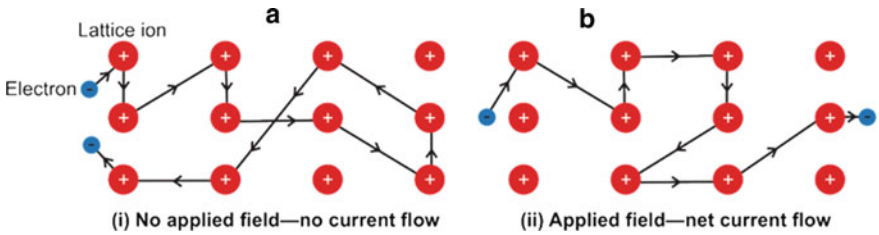

Fig. 2.2 Free electron motion in a lattice of a metal A in the absence of an electric field B in the presence of an electric field

frequency. In the absence of an electrical potential, electrons do get scattered by these ions but randomly, such that they do not drift in a particular direction. Therefore, there is no current flow. In the presence of an electric potential, electrons still get scattered by the ions but now they drift in a particular direction, which is opposite to that of the applied potential. A net current thus flows through the conductor. When electrons are scattered by ions they lose energy, which is absorbed by the lattice in the form of heat, called dissipation. Thus in a sense, electrons face resistance in their free movement when scattered by the lattice ions vibrating at quantized frequencies, called phonons. In what follows, we will refer to this mechanism as electron–phonon interaction. Figure 2.2 shows schematically the electron motion in a lattice under these two different situations. If impurities are present in the lattice, they too will scatter electrons and will add an additional term to the resistivity. What is surprising is that the electrical resistance of most materials is governed by a simple law, the Ohms Law ($V = I \times R$), and strangely enough this relationship is found valid over a large resistance range of the order of 10^{24}.

Temperature variation of resistance in metals has been the next most exciting problem researchers aimed at after the liquefaction of helium. Around ambient temperature resistivity usually shows a linear variation with temperature. The behaviour may become quite different at low temperature. In metals well below Debye temperature ($T \ll \theta_D$), the resistance varies as ~ T^5. What will happen to resistance just a few K above the absolute zero had been a curiosity of the physicists all along. In fact, this curiosity has been a motivation for getting to lower and lower temperatures. Before Kamerlingh Onnes succeeded in liquefying helium, there were different conjectures as to what will happen to resistivity at absolute zero. As shown in Fig. 2.3, James Dewar had predicted the resistivity to become zero as the temperature approaches zero K because the phonon scattering too should die down. Kelvin believed that the resistivity should decrease to a minimum and rise again at still lower temperature as the electron motion will freeze. Matthiessen's prediction that resistance will saturate at a finite value close to absolute zero turned out to be the most accurate one.

According to Matthiessen's Rule the resistivity at low temperature consists of two dominant components. One ρ_0, the residual resistivity which is temperature independent and is caused by the scattering of electrons by impurities and imperfections and

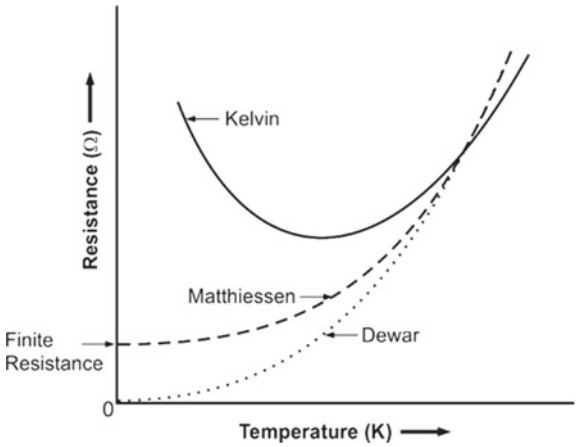

Fig. 2.3 Three different predictions about the possible resistivity–temperature behaviour in metals as one approaches zero absolute

another ρ_i, the intrinsic resistivity caused by the scattering of electrons by phonons and is strictly temperature dependent. The intrinsic resistivity ρ_i always decreases with the fall of temperature. Dewar, after liquefying hydrogen, measured the resistivity of pure silver and gold down to 16 K but always found it to be saturating to a finite value (Fig. 2.4). He believed that there is always an impurity. This was precisely the reason that Kamerlingh Onnes chose to study resistivity of mercury, which can be

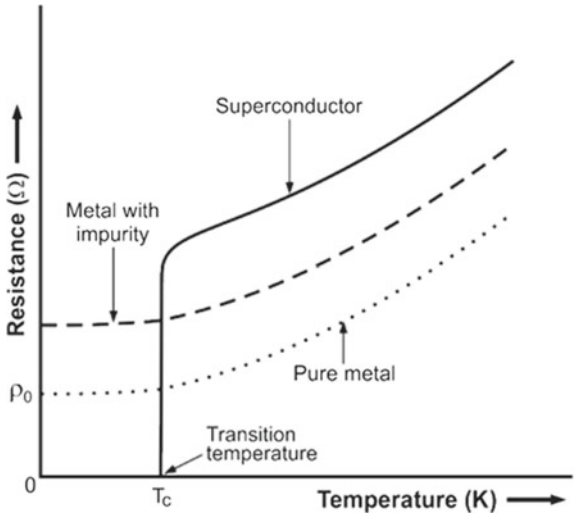

Fig. 2.4 Electrical resistance behaviour at low temperature (close to 0 K) of pure metals and a superconductor. Impurity in a metal raises the residual component of the resistance, ρ_0

obtained in ultra-high purity form by multiple-distillation process. What he observed in mercury at 4.2 K became a history and is the subject matter of the book.

$$\rho = \rho_0 + \rho_i \tag{2.1}$$

2.2 The Phenomenon of Superconductivity

As discussed in Chap. 1, superconductivity was discovered by Kamerlingh Onnes [1] in mercury in 1911 at 4.2 K. The temperature at which superconductivity occurs is called the 'transition temperature' or the 'critical temperature', T_c. Kamerlingh Onnes also concluded that the purity of mercury was not of consequence and superconductivity was an intrinsic property of mercury. Soon, he found superconductivity in Sn at 3.7 K and in Pb at 7.2 K. Intense research continued for discovering more and more superconductors across the periodic table. There was no rule to govern which particular element should become superconductor and which should not. Characteristic parameters like melting point and crystal structure did not show a particular trend for the occurrence of superconductivity. The position of the superconducting elements in the periodical table has been marked with their transition temperature (T_c), the critical field (B_c), the penetration depth (λ) and the coherence length (ξ) values in Table 2.1. The critical field parameter (B_c) will be introduced and discussed in next section. As seen from the table, the T_c of these elements varies from as low a value as 0.0003 K for Rh to a maximum of 9.3 K for Nb. In addition, there are elements, which are superconducting only under high pressure [2]. These are shown as shaded in Table 2.1. Pressure at which they become superconducting has been indicated in kbar unit. One striking feature of the periodic table, however, is the absence of superconductivity in the best-known electrical conductors, namely copper, silver and gold.

2.3 The Critical Magnetic Field

Soon after the discovery of superconductivity, Kamerlingh Onnes realized the importance of these materials for winding magnets to produce high fields without dissipation but to his dismay, he found in early 1913 that superconductivity is destroyed when exposed to small magnetic field. Each superconductor was found to have a characteristic value of this field, called B_c, the critical magnetic field. B_c is maximum at $T = 0$ K and continuously decreases with the increase of temperature and becomes zero at T_c. It is shown in Fig. 2.5 that the material at point 'A' in the superconducting state can be driven to normal state by increasing either the temperature or the magnetic field and taking it outside the parabolic curve. Unfortunately, the value of B_c for most of the elemental superconductors is very low, of the order of few hundred Gauss. B_c

Table 2.1 Elements in the periodic table showing superconductivity, with their T_c, B_c, λ and ξ values
Shaded elements show superconductivity at high pressure only, T_c (K) and pressure values (kbar) are mentioned. Elements with * turn superconducting under high pressure or in thin film form only. Parameter values compiled from my lecture notes, large number of publications and [2] (Copyright Wiley-VCH Verlag GmbH & Co. KGaA. Reproduced with permission.)

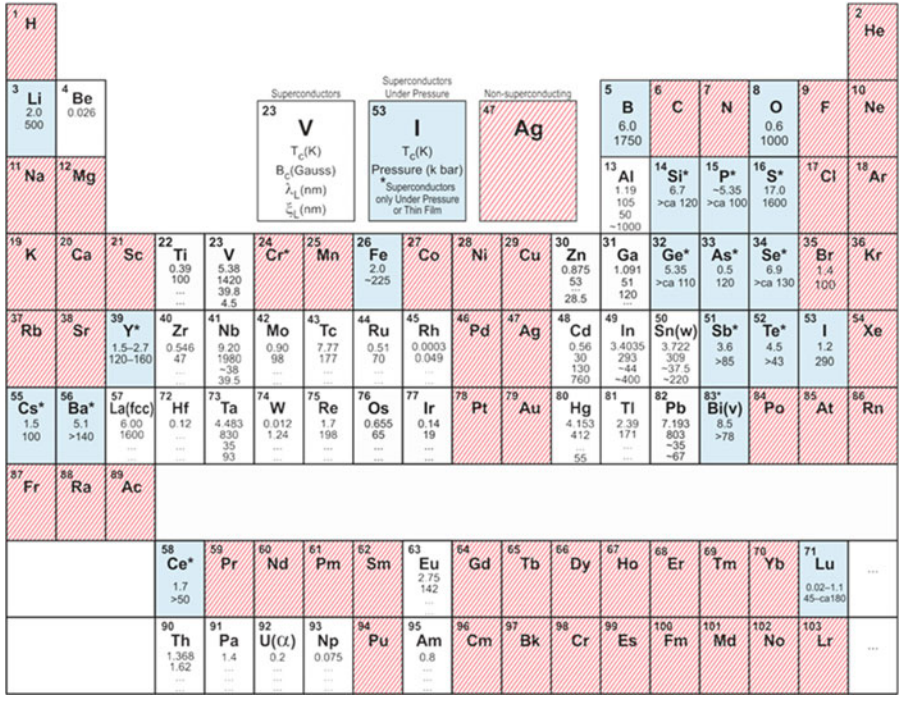

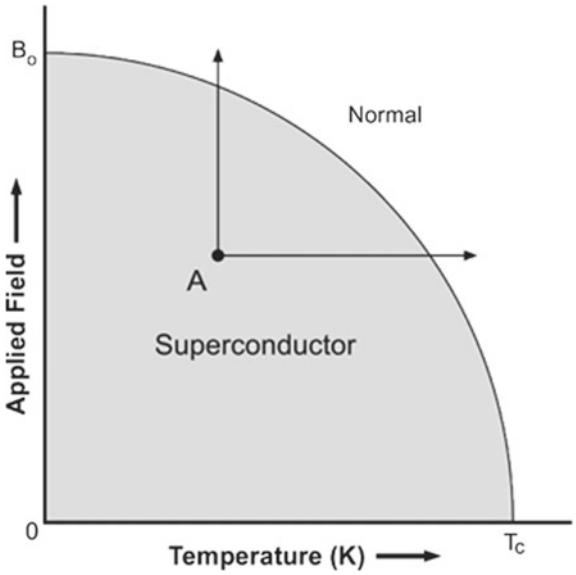

Fig. 2.5 Parabolic B–T curve represents the boundary between the superconducting state and the normal state

of Nb metal happens to be maximum ~ 1980 Gauss. Values of the B_c for most superconductors are shown in the periodic Table 2.1. The variation of B_c with temperature is parabolic and can be expressed by the expression (2.2).

$$B_c = B_0\left[1 - (T/T_c)^2\right] \tag{2.2}$$

B_c is maximum ($= B_0$) at $T = 0$ and drops to zero at the T_c. The transition to normal state in magnetic field can be very sharp depending upon the purity and perfection of the material. Transition also depends strongly upon the direction of the applied magnetic field. Transition is sharp if the field is parallel to the axis of the cylindrical sample. Transition starts at $B_c/2$ if the field is perpendicular to the axis. Figure 2.6 shows the plots of B_c versus tempearture for a number of metal superconductors. Niobium turns out to be the best elemental superconductor with highest $B_{c(0)}$.

Francis Silsbee [3] proposed in 1916 that a superconductor has a critical value of current too which will produce a self-field equivalent to B_c and destroy superconductivity. We thus have three critical parameters characterizing a superconductor, namely critical temperature (T_c), the critical field (B_c) and the critical current (I_c). All the three parameters are interdependent. Thus a superconductor remains superconducting within the confine of these three critical parameters and turns normal, and the moment any of critical parameters is exceeded as shown in Fig. 2.7.

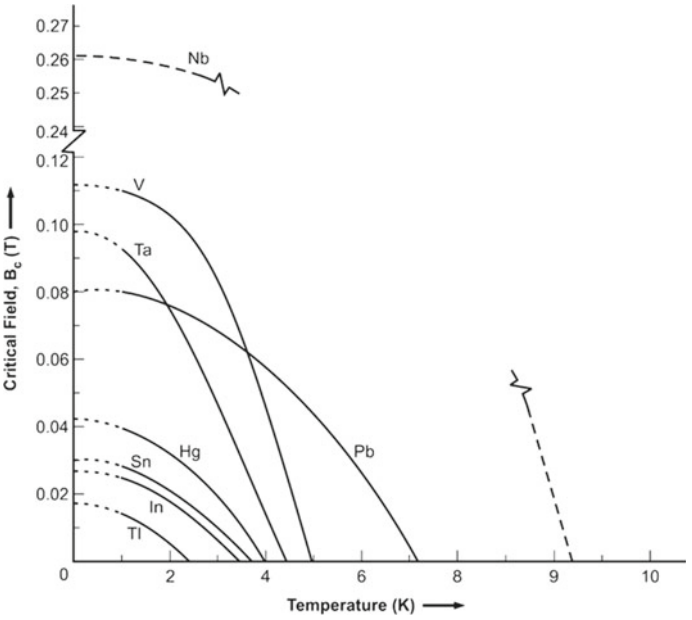

Fig. 2.6 B_c versus temperature plots of some of the metallic superconductors (Data from 'Superconductivity' by Shoenberg, 1952, page 224) (Reproduced with the permission of Cambridge Uni. Press)

2.4 The Meissner Effect (Field Expulsion)

Low-temperature research spread beyond the confines of the Low Temperature Laboratory of Leiden around the world after 1930. Race to discover superconductivity in a variety of materials and especially in alloys continued unabated. Something very extraordinary happed in 1933 when Meissner and Ochsenfeld [4] at Berlin found out that a magnetic field is not frozen within the body of a superconductor when cooled down to below its critical temperature T_c. Instead, the field is expelled from the interior of the superconductor. This observation was quite startling and unexpected. It was expected that a magnetic field will freeze inside a superconductor (being a perfect conductor) until the superconductor is warmed up above T_c. We know, a perfect conductor cannot sustain an electric voltage, that is $E = 0$, it therefore follows from Maxwell equations

$$\nabla \times E = -\frac{\partial B}{\partial t} \tag{2.3}$$

$$E = 0 \Rightarrow \frac{\partial B}{\partial t} = 0 \tag{2.4}$$

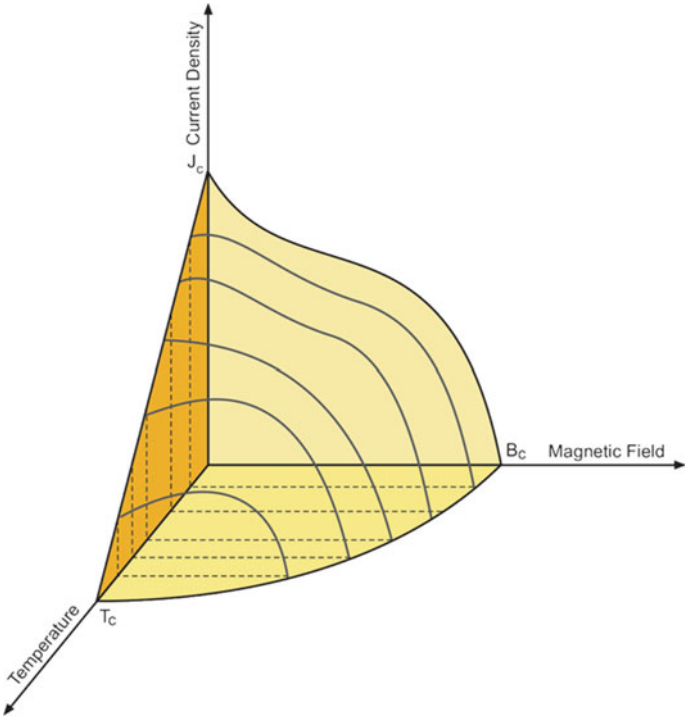

Fig. 2.7 Critical surface of a superconductor. Notice that the three critical parameters are interdependent

This implies that $\partial \mathbf{B} = 0$ or the magnetic flux B inside a superconductor should be constant. This means that if a perfect conductor is placed in a magnetic field and then cooled down to $T_\mathbf{c}$, the magnetic flux remains trapped inside even when the field is removed. Meissner and Ochsenfeld, however, observed that it does not happen in a superconductor. They found that the flux is expelled from the body of the superconductor the moment it is cooled down to below $T_\mathbf{c}$. Irrespective of the fact whether the superconductor is kept in a magnetic field and cooled below $T_\mathbf{c}$ or it is cooled below $T_\mathbf{c}$ first and then a field is applied, the magnetic flux does not enter a superconductor. The lines of force now pass around the sample as shown in Fig. 2.8b. A superconductor thus behaves like a perfect diamagnet.

We can therefore state that a superconductor is a perfect conductor as well as a perfect diamagnet below its transition temperature $T_\mathbf{c}$. Field expulsion can be explained in terms of screening current running across the surface so as to produce a magnetic field equal and opposite to the applied field. The consequence of this induced field is that a magnet will levitate over a superconductor provided, of course, the weight of the magnet is less than the force of levitation. Figure 2.9 is a typical picture of a superconductor floating over a permanent magnet. One can also levitate a magnet over a superconductor.

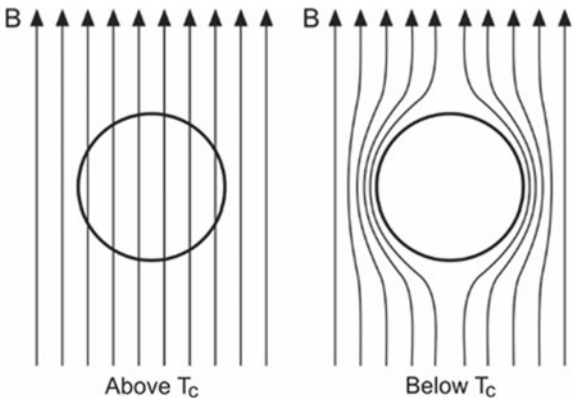

Fig. 2.8 Magnetic flux is expelled from the body of a superconductor the moment it enters the superconducting state (cooled to below T_c) as shown on the right

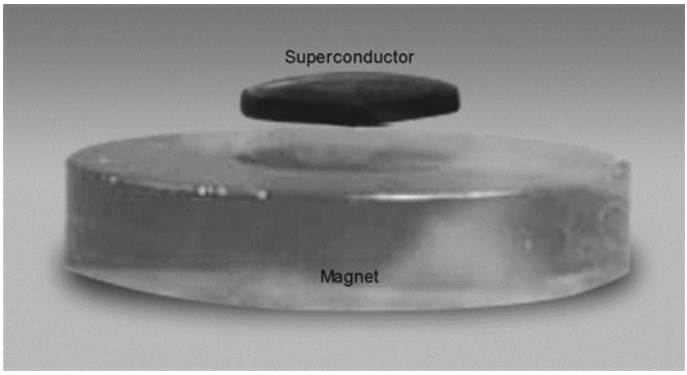

Fig. 2.9 A superconductor floating above a magnet

2.4.1 Perfect Diamagnetism

One immediate consequence of Meissner effect is that superconductivity is a thermodynamical phase as far as the final state of magnetization does not depend upon the sequence of cooling below T_c and applying a magnetic field. This behaviour is totally different to that observed in a normal metal. The fact that the magnetic flux inside a superconductor remains zero ($B = 0$) when an external field B_a is applied implies that a magnetization is induced in the superconductor which exactly cancels out this magnetic flux. Thus,

$$\text{The magnetic flux} = (\mathbf{B_a} + \mathbf{M}) = 0 \tag{2.5}$$

Or

$$\chi = \mathbf{M}/\mathbf{B_a} = -\mathbf{1} \tag{2.6}$$

A superconductor thus has a magnetic susceptibility of − 1 and is a perfect diamagnet but quite distinct from the known diamagnetic materials.

As stated earlier, the screening currents flow along the surface of a superconductor to prevent the entry of the flux. Since the resistance of a superconductor is zero, these currents never decay (supercurrents) and flow persistently without Joule heating.

2.4.2 The Penetration Depth

The just discussed Meissner effect or the so-called perfect diamagnetic property of a superconductor implies that screening currents flow along the external surface of the superconductor. If these currents were to flow only at the surface, the current density will be infinite which will be an impossible proposition. Current sheet should therefore extend in to the material to a depth of an atomic dimension. In fact, the magnetic field penetrates a superconductor a very small distance, falling exponentially to zero with a characteristic depth, called the 'penetration depth' λ. This is shown in Fig. 2.10. This penetration depth in most pure metals turns out to be of the order of 10–100 nm. The flux at a distance of x inside the material is given by the expression:

$$B(x) = B_0 e^{-(x/\lambda)} \tag{2.7}$$

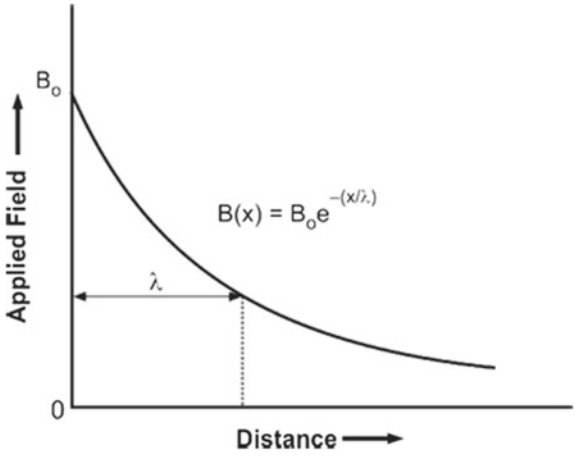

Fig. 2.10 Field penetration in a superconductor. The magnetic flux drops exponentially inside the material. Penetration depth λ is defined as the depth at which the flux density drops to its eth value

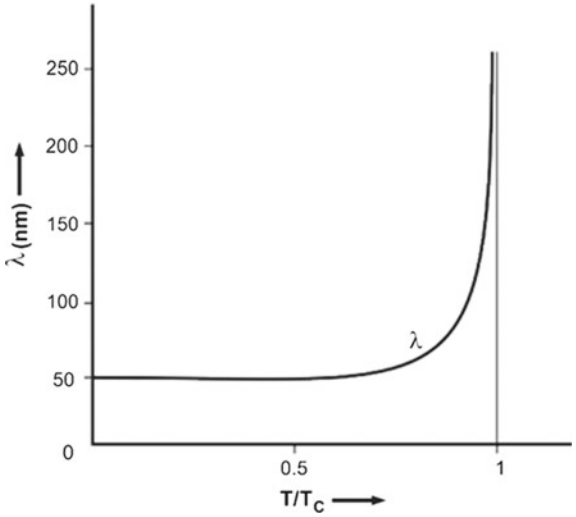

Fig. 2.11 Penetration depth is nearly constant until about 0.8 T_c and rises sharply thereafter, reaching infinite at T_c

It is rather difficult to measure the penetration depth in bulk material, flux penetration being so small. In specimens of the dimension of λ, the field penetration could be across the material and can therefore be estimated to some accuracy.

The penetration depth is not constant but varies widely with temperature. Well below T_c and until 0 K there is hardly any variation but close to T_c (> 0.8 T_c) λ rises exponentially to infinity at T_c. Figure 2.11 is a typical λ–T curve for a superconductor. Equations (2.8) and (2.9) represent the observed λ–T behaviour.

$$\lambda(T) = \frac{\lambda_0}{\left[1 - \left(\frac{T}{T_c}\right)^4\right]^{\frac{1}{2}}} \tag{2.8}$$

Very close to T_c

$$\lambda(T) = \frac{\lambda_0}{\left[1 - \left(\frac{T}{T_c}\right)\right]^{\frac{1}{2}}} \tag{2.9}$$

Table 2.2 gives typical values of λ at 0 K for Pb, In and Al. The exponential variation of λ near T_c makes measurements close to T_c most difficult. The technique employed to measure field penetration is to have cylindrical superconductor of possibly high purity snugly fitted in to a solenoid magnet. The inductance of this system will depend upon the extent of field penetration. If this inductance is connected

Table 2.2 Penetration depth of some metals at 0 K

S. No	Metal	Penetration depth at 0 K (nm)
1	Pb	39
2	In	64
3	Al	50

to a LCR circuit, change in inductance can be evaluated in terms of frequency, which can be measured with high accuracy.

2.4.3 Magnetization in Superconductors

We have already discussed in Sect. 2.4.1 that superconductivity is an equilibrium thermodynamic state and a magnetization is induced in the superconductor when an external field B_a is applied. This behaviour too is different from that of the normal metal. From Figs. 2.5, we find that at temperature higher than T_c and in field higher than B_c, a normal state is more stable. The magnetic flux inside a superconductor remains zero, but the flux enters the material rather sharply as soon as the field exceeds B_c and the material turns normal. This is shown in Fig. 2.12a. The magnetization versus field behaviour is shown in Fig. 2.12b. In the superconducting state, magnetization rises with the increase of magnetic field to oppose the field penetration and drops to zero as soon as B_c is reached. Interestingly, both these processes turn out to be reversible confirming the thermodynamical nature of superconductivity.

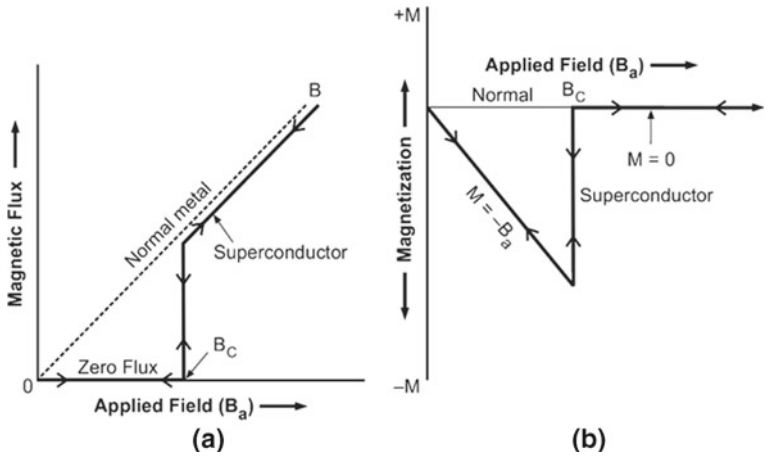

Fig. 2.12 Magnetic flux (**a**) and magnetization (**b**) behaviour of a superconductor in an applied magnetic field

2.4.4 The Intermediate State

The value of critical field B_c usually gets modified because of the concentration of field lines at the surface. This, the so-called the demagnetization effect, depends upon the shape of the material and the field orientation. For example, a long-thin-cylindrical superconductor has no demagnetization effect if the magnetic field is parallel to its axis. In perpendicular field, however, the field penetration starts at $1/2B_c$, that is, the demagnetization factor is 1/2. For a sphere, the demagnetization factor is 1/3. The uniform field B_i inside the superconductor in an applied field B_a is given by the expression

$$B_i = B_a/(1 - n) \tag{2.10}$$

where n is the demagnetization factor. Since $n = 1/3$ for a superconducting sphere, at $B_a = 2/3\ B_c$, $B_i = B_c$ and the sphere has to turn normal. If, however, it turns normal $M \approx 0$ and $B_i = 2/3B_c$ which is less than the critical field B_c and the sphere has to stay superconducting. This simply means that between 2/3 B_c and B_c the sphere can neither be fully normal nor fully superconducting. Instead, the sphere undergoes an intermediate state. Figure 2.13 schematically shows the splitting of the material in to laminae of alternate normal and superconducting material parallel to the field in a long thin cylinder when the field exceeds $1/2B_c$. As field increases superconducting fraction diminishes and the normal regions grow at the expense of the superconducting regions. At B_c, the entire material turns normal. Consequently, there is a continuous increase of resistance. These laminae are parallel to field. Since magnetic induction in the normal regions is parallel to field and goes to zero in superconducting regions, the boundary has to be parallel to the field direction only. That the laminae extend right through the sample is confirmed by the observation of a finite resistance in the intermediate state. Finite resistance obviously comes from

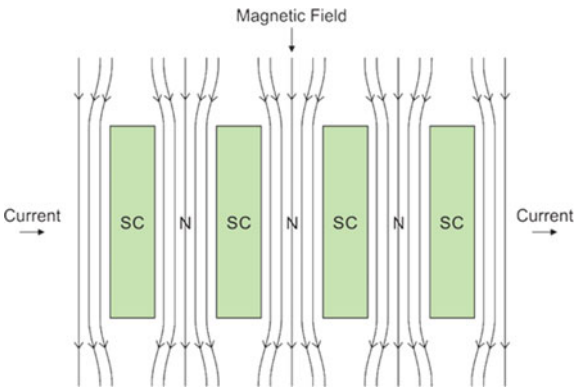

Fig. 2.13 A superconductor between the initial penetration and B_c splits in to the laminae of alternate normal and superconducting material parallel to the field

the current flow through the normal regions, without being short-circuited by the superconducting regions.

Free energy calculations show that the intermediate state is more favourable than the wholly superconducting state as the effective field on the superconducting regions is greatly reduced. Stability of such a structure requires a positive surface energy, which in turn implies finite width δ of the boundary layer between the laminae given by the expression

$$\alpha_{ns} = \delta(B_c)^2/8\pi \tag{2.11}$$

where α_{ns} is the boundary energy per unit area and $(B_c)^2/8\pi$ is the free energy difference between the normal and superconducting state. δ turns out to be of the order of 1000 nm and can be identified with Pippard's coherence length, to be discussed in a later section.

2.5 Two-Fluid Model

To explain the zero resistivity and the perfect diamagnetism in superconductors, Gorter and Casimir [5] in 1934 at Leiden proposed a hypothesis what is popularly called as two-fluid model. According to this model, below the transition temperature the normal electrons start condensing in to superelectrons which only carry super-current. At $T = 0$ K all the electrons are superelectrons and at T_c all the electrons are normal electrons. These superelectrons can be identified with Cooper pairs of the BCS microscopic theory, to be discussed in chapter four. The variation of the normal electron density and the superelectron density with temperature is shown in Fig. 2.14. At any given temperature, the electron density is given by;

$$n = n_n + n_s \tag{2.12}$$

The superconducting electron density n_s at any temperature is given by the expression;

$$n_s = n_0\left\{1 - (T/T_c)^4\right\} = n_0\left(1 - t^4\right) \tag{2.13}$$

where $t = T/T_c$.

Here n_0 is the superconducting electron density at $T = 0$ K. n_s is also taken as an order parameter. Using this model, Gorter and Casimir were able to account well for the specific heat anomaly at T_c discovered in Tin [6] and later in Thallium [7]. The peak in specific heat at T_c is caused by the extra energy required to excite the superelectrons to normal electrons at T_c.

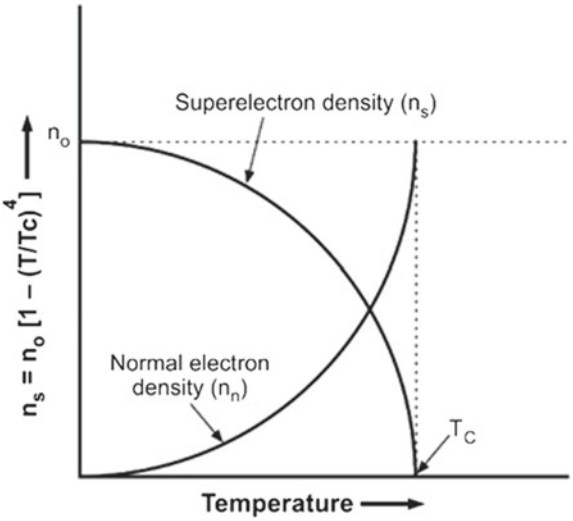

Fig. 2.14 Variation of the densities of the normal electrons and the superelectrons with temperature

2.6 Thermodynamics of Superconductors

Thermodynamics of superconductors is equally interesting. Some of the thermodynamical properties are conventional, while some others are quite different and unique. We discuss some of the thermodynamical properties in the following sub-sections.

2.6.1 The Gibbs Free Energy

In Sect. 2.4.2, we have seen that the magnetization induced in a superconductor depends upon the magnetic field and is reversible thermodynamically under the two variables, temperature and magnetic field. The destruction of superconductivity at the critical field $B_{\mathbf{c}}$ indicates that the normal state is energetically more favourable at $B_{\mathbf{c}}$. Let us see how much is the increase in the potential energy of the superconductor in presence of $B_{\mathbf{c}}$. The work done in bringing a superconductor in an applied field $B_{\mathbf{a}}$ is given by

$$W = -\mu_0 \int_0^{B_a} M \mathrm{d}B \tag{2.14}$$

Since $M = -B$ in a superconductor, W turns out to be

$$W = \mu_0 \left(\frac{B_a^2}{2} \right) \tag{2.15}$$

The Gibbs free energy of a superconductor in an applied field B_a is thus given by

$$g_s(T, B_a) = g_s(T, 0) + \mu_0 B_a^2/2 \tag{2.16}$$

Therefore, the Gibbs free energy of a superconductor at B_c will be:

$$g_s(B_c) = g_s(0) + \mu_0 \left(\frac{B_c^2}{2} \right) \tag{2.17}$$

At B_c the free energies of the superconducting phase and the normal phase are equal, that is, $g_s(B_c) = g_n$. Thus from (2.17), we have the energy difference between the normal state and the superconducting state:

$$g_n - g_s = \mu_0 \left(\frac{B_c^2}{2} \right) \quad \text{(a positive quantity)} \tag{2.18}$$

Critical field B_c thus turns out to be an important parameter linking up the free energies of the normal and the superconducting states in a superconductor and can be measured experimentally with precision. Figure 2.15 shows Gibbs free energy in the superconducting state and the normal state plotted against magnetic field. At B_c normal state becomes more stable.

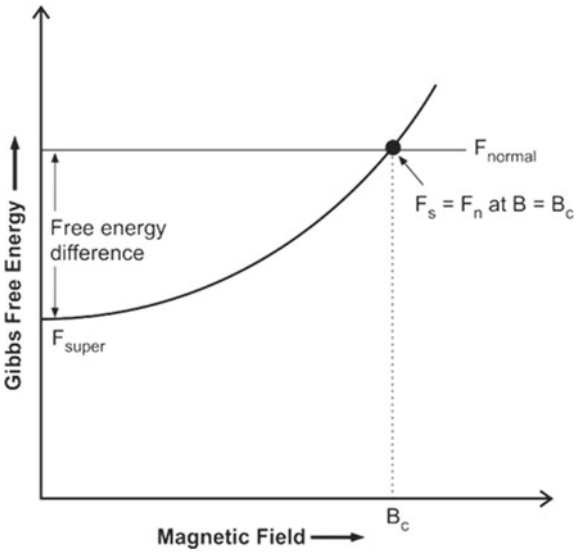

Fig. 2.15 Gibbs free energy in the superconducting state and the normal state plotted against magnetic field. Beyond B_c normal state becomes more stable

2.6.2 Specific Heat

From the free energy difference equation, it is easy to calculate the difference in entropies and the specific heats in the normal and superconducting states. From the first law of thermodynamics entropy,

$$S = -\left(\frac{\partial g}{\partial T}\right)_{p, B_a} \tag{2.19}$$

Thus, differentiating $g_{\mathbf{n}}$ and $g_{\mathbf{s}}$ with respect to T in (2.18) we get

$$S_n - S_s = -\mu_0 B_c \left(\frac{dB_c}{dT}\right) \tag{2.20}$$

Since $B_{\mathbf{c}}$ always decreases with the rise of temperature in all the known superconductors the quantity $\left(\frac{dB_c}{dT}\right)$ is negative. This means $S_{\mathbf{n}} - S_{\mathbf{s}}$ is always positive, that is the entropy of a material is lower in superconducting state than in its normal state. Superconducting state is therefore an ordered state as also predicted by the two-fluid model discussed in Sect. 2.5. It also follows from (2.20) that at $T_{\mathbf{c}}$ the critical magnetic field $B_{\mathbf{c}}$ is zero and therefore the two entropies are same at $T_{\mathbf{c}}$. Similarly, from the third law of thermodynamics the two entropies should again converge to the same value, that is, zero at 0 K. The entropies in the two states of Sn are shown in Fig. (2.16). Between $T_{\mathbf{c}}$ and 0 K, the entropy of the superconducting state is lower than in the normal state. Between these two temperatures, one can go from the superconducting state to normal state by applying an appropriate magnetic field. The above curves have an interesting consequence. For example, if we move from low entropy point

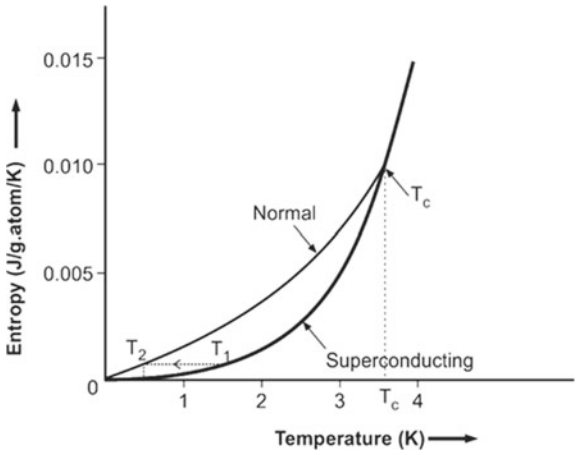

Fig. 2.16 Typical entropy curves of Sn in normal state and in superconducting state. The entropies of the normal state and the superconducting state are the same at $T_{\mathbf{c}}$ and at 0 K

1 in superconducting state to high entropy point 2 in normal state by applying a field, cold will be produced if the process is carried out under adiabatic condition. This may be called as 'adiabatic magnetization' as opposed to the usual 'adiabatic demagnetization', a popular method to produce ultra-cold using paramagnetic salt (electron spins) or the nuclear bundle such as copper (nuclear spins).

We can now derive an expression for the specific heat difference using expression (2.20). We know that the specific heat of a material is given by

$$C = VT\frac{\partial s}{\partial T} \tag{2.21}$$

where V is the volume per unit mass. Differentiating (2.20), we obtain

$$C_{\mathrm{s}} - C_{\mathrm{n}} = VT\mu_0 B_{\mathrm{c}}\frac{\mathrm{d}^2 B_c}{\mathrm{d}T^2} + VT\mu_0\left(\frac{\mathrm{d}B_{\mathrm{c}}}{\mathrm{d}T}\right)^2 \tag{2.22}$$

At the transition temperature $T_{\mathbf{c}}$, the magnetic field $B_{\mathbf{c}} = 0$. At $T_{\mathbf{c}}$, the (2.22) will therefore reduce to

$$(C_{\mathrm{s}} - C_{\mathrm{n}})_{T_{\mathrm{c}}} = VT_{\mathrm{c}}\mu_0\left(\frac{\mathrm{d}B_{\mathrm{c}}}{\mathrm{d}T}\right)^2_{T_{\mathrm{c}}} \tag{2.23}$$

which is a positive quantity. Superconducting state thus has higher specific heat value than the normal state at $T_{\mathbf{c}}$. This jump in the specific heat at $T_{\mathbf{c}}$ (Fig. 2.17) is a characteristic feature of all the superconductors and has been well explained on

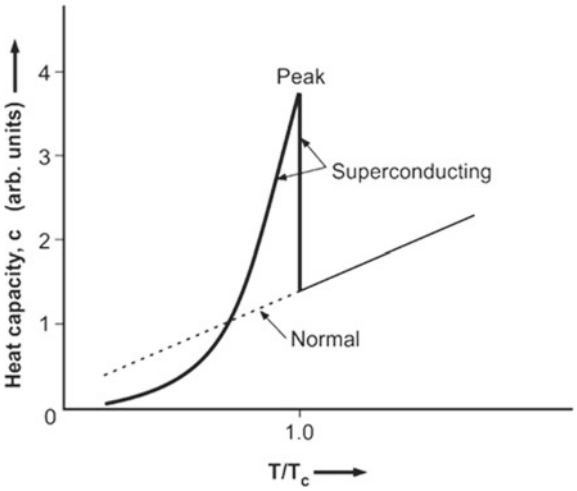

Fig. 2.17 Specific heat of a superconductor shows a jump at $T_{\mathbf{c}}$ and decreases exponentially below its value for the normal state as it approaches 0 K

the basis of two-fluid model [6, 7]. The specific heat of a metal is composed of two components. One is the lattice contribution proportional to T^3 and the other, electronic contribution proportional to T. The specific heat can therefore be represented by the following equation:

$$C_{\mathrm{n}}(T) = \gamma T + \beta T^3 \tag{2.24}$$

Here γ is the density of electron states at Fermi level. The first term is the electronic term, and the second is the lattice term. A plot of $\left[\frac{C_{\mathrm{n}}(T)}{T}\right]$ versus T^2 gives a straight line with a slope β and the intercept γ. Since superconductivity affects only the electrons and not the lattice at the transition, it is reasonable to assume that the lattice contribution to specific heat, βT^3 is the same in the normal state as well as in the superconducting state. Using this substitution, electronic specific heat has been evaluated experimentally well below $T_{\mathbf{c}}$, and it turns out to be of the form

$$C_{\mathrm{es}}(T) = A \exp\left(\frac{-\Delta}{k_{\mathrm{B}} T}\right) \tag{2.25}$$

Experimental data fit well to (2.25) as shown in Fig. (2.18). This form of exponential dependence implies the existence of an energy gap between the energy levels of the so-called superelectrons and the normal electrons. Superelectrons exist in a special lower energy state separated by a gap from the normal electrons. Extra heat is to be supplied to convert superelectrons into normal electrons to maintain the

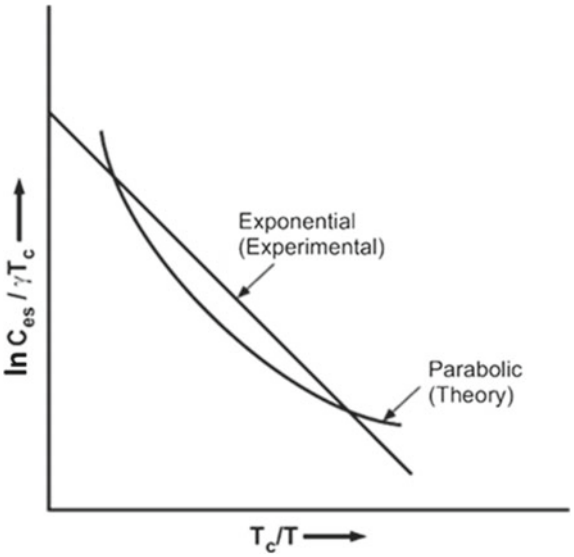

Fig. 2.18 Exponential behaviour of the electronic specific heat in superconducting state below $T_{\mathbf{c}}$

superelectrons' density compatible with the temperature (as per $x = 1 - (T/T_{\mathbf{c}})^4$). At low temperature, the change in 'x' is small and exponential at high temperature. Number of normal electrons thermally excited rises exponentially with temperature and hence the exponential behaviour of the specific heat. Thermal conductivity below $T_{\mathbf{c}}$ is expected to be lower as the number of normal electrons carrying entropy is reduced. Superelectrons do not transport entropy.

2.6.3 Phase Transition

Let us recall (2.18) which gives the difference between the free energy in superconducting state and the normal state to be $\mu_0 B_{\mathrm{c}}^2/2$. Since at $T_{\mathbf{c}}$ the value of $B_{\mathbf{c}}$ is zero the two free energies, $g_{\mathbf{s}}$ and $g_{\mathbf{n}}$ are equal. This means, the free energy at $T_{\mathbf{c}}$ is continuous. From (2.20), the difference between the entropies of the two states at $T_{\mathbf{c}}$ again turns out to be zero ($B_{\mathbf{c}}$ being zero). The fact that not only the free energy but also the entropy is continuous at the transition temperature shows that in the absence of the magnetic field the normal to superconducting transition is of the second order. There is no latent heat involved either, at the transition ($\mathrm{d}Q = T \quad \mathrm{d}S = 0$). Second-order phase transition is also confirmed by the jump in the specific heat at $T_{\mathbf{c}}$ as discussed in Sect. 2.6.2 and shown in Fig. 2.17.

Phase transition from superconducting to normal state at $T_{\mathbf{c}}$ in presence of a magnetic field, however, turns out to be of the first order. The latent heat $\mathrm{d}Q = T\ (S_{\mathbf{n}} - S_{\mathbf{s}})$ now is finite (2.18), $B_{\mathbf{c}}$ being no longer zero.

2.7 Thermal Conductivity

Thermal conductivity in superconducting state is found to be smaller than in the normal state. The reason is that the superelectrons do not interact with the lattice and therefore do not transport heat from one part of the material to another. As the temperature goes down, the thermal conductivity keeps decreasing. Far below $T_{\mathbf{c}}$, it becomes orders of magnitude smaller. For example, in Pb the thermal conductivity at 1 K is reduced by a factor of 100. No wonder therefore superconductors like Pb and Sn are routinely used as thermal switches in the milli Kelvin and lower temperature region to break the thermal contact between different cooling stages. Thermal conductivity can, however, be restored by applying a small magnetic field just above $B_{\mathbf{c}}$ or by winding a small heating coil to raise the temperature just above $T_{\mathbf{c}}$.

2.8 Thermoelectric Power

There is no thermo-emf in a thermocouple made up of two superconductors, when the two junctions are held at different temperatures. This is for the simple reason that any thermo-emf howsoever small will lead to current flowing at a critical value irrespective of the magnitude of the temperature difference at the junctions. In other words, the Seebeck coefficient S $(= \mathrm{d}V/\mathrm{d}T)$ is zero. Likewise, the two other thermoelectric effects, namely Peltier effect and the Thomson effect are also absent in the superconductors, and all the three effects being inter-related. Both the Peltier coefficient $(\Pi = S.T)$ and the Thomson coefficient $(\mu = \mathrm{d}S/\mathrm{d}T)$ are zero in superconductors. This property makes a superconductor an ideal standard to measure the absolute thermoelectric power of a material if coupled with it and had been widely used for the calibration of temperature sensors below $T_{\mathbf{c}}$.

2.9 The Energy Gap

The exponential behaviour of specific heat with temperature in superconducting state gave the first hint of the existence of an energy gap in the energy spectrum of the electrons. One needs, as though, an energy equal to the gap to excite a superelectron to the normal state. The energy gap turns out to be of the order of $3.5\, k_{\mathbf{B}} T_{\mathbf{c}}$. This energy gap is reminiscent of a similar gap between the valence band and the conduction band in semiconductors, but the gap here is of the order of 10^{-4} eV, some three orders of magnitude smaller than in semiconductors. Table 2.3 gives the values of the energy gap ratio of some of the metal superconductors [8]. The presence of an energy gap implies that a photon of energy less than 2Δ is not absorbed by the superconductor. A superconductor is thus more reflective than in its normal state for frequencies $< 2\Delta/h$. Figure 2.19 shows the absorption of EM radiation in superconductors normalized to that in the normal state $(P_{\mathbf{s}} - P_{\mathbf{n}})/P_{\mathbf{n}}$ plotted against frequency (in wave numbers) [9] of the EM radiation for Pb, V, Sn, Nb, Hg, In and Ta. All the curves show a peak

Table 2.3 Energy gap ratio $(2\Delta/k_{\mathbf{B}} T_{\mathbf{c}})$ for metal superconductors at zero temperature $(T = 0\ \mathrm{K})$

Metal	Energy gap $(2\Delta/k_{\mathbf{B}} T_{\mathbf{c}})$ ratio	Metal	Energy gap $(2\Delta/k_{\mathbf{B}} T_{\mathbf{c}})$ ratio
Aluminium	3.3	Thallium	3.57
Zinc	3.2	Lead	4.38
Gallium	3.5	Vanadium	3.4
Cadmium	3.2	Niobium	3.80
Indium	3.6	Molybdenum	3.4
Tin	3.5	Lanthanum	3.7
Mercury	4.6	Tantalum	3.60

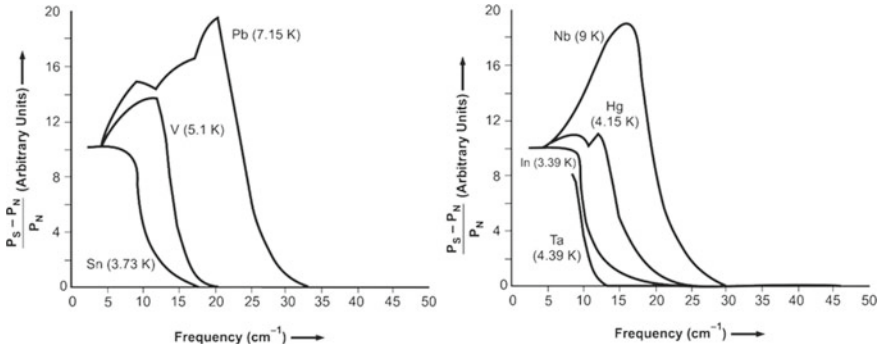

Fig. 2.19 Absorption curves for seven metal superconductors normalized to the normal state plotted against the frequency (in wave number). T_c of each metal is written within the bracket [9] (With permission from APS) http://journals.aps.org/pr/abstract/10.1103/PhysRev.119.575

followed by a steep drop to zero at a characteristic frequency, which is different for different metals. This frequency is a function of temperature and increases as the temperature approaches zero. At T_c, this frequency drops to zero.

The energy gap and its variation with frequency at different temperatures can be measured directly by electron tunnelling measurements. The energy gap is maximum at 0 K and decreases with the rise of temperature and becomes zero at T_c. Reduced energy gap $\Delta(T)/\Delta(0)$ plotted against reduced temperature T/T_c for a number of pure metal superconductors has a universal behaviour. Interestingly, the data for all the superconductors lie on a universal curve (within the width of the curve in the middle) as shown in Fig. 2.20. The data are also in good agreement with the BCS theory.

2.10 The Isotope Effect

Different isotopes of several metal superconductors showed a variation in T_c with the atomic mass number [10, 11]. Most of the data can be fitted to the expression of the type $M^{\alpha}T_c = \text{constant}$. Experimentally, the average value of α turns out to be 0.5, that is, T_c is inversely proportional to the square root of the atomic mass.

$$T_c \propto \frac{1}{\sqrt{M}} \tag{2.26}$$

This leads to an interesting conclusion that the lattice does not seem to play a direct role in the phenomenon of superconductivity as the lattice does not show change in going from normal to superconducting state but does influence the behaviour of the electron in a very subtle way. The isotope effect in fact provided an important clue to the role of lattice in superconductivity. Figure 2.21 is the logarithmic plot of T_c of

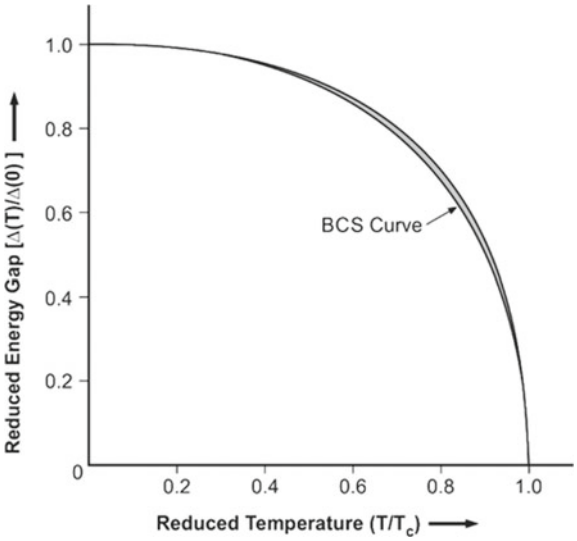

Fig. 2.20 Reduced energy gap $\Delta(T)/\Delta(0)$ plotted against the reduced temperature T/T_c for most metal superconductors lie on a universal curve and fit well with BCS theory within the width in the curve

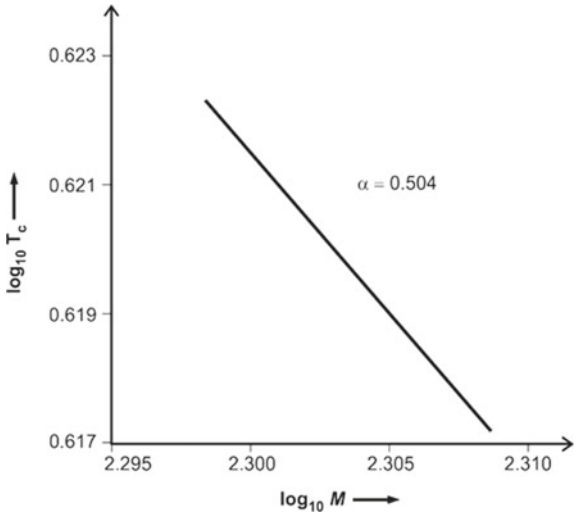

Fig. 2.21 Logarithmic plot of T_c of the different isotopes of mercury and the average mass number. The data fit well with the formula $T_c \propto \frac{1}{\sqrt{M}}$ ([11]) (With permission from APS) http://journals.aps.org/pr/abstract/10.1103/PhysRev.84.691

Table 2.4 Measured values of α in the formulae $M^{\alpha}T_c$ = constant of some metal superconductors

Metal superconductor	Value of α in $M^{\alpha}T_c$ = constant
Zinc	0.45 ± 0.05
Cadmium	0.32 ± 0.07
Mercury	0.50 ± 0.03
Thallium	0.61 ± 0.10
Tin	0.47 ± 0.02
Lead	0.49 ± 0.02

the different isotopes of mercury [11] and the average mass number. The data fit well with the formula $T_c \propto \frac{1}{\sqrt{M}}$. The experimental values of exponent α in the formula $M^{\alpha}T_c$ = constant for a few metal superconductors are listed in Table 2.4.

2.11 Flux Quantization

F. London going through the peculiar behaviour of superconductors postulated [12] that a magnetic flux inside a superconducting cylinder or in a ring (Fig. 2.22) will always be an integral multiple of (h/e) where h is the plank constant and e the electronic charge. It was indeed a remarkable prediction that the magnetic flux in the

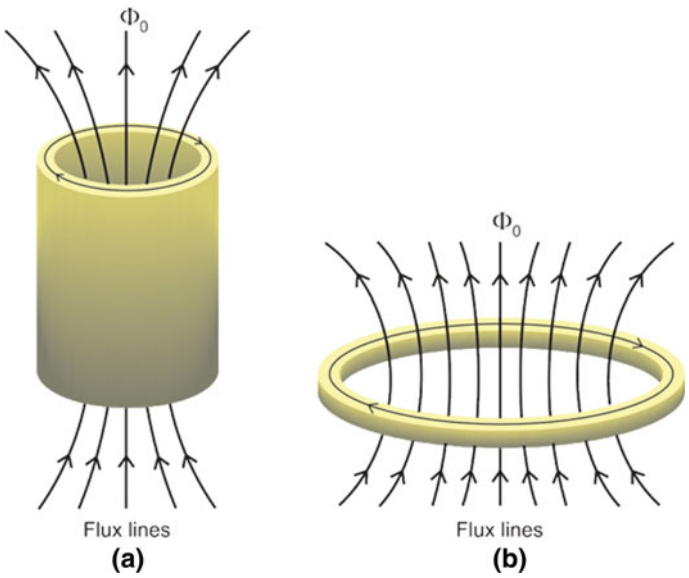

Fig. 2.22 Flux inside a superconducting cylinder (**a**) or a superconducting ring (**b**) is always found to be an integral multiple of the quantum of flux, $\Phi_0 = h/2e$

free space is a multiple of h/e simply because it is surrounded by a superconducting cylinder. This quantum of flux is small only about 4×10^{-15} Wb or 4×10^{-15} T m^2. The experimental confirmation of this so-called flux quantization came through precision experiments by Deaver and Fairbank [13] at Stanford and Doll and Näbauer [14] at Munich in 1961. The trapped flux was, however, found to be quantized in units of (h/2e) and not in units of (h/e). The flux quantum thus turns out to be exactly 2.067833×10^{-15} T m^2 and is represented by Φ_0.

Deaver and Fairbank [13] carried out measurement on a Sn (hollow) cylinder by depositing a 5-μm-thick tin layer over a copper wire (cylinder) of 13 μm diameter. The composite wire was cooled below T_c in a small magnetic field of about 0.1 Gauss. The magnetic flux in copper was determined by measuring the emf in an electrical pick up coil while moving the sample up and down in the coil at a rate of 100 cycles/s. The measured flux remained confined to values to $nh/2e$ for integral values of $n = 1, 2, 3$. Döll and Näbauer [14] on the other hand used a torque method to determine the magnitude of flux contained in a lead cylinder. They coated lead on a quartz fibre and suspended with a quartz fibre and made to oscillate in a liquid helium bath. The frozen flux was measured by the torque produced by the application of a magnetic field perpendicular to the axis of the cylinder. Flux was again found to be quantized in the unit of $h/2e$.

The factor $2e$ above is of great significance as far as it represents the charge of the superelectron responsible for superconductivity. These superelectrons are identified with Cooper pairs in the theory of superconductivity, the BCS theory [15] which will be discussed in Chap. 4.

2.12 The Concept of Coherence Length and Positive Surface Energy

The coherence length represented by ξ is yet another fundamental characteristic length, which defines a superconductor. The other similar characteristic length already introduced is the penetration depth λ. One of the many observed unique features of superconductivity that the transition temperature could be as sharp as 10^{-5} K in a pure metal, led sPippard [16] to believe that superconductivity is a cooperative phenomenon. A large number of entity (superelectrons) over a long range take part in the process. There is a long-range coherence among the superelectrons. All superelectrons move in phase. According to the two-fluid model, superelectron density n_s increases as the temperature decreases below T_c and so does the degree of order of the superconducting phase. The superelectron density n_s in fact can be identified with this order. Pippard arrived at a conclusion [16] that this order parameter cannot change abruptly at the S–N boundary but will do so smoothly over a finite distance of the order of 1000 nm in pure metals. This distance is referred to as the coherence length, ξ. It has the maximum value at $T = 0$ K, for the purest form of the metal and is represented by ξ_0. The value of ξ_0 is an intrinsic property of a

superconductor. As the temperature increases, the coherence length decreases and drops to zero at T_c.

Another property of coherence length is that it is strongly dependent upon the purity of the metal. ξ is found to be proportional to the electronic mean free path ℓ_e and is shorter for impure material. At high level of impurity, the coherence length becomes equal to ℓ_e. Coherence length ξ is related to ξ_0 through the equation of the type

$$\xi = (\xi_0 \ell_e)^{1/2} \tag{2.27}$$

The value of the intrinsic coherence length ξ_0 can be calculated from (2.27) by substituting the values of the Fermi velocity v_f, Boltzmann constant k_B and T_c

$$\xi_0 = 0.18 \frac{\hbar v_f}{k_B T_c} \tag{2.28}$$

Table 2.5 gives typical values of ξ_0 and λ for a few metal superconductors. In fact, the ratio of ξ/λ determines the nature of superconductor whether it belongs to type I or type II class of superconductors.

Let us now attend to the surface energy issue. Figure 2.23 shows [17] the boundary between the normal and the superconducting regions. In order to have a stable boundary, it is necessary that the two regions be in equilibrium. This means that at the boundary, the free energy per unit volume in both the regions is same. Inside the superconducting region, however, there are two contributions to the free energy. Since electron ordering takes place in the superconducting region over a distance of ξ there is a decrease in free energy equal to $g_n - g_s = \mu_0 B_c^2/2$. The other contribution to free energy is due to the magnetization, which it acquires to expel the flux. It contributes a positive magnetic energy equal to $\mu_0 B_c^2/2$ over a distance of the penetration depth λ. So well inside the superconductor, both these contributions cancel each other but since $\xi \gg \lambda$ in most of the metal superconductors but close to the boundary there is a net small positive energy. The value of this energy is approximately equal to $\mu_0 B_c^2/2(\xi - \lambda)$ per unit area of the boundary. Positive surface energy

Table 2.5 Typical values of the intrinsic coherence length ξ_0 and penetration depth, λ at 0 K for some metal superconductors

Metal (superconductor)	Intrinsic coherence length, ξ_0 (nm)	London's penetration depth, λ (nm)	Ratio ξ_0/λ
Aluminium	1600	16	100
Niobium	38	39	0.98
Cadmium	760	110	6.9
Tin	170	30	5.67
Lead	510	37	13.8
Indium	360	24	15

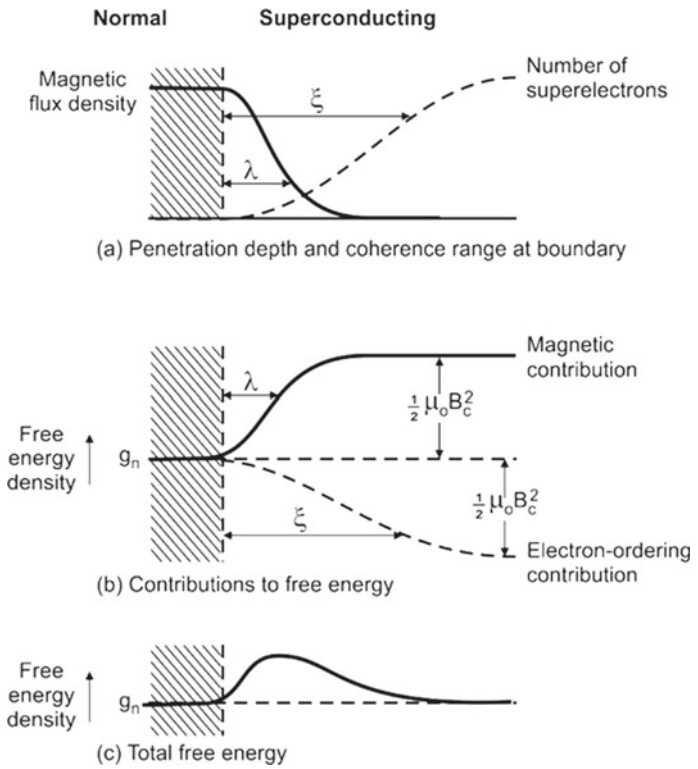

Fig. 2.23 Interface at the superconducting and normal boundary in a type I metallic superconductor has a positive surface energy [17] (With permission from Elsevier)

turned out to be an important characteristic parameter of the metallic superconductors as opposed to alloy superconductors, which are characterized with a negative surface energy and are termed as type II superconductors. Metallic conductors are likewise termed as type I superconductors. We will discuss type II superconductors in subsequent sections.

2.13 Determination of Energy Gap (Single Particle Tunnelling)

One easy and simple technique to measure the energy gap in superconductors is through the single particle tunnelling experiment. As shown in Fig. 2.24a, thin film of metal is deposited on a suitable substrate. The metal surface is then oxidized to form an insulating layer of the order of 10 Å thick. A superconducting layer is now deposited on this oxide layer. *I–V* characteristics of the junction are studied after

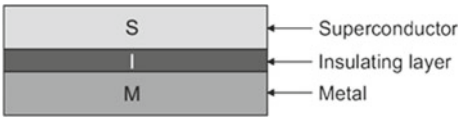

Fig. 2.24 Cross section of a tunnel junction consisting of a metal, an insulator and a superconductor. The insulator is usually the oxidized metal surface itself

making usual current and voltage contacts with the layers. A typical I–V behaviour of such a (MIS) junction as observed by Giaever [18] is shown by solid line in Fig. 2.25. For comparison, the I–V characteristics of a tunnel junction consisting of a metal–insulator–metal (MIM) has also been shown in this figure. The I–V plot for MIM junction is a straight line, that is, current and voltage are proportional. For the MIS junction, the current jumps sharply at a voltage of Δ/e where 2Δ is the energy gap of the superconductor.

The energy versus density of electronic states for a superconductor and normal metal are plotted in Fig. 2.26. The energy gap in the superconductor is distinctly shown in the figure (left). At 0 K, no current flows unless the voltage is raised to $E_g/2e = \Delta/e$. The current rises sharply [19] at $eV = \Delta$ (Fig. 2.25). The gap separates the normal electrons from the superelectrons. At nonzero temperature, there is a small current flowing even at lower voltage because the normal electrons are thermally excited across the energy gap.

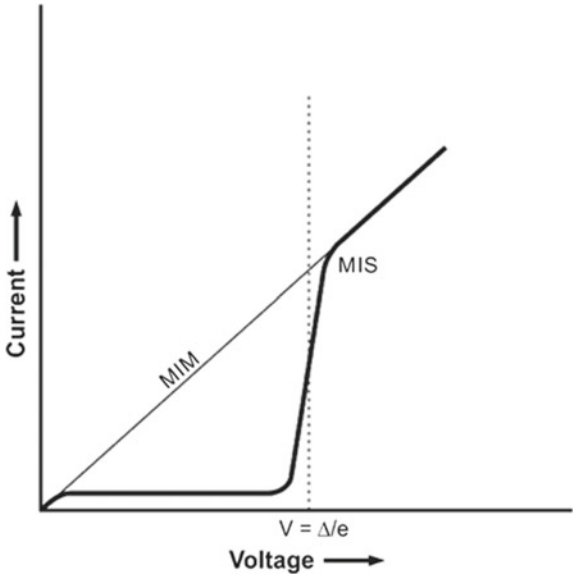

Fig. 2.25 Typical current–voltage behaviour of a metal–insulator–superconductor (MIS) tunnel junction. The straight line is the I–V characteristic of a metal–insulator–metal (MIM) junction

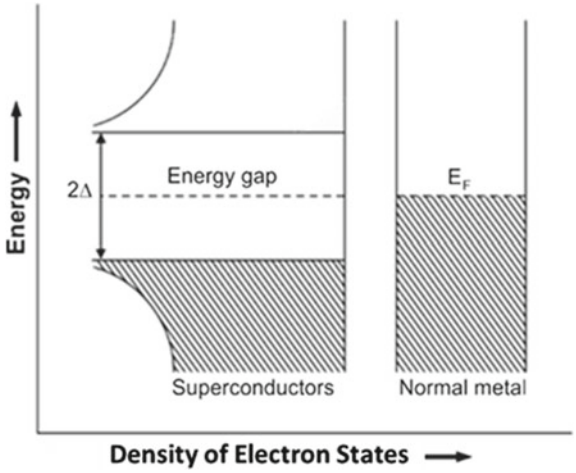

Fig. 2.26 Energy versus density of electronic states plots for a superconductor and in a normal metal

2.14 The Josephson Effect (Pair Tunnelling)

In 1962, Josephson [20], a graduate student at the University of Cambridge, made a startling prediction that a supercurrent (zero voltage) will flow across a tunnel junction consisting of two superconductors, A and B separated by a thin insulating layer, about 10 Å thick. These two superconductors can be either identical or different. The prediction came true, and the effect was observed experimentally. In the picture of BCS theory [15] of superconductivity (to be discussed in Chap. 4), the electrons start pairing up via a virtual phonon interaction process as the temperature is reduced to below T_c. These pairs, called Cooper pairs, condense to a ground state and are responsible for the supercurrent flow in superconductors. These Cooper pairs are identified with the superelectrons in the Gorter's two-fluid model. Interestingly, all the pairs in a superconductor are in the same quantum mechanical phase ϕ (phase coherence) and can be represented by a single macroscopic wave function or the order parameter (Fig. 2.27).

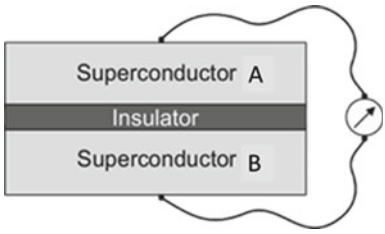

Fig. 2.27 A Josephson junction has two superconductors A and B separated by a thin (~ 10 Å) oxide insulating layer

$$\psi(\vec{r}, t) = |\psi(\vec{r}, t) \exp\left[i\phi(\vec{r}, t)\right] \tag{2.29}$$

This theory explained well most of the observed behaviour of the metallic superconductors, like zero resistance, Meissner effect and flux quantization.

2.14.1 DC Josephson Effect

Josephson effect [20] was yet another important manifestation of the same macroscopic quantum nature of superconductors. Here the pairs tunnel through the insulating barrier without encountering resistance. This flow of pairs constitutes a supercurrent. The supercurrent I generates a phase difference $\Delta\phi$ between the order parameters of the two superconductors according to the equation

$$I = I_c \sin(\Delta\phi) \tag{2.30}$$

where I_c is the critical current of the junction which depends upon the temperature and the junction parameter. For current, less than I_c the phase difference $\Delta\phi$ adjusts to facilitate the passage of the Cooper pairs across the junction with a constant value of $\Delta\phi$ or for a zero voltage. For currents larger than the critical current, a finite voltage appears. This is DC Josephson effect. A typical ideal current–voltage (I–V) characteristic of a Josephson tunnel junction is shown in Fig. 2.28. The DC Josephson effect was first observed experimentally in a crossed film junction by Anderson and Rowell [21].

2.14.2 AC Josephson Effect

At finite voltage, supercurrent still exists but oscillates with time with a frequency given by

$$\nu = \frac{2eV}{h} = \frac{V}{\phi_0} \tag{2.31}$$

This frequency turns out to be 484 MHz/μV. These oscillations persist up to frequencies of the order of 10^{12} Hz or more. This is AC Josephson effect and can be experimentally observed by irradiating the Josephson junction (J–J) by microwave of frequency, f. The I–V characteristic now shows a series of current steps at constant voltage

$$|V_n| = \frac{nhf}{2e}, \text{ where } n \text{ is an integer} \tag{2.32}$$

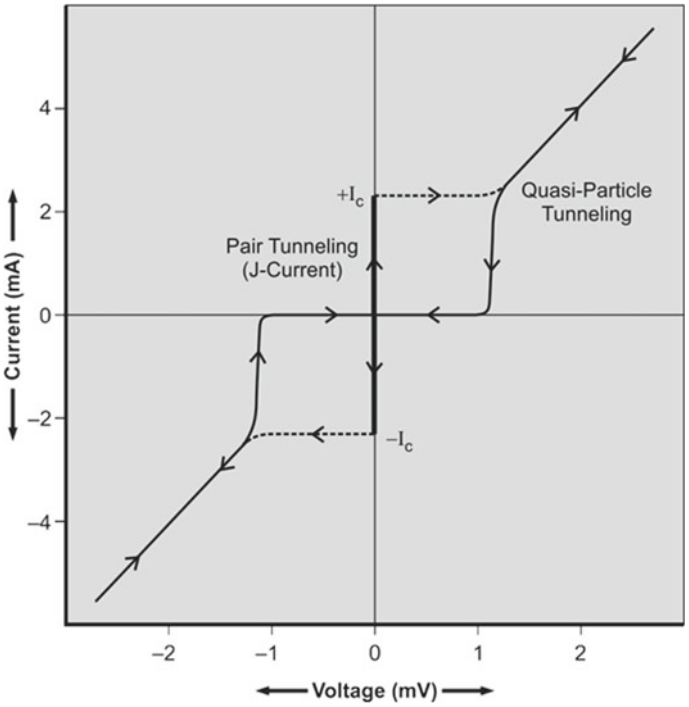

Fig. 2.28 A typical *I*–*V* behaviour in a Josephson tunnel junction. Note the hysteresis when the current is swept from − 5 to + 5 mA and back

The *I*–*V* characteristics with and without microwave irradiation are shown in Fig. 2.29. The height of the current steps and the range of current for which voltage remains constant oscillate with microwave frequency, f. This microwave frequency mixes up with the Josephson currents whose frequency ν depends upon the voltage across the J–J. Whenever $\nu \pm nf = 0$, there is a zero frequency beat and a current step appears. When the J–J is biased at voltage V, energy difference between Cooper pairs on the two sides is $= 2\ eV$ and whenever $2\ eV = nhf$, pairs can tunnel through the barrier coherently with the emission or absorption of n microwave photons. Please notice here that the voltage is related to frequency through the universal constants h and e, which are invariant of time and place. Consequently, international standard volt has now been defined as the voltage step that will be produced in a J–J irradiated by microwave of frequency 483,597.9 GHz. It is, however, necessary to prepare an array of a large number of Josephson junctions. An array of a large number of Nb J–J is used to generate 10 V for voltage standard routinely by the international laboratories. The voltage can be measured to better than 0.03 ppm accuracy. Josephson effect studies can be carried out on a variety of junctions prepared by different routes, and three of such most popular configurations [22] are depicted in Fig. 2.30. Figure 2.30a is a crossed film Josephson junction consisting of an insulating layer sandwiched

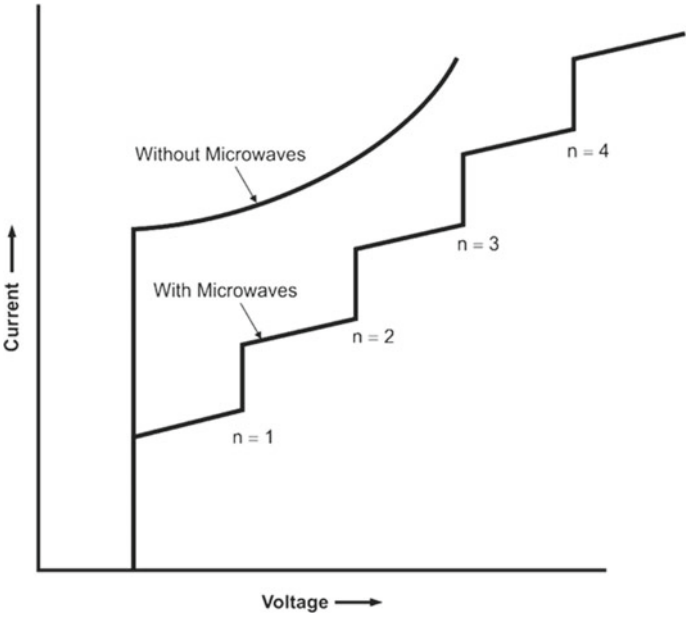

Fig. 2.29 I–V characteristics of a Josephson junction with and without microwave radiation. Current steps appear at constant voltage $|V_n| = \frac{nhf}{2e}$. These steps are shown for $n = 1, 2, 3$ and 4

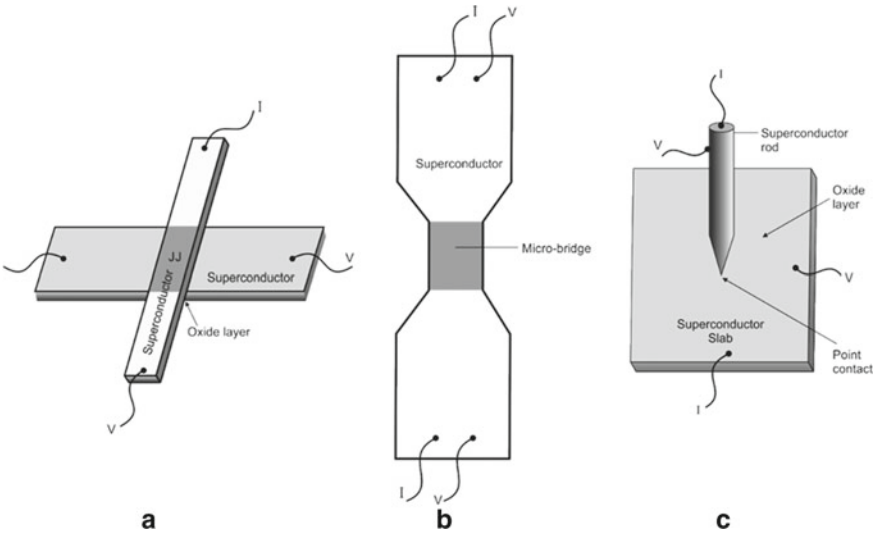

Fig. 2.30 Three different configurations of the J–J, **a** a 'crossed film Junction', **b** a 'weak link' or a 'microbridge', **c** a 'point contact' [22] (With permission of AIP)

between two superconductors. The first superconductor film is oxidized to form an insulating barrier, and a film of second superconductor is then deposited. Figure 2.30b is yet another form of J–J which has a broad superconducting film with a constriction in the middle and is called a 'weak link' or a microbridge. Figure 2.30c is a point contact J-J consisting of a superconducting screw pressing a bulk-superconducting slab, mostly niobium, at a point. A niobium oxide film formed on the slab at room temperature serves as the barrier between the slab and the screw.

2.14.3 The SQUID

SQUID stands for 'Superconducting Quantum Interference Device' and is perhaps the most widely exploited application of Josephson effect and the flux quantization. SQUID is a device, which can measure feeble magnetic field of the order of 10^{-15} T, such as produced by the neural activity in human brain, to unprecedented accuracy. SQUID is used in biomagnetism and geomagnetism for prospecting as also in solid-state physics. By coupling a small coil, a SQUID can as well be used as an ultra-low noise parametric amplifier for voltage and current signals from a variety of transducers. A SQUID could be either a dc SQUID or an rf SQUID. The prefix indicates the method of coupling of the electronics to the device. Figure 2.31 is the schematics of DC SQUID [23], which consists of two Josephson junctions (weak links), J–J1 and J–J2 mounted on a superconducting ring with two side arms. External current applied to the SQUID (bias current) enters from the left and branches out into two arms of the device and combines and exits at the right end. When the current in the weak links (J–J1) and (J–J2) is greater than the critical current, a voltage appears across the SQUID. The junction critical current (supercurrent) is extremely sensitive to the flux applied to the ring and is maximum for zero flux. If now the magnetic flux threading the ring is increased, the critical current starts decreasing and reaches to a minimum at half the integer of flux quantum Φ_0. Critical current increases again to a maximum at full integer of Φ_0. The voltage across the SQUID thus oscillates with a periodicity of one flux quantum Φ_0 as shown in the lower part of Fig. 2.31. The above effect is similar to the one observed in optics when a coherent light beam from a laser source passes through two parallel slits and interfere with each other to produce dark and bright fringes. In a superconductor, all the Cooper pairs are in phase and are described by a single wave function. In a SQUID, the wave functions at the two weak links (JJ) interfere with each other and produce current and voltage fluctuations. As shown in Fig. 2.32a.

SQUID in a magnetic field has a critical current versus magnetic field pattern very much similar to the diffraction pattern formed by the interference between the monochromatic light coming from the two slits. In a SQUID, the quantum mechanical interference takes place between the currents flowing through the two separate Josephson junctions. This interference gives rise to the periodicity of current associated with flux enclosed in the area between the two junctions. The other periodicity, of course, is associated with the flux contained in a single junction. It is clear from the

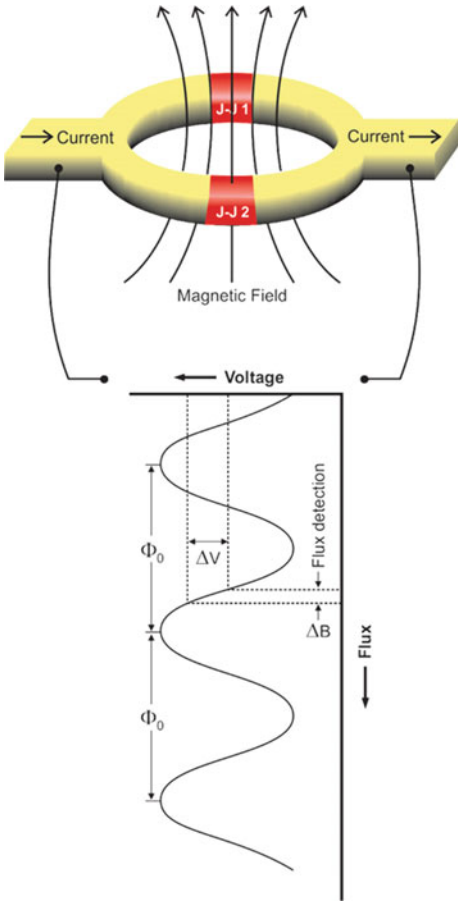

Fig. 2.31 A DC SQUID with two Josephson junctions (J–J1 and J–J2) mounted on a superconducting ring (*top*) and SQUID voltage oscillations with flux (*bottom*). One can measure a fraction of the flux quanta accurately in terms of voltage [23]. *Courtesy* 'Ian Worpole/Scientific American'

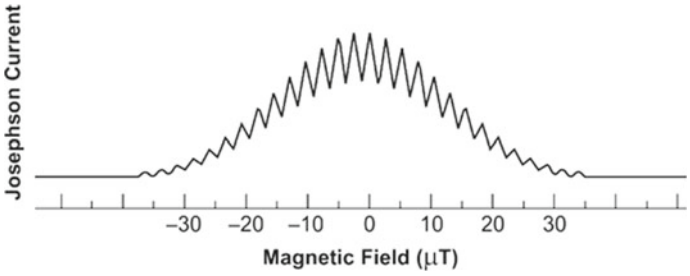

Fig. 2.32 A typical Josephson current versus magnetic field pattern in a DC SQUID

above discussion that a SQUID can detect and measure a fraction of a flux quantum digitally and accurately. SQUIDs are widely used as sensitive magnetometers. Clarke [22, 23], who contributed a great deal to this field, has written very good reviews on SQUIDs.

With the commercial availability of SQUIDs, a new field of research 'Magnetoencephalography (MEG)' has emerged wherein one can map feeble magnetic field generated by neuroelectric activities in the brain. Neurosurgeons can pin point the source of epileptic seizure and can study real time brain activity. A combination of MEG and MRI can enable a surgeon to have detailed brain map and remove only the damaged tissues. MEG machines with as much as 600 SQUIDs on a helmet-shaped headgear are commercially available to map the entire area of the brain.

It is easier to fabricate rf SQUIDs as it uses a single Josephson junction as shown in Fig. 2.33. Here the interferometer is coupled to an inductance–capacitance–resistance (LCR) resonant circuit. An AC current flows in the circuit at its resonant frequency. The voltage across this circuit oscillates with a period of one flux quantum Φ_0 with the flux threading the superconducting ring. The applied flux modulates the critical current of the J–J as also the voltage. In rf SQUID, the resonant circuit too is kept at liquid helium temperature. Both the DC and the rf SQUIDS have comparable sensitivity.

The photographs of a commercial MEG machine TRIUX™ neo produced and marketed by MEGIN Oy are shown in Fig. 2.34. The patient can lie on a patient table (left) or can sit comfortably with the head fitted into a helmet-shaped gear housing few hundred SQUIDS, cooled to 4.2 K. This sophisticated MEG system has become popular with the neurosurgeons who use it for pre-surgical localization of epilepsy and for mapping eloquent cortex, including motor functions, hearing and vision. The system has a 'zero-boil-off' liquid helium cryostat with virtually zero helium

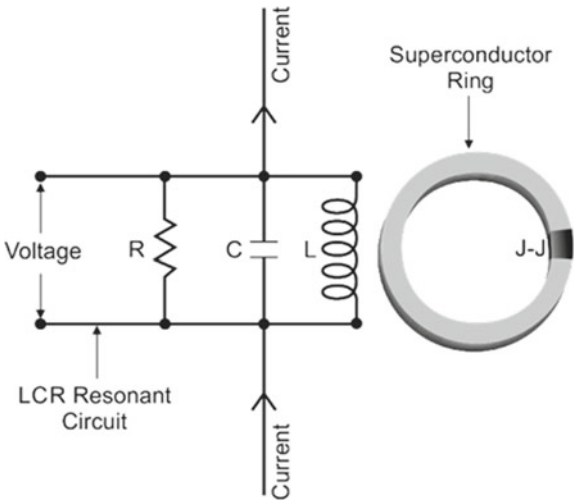

Fig. 2.33 An rf SQUID has a single J–J on a superconducting ring and is coupled to an LCR circuit

Fig. 2.34 Two versions of the TRIUX™ neo commercial MEG machine produced and marketed by MEGIN Oy. The patient head fits in a helmet-shaped gear having 306 SQUID channels mounted on it for mapping the whole brain area. It has a patient table (*left*) or a chair (*right*) for patient comfort. The inset of the left picture shows SQUIDs mounted on a helmet-shaped headgear which are cooled to 4.2. Courtesy of MEGIN Oy

consumption, has a high tolerance for magnetic interferences and improved patient comfort. This has made TRIUX™ neo an important tool for neurological studies, clinical use and for research. Figure 2.34 shows two versions of the MEGIN machine with a patient on the table (*left side*) and sitting on a chair (*right side*). The inset of the left figure shows how the multiple SQUIDS are mounted on a helmet-shaped headgear.

2.15 Type II Superconductors—Abrikosov's Concept of Negative Surface Energy

After having studied superconductivity in metals across the periodic table, and the consequent disappointment with low T_c values, the researchers in the field of superconductivity changed track and started looking for superconductivity in alloys and compounds. Superconductivity was indeed discovered in a large number of alloys and compounds at higher T_c. These new superconductors, however, displayed a strange behaviour insofar as they did not show perfect diamagnetism like in pure metals. Instead, they exhibited partial flux penetration. At first instance, it was thought to be either an experimental artefact or an impurity effect. Abrikosov [24], however, predicted in 1957 a new class of superconductors, now called type II with anomalous properties. He emphasized that it is a new class of superconductors and not a trivial impurity effect. He argued that in metal superconductors, referred to as type I superconductors, occurrence of perfect diamagnetism implies that there is a positive surface energy at the normal–superconducting boundary. Now consider a normal region in a type I superconductor in a magnetic field $B_a < B_c$ the free energy of normal regions/unit volume is greater than for the superconducting region (diamagnetic state) by $\frac{\mu_0}{2}\left(B_c^2 - B_a^2\right)$. Thus in a type I superconductor, the free energy will

increase if the normal regions were to grow. This is energetically unfavourable, and therefore, it remains superconducting until a field B_c is reached. Let us now assume a negative surface energy [17] at the superconducting–normal boundary. This implies that the energy will reduce if normal regions are formed in the superconductor. When a field is applied, a large number of normal regions are formed resulting in a large negative energy. It thus becomes energetically favourable to allow partial flux penetration than carrying the burden of expelling the field completely (Fig. 2.35).

To understand the concept of negative surface energy, we should recall that type II superconductivity is observed mostly in alloys and compounds (with a few exceptions like Nb, V and T_c) where the mean free path is very small and so is the coherence length. Thus, type II superconductors are characterized by a coherence length ξ much smaller than the penetration depth λ. We have shown in Fig. 2.23 that in type I superconductors, where $\xi \gg \lambda$, the surface energy is positive. The surface energy in type II superconductors ($\xi \ll \lambda$) is, however, negative close to the N–S boundary.

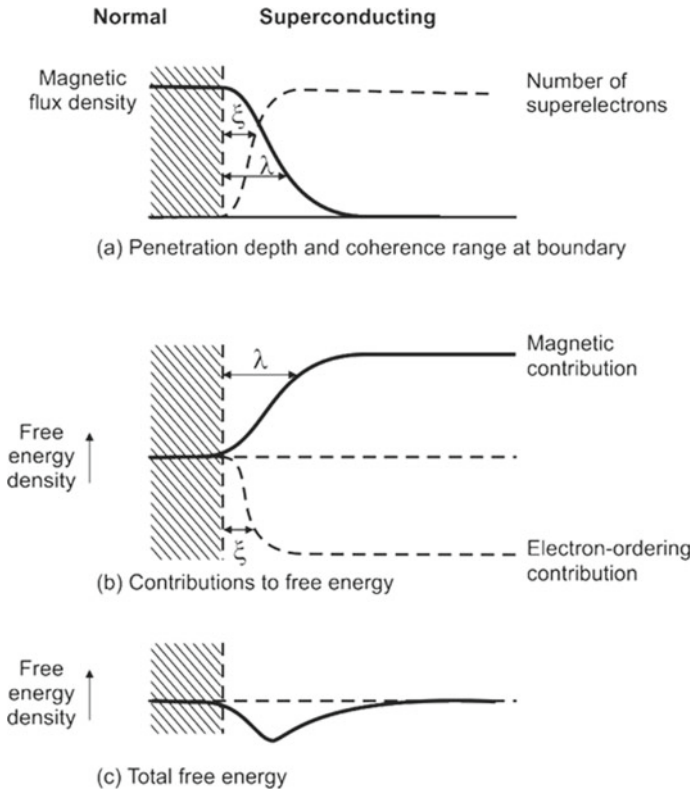

Fig. 2.35 Interface at the superconducting and normal boundary in a type II superconductor has a negative surface energy as lowering of energy due to pair formation is more than the increase in energy due to magnetic contribution close to the N–S boundary [17] (With permission from Elsevier)

Here we see that well inside the material the two contributions to free energy, that is, electron ordering contribution and the magnetic contribution cancel each other but close to the boundary there is now a net negative energy.

2.15.1 Lower and Upper Critical Magnetic Field

Figure 2.36 shows the magnetic phase diagrams of the type I and type II superconductors. Figure 2.36a is the same as Fig. 2.5 for the type I superconductor, whereas Fig. 2.36b is the phase diagram for type II superconductors. As seen in the figure, type II superconductors are now characterized by two critical magnetic fields instead of one for type I. A type II superconductor shows perfect diamagnetism only up to a magnetic field, B_{c1}, called the lower critical magnetic field. This field is a fraction of the thermodynamical magnetic field B_c. Material, however, stays superconducting (zero resistance) up to a magnetic field which is significantly higher than B_c and is called the upper critical magnetic field, B_{c2}. A type II superconductor can thus sustain a very high magnetic field and can still carry large current. It is for this reason that only type II superconductors are of technological importance and are widely used for magnet construction. All the three critical magnetic fields are interrelated in the following way;

$$B_c = [8\pi(g_n - g_s)]^{\frac{1}{2}} \tag{2.33}$$

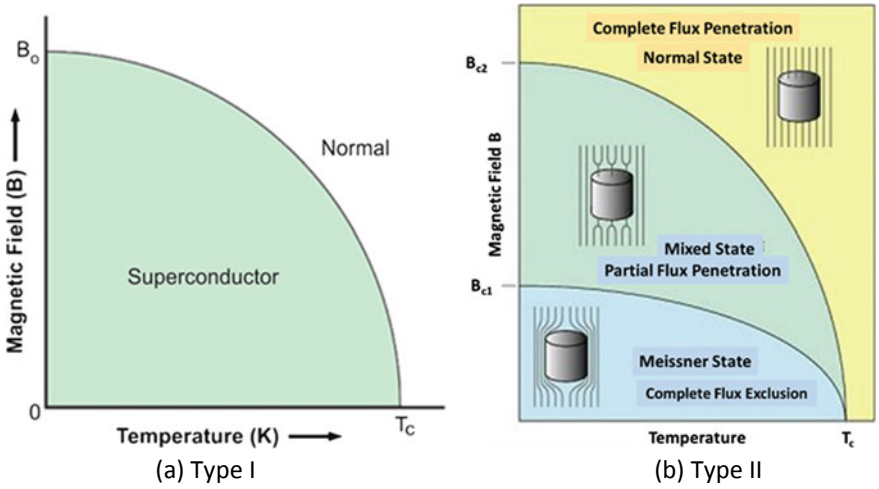

Fig. 2.36 **a** Magnetic phase diagrams of type I superconductor and **b** magnetic phase diagrams of type II superconductor showing type I (Meissner state), type II (mixed state) and non-superconducting regions (normal state) (Modified Open access under CCA, Phys. Rev. Authors—M. G. Alford and G. Good, https://doi.org/10.1103/PhysRevB.78.024510)

Table 2.6 κ values for type II pure metal superconductors

Metal superconductor	κ Value
Nb	0.78
V	0.85
T_c	0.92

$$B_{c1} = \frac{B_c}{\left(\kappa\sqrt{2}\right)^{0.65}} \tag{2.34}$$

$$B_{c2} = \left(\sqrt{2}\right)\kappa B_c \tag{2.35}$$

$(g_n - g_s)$ is the energy difference between the normal state and the superconducting state and κ is the G–L parameter ($= \lambda/\xi$). As κ increases, B_{c1} decreases with respect to B_c and B_{c2} increases. The value of κ is given by the G–L theory:

$$\kappa = \frac{\left(\sqrt{2}\right)2\pi\lambda^2\mu_0 B_c}{\Phi_0} \tag{2.36}$$

where $\Phi_0 = h/2e = 2 \times 10^{-15}$ T m^2, the flux quanta. It is pertinent to note here that in alloys, electron mean free path is short which means the coherence length ξ decreases and λ increases thus making κ large. For type I superconductor $\kappa < 0.71$ and for type II $\kappa > 0.71$. However, κ can be more than 0.71 even for pure metals in exceptional cases as shown in Table 2.6.

For pure metals κ increases with impurity and thus with normal state resistivity as per the relation below:

$$\kappa = \kappa_0 + 7.5x\sqrt{10} \times 10^5 \gamma^{\frac{1}{2}}\rho \tag{2.37}$$

where κ_0 is the value of κ for pure metal, ρ and γ are normal state resistivity and coefficient of electronic specific heat, respectively. Further, some metals and alloys behave like type I superconductor at T_c but turn type II at lower temperature. For example $Pb_{0.99}$ $Tl_{0.01}$ $\kappa = 0.58$ at T_c ($= 7.2$ K) but increases to 0.71 at $T = 4.3$ K. For pure vanadium $\kappa = 0.85$ at T_c ($= 5.4$ K) and increases to 1.5 at $T = 0$ K.

2.15.2 The Mixed State

It will be interesting to know what happens to a type II superconductor between the lower critical field B_{c1} and the upper critical field B_{c2}. The existence of a negative surface energy at the N–S boundary favours partial field penetration of the material. As shown in Fig. 2.37, between B_{c1} and B_{c2} the material undergoes 'mixed state'. It is energetically favourable that the flux lines, each carrying a unit quantum of flux

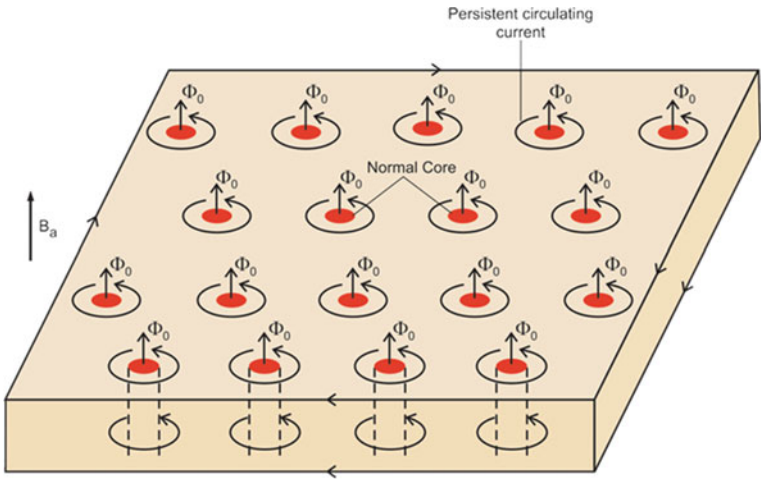

Fig. 2.37 Between B_{c1} and B_{c2}, a type II superconductor undergoes mixed state. The material is threaded by flux lines (Φ_0) produced by vortices of persistent current with a sense of rotation opposite to the surface screening current

Φ_0 ($= h/2e$) parallel to the applied field penetrate the material. These flux lines form a triangular lattice and are normal cores of small dimension of the order of diameter 2ξ. Mixed state is a fine structure with a periodicity of $< 10^{-6}$ and is an intrinsic property of type II superconductors.

The favourable configuration for the normal cores to thread the superconductor is a cylinder with a maximum surface to volume ratio, parallel to the applied field. Each flux line is produced by a vortex of persistent current with a sense of rotation opposite to the surface screening current. The material remains diamagnetic being protected by the surface screening current, and the supercurrent still flows. In type II superconductors, current flows through the entire cross section as compared to type I where the current flows along the surface. As field strength increases, the density of normal cores increases at the expense of superconducting volume fraction and at the upper critical field B_{c2} the entire structure collapses. The material turns normal.

2.15.3 Current Flow and Mixed State

Type II superconductors are known to carry very large current in presence of high magnetic fields. Let us see how current is carried by a type II superconductor in mixed state. In the mixed state, the current is not impeded by the presence of flux lines, the size of the normal cores being very small (~ 2 ξ). The vortices repel each other so that the normal cores are confined to small area and the current flows without hindrance as long as it does not disrupt vortices. The flux lines, however, experience a Lorentz force, F_L under the influence of the transport current and the perpendicular

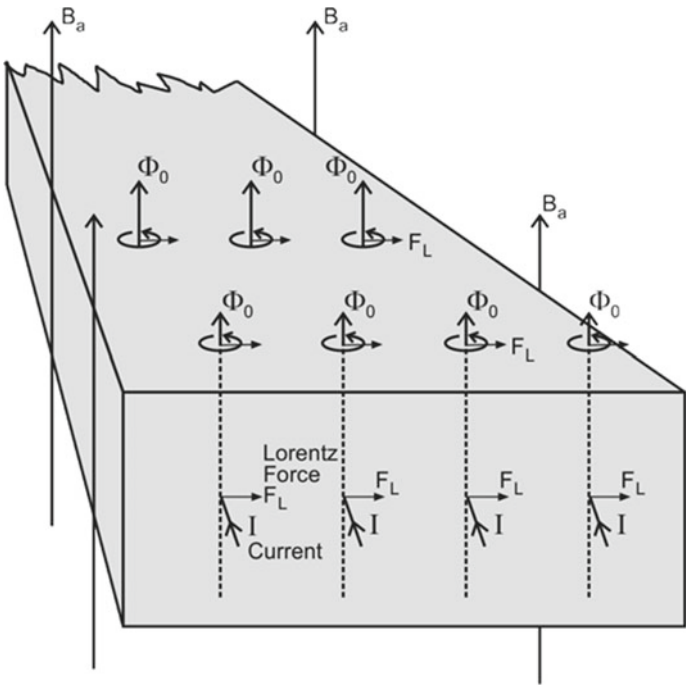

Fig. 2.38 In the mixed state flux lines (normal cores) experience Lorentz force ($F_{\mathbf{L}}$) when a longitudinal current flows through the superconductor. Movement of flux line is prevented by flux pinning mechanism

transverse field, which tries to move it in the third perpendicular direction (Fig. 2.38). The movement of the flux lines generates a finite voltage and a resistance appears. The flux lines are, however, held back by the crystal lattice through a pinning force $F_{\mathbf{P}}$. Imperfections, defects and impurities are introduced in to the superconducting materials to create pinning sites. The pinning force is thus increased significantly, and the superconductor can carry a much larger current.

The flux lines do not move until the time Lorentz force exceeds the pinning force. This happens at a current density value, called the critical current density $J_{\mathbf{c}}$ of the superconductor. Once the $J_{\mathbf{c}}$ is exceeded, flux lines start moving, a voltage appears and the material reverts to normal state.

Figure 2.39 shows two typical plots of $J_{\mathbf{c}}$ versus the magnetic field. The lower plot is for a clean, defect-free type II superconductor, and the upper plot is drawn for the 'dirty' superconductor with defects or the so-called pinning centres. As seen from the figure, $J_{\mathbf{c}}$ drops sharply to low value for a pure superconductor at low field and is hardly of use for practical applications. The dirty superconductors normally referred to as 'hard superconductors' with pinning sites (defects) on the other hand carries large useful current at high magnetic field. Defects are substituted intelligently in a superconductor to create pinning sites, which increase the pinning force many

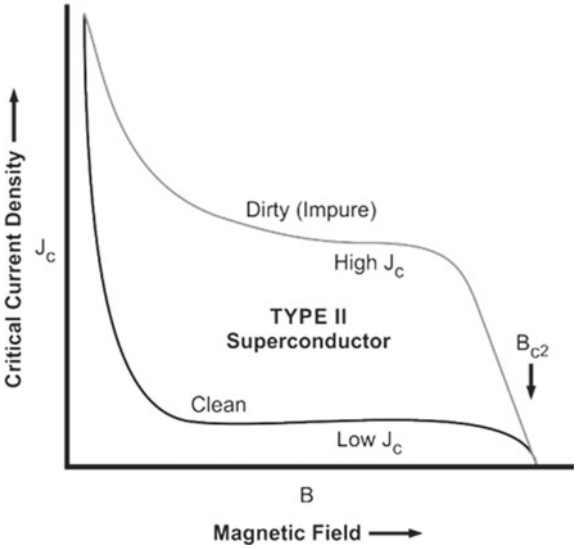

Fig. 2.39 J_c versus magnetic field for type II superconductors in clean limit and the dirty limit with pinning centres. J_c in both the cases drops to zero at B_{c2}, but the dirty superconductor carries high current in the intermediate field region between B_{c1} and B_{c2}

fold. The critical current increases dramatically whereby the superconductor can be used for magnet applications like in accelerators and the fusion reactors where the superconducting cables carry several tens of kA current and in high magnetic field.

2.15.4 Measuring Transport Critical Current

Critical current density (J_c) in magnetic field is the single most important parameter for characterizing a superconducting wire. Critical current (I_c) in a mono-core superconducting wire can be measured accurately using a short sample and making the voltage contacts close to the current contacts. The sample is mounted on a sample holder and kept in a perpendicular magnetic field. An increasing current is then flown through the sample. The voltage is continuously recorded which remains zero until the current exceeds a critical value when the voltage rises sharply. This current is the critical current I_c. The I_c is always measured as a function of magnetic field, I_c being a strongly field dependent parameter and is important for designing magnets or other such devices.

I_c measurements on multifilamentary (MF) superconducting wires have to be carried out on a hair-pin-shaped specimen as shown in Fig. 2.40. While measuring critical current in a MF wire with several concentric layers of filaments around the central core, it is important that the voltage contacts are made far away from the current contacts. There is a current transfer length, [25, 26] which can be many times

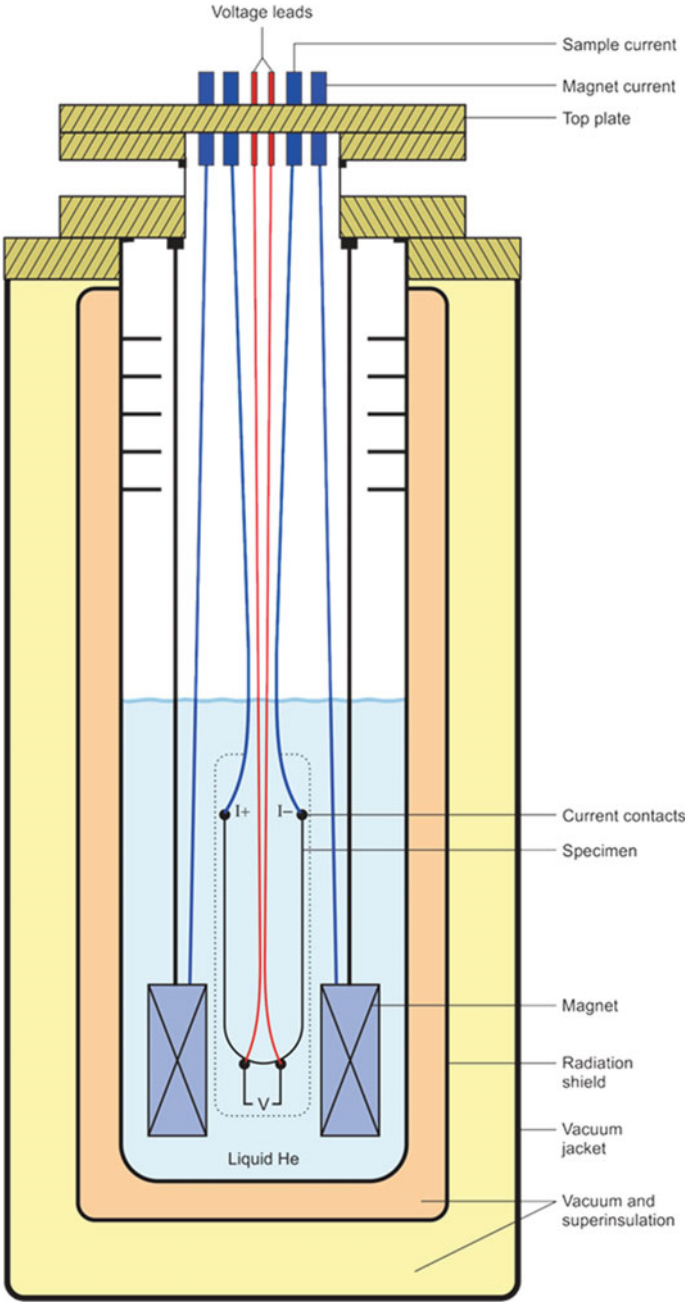

Fig. 2.40 A schematic of the superconducting magnet system used for critical current measurement. Voltage contacts on the multifilamentary wire sample are made far away from the current contacts

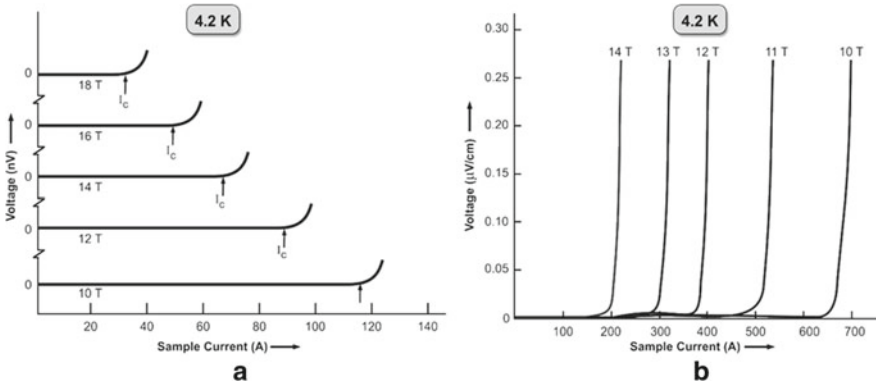

Fig. 2.41 Typical critical current, (I_c) plots at different fields. I_c decreases as the magnetic field increases

the wire diameter depending upon the matrix resistance. All the layers of filaments must share the current uniformly. Voltage contacts are made on the horizontal part of the sample, which is kept in the perpendicular magnetic field. The sample is kept dipped in liquid helium at 4.2 K. A variable DC current is passed through the sample from a power supply, and the voltage across the sample is monitored using a nanovoltmeter and a plotter. In this case, also there is practically no voltage across the sample with increasing current until a current equal to critical current I_c is reached. There is a sharp jump in voltage at I_c as shown in Fig. 2.41. This voltage rise is caused by the flux flow resistivity of the sample which is different from the Ohmic resistivity and is proportional to the normal state resistivity. At still higher current, the voltage becomes resistive and follows an Ohmic behaviour. I_c is determined at different values of the magnetic field. It is advisable to start from the highest magnetic field so that the current to be passed through the sample is minimum, I_c being low. As the field is reduced, sample carries larger currents (I_c) which enhances the possibility of burnt-out of the sample. A shunt across the sample is therefore always advisable to save the sample from burnt-out. The criterion to determine I_c is usually 0.1–1.0 μV/cm voltage drop across the sample. The engineering critical current density, J_c is calculated by dividing I_c by the area cross section of the wire.

The author has made detailed I_c-measurements on a 19 core V_3Ga wires [27] in both the geometries, that is, voltage contacts (V_1) were made far away from the current contacts as well as close to current contacts (V_2) on hairpin samples. Voltage V_1 showed the normal behaviour of the horizontal line in the I–V plots followed by a sharp rise of voltage at I_c. V_2 on the other hand showed steady increase of voltage with increasing current (similar to observed in short sample geometry) followed by a sharp rise of voltage at the same value of I_c. The important finding of these I_c measurements thus was that the I_c values in both the geometries are almost equal if one ignores the slope of I–V plots of V_2. It appears that the current is shared by copper matrix close to the current contacts in MF wires and the plot therefore shows

a resistive (current transfer) behaviour (V_2) resulting in a finite slope. The second sharp jump in the voltage appears at I_c when filaments finally turn normal.

2.15.5 *Magnetization in Type II Superconductors*

A type II superconductor behaves exactly like type I below the critical field B_{c1} and is a perfect diamagnet with magnetization equal to $-B_a$. Beyond B_{c1} flux lines start penetrating the material (mixed state) and the magnetic flux inside the material is no longer zero as shown in Fig. 2.42a. As the magnetic field is increased magnetic flux density continues rising till B_{c2} is reached. The material is completely taken over by the flux, turning it in to the normal state. The curve retraces its reverse path in pure ideal superconductors when the field is ramped down to zero. The corresponding magnetization versus field behaviour is shown in Fig. 2.42b. As shown, magnetization increases with magnetic field until B_{c1} and starts decreasing in field higher than B_{c1}. The magnetization continues to decrease until it becomes zero at B_{c2}. Between B_{c1} and B_{c2} flux lines (normal cores) enter the material. The density of flux line is governed by the equilibrium between the reduction in free energy and the mutual repulsion between the vortices. In increasing field, normal cores pack closer together, so the average flux density increases in the material and the magnetization decreases. At B_{c2}, there is a discontinuous change in the slope of the flux density

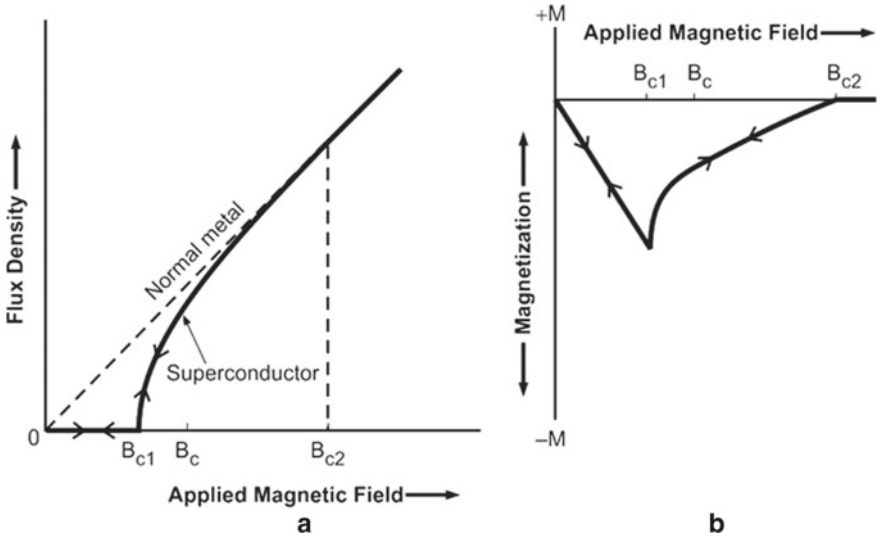

Fig. 2.42 **a** Magnetic flux density inside a type II superconductor is zero up to B_{c1} and increases in higher field. At B_{c2} flux penetrates the whole of the material. The process is reversible in ideal pure material, **b** negative magnetization increases with magnetic field, peaks at B_{c1} and then decreases to zero at B_{c2}. This process too is reversible for pure ideal material

and the magnetization. The material now is in normal state with flux density equal to $\mu_0 B_a$ and magnetization zero.

Magnetization measurement can be used for the determination of κ by finding the slope of the M–H curve near the field B_{c2} as per the formula:

$$\left[\frac{dM}{dH}\right]_{B_{c2}} = \frac{-1}{1.16(2\kappa^2 - 1)} \tag{2.38}$$

The procedure is, however, valid only if the magnetization is reversible, which means that the same curve should be traced while increasing and decreasing the magnetic field.

2.15.6 Irreversible Magnetization

Only ideal type II superconductors without pinning show reversibility, but real type II superconductors (hard superconductors) show irreversibility in their magnetization behaviour as shown in Fig. 2.43. The reason for this magnetic irreversibility is that the flux lines or the normal cores are pinned in the bulk by imperfections and are not free to move. Consequently, on increasing the field from zero there is no sudden entry of flux inside the material at B_{c1}. Instead, there is rounding in the flux density and the magnetization curves at B_{c1}. Likewise on reducing the field from above B_{c2}, the two curves do not retrace their paths, but show hysteresis. Flux may be left trapped permanently as some flux line remain pinned and are not able to detach and

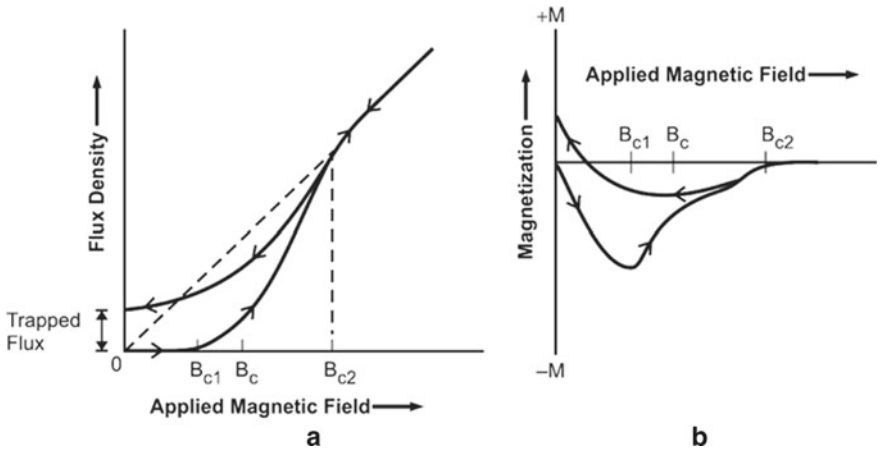

Fig. 2.43 **a** A real type II superconductor has imperfection and show magnetic irreversibility in flux density. Material can retain finite flux even after the field is reduced to zero. **b** Similarly, a real type II superconductor with imperfections show magnetic irreversibility in magnetization. Material can retain finite magnetization even after the field is reduced to zero

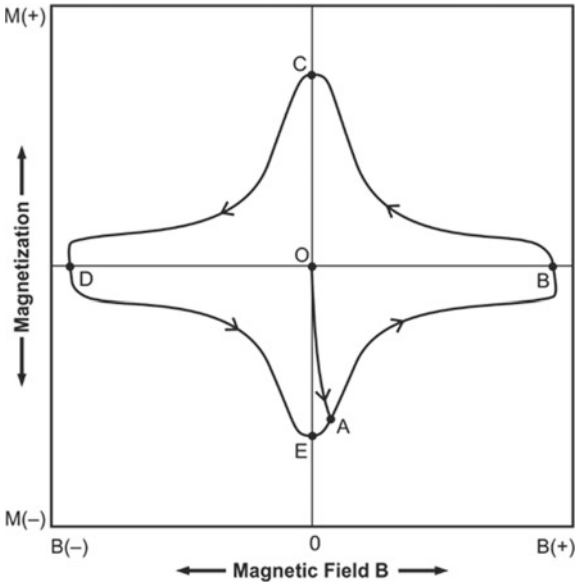

Fig. 2.44 Typical plot of magnetization versus magnetic field of a multifilamentary hard superconductor between $+B$ to $-B$. Starting from $M = 0$ and $B = 0$ point the curve traverses an irreversible path showing hysteresis. M does not drop to zero even at $B = 0$ after tracing the full cycle. M can only be reduced to zero only by warming the sample to above T_c

move out. Imperfections like dislocations, grain boundaries and impurities can cause this type of magnetic irreversibility. The magnetic field has to be reversed to bring down magnetization M to zero. The trapped flux at $B = 0$ can be s retrieved only by warming the material to normal state.

Figure 2.44 shows a typical magnetization versus magnetic field loop observed in a multifilamentary conductor. To draw the full M–B loop, we start from point O ($M = 0, B = 0$). The negative magnetization M increases with field up to the field B_{c1} (point A) and starts decreasing with the further increase of the field. Magnetization drops to zero at B_{c2} (point B). The anomalous behaviour of these hard superconductors is that when the field starts decreasing, the M–B curve does not retrace the earlier path. Instead, magnetization changes sign and starts increasing to oppose the changing magnetic field attaining a peak value at C. Now if we reverse the direction of the magnetic field and start increasing it, M again drops to zero at point D. With the decreasing field, M again increases in the negative direction to a peak value at point E. Thus, we find that even after a full cycle from $+B$ to $-B$, the magnetization does not drop to zero at zero field. Warming of the superconductor to normal state seems to be the only way-out.

Notice that the curve is almost a straight line until a small field ($= B_{c1}$) and then it traverses an irreversible path showing hysteresis. It is shown from Fig. 2.44 that the reversibility behaviour is associated with the hysteresis and the consequent dissipation. It is interesting to note that the curve is not symmetric around the horizontal

axis. This asymmetry is caused by the magnetic moments produced by the surface screening currents opposing the flux entry. Area of the hysteresis loop is the measure of the dissipation. The dissipation can be estimated from the area of the loop using the formula:

$$Q_{\text{hys}} = \oint M(B)\mathrm{d}B \tag{2.39}$$

This energy dissipation appears as frictional heat and is caused by the movement of the flux bundles in and out of the conductor. This is important for superconducting magnets in accelerators where the conductor is exposed to time-varying field. Precise calculation of heat generation is thus extremely important to work out the cryogenic refrigeration requirement. Hysteresis is an indication of an effective pinning of flux lines by imperfections which causes sharp increase of critical current density in type II superconductors, making them most suitable for magnet applications.

2.15.7 The Bean's Critical-State Model and Magnetization

Superconducting magnets built during 1960s using hard superconductors performed poorly and quenched at operating currents far below the expected value. Flux jumping was found to be the main reason behind this disappointing performance. Flux jump is caused by the magnetization currents penetrating the surface deeper as the external field keeps increasing. The problem was solved in the subsequent years, and ingenious techniques to produce multifilamentary wires were perfected. These conductors showed no flux jumping, and the magnets performed just as predicted. AC losses in hard superconductors is another problem faced, which again is a manifestation of the magnetization effects.

The first phenomenological theory of magnetization was given by Bean [28, 29]. Even though the mixed state is well explained by the vortex structure postulated by Abrikosov and verified experimentally. Bean assumed a 'filamentary mesh structure' (also referred to as 'Sponge model') postulated by Mendelssohn [30] for the sake of simplified calculations. According to this model, the mesh consists of filaments, which have diameter less than London's penetration depth. These filaments sustain supercurrent up to a critical current density $J_{\mathbf{c}}$ that is a function of magnetic field and becomes zero at the critical field of the filament. The sponge model is equivalent to a picture of multiply connected internal structure of high critical field material surrounded by a matrix of soft superconductor with low critical magnetic field.

Bean, however, assumed that the critical current density is independent of the magnetic field, which would simply mean that the field is far less than the critical field of the filaments. He also envisaged that the mesh interstices are filled with soft superconductor of critical field $B_{\mathbf{c}}$ which shields the material against the magnetic field up to $B_{\mathbf{c}}$. The shielding beyond $B_{\mathbf{c}}$ is provided by the magnetizing currents

induced in the filaments at a critical value $J_{\mathbf{c}}$. These currents flow in a depth necessary to reduce the field to $B_{\mathbf{c}}$. Bean drew the magnetization curve of a virgin hard superconductor cylinder of radius R in a magnetic field parallel to the axis. He calculated internal field $B_{\mathbf{i}}$ as a function of external field B and the position in the superconductor. Writing the magnetization equation:

$$4\pi M = \frac{\int_0^v (B_{\mathrm{i}} - B_{\mathrm{e}})\mathrm{d}v}{\int_0^v d} \tag{2.40}$$

where v is the sample volume and the integrals are over the whole volume. For field less than $B_{\mathbf{c}}$, the shielding will be full if the radius R is much greater than London's penetration depth, that is

$$B_{\mathrm{i}} = 0, \quad 0 \le r \le R \quad \text{and} \quad 0 \le B \le B_{\mathrm{c}} \tag{2.41}$$

For field greater than $B_{\mathbf{c}}$ the soft superconductor surrounding the filaments becomes normal and for higher fields shielding, currents are induced in the filaments flowing within a depth $D_{\mathbf{p}}$, given by the circuital form of Ampere's law

$$D_{\mathrm{p}} = 10(B - B_{\mathrm{c}})/4\pi J_{\mathrm{c}} \tag{2.42}$$

This field-dependent and macroscopic penetration depth is an interesting result of this model. Here a new field B^* can be defined as:

$$B^* = 4\pi J_{\mathrm{c}} R/10 \tag{2.43}$$

This step simplifies the analytic expressions and B^* signifies the field that should be applied in excess of the bulk critical field which induces magnetization current to flow throughout the sample. Under such condition, the penetration depth $D_{\mathbf{p}}$ will simply be equal to R. Under conditions when all the bulk superconducting characteristics are destroyed and only shielding currents flow through the filaments:

$$B_{\mathrm{i}} = B - B^*(1 - r/R); \quad 0 \le r \le R \quad B^* + B_{\mathrm{c}} \le B \tag{2.44}$$

After a few mathematical steps, the expressions for magnetization turn out to be

(i) For $0 \le B \le B_{\mathbf{c}}$

$$4\pi M = -B \tag{2.45}$$

(ii) For $B_{\mathbf{c}} \le B \le B^* + B_{\mathbf{c}}$

$$4\pi M = -B + \frac{\left(B^2 - B_{\mathrm{c}}^2\right)}{B^*} + \frac{\left[B_{\mathrm{c}}^2(3B - 2B_{\mathrm{c}}) - B^*\right]}{3B^{*2}} \tag{2.46}$$

(iii) For $B \geq B^* + B_c$

$$4\pi M = -B^*/3 \tag{2.47}$$

The most striking result of this model is that the magnetization in hard superconductors is dependent on the macroscopic dimension of the sample. Rightly so, because critical current is carried by all the filaments, the number of which are proportional to the sample size. There is an excellent fit between the experimental magnetization data on Nb_3Sn specimens and the theoretical calculations.

The essence of Bean's critical state model thus turns out to be (i) that each hard superconductor is characterized by a limiting critical current density J_c (B) and (ii) that any smallest electromotive force induces this full current that flows locally. The consequences of this model are that the regions inside a superconductor not experiencing magnetic field will carry zero current, full current at J_c will flow in regions perpendicular to the field axis. The polarities of the current depend on the polarity of the electromotive force caused by the earlier field change. The field profile in a slab of large dimensions along the Y and Z axes and finite thickness $2a$ along the x-axis is shown in Fig. 2.45a for $B = 0$, $B = B^*/2$, $B = B^*$ and $B = 2B^*$. The magnetic field is parallel to the surface. The corresponding critical currents with opposing polarities ($+ J_c$ and $- J_c$) for different fields are shown in Fig. 2.45b. It can be noticed that the polarities of the critical currents along the outer and inner surface sheaths on the right and left of the mid-axis are in opposite directions.

Figure 2.46 shows the plots of the local field and critical current density in a slab of hard superconductor after a field B_0 is applied in a virgin state and removed. When the field B_0 is applied, it penetrates the slab to a depth determined by the critical current to oppose this field shown in Fig. 2.46a. As we remove the field, an

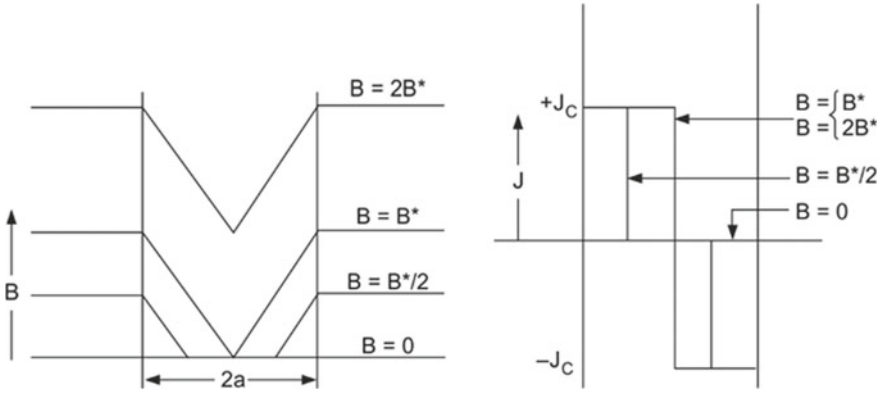

Fig. 2.45 Local field (**a**) and critical current density (**b**) configuration in a hard superconductor for increasing external field, $B = 0$, $B = B^*/2$, $B = B^*$ and $B = 2B^*$ in Bean's model. The J_c is assumed independent of field [29] (With permission from APS) http://journals.aps.org/rmp/abstract/10.1103/RevModPhys.36.31

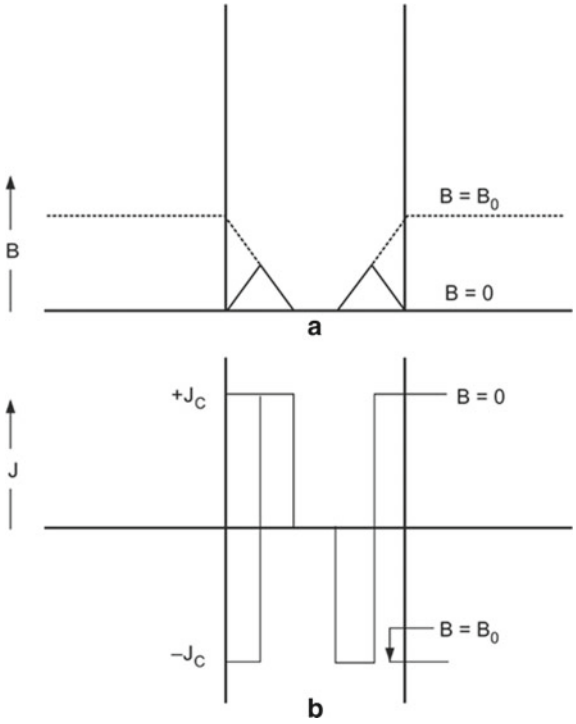

Fig. 2.46 Local fields (**a**) and current density (**b**) configuration in the slab after a field B_0 has been applied and removed [29] (With permission from APS) http://journals.aps.org/rmp/abstract/10.1103/RevModPhys.36.31

electromotive force is generated directed in opposite direction to the one at the time of increasing field. As a result, the surface currents reverse as shown in Fig. 2.46b wherein the two surface sheaths have oppositely directed currents. The remnant flux density or the trapped flux as shown in Fig. 2.46a is exactly half the flux penetration at $B = B_0$.

2.15.8 The Kim Model

Kim et al. [31] generalized Bean's critical state model and assumed that the entire region of the superconductor carries critical current, which is determined only by the local field in the region. They compared experimental data on a thin walled hollow cylinder with theory. When an increasing external field (along the axis) is applied, currents are induced in the surface to counter the field. As the field keeps increasing, current penetrates the specimen deeper inside and eventually reaches a critical state. Any further increase in the field brings down the critical current density. Based upon

their experimental data on hollow Nb–Zr and Nb_3Sn tubes, they postulated that the critical state is a body current in saturation and the concept of critical current applies to each macroscopic part of the sample. This critical current density is unique and a function of local magnetic field only. The state of magnetization can then be determined from this unique $J_c(B)$. A rapid sweep in the magnetic field in critical state generates an electric field, which may result in a normal current flow and heating. The heating is found severe in regions where the magnetization curve is steep. This is supported by experiments which indicate that a critical state is difficult to be realized when the magnetization curve is steep. This implies that going from one critical state to another is very difficult unless the heat generated by the normal current is dissipated away fast. If the heat removal is not fast enough, the raise in temperature might quench a part of the superconductor, which in turn will generate more heat. Since this additional heat is proportional to M^2, flux jumps have been found frequent in materials with large magnetization. This is the primary reason why the critical state is difficult to be realized in bulk material of large dimensions. Another interesting result of Kim model is that Lorentz force is an important parameter for the determination of the critical current density. They found a simple relationship

$$\alpha(T) = J_{cr}(B + B_0) \tag{2.48}$$

where $\alpha(T)$ and B_0 are constants. Parameter $\alpha(T)$ is structure sensitive and strongly dependent on temperature. The strong temperature dependence of $\alpha(T)$ and the fact that the critical current decays slowly in hard superconductors prompted Anderson [32, 33] to propose the theory of 'flux creep' in these materials.

We will return to the problem of flux jumping in detail in Chap. 5 (Conventional Practical Superconductors) and describe how the problem has been solved successfully by providing stability to the conductors carrying several *kA* current.

2.15.9 Flux Creep

Anderson built up over the critical state model proposed by Bean and modified by Kim and argued that if the critical current J or the field B exceed the critical values in equation 2.48, flux bundles leak through the material and the material returns to critical state. Flux lines closer than London's penetration depth may be considered bound together via their mutual field interaction and move as flux bundle of dimension ~ 10^{-5} to 10^{-6} cm. This flux motion has been termed [32] as 'flux creep'. Anderson gave a theory [32, 33] of flux creep in terms of the thermally activated movement of flux bundle caused by an interplay between the Lorentz force ($J \times B$) and pinning force. The flux movement is viscous and highly dissipative. Even when the pinning force exceeds the driving force ($F_{\mathbf{P}} > F_{\mathbf{L}}$), at a finite temperature ($T > 0$ K) the flux bundles may still hop from one pinning centre to another or from one potential well to another potential well. This is because by the thermal energy associated with the driving force of flux density gradient may force the flux bundles to move. Flux

creep is revealed in two ways. One, the trapped magnetic flux shows a slow variation leading to a logarithmic decay [33] of flux with time (t) as

$$\partial B \propto k_B \ln(t) \tag{2.49}$$

This creep is unobservable slow unless the flux density gradient is close to the critical value. Second, the flux creep leads to a longitudinal resistive voltages caused by the drifting of the flux bundles under the influence of current flow through the conductor. This voltage is proportional to the average creep velocity of the flux bundle.

The theory of Anderson clearly establishes a marked variation of J_c with temperature in the range of 0.5–0.1 T_c. The movement of flux bundles is blocked at the pinning centres by an energy barrier (potential well). When a field is applied, the flux density in the material is not uniform because of this pinning. In the presence of a transport current, the Lorentz force exerts a force on the flux bundles and modifies the local free energy which turns the barrier structure spatially 'downhill' direction in a 'stair case' style. At finite temperature below T_c, the flux bundle jumps over the barrier under thermal excitation. The bundle jumps at the rate

$$\nu = \nu_0 \exp[-U(B, T, J)/k_B T] \tag{2.50}$$

where ν_0 is a characteristic frequency of flux bundle vibration assumed to be 10^5–10^{11} s^{-1} and $U(B, T, J)$ is the activation free energy.

In high T_c oxide superconductors (HTS), to be introduced in the next chapter, the problem of thermally activated flux creep has been found [34–37] to be severe. Several models based upon the classical theory have been developed. Two models, namely the 'giant flux creep model' [34] and the 'thermally assisted flux flow model' [38] assume that all HTS materials have intrinsically low pinning barriers $(U_0/k_B T_c) < 10$. Here U_0 is the effective pinning potential height and $k_B T_c$ is the thermal energy. The studies have shown that the relaxation is considerably faster in HTS in comparison with the conventional superconductors, though the logarithmic law is followed in both the types of materials. In HTS single crystals, the value of U_0 has been found [34] to be 0.02 eV, which is about two orders of magnitude smaller than in conventional metallic superconductors. On the other hand, the expected temperature of 77 K for the operation of HTS is high. This makes the height of the pinning barrier $(U_0/k_B T_c)$ extremely small, which results in 'giant flux creep'. The value of U_0 in practical HTS conductors has been increased significantly by introducing suitable effective pinning centres.

2.15.10 Critical Current by Magnetization Method

It is possible to calculate critical current density J_c through the magnetization method using Bean Model [28, 29]. Following expression can be used to calculate J_c from

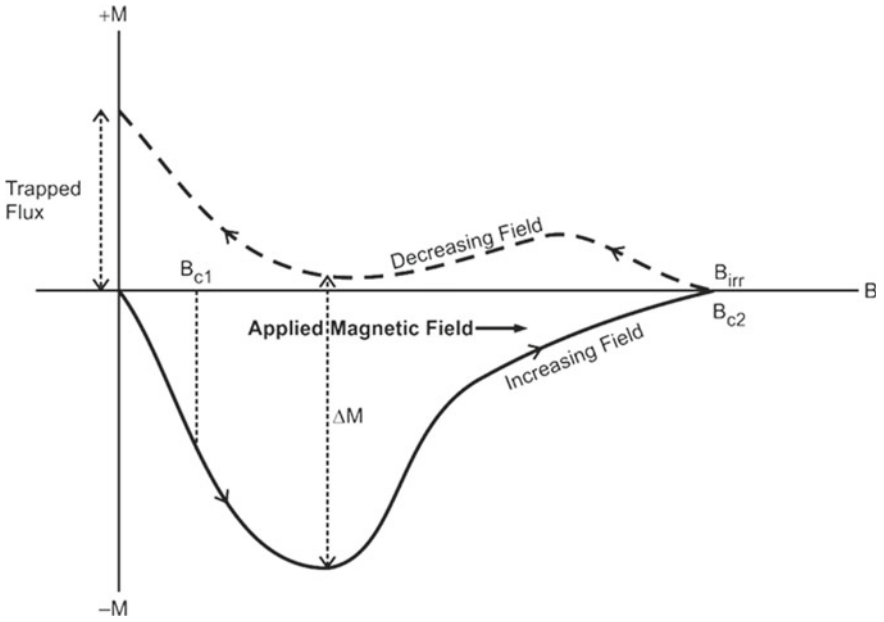

Fig. 2.47 A typical *M–B* plot of a inhomogeneous type II superconductor. J_c can be calculated from the measured ΔM value using the expression (2.52)

the measured magnetization in increasing and decreasing magnetic field (Fig. 2.47):

$$J_c = 2(M_+ - M_-)/d = 1.59 \times 10^6 \mu_0 \Delta M/d \tag{2.51}$$

where J_c is in A/m^2, $\mu_0 \Delta M = \mu_0(M_+ - M_-)$ is in tesla and d is the diameter of the sample grain in metres. The equation in cgs units reduces to:

$$J_c = 20 \Delta M/d \quad \left(\text{A/cm}^2\right) \tag{2.52}$$

where d is in cm.

2.16 Surface Superconductivity—Critical Magnetic Field B_{c3}

Saint James and de Gennes [39] in 1963 deduced theoretically that in a finite size-superconducting specimen superconductivity exists close to the surface of the superconductor in contact with a dielectric, including vacuum in field higher than B_{c2}. This new critical field is termed as B_{c3}, which is 1.695 times B_{c2}. The bulk material though is normal. This superconducting surface layer is found to occur in superconductors

with $\kappa > 0.42$ and usually in type II superconductors. B_{c3} depends upon the angle the applied field makes with the surface. It has a maximum value if the field happens to be parallel to the surface and is given by

$$B_{c3} = 2.4\,\kappa\, B_c = 1.7 B_{c2} \tag{2.53}$$

B_{c3} decreases with the angle and is minimum when the applied field is perpendicular to the surface. B_{c3}(min) reduces to B_{c2} for type II superconductors. An indicative magnetic phase diagram (B–κ plots) incorporating B_c, B_{c1}, B_{c2} and B_{c3} has been shown in Fig. 2.48. A type II superconductor now has superconducting state, mixed state, surface superconductivity and the normal state at different field values. Since surface superconductivity occurs for materials with $\kappa > 0.41$ the phenomenon is observed even in Type I superconductors. For example, in Pb, κ increases from 0.37 (at $T_c = 7.3$ K) to a value of 0.58 at $T < 1.4$ K and surface superconductivity is indeed observed. Surface superconductivity is observed at the interface of the material and a dielectric (or vacuum). Surface superconductivity does not occur at the interface of the superconductor and a metal. So, no surface superconductivity is observed if a type II superconductor is coated with metal. For field higher than B_{c2}, the surface layer shrinks to two strips along the length of the specimen. Close to B_{c3}, these

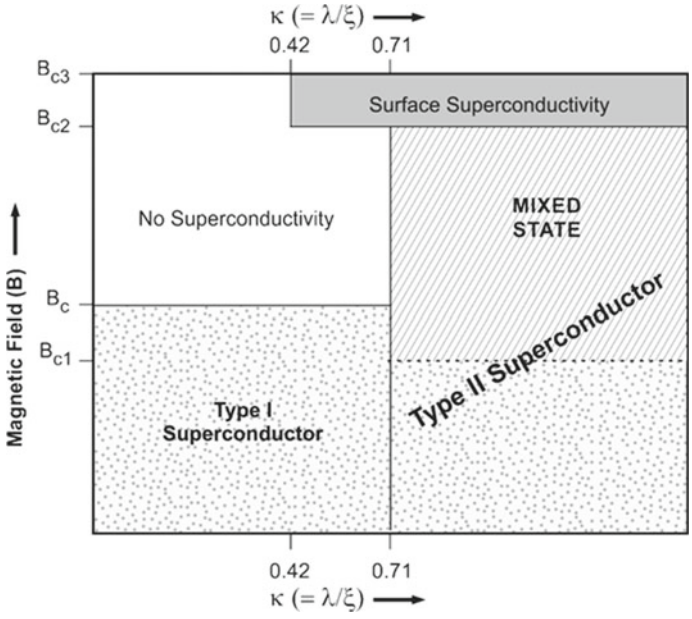

Fig. 2.48 An indicative magnetic phase diagram of a superconductor in contact with a dielectric, showing B–κ plots for B_c, B_{c1}, B_{c2} and B_{c3} and the existence of surface superconductivity for $\kappa > 0.42$

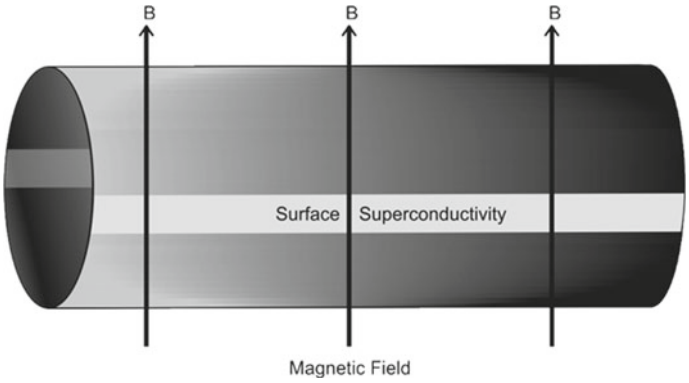

Fig. 2.49 For perpendicular field greater than B_{c2} surface superconductivity reduces to two strips parallel to the two sides of the specimen

strips reduce to just two lines where the field happens to be parallel to the surface (Fig. 2.49).

2.17 Paramagnetic Limit

B_{c2} in type II though is high and still increases at reduced temperatures but cannot be increased open-endedly, even if κ too is made high. In fact, the B_{c2} of the best-known superconductor is limited to a value much smaller than the predicted one. In high magnetic field, the electron spins tend to align themselves along the direction of the field. This lowers the magnetic energy considerably, which is not conducive to superconductivity that envisages anti parallel spins to form Cooper pairs. At high enough field, it may be energetically favourable for the material to go to normal paramagnetic state rather than remaining in a superconducting state. Experimentally, the highest value of B_{c2} has been found limited to what is known as the paramagnetically limited field, $B_p = 1.6 \times 10^6\ T_c$ (A m^{-1}) beyond which superconductivity does not exist, irrespective of how large is the value of κ.

References

1. H.K. Kamerlingh Onnes, Commun. Physics Lab. Univ. Leiden **29** (Nov 1911)
2. W. Buckel, R. Kleiner, *Superconductivity Fundamental and Applications* (Wiley_VCH Verlag GmbH & Co KGaA, Weinheim, 2004)
3. F.B. Silsbee, J. Wash. Acad. Sci. **6**, 597 (1916)
4. W. Meissner, R. Ochsenfeld, Naturewissenschaften **21**, 787 (1933)
5. C.J. Gorter, H.B.G. Casimir, Phys. Z. **35**, 963 (1934)
6. W.H. Keesom and J.v.d. Ende, Comm. Leiden, 219b

7. W.H. Keesom, J.A. Kok, Comm. Leiden, 221e and Physica **1**, 175 (1934)
8. D.H. Douglass Jr., L.M. Felicov, Prog. Low Temp. Phys. **4**, 97 (1964)
9. P.L. Richards, M. Tinkham, Phys. Rev. **119**, 575 (1960)
10. E. Maxwell, Phys. Rev. **78**, 477 (1950)
11. C.A. Reynold, B. Serin, W.H. Wright, L.B. Nesbitt, Phys. Rev. **84**, 691 (1951)
12. F. London, *Superfluids*, vol. **1** (Willey, 1950)
13. B.S. Deaver Jr., W.M. Fairbank, Phys. Rev. Lett. **7**, 43 (1961)
14. R. Doll, M. Nabauer, Phys. Rev. Lett. **7**, 51 (1961)
15. J. Bardeen, L.N. Cooper, J.R. Schrieffer, Phys. Rev. **108**, 1175 (1957)
16. A.B. Pippard, Physica **19**, 765 (1953)
17. A.C. Rose-Innes, E.H. Rhoderidz, "Introduction to Superconductivity" Copyright © Pergamon Press, Library of Congress Catalog Card No. 79-78591 (1969)
18. I. Giaever, Phys. Rev. Letters **5**, 464 (1960)
19. I. Gaiever, K. Megerle, Phys. Rev. **122**, 1101 (1961)
20. B.D. Josephson, Phys. Lett. **1**, 251 (1962)
21. P.W. Anderson, J.M. Rowell, Phys. Rev. Lett. **10**, 230 (1963)
22. J. Clarke, *Physics Today*, **24**, 30 (August, 1971)
23. J. Clarke, *Scientific American*, **271**, 46 (August, 1994)
24. A.A. Abrikosov, ZhETF **32**, 1442; Sov. Phys. JETP **5**, 1174 (1957)
25. J.W. Ekin, J. Appl. Phys. **49**, 3406 (1978)
26. J.W. Ekin, A.F. Clark, J.C. Ho, J. Appl. Phys. **49**, 3410 (1978)
27. R.G. Sharma, Y. Tanaka, K. Tachikawa, Cryogenics **25**, 381 (1985)
28. C.P. Bean, Phys. Rev. Lett. **8**, 250 (1962)
29. C.P. Bean, Rev. Mod. Phys. **36**, 31 (1964)
30. K. Mendelssohn, Proc. Roy. Soc. (London) **A152**, 34 (1935)
31. Y.B. Kim, C.F. Hemstead, A.R. Strnad, Phys. Rev. **129**, 528 (1963)
32. P.W. Anderson, Phys. Rev. Lett. **9**, 309 (1962)
33. P.W. Anderson, Y.B. Kim, Rev. Modern Phys. **36**, 39 (1964)
34. Y. Yashurun, A.P. Malozemoff, Phys. Rev. Lett. **60**, 2202 (1988)
35. T.T.M. Palstra, B. Batlogg, L.F. Schneermeyer, J.V. Waszczak, Phys. Rev. Lett. **61**, 1662 (1988)
36. D. Shi, M. Xu, A. Umezawa, R.F. Fox, Phys. Rev. **B42**, 2026 (1990)
37. Y. Yashrun, A.P. Malozemoff, T.K. Warthington et al., Cryogenics **29**, 258 (1989)
38. P.S. Kes, J. Aarts, J. van der Berg et al., Supercond. Sci. Techno. **1**, 242 (1989)
39. D. Saint James, P.G. de Gennes, Phys. Lett. **7**, 306 (1963)

Chapter 3
High-Temperature Cuprate Superconductors and Later Discoveries

Abstract The discovery of superconductivity at 30 K in an oxygen deficient $La_4Ba_1Cu_5O_{5(3-y)}$ compound by Bednorz and Muller in 1986 marked a turning point in the history of superconductivity. The discovery at last lifted the despondency under which the superconductivity community was reeling since 1973 when a highest T_c = 23 K was recorded in sputtered Nb_3Ge films and the T_c went no further. Chu raised T_c of this compound to 40 K by applying pressure and Cava to 36 K after substituting Sr at the La site. A breakthrough came in early 1987 when Wu and Chu announced a record $T_c = 93$ K in $Y_1Ba_2Cu_3O_7$. T_c thus crossed the 77 K mark first time. Soon Maeda discovered superconductivity at 110 K in another cuprate of the type $Bi_2Sr_2Ca_2Cu_3O_{10}$ (Bi-2223 with 3 CuO_2 layers). These layered curates have large anisotropy. The superconductivity is strong in the a-b planes (CuO_2 layers) and weak along the *c*-axis. Critical parameters B_{c2} and J_c too are high in the *a–b* plane and low along *c*-direction. Both the materials, Bi-2223 and YBCO are produced commercially and used for selected applications. The new improved 2G YBCO wires are coated thin film conductors produced by employing sophisticated techniques and getting popularity among the community. Two more cuprates with still higher T_c and analogous to Bi-system were discovered. A $T_c = 125$ in $Tl_2Ca_2Ba_2Cu_3O_x$ (Tl-2223) and 135 K in $Hg_1Ba_2Ca_2Cu_3O_{6+\delta}$ (Hg-1223) were reported. These materials were, however, not pursued for commercial production because of the toxicity involved. Superconductivity was also discovered in MgB_2 at 39 K by Nagamatsu in 2001. MgB_2 behaves like a BCS superconductor but is characterized by two widely differing energy gaps, namely, 6.8 meV and 1.8 meV, two coherence lengths (13 and 51 nm) and two penetration depths (47.8 and 33.6 nm), respectively. This hinted at the presence of two species of electrons (σ bonding and π bonding) forming Cooper pairs. The material has low anisotropy of upper critical field $\left(\frac{B_{c2}^{ab}}{B_{c2}^{c}} = 1.1 - 1.7\right)$, high critical field, B_{c2} of up to 60 T and irreversible field B_{irr} up to 40 T. MgB_2 carries large self-field as well as in-field critical current at 20 K. One more surprise came when Hosano reported superconductivity in iron-based oxypnictides of the type LaFeAsO 1111 at 26 K. T_c in excess of 50 K were reported in Sm and Nd-based pnictides. The strategy adopted to enhance T_c has been to dope the insulating La_2O_2 layer suitably whereby a charge, electron/hole is transferred to the Fe_2As_2 conduction layer. Thus, a $T_c = 38$ K was reported in a K-doped $(Ba_{0.6}K_{0.4})Fe_2As_2$ 122 compound. Record high $T_c = 203$ K has been reported in sulphur hydride which has been found to be

R. G. Sharma, *Superconductivity*, Springer Series in Materials Science 214,
https://doi.org/10.1007/978-3-030-75672-7_3

a BCS superconductor. More recently, a $T_c = 288$ K (15 °C) has been reported in a C-S-H compound under a pressure of 267 GPa. This value of T_c is almost the room temperature.

3.1 Discovery of Superconductivity in La-Ba-Cu-O System ($T_c = 35$ K)

The search for superconductivity among the elements in the periodical table, in alloys and compounds continued unabated after the discovery of this fascinating phenomenon. Superconductivity was indeed discovered in a variety of families (listed in Table 3.1), but the T_c still remained confined to low value, necessitating the use of liquid helium for operation. The highest T_c was obtained in 1973–1974 in thin films of Nb_3Ge by Gavaler [1] and Tastardi et al. [2] by optimizing the deposition parameters. There was a lull for next 12 years until in 1986 all of a sudden, something very extraordinary happened. Two research scientists at IBM, Zűrich, namely, Bednorz and Muller discovered [3] superconductivity at 30 K in an oxide compound of the type $La_{5-x}Ba_xCu_5O_{5(3-y)}$. The compound was prepared by co-precipitation of the nitrates of La, Ba and Cu taken in appropriate ratios. This was followed by the solid-state reaction at 900 °C in a reduced atmosphere. Samples were finally prepared in the form of pellets sintered at 900 °C. The resistivity behaviour of these samples is shown in Fig. 3.1. Clearly, the resistivity drops with the fall of temperature nearly linearly, then rises logarithmically and then drops sharply by three orders of magnitude. The onset transition temperature is 30 K. Three phases were detected in the material: (i) a cubic phase dependent upon Ba composition, (ii) a superconducting phase $La_{1.8}Ba_{0.2}CuO_4$ and (iii) Perovskite layered phase of the type K_2NiF_4 with $a = 3.79$ Å and $c = 13.2$ Å. The resistivity was found to be changing with measuring sample current indicating that the superconductivity is granular in nature. The material turns out to be an O^{2-} deficient phase with mixed valence Cu constituents, namely, Jahn–Teller ions Cu^{2+} and non-Jahn—Teller ions Cu^{3+} resulting in a large λ (the electron–phonon coupling parameter) and large metallic conductivity. The ideal perovskite La_2CuO_4 structure is shown in Fig. 3.2 is orthorhombic at room temperature and becomes tetragonal at 500 K. Pure La_2CuO_4 is insulating and antiferromagnetic with a Neel temperature of 290 K. Ba and Sr substitute at La sites and the compound $La_{2-x}M_xCuO_4$ shows a T_c of 35 K at M = 0.15 and 0.2 for Ba and Sr, respectively. The doped material has a tetragonal structure at room temperature and turns orthorhombic at 180 K. It was not the first time that superconductivity was observed in oxides. As early as 1973, Johnston et al. [4] reported superconductivity in a Li-Ti-O system with a $T_c = 13.7$ K. The X-ray analysis showed the presence of three crystallographic phases. One phase with a spinel structure had the highest T_c with a comparatively low carrier concentration of $n = 2$–$4 \times 10^{21}/cm^3$. Soon after Sleight et al. [5] reported a $T_c = 13$ K in a mixed valence $BaPb_{1-x}Bi_xO_3$ system which also has a perovskite structure. Strong electron–phonon coupling was believed to be responsible for superconductivity. Prior to the discovery by Bednorz and Muller, scientists had almost given-up hopes of

Table 3.1 Different families of superconductors with corresponding T_c values (most values from [8], Courtesy R. P. Aloysius)

S. No.	Type of superconductor	Example	Max. T_c (K)
1.	Pure elements	Nb	9.2
2	Transition metal alloys	MoRe	12
3	Carbides	NbC	11
4	Nitrides	NbN	15
5	Amorphous superconductors	VGa	8.4
6	Nitrocarbides	$NbN_{0.7}C_{0.3}$	18
7	Laves phase (C-15 structure)	$CeRu_2$	6.1
8	Cheveral phase	$PbMo_6S_8$	12–14
9	A-15 (β-Tungsten)	Nb_3Sn-Nb_3Ge	18–23
10	Organic superconductors	$(TMTSF)_2PF_6$	1 (at 12 kbar)
11	Intercalated superconductors	$TaS_2(C_5H_5N)_{1/2}$	3.5
12	Heavy fermionic superconductors	UPt_3-$CeCoIn_5$	0.48–2.3
13	Magnetic superconductors	$ErRh_4B_4$	8.6
14	Semimetal superconductors	La_3Se_4	10
15	First oxide superconductors	$BiPb_{1-x}Bi_xO_3$	13 ($x = 0.25$)
16	K-doped Ba-Bi oxide, supercond.	$(Ba_{0.6}K_{0.4})BiO_3$	31.5
17	Boro-carbides	YNi_2B_2C	15
18	Rare earth cuperates	$YBa_2Cu_3O_{7-\delta}$	92
19	Lanthenate (discovery of high-T_c superconductor)	$La_{5-x}Ba_xCu_5O_{5(3-y)}$	35
20	Bismuth oxide superconductors (Bi-2223)	$Bi_{1.7}Pb_{0.4}Sr_{1.8}Ca_2Cu_{3.5}O_y$	110
21	Mercury oxide superconductors (Hg-1223)	$HgBa_2Ca_2Cu_3O_{8+\delta}$	155 (15 GPa)
22	Thallium oxide superconductors (Tl-2223)	$Tl_2Ca_2Ba_2Cu_3O_x$	125
23	Fullerides	Rb_2C_{60}	45
24	Magnesium diboride	MgB_2	39
25	Iron pnictides	$NdFeAsO_{0.82}F_{0.18}$	51
26	F-doped La-Fe-As compounds	$NdFeAsO_{0.82}F_{0.18}$	55 K
27	Iron chalcogenides	$Tl_{0.6}Rb_{0.4}Fe_{1.67}Se_2$	33

achieving high T_c in superconductors under the belief of the theoretical predictions made around the time. On the basis of the BCS theory even with highest values of the electron density of state and the electron–phonon coupling parameter, the T_c would not go beyond 30 K. What happened after the publication of the celebrated paper by Bednorz and Muller was something unprecedented and quite unexpected. Superconductivity was reported in oxide systems one after another with higher and

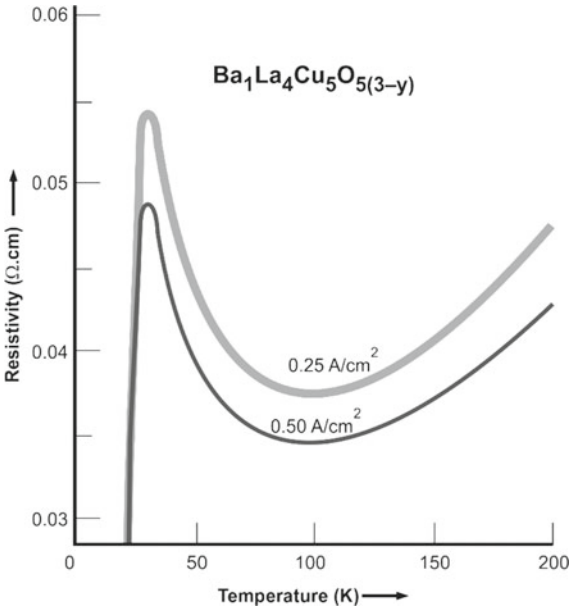

Fig. 3.1 Electrical resistivity plotted against temperature for the compound $La_4Ba_1Cu_5O_{5(3-y)}$. Superconducting transition occurs at ~ 30 K and the resistivity shows variation with measuring current [3]. With permission of Springer Science + Business Media

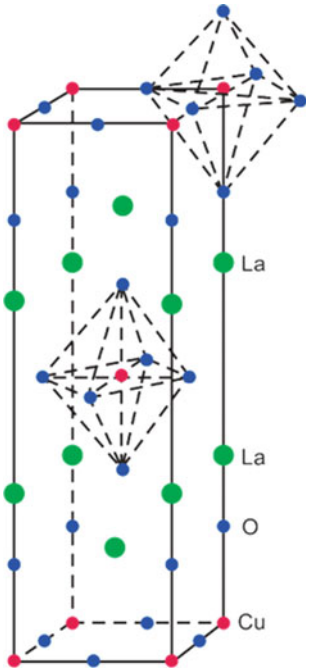

Fig. 3.2 Ideal La_2CuO_4 (K_2NiF_4) crystal structure. Superconductivity sets in with Ba/Sr substitution at the La site

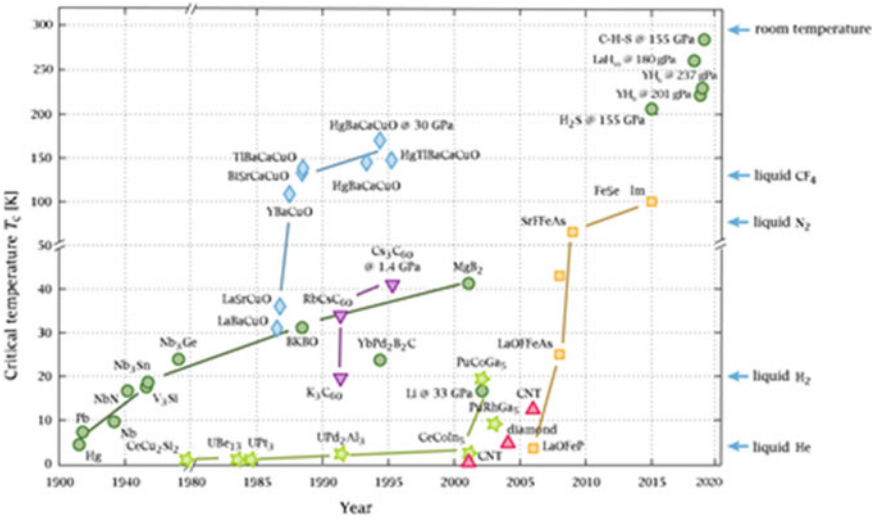

Fig. 3.3 Transition temperature (T_c) versus the year of discovery of the superconductor. The curve rose sharply in 1987 with the discovery of cuprates, in 2008 in iron based superconductors and in 2015 in sulphur hydride. Green circles are BCS superconductors, green stars heavy fermions, red triangles carbon allotropes, purple triangle buckminsterfullerenes, orange squares are iron–pnictogens and the blue diamonds are the cuprates. (Adapted from PJ Ray—CC BY-SA 4.0)

higher transition temperature, climbing well above the liquid nitrogen temperature (77 K) mark. Within a couple of years, T_c rose to as high as 150 K making the T_c/year graph rising almost exponentially (Fig. 3.3).

Chu et al. [6] at the University of Houston raised the T_c of the compound $(La_{0.85}Ba_{0.15})_2CuO_{4-y}$ from 36 K at ambient pressure to 40 K after applying a pressure of 13 K bar. Cava et al. [7], on the other hand, partially replaced La by Strontium replicating chemical pressure. The compound studied had the chemical composition $La_{1.8}Sr_{0.2}CuO_4$. Undoped La_2CuO_4 structure is slightly orthorhombic distortion of K_2NiF_4, all the copper ions are in Cu^{2+} state and no superconductivity is observed down to 4.2 K. Substitution of La by Sr stabilizes tetragonal undistorted K_2NiF_4 and oxidizes some Cu to Cu^{3+} state resulting in a mixed valence compound. The compound had been annealed in air as well as in oxygen [7]. Sample annealed in air revealed the presence of a mixture of a metallic phase, a semiconducting phase and a superconducting phase. Oxygen anneal on the other hand leads to a metallic and a superconducting phase. Oxygen anneal also improves the onset T_c from 36.5 to 38.5 K. Thus, Sr and oxygen both are important for the oxidizing condition. Oxygen pressure influences Cu^{3+}/Cu^{2+} valence ratio as well as charge compensation by O-vacancies.

The discovery of superconductivity by Bednorz and Műller in an oxide system opened the flood gate to the discovery of a larger family of oxide systems containing copper. Many superconductors containing Cu-O layers, now called cuprates with higher and higher T_c values rising far above the boiling temperature of nitrogen, 77 K

were discovered. This evoked great excitement among the scientific community of all shades who hoped that an engineering revolution will soon take place where the conventional superconductors used in large-scale applications will be replaced by these oxide superconductors. Although the hope of using these superconductors at 77 K for producing high magnetic fields has not been realized, yet selected cuprates have been produced commercially and are being increasingly used in a variety of power applications where high-current densities in presence of high magnetic field are not required. They have nevertheless been found suitable for high-field production, when operated below 65 K. A vast family of cuprate superconductors is tabulated along with their T_c values in Table 3.2.

Below we briefly discuss the discovery of important superconductors that surpassed the T_c of the previous superconductors.

3.2 The Y-Ba-Cu-O (YBCO) System—First Superconductor with T_c Above 77 K

A real breakthrough occurred in the history of superconductivity in March 1987 when Wu et al. [9] discovered superconductivity in a $Y_1Ba_2Cu_3O_{7-x}$ (or simply YBCO or also called just Y123) system at a T_c of 93 K making it possible first time to cool down a superconductor below its T_c using liquid nitrogen instead of liquid helium. Figure 3.4 shows the resistivity/temperature plots at different magnetic field reported by Wu et al. [9]. The superconducting phase was identified to be $Y_1Ba_2Cu_3O_7$ which is an oxygen deficient triplet perovskite unit cell of the type ABO_3. The triplet cell would have been $(Y_1Ba_2)Cu_3O_9$ but the superconducting phase is oxygen deficient that is, $Y_1Ba_2Cu_3O_7$ and has a $T_c = 93$ K. $Y_1Ba_2Cu_3O_7$ has an orthorhombic distorted structure and is shown in Fig. 3.5. Clearly, Cu ion has two distinct crystallographic and dissimilar sites Cu(1) and Cu(2). Cu(1) is surrounded by a squashed square planar O configuration in the *b*–*c* plane and linked to similar sites in a one dimension along the *b*-axis. Cu(2) site is 5 coordinated by a square pyramidal arrangement of O. The vertex of the pyramid is at O(4) site along the *c*-axis. The Y ion is at the centre of the two Cu-O sheets eight O-coordinated and Ba 10 O-coordinated. We thus find that Cu-O network is important for cuprates. Cu(1)–O(1) chains are crucial to superconductivity in this material. Cu(2)–O(2) and Cu(2)–O(3) do not seem to be so crucial for 90 K transition.

Cu(1)–O(4) bond is much stronger than Cu(1)–O(1), bond lengths being 1.85 Å and 1.943 Å, respectively. Oxygen vacancies occur on O(1) sites easily which brings down the transition temperature. At stoichiometric O_7, copper exists in divalent and trivalent state as per the expression below:

$$\text{At } O_7 \; Y_1Ba_2Cu_3O_7 \Rightarrow Y^{3+}Ba_2^{2+}Cu^{3+}(1)Cu_2^{2+}(2)O_7^{2-} \tag{3.1}$$

Table 3.2 Large variety of cuprate superconductors with their T_c values. 'n' represents the number of CuO_2 layers in the compound

S. No.	Compound	T_c (K)
1	$La_{1.85}(Ba/Sr)_{0.15}CuO_4$	35
2	$La_2CuO_{4+\delta}$	45
3	$La_{1.6}Sr_{0.4}CaCu_2O_{6+\delta}$	60
4	$Y_1Ba_2Cu_3O_7$	92
5	$Y_1Ba_2Cu_3O_8$	82
6	$TlBa_2Ca_{n-1}Cu_nO_{2n+3}$	120 ($n = 3$)
7	$TlBa_2Ca_{n-1}Cu_nO_{2n+4}$	127 ($n = 3$)
8	$Bi_2Sr_2Ca_{n-1}Cu_nO_{2n+4}$	110 ($n = 3$)
9	$HgBa_2Ca_{n-1}Cu_nO_{2n+2+\delta}$	134 ($n = 3$)
10	$CuBa_2Ca_{n-1}Cu_nO_7$	120
11	$Sr_2Ca_{n-1}Cu_nO_4$	90
12	$Pb_2Sr_2(Ca,Y,Nd)Cu_3O_8$	70
13	$Pb_2(Sr,La)_2Cu_2O_6$	32
14	$PbBaSrYCu_3O_8$	50
15	$(Pb,Cu)(Ba,Sr)_2(Y,Ca)Cu_2O_7$	53
16	$Pb_{0.5}Sr_{2.5}(Y.Ca)Cu_2O_7$	104
17	$(Pb,Cu)(Sr,La)_2CuO_5$	32
18	$(Nd,Ce)_2CuO_{4-\delta}$	24
19	$(Nd,Ce,Sr)CuO_{4-\delta}$	28
20	$(Pb,Cu,Eu,Ce)_2(Sr,Eu)_2Cu_2O_9$	25
21	$(EuCe)_2(Ba,Eu)_2Cu_3O_{10}$	43
22	$Bi_2Sr_2(Gd,Ce)_2Cu_2(CO_3)O_7$	34
23	$Tl_{0.5}Pb_{0.5}Sr_4Cu_2(CO_3)O_7$	70
24	$(BaSr)_2CuO_2(CO_3)$	40
25	$Sr_{4-x}Ba_xTlCu_2(CO_3)O_7$	62
26	$Tl_{0.5}Pb_{0.5}Sr_2Gd_{2-x}Ce_xCu_2O_{9-\delta}$	45
27	$NbSr_2(Gd,Ce)_2Cu_2O_y$	27
28	$Bi_2Sr_{6-x}Cu_3O_{10}(CO_3)_2$	40
29	$(Cu_{0.5}C_{0.5})Ba_2Ca_{n-1}Cu_nO_{2n+3}$	117 ($n = 4$)
30	$YCaBa_4Cu_5(NO_3)_{0.3}(CO_3)_{0.7}O_{11}$	82
31	$CuSr_{2-x}La_xYCu_2O_7$	60
32	$GaSr_2Ln_{1-x}Ca_xCu_2O_7$	73
33	$(C_{0.35}Cu_{0.65})Sr_2(Y_{0.73}Ce_{0.27})_2Cu_2O_x$	18
34	$Bi_4Sr_4CaCu_3O_{14+x}$	84

Data from [8], Courtesy R.P. Aloysius

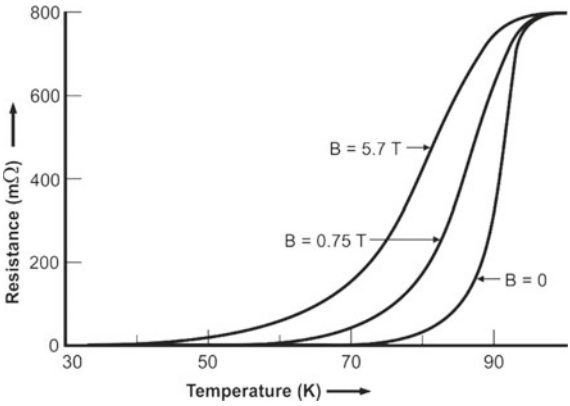

Fig. 3.4 Resistivity/temperature plot of Y-Ba-Cu-O at different magnetic fields by Wu et al. [9]. With permission from APS. http://journals.aps.org/prl/abstract/10.1103/PhysRevLett.58.908

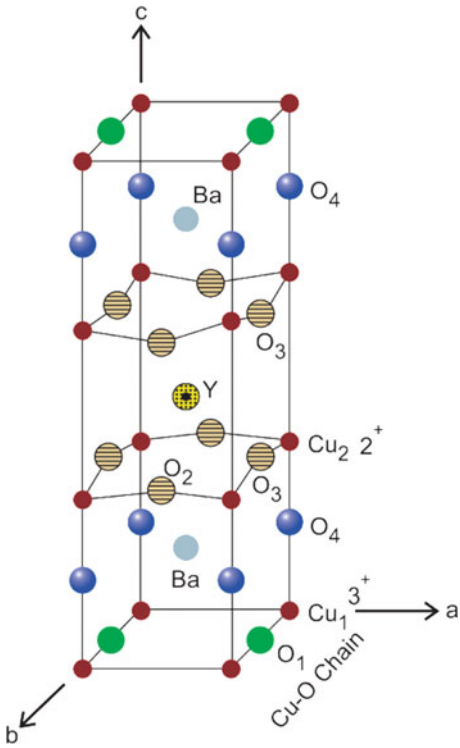

Fig. 3.5 Crystal structure of $Y_1Ba_2Cu_3O_7$. Notice two Cu-O sheets in the *a*–*b* plane sandwiching Y-atom and the Cu-O chains along the *b*-axis.

Oxygen depletion leads to change in structure from orthorhombic to tetragonal. T_c starts decreasing with oxygen loss and so does the oxidation state of Cu. As O-content decreases from 7 to 6.5, T_c decreases from 93 to 55 K and Cu(1) and Cu(2) are in divalent state. At O = 6.5, the material becomes semiconducting. In fact, there is a plateau in the T_c versus O-content curve at $O_{6.5}$. As O-content decreases further,

T_c decreases too and at O = 6, and the material turns in to an insulator. The oxidation state of Cu reduces to univalent. The oxidation states of Cu at O_6 and $O_{6.5}$ can be expressed like this:

$$\text{At } O_{6.5} \quad Y_1Ba_2Cu_3O_{6.5} = Y^{3+}Ba_2^{2+}cu^{2+}(1)Cu_2^{2+}(2)O_{6.5}^{2-} \tag{3.2}$$

$$\text{At } O_6 \quad Y_1Ba_2Cu_3O_6 = Y^{3+}Ba_2^{2+}Cu^{1+}(1)Cu_2^{2+}(2)O_6^{2-} \tag{3.3}$$

There is a striking correlation between the T_c and the oxidation state of Cu. T_c is found to be maximum when the oxidation state of Cu is $^{+}2.2$ which is found to correspond to O_7 stoichiometry. Both T_c and the copper oxidation state scales with the oxygen stoichiometry almost identically as seen from Fig. 3.6. T_c thus seems to be strongly dependent on the valence state of Cu which is controlled by the oxygen stoichiometry. One can explain this correlation between the valence state and T_c on the basis of the so-called charge transfer model. A detailed crystal structure of YBCO system, a repeat unit cell, is shown in Fig. 3.7. The CuO_2 planes sandwiching the Y-atom constitute the conduction layers. These double CuO_2 planes are separated by the so-called charge reservoir layers or the intercalating layers which consists of metal-oxygen layers of Cu, Ba and oxygen. Many cuprate superconductors have been discovered by manipulating the number of CuO_2 planes, metal atoms in the charge reservoir layer and crystal structure. Quite a few of these cuprates are tabulated along with their T_c values in Table 3.2. YBCO has two Cu-atoms per unit cell in the conduction layer and one Cu-atom in charge transfer layer forming Cu-O chains.

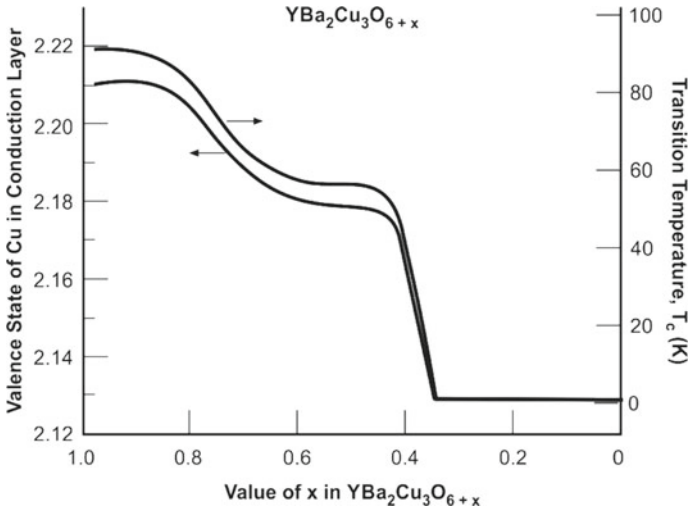

Fig. 3.6 T_c and the valence state of Cu in YBCO plotted against O-contents. T_c decreases as the oxygen content decreases from 7 to 6. Note the similarity in the two curves. Highest T_c occurs at $Cu^{+2.1}$. From my lecture notes, original data source could not be traced

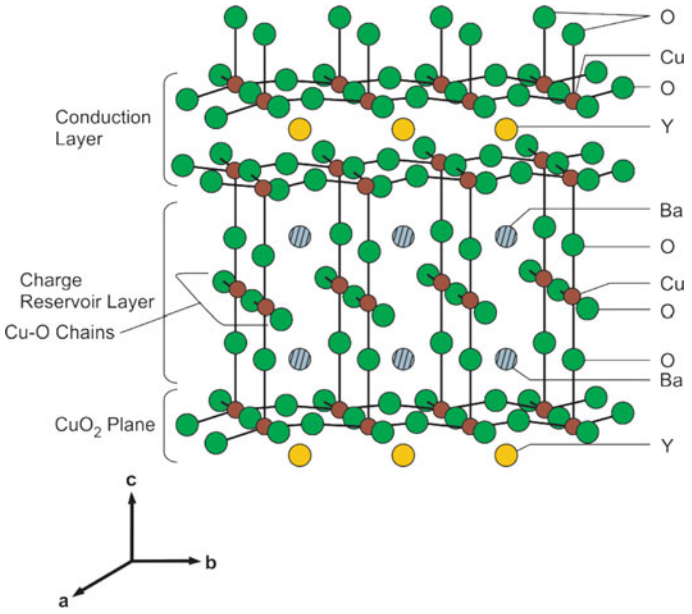

Fig. 3.7 Repeat unit cell structure of $Y_1Ba_2Cu_3O_{7-x}$. The CuO_2 planes on either side of Y-atom are the conduction layers and the Cu-O chains and the Ba-O planes constitute the charge reservoir layers

A reduction of O from 7 to 6 leads to equal distribution of O along the '*a*' and '*b*' axes and the structure changes from orthorhombic to tetragonal. The tetragonal phase is not superconducting. Holes are created in the conduction layers as the electrons are transferred to charge reservoir layers'. This changes the oxidation state of Cu to optimum value ($Cu^{+2.1}$) in the conduction layer causing the material to turn superconducting.

Even though YBCO remains to be the most studied and developed system, yet Y can be replaced by almost all the rare earth elements except Pr and Cs yielding this 123 compound with a $T_c = 90$ K. Even the magnetic material Gd yields Gd123 superconductor with $T_c = 90$ K.

3.2.1 Method of Synthesis of YBCO

The most popular technique for synthesizing Y123 is the standard technique of solid-state diffusion [10]. Appropriate quantities of Y_2O_3, $BaCO_3$ and CuO as per the formula unit $Y_1Ba_2Cu_3O_{7-x}$ are mixed thoroughly and ground in a pestle mortar. The fine powder so prepared is calcined at around 900 °C for about 20 h. This powder is finely crushed and calcined again. This process is repeated about three times when a homogenous mixture is obtained. The powder is now pressed in to the form of a pellet

or a bar and sintered at 920 °C for 20–25 h under flowing oxygen. Pieces of desired dimensions can now be cut from this pellet for different types of measurements. It is important to cool the sample slowly from the sintering temperature to have the stoichiometric oxygen (O_7) in the compound. Our experience shows around 60 °C/h. cooling rate is optimum [11]. Fast cooling changes the orthogonal phase in to the tetragonal phase and makes the material non-superconducting. Target pellets are also prepared for thin film deposition following this method. Adequate oxygen supply during the sintering process is essential to get oxygen stoichiometry to 7.0. This becomes rather difficult while supplying oxygen to Ag-clad wires. The author has used successfully an addition of HgO to the bulk YBCO before calcination which provides an internal source of oxygen [12–14]. A perfect O_7 stoichiometry has been obtained using this technique.

3.2.2 Some Peculiar Properties of YBCO

These cuprate superconductors are highly anisotropic materials and have widely different characteristic parameters and properties in the *a–b* plane and along the *c*-axis. Among the family of cuprates YBCO is, however, the least anisotropic. A well-oxygenated stoichiometric YBCO superconductor, for example, has the following typical parameters (Table 3.3).

Another peculiar property observed in these cuprates was the linear variation of the normal state resistivity with temperature down to T_c. This linear ρ–T behaviour in these compounds cannot be explained on the basis of electron–phonon interaction since the mean free path (~ 100–200 Å) is much greater than the lattice parameter (~ 3.8 Å).

Table 3.3 Typical parameters of a stoichiometric $Y_1Ba_2Cu_3O_7$ in the *a–b* plane and along the *c*-axis

Parameter	$Y_1Ba_2Cu_3O_7$
Critical temperature, T_c (K)	93 K
Lattice parameters	$a = 3.8591$ Å $b = 3.9195$ Å $c = 11.8431$ Å
Coherence length (0 K)	ξ_{ab} (0) = 15 Å ξ_c (0) = 3 Å
London penetration depth	λ_{ab} (0) = 1400 Å λ_c (0) = 7000 Å
Normal state resistivity	$\rho_{ab} = 0.5$ mΩ cm and metallic $\rho_c = 20$ mΩ cm and semiconducting

3.2.3 YBCO Wires and Tapes

High hopes were generated, first time, to use this material for high-field superconducting magnets and operate them at 77 K but the results were disappointing. The critical current in bulk YBCO superconductor drops down sharply with the application of magnetic field for a variety of reasons. One important reason is that these materials happen to be granular [10, 15] with grain boundaries which are weakly superconducting or even insulating. High critical current densities have however been reported in epitaxially grown YBCO films [16] and in YBCO single crystals [17]. This resulted in high expectation of developing this material with high critical current densities needed for high-field applications. The critical current within the grain has been found to be quite high ~ 10^6 A cm^{-2} at 77 K. After a few years of intensive research, the focus of R&D activity shifted from research laboratories to industry for their commercial production. American Superconductors, Furukawa, SuperPower and Sumitomo are some leading companies marketing HTS wires, tapes and current leads. 2G YBCO or rather 2G REBCO-coated conductors are increasingly used for power devices like fault current limiter (FCL), transformer and rotating machine. More recently, ingenious methods have been developed to produce REBCO cables capable of carrying tens of kA current. Full details of the fabrication techniques employed to produce these wires and cables will be discussed in Chap. 6 titled 'Practical Cuprate Superconductors'.

3.3 The Bi-Sr-Ca-Cu-O (BSCCO) System

Soon after the discovery of superconductivity in YBCO system at 93 K, Maeda et al. [18] reported superconductivity above 100 K in a Bi-Sr-Ca-Cu-O system, first high-T_c material without a rare earth element. Figure 3.8 shows the redrawn version of the original curve of the resistance versus temperature behaviour of this compound which happens to be a multiphase superconductor. This was the first observation made by Maeda's group on 24 December 1987. An onset of superconducting transition was observed at 114 K with a tendency to go to zero resistivity at 105 K. A second transition is observed showing zero resistivity at 80 K. Their initial attempts to isolate the high-T_c phase failed and they announced the discovery on 21 January 1988. Takano et al. [19], however, succeeded in stabilizing the high-T_c phase (= 110 K) through the partial substitution of Bi by Pb. Further studies established the coexistence of three distinct crystallographic phases, namely the $Bi(Pb)_2Sr_2Ca_2Cu_3O_x$ phase, $Bi_2Sr_2Ca_1Cu_2O_y$ phase and the $Bi_2Sr_2CuO_z$ or simply referred to as Bi-2223, Bi-2212 and Bi-2201 phases with T_c values of 110 K, 80 K and 10 K, respectively. In our laboratory, we have been obtaining phase pure Bi-2223 material by solid-state and also by solution technique with a T_c of 110 K. Best results have been obtained on nominal composition like $Bi_{1.6}Pb_{0.4}Sr_2Ca_{2.2}Cu_{3.5}O_y$ [20] and $Bi_{1.7}Pb_{0.4}Sr_{1.8}Ca_2Cu_{3.5}O_y$ [21] which are rich in Ca and Cu and deficient in

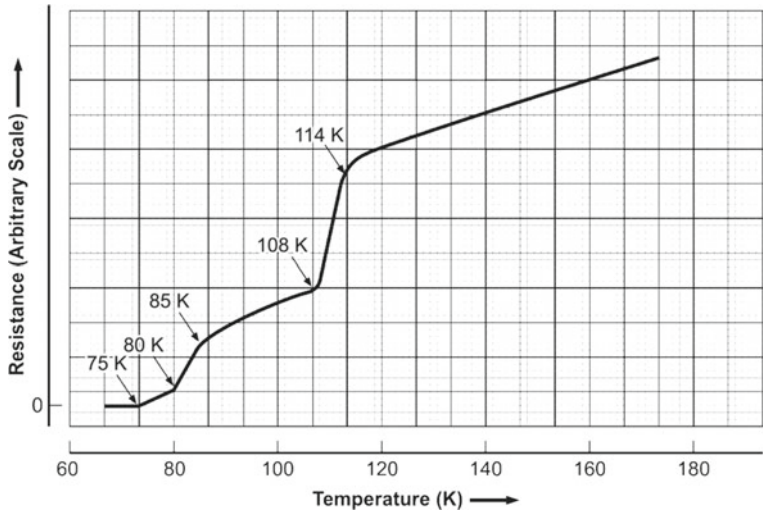

Fig. 3.8 Replicated original resistance versus temperature plot of Bi-Sr-Ca-Cu-O by Maeda et al. The curve shows multiple superconducting transitions at 114, 108 and 85 K [18]

Sr. These Bi-cuprates have orthorhombic structure and have Cu-O layers separated by Sr-O and Ca-O layers and two double Bi-O layers at the two ends of the unit cell. As seen from Fig. 3.9, the *c*-axis increases with the number of Cu-O layers. The *c*-axis is 24.6 Å for the 2201 phase, 30.89 Å for 2212 phase and 37.1 Å for the 2223 phase. There is one Cu-O layer in the 2201 phase, two Cu-O layers in 2212 phase and three Cu-O layers in the 2223 phase. It appears that T_c goes up as the number of Cu-O layers increase. T_c has however been found decreasing if the number of layers increases beyond three. Crystals of Bi-cuprates have mica like morphology. The 80 K Bi-2212 compound show modulation in the ab plane structure with 4b periodicity. The modulation is related to oxygen content and the Bi-O layers but does not play role in superconductivity. Inter-growth of the phases is a problem in the synthesis of Bi-compounds. Sometimes, this intergrowth has been found [21, 22] to provide effective flux pinning enhancing critical current density, J_c in Bi-2223 system.

3.3.1 Bi-2223 Wires and Tapes

Until the arrival of 2G, YBCO-coated tape conductors, Bi-2223 was the only material which has been commercially produced and used in applications like magnets, current leads high-gradient magnetic separators, fault current limiters and the likes. Bi-2223 had been the favourite high-T_c material for manufacturing because one needs to use a simple PIT technique followed by mechanical drawing, rolling and re-bundling

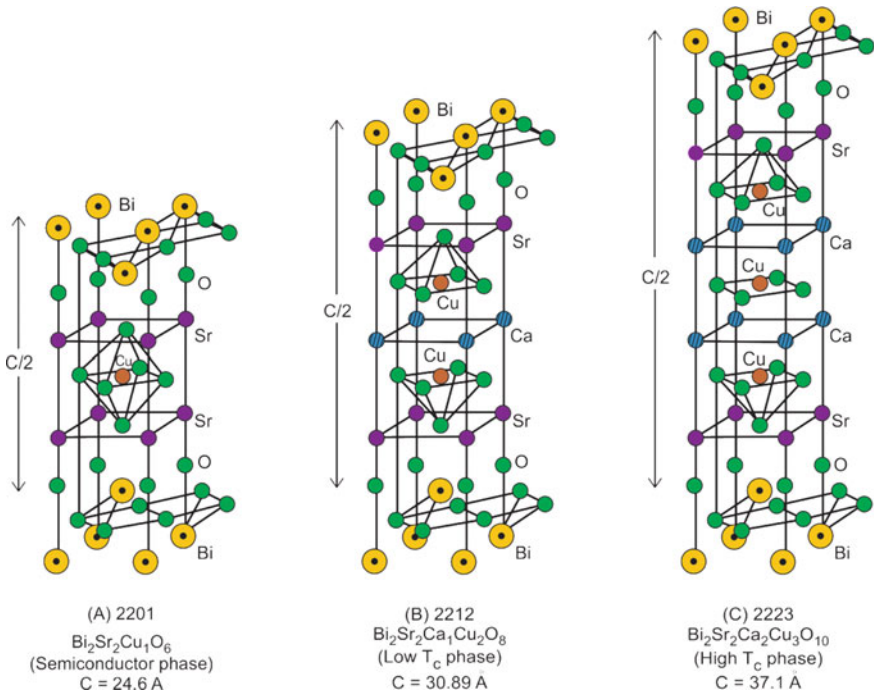

Fig. 3.9 Unit cells of the three Bi-compounds with compositions 2201, 2212 and 2223 having one, two and three Cu-O layers and increasing *c*-axis value, respectively

with intermediate heat treatments. Typical cross section of a circular wire and a rectangular tape with multifilaments are shown in Fig. 3.10. Another more subtle reason is that the *c*-axis grain alignment can easily be achieved when shaped in to the form of tapes. Grain alignment is achieved during the rolling process when compressive stress forces the plate-like Bi-2223 grains to align parallel to the tape surface. Weak link problem is thus minimized in this material. Bi-2212 on the other hand needs heat treatment of the partially melted material followed by solidification after the tape forming to get the grain alignment. NRIM (now NIMS) together with

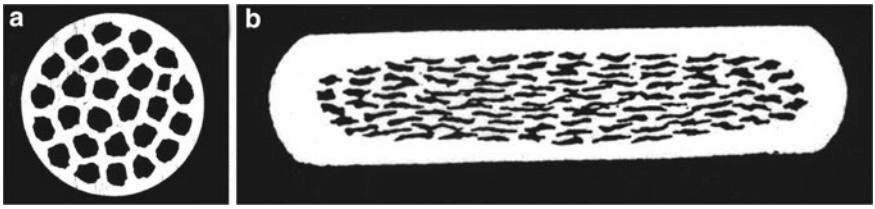

Fig. 3.10 Cross section of the multifilamentary Ag/B(P)SCCO wires and tapes [8]. *Courtesy* R. P. Aloysius

Asahi Glass and Hitachi Cable Group in Japan had produced a field of 21.8 T at 1.8 K by using a Bi-2212 coil [23] as the innermost insert. A background field of 18 T was provided by a combination of Nb-Ti and Nb_3Sn coils. The tapes were fabricated following the doctor-blade technique. More recently, round wires of Bi-2212 have been produced with high J_c by eliminating bubble formation in the grains through over-pressure heat treatment. This will be discussed in detail in Chap. 6.

The problem with high-T_c material is that the critical current density, J_c in these materials drops rather sharply in increased magnetic field when operated at high temperature, 77 K. This is primarily due to the weak pinning at these temperatures and the large anisotropy of J_c. Both are caused by the 2D nature of the structure of BSCCO system. Weakly superconducting or non-superconducting oxide layers separate the CuO_2 layers where the superconductivity resides. When a magnetic field is applied parallel to the layers (along the ab plane), vortices pass through the weakly superconducting layers (charge transfer layers), but CuO_2 layers prevent the vortex movement in the perpendicular direction. This is the new type of pinning force called 'intrinsic pinning' [24]. BSCCO tapes in parallel field configuration can thus be used even at 77 K and still carry significant current. In field parallel to *c*-axis, the vortex is divided into segments by non-superconducting layers because of extremely small coherence length along this axis. This segment is referred to as 'pancake vortex' [25] and is confined within the CuO_2 layer and free to move because it is not strongly connected with the vortex in the next layer. In our initial studies on MF Ag/BSCCO tapes [21], we found a variety of impurity induced defects which probably served good pinning centres in a low purity commercial (CuO 99%) grade material tapes. Figure 3.11a shows dislocation network in a (001) basal plane in a Ag/BSCCO-2223 tape with a core thickness of 140 μm. The same tape is further rolled to small thickness where the core thickness is reduced to 7 μm. As shown in Fig. 3.11b, the

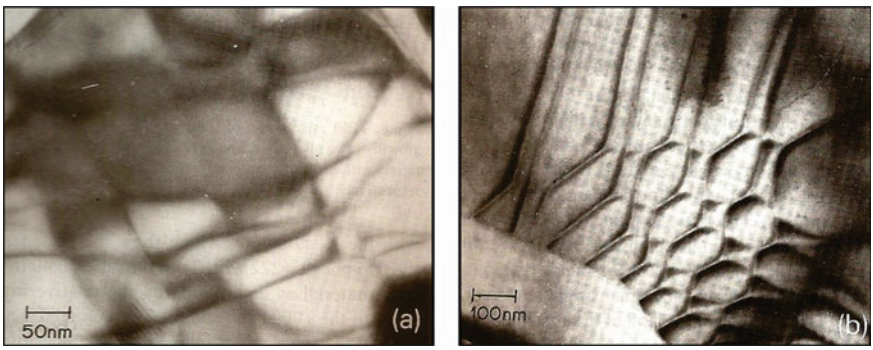

Fig. 3.11 Transmission electron micrographs of the core material of a Ag/BSCCO-2223 tape prepared using commercial grade oxides and carbonates. **a** is a tape with 140 μm thick core and shows dislocation network in (001) basal plane. **b** is the same tape rolled down to a core thickness of 7 μm and re-sintered. The density of dislocation increases in (b) sample. The dislocation network corresponds to the low-angle twist grain boundaries. J_c too increases [21]. With permission from Elsevier

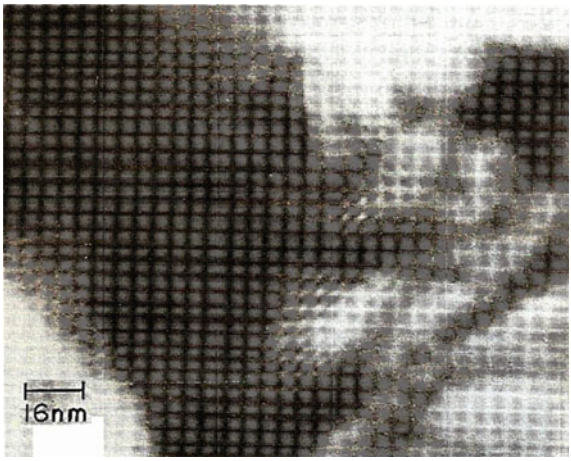

Fig. 3.12 TEM micrograph of (b) sample of Ag/BSCCO-2223 tape, rolled to fine size (7 μm core) and re-sintered, which shows the intergrowth of low T_c (2212) and high-T_c (2223) phases [21]. With permission from Elsevier

dislocation density increases and improves the flux pinning. The dislocation network corresponds to the low-angle grain boundaries. The J_c value of the 7 μm (b) sample is 6.14×10^3 A m^{-2} (77 K, self-field) and 1.49×10^5 A cm^{-2} (4.2 K, self-field). Yet another type of defect structure observed in the (b) sample is the inter-growth of the two phases, viz.; the low T_c (2212) and the high-T_c (2223) phase with a *c*-axis parameters of 30.89 Å and 37.1 Å, respectively. The J_c value after the rolling and re-sintering process is found to increase substantially. The commercial grade CuO (99 %) was found to have 60 ppm Fe which preferentially occupies the Cu(II) square pyramidal site as revealed by Mössbauer studies. This results in stacking faults and the intergrowth of the 2212 and 2223 phases (Fig. 3.12). These defects may be responsible for effective flux pinning and the higher J_c, as observed experimentally.

Among several manufacturers of the Ag/BSCCO wire, American Superconductors (AMSC) of USA and Sumitomo Electric Company (SEC) of Japan were the main players supplying this material for different applications. SEC of Japan had been marketing Ag-matrix clad BSCCO wires in long lengths under the code name DI-BSCCO wires [26]. AMSC mainly supplied two types of wires. One code named 1G-HSP HTS (high-strength plus HTS wire) meant for applications where high mechanical strength was required. This wire had BSCCO-based multifilaments (MF) and was encased in a Ag-alloy matrix with a SS lamination. We will discuss the cuprate wires and cables and their present status in Chap. 6 on 'Cuprate Practical Superconductors'.

3.3.2 First Generation (1G)-BSCCO Current Leads

One most popular use of BSCCO superconductor had been in current leads employed in superconducting magnets both bath-cooled and conduction-cooled. The BSCCO

Fig. 3.13 Bulk and encased current leads marketed by M/S 'Can Superconductors' and used in author's lab (IUAC New Delhi)

current leads capable of transporting current in excess of 3000 A have been commercially marketed for decades now. 'Can Superconductors' of Czech Republic, American Superconductors of USA and Bruker Energy & Supercon Technologies are some of the suppliers of these current leads. Current leads are generally used to transport current from 77 K thermal shield to magnet maintained at ~ 4 K with no Joule heating. Moreover, the thermal conduction through the leads too is poor which makes the magnet system energy efficient. Current carrying capacity almost doubles if the higher temperature end is kept at around 64 K instead of 77 K. Typically, a current lead with $I_c = 1500$ A between 77 and 4 K has a conductive heat leak of 0.6 W, whereas if used between 64 and 4 K the heat leak reduces to only 0.4 W. Current leads can be bulk tube type or encased for protection (Fig. 3.13).

Copper studs or copper braids are provided for jointing/soldering purpose. Figure 3.14 is a 100 A pair of BSCCO-2223 current leads developed [8] by the NIIST, Thiruvananthapuram. The development of BSCCO current leads made it possible to build cryo-free superconducting magnets, which found popularity in low temperature laboratories in last three decades. The reduction in heat generation in the current leads had been so significant that a closed-cycle refrigerator (CCR) with a cooling capacity of 1.5 W can cool a medium size magnet to ~ 3 K in a reasonable time of few hours. In Chap. 9, we will discuss the construction of a cryo-free magnet with a special reference to a 6 T room temperature bore magnet built in author's laboratory using a 1.5 W CCR of Sumitomo make many years ago.

Fig. 3.14 Pair of 100 A, BSCCO-2223 current leads developed by NIIST, Thiruvananthapuram. Leads with higher current rating available [8]. *Courtesy* R. P. Aloysius

3.4 The Tl-Ba-Ca-Cu-O System

The race to discover still higher T_c superconductors continued and yet one more cuprate superconductor of the type Tl-Ba-Ca-Cu-O with T_c of greater than 90 K was discovered by Sheng and Hermann [27] in 1988 itself. The zero resistivity in this compound was obtained at 81 K. Soon a T_c of 120 K was reported by the same authors [28] in a compound $Tl_{1.86}CaBaCu_3O_{7.5+y}$. This was the highest T_c cuprate without a rare earth constituent. Since Tl_2O_3, the ingredient of the compound has a low melting point of 717 °C and starts decomposing at 100 °C, and the preparation method for this compound is different. Sheng and Hermann have followed a 'short high temperature and quenching technique'. Appropriate amounts of $BaCO_3$ and CuO were mixed, ground and heated to 925 °C for > 24 h in air with several intermediate grindings. Black compound like $BaCu_3O_4$ or $Ba_2Cu_3O_5$ is formed during this process. Right amount of Tl_2O_3 was then added, pressed in to a pellet and kept in a tubular furnace already heated to about 900 °C under flowing oxygen. The pellet was kept for 2–5 min and quenched in air to room temperature and used for studies.

Still higher T_c of 125 K was reported [29] in quick succession in the same compound with stoichiometry $TlCa_2Ba_2Cu_3O_x$ (Tl-2223) quite analogous to Bi-2223 compound. The unit cell of this compound is bcc tetragonal containing three Cu perovskite like units separated by bilayers of TlO. T_c ranges between 118 and 125 K depending on the preparation parameters. Another compound with composition $Tl_2Ba_2Ca_1Cu_2O_x$ (2212) is a bulk superconductor with $T_c = 95$–108 K. This compound has two Cu perovskite units similar to Bi-2212 compound.

Figure 3.15 shows how T_c increases with the number of CuO layers from one to three. Tl compounds can be expressed with the general formula $Tl_2Ba_2Ca_{n-1}Cu_nO_{2n+4}$ and are tetragonal with two Tl-O layers and n Cu-O layers. T_c values are 80 K, 110 K and 125 K for three compounds with $n = 1$, 2 and 3, respectively. T_c is found increasing with the increase of Cu-O layers only up to $n = 3$. T_c decreases for $n > 3$. Tl being a toxic material, no attempts have been made to

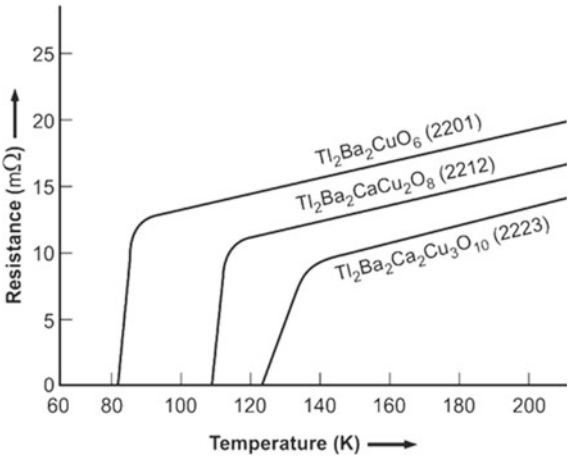

Fig. 3.15 Superconducting transition in three compositions of Tl compounds, viz.; 2201, 2212 and 2223. T_c increases with the number of Cu perovskite units 1, 2 and 3, respectively

produce wires/tapes of this material either on a laboratory scale or on a commercial scale for applications.

3.5 The Hg-Ba-Ca-Cu-O System

After a lull of about 5 years, once again a new superconductor was discovered with T_c of 94 K by Putillin et al. [30] in a compound $HgBa_2CuO_{4+y}$ or simply called Hg-1201 (as Ca is absent). This is very high T_c in contrast to the similar Tl-1201 compound which has a T_c of < 10 K. This compound has one Cu-O_2 sheet. Mercury compounds can in general be described by a formula of the type $HgBa_2Ca_{n-1}Cu_nO_{2n+2+y}$ where n can take different values starting from 1 onwards. Soon superconductivity was discovered at 130 K by Schilling et al. [31] in a multiphase Hg-compound with $n = 1$, 2 and 3. Soon the pure phase $HgBa_2Ca_2Cu_3O_{8+\delta}$ was synthesized with $n = 3$ and a $T_c = 135$ K was obtained. The unit cell structure of the three Hg-compounds with $n = 1$, 2 and 3 are shown in Fig. 3.16. Evidently, c-axis increases with the number of CuO_2 layers. Analogous to Tl-system, Hg-system too has a tetragonal structure with 'a' and 'c' parameters as given in the figure for the three phases. An enhancement in T_c with pressure in copper containing superconductors with hole conductivity is well known. Chu et al. [32] reported a T_c of 153 K for the compound $HgBa_2Ca_2Cu_3O_{8+\delta}$ (1223) at a pressure of 150 kbar. In a systematic study, Gao et al. [33] found continuous increase in T_c of all the Hg-compound (1201, 1212 and 1223) up to a pressure of 45 GPa, viz.; 164 K for 1223, 154 K for 1212 and 118 K for the compound 1201. Antipov et al. [34] report that the T_c values increase with increasing pressure for all the Hg-compounds with $n = 1, 2, 3$ and 4 as shown in Fig. 3.17. In all the compounds T_c increases with pressure and tends to saturate at high pressure. It has been conjectured that it may be possible to get T_c values as high as 164 K under

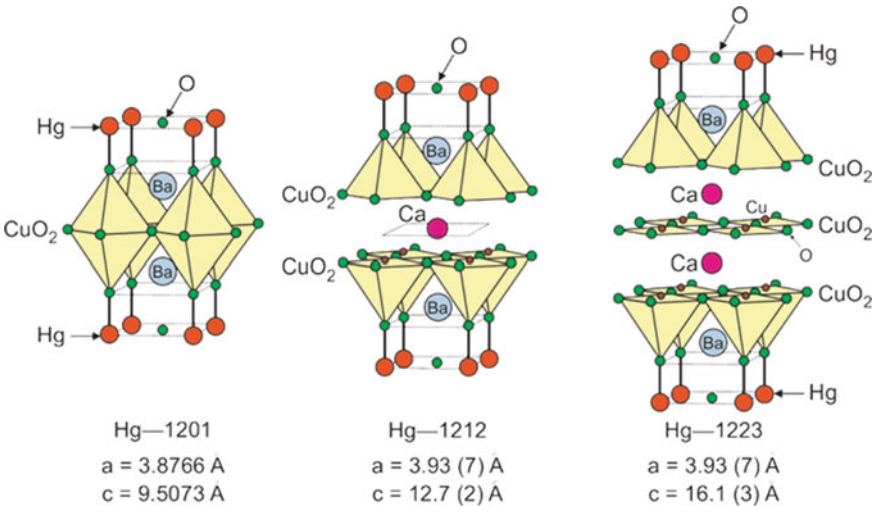

Fig. 3.16 Unit cell structure of $HgBa_2CuO_{4+\delta}$ (1201), $HgBa_2Ca_1Cu_2O_{6+\delta}$ (1212) and $HgBa_2Ca_2Cu_3O_{8+\delta}$ (1223) with one, two and three CuO_2 layers, respectively [34]. With permission from IOP

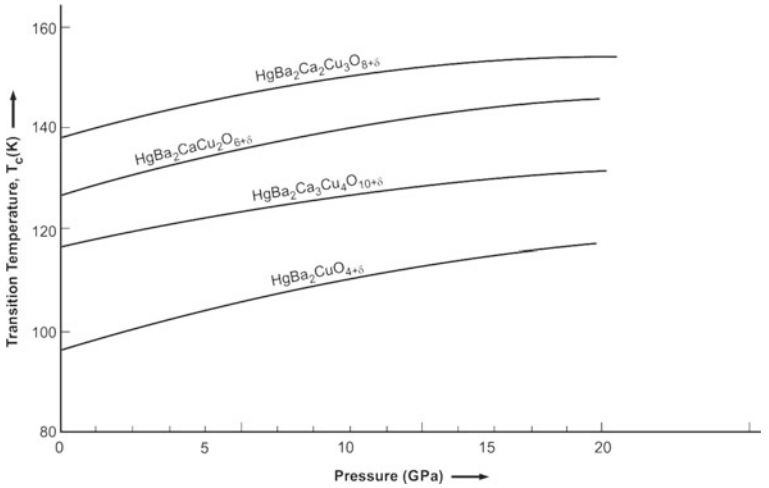

Fig. 3.17 T_c increases with pressure for Hg-compounds and with the number of CuO_2 layers up to $n = 3$. T_c decreases with pressure for compound Hg-1234 ($n = 4$). T_c is thus highest for Hg-1223 ($n = 3$) [34]. With permission from IOP

ambient pressure in optimally doped compounds through substitution if the Cu-O distances can stabilize.

Synthesis of Hg-compound is little complicated because of the toxicity of Hg and decomposition of HgO in to Hg and oxygen at comparative low temperature (430 °C). Samples are prepared in sealed quartz ampoules or in platinum or gold containers to prevent reaction. The synthesis is a two-step process. In the first step, stoichiometric mixture of barium carbonate (oxalate, nitrate or oxide), copper and calcium oxides is prepared and annealed at 600–1000 °C in air, oxygen flow or vacuum. The precursor so prepared is extremely hygroscopic and absorb CO_2 fast. All the operations are therefore carried out in a dry box. HgO is then added to the mixture and sealed in an ampoule for further annealing. T_c of these compounds has been found extremely sensitive to the presence of carbon and steps should therefore be taken to avoid carbon contents in the starting materials. An excellent topical review on the structure and synthesis of Hg-compounds has been written by Antipov et al. [34] on Hg-compounds. Hg-compound wires and tapes have not been exploited commercially for applications.

3.6 Flux Vortices, Critical Current Density and Flux Pinning in High-T_c Superconductors

The irreversible magnetic properties and critical current in type II superconductors especially in anisotropic HTS involve numerous complex mechanisms. A pure type II superconductor is well defined with T_c, B_{c1} and B_{c2} values which are the intrinsic properties of the material but same is not true for critical current density, J_c which can change widely with defects which are influenced by the fabrication process. Because of the high T_c, the J_c of HTS is also affected by thermal activation which in turn leads to flux creep and a power law I–V characteristic so that J_c is determined by an arbitrary electric field criterion. Further, J_c controls the irreversible magnetic properties of type II superconductors that are explained by the Bean critical state model [35, 36] and already discussed in Chap. 2. J_c thus is an extrinsic property of a superconductor.

Let us recall that a type II superconductor, in mixed state, ($B_{c1} < B < B_{c2}$) is threaded by flux lines each carrying a flux quantum ($\Phi = 2 \times 10^{-15}$ T m^2) or the vortices which form a triangular lattice as proposed by Abrikosov [37] and shown in Fig. 3.18. The vortices are produced by the circulating current flowing in a direction opposite to the surface screening current. The vortex is a normal cylindrical core of radius, ξ and has a region of suppressed order parameter (ψ or n_s) which is zero at the centre of the vortex. The magnetic flux at the core spreads out in the material over a distance of ~ 2λ as shown in the figure. Most interesting thing that one notices from this figure is that current in type II superconductors is carried by the entire bulk of the material unlike the type I superconductors in which the current flows only

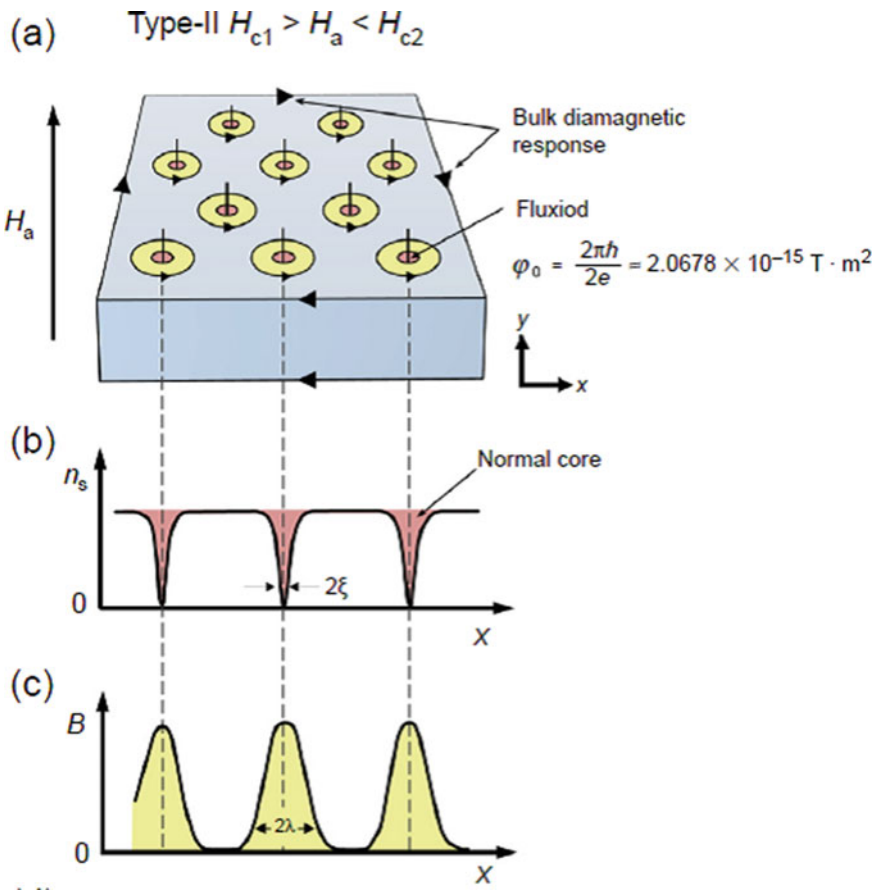

Fig. 3.18 **a** Type II superconductor in mixed state ($B_{c1} < B < B_{c2}$) is threaded by flux lines(normal cores) of dia. 2ξ, produced by current vortices flowing in a direction opposite to surface screening current along the periphery. **b** Magnetic field at the core spreads over a distance 2λ. Order parameter (ψ or n_s) drops to zero at the centre of the cores. **c** Variation of the magnetic flux density. With permission from Elsevier, 'Fundamentals of Superconductivity by C M Rey and A P Malozemoff'

through a small surface thickness (~ λ). Further, J_c in these materials is controlled by defects which may act as flux pining centres and increase J_c to high values.

Let us see how J_c in type II superconductors is controlled by defects and can be enhanced by great margin. From Ampere's law:

$$\nabla x\ B = \mu_0 J \tag{3.4}$$

Which for one dimension, reduces to:

$$\mathrm{d}B/\mathrm{d}x = \mu_0 J \tag{3.5}$$

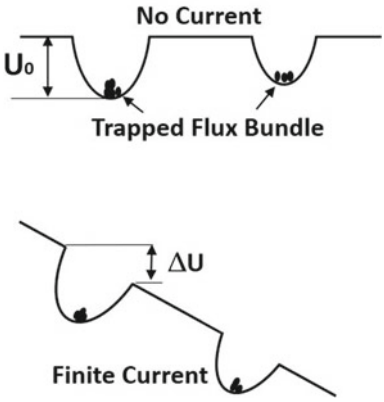

Fig. 3.19 Pinning potential without current flow (top curve) and with current flow (bottom curve). The potential wells display slope proportional to driving force when a current flows. This reduces the effective depth of the well. *Courtesy* Ajit Nandawadekar

It turns out from this expression that a supercurrent can flow in a superconductor if the field (flux line bundle) enters the bulk material and a gradient in flux line density exists. In a defect-free superconductor, however, Abrikosov lattice is in an equilibrium state. A gradient can only be created by introducing defects that will pin the flux lines. The pinning centres are represented by potential wells (Fig. 3.19) of average depth U_0 and width a. Bundle of flux quanta with an average flux $n\Phi_0$ are captured by the potential well. When no current flows, the probability of flux leaving the potential well is proportional to Boltzmann factor:

$$P_0 \propto \exp(-U_0/k_B T) \tag{3.6}$$

When a current of density J flows through the superconductor the potential acquires a slope (Fig. 3.19) proportional to the driving Lorentz force $F \propto n\Phi_0 J$. The slope is equivalent to a reduction in the effective potential well depth to $U = U_0 - \Delta U$

$$\text{Here } \Delta U \approx n\ \Phi_0 J a\ \ell \tag{3.7}$$

where ℓ is the length of the flux bundle. The increased probability of the escape of the flux P is now given by:

$$P = P_0 \exp(+\Delta U/k_B T) \tag{3.8}$$

The flux line gradient grows steeper, following Ampere's law, if the current density is increased in the type II superconductor. This generates increasing Lorentz force which at a certain maximum value overcomes the pinning force and starts pushing the flux lines out of their defect potential wells. As already discussed in Chap. 2, this current density is the critical current density J_c at which the pinning force, F_P becomes equal to the Lorentz force, F_L ($= B \times J_c$). Thus, the pinning force

in a defect superconductor can be determined from the measurement of J_c at a given field and at a given temperature. This flux pinning force, however, can be increased by introducing pinning centres such as dislocations, voids, secondary phase precipitations or elemental additions to the material. For illustration, we present some flux pinning data from Selvamanickam's group [38] on YBCO films as shown in Fig. 3.20. The figure shows field dependence of flux pinning force, F_P ($B//c$) at 4.2 K for 7.5 and 15 mol.% Zr-doped YBCO films. The flux pining force increases to an ultra-high value = 1.7 TN/M^3 for film doped with 15% Zr which is twice the value obtained for the film doped with 7.5% Zr. Surprisingly, the pinning force (F_P) does not show a drop with increasing field between 8 and 31 T ensuring high-current density in doped films right up to 31 T.

High pinning performance in these doped films has been attributed to spontaneous formation of the $BaZrO_3$ (BZO) defect columns during film growth.

When current through a type II superconductor exceeds J_c the flux lines or the vortices start moving and there is a sharp jump in the voltage in the I–V plots. This sharp jump in the voltage gets smeared if J_c distribution within the superconductor is not homogeneous. The right kind of J_c distribution can however cause a power law dependence $V \sim I^n$ [39], where the power index n is a function of inhomogeneity distribution in the material. Such a power law curve can also arise from flux creep, which is particularly relevant to HTS materials. Very high J_c values have been achieved in all the practical superconductors including HTS like the 2G YBCO-coated conductors [40] following innovative fabrication techniques and introducing efficient pinning centres. Naturally occurring pinning centres, like dislocations, voids, stacking faults, crystal twin boundaries, chemical precipitates, and such

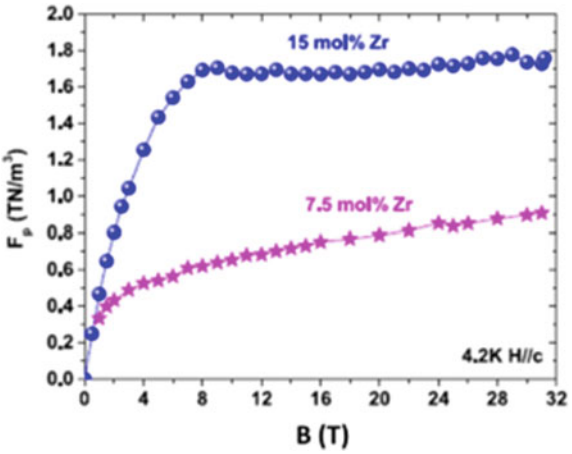

Fig. 3.20 Flux pinning force, F_P ($B//c$) at 4.2 K plotted against magnetic field for 7.5 and 15 mol.% Zr-doped YBCO films. Note ultra-high F_P = 1.7 TN/M^3 for film doped with 15% Zr. There is hardly a drop of F_P between 8 and 31 T field ensuring high-current density in field up to 31 T. With permission from V. Selvamanickam; Open access under CCA, A. Xu et al. App. Phys. Lett., MATERIALS **2**, 046111 (2014), http://dx.doi.org/10.1063/1.4872060

other defects, provide much of the pinning force. Pinning centres are also introduced by creating particular type of defects in to the substrate which get replicated in to the epitaxially grown films. Radiation-induced defects too can increase the number of pinning centres and increase the magnitude of the pinning force, F_P as reported by Weber [41].

3.7 Critical Surface of High-T_c Superconductors

The mixed state of HTS reveals the existence of a well-defined irreversibility temperature (T_{irr}) up to which magnetic irreversibility persists. This temperature is a characteristic feature of a superconductor and depends on the applied field. T_{irr} can be determined [42] from zero-field cooled (ZFC) and field cooled (FC) magnetization as a function of temperature plots as shown in Fig. 3.21. Magnetic irreversibility in these materials originates from the movement of vortices overcoming the pinning force. Below T_{irr}, the vortices are trapped by the pinning centres.

Above T_{irr} the system is magnetically reversible due to high thermal energy. When temperature is lowered below T_{irr}, many of the grains become coupled and strong irreversibility effects are observed in the magnetization curve. An irreversible line can be plotted from the reversibility data obtained on a superconductor sample as a function of field (B) and temperature (T). The critical surface of a HTS thus looks like [43], the one shown in Fig. 3.22. The irreversible line separates high-temperature magnetically reversible region from low temperature magnetically irreversible region. In conventional metal superconductors with low T_c, the critical surface is very close to the upper critical field B_{c2} and the critical current density J_{co} which is unaffected by flux creep. In HTS, the critical surface is diminished and shifts downwards as indicated by the arrows. The critical surface is now bound by the irreversibility line $B_{irr}(T)$ and

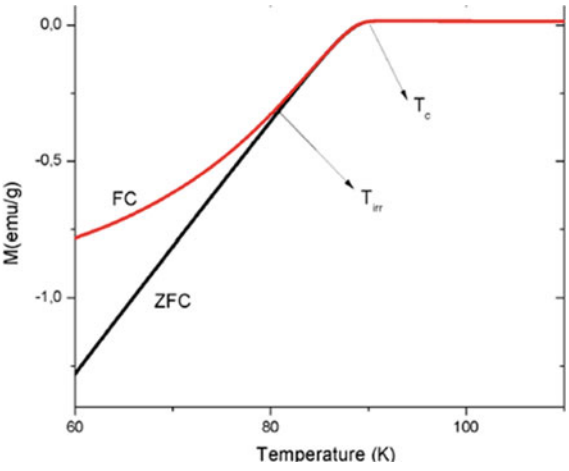

Fig. 3.21 Typical zero-field cooled (ZFC) and field cooled (FC) magnetization of a $Y_{0.6}Lu_{0.4}Ba_2Cu_3O_{7-\delta}$ sample as a function of temperature [42]. With permission from Armando Sarmiento Santos, Escuela de Física—UPTC; Open Access under CCA, Journal of Physics: Conference Series **480**, 012036 (2014), http://dx.doi.org/10.1088/1742-6596/480/1/012036

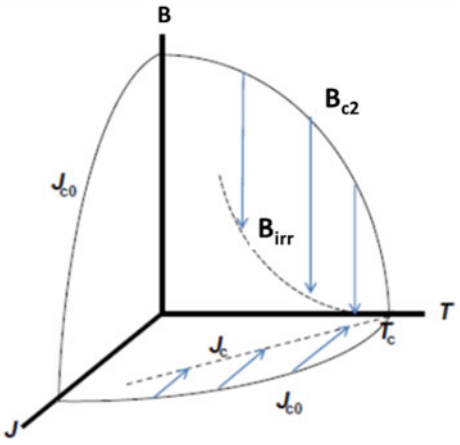

Fig. 3.22 Typical critical surface bound by of field B, temperature T and current density J in a HTS within which, a supercurrent can persist. The superconducting parameters, however, shrink because of thermal activation and flux creep as shown by arrows. The critical surface now is bound by B_{irr} line and the flux-creep-reduced critical current density, $J_c(T)$ [43]. With permission from Elsevier

the critical current density $J_c(T)$ which is now reduced by flux creep. Nevertheless, the energy gap and the vortex current around the vortices persist within the bulk of superconductor until B_{c2} is reached. Between B_{c2} and B_{irr} the vortices are in a liquid-like state called a 'vortex liquid'. Below B_{irr}, the vortices are in a disordered state if the pinning centres are disordered and the state is called a 'vortex glass state'.

3.8 The Depairing Current

The critical current density of a superconductor as a function of temperature and magnetic field is the most important parameter for building a superconducting device. Large efforts have continuously been made to enhance the critical current in practical superconductors largely through new fabrication techniques and by adding effective pinning centres. There is however a theoretical thermodynamic limit beyond which critical current density cannot be raised. We have learnt in Chap. 2 that a normal to superconducting phase transition is of the second order (no latent heat involved) and the free energy is reduced. Now consider the transport current in a superconductor. Contrary to this decrease in energy during the normal to superconducting transition, the kinetic energy of the electron pairs (Cooper pairs) increases as the transport current increases. At a certain high enough current value, this increase in energy may exceed the decrease in energy while entering the superconducting state. It would then be favourable for a superconductor to get back to normal state. This current is called the depairing current, J_d. This is the upper theoretical limit of the maximum current density that can be achieved in a superconductor no matter how strong is the flux pinning. We can thus define depairing current density as the current density at which the kinetic energy of the electron pair is equal to the binding energy of the pair. Beyond this current, the energy gap vanishes and superconductivity is completely destroyed. The depairing current J_d thus becomes an intrinsic critical parameter

together with T_c, J_c and B_{c2} characterizing a superconductor. A rough estimation of J_d can be made [44] from the London equations by equating the kinetic energy of the pair with the free energy density;

$$\frac{1}{2} n_s m^* v_s^2 = \frac{B_c^2}{2\mu_0} \tag{3.9}$$

Substituting $v_s = \frac{J_s}{2en_s}$ and $n_s = \frac{m^*}{4\mu_0 e^2 \lambda^2}$

$$J_d = \frac{B_c}{\mu_0 \lambda} \tag{3.10}$$

The above equation is only an approximation because n_s has been assumed here to remain unaffected by the current approaching J_d which is not realistic. The equation however establishes the fact that J_d is strongly dependent on critical magnetic field and the penetration depth. Similar expression has been derived for type II superconductors following the Ginzberg–Landau theory yielding:

$$J_d(0) = 5.56 \times 10^{-3} \times \frac{\sqrt{B_{c2}(0)}}{\lambda^2(0)} \tag{3.11}$$

where J_d is in A/m^2, B_{c2} is in Tesla and λ is in metres. The theoretical limit of J_d can only be reached in samples with very high pinning force with J_d approaching 10^{12}–10^{13} A/m^2.

For almost all applications, only three critical parameters, T_c, J_c and B_{c2} of a superconductor are considered routinely and not the J_d. In fact, J_d is hardly measured partly because of the technical difficulties related to excessive heating and burnt out of samples at high currents. Also, at very high current, the critical temperature, T_c too shifts to lower temperature. Most measurements are therefore carried out using short-pulse currents with short duration of about 50 ns to prevent burnt out of the samples. For example, the depairing current density in $YBa_2Cu_3O_{7-x}$ is of the order of 10^8 A/cm^2 (4.2 K), and therefore, ultra-thin films of $YBa_2Cu_3O_{7-x}$ patterned to microbridges have been used to allow for an effective heat transfer into the MgO substrate. Arpaia et al. [45] measured J_d in YBCO nanowire with a protecting gold capping layer. They measured multiple YBCO bridges with cross sections as small as 50×50 nm^2 and reported $J_d = 1 \times 10^8$ A/cm^2 in bridges covered with Au capping. The measured J_d is found to be close to values predicted by Ginzburg–Landau theory.

3.9 Grain Boundary Problem in High-T_c Superconductors

High-T_c superconductors are not only characterized by high T_c and high B_{c2} but also by poor grain connectivity and strong anisotropy of superconducting properties along

the *a*–*b* (CuO_2) planes and along the *c*-axis. Lack of perfect stoichiometry especially the oxygen content is another problem. Critical current density, J_c depends strongly on the method of preparation as well. For example, J_c in bulk YBCO, prepared by solid-state diffusion method, and remains confined to 10^3 A/cm^2 at 77 K. In melt textured samples, where number of grain boundaries (GB) decrease, J_c increases and can reach a value of 10^5 A/cm^2 (77 K). It increases further to 10^6 to 10^7 A/cm^2 in epitaxial films with preferred grain orientation. Chaudhuri et al. [16] did report high J_c in epitaxially grown YBCO films and Dinger et al. [17] reported similar high J_c values in YBCO single crystals. Inter-grain J_c, however, was found to be very small which turned out to be a stumbling block in realizing high transport J_c in bulk material and in wires and tapes prepared by powder-in-tube (PIT) method.

Large anisotropy in these ceramic superconductors is another difficulty which needs resolution. Widely different coherence lengths in YBCO along the *a*–*b* plane, $\xi_{ab} = 1$–2 nm and along the *c*-axis, $\xi_c = 0.3$ nm lead to anisotropy in various superconducting properties including J_c which now depends on the crystallographic orientation of the grains. Misorientation of grain reduces inter-grain $J_{c(GB)}$ and larger the misorientation angle greater is the reduction in $J_{c(GB)}$. In fact, several factors are responsible for poor quality of grain boundaries (GB) which are dependent upon the process followed for the synthesis of this ceramic superconductor. Two HTSs which have been pursued for application are the BSCCO and YBCO superconductors. The third one, Bi-2212 is also close to commercial production. For operation at 77 K in magnetic field, BSCCO (2223) tapes are preferred because of its higher $T_c = 110$ K and better flux pining properties. The popular approach to make YBCO tape wires is the so-called coated conductor technique in which the superconductor is deposited on a textured tape substrate with *c*-axis normal to the direction of current flow. These 2G REBCO-coated conductors now have very high J_c. The polycrystalline films, however, have severe problem of the inter-grain interfaces (GB). Misalignment of the *a* and *b* axes of more than a few degrees causes week links similar to Josephson junctions with critical current significantly lower than inside the bulk grain. The grain boundary problem has been solved at least partially through a variety of techniques to be described in Chap. 6.

3.10 Discovery of Superconductivity in Magnesium Diboride (MgB_2)

Over a thousand condensed matter physicists presented their work on the newly discovered superconductor, Magnesium Diboride (MgB_2) [46] on 12 March 2001 at the American Physical Society meeting held in the Grand Ballroom of the Westin Hotel in Seattle. The session lasted for more than 5 h. Most surprising part of the discovery has been that MgB_2 was a known material since 1953 and yet it had to wait for nearly 50 years to be known as a superconductor, with a $T_c = 39$ K. Studies on this material proceeded at great speed and within a few years physics of this material was

well understood. Soon, the material positioned itself as a practical superconductor [47, 48] to be used at 20 K with superconducting parameters superior to Nb_3Sn. Long lengths of multifilamentary MgB_2 wires and tapes with increased J_c and B_{c2} are being manufactured now and used for magnets and other applications. MgB_2 has several advantages over HTSs. It is inexpensive and wire fabrication does not need costly silver. Its T_c is 39 K and thus has an operational window of 20–30 K. Magnets and other devices can thus be conduction cooled and operated using closed-cycle refrigerators (CCR). Some other advantages can be summarized as below:

- A number of diborides are known [49] to be superconducting but with only within a T_c range of 0.62 K (NbB_2) and 9.5 K (TaB_2). Only MgB_2 has the highest T_c of 39 K.
- There are no grain boundaries weak links in MgB_2 restricting the critical current to low values like in HTSs. Standard powder-in-tube (PIT) technique is employed to manufacture long lengths of wires/tapes. This is in contrast to 2G-coated conductors which need very sophisticated thin film deposition techniques which makes it very expensive.
- It has much smaller anisotropy of upper critical field compared to HTS. $\frac{B_{c2}^{ab}}{B_{c2}^{c}}$ in MgB_2 is just 1.1–1.7.
- Enhancement of transport critical current continues to be made. MRI scanners using MgB_2 magnets (0.5 T) are already in the market. 3 T MRI scanner might hit the market sooner than expected.
- MgB_2 has low density, 2.57 g/cc and is thus a potential candidate for space-oriented superconducting applications.

3.10.1 Peculiar Properties of MgB_2

Magnesium diboride, MgB_2, a low cost material, known since 1953, was found superconducting when cooled to 39 K by Nagamatsu [46] in 2001. The original plots of magnetic susceptibility versus temperature under zero-field cooled (ZFC) and field cooled (FC) conditions and the electrical resistivity versus temperature are shown in Fig. 3.23a and b, respectively. Both the measurements confirm a sharp superconducting transition at 39 K. MgB_2 though is considered to be a superconductor of conventional type, nevertheless, has peculiar properties. The material is characterized by two widely differing energy gaps. The presence of two energy gaps has been theoretically understood by assuming two species of electrons at the Fermi surface in its electronic structure, namely the 'sigma-bonding' and the pi-bonding electrons. Using the measured values of the two energy gaps 6.8 and 1.8 meV for sigma and pi bands, respectively and employing BCS theory the sigma and pi bands of electrons are found to have two coherence lengths, 13 and 51 nm, respectively. The corresponding penetration depths are 47.8 and 33.6 nm. The Ginzberg–Landau (G-L) parameter κ turns out to be =3.68 for sigma-bonding and 0.66 for pi-bonding. The first term is more than $1/\sqrt{2}$ and the second term less than $1/\sqrt{2}$. Thus, the

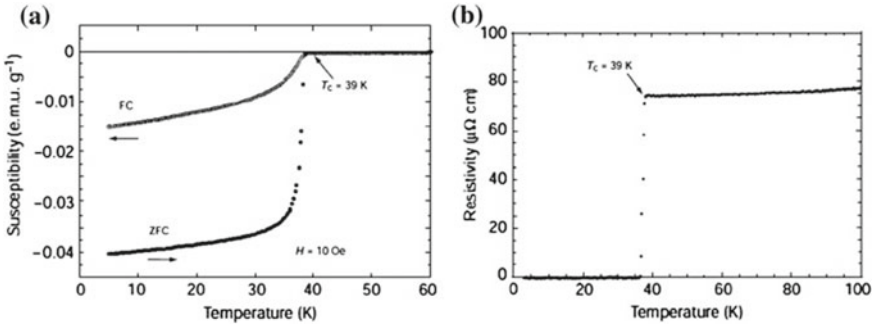

Fig. 3.23 **a** Magnetic susceptibility versus temperature plots of MgB_2 under zero-field (ZFC) and field cooled (FC) conditions. **b** The electrical resistivity versus temperature plot for MgB_2. Both the measurements show a sharp superconducting transition at 39 K [46]. With permission from Nature Publishing Group

sigma-bonding superconductivity is of type II and the pi-bonding superconductivity of the type I. MgB_2 has been termed by some as a superconductor of 'one and a half' (1.5) type [50].

3.10.2 Crystal and Electronic Structure and Energy Gaps in MgB_2

MgB_2 is a metal with a layered hexagonal structure where the B atoms form a graphite-like honeycombed layers and the magnesium atoms sit at the centre of the hexagons in between the boron planes as shown in Fig. 3.24. The electronic states at the Fermi level are mainly either σ or π-bonding boron orbitals. The σ-bonding states

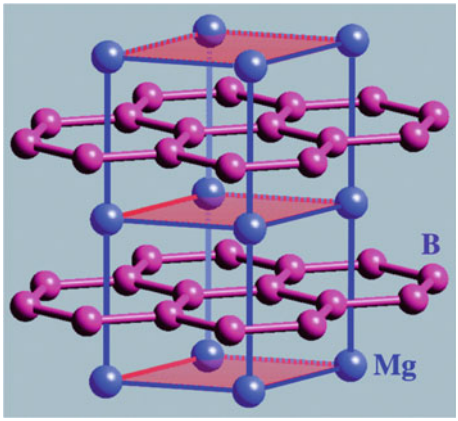

Fig. 3.24 B atoms form a graphite-like honeycombed layers and the magnesium atoms occupy the centre of the hexagons in between the boron planes (Taner Yildirin, Materials Today, **5**, 40 (2002) ISSN:1369 7021 © Elsevier Science Ltd 2002Open access under CBY-NC-ND license)

are confined in the boron planes and couple very strongly to the in-plane vibration of boron atoms. Based upon the strong-coupling formalism of superconductivity by Eliashberg, Choi et al. [51] showed from the first principle that this strong-coupling results in strong electron-pair formation of the σ-bonding states with an energy gap of 6.8 meV. This pairing is strong and confined to the boron planes and Fermi surface partially. This strong pairing, in fact, is the principal contribution responsible for the occurrence of superconductivity in MgB_2. The π-bonding states, on the remaining parts of the Fermi surface form much weaker pairs with an energy gap of 1.8 meV. This pairing is enhanced by the coupling with σ-bonding states. MgB_2 though has high T_c nevertheless is similar to conventional metal superconductors. It remains metallic all through unlike the cuprates which are insulators without doping. The major difference with metal superconductors is that MgB_2 is characterized by two energy gaps corresponding to two types of pairing.

Choi et al. [51] carried out calculations and obtained numerical values of the two energy gaps and their effects on the measurable parameters. They were successful in accounting for the high T_c, the anomalous specific heat versus temperature behaviour and for the isotopic behaviour. The calculated energy gaps versus temperature plots are shown in Fig. 3.25. As seen in the figure the energy gap corresponding to σ-bonding states is large, 6.8 MeV which drops with increasing temperature and faster close to T_c than the smaller energy gap (1.8 MeV) corresponding to the π-bonding states. Both the energy gaps, however, merge and disappear at T_c. The experimental energy gap parameters fit well with the calculated values. The temperature variation of the energy gaps can be expressed by the following equation:

$$\Delta(T) = \Delta(0)\left[1 - \left(\frac{T}{T_c}\right)^p\right]^{1/2} \tag{3.12}$$

here $p = 2.9$ for the larger energy gap corresponding to the σ-bonding states and $p = 1.8$ for the smaller energy gap corresponding to the π-bonding states. This

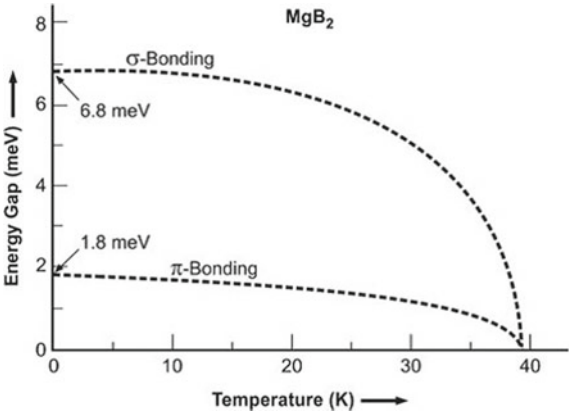

Fig. 3.25 Two superconducting energy gap parameters plotted against temperature. Both the gaps merge and become zero at T_c [51]. With permission from Nature Publishing Group

temperature variation of the energy gaps has been verified experimentally through tunnelling, optical and specific heat measurements. Parameter $2\Delta(0)/k_B T_c$ for the σ-bonding comes out to be =4.0 and for the π-bonding 1.06, k_B being the Boltzmann constant. Two-gap superconductivity was also inferred from measurements using Raman spectroscopy, photoemission, penetration depth and tunnelling. That MgB_2 is a BCS type conventional superconductor, with an intermediate to strong s-wave coupling, has been borne out by a plethora of experimental data. The existence of Cooper pairs with charge 2e has been confirmed through AC and DC Josephson effect [52] studied on break junctions of MgB_2. Observation of isotope effect in this material, to be discussed in the next section, further confirmed the role of phonons in the formation of the Cooper pairs and the occurrence of superconductivity. Because of comparative ease, studies on MgB_2 have been fast and very passionate. Studies were carried out on almost all aspects of this material and a very large number of papers published. Two widely different energy gaps arise from a weak electron–phonon coupling in the 3D π-bands (smaller gap) and a strong coupling in 2D σ-band (larger gap). In MgB_2, the two sets of electrons do interact, though weakly, through Coulomb repulsion and scattering from states in one band to states in the other band. That, such a weak interaction can cause both the bands go superconducting at the same temperature with two widely different energy gaps, is the striking property of this superconductor.

3.10.3 The Boron Isotope Effect

One single most credible evidence of BCS type superconductivity is the observation of isotope effect which confirms the phonon mediated Cooper pair formation mechanism. As per the classical form of the BCS theory [53], the isotope coefficient α in the formula $T_c \propto M^{-\alpha}$ is 0.5. Here M is the atomic mass of the element. The Boron isotope effect was reported by Budko et al. [54] as early as 2001. Careful resistivity and magnetization experiments were performed on two types of bulk samples, viz.: $Mg^{10}B_2$ and $Mg^{11}B_2$ by exposing isotopic pure ^{10}B and ^{11}B to magnesium vapours. Figure 3.26 is the plot of resistivity of MgB_2 against temperature [55]. It shows a resistive superconducting transition close to 40 K. The upper insert shows the effect of replacing ^{10}B by ^{11}B in MgB_2 on the resistive T_c and the lower inset on magnetization T_c. In both the experiments, T_c is found to reduce by 1 K, that is, from 40.2 K for $Mg^{10}B_2$ to 39.2 K for $Mg^{11}B_2$. The value of exponent α for boron isotope in MgB_2, comes out to be $=0.26 \pm 0.03$. This value is quite close to the values found in YNi_2B_2C and $LuNi_2B_2C$ borocarbides. No isotope effect was observed when ^{24}Mg was substituted for ^{25}Mg. It thus appears that only boron phonons take part in pair formation. There are indications that high-frequency boron A1g optical modes are responsible for the onset of superconductivity in MgB_2.

For a BCS superconductor, a $T_c = 39$ K is considered high. Looking at the BCS expression for T_c one finds that T_c depends upon the phonon energy, $\hbar\omega$, the electron density of states $N(0)$ and the electron–phonon interaction parameter V. The phonon

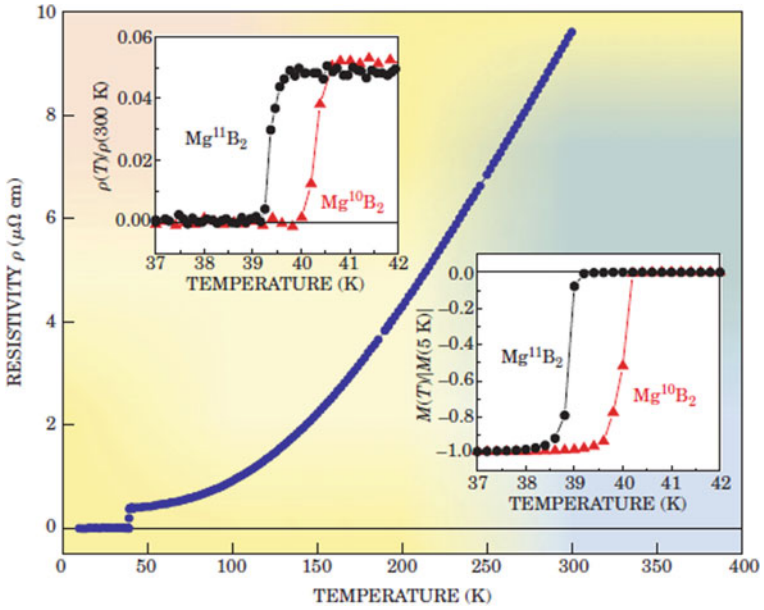

Fig. 3.26 Resistive superconducting transition in MgB_2 at 40.2 K. Upper inset: Effect of replacing $^{10}B_2$ by $^{11}B_2$ on the resistive T_c in MgB_2. The resistivity has been normalized to 300 K Lower inset: Effect of replacing $^{10}B_2$ by $^{11}B_2$ in MgB_2 on T_c through magnetization experiments. The data have been normalized to -1 at 5K. The transition temperature, T_c of MgB_2 is reduced by 1 K when $^{10}B_2$ is replaced by $^{11}B_2$ as confirmed by both the types of experiments [55]. Reproduced from 'Physics Today, 56, 34 (2003), with the permission of the American Institute of Physics'

energies of MgB_2 are indeed high

$$kT_c = 1.14\hbar\omega \exp\left[-\frac{1}{N(0)V}\right] \tag{3.13}$$

but so are the energies of other borides and light element binary alloys but all have low T_c. The density of states is low because MgB_2 does not have d-electrons. The only other parameter left, which may lead to high T_c, is the strong electron–phonon interaction represented by 'v'. Perhaps, the selective coupling between the specified electron states and specified phonons is responsible for high-T_c (~ 40 K) superconductivity.

3.10.4 Some Physical Properties of MgB_2

We briefly describe some physical properties and interesting studies that have been carried out on this material. The Hall effect measurements by Elstev et al. [56] on MgB_2 single crystal reveal that it has two types of charge carriers, holes in the plane

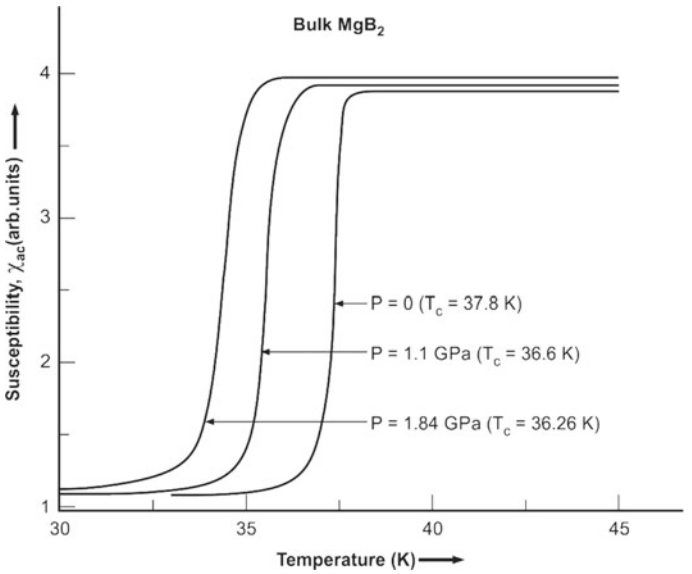

Fig. 3.27 Plots of AC susceptibility of bulk MgB_2 against temperature at different pressure up to 1.84 GPa. T_c shifts to lower temperature with increasing pressure [57]. With permission from the American Physical Society. http://journals.aps.org/prb/abstract/10.1103/PhysRevB.64.012507

and electrons along the *c*-axis. There is anisotropy in electrical resistivity along the plane and in the perpendicular direction such that $\rho_c/\rho_{ab} = 3.5$. Normal state Hall coefficient is positive in plane (*B*//*c*, *I*//*ab*) and negative in the out-of-plane (*B*//*ab*, *I*//*c*) confirming that the electronic structure of MgB_2 is multiband.

Pressure is another important parameter which has been exploited to study this material. Lorenz et al. [57] have made detailed studies on ac susceptibility and Seebeck coefficient with increasing pressure up to 1.84 GPa. T_c always decreases with increasing pressure and is linear with pressure. As shown in Fig. 3.27, T_c drops down with the increase of pressure till the highest pressure of 1.84 GPa. This drop in T_c is rather fast at a rate of $-$ 1.6 K/GPa and is close to the theoretically calculated value of $-$ 1.4 K/GPa.

The Seebeck coefficient has been found to be positive and relatively small. It decreases with the decrease of temperature similar to in a metal with hole-type carriers. Substitution at Mg as well as B sites with a host of elements always resulted in the decrease of T_c. Some of the materials tried are C, Al, Li, Si, Be, Cu, Mn, Nb, Ti, Fe, Co, Ni and Zn. Decrease in T_c is severe in case of substitution with Mn, Co and C and slow with Si and Li. Least decrease in T_c occurs with Zn substitution. The coherence length values, as calculated from B_{c2}, range between 6.1 and 6.5 nm in ab plane and between 2.5 and 3.7 nm along the *c*-axis. The most accurate data for a single crystal gives $\xi_{ab}(0) = 6.1$–6.5 nm and $\xi_c(0) = 2.5$–3.7 nm. The penetration depth as evaluated from B_{c1} values range between 85 and 203 nm. The lower critical magnetic field (B_{c1}) as reported by several investigators range from 25 to 48 mT.

Upper critical magnetic field B_{c2} has been reported for material in different forms like bulk, single crystal and thin films and in different orientations over a wide range of values ranging from 2.5 to 32 T. The highest value of B_{c2}, 32 T has been reported for films with $T_c = 39$ K. Higher $B_{c2} = 40$ T has been reported by Patnaik et al. [58] for films with lower T_c. B_{c2} drops almost linearly with increasing temperature saturating at low temperature. The B_{c2} anisotropy ratio $= B_{c2}^{ab}/B_{c2}^{c} = 1.1-1.7$ is reported for textured bulk and partially oriented crystallites. Higher ratio = 1.8–2.0 has been reported [58] for *c*-axis oriented MgB_2 film. The irreversible field extrapolated to 0 K, range from 6 to 12 T for MgB_2 in bulk, thin film, powder, tape and wire. B_{irr} thus is $=0.5\ B_{c2}$ in MgB_2 instead of $=0.8\ B_{c2}$ for conventional low temperature superconductors. Impurity additions are known to increase B_{c2} in type II superconductors as the mean free path is reduced and so does the coherence length $\xi(0)$. Braccini et al. [59] do report significant enhancement of B_{c2} in C-alloyed MgB_2 films irradiated with He-ions. The disorder thus introduced, raises in-plane B_{c2} to 51 T (4.2 K) and along the *c*-axis to 35 T (4.2 K). These are very promising values and show the potentiality of use of this material with high J_c in high magnetic field. Extrapolation of data to $T = 0$ K shows that B_{c2}^{ab} might lead to paramagnetic limit of 70 T. Various properties of MgB_2 that we have discussed in the preceding sections are summarized below and also tabulated in Table 3.4.

Table 3.4 Important superconducting parameters of MgB_2

Parameter	Unit	Value
Crystal structure		Hexagonal AlB2-type
Unit cell parameter	Å	$a = 3.14326 \pm 0.0315$ $c = 3.51936 \pm 0.0323$
Isotope coefficient for Boron, α_B in $\left(T_c \propto M^{-\alpha}\right)$		$\alpha = 0.266 \pm 0.03$
Transition temperature, T_c	K	39
Penetration depth, λ	nm	85–203
Coherence length, ξ_{ab}	nm	6.1–6.5
Coherence length, ξ_c	nm	2.5–3.7
Coherence length, ξ_{ab} single crystal	nm	6.1–6.5
Coherence length, $\xi_c(0)$ single crystal	nm	2.5–3.7
Lower critical field, H_{c1}	mT	25–48
Highest upper critical field (film)	T	32–40
$\frac{H_{c2}^{ab}}{H_{c2}^{c}}$ anisotropy (textured bulk/partially oriented crystallites)		1.1–1.7
Irreversible field, H_{irr} (0 K)	T	6–12
Energy gap (σ band)	meV	6.8
Energy gap (π-band)	meV	1.8
Room temperature resistivity	$\mu\Omega$ cm	10
Resistivity close to T_c	$\mu\Omega$ cm	0.5
Estimated paramagnetic limited field, B_{c2}^{ab}	T	70

3.10.5 Summery of the Various Properties of MgB_2

- Transition temperature T_c always decreases with elemental substitution at Mg and B sites and is more severe in case of substitution with Mn, Co and C but moderate with Si and Li. Least decrease in T_c occurs with Zn substitution.
- Most reliable coherence length values in a single crystal come out to be $\xi_{ab}(0) =$ 6.1–6.5 nm and $\xi_c(0) = 2.5$–3.7 nm.
- The penetration depth as evaluated from B_{c1} values range between 85 and 203 nm.
- The lower critical magnetic field B_{c1}, as reported by different groups range from 25 to 48 mT.
- Upper critical magnetic field B_{c2} has been reported for MgB_2 in its different forms like bulk, single crystal and thin films and in different crystal orientations in the range of 2.5–40 T. The highest value of $B_{c2} = 40$ T has been reported by Patnaik et al. [58] for films with lower T_c.
- B_{c2} drops almost linearly with increasing temperature and saturating at low temperature.
- The B_{c2} anisotropy ratio, $\frac{B_{c2}^{ab}}{B_{c2}^{c}} = 1.1-1.7$ is for textured bulk and partially oriented crystallites.
- Higher ratio, $\frac{B_{c2}^{ab}}{B_{c2}^{c}} = 1.8-2.0$ has been reported [58] for c-axis-oriented MgB_2 film.
- B_{irr}, the irreversible magnetic field extrapolated to 0 K, range from 6 to 12 T for MgB_2 in bulk, thin film, powder, tape and wire. B_{irr} thus is $=0.5\ B_{c2}$ in MgB_2 instead of $=0.8\ B_{c2}$ for conventional low T_c superconductors.
- B_{c2} of type II superconductors is known to increase with the increase of normal state resistivity as the mean free path is reduced and so does the coherence length $\xi(0)$.
- Braccini et al. [59] report significant enhancement of B_{c2} in C-alloyed MgB_2 films irradiated with He-ions. The disorder thus introduced, raises in-plane B_{c2} to 51 T (4.2 K) and B_{c2} along the c-axis to 35 T (4.2 K).

The critical parameters of MgB_2 are very impressive and have already been exploited commercially and are being used for a variety of conduction-cooled magnets. Conduction-cooled MgB_2 magnet-based MRI scanners are expected to flood the market in very near future. We will devote a full chapter (no. 7) on the fabrication techniques of MgB_2 wires and cables planned to be used in superconducting magnet projects. Table 3.4 summarizes the important superconducting parameters of MgB_2.

3.11 The Discovery of Iron-Based Superconductors—LaFeAsO 1111 Compounds

One more surprise came from the Japanese group, Kamihara et al. [60] headed by Hideo Hosano when they reported a high T_c of 26 K in iron-based oxypnictides, of the type $La(O_{1-x}F_x)FeAs$ layered superconductor containing magnetic materials like Fe, Co and Ni. Iron was earlier believed to be an enemy to superconductivity. Here, the contradiction was between the static spin ordering in iron and the dynamic formation of Cooper pairs (electrons with opposite spins) in a superconductor. In $La(O_{1-x}F_x)FeAs$, x varies from 5 to 12%. The crystal structure of this superconductor [61] is shown in Fig. 3.28. The conduction layers Fe_2As_2 are sandwiched between the insulating La_2O_2 layers. It has a tetragonal structure of the type (ZrCuSiAs) with p4/nmm space group. The room temperature lattice parameters of the undoped samples are $a = 0.403552(8)$ nm and c = 0.87263(3) nm. The lattice constants decrease with F-doping. Thus, for example, the lattice parameters for 5% F-doping are: $a = 0.40320(1)$ nm and $c = 0.87263(3)$ nm. The electrical resistivity of $La(O_{1-x}F_x)FeAs$ is plotted against temperature up to 40 K as shown in Fig. 3.29. The undoped sample does not show superconductivity down to the lowest temperature. Highest value of T_c (= 26 K) is obtained for 11 at% F-doped sample. Higher doping leads to a drop in T_c. Superconductivity was not observed when doping was done with Ca^{2+} instead of with F. This gives a strong signal that superconductivity is induced by electron (F^-)-doping and not by hole (Ca^{2+})-doping. The material LaOFeAs was prepared following the solid-state method. Powders of dehydrated La_2O_3, lanthanum arsenide and iron arsenide were thoroughly mixed and sealed in a silica tube filled with Ar-gas. The tube was heated to 1250 °C for 40 h. Right quantities of CaO and

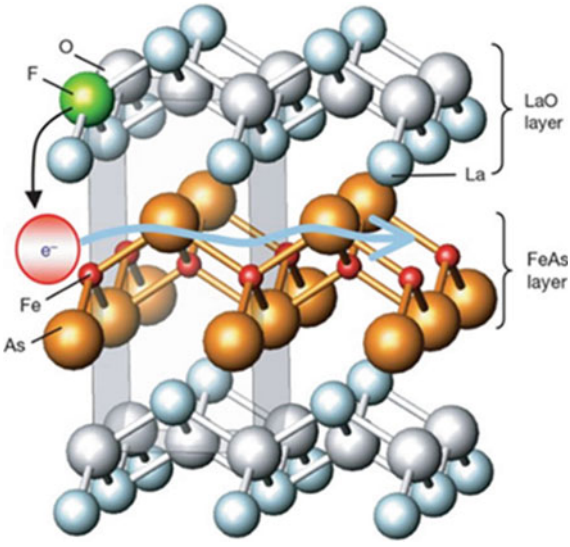

Fig. 3.28 Crystal structure of LaFeAsO, 1111 compound. The Fe_2As_2 conduction layers are sandwiched between the insulating La_2O_2 layers. The structure is of the type (ZrCuSiAs) electron carriers generated by F^- doping at the oxygen site are transferred to FeAs conduction layer [61]. Reproduced with the permission from Springer Nature

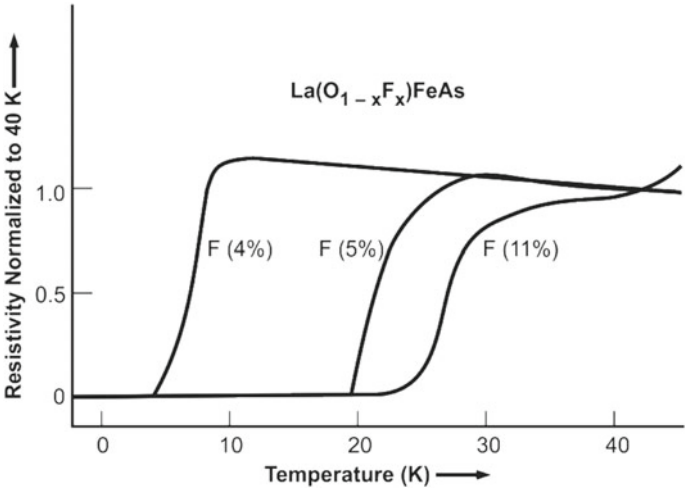

Fig. 3.29 Electrical resistivity plotted against temperature for $La(O_{1-x}F_x)FeAs$ for 0, 4, 5 and 11%) of F-doping [60]. With permission from American Chemical Society

1:1 mixture of LaF_3 and La were added to the starting material for doping with Ca^{2+} and F^-, respectively. This was followed again by the same heating schedule.

3.11.1 High T_c (> 50 K) in Sm and Nd-Based Oxypnictides

Significantly, high values of T_c have been reported for these oxypnictides by replacing La by different rare earths. For Ce-compound the T_c rises to above 40 K and above 50 K for Nd, Pr, Sm and Gd. Jaroszynski et al. [62] reported T_c higher than 50 K for their Sm and Nd-based materials. They carried out high-field studies on three REFeAsO 1111 materials with RE as La, Sm and Nd. Superconductivity was induced either by doping F at O-sites or creating O-vacancies by synthesizing O-deficient materials. Three compounds studied, viz.; $LaFeAsO_{0.89}F_{0.11}$, $SmFeAsO_{0.85}F_{0.15}$ and $NdFeAsO_{0.94}F_{0.06}$ yield $T_c = 28$ K, 53.5 K and 50.5 K, respectively. These values have been tabulated in Table 3.5. It is to be mentioned that these materials were synthesized at high pressure and high temperature following the solid-state reaction route. Pre-sintered powders of LaAs. SmAs and NdAs were mixed together with powders of Fe, Fe_2O_3 and FeF_2 in right stoichiometric proportions ground and pressed in to pellet form. The pellets were sealed in boron nitride (BN) tubes and heated at 1250 °C under 6 GPa pressure for 2 h. Interestingly, the highest values of T_c obtained for optimal doping show that the optimal level is different for different doping materials, viz.; 11%, 15% and 6% for La, Sm and Nd, respectively. A detailed review article by Aswathi et al. on oxypnictides had appeared in the literature [63].

Table 3.5 Superconducting parameters of REFeAsO 1111 oxypnictides with RE as La, Sm and Nd [62]

Parameter	Unit	$LaFeAsO_{0.89}F_{0.11}$	$SmFeAsO_{0.85}F_{0.15}$	$NdFeAsO_{0.94}F_{0.06}$
Transition temperature, T_c	K	28	53.5	50.5
Optimum doping of F	%	11	15	6
Upper critical field, B_{c2}	T	36	150	204

The upper critical field B_{c2} of La $FeAsO_{1-x}F_x$ 1111 compounds turns out to be high. The B_{c2} values as evaluated from resistive (ρ–B plots) using Werthamer–Helfend–Hohenberg (WHH) formula,

$$B_{c2} = -0.693\ T_c\ [dB_{c2}/T]_{T_c} \tag{3.14}$$

and extrapolated to 0 K for La, Sm, Nd, Pr and Ce 1111 compounds are [62] 36 T, 150 T, 204 T, 72 T and 43 T, respectively (Table 3.6). B_{c2} has been found to decrease with increasing F^- doping even though T_c shows an opposite trend. For $CeFeAsO_{0.8}F_{0.2}$, the B_{c2} is 43 T and T_c is 42.5 K and for $CeFeAsO_{0.9}F_{0.1}$ the B_{c2} value is 94 T and T_c is 38.4 K. Similar variation of B_{c2} is reported for $LaFeAsO_{1-x}F_x$. For $LaFeAsO_{0.95}F_{0.05}$, the B_{c2} is 63-65 T, and for $LaFeAsO_{0.89}F_{0.11}$, it is 36 T. Sm 1111 compound also show similar behaviour. Like the T_c of this compound, B_{c2} of the 1111 compounds also increases if the compound is prepared by high-pressure route. B_{c2} up to 230 T and T_c of 51 K have been reported [63] in $NdFeAsO_{0.82}F_{0.18}$. The field anisotropy B_{c2ab}/B_{c2c} is about five, much smaller than in YBCO compound. The values of irreversible field, B_{irr} are also correspondingly high as compared to MgB_2. Tables 3.5 and 3.6 indicate beyond doubt that these materials can have high T_c and B_{c2} once the process parameters are optimized.

In spite of high B_{c2} and high T_c, these compounds suffer from the problem of granularity similar to cuprates. Thus, the inter-grain critical current J_{cgp} is far smaller

Table 3.6 Superconducting parameters of REFeAsO 1111 oxypnictides with RE as La, Sm, Nd, Pr and Ce [66]

Oxypnictide	T_c (K)	B_{c2} (0 K)
$LaFeAsO_{0.89}F_{0.11}$	28	36
$SmFeAsO_{0.85}F_{0.15}$	53.5	150
$NdFeAsO_{0.94}F_{0.06}$	50.5	204
$PrFeAsO_{0.94}F_{0.06}$		72
$CeFeAsO_{0.8}F_{0.2}$	42.5	43
$CeFeAsO_{0.9}F_{0.1}$	38.4	94
$NdFeAsO_{0.82}F_{0.18}$ [63]	51	230

than the intragrain critical current J_{cg}. Through magneto-optical measurements (low temperature laser scanning electron microscopy) on Sm 1111 compounds, Kametani et al. [64] have shown that the transport current though is high within the grains but is low at the grain boundaries in very low field. Great advancements have been made in recent times to develop IBSC conductors and in good lengths and with high J_c. This is a significant step towards the exploitation of these materials on a commercial scale. These developments will be discussed in Chap. 8 on 'Iron-Based Practical Superconductors'.

3.11.2 Superconductivity in K-Doped $BaFe_2As_2$ 122 Compounds

A new member of the Fe-As superconductor family was discovered in 2008 raising the T_c to all time high 55 K in $SmFeAsO_{1-x}$ system. This was achieved by F^- doping or creating oxygen deficiency (electron-doping) in the Fe_2As_2 conducting layer which suppresses the structure phase transition (at 135–140 K) and induces superconductivity. Hole doping too has been reported to induce superconductivity in the $(La_{1-x}Sr_x)FeAsO$ system but the T_c was limited to 25 K.

Rotter et al. [65] discovered superconductivity first time in an oxygen-free pnictide.

A T_c of 38 K has been reported in a compound, $(Ba_{0.6}K_{0.4})Fe_2As_2$ prepared by partially replacing Ba with K. The parent compound $BaFe_2As_2$ has a tetragonal $ThCr_2Si_2$ type crystal structure with I4/mmm space group and consisting of $(FeAs)^-$ layers separated by Ba^{2+} ions as shown in Fig. 3.30. $BaFe_2As_2$ is a poor metal with Pauli paramagnetism. It shows a spin density wave (SDW) anomaly at 140 K similar to the anomaly in LaFeAsO compound at 150 K. The anomaly is accompanied with a structural and magnetic phase transition and anomalous specific heat, resistivity and susceptibility. Hole doping in $(FeAs)^-$ layers by partial substitution of K^+ on the Ba^{2+} sites suppresses this SDW anomaly and induces superconductivity. This SDW anomaly seems to be a pre-requisite for superconductivity. The structural phase transition can be suppressed by electron-doping or hole-doping in the Fe-As layer which leads to the appearance of superconductivity. Through this substitution, Rotter et al. [65] have found superconductivity in $(Ba_{0.6}K_{0.4})Fe_2As_2$ at 38 K. The resistive superconducting transition is shown in Fig. 3.31. Thus, a new category of oxygen-free Fe-As compounds was added to the list of Fe-As-based superconductors.

3.11.3 Superconductivity in Iron-Chalcogenides

After the discovery of superconductivity in Fe-oxypnictides of the type LaFeAsO, these compounds became the most studied materials with an object of getting higher T_c. Report of T_c as high as 55 K in oxygen deficient $SmFeAsO_{0.85}$ [62] inspired

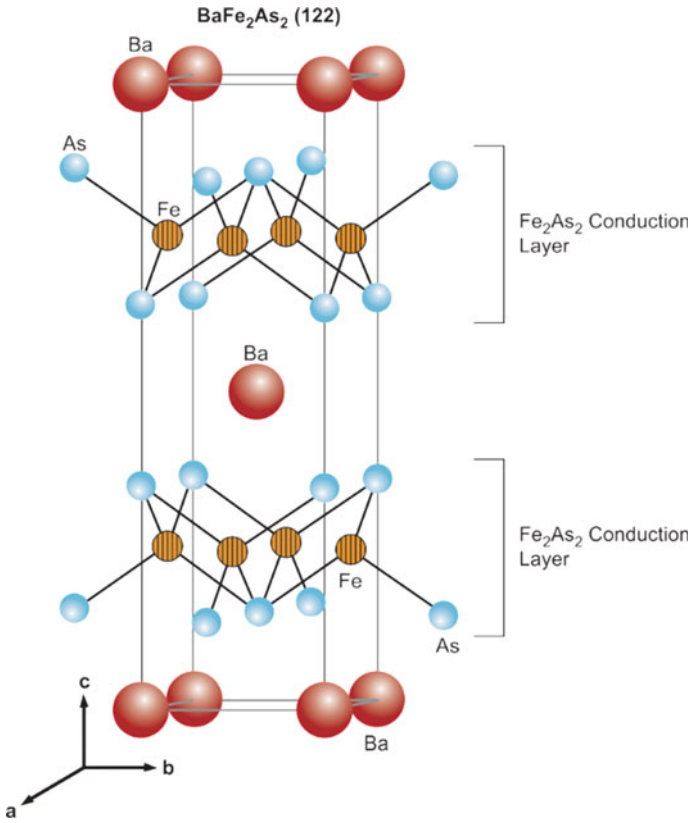

Fig. 3.30 Crystal structure of $BaFe_2As_2$ 122 compound (of the type $ThCr_2Si_2$) with space group I4/mmm [65]. With permission from APS. http://journals.aps.org/prb/abstract/10.1103/PhysRevB.82.180520

researchers to continue to look for Fe-based superconductors with still higher T_c. Superconductivity was indeed reported in a new material, Fe-Se or referred to as (11) iron-chalcogenide at 8 K by Hsu et al. [66]. This compound has a simple structure of Fe-Se layers without intercalating cations, something quite different from the oxypnictides. Static magnetic ordering too does not occur up to a pressure of 38 GPa. Tellurium doping ($FeSe_{0.42}Te_{0.58}$) raises the T_c to 15 and 37 K at high pressure. Guo et al. [67] reported superconductivity in a compound of the composition $K_{0.8}Fe_2Se_2$ at 30 K at ambient pressure. The compound was synthesized through intercalation of Fe-Se by K. Figure 3.32 shows the crystal structure of this compound. Single crystal grown by flux method shows a tetragonal structure with $a = 3.9136(1)$ Å and $c = 14.0367(7)$ Å and space group I4/mmm. Obviously, the intercalation increases the c-axis parameter significantly. The carrier density as evaluated from Hall effect measurement turns out to be $1.76 \times 10^{21}/cm^3$. The Hall coefficient R_H is negative and constant above 105 K. The electrical conduction is thus electron dominated.

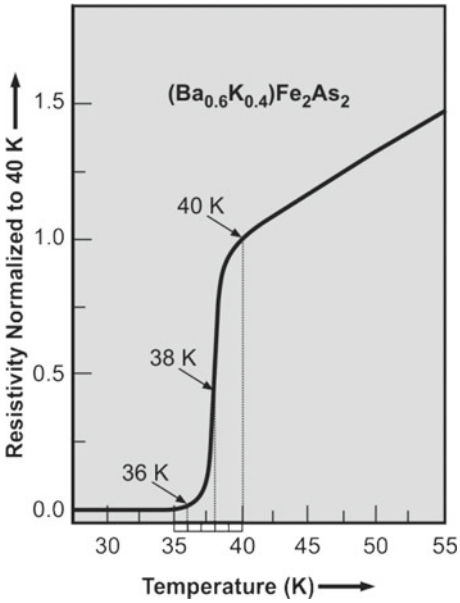

Fig. 3.31 Resistive superconducting transition in $(Ba_{0.6}K_{0.4})Fe_2As_2$ [65]. With permission from APS. http://journals.aps.org/prb/abstract/10.1103/PhysRevB.82.180520

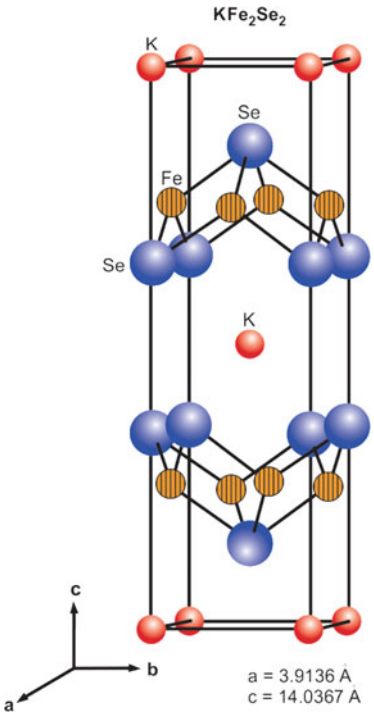

Fig. 3.32 Crystal structure of KFe_2Se_2 of the type $(ThCr_2Si_2)$ $a = 3.9136(1)$ Å and $c = 14.0367$ Å [67]. With permission from APS. http://journals.aps.org/prb/abstract/10.1103/PhysRevB.82.180520

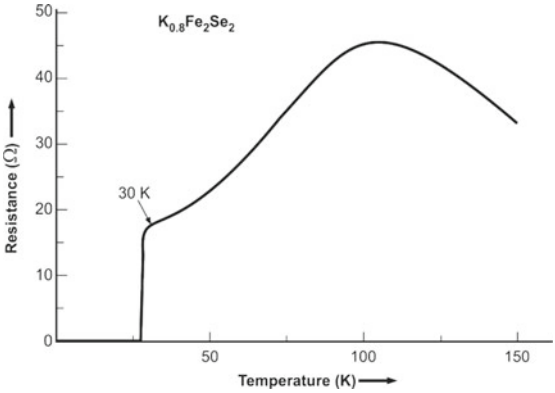

Fig. 3.33 Resistance–temperature behaviour of $K_{0.8}Fe_2Se_2$, below 150 K. Superconducting transition occurs at 30 K [67]. With permission from APS. http://journals.aps.org/prb/abstract/10.1103/PhysRevB.82.180520

The compound has a semiconductor behaviour in electrical resistivity between room temperature and 105 K below which it turns metallic and finally superconducting (at 30 K). The resistive transition of the $K_{0.8}Fe_2Se_2$ compound is shown in Fig. 3.33. The lower critical magnetic field B_{c1} and upper critical magnetic field B_{c2} have been calculated to be 0.2 T and 9 T, respectively.

The superiority of IBSCs over HT cuprates in many respects made them very attractive materials for research as well as for exploiting them for practical applications especially the high-field magnets. The deluge of papers that appeared within the first year of the discovery by Hosono is the testimony to the potential of these superconductors. The structural phase transition in these IBSC is very interesting. The interplay between the superconductivity and antiferromagnetic ordering (SDW) is quite fascinating. At the same time, the $J_c = 10^5$ A/cm^2 (4.2 K, 10 T) in these materials has already crossed the threshold of practical conductors. We will therefore discuss these IBSCs again in a separate Chap. 8 in greater detail.

3.12 Superconductivity at 203 K in Sulphur Hydride (H_3S)

After attaining a T_c well above 100 K in cuprates the next target for discovery became the room temperature superconductor. Luckily, the Eliashberg formulation of the BCS theory does not envisage an upper limit to T_c in a superconductor. A high-T_c BCS superconductor needs (i) high phonon frequency, (ii) very strong electron–phonon interaction and (iii) high density of states per spin per atom. Ashcroft [68] focused on hydrogen the lightest atom which has very high vibrational frequency and provides strong electron–phonon interaction. Mcmahon et al. [69] made calculations and predicted that metallic hydrogen should show superconductivity at 100–140 K in molecular phase and 300–350 K in atomic phase at a pressure of 500 GPa. Even though no superconductivity has been detected in hydrogen yet, several hydrogen-rich covalent hydrides like SiH_4, SnH_4 and H_2S were chosen for

studies. Hydrogen has high Debye temperature and thus high Debye frequency ($\theta_D = \hbar\omega_D/k_B$). Combining hydrogen with the heavier elements may also help to induce superconductivity as they contribute to low frequency known to enhance electron–phonon interaction. Besides, very high pressures needed to metallize pure hydrogen are no longer needed. Drozdov et al. [70] investigated H_2S which showed metallicity at ~ 96 GPa which improves further with increasing pressure. At 200 GPa, it has a resistivity of 3×10^{-7} Ω. They also observed that H_2S gets dissociated in to H_3S and elemental S, a favourable situation indeed. Superconductivity was confirmed with the observation of Meissner effect. Magnetic susceptibility measurements show a sharp transition from the diamagnetic to paramagnetic state for zero-field-cooled (ZFC) sample at T_c. Drozdov et al. [71] reported a record onset T_c of 203 K. Magnetization measurements reveal a pronounced hysteresis which indicated that it is a type II superconductor. The lower critical field B_{c1} is found to be < 30 mT. The T_c of sulphur hydride rises sharply as the pressure exceeds 150 GPa as shown in Fig. 3.34a. The T_c of the sulphur deutride stays lower than the T_c of the hydride at all pressures as expected in a BCS superconductor. Figure 3.34b shows the resistive superconducting transition at 185 K and 90 K, respectively, for the sulphur hydride and sulphur deutride. Highest T_c reported by Drozdov et al. for the sulphur hydride is 203 K [71]. Figure 3.34c shows the temperature dependence of the magnetization of sulphur hydride at 155 GPa in zero-field cooled (ZFC) and 20 Oe field cooled (FC) modes. The magnetization measurements clearly show an onset of superconductivity at 203 K. Optical micrograph of the sulphur hydride at 155 GPa is shown in the inset.

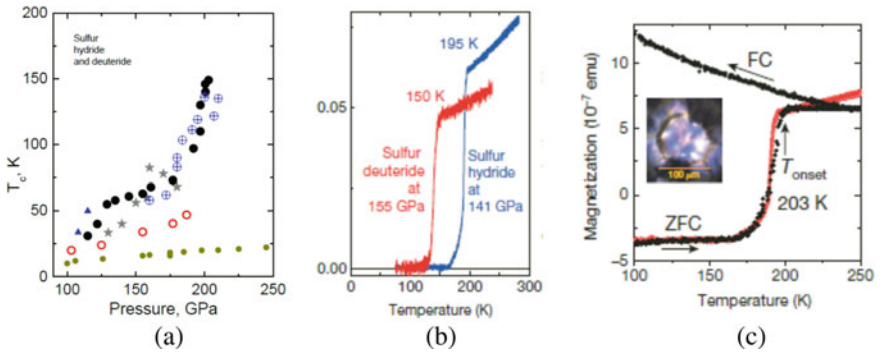

Fig. 3.34 **a** Dependence of T_c of sulphur hydride (different runs) and sulphur deutride (open circles) with pressure. Note the sharp rise of T_c at $p > 150$ GPa. T_c of sulphur deutride in the entire pressure range is lower than the T_c of sulphur hydride. The bottom plot (small circles) is for pure sulphur. **b** Superconducting transition at 150 K (@ 155 GPa) in sulphur deutride and at 195 K (@ 141 GPa) in sulphur hydride. **c** The temperature dependence of the magnetization of sulphur hydride at 155 GPa in zero-field cooled (ZFC) and 20 Oe field cooled (FC) modes. The $T_{c\ onset}$ is 203 K. Optical micrograph of the sulphur hydride at 155 GPa is also shown in the inset under cooled conditions [71]. With permission from Springer Nature

The synchrotron X-ray diffraction measurements by Einaga et al. [72] confirmed the presence of hydrogen-rich hydride, H_3S phase which is responsible for the emergence of superconductivity. It turned out that H_2S (D_2S) dissociates in to H_3S (D_3S) and elemental sulphur under high pressure $3H_2S \rightarrow 2H_3S + S$. The authors report that the compound in normal state as well as in superconducting state has the same structure as revealed from the XRD data obtained at room temperature and at low temperatures. Two superconducting phases with bcc structures have been identified. One with a crystal structure which correspond to R3m symmetry as shown [73] in Fig. 3.35a and b. This phase has a T_c of 120 K and is called the low T_c phase. Second phase appears when pressure increases to 150 GPa. This phase, called the high-T_c phase, has a structure with Im-3M symmetry (Fig. 3.35c) and is responsible for the

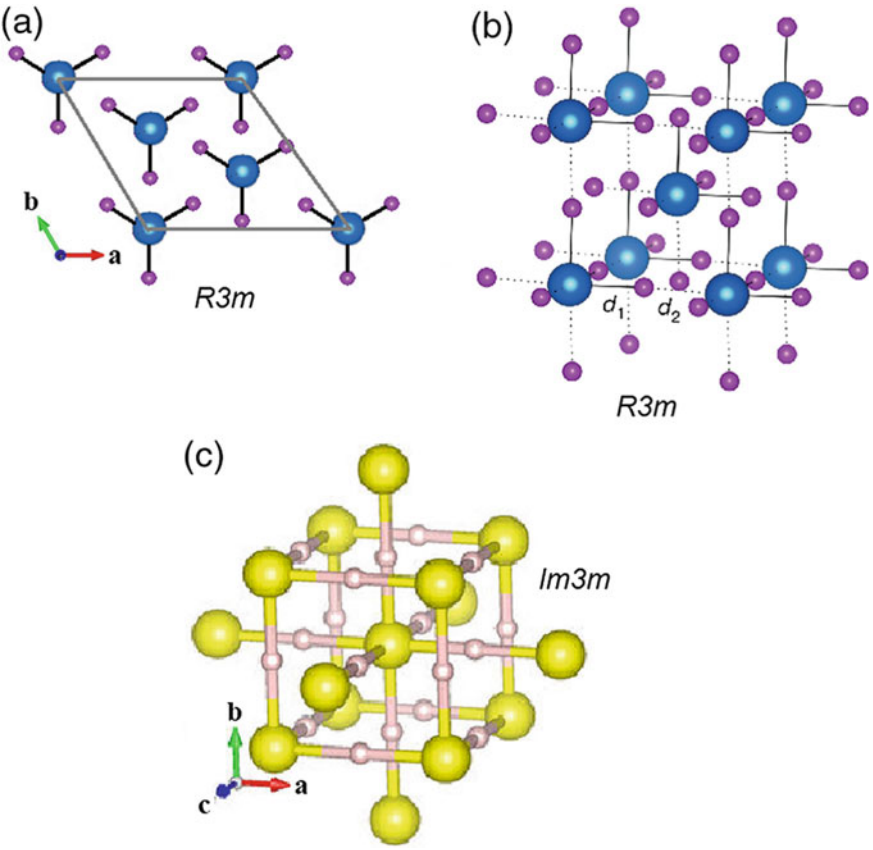

Fig. 3.35 Structures of the low T_c phase with R3m symmetry and $T_c = 120$ K (**a**) top view—large spheres are sulphur atoms and small spheres hydrogen (**b**) side view; one can see that d1 $\neq d_2$, d_i ($i = 1.2$) are the distances between the H ion and neighbouring S ions. **c** Structure of the Im-3m high-T_c (200 K) phases [73]. With permission from Am. Phys. Soc.

record $T_c \approx 203$ K. Even though the transition temperature increases with pressure, yet the structure does not change within a pressure range of 92–173 GPa. This appears contradictory to the sharp jump observed at 150 GPa in H_3S and 160 GPa in D_3S (Fig. 3.34 c). It is seen from this figure that the pressure dependence of T_c is different in the R3m phase at lower pressures and in the Im-3m phase at higher pressures. X-ray diffraction data are however found to be the same in the two phases and differ only in ordering of hydrogen atoms in the two pressure domains. It has been conclusively proven that the highest critical temperature of 203 K corresponds to the Im-3m phase of H_3S. The pressure dependence of T_c, however, reverses after the $T_{c\,max}$ has been reached. The T_c decreases upon further increase in pressure. This decline is however slow indicating that the pressure dependence of T_c is strongly asymmetric with respect to $T_{c\,max}$, which is somewhat unusual.

It will be of interest to look for other hydrides which may turn superconducting at still high temperature and possibly at room temperature. Indeed, many groups have carried out theoretical calculation and have predicted superconductivity with high T_c in several hydrides. Peng et al. [74] and Wang et al. [75] made many interesting predictions based on their theoretical calculations. Thus, for example, Wang et al. predicted superconductivity in calcium hydride, CaH_6 at 240 K, Li et al. [76] in YH_6 at 264 K. Feng et al. [77] also predicted superconductivity in MgH_6 at 264 K at a pressure of > 300 GPa. There are others who have predicted room temperature superconductivity but the moot question is that can we realize superconductivity which would be stable at ambient pressures which is a requirement of a practical superconductor.

3.13 Superconductivity at Room Temperature ($T_c = 288$ K @ 267 GPa)

The group led by Mikhail Eremets at the MPI for Chemistry, Mainz, Germany reported [78] still higher T_c of 250 K in LaH_{10} within the Fm3m structure at a pressure of 170 GPa. Superconductivity was confirmed through the observation of zero-resistance, isotope effect, and the dependence of T_c on external magnetic field. These magnetic field measurements yielded a value of the upper critical magnetic field B_{c2} (0 K) as ~ 120 T. This 50 K jump in T_c in hydrides gave strong indications that room temperature superconductivity is achievable using high pressure technique.

The record of $T_c = 250$ K in LaH_{10} too was broken in the following year (2020) by a team led by Ranga Dias of university of Rochester, USA [79] when the team reported an all-time high T_c of ~ 288 K in a compound containing C, H and S at a pressure of 267 GPa. Dias technique had merit in so far as the LaH_{10} was formed at high temperature by Drozdov et al. [78] but Dias used a milliwatt green laser into the diamond anvil cell (DAC) containing C-H-S mixture for several hours at 4GPa pressures before raising the pressure further. Their DAC also contained probes that recorded electrical resistance dropping to zero and confirmed superconductivity

through magnetic measurements. The Dias's team added a third component C to the sulphur hydride system in the hope to observe more structures and more chances to find higher T_c.They succeeded and discovered superconductivity almost at room temperature (RT), that is, 288 K (15 °C). The composition of the compound could not be ascertained but is believed to be in the range of CSH_6 to CSH_8.

A resistive sharp superconducting transition is observed in the C-H-S compound as shown in Fig. 3.36a. The T_c increases with increasing pressure and the highest T_c = 288 K is obtained at a pressure of ~ 267 GPa. Fig.3.36b shows the microphotographs of the sample during the photochemical process. The electrical leads in a four-probe configuration for resistance measurements can also be seen in the microphotograph. As seen from Fig. 3.36c T_c rises gradually with increasing pressure from 140 GPa up to a pressure of 220 GPa when a T_c = 194 K is reached. As the pressures is increased further T_c rises rather sharply until a highest value of 288 K is attained at a pressure of 267 GPa. The T_c of the samples was determined from the electrical resistance (R) and a.c. susceptibility (χ) measurements. A discontinuity appears at around 225 GPa between the two pressure regimes at which the rise of T_c with pressure becomes sharper. This method of pressure induced metallization followed by superconductivity thus appears to be a promising route to room temperature superconductivity. The next challenge will be to find an alternate route perhaps a chemical route to mimic such high pressure during the synthesis of material and yet realize room temperature superconductivity at ambient pressure.

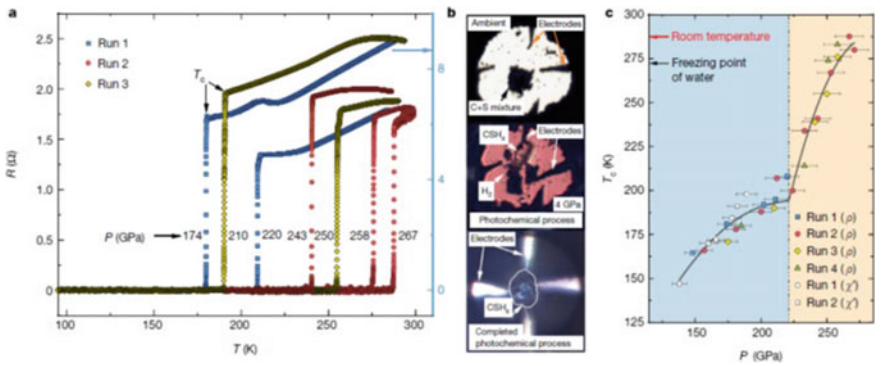

Fig. 3.36 **a** Resistive superconducting transition in C-H-S compound at different pressures. Highest T_c is obtained at ~ 288 K at a pressure of ~ 267 GPa. The vertical (R) axis on right is for two samples measured in a separate experimental run (shown by arrow). **b** Microphotographs of the samples during photochemical process in the C–S–H compound. Electrical leads in a four-probe configuration for resistance measurements are also shown. **c** Pressure dependence of T_c, as determined from the electrical resistance (R) and a.c. susceptibility (χ) measurements. Highest T_c = 288 K is observed for a pressure of 267 GPa (With permission from Springer Nature)

References

1. J.R. Gavaler, Appl. Phys. Lett. **23**, 480 (1974)
2. L.R. Tastardi, J.H. Wernick, W.A. Royer, Solid State Commun. **15**, 1 (1974)
3. J.G. Bednorz, K.A. Muller, Z. Phys. B: Condens. Matter **64**, 189 (1986)
4. D.C. Johnston, H. Prakash, W.H. Zachariasen, R. Viswanathan, Mater. Res. Bull. **8**, 777 (1973)
5. A.W. Sleight, J.L. Gillson, F.E. Bierstedt, Solid State Commun. **17**, 27 (1975)
6. C.W. Chu, P.H. Hor, R.L. Meng et al., Phys. Rev. Lett. **58**, 405 (1987)
7. R.J. Cava, R.B. van Dover, B. Batlogg, E.A. Rietman, Phys. Rev. Lett. **58**, 408 (1987)
8. R.P.Aloysius, Ph.D. Thesis, 2002, Cochin University of Science & Technology, Cochin
9. M.K. Wu, J.R. Ashburn, C.J. Torng et al., Phys. Rev. Lett. **58**, 908 (1987)
10. R.G. Sharma, Y.S. Reddy, S.R. Jha, S.S. Dubey, Pramana—J. Phys. **30**, L-81 (1988)
11. S.R. Jha, Y.S. Reddy, D.K. Suri, K.D. Kundra, R.G. Sharma, Deepak Kumar, Pramana—J. Phys. **32**, 277 (1989)
12. A. Pandey, R. Rajput, B. Sarkar, Y.S. Reddy, R.G. Sharma, Physica C **256**, 335 (1996)
13. A. Pandey, Y.S. Reddy, R.G. Sharma, J. Mater. Sc. **32**, 3701 (1997)
14. R.G. Sharma, S. Lahiry, A. Pandey, D. Bhattacharya, Bull. Mater. Sci. **22**, 265 (1999)
15. R.G. Sharma, Y.S. Reddy, S.R. Jha, Rev. Solid State Sci. **2**, 409 (1988)
16. P. Chaudhuri, R.H. Koch, R.B. Laibowitz et al., Phys. Rev. Lett. **58**, 2684 (1987)
17. T.R. Dinger, T.K. Worthington, W.J. Gallagher, R.L. Sandstorm, Phys. Rev. Lett. **58**, 2687 (1987)
18. H. Maeda, Y. Tanaka, M. Fukutomi, T. Asano, Jpn. J. Appl. Phys. **27**, L665 (1987)
19. M. Takano, J. Takada, K. Oda et al., Jpn. J. Appl. Phys. **27**, L1652 (1988)
20. B. Sarkar, Y.S. Reddy, R.G. Sharma, Mater. Res. Bull. **28**, 629 (1993)
21. S.R. Shukla, D.K. Pandya, N. Kumar, S.K. Sharma, R.G. Sharma, Physica C **219**, 483 (1994)
22. S.R. Shukla, Y.S. Reddy, N. Kumar, S.K. Sharma, R.G. Sharma, Pramana—J. Phys. **41**, 285 (1993)
23. H. Maeda, K. Innoue, T. Kiyoshi, T. Asano et al., Physica B **216**, 141 (1996)
24. M. Tachiki, S. Takahashi, Solid State Commun. **70**, 291 (1989)
25. K. Kadowaki, *Electronic Properties and Mechanism of High T_c Superconductors*, ed. by T. Oguchi, K.Kadowaki, T. Sasaki (North-Holland, Amsterdam, 1992), p. 209
26. M. Kikuchi, N. Ayai, T. Ishida et al., SEI Tech. Rev. No. **66**, 73 (2008)
27. Z.Z. Sheng, A.M. Hermann, Nature **332**, 55 (1988)
28. Z.Z. Sheng, A.M. Hermann, Nature **332**, 138 (1988)
29. S.S.P. Parkin, V.Y.Lee, E.M. Engler et al., Phys. Rev. Lett. **60**, 2539 (1988)
30. S.N. Putillin, E.V. Antipov, O. Chmaissem, M. Marezio, Nature **362**, 226 (1993)
31. A. Schilling, M. Cantoni, J.D. Guo, H.R. Ott, **363**, 56 (1993)
32. C.W. Chu, L. Gao, F. Chen et al., Nature **365**, 323 (1993)
33. L. Gao, Y.Y. Xue, F. Chen et al., Phys. Rev. **B50**, 4260 (1994)
34. E.V. Antipov, A.M. Abakumav, S.N. Putillin, Supercond. Sci. Technol. **15**, R-31 (2002)
35. C.P. Bean, Phys. Rev. Lett. **8**, 250 (1962)
36. C.P. Bean, Rev. Mod. Phys. **36**, 31 (1964)
37. A. A. Abrikosov, Zh. Eksperim. i. Fiz. **32**, 1442 (1957); Sov. Phys.—JETP **5**, 1174 (1957)
38. A. Xu, L. Delgado, N. Khatri, Y. Liu, V. Selvamanickam et al., Appl. Phys. Lett. Mater. **2**, 046111 (2014)
39. W.H. Warnes, D.C. Larbalestier, Cryogenics **26**, 643 (1986)
40. A.P. Malozemoff, Y. Yamada, in *100 years of Superconductivity*, ed. by H. Rogalla, P. Kes (CRC Press, Taylor & Francis Group, Boca Raton, FL, 2012), p. 689e702
41. H.W. Weber, Int. J. Mod. Phys. E **20**, 1325e1378 (2011)
42. J.F. Cepeda Grimaldos, M.V. Chiquillo, G.I. Supelano, D. Martínez et al., J. Phys.: Conf. Ser. **480**, 012036 (2014)
43. C.M. Ray, A.P. Malozemoff, Chapter 2, *Superconductors in Power Grid—Materials and Applications* (Woodhead Publishing Series in Energy, 2015), pp. 29–73

44. M. Liang, Depairing Current Density of Cuprate Superconductors. Ph.D. Thesis, University of South Carolina, USA (2013)
45. R. Arpaia, S. Nawaz, F. Lombardi, T. Bauch, IEEE Trans. Appl. Supercond. **23**, 1101505 (2013)
46. J. Nagamatsu, N. Nakagawa, T. Muranaka et al., Nature **410**, 63 (2001)
47. P.C. Canfield, S.L. Budko, Sci. Am. **292**, 80 (2005)
48. S.L. Budko, P.C. Canfield, Physica C **514**, 142 (2015)
49. N. Varghese, Ph.D. Thesis, Cochin University of Science & Technology, Cochin, India
50. V.V. Moshchalkov, M. Menghini, T. Nishio, Q. Chen, A. Silhanek et al., Phys. Rev. Lett. **102**, 117001 (2009)
51. H.J. Choi, D. Roundy, H. Sun, M.L. Cohen, Nature **418**, 758 (2002)
52. R.S. Gonelli, A. Calzolari, D. Deghero et al., Phys. Rev. Lett. **87**, 097001 (2001)
53. J. Bardeen, L.N. Cooper, J.R. Schrieffer, Phys. Rev. **108**, 1175 (1957)
54. S.L. Bud'ko, G. Lapertot, C. Petrovic, C.E. Cunningham et al., Phy. Rev. Lett. **86**, 1877-1880 (2001)
55. P.C. Canfield, G. Crabtree, Phys. Today **56**, 34–40 (2003)
56. Y. Elstev, K. Nakao, S. Lee et al., Phys. Rev. **B 66**, 180504 (2002)
57. B. Lorenz, R.L. Meng, C.W. Chu, Phys. Rev. B **64**, 012507 (2001)
58. S. Patnaik, L.D. Cooley, A. Gurevich et al., Supercond. Sci. Technol. **14**, 315 (2001)
59. V. Braccini, A. Gurevich, J.E. Giencke et al., Phys. Rev. **B 71**, 012504 (2005)
60. Y. Kamihara, T. Watanabe, M. Hirano, H. Hosono, J. Am. Chem. Soc. **130**, 3296 (2008)
61. H. Takahashi, K. Igawa, K. Arii, Y. Kamihara, M. Hirano, H. Hosono, Nature **453**, 376 (2008)
62. J. Jaroszynski, C. Scott, F. Riggs et al., Phys. Rev. B **78**, 064511 (2008)
63. P.M. Aswathy, J.B. Anuja, P.M. Sarun, U. Syamaprasad, Supercond. Sci. Technol. **23**, 073001 (2010)
64. F. Kametani, P. Li, D. Abrrimov et al., Appl. Phys. Lett. **95**, 142502 (2009)
65. M. Rotter, M. Tegel, D. Johrendt, Phys. Rev. Lett. **101**, 107006 (2008)
66. F.C. Hsu, J.U. Luo, K.W. Yeh et al., Proc. Natl. Acad. Sci. USA **105**, 14262 (2008)
67. J. Guo, S. Jin, G. Wang et al., Phys. Rev. B **82**, 180520(R) (2010)
68. N.W. Ashcroft, Phys. Rev. Lett. **21**, 1748 (1968)
69. J.M. McMahon, M.A. Morales, C. Pierleoni, D.M. Ceperley, Rev. Mod. Phys. **84**, 1607 (2012)
70. A.P. Drozdov, M.I. Eremets, I.A. Troyan, Conventional superconductivity at 190 K at high pressures, preprint at http://arXiv.org/abs/1412.0460 (2014)
71. A.P. Drozdov, M.I. Eremets, I.A. Troyan, V. Ksenofontov, S.I. Shylin, Nature **525**, 73 (2015)
72. M. Einaga, M. Sakata, T. Ishikawa, K. Shimizu et al., Nat. Phys. **12**, 835 (2016). https://doi.org/10.1038/nphys3760
73. L.P. Gor'kov, Rev. Mod. Phys. **90**, 011001–011011 (2018)
74. F. Peng, Y. Sun, C. Pickard, R. Needs, Q. Wu, Y. Ma, Phys. Rev. Lett. **119**, 107001 (2017)
75. H. Wang, J. Tse, K. Tanaka, T. Litaka, Y. Ma, Proc. Natl. Acad. Sci. USA **109**, 6463 (2012)
76. Y. Li, J. Hao, H. Liu, J. Tse, Y. Wang, Y. Ma, Sci. Rep. **5**, 9948 (2015)
77. X. Feng, J. Zhang, G. Gao, H. Liu, H. Wang, RSC Adv. **5**, 59292 (2015)
78. A.P. Drozdov, P. P. Kong, V. S. Minkov, S. P. Besedin et al., Nature **528**, 773 (2019
79. E. Snider, N. Dasebrok, N. Dasenbrock-Gammon, R. McBride et al. Nature **586**, 377 (2020)

Chapter 4
A Review of Theories of Superconductivity

Abstract The first ever phenomenological theory of superconductivity was propounded by London brothers (Fritz and Heinz) by correlating the current in a superconductor with a vector potential and using Maxwell equations. Theory explained well the vanishing of resistivity and the occurrence of Meissner effect in metallic superconductors. An expression for Londons' penetration depth λ was given which was confirmed experimentally. Another phenomenological theory was proposed by Ginzberg and Landau (G-L theory) introducing the concept of an order parameter and a temperature-dependent coherence length which close to 0 K is similar to the temperature-independent Pippard coherence length. The most successful theory, the microscopic BCS theory ultimately came from three physicists Bardeen, Cooper and Schrieffer in 1957. They argued that two electrons with equal and opposite momenta form a bound pair (Cooper pair), a boson, via the exchange of a virtual phonon overcoming the Coulomb repulsion. These pairs (bosons) condense into a ground state, a gap appears in the energy spectrum, and the system turns superconducting. The energy gap goes down to zero at T_c. Theory however could not explain the so-called high-temperature cuprate superconductors (HTS) which are similar to BCS superconductors in several respects but differ drastically in many others. There is no evidence of phonon mediation in pair formation in these materials as evidenced from the absence of isotope effect. After many attempts and a long turmoil, two theories have found some acceptance. First is the RVB resonance valence bond (RVB) theory proposed by P. W. Anderson, and the other is spin fluctuation theory proposed by P. Monthoux. The two concepts are qualitatively described briefly in this chapter. Recently, Christoph Renner through their STM studies observed Caroli–de Gennes–Matricon states (vortex-core states) in YBCO under magnetic field supporting the strong belief that superconductivity in cuprates may be of the BCS type. Li et al., based upon their ARPES data, have proposed a positive feedback mechanism. They argue that the incoherent correlations associated with the strange-metal normal state do not disappear; instead, they convert to strongly renormalized coherent state at temperature well above T_c as soon as the superconducting fluctuations set in. More recently, Yanagisawa et al. have proposed that superconductivity in high-T_c cuprates is induced by the strong on-site Coulomb interaction. The phase diagrams for 2D Hubbard model and the three-band d-p model show different regions of superconductivity, paramagnetic and ferromagnetic phases. Last word on the theory of high-T_c

R. G. Sharma, *Superconductivity*, Springer Series in Materials Science 214,
https://doi.org/10.1007/978-3-030-75672-7_4

superconductivity is, however, yet to come. MgB_2 superconductor discovered in 2001 with $T_c = 39$ K has fortunately turned out to be a BCS superconductor as also supported by the isotope effect. Origin of superconductivity in iron-based superconductors (IBSCs) with T_c as high as 55 K and more recently 100 K in a monolayer, discovered in 2008, has proved to be more complicated than the cuprates. Many groups of IBSCs [such as 1111, 111, 11 and 122] with different electronic structures pose problems in finding the right type of pairing mechanism. Newly discovered superconductor, sulphur hydride (H_3S) with record $T_c = 203$ K has been found to be a typical BCS superconductor. High T_c has been well accounted by the BCS theory with high-frequency optical phonons mediating in pair formation. It appears that the celebrated BCS theory may triumph one day and explain superconductivity in all types of superconductors after taking the peculiar structural parameters into account.

4.1 A Chronology of Theories of Superconductivity

In this chapter, we will review the development of important theories culminating into a successful microscopic theory formulated by Bardeen et al. [1] which explained all the important features of metal superconductors quite well. The first theory to explain the occurrence of superconductivity in metallic superconductors was given by London brothers [2] (Fritz London and Heinz London) in 1935. They had set out to formulate a law similar to the versatile Ohm's law valid for normal conductors. Ohm's law, however, cannot account for superconductors because current in a superconductor flows without a voltage. The formulation has also to explain Meissner effect which characterizes a superconductor and distinguishes it from a perfect conductor. Since Meissner state is a fundamental equilibrium state, the current flow must correlate with the applied magnetic field and not with the voltage. They drew a connection between the current density J and an electromagnetic vector potential A and employed Maxwell's expressions. The theory accounted well for the infinite conductivity as also for the Meissner effect. Another important landmark in this journey was the so-called GL theory proposed by Ginzburg and Landau [3]. The theory in its original form was a phenomenological theory in which they argued that free energy of a superconductor can be expressed in terms of a complex wave function $\Psi(r)$ which is an order parameter $\left(n_s = |\Psi(r)|^2\right)$ within the general theory of Landau of second-order phase transition. Gorkov [4] in 1959 did, however, show that the GL theory was a limiting case of the microscopic theory of BCS valid near T_c, where $\Psi(r)$ is proportional to the energy gap parameter. But the answer to the question that how a single wave function describes a superconductor not only at $T = 0$ but also at all temperatures below T_c came in 1957 from the BCS theory. These three gentlemen proposed that in a superconductor electron pairing takes place via the exchange of a virtual phonon and the pairs condense to a ground state. This was the first successful microscopic theory which accounted well for all the peculiar properties of the superconductor observed experimentally. These theories will be briefly

discussed. A concise description of the theories, as they existed in 1990, was given by Ramakrishnan and Rao [5]. A summary of theories proposed by various schools of thought to explain the occurrence of superconductivity in the cuprate superconductors or the so-called high-temperature superconductors (HTSs) will be discussed towards the end of this chapter. Rigorous treatment of any theory is outside the scope of the book.

4.2 Londons' Theory

London brothers started with the logic that if the electrons do not encounter resistance (superelectrons) they will continue to accelerate in an applied electric field such that

$$\frac{\mathrm{d}v}{\mathrm{d}t} = \frac{eE}{m} \tag{4.1}$$

where e, m and v are the charge, mass and velocity of the electron, respectively, and E the electric field. If we multiply both sides with the density of these superelectrons and the charge e, we get

$$\frac{\mathrm{d}}{\mathrm{d}t}(n_s ev) = \left[\frac{n_s e^2}{m}\right] E \tag{4.2}$$

But since $(n_s ev)$ in (4.2) is just the electric current density J_s, we now have

$$\frac{\mathrm{d}}{\mathrm{d}t}(J_s) = \left[\frac{n_s e^2}{m}\right] E \tag{4.3}$$

London(s) expressed the electromagnetic field in terms of a vector potential A. We thus have the relation between magnetic flux and the electric field,

$$B = \nabla \times A \tag{4.4}$$

And

$$E = -\left|\frac{\partial A}{\partial t}\right| \tag{4.5}$$

Combining (4.3) and (4.5), we get

$$\frac{\mathrm{d}}{\mathrm{d}t}(J_s) = -\frac{n_s e^2}{m}\left[\frac{\partial A}{\partial t}\right] \tag{4.6}$$

The expression for J_s can now be obtained by integrating (4.6). J_s is thus given by

$$J_{\mathrm{s}} = -\left(\frac{n_{\mathrm{s}} e^2}{m}\right) A \tag{4.7}$$

London(s) assumed the constant of integration to be zero so that the relation (4.7) is unique and which accounts well for the zero electrical resistivity.

The expression for the magnetic field B can be obtained by employing Amperes law

$$(\nabla \times B) = \mu_0 J_{\mathrm{S}} \tag{4.8}$$

Using (4.4) and (4.7), we can eliminate J_s and have an expression for B

$$\nabla \times (\nabla \times B) = -\left[\frac{n_{\mathrm{s}} e^2}{m}\right] \mu_0 B \tag{4.9}$$

Assuming the field along the z direction, we get London equation for field inside the superconductor along the x direction as given by

$$\frac{\mathrm{d}^2 B(x)}{\mathrm{d}x^2} = \frac{\mu_0 n_{\mathrm{s}} e^2}{m} B(x) \tag{4.10}$$

which has a solution of the type

$$B(x) = B_0 \exp(-x/\lambda) \tag{4.11}$$

The solution matches with the experimental observation that the magnetic flux is maximum at B_0 on the superconductor surface and drops exponentially inside it to $1/e$th value at a distance of λ, called Londons' penetration depth or just the penetration depth. The equation for the penetration depth λ thus becomes

$$\lambda^2 = \frac{1}{\mu_0}\left[\frac{m}{n_{\mathrm{s}} e^2}\right] \tag{4.12}$$

The penetration depth thus turns out to be inversely proportional to the square root of n_s, the superelectron density which changes with temperature. As the temperature increases, n_s decreases, and the flux penetration increases. At T_c, n_s decreases to zero, and the whole material is penetrated with magnetic field, thus turning the superconductor into the normal state. Although Londons' theory did explain the infinite electrical conductivity and the Meissner effect, yet the expressions (4.11) and (4.12) are only approximate insofar as the calculated values of λ differ from the experimentally determined values. This may be due to the uncertainty of the values of n_s, e and m taken for free electrons, which obviously cannot be justified.

The parameters like the superelectron density, n_s, their effective charge and effective mass have to be taken into account. After all, a superconductor cannot be treated as a free electron metal. Instead, superelectrons in a superconductor interact coherently.

4.3 The Ginzburg–Landau Theory

The Ginzburg-Landau theory of superconductivity or called just G-L theory [3] is a phenomenological theory and valid close to the transition temperature. Nevertheless, it accounts well for the main characteristic properties of the superconductors. Recognition of this theory came after Gorkov [4] showed that the theory can as well be derived from the microscopic BCS theory. Since superconductivity is caused by a second-order phase transition, this theory draws an analogy with the similar second-order ferromagnetic phase transition in metals like iron and nickel. The order parameter M, the magnetization in ferromagnets, has now been replaced by a macroscopic quantum wave function $\psi(r)$. The theory expresses the free energy of a superconductor in terms of the expansion of $\psi(r)$. Ginzburg and Landau treated the order parameter $\psi(r)$ as the wave function of the superconducting state which can vary with the location r. They expressed the order parameter $\psi(r)$ as $|\psi(r)|e^{i\varphi(r)}$ where $\varphi(r)$ is the phase. The gradient of the phase at r is related to the momentum, that is, the current flowing at the point r. Ginzburg and Landau expanded the free energy as a functional power series for small values of $\psi(r)$ and for its slow spatial variation as below

$$F\{\psi(r)\} = \int a|\psi(r)|^2 + (b/2)|\psi(r)|^4 + d\xi^2\left|\nabla\psi(r) - \left(ie^*/\hbar\right)A\psi(r)\right|^2 + (1/2)\mu_0\int |B(r)|^2 \mathrm{d}r \tag{4.13}$$

Terms *a, b and d* are the energy density terms. It is assumed that the term *'a'* is temperature-dependent and given by $a = a_0\,[(T - T_c)/T_c]$ and the terms b and d are assumed to be temperature-independent. The third term which is proportional to the squire of the gradient of ψ indicates the uniform value of $\psi(r)$ at minimum energy. The quantity ξ has the dimensions of length and represents a characteristic length scale over which $\psi(r)$ varies and can thus be identified with the coherence length. It is to be noticed that this square term also has the electromagnetic potential A because $\nabla\psi(r)$ is proportional to current which too depends upon A. Magnetic field energy is represented by the last term in (4.13). The free energy expression above assumes a configuration $\psi(r)$, yielding minimum free energy condition controlled by external parameters like temperature and magnetic field. Quite a few solutions of equation (4.13) are possible which yield various superconducting parameters.

The term ξ in (4.13), called Ginzburg–Landau coherence length, is given by

$$\xi_{GL} = \frac{\hbar}{|2m^* a(T)|^{1/2}} \tag{4.14}$$

This characteristic length is the distance over which $\psi(r)$ can change without appreciable energy increase. In a pure superconductor close to 0 K, $\xi_{GL} \approx \xi_0$ similar to temperature-independent Pippard coherence length. ξ_{GL}, however, diverges as $(T_c - T)^{-1/2}$ since 'a' vanishes as $(T - T_c)$. These two coherence lengths though based on the same concept yet are two different quantities. Coherence length decreases with the addition of impurity to the superconductor as the electronic mean free path decreases. In pure metal superconductors, the coherence length is of the order of few hundred nm and can be reduced to few tens of nm on alloying.

4.3.1 Flux Exclusion and Zero Electrical Resistance

The GL theory too leads to a London type relation between the electromagnetic vector potential 'A' and the electric current. Taking current density of a system of charges in a vector potential as the rate of change of its energy with vector potential 'A', we can write

$$j_s(r) = -[\partial F / \partial A(r)] \tag{4.15}$$

$$= -d\xi^2 \frac{ie^*}{\hbar}\left[\psi^*(r)\left(\nabla - \frac{ie^*}{\hbar}A\right)\psi(r) + c\right] \tag{4.16}$$

In a region where order parameter is uniform, that is, $\nabla\psi(r) = 0$, J_s is given by

$$j_s = -d\xi^2 |\psi|^2 \left(\frac{e^{*2}}{\hbar^2}A\right) \tag{4.17}$$

Which is the London equation. The constant of proportionality depends upon the order parameter $|\psi|^2$. As the order parameter decreases, penetration length increases. Since near T_c $|\psi|^2 \propto (Tc - T)$, the penetration depth λ should be proportional to $(T_c - T)^{-1/2}$. This variation of λ with temperature is indeed experimentally observed as shown in Fig. 2.11. The assumption that ψ does not vary spatially implies that London results are valid if ξ, the length scale of the variation of ψ, is much smaller than λ ($\xi \ll \lambda$). This condition is satisfied only in type II superconductors.

4.3.2 *Flux Quantization*

Londons' postulate that the flux inside a superconducting ring is quantized also follows as a consequence of GL theory. We know from our discussion on Meissner effect that the flux penetrates a superconductor a small depth λ only, being protected by the surface screening current. Deep inside the ring (contour C) the supercurrent as well as the field will be zero. Thus, (Fig. 4.1)

$$j_s = \psi^*(r)\left[\nabla - \frac{ie^*A}{\hbar}\right]\psi(r) = 0 \tag{4.18}$$

Since $\psi(r) = |\psi|e^{i\varphi}(r)$, (5.18) can be written as,

$$\nabla\varphi(r) - \frac{e^*A(r)}{\hbar} = 0 \tag{4.19}$$

The order parameter should have a unique value with minimum energy at every point along the circular path. In going round the circular path, phase $\varphi(r)$ should change only by an integral multiple of 2π. Thus, from (4.19),

$$\oint \nabla\varphi \cdot dl = \Delta\varphi = 2n\pi \tag{4.20}$$

Or

$$\frac{e^*}{\hbar}\oint A \cdot dl = \frac{e^*}{\hbar}\varphi \tag{4.21}$$

Or

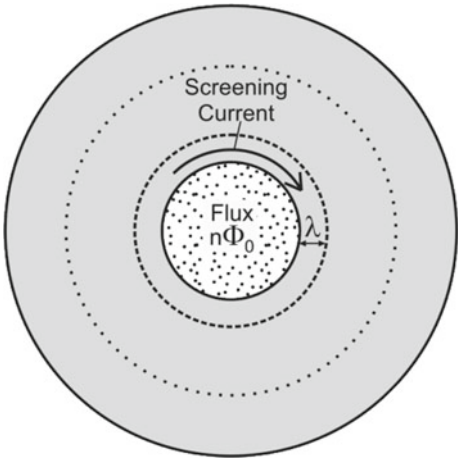

Fig. 4.1 The flux contained in a superconducting hollow cylinder or a circular ring is always an integral multiple of the unit quantum of flux $\varphi_0 = h/2e$

$$\varphi = \frac{nh}{e^*} = \varphi_0 \tag{4.22}$$

We thus find that the single valuedness of the order parameter leads to the flux quantization. The quantity e^* turns out to be equal to $2e$ in the microscopic theory.

4.3.3 GL—Parameter and Type II Superconductors

The ratio of Londons' penetration length λ and the GL coherence length ξ is called the GL parameter represented by κ, that is,

$$\kappa = \lambda/\xi \tag{4.23}$$

Since both the parameters λ and ξ diverge as $(T_c - T)^{-1/2}$, the GL parameter, κ remains temperature-independent. For typical classical metallic superconductors, λ is much smaller than ξ, and the ratio κ is smaller than 1. In fact, the value of the GL parameter distinguishes between two classes of superconductors type I and type II. For most metallic superconductor, $\kappa < 1/\sqrt{2}$, and for type II superconductors (like alloy superconductors and high-T_c superconductors), this ratio is $\kappa > 1/\sqrt{2}$. Thus, $\kappa = 1/\sqrt{2}$ (< 0.71) is the dividing line between the two classes of superconductors.

4.3.4 Josephson Effect

From the aforesaid discussion, we understand now quite clearly that a superconductor is defined by an order parameter $\Psi(r)$ with a phase which is constant within a superconductor. This phase can however be changed by an external magnetic field. Variation of phase causes a current to flow. If two superconductors with two different phases φ_1 and φ_2 are coupled weakly (like in a microbridge or a point contact), a current tends to flow across the weak link or the junction. This current is dependent on the phase difference $(\varphi_1 - \varphi_2)$. The expression for the current that flows through the weak link can be written as

$$i = i_c \sin(\varphi_1 - \varphi_2) \tag{4.24}$$

No current will flow if the phase difference $\varphi_1 - \varphi_2$ is zero. I_c in the above equation is the critical current of the junction and depends upon the junction strength. This is DC Josephson effect [6], and we have discussed it in some details in Chap. 2, Sect. 2.14. This current flows without a potential difference. In a geometry, like a superconducting ring, the phase difference will change with the flux in the ring which is quantized. Equation (4.24) will now take the form

$$i = i_c \sin\left[(\varphi_1 - \varphi_2) + 2\pi\varphi_{\text{junction}}/\varphi_0\right] \tag{4.25}$$

In a SQUID (Fig. 2.31), the two arms acquire different phases equal to 2π times the unit quantum of flux, φ_0 depending on the enclosed flux. The current will be maximum when the phase difference is 2π times φ_0 and minimum when the phase difference is an odd multiple of π. The current pattern is thus oscillatory when plotted against the magnetic field passing through the SQUID (Fig. 2.31).

An expression for the AC Josephson effect can be derived from the equation (4.22) by differentiating with respect to time, that is,

$$\nabla\frac{\partial\varphi}{\partial t} = \frac{e^*}{\hbar}\left(\frac{\partial A}{\partial t}\right) \tag{4.26}$$

Since the rate of change of vector potential A is V

$$\frac{\partial\varphi}{\partial t} = \frac{e^* V}{\hbar} \tag{4.27}$$

Thus, the phase difference between the two superconductors in a Josephson junction turns out to be

$$\Delta\varphi = \left[\frac{2eV}{\hbar}\right]t \tag{4.28}$$

Thus, if a voltage V is applied across the junction, an AC current with a frequency $2e\ V/\hbar$ will flow. We thus find that G-L theory accounts well for most of the characteristic parameters of a superconductor and establishes the fact that the free energy of a superconductor can be expressed as a function of an order parameter, which is influenced by external electromagnetic field.

4.4 The BCS Theory of Superconductivity

The sharp transition temperature (~ 10^{-5} K) in superconductors had long established the fact that superconductivity is a cooperative phenomenon in which a large number of entities (conduction electrons) take part. There are, however, two major difficulties. One that the electrons are fermions and obey Fermi–Dirac statistics according to which no two electrons can occupy the same quantum energy state. A cooperative phenomenon or the coherence among electrons is thus not feasible. Secondly, electrons experience Coulomb repulsion which will prevent them from coming together howsoever weak the Coulomb repulsion may be. Suggestion, that two electrons can have an attractive interaction via a lattice distortion overcoming the Coulomb repulsion, came first time from Fröhlich [7] in 1950. Fröhlich argued that electron–phonon interaction, which is associated with either the emission or the absorption of a phonon,

could lead to a new state of superconductivity. As the two electrons attract each other and form a bound pair, they behave like a boson obeying Bose–Einstein statistics. All the bosons can then condense coherently into a single quantum state. Confirmation of the electron–phonon (lattice) interaction responsible for superconductivity came from the discovery of isotope effect [8, 9] (discussed in Chap. 2, Sect. 2.10) in metal superconductors. In the same year (1950), Bardeen independently developed a theory [10] of electron–electron interaction via the exchange of a virtual phonon on similar lines.

4.4.1 The Cooper Pairs

Electron–electron attractive interaction via the lattice vibrations originally proposed by Fröhlich [7] can be understood using the following argument [11]. Let us assume that an electron passes through the lattice distorting it by attracting positive ions (Fig. 4.2). This lattice distortion, because of the large inertia, will lag behind the moving electron by a distance

$$d \approx v_{\mathrm{F}} \frac{2\pi}{\omega_{\mathrm{D}}} \approx 100 - 1000 \text{ nm} \tag{4.29}$$

where ω_{D} is the Debye frequency. This lattice deformation, because of the accumulation of positive charge, will attract another electron passing through this region. This attraction will be maximum when the second electron moves along the track left by the first electron and is a distance d away. This attractive force is a polarization force and lasts much longer as compared to the coulomb repulsive force between these two electrons, which is instantaneous. It is for this reason that even if the lattice distortion is weak, the attractive force mediated by it overcomes a stronger instantaneous Coulomb repulsion.

Cooper [12] studied to find what happens when two electrons with equal and opposite momenta $\vec{p}_1 = -\vec{p}_2$ with magnitude slightly more than the Fermi momentum

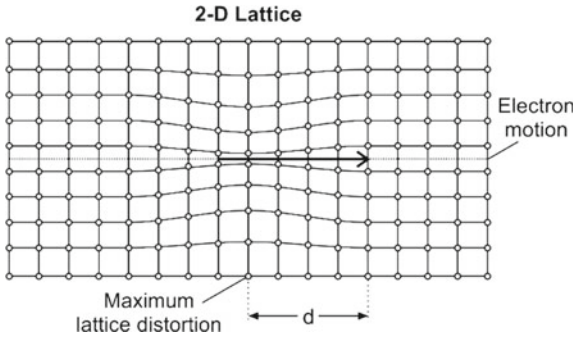

Fig. 4.2 Lattice deformation caused by the passage of an electron

p_F are added to a filled Fermi sphere. Because of the Pauli exclusion principle, these electrons cannot occupy energy state below the Fermi level being fully occupied. Instead, they tend to come together via the exchange of a virtual phonon and form a bound state. These pairs, called Cooper pairs have a binding energy of 10^{-3}–10^{-4} eV. To preserve this binding energy against thermal excitations, it is necessary to maintain the temperature low. The binding is strongest when the electrons have equal and opposite momentum so that the total momentum of the pair is zero and the pairs are in spin-singlet state. The size of the Cooper pair, 'r', can be calculated using the relationship

$$r = \left[\frac{\hbar v_F}{E_B}\right] \tag{4.30}$$

where E_B is the binding energy and v_F the Fermi velocity. Taking the E_B as 10^{-3}–10^{-4} eV and $v_F = 10^8$ cm/s in a metal, 'r' turns out to be 100–1000 nm, the same as d in (4.29).

Thus, we find that the size of the Cooper pair is quite large compared to the distance between two electrons (~ 0.01 nm) and thus is an extended entity. This implies that there will be a considerable overlapping of the Cooper pairs. As shown in Fig. 4.3, there will be hundreds of thousands of other pairs within the space occupied by one Cooper pair. Once electrons form a bound pair, all other electrons tend to realign into bound pairs as well. Bardeen Cooper and Schrieffer showed that the energy of

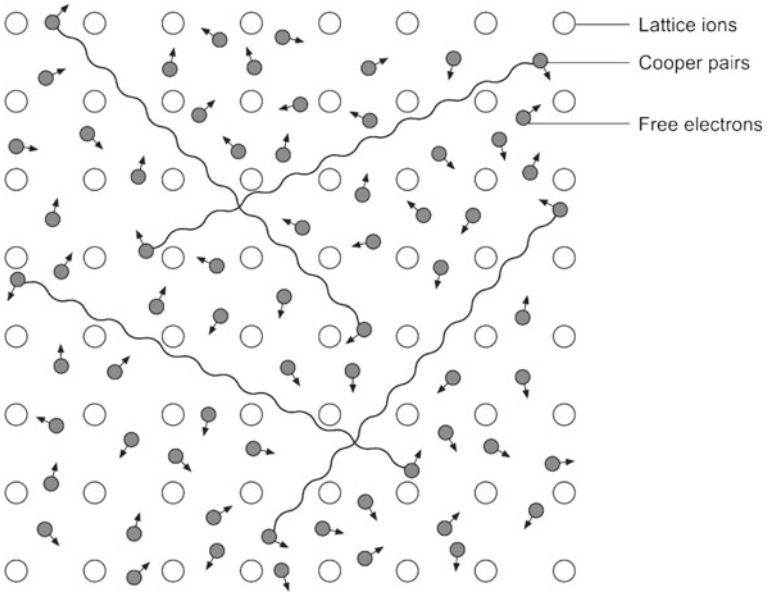

Fig. 4.3 Single electron and Cooper pairs in a metal lattice. Pairs extend over long distance

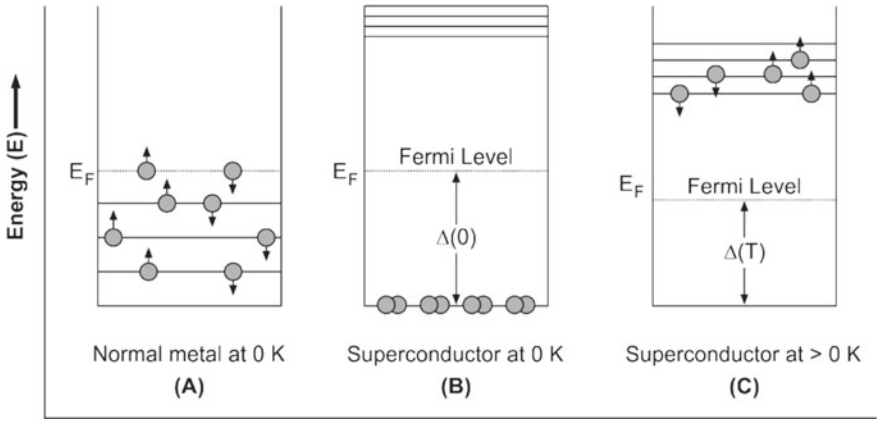

Fig. 4.4 Pictorial depiction of the energy spectrum of a metal and a superconductor

the system is lowest when all the pairs have the same momentum, that is, zero and have phase coherence.

The energy level diagram of a normal metal ($T = 0$), a superconductor at $T = 0$ and at $T > 0$, has been shown in Fig. 4.4. All the levels below Fermi level are filled in a metal, and those above Fermi level are empty. In a superconductor at $T = 0$, all the electrons form bound pairs and condense to the ground state, and an energy gap $= 2\Delta$ appears in the energy spectrum. A pair can be broken into quasi-electrons only when an energy equal to 2Δ is supplied to the superconductor. These electrons will occupy the empty levels above the energy gap. At finite temperature (below T_c), bound pairs as well as single electrons are interspersed. All the pairs occupy the ground state, and the single electrons occupy the levels above the energy gap.

4.4.2 Formulation of the Microscopic Theory

With the plethora of crucial experimental data on superconductors available and the phenomenological and semiphenomenological theories already developed, the time was just ripe for Bardeen, Cooper and Schrieffer to formulate their microscopic theory for superconductors. BCS set for themselves the task to formulate a theory that accounts for all the experimental observations, namely (i) the zero electrical resistance below T_c, (ii) second-order phase transition at T_c, (iii) Meissner effect, (iv) an energy gap of right magnitude, (v) a jump in specific heat at T_c and an exponential term in the electronic specific heat in superconducting state, (vi) dependence of T_c on isotopic mass and (vii) the penetration depth and its temperature variation.

The theory was built around the Cooper pair formation involving electron–electron interaction via the exchange of virtual phonon discussed above. This interaction is attractive when the energy difference between the electron states is smaller than the

phonon energy $\hbar\omega$. Superconducting phase is formed when this attractive force is greater than the repulsive screened Coulomb interaction. With the electrons now forming bound state, the energy is lowered, and pairs condense to the BCS ground state. An energy gap appears in the energy spectrum. An energy equal to this gap energy is required to break a pair. All the pairs in the ground state are indistinguishable and are in the same phase. They keep on changing their partners within a narrow energy band around the Fermi level. Momentum is conserved when a pair is formed $(k_1 + k_2) = \left(k_1' + k_2'\right)$. Here, k_1 and k_2 are the wave vectors of electron one and electron two before pairing, and k_1' and k_2' are the respective wave vectors after pairing. According to BCS theory, all the pairs can be represented by a single wave function. The state so produced is highly ordered. This order extends over the entire lattice and is responsible for most of the exotic properties of the superconductors.

A detailed analysis of the BCS theory is outside the scope of the book, and I refer to their original paper [1]. We, however, summarize below the important results and relationship between different superconducting parameters calculated by BCS.

4.4.3 Transition Temperature

In the weak coupling limit ($kT_c \ll \hbar\omega$), the expression for the transition temperature has been obtained by solving ground-state energy equations and is given by the expression

$$kT_c = 1.14\hbar\omega \exp\left[-\frac{1}{N(0)V}\right] \tag{4.31}$$

where $N(0)$ is the density of electron states of one spin per unit energy at the Fermi level and V the electron–phonon interaction parameter. Here, we find that T_c is proportional to the phonon frequency $\hbar\omega$ that is consistent with the observation of the isotope effect in superconductors. We also notice in (4.31) that T_c is a strong function of the electron concentration as the density of state enters in the exponential term. It is thus possible for one to make calculations for the change in T_c as a result of alloying or applying pressure.

4.4.4 The Energy Gap

Another remarkable finding of the BCS theory is that it predicts a relationship of T_c with the energy gap, which is given by

$$2\Delta = 3.5kT_c \tag{4.32}$$

It is interesting to note that the energy gap normalized to the zero temperature value when plotted for various superconductors against the reduced temperature, T/T_c, lies on a single universal curve as already shown in Fig. 2.20. The law of corresponding state does predict this ratio to be the same for all superconductors. As seen in Fig. 2.20, the energy gap at $T = 0$ is almost independent of temperature. Close to T_c, gap versus temperature relationship is given by

$$2\Delta = 3.2kT_c[1 - (T/T_c)]^{\frac{1}{2}} \tag{4.33}$$

4.4.5 Critical Field and Specific Heat

BCS theory predicts the critical field B_c to vary as $1 - (T/T_c)^2$ which is in conformity with the Gorter–Casimir two-fluid model [13]. Most of the B_c experimental data fall between the BCS curve and the $1 - (T/T_c)^2$ plot. The maximum deviation is 4%. The critical field at $T = 0$ is given by

$$B_{co} = [4\pi N(0)]^{\frac{1}{2}}\Delta(0) = 1.75[4\pi N(0)]^{\frac{1}{2}}kT_c \tag{4.34}$$

where $2\Delta(0)$ is the energy gap at $T = 0$, and the density of states $N(0)$ has been taken for a unit volume. On the basis of law of corresponding states, Eq. (4.34) yields

$$\gamma T_c^2/B_{co}^2 = \frac{1}{6}\pi[kT_c/\Delta(0)]^2 = 0.170 \tag{4.35}$$

Here, γ is the coefficient of the electronic specific heat of the normal state ($C_{en} = \gamma T$) and is given by

$$\gamma = \frac{2}{3}\pi^2 N(0)kT \tag{4.36}$$

The two-fluid model gives the value of the ratio in (4.34) as 0.159 quite close to the BCS value.

At T_c, the energy gap disappears, and the specific heat drops to normal state value. This peak in specific heat is caused by the onset of second-order phase transition. The ratio of the excess specific heat to normal state value at T_c turns out to be

$$\left.\frac{C_{es} - \gamma T_c}{\gamma T_c}\right|_{T_c} = 1.52 \tag{4.37}$$

The value of this ratio as given by Gorter–Casimir model is 2.00. Experimental values fall between 1.52 and 2.00. The experimental data on Sn fit extremely well with the BCS curve. BCS value near the T_c was later corrected, and the intercept at

$T = T_c$ became 2.52. The two curves thus almost overlap all through. The electronic specific heat can be expressed as

$$\frac{C_{es}}{\gamma T_c} = ae^{-bT_c/T} \tag{4.38}$$

Corak et al. [14] have reported their specific heat data on V and Sn which fit with the above expression quite well for $T_c/T > 1.4$ with parameters, $a = 9.10$ and $b = 1.50$. The BCS theory thus gives a very good account of the thermodynamical properties of the superconductors.

The BCS theory also yields expressions for all other superconducting parameters like critical current, coherence length and the penetration depth. It deals very successfully with Meissner effect and electro-dynamical properties of the superconductors. At the same time, the theory does not invalidate any of the then existing phenomenological theories. BCS theory remains to-date the successful microscopic theory of superconductivity. It stood the test of time and was awarded Nobel Prize only in 1972 a good 15 years after it was formulated. It explains well the behaviour of at least type I superconductors. Theory, however, does not predict which material should become superconductor and which should not. It has also not been successful in its existing form to explain the occurrence of superconductivity in so-called HTS cuprate superconductors.

4.5 Anomalous Properties of the Cuprates

As discussed in detail in Chap. 3, the discovery of superconductivity at 30 K in La-system [15] then at 92 K in YBCO [16] and at 110 K in BSCCO [17] caused unprecedented excitement among the superconductivity community. A race started to look for newer materials with higher and higher T_c. The discovery also threw a challenge to theoreticians to find a suitable theory which can account for high-T_c values far beyond what could have been accounted for by the BCS theory. While companies have been engaged in exploiting these materials for magnet and power applications, theoreticians remain entangled in solving the mystery. Leading theory groups have been putting forth various theories and hypothesis at times contradicting each other's viewpoint. High-T_c superconductors have several features quite common to the conventional superconductors but have many properties that are anomalous and at variance with conventional superconductors. This riddle continues to be unresolved to-date. We discuss below the anomalous properties that these superconductors display.

4.5.1 Temperature-Hole Concentration Phase Diagram

Cuprates are unique materials as far as they transform from insulating state to a superconducting state at an optimum level of doping. Oxides in general are supposed to be insulating in their solid state, but some of them, mostly binary and ternary oxides of transition metals, do show transition to metallic state under suitable condition of temperature, pressure and doping. What surprised us all in 1986 was that La_2CuO_4, which is an antiferromagnetic insulator with a Neel temperature of 290 K, turned metallic and subsequently showed superconductivity at 30 K when it was doped suitably with Ba or Sr. La is in La^{3+} valence state, Cu in Cu^{2+} valence state and O in O^{2-} valence state in the undoped La_2CuO_4 compound. If, however, La^{3+} is replaced by Sr^{2+}, either Cu has to be in Cu^{3+} state or O has to be in O^{1-} state. Spectroscopic evidence does suggest the presence of O^{1-} state, thus adding a hole in the otherwise filled p-shell. This hole concentration is proportional to the doping concentration x in $La_{2-x}Sr_xCuO_4$. The movement of holes leads to metallicity and ultimately to superconductivity.

The temperature-Sr doping (x) phase diagram [18] of this system is shown in Fig. 4.5. In the underdoped region, the material is an antiferromagnetic insulator. Below a temperature T^* and above T_c, the material has a pseudo-gap phase. The transition between the Fermi liquid and strange metal occurs gradually, and there is no sharp boundary between the two phases. Superconductivity occurs between $x = 0.06$ and $x = 0.28$, and the highest value of T_c is found for $x = 0.2$. QCP indicates quantum critical point at which T^* becomes zero. At increased doping level (over-doped), different phases are obtained at different temperatures. Superconducting phase occurs below T_c for a doping level $x = 0.05$ to $x = 0.28$. Thus, we find that the doping level is very crucial for the occurrence of superconductivity in cuprates. For very low doping called 'underdoping', the material is in a long-range antiferromagnetic

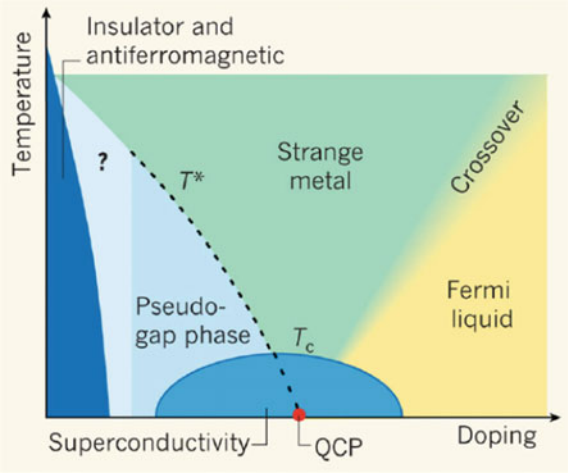

Fig. 4.5 Phase diagram of a hole-doped ($La_{2-x}Sr_xCuO_4$) cuprate, showing superconductive (SC), antiferromagnetic (AF), pseudo-gap, strange metal and Fermi liquid (FL) metal regions. Neel temperature (T_N), superconducting transition temperature (T_c) and pseudo-gap temperature scale (T^*) are indicated in figure [18]. *Courtesy* Chandra Varma and with permission from Nature Publishing House

state, it is superconducting for 'optimum doping', and finally, superconductivity disappears in 'over-doped' systems. T_c turns out maximum close to 0.2 holes/CuO_2 layer doping. The normal states above the superconducting dome at high temperature are abnormal in contrast with known states of matter found in nature. As shown in Fig. 4.5, the normal region can be divided into three parts, namely the pseudo-gap region for underdoped (small x), the strange-metal region (intermediate values of x) and a conventional metal (large x) in the over-doped region. Quite unlike a real-phase transition, the pseudo-gap state crosses over and goes into the strange-metal phase above a temperature scale shown as the pseudo-gap scale T^*.

4.5.2 Normal State Resistivity

The electrical resistivity of the cuprates is anomalous. As discussed, earlier cuprates are highly anisotropic materials. The resistivity in the Cu-O planes (ab planes) is quite different from that along the c-axis. Resistivity in ab plane is metallic over a wide range of temperature down to T_c where the material goes superconducting. Resistivity along the c-axis, on the other hand, is semiconducting, even though the material displays superconductivity at the same temperature, T_c. Thus, below T_c, one observes superconductivity in both the orientations. Cuprates also exhibit strong anisotropy in their J_c and B_{c2} behaviour.

Another anomalous behaviour of normal state resistivity is that in the ab-plane the resistivity varies linearly over a wide temperature range of several hundred K down to T_c as shown in Fig. 4.6. In normal free electron metals, well above Debye temperature (Θ_D) the resistivity is linear in temperature, but below Θ_D, it decreases rather fast ~ T^5. Resistivity in metals is caused by the scattering of electrons by phonons, lattice imperfections and other electrons. None of the above scattering mechanisms accounts for the observed variation of resistivity in cuprates.

This perfect linearity of resistivity with temperature all through, from the high temperature to near T_c, is a function of doping as well. This is seen from Fig. 4.7 for the compound $La_{2-x}Sr_xCuO_4$ [19] for different values of doping ($x = 0.07$, 0.15 and 0.34). The R-T plot is perfectly linear throughout the large temperature range for $x = 0.15$, that is for optimum doping. For underdoped and over-doped compound, the curves deviate from perfect linearity. This linear resistivity behaviour is certainly non-Landau's Fermi-liquid like and thus quite different from the normal metals. The underdoped regime ($x = 0.07$) marks the pseudo-gap causing a dip in resistivity below a certain temperature. Over-doped regime ($x = 0.34$) hints at the recovery of Landau's Fermi-liquid behaviour. Very strangely this linearity in R-T plot is found in all the cuprates with differing T_c values right from 20 to 120 K with almost similar slope.

Besides the anomalous linear resistivity/temperature behaviour, the cuprates also display normal state properties like Hall effect and frequency dependence of the electrical conductivity quite different from the normal metals. The electrical conductivity, $\sigma(\omega)$, for example, decreases as ω^{-1} instead of ω^{-2} expected for the normal

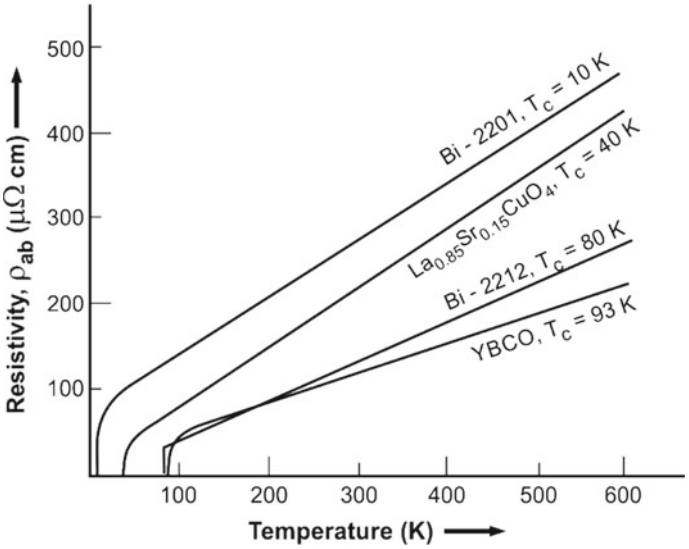

Fig. 4.6 Typical normal state resistivity of LSCO, YBCO, BSCCO-2201 and BSCCO-2212 in ab plane plotted against temperature. ρ-T is linear over a wide range of temperature. Adapted from [5]

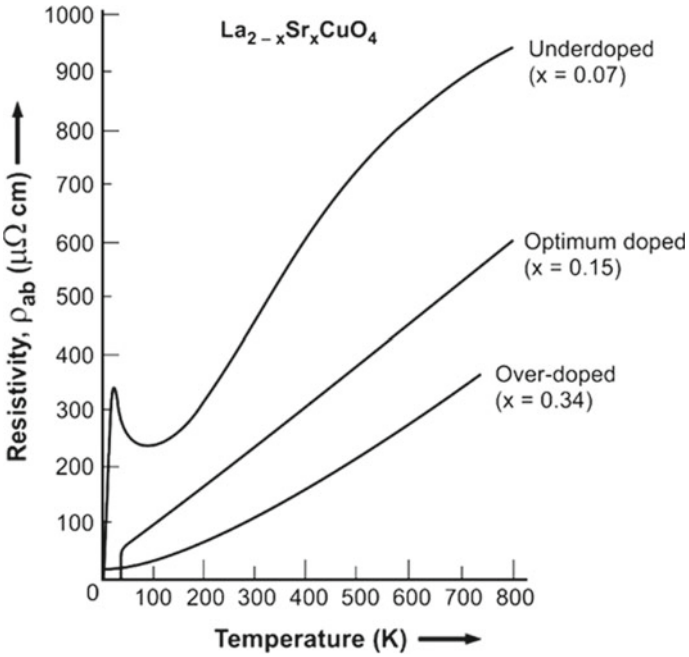

Fig. 4.7 Electrical resistivity of $La_{2-x}Sr_xCuO_4$ in ab plane for different doping levels ($x = 0.07$, 0.15 and 0.34). The perfect linearity for optimum doping ($x = 0.15$) and deviations for underdoped and over-doped compound are distinctly visible [19]. With permission from Elsevier

metal. Hall effect measurements yield parameters, namely Hall angle $\left(\theta_H \propto T^{-2}\right)$, Hall resistivity $\left(\rho_{xy} \propto T^{-1}\right)$ and the transverse magneto-resistance $\left(\Delta\rho/\rho \propto T^{-4}\right)$. In addition, the photo-electron spectroscopy shows that over a large energy range, the spectral function is dominated by an incoherent function. All these observations strongly hint at the failure of the Landau's Fermi-liquid theory in the optimally doped cuprates. The measurements on momentum transport scattering rate in resistivity in normal state show the processes dominated by electronic scatterings and not by electron–phonon scattering. There is enough evidence that the inverse lifetime increases with energy linearly and not quadratically as expected in normal metals. As seen from the phase diagram (Fig. 4.5), superconductivity occurs in a narrow region of optimal doping by holes. If more holes (0.3–0.4) are doped, the resistivity curve (Fig. 4.7) shows an upward turn which can be expressed by $\rho = \rho_0 + \rho' T^2$. The T^2 law is reminiscent of quasi-particle—quasi-particle scattering in Landau-Fermi liquids. The over-doped region thus tends to be closer to the Landau-Fermi liquid theory.

4.5.3 Presence of Pseudo-Gap in Highly Underdoped Superconductors

Several precision experiments like the specific heat, angle-resolved photoemission spectroscopy (ARPES) and the scanning tunneling microscopy (STM) have revealed the existence of a pseudo-gap in the energy spectrum of highly underdoped cuprates (Fig. 4.5), a strange behaviour indeed. This energy gap is quite different from the usual energy gap in superconductors which appears at T_c. The pseudo-gap exists over a wide range of temperature and doping. The understanding of the origin of this pseudo-gap may play a crucial role in understanding the mechanism responsible for the occurrence of superconductivity in these high-T_c superconductors. This energy gap is termed 'pseudo-gap' because it has no direct relationship with T_c. Through a systematic study on a heavily underdoped Bi(2212) system with $T_c = 30, 40$ and 50 K using ARPES technique, a Stanford group had observed distinctly two energy gaps along the Fermi surface in different parts of the momentum space. Their observation hints at the presence of a small gap with a sharp coherent peak near the nodal region identified with pseudo-gap and a larger gap at the antinodal region identified as the normal–superconducting gap. The two gaps, however, display opposite behaviour on doping. The magnitude of the larger gap scales with T_c in conformity with the BCS theory.

The presence of a pseudo-gap is the unique features of cuprates, and its origin may as well throw light on the occurrence of superconductivity in these materials. Above experiments also confirm that the pseudo-gap is not a precursor to superconductivity. Instead, this state competes with the superconducting state. These studies reveal that superconductivity in the underdoped state is weakened by the loss of coherence due to a reduction in the superfluid density and weakening of the pair amplitude. The

reduction in the superconducting gap may be related to the shrinkage of the Fermi surface due to underdoping, leading to a reducing phase space for pairing.

4.5.4 Comparison with Conventional Metallic Superconductors

Although cuprates have many similarities with the conventional superconductors, yet they behave very differently in many respects. For example, the following three experimentally determined dimensionless ratios for cuprates are all within the range of conventional superconductors. These ratios are

$$\text{(i)}\ \frac{2\Delta}{kT_c} \approx 3.5 - 4.8 \tag{4.39}$$

$$\text{(ii)}\ \frac{2\Delta}{\gamma T_c} \approx 1.5 \tag{4.40}$$

$$\text{(iii)}\ \frac{B_c}{4\pi N(0)^{\frac{1}{-\Delta}}} \approx 1 \tag{4.41}$$

2Δ being the energy gap.

Formation of Cooper pairs ($e^* = 2e$) has been confirmed in cuprates experimentally through the observation of DC/AC Josephson effect.

Existence of an energy gap in the single particle energy spectrum is confirmed, though high in comparison with the transition temperature thermal energy.

Isotope ^{18}O has been substituted in place of normal ^{16}O, but the decrease in T_c observed is small, putting a question mark on the exact role of lattice in pair formation in cuprates.

Flux quantization $\left(\varphi = \frac{h}{2e}\right)$ too has been confirmed in these materials.

Cuprates are extreme type II superconductors, that is, $(\lambda/\xi \gg 1)$, meaning thereby that the field penetration is large because of low carrier concentration $\approx 2 - 5 \times 10^{21}/\text{cm}^3$. Consequently, these superconductors also show poor Meissner shielding. In clean limit, $\xi_{T=0} \ll$ mean free path which is of the order of 10–20 nm near T_c. Following the BCS expression for coherence length $\xi = \hbar v_F/\pi\Delta(0)$ and taking the Fermi velocity $v_F = 1.1 \times 10^7$ cm/s and the gap parameter $2\Delta(0) = 6kT_c$ coherence length, ξ_{ab} turns out to be 1.5 nm which is a typical value for YBCO in ab plane. However, the coherence length along the c-axis, $\xi_c = 0.15$–0.3 nm, is much smaller than in the ab plane. This low value of ξ_c indicates that the CuO_2 layers are weakly coupled because of large charge reservoir layers.

The concept of short coherence length is interesting as far as it indicates at low carrier concentration < 1 per CuO_2 layer. Since coherence volume ξ^3 contains 5–10 CuO_2 units, it has less than five pairs far less than the 10^4 pairs in aluminium superconductor. This leads to pronounced fluctuation effects. The $B_{c2} = \varphi_0/2\pi\xi^2$ of

these superconductors turns out of the order of 100 T which is almost four to five times the B_{c2} value for conventional best superconductor, the Nb_3Sn. Peculiar features like different mobilities, the layered structure and the granular nature of these materials make it very difficult to work out transport parameters. These materials characterized by short coherence length and high penetration depth also display most unusual vortex state.

Another complication in high-T_c cuprates comes in their J_c-B behaviour. These materials show sharp drop in J_c with increasing magnetic field because of the large angle grain boundaries, which block the grain-to-grain current flow. Grains are thus weakly coupled as discussed in detail in Chap. 3. J_c is therefore quite different within the grain and in the inter-grain region. Intragrain J_c is usually very high. Material being highly anisotropic J_c in *ab* plane is much higher than along the *c*-axis. These materials show enhanced flux creep and flux flow effects because of high operating temperature (high T_c) and low pinning potential. The flux creep or the so-called thermal activation leads to a time decay of J_c from J_{co}, the value without thermal activation. Several techniques have been tried to introduce defects to pin the flux motion. Highest value of J_c has been obtained by growing highly oriented epitaxial films and highly pure single crystals.

HT cuprates are thus very unconventional but fascinating materials. What causes the carriers to pair up below T_c is still an unresolved issue.

4.6 Possible Theories of HTS

A detailed account of the theories proposed during this period of more than three decades by very many theorists is outside the purview of the book, and we just mention about a couple of serious attempts made to explain the occurrence of superconductivity in these cuprates. Formation of charge carrier pairs in these materials is well established experimentally, but to find the mechanism of formation of the pair has proved to be a daunting task.

In BCS superconductors, T_c increases with the lattice frequency and the electron–phonon coupling parameter. Even after taking the largest possible values of these two parameters for the known materials, T_c cannot exceed 35–40 K if the pair formation is assumed to be phonon mediated. Obviously, a new possible mechanism for the Cooper pair formation is to be worked out, and the ensued theory should be able to explain all the normal and anomalous properties of the cuprates. We just give a summary of a few credible attempts made by the theorists.

Various theories were proposed by many theory groups during last 34 years ranging from the extension of the BCS theory (attraction mediated by phonons), the excitonic mechanism based on electronic polarization, the marginal Fermi liquid theory, spin bipolaron (or spin bag), the resonating valence bond (RVB) theory and the spin fluctuation theory. After a long time of fights and turmoil, people have by now come to accept two theories on which the work still continues.

4.6.1 The Resonating Valence Bond (RVB) Theory

The concept of resonating valence bond (RVB) was originally introduced by Linus Pauling [20] in the context of pπ bond states of some organic molecules. The valence bond develops between a pair of atoms bonded by sharing of unpaired valence electrons of the atoms at the outermost levels. The bonded electrons form a singlet which resides in between the atoms. This singlet can also be considered a dimer. In a lattice when valence bonds or dimers between a pair of atoms (nearest neighbours) stabilize into a configuration of many body singlet pairs, a stable state is formed which is actually a resonating valence bond state. This state is a superposition of all the possible singlets. It also shows that these singlets move freely between the pair of atoms and thus can give rise to even a metallic state. However, this superposition gives rise to an energy gap at $T = 0$ with respect to any state with long-range charge fluctuations and therefore, the resonating valence bond state in its pure form cannot be a metal.

Anderson [21] revived this concept for describing the ground state of the Mott insulators where electron–electron correlation in systems with one electron per unit cell yields an insulating ground state while forming singlet pairs. The spin-1/2 excitations in these systems could either form an antiferromagnetic Neel state at $T = 0$ or a fluctuating resonating valence bond state with superposition of singlet pairs. The fluctuations are quantum in nature which is further enhanced in lower dimension and geometric frustration. The Neel state is a solid, while the RVB state is a liquid. In one dimension, both the states are identical, and there is no energy difference between them. However, in two dimensions, the RVB state is found to be more stable with lower free energy. This can be easily understood in a triangular lattice of spin-1/2 particles. The antiferromagnetic coupling between a pair of spins cannot yield a stable configuration while satisfying the condition of spin pairing between any two nearest neighbours. Therefore, the stable state is the one which is a superposition of the fluctuating states—a resonating valence bond state. Soon after the discovery of cuprate superconductors, Anderson [22] realized that the essential physics of the origin of superconductivity is contained in the electronic states of the Cu-O planes which are present in all the cuprates. The Cu-O planes with spin-1/2 excitations yield a fluctuating spin liquid—essentially a RVB liquid state. Once again, this state appears with a gap with respect to the long-range charge fluctuations and, therefore, is an insulator. The statistics of these spin-1/2 particles appear to be different from normal Fermi–Dirac statistics of indistinguishable particles such as electrons. These localized spin singlets (notwithstanding the fluctuations) do not conduct electricity. Only when this Mott insulator is doped by creating holes in the electron states, the electrons flow and carry current and thus induce metallicity.

Interestingly, it has been found that the collectivfve behaviour of the strongly interacting localized spins and delocalized holes leads to fractionization and these quantum particles acquire two different dispersion patterns and are clearly distinguishable from each other—spin-1/2 particles (spinons) are more like fermions (ordinary electrons), while the charged particles are spinless bosons (holons). Separation

of spin-charge spectra in two-dimensional Cu-O layers is an important outcome of the RVB concept. Depending on the doping level x, a certain number of spin-singlet states thus get charged and form Cooper pairs. They condense following either Bose or Kosterlitz–Thouless condensation and give rise to the superconducting state. One important point worthy of mention here is that the RVB state of spin-singlet pairs gives rise to a pseudo-gap at T^* ($> T_c$) at which the pairs break. Experimental observation of the pseudo-gap [23] in cuprate superconductors points out that the RVB state does form and offers the background for superconductivity to emerge. However, recent experiments offer a contradictory picture as far as the superconductivity within RVB context is concerned. In Anderson's theory, the pseudo-gap is a precursor of the superconducting gap, and therefore, it should vanish at T_c. Yoshida et al. [24] on the other hand have confirmed, through ARPES experiments on LSCO system, the coexistence of pseudo-gap together with superconducting gap below T_c. It thus appears that the Cooper pairs do not originate from the charging of the spin-singlet pairs. Instead, they originate elsewhere even though the collective modes of the background RVB state do bind them. The doped hole actually resides in oxygen ions instead of Cu 3d levels [25]. This, in turn, breaks the spin singlets and creates free d-electrons instead of d holes. These free d-electrons form the Cooper pairs while retaining the RVB background and the pseudo-gap. The theory has been built further by Anderson and co-workers [26–28].

4.6.2 The Spin Fluctuation Theory

The second theory is the spin fluctuation theory developed by Monthoux and coworkers [29–31] that finds wider acceptability within the superconductivity fraternity. The theory is based upon the premise that the full treatment of charge and spin degree of freedom of the electrons is essential which predicts an attractive component of the interaction between electrons without invoking the phonon mediation. Cooper pair formation is possible through the involvement of spin fluctuations. The theory envisages that in an undoped cuprate the magnetic field, produced by the antiferromagnetically aligned spins of the outer most electrons of copper atoms, locks the electrons in place. So, it remains an insulator. Doping makes these electrons mobile rendering them free to move. A passing electron may set up a pulsating pattern of spins quite similar to the lattice distortion in conventional superconductors. This distortion can pull another electron allowing the two electron pair up to form a Cooper pair. This leads to unconventional type of superconductivity in materials like the cuprates which show sensitivity to the fine details of the crystal structure, the electronic property and the magnetic property of the material. This theory too rules out the role of lattice in the occurrence of superconductivity for the same reason of not finding isotope effect in these materials like we found in conventional superconductors.

The focus of the theory has been to understand the origin of the physical properties of the cuprates in their normal state which can give a clue to the occurrence of superconductivity at high temperatures. It is argued that strong antiferromagnetic correlations of the nearly localized Cu^{2+} d orbitals are responsible for the unusual normal state properties. The same correlations are responsible for the existence of superconductivity with high T_c. The theory deals with the interaction of quasi-particles having same charge and spin but not the same mass. In a real metal, an electron with its moving cloud can be considered as a quasi-particle. Its effective mass can be two or more orders of magnitude higher than the mass of an electron.

It was established earlier that quasi-particle scattering [32] by paramagnons results in electrical resistivity which varies linearly with temperature. This quasi-particle interaction produced by magnetic excitations leads to superconductivity at higher T_c with a d-wave gap. The presence of conventional s-wave pairing has been ruled out by the detailed NMR studies on these materials. Enough experimental evidence exists which confirms the presence of a d-wave pairing. Schrieffer et al. [33] too believe that antiferromagnetic correlations play important role in the determination of T_c of the superconductors but argue that the coupling between the quasi-particles and spin fluctuations is so strong that the normal state excitations are solitons (spin bag). They go to the second-order spin fluctuation exchange to get s-wave superconductivity rather than going to first-order term to get d-wave superconductivity.

The important results obtained by Monthoux et al. [29] can be summarized as

(a) $$T_c = \alpha \hbar \omega_{SF}(T_c) \frac{\xi^2(T_c)}{\alpha^2} \exp\left[-\frac{1}{\lambda(T_c)}\right] \tag{4.42}$$

$$\cong \alpha \frac{\Gamma(T_c)}{\pi^2} \exp\left[-\frac{1}{\lambda(T_c)}\right] \tag{4.43}$$

where ω_{SF} is the paramagnon energy, the dimensionless effective coupling constant—$\lambda(T_c) = \eta g_{eff}^2(T_c)\chi_0(T_c)N(0)$ varies from 0.48 to 0.33 in the compounds. α and η are the constants of the material and are of the order of unity.

(b) In spite of the poor coupling below T_c, the energy gap does open up rapidly reaching a maximum. This energy gap is larger than the gap in weak coupling BCS superconductors. The results are in conformity with the experiments.

(c) Smaller values of T_c and larger values of $\Delta_{max}(0)/k_{BTc}$ are, however, obtained if the antiferromagnetic correlations happen to be strong.

(d) The temperature variation of the calculated planer spin susceptibility is found to be of right magnitude and matches well with experiments [34].

(e) The coupling constant $g_{eff}^2(T_c)$ evaluated from λ accounts well the anomalous resistivity as well as the optical properties of the normal state.

NMR experiments [35, 36] on $Y_1Ba_2Cu_3O_7$ in superconducting state have confirmed, first time, the presence of unconventional superconductivity in this material. The experimentally measured temperature-dependent anisotropy of the relaxation rates of the ^{63}Cu and ^{17}O nuclei for field in plane and perpendicular to plane rule out the possibility of s-wave pairing being responsible for superconductivity in this system. Bulut and Scalapino [37] also confirm that the superconductivity is of the d-wave pairing type.

We thus find that the spin fluctuation-mediated coupling model is quite an attractive one. The strong electron correlation between the local moment and the conduction electron leads to an anisotropic pair wave function in k-space with nodes on the Fermi surface. This d-wave symmetry of the pair wave function or the superconducting gap has been observed experimentally as well. A good successful theory has, however, yet to come which can explain everything and make good sense of huge data reported in literature till now.

Since last word on the theory of HTS has not been said, various mechanisms to explain superconductivity in HTS continue to be proposed by theorists. Let us discuss briefly a few of them.

4.6.3 Revisiting BCS Theory to Explain HTS Superconductors

Since HTSs exhibit some of the properties which are at odd with conventional BCS superconductors, the general belief has been that the BCS theory does not explain these superconductors adequately and theorists started looking into a theory which is fundamentally different from BCS. Specifically, the Abrikosov vortices fail to exhibit localized states in HTS which are observed in all clean superconductors. Berthod et al. [38] combined local tunneling measurements with large-scale theoretical modelling and identified the elusive vortex states in $YBa_2Cu_3O_{7-\delta}$ actually present, though weak. On the basis of the observation of vortex states in HTSs, which is a crucial feature of the BCS theory, the authors argued that superconductivity in HTSs is of conventional nature. Abrikosov vortices act as potential barrier confining non-superconducting electrons which results in bound states with discrete energies, known as Caroli–de Gennes–Matricon states [39]. The non-observation of these states in cuprates led the theorists to search for a theory other than the BCS theory. Let us go through briefly the arguments put forward by the team [38] in favour of BCS theory for HTS which are based upon their scanning tunneling spectroscopic measurements.

Vortices can be observed using scanning tunneling spectroscopy (STS) in which a tip scanning over the superconductor surface records a peak at the centre of the vortex core which corresponds to zero electrical bias between the tip and the superconductor. Fischer et al. [40] had earlier observed discrete states at energies close to one quarter of the superconductor's pseudo-gap through their STS studies in $YBa_2Cu_3O_{7-\delta}$

which was not in conformity with BCS predictions. Subsequently, Renner's group concluded from their STS experiments that those sub-gap features were not related to vortices. Instead they decided to isolate superconducting states from other collective electronic states, such as charge order, spin order and pseudo-gap states, which may coexist with superconductivity in cuprates. Thus, two different 'channels' of electrons, a superconducting (SC) one and a non-superconducting (NSC), will affect the material's electronic properties. The NSC channel, with higher electron density than in the SC channel, can mask the SC channel and complicate the investigation of vortex states. Assuming the two contributions additive, they applied a magnetic field and subtracted the conductance measured inside the vortices from that measured outside of the vortices. Since the NSC channel is not affected by the vortices, this leaves out only the conductance in SC channel. The SC channel signal thus derived showed clear zero-bias conductance peaks (ZBCPs) corresponding to vortex-core states. The authors identified 19 vortex cores in a scan of a $90 \times 90\ \text{nm}^2$ $YBa_2Cu_3O_{7-\delta}$ sample. The authors interpreted these peaks as Caroli–de Gennes–Matricon states inside the vortex cores, thus conforming to BCS theory. Renner and co-workers observed experimentally that vortex states are produced when a magnetic field is applied to YBCO quite similar to in conventional type II BCS superconductors. This inference finds support in newly discovered superconductors with high T_c such as monolayer FeSe films with $T_c > 65$ K [41] and pressurized H3S with $T_c = 203$ K [42] which can be explained by BCS theory. These claims have however been disputed by other theorists. In fact, for wider acceptance of the validity of BCS theory for HTS need more STM spectral studies in other cuprate superconductors. Also, equations for the calculation of various superconducting critical parameters need to be derived and verified experimentally. Renner and co-workers also have to produce justification for the additiveness of the tunnelling conductance from SC and NSC channels [43]. Nevertheless it is a bold attempt to find a unified theory for a wide family of high-T_c superconductors.

4.6.4 Positive Feedback Mechanism for High-T_c Superconductivity

Li et al. [44, 45] have proposed yet another pair mechanism, referred to as the positive feedback mechanism based upon their angle-resolved photoemission spectroscopy (ARPES) measurements on Pb-doped Bi-2212 cuprate superconductor. The authors argue that electrons in normal state of the cuprates are correlated quite differently than in other types of superconductors including conventional BCS superconductors. Most of these superconductors have strongly coherent electronic correlations. On the contrary, the cuprates in their normal state have strongly incoherent 'strange-metal' electron correlations. These incoherent correlations associated with the strange-metal normal state do not wither away when cuprates become superconducting. Instead, these incoherent correlations convert into strongly renormalized coherent

states which lead to stronger superconducting state renormalization. This conversion starts as soon as the superconducting fluctuations set in, that is, at temperature well above the T_c. This conversion increases the number of states that can form pairs. This amounts to a type of a 'positive feedback'—the conversion creating the pairing and pairing enhancing the conversion. The authors emphasize that such a positive feedback mechanism can be the basis for superconducting paring in cuprates.

This strong positive feedback effect stabilizes and strengthens superconductive pairing favouring an anisotropic (d-wave) superconducting gap. This mechanism allows much stronger pairing than the conventional strong coupling in the framework of the BCS theory. It also makes a fully electronics mechanism possible for the occurrence of superconductive pairing without the involvement of phonons.

4.6.5 Pairing in Strongly Correlated Electron Systems

After the broad consensus reached among the theorists that the pair formation in cuprates is not phonon mediated, many investigators switched over to electronic interactions [46–48]. Yanagisawa [48] for example argued that strong electron correlations are responsible for the onset of superconductivity in cuprates. Following the optimization variational Monte Carlo method, they showed that a high-temperature superconducting phase does exist in the strongly correlated region. Similar to BCS superconductors, critical temperature of HTS too may have a strong correlation with the energy scale of the interaction which causes electron pairing. HTSs are a typical correlated electron system having nodes in the superconducting gap, indicating that the Cooper pairs are anisotropic. This confirms the fact that superconductivity in cuprates is unconventional. Several established facts about HTSs led Yanagisawa's group to believe that strong Coulomb interactions may induce superconductivity in HTS.

Vast amount of experimental results obtained on HTS brought out several characteristic features of HTS unambiguously, which drove theorists to explore alternate mechanisms of pair formation. Most crucial facts which aided them are: the Cooper pairs in HTS have d-wave symmetry, their parent materials are Mott insulators, the superconducting phase exists adjacent to antiferromagnetic phase, the CuO_2 planes are present in all cuprates, these planes are highly anisotropic and coupled weakly like Josephson junctions. The on-site Coulomb repulsive interaction works between d-electrons, and the size of the Cooper pair is very small about 2Å. It is conceivable that Coulomb interaction within the atom can account for the above-mentioned experimental observations. Since the energy scale of the Coulomb interaction is very large, of the order of eV, high critical temperature T_c is possible in these superconductors.

Several approaches were applied to investigate high-T_c superconductivity in strongly correlated electron systems but with mixed luck. Zhang et al. [49, 50] proposed quantum Monte Carlo methods in the two-dimensional Hubbard model which did not support the existence of high-T_c superconductivity. In quantum Monte Carlo calculations, the strength of the Coulomb interaction U is not large enough

to account for high-temperature superconductivity, the range of accessible U being quite restricted.

In an earlier publication, Yanagisawa [51] had confirmed that high-temperature superconductivity is a strongly correlated electron system. He had shown that the strength of Coulomb interaction U in quantum Monte Carlo calculations in a 2D Hubbard model is not large. Instead, he focused on the simplest wave function of superconducting state with strong electron correlations, the Gutzwiller-projected BCS wave function:

$$\psi_{\mathrm{BCS-G}} = P_{\mathrm{G}} \prod_{k} \left(u_k + \; v_k \;\; c^{+}_{k\uparrow} \, c^{+}_{-k\downarrow} \right) |0\rangle \tag{4.44}$$

Yanagisawa calculated the order parameter Δ which is treated as a variational parameter. The wave function $\psi_{\mathrm{BCS-G}}$ is, in fact, the wave function proposed by Anderson for the resonating valence bond (RVB) state [22]. Using the variational Monte Carlo method in the two-dimensional Hubbard model, the author showed that the ground-state energy has a minimum at finite Δ for the BCS-Gutzwiller wave function which has the d-wave symmetry. Setting the transfer integral t at 0.5 eV, the value of the superconducting condensation energy per site in the limit of large size system turned out to be

$$E_{\mathrm{cond}}/_{N} = \cong 0.2 \text{ meV} \tag{4.45}$$

These results are similar to those reported earlier by Yanagisawa et al. [52] for three-band d-p model. The condensation energy per atom turns out to be of the order of 10^{-4} meV confirming the role of Coulomb repulsive interaction in pair formation. The value of superconducting condensation energy for YBCO as calculated from the specific heat and critical magnetic field data comes out to be 0.17–0.26 meV per Cu atom which is close to the experimental value. This match between the theoretical and experimental values is indeed very significant and strengthens the concept that strong electron correlation and the 2D Hubbard model explain the essential features of the high-T_{c} curates remarkably well.

The optimization Monte Carlo method in two-dimensional Hubbard model leads to superconducting state [48] which becomes stable when the Coulomb interaction U is large, of the order of the bandwidth. Figure 4.8 shows the variation of the ground-state energy with superconducting gap Δ [48] for the optimized wave function ψ_{λ} for the Hubbard model on a 10×10 lattice with $U/t = 18$ and $\acute{t} = 0$. The electron density n_{e} has been kept 0.88.

Figure 4.9 shows the superconducting (SC) and antiferromagnetic (AF) order parameters as a function of the Coulomb interaction strength U. The AF order parameter shows a peak at $U/t \sim 10$ which is of the order of the bandwidth, whereas the SC order parameter has a peak at U_{c} which is greater than the bandwidth. This gives a strong indication that superconductivity in HTS occurs in strongly correlated region. The AF correlation has a maximum at a critical value, U_{c}, and decreases as U increases beyond U_{c}. The gap functions of AF and SC states as a function of U

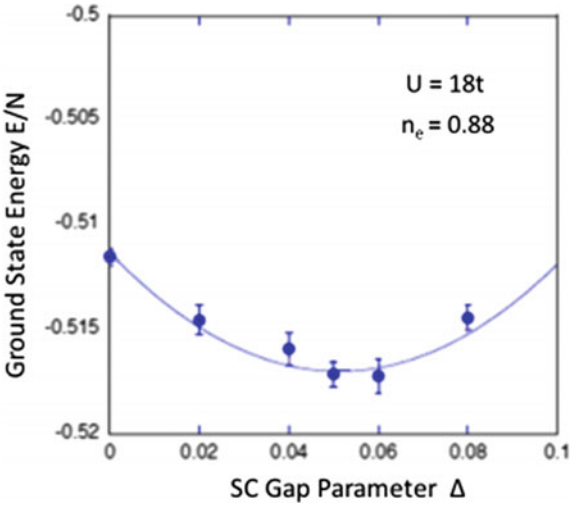

Fig. 4.8 Variation of ground-state energy with superconducting gap parameter, Δ, for the optimized wave function ψ_λ for the Hubbard model on a 10×10 lattice with $U/t = 18$ and $\acute{t} = 0$. The electron density, $n_e = 0.88$. [48]. Open access under the Creative Commons Attribution license Yanagasawa, Condense Matter, **4**, 57 (2019), https://doi.org/10.3390/condmat4020057

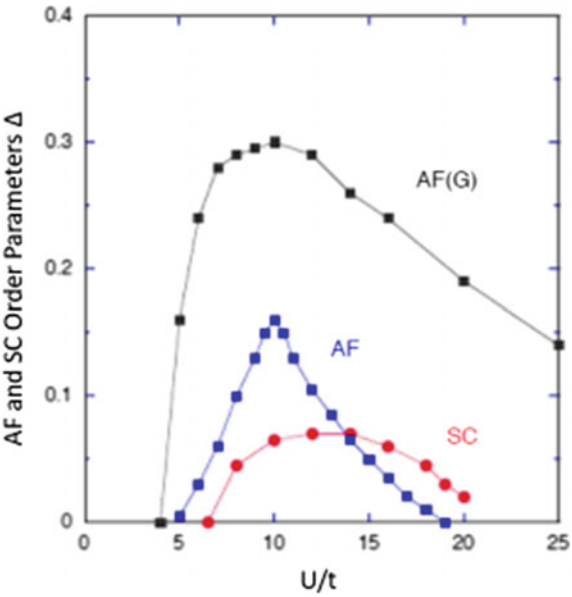

Fig. 4.9 Plots of AF and SC order parameters as a function of U/t when $N_e = 0.88$ for the 2D Hubbard model on a 10×10 lattice. AF(G) is the curve obtained for the simple Gutzwiller function [48]. Open access under the Creative Commons Attribution license Yanagasawa, Condense Matter, **4**, 57 (2019), https://doi.org/10.3390/condmat4020057

for the 2D Hubbard model are shown in Fig. 4.10. Evidently, there is a crossover between the AF and the SC states as one moves from a weakly correlated region to the strongly correlated region. The superconducting state dominates as the AF correlations are suppressed in the strongly correlated region. Thus, high-temperature superconductivity is favoured in the strongly correlated region where the Coulomb interaction strength U is larger than the bandwidth D.

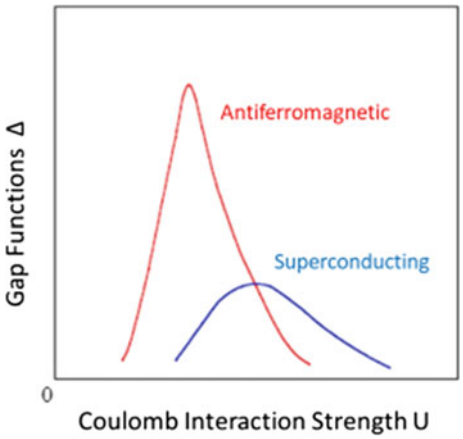

Fig. 4.10 Gap functions of AF and SC states as a function of Coulomb interaction strength, U for the 2D Hubbard model [48]. Open access under the Creative Commons Attribution license Yanagasawa, Condense Matter, **4**, 57 (2019), https://doi.org/10.3390/condmat4020057

Yanagisawa [48] also worked out the phase diagram when holes are doped in the CuO_2 layer. The lowering of energy ΔE is evaluated as

$$\Delta E = E(\Delta = 0) - E(\Delta_{\min}) \tag{4.46}$$

where $E(\Delta)$ takes a minimum at $\Delta = \Delta_{\min}$. The condensation energy per site ΔE/N as a function of the hole doping x is plotted in Fig. 4.11 for $U/t = 18$ and $t_0 =$

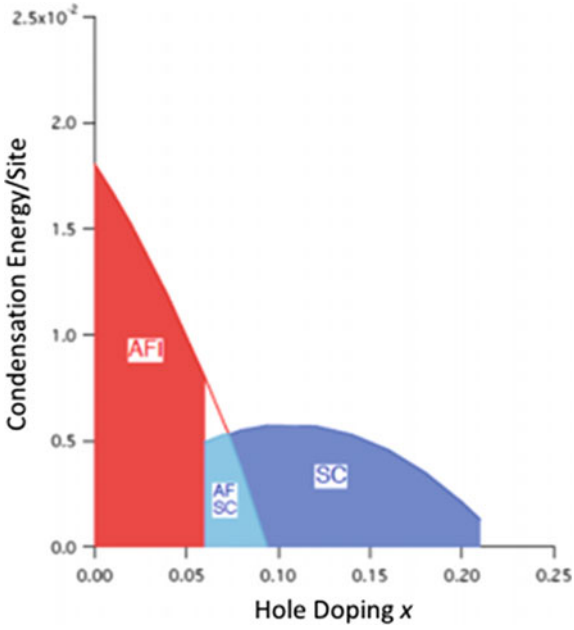

Fig. 4.11 Phase diagram showing condensation energy per site for the 2D Hubbard model as a function of the hole doping on a 10 × 10 lattice, $t_0 = 0$ and $U/t = 18$. AFI—antiferromagnetic insulating state, SC—d-wave SC phase and AF-SC—coexistent state [48]. Open access under the Creative Commons Attribution license Yanagasawa, Condense Matter, **4**, 57 (2019), https://doi.org/10.3390/condmat4020057

0. We see three distinct phases in this phase diagram, namely an antiferromagnetic insulator (AFI) phase, a coexistent (AFSC) phase and a superconducting (SC) phase. The pure d-wave state is stable for $x \geq 0.09$ where the high-T_c phase, going up to room temperature, is possible. The phase diagram also shows the coexistence of an AF phase and the SC phase. In the underdoped region, $0.06 < x < 0.08$–0.09, both the AF phase and the SC phase coexist. There is a transition at the AFSC-SC phase boundary (Fig. 4.11). The antiferromagnetic insulating (AFI) state exists near half-filling ($x < 0.06$) because the doped holes form clusters which are localized and thus do not conduct. This AFI phase is closely related to phase separation [53] when the hole density is very low.

4.6.6 Three-Band d-p Model

In three-band d-p model, the AF correlations are strong, and the AF state is more stable than in the single-band Hubbard model, d-electrons being localized and can magnetically order easily [54]. For the occurrence of high-temperature superconductivity in the d-p model, one has to look for regions of weak AF order. The strength of the AF correlations in the d-p model is controlled by factors such as the Coulomb repulsion between d-electrons, U_d, the level difference, $\Delta d_p = \varepsilon_p - \varepsilon_{d,}$ and the hole density, x. The $U_d - \Delta_{dp}$ phase diagram showing AF, PM and on-site attractive regions in a d-p model for a hole density $x = 0.1875$ is shown in Fig. 4.12. High-temperature superconductivity should appear near the boundary between the antiferromagnetic (AFM) and paramagnetic (PM) metal regions when Δ_{dp} is small. Yet one more region the 'on-site attractive region' exists for large Δ_{dp} where two d-electrons prefer to occupy the same site. It is this region where a charge-density wave or an s-wave superconducting state will occur.

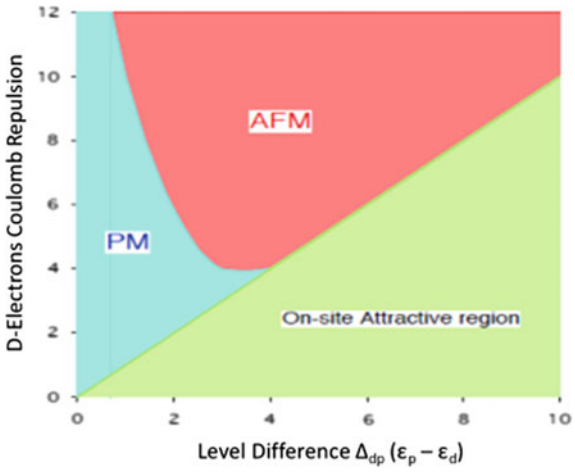

Fig. 4.12 $U_d - \Delta_{dp}$ phase diagram showing antiferromagnetic (AFM), paramagnetic (PM) metal regions and 'on-site attractive region' in a three-band d-p model [48]. Open access under the Creative Commons Attribution license Yanagasawa, Condense Matter, **4**, 57 (2019), https://doi.org/10.3390/condmat4020057

We can draw the following inferences from the discussion above:

1. Superconductivity in high-T_c cuprates can be explained on the basis of strong correlation between electrons.
2. The phase diagrams for the 2D Hubbard model and the three-band d-p model display the characteristic properties of cuprate superconductors.
3. The electron-pair formation must be due to the strong on-site repulsive Coulomb interaction.
4. The SC phase exists near the AF phase.
5. The AF phase and the SC phase coexist for a hole concentration $0.06 < x < 0.09$. This coexistence may be related to the anomalous metallic behaviour in the underdoped region.
6. The AF phase near half-filling ($x < 0.06$) is insulating.
7. For $x > x_{dsc,}$ there is a pure d-wave phase.
8. High-temperature superconductivity in the d-p model occurs in the region of weak AF order.
9. The strength of the AF correlations in the d-p model is controlled by factors such as the Coulomb repulsion between d-electrons, U_d, the level difference, $\Delta_{dp} = \varepsilon_p - \varepsilon_{d,}$ and the hole density, x.
10. High-temperature superconductivity in d-p model is more likely to occur near the AF–PM boundary when the level difference Δ_{dp} is small.
11. The crossover between weakly correlated region and the strongly correlated region appears to be universal in several other correlated systems.

4.7 Theories of Newly Emerged Superconductors

While the theorists were still struggling to reach a consensus over the mechanism of pair formation in HTS, superconductors of different varieties were discovered in quick succession. Prominent among them were MgB_2 discovered in 2001 and iron-based superconductors discovered in 2008. Efforts to understand the mechanism of superconductivity in these materials were made afresh on the basis of the huge experimental data collected on these materials. Below we discuss briefly the theories proposed to explain the occurrence of superconductivity in these materials.

4.7.1 Theory of Superconductivity in MgB_2

The discovery of superconductivity in MgB_2 in 2001 with highest T_c (39 K) among the inter-metallic compounds broke the BCS limit first time. This raised an important question whether the high T_c in this new system can be understood within the framework of the conventional BCS theory or a new non-phonon mechanism is responsible for the pair formation. Measurements on isotope effect, de Haas-van Alphen (dHvA) effect, Raman scattering, inelastic neutron (INS) and X-ray scattering (IXS) on MgB_2

were carried out at many centres because these parameters give reliable information about the role of phonons in superconducting pairing. Phonon density of states (DOS) and phonon dispersion curve in MgB_2 have been studied in detail. The calculations of the electron–phonon coupling constant reveal strong coupling of the electron to the E_{2g} optical phonon, while the interaction with other three modes, namely E_{1u}, A_{2u}, and B_{1g}, is very weak [55]. These four optical phonon modes with arrows pointing the direction of atom vibration are shown in Fig. 4.13. Crucial support for strong electron–phonon interaction came from the isotope effect observed in MgB_2 (Fig. 3.26 in Chap. 3). The isotop effect in MgB_2 [56] shows that T_c increases by about 1 K when ^{11}B is replaced by ^{10}B. The isotope effect follows the relation $T_c \propto M^{-\alpha}$ with exponent $\alpha = 0.26(3)$ for MgB_2.

The value of isotope effect coefficient, α, for Boron calculated based on BCS theory comes out to be 0.30(1) [57]. For Mg, the value of the coefficient is quite small = 0.02(1). These results confirm that mostly B phonons are involved in superconducting pairing and Mg phonons contributing very little to it. Further, the isotope coefficient value $\alpha = 0.03$ observed in MgB_2 is smaller than 0.5 observed in pure metallic superconductors like Hg, Pb and Sn indicates that MgB_2 is a intermediate

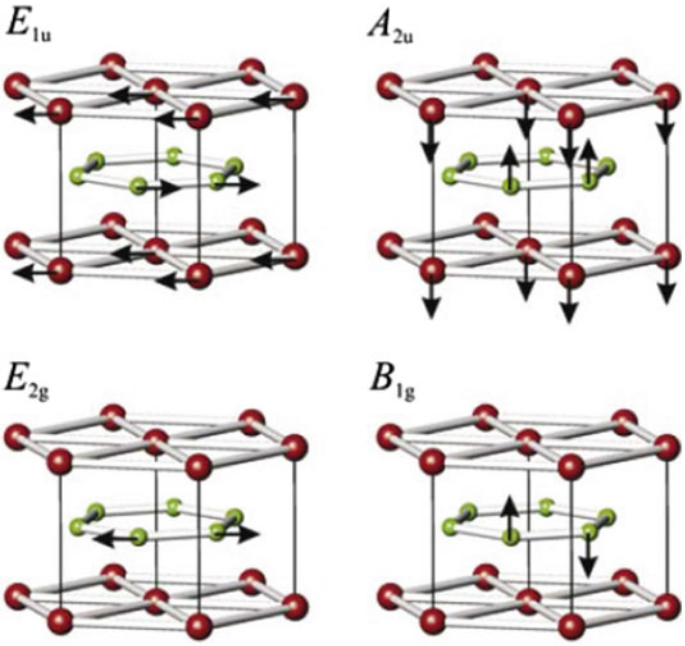

Fig. 4.13 Calculated four distinct optical phonon modes in MgB_2. 1. E_{1u} (in-plane B and Mg displacement, 40–42 meV). 2. A_{2u} (out-of-plane B and Mg displacements, 48–52 meV). 3. E_{2g} (B in-plane bond stretching, 58–82 meV). 4. B_{1g} (B out-of-plane bond bending, 84–86 meV). Arrows show the direction of atom vibration [55]. Open access under the Creative Commons Attribution license. T. Muranaka and J. Akimitsu, Z. Kristallogr. 226, 385 (2011), https://doi.org/10.1524/zkri.2011.1384

to strong coupling superconductor. The low value of the isotope effect coefficient could be due to the complex material properties and would require a larger electron phonon coupling constant, λ and larger repulsive electro-electron ineraction parameter μ^* than found in most simple superconductors. The most unusual feature of MgB_2, discussed in Chap. 3, is that it has two energy gaps at 1.8 and 6.8 meV as also confirmed by specific heat data and direct measurement by ARPES technique. With these two gaps (on 2D σ-band and 3D π-band), MgB_2 is now recognized as the first superconductor containing intrinsic multigaps. Band structure calculations and MEM density reveal that MgB_2 is metallic through electron transfer from π bands (pz orbitals) to in-plane σ bands (pxy orbitals). Superconductivity in MgB_2 predominantly occurs in σ bands, though both π and σ bands contribute to it. The electronic specific heat of a polycrystalline MgB_2 sample plotted as $\Delta C_p/T$ against temperature [58] shows a shoulder at around 8 K in zero field is a clear indication of a second (smaller 1.8 meV) energy gap. This specific heat peak nearly disappears as the field strength is increased. The sharp drop of specific heat at T_c matches with BCS curve closely, but the shoulder at ~ 8 K deviates from the BCS curve. This unusual behaviour is thought to be a consequence of the anisotropic band structure of MgB_2.

Two main bands cross the Fermi level. The π band consists of electrons and holes in the 3D band (~ 56% of total DOS), and the σ band consists of holes in the 2D band (~ 44% of total DOS). These two types of carriers induce two energy gaps at 0 K, $2\Delta_\pi = 1.8$ meV and $2\Delta_\sigma = 6.8$ meV, and both the gaps disappear at T_c. These values are in good agreement with band structure calculations and direct measurement of the gaps by ARPES. BCS theory thus explains well the occurrence of superconductivity in MgB_2.

4.7.2 Theory of Iron-Based Superconductors (IBSC)

The discovery of iron-based superconductors (IBSC) by kamihara et al. [59] in 2008 generated unprecedented interest in superconductivity community because of their great potential for applications. These superconductors have high T_c and very high B_{c2} values. For example, the compound $SmFeAsO_{0.85}F_{0.15}$ has a $T_c = 53.5$ K and $B_{c2} = 150$ T and $NdFeAsO_{0.94}F_{0.06}$ $T_c = 50.5$ K and $B_{c2} = 204$ T. Many reviews have appeared on a variety of studies and theories of IBSCs. See, for example, a comprehensive review by Bang and Stewart [60] and several references therein. These IBSCs are diverse groups like pnictides, chalcogenides, inter-metallics and oxides. Each group has its own distinct features even though some important properties in all the groups are quite similar. It was felt that these materials might be less complicated than the cuprates because they are less strongly correlated. They, however, turned out to be more complicated because they turned out to be multiband systems. Explanation for superconductivity in IBSC needs expertise in electronic structure theory as well as phenomenology and microscopic modelling. Various viewpoints and theories for pair mechanisms have been proposed since 2008, but a consensus has not been built

up. Hirschfeld and co-workers [61, 62] have been working very actively to resolve the problem related to the pairing mechanism operating in IBSCs.

Hirschfeld in his 2016 review [62] has discussed theoretical concepts and experimental results vis-à-vis the gap structure and symmetry of the Fe-based superconductors. It is possible in this system to influence the interactions by small changes in pressure, doping or the disorder. Interactions underlying IBSCs can thus be understood by monitoring order parameter by changing these parameters. The spin fluctuation pairing theory assumes that the repulsive Coulomb interaction produces this effective interaction proportional to magnetic susceptibility. The Hirschfeld group performed random phase approximation (RPA) calculations of the magnetic susceptibility and pairing interaction within a 5-band model. They also took Hubbard and Hund's rule interactions on each Fe site into account and discussed the results of their calculations for different band structures, doping and different interaction strengths. They report an anisotropic, sign-changing s-wave state and a d-state to be almost degenerate because of the near nesting of cylindrical Fermi surface sheets. They had considered a 5-band model based on the density functional theory (DFT) calculations of Cao et al. [63] yielding the Fermi surface. For undoped systems, the peak is observed in (q, w) at $(\pi, 0)$ in the reduced Brillouin zone. On the other hand, for finite doping, Hund's rule coupling becomes incommensurate which might give rise to phenomena like order parameter collective modes.

The existence of spin-singlet sign-changing *s*-wave superconducting gaps on multibands ($s^{\pm}$-wave state) is supported by a variety of experiments [60]. This multiband $s^{\pm}$-wave state is a very unique gap state displaying many interesting superconducting properties. Curiously, these properties can easily be mistaken as evidence for a nodal gap state such as a *d*-wave gap, on the basis of a single type of experimental probe. However, enough experimental evidence has been found to confirm that all nodal gap conceived in IBSCs have multiple *s*-wave full gaps, but often exhibit nodal gap-like behaviours in different superconducting properties which is in tune with the basic $s\pm$-wave pairing state. Identifying the gap symmetry and gap function certainly helps in finding a correct theory, but it does not identify the pairing mechanism which is only a concept and can only be verified through circumstantial experimental evidence.

At the moment, a non-phononic BCS pairing mechanism for the IBSCs is not a very exciting idea, but at least it is very much consistent with the $s \pm$ -wave pairing model. Thus, we find that the picture of $s^{\pm}$ superconducting states formed by $(\pi, 0)$ spin fluctuations was quite intuitive. Notwithstanding this partial success, much higher T_c (= 60–100 K) found in the monolayer of heavily electron-doped iron selenide (HEDIS), $FeSe/SrTiO_3$ [64] has added a new dimension to the problem of understanding superconductivity of IBSCs. Serious attempts have been made to investigate the pairing mechanism and to find if $SrTiO_3$ also plays a role [65, 66]. The discovery of newer and different classes of IBSCs, which continues to take place at regular intervals, poses even bigger challenge to build a theory explaining superconductivity in this diverse group of materials.

4.7.3 Superconductivity in Sulphur Hydride (H_3S)

Very interestingly, newly discovered superconductor, sulphur hydride (H_3S) with record $T_c = 203$ K has been found to be a typical BCS superconductor. High T_c has been well accounted by the BCS theory with high-frequency optical phonons mediating in pair formation. Gorkov and Kresin [67] believe that superconductivity in sulphur hydrides is caused by the electron–phonon interaction, but it differs from that in the conventional superconductors in many ways. The phonon spectrum of sulphur hydride is quite broad, up to 200 meV and structurally quite complex. Sulphur hydrides show remarkable presence of strong electron–phonon coupling together with high-frequency optical phonons. Superconductivity occurs in H3S mainly due to strong coupling between electrons and high-frequency optical modes, although the acoustic phonons also do take part. Superconductivity can be anticipated at even higher temperatures as long as Migdal adiabaticity criterion is not violated. Gorkov and Kresin obtained an analytical expression for T_c by generalizing the standard treatment of the phonon mechanism by employing two coupling constants λ_{opt} and λ_{ac} together with appropriate frequencies. The expression for T_c can be written as

$$T_c = \left[1 + 2\frac{\lambda_{ac}}{\lambda_{opt-\mu^*}} \frac{1}{1 + \frac{\pi T_c^0}{\theta_{ac}}}\right] \tag{4.47}$$

Taking $T_c = T_c^0 + \Delta T_c^{ac}$ and $T_c^0 \equiv T_c^{opt}$ and assuming $\Delta T_c^{ac} \ll T_c^0$.

Here, θ is the Debye temperature roughly the characteristic phonon frequency, λ is the electron–phonon coupling parameter, and μ^* is the Coulomb pseudo-potential which characterizes the direct electron–electron repulsion, μ^* being $\approx$ 0.1–0.15. Further, these hydrides display isotope effect which is different from the conventional superconductors. The isotope coefficients in sulphur hydride and sulphur deutride vary with the pressure which is a reflection of the relative contributions of the two phonon modes. They argued that the rise in T_c from 120 K up to 200 K over a narrow pressure interval near 150 GPa is a sign of a first-order structural phase transition into the high-T_c phase along with the appearance of additional small Fermi pockets. Consequently, a two-gap structure appears which should be observable by tunneling spectroscopy.

A unified theory capable of explaining superconductivity not only in diverse groups of IBSCs but also in other exotic superconductors like cuprates and heavy fermions is something which should be the dream of most of the theory groups. Will the celebrated BCS theory triumph one day and explain superconductivity in all types of superconductors after taking the peculiar structural parameters into account?

References

1. J. Bardeen, L.N. Cooper, J.R. Schrieffer, Phys. Rev. **108**, 1175 (1957)
2. F. London, H. London, Proc. Roy. Soc. (London) **A149**, 71 (1935)

3. V.L. Ginzburg, L.D. Landau, Zh. Eksperim i Teor. Fiz. **20**, 1064 (1950)
4. L.P. Gorkov, Z. Eksperim. i Teor. Fiz., **36**, 1918 (1959) [Sov. Phys.-JETP, **9**, 1364 (1959)]
5. T.V. Ramakrishnan, C.N.R. Rao, *Superconductivity Today*, Chapter 4 (Wiley Eastern Ltd. 1992)
6. B.D. Josephson, Phys. Lett. **1**, 251 (1962)
7. H. Fröhlich, Phys. Rev. **79**, 845 (1950)
8. E. Maxwell, Phys. Rev. **78**, 477 (1950)
9. C.A. Reynold, B. Serin, W.H. Wright, L.B. Nesbitt, Phys. Rev. **78**, 487 (1950)
10. J. Bardeen, Phys. Rev. **80**, 567 (1950)
11. H. Ibach, H. Luth, *Solid State Physics*, 2nd edn. (Springer, Berlin, 1996).
12. L.N. Cooper, Phys. Rev. **104**, 1189 (1956)
13. C.J. Gorter, H.B.G. Casimir, Phys. Z. **35**, 963 (1934)
14. W.S. Corak, B.B. Goodman, C.B. Satterthwaite, A. Wexler, Phys. Rev. **102**, 656 (1956)
15. J.G. Bednorz, K.A. Muller, Z. Phys, B-Cond. Matter **64**, 189 (1986)
16. M.K. Wu, J.R. Ashburn, C.J. Torng et al., Phys. Rev. Lett. **58**, 908 (1987)
17. H. Maeda, Y. Tanaka, M. Fukutomi, T. Asano, Jpn. J. App. Phys. **27**, L665 (1987)
18. S. Banerjee, C. Dasgupta, S. Mukerjee, T.V. Ramakrishnan, K. Sarkar, *AIP Conference Proceedings* (2018), pp. 020001. https://doi.org/10.1063/1.5050718
19. B. Betlogg, Solid State Commun. **107**, 639 (1998)
20. L. Pauling, *Nature of Chemical Bond* (Cornell University Press, New York, 1960).
21. P.W. Anderson, Mater. Res. Bull. **8**, 153 (1973)
22. P.W. Anderson, Science **235**, 1196 (1987)
23. See, for example, S. Hufner, M.A. Hossain, A. Damascelli, G.A. Sawatzky, Rep. Prog. Phys. **71**, 062501 (2008)
24. T. Yoshida, M. Hashimoto, S. Ideta et al., Phys. Rev. Lett. **103**, 037004 (2009)
25. M.-L. Chen, arXiv: 1206.0862v3 (2012)
26. G. Baskaran, Z. Zou, P.W. Anderson, Solid State Commun. **63**, 973 (1987)
27. G. Baskaran, P.W. Anderson, Phys. Rev. B **37**, 580 (1988)
28. G. Baskaran, Phys. Rev. **B64**, 092508 (2001)
29. P. Monthoux, A.V. Balatsky, D. Pines, Phys. Rev. Lett., **67**, 3448, (1991)
30. P. Monthous, A.V. Balatsy, D. Pines, Phys. Rev. B **46**, 14803 (1992)
31. P. Monthoux, D. Pines, G.G. Lonzarich, Nature **450**, 1177 (2007)
32. H. Monien, M. Takigawa, D. Pines, Phys. Rev. **B43,** 258 (1991): H. Monien, P. Monthous, D. Pines, **B43**, 275 (1991)
33. J.R. Schrieffer, X.G. Wen, S.C. Zhang, Phys. Rev., **B39**, 11663 (1989); A. Kampf, J.R. Schrieffer, Phys. Rev. **B41**, 6399 (1990); **B42**, 7967 (1990)
34. S.E. Barrett, D.J. Durand, C.H. Pennington et al., Phys. Rev. B **41**, 6283 (1990)
35. S.E. Barrett, J.A. Martindale, C.H. Pennington et al., Phys. Rev. Lett. **66**, 108 (1991)
36. M. Takigawa, J.L. Smith, W.L. Hults, Phys. Rev. B **44**, 7764 (1991)
37. N. Bulut, D.J. Scalapino, Phys. Rev. Lett. **68**, 706 (1992)
38. C. Berthod, I. Maggio-Aprile, J. Bruér, A. Erb, C. Renner, Phys. Rev. Lett. **119**, 237001 (2017)
39. C. Caroli, P.G. De Gennes, J. Matricon, Phys. Lett. **9**, 307 (1964)
40. Ø. Fischer, M. Kugler, I. Maggio-Aprile, C. Berthod, C. Renner, Rev. Mod. Phys. **79**, 353 (2007)
41. W. Qing-Yan, L. Zhi, Z. Wen-Hao, Z. Zuo-Cheng et al., Phys. Lett. **29**, 037402 (2012)
42. A.P. Drozdov, M.I. Eremets, I.A. Troyan, V. Ksenofontov, S.I. Shylin, Nature **525**, 73 (2015)
43. C.-L. Song, Q.-K. Xuey, Physics **10**, 129 (2017)
44. H. Li, *Angle-Resolved Photoemission spectroscopy Study of High Temperature Superconductor Cuprate, and Potential High Temperature Superconductors K-Doped p-Terphenyl and Trilayer Nickelate* (University of Colorado Boulder, 2017)
45. H. Li, X. Zhou, S. Parham, T.J. Reber, H. Berger, Nature Commun. **9**, Article number: 26 (2018)
46. S.A. Kivelson, Sci. Bull. **61**, 911 (2016)
47. L.J. Dunne, E.J. Brändas, H. Cox, Chapter 9. Adv. Quantum Chem. **74**, 183–208 (2017). https://doi.org/10.1016/bs.aiq.2016.06.003

48. T. Yanagisawa, Condens. Matter **4**, 57 (2019)
49. S, Zhang, J. Carlson, J.E. Gubernatis, Phys. Rev. **B55**, 7464 (1997)
50. S, Zhang, J. Carlson, J.E. Gubernatis, Phys. Rev. Lett., **78**, 4486 (1997)
51. T. Yanagisawa, J. Phys. Soc. Jpn., **85**, 114707 (2016)
52. T. Yanagisawa, M. Miyazaki, K. Yamaji, J. Phys. Soc. Jpn. **78**, 031706 (2009)
53. K. Kapcia, S. Robaszkiewicz, R. Micnas, J. Phys. Condens. Matter, **24**, 215601 (2012)
54. T. Yanagisawa, S. Koike, K. Yamaji, Phys. Rev. B **64**, 184509 (2001)
55. T. Muranaka, J. Akimitsu, Z. Kristallogr. **226**, 385 (2011)
56. P.C. Canfield, G. Crabtree, Phys. Today **56**, 34–40 (2003)
57. D.G. Hinks, H. Claus, J.D. Jorgensen, Nature **411**, 457 (2001)
58. F. Bouquet, R.A. Fisher, N.E. Phillips, D.G. Hinks, J.D. Jorgensen, Phys. Rev. Lett. **87**, 047001 (2001)
59. Y. Kamihara, T. Watanabe, M. Hirano, H. Hosono, J. Am. Chem. Soc. **130**, 3296 (2008)
60. Y. Bang, G.R. Stewart, J. Phys. Condens. Matter, **29**, 123003 (2017)
61. A. Chubukov, P.J. Hirschfeld, Phys. Today **68**, 46 (2015)
62. P.J. Hirschfeld, C R Phys. **17**, 197 (2016)
63. C. Cao, P.J. Hirschfeld, H.-P. Cheng, Phys. Rev. B **77**, 220506 (2008)
64. J.-F. Ge, Z.-L. Liu, C. Liu, C.-L. Gao, D. Qian et al., Nat. Mater. **14**, 285–289 (2015)
65. A. Linscheid, S. Maiti, Y. Wang, S. Johnston, P.J. Hirschfeld, Phys. Rev. Rev. Lett. **117**, 077003 (2016)
66. Z.-X. Li, F. Wang, H. Yao, D.-H. Lee, Sci. Bull. **61**, 925 (2016)
67. L.P. Gor'kov, V.Z. Kresin, Rev. Mod. Phys., **90**, 011001-1 (2018)

Chapter 5
Conventional Practical Superconductors

Abstract All superconductors exhibit thermal and EM instabilities because of their poor thermal conductivity and worst electrical conductivity in their normal state. These instabilities lead to premature quench in superconducting magnets. To circumvent the problem, practical superconductors are produced in the form of fine filaments in high conductivity copper matrix. Most popular superconductor Nb-Ti had been produced this way by co-processing it with Cu and used universally up to a field of 8–9 T. To meet the stringent requirement of high J_c and low AC losses for accelerator and fusion reactor magnets, impressive improvements have been made in the production techniques of Nb-Ti. Conductors with fine filaments 1–5 μm diameter cladded with diffusion barriers, with low filament spacing to dia. ratio (~ 0.15), resistive matrix to reduce filament coupling and low fraction of Cu have been produced. Conductors carrying large J_c of 50–70 kA in Rutherford and cable-in-conduit conductor (CICC) configuration have been produced. For future accelerators and fusion reactors, high-field A-15 Nb_3Sn superconductor cables with high J_c have been produced by bronze technique, internal tin (IT) method, improved distributed tin (DT) method, RRP and the jelly roll (JR) methods. The DT technique has yielded Nb_3Sn wire with 2–3 μm filament dia. with $J_c = 10^5$ A/cm^2 (12 T, 4.2 K) and AC loss = 300 kJ/m^3 (± 3 T, 4.2 K) suitable for ITER application. JAERI has produced CICC Nb_3Al cable by JR technique, which produces a field of 13 T at a current of 46 kA. NRIM, KEK and FNAL have jointly developed Nb_3Al Rutherford cable (14 × 1.84 mm) using 27 strands prepared by the so-called rapid heating quench technique (JR-RHQT) for the luminosity upgradation of the LHC. V_3Ga conductors too are being developed by PIT technique for the future DEMO fusion power reactor to take care of the induced radioactivity by the 14 MeV neutrons released by the D + T reaction.

5.1 Superconductors Useful for Magnet Application

Even before the discovery of the high-temperature superconductors or the so-called cuprate superconductors, over two thousand conventional metallic superconductors were known to us, yet precisely only three superconductors, namely Nb-Ti, Nb_3Sn and V_3Ga were produced commercially during 1970s and 1980s. The latter two

R. G. Sharma, *Superconductivity*, Springer Series in Materials Science 214,
https://doi.org/10.1007/978-3-030-75672-7_5

superconductors belong to A-15 class of crystal structure and are extremely brittle. In the later years, even the commercial production of V_3Ga stopped in favour of Nb_3Sn. There are several other superconductors mostly belonging to A-15 class which hold promise to become available for applications in future, as they have high values of B_{c2} and J_c. Their inability to be fabricated in desired multifilamentary form remains a hurdle. These superconductors are listed in Table 5.1. The upper critical field (B_{c2}) of some of these potential superconducting alloys and compounds is quite high and is plotted [1] in Fig. 5.1. Materials are available with B_{c2} as high as 60 T ($Gd_{0.2}PbMo_6S_8$) only if the techniques are developed to produce them in long length

Table 5.1 High-field superconducting materials having potential for technological applications

Material	Crystal structure	T_c (K)	B_{c2} (T) at 4.2 K	J_c (A cm^{-2}) at 4.2 K at B (T)
Nb-Zr	A-2	9.5	11	1×10^4 (6 T)
Nb-Ti	A-2	9.3	11	1×10^6 (7 T)
Nb_3Sn	A-15	18.3	23	2×10^4 (20 T)
Nb_3Al	A-15	18.9	32	1.5×10^4 (16 T)
$Nb_3(Al,Ge)$	A-15	20.5	41	1×10^4 (12 T)
Nb_3Ga	A-15	20.3	34	
Nb_3Ge	A-15	23.2	37	1×10^5 (21 T)
V_3Si	A-15	17.0	23.5	1×10^3 (10 T)
V_3Ga	A-15	15.2	23	1×10^5 (20 T)
$V_2(Hf,Zr)$	C-15	10.1	23	3×10^5 (6 T)

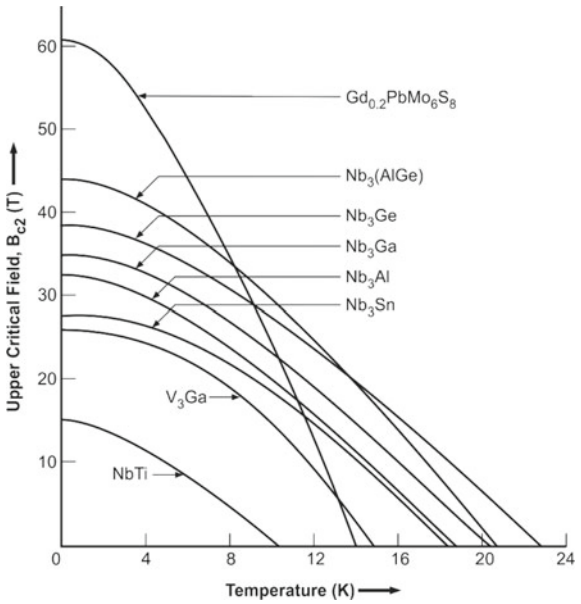

Fig. 5.1 Upper critical field B_{c2} versus temperature plots of potential superconductors for applications. Highest B_{c2} (60 T) is for Cheveral phase compound $Gd_{0.2}PbMo_6S_8$ [1]. With permission of Oxford University Press

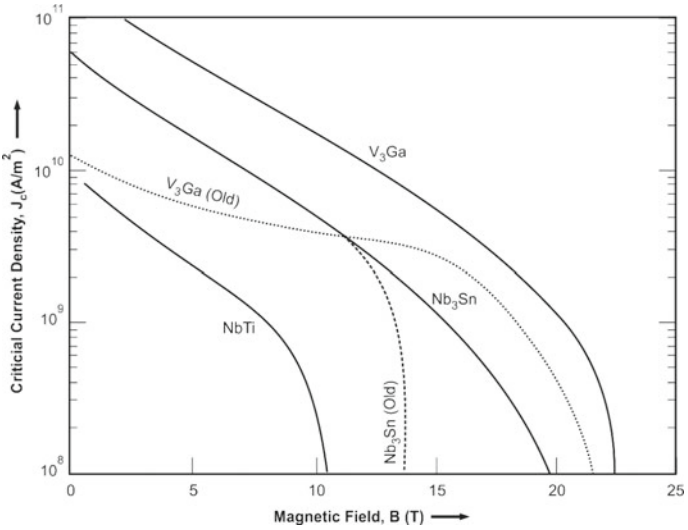

Fig. 5.2 J_c versus B plots for the three commercial superconductors, namely ductile Nb-Ti, Nb_3Sn and V_3Ga. The last two superconductors are highly brittle inter-metallic compounds

and in multifilamentary configuration. Predictably, one of these materials, Nb_3Al, has been recently produced by the NIMS (earlier called National Institute for Materials, NRIM) in Japan. Figure 5.2 shows the J_c versus B plots for these three commercial materials. Clearly, Nb-Ti superconductor is the obvious choice for field production up to 9 T. Since Nb-Ti is a ductile alloy and easy to be manufactured, it has been the workhorse so far in entire electro-technical applications, laboratory magnets, particle accelerators and fusion reactors. However, wherever the field requirement is in excess of 9 T one had to switch over to either Nb_3Sn or V_3Ga, both belonging to A-15 family of superconductors. We will discuss this class of materials separately in subsequent sections. Between these two materials, V_3Ga was traditionally considered a superior material for high-field application. The reason being that the value of γ (ratio of specific heats) for V_3Ga is 3.04 much higher than the corresponding value of 1.42 for Nb_3Sn, and since J_c is proportional to $\gamma^{\frac{3}{2}}(T_c - T)^{\frac{5}{2}}$, the J_c of V_3Ga tends to be roughly twice the J_c for Nb_3Sn. However, since the T_c for V_3Ga is little lower (15.2 K) than for Nb_3Sn (18.2 K), there is a crossover in the J_c–B plots for the two industrial superconductors in a field region of ~ 12 T. This crossover is shown by the dotted lines for the two superconductors in Fig. 5.2. Great improvement in J_c has, however, been achieved for Nb_3Sn over the years, and it is now routinely used for field production up to 20 T. The solid curves for the two materials are the improved J_c values achieved through elemental additions and the microstructural control. Nb_3Sn being significantly cheaper than V_3Ga becomes the material of choice for applications in high-field magnets.

Why out of thousands of known superconductors only three superconductors have been produced on an industrial scale, is a pertinent question. There are stringent

conditions to be met while fabricating these superconductors in wire and cable form. These so-called industrial superconductors are to be fabricated in the form of wires consisting of a large number of very fine superconducting filaments embedded in a high conductivity material like copper. These wires are then twisted and transposed to make cables. Co-processing of high-field brittle A-15 superconductors with copper becomes a challenge. Fine size filaments and conducting matrix are essential to counter the problem of the thermal and electromagnetic instability of superconductors caused by their peculiar properties. We will discuss this topic a bit in detail in the following section.

5.2 Thermal and Electromagnetic Instability Problem—The Multifilamentary Superconductors

All superconductors are poor conductors of heat because Cooper pairs do not transport entropy and worst conductor of electricity in their normal state (above T_c) as most type II superconductors are either alloys or compounds. As shown in Table 5.2, the electrical resistivity of a pure metal like copper is 3–4 orders of magnitude smaller than a superconductor in its normal state, and the thermal conductivity of a normal conductor is about three orders of magnitude larger than of a superconductor. The table also shows that the magnetic diffusivity in a superconductor is 3–4 orders of magnitude higher than in a normal metal, while the thermal diffusivity in normal metal is 3–4 orders of magnitude higher than that in a superconductor. This, in simple words, means that heat travels faster in a normal conductor than in a superconductor, and magnetic flux travels faster in a superconductor than in a normal metal. The result is that magnetic flux takes over a superconductor before the heat is dissipated away to the surrounding. Under such a situation, the temperature of the superconductor may rise above T_c and the material may turn normal. This is termed as 'quenching'.

Table 5.2 Typical thermal, electrical and magnetic parameters of copper and a superconductor in its normal state

Parameter	Superconductor in normal state	Pure metal like copper
Resistivity, ρ (Ω cm)	~ 10^{-5} to 10^{-4}	~ 10^{-8}
Thermal conductivity, λ (W cm^{-1} K^{-1})	~ 10^{-3} to 10^{-2}	~ 1–10
Heat capacity, S (J cm^{-3})	~ 10^{-3} to 10^{-2}	~ 10^{-3}
Thermal diffusivity, D_H	~ 1	~ 10^3–10^4
Magnetic diffusivity, D_M	~ 10^3–10^4	~ 1

5.2.1 Degradation and Flux Jump

Early magnets wound using superconducting wires quenched at current densities significantly smaller than the values quoted based on short sample tests. This was believed to be partly due to 'flux jumps' or the 'premature quenching'. The flux jump can be understood this way. Suppose, we apply a small magnetic field to a superconductor, surface screening currents will start flowing in a surface layer to protect the superconductor against the flux penetration. Flux will, however, penetrate the superconductor a small distance equal to the penetration depth λ. The resulting heat of magnetization will cause a small temperature increase in the superconductor by a small amount, say ΔT_1. This increase in temperature will bring down the screening current density allowing an additional small field penetration and a further raise in temperature, say by an amount ΔT_2. If this temperature rise ΔT_2 is greater than ΔT_1, further increase in magnetic field will raise the conductor temperature further by a small amount say, ΔT_3, and the process will continue until the superconductor quenches to normal state. We refer it as 'thermal runaway' or 'flux jump'. Let us assume that ΔT_2 happens to be smaller than ΔT_1 and ΔT_3 smaller than ΔT_2, the material can be stabilized against flux jump. This can be achieved by either resorting to

1. Adiabatic stability criterion or
2. Dynamic stability criterion.

Let us discuss these two criteria to stabilize a superconductor against flux jumps in detail. Figure 5.3 shows the magnetic field penetration of a superconductor of diameter 2a. Field penetration increases with increasing field strength, and at a certain value B_F, the superconductor is fully penetrated. The energy stored by the magnetization currents corresponding to this full penetration field B_F is given by

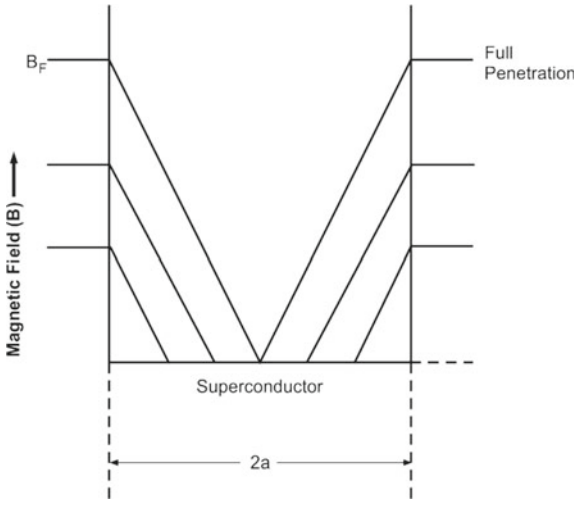

Fig. 5.3 Field penetration of a superconductor of the diameter 2a. Field B_F corresponds to the full penetration

$$Q = \left(\frac{2\pi}{3} \times 10^{-9}\right) J_c^2 a^2 \tag{5.1}$$

or

$$Q = \left(B_F^2\right)/\left(24\pi \cdot 10^7\right) \tag{5.2}$$

Since $B = \frac{4\pi}{10} J_c x$.

It is, thus, seen from (5.1) that for a given value of J_c the heat produced during field penetration is proportional to the square of the thickness of the superconductor. This simply means that if the dimension of the superconductor or the radius of the circular wire is reduced to very fine filament size, the heat generated during the field sweep can be reduced to a very small value, which can be absorbed by the superconductor itself without a serious rise in temperature. This will fulfil the stability criterion of $\Delta T_3 \ll \Delta T_2 \ll \Delta T_1$. This is called the 'adiabatic' or the 'intrinsic' stability criterion because it assumes that no heat escapes to the surrounding. Thus, if the wire diameter is reduced by a factor of 10, the heat produced Q will be reduced by a factor of 100.

The other alternative technique to stabilize the superconductor against flux jumps is to laminate a superconductor with a high conductivity material like copper. In such a composite superconductor, the heat generated during field sweep is dissipated away through copper. This is called the 'dynamic' stability criteria. Copper, in fact, not only provides dynamic stability but also provides the cryostatic stability to the superconductor by working as a shunt resistance. In the event of a part of superconductor turning normal (becoming highly resistive), the current will flow through the copper shunt instead of the superconductor. How to realize these two stability criteria will be discussed in the following sections.

5.2.2 *The Adiabatic or Intrinsic Stability*

Figure 5.4 shows a superconductor under an external magnetic field B. The superconductor is protected against flux penetration by the screening currents flowing at a density of J_c allowing a field penetration of x (cm). Let us see what happens if a disturbance causes a small temperature rise ΔT_1 in the conductor. Following sequence of events is likely to follow

1. The screening current density, J_c will decrease by a small amount, say ΔJ_c given by

$$\Delta J_c = \left(\frac{dJ_c}{dT}\right) \Delta T_1 \tag{5.3}$$

2. This decrease in J_c allows an extra flux penetration, say Δx, given by

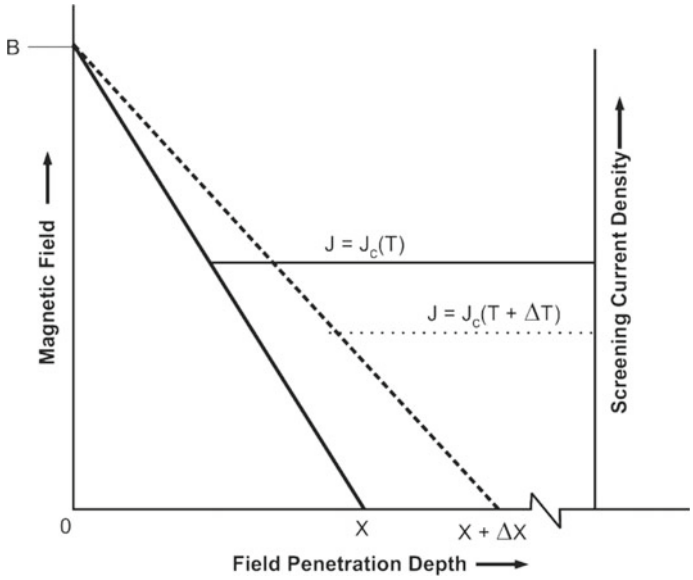

Fig. 5.4 Adiabatic stability criterion: the conductor dimensions are reduced such that the heat generated due to field penetration is so small that it is absorbed by the conductor without a serious rise in temperature

$$\Delta x = -\frac{10}{4\pi}\left(\frac{B}{J_c}\right)\left(\frac{\Delta J_c}{J_c}\right) \tag{5.4}$$

3. This flux movement will generate heat ΔQ per unit volume given by

$$\Delta Q = 10^{-8}\left(\frac{J_c B \Delta x}{3}\right) \text{J/cm}^3 \tag{5.5}$$

4. Since thermal diffusivity D_H in a superconductor is very small, this heat is not likely to be dissipated away. Instead, the material itself under adiabatic situation will absorb it. Thus, there will be a further rise in temperature, say ΔT_2, depending upon the heat capacity of the conductor and will be given by

$$\Delta T_2 = \frac{\Delta Q}{S} \tag{5.6}$$

where S is the heat capacity of the superconductor in J/cm^3/K. Thermal runaway will occur if ΔT_2 happens to be greater than ΔT_1. The superconductor will, however, remain stable in case ΔT_2 turns out smaller than ΔT_1. The system will then be stable against small disturbances.

Taking the values of ΔT_1 and ΔT_2 from expressions (5.3) and (5.6), the condition $\Delta T_2 \ll \Delta T_1$ for conductor stability against small disturbance/perturbation leads to

$$B < \left(12\pi 10^7 S J_R\right)^{\frac{1}{2}} \tag{5.7}$$

Here

$$J_R = \frac{J_c}{-\mathrm{d}J_c/\mathrm{d}T} \tag{5.8}$$

Since B and J_c are related through the relation

$$B = \left(\frac{4\pi}{10}\right) J_c x \tag{5.9}$$

Equation (5.7) can as well be written as follows:

$$x < \left(\frac{3 \cdot 10^9 S J_R}{4\pi}\right)^{\frac{1}{2}} \left(\frac{1}{J_c}\right) \tag{5.10}$$

In the above calculations, we have assumed a uniform distribution of energy released by the flux motion, which is not likely to happen in an adiabatic process. For a perfect adiabatic condition, the above two equations (5.7) and (5.10) will get modified to

$$B < \left(\pi^2 10^7 S J_R\right)^{1/2} \tag{5.11}$$

and

$$x < \frac{\left(10^9 S J_R\right)^{1/2}}{4 J_c} \tag{5.12}$$

If we assume typical values of $S = 2 \times 10^{-3}$, $J_R \sim 4$ and a J_c value of 3×10^5 A cm^{-2} for Nb-Ti, a wire of 24 μm dia. will be stable against flux jump. For larger diameter, 'flux jumps' will occur before the full flux penetration of the superconductor.

5.2.3 The Dynamic and Cryostatic Stability

Dynamical stability criterion is an alternate route to stabilize a superconductor by laminating it with high conductivity material such as copper. Conditions get modified when we consider composite of a superconductor and a conducting normal matrix. This arrangement slows down the flux movement in the superconductor by reducing the value of the magnetic diffusivity, D_M. This slowdown of flux movement permits time for most of the heat to escape from the superconductor to the surrounding via thermal conduction through copper. The D_H will now be greater than the D_M, and therefore energy dissipated by flux motion will distribute uniformly throughout the composite. The current density will be the mean current density $= \lambda J_c$. (λ being the superconducting fraction). Similarly, the specific heat too will have to be averaged out over the whole composite. When the flux penetration x is less than the half width of the composite, the heat release will be distributed over the entire composite cross section. This will reduce ΔT_2 by a fraction x/a (2a being the composite diameter) and improve the stability of the composite. Copper lamination not only provides dynamic stability but also provides cryostatic stability to the superconductor by way of sharing the current in the event of the formation of a hot spot.

As shown in Fig. 5.5, the composite consists of alternate sheets of the superconductor and a normal matrix, usually copper for its excellent bonding properties and high thermal conductivity. The superconductor sheet has a thickness of w (cm) and constitutes a fraction λ_s of the whole composite. Let the electrical resistivity of copper be ρ (Ω cm). The composite conductor (Fig. 5.5) is shielded against an external magnetic field, B by the screening currents flowing at a mean current density of $\lambda_s\ J_c$ extending to a depth of x cm.

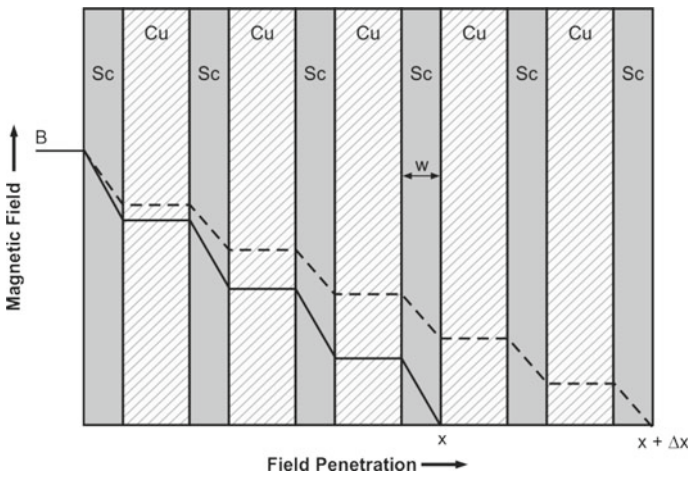

Fig. 5.5 Dynamic stability criterion: the composite now consists of alternate sheets of copper and superconductor. Heat dissipates away via copper before the conductor turns normal

We can again start from a disturbance say, an increase of temperature by ΔT_1 and construct the following sequence of events

1. This increase in temperature ΔT_1 will reduce the screening current J_c by an amount

$$\Delta J_c = \left(\frac{dJ_c}{dT}\right)\Delta T_1 \tag{5.13}$$

2. This decrease in shielding current will allow further field penetration by a small amount, say Δx given by

$$\Delta x = -\left(\frac{10}{4\pi}\right)\left(\frac{B}{\lambda_s J_c}\right)\left(\frac{\Delta J_c}{J_c}\right) \tag{5.14}$$

3. The rate of heat release/cm^3 in the filament will be

$$\frac{dQ}{dt} = \frac{\Delta Q}{1/2T_m} \tag{5.15}$$

Here

$$\Delta Q = 10^{-8} J_c B \Delta x/3 \tag{5.16}$$

and

$$T_m = \left(\frac{16}{10^9\pi}\right)\left(\frac{x^3}{\rho}\right)(1-\lambda_s) \tag{5.17}$$

4. The effective resistivity being $\left(\frac{\rho}{1-\lambda_s}\right)$. Assuming that there is no temperature rise of the normal metal, the average temperature rise in the superconductor will be

$$\Delta T_2 \cong \left(\frac{dQ}{dt}\right)\frac{w^2}{12k_s} \tag{5.18}$$

where k_s is the thermal conductivity of the superconductor in W cm^{-1} K^{-1}. According to our stability criterion, $\Delta T_2 < \Delta T_1$, we combine (5.13) and (5.18) and obtain

$$B^2 \leq 12\left(\frac{J_R k_s}{\rho}\right)\left(\frac{x}{w}\right)^2 \lambda_s(1-\lambda_s) \tag{5.19}$$

Here $J_R = \frac{J_c}{-dJ_c/dT}$ same as in (5.8).
Since $B = \left(\frac{4\pi}{10}\right)\lambda_s J_c x$ (5.19) can as well be written as follows:

$$x^2 \leq 8\left(\frac{J_R k_s}{\rho}\right)\left(\frac{1-\lambda_s}{\lambda_s}\right)\left(\frac{1}{J_c^2}\right) \tag{5.20}$$

Taking typical values of parameters for Nb-Ti superconductor, $J_R = 4$, $J_c \sim 3 \times 10^5$ (A cm^{-2}), $k_s \sim 10^{-3}$ (W cm^{-1} K^{-1}), $\rho \sim 2 \times 10^{-8}$ (Ω cm) and $\lambda_s \sim 0.5$, we find that a wire 40 μm in diameter will be stable. Lower λ_s values, that is, larger copper fraction will lead to larger filament diameter. For example for $\lambda_s = 0.3$, a filament diameter of 55 μm can be tolerated if one goes by the dynamical stability criterion. It is, however, advisable that the filament diameter be chosen as per the adiabatic stability criterion so that individual filaments are intrinsically stabilized. If we exceed the diameter given by (5.12), there is a danger that local instabilities may occur within the individual filaments or the superconducting layer which may not be sufficiently damped by the copper lamination if the bonding is not perfect. Further, our assumption of temperature rise only in the superconducting part may not be valid. The conduction paths in a composite system in fact are quite complicated, as the composite not only involves superconductor and the cladding metal but other components like electrical insulation, inter-layer and potting material. Notwithstanding these limitations, above equations have served admirably well for the design and the production of industrial multifilamentary superconductors capable of transporting large currents and used in DC applications. Filament diameter of the commercial wires ranges from 5 to 50 μm depending upon the application. For AC applications, the filament diameter is kept much smaller in the range of 1–10 μm. Wilson [2] has published a good review on Nb-Ti conductors with low AC and eddy current losses.

5.2.4 Multifilamentary Superconducting Wires

From the above discussion, we can conclude that a practical superconductor has to be manufactured in the form of fine filaments of a few micron size. However, all practical superconductors are required to carry large current, and since a single filament can carry only a very small current, a superconducting wire should have a bundle of such fine filaments. The best way to produce such a material on an industrial scale is to combine both the stability criteria. Thus, the practical way to produce the material is in the form of a large number of filaments embedded in pure copper.

Figure 5.6 shows the schematic of the manufacturing process for stabilized Cu/Nb-Ti superconducting wires. The Nb-Ti alloy happens to be ductile enough to be co-processed with copper. The process for manufacturing the composite copper/Nb-Ti wires can briefly be described this way. The Nb-Ti composition is roughly 50:50 with Ti concentration varying from 47% to 56 wt%. The Nb-Ti alloy is usually prepared by arc melting or the electron beam melting technique under controlled metallurgical conditions yielding mass with desired microstructure and ductility. The alloy ingot is extruded and hot rolled into thick rods of a few cm diameter depending upon the dimensions of the composite billet needed to produce required length of the wire. These rods are annealed at about 1000 °C and quenched to room temperature. A large number of these rods are inserted into the holes drilled in a large size copper billet in a predetermined geometry. The billet ends are plugged with thick copper lids, which are electron beam welded after proper evacuation. No trace of oxygen is left.

The sealed billet is preheated and extruded at high temperature under inert atmosphere. High temperature at this stage is needed to have good metallurgical bonding between the superconducting rods and copper matrix. These billets can be massive with large diameters and long lengths depending upon the required diameter and the length of the conductor. Typical dimensions of a large billet could be as much as

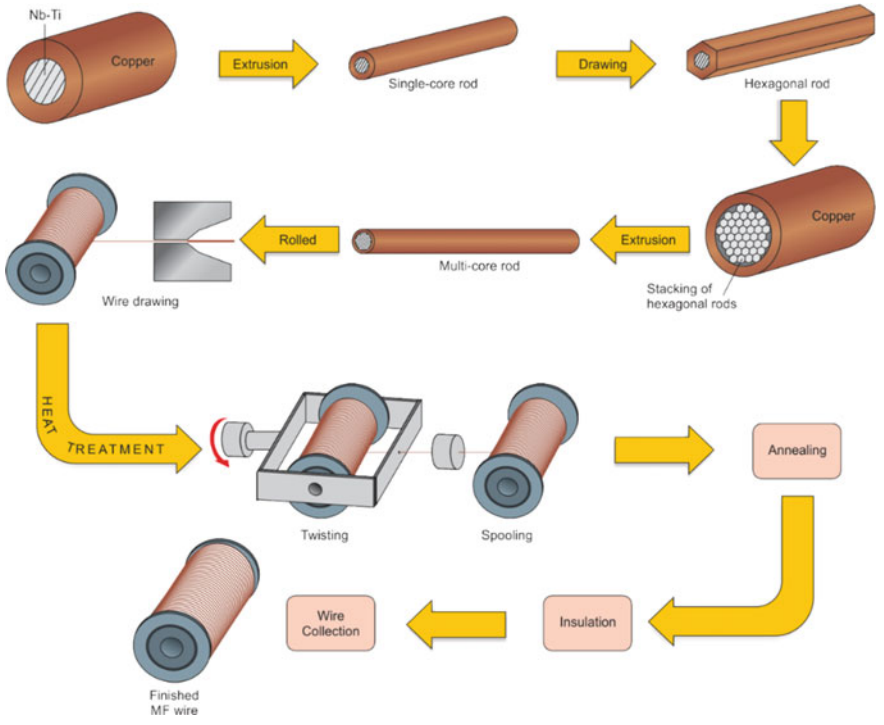

Fig. 5.6 Schematic diagram of the manufacturing process of a mutifilamentary composite superconductor

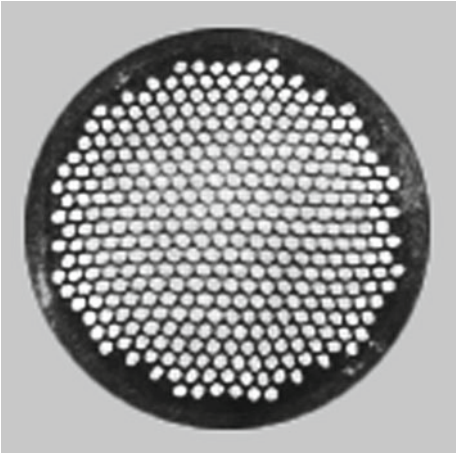

Fig. 5.7 Typical cross section of a multifilamentary wire with copper stabilizer

250 mm diameter and 800 mm length. For industrial production, a billet may weigh as much as 250–300 kg. After hot extrusion, the billet takes the shape of a long rod, which is then rolled to a hexagonal shape and cut into many pieces to prepare another billet. Several of these hexagonal rods are packed together and inserted inside a copper stabilizer tube. The new billet so prepared is evacuated and sealed as before and cold extruded. This multicore rod is then rolled, swaged and drawn to wires of desired size. This process can be repeated until one gets the required number of filaments. A typical cross section of a multifilamentary wire is shown in Fig. 5.7. The multifilamentary wire, thus, produced is suitably heat treated and twisted along its axis to decouple the filaments in the metal matrix. We will deal with this issue in the next section. The twisted wire is usually subjected to a series of heat treatment and cold work schedule to introduce defects, which serve as flux pinning sites and enhance J_c. The twisted and annealed wire is finally insulated. For high-current application, several of such wires (strands) are woven in the form of braids to counter the self-field affects, yet to be discussed in the next section.

5.2.5 Twisting and Transposition of the Multifilamentary Wires

The technique discussed above to produce multifilamentary superconducting wires with filaments embedded in copper matrix looked as though the problem of flux jumps has been solved once for all, but turned out to be not enough. Magnets wound using multifilamentary wires practically behaved quite the same way as with using the equivalent single solid core wire. These magnets too quenched prematurely. It turned out that copper did provide dynamic stability to the superconductor but also coupled the filaments electrically. In a static field, the composite superconductor

is protected against flux inclusion by the surface shielding (magnetization) current flowing along the surface of an individual filament. However, under the influence of a rapidly changing magnetic field, enough voltage is induced which drives the shielding currents from one filament to another across the copper (resistive) matrix. Shielding current loops are formed (Fig. 5.8) occupying the whole of the composite instead of confining to individual filaments. All the filaments are, thus, electrically coupled, and the very purpose of having isolated fine filaments is defeated. On the other hand, if the magnetic field increases sufficiently slowly, there will be very small associated voltage and very little shielding current will cross the copper matrix. Shielding current loops will, thus, form within the individual isolated filaments. Based on these arguments, Smith et al. suggested that these composites should be twisted along the axis so that the induced voltage changes the polarity with the period of the twist. It has been pointed out that for a given field sweep $\dot{B}$ ($= \mathrm{d}B/\mathrm{d}t$), there is a critical length of the composite conductor which allows all the current in the filament to cross the matrix. Below this critical length, the shielding currents will form a close loop within the filament. We can estimate this critical length, ℓ_c in the following way. Let us consider two superconducting blocks of thickness t (cm) each separated by the normal matrix of width d and of resistivity ρ (Ω cm) as shown in Fig. 5.8. The total length of the composite block is 2ℓ (cm). A varying external magnetic field $\dot{B}$ (Gauss/s) is applied along the z direction. Under steady state, let us find out the critical length ℓ_c at which the induced voltage is large enough to allow all the current to cross the matrix. Consider a small element dx at a distance x (cm) from the mid-point. The critical length ℓ_c can be estimated mathematically like this:

1. The voltage across XY

$$= \left(\frac{\dot{B}}{10^8}\right)(xd) \tag{5.21}$$

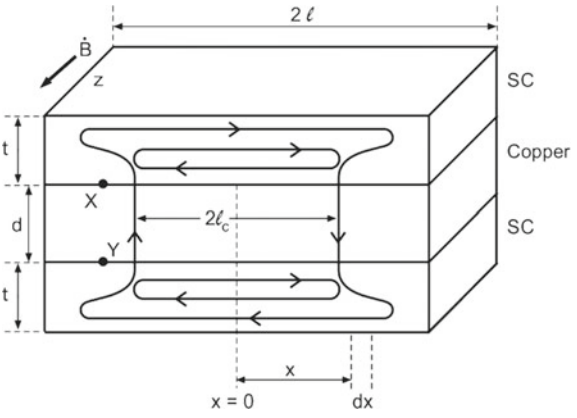

Fig. 5.8 Critical length ℓ_c of the wire in a composite of two superconducting blocks separated by a normal matrix. Twisting the wire with a twist pitch smaller than ℓ_c prevents the coupling of filaments across the matrix

2. Resistance across XY

$$= \frac{\rho d}{z \mathrm{d}x} \tag{5.22}$$

3. Current across XY

$$= \frac{\dot{B}}{10^8}\left(\frac{z}{\rho}\right) x \, \mathrm{d}x \tag{5.23}$$

Integrating current from 0 to ℓ and equating it to $J_c z t$ we get

4. $J_c z t$

$$J_c z t = \int_0^{\ell} \frac{\dot{B}}{10^8}\left(\frac{z}{\rho}\right) x \, \mathrm{d}x = \left(\frac{\dot{B}}{10^8}\right)\left(\frac{\ell^2 z}{2\rho}\right) \tag{5.24}$$

5. or

$$\ell^2 = \ell_c^2 = \left(\frac{2 \times 10^8 \rho J_c t}{\dot{B}}\right) \tag{5.25}$$

For a multifilamentary system, J_c in (5.25) is to be multiplied by a space factor, λ, the superconducting volume fraction. To account for fine size filaments, the right-hand side of (5.25) is to be multiplied by a factor $d/(d + t)$. Thus, the final equation for ℓ_c gets modified to

$$\ell_c^2 = \left(\frac{2 \times 10^8 \rho J_c \lambda t}{\dot{B}}\right)\left(\frac{d}{d + t}\right) \tag{5.26}$$

Thus, by substituting typical values for Cu/Nb-Ti composite, for the typical sweep rate of $\dot{B} = 1$ T/s, $J_c = 3 \times 10^5$ A/cm^2, $\lambda = 0.5$ ($d = t = 50$ μm), ℓ_c turns out to be 30 mm for copper composites. A magnet built by untwisted superconductor multifilamentary wire will show solid conductor behaviour and quench at low-current value. However, if the composite conductor is twisted along its axis cutting effectively the length equal to one quarter of the twist pitch, it behaves as a collection of isolated filaments. For conductor length $\ell > \ell_c$, transverse current equal to magnetization currents crosses the matrix in a distance of ℓ_c at each end. If, however, the conductor length $\ell < \ell_c$, only a small fraction, of the current can cross the matrix, the remaining

current is being confined to individual filament. A sweep rate range is, thus, specified for a given multifilamentary composite superconductor by the manufacturer. Loss or the magnetization of the composite conductor becomes smaller as the twist rate is increased. Direct experimental confirmation of (5.25) and (5.26) came from the magnetization and loss measurements carried out by Critchlow et al. [4]. These authors made use of the expression for magnetization versus the field sweep rate for a fixed twist pitch for a composite conductor given by Smith et al. [3], viz

$$M = M_0\left(1 + \frac{3\pi}{4\lambda^{1/2}}\right)\frac{\dot{B}}{\dot{B}_c} - \cdots \tag{5.27}$$

(Ignoring the higher order terms).

Here M_0 is the magnetization of the bare filament, and $\dot{B}_c$ is the magnetic sweep rate at which the effective length is equal to the critical length. Since $\dot{B}_c$ depends on the critical current density, above equation should be used for a constant external magnetic field. Figure 5.9 gives the plots between the magnetization (M) and field sweep $\dot{B}$ for Cu/Nb-Ti composite superconductor containing 121 strands each 0.009 mm (9 μm) dia. in a 0.2 mm copper matrix [4]. The plots qualitatively fit with (5.27) and yield a value of right magnitude of the matrix resistivity. As seen from this figure, magnetization is high for composite without twist that decreases as the twist rate increases. For high pitch rate, the magnetization reduces to the bare filament value, M_0. Magnets using twisted filamentary conductors and suitably impregnated

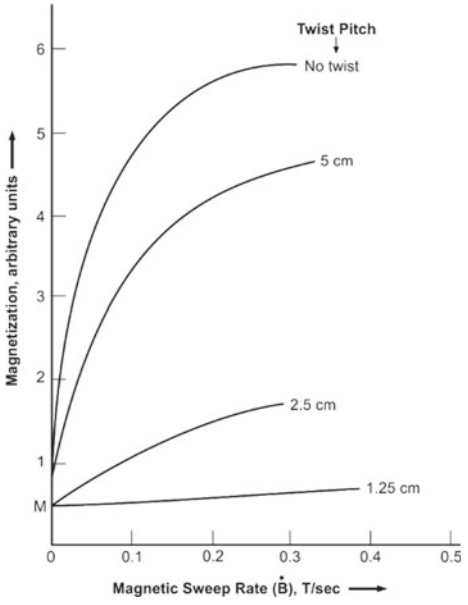

Fig. 5.9 Plots of magnetization versus field ramp rate plots at 1 T of a Cu/Nb-Ti wire with 121 strands each 0.009 mm dia. in a 0.2 mm Cu matrix composite [4]. With permission of Elsevier

performed as per the expectation. When large cross-sectional composite superconductors with much larger number of filaments, in multiple layers around the central core, were developed, it was found that twisting was not enough and the conductors exhibited losses. This has been attributed to the 'self-field effect'. The self-field produced by the transport current causes unequal distribution of current across the cross section of the MF wire. The outer layers of the filaments carry larger current than the inner layers. Twisting does not eliminate the self-field effect, as the radial positions of the filaments remain unaffected. Twisting proved to be effective only for a single layer of filaments around the central core. In large cross-sectional wires, self-field can be eliminated by transposing the wires/strands. High-current multifilamentary conductors are, thus, produced in braided form. A typical braded cable flat rolled in a Rutherford style is shown in Fig. 5.10. Such cables are the standard conductors used for winding magnets for accelerators. A cable contains a large number of strands; each strand contains thousands of Nb-Ti fine filaments. Several of these strands are then braided into flat cables. The filament diameter for such application is as small as 3 μm, and the cable has very low losses.

Figure 5.11 shows the cross sections of typical commercial superconductors. Circular wires in the diameter range of 0.4–1 mm are routinely used for small DC laboratory magnets. The square and rectangular conductors with large cross section are used for large size magnets. Typical dimensions of the conductor are 2 mm^2 and rectangular as 3.0 mm × 1.25 mm. Hollow conductors are used for the circulation of supercritical helium for efficient cooling of the coil. Figure 5.12 shows a variety of high-current multistrand cables manufactured by Europa Metalli (now KME), Italy, for applications in accelerator and fusion reactor magnets. The cable is reinforced with a stainless steel casing too, which provides mechanical strength for withstanding large stresses during the operation of the magnets. Cooling channels are at times provided within the conductor cross section. Cable-in-conduit conductor (CICC) is a popular choice for toroidal magnets in fusion reactor.

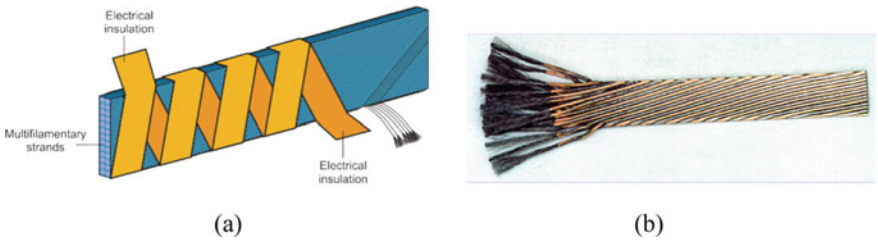

Fig. 5.10 **a** Sketch of a braded superconducting cable in Rutherford style. Each strand in the braid contains thousands of superconducting filaments. **b** Photograph of a typical Rutherford cable. The strands and the filaments are clearly visible. The strands are bradded around a central core and flat rolled. Such cables have been used for magnets in accelerators

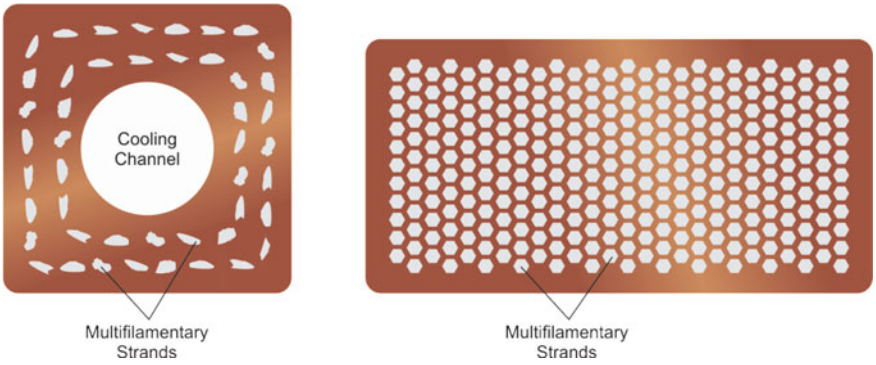

Fig. 5.11 Typical squire cross-sectional commercial Nb-Ti superconductors with a central cooling channel (left) and a rectangular superconductor with multifilamentary strands (right)

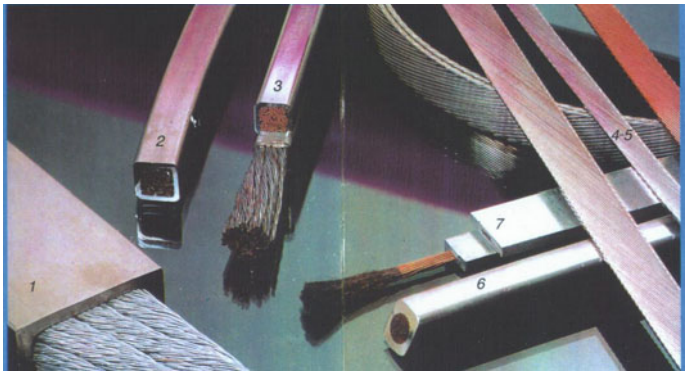

Fig. 5.12 Variety of high-current multifilamentary cables manufactured by Europa Metalli, Italy, for specific applications in accelerator magnets and fusion reactors. From an old brochure of Europa Metalli

5.3 Losses in Practical Superconductors

Mutifilamentary superconductors (filaments in copper matrix) did serve admirably well for DC applications. Magnets large and small going up to record fields were built and operated successfully. Problems cropped up when the magnets were ramped fast or used for pulsed operation. Large dissipation was observed in these magnets when used in circular accelerators, synchrotrons and magnet coils in fusion reactors. For fields less than B_{c1}, ideal homogeneous type II superconductors are loss free. So long as the amplitude of the AC field stays below the value determined by the intrinsic critical surface current densities, losses remain insignificant. In case the field exceeds B_{c1}, cyclical flux movement occurs inside the superconductor in its mixed state. This flux flow causes AC losses inside the superconductor and eddy current losses in the metal matrix. In a non-ideal real superconductor, these losses are much higher

arising from flux pinning. Inhomogeneities are introduced in a superconductor to create strong pinning sites, which pin the flux lines (vortices) effectively and lead to high DC transport current density. The AC losses appear as heat and put excess load on the cryogenic system.

Superconductors, exposed to changing magnetic field, experience energy loss of various kind, which can broadly be categorized as follows:

1. Hysteresis losses
2. Filament coupling (intrastrand and inter-strand)
3. Proximity coupling losses
4. Eddy current losses
5. Self-field losses.

Let us describe these losses a bit in detail.

5.3.1 Hysteresis Losses

Hysteresis losses in type II superconductors arise because of the irreversible nature of the magnetization (Fig. 2.43b). In the mixed state ($B_{c1} < B < B_{c2}$), the flux enters a type II superconductor but does not leave it precisely in the same manner as it gets pinned to the pining sites. The area enclosed by the cyclic M–B curve (Fig. 2.44) represents the hysteresis loss per cycle. The vortices exit the material only when they are depinned from the pinning sites. This movement of vortices in the material is an irreversible dissipative process and generates heat. This dissipative heat increases with the increase of the pining strength. Thus, a conductor with high critical current has larger hysteresis losses too. The area of the hysteresis loop represents the amount of heat produced in a full M–H cycle, provided no transport current is flowing, and is given by:

$$Q = \mu_0 \int M \, \mathrm{d}H \tag{5.28}$$

The AC loss power $\dot{Q}$ (W/m^3) in a semi-infinite wire of diameter 'd' in a transverse field turns out [2] to be

$$\dot{Q} = \dot{B} M = \dot{B} J_c \frac{2d}{3\pi} \tag{5.29}$$

Equation (5.29) tells us that $\dot{Q}$ can be minimized either by reducing the wire diameter or by lowering J_c. Since lowering J_c is not a good proposition, the only option available then is that we reduce the diameter of the round wire or the width ($\perp$ to field) of a rectangular tape. Filaments of diameter 5–10 μm have been found optimum to keep the AC losses in Nb-Ti conductors small. Any field change which does not depin the vortices from the pinning centres in the superconductor, will not cause AC loss.

5.3.2 Losses Due to Filament Coupling

Copper matrix though provides stability to the conductor but also couples the filaments as the induced voltage during field ramping drives the magnetizing currents from one filament to another across the matrix. This results in Joule heating. The coupling between the intrastrand filaments is minimized by twisting the strand with a pitch determined by the desired ramp rate as discussed in Sect. 5.2.5. Further, the individual filaments are now routinely cladded with a diffusion barrier, usually niobium that reduces filament coupling. Coupling between the filaments also increases the eddy current loss. Exact computation of the inter-filamentary and inter-strand coupling losses is difficult because of the non-uniform matrix resistivity and the contact resistances between the filaments/strands and the matrix.

5.3.3 Proximity Coupling Losses

A new type of loss mechanism, proximity coupling loss, has been found in composite conductors when Gregory [5] at Supercon reported a significant enhancement in J_c of Nb-Ti by reducing the inter-filament separation to filament diameter ratio (S/D) to 0.15 without using the diffusion barrier. The losses were, however, found to be high. This has been attributed to proximity coupling of the filaments. The magnetization currents will flow through the filaments in one direction on one side of the wire and flow back in reverse direction through the filaments on the other side of the wire after crossing the normal matrix. The proximity coupling currents do not decay with time like the eddy currents but flow persistently. It is, therefore, advisable to keep the filament diameter large enough to avoid proximity coupling. Coupling currents can be strongly diminished by the introduction of magnetic impurities in copper as shown by Collings [6]. Best results have been obtained by adding Mn (0.5 wt%) to the copper matrix. The addition of Mn can, however, degrade the stability of the conductor and affect adversely the quench protection. Pure copper is, therefore, used as the central core as well as the outer overlay which provides excellent stability.

5.3.4 Losses Due to Eddy Currents

Eddy currents are the surface loop currents induced in the conducting matrix by the change in field and generate Joule heating. To calculate the eddy current losses, one needs to have an estimate of the effective transverse resistivity across the matrix. Duchateau et al. [7] have given a comprehensive treatment of the transverse resistivity in complicated geometries. Losses due to eddy currents, generated during fast charging and discharging of magnets, can be minimized by having a resistive matrix like Cu-Ni matrix. As an example, the conductor which was intended to be used in

Superconducting Super Collider (SSC) project (abandoned) had a design in which each filament was encased in a Cu-Mn (0.6 wt%) shell and 199 of such filaments were grouped in a cluster. Each cluster was jacketed in a copper matrix, and 114 of these clusters were enclosed in a copper jacket and drawn to 0.65 mm diameter strand. The strand at the end of the drawing process had 22,686 filaments of diameter of 2.6 μm with an inter-filamentary separation of 0.4 μm. As expected, the final wire did not exhibit any significant proximity coupling effects.

5.3.5 Losses Due to Self-field Effect

Twisting proved inadequate when high-current conductors with large cross-sectional composite superconductors with much larger number of filaments were produced. Filaments in such conductors are configured across the cross section in concentric multilayers around a central core. These conductors exhibited large losses caused by self-field effect already discussed in Sect. 5.2.5. Twisting alone does not eliminate the self-field effect because the radial positions of the filaments in a strand remain unaffected in twisting. Smaller number (optimum) of filaments are, thus, recommended to be kept in a strand. The optimum strand diameter kept for high-current cables is about 0.8 mm. Self-field effects have been eliminated in practical high-current multifilamentary conductors, produced in flat rolled braided Rutherford style as shown in Fig. 5.10 and used in accelerators. Another important cable configuration is the high-current cable-in-conduit conductor (CICC) used in most fusion reactors. CICC conductors are hollow conductors, which allow the circulation of cooling fluid (liquid helium or supercritical helium (@ 4.5 K) for efficient cooling of the coils. We have already seen the variety of high-current cables in Fig. 5.12.

5.3.6 Losses Due to Transport Current

The transport current too contribute to the losses. The energy of the self-field comes from the power supply used for the transport current. As the transport current increases, the flux flow losses too increase. This is because more and more vortices are depinned from the pinning sites, which start moving out. Self-field losses do dominate in the initial stages but soon overtaken by the flux flow losses as the current keeps increasing. The transport current losses dominate and become quite significant. These losses can be reduced by choosing the right combination of current and temperature.

5.3.7 AC Losses in High Temperature Oxide Superconductors

Broadly, the sources of AC losses and the loss analysis techniques in HTS are same as in conventional metallic conductors except that the HTS have anisotropic critical field and critical current density because of the 2D nature of the CuO_2 planes, which host superconductivity. Thus, typical operating conditions like current and field parallel or perpendicular to the Cu-O plane impact AC losses. Losses need to be calculated for the two orientations of the HTS tape. HTS have some advantages too. Since HTS are operated at higher temperature (20–77 K), they have higher specific heat which enhances conductor stability and higher losses may be sustained.

Magnetization loss is mostly the hysteresis loss like in a single long filament. Losses due to transport current arise even in the absence of the magnetic field. As discussed earlier, an effective way to reduce the magnetization losses is to reduce the size of the loop by subdividing the filaments, that is, by producing high T_c wires/tapes in multifilamentary form in a silver matrix. This is, however, not enough for AC use. The induced coupling current flows between the outer filaments through the matrix, couples the filaments and increases the hysteresis losses again. The coupling current generates Joule heating termed as the coupling loss. Twisting the filaments reduces these losses, which are proportional to the square of the twist pitch. Thus, for example, Sumitomo electric produced [8] commercial DI-BSCCO tapes (AC Type) for AC applications by reducing the tape dimensions and twisting the filaments with a twist pitch of 3 mm. Transport current losses comprise resistive loss, self-field loss and dynamic resistance. All these losses in turn have two field components corresponding to field parallel and perpendicular to tape width. The resistive loss is found to be proportional to $I^{(n+1)}$ where n is the quality factor of the tape, the exponent in the I–V relation. The self-field loss component too depends on current density being proportional to I^k where k varies between 3 and 4. Dynamic resistance loss too depends upon I varying as I^2. Twisting does not affect the self-field losses. The resistance loss can, however, reduce the dynamic resistive loss. Transport current loss can best be reduced by operating the device at a lower current level and at a reduced temperature but such a measure will increase the magnetization loss and raise the cost. SuperPower quotes AC loss value for its transmission cable as low as 0.36 W/kA/m. The material is quite popular and is increasingly used in power applications.

Situation may be different in different devices, and the loss pattern will change. Some models [9] have been developed and may be used for calculating different components of the AC losses but not too accurately. Device design, conductor configuration, filament dimensions, matrix resistivity, orientation of the grains and several other parameters discussed above play crucial role in AC loss estimation.

5.4 AC Loss Measurement Methods

Measurement of AC losses in superconductors is important and has to be carried out under situation in which it is going to be used in the device. Such situations are to be simulated during the AC loss measurements. There are three popular methods to measure AC losses, namely (1) electric method, (2) magnetization method and (3) calorimetric method. All the three methods have advantages and disadvantages. These methods are briefly described below.

5.4.1 Electric Method

This method is based upon the measurement of the voltage component, which is in-phase with the current. Here one measures the voltage along the superconductor, multiplies with the transport current and integrates over a full cycle. The influence of external magnetic field on the transport current loss is easily detected by this method. An alternating field, however, may induce spurious voltages, which have to be accounted for, to estimate the transport current loss with reasonable accuracy. This method has the advantage that it can measure different components of the losses at all temperatures and takes care of the anisotropy effects unlike the calorimetric method, which can measure only total loss, and at a fixed bath temperature such as a 4.2 K or 77 K.

5.4.2 Magnetization Method

Any change in magnetic field induces surface screening currents in the superconductor and causes magnetization losses. The energy dissipated by these screening currents comes from the magnet power supply. Dissipation also occurs when a transport current (AC or DC) flows through the superconductor. Magnetization method measures the losses from the hysteresis loop in the magnetization curve of the superconductor by integrating signals from the pickup coils wound around the sample. This ‘pickup coil and Hall probe method’ is most suitable for measuring magnetization losses. A four point measuring technique using voltage taps is also a popular technique for measuring transport current losses.

5.4.3 Calorimetric Method

In this method, one can measure the total AC losses, that is, the sum of the magnetization loss and the transport current loss. In this method, the superconductor sample

or the device is kept in a 77 K liquid nitrogen bath or a 4.2 K liquid helium bath, and the quantity of the gas (N_2 or He) evaporated is measured. Alternatively, one can measure the raise in temperature of the conductor sample. Though the calorimetric method is relatively simple, yet it has many limitations and disadvantages. First, it does not distinguish between the magnetization loss and the transport current loss. Further, the temperature variation of the loss cannot be measured, as it needs a fixed temperature bath such as liquid nitrogen or liquid helium bath. This method has low sensitivity and cannot be used for small conductor samples. Since the heat of evaporation of liquid nitrogen is high (200 kJ/kg) some ten times, the heat of evaporation of liquid helium (21 kJ/kg) short samples of HTS conductor cannot be measured. Small increase in the temperature of the sample makes this technique less sensitive to power dissipation.

5.5 Practical Superconductors—The Ubiquitous Nb-Ti Superconductor

The most versatile and pervading practical superconductor is the ductile multifilamentary Nb-Ti conductor discovered in 1961. Since then, the material has been exclusively used for building magnets, small and big size producing field up to 9 T. Great advancements have been made to enhance the critical current density, J_c of this material. The design of the Nb-Ti cables has also been suitably altered and optimized which enabled the production of the Nb-Ti cables with very low AC losses. This made Nb-TI cables the material of choice for particle accelerators magnets exemplified by Large Hadron Collider (LHC) and for fusion reactors magnets exemplified by International Thermo-Nuclear Experimental Reactor (ITER).

5.5.1 Emergence of Nb-Ti as a Superconductor for Magnets

The superconductivity in Nb-Ti alloy system in the composition range of 50 at. % was reported first time by Hulm and Blaugher [10] with a $T_c = 9$ K. The first 9.2 T superconducting magnet using Nb-Ti wire was built at Westinghouse, USA, by Coffey et al. [11]. The magnet was built in five sections. A background field of > 5 T was produced using two outer coils of copper-coated Nb-Zr (25 at.%) wire, and the inner three coils were wound using copper-coated Nb-Ti (56 at.%) wire. The invention of copper-stabilized multifilamentary Cu/Nb-Ti composite wires and cables in 1970s firmly established the monopoly of this cheap, ductile, lighter and high-performing material for fields up to 9 T.

5.5.2 The Phase Diagram of Nb-Ti

The relevant useful part of the Nb-Ti phase diagram [4] is reproduced in Fig. 5.13. The useful composition of Nb-Ti is from 45 wt% to 56 wt% Ti. Composition with 47 wt% Ti has emerged as the most preferred material for commercial production. At high temperature, only a single bcc-(β) phase forms, whereas at lower temperatures pure Ti- (α) phase is formed. In between these two limits, a mixture of both the phases α and β exists. The phase boundaries shown are not stable, rather depend upon the interstitial oxygen. Oxygen interstitials do enhance precipitation of α-phase, but if oxygen exceeds 2000 ppm, it can lead to poor ductility. Heat treatment in the α + β phase region can cause precipitation of the metastable ω phase in a very fine structure. These precipitates can serve as excellent pinning sites but causes severe work hardening, which makes the extrusion process rather difficult. Formation of this phase should, therefore, be avoided. The starting material and the rate of cooling determine the actual yields of the α and β phase materials. β phase is, however, retained irrespective of the cooling rate if the Nb contents are greater than 50%.

This perhaps may be because the α-phase precipitation is too sluggish to occur in the low-temperature region obtained by the extrapolation of the (β, α + β) phase boundary. Further, the α phase precipitation can still be prevented in the 20–50% Nb region by quenching the melt to room temperature to preserve β phase. However, as the Nb contents are reduced α precipitation increases as the temperature is lowered. The two vertical arrows indicate the two popular compositions (47 and 56 wt% Ti) in Fig. 5.13. At 47% Ti, B_{c2} peaks [12] at 11.7 T but the T_c drops to 9 K from its peak value of 9.68 K at a lower Ti concentration.

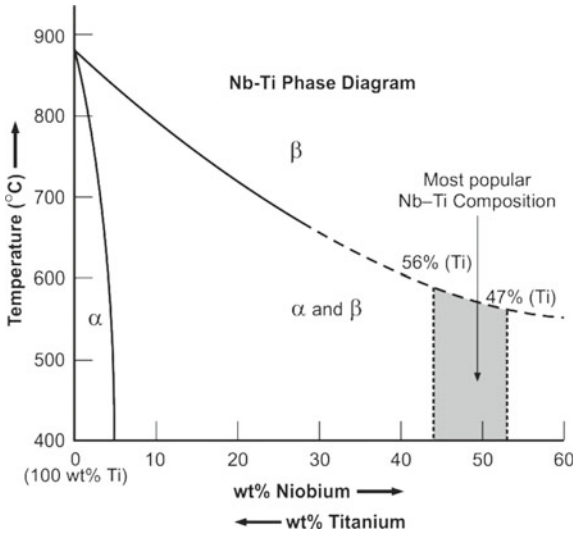

Fig. 5.13 Relevant part of the Nb-Ti phase diagram [4]. With permission of Elsevier

5.5.3 *Optimization of J_c in Nb-Ti Wires*

The detailed processing technique to produce multifilamentary conductors has already been discussed in Sect. 5.2.4. For processing the material for wire/cable production, Nb-Ti alloy is hot extruded and quenched to room temperature to retain the β phase. It is, however, crucial that the microstructure of the material is suitably controlled through the optimization of thermo-mechanical treatment of the final product to have high value of the critical current density, J_c. Cold working of the material is known to produce dislocations, which have been found effective pinning sites. Dislocation cell structure provides even more effective pinning in Nb-Ti as revealed by critical current studies [13]. A dislocation network with a cellular structure has been observed in Nb-Ti cold worked to the extent of 99%. The average separation between cell walls is of the order of a few hundred Å. This dislocation network provides more effective flux pinning. The X-ray and electron diffraction data show the presence of only β phase. This confirms that under cold work condition the pinning is mainly caused by the dislocation cell structure and not by α or ω phase precipitations. Figure 5.14 shows the J_c versus B data of a Nb-Ti alloy containing 56 wt% Ti in cold-worked state as well as after annealing it at 375 °C

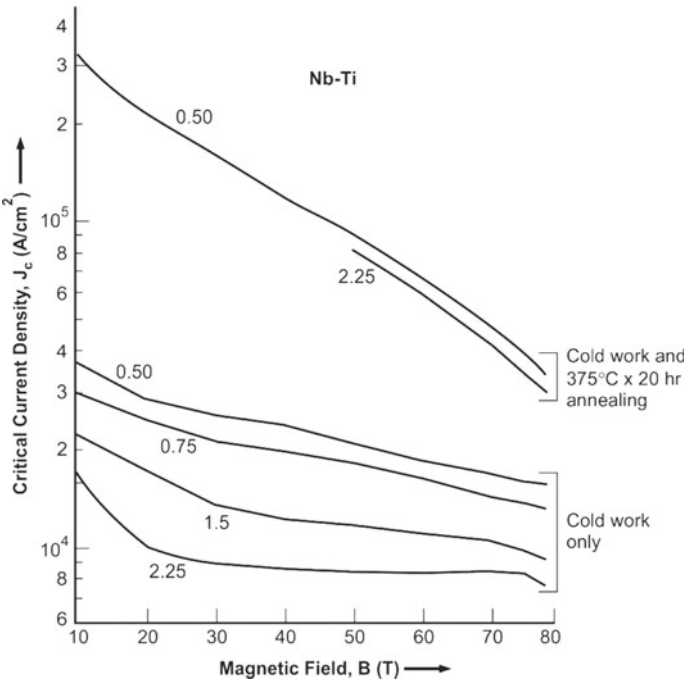

Fig. 5.14 J_c–B plots of Nb-Ti alloy containing 56 wt% Ti. Cold working leads to increased J_c. Successive annealing (375 °C × 20 h) raises the J_c to still higher values [4]. With permission from Elsevier

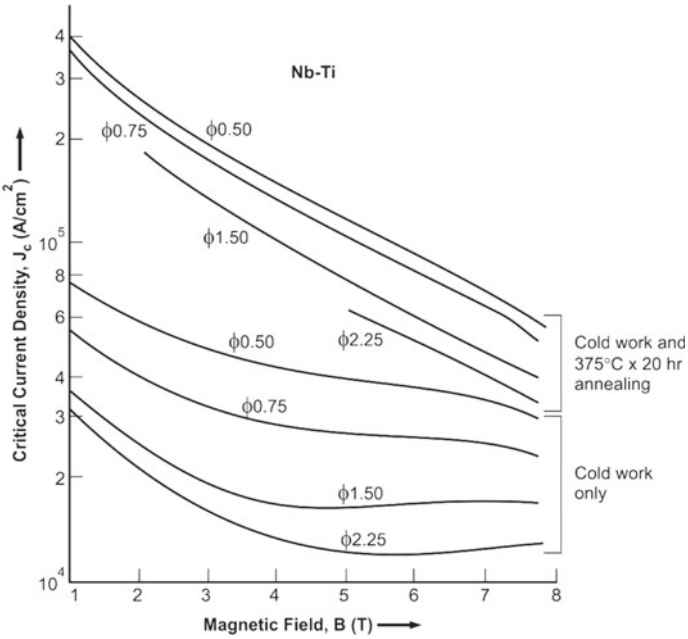

Fig. 5.15 J_c–B plots of Nb-Ti alloy containing 45 wt% Ti. Cold working followed by annealing (375 °C × 20 h) leads to enhanced J_c values [4]. With permission from Elsevier

for 20 h. Evidently, J_c increases with cold working and still more significantly after annealing them. Similar effect has been observed in Nb-Ti wires containing 45 wt% Ti (Fig. 5.15). Increase in J_c value depends strongly on the degree of cold work to which the wire was subjected. J_c is higher for heavily cold-worked wires. The increase in J_c after heat treatment is believed to have been caused by α (pure Ti) precipitation. This is confirmed by the X-ray and electron diffraction studies but not by the electron micrographs. This would then mean that these precipitates are very fine and nucleate at the dislocation cell walls. Intermediate annealing has been found even more beneficial for Nb-Ti conductors. The conductor after annealing treatment is cold worked to final size. Heat treatment causes some recovery and cell rearrangement in the highly deformed material. Heat treatment also produces α precipitation. If the material is deformed again, dislocations are produced which form tangles around the precipitates and along the cell walls. The new structure leads to even more effective pinning and higher J_c. During the entire thermo-mechanical process, care is, however, taken that the ductility of the composite is maintained all through the processing. This intermediate heat treatment has been proven most effective pinning process especially in high-field region. A $J_c = 10^5$ A cm^{-2} (4.2 K, 6 T) is invariably achieved in practical MF Cu/Nb-Ti conductors.

5.5.4 *Developments in the Fabrication Process of MF Cu/Nb-Ti Composite Conductors*

By the end of 1970s, Nb-Ti was accepted as the best choice for magnet systems designed to generate field below 10 T. The reason for this success was its extreme ductility and the consequent ability to be produced in fine filamentary structure. The challenge to this material came in early 1980s when strong interest grew in using this material for pulse magnets for particle accelerators. The hysteretic AC losses encountered in such applications turned out to be a big hurdle. The problem was, however, surmounted by reducing the filament to 5–10 μm size. A filament of 5 μm dia. is stable up to a ramp rate of 1 T/s. Losses can be greatly reduced by increasing the ramp time and retaining the filament diameter to 5–10 μm range to reduce the field errors caused by superconductor magnetization. This leads to high-quality field shape in the accelerator dipole magnets. Since these wires were required to transport several thousand of Ampere current, conductors were produced with thousands of fine filaments. For small number of filaments conductor (up to few hundred), Nb-Ti rods in copper tubes with outer hexagonal geometry are staked in an outer Cu-billet tube and processed as described in Sect. 5.2.4. For several thousand filamentary conductors, the hexagonal composite rod becomes very small and difficult to bundle in desired geometry. In an alternate technique, to fabricate conductor with several thousand filaments, a two-stage stacking process [14] has been followed involving hexagonal staking at two stages of the billet assembly. Figure 5.16a shows the cross section of a standard composite Cu/Nb-Ti conductor with 54 filaments, and Fig. 5.16b shows a conductor with 8670 (102 × 85) filaments fabricated with double stacking process. The conductor contains 102 strands, and each strand has 85 filaments [14].

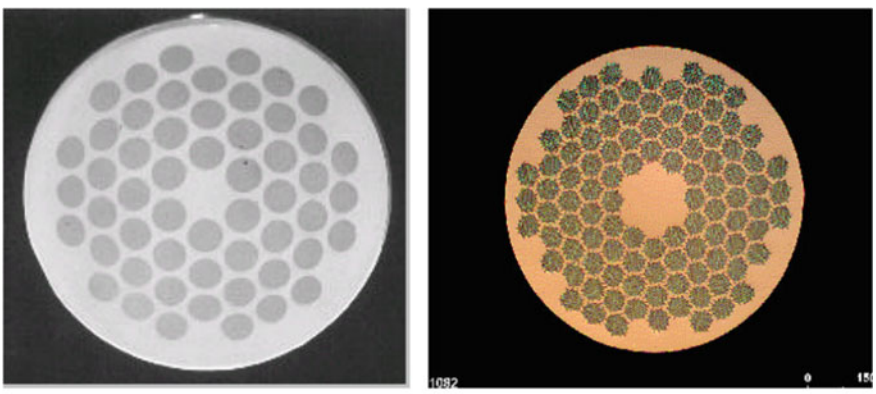

Fig. 5.16 **a** Standard composite Cu/Nb-Ti conductor with 54 filaments. **b** A conductor with 8670 (102 × 85) filaments fabricated with double stacking process [14]. *Courtesy* Helmut Krauth

The hysteretic AC loss problem becomes truly formidable in power engineering where the devices operate at 50–60 Hz. Wires with 1 million filaments of 0.1 μm dia. were developed but attempts to commercialize the technology failed on the consideration of economics.

5.5.5 *Use of Diffusion Barrier and Filament Spacing*

While developing these high-current, tailor-made conductors, one drawback came to the fore. As discussed in Sect. 5.2.4, one hot extrusion of the virgin billet is invariably followed to have large area reduction ratio and good metallurgical bonding. This hot extrusion and the successive heat treatments were found to lead to the formation of Cu-Ti inter-metallic on the filament surface [14]. These hard particles cause sausages of the filaments (varying dia. of the filaments along the length as shown in Fig. 5.17a) and bring down the J_c significantly. The problem is solved by using a Nb diffusion barrier around each filament. This is achieved by preparing monocore Nb-Ti/Nb/Cu composite rods for the initial stacking of the billet tube. The thickness of the Nb barrier is such that down to the last diameter of the wire no Cu-Ti inter-metallic is formed during the heat treatment. Figure 5.17b shows the uniformity of the filaments achieved by the use of Nb barrier.

Another important factor affecting the J_c in Nb-Ti conductors has been reported by Gregory [5] at Supercon Inc., namely the filament spacing to diameter ratio (S/D). A detailed analysis of the data on conductors from different manufacturers yielded the result that the sausaging problem is far less in conductors having closely spaced filaments. Supercon reports a $J_c = 2.3 \times 10^5$ A cm^{-2} (4.2 K, 5 T) for S/D ratio

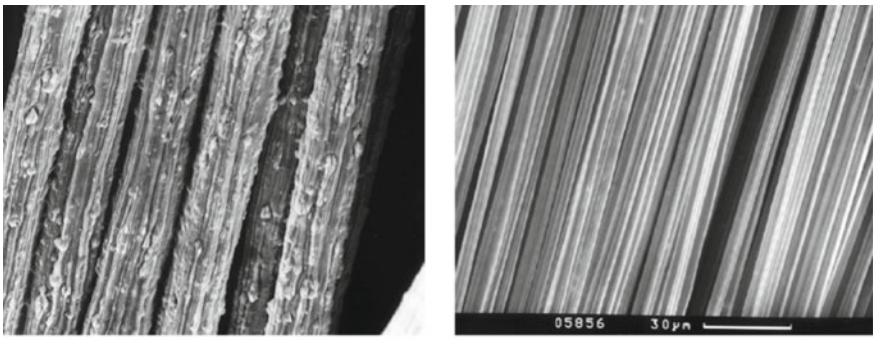

Fig. 5.17 Problem of sausages of the Nb-Ti filaments solved by using Nb diffusion barrier around each filament **a** Nb-Ti filaments with sausages caused by Cu-Ti inter-metallic particles. **b** Very uniform Nb-Ti filaments when the filaments are covered by the Nb diffusion barrier [14]. *Courtesy* Helmut Krauth

of 0.24 without the use of Nb diffusion barrier. Supercon designed conductors for Superconducting Super Collider (SSC, abandoned in 1990s) and Relativistic Heavy Ion Collider (RHIC) with *S*/*D* ratio of 0.15 which carried a $J_c = 3.45 \times 10^5$ A cm^{-2} with good uniformity of the filaments.

The disadvantage of having closely spaced filamentary conductor is that at low filament diameter and low magnetic field, filaments get coupled as the Cooper pairs tunnel through copper via the proximity effect. Supercon solved this coupling problem by employing spin flip scattering by magnetic impurity like Mn, Fe and Cr, which are known to possess a magnetic moment. In the first technique, 40% of the spacing between the filaments is filled up with 70/30 Cu-Ni. The filaments remain decoupled even when the filaments are spaced 0.3 μm apart without causing stability or quench problem. This technique can work for all the filament diameters. In the second technique, Supercon experimented with a matrix Cu-Mn (0.5 wt%) and found filaments as small as 0.35 μm are completely decoupled. The presence of Mn can, however, affect adversely the stability of the conductor and the quench protection. In large billets, the effect will be minor because Cu-Mn is used only between the filaments. The central part of the billet and outside the filaments is pure copper. By carefully choosing proper design and combining the three constituents, viz Nb-Ti, Cu-Mn and Cu in such a geometry and in right proportion so that the AC losses can be cut down to the minimum without sacrificing the stability and the ductility of the conductor.

5.5.6 Nb-Ti Cable-in-Conduit Conductors (CICC)

For upcoming fusion reactors like ITER where the current requirement is 70 kA, cable-in-conduit conductors (CICC) type cable is considered most appropriate. Magnets in fusion reactors are subjected to fast changes not only by the ramping of the magnets but also by frequent plasma disruptions. Several wires containing large number of fine filaments are twisted together to form strands, and several strands are transposed around a central spiral for uniform current sharing in the cable. CICC cables have several advantages over other geometries. Figure 5.18 is the cutaway view of the cross section of a typical CICC cable containing Nb_3Sn or Nb-Ti strands cabled together with copper in a multistep process and jacketed in a structural SS 316 N shell used for TF/CS and PF coils of the ITER, respectively. The central spiral and voids (about 30 vol.%) facilitate SHe or liquid helium flow for cooling the magnets. The fabrication of the jacketed CICC Nb_3Sn cables used in ITER will be discussed further in Chap. 11 on fusion reactors.

The Nb-Ti superconductor, thus, continues to remain unrivalled as it has demonstrated the ability to be drawn into filaments of sub-micron size and in the desired filament configuration. State-of-the-art technologies have been developed for use in magnets of the future accelerators and fusion reactors.

Fig. 5.18 Cross section of a typical CICC cable containing Nb_3Sn or Nb-Ti strands cabled together with copper and jacketed in a structural SS shell used for TF/CS and PF coils of the ITER, respectively. The central spiral and voids facilitate SHe or liquid helium flow for cooling the magnets. *Credit* © ITER Organization, http://www.iter.org/

5.6 The Discovery of A-15 Nb_3Sn Superconductor

Hardy and Hulm [15] discovered superconductivity in A-15 class of inter-metallic compound in 1953. They reported, first time, superconductivity at 17 K in vanadium silicide, V_3Si, a compound with A-15 ($\beta - W$) structure. Soon in 1954, Matthias et al. [16] at Bell Laboratories reported superconductivity at still higher temperature of 18 K in Nb_3Sn. The inductive transition to superconductivity at 18 K in Nb_3Sn as reported first time by Matthias et al. is reproduced in Fig. 5.19. This was the highest ever reported T_c value until then. Because of the large mismatch of the melting points of Nb and Sn, the compound was prepared following a liquid diffusion process by dipping the Nb sample into a molten Sn-bath kept at 1200 °C in a quartz tube.

Figure 5.20 is the Nb-Sn phase diagram taken from Charlesworth et al. [17]. Nb_3Sn phase is stable rather over a wide range, 18–23 at.% of Sn. This gives enough flexibility to prepare this material. Below 930 °C, however, low T_c phases like Nb_6Sn_5 ($T_c = 2.6$ K) and $NbSn_2$ ($T_c = 2.1$ K) are formed which should be prevented by cooling the ingot below 930 °C rather fast. Nb_3Sn undergoes a phase transformation from A-15 cubic phase to tetragonal phase below 43 K. Nb_3Sn happens to be the highest T_c and B_{c2} material (Table 5.1) even among the A-15 superconductors which has been produced in multifilamentary form. Some important superconducting parameters of Nb_3Sn are listed in Table 5.3. Nb_3Sn is the most successful and in fact, the only superconductor in use for field generation up to 20 T. It belongs to the family of A_3B type of inter-metallic compounds having a crystal structure of β-wolfram/Cr_3Si or the so-called A-15 class. In these compounds, A is a transition metal and B can be either a transition metal or a non-transition metal. It has a cubic unit cell. Atoms A (Nb) form chains along the faces of the cube, and the B-atoms (Sn) occupy the

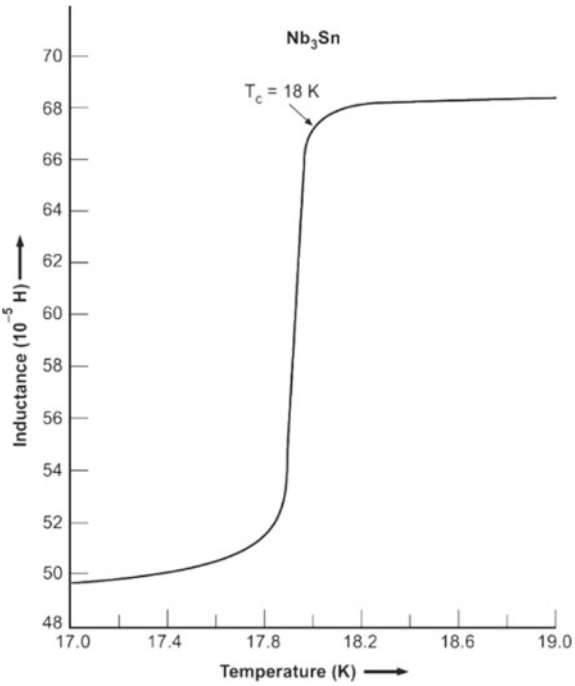

Fig. 5.19 Superconducting transition in Nb_3Sn as reported first time by Matthias et al. at 18 K [16]. With permission from APS. http://journals.aps.org/pr/abstract/10.1103/PhysRev.95.1435

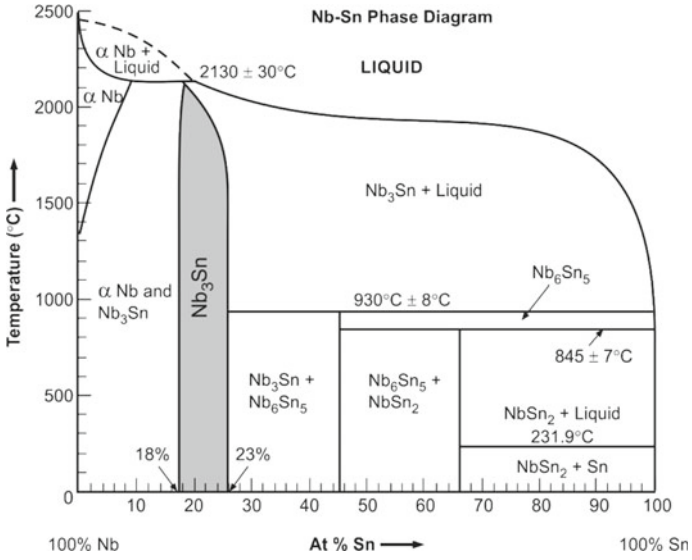

Fig. 5.20 Phase diagram of Nb-Sn [17]. With permission from Springer Publishing Company

Table 5.3 Some important superconducting parameters of Nb_3Sn (B_{sh} is the superheating critical magnetic field relevant while using Nb RF SC cavities, ℓ is the mean free path, other parameters carry their usual meanings)

Parameter	T_c (K)	B_c (mT)	B_{sh} (mT)	B_{c1} (mT)	B_{c2} (T)	$\Delta(0)/kT_c$	ξ_o (nm)	λ_L nm	ℓ nm
Nb_3Sn	18.2	535	400	20	22	2–2.2	6	60	1

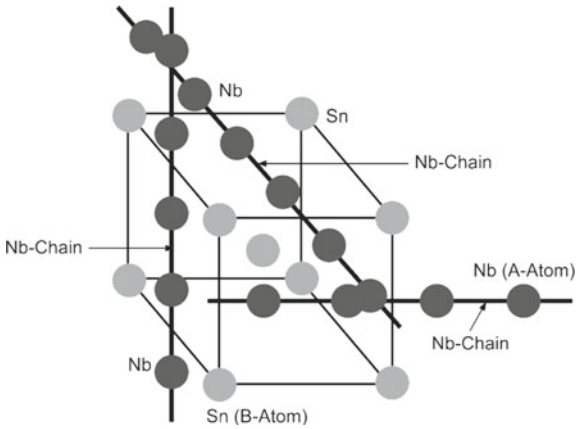

Fig. 5.21 Crystal structure of the Nb_3Sn of the type A_3B of compounds. Transition metal atoms Nb form mutually orthogonal chain along the cubic faces and Sn atoms occupy the corners and the centre of the cube

corners and the centre of the cube. The peculiar feature of A-15 structure is that the A atoms form three mutually orthogonal chains, which run throughout the lattice as shown in Fig. 5.21. The lattice parameter 'a' of Nb_3Sn is 5.2908 Å. The extraordinary properties of this class of superconductors are believed to be caused by the integrity of these A atom chains. The most important A-15 superconductors, which are mostly Nb or V based, are listed in Table 5.1. In the rest of the chapter, we will concentrate on three A-15 compounds, viz Nb_3Sn, V_3Ga and Nb_3Al only, which either have been produced commercially or stand good chance of being produced in near future.

5.6.1 Emergence of Nb_3Sn as High-Field Superconductor

The real breakthrough for Nb_3Sn to emerge as an industrial material for high-field application came from Bell Laboratories in 1961 when Kunzler [18] demonstrated first time that Nb_3Sn carries a current density of ~ 10^5 A/cm^2 in a field of 8.8 T and magnets producing field in excess of 10 T became a possibility. He produced Nb_3Sn by two techniques, namely (1) by the standard solid-state ceramic technique and (2) by the powder-in-tube (PIT) technique. In PIT technique Nb tubes were packed with the mixture of Nb and Sn powder having 10% extra Sn powder. These tubes were mechanically reduced to wires of 0.38 mm dia. and heat treated between 970 and

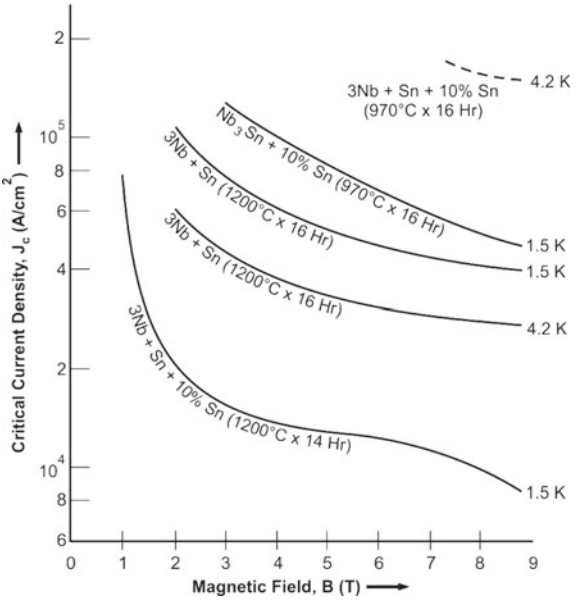

Fig. 5.22 Critical current density versus magnetic field plots of Nb_3Sn at 4.2 and 1.5 K as reported by Kunzler et al. Highest J_c (~ 10^5 A/cm^2 at 4.2 K, 8.8 T) is observed for sample heat treated at 970 °C for 16 h [18]. With permission from American Physical Society. http://journals.aps.org/prb/abstract/10.1103/PhysRevB.82.180520

1400 °C for several hours. The J_c versus field data on these samples are shown in Fig. 5.22. Evidently, J_c is the highest for samples heat treated at 970 °C. A J_c value of ~ 10^5 A/cm^2 (at 4.2 K and 8.8 T) is reached for a sample heat treated at 970 °C for 16 h. High-temperature heat treatment lowers the J_c. Great efforts were made in research laboratories, R&D institutions and companies to produce this material for high-field magnets.

The brittle nature of Nb_3Sn hampered the development of stabilized multifilamentary Cu/Nb_3Sn composites, and the material was produced in the form of flexible tapes of Nb suitably coated with Nb_3Sn either by a liquid diffusion method (perfected by General Electric Company, GEC) or by the chemical vapour deposition (CVD) process (perfected by RCA). Initial 10 T magnets were wound using these tapes in pancake structure. They were, however, not stable against flux jumps. We will not discuss these techniques because they became obsolete after the arrival of multifilamentary Nb_3Sn conductors. A brief discussion on these techniques can, however, be found in my old review of 1983 [19].

In the beginning of 1970, alternate technologies were developed to realize multifilamentary composites of Cu/A-15 superconductors. The common strategy adopted in these techniques is that the brittle A-15 phase is formed at the final stage of fabrication of the application or the device. Many techniques have been tried in the past to realize multifilamentary A-15 composite conductors with varying degree of success. The author reviewed various techniques of fabrication of stabilized A-15 MF superconductors in 1987 [20]. We will, however, discuss here only the techniques already in use for commercial production or very close to being exploited in immediate future. These techniques are (1) the bronze process, (2) the internal tin (IT) process

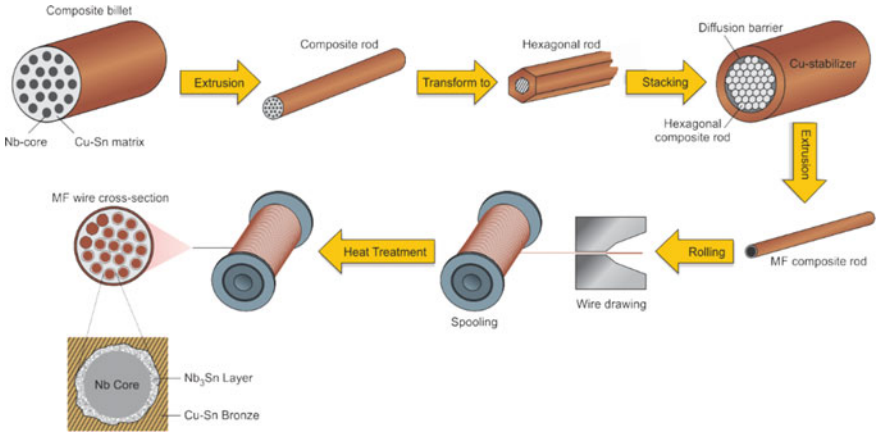

Fig. 5.23 Bronze process is shown schematically. For large number of filaments, composite rods are repeatedly bundled. Heat treatment to convert Nb into Nb_3Sn is carried out in the last stage, that is, after winding the wire into the device

(3) the jelly roll (JR) process, (4) rod-restacking process (RRP) and (5) the in situ process. Good reviews have been published by Tachikawa [21, 22] summarizing the state-of-the-art techniques of manufacturing metallic superconductors.

5.6.2 The Bronze Process

The bronze process was first time proposed by Kaufman and Pickett [23] for Nb_3Sn and by Tachikawa [24] for V_3Ga at the same conference, ICEC-3, in 1970. In this process for Nb_3Sn, one prepares an ingot of bronze of Cu–Sn containing 13–16 wt% Sn. This bronze is used as a matrix for the billet. A desired number of holes are drilled in this billet in a predetermined geometry as per the conductor design for specific application and Nb rods are inserted in these holes. The composite billet is extruded, rolled, swaged and drawn to final size in a hexagonal cross section with a few intermediate heat treatments to maintain ductility. These wires are usually bundled together repeatedly to obtained a conductor with several thousands of filaments. This bronze process is schematically shown in Fig. 5.23.

5.6.3 Parameters to Be Optimized

A. **Filament to Bronze Volume Ratio**

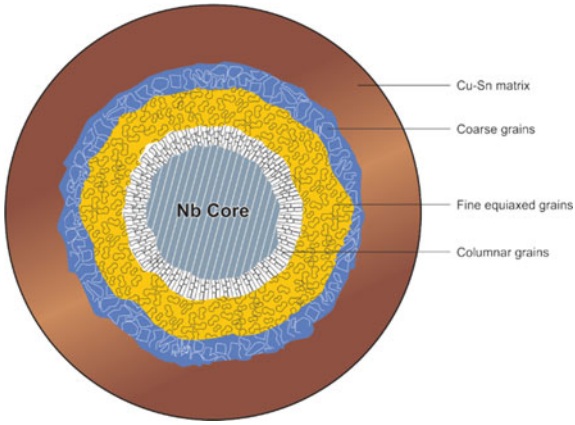

Fig. 5.24 Geometrical drawing of the cross section of a bronze route Nb_3Sn wire showing three distinct regions of grains—columnar grains close to Nb core, equiaxed grains in the middle of the layer and coarse grains close to the matrix

This ratio determines the amount of Nb_3Sn formed during the heat treatment and the compressive strain experienced by the Nb_3Sn layer when the composite wire is cooled to 4.2 K. The compressive strain is caused by the mismatch of the thermal contraction of Nb_3Sn and the matrix, which increases with bronze volume.

B. Optimization of Heat Treatment

The heat treatment of bronze composites is the most critical parameter, which needs to be optimized to achieve high J_c. During heat treatment, Sn from the bronze matrix diffuses into Nb rods and forms Nb_3Sn layer along the outer surface. The typical grain morphology of the Nb_3Sn layer formed is shown in Fig. 5.24. The Nb_3Sn layer is found to have three distinct regions, the central region consisting of equiaxed fine grains, the region with coarse grains towards the matrix interface (Sn deficient) and the third region of columnar grains towards the Nb interface. It is the central fine grain region, which is responsible for high J_c as the grain boundaries are known [25] to be the best pinning sites in A-15 superconductors.

Heat treatment controls J_c through a number of metallurgical factors. First, the volume of the central fine grains of the Nb_3Sn layer increases with the duration of heat treatment. Second, for high J_c, the grain size has to be kept minimum, and therefore, a lower reaction temperature is to be preferred. For Nb_3Sn, a temperature of 650–700 °C has been found ideal. The third important parameter to be controlled is the perfect stoichiometry of the A-15 layer, which too depends strongly on heat treatment. The Nb/Sn stoichiometry shows a large variation of Sn when the composite is reacted at lower temperature. Sn concentration is higher at the matrix end and lower at the Nb end. Heat treatment at higher temperature on the other hand leads to better Nb_3Sn stoichiometry and to higher B_{c2}. J_c therefore increases. Thus, a combination of two heat treatments is preferred. A long lower-temperature reaction leading to fine grain structure followed by a higher-temperature reaction for shorter duration. The high-temperature heat treatment improves the Nb_3Sn compositional stoichiometry and therefore B_{c2}. Table 5.4 gives the thicknesses of the Nb_3Sn layer in the three regions

Table 5.4 Grain morphology in bronze-processed Nb_3Sn after a two-step heat treatment

Heat reaction	A-15 layer thickness (μm)				J_c, A/cm^2 (4.2 K)	
	Columnar grains	Equiaxed grains	Coarse grains	Total, μm	10 T	14 T
730 °C/2 days	0.4	0.8	0.5	1.7	5.0×10^4	2.0×10^4
700 °C/4 days + 730 °C/2 days	0.5	1.2	0.4	2.1	6.7×10^4	2.8×10^4

Lower-temperature reaction yields small grains and high J_c, high-temperature reaction improves stoichiometry and increases H_{c2} again leading to high J_c [26]

and the corresponding J_c values following two different heat treatment schedules of the Nb_3Sn conductor produced by Airco [26]. The Airco bronze Nb_3Sn wire dia. was 0.7 mm with 2869 filaments and used a matrix of Cu-Sn (13 wt%). A two-step heat treatment has been found to increase the J_c up to 14 T. The wire was heat treated in two steps, namely 700 °C × 4 days followed by 730 °C × 2 days. The first heat treatment results in fine grains of ~ 72 nm and a $J_c = 2 \times 10^4$ A/cm^2 (4.2 K, 14 T). The second heat treatment coarsens the grains a bit to ~ 76 nm but still increases the J_c through an increase in B_{c2} due to improved stoichiometry. After the second treatment, J_c goes up to 2.8×10^4 A/cm^2 (4.2 K, 14 T). Figure 5.25 shows how the Nb-Sn stoichiometry improves with two-step heat treatment.

C. Filament Size

A small filament diameter needs a shorter heat treatment and is thus ideal for attaining high J_c.

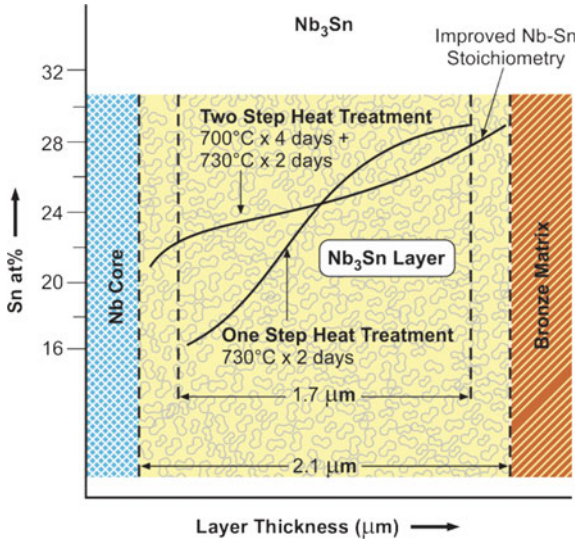

Fig. 5.25 Two-step heat treatment, 700 °C × 4 days followed by 730 °C × 2 days leads to high J_c due to small grain size and high B_{c2} due to better Nb/Sn stoichiometry [26]. With permission from Elsevier and Springer

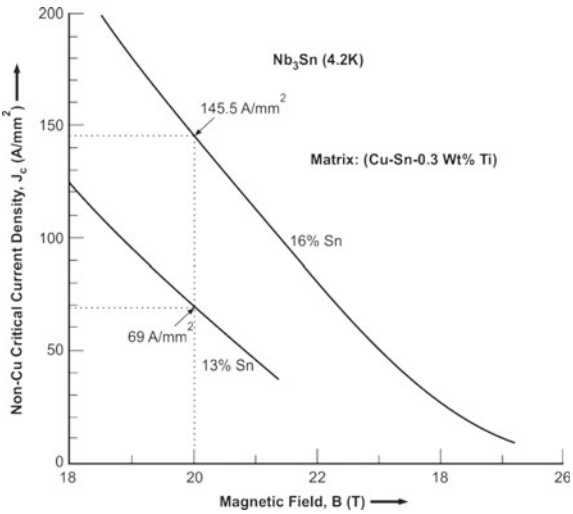

Fig. 5.26 Non-Cu J_c versus magnetic field plots of bronze-processed Nb_3Sn as a function of Sn concentration. J_c rises by almost a factor of two for bronze with 16 wt% Sn. The bronze had 0.3 wt% Ti as well. Adapted from [27]

D. **High Tin Content in Bronze**

Yet another milestone [27] was reached in enhancing the J_c of bronze-processed Nb_3Sn twofold when the Sn concentration in the bronze matrix was increased from 13 to 16 wt%. Figure 5.26 shows significant increase in J_c when Sn contents are increased from 13 to 16 wt%. The matrix also had 0.3 wt% Ti added to it.

5.6.4 Elemental Additions to Nb_3Sn

Impressive improvements in J_c of bronze Nb_3Sn superconductors have been made using elemental additions to the Nb core, to the Cu-Sn matrix or to both. These additives either refine the grains and increase J_c up to a field of 10 T or increases B_{c2} that leads to higher J_c in high fields. We will discuss below some of the interesting developments that have taken place to produce Nb_3Sn conductors with high J_c for the International Thermonuclear Experimental Fusion Reactor (ITER). Among many elements, Ti addition to the Nb core and/or the Cu-Sn matrix has been found to raise J_c significantly [28]. Ti has been found to be incorporated in the Nb_3Sn layer better if Ti is added to the matrix. Kamata et al. [29] at Hitachi Cable Co., Japan, successfully produced high J_c Nb_3Sn conductor using a matrix of Cu-7.5 at.% Sn-0.4 at.% Ti heat treated at 690 °C for 200 h. The conductor had 4.7 μm diameter 10,261 filaments. An overall J_c of 3.5×10^4 A/cm^2 (4.2 K, 15 T) was achieved in these conductors as shown in Fig. 5.27. Superconductors with improved J_c in rectangular tape form (9.5 × 1.8 mm) consisting of 5 μm diameter 349 × 361 filaments have been successfully fabricated in a full-scale production using a three-step hydrostatic extrusion process. These conductors have been widely used in fabricating 16 T magnets on a routine

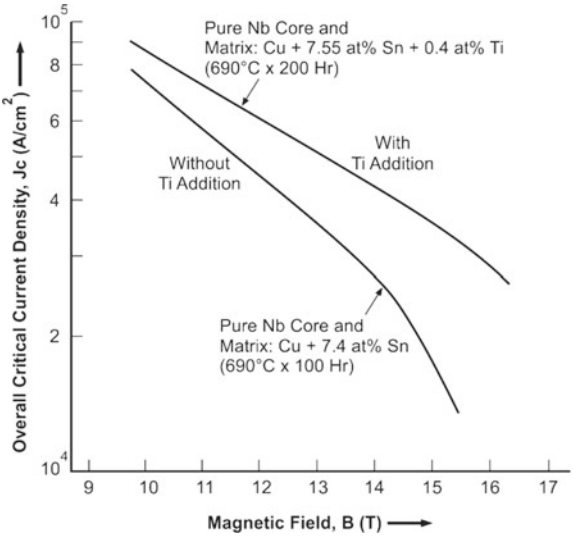

Fig. 5.27 Overall J_c (4.2 K) of 4.7 μm diameter 10,261 filament Nb_3Sn composite wire produced by Hitachi Cable Co. in Japan increases significantly by adding 0.4 at.% Ti to the Cu-7.5 at.% Sn matrix. Wire heat-treated at 690 °C for 200 h. Adapted from [20, 29]

basis. V_3Ga, and HTS YBCO or BSCCO inserts have been used in a hybrid formation to reach fields in 20–21 T range with a 16 T background field provided by Nb-Ti/Nb_3Sn combination. Bronze-processed Nb_3Sn conductor with 16 wt% Sn and 0.3 wt% Ti matrix has become the norm for many companies to produce high-performing Nb_3Sn conductor.

Such conductors have been used successfully by Kiyoshi et al. [30] in building high-frequency 930 MHz NMR magnet producing a field of 21.9 T (@ 1.5 K) using this material at NIMS, Tsukuba, Japan. Further, this material is in wide use for building cryofree (CCR cooled) magnets in the field range of 15 T for a variety of applications.

The international programme ITER has given new impetus to the development of high performance Nb_3Sn cables. Japan Atomic Energy Agency (JAEA) has produced [31] bronze-processed conductors with more than 11,000 filaments each of 3 μm dia. for ITER. To fabricate a cable-in-conduit conductor (CICC) a large number of such strands, and copper wires are twisted together in a multistage process and encased in a long SUS 316 LN jacket. Some important parameters of the bronze-processed strand used in ITER conductor are given in Table 5.5.

Bronze technique has also been used to manufacture Nb_3Sn conductors for AC applications. To minimize hysteresis losses, the filament size has been reduced to as small as 0.2 μm. The Sn concentration in bronze is reduced, and a small amount of Ge is added to make the matrix resistive for effective decoupling of the filaments. Because of the very small size of the filaments, the heat treatment temperature is now reduced to 500–550 °C. J_c in these wires do not show degradation up to a bending strain of 4%. This enables the wire to be used in a 'react and wind' mode. A-2 T, 50 mm bore magnet using Nb_3Sn wire has been operated by Tachikawa et al. [32] at 53 Hz with an AC loss of only 0.013% of the coil energy.

Table 5.5 Important specifications of the bronze-processed Nb_3Sn conductor developed for ITER [31]

Parameter	Unit	Value
Dia. of Cr-plated wire	mm	0.826
Bronze composition	wt%	Cu + 15.5 Sn + 0.3 Ti
Filament composition	wt%	Nb + 1.0 Ta
Barrier material		Nb
Filament dia.	μm	3
No. of filament		19 × 583 = 11,077
Non-Cu J_c	A/mm^2	820 (12 T, 4.2 K)
Hysteresis loss	kJ/m^3	620 (±3 T, 4.2 K)

5.6.5 *The Internal Tin (IT) Process*

The internal tin (IT) method of fabricating Cu-Nb_3Sn composite wires is based on the old work of Hashimoto [33]. In this process, Sn or Sn alloy contained as core is made to diffuse out into the composite. The problem of intermediate annealing associated with bronze process due to work hardening is, thus, circumvented. In this process, [33], as shown in Fig. 5.28, the copper billet consisting of Nb rods has a central hole, which is filled with Sn. The composite billet is reduced to hexagonal-shaped rods suitable for restacking. The desired number of these 'sub-elements' is stacked together in a stabilizing Cu tube lined with a thin tantalum diffusion barrier and cold drawn to final size of the wire. Since all the components, that is, Cu, Sn,

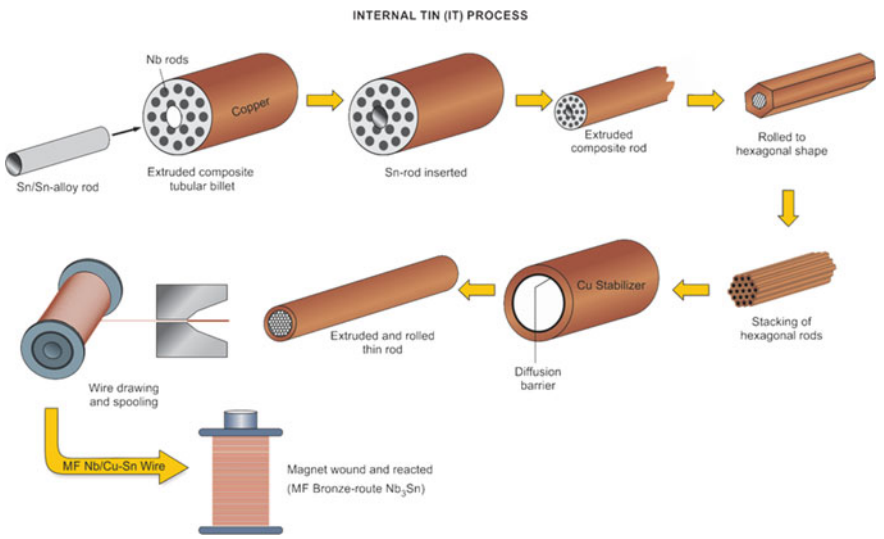

Fig. 5.28 Sequence of steps followed in the internal tin process to produce Cu/Nb_3Sn composite wire

Ta and Nb are ductile; their co-processing is easy and economical. No intermediate annealing is needed. For high-current applications, the wires can be cabled into a desired configuration. Diffusion of Sn from the centre is carried out in a multistep homogenization process between 200 and 500 °C for several days. The final reaction to form Nb_3Sn is carried out at 650–750 °C for a few days, depending upon the sub-element size, filament size, volume fraction of Sn and the desired magnetic field. IGC [34] as early as 1985 prepared 27-km-long wire with this process with an overall J_c (excluding the barrier and the stabilizing Cu) = 10^5 A/cm^2 (4.2 K, 10 T).

The bronze process has the limitation that the solubility limit of Sn in Cu is 15.8 wt%, whereas larger Sn concentration is possible in the IT process which results in high non-Cu J_c in the wire. IT process is also being used for wire production for fusion programme including ITER. Similar to in bronze process addition of Ti to the Sn core leads to higher J_c values in IT processed Nb_3Sn wires. The IT process has a drawback that pure Sn used as a core melts during extrusion. Further, the diffusion of Sn causes a void at the centre after the heat treatment. Nb_3Sn filaments in IT process tend to bridge after the heat treatment causing an increase in AC losses. Thus, they do possess higher J_c but AC losses go up in comparison with the bronze-processed conductors.

The benefit of Ti addition to Nb_3Sn to raise J_c is realized in IT process by adding Ti to the Sn component. Ti addition also increases the hardness of Sn to make it more compatible with Cu and Nb for co-processing. A few variants of the IT techniques have been invented which are summarized in the next subsections.

A. The Distributed Tin (DT) Technique

Uniform availability of Sn to the filaments across the cross section of the conductor is a prerequisite of any fabrication technique for the growth of Nb_3Sn with perfect stoichiometry. Uniform distribution of Sn across the cross section is accomplished in the so-called distributed tin (DT) technique [35]. In this design, the distances for Sn to diffuse in Nb have been reduced drastically. Two elements, namely Nb-Cu (Nb rods in Cu tubes) and Sn-Cu (Sn rods in Cu tubes), are packed uniformly across the cross section of a Cu stabilizer tube in a predetermined geometry as shown in Fig. 5.29. The volume ratio of Nb:Sn is kept at 3:1 across the wire. Table 5.6 gives the specifications of a wire prepared with a typical DT configuration. A non-Cu J_c of 2.07×10^4 A/cm^2 (4.2 K, 20 T) has been achieved. Uniform grain size distribution has been realized in this technique, which has resulted in high J_c values. The AC losses are, however, high reaching a level of 3850 kJ/m^3 at $\pm$ 3 T at 4.2 K.

B. The Modified IT Process with Radial Nb Filaments

The Mitsubishi Electric Co. later modified the DT process and developed [36] low-loss Nb_3Sn wire by having a modified radially arranged Nb filaments across the cross section of the sub-elements as shown in Fig. 5.30. The Mitsubishi wire of 0.82 mm dia. had 91 sub-elements. Each sub-element has a central Sn core with three layers of 84 Nb filaments of 2.7, 3.3 and 3.9 μm dia. from inner to outer layer, respectively. The twist pitch was 25 mm. A Ta barrier has been used at the Cu stabilizer interface.

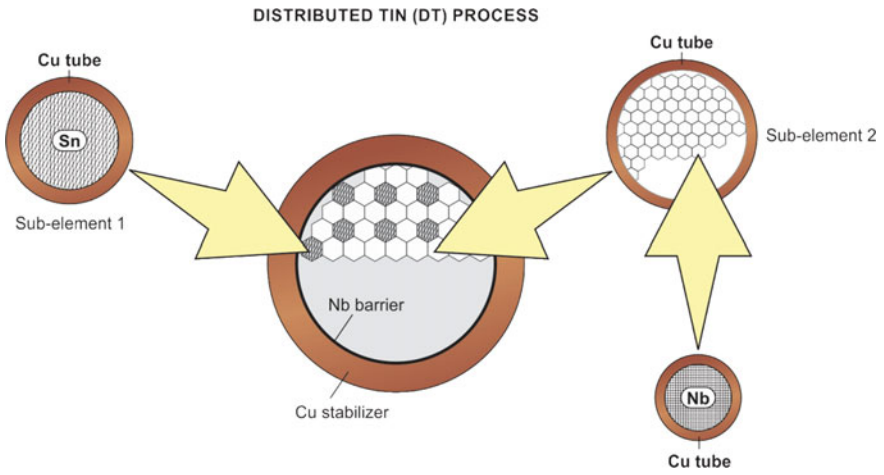

Fig. 5.29 Schematic drawing of the distribution of Nb-Cu and Sn-Cu sub-elements in a conductor cross section prepared by the so-called distributed tin (DT) technique. Adapted from [22, 35]

Table 5.6 Specifications of a typical DT-type conductor

Parameter	Unit	DT wire
Wire dia.	mm	1.0 × 0.7
No. of Nb in Cu tube elements		138
No. of Sn in Cu tube elements		61
Cu to non-Cu ratio		0.8
Filament dia.	μm	3.0/2.1
No. of filaments		27,462
Barrier material		Nb
J_c @ 4.2 K	A cm^{-2}	2.07 × 10^4 (20 T)

Data compiled from [35]

The stabilizing Cu was 51.5 vol.%. The volume fraction of Cu, Nb and Sn in a sub-element was 25.4%, 12.8% and 10.3%, respectively. This filament arrangement opened many Sn diffusion paths and prevented circumferential filament coupling. This resulted in higher J_c and low AC losses. A non-Cu J_c of 1.15 × 10^5 A/cm^2 (4.2 K, 12 T) was achieved. AC losses were reduced to 301 kJ/m^3 at ± 3 T and 4.2 K. It, thus, appears that the performance of the IT conductor is strongly linked to the design of the cross section. The present-day performance of the IT wires matches well with the specifications, set for the ITER conductor.

Both the techniques, namely, bronze and the IT, have been used successfully to produce Cu-$(Nb,Ti)_3Sn$ wire of lengths up to 20 km which are cabled to fabricate cable-in-conduit conductors (CICC) carrying currents up to 80 kA at 10 T field. Japan Atomic Energy Research Institute (JAERI) has already tested the central

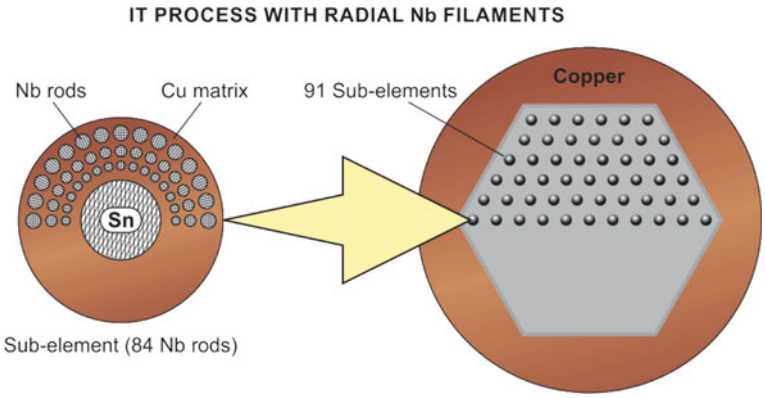

Fig. 5.30 Geometrical arrangement of Nb rods in a sub-element and the sub-elements in a wire cross section of an IT wire by Mitsubishi Electric Co. for the production of a low-loss Nb_3Sn wire. Note the radially arranged Nb filaments in a sub-element. Adapted from [36]

solenoid model coil (CSMC) for ITER. Coils have been wound using combination of conductors produced by bronze and IT processes.

5.6.6 The Jelly Roll Process

The jelly roll (JR) process was introduced by McDonald et al. [37] at Teledyne Wah Chang Albany, for producing composite Nb_3Sn MF conductors. In this process, thin foils of Nb and Cu-Sn bronze are laminated and wrapped around a Cu cylinder with a Ta diffusion barrier on the cylinder, and the assembly is inserted in a hexagonal-shaped Cu container. Several of these hexagonal containers are bundled together in another Cu tube. The composite billet is extruded and reduced to fine wires as in conventional bronze or IT process. The advantage of this JR process is that the conventional bronze core is replaced by a Cu core surrounded with a barrier. The barrier prevents the Sn infiltration into copper and enhances the conductor stability. This technique also makes the availability of bronze around each filament uniform. By contrast, the conventional bronze core leads to a strong radial Sn gradient that produces marked differences in the local Sn composition and the grain morphology of the Nb_3Sn layer. Detailed work on this JR technique by changing matrix to filament ratio, using pure Nb and Nb-0.8 wt% Ti sheets and using a heat treatment at 725 °C for 50–200 h, has led to high J_c values $= 1.3 \times 10^4$ A/cm^2 (4.2 K, 16 T).

Tachikawa et al. [38] at Tokai University, Japan, used the JR technique to produce composite Nb_3Sn conductor with high J_c and B_{c2} values. Thin sheets of Nb laminated with the sheet of one of the Sn-based alloys like Sn-Ta, Sn-B or Sn-Nb are wrapped spirally over a Nb-Ta (3.3 at.%) core and covered again with the Nb-Ta sheet. The composite assembly is rolled and drawn to wires and heat treated at 725–750 °C

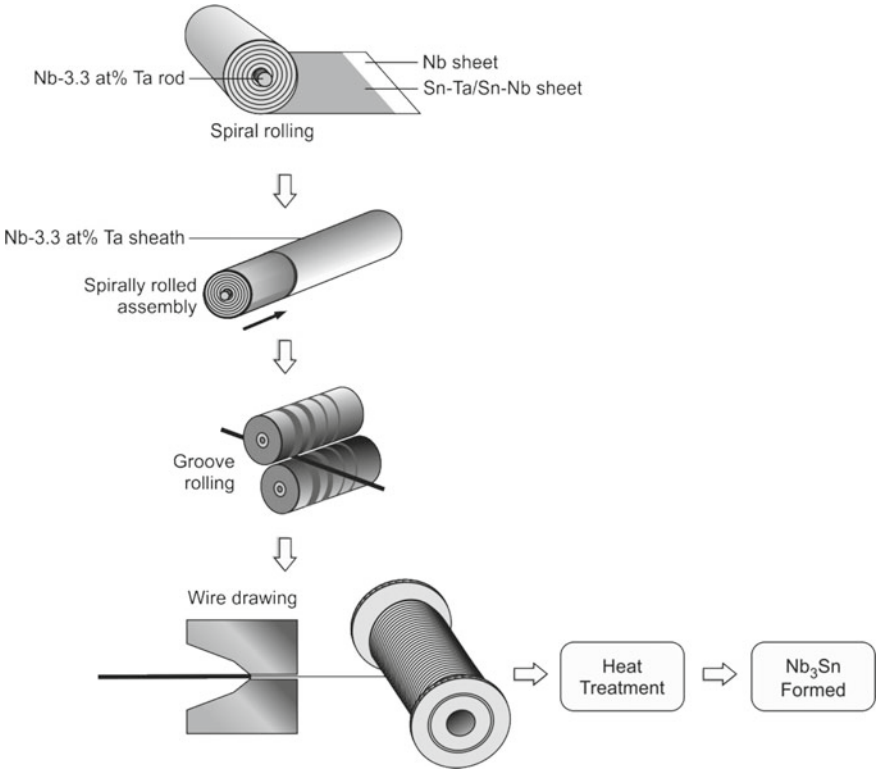

Fig. 5.31 Schematics of the JR process for producing Nb_3Sn conductor

for long periods. A sharp $T_c = 18.1$ K, $B_{c2} = 26.5$ T and a non-Cu $J_c = 1.5 \times 10^4$ A/cm^2 (4.2 K, 22 T) has been achieved. Still better performance can be attained by optimizing parameters leading to a uniform and stoichiometric Nb_3Sn layers. The JR process used by Tachikawa et al. is schematically shown in Fig. 5.31.

5.6.7 The Rod Restacking Process (RRP)

The rod restacking process (RRP) [39] gained popularity in the beginning of 2000, replacing the MJR process, for facilitating large-scale production. The unique feature of this process is that the barriers are distributed over the cross section and is built up of two types of sub-elements. Sub-element 1 in RRP is a Sn rod encased in a Cu tube which is surrounded by a stack of the sub-elements 2 which is a Cu tube stacked with a large number of Nb rods each of which is encased in a Cu tube. Sub-element 1 and sub-elements 2 are packed uniformly in a Cu stabilizer lined with a barrier. The composite billet is then processed as usual. The Cu/Nb area ratio of the Cu clad Nb

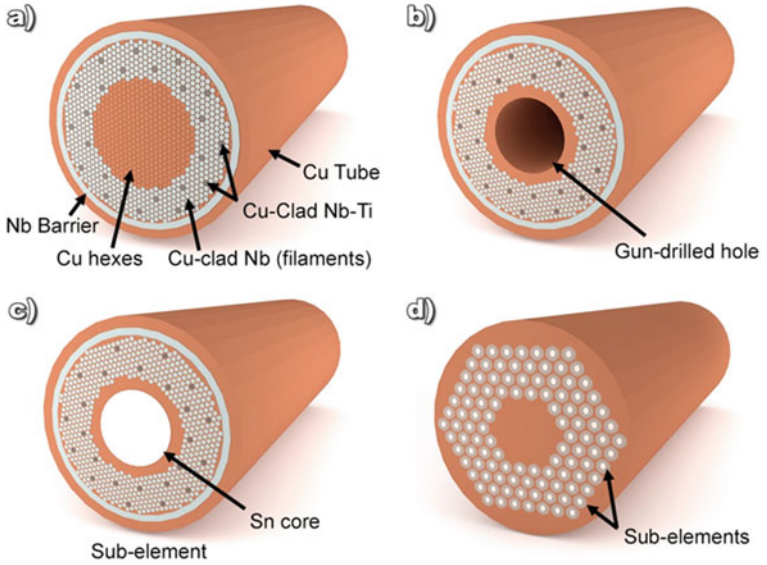

Fig. 5.32 Fabrication sequence of high J_c Nb_3Sn wires by rod restacking process (RRP) technique. *Courtesy* Charlie Sanabria. Image by Charlie Sanabria licensed under a Creative Commons Attribution 4.0 International License. Based on a work at the National High Magnetic Field Laboratory

rods can be chosen as per the demand of the application. During the heat treatment, Sn gets diffused out through Cu and reacts with Nb core in sub-elements 2 converting Nb core into Nb_3Sn. Oxford Superconducting Technology (OST) achieved a non-Cu J_c of 3000 A/mm^2 (4.2 K, 12 T) in early 2000, following the RRP technique with the best values of about 3300 A/mm^2 [39].

Figure 5.32 shows the steps involved in the fabrication of Nb_3Sn wire following the RRP method. Figure 5.32a is the sketch of a billet consisting of hexagon of Cu and the Nb rods cladded with Cu, all contained in an outer Cu tube lined with Nb barrier. Some Cu clad Nb-Ti rods have also been introduced for doping to increase J_c. The billet is hot extruded for good bonding between various components. A gun hole is now drilled at the centre of the billet for inserting a Sn rod (Fig. 5.32b). The composite billet after the insertion of Sn rod and cold drawing constitutes a sub-element (Fig. 5.32c). A large number of these sub-elements are stacked again in a Cu jacket with a Cu central core and finally processed to wires of desired diameter.

5.6.8 The Powder-in-Tube (PIT) Process

PIT process is similar to what Kunzler [18] used for making Nb_3Sn wires in 1961. The present-day PIT differs in one respect that Nb + Sn powder is mixed with Cu

powder to bring down the reaction temperature to 650–700 °C. The technique was used first time [40] by ECN, the Netherland Energy Research Foundation in 1977. In this technique, Sn-rich inter-metallic $NbSn_2$ in powder form is mixed with small amounts of Cu powder and filled into a thin Cu tube. This Cu tube in turn is inserted into a Nb (or Nb-7.5 wt% Ta) tube. The composite is finally fitted into an outer Cu stabilizer. In these wires, Nb left unreacted in each filament serves as the barrier. The processed wire is reacted at 650–700 °C, whereby the A-15 Nb_3Sn phase with fine grains is formed. To improve the Sn to Nb ratio, extra elemental Sn is added. The process needs a heat treatment at 650–700 °C for 50–75 h for Nb_3Sn formation.

This process leads to strands [41] with high non-Cu critical current densities ~ 2500 A/mm^2 (4.2 K, 12 T) with fine filaments of diameter down to 30 μm. Lindenhovius et al. [42] at Shape Metal Innovation (SMI) obtained high non-Cu J_c = 217 A/mm^2 (4.2 K, 20 T) and B_{c2} = 25.6 T in PIT processed strands of $(Nb\text{-}Ta)_3Sn$. These values were obtained by optimizing the heat treatment and adding 7.5 wt% Ta to Nb. The SMI has developed a PIT binary Nb_3Sn conductor with 504 filaments of 20 μm diameter that had a non-copper current density of 2680 A/mm^2 (4.2 K, 10 T). This conductor has been developed for a 10 T, wide bore model separator dipole magnet for the LHC.

5.6.9 Conductor for High-Luminosity LHC Quadrupole Magnets

CERN will be replacing the main ring inner triplet quadrupoles (MQXF), adjacent to the main ring intersection regions for its high-luminosity upgrade of the Large Hadron Collider (HL-LHC) project. After evaluating the performance of superconducting cables at LARP (the US LHC Accelerator R&D Program), Cooley et al. [43] have frozen the specifications of the Ti-alloyed Nb_3Sn conductor for MQXF magnets. The conductor will have 0.85 mm diameter, restack 108 × 127 and a copper fraction of 52.4%. The strand critical current will be ≥ 631 A (4.22 K, 12 T) and ≥ 331 A (4.22 K, 15 T). The residual resistance ratio (RRR) will be of not less than 150. These new specifications allow a small increase of the sub-element diameter from 50 to 55 μm, and in Nb:Sn molar ratio from 3.4 to 3.6. Alloying with Ti improves the growth rate of Nb_3Sn layer formation at a reaction temperatures of 635–665 °C that results in high RRR. However, this low reaction temperature yields the 4.2 K extrapolated upper critical field B_{c2} value of 25–26 T, somewhat lower than the highest value of 27.8 T. Enhancing the ratio Nb:Sn will provide better control over RRR and flexibility for heat treatment schedule. The specifications are tabulated in Table 5.7.

It, thus, appears from the description of the most promising techniques discussed in preceding sections, which have reached almost the limit of J_c and B_{c2} for Nb_3Sn conductors. According to an analytical model [44], the maximum Nb_3Sn fraction can reach 65% just 5% more than what is presently found in best RRP conductors. The best value of B_{c2} reached in RRP strands at 4.2 K is ~ 28 T, almost the

Table 5.7 Specifications of the Ti-alloyed Nb_3Sn RRP round wire to be used for replacing the main ring inner triplet quadrupoles (MQXF) for its high-luminosity upgrade of the Large Hadron Collider (HL-LHC) project (compiled from [43])

Parameter	Value	Units	Parameter	Value	Units
Type of conductor	Ti-alloyed Nb_3Sn		Critical current (4.22 K, 12 T)	$\geq$ 632	A
Conductor diameter	0.85	mm	Equivalent Je	2450	A/mm^2
Re-stack	108 × 127		Critical current (4.22 K, 15 T)	$\geq$ 331	A
Heat treatment	210 °C 48 h + 400 °C 48 h + 665 °C 75 h		Equivalent J_c	1285	A/mm^2
Cu:non-Cu ratio	1.2		Sub-element dia.	55	μm
RRR	150		Peak field (@ 1.9 K)	11.4	T
Nb:Sn mole ratio	3.6		Max operating current	17.8	kA
No. of sub-elements	$\geq$ 108		Max current/strand	445	A

highest reported so far. Further improvement in J_c seems unlikely through more comprehensive optimization of the compositions of Sn/Cu/Nb, heat treatment and microstructural control. At times, improvement in one superconducting parameter turns detrimental for another parameter. For example, a high-temperature treatment improves the stoichiometry of Nb_3Sn and hence B_{c2}, but it increases the grain size and brings down the J_c. Optimization of parameters is, therefore, carried out by making a trade-off between these controlling factors. The only hope could be that the grain size in RRP technique at 125–150 nm is still larger than the lowest limit of 15 nm that can be reached theoretically, and thus a further reduction of grain size can perhaps enhance flux pinning and J_c though only marginally.

5.6.10 The In Situ Process

Though the in situ process has not been exploited for commercial production, yet I am including it here because it is an interesting process insofaras the multiple and very fine filaments are formed in situ. The technique is a fall-out of a paper by Tsuei [45] and soon followed by Sharma and Alekseevskii [46] in which superconductivity was found at 18 K (= T_c of Nb_3Sn) in an alloy $Cu_{93}Nb_5Sn_2$ when drawn into fine wires and suitably heat reacted. The in situ technique is based upon the near negligible solubility of Nb in Cu at ambient temperature. Large amount of Nb can mix with Sn in the molten state but as soon as the liquidus line at 1700 °C is crossed, most Nb gets precipitated out in the Cu matrix. Below the peritectic temperature (1090 °C),

the solubility of Nb in Cu is only ~ 1.5 wt% and that of Cu in Nb ~ 2 wt%. These compositions are retained if the cooling is fast.

Figure 5.33 shows the SEM micrographs of the Cu-Nb (20 at.%) alloy in three different stages of the process reported by Sharma et al. [20, 47]. The cast alloy prepared by arc melting shows typical dendrite structure of the Nb precipitates in Cu matrix (Fig. 5.33a). Ingots when rolled and/or drawn to fine size of wire, these precipitates get elongated and take the shape of fine filaments which tend to curl and fold being constrained by the matrix (Fig. 5.33b). Figure 5.33c is the SEM micrograph of the cross section of a 0.21 mm wire, which shows very high density of the filaments. As seen from this figure, the filaments are ribbon-shaped because typically the bcc Nb crystals deform in a plane strain rather than having an axially symmetric flow. This high density of Nb filaments causes high density of Cu-Nb interfaces increasing the yield strength of the composite manifold, much more than what the rule of mixture would predict. This structure also leads to increased J_c because of increased surface flux pinning caused by the high density of interfaces.

The drawn wires are then coated with optimized amount of Sn and heat treated at ~ 550 °C for 50–200 h. Note that this temperature is much smaller than needed (~ 700 °C) in bronze process. Figure 5.34 shows the J_c–B behaviour of the in situ

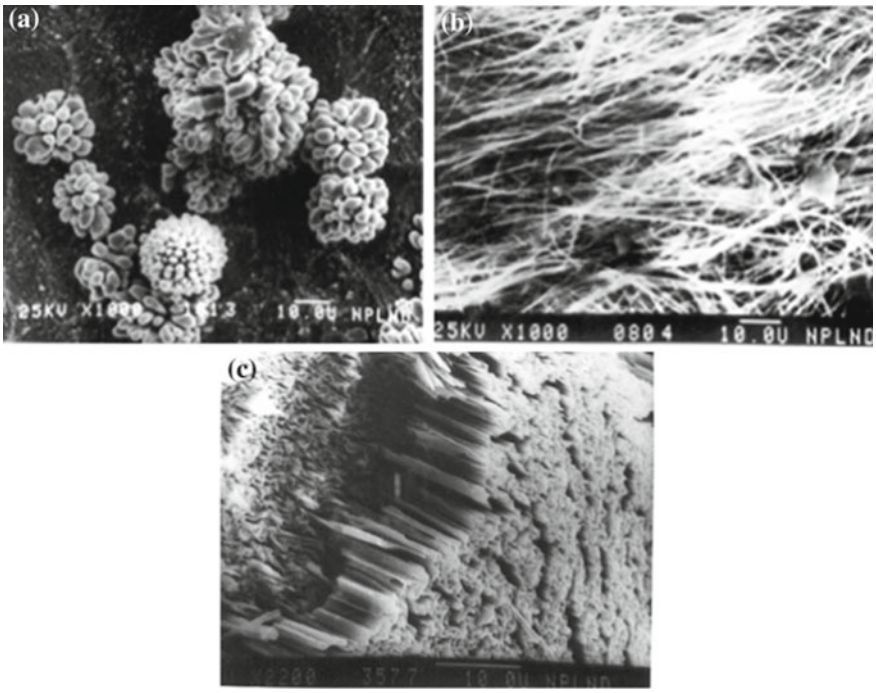

Fig. 5.33 **a** Typical Nb dendritic structure in a Cu-Nb (5 at.%) ingot quenched from the melt. **b** Filamentary morphology of a Cu-Nb (20 at.%) wire drawn to 0.21 mm dia. **c** Cross section of a 0.21 mm dia. Cu-Nb (20 at.%) wire. High density of ribbon-shaped filaments is visible [47]

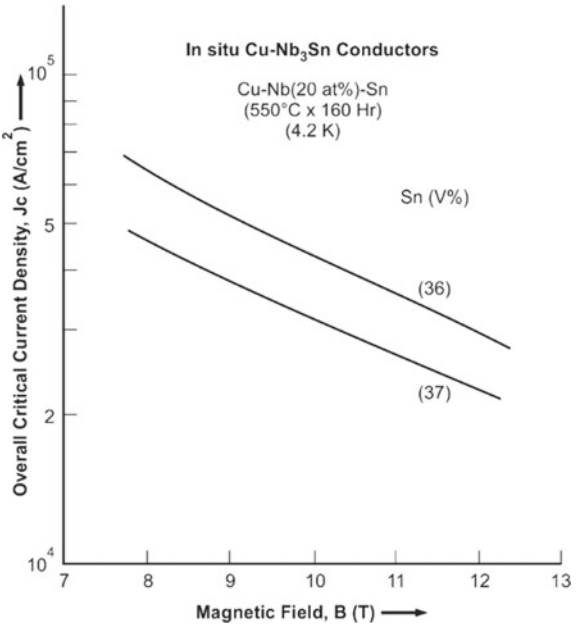

Fig. 5.34 Overall J_c of the Cu/Nb_3Sn 0.21 mm dia. in situ wires reacted at 550 °C for 160 h. Upper curve has Sn 36 vol.% and the lower curve Sn 37 vol.% [47]

Cu/Nb_3Sn wires of 0.21 mm dia. coated with 36–37 vol. % Sn and reacted at 550 °C for 160 h. Cu-Nb ingots were prepared using an arc furnace. An overall $J_c = 3 \times 10^4$ A/cm^2 (4.2 K, 12 T) has been obtained as shown in Fig. 5.34. Impressive results were reported on in situ Nb_3Sn and V_3Ga conductors by Bevk's group at Harvard University, Finnemore's group at Iowa State University, Freyhardt at Gottingen University, Roberge's group at Quebec, Canada, and Tachikawa' group at National Research Institute for Metals (now NIMS). For details of results from these groups, please, see the review paper by the author [20]. The J_c of in situ conductors are comparable or better than obtainable from conventional bronze and IT techniques, nevertheless suffer from the high AC losses because of the intimate coupling between the closely spaced filaments.

This technique has several advantages not available with other techniques. The technique is much simpler as there are no repeated bundling to make MF, and there are no intermediate annealing treatments. The ductility of the Cu-Nb ingot allows processing of the wire down to fine size without annealing. Very fine filaments obtainable in in situ conductors (~ 0.2–0.5 μm) need low-temperature heat treatment temperature (500–600 °C) which leads to fine grain structure of the Nb_3Sn layer resulting in high J_c. Very fine size of the filaments and small inter-filamentary distances lead to exceptionally high filamentary bonding. As a result, local strain is transferred to the entire cross section. This results in exceptionally high mechanical strength. The ultimate tensile strength σ_{UTS} of the bronzed processed Cu/Nb_3Sn composite is 292 MPa, whereas the in situ composite has a σ_{UTS} of 513 MPa at room temperature and increases further by 25% to 690 MPa at 77 K. In situ conductors are less sensitive to stress–strain behaviour than their counter part in bronze

Table 5.8 Engineering J_e values of different compositions of the in situ processed Cu/Nb_3Sn composite conductors reported by different groups

Reference	Author	J_c (A/cm^2)	Temp, field	Composition
[47]	Sharma et al.	3×10^4	4.2 K, 12 T	Cu-Nb 20 at.%-Sn 36 vol.%
[48]	Harbison et al.	2×10^3	4.2 K, 12 T	Cu-Nb 10 at.%-Sn 2 at.%
[49]	Verhoeven et al.	6×10^4	4.2 K, 8 T	Cu-Nb 20 wt%-Sn 9.3 wt%
[50]	Fihey et al.	1×10^4	4.2 K, 14 T	Cu-Nb 36 wt%-Sn 20 wt%
[51]	Verhoeven et al.	8×10^3	(4.2 K, 12 T)	Cu-Nb 20 wt%-Sn 10 wt%

process. For example, the bronze conductor shows J_c degradation at a strain level of 0.3%, whereas the in situ conductor shows the J_c degradation at only 0.6% strain. Filament strength too in these composites is high because of small grain size (Hall Patch effect), and dislocation movement is inhibited due to the high density of the filaments causing obstacles due to Orowan mechanism. All the unique properties of these in situ conductors depend upon two factors, one, the superconducting volume fraction (SVF) and the other area reduction ratio (ARR). The SVF has to be well above the percolation threshold (~ 17 vol.%) and as high as permitted by the need to maintain ductility. The area reduction ratio (ARR) will depend upon the starting billet size but an area reduction of 3000–4000 has been found optimum for laboratory scale production.

In situ Nb_3Sn conductors with impressive values of J_c, high strain tolerance, exceptionally high mechanical strength have been produced on laboratory scale with ingots up to 40 kg. Different techniques have been used to prepare the alloy ingots. These include induction melting, arc melting, chill cast, levitation technique, high-temperature gradient arc melting and continuous arc casting. The basic objective in preparing the ingot has been to obtain a homogenous mixture of Cu and Nb at high temperature and quench fast to retain homogeneity and keep the precipitate small. Table 5.8 gives the representative J_c values for different compositions of Cu-Nb-Sn reported by a few groups and prepared by different techniques. It is important to note that all these J_c values are overall engineering J_e values, that is, it takes the entire cross section of the composite wire in the calculation of J_c.

There may be a revival of interest in the in situ technique in future as the reports suggest that in situ conductors are less prone to radiation damage.

5.7 The A-15 Nb_3Al MF Superconductor

Nb_3Al is yet another superconductor belonging to the family of A-15 class/β-W structure compounds and is tipped to be the material of future for magnets needed for high-energy particle accelerators, nuclear fusion reactors and high-frequency NMR spectrometers. This material is superior to Nb_3Sn in two respects, one, the upper critical field of Nb_3Al is about 32 T much higher than that for Nb_3Sn, and the

other is its high strain tolerance. Its T_c at 18.8 K is comparable to that of Nb_3Sn. The complicated phase diagram of Nb-Al had put the hurdle in perfecting the technology of the production of multifilamentary Nb_3Al that has now been solved by the NIMS group.

5.7.1 *Phase Diagram of Nb-Al System*

The phase diagram of the binary phase of Nb and Al is shown [52] in Fig. 5.35. The phase diagram of Nb-Al has a similarity with the Nb-Sn system insofaras the A-15 phase is formed by a peritectic reaction from bcc phase + liquid to A-15 phase at 2060 °C. The bcc solid solution phase Nb(Al)ss, however, extends over a wide range of composition. The solubility limit of Al is 21.5 at.% at 2060 °C and 9 at.% up to 100 °C. On both sides, that is, Al-rich side as well as Nb-rich side, the phase limits of the A-15 phase depend strongly upon temperature. On the Al-rich side, the A-15 phase includes the stoichiometric composition at the second peritectic temperature of 1940 °C. This limit, however, shifts to lower Al concentration of 21.5 at.% at 1000 °C. The Al content on the Nb-rich side varies from 19 at.% at 1500 °C to 22.5 at.% at the peritectic temperature. This extensive variation of A-15 phase stoichiometry at low temperatures creates problem in fabricating Nb_3Al conductors with acceptable J_c and B_{c2} values. Even the stoichiometric bulk Nb_3Al (3:1) material has low T_c of

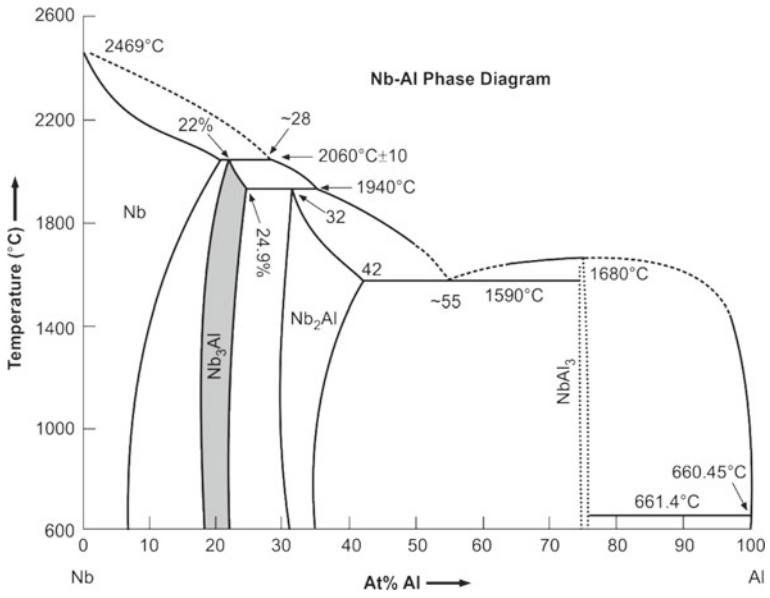

Fig. 5.35 Binary phase diagram of Nb and Al [52]. *Courtesy* Takao Takeuchi and with the permission of Taylor and Francis Group LLC, a division of Informa plc

12 K when heat treated at below 1000 °C. This T_c, in fact, corresponds to a Al-rich limit of 21 at.%. Al. Low-temperature heat treatment below 1000 °C is thus ruled out for fabricating Nb_3Al wire conductors. The ternary Cu-Nb-Al phase diagram too is complicated and has proved to be a big hurdle in adopting the so-called bronze technique to produce MF Cu-Nb_3Al stabilized conductors. Several unwanted ternary phases are formed which block the tie line routes between Cu-Al bronze and the Nb solid solution through the A-15 Nb_3Al phase. It was for this reason that conventional bronze process could not be applied to Nb_3Al wire fabrication. Production of Nb_3Al conductor, thus, had to wait for the development of an alternate method. Nb_3Al has the β-wolfram (β-Tungsten) crystal structure similar to that of Nb_3Sn shown in Fig. 5.21 with the difference that Sn atoms are now replaced by Al atoms. The lattice parameter, of Nb_3Al is, $a = 5.183 \pm 0.002$ Å.

5.7.2 *Mass Production of JR Nb_3Al Conductors by JAERI for ITER*

The strategy for the successful manufacture of Nb_3Al wires has been to follow a three-step process. One, that the A-15 stoichiometric composition should be attained at high temperature (~ 1900 °C) by forming a bcc solid solution $(3Nb.Al)_{SS}$. Two, the stoichiometry should be retained by quenching the alloy fast (~ 10^4 °C/s), the alloy though is in bcc phase. Third, the diffusion temperature to convert bcc phase into A-15 phase should be kept below 1000 °C in order to keep the grain size small. This three-step procedure, thus, leads to perfect stoichiometric composition (25 at.% Al) with high T_c, high B_{c2} and high J_c in higher fields. Lower diffusion temperature restricts the grain size, which helps in achieving high J_c, grain boundaries being the most effective pining centres in A-15 superconductors. Japan Atomic Energy Research Institute (JAERI) followed the jelly roll method to make long length A-15 MF Nb_3Al conductors, wherein thin sheets of Nb and Al are laminated and wound over a Cu rod and encased in a Nb sheet. The composite billet is extruded and drawn to hexagonal-shaped JR sub-elements. These sub-elements are stacked together in the desired geometry in a Cu tube and processed to wires of required diameter.

The JAERI in collaboration with Sumitomo Electric Co. produced Nb_3Al CICC [53, 54] for ITER magnets. Figure 5.36 is the cross section of a strand 0.81 mm in diameter with 96 JR processed sub-elements, and Fig. 5.37 on the other hand is the cross section of the CICC with 1152 such strands. These JR processed wires are heat treated at a temperature of 750 °C to facilitate the formation of Nb_3Al through the diffusion reaction. A non-Cu J_c of ~ 1.0×10^5 A/cm^2 (4.2 K, 12 T) has been attained. JAERI established the facility to process 70 kg billets producing JR Nb_3Al wires of length as much as 16 km and weighing about 1000 kg. This conductor has been used for an insert coil of the ITER central solenoid producing a field of 13 T at 4.2 K. The hysteresis losses are found to be limited to 600 mJ/cm^3 at ± 3 T and a residual resistivity of the chrome-plated wire less than 1.6×10^{-10} Ωm. JAERI has

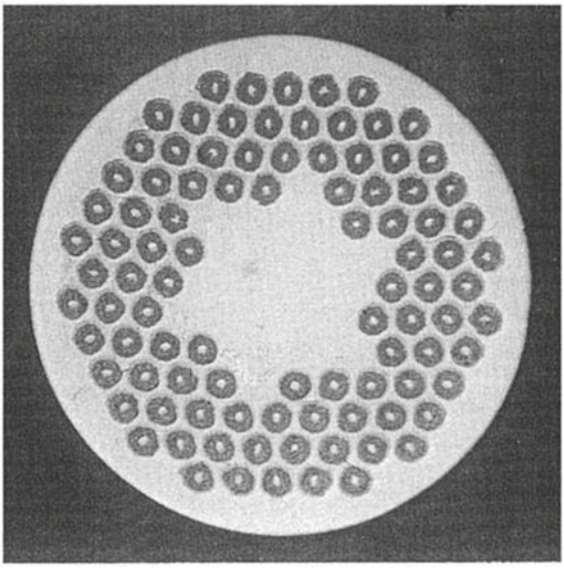

Fig. 5.36 Cross section of a 0.81 mm dia. strand with 96 sub-elements of Nb_3Al processed by JR technique, for the insert coil of the central solenoid of ITER [53]. With permission from Elsevier

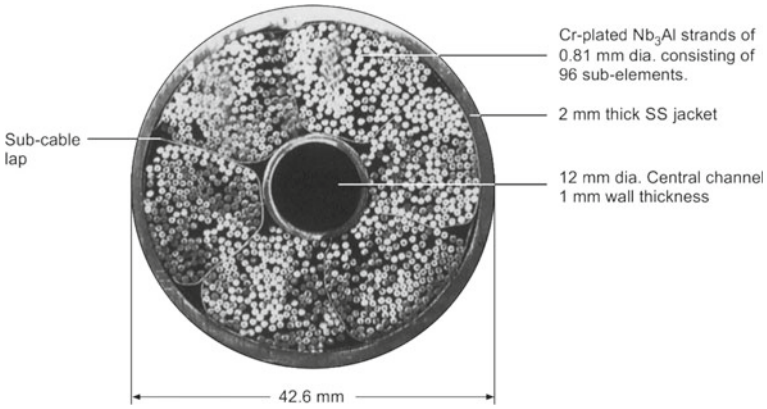

Fig. 5.37 Cross section of the JR processed Nb_3Al-CICC for ITER TF coils (13 T @ 46 kA) [54]. With permission from Elsevier

since tested successfully a stainless steel (SS) jacketed JR-processed Nb_3Al CICC conductor in a 'react and wind' form carrying a current of 46 kA at 13 T, 4.2 K as a candidate for the TF coils of the ITER.

5.7.3 The Rapid Heating, Quench and Transformation (RHQT) Technique

Though JAERI has been successful in developing Nb_3Al CICC by JR method suitable for ITER applications, yet the technique suffers from an inherent problem of direct diffusion reaction between Al and Nb at a temperature of 750 °C at which the phase composition deviates from the normal A-15 stoichiometry. This resulted in a low B_{c2} of 22 T significantly lower than the expected value of 30 T. Alternatively, diffusion can be carried out at high temperature (~ 1800 °C) but coarser grains, formed at this temperature, lower the J_c thus wiping out any benefit from high B_{c2}.

The twin objective of fine grains and perfect stoichiometric composition can best be met by the rapid heating, quench and transformation technique (RHQT) developed at NRIM (NIMS) and pioneered by Takeuchi [55, 56]. In this technique, a metastable bcc supersaturated Nb solid solution containing 25 at.% Al, that is, (3Nb.Al)ss is obtained at high temperature and quenched fast to retain its composition. In the next step, this bcc supersaturated solid solution is transformed into A-15 phase through a suitable heat treatment carried out at ~ 800 °C. Here, the transformation only changes the crystal structure (from bcc to A-15) and not the composition, and the twin objective of fine grains and perfect composition is thus met intelligently. After trying liquid quenching technique in the beginning, NIMS finally perfected the so-called RHQT technique [56] for the manufacture of long lengths of Nb_3Al tapes/wires.

The schematic diagram of the system developed at the NIMS to produce long lengths of Nb_3Al conductor is shown in Fig. 5.38. In this technique, the precursor multifilamentary Nb_3Al wire is prepared by the usual JR method. Foils of Nb and Al are laminated together and are spirally wound on a Nb rod and wrapped around by a Nb sheet at the outside. The composite is encased in a Cu can which should be removed after the extrusion and drawing processes are complete. The standard multifilamentary wire, thus, has the Nb matrix only. NIMS and Hitachi cable Ltd. produced 2.6 km wire using a 50 kg billet of the size 140 mm × 450 mm. As shown in Fig. 5.38, the precursor wire is fed from pay-off reel to a Cu wheel (working as an electrode) and then to a pulley dipped in molten Ga and is collected on another spool. A uniform RHQ treatment along the length of the wire is crucial for this scale up system. The wire is Ohmic heated between the copper wheel and Ga bath to a temperature of about 1950 °C where the bcc solid solution extends to 25 at.% Al. The wire is then quenched in the molten Ga bath kept at ~ 50 °C followed by annealing at ~ 800 °C to transform the bcc solid solution to A-15 Nb_3Al phase. The speed of the moving wire was kept 20 m/min. The bcc (3Nb.Al)ss solid solution is ductile at room temperature and therefore enables convenient cabling and winding before the final annealing for phase transformation.

Copper stabilizer is incorporated with the wire after quenching by mechanical cladding. Drawing the wire at room temperature in the bcc phase has been found to increase J_c by a factor of two in the annealed wire. For comparison, the non-Cu J_c of the RHQT wire has been plotted against field together with three Nb_3Sn wires in Fig. 5.39. Evidently, the RHQT Nb_3Al wire stands out to be superior to other wires

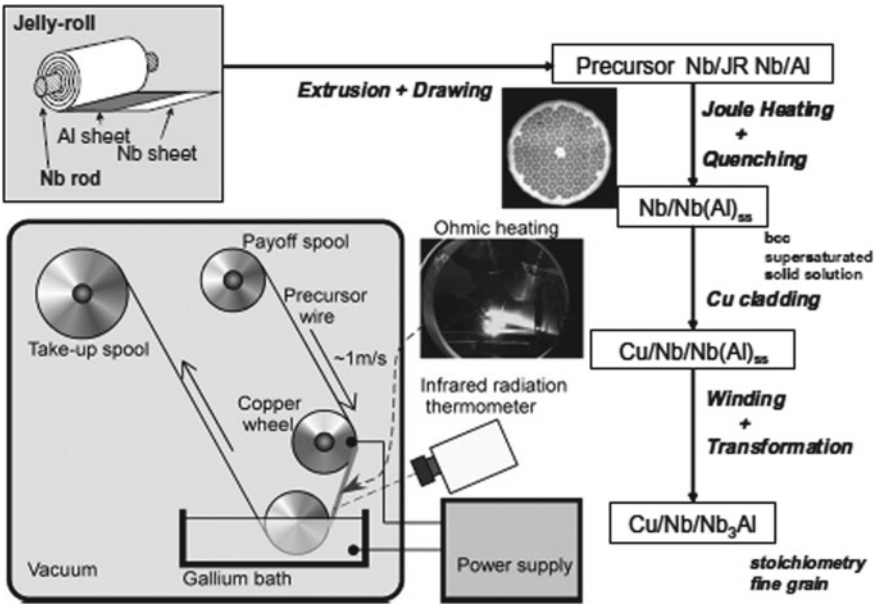

Fig. 5.38 Schematic diagram of the RHQT technique developed at NIMS for the production of long length Nb_3Al conductors. The JR Nb_3Al precursor wire is Ohmic heated to 1950 °C, quenched to 50 °C in Ga bath and annealed at 800 °C [56]. *Courtesy* T. Takeuchi and with permission from Elsevier

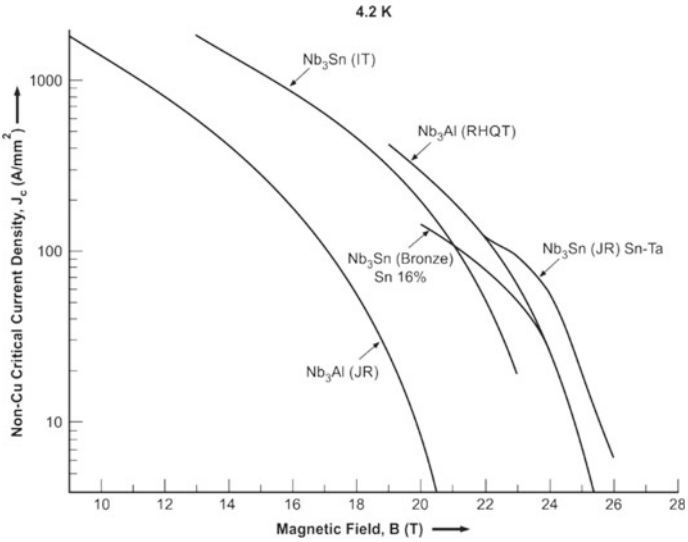

Fig. 5.39 Comparison of non-Cu, J_c of RHQT processed JR Nb_3Al wire with data on Nb_3Sn wires prepared by different techniques. The superiority of RHQT wire is quite noticeable at 20–22 T field [22]. With permission from Alex Braginski (ESNF) and K. Tachikawa

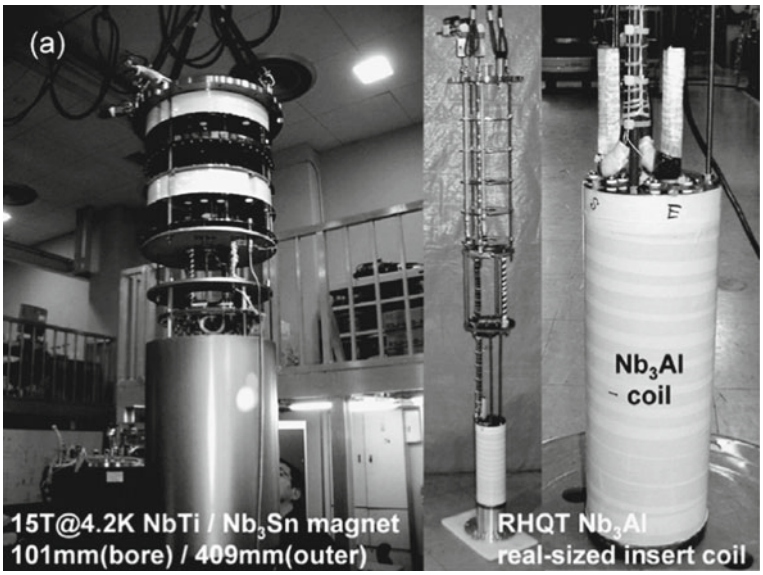

Fig. 5.40 RHQT Nb_3Al insert coil built at NIMS, Japan. The coil produced a field of 19.5 T in a background field of 15 T generated by a Nb-Ti/Nb_3Sn combination magnet [57]. *Courtesy* T. Takeuchi and with permission from Elsevier

in the field range of 20–22 T. The J_c of this wire is surely much higher than the ordinary JR-processed wire by JAERI.

A test insert coil of RHQT Nb_3Al wire has been successfully tested at NIMS (Fig. 5.40) producing a field of 19.5 T at a current of 242.3 A in a background field of 15 T provided by a combination Nb-Ti/Nb_3Sn magnet [56]. The technique is now being used for making Nb_3Al Rutherford cables for next generation high-field particle accelerators magnets [57] because of its high strain tolerance.

5.8 The V_3Ga Tapes and Multifilamentary Wires

Superconductivity in the A-15 inter-metallic V_3Ga superconductor was discovered by Matthias [58] in 1956. In contrast to worldwide development of Nb-Ti and Nb_3Sn superconductors, work on the development of V_3Ga superconductor has been followed religiously in Japan at NRIM only. As discussed earlier in this chapter, V_3Ga has a great potential to carry much larger transport current compared to Nb_3Sn at high magnetic fields. V_3Ga also has better mechanical properties and is less sensitive to strain. It has an added advantage that one needs lower heat treatment temperature for the formation of V_3Ga layer, of the order of 600 °C. The decomposition temperature of V_3Ga is 1300 °C which is much lower than 2100 °C for Nb_3Sn. Thus, for the same grain size, V_3Ga has to be heated at lower temperature. V_3Ga is also an

attractive material for fusion magnets because it has shorter decay time of induced radioactivity, 10 years compared to 2×10^4 years for Nb-based superconductors in a DT fusion environment.

5.8.1 The V-Ga Binary Phase Diagram

The binary phase diagram of V-Ga [59] is shown in Fig. 5.41. V_3Ga has a wide range of composition from 21.3 to 31.5 at.% Ga at 1010 °C, however falls to 21–29 at.% at a lower temperature of 600 °C. This wide range of composition of the A-15 phase makes it an attractive material for application. The highest T_c recorded for the stoichiometric V_3Ga is 15.2 K. T_c decreases as one moves away from the 3:1 stoichiometry. V-Ga system has several other inter-metallic compounds that are Ga-rich. These compounds are V_6Ga_5, V_6Ga_7, V_2Ga_5 and V_8Ga_{41}. However, only compound V_3Ga crystallizes in β-tungsten (Cr_3Si) structure and displays superconductivity. The lattice parameter of V_3Ga is $a = 4.186$ Å. This crystal structure persists up to 20 K below which it undergoes a martensitic transformation quite similar to in several A-15 Nb and V-based superconductors.

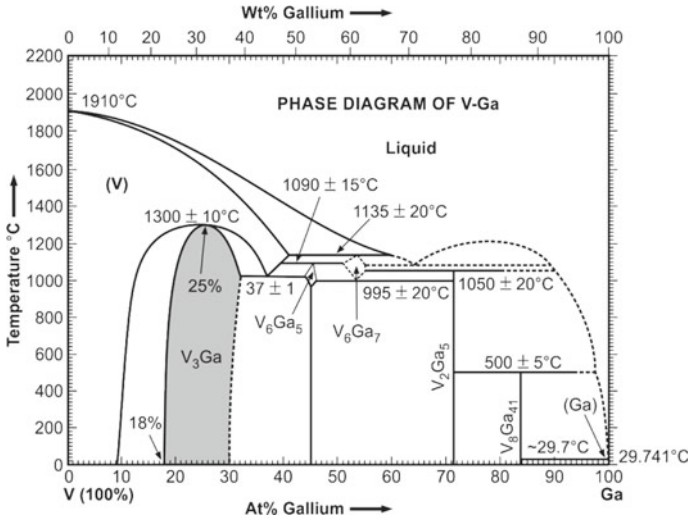

Fig. 5.41 The V-Ga binary phase diagram [59]. With permission from Springer, copyright © 1981, Springer

5.8.2 V_3Ga Diffusion Tapes

The importance of V_3Ga as a high-field practical superconductor was realized by Tachikawa at NRIM as early as 1960s. Tachikawa and Tanaka developed a surface diffusion technique [60] to fabricate long length of flexible V_3Ga tapes. The process consists of two steps. In the first step, a 50-μm-thick V-tape is passed through a molten Ga bath heated at 500–600 °C and then through a tube furnace kept at 800 °C. During this process, about 10-μm-thick layers of V_3Ga_2 and VGa_2 are formed on both sides of the V substrate. In the second step, the tape is electroplated with a 5-μm-thick Cu layer and heat treated at 650 °C. Cu diffuses fast into V_3Ga_2 and VGa_2 to form a ternary Cu-V-Ga alloy of low melting point (700–800 °C) which supplies Ga to form a thick layer of V_3Ga. High J_c in Zr-doped tapes were obtained for tapes heat treated at 650 °C for 100 h. Tapes had approximately 30-μm-thick V sandwiched between 8 and 10 μm V_3Ga layers on either side and outer Cu-Ga layer.

Indeed world's first highest field (17.5 T) was produced [61] in 1976 by a superconducting magnet that used V_3Ga as a central coil prepared by the surface diffusion technique at NRIM. The outer Nb_3Sn coils provided the background field. Figure 5.42 shows the magnet with support system without the cryostat on the left

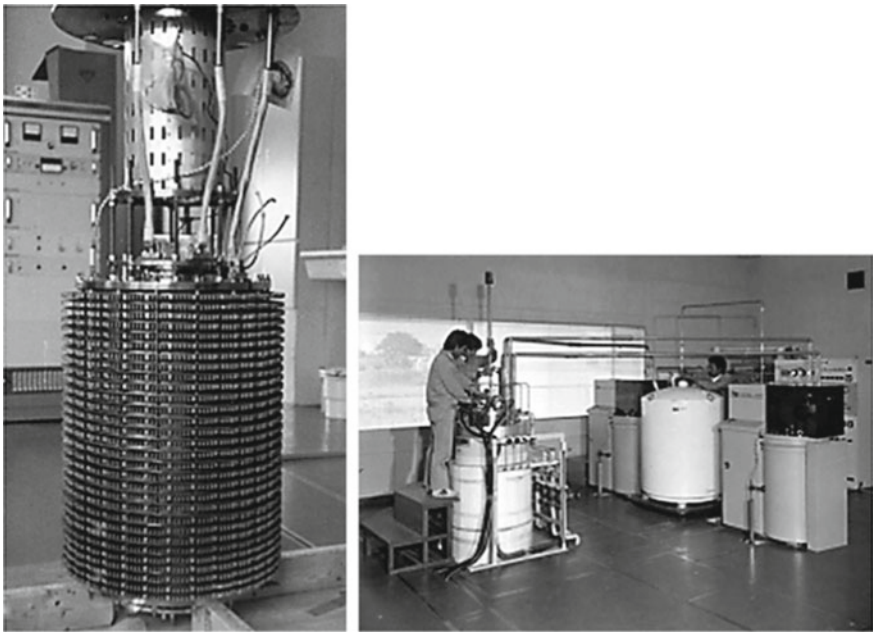

Fig. 5.42 World's first 17.5 T superconducting magnet operated at NRIM, Japan, in 1976. Innermost coil used V_3Ga diffusion tape [61]. Left: the magnet without the LHe cryostat. Right: the magnet under operation cooled by two He liquefiers. *Courtesy* K. Tachikawa and permission from Cryogenics and Superconductivity Society of Japan

and the complete system under operation on the right. The magnet was cooled down with two helium liquefiers perhaps because large liquefiers may not have been available around the time. It had a working bore of 31 mm, outer diameter 400 mm and the height 600 mm.

5.8.3 *Bronze-Processed V_3Ga MF Conductors*

Tachikawa [60] while preparing V_3Ga diffusion tapes found the exemplary role played by Cu in the growth of the V_3Ga layer through its addition to Ga. This finding led Tachikawa to propose the so-called bronze process [24] for the production of MF V_3Ga wires. The technique has already been discussed in Sect. 5.6.1 for the MF Nb_3Sn superconductors. The methodology is the same except the Nb core is now replaced by V core and the Cu-Sn matrix by the Cu-Ga (15–20 at.%) matrix. As discussed earlier, heat treatment temperature for the formation of V_3Ga layer is smaller at 600–650 °C. Significant improvement in J_c of V_3Ga has been achieved by adding elemental impurities to core and/or to the matrix and also by changing the fabrication geometry. Tachikawa et al. [62] reported an improved $J_c = 1 \times 10^5$ A/cm^2 (4.2 K, 20 T) by adding simultaneously 6 at.% Ga to the V core and 0.5 at.% Mg to the Cu-Ga (19 at.%) matrix as shown in Fig. 5.43. The enhancement of J_c is primarily caused by grain refinement of V_3Ga and an accelerated layer growth. In these attempts, efforts have been made to achieve two objectives. First, that, Ga has high solubility in V (~ 8 at.%) at 600 °C. A significant amount of Ga migrates from the matrix and is dissolved into V core before V_3Ga formation starts. This reduces the availability of Ga for V_3Ga layer formation. The pre-addition of 6 at.% of Ga in V core prevents the depletion of Ga in the matrix and consequently results in an accelerated layer growth and a better stoichiometry of the V_3Ga. The second objective is to restrict the grain growth through Mg addition to the matrix, which increases the pinning strength and J_c.

High J_c values of V_3Ga were also reported by Sharma et al. [63, 64] by fabricating monofilamentary and multifilamentary Cu-V_3Ga composite wires and tapes by reversing the geometry of the starting billet and using Ga and Mg additions. Figure 5.44 shows two types of configurations in which the composite billets were prepared. Configuration 1 is the normal one in which the V core is kept inside the Cu-Ga matrix. Configuration 2 is a sort of a reverse geometry. The matrix is now used as core inside a V tube with Cu cladding. Since the matrix has a larger thermal expansion coefficient than V, V_3Ga layer in configuration 2 is formed under compression at the reaction temperature of 600 °C. The layer growth in this new configuration is much faster than in the normal configuration. The addition of 6 at.% Ga in V and 0.5 at.% Mg in Cu-Ga matrix was also used in both the configurations. The typical V_3Ga thickness for a 0.65 mm dia. monocore composite wire heat treated at 600 °C for 212 h is 1.9 μm prepared in configuration 1, 2.2 μm when prepared in configuration 2 and 4.7 μm when prepared in new geometry (configuration 2) and with Ga and Mg additions. The Mg addition leads to fine grains and accelerated V_3Ga growth through

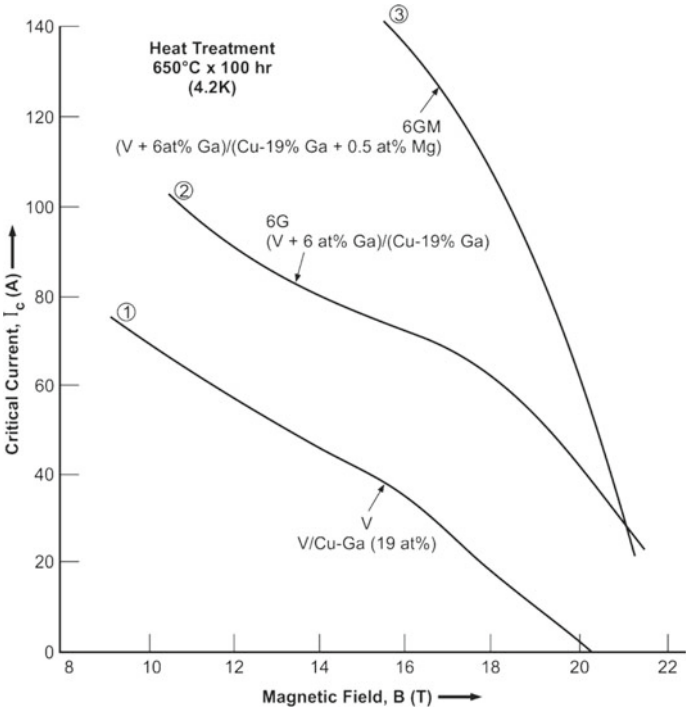

Fig. 5.43 I_c values of the bronze V_3Ga composite tapes plotted against magnetic field. 3G and 6G samples have 3 at.% and 6 at.% Ga, respectively, in the V cores. M represents 0.5 at.% Mg addition to the Cu-Ga (19 at.%) matrix [22, 62]. *Courtesy* K. Tachikawa

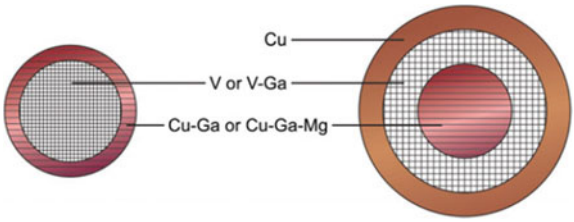

Fig. 5.44 Composite billets prepared in two different configurations. Configuration 1 has V core in Cu-Ga matrix, configuration 2 has matrix inside the V tube and cladded with Cu [63]. With permission of Elsevier

grain boundary diffusion. The critical current I_c versus B plots for these materials with additives and in two different geometries can be seen in Fig. 5.45. At all fields and up to 16 T the I_c is higher for configuration 2 compared to those prepared in conventional configuration 1 and still higher for Ga and Mg additions. The best J_c of V_3Ga turns out to be 7.0×10^5 A/cm^2 (4.2 K, 15 T). The typical V_3Ga layer formed in a sample prepared in configuration 2 and heat treated at 600 °C for 212 h is shown

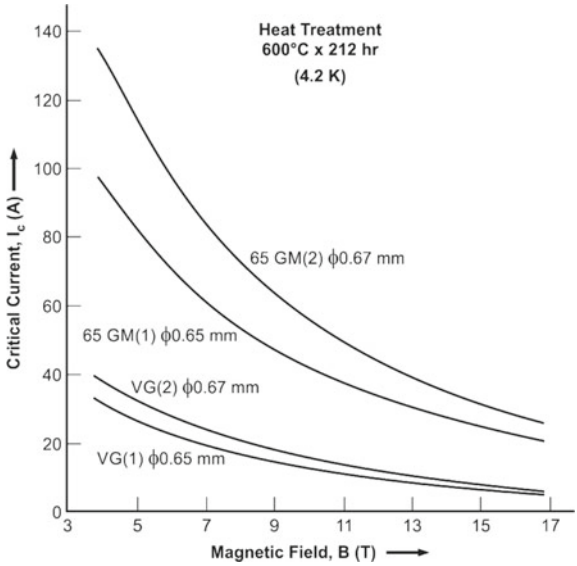

Fig. 5.45 Critical current, I_c of bronze-processed V_3Ga composite wires (heat treated 600 °C × 212 h) plotted against field. Samples (1) are prepared in conventional geometry and (2) in reverse geometry. 65GM samples have 6 at.% Ga in V and 0.5 at.% Mg in Cu-Ga (19 at.%) matrix [63]. With permission of Elsevier

in Fig. 5.46. Note that the Cu-Ga matrix is now inside the V tube as a core and that a very thin layer (~ 2 μm) of V_3Ga is formed. It is this ~ 2-μm-thick V_3Ga layer which carries the entire super current out of the whole cross section of the wire.

We used the results of these studies in fabricating Cu-V_3Ga composite wires with 19 composite cores [64]. Each core was now a V tube filled with the matrix and

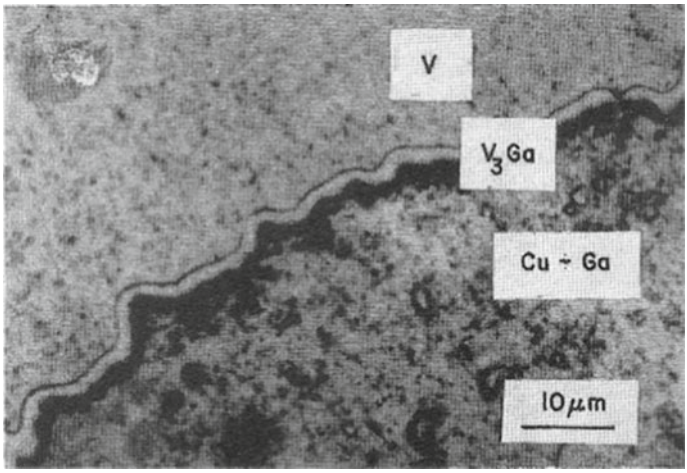

Fig. 5.46 Typical V_3Ga layer formed in a configuration 2 sample heat treated 600 °C for 212 h. Cu-Ga matrix has been used as core inside the V tube. It is this thin V_3Ga layer, which carries entire supercurrent [63]. With permission of Elsevier

finally cladded with a Cu sleeve. The composite was drawn to wires and rolled to tapes. The geometrical cross section of the composite is shown in Fig. 5.47a. Two layers of V_3Ga are now formed on either side of the V tubes as shown in Fig. 5.47b. The inner layer has a much faster growth rate compared to the outer layer per unit matrix volume to surface area ratio and reaches saturation in a shorter time. The overall J_c of this wire with 19 composite cores was significantly higher than the conventional 19 core wires. These studies again confirm the beneficial effect of Ga and Mg addition in increasing the J_c of V_3Ga conductors.

The bronze-processed Cu-V_3Ga composite MF wires/cables were manufactured by Furukawa Electrical Co. [65] on a commercial scale in 1974. Wires were prepared

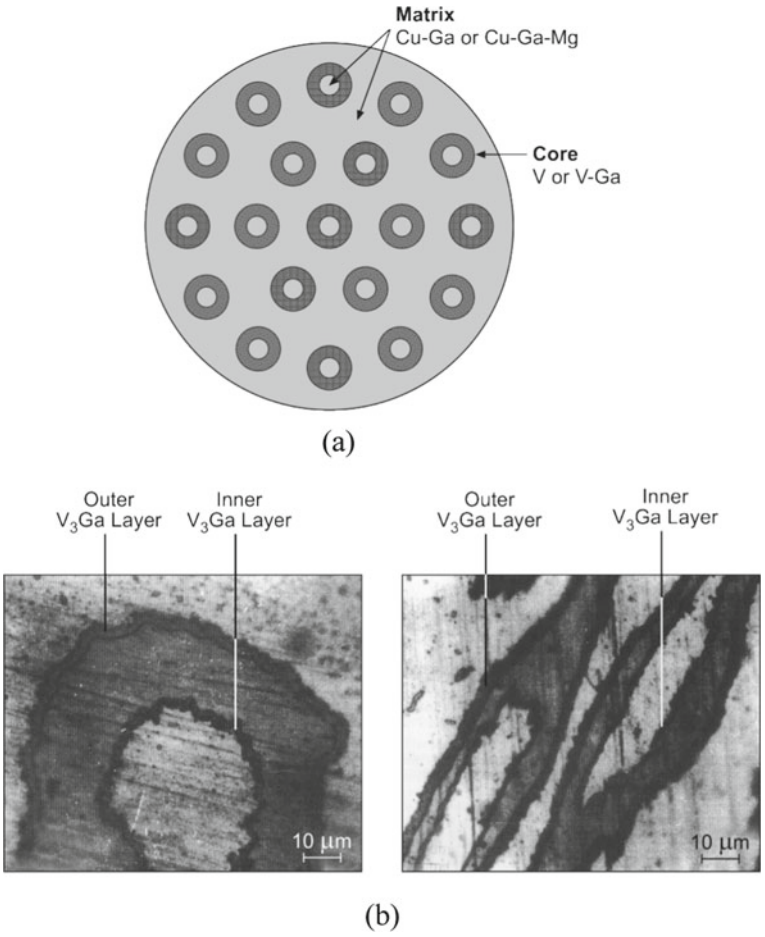

Fig. 5.47 **a** Geometrical cross section of the billet with 19 composite cores. Each core is a V (or V–Ga) tube filled with Cu–Ga (or Cu–Ga–Mg). **b** V_3Ga layers are formed on both the side of the core. The composite billet was drawn to wires and also rolled to tapes [64]. With permission of Elsevier

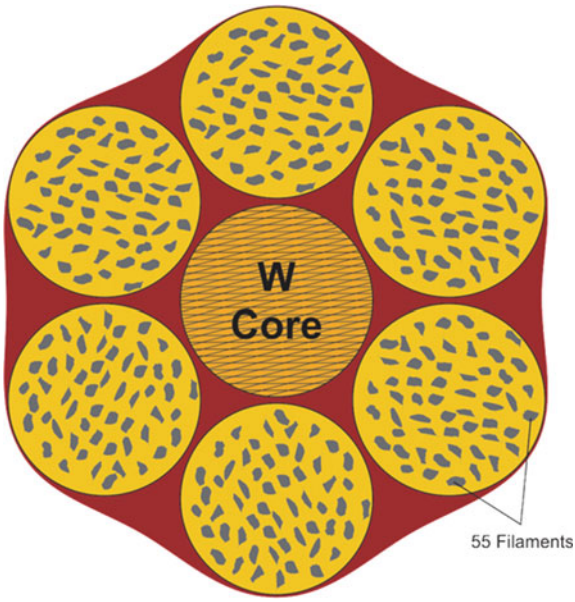

Fig. 5.48 Geometrical scheme of the cross section of six twisted wires Cu-V_3Ga each having 55 filaments manufactured by Furukawa Electric Co. in 1970s by bronze process. In the centre is a tungsten core (for strength), overall $J_c = 3.3 \times 10^4$ A/cm^2 (4.2 K, 15 T) [65]

by bronze process using a matrix of Cu-Ga (19 at.%) and 55 V cores. Some unspecified percentage of Zr too was added to the V cores. The wires were drawn to 0.12 mm dia. size. Six of these wires were twisted with tungsten wire at the centre with a pitch length of 5 mm. The tungsten core provided mechanical strength to the cable. The geometrical cross section of the cable is shown in Fig. 5.48. The cable had a final diameter of 0.37 mm and the filament dia. about 10 μm. A heat treatment of 700 °C × 100 h. resulted in a V_3Ga layer of 2.9 μm thick. The cable was impregnated with In. An overall $J_c = 3.3 \times 10^4$ A/cm^2 (4.2 K, 15 T) and $B_{c2} = 21$ T were obtained. No degradation in J_c was observed down to a bending dia. of 20 mm. A 13 T magnet with 50 mm bore was successfully operated using this MF V_3Ga wire. The bronze technique, thus, works well for V_3Ga composites similar to for Nb_3Sn.

5.8.4 V_3Ga Conductor by PIT Method

As of today, Cu-Nb_3Sn composite wires and cables are universally used for high-field magnet applications; however, interest in the revival of V_3Ga conductor might grow because of the two superior properties of this compound vis-à-vis Nb_3Sn. V_3Ga has intrinsically better mechanical properties and a much shorter decay time of induced radioactivity. The later characteristic property is most relevant at the present time in the context of its application in future advanced fusion reactors. Advanced fusion reactors or power plants will have high magnetic fields to confine and maintain burning deuterium (D)-tritium (T) fusion plasma in steady state. It is estimated that

burning plasma will generate 14 MeV fusion neutrons during DT reaction. These neutrons will stream to penetrate superconducting magnets via the numerous ports provided in the reactor for various inserts. Nb_3Sn magnets are considered safe for ITER as the neutrons penetrating the magnets will be of the order of 10^{11} n m^{-2} s^{-1} (> 0.1 MeV). Since future reactors will require long steady-state operation to produce power, neutron streaming and penetration will increase by orders of magnitude. The magnets will, thus, be operated in harder neutron irradiation environment than the ITER. Studies show that the decay time of induced radioactivity of the nuclide of ^{94}Nb nuclear transformed from ^{93}Nb is over ten thousand years. The estimated half-life is ~ 2×10^4 years. The decay time of all the V superconductors, on the other hand, is of the order of 10 years.

Realizing the merit of V_3Ga superconductor for its excellent property of the short decay time for induced radioactivity, Hishinuma et al. [66] at the National Institute for Fusion Science (NIFS), Japan, have preferred to produce Cu-V_3Ga composite wires by the powder-in-tube (PIT) technique and using high Ga contents. Best superconducting parameters are obtained for 30 at.% Ga samples and heat treated at 700 °C for 50 h. The J_c of the V_3Ga layer is plotted against field B in Fig. 5.49. The best value of $J_c = 4 \times 10^4$ A/cm^2 (4.2 K, 17 T) is obtained for the 700 °C heat-treated sample. Much higher J_c and B_{c2} of V_3Ga can be expected with suitable elemental additions in PIT technique similar to that achieved in the bronze-processed V_3Ga. Hishinuma et al. [67] later reported enhanced J_c and B_{c2} in PIT V_3Ga multifilamentary wires having 12 filaments for high contents of Ga (50 at.%) and by adding small amount (within 1 at.%) of Mg. The high Ga content produced a nearly stoichiometric compound with the B_{c2} value of 23 T.

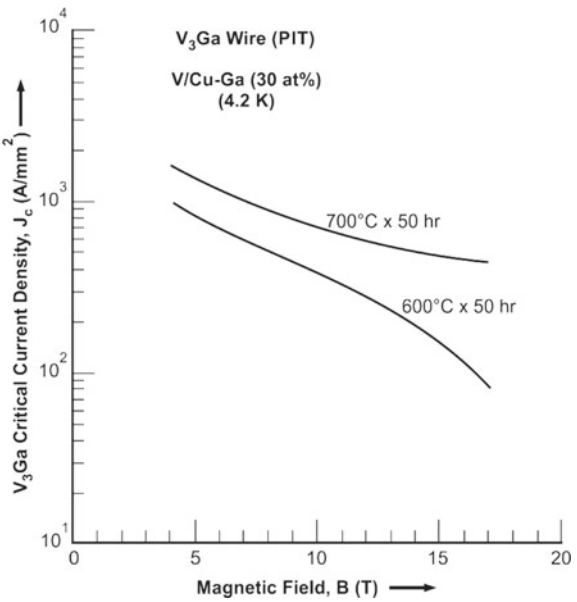

Fig. 5.49 V_3Ga layer J_c versus B for a monofilamentary PIT wire. Best J_c obtained for heat treatment at 700 °C for 50 h and for a matrix Cu-Ga (30 at.%) [66]. © IOP Publishing. Reproduced by permission of IOP Publishing

Our discussion on conventional practical superconductors shows that Nb-Ti and Nb_3Sn will remain the workhorse for a long time for field generation of 8–9 T and 16–18 T, respectively. Nb_3Al too might be the material close to commercial production and could be used for generating field in the range of 19–20 T. Commercial production of V_3Ga seems to be a possibility in near future as the work on future advanced fusion reactors and accelerators progresses. Although ultra-high-current cables of REBCO are being developed with an eye on future accelerators and fusion reactors, yet high cost of REBCO conductor will be a hurdle.

References

1. M.N. Wilson, *Superconducting Magnets* (Clarendon Press, Oxford, 1983)
2. M.N. Wilson, Cryogenics **48**, 381 (2008)
3. P.F. Smith, M.N. Wilson, C.R. Walter, J.D. Lewin, in *Proceedings of the Summer Study on Superconducting Devices* (Brookhaven National Laboratory, 1968), p. 967
4. P.R. Critchlow, E. Gregory, B. Zeitlin, Cryogenics **11**, 3 (1971)
5. E. Gregory, Cryogenics **27**, 290 (1987)
6. E.W. Collings, Adv. Cryog. Eng. **34**, 867 (1988)
7. J.L. Duchateau, B. Turk, D. Ciaznski, in *Chapter B 4.3 Handbook of Applied Superconductivity*, ed. by B. Seeber (Institute of Physics, London, 1998)
8. Masashi Kikuchi, Naoki Ayai, Tomonobu Ishida et al., SEI Rev. **66**, 73 (2008)
9. M.P. Oomen, R. Nanke, M. Leghissa, Supercond. Sci. Technol. **16**, 339 (2003)
10. J.K. Hulm, R.D. Blaugher, Phys. Rev. **123**, 1569 (1961)
11. H.T. Coffey, J.K. Hulm, W.T. Reynolds et al., J. Appl. Phys. **36**, 128 (1965)
12. http://boulder.research.yale.edu/Boulder-2000/lectures/larbalestier/larbalestier3.pdf (PPT)
13. A.V. Narlikar, D. Dew-Hughes, J. Mater. Sci. Eng. **1**, 317 (1966)
14. H. Krauth, Fabrication and applications of NbTi and Nb_3Sn superconductors, in *Niobium, Science & Technology": Proceedings of the International Symposium, Nb 2001*, Orlando, Florida, USA, 2–5 Dec (2001). http://cbmm.com.br/portug/sources/techlib/science_techno/table_content/su b_3/images/pdfs/014.pdf
15. G. Hardy, J.K. Hulm, Phys. Rev. **89**, 884 (1953)
16. B.T. Matthias, T.H. Geballe, S. Geller, E. Corenzwit, Phys. Rev. **95**, 1435 (1954)
17. J. Charlesworth, I. MacPhail, P. Madsen, J. Mater. Sci. **5**, 580 (1970)
18. J.E. Kunzler, E. Buehler, F.S.L. Hsu, J.H. Wernick, Phys. Rev. **6**, 89 (1961)
19. R.G. Sharma, J. Sci. Ind. Res. **42**, 64 (1983)
20. R.G. Sharma, Cryogenics **27**, 361 (1987)
21. K. Tachikawa, Cryogenics **48**, 337 (2008)
22. K. Tachikawa, European Superconductivity News Forum (ESNF), No. 16 Apr 2011, pp. 1–30
23. A.R. Kaufman, J.J. Pickett, Bull. Am. Phys. Soc. **15**, 883 (1970)
24. K. Tachikawa, in *Proceedings of the International Cryogenic Engineering Conference (ICEC-3)*, Iliffle Science and Technical Publications, Surrey, UK (1970), p. 339
25. E. Nembach, K. Tachikawa, J. Less Common Met. **19**, 359 (1969)
26. M. Hong, I.W. Wu, J.W. Morris Jr. et al., Adv. Cryog. Eng. **28**, 435 (1982)
27. T. Miyazaki, H. Kato, T. Hase et al., IEEE Trans. Appl. Supercond. **14**, 975 (2004)
28. H. Sakine, Y. Iijima, K. Tachikawa, J. Appl. Phys. **53**, 5354 (1982)
29. K. Kamata, H. Moriai, N. Tada et al., IEEE Trans. Magn. **21**, 277 (1985)
30. T. Kiyoshi, S. Matsumoto, A. Sato, IEEE Trans. Appl. Supercond. **15**, 1330 (2005)
31. K. Okuno, H. Nakajima, N. Koizumi, IEEE Trans. Appl. Supercond. **16**, 880 (2006)

32. K. Tachikawa, K. Miyashita, K. Sugiyama et al., 2T-class 50 Hz AC magnet of 50 mm bore made by bronze-processed submicronic filament new Nb_3Sn cables, in *Proceedings of the ICEC 17*, ed. by D. Dew-Hughes, R.G. Scurlock, J.H.P. Watson (IOP, Bristol, 1998), pp. 439–442
33. Y. Hashimoto, K. Yoshijaki, M. Tanetia, in *Proceedings of the Fifth International Cryogenic Engineering Conference* (IPC Science and Technology Press, Guildford, UK, 1974), p. 332
34. B.A. Zeitlin, G.M. Ozeryansky, K. Hemachalam, IEEE Trans. Magn. **MAG-21**, 293 (1985)
35. K. Egawa, Y. Kubo, T. Nagai, T. Sone et al., Adv. Cryog. Eng. (Mater.) **50B**, 403 (2004)
36. Y. Kubo, K. Egawa, T. Nagai, T. Sone et al., IEEE Trans. Appl. Supercond. **16**, 1232 (2006)
37. W.K. McDonald, C.W. Curtis, R.M. Scalan et al., IEEE Trans. Magn. **MAG-19**, 1124 (1983)
38. K. Tachikawa, T. Ando, H. Sasaki et al., IEEE Trans. Appl. Supercond. **21**, 2533 (2011)
39. J.A. Parrell, Y.Z. Zhang, M.B. Field, P. Cisek, S. Hong, IEEE Trans. Appl. Supercond. **13**, 3470–3473 (2003)
40. J.D. Elen, C.A.M. van Beijnen, C.A.M. van der Klein, IEEE Trans. Magn. **13**, 470–473 (1977)
41. A. Godeke, A. den Oudenb, A. Nijhuisb, H.H.J. ten Kateb, Cyogenics **48**, 308 (2008)
42. J.L.H. Lindenhovius, E.M. Hornsveld, A. den-Ouden, W.A.J. Wessel, H.H.J. ten-Kate, IEEE Trans. Appl. Supercond. **10**, 975 (2000)
43. L.D. Cooley, A.K. Ghosh, D.R. Dietderich, I. Pong, IEEE Trans. Appl. Supercond. **27**, 6000505 (2017)
44. Xu Xingchen, Supercond. Sci. Technol. **30**, (2017)
45. C.C. Tsuei, Science **180**, 57 (1973); IEEE Trans. Magn. **MAG-11**, 272 (1975)
46. R.G. Sharma, N.E. Alekseevskii, J. Phys. **D8**, 1783 (1975)
47. R.G. Sharma, Y.S. Reddy, M.M. Krishna, Indigenous development of A-15 superconductors through in situ technique, in *Workshop on Superconducting Magnets and Cryogenics, ICFA*, Brookhaven National Laboratory, Upton, New York, USA, 12–16 May 1986, pp. 127–131
48. J.P. Harbison, J. Bevk, J. Appl. Phys. **48**, 5180 (1977)
49. J.D. Verhoeven, D.K. Finnemore, E.D. Gibson et al., Appl. Phys. Lett. **33**, 101 (1978)
50. J.L. Fihey, M. Neff, R. Roberge, M.C. Flemings et al., Appl. Phys. Lett. **35**, 715 (1979)
51. J.D. Verhoeven, F.A. Schmidt, E.D. Gibson et al., Appl. Phys. Lett. **35**, 555 (1979)
52. D.A. Cardwell, D.S. Ginley (eds.), *Handbook of Superconducting Materials*, vol. 1 (2003). ISBN 07503 04324. Fig. 3.3.4.1(a), p. 674. Contribution B 3.3.4 "Processing of low Tc conductors: the composite Nb_3Al", Author Takao Takeuchi
53. Y. Yamada, N. Ayai, A. Mikumo et al., Cryogenics **39**, 115 (1999)
54. N. Koizumi, Y. Takahashi, Y. Ninoya et al., Cryogenics **42**, 675 (2002)
55. T. Takeuchi, Topical review 'Nb_3Al conductors for high-field applications'. Supercond. Sci. Technol. **13**, R101 (2000)
56. T. Takeuchi, A. Kikuchi, N. Banno et al., Cryogenics **48**, 371 (2008)
57. K. Tsuchiya, A. Kikuchi, T. Takeuchi et al., IEEE Trans. Appl. Supercond. **21**, 2521 (2011)
58. B.T. Matthias, E.A. Wood, E. Cobbnzwit, J. Bala, J. Phys. Chem. Solids **1**, 188 (1956)
59. The Ga-V (Gallium-Vanadium) system. Bull. Alloy Phase Diagr. **2**, 201 (1981)
60. K. Tachikawa, Y. Tanaka, Jpn. J. Appl. Phys. **5**, 834 (1966)
61. K. Tachikawa, in *European Superconductivity News Forum IESNF*, 16 Apr 2011, pp. 1–30
62. K. Tachikawa, Y. Tanaka, Y. Yoshida et al., IEEE Trans. Magn. **Mag-15**, 391 (1979)
63. R.G. Sharma, Y. Tanaka, K. Tachikawa, Cryogenics **21**, 165 (1981)
64. R.G. Sharma, Y. Tanaka, K. Tachikawa, Cryogenics **25**, 381 (1985)
65. Y. Furuto, T. Suzuki, K. Tachikawa, Y. Iwasa, Appl. Phys. Lett. **24**, 34 (1974)
66. Y. Hishinuma, A. Kikuchi, Y. Iijima et al., Supercond. Sci. Technol. **20**, 569 (2007)
67. Y. Hishinuma, A. Kikuchi, Y. Iijima, T. Takeuchi et al., IEEE Trans. Appl. Supercond. **19**, 2670 (2009)

Chapter 6
Practical Cuprate Superconductors

Abstract Sustained research at R&D centres in several countries yielded huge success in the production of three most popular cuprates, namely REBCO, Bi-2223 and Bi-2212. The best superconductor the so-called 2G REBCO-'coated conductor' is produced by depositing highly oriented thin film of (GdY)BCO on biaxially textured Hastelloy substrates buffered with a number of oxide layers. The tape conductor is suitably laminated with Ag-alloy and then a high conducting hardened copper for stability and increased mechanical strength. Critical current density, $J_c = 20$ MA/cm^2 (30 K, 3 T), has been achieved in (GdY)BCO tape (0.1 mm thick) deposited on a 30 μm Hastelloy substrate and doped with 25 mol% Zr. The BZO nanocolumns introduced act as pining centres and enhance the J_c to high value. Engineering current density, $J_e = 586$ A/mm^2 (4.2 K, 20 T), has been obtained in round wires of (GdY)BCO, fabricated by winding number of narrow tapes over a central Cu former under condition of 15 mm radius bending. Cables capable of carrying currents as high as 90–100 kA have been designed for future fusion machine EU-DEMO and future accelerator detector magnets. Another promising cuprate, Bi-2212 conductor is produced in the form of round wire by the PIT method using pure Ag matrix. The round Bi-2212 wire generates a dominant a-axis growth texture and aligns the c-axis of its polycrystals along the filament axis making Bi-2212 to display a macroscopic isotropic behaviour. In a landmark development, it was found that J_c in Bi-2212 is limited by the presence of bubbles in the filaments formed by the agglomeration of porosity in the PIT wires during the heat treatment. These bubbles hindered the current flow. The bubble problem was overcome by employing an over-pressure heat treatment which densifies the core material to nearly 100% and allowed Bi-2212 to regrow inside the bubbles. NHMFL developed PIT Bi-2212 flexible round wires under 100 bar over-pressure which carried a $J_e = 900$ A/mm^2 (4.2 K, 5 T). The wire was used for winding a small insert magnet which produced a magnetic field of 2.6 T in a background field of 31 T, thus generating a record field of 33.6 T. Bi-2223 is a tape conductor with anisotropic properties, yet it has sufficiently high J_c in the ⊥ field direction. Grain texture and high density in Bi-2223 are achieved by rolling and sintering the tapes under pressure. The tapes are produced through the standard PIT technique involving multiple drawing and rolling followed by sintering under pressure. For high strength, Bi-2223 tapes are laminated with either SS, Cu-alloy or Ni-alloy. Sumitomo, the only manufacturer of Bi-2223 tape wires, produces a variety

R. G. Sharma, *Superconductivity*, Springer Series in Materials Science 214,
https://doi.org/10.1007/978-3-030-75672-7_6

of Bi-2223 wires suitable for different types of applications. The maximum critical tensile stress is 400 MPa for the HT-NX wires. HT-G wire has Ag-Au matrix and used for current leads because of its very low thermal conductivity. HT-AC wires have very low AC losses. Bi-2223 wires find application in power transmission and other devices.

6.1 Introduction

High-temperature superconductors (HTSs) continue to be most attractive superconductors for applications because of their high critical temperature, T_c, and high upper critical field, B_{c2}. HTSs however suffered from the problem of poor inter-grain connectivity and large anisotropy in B_{c2} and J_c. As a result, the critical current in these materials drops sharply with the application of magnetic field. This prevented their quick acceptance as high-field/high-current superconductors for the production of high magnetic field. For the same reason the hope of replacing conventional superconductors like Nb-Ti and Nb_3Sn with HTSs was not realized for decades. The grain boundary problem has however been circumvented to a great extent by using innovative fabrication techniques which though are complex. The confidence in producing high-current superconductors has grown rapidly, and a record magnetic field of 45.5 T has been achieved at NHMFL USA in 2019. Not limited to this, the design of the high-current REBCO-coated conductor strands and cables for use in futuristic high-luminosity LHC dipoles and in toroidal magnets for DEMO fusion reactor is going on at fast pace. Out of a large number of known cuprates, only three have been identified and pursued to the level of commercial production. These are $REB_2Cu_3O_x$ (REBCO), $Bi_2Sr_2Ca_2Cu_3O_x$ (Bi-2223) and $Bi_2Sr_2CaCu_2O_x$ (Bi-2212). As discussed in Chap. 3, these materials have layered structure formed during a high-temperature reaction. Besides having large anisotropy in critical current and critical field, the superconducting properties of these compounds are extremely sensitive to the oxygen stoichiometry which needs precise control. Further, the conventional copper cannot be used as matrix for fabricating HTS wires or tapes because of their strong reactivity. Only silver or silver alloy can be used which makes the conductors rather expensive. In the following sections, we discuss these materials how the fabrication techniques evolved over last more than three decades and used for commercial production.

6.2 2G REBCO Tape Wires (Coated Conductors)

The granular nature of REBCO superconductor was one important reason that J_c in bulk material was disappointingly low and dipping sharply in magnetic field. The grain boundaries in curates have been found weakly superconducting or even insulating. High critical current densities have however been reported by Chaudhuri et al. [1] in epitaxially grown YBCO films and by Dinger et al. [2] in YBCO single crystals.

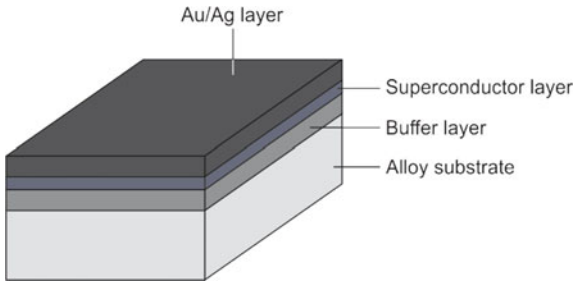

Fig. 6.1 General scheme of deposition of multilayered structure used for producing second-generation 2G REBCO wires

The critical current within the grain has been found to be quite high ~ 10^6 A cm^{-2} at 77 K. After a few years of intensive research, the focus of R&D activity shifted from research institutes to superconductor industries culminating in their commercial production. The straight forward method to fabricate flexible wires and tapes with powder materials is the usual powder-in-tube technique or the so-called PIT technique. Thermal stability criterion requires superconductor to be co-processed with high conductivity material like copper, but HTS cuprates have been found reacting with copper during heat treatment. Soon after the discovery of superconductivity in $Y_1Ba_2Cu_3O_x$, the author, through a systematic study on a number of materials, had found only silver to be a safe cladding material [3] for YBCO wires and tapes. Silver addition as much as 60 at % was found neither affecting the crystal structure of YBCO nor the T_c. Ag tubes have therefore been used to fabricate YBCO wires and tapes. Since silver is too soft a material, Ag-alloys have been specially developed to process wires to have higher mechanical strength. Weak superconductivity in grain boundaries proved to be the stumbling block in achieving reasonably high transport J_c in cuprates. The strategy adopted to make wires with high J_c therefore shifted to deposition of highly oriented thin film of YBCO on biaxially textured substrates with grain misalignment < 5° and suitably laminating with Ag-alloy. This in turn is then laminated with a high conducting hardened copper for stability and mechanical strength. The general scheme of various layers deposited is shown in Fig. 6.1. Sophisticated techniques such as ion beam-assisted deposition (IBAD), rolling-assisted biaxially textured substrate (RABiTS) and inclined substrate deposition (ISD) have been employed by various R&D laboratories. American Superconductors (AMSC) markets this product under the brand name Amperium wire having a single coat of 1.2-μm-thick YBCO film. This 2G HTS wire has a critical current (I_c) of 500 A/cm w (77 K, self-field). The two techniques used for the production of the 2G superconductor, IBAD and RABiTS, were developed under DAE (USA) programme at Los Alamos National Laboratory (LANL) and the Oak Ridge National Laboratory (ORNL), respectively. The LANL perfected IBAD process. It involves pulse laser deposition of the preferentially oriented buffer layer on the top of commercial Hastelloy tape. Four ion beams are used to grow yttria-stabilized zirconia (YSZ) crystals with one orientation on top of the ceramic oxide buffered Hastelloy. Excellent lattice match between YBCO and YSZ leads to highly oriented YBCO film. The ORNL followed RABiTS which involves the fabrication of long lengths of biaxially

textured Ni tapes. Suitable oxide buffer layers are then grown to transfer the orientation to the YBCO layer. In both the processes, YBCO is deposited using pulse laser deposition (PLD). Even at 64 K, 2G tapes have J_c better than traditional Nb-Ti and Nb_3Sn conductors which need liquid helium for operation. The temperature (64 K) is conveniently provided by pumped liquid nitrogen or by cryocoolers. It is far superior to the first-generation BSCCO-2223 tapes (to be discussed in this chapter). Even along the c-direction, J_c in 2G tapes at 64 K and 8 T field is much higher than the J_c value for the BSCCO-2223 at 77 K and self-field.

Figure 6.2 shows the architecture of the 2G HTS tape manufactured by SuperPower. To begin with, a Hastelloy C-276 substrate 12 mm wide is electroplated to have a clean and smooth surface for the deposition of the buffer and superconducting layers. Preferentially oriented buffer layers are then grown on the substrate by IBAD/magnetron sputtering over which (RE)BCO film of 1 μm thickness is deposited by metal organic chemical vapour deposition (MOCVD) technique. A 2 μm silver layer is deposited next by sputtering. The composite tape is finally laminated on both sides with 20-μm-thick layers of hardened high conducting copper which provides strength and stability. The Hastelloy C-276 substrate provides high mechanical strength to the tape. The stress limit rises to 700 MPa and the yield stress to 970 MPa (77 K) @ 0.92% strain. High I_c value of 310 A/cm width (77 K) for a 1.1-μm-thick HTS film has been obtained by doping with Zr and by introducing nanodefects. These defects create efficient pining sites and increase J_c. A world record of magnetic field of 27.4 T was established in 2009 at NHMFL (Florida State Uni.) using this 2G HTS central coil in a background field of 19.9 T. Later, in 2012, NHMFL has generated a field of 32 T (@4.2 K) using 2G REBCO tape in a background field of 20 T provided by the resistive magnet. More recently, NHFML produced a record field of 45.5 T using the innermost coil of REBCO-coated conductor.

The lift factor defined as I_c(T, B) / I_c (77 K, sf), the ratio of the critical current I_c at a temperature and field to the value at 77 K and self-field of the SuperPower 2G wires

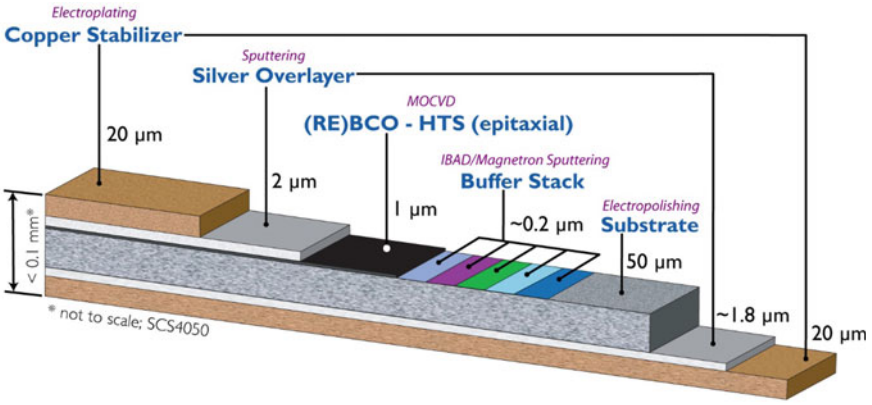

Fig. 6.2 Architecture of the 2G HTS (REBCO) tape conductor, manufactured by SuperPower. Copyright SuperPower Inc. 2014, image provided courtesy of SuperPower

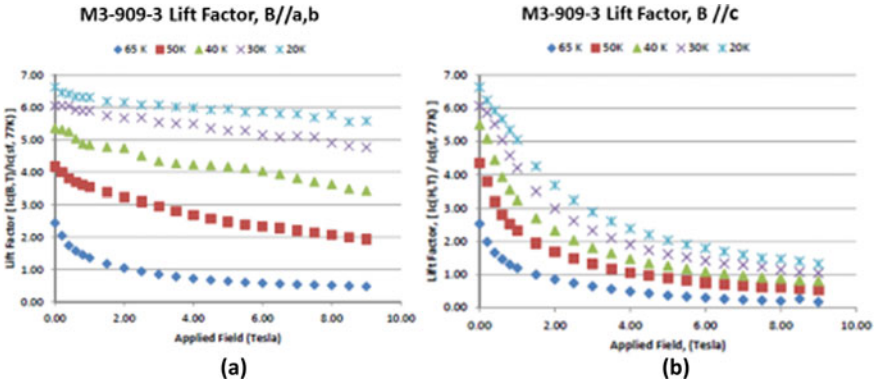

Fig. 6.3 Dependence of the lift factor, I_c(T, B)/I_c(77 K, sf) on magnetic field in SuperPower 2G HTS-coated conductor SP wire ID M3-909–3 at 65 K, 50 K, 40 K and 20 K (data 2014). **a** Field parallel to *a–b* plane and **b** field parallel to *c*-axis. Copyright SuperPower Inc. 2014, images provided courtesy Yifei Zhang

are plotted in Fig. 6.3 in two orientations. The current, I_c, in B//ab plane orientation shows very little drop with magnetic field compared to the B//c-axis orientation up to 9 T. The lift factor goes up by a factor of more than 6 as the temperature is lowered from 77 K to 4.2 K. In B//ab plane, I_c goes up to still higher values.

Figure 6.3 shows dependence of the lift factor, I_c(T, B)/I_c(77 K, Sf) on magnetic field in SuperPower 2G HTS-coated conductor SP wire ID M3-909-3 at 65 K, 50 K, 40 K and 20 K in field parallel to *a–b* plane and field parallel to *c*-axis. This wire is an advanced pinning (AP) type. $BaZrO_3$ (BZO) nanocolumns were introduced into the REBCO layer and engineered along the c-axis to enhance the in-field performance. At low fields, the enhancement of I_c at reduced temperature is very significant. At 4.2 K, the wire carried a current of 500 A/cm width in a field of 17 T//*c*-axis in 2014. By 2020, the critical current was improved to as much as 813 A/cm width an impressive increase of about 60%. In B//*a–b* orientation, I_c will further go up by a factor of 5–6. Such high values of I_c established the efficacy of the material as a high-field conductor. The engineering current density J_e of these wires measured at NHMFL up to 30 T field is ~ 3000 A/mm^2 at 4.2 K in B//*a–b* orientation. This value is far above the values for the best Nb_3Sn conductor. The I_c-B behaviour of SuperPower 2G HTS tapes in B//c orientation at temperatures ranging between 77 and 4.2 K in the year 2014 and the year 2020 is shown in Fig. 6.4a, b, respectively. It is noticed from the set of these two figures that the improvement in I_c-B behaviour of the SuperPower over last five years had been very impressive. Intense work is going on in the development of high-current cables for future accelerators and fusion reactors. Detailed description of the SuperPower 2G-coated conductors can be found in [4].

High values of J_c in 2G HTS manufactured by SuperPower [5] are attributed to the introduction of nanoscale flux pining centres through RE-substitution (replacing *Y* partially by other RE) and with elemental addition to the precursor. The thickness of

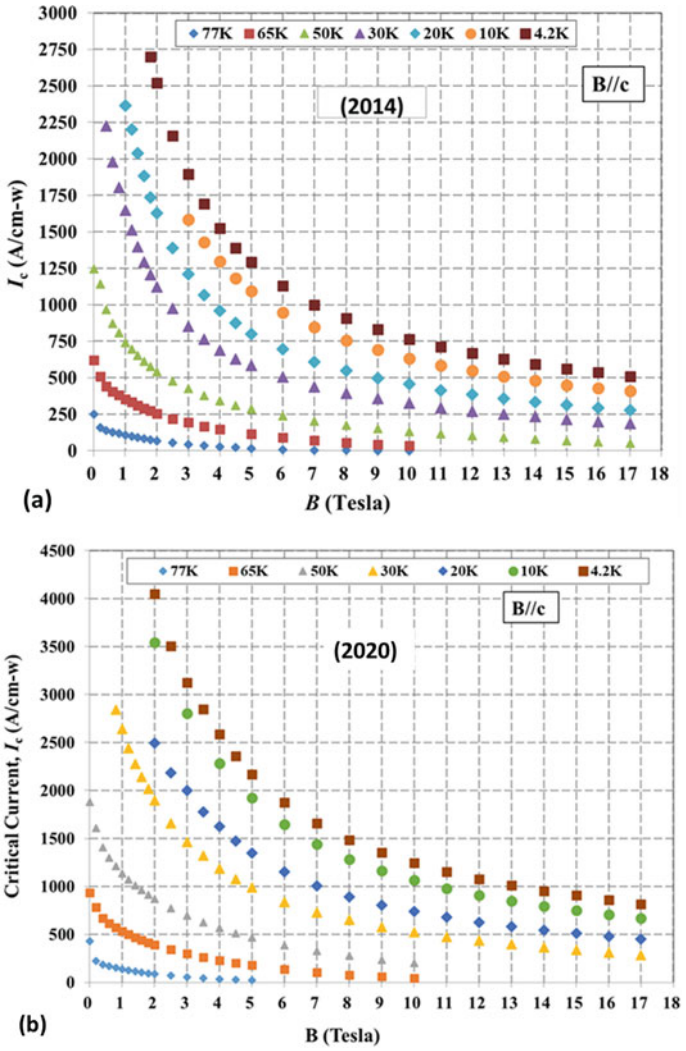

Fig. 6.4 **a** I_c-B behaviour of SuperPower 2G HTS tapes in B//c orientation. Notice $I_c = 500$ A/cm width (4.2 K, 17 T) in 2014, **b** in 2020, the I_c has improved to 813 A/cm width in B//c orientation. These I_c values will go up further by a factor of 5–6 in B//*a*–*b* plane. Copyright SuperPower Inc. 2014, 2020, images provided courtesy of Yifei Zhang, SuperPower

the finished tape is only 0.095 mm which increases engineering current density significantly. The resistive substrate, Hastelloy, provides high strength to the conductor, reduces AC losses, minimizes eddy current losses and also reduces ferromagnetic losses. The critical stress for I_c degradation too is high at 700 MPa depending upon the copper fraction. The wide tape can be spliced into narrow 2-mm-wide tapes which have been successfully used for fabricating high-current cables by winding the tape

around a central core in multi-layer configuration, the so-called conductor on round core (CORC). Coated 2G conductors are increasingly used for building high-field magnets and for power applications.

6.2.1 Enhancement of J_c Through Heavy Doping

Great advancement has been made in enhancing critical current density of REBCO-coated conductors through heavy doping by Selvamanickam et al. [6–8]. Critical current density, J_c, as high as 20×10^6 A/cm^2 (30 K, 3 T) has been reported [6] in (GdY) $Ba_2Cu_3O_x$ films doped with as much as 25 mol % Zr. Pinning force as high as 1000 GN/m^3 (20 K, 5–7 T) has been obtained in these tapes. High J_c in the doped films is caused by an effective flux pinning by highly *c*-axis aligned barium zirconate ($BaZrO_3$ or BZO) nanocolumns defects with a defect density of 7×10^{11}/cm^2, and the particles rich in Cu and Zr of 2–3 nm size observed in the microstructure. The sample had high lift factor in I_c at 30 K. It thus turns out that tapes having J_c below 4×10^6 A/cm^2 (77 K, sf) should have high (Ba + Zr)/Cu composition ratio between 0.7 and 0.8 and well-aligned BZO nanocolumns in order to have a high lift factor ($\sim$ 6) at 30 K, 2.5 T.

The I_c of the 12-mm-wide tape at 30 K and at 3 T field turns out to be 2195 A which corresponds to an engineering current, $J_e = 1829$ A/mm^2, taking the thickness of the tape as 0.1 mm and that of copper stabilizer as 40 μm. The composition of the film measured by inductively coupled plasma spectroscopy shows the ratio Ba: Zr: Cu to be 0.394: 0.032: 0.574 an ideal composition to achieve a lift factor $\frac{J_c(30\ K,3\ T)}{J_{c(77\ K,0\ T)}}$ of $\geq$ 6(30 K, 3 T). A lift factor of > 6 has indeed been obtained in these tapes.

Selvamanickam's group deposited epitaxial films of GdYBCO with Zr addition on $LaMnO_3$-terminated biaxially textured buffer layers of MgO deposited by ion beam-assisted deposition (IBAD) on a 50-μm-thick and 12-mm-wide Hastelloy C276 substrate. MOCVD using a liquid precursor delivery system was followed for growing the films. Standard tetramethyl heptanedionate (thd) precursors were used for all components. Precursor flow rate controlled the deposition rate of the film to 0.1 μm/min. Films 0.9 μm and 1.1 μm thick were grown for several studies. 2.2-μm-thick films were also deposited in two passes 1.1 μm thick in each pass. Film thickness is controlled by the speed of the substrate movement. Figure 6.5 shows the dependence of critical current of a 2.2-μm-thick GdYBCO tape with 20 mol% Zr along with the best 0.9-μm-thick films with 7.5%, 15% and 25% Zr addition at 30 K and in field parallel to c-axis [7]. A high value of critical current, $I_c = 2797$ A (30 K, 5 T), for the 12-mm-wide and 2.2-μm-thick 20 mol % Zr-added film has been achieved. The lift factor of 5.1 found in critical current at 30 K, 3 T is about 2.4 times the lift factor of the commercial 7.5 mol % Zr-added tapes.

Detailed critical current measurements bring out the fact that the values of critical current, I_c, and critical current density, J_c, of 2.2 μm GdYBCO tape with the addition of 20 mol % Zr are quite high up to the measured fields of 9 T applied along the

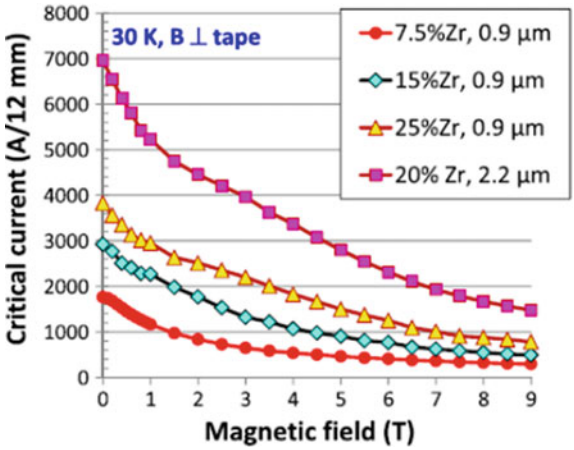

Fig. 6.5 Dependence of critical current, I_c, of a 2.2-μm-thick GdYBCO tape with 20 mol% Zr along with the best 0.9-μm-thick films with 7.5, 15% and 25 mol% Zr addition at 30 K and field ⊥ tape [7]. Courtesy V. Selvamanickam and permission from IOP

c-axis and in the temperature range of 30–77 K as shown in Fig. 6.5. The typical engineering current, J_e, at 40 K and in 3 T field comes out to be 236 A/mm^2 taking the typical thickness of the copper stabilizer as 40 μm. This value happens to be 3.8 times higher than the J_e value of the best commercial HTS tapes. Table 6.1 gives the values of I_c and J_c measured in a magnetic field of 3 T and at different temperatures, namely 40 K, 50 K, 65 K and 77 K. Figure 6.6 shows the plots of critical current (I_c) and critical current density (J_c) of a 2.2-μm-thick GdYBCO + 20 mol% Zr against magnetic fields up to 9 T applied along the *c*-axis at different temperatures between 30 and 77 K.

The target critical current for the group was to achieve 3000 A/12 mm width at 30 K and 2.5 T required for a 10 MW wind generator. The measured value of I_c was found to be 4206 A/12 mm width (30 K, 2.5 T) thus far exceeding the target value. In fact, this value of I_c was more than 5 times the best I_c available in commercial-coated conductors at the time.

Table 6.1 Critical current (I_c) and critical current density (J_c) of a 2.2-μm-thick GdYBCO + 20 mol% Zr tape in a magnetic field of 3 T (B//c) at different temperatures (40–77 K)

Parameter	Unit	Temperature			
		40 K	50 K	65 K	77 K
Critical current/12 mm, width, I_c @ 3 T	A	2833	1881	805	184
Critical current density, J_c @ 3 T	MA/cm^2	10.1	7.1	3.1	0.7

Data compiled from [7]

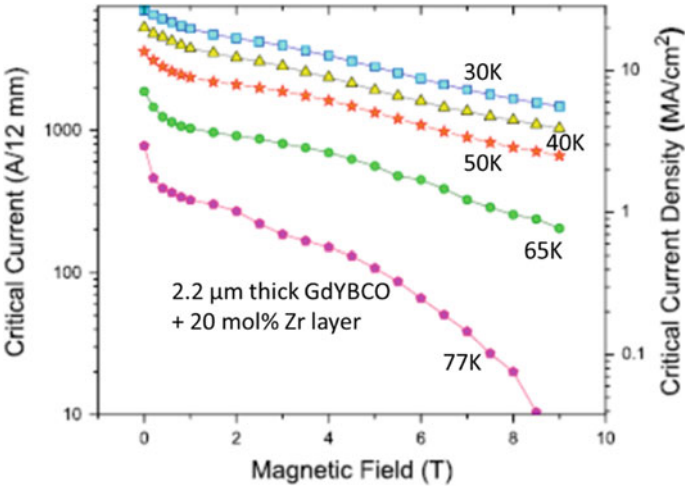

Fig. 6.6 Dependence of critical current (I_c) and critical current density (J_c) of a 2.2-μm-thick (GdYBCO + 20 mol% Zr) tape on magnetic fields up to 9 T. Field is applied along the *c*-axis at different temperatures between 30 and 77 K [7]. Courtesy V. Selvamanickam and permission of IOP

6.2.2 Development of Flexible Fine Round REBCO Wires with High Mechanical Strength

Ultra-high field REBCO tapes have not so far been fully exploited for building magnets generating field, far above 20 T. This is because of its geometry with large aspect ratio and high axial strain close to the irreversible strain (ε_{irr}) experienced under large Lorentz force. Selvamanickam and co-workers developed round wires [9] with 1.6 mm diameter by winding helically a single layer 2-mm-wide REBCO tape around a 0.81 mm copper former. High critical current has been obtained in these wires by using the best tape and optimizing twist pitch under combined torsion and compressive strains. Use of small diameter of the Cu former and small thickness of the REBCO tape make these wires extremely flexible which is essential for winding magnet coils. Flexibility of the wire also helps in reducing strain experienced by the REBCO layer due to the shift of neutral axis close to REBCO layer. The architecture of the composite REBCO tape chosen is one which uses a thinner substrate and thinner Cu stabilizer on one side only. These wires were characterized for critical current vis-à-vis effect of bending over a wide range under torsion as also under compressive strain. The authors [9] have studied several architectures of REBCO tapes with different thicknesses of the substrate and the Cu stabilizer. The architecture was so optimized that tapes were produced with maximum flexibility and with sufficiently high I_c which is not affected by bending the tapes over small diameter.

Three architectures of the REBCO tape, namely S2, S3 and S4 were chosen. The substrate thickness in all the three tapes was kept 22 μm instead of standard 50 μm and the thickness of the Cu stabilizer as 20 μm, 10 μm and 30 μm, respectively. All

Table 6.2 Architectural parameters of three REBCO-coated conductors (S2, S3 and S4) with different thicknesses of Cu stabilizer

Parameter	Unit	REBCO-coated conductor		
		*S*2	*S*3	*S*4
Silver back layer	μm	1	1	1
Hastelloy substrate	μm	22	22	22
Buffer layers	μm	0.2	0.2	0.22
REBCO layer	μm	1	1	1
Silver overlayer	μm	2	2	2
Copper stabilizer	μm	20	10	30

Data compiled from [9]

the architectural parameters of the 3 tapes are given in Table 6.2. These tapes were wound spirally over a 0.81 mm diameter Cu former with different pitch lengths of 2.8, 3.3, 4, 6 and 8 mm. In the winding, REBCO layer faced inward and Hastelloy outwards. I_c measurements were carried out on flat tapes as well as after bending them over the 0.81 mm former. The *S*2 tape in which the REBCO layer remains close to the neutral axis (zero strain) and experiences minimum strain turned out to be the best with little impact of compressive strain on I_c. This tape was flexible and had enhanced mechanical strength and thus did not show degradation in I_c at a small diameter of 0.81 mm. Thus, 20-μm-thick Cu stabilizer was accepted as the optimum value for providing high I_c retention and at the same time keeping the overall diameter of a six-layered round wire small.

An engineering critical current density, $J_e = 141$ A/mm^2 (77 K, sf), was obtained in this tape in a straight condition. No I_c degradation was observed when the six-layer round wire was bent over 6 cm diameter. I_c however decreased by 17% when the wire was bent over a diameter of 3 cm yielding a $J_e = 117$ A/mm^2 (77 K, sf). These results are quite encouraging and make these fine round wires of REBCO-coated conductor attractive for high-field magnets. NHFML has indeed generated a record field of 45.5 T in 2019 using ultra-thin REBCO tapes.

6.2.3 Next Generation High-Current REBCO STAR Wire for Compact Magnets

After the successful development of flexible and small diameter high-current round wires, the Selvamanickam group proceeded to fabricate highly flexible high-current symmetric tape round (STAR) REBCO wires which meet the requirement of compact magnets to be used in accelerators, like the canted cosine theta (CCT) magnet. The conductor suitable for a CCT magnet must have a $J_e = 540$ A/mm^2 (4.2 K, 21 T) and a bending radius as small as 15 mm. Luo et al. [10] fabricated STAR wires of diameter ranging between 1.68 and 1.97 mm using six and eight layers of thin REBCO tapes of

2.5 mm width. To prevent I_c degradation due to bending strain effect, the tapes were always wound at an angle of 45°. Engineering current densities, J_e, of 438 A/mm^2 (4.2 K, 20 T) and 299 A/mm^2 (4.2, 31.2 T) were obtained under condition of 15 mm radius bending. Sample designated as STAR wire no. 5 in [10] containing eight layers and filled with Indium after bending exhibited an $I_c = 909$ A (4.2 K, 31.2 T). Each layer of the wire had one 2.5-mm-wide tape with thicker copper layer facing inward. Winding of tapes of fixed width in each layer resulted in a gap between the turns which increases with increasing layer number. These gaps reduce the excessive strain on the tapes by allowing the tapes to slide and adjust, while the STAR wire is bent to a smaller radius. A highest value of $J_e = 296$ A/mm^2 (4.2 K, 31.2 T) has been reported.

The Selvamanickam group miniaturized the REBCO tapes and the STAR wires and yet the wires carried large current in high field and did not show degradation while bending the wires to 15 mm radius. Kar et al. [11] recently followed an innovative process to realize highly flexible isotropic round STAR wires with J_e almost 30% higher than the value reached by them a year ago. They were able to get a $J_e =$ 600 A/mm^2 (4.2 K, 20 T) at a bend radius of 15 mm. The strategy adopted by them was to prepare ultra-thin REBCO tapes, as thin as 50 μm by using 10–18-μm-thick Hastelloy substrate. The 12-mm-wide tape was laser slit to 1.4–2.6-mm-wide tapes. Silver (2–3 μm thick) was deposited on the REBCO layer and 1 μm on the substrate side by magnetron sputtering. Silver layer helps in the electrodeposition of Cu stabilizer. Optical shields were developed to deposit Ag on the REBCO film side primarily to bring neutral plane close to REBCO layer. The neutral plane may however shift because of the poor yield strength of Cu or in case the yield strength of Hastelloy is exceeded during plastic deformation caused by the winding of the tapes on Cu former. Two formers of diameter 0.81 and 0.51 mm were used in the studies. Since the tape is composite in nature, its neutral plane is not the centre of the tape, and the thickness of the copper stabilizer was adjusted in relation to the substrate thickness to position the REBCO film near the neutral plane.

The new series of STAR wires, named by the authors as 'Next Generation STAR' (NGS) wires have been designed on the basis of locating the neutral plane in the tape as a function of bending radius, that is, the former diameter and the number of layers. To increase the ratio of REBCO to Cu, the width and thickness of the symmetric tapes were varied in each layer. Tapes with thinner substrates (10 μm) and small widths were wound in the inner layers, while the tapes with 18-μm-thick substrates and 2.6 mm widths were wound in the outer layers. This is the key feature of the NGS wire that led to high J_e, enhanced mechanical performance and made them amiable to small diameter bending without I_c degradation. For carrying out comprehensive superconducting parametric studies, Kar et al. [11] prepared a number of NGS wires in different configurations. They chose different former diameters, different widths and thicknesses of the tapes, different number of layers and finally prepared wires of diameters 1.3, 1.75, 1.98 and 2.04 mm. Specifications of these NGS wires in straight form and at 15 mm radius bending and the I_c and J_e values (77 K, sf) are tabulated in Table 6.3. The thickness of the REBCO tape used in all the wires was ≈ 50 μm. Table 6.4 gives measured critical current and engineering current density data of all

Table 6.3 Specifications and critical currents in four NGS[a] wires *S*1, *S*2, *S*3 and *S*4 at (77 K, sf) in straight form and at 15 mm radius bending, REBCO tape thickness ≈ 50 μm in all the wires

NGS wire No	Cu former diameter (mm)	Number of layers[b]	Total width of the tape used (mm)	NGS wire diameter (mm)	I_c in straight wire (A)	J_e in straight wire (A/mm^2)	I_c in 15 mm Bending (A)	J_e in 15 mm Bending (A/mm^2)
*S*1	0.81	8	19	1.75	571	237.5	494	205.8
*S*2	0.81	9	23	1.98	> 600	> 195	548	178.1
*S*3	0.51	6	11.4	1.30	422	318.3	400	301.5
*S*4	0.51	12	27	2.04	> 600	> 183.6	766	234.5

[a]*NGS wires* New generation star wires
[b]Different layers use different widths of the REBCO as explained in the text
Data compiled from [11]

Table 6.4 Critical current, I_c, and engineering current density, J_e, of the 4NGS wires, *S*1, *S*2, *S*3 and *S*4 at 4.2 K and field as indicated in the column

Wire Sample		I_c (A)			J_e (A/mm^2)		
No	Wire Diameter (mm)	Value	Temperature (K)	Field (T)	Value	Temperature (K)	Field (T)
*S*1	1.75	966.5	4.2	20	402	4.2	20
*S*2	1.98	734	4.2	26	208.5	4.2	20
*S*3	1.30	778	4.2	20	586	4.2	20
					416	4.2	31.2
*S*4	2.04	1331	4.2	26	353.8	4.2	20
		1100	4.2	30			
		1300	4.2	23			

Data compiled from [11]

the 4 NGS wires at 4.2 K and different fields. Sample *S*4 with maximum tape width of 27 mm and maximum diameter has the maximum I_c, but the J_e turns out to be the highest in NGS wire *S*3 at all fields up to 31.2 T. The wire *S*3 has the smallest diameter of 1.30 mm and exhibits highest retention of I_c (95% at 77 K) in 15 mm radius bending.

The *S*3 wire sustained a Lorentz force of 15.5 kN/m at a J_e of 586 A/mm^2 (4.2 K) and no degradation was observed. Three reasons seem to be pertinent to the excellent performance of these wires. (1) Very thin former 0.51 mm diameter which makes the wire ultra-flexible making them capable of bending over very small (15 mm) radius without degradation in I_c, (2) variation in tape thickness in each layer results in high level of retention of I_c in bend state, and (3) variable twist pitch in different layers causes inter-turn gaps allowing tapes to slide under high Lorentz force. By

all accounts, it appears that these highly flexible NGS wires are going to fulfil the requirements of the CCT magnets sooner than expected.

6.2.4 High Engineering Current Density (J_e) in REBCO Wires

High irreversibility field and high mechanical strength possessed by the HTS 2G REBCO-coated tape wires have made this material very attractive for magnet-based applications. High-field magnets require very high engineering current density. SuperPower followed a novel technique to increase J_e by about 35% by changing the architecture of the conductor. SuperPower found an innovative way to increase J_e by reducing the cross section of the wire without affecting the superconducting parameters of the REBCO film. The complete process followed at SuperPower is like this: Hastelloy C-276, 12-mm-wide and 30-μm-thick tape electro-polished with a surface finish of 1 nm has been used as the substrate. Next, amorphous layers of alumina and yttria were sequentially deposited on the substrate at room temperature by reactive magnetron sputtering of the metal targets. Alumina serves as a diffusion barrier to the cations from the substrate, and yttria provides a pristine surface for the nucleation of the ion beam-assisted deposition (IBAD) MgO film which was deposited by ion beam sputtering of MgO at room temperature with texture control. To provide a good lattice match with REBCO, a cap layer of $LaMnO_3$ (LMO) is deposited next. MgO and LMO are also deposited sequentially in the pilot-buffer system. Various parameters like texture, grain-grain alignment (110), pole figure, etc., of LMO were measured and controlled during the deposition to monitor and maintain the quality of the film. The REBCO layer was deposited using a MOCVD system with 7.5% Zr-doped precursor. At this stage, a 2-μm-thick Ag overlayer was deposited on the REBCO layer by cylindrical magnetron sputtering. This was followed by the deposition of 2 μm of Ag, oxygen annealing and the deposition of Cu stabilizer of desired thickness. Ag protects the REBCO layer from reaction contamination, provides good current transfer to the REBCO layer and ensures oxygen supply during annealing being transparent to oxygen diffusion.

6.2.5 REBCO Deposition on 30 μm Hastelloy Substrate and High J_e

Sundaram et al. [5] at SuperPower reported an increase in J_e by a factor of 2.5 by reducing the thickness of the Hastelloy C 276 from 50 to 30 μm without causing any adverse effect in the superconducting properties of the wire. The I_c and J_c of the wire increase by 30–45% depending upon the quantity of copper stabilizer incorporated. These 2G wires with high J_e will be very attractive for building high-field magnets

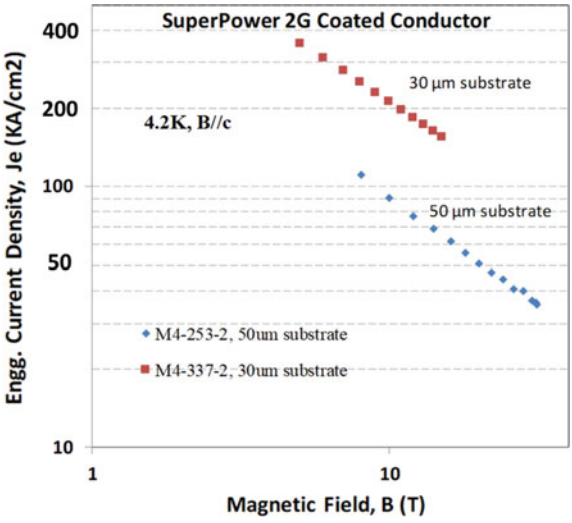

Fig. 6.7 Magnetic field dependence of the engineering current density, J_e, of 2G REBCO doped with 7.5% Zr tape form wires produced by SuperPower Inc. by IBAD-MOCVD process using 50- and 30-μm-thick Hastelloy substrates. There is a significant increase of J_e in REBCO layer when deposited on a thinner substrate. Copyright SuperPower Inc. 2020, images provided courtesy of Yifei Zhang, SuperPower

needed for magnetic resonance imaging (MRI), nuclear magnetic resonance (NMR), fusion machines, particle accelerators and high-field magnets for laboratory research. Figure 6.7 shows the field dependence of the engineering current density, J_e of 2G YGdBCO tape wires produced by SuperPower Inc. by IBAD-MOCVD process. This paper thin (0.043 mm) tape had the YGdBCO film doped with 7.5% Zr deposited on a 30-μm-thick Hastelloy substrate instead of the usual 50-μm-thick substrate. The reduction in cross section of the tape thus leads to higher J_e. Hahn et al. [12] at the National High Magnetic Field Laboratory (NHFML), Tallahassee, Florida, which held a world record of 45 T produced by a hybrid magnet (resistive and superconducting) for about two decades, were quick to exploit this material for producing a record field of 45.5 T [12]. They used a paper thin, 0.043 mm (43 μm) (YGd)BCO tape without any insulation. The background field of 31.1 T was provided by the resistive coil consuming 31 MW of power. The 2G YGdBCO insert coil produced an additional field of 14.4 T, and thus, a new record of 45.5 T was established in 2019. We will discuss the details of this magnet in Chap. 9.

6.2.6 High-Current CORC Cables

The SuperPower 30 μm substrate wires SCS 3030 have been used by Advanced Conductor Technologies LLC (ACT) for developing high-current cables, conductor on round core (CORC) for next generation accelerator magnets which need an engineering current density, J_e, of 300–600 A/mm^2 at 4.2 K and 20 T and a minimum bending diameter of about 40 mm. ACT fabricated CORC wires by winding 2-mm-wide 2G REBCO tapes on 30-μm-thick Hastelloy substrate in two different layouts.

Table 6.5 Specifications of a typical CORC®-30 wire developed by Advance Conductor Technologies LLC (ACT)

Parameter	Unit	Value
Cu-core diameter	mm	2.58
Tapes used		SuperPower SCS 2030
Tape width	mm	2
Critical current	A	50–70 A @ 77 K
Number of tapes wound		30
Number of layers		112
Hastelloy substrate thickness	μm	30
Copper plating thickness	μm	5
CORC wire diameter	mm	3.8
Gap spacing	mm	0.3–0.4
Winding angle	(°)	30–47

Data compiled from [13]

The central core in both the wires was a 2.58 mm diameter annealed solid copper. Cable produced by ACT, code named CORC®-27, had 27 REBCO tapes, and the wire CORC®-30 had 30 tapes wound around the central Cu core. Both the tapes had I_c = 50–70 A (77 K, sf) and were wound in 11–12 layers at a winding angle of 30°–47°. Each tape layer was wound with opposite pitch with respect to the adjacent layer. Table 6.5 gives the specifications of a typical CORC®-30 wire.

In accelerator magnets, these wires will be subjected to large Lorentz forces due to the combination of high engineering current density and high magnetic field. This may cause irreversible degradation to cable's performance. Danko van der Laan et al. [13] at ACT have carried out studies on the effect of axial tensile stress on the critical current at 77 K and report that CORC cables do not show significant change in critical current until the irreversible stress limit, as high as 177 MPa, is reached. This limit depends on the yield strength of the Cu former, the number of 2G REBCO tapes wound and the angle at which the tapes are wound. The helical style of winding of the tapes leads to high irreversible strain limit of 0.85% far above the strain limit of single tape. As long as the peak stress remained below the irreversible stress limit, the cable did not show any degradation in performance over 100,000 tensile stress fatigue cycling. These studies established the fact that CORC cable is a robust high-current superconductor capable of producing high magnetic field and withstanding high tensile stress and strain. There is still scope for increasing the irreversible stress by changing to stronger core material (like cold-worked Cu) and tensile strain limit by optimizing the winding angle. Figure 6.8 shows the photograph of typical CORC wires [14] with 2G REBCO tapes wound over a central solid Cu core of different diameters. Different number of REBCO tapes have been used for winding, and the tapes had different thicknesses of the Hastelloy substrate, viz 50, 30 and 25 μm in three wires. The ACT-manufactured CORC cable has a diameter of 5.1 mm with a J_e = 344 A/mm^2 (4.2 K, 17 T). The company hopes to achieve a J_c = 600 A/mm^2 at 4.2 K and 20 T field shortly. The critical stress beyond which the degradation in

Fig. 6.8 Typical CORC wire with different number of 2G REBCO tapes wound over a central solid Cu core from Advanced Conductor Technologies LLC for different Hastelloy substrate 50, 30 and 25 μm thick. Copyright Advanced Conductor Technologies, courtesy Danko van der Laan

J_c is irreversible, in a CORC wire with 30 tapes, is measured to be 175 MPa. In zero stress, a critical current, I_c, ∼ 1500 A at 77 K has been recorded.

In view of the significantly high critical current density and high stress tolerance, the CORC® wires seem to be good candidate for future accelerator magnets. The measured maximum irreversible stress 175 MPa at 77 K is smaller than what it should be on the basis of rule of mixture (ROM). As per ROM, the yield strength of CORC wire should have been about 290 MPa taking the yield strength of 110 MPa for the annealed Cu core and 1093 MPa for the REBCO tapes at 77 K. This discrepancy is attributed to helical mode of winding instead of being parallel to the core. The helical winding however results in an irreversible strain limit of as high as 0.74–0.85% in CORC wires. Another favourable feature of the CORC wires is that the critical current is not degraded significantly under fatigue up to 100,000 cycles as long as the peak stress remained below the irreversible stress limit. Major improvement in mechanical properties of CORC wires is expected if the annealed Cu is replaced by a cold-worked Cu.

CERN in collaboration with the University of Twente [15] is developing the CORC CICC cables for use in the future circular collider (FCC) magnets and bus bars. Figure 6.9 a shows the conceptual drawings of the six-around-one type of CICC cables being presently evaluated for critical parameters at CERN. Figure 6.9b is the picture generated for a demonstration racetrack coil. The coil is wound in two layers with eight turns each using 7.96 m long CORC wire of 3.45 mm diameter manufactured and supplied by ACT. The coil is 189 mm long and has a bore of 40 mm. The CORC wire was fabricated with 27 REBCO tapes, and 11 layers helically wound over a copper core of diameter of 2.35 mm. The expected critical current was 1.8 kA (77 K, sf) and 5.25 kA (4.2 K, 10 T). The coil had an inductance of 50 μH and a field factor of 0.38 T/kA. A critical current of 4.5 kA was recorded at 4.2 K and in 10 T field. The minimum bending diameter was 40 mm. It turned out that the 3.4 mm diameter wire with REBCO tape on 30 μm-thick-substrate is still too thick

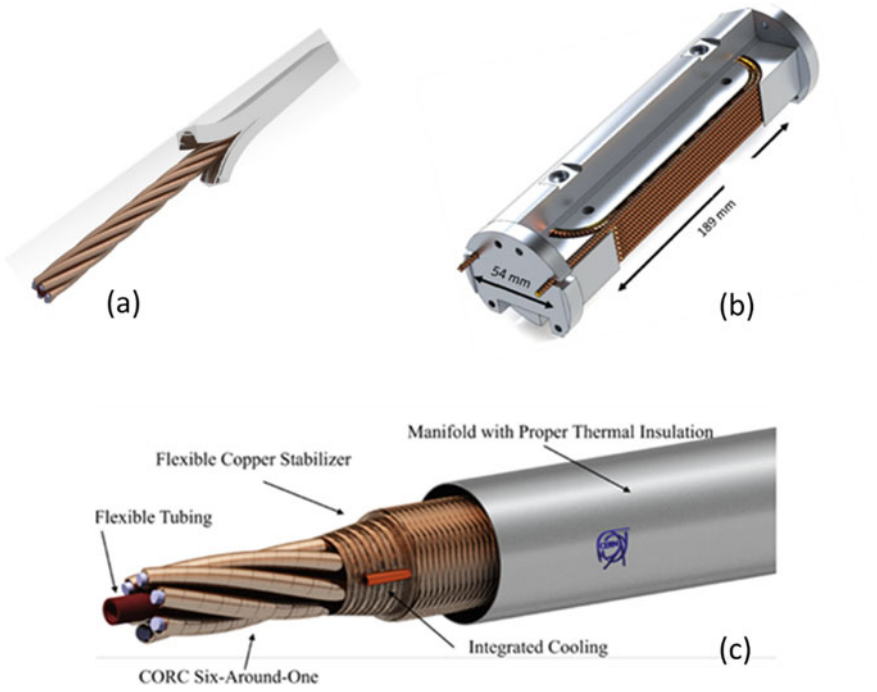

Fig. 6.9 **a** The drawing of the 'six-around-one' type of CORC cable-in-conduit conductor (CORC-CICC) under development at CERN. **b** 3D computer generated picture of a demonstration racetrack coil built by CERN using CORC wire supplied by ACT. The dimensions of the coil are given in the picture. **c** Conceptual image of CORC 'six-around-one' bus bar under development at CERN. The 'six-around-one' bundle has multiple layers of copper braid wrapped around it for stability. A central tube and the gaps between the layers provide cooling channels [15]. Pictures courtesy of Herman ten Kate, CERN and University of Twente

and should be reduced further. Figure 6.9c is the image of six-around-one CICC cable being developed for bus bars to carry current to the twin-solenoid and the forward-solenoid detector magnets. The bus bars, 400 m long, will be required to carry a current of 80 kA to the twin-solenoid magnets at a temperature of 55 K down the 350 m deep tunnel in a 1 T field environment. The bus bars have already been tested up to 30 kA at 70 K in a background field of 1 T. An appropriate amount of copper has to be incorporated with the cable to protect the magnet and the bus bar itself in a situation of quench of the magnet depending upon the maximum allowable hot spot temperature. The bus bars can be cooled using liquid helium or through conduction via the integrated cooling line within the bundle or around it.

More recently, Laan et al. at ACT have reported [16] a high magnetic field of 15.86 T produced by an insert coil of CORC wire in a background field of 14 T. The magnet operated at a current of 4.4 kA ($J_e = 282$ A/mm^2) and generated a hoop stress of 275 MPa. The peak field at the conductor was 16.77 T. This was the first

time that a magnet was operated at such a high current using a HTS material. By all accounts, REBCO CORC wires have established its dominance to be a high current, high current density, high field with high stress tolerance practical superconductor for future applications.

6.2.7 REBCO–CORC Cable-In-Conduit Conductors (CORC-CICC)

The most critical requirement of the fusion toroidal coils is the high-current superconducting cables to limit high voltages generated during fast discharge or quench. High current in conductor means that smaller number of turns are needed to produce the same field, reducing thereby the inductance and hence the induced voltage. Another requirement for the TF conductor is low AC loss because additional heating by AC loss reduces the temperature window for safe operation of the TF coils. Future fusion machines and particle detector magnets will need very high operating currents anywhere between 80 and 100 kA for which a large number of superconducting subcables or strands are required to be bundled together. To withstand large stresses, these cables are to be embedded in a metallic jacket with cooling channels inside to assume the form of a high-current CICC. These CICCs are cooled with liquid helium or with forced-flow supercritical helium (SHe). The introduction of conductor on round core (CORC) cables was a consequence of high tolerance of REBCO-coated conductors to axial tensile and compressive strain. The tolerance of irreversible strain in REBCO under axial compression is about twice to that under axial tension. The motivation behind the development of CORC was to produce a high-performing round cables which are mechanically and electrically isotropic. Major efforts for the development of such REBCO high-current cable conductors have been made by Advanced conductor Technologies (ACT) in collaboration with a number of research institutes, and the status of this development was published recently by van der Laan et al. [17]. A variety of CICC have been produced in the laboratory and experimented with. The focus has been on the development of two varieties of CICC, one required for high-field fusion magnets and the other for accelerator detector magnets. These conductors are being developed at ACT with the support of the U.S. DOE and in collaboration with MIT, LBNL, NHFML, CERN, KIT, Uni. of Twente and Paul Sherrer Institute. The varieties of such cables are described in the following subsections.

A. **Development of REBCO-CORC-CICC**
We have already discussed that the CICC cables not only have to carry large current but should also be mechanically strong. Further, these cables have to be flexible enough to be wound as coils without degrading superconductivity. The flexibility will depend upon the twist pitch length at which the CORC strands are wrapped around, the thickness of the strand and their ability to slide within the bundle during the bending of the bundle. Few tens of CORC wires are wound around a cooling tube with a short pitch of 100–300 mm [17].

Short pitch leads to excellent transposition of strands and makes the cable quite flexible. High level of transposition minimizes the self-field effect, enhances uniformity of current distribution among the strands and consequently reduces ramping losses. Typically, a model CORC-CICC sample has 13 copper strands of diameter 3.85 mm, and one REBCO CORC wire of diameter 3.65 mm sandwiched between two SS strands of diameter 4.1 mm. The whole bundle is then jacketed in a SS casing. The slightly larger diameter of the SS strand prevents the jacket compressing the CORC wire during bending. This CICC was bent to different diameters down to 1 m and studied for critical current behaviour. The I_c of the CORC-CICC is reduced to 82% of the initial I_c value after bending to 1 m diameter.

As part of the development, two 3 m long CORC-CICC were made by Mulder et al. [18, 19] one each for fusion magnet and another two for accelerator detector magnet. Six CORC cables were wound over a central cooling SS tube in a so-called 6-around-1 configuration with a twist pitch of 0.4 m and inserted in a SS jacket for fusion magnet and in a copper jacket for detector magnet. The conductor for detector magnet can also be cooled by conduction from outside the jacket. The cables were characterized for critical current in 7–10.9 T field and at different temperatures of 4.2 K, 40 K, 45 K and 50 K at SULTAN test facility at PSI, Switzerland. These measurements were limited to 30 kA because of the degraded CORC-CICC which was connected in series while measuring I_c. It is hoped that the designed value of 80 kA at 4.2 K has been achieved at ACT. The reason for degradation of I_c in CORC-CICC for detector magnets during operation is believed to have been caused by the accumulation of stresses due to error in tolerances in cable and jacket manufacturing. This error might have resulted in the movement of the CORC strands within the bundle. The way to overcome this problem was to decouple the CORC strands by following the ENA design of laying the CORC strands inside an extruded spiral groove-structure of copper or aluminium which has a central circular cooling channel. The structure with CORC strands is inserted in a circular metallic jacket. The fins in the structure fit well to the inner surface of the jacket, and the CORC strands remain in position in the grooves between the fins. The CICC had 12 CORC strands.

B. **Recent Work on CORC-CICC Conductors at CERN**

Recently, CERN [20] has tested three samples of CORC-CICCs prepared in three different configurations using CORC ‘six-around-one’ cables. The conductor in fusion application has to carry large current, withstand high mechanical loads and provide adequate cooling as the heat loads are high. The CORC strands having 42 REBCO tapes are wound over a 5 mm diameter central solid copper rod, and the bundle of strands is housed in a SS jacket. Voids between the strands serve as cooling channels for forced flow. Two other CORC-CICC developed and referred to as CICC-Cu1 and CICC-Cu2 have the same number of strands and tapes as in CICC-SS1 but have a copper jacket. The conductor CICC-Cu1 has an option of cooling by internal forced flow or/and cooling by conduction for which a cooling line is provided in the jacket. This conductor has been primarily designed for use as bus bar. More recently, one

more CICC referred to as CICC-Cu2 has been prepared with a better mechanical design compared to the previous samples. This new 'six-around-one' CORC-CICC contained 42 REBCO tapes which had slightly better performance rating compared to the tapes in the other two samples. The diameter of the central solid copper core was increased from 4 to 5 mm for better tolerance to large electromagnetic loads. To further improve the mechanical strength of the strands, the voids were completely filled with BiSnPb solder. The joint terminals are filled with indium for a very low contact resistance $\sim$ 1 nΩ (4.2 K, 12 T). Cooling of the conductor is provided only through conduction by the cooling line soldered in the conductor's copper jacket. The complete specifications of the three CORC-CICC are given in Table 6.6.

The critical current of the CICC-SS1 is close to the expected value of 90 kA and showed no degradation on thermal cycling. Both cooling routes, internal forced-flow cooling as well as conduction cooling, have been found successful. Copper-jacketed CICC-Cu1 was specifically designed to carry a critical current of 100 kA at 4.5 K, 10 T. This cable is also planned to be used for high-current bus bars and large magnets

Table 6.6 Specifications of the three CORC-CICC cables, one for fusion magnets and two for detector magnets

Parameter	Unit	CICC for fusion magnet (SS1)	CICC for detector magnet (Cu1)	CICC for detector magnet (Cu2)
Year		2017	2017	2019
Cable name		CICC-SS1	CICC-Cu1	CICC-Cu2
Cable length	m	2.8	2.8	2.8
Tape code		SCS 4050	SCS 4050	SCS 4050
Hastelloy substrate	μm	50	50	50
Number of tapes		42	42	42
Number of layers		14	14	14
Copper plating	μm	10	10	10
Core material		Cu	Cu	Cu
Core diameter	mm	5	4	5
Jacket material		SS	Cu	Cu
Strand outer diameter	mm	7.7	7.7	7.7
Cooling through		Voids	Voids/channels	Conduction cooling
Impregnation		No	No	Voids filled with solder (BiSnPb)
Expected I_c (4 K, 10 T)	kA	90	90	100

Data compiled from [20]

for detectors at 4.5 K. Copper jacket enables conduction cooling through a cooling line provided within the jacket itself.

6.2.8 The Roebel Bar Cable

Future accelerators and fusion machines need cables with low AC loss current of several kA for magnets and many power applications which can be operated at higher than 4.2 K for economic reasons. The natural choice falls on the 2G REBCO cables which can be operated at 30–50 K and yet carry low-loss large current under high field. Besides, they are mechanically strong and have high stress tolerance. The hysteresis losses in REBCO tapes are however high because of the large aspect ratio of the tape cross section. A filament architect and twisting to reduce losses is however difficult to realize in such tape geometry. Roebel bar cable configuration and Rutherford cables seem to be good alternatives. The concept of Roebel cables is based upon the strategy of dividing the current among many tape wires and provide a full transposition of the wires along the cable direction. The Roebel concept, invented for copper cables some hundred years ago, was adapted by the Karlsruhe Institute of Technology (KIT) in 2006 [21] for the production of low-loss high-current cables using 2G-coated conductors. In this process, meandered strand tapes are prepared by punching a wide 2G tape instead of bending it in-plane. A computer controlled feedback system was used during punching and cabling.

Goldacker et al. [21] carried out feasibility study by fabricating a 35 cm long Roebel cable based upon the idea of pre-shaping the Roebel wire structure from a 2G tape and stack a number of them together to transport required current. Copper strands are added to the cable for stabilization. Goldacker group prepared a strand of 4-mm-wide DyBCO-coated conductor (CC) wires (from THEVA GmbH Germany) cut from 10-mm-wide CC tapes with a twist pitch of 180 mm. Each wire carried an average of 157 Amps/cmwidth, and these were assembled into a sub-cable with five strands and a final cable with 16 strands. The I_c of the 5 strand cable was > 300 Amps at 77 K, almost five times the I_c for an individual strand. The 16 strand cable however carried 500 A only, because of poor stabilization. A pulse current load however indicated a current carrying potential of the cable > 1 kA. A topical review has been published by Ugliatti [22] which gives a detailed account of commercial wires, tapes and cables capable of carrying large low-loss currents needed for power sector and for high-field magnets in accelerators and fusion reactors. Figure 6.10 shows the photographs of two typical REBCO Roebel cables developed at KIT in Goldacker's laboratory.

The work on the development of low-loss high-current Roebel cables has been pioneered by Goldacker and co-workers. The group has successfully developed Roebel cables consisting of up to 50 tapes [23] and with a current carrying capacity of up to 2.6 kA (77 K, sf). This current capacity however falls short of the requirement for bus bars and fusion magnets current which stands at 10–20 kA.

Fig. 6.10 Typical REBCO Roebel cables developed at Karlsruhe Institute of Technology (KIT). *Courtesy* Wilfried Goldacker, KIT

6.2.9 HTS CroCo Cable Development for DEMO Fusion Reactor

Buoyed with the success of REBCO-coated conductors in producing high current and mechanically strong CORC cables, efforts started using this material for developing cables which can be used in the toroidal field (TF) coils for EU-DEMO, the successor of ITER fusion reactor. Such a machine can be made compact and with reduced cost. EU-DEMO is designed to produce 2000 MW power with an input power of 80 MW with a gain factor of 25. The central plasma field in EU-DEMO will be 6.8 T, and the peak field at the conductor is estimated to be 13.3 T. The TF conductor should have low AC losses and about $\sim$ 12 K as the temperature margin for operation. Fietz et al. [24] at KIT have proposed a method of producing long length of high J_e REBCO cables named as HTS CroCo (cross conductor) cable. In this process, two REBCO tapes of different widths are arranged in a cross structure, twisted and produced in long length. This assembly is compacted in a Cu-casing which is then filled up with molten solder. All the voids are thus filled up. The cable has been named as HTS CroCo. The Rutherford cable proposed for DEMO TF coils has 11 HTS CroCos transposed over a rectangular metallic core and inserted in a SS jacket. Each HTS CroCo has a diameter of 9 mm and contains twenty 6-mm-wide and ten 4-mm-wide REBCO tapes. This HTS CroCo had a critical current, I_c, of $\approx$ 30 kA (4.2 K, sf) and will have $I_c = 7.6$ kA at 13.5 T, the calculated maximum field felt at the conductor in the TF coils. The critical current value (7.6 kA) has been calculated on the basis of the I_c of the REBCO tapes available. Thus, the I_c of the Rutherford cable with 11 HTS CroCos is expected to have $I_c = 84$ kA (4.2 K, 13.5 T). Taking the 2016–17 J_c value of the REBCO-coated conductor into account, the expected I_c of this HTS CroCos cable is high at 154 kA and thus quite suitable for use in DEMO TF coils. Future improvement in critical current performance of the REBCO tapes will push up the I_c of the HTS CroCos further and may overshoot the designed value by a big margin. Since the present aim is to operate DEMO TF coils at 50–60 kA, the TF coils

can produce still higher magnetic field or the TF coils can be operated at a higher temperature or use smaller quantity of the tape.

A 9.7 mm diameter CroCo composed of layers of 4- and 6-mm-wide REBCO tapes carries a current more than 4000 A at 70 K which can be provided by liquid nitrogen. At 20 K, this CroCo will carry over 20,000 A of DC current without loss. Table 6.7 gives the I_c data on a few REBCO CroCos fabricated using different combinations of tapes in different numbers and of different widths at temperatures of 4 K, 30 K and 77 K in different values of magnetic field (Fig. 6.11).

KIT produced very high-current cables in 2018 [25] by combining several HTS CroCo strands that carried a DC current of 35 kA at 77 K. In 2018, KIT produced 3 m long demonstrator cable using 12 CroCo strands around a central core of diameter of 130 mm which carried a DC current of 35 kA at 77 K. This cable was the one third scale down of the main target of producing a cable carrying a current of 104 kA which

Table 6.7 Specifications of typical REBCO CroCo strands using combinations of different number of tapes and of different widths

Parametric detail	CroCo 6/4	CroCo 4/3	CroCo 3/2
Number of REBCO tapes × width	22 × 6 mm 10 × 4 mm	28 × 4 mm 10 × 3 mm	18 × 3 mm 10 × 2 mm
Cross diagonal	7.2 mm	5.0 mm	3.6 mm
I_c (77 K, self-field)	3100 A	2090 A	1460 A
I_c (30 K, 2 T)	20,000 A	14,000 A	9000 A
I_c (4 K, 12 T)	> 10,000 A	~ 9500 A	6000 A
Minimum bending radius (R_{min})	60 cm	45 cm	30 cm

Data compiled from [25]
I_c depends on the tape used

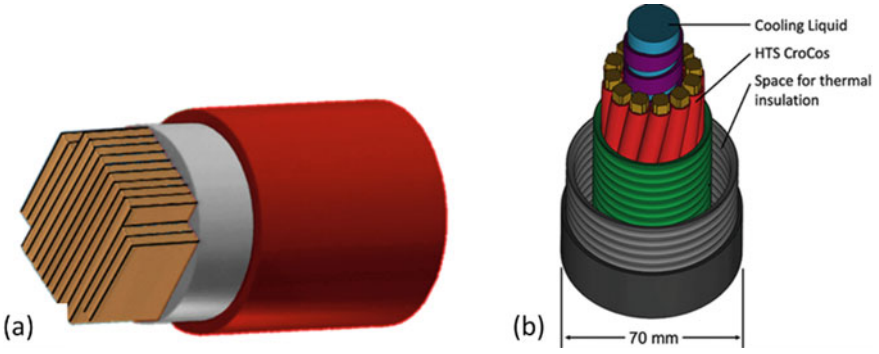

Fig. 6.11 **a** Cross section of the cross conductor (CroCo) billet prepared by packing two types of long tapes of different widths in a cross structure, twisted, and finally compacted in a Cu-casing. The casing is then filled up with molten solder, **b** several REBCO CroCos processed into a cable capable of carrying a current of 35 kA (*Courtesy* Walter H. Fietz, KIT) https://www.sek.kit.edu/downloads/2019-datasheet-superconductor-hts-croco.pdf

would have 36 CroCo strands along the same periphery with 130 mm diameter. The strands used 22 tapes of 6 mm width and ten tapes of 4 mm width. The design of the cable was worked out by making FEM calculations using COMSOL software tool. The configuration of the tapes within the strands was such that the influence of the magnetic field is minimized. The tapes were oriented such that the tape surface lies parallel to magnetic field because of the strong field anisotropy of the tapes.

The REBCO CroCo high-current cables are also the serious contender for the TF coils of the EU-DEMO. To study quench performance of the cable, the thermal hydraulic analysis has been performed [26] using the THEA code. The structural analysis carried out on the winding pack of the TF coil puts constraint on the aspect ratio of the cable space inside the jacket. This led to a round cable of 31.2-mm diameter. Studies were conducted on the number and the constitution of HTS CroCo strands and the volume percentage of copper central core vis-à-vis the quench performance of the cable. The cable is jacketed in a SS casing and cooled by 4.5 K supercritical helium (SHe). The simulations yield the hot spot temperatures of the HTS CroCo, copper core and the jacket during a fast quench of the magnet with a time constant of $\tau = 27$ s after reaching the quench voltage of 100 mV. General design principles for HTS TF coils have been drawn for fusion magnets based upon simulation data on the dependence of hot spot temperature on different parameters related to the geometry, the material and the thermal properties of the conductor.

6.2.10 Supremacy of REBCO-Coated Conductors

During last one decade, REBCO-coated conductor has established its superiority over the conventional superconductors where field requirements are in excess of 20 T. Realizing the future potential of this emerging practical superconductor, several companies have started manufacturing and supplying these conductors across the world. Prominent among these companies are: American Superconductor Corp. (AMSC) (US), SuperPower Inc. (US), Fujikura Ltd. (Japan), SuNAM Co., Ltd. (Korea), Shanghai Superconductor Technology Co., Ltd. (China), SuperOx Japan LLC (Japan) and SWCC Showa Cable Systems Co., Ltd. (SWCC) (Japan). Table 6.8 gives the dimensions, fabrication technique, critical current, I_c, (77 K, sf) and n-value of the REBCO-coated conductors marketed by different companies.

All the companies use a biaxially textured templates consisting of a flexible Hastelloy tape with a set of buffer layers and epitaxial REBCO layer. The buffer layers are deposited on Hastelloy substrates and are textured by ion beam-assisted deposition (IBAD). AMSC's template is however prepared by deforming a Ni-W substrate with roll-assisted biaxially textured substrate (RABiTS) technology. The epitaxial REBCO layers of these conductors are grown by different methods like metal organic deposition (MOD), pulsed laser deposition (PLD), reactive co-evaporation (RCE) and metal organic chemical vapour deposition (MOCVD) technique. Thickness of the substrate and the copper stabilizer used have been varied to optimize the engineering

Table 6.8 Dimensions, fabrication technique, critical current, I_c (77 k,) and n-value of the REBCO-coated conductors marketed by different companies

Conductor	Dimensions $W \times t$ (mm)	Fabrication technique	Substrate thickness (μm)	Cu stabilizer thickness (μm)	I_c (77 K, sf) (A)	*n*-value
AMSC 8501–130	4.8 × 0.20	RABiTS/MOD	(NiW) 75	60	144.5	37
Fujikura FYSC-SCH04	4.1 × 0.12	IBAD/PLD	Hastelloy 75	20	225.5	34
Shanghai SC	4.8 × 0.07	IBAD/PLD	Hastelloy 50	10	145	27
SuNAM HCKNK04150	4.1 × 0.10	IBAD/RCE	Hastelloy 75	20	217	43
SuperOx	4.0 × 0.15	IBAD/PLD	Hastelloy 60	40	132	36
SuperPower SCS4050-CF	4.0 × 0.09	IBAD/MOCVD	Hastelloy 50	20	116	31
SuperPower SCS4050-AP	4.0 × 0.10	IBAD/MOCVD	Hastelloy 50	20	156	30
SuperPower SCS4050-AP-low	4.0 × 0.10	IBAD/MOCVD	Hastelloy 50	20	87	29
SuperPower SCS4030-AP-sp	4.0 × 0.045	IBAD/MOCVD	Hastelloy 30	5	150	29
SWCC SW2G04-N	4.2 × 0.22	IBAD/MOD	Hastelloy 100	41	156	34

Data compiled from [27]

current density, J_e, of the conductors. Tsuchiya et al. [27] have carried out an interesting comparative study on the I_c-B behaviour of the coated conductors marketed by these companies in 2016–17. The I_c values have however improved further since then, through innovative measures.

The critical current, I_c, of all the conductors listed in Table 6.8 measured at 4.2 K in perpendicular magnetic field is plotted against the field (B) in Fig. 6.12. The SuperPower-AP-SP conductor with highest I_c stands out to be the best conductor. High J_c in these conductors is attributed to Zr-doping (7.5%) and the presence of advanced pining centres (APC). The introduction of APC causes the I_c (4.2 K, 18 T) to go up by a factor of 2.5. It is also evident from Fig. 6.12 that the I_c of SuperPower-AP-SP conductors is about 1.3 times higher than the I_c of SuperPower-AP conductors. The only difference between the two conductors is the small thickness of the Hastelloy substrate (30 μm) used in the AP-SP compared with 50 μm in AP conductors. Reduced substrate thickness results in increased flexibility of the wire which in turn may enhance irreversible critical strain, ε_{irr}. Other difference between the two conductors is the use of thinner Cu stabilizer 5 μm in AP-SP conductor instead of 20 μm used in AP conductor. Reduced cross section of the

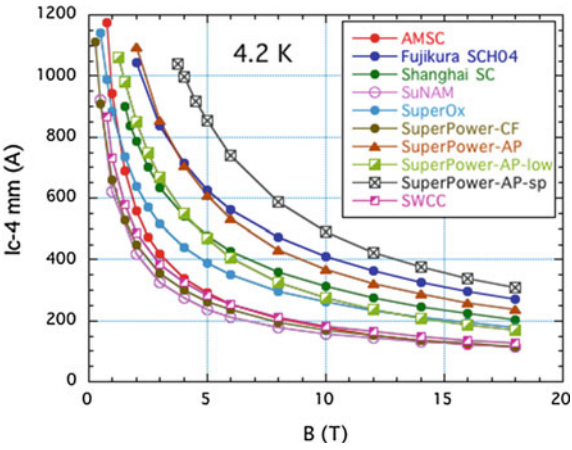

Fig. 6.12 Magnetic field dependence of transport critical current, I_c, for 4-mm-wide REBCO tape wire manufactured by different companies. SuperPower-AP-SP has the highest I_c in the entire range of field up to 18 T [27]. With permission from Elsevier

conductor increases J_e of the conductor. Different types of pinning mechanism might be operating in conductors prepared by different methods. The indications from Table 6.8 are that IBAD/PLD technique leads to higher I_c. Other finding of these studies is that 4-mm-wide conductors have a high $J_c = 1000–2000$ A/mm^2 (4.2 K, 18 T) and 1200–3000 A/mm^2 (4.2 K, 12 T).

6.3 The Promising $Bi_2Sr_2CaCu_2O_x$ (Bi-2212) Practical Wires and Cables

Even though Bi-2212 was one of the first HTS materials to enter the superconductor market yet its large anisotropy, low critical current density and the complexity of manufacturing wires of long lengths in polycrystalline conductor form prevented its use in potential applications. Low critical current in this material is largely caused by the great current blocking effects of randomly oriented grain boundaries (GBs). The common approach to overcome this problem until recently has been to avoid grain boundaries. Quite early in 1989, it was observed that the routing through the melt phase of Bi-2212 [28] could lead to a self-organized, local grain alignment which will increase the J_c significantly well above the J_c in randomly oriented polycrystalline material. Fortunately, Bi-2212 could be conveniently melted inside a Ag-alloy sheath, and it appeared that Bi-2212 might challenge Bi-2223 soon. This was however not to be as its sibling $(BiPb)_2Sr_2Ca_2Cu_3O_{10}$-x or just Bi-2223, with its higher $T_c = 110$ K and comparatively high J_c at 77 K superseded it. We will discuss Bi-2223 conductors in the next section.

Bi-2212 however scores over Bi-2223 insofar as the round Bi-2212 wire generates a dominant a-axis growth texture and imposes a local biaxial texture (FWHM < 15°). Simultaneously, it aligns the c-axis of its polycrystals along the filament axis making Bi-2212 to display a macroscopic isotropic behaviour. Bi-2223, on the other hand,

displays only a uniaxial (FWHM < 15°) *c*-axis texture perpendicular to the tape plane but not in the in-plane texture. Consequently, Bi-2212 round wire does not show J_c (B) hysteresis during increasing and decreasing field in contrast with Bi-2223 which exhibits hysteresis. As mentioned earlier, the main attraction of the HTS (REBCO, Bi-2212 and Bi-2223) conductors is that they have very high B_{c2} (~ 100 T) and therefore the critical current shows a plateau in high-field region up 45 T in contrast to Nb_3Sn conductors which shows sharp drop in critical current at 20 T field, B_{c2}, being about 30 T only. Another parameter which influences J_c in HTS conductor is the ratio of superconductor to the normal matrix. Presently, it is only 1–2% for REBCO-coated conductors, 25–40% for Bi-2212 and Bi-2223 compared to 50% for Nb-Ti and Nb_3Sn.

6.3.1 Development of a 10 kA Bi-2212 Conductor

The development of a 10 kA Bi-2212 conductor for a conceptual fusion device by Isono et al. [29] in 2003 confirmed the superiority of isotropic round wires of Bi-2212 over REBCO and Bi-2223. The fusion device was designed by Japan Atomic Energy Research Institute (JAERI) which envisaged a toroidal field of 16.5 T and a peak field of 23 T. The JAERI team fabricated a round Bi-2212 conductor which carried a current of 10 kA (4.2 K, 12 T). The conductor used 729 round Ag-alloy sheathed Bi-2212 strands, which had best J_c (4.2 K, 16 T) at the time. The specifications of the strands and the cable are listed in Table 6.9. The cable had a final target of reaching 100 kA in a field of 16.5/23 T and at an operating temperature of 20 K.

Table 6.9 Parameters of the strand and cable of Ag-alloy sheathed Bi-2212 prepared by PIT and repeat bundling technique

Strand specifications			Cable specifications		
Parameter	Unit	Value	Parameter	Unit	Value
Diameter	mm	0.80	Diameter	mm	34
Filament diameter	mm	10–13	Number of strands	3 × 3 × 81	729
Matrix		Pure Ag	Twist pitch	mm	20, 60, 550
Outer sheath		AgMgSb	Conductor length	m	1.5
AgMgSb:Ag:SC		1.8:2.3:1	Outer coating		Pb-based solder
Critical current, I_c	A (4.2 K, 0 T)	~ 400	Critical current, I_c	kA (20 K, 12 T)	10
Critical current, I_c	A (4.2 K, 12 T)	~ 100			

Data compiled from [29]

Higher operating temperature is attractive as it brings down the cryogenic cost. The conductor had 729 round strands of Bi-2212, each of diameter 0.8 mm, fabricated in a configuration of $3 \times 3 \times 81$ strands with twist pitches of 20 mm, 60 mm and 550 mm, respectively, in three stages. The cable is heat treated after the final configuration and coated with a layer of Pb solder. The Pb solder has large heat capacity at 20 K, matching with the heat capacity of supercritical helium (SHe) which provides good thermal stability to the conductor. These Ag-cladded strands had an outer layer of a silver alloy of the type AgMgSb which provided strong mechanical support to the strands. The impressive performance of these cables at 20 K, 12 T gave good impetus to further development of Bi-2212 as a high-field conductor.

6.3.2 Bubble Formation in PIT Bi-2212 Wire Filaments and Current Blockage

Even though the isotropic flexible round wires of Bi-2212 with high irreversible field ($B_{irr} = \sim 100$ T) meet most criteria of a practical superconductor and appear to be moving consistently towards its dominance over its competitors, yet it has not attained its full potential as the J_c had been found limited by filament connectivity. The subtle nature of this connectivity was revealed by Kametani et al. [30] through a comprehensive microstructural study on Bi-2212 round wires during the formation of 2212 phase in various stages of heat treatment. As discussed earlier, partial melting of Bi-2212 phase is critical to achieve high J_c in this material. The temperature of Bi-2212 is raised above the peritectic temperature whereby a liquid is formed which contains all the constituent elements, Ag, solid alkaline earth cuprate (AEC) $(Sr, Ca)_{14}\ Cu_{24}\ O_x$ and copper free (CF) $Bi_9\ (Sr, Ca)_{16}\ O_x$ phases. During slow cool-down, this mixture solidifies by nucleation of Bi-2212 grains below $\sim$ 872 °C. Controlling composition and cooling rate does enhance J_c to some extent, but major issue of poor connectivity of the filaments remained unresolved for long. Round wires of Bi-2212 have an added advantage that it can be manufactured in long lengths by inexpensive powder-in-tube (PIT) process [30]. One inherent problem with the PIT technique is however the porosity of the material which may vary from 30 to 40% and is one of the reasons for the degradation of J_c. The authors carried out studies on a variety of wires with different configurations supplied by OST (now Bruker OST).

What Kametani et al. found through their microstructural investigations was startling. They found that the porosity in the unreacted wire agglomerated into bubbles during the heat treatment. The carbon, hydrogen from powder and sheath may lead to the formation of gas-filled bubbles. These bubbles divided the filaments in discrete sections reducing the effective cross section of the filaments at bubble spots. In other words, the grain-to-grain connectivity is diminished intermittently. Surprisingly these bubbles do not disappear during subsequent heat treatment but are only partially filled by Bi-2212 grains as the Bi-2212 phase is formed during cooling. The SEM picture of the transverse and longitudinal cross section of the

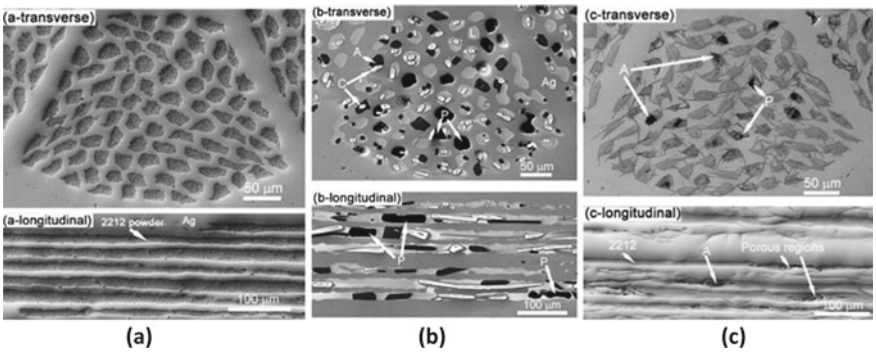

Fig. 6.13 SEM pictures of the 85 × 7 wires at various stages of heat treatment: **a** as-drawn, unreacted state, **b** Quenched from the melt region at 872 °C, **c** fully processed state. Transverse and longitudinal cross sections are shown for each stage. L = liquid; A = AEC (Alkaline earth cuprate); C = CF (Cu-free) and P = porosity [30]. With the permission of IOP

same wire after it was quenched from the melt at 872 °C but before Bi-2212 begins to form reveals a frozen liquid phase containing ~5 at % Ag, the alkaline earth cuprate (AEC) and copper free (CF) phases. The key feature of the quenched (from the melt) wire is the presence of bubbles. These bubbles are completely hollow spaces. Some of them are spherical of diameter approximately 20 μm, and others appear to have agglomerated into 50–200 μm long bubbles On cooling, AEC and CF react with the liquid to form plate-like Bi-2212 grains, but this reaction forming 2212 is rarely completed, leaving residual unreacted AEC and CF phases in the fully processed wire. Figure 6.13 is the SEM picture of the longitudinal cross section of the same wire after it was fully processed, that is fully reacted and cooled down. The micrograph of the fully processed wire in the figure still shows the presence of bubbles though reduced in number. These bubbles thus prevent the full realization of high J_c in Bi-2212 conductors.

The longitudinal cross section of a filament extracted by etching away silver from the Bi-2212 wire quenched from 867 °C, just above the onset temperature of Bi-2212 phase re-growth, shows large bubbles. These bubbles fill the filament diameter almost completely at many places with a quite non-uniform distribution as seen from Fig. 6.14. The average separation between the bubbles is about 140 μm. The SEM micrograph also reveals that the bubbles are not re-distributed, eliminated or reduced in size, as the bubble density (~ 70 bubbles/cm) remains almost unchanged. Instead, the bubbles are found to agglomerate out of residual porosity of the filaments in the melt phase. Bubbles are not removed during the heat treatment. The current path in the filament is strongly suppressed resulting in a drop in J_c. During subsequent cooling, Bi-2212 grains start to grow inside the bubbles allowing filaments to carry current. Measured I_c = 120 A (4.2 K, sf) in the 27 × 7 wire does confirm current flow through the filaments as there is no current transfer from filament to filament in this wire, filaments being sparsely distributed. It can thus be concluded from

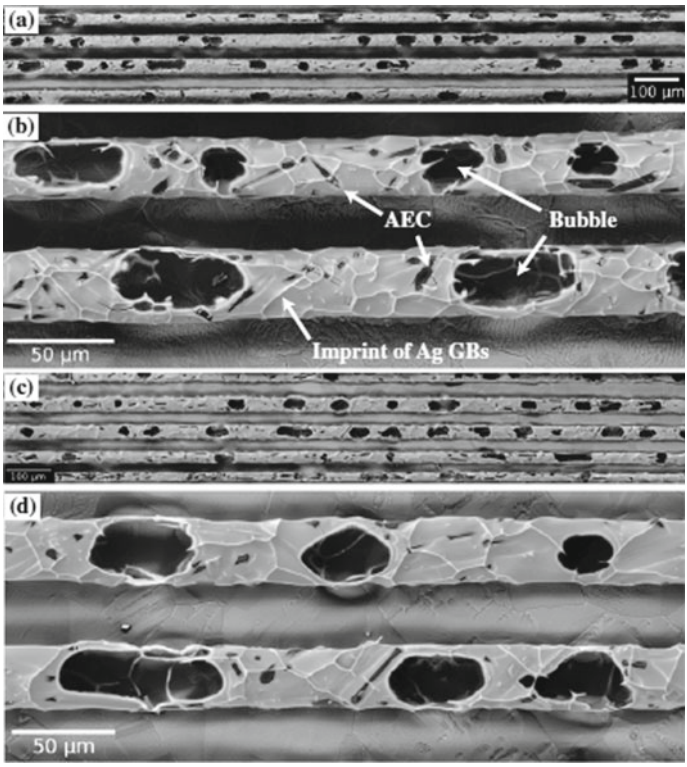

Fig. 6.14 SEM pictures of the filaments in the 27 × 7 wires **a**, **b** quenched from the melt state at 887 °C, **c**, **d** quenched from 867 °C, just above the Bi2212 re-formation onset temperature. Large bubbles almost completely fill the filament diameter at many places with a quite non-uniform distribution. *Courtesy* Fumitake Kametani

these microstructural studies that the bubbles agglomerated out of porosity in Bi-2212 filaments during melt phase are the key factor limiting the current density in round PIT multifilamentary Bi-2212 wires. Bubbles block the continuous current path through individual Bi-2212 filament and force current to flow through Bi-2212 grains that span the bubbles or through a thin Bi-2212 layer at the interface between the bubble and the Ag matrix. Elimination of bubbles thus is essential to achieve high J_c in Bi-2212 round wires.

6.3.3 High J_c in Round Bi-2212 Wires Through Over-Pressure Heat Treatment

The microstructural investigations discussed in the previous section have clearly established the fact that mass density of the filaments in a PIT Bi-2212 wires remained

a bottle neck in raising the J_c in these wires to its expected value. Miao et al. [31] at OST in collaboration with ASC-NHMFL were able to densify the Bi-2212 filaments in as-drawn wire prior to melting stage by employing the process of swaging to 90% corresponding to a swaging area reduction of 20%. The cold isostatic pressing (CIP) at pressures up to 1400 MPa raised the core density of the powder to above 90% of the theoretical value. OST manufactured high J_e Bi-2212 round wires in several configurations depending on the current requirement. OST used Nexans granulate powder with the optimized composition of $Bi_{2.17}$ $Sr_{1.94}$ $Ca_{0.89}$ $Cu_{1.98}$ O_x for all wire fabrication. The configurations of the wires were of the type: 19 × 36, 37 × 18, 85 × 18, 121 × 18 with wire diameters of 0.8 mm, 1.2 mm and 1.4 mm, respectively. Since the filament diameter was kept at the optimum value of 15 μm, the number of filaments was increased as per the current requirement of the wire. Wire diameter is thus increased for carrying high current.

Microstructural studies at OST reveal that the as-drawn wire samples quenched from the melt show many large (filament-sized) bubbles. However, after CIPing (cold isostatic pressing) at 650 MPa, fewer bubbles are seen during the melting process. The 0.8 mm diameter 37 × 18 wire does show reduced void fraction in the melted filaments which results in an increase of J_c by a factor of two. A J_e = 320 A/mm^2 (4.2 K, 15 T) was obtained in the as-drawn wires which increased to 470 A/mm^2 (4.2 K, 15 T) after core densification by swaging and CIPing. All the Bi-2212/Ag wires were heat treated using a partial melt-solidification process under flowing oxygen at 1 atmosphere. To improve the J_e further, an over-pressure heat treatment was carried out at Applied Superconductivity Center of National High Magnetic Field Lab (ASC-NHMFL). This process prevents wire swelling during heat treatment and improves wire performance significantly. An engineering current density, J_e, of 550 A/mm^2 (4.2 K, 15 T) has been achieved in a 1.2 m long sample after CIPed at 650 MPa and heat treated at an over-pressure (OP) of 10 bar. Still higher J_e has been obtained at an over-pressure heat treatment at 100 bar. Twisting of the OP heat-treated Bi-2212 has been found to reduce AC loss significantly without any degradation of the critical current.

6.3.4 Isotropic Round OP Bi-2212 Wires Generate a Field of 33.6 T

The finding of Miao et al. [31] at OST that bubble formation in Bi-2212 round wires during the melt phase limits the J_c and that these can be eliminated though over-pressure heat treatment turned out to be a game changer. Bi-2212 though does not have macroscopic texture and contains many high-angle grain boundaries (HAGBs), yet attains a very high J_c of 2500 A/mm^2 (4.2 K, 20 T) in PIT round wires heat-treated at high pressure (10–100 bar). Larbalestier et al. [32] at ASC-NHMFL in collaboration with CERN developed PIT Bi-2212 flexible round wires under 100 bar over-pressure which carried a J_e = 900 A/mm^2 (4.2 K, 5 T). The wire used for winding

a small magnet produced a magnetic field of 2.6 T in a background field of 31 T, thus generating a total of 33.6 T field, a record for Bi-2212. This demonstrates that grain boundary limitations to high J_c can be overcome by resorting to alternate technique of over-pressure heat treatment. This has been a most interesting development, and we will like to discuss it in detail.

The Bi-2212 round wire was produced by the PIT process using the methods of swaging and CIP for densification. The wire had the 37 × 18 configuration, that is, 18 strands each consisting of 37 filaments of 15 μm diameter embedded in high-purity Ag matrix which in turn is cladded with a Ag + 0.2 wt. % Mg sheath for increased mechanical strength. The filaments are composed of Bi-2212 powder which needs to be melted to create full continuity along each filament. During the molten stage, however, large bubbles are formed in filaments which block the current paths along the filaments. These bubbles can be seen clearly in Fig. 6.15c in samples quenched from the molten stage. After full heat treatment, these bubbles are generally not visible because Bi-2212 grains 10–40 μm in length grow across the bubbles, thus providing very poor grain connectivity which reduces the long range J_c. Figure 6.15d, e shows the two topographic views (after 45° rotation) of longitudinal cross section of a single filament of the fully heat-treated wires. Highly aspected Bi-2212 grains can be seen in the figure. Figure 6.15f is the electron backscatter diffraction (EBSD) image of a polished dense filament section. The colours indicate grain orientation. Although the EBSD image depicts local grain-to-grain texture, multiple HAGBs and Bi-2201 phase formed out of residual liquid, yet the J_c of the wire is high. One important finding of these studies is therefore that the HAGBs do not obstruct reaching high J_c in this material. This figure also shows the crystallographic details of the reacted filament and the orientations of the grains. The melt stage is followed by the final heat treatment and cooling which initiates the re-growth of Bi-2212 phase with large grains.

The above microstructural studies strongly suggest that to achieve the best J_c value in Bi-2212 wires, the formation of bubbles in the filaments has to be prevented. The solution lies in applying over-pressure to the wire during heat treatment. Over-pressure will also prevent creep de-densification caused by the internal gas pressure during heat treatment at 1 bar. Heat treatment under over-pressure densifies 2212 phase making use of creep of Ag and also enhances the mechanical and superconducting performance of the wire. Wire samples were sealed at the two ends so that the gas generated internally during heating does not escape out as it would be in long lengths. Bi-2212 densities greater than 95% were attained for pressure > 50 bar heat reaction. Figure 6.16 shows how the J_e continuously increases with over-pressure up to 100 bar at which J_e reaches a value of ~ 1000 A/mm^2 (4.2 K, 5 T). X-ray tomographs of the 1 and 100 bar pressured samples show the deep contrast between the de-densified 1 bar sample and almost fully and uniformly densified 100 bar pressurized sample. Figure 6.16 shows that even though Bi-2212 occupies just about 25% of the total cross section of the wire, yet the J_e attains a value ~ 1000 A/mm^2 (4.2 K, 5 T) in 100 bar OP processed Bi-2212 wire. The J_c of Bi-2212 wires is ~ 4000 A/mm^2 which is higher than the J_c of optimized Nb-Ti at 4.2 K and 5 T (Fig. 6.17).

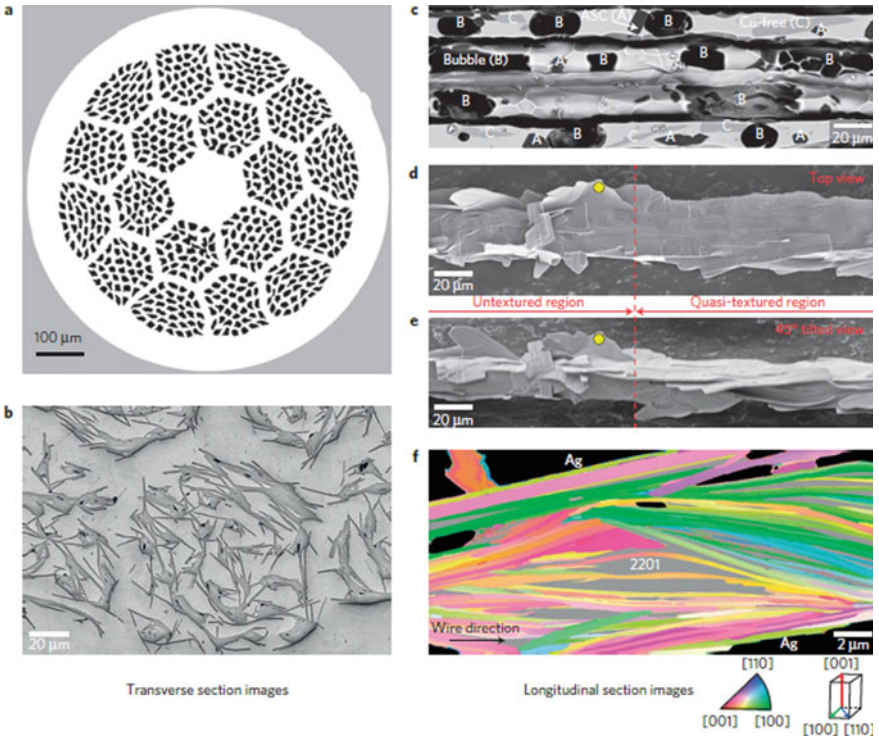

Fig. 6.15 **a** Cross section of as-drawn 0.8 mm diameter Bi-2212 wire of 37 × 18 configuration with 666 filaments of 15 µm dia, **b** cross section of the same wire after final heat treatment showing Bi-2212 grains of large aspect ratio formed during final heat treatment, **c** longitudinal cross section of the wire during the molten stage showing the presence of large bubbles agglomerated out of porosity in the filaments, **d** and **e** longitudinal cross section of a single filament after the final heat treatment showing Bi-2212 grains with large aspect ratio. The yellow circular dot is the same on the filament in two views rotated by 45°, **f** electron backscatter diffraction (EBSD) image of a polished dense filament section. The colours correspond to the orientation of the grains. The EBSD image confirms local grain-to-grain texture, multiple HAGBs and residual liquid that has converted to Bi-2201 phase. Yet the wire has high J_c. The filaments shown in **c**–**e** were exposed by removing the Ag matrix by etching [32]. Copyright © Springer Nature, with permission from Springer Nature

Impressive J_e values, 700 A (4.2 K, 15 T), 630 A (4.2 K, 20 T) and 500 A (4.2 K, 30 T), obtained in round OP processed Bi-2212 wires made this material attractive enough for winding high-field NMR magnets beyond the limit of 1 GHz proton resonance put by Nb_3Sn conductor. For a high-field magnet, high J_e is important to keep the magnet compact, the central field, B_0, being given by

$$B_0 = 2\mu_0 J_e d \tag{6.1}$$

where d is the winding width. High J_e magnet will have low inductance and therefore low stored energy density $\left(= B^2/2\mu_0\right)$ which helps in managing the quench.

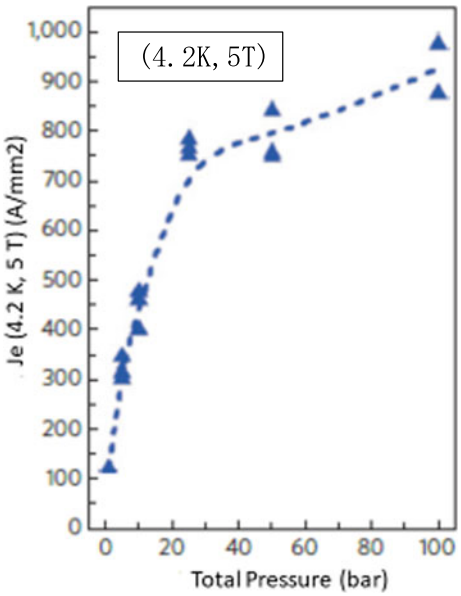

Fig. 6.16 Overpressure dependence of the engineering current density, J_e (4.2 K, 5 T). The over-pressure is applied during the heat treatment of Bi-2212 wire [32]. Copyright © Springer Nature, with permission from Springer Nature

Compact size magnet (low winding thickness) also minimizes the Hoop stresses given by

$$\sigma_{\text{Hoop}} = B_0 J_e R \tag{6.2}$$

where B_0 is the central field, J_e current density in the winding and R is the winding radius. Too high a J_e value can also cause problem during quench because of the slow quench velocities of HTS conductors and the need for restricting current density in the Cu/Ag stabilizer generating heat during magnet quench. As mentioned earlier, the Applied Superconductivity Centre of the National High Magnetic Field Laboratory (ASC-NHMFL) had built a small insert magnet using 30 m of this Bi-2212 round OP processed wire which produced a field of 2.6 T in a background field of 31 T. In coming years, the popularity of Bi-2212 conductors is bound to grow fast once long lengths are commercially produced. The wire will be much cheaper than other HTS wires especially REBCO-coated conductors. Only drawback at the present time is that these wires are of 'wind-and-react' type but this technology is well developed for Nb_3Sn.

6.3.5 AC Loss in Bi-2212 Cable-In-Conduit Conductors

The excellent performance of the round OP processed Bi-2212 wires caught the attention of the superconductor community to produce Bi-2212 cables for high current

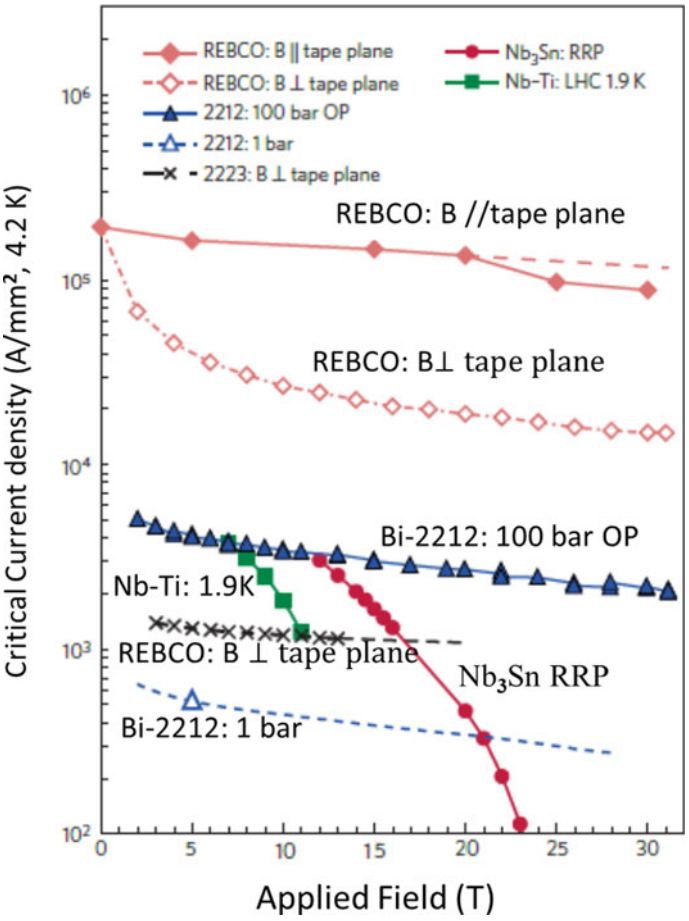

Fig. 6.17 Comparison of J_e of the best-known practical superconductors. Note that the J_c of Bi-2212 OP 100 bar at 4000 A/mm^2 (4.2 K, 5 T) is slightly higher than in Nb-Ti (1.9 K, 5 T) and superior to Nb_3Sn in fields above 20 T [32]. Copyright © Springer Nature, with permission from Springer Nature

cable applications. Thus, Quin et al. [33] at the Institute of Plasma Physics (IPP-CAS) designed and fabricated a sub-size cable consisting of 42 strands in cable-in conduit conductor (CICC) architecture and reported AC loss measurements. The conductor is being developed for their proposed 'Chinese Fusion Engineering Test Reactor' (CFTER) which will need conductor producing field of 15 T in the central solenoid and the TF coils. This field is higher than the field of ITER magnets. The main issue in fabricating CICC is the degradation of critical current during cabling process because of the high strain sensitivity and brittleness of Bi-2212. Strands were made following the PIT technique. Every strand had 18 sub-strands each having 36 filaments. Forty-two strands were then twisted together in three stages

Table 6.10 Parametric specifications of the strand and the CICC sub-cable of Bi-2212. The sub-cable had 42 twisted strands in three stages with different twist pitches. Sub-cable is inserted in a Ag tube and finally jacketed in a casing

Strand specifications			Sub-cable specifications		
Parameter	Unit	Value	Parameter	Unit	Value
Diameter	mm	1.0	Number of strands		42
Matrix		Pure Ag	Layout		$2 \times 3x(6 + 1)$
Outer sheath		Ag + Mg	Twist pitch stage 1	mm	20
Filament No		36×18	Twist pitch stage 2	mm	50
Ag-Mg:Ag: Bi-2212		1.8:1:0.9	Twist pitch stage 3	mm	87
I_c (4.2 K, sf)	A	~ 400	Ic (4.2 K, sf)	kA	10
I_c (4.2 K, 12 T)	A	~ 146	Diameter no compaction	mm	10
			Diameter after compaction	mm	9.0
			Cladding material		Ag
			Jacket material		SS

Data compiled from [33]

$[2 \times 3 \times (6 + 1)]$ with different twist pitches. The cable was then inserted into Ag tube and finally in a SS jacket. Since the Bi-2212 has to be heat-treated in an oxygen environment, direct contact between Bi-2212 and the SS jacket has to be prevented. The Ag tube thus was used to separate the cable and SS jacket. The conductor was heat treated at 890 °C for 30 min, and then, the temperature reduced to 830 °C at the rate of 5 °C/h and kept at this temperature for 48 h under oxygen environment. The measured I_c of the cable was 13.1 kA (4.2 K, sf) some 15% lower than the expected value of 15.4 kA. The n-value was 12. The lower value of I_c might have been caused by strand deformation during processing or even during heat treatment. The specifications of the strand and the cable are given in Table 6.10.

AC loss measurements on Bi-2212 cable were carried out using VSM with magnetic field amplitude from − 3 T to + 3 T at different ramp rates at temperatures 4.2 K, 20 K and 50 K with magnetic field perpendicular and parallel to the sample axis. Since the hysteresis loss per cycle at low excitation (< 100 mT/s) is independent of the ramp rate, the coupling loss was separated from the hysteresis loss by applying different frequencies. The measured AC loss data yield the coupling loss time constant with perpendicular magnetic field as 121, 58 and 5.4 ms for 4.2, 20 and 50 K, respectively. For parallel magnetic field, these values turned out to be 4.58, 4.09 and 0.71 ms for 4.2, 20 and 50 K, respectively. The coupling loss time constant of Bi-2212 at 4.2 K was found roughly one order of magnitude higher than that of Nb_3Sn wire. This must be due to the much lower matrix (silver) resistivity in Bi2212 wire than the matrix (bronze) in Nb_3Sn wire. Uniformity in the wire was also confirmed by the AC loss measurements on different samples of this wire which yielded same results. The AC loss measurements were also carried out on one cable section under applied transverse load, to simulate Lorentz force, but no significant

effect was observed on the AC losses up to a load of 53 kN/m. The hysteresis loss as well as the coupling loss remained unchanged. These results auger well for the application of Bi-2212 CICC cables to fusion magnets.

6.3.6 PIT-OPHT Bi-2212 Rutherford Cable

The invention of the over-pressure heat treatment (OPHT) by Kametani et al. [30] appeared to have solved the problem of gas bubbles in round Bi-2212 wires once for all and enabled to reach highest possible J_e. Soon, a new problem was detected by Zhang et al. [34] that of the leakage of Bi-2212 out of the Ag cladding during the melt phase of the heat treatment. This leakage was detected when the racetrack coil was being heat treated after the winding. The critical current was found to be disappointingly low compared to value specified by OST when racetrack coils were tested for their performance. Three racetrack coils, RC1, RC2 and RC3, were wound at Lawrence Berkeley National Laboratory (LBNL) using Rutherford cable of the Bi-2212 PIT-OPHT wire supplied by OST. The Bi-2212 Rutherford cable had 17 strands each of diameter 0.8 mm with the architecture of 36 × 19 and 18 × 37 and had the dimensions of 7.8 mm × 1.44 mm. The racetrack coils were wound and heat treated following the OPHT process. The transverse cross sections of the two strands and the longitudinal cross section of the Rutherford cable are shown in Fig. 6.18.

Being the first attempt to use over-pressure heat treatment (OPHT) processed conductor for accelerator coils, many problems came to the fore. First problem was the Rutherford cable itself because when the strands are twisted and rolled, the filaments get deformed heavily especially at the edges of the cable. This degrades the J_c of the cable. Reacting the coils, with large mass, under high density, high-pressure (25–50 bar) gas mixture of Ar and O_2 (partial pressure 1 bar) in SS or Inconel fixtures of fixed shape was another problem as these materials may react with O_2. Choosing the peak reaction temperature and duration of melt stage also needs great expertise. For OPHT, the coils were heat treated at 450 °C for 4 h in flowing O_2 at 1 bar to get rid of the organic sizing in the braided Mullite insulation braided sleeve. The ends of all the strands were sealed to prevent the escape of the gas during heat treatment. The coils, each weighing ~ 8.5 kg and measuring 370 mm × 120 mm × 31 mm, were then reacted in a NHMFL over-pressure furnace at 892 °C in a flowing mixture of Ar and O_2 (Ar:O_2 = 49:1).

Three racetrack coils, RC1, RC2 and RC3, were built, reacted and tested for their quench currents. The quench currents of RC1 and RC2 reached 5268 A and 5781 A, respectively. The surprise however was that these coils displayed leakage of Bi-2212 to the surface at several places. RC1 and RC2 were built using the cables with strands in configuration (36 × 19) and (18 × 37), respectively. RC3 used the same cable as used for coil RC2, but the cable used in Rc3 was painted with several coats of TiO_2-polymer slurry before being insulated with the same Mullite sleeve as used for the cables for RC1 and RC2. After eliminating most of the leakages using this modified insulation scheme, the quench current of RC3 reached 6485 A. This value is about

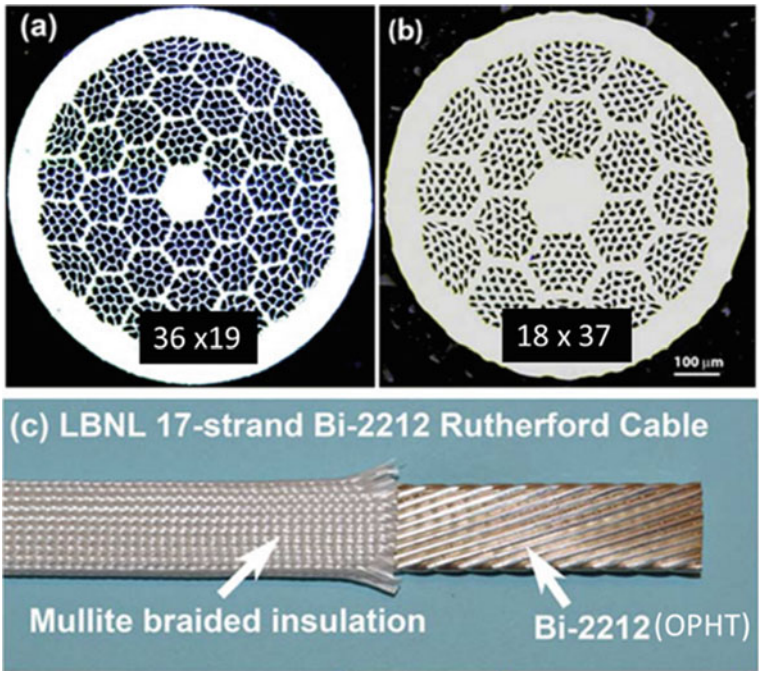

Fig. 6.18 **a** Transverse cross section of the Bi-2212 OPHT strand used in racetrack coil, RC1, with 36 bundles of 19 filaments, **b** Transverse cross section of the Bi-2212 OPHT conductor used in racetrack coils, RC2 and RC3, with 18 bundles of 37 filaments, **c** Rutherford cable with 17 Bi-2212 OPHT strands shown in (**a**) and (**b**) covered by Mullite braided insulation sleeve [30]. With the permission from IOP

three times the average quench current of a few racetrack coils tested previously, using Rutherford cables fabricated in the conventional 1 bar heat treatment. Another interesting result of these studies is that the quench current in the Bi-2212 racetrack coils increases with ramp rate in contrast with Nb-Ti and Nb_3Sn coils which show a decrease in quench current with increasing ramp rate. These results not only confirm the efficacy of OPHT technology but also demonstrate that Bi-2212 conductor is superior to Nb-Ti and Nb_3Sn in many respects and could be a material of choice in near future.

6.4 The Bi-2223 Conductors

The Bi-2212 conductors discussed in the previous section are indeed very promising conductors that are available as round wires with twisted filaments and a biaxial melt-growth texture. The disadvantage is however that the wire has to be reacted after coil

winding at around 888° C within only a few degrees Celsius window in an oxygen-rich environment. The selection of electrical insulation and the coil-former material thus becomes very demanding. Furthermore, to achieve high J_c and densification > 95%, the final heat treatment has to be carried out at an over-pressure of 25 to 100 bar in an oxygen-inert gas mixture which adds to complications. Bi-2223 on the other hand has many advantages and in fact was the first commercially available 'first generation HTS conductor'. It was produced commercially by Sumitomo Electric Industries (SEI) within a year of the discovery of this material by Hiroshi Maeda in 1987 [35]. Besides having high critical magnetic field, Bi-2223 scores over Bi-2212 as its T_c is much higher (110 K). Even though it is a tape conductor with anisotropic properties, yet it has sufficiently high critical current density in the $\perp$ field direction (B $\perp$ ab plane). Grain texture and high density in Bi-2223 are achieved by rolling and sintering under pressure. Great advantage with Bi-2223 conductor is that in contrast to Bi-2212, this conductor is available in reacted tape form. The tapes are produced through the standard PIT technique involving multiple drawing and rolling followed by sintering under pressure. Similar to Bi-2212, the matrix used in Bi-2223 is mechanically weak Ag/Ag-alloy in which the Bi-2223 filaments are embedded. For high strength, Bi-2223 tapes are laminated with either SS or Cu-alloy.

The Bi-2223 tapes produced commercially by Sumitomo Electric [36] during mid 1990s had critical current of a few tens of amperes only. Soon, American Superconductor (AMSC) started making Bi-2223 tapes and by the end of the 1990s achieved critical current of 150 A. In 2005, Otto et al. [37] at AMSC reported a two-fold increase in the size of the axial strain window with reinforcing materials bonded to the outside of Bi-2223/Ag tape while retaining the critical current. Expecting a good future of the material, a number of companies came into being in the beginning of 2000. These companies were Intermagnetics General (USA), Trithor GmbH (Germany), Nordic Superconductor Technologies (Denmark) and Innova Superconductor Technology (China). In 2005 Sumitomo [38] introduced controlled over-pressure (CT-OP) sintering process which increased the critical current, I_c, of Bi-2223 tape wires by more than 30%, The CT-OP process increases the relative density of the core to almost 100% which in turn leads to higher phase purity, higher grain alignment and better grain connectivity than in tapes made with a conventional normal pressure sintering process. Densification of the core also prevents liquid nitrogen diffusion in the tape during long-term exposure to liquid nitrogen when used in power cable applications. The CT-OP processed Bi-2223 wire also prevents ballooning which may occur during warming to room temperature as the trapped nitrogen expands. Production yield was increased over 1 km and I_c exceeded 200 A (77 K, sf). Bi-2223 was used in current leads and inserts for high-field magnets, but use in electrotechnical devices remained limited to demonstration stage only. Around the same time, interest grew in REBCO-coated conductors, already discussed in Sect. 6.2, and research activity in Bi-2223 reduced gradually. Sumitomo is now the only manufacturer producing Bi-2223 wires in km lengths with I_c > 200 A–250 A in piece length of few hundred metres. High-current tapes are usually composed of non-twisted filaments in Ag matrix.

6.4.1 The Controlled Over-Pressure (CT-OP) Processed Bi-2223 Superconductors

Sumitomo Electric had continued to improve the superconducting parameters of the Bi-2223 tape wires especially the critical current, I_c, and the mechanical strength so as to make the wire suitable for a range of applications and named these wires as 'dynamically innovative' (DI-BSCCO) wires. In earlier publications, these wires were, however, referred to as 'dramatically innovative' so DI-BSCCO still stays. The I_c in Bi-2223 wires increased significantly after the introduction of the controlled over-pressure (CT-OP) sintering process in 2004 [38]. In long length wires of up to 2 km and with a cross section of 1 mm^2, the I_c reached 180 A (77 K, sf) and in short length as high as 200 A. This value of I_c is sufficient for use in various equipment such as high-field magnets, motors and cables for power transmission. The manufacturing process of DI-BSCCO wires [39] is based upon the PIT technique. Precursor powder of $(BiPb)_2Sr_2Ca_2Cu_3O_x$ is packed in a Ag tube which is rolled and drawn into thin rods. A certain number of these drawn thin rods are bundled together and inserted into an Ag-alloy tube. This composite tube is rolled, drawn and flat rolled into the form of thin tape. The advantage of this process is that each step of processing can be controlled easily which makes this process most suitable for the production of high-homogeneity long wires. Sumitomo Electric employed the controlled over-pressure (CT-OP) sintering process at the second stage of sintering by applying a gas pressure up to 30 MPa to the tape and controlling the temperature and oxygen partial pressure. The superconducting parameters of Bi-2223 improve dramatically. We recall here that a Bi-2223 unit cell has a layered structure in which the Cu-O layer is sandwiched between two insulating layers. Besides, Bi-2223 cleaves easily because of the somewhat weak bonding between the double Bi-O layers within each insulating layer. Thus, even though the filaments are not very ductile, yet they along with Ag/Ag-alloy are comfortably drawn. During the rolling process, the filaments get oriented along the c-axis.

High value of critical current, I_c, of a practical superconductor, no doubt, is the single most important parameter, yet for a variety of applications, mechanical strength and low AC losses become a priority. To meet such requirements, Sumitomo Electric manufactures diverse variety of DI-BSCCO conductors [40] code named Type H (conventional wire with high I_c), Type S (slim), Type HT (high critical current and tough), Type ST (slim and tough), Type AC (for AC applications) and Type G (wire with Ag + Au 5.4 wt. % matrix) for current leads. Type H is the conventional high I_c wire of 1 mm^2 cross section processed by CT-OP method. Type S is a slim wire with 50% cross section of the core material and half the cost. Type HT wires are the high-current wires toughened by laminating the basic H Type wire with metallic tapes of SS, Cu-alloy or Ni-alloy. These wires have increased mechanical strength. Type HT-SS has the lamination of stainless steel, Type HT-CA has the lamination with Cu-alloy, and wire HT-NX has the lamination with Ni-alloy and has the maximum tensile strength. These wires have the same I_c values as Type H but display unusual high mechanical strength. Type AC wire has the lowest AC loss and is ideal for AC

applications. Table 6.11 lists these wires with their important parameters. Type G wire though processed by CT-OP technique but has Ag-Au (5.4 wt.%) matrix and is more expensive. This wire has very low thermal conductivity compared to the basic Type H wire and has been used widely for current leads in superconducting magnet

Table 6.11 Specifications of different types of DI-Bi-2223 wires manufactured by Sumitomo Electric Industries by CT-OP process [40]

		Type H	Type HT-SS	Type HT-CA	Type HT-NX	Type G
Parameters	Unit	High current	High current and toughened with SS	High current and toughened with Cu-alloy	High current and toughened with Ni-alloy	Low thermal conduct
Width of the tape	mm	4.3	4.5	4.5	4.5	4.3
Thickness of the tape	mm	0.23	0.29	0.34	0.31	0.23
Length	m	2000	Up to 500			
Matrix		Ag	Ag	Ag	Ag	Ag + Au 5.4 wt.%
Critical current, I_c	A	200	200	200	200	200
Critical tensile strength @ 77 K	MPa	130	270	250	400	130
Critical tensile strain @77 K	%	0.2	0.4	0.3	0.5	
Critical bending diameter @ room temperature	mm	80	60	60	40	80
Critical wire tension @ room temperature	N	≥ 80	$> \geq 230$	$\geq > 280$		
Critical double bending diameter @ room temperature	mm	180	140	140		80

Data compiled from Brochure SEI, Courtesy: Yuichi Yamada

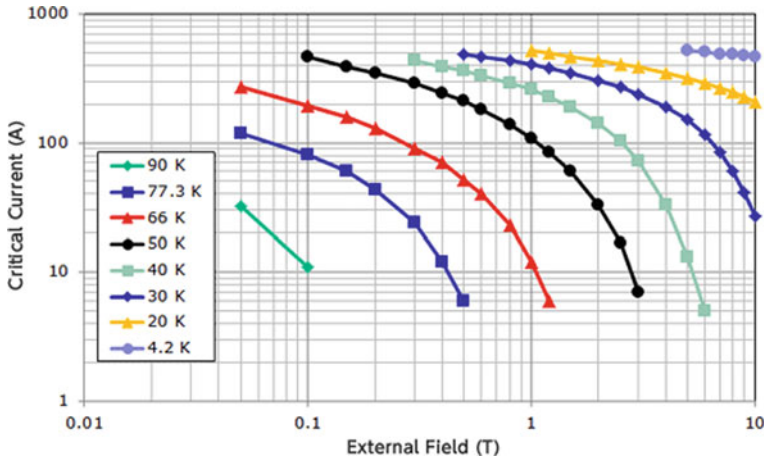

Fig. 6.19 Dependence of Ic in Type H and Type HT DI-Bi-2223 tape wires on external applied magnetic field up to 10 T at different temperature ranging between 4.2 and 90 K [38]. *Courtesy* Yuichi Yamada, Sumitomo Electric Industries

systems. SEI data show that at 50 K the thermal conductivity of Type G wire is only ~ 70 W/m/K compared to ~ 310 W/m/K in Type H wire. These values at 100 K read 100 W/m/K and 250 W/m/K, respectively, for these two types of Bi-2223 wires. The 70 kA current leads developed by KIT for ITER–TF coils are one such example.

Figure 6.19 shows the dependence of I_c in Type H and Type HT DI-Bi-2223 wires on external magnetic field up to 10 T at different temperatures ranging between 4.2 and 90 K [40]. As expected, at 77 K, the critical current drops rather fast with increasing magnetic field, but as the operating temperature is reduced, the curves tend to become flat, and at 4.2 K, the drop in I_c with increasing field is insignificant. This is a unique feature of all the HTS conductors as evidenced from Fig. 6.19 because of very high B_{c2} in the HTS. The I_c of Type H and Type HT at 4.2 K and 10 T field is > 450 A/mm^2 an impressive value indeed.

Figure 6.20 shows the temperature dependence of the thermal conductivity of DI-2223 tape wires manufactured by Sumitomo Electric Industries. Type G wires with Ag + Au (5.4 wt.%) matrix have the lowest value of the thermal conductivity at all temperatures. At 10 K, the thermal conductivity of G type wire is about 20 W/m/K compared to about 800 W/m/K for DI-Bi2223 H type wires. This wire has been especially designed and produced by Sumitomo for current leads and has been very popular for use in magnet systems. IPP of China has used DI-Bi-2223 type G wires for fabricating about 60 current leads of current capacities ranging between 10 and 68 kA for ITER magnets. LHC (CERN) too had used these wires for fabricating over a thousand current leads for charging its fleet of dipoles, quadrupole and correction magnets and saved a very substantial amount of power.

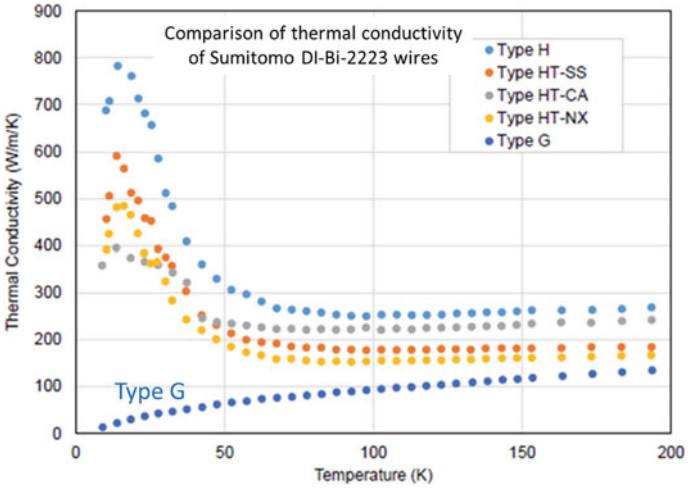

Fig. 6.20 Temperature dependence of thermal conductivity of various types of DI-Bi-2223 tape wires. Type G wires with Ag + Au (5.4 wt.%) have the minimum thermal conductivity at all temperature and are the most suitable wires for fabricating current leads for magnet systems [38]. *Courtesy* Yuichi Yamada, Sumitomo Electric Industries

6.4.2 Suitability of DI-Bi-2223 for High-Field Magnets

DI-(Bi-2223) wires became quite attractive for use in inserts of magnets for producing magnetic field in the range of 30 T. The wire fulfils the requirements of high I_c and high mechanical strength. Excellent grain texture and high densification of the Bi-2223 during rolling and CT-OP sintering led to high I_c and metallic lamination provided enough tensile strength. The wire HT-NX has a critical strength as much as 400 MPa (@ 77 K) for Ni-alloy lamination (Table 6.12). Godeke et al. [41] have carried out a detailed study on various parameters of this wire relevant to its use as magnet insert. The authors have characterized this wire for stress–strain behaviour under EM loads in magnetic field ranging up to 31.2 T and a number of small 20

Table 6.12 Normalized AC losses in Type H and Type AC Bi-2223/Ag wires processed by CT-OP technique [40] at SEI

Wire type	Width	Thickness	Pitch length P_L	Critical current I_c	AC loss (W/kA/m)	
	mm	mm	mm	A	B⊥@ 0.2 T, (77 K, 50 Hz)	B// @ 0.07 T (77 K, 50 Hz)
Type AC	2.0	0.17	3	32	21	0.16
	2.4	0.18	8	53	17	0.17
Type H	4.0	0.23	–	180	20	0.57

Data compiled from Brochure of SEI, courtesy Yuichi Yamada

turn coils in a background field going up to 17 T. The critical stress and strain limits observed in longitudinal tensile tests are 516 MPa and 0.57%, respectively. Other tests performed were single- and double-bend tests, coil sections with a single-pitch and a single-pitch plus s-bend through low-temperature tensile experiments. The maximum allowable stress and strain limits however were substantially higher in bending, and coil sections and 20-turn coils. Calculations under elastic limits show much higher strain limits going up to 0.92% in other formations, namely pure bending, large hoop stress with small bending and large bending strain with small hoop strain. This value of strain limit can thus be taken into account for coils with single bend during winding together with hoop stress. This strain limit is little more than in REBCO tapes (0.65%), but REBCO tape has higher critical stress if the copper fraction in the cross section reduced which is the case in magnets without insulation. In view of sufficiently high critical current and excellent stress–strain behaviour displayed by Sumitomo's DI-(HT-NX) wire, it is most suitable to be used as magnet insert for producing field of 30 T. The added advantage is that it can be obtained in reacted form with insulation.

6.4.3 Low AC Loss Bi-2223 Conductors

The anisotropy of critical field and critical current which characterizes a HTS adds new dimension to AC loss estimations in these conductors. Thus, typical operating conditions like current and field parallel or perpendicular to the Cu-O plane impact AC losses. Bi-2223 has been a chosen material for AC applications like in transmission cables, motors and fault current limiters. We have seen that for low AC loss the conductor has to be divided in fine filaments in a metallic matrix (Ag in HTS) to minimize the hysteresis loss and twisted such that the induced magnetization currents which couple the filaments across the conducting matrix are attenuated and heat generation is minimized. It is known that the coupling loss is proportional to the square of the twist pitch. So, reducing the twist pitch to half will reduce the coupling loss by a factor of 4. SEI optimized the process parameters and produced low AC loss type slim wire with a twist pitch of 3 mm. The AC loss per unit length has been normalized by I_c, so that a comparison can be done equally on various samples with different I_c values. If the Ag fraction is same in all the samples, the critical current density, J_c, will be different in different samples. The coupling current corresponding to high J_c may not flow through the matrix because of a higher resistance. In such a case, the coupling loss is bound to decrease. It is because of this reason that the samples with different I_c have different AC losses even though all the samples are prepared by an identical process.

The normalized magnetization loss in Type AC wires, measured in an alternating parallel magnetic field of 0.07 T at a frequency of 50 Hz, is found to be about 0.12 W/kA/m/cycle which is almost one third of the loss in Type H wire. Further, the reduction of the twist pitch length (8–3 mm) results in bringing down the magnetization loss but only at lower frequencies. Loss reduction at higher frequencies is

however mainly due to the slimming of Type H wire to half the cross section. Fortunately, AC motors commonly use low frequencies ~ 20 Hz, and Type AC wires are ideal for use in AC motors and cables. The mechanical properties of the AC wires have been improved dynamically through lamination with SS tapes and supplied as a low AC and mechanically strong wire under the brand name—Type ACT wire.

6.4.4 A Comparison Between B-2212 and Bi-2223 Wires

The two siblings Bi-2212 and Bi-2223 appear to be in tough competition. Both have some advantages over the other. Bi-2212, besides having high J_c and high mechanical strength, is available in the form of isotropic round wire. Bi-2223 on the other hand has the advantage of having much higher T_c (110 K) and is available in reacted form. A comparative growth texture study has been carried out by Kametani et al. [42] on round Bi-2212 wires and flat Bi-2223 tape wires in relation to high critical current density, J_c. One can note two striking features of the two BSCCO superconductors in Fig. 6.21 which shows the dependence of the critical current density, J_c, on magnetic field, B, of the Bi-2223 tape and the Bi-2212 round wire. The field, B, was applied

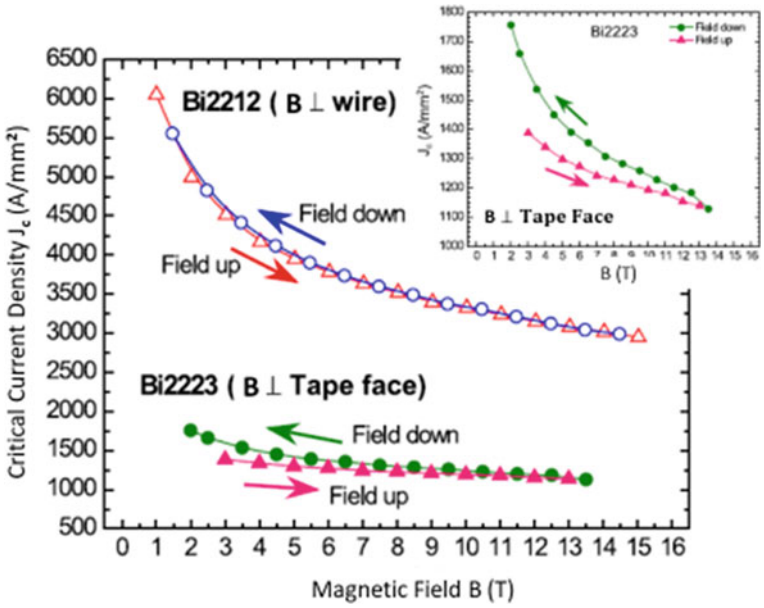

Fig. 6.21 Dependence of critical current density, J_c, on magnetic field of the Bi-2223 tape and the Bi-2212 round wire. The field B was applied normal to the wire axis for Bi-2212 and normal to the tape face for Bi-2223. The J_c of Bi-2212 round wire is bout 3 times larger than in Bi-2223 flat tape. J_c in Bi-2212 shows no hysteresis, whereas J_c in Bi-2223 shows hysteresis [42]. SpringerNature, Open access article under CCA, Kametani et al. https://doi.org/10.1038/Srep08285

normal to the wire axis for Bi-2212 and normal to the tape face for Bi-2223. J_c was measured in increasing field as well as in decreasing field. Apparently, the J_c of Bi-2212 round wire is bout 3 times larger than in Bi-2223 flat tape. Further, J_c in Bi-2212 shows no hysteresis, whereas J_c in Bi-2223 shows hysteresis in increasing and decreasing field. As expected, J_c is higher in decreasing field (inset of Fig. 6.21). The hysteresis observed in Bi-2223 tapes indicates the presence of weak links in the polycrystalline network. Surprisingly, the Bi-2212 round wire showed no hysteresis in J_c/B behaviour and thus no weak links, even though both the conductors were densified to ~ 95% by the same CT-OP process. Besides this, Bi-2223 is phase pure, and Bi-2212 is less phase pure because of the presence of larger AEC, Cu-free (CF) or Bi-2201 and void fraction.

Detailed microstructural studies by Kametani et al. revealed that the Bi-2212 grains are plate like in shape and similar in thickness to Bi-2223 grains but they are much longer, 300 mm almost 10 times the Bi-2223 grains. The lateral grain growth is however restricted by the constraint of the filaments. The dominant grain boundaries (GBs) in Bi-2223 are parallel to the ab planes. The grains in both the superconductors tend to stack on each other in a colony structure with all the grains having the same c-axis. A practical conductor is targeted to have an overall conductor current density, J_e, exceeding 300–500 A/mm^2 in a range of B and T of interest. No doubt, both Bi-2223 and Bi-2212 wires meet this requirement at 4.2 K in fields well over 20 T with filling factors of 40% for Bi-2223 and 25–30% for Bi-2212. However, for the future development of these materials, it is of great interest to understand what fraction of the superconductor cross section actually carries current. Since both the conductors are more than 95% dense having been heat treated under an external over-pressure, voids cannot be the current-limiting obstacles. The implication is that the GBs are responsible for the dominant current-limiting mechanism. It is very difficult to evaluate to what extent J_c contributed by flux pining within the grains is limited by the blockage of current by GBs, non-superconducting secondary phases, cracks or such other obstacles. The remarkable differences in the texture observed in the microstructural studies hint strongly that the distribution of the misorientations within the grain boundary network is the key to current limitating phenomenon in the two superconductors.

We should also consider that Bi-2212 round wire is not as perfectly biaxial as the REBCO-coated conductors in which grain misorientation in-plane and in out of plane is minimized to below 5°. Studies show that misorientation of the grain boundaries in Bi-2212 is normally 10°–15° which is higher than the critical angle, 2°–3°, found in thin film bicrystals with planar GBs parallel to the film normal. Notwithstanding this higher misorientation angle, the weak links are absent in Bi-2212 similar to in biaxially textured coated conductors, in contrast with Bi-2223. This would imply that Bi-2212 GBs are less obstructing. The presence of a unique biaxially aligned microstructure in high J_c Bi-2212 round wire suggests that it should be possible to tailor a melt-driven route for making round wires with high J_c from other HTS materials too.

Having discussed the J_c/B behaviour of the predominant practical HTSs, let us have a look at all the practical superconductors available to-date, where do they stand

vis-a-vis their applicability for building magnets. Figure 6.22 presents a comparison of the in-field engineering current density, J_e, of all the practical superconductors conventional (Nb-Ti and Nb_3Sn), MgB_2 and HTS (REBCO and BSCCO, 2212 and 2223). Evidently, REBCO conductors turn out to be the best practical conductors in high fields. Cables capable of transporting currents as high as 90 kA in high fields have been tested in the laboratory. The next best material could be the round wires of Bi-2212 superconductor which is expected to be cost-effective as well.

We can clearly learn from the above discussion that the performance of REBCO-coated conductor has improved to the extent that it has established itself as the high-field superconductor of the future. It is also hoped that it will be produced soon in longer lengths and at an economical cost. It is because of this confidence in this material that many large future projects, which will be using coated REBCO wires, have been launched. For example, CERN has begun study on a conceptual design of the future circular collider (FCC) which will use 20 T dipole magnets. The proposed muon collider project in the USA will need solenoids which will generate field in the range of 30–50 T. As discussed in previous sections DEMO, the future power fusion reactor is evaluating REBCO cables for its monstrous toroidal field (TF) coils. These conductors are slated to be used in higher range of temperature 30–50 K which will bring down cryogenic cost. No wonder, therefore, several companies have got involved in the production of high critical current REBCO conductors.

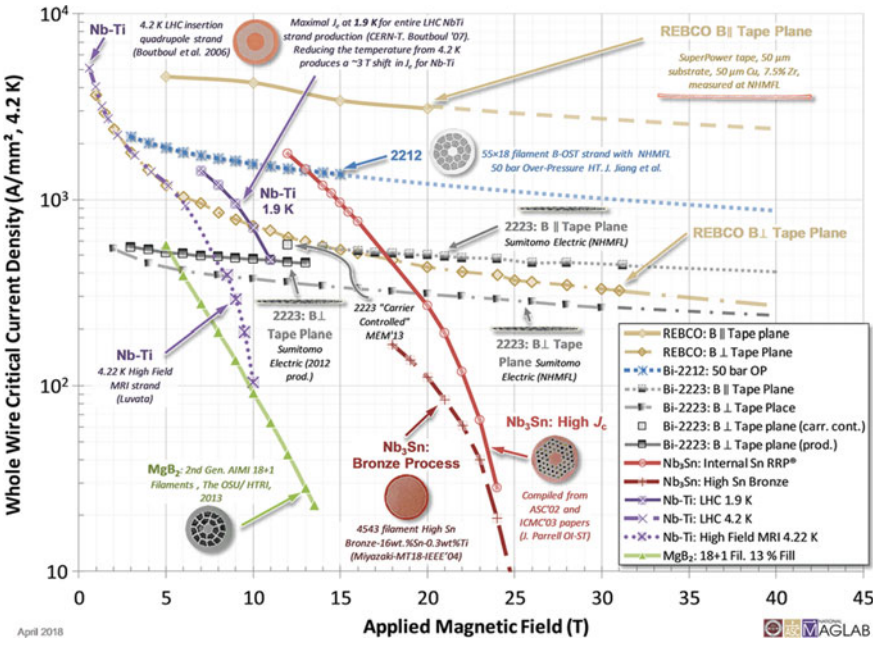

Fig. 6.22 Superiority of J_e of 2G REBCO-coated conductors prepared by IBAD or RABiTS over conventional superconductors, Nb-Ti and Nb_3Sn, at 4.2 K. BSCCO and MgB_2 too are left behind. *Courtesy* Peter J. Lee, National High Magnetic Field Laboratory

References

1. P. Chaudhuri, R.H. Koch, R.B. Laibowitz et al., Phys. Rev. Lett. **58**, 2684 (1987)
2. T.R. Dinger, T.K. Worthington, W.J. Gallagher, R.L. Sandstorm, Phys. Rev. Lett. **58**, 2687 (1987)
3. R.G. Sharma, Y.S. Reddy, S.R. Jha et al., Pramana-J. Phys. **30**, L75 (1988)
4. http://www.superpower-inc.com/content/2g-hts-wire
5. A. Sundaram, Y. Zhang, A.R. Knoll, D. Abraimov, P. Brownsey et al., Supercond. Sci. Technol. **29**, 104007 (2016)
6. V. Selvamanickam, M.H. Gharahcheshmeh, A. Xu, E. Galstyan et al., App. Phys. Lett. **106**, 032601 (2015)
7. V. Selvamanickam, M.H. Gharahcheshmeh, A. Xu, Y. Zhang, E. Galstyan, Supercond. Sci. Technol. **28**, 072002 (2015)
8. V. Selvamanickam, M.H. Gharahcheshmeh, A. Xu, Y. Zhang, E. Galstyan, Supercond. Sci. Technol. **28**, 104003 (2015)
9. S. Kar, W. Luo, V. Selvamanickam, IEEE Trans. App. Supercond. **27**, 6603 (2017)
10. W. Luo, S. Kar, X. Li, E. Galstyan et al., Supercond. Sci. and Technol., **31** (2018)
11. S. Kar, J.S. Sandra, W. Luo, M. Kochat et al., Supercond. Sci. Technol. **32**, 10LT01 (2019)
12. S. Hahn, K. Kim, K. Kim, X. Hu, T. Painter et al., Nature, **570**, 496 (2019)
13. D.C. van der Laan, D.M. McRae, J.D. Weiss, Supercond. Sci. Technol. **32**, 054004 (2019)
14. https://www.advancedconductor.com/corccable/accelerator-cables-and-wires/brochureofadvancedconductortechnologiesllc
15. T. Mulder, *Advancing REBCO-CORC Wire and Cable-in-Conduit Conductor Technology for Superconducting Magnets*, Ph.D. Thesis (University of Twente, 2018)
16. D.C. Van Der Laan, J.D. Weiss, U.P. Trociewitz, D. Abraimov et al., Supercond. Sci. Technol. **33**, 05LT03 (2020)
17. D.C. van der Laan, J.D. Weiss, D.M. McRae, Supercond. Sci. Technol. **32**, 033001 (2019)
18. T. Mulder, D. van der Laan, J.D. Weiss, A. Dudarev, et al., IOP Conf. Ser.: Mater. Sci. Eng. **279**, 012033 (2017)
19. T. Mulder, *Advancing ReBCO-CORC Wire and Cable-In-Conduit Conductor Technology for Superconducting Magnets*, PhD Dissertation (University of Twente, 2018)
20. T. Mulder, J. Weiss, D. van der Laan, A. Dudarev, H. ten Kate, IEEE Trans. Appl. Supercond. **30**, 4800605 (2020)
21. W. Goldacker, R. Nast, G. Kotzyba, S.I. Schlachter, et al., J. Phys. Conf. Ser. **43**, 901 (2006); 7th European Conference on Applied Superconductivity
22. D. Uglietti, Supercond. Sci. Technol. **32**, 053001 (2019)
23. S.I. Schlachter, W. Goldacker, F. Grilli, A. Kudymow et al., IEEE Trans. Appl. Supercond. **21**, 3021 (2011)
24. W.H. Fietz, R. Heller, M.J. Wolf, P.V. Gade, Fusion Eng. Des. **125**, 290 (2017)
25. K.-P. Weiss, W.H. Fietz, M. Heiduk, C. Lange, et al., J. Phys. Conf. Ser. **1559** (2020) 012082
26. R. Heller, P. Blanchier, W.H. Fietz, M.J. Wolf, IEEE Trans. App. Supercond. **29**, 4703111 (2019)
27. K. Tsuchiya, A. Kikuchi, A. Terashima, K. Norimoto, M. Uchida et al., Cryogenics **85**, 1 (2017)
28. K. Heine, J. Tenbrink, M. Thöner et al., Appl. Phys. Lett. **55**, 2442 (1989)
29. T. Isono, Y. Nunoya, T. Ando, K. Okuno, M. Ono, A. Ozaki, IEEE Trans. APP. Supercond. **13**, 1512 (2003)
30. F. Kametani, T. Shen, J. Jiang, C. Scheuerlein, A. Malagoli et al., Supercond. Sci. Technol. **24**, 075009 (2011)
31. H. Miao, Y. Huang, S. Hong, M. Gerace, J. Parrell, J. Phys. Conf. Ser. **507**, 022020 (2014)
32. D.C. Larbalestier, J. Jiang, U.P. Trociewitz, F. Kametani, C. Scheuerlein et al., Nat. Mater. **13**, 375 (2014)
33. J. Qin, Y. Shi, Y. Wu, J. Li, Q. Wang, Y. He, C. Dai et al., Supercond. Sci. Technol. **31**, 015010 (2018)

34. K. Zhang, H. Higley, L. Ye, S. Gourlay, S. Prestemon, et al., Supercond. Sci. Technol. **31**, 105009 (2018)
35. H. Maeda, Y. Tanaka, M. Fukutomi, T. Asano, Jpn. J. Appl. Phys. **27**, L665 (1987)
36. T. Hikata, K. Sato, H. Hitotsuyanagi, Jpn. J. App. Phys. **28**, L 82 (1989)
37. A. Otto, E.J. Harley, R. Mason, Supercond. Sci. Technol. **18**, S308 (2005)
38. S. Kobayashi, K. Yamazaki, T. Kato, K. Ohkura et al., Physica C **426**, 1132 (2005)
39. M. Kikuchi, N. Ayai, T. Ishida, K. Tatamidani, K. Hayashi, et al., SEI Tech. Rev. 66 (2008)
40. Sumitomo Electric Industries (SEI) Brochure: DI-BSCCO (Dynamically Innovative), 2019 vol. **1** (201909)
41. A. Godeke, D.V. Abraimov, E. Arroyo, N. Barret, M.D. Bird et al., Supercond. Sci. Technol. **30**, 1 (2017)
42. F. Kametani, J. Jiang, M. Matras, D. Abraimov, E.E. Hellstrom, D.C. Larbalestier, Sci. Rep. **5**, 8285 (2015). https://doi.org/10.1038/srep08285; www.nature.com/scientificreports

Chapter 7
Practical Magnesium Diboride (MgB_2) Superconductor

Abstract Even though the T_c of MgB_2 is 39 K only, much lower than the HTSs, yet it has been exploited for the manufacture of wires and cables for a variety of applications within a short span of time. It has already positioned itself as a practical superconductor to be used at 20 K and thus superior to Nb-Ti and Nb_3Sn which need liquid helium for operation. Long lengths of multifilamentary MgB_2 wires and tapes are being commercially manufactured with increasing J_c and B_{c2}. The cross section of the wire contains MgB_2 filaments in a Nb, Ta or Ti diffusion barrier, Cu-Ni, SS, Ni or Fe metal casing and Cu core and/or outside for stability. Most popular techniques for manufacturing MgB_2 multifilamentary wires/cables are powder-in-tube (PIT) technique, the internal magnesium diffusion (IMD), a hybrid method combining the IMD and PIT techniques and the thin-film-coating technology. High J_c values have been reported for IMD processed multifilamentary MgB_2 wires, typically 9.9×10^4 A/cm^2 (4.2 K, 10 T) and 3.3×10^5 A/cm^2 (20 K, 1 T) without impurity doping. IMD-processed MgB_2 wires, doped with 5 mol% C using coronene ($C_{24}H_{12}$) as C source, had $J_c = 1.0 \times 10^5$ A/cm^2 (4.2 K, 10 T) and high $H_{irr} = 25$ T. Among many thin film deposition techniques, the hybrid physical–chemical vapour deposition (HPCVD) technique has turned out to be the best technique to achieve high J_c. An HPCVD epitaxial 1.7-μm-thick film of MgB_2 on sapphire substrate achieved a $J_c = 1.5 \times 10^6$ A/cm^2 (30 K, 0 T) and a $T_c = 40.5$ K. HPCVD film deposited on Hastelloy tape yielded a $J_c = 1.9 \times 10^6$ A/cm^2 (20 K, 0 T). The material is being exploited for the development of high-current Rutherford cable and the cable-in-conduit (CIC) conductor. The fast development of this superconductor for magnet application can be attributed to a variety of reasons. The material is cheap, the wire does not need expensive silver like the HTSs, has small anisotropy of Hc_2 and J_c and the high T_c enabling the MgB_2 devices to operate at 20 K. These devices are therefore conduction cooled by the closed-cycle refrigerators (CCRs). The ASG superconductor is already marketing a conduction-cooled MRI scanner with the brand name 'Paramed MROpen System' using MgB_2 magnets.

R. G. Sharma, *Superconductivity*, Springer Series in Materials Science 214,
https://doi.org/10.1007/978-3-030-75672-7_7

7.1 Introduction

We have already discussed at length the discovery of magnesium diboride (MgB_2) by Nagamatsu and Nakagawa [1] and its peculiar properties in Chap. 3. Even though the T_c of MgB_2 is 39 K only, much lower than the HTSs, yet it has been exploited for the manufacture of wires and cables for a variety of applications. Within a short span of time, it has already proved itself as a practical superconductor to be used at 20 K and thus superior to Nb-Ti and Nb_3Sn which need liquid helium for operation. This superiority can be clearly seen from Fig. 7.1 [2]. The reasons for such a fast development being (i) the material is cheap, (ii) it has low anisotropy of B_{c2} and J_c (1.1–1.7), (iii) can be produced by convenient PIT technique, (iv) does not need expensive silver which constitutes about 70% of the cross section in HTS, (v) MgB_2 devices can operate at 20 K and therefore can be conduction cooled by CCRs, (vi) does not have grain boundary problem like in HTSs, (vii) it has low density 2.57 g/cm^3 and thus can be a potential candidate for use in space-related superconducting applications.

Many innovative techniques for the fabrication of MgB_2 multifilamentary wires and high current cables have been developed for its commercial production. The material is also being exploited for the development of high-current Rutherford cable and cable-in-conduit (CIC) conductors for use in accelerators and fusion machines. The ASG superconductor is already marketing a conduction-cooled MRI scanner with the brand name 'Paramed MROpen System' using MgB_2 magnets. It is hoped that the whole body 3 T MRI scanner using conduction-cooled MgB_2 magnet will appear in market in the near future.

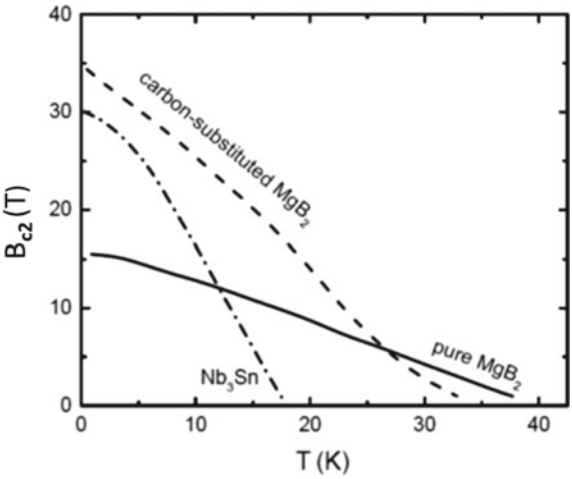

Fig. 7.1 Upper critical magnetic field B_{c2} as a function of temperature for Nb_3Sn, pure MgB_2 and C-doped (~ 5% C) MgB_2 [2]. With the permission from Elsevier

7.2 Preparation of Bulk MgB_2, Single Crystal and Thin Film

The virgin MgB_2 superconductor has a low value of $B_{c2} = 18$ T (4.2 K) as compared to 23 T of Nb_3Sn. Further, the material displays weak flux pinning behaviour which results in low irreversibility field B_{irr} (= 10 T at 4.2 K) and a sharp drop in J_c under magnetic field. Low density and high porosity in 'in situ' MgB_2 (almost 50%) is yet another problem faced while fabricating MgB_2 wires. This leads to poor homogeneity within the material and low J_c. Even though the dominant pinning sites in Nb_3Sn as well as in MgB_2 are same, that is, grain boundaries but MgB_2 has much cleaner grains and the size of the grains is also large. Through band structure calculations, Gurevich [3] has shown that B_{c2} in MgB_2 can be enhanced to more than 50 T (at 4.2 K) by adding non-magnetic impurity such as carbon. Further, core flux pinning and therefore in-field J_c in MgB_2 can be enhanced through doping with nanoparticles through a grain refining process. Enhanced J_c values ($= 2 \times 10^4$ A/cm^2 (5 K, 10 T) have indeed been reported by doping MgB_2 with amorphous SiC [4] and Malic acid [5]. Thus, a combination of core pinning by nanoparticles, grain refinement and enhancement of H_{c2} through carbon alloying can lead to high J_c suitable for magnet application.

Magnesium diboride is commercially available from chemical suppliers, but the purity has to be ascertained. In the laboratory, MgB_2 has been synthesized in various forms such as polycrystalline bulk, single crystal, thin film, wires and tapes following different techniques. Nagamatsu and Nakagawa [1] had prepared the first MgB_2 sample by the solid-state reaction method. Appropriate quantities of Mg and B in the ratio 1:2 were mixed, ground and pressed in pellet form. The pellet was heated to 700 °C under 196 MPa argon pressure using a hot isostatic pressing furnace for 10 h. The material can also be synthesized under ambient or in an inert atmosphere. One can prepare bulk MgB_2 in a sealed ampoule to prevent the loss of Mg because of its volatile nature. Single crystals of the size $1.5 \times 0.9 \times 0.2$ mm^3 and weighing up to 230 μg have been grown by Kapinski and Kazakov [6] at high pressure through the peritectic decomposition of MgB_2. The single crystals have a T_c in the range of 37–39 K. Techniques for depositing MgB_2 film are co-evaporation, pulse laser deposition (PLD), magnetron sputtering, deposition from suspension and Mg diffusion. Films have been deposited on a variety of substrates such as, SiC, Si, $LaAlO_3$, $SrTiO_3$, MgO, Al_2O_3 and SS. The choice of substrate is thus very wide because perhaps the hexagonal structure of MgB_2 can grow on a variety of substrates with different lattice parameters. The volatility of Mg has to be kept in mind. Target for sputtering therefore has to be kept Mg rich. Bulk MgB_2 is also prepared in sealed ampoules for the same reason. Mg diffusion technique (diffusion of Mg in B) has proved to be the best technique, be it bulk, films or wires.

7.3 MgB_2 Wires, Tapes and Cables

For magnet coils, we need superconducting material in the form of stabilized multifilamentary wire or a tape. Two methods are available to prepare the material in this form. One is the coating technique and the other PIT (powder-in-tube) technique. In the first technique, a moving ribbon mostly Hastelloy is coated with MgB_2. Komori et al. [7] prepared MgB_2 tapes on Hastelloy with a $J_c = 1.1 \times 10^5$ A/cm^2 (4.2 K, 10 T). B_{c2} as high as 55 T and an irreversible field of 40 T has been reported by Ferrando et al. [8] in a carbon-alloyed MgB_2-coated conductor by a hybrid physical–chemical vapour deposition technique.

The coating technique discussed above though provides tapes with superior quality, nevertheless is not an ideal technique to produce long lengths (several km). PIT is a viable and preferred technique for commercial production. In this technique, well-prepared fine powder is packed at a high density in a metal tube and rolled/drawn to fine size of wires or tapes in a series of steps of rolling and intermediate annealing to maintain ductility. The sheath material should be such that it does not react with the core material and provides sufficient mechanical strength to the composite wire/tape. Copper has to be incorporated somehow in the cross section of the wire/tape to provide thermal stability to the superconductor. Several metals such as Fe, Mo, Nb, Ta, Hf, W, Cu, Ag, Cu-Ni and SS have been used for cladding with varying degree of performance. The starting core material can be either preformed MgB_2 or a mixture of Mg and B in right proportion. In the later case, a heat reaction at 900–1000 °C is required so as to form stoichiometric MgB_2 core. High-temperature treatment is not needed [9] in the case of preformed MgB_2. Critical current density J_c and the stoichiometry, however, improve with heat treatment after the drawing process. Kumakura et al. [10] reported $J_c = 10^4$ A cm^{-2} (4.2 K, 5 T) values in a single-core and a 7-core MgB_2 tapes fabricated using PIT technique with SS and Cu-Ni sheath material (Fig. 7.2). The higher value of J_c for SS sheathed tape is achieved because of the higher packing density attainable. SS also provides higher mechanical strength. Fang et al. [11] prepared 1 mm dia. wires by PIT technique using 1020 Fe sheath and following a wind-and-react method. Annealing was done under Ar atmosphere at a temperature of 850 °C for 30 min. They report a J_c value of 1×10^4 A cm^{-2} (4.2 K, 6 T) and 1.8×10^5 A cm^{-2} (20 K, 0 T). Fe, Ni and SS turn out to be the most suitable cladding materials. Copper has to be used with Nb or Ta barrier for thermal stability.

Sumption et al. [12] developed 7, 19 and 37 filament MgB_2 wires following the ex situ route. In some sample, 30-μm-size particles and in some samples excess Mg were incorporated. Single-step heat treatment at 700–800 °C for 10–30 min was given. All the wires used either Nb or Fe as filament barrier. Filament size ranges between 80 and 150 μm. A $J_c = 1.75 \times 10^5$ A cm^{-2} (4.2 K, 5 T) has been achieved. At 20 K, the intrinsic J_c appears to be reaching 10^6 A cm^{-2}. All these studies auger well for the potential application of MgB_2 superconducting wires for magnets operating with closed-cycle refrigerators. The product is already marketed by two companies, namely Columbus Superconductors of Italy and Hypertech Research Inc. of USA.

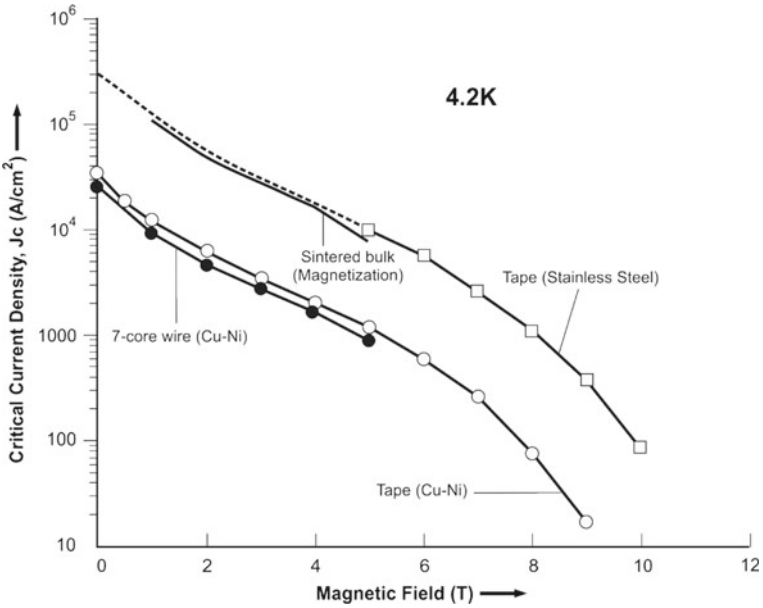

Fig. 7.2 Transport J_c versus magnetic field plots for Cu-Ni sheathed monocore tape and Cu-Ni sheathed 7-core wire and SS sheathed monocore tape at 4.2 K [10]. With the permission of AIP Publishing LLC

Hitachi, Japan, too is keen to manufacture this conductor in collaboration with NIMS, Japan.

7.3.1 Different Variants of PIT Technique—The In Situ PIT Technique

The powder-in-tube (PIT) technique has emerged as the most favoured technique to produce long lengths of wires of brittle and hard ceramic-type materials because it is comparatively simple and cost effective. The technique though suffers from the problem of low packing density and consequently low self field/in-field J_c, counter-measures have been adopted and the problem has been largely solved. High packing densities, leading to high J_c values, have been attained. There are a few variants of these PIT techniques to produce MgB_2 strands, namely (i) in situ, (ii) ex situ and (iii) the IMD route, all resulting in encouraging values of J_c under in-field and self-field conditions. We discuss these techniques below.

In this process, MgB_2 is formed in situ after the wire is drawn and reacted at a temperature (~ 650 °C) which is significantly lower than needed in ex situ technique. The starting material is the mixture of Mg and B powders with particle size in nm range. The mixture is packed in an Nb tube which works as a diffusion barrier. Nb

tube is in turn is inserted into a Cu-Ni (70:30) tube and rolled and drawn to wires of 2–3 mm diameter. Several of these monofilamentary wires are stacked into a Ni or Monel tube surrounded by outer OFHC Cu stabilizing tube. The composite billet is again rolled and drawn to the final size of the strand about 0.8 mm in diameter. For making tape, the wire, when about 2 mm of diameter, is first twisted and then flat rolled to desired thickness. In situ technique, however, leads to wires with large porosity because of low bulk density (~ 50%). Lower heat temperature (650 °C) is certainly attractive as the reaction layer at the metallic sheath is reduced. Lower reaction temperature also leads to small grains and thus to higher grain boundary density. This results in high J_c because grain boundaries provide efficient flux pining in this material. At the same time, C can be substituted into the B at such temperatures. Li et al. [13] have reported a high value of $J_c = 1 \times 10^4$ A/cm^2 (4.2 K, 13.2 T) in in situ multifilamentary MgB_2 strand of dia. 0.8 mm dia. The starting material was B powder of 100 nm size, pre-doped with various C contents by plasma spray synthesis and the 99% Mg powders of 25 μm size. Multifilamentary wires of 0.83 mm diameter with a Nb barrier and a Monel outer sheath (MgB_2/Nb/Monel) were reacted at 700 °C for 40 min. The final MgB_2 filament had 2.54 mol% of C. The in situ wires were developed at the University of Genova and produced on an industrial scale by Hyper Tech Research in collaboration with Ohio State University.

7.3.2 The Ex Situ PIT Technique

The ex situ process is the most suitable technique for producing uniform, strong and long-length MgB_2 conductors This technique is similar to the in situ PIT technique except that one uses preformed MgB_2 powder in place of the mixture of Mg and B while preparing the billet. In the first phase, fine MgB_2 powder is prepared through a controlled solid-state reaction between boron and magnesium. In the second metallurgical stage, the powder produced by the reaction is packed inside a Nb tube surrounded by a metal tube and an outermost Cu tube for stability. The composite billet then undergoes swaging, rolling and drawing to produce a monofilament MgB_2 wire with the desired cross section. Required number of wire pieces possibly combined with additional wire constituents are stacked inside a second Ni or Monel tube and subjected to a similar metallurgical process of swaging, rolling and drawing in order to obtain the MF wire of desired diameter, shape and length of the conductor. A known % of OFHC needs to be added to the total cross section of the conductor either as a core, as an outermost section or spread uniformly within the cross section. Nb diffusion barrier around the filaments is essential so as to prevent diffusion of metal matrix into MgB_2. Finally, the multifilamentary conductor is heat treated at optimized temperature and duration so as to carry acceptable in-field critical current, I_c. For fabricating a tape, the wire dia. is kept about 2 mm which is twisted and flat rolled to tapes typically of the size 3.6 mm × 0.65 mm as marketed by Columbus Superconductors. The tapes are heat treated for recrystallization at 965 °C for 4 min. The ex situ wires produced by Columbus (ASG) Superconductors

have $J_c = 3 \times 10^5$ A/cm^2 (4.2 K, 3 T), 5×10^4 A/cm^2 (4.2 K, 5 T) for undoped wires and 4×10^6 A/cm^2 (4.2 K, 7 T) for C alloyed wires [14, 15]. These J_c values are lower than those for the other two processing routes, but ex situ wires are capable to be produced in km lengths and display the highest homogeneity over long lengths.

7.3.3 *The Internal Magnesium Diffusion (IMD) Technique*

The PIT technique (in situ and ex situ) discussed in previous sections though widely used for producing long lengths, nevertheless suffers from some inherent problems which limit J_c to low values. Ex situ PIT suffers from poor grain connectivity, MgB_2 being a hard ceramic. The in situ PIT technique on the other hand has a porosity problem because of the volume shrinkage during MgB_2 formation reaction. Alternate techniques are therefore being developed to achieve high J_c in this superconductor. A new technique called internal magnesium diffusion (IMD) technique developed originally by Giunchi et al. [16] has caught up with several research teams leading to a significant improvement in J_c. In the IMD technique [17], an Mg rod is kept at the centre of a metal (SS, Fe, Cu-Ni, Ni or Monel) tube with a lining of Ta or Nb tube inside as a diffusion barrier. The interspace between the Mg rod and the outer metal barrier is filled with B (or B with additive like SiC, $C_{24}H_{12,}$ etc.).

The composite billet is now cold processed through swaging, rolling and drawing to wires of desired diameter and subjected to heat treatment at 640–650 °C. During heat reaction liquid Mg infiltrates into B and reacts to form MgB_2 layer leaving a hole at the centre because of volume shrinkage. IMD-processed wire is sometimes referred to as *hollow wires*. When Giunchi et al. published their first results [16] in 2003, they reported a $J_c = 3 \times 10^2$ A/cm^2 (4.2 K, 10 T) but improved it in 2007 [18] by partially substituting C at B positions and reported a $J_c = 5 \times 10^3$ A/cm^2 (4.2 K, 10 T). Giunchi et al. refer this method as Mg-reactive liquid infiltration (Mg-RLI) process.

Data on J_c of IMD wires from a number of research groups are given in Table 7.1. A detailed review on IMD technique has been published by Shujun and Kumakura [26]. The table gives the J_c values of the MgB_2 layer only but what matters for application is the engineering (or overall) critical current density, J_e which takes into account the total cross section of the conductor which contains superconducting as well as normal metal components. Compared with the J_c values given in Table 7.1, the J_e values will be about one order of magnitude smaller depending upon the shape cross section and the constituents' percentage. Thus, J_c and J_e values of MgB_2 wires at 20–30 K temperature and magnetic fields (> 5 T) need significant improvement so as to qualify for large-scale applications. The key factors that influence the critical current of MgB_2 processed by IMD technique can be summarized thus:

1. The reactive liquid (Mg) infiltration (RLI) increases grain connectivity.
2. Use of nanosized B reduces grain size which helps in increasing J_c.

Table 7.1 Some important critical current density, J_c data, from a few research groups on IMD-processed MgB_2

Author	Year	Additive	Other details	Critical current density (J_c)			References
				Value (A/cm^2)	Temp. (K)	Field (T)	
Giunchi et al.	2003	Undoped	Nb barrier/SS sheath	3×10^2	4.2	10	[16]
Giunchi et al.	2007	C-doped		2.5×10^3 5×10^3	4.2 4.2	12 10	[18]
Hur et al.	2008	SiC 5 mol% 5 mol%	Fine B/Fe sheath	4.1×10^4	4.2	10	[17]
Togano et al.	2009	SiC nano 10 mol%	Ta barrier/Cu-Ni sheath	1.0×10^5	4.2	9	[19]
Togano et al.	2010	SiC nano 10 mol%	Ta barrier/Cu-Ni sheath Mono/7 fil.	9.9×10^4 3.3×10^5	4.2 20	10 1	[20]
Ye et al.	2011	SiC +liq. Aromatic Hydro. C	Monofilament	4.9×10^4	4.2	10	[21]
Li et al.	2012	C 2 mol% Nano B	Wire ϕ 0.55 mm monofilament	1.07×10^5	4.2	10	[22]
Li et al.	2013	C 3 mol%	Monofilament	1.5×10^5	4.2	10	[23]
Ye et al.	2013	C 4 mol% + dimethyl benzene	Wire ϕ 0.6 mm Ta/Fe sheath and Ta/Cu-Ni sheath	1.2×10^5	4.2	10	[24]
Ye et al.	2014	Nano B + coronene ($C_{24}H_{12}$)	Wire ϕ 0.6 mm	1.1×10^5	4.2	10	[25]

Data compiled from [16–25]

3. IMD allows lower temperature of reaction, ~ 650 °C which is conducive to form small grains (high grain boundary density) which leads to an effective flux pinning and high J_c.
4. Addition of carbon-containing dopant to B powder has been found quite effective in enhancing J_c and J_e.
5. For adiabatic (thermal and EM) stability filament size should be reduced to below 100 μm.
6. Cu and Al provide good dynamic (thermal) stability to conventional superconductors like Nb-Ti and Nb_3Sn, but these metals cannot be used as matrix for MgB_2 wires because of the high reactivity of Mg. High conductivity Cu though has to be in the cross section either as a core or on the outside the wire.

7. To prevent reaction of MgB_2 with stabilizing metal, filaments are encased in Nb or Ta as a diffusion barrier. In fact, Giunchi et al. [27] have proposed Mg itself the metal for stabilization.

As discussed in the previous section, during the reaction molten Mg reacts aggressively with B within the annulus of the billet to form MgB_2. Since the volume is fixed and the density of MgB_2 is higher than those of Mg and B, voids (pores) are formed within the cross section reducing the superconducting volume fraction. Pores reduce the current transfer capability which brings down J_c. An elongation of pores along the length will increase the effective superconducting area percentage within the cross section and enhance J_c and J_e. One interesting method of elongating pores has been the use of coarse Mg. Elongated pores are indeed observed when coarse (100 mesh) Mg powder is used. This results in a reduced pores area cross section along the longitudinal direction of the IMD MgB_2 wire which has a central hole and a dense MgB_2 layer with high J_c. The central Mg rod, in fact, is akin to an extremely coarse Mg and the entire porous area joins to appear as a hole. The IMD wires thus have increased connectivity and high J_c and J_e. The J_c and J_e of the IMD wires can be increased further through the addition of impurities or structural imperfections which will serve as efficient flux pining centres.

7.3.4 Enhancement of J_c Through Optimization of Process Parameters and Doping

High in-field critical current density, J_c and the engineering current density, J_e in practical superconductors have always been a goal for developing material for application. The goal is usually achieved through the optimization of the process parameters and doping in superconductors. Table 7.1 summarizes the J_c data reported for MgB_2 conductors by several groups [16–25]. The factors affecting J_c are (i) selection of B and carbon containing additive, (ii) porosity within MgB_2 layer, (iii) unreacted B, (iv) grain size and grain connectivity, (v) flux pinning, (vi) wire diameter, (vii) maximum Mg infiltration distance, (viii) mono- or multifilamentary, (ix) heat treatment conditions (temperature, duration and ambience) and (x) sheath material. We will very briefly discuss some of these factors in the next few sections.

(A) **Selection of Boron**

The B powder particle size should be in nm size range. Using the μm size B powder, the earlier workers obtained low J_c because of the long diffusion distance that Mg atoms from the Mg rod have to travel to diffuse into B to form MgB_2. Consequently, Mg does not diffuse till the centre of B particle leaving the central part of B particles unreacted. This reduces the volume fraction of superconducting MgB_2. Fine B particles will thus result in an increased superconducting volume fraction and higher J_e.

(B) Enhancement of J_c Through Carbon Doping

Carbon doping implemented in a variety of ways in MgB_2 has been found to be most effective in raising J_c. Carbon replaces B atoms and increases resistivity which in turn increases B_{c2} and thereby J_c. By now, there is broad consensus on this additive but the route through which C can be added is being experimented with. Numerous attempts have been made to achieve high J_c and high J_e values through the adjustment of strand diameter, filament size, number of filaments and carbon concentration through different chemical routes.

(C) SiC-Doping and Multifilamentary MgB_2 Wires

SiC doping has been popular among the earlier groups for attaining high J_c. Following the IMD technique, Kumakura et al. [28] obtained a J_c value of 1.1×10^5 A/cm^2 (4.2 K, 10 T) for a monofilamentary MgB_2 wire doped with 10 mol% SiC and reacted at 600 °C. This J_c value is significantly higher than the value of the undoped wires. Togano et al. [20] carried out studies on the development of MgB_2 wires using IMD technique with an objective to fabricate multifilamentary wires and optimize the heat treatment parameters. These parameters depend upon the configuration of the cross section and strongly depend on the filament dimensions and filament area fraction within the cross section. Accordingly, they prepared mono, 7 and 19 filaments wires using a mixture of B (99.9%—300 mesh) and 10 mol% SiC. The billet had a Ta tube of outer dia. 6 mm and 3.5 mm inner dia. The Mg rod at the centre is 2 mm in diameter. The annular interspace between the Mg rod and Ta tube was packed tightly with B + SiC mixture. With this geometry, the Mg: B ratio was 1.3: 1, that is, Mg has been in excess to the stoichiometric ratio. For the monofilamentary wire, the Ta tube (without the outer jacket of Cu-Ni) was processed (swaged, groove rolled and drawn) to 4 mm wire. The wire was inserted in a Cu + 10 wt% Ni tube of inner dia. 4 mm and outer dia. 6 mm and processed to 0.8–1.0 mm dia. strand. For multifilamentary conductors, the Ta clad billet was processed further down to 1.3 mm and 0.8 mm dia. for fabricating 7 and 19 filament wires, respectively. Seven and nineteen pieces of these two strands were assembled together in an outer Cu-Ni tube. These three billets having same size 4 mm × 6 mm Cu-Ni tube were again rolled and drawn to final size of the wire, 1.3 mm dia. The wires were heat treated at 590–800 °C for 1 h. During this heat treatment, Mg infiltrates into the composite powder of B and SiC and reacts to form a dense layer of MgB_2. The transport I_c in all the wires is maximum for the heat treatment temperature of 640–645 °C which is just below the melting temperature of Mg. Strangely, all the three samples had almost the same J_c values, which were 8.2×10^4 A/cm^2, 8.6×10^4 A/cm^2 and 9.9×10^4 A/cm^2 at 4.2 K and 10 T for the single, 7 and 19-filament wires, respectively.

A significant part of the B + SiC mixture was found unreacted in monofilamentary wires which is the basic reason for low J_c. On increasing the reaction temperature I_c decreases rather fast even though layer thickness grows. The highest layer J_c has been obtained for 7 and 19 filament wires heat treated between 640 and 645 °C for 1 h. The J_c values obtained were 9.9×10^4 A/cm^2 (4.2 K, 10 T) and 3.3×10^5 A/cm^2 (20 K, 1 T), respectively, for 7 and 19 filament wires [20].

Table 7.2 Critical current density, J_c of undoped and 10 mol% SiC-doped IMD 37 filaments MgB_2 wires. J_c has been measured at temperature between 4.2–30 K and in magnetic field between 1 and 10 T (data compiled from [24])

Temperature (K)	Magnetic field (T)	Critical current density, J_c (A/cm^2)	
		Undoped	Doped (10 mol% SiC)
4.2	10	1.1×10^4	7.6×10^4
15	8	2.8×10^3	1.7×10^4
20	6	5×10^3	8.0×10^3
20	3	1.5×10^5	1.1×10^5
25	3	–	2.0×10^4
30	1	1.1×10^5	7.0×10^3

The same NIMS group [24] went on to produce 37 filament wire with and without nano-SiC doping. The maximum J_c value for the undoped wire was $= 1.6 \times 10^5$ A/cm^2 (20 K, 3 T) and $J_e = 2.8 \times 10^3$ A/cm^2 (20 K, 3 T). The authors also studied the critical current behaviour of 37 filament wires without doping as well. A comparison shows that J_c of the IMD MgB_2 wires doped with SiC is higher in high magnetic field and low temperature, whereas J_c is higher at higher temperature and lower field in undoped wires. The low values of J_c and J_e in both doped and undoped wires are attributed to a very low superconducting volume fraction in the wire. This is because of the thick Ta and Cu-Ni tubes and the central hole created by the shrinkage of volume during MgB_2 formation. These results indicate rather strongly that the diameters of all the components in the billet cross section need to be optimized to increase the superconducting volume fraction in the wire. The high critical current densities achieved in multifilamentary wires are primarily caused by much shorter Mg diffusion paths produced in these MF wires. Infiltration of liquid Mg into B increases which reduces the central unreacted volume of B substantially. As a result, J_c increases. These studies established the fact that optimization of process parameters especially doping, number of filaments and heat treatment is strongly dependent on the final application to which the conductor will be used (Table 7.2).

(D) Dependence of J_c on Carbon Concentration and Number of Filaments

A systematic study has been carried out by Li et al. [23] at Ohio University on the effect of the C concentration and the number of filaments on J_c and J_e in an IMD MgB_2 strand. The objective has been to enhance J_c to high value by optimizing these two extremely important parameters. The layer J_c in IMD wires has been quite impressive, but the J_e is low. The main reason for low J_e has been a small fill factor of the MgB_2 layer within the whole cross section of the strand. A larger number of small diameter filaments seem to be the best option to increase the volume fraction of MgB_2 and therefore J_e. Strands with large number of fine filaments are any way required for low AC loss cables. These authors had previously [22] achieved high J_c of the IMD processed conductors by optimizing B powder, different wire diameters, heat treatment parameters, wire geometry and fabrication. A maximum layer J_c of 1.1×10^5 A/cm^2 (4.2 K, 10 T) and a maximum J_e of 1.7×10^4 A/cm^2 (4.2 K, 10 T)

were reported. The engineering critical current, J_e in these samples was much higher than in the best PIT conductors. The strands with high optimized J_e were designated as 'second generation or 2 G MgB_2 IMD wires' or 'advanced internal Mg infiltration (AIMI)' wires.

The J_c optimized strands studied by this Ohio Uni. group were manufactured by Hyper Tech Research Inc. (HTR). Three types of samples, namely monofilament and 18-filament IMD strands and the third 36 filaments PIT strands, were studied for comparison. In all the samples, a C-doped (2–4 mol%) B supplied by SMI (Specialty Materials Inc.) was used. Two carbon concentrations (3 mol% and 4 mol%) were used in these studies in place of 2 mol% C used in IMD and PIT strands in their earlier studies [22]. Strands were fabricated [23] by processing the billet comprising of a central Mg rod inside a Monel tube with Nb lining and packing the space between the Mg rod and the Monel tube with C-doped (SMI) B. For monofilament, the billet was processed to wire of diameter 0.55 mm. For MF strands, 18 pieces of this wire along with a central Cu-Ni filament were restacked in another Monel tube and processed to 0.83 mm dia. strand. At the same time, PIT 36 filaments strands of 0.92 mm dia. were also made with varying amount of C-doping (2–4 mol%) by the same restacking process. Heat treatment (HT) was carried out at 675 °C for varying periods ranging between 1 min and 4 min. Longer HT will lead to grain growth which will pull down J_c. The layer J_c of MgB_2 AIMI strands with 3 and 4 mol% C doping and heat treated at 675 °C for 1 h are plotted against magnetic field between 4 and 13.5 T field range in Fig. 7.3. For comparison layer J_c of a 2 mol% C-doped 2G-IMD strand heat treated 675 °C for 1 h has also been plotted in Fig. 7.4. It is evident from the figure that the sample A3 with 3 mol% of C doping and heat treated for 4 h has the highest $J_c = 1.5 \times 10^5$ A/cm^2 (4.2 K, 10 T), whereas sample A1 heat treated 675 °C for 1 h has $J_c = 1.3 \times 10^5$ A/cm^2 (4.2 K, 10 T) and sample A2 heat treated 675 °C for 2 h has the J_c

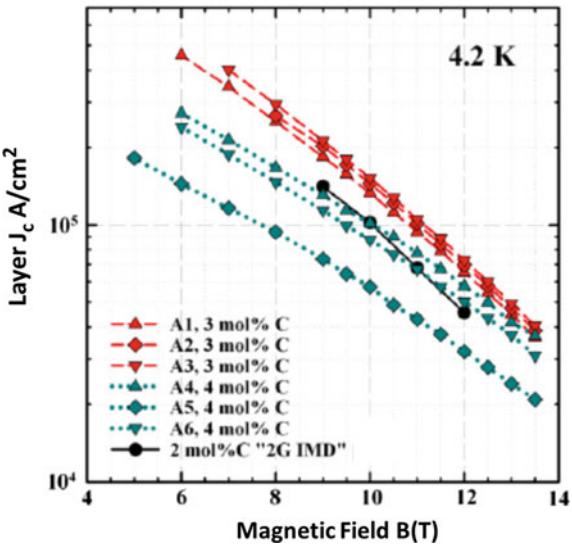

Fig. 7.3 Layer J_c of the monofilamentary AIMI strands with 3 and 4 mol% C at 4.2 K plotted against applied magnetic field. J_c of a 2G-IMD strand with 2 mol% C too has been plotted [23]. With the permission from IOP

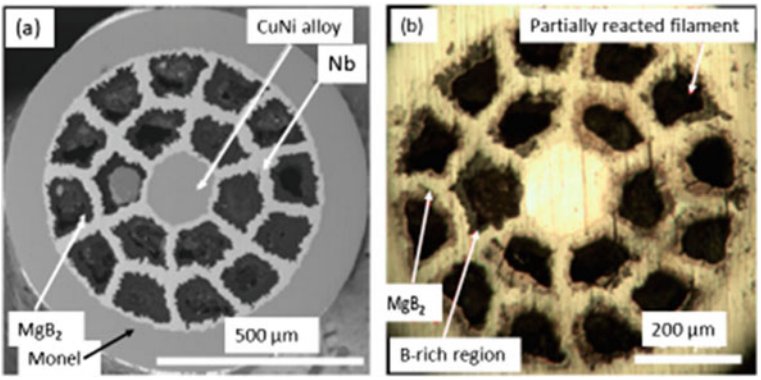

Fig. 7.4 SEM (**a**) and optical microscope (**b**) pictures of the transverse cross section of a 2 mol% C-doped AIMI-B1 sample with 18 strands. Grey B-rich regions seen on the periphery of annulus MgB_2 layer (**b**) indicates that not all B has been converted to MgB_2 [23]. With the permission from IOP

$= 1.4 \times 10^5$ A/cm^2. The J_c data and other typical specifications of the AIMI MgB_2 strands (A3 and B1) with 3 mol% and 2 mol% C doping, respectively, are given in Table 7.3. The data clearly establish that layer J_c increases with the duration of heat treatment.

The MgB_2 layer J_c though increases with C doping up to 3 mol%, but surprisingly the layer thickness in 3 mol% sample come out to be less than a quarter of thickness obtained in 2 mol% C-doped IMD sample under same heat treatment conditions. The annular MgB_2 layer is surrounded by another layer which is B rich. SEM and optical microscope pictures [23] of the transverse cross section of a 2 mol% C-doped AIMI sample designated as B1 in Table 7.3 are shown in Fig. 7.4. Figure 7.4a shows a uniform deformation of the filaments of about 100 μm in diameter with Cu-Ni alloy at the centre. The outermost cladding is of Monel. MgB_2 is formed between Nb lining and the hole at the centre of each filament. In optical microscope image (Fig. 7.4b), one can see the MgB_2 layer of 0–30 μm with grey unreacted B areas on the outer periphery of MgB_2. It is also seen from Table 7.4 that in AIMI strands the MgB_2 fill factor (FF) in both the types of strands (monofilamentary A type and 18-filament B type), are significantly small, 5.2% and 13.2%, respectively, in comparison with PIT strands. Strand B1 with 2 mol% C turns out to be best performing strand with a J_c value of 4.3×10^5 A/cm^2 (4.2 K, 5 T) and 7.1×10^4 A/cm^2 (4.2 K, 10 T) over twice the best J_c value of a 3 mol% C-doped PIT strand. The highest layer J_c for monofilamentary AIMI strands with 3 mol% C and heat treated at 675 °C for 4 h was 1.5×10^5 A/cm^2 (4.2 K, 10 T). The transport critical current measurement at 4.2 K on short samples and 1 m segments of 18-filament C-doped AIMI strands yielded layer $J_c = 4.3 \times 10^5$ A/cm^2 (4.2 K, 5 T) and 7.1×10^4 A/cm^2 (4.2 K, 10 T), twice as high as that of the best PIT strands.

Thus, the data show that C composition, which yields highest J_c, is different for mono- and multifilamentary conductors. Further, the J_c of 18-filament conductors

Table 7.3 Detailed specifications of the AIMI MgB_2 strands (A3 and B1) with 3 and 2 mol% C doping, respectively, and discussed in the text (data compiled from [24])

Sample name	No. of filaments	C (mole %)	Central filament	MgB_2 fill factor, FF(%)	Filament to strand fraction (%)	MgB_2 (%) in filament	Dia. mm	HT ($^oC \times h$)	Layer J_c A/cm^2 (4.2 K)
A3	Monofilament	3	none	5.2	32.5	16	0.55	675×4	4.3×10^4 (13 T) 1.5×10^5 (10 T)
B1	18 filament	2	Cu-Ni	13.2	33.8	39.1	0.83	675×1	7×10^4 (10 T) 4.3×10^5 (5 T)

Table 7.4 Engineering current density, J_e (4,2 K, 5 T) of Hyper Tech Research multifilamentary AIMI second-generation MgB_2 wires

Sample wire	No. of filaments	J_e (4.2 K, 5 T) A/cm^2
CTFF-1	36	2.6×10^4
CTFF-2	18	5.8×10^4
CTFF-2	1	12.2×10^4

decrease when heat treated for 2 h as compared to samples heat treated for one hour. Thus, even the heat treatment conditions for obtaining best value of J_c are different for mono- and multifilamentary strands. Conspicuously, the AIMI 18-filament strands have been found to be uniform along 1 m length, a good sign for large-scale production. Figure 7.5a shows the magnetic field dependence of the engineering current density, J_e of the multifilamentary AIMI MgB_2 wires manufactured by HTR (Hyper Tech Research), while Fig. 7.5b shows the magnetic field dependence of the critical current density, J_c of the C-doped 0.84 mm diameter monofilamentary MgB_2 strand manufactured by HTR at different temperatures between 4.2 and 30 K.

Table 7.4 gives the J_e values of the three wires at 4.2 K and 5 T field. It is shown from the table that J_e is reduced as the number of filaments is increased. It is possible that during the wire fabrication, the filaments in a MF strand get very fine and non-uniform along the length. Nb barrier may also puncture and allow Cu to leak and contaminate MgB_2 layer. All these factors would bring down J_c in MF strands.

We can now summarize the main results of these studies as below:

1. C doping is beneficial to raise J_c as it increases B_{c2}, reduces anisotropy and provides extra pinning centres. The doping level of 3 mol% appears optimum.

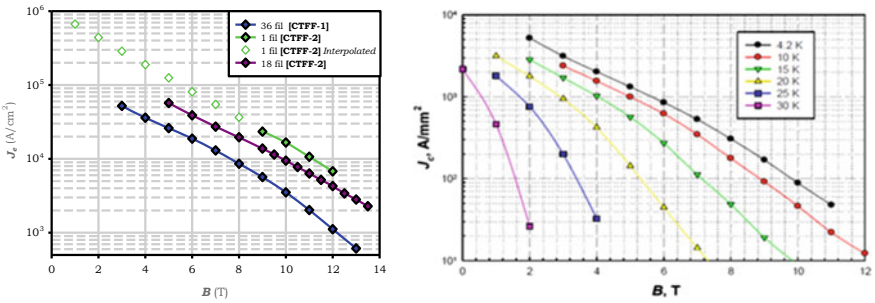

(a) (b)

Fig. 7.5 **a** Magnetic field dependence of the engineering current density, J_e of the multifilamentary AIMI MgB_2 wires with 1, 18 and 36 filaments manufactured by Hyper Tech Research. **b** Magnetic field dependence of the critical current density, J_c of the C-doped 0.84-mm-diameter monofilamentary MgB_2 strand (manufactured by Hyper Tech Research) at different temperature between 4.2 and 30 K. Pictures copyright Hyper Tech Research, courtesy David Doll

Doping C with more than 3 mol% damages grain connectivity and brings down J_c.

2. Multifilamentary strands are found to carry larger transport current as the Mg infiltration distances are reduced and most of B is used-up in the formation of MgB_2. Contents of unreacted B are reduced significantly increasing thereby J_c. However, the geometry of the starting billet is important. During the wire fabrication if the filaments in a MF strand get very fine and become non-uniform along the length and are punctured by Nb barrier, Cu may leak and contaminate MgB_2 layer. All these factors would degrade J_c.
3. Heat treatment conditions too are quite different for mono- and multifilamentary strands. The precursor B layer in a MF strand is only about 20 μm thick, and 1 h heat treatment is just optimum but in a monofilamentary strand, which has a B layer more than 50 μm thick, needs 4 h of heat treatment. During this prolong heat treatment, complete transformation of B into MgB_2 layer takes place, MgB_2 layer thickness increases and so does the J_c.
4. A short time of heat treatment needed for MF strands is also conducive to small gains which increase the J_c. Prolong heat treatment time leads to grain coarsening and oxidation of copper, both of which cause J_c to decrease. To this end, MF strands are desirable as they have thinner precursor B layer and needs shorter reaction time.
5. The advanced internal Mg infiltration (AIMI) MF strands are superior to PIT strands, which are plagued with porosity. AIMI strands are highly thermally stable, uniform along long lengths and can carry a transport current of 1000 A (4.2 K, 1 T).

In conclusion, we find that these studies establish the fact that the addition of SiC to MgB_2 has two effects. One is that C substitutes B which increases resistance and thus B_{c2} and J_c. The other effect is that it decreases T_c which brings down the J_c at high temperature and low magnetic field. The consequence is that the extent of SiC addition depends upon the temperature and the magnetic field range at which the conductor is intended to be used.

(E) Using Coronene ($C_{24}H_{12}$) as an Active Source of Carbon

In previous sections, we have seen that C substitution for B leads to high upper critical magnetic field, B_{c2} and the critical current density, J_c in PIT and IMD MgB_2 wires. This has been confirmed by most of the research groups. The choice of C containing dopant, however, remained an option. SiC dopant was used by several research groups but Si impurity limited the increase of J_c. Ye et al. [25] opted for the use of coronene ($C_{24}H_{12}$), an aromatic hydrocarbon, has a large contents of C but a low content of hydrogen. Coronene is a yellow powder, has a melting point of about 438 °C, boiling point 525 °C and decomposes into graphite nanoparticles above 600 °C. Coronene has several advantages as a carbon source.

1. Coronene has 96 wt% C and only 4 wt% hydrogen.
2. Heating coronene to 400 °C removes small absorbed impurities.

3. Molten coronene, when heated above 480 °C, will uniformly diffuse and penetrate into the B and Mg particles in PIT and into B particles in IMD process. Since the particles are of nanosize, the surface area is enormous and thus large amount of C is adsorbed.
4. In fact, in the IMD process the B particles are coated uniformly with coronene which decomposes at a temperature above 600 °C into graphite nanoparticles.
5. This temperature is close to the temperature at which reaction between Mg and B takes place. As a result, fresh carbon substitutes B uniformly in the MgB_2 lattice
6. Use of coronene permits good control over the extent of carbon substitution as most of the coronene is converted into graphite nanoparticles. One can therefore control the C substitution by controlling the amount of coronene.

In the IMD fabrication process, the coronene and B nanoparticle powders are mixed together thoroughly and packed in the annular space between the Mg tube and the Ta/Nb barrier lined inside the outer Fe/Cu-Ni tube. For PIT, one can mix coronene with Mg and B powders in the initial stage and proceed as usual. The composite billet is then groove rolled and drawn to wires of dia. 0.6 mm (small) so as to keep the diffusion paths short. To optimize the C concentration, IMD wire samples were prepared without doping and with doping carbon content of 2, 5, 10 and 15 mol%. All the samples were heat treated at 670 °C for 6 h. TEM pictures show that the carbon layer coated on the B powder is about 4 nm thick and quite uniform. The carbon coating is amorphous, and its thickness can be varied by controlling the initial addition of $C_{24}H_{12}$. Ye et al. [25] studied PIT wires as well as IMD wires using $C_{24}B_{12}$ as C source. The PIT wires were drawn to 1 mm diameter and the IMD wires to 0.6 mm to keep the Mg diffusion path short. The wires were Fe clad and were reacted at 700 °C for 1 h.

Figure 7.6a shows the J_c versus field plots for the wires fabricated following the usual PIT technique and using coronene for C doping. These wires drawn to 1 mm diameter contain 0% (undoped), 2, 5, 10 and 15% C and have been heat treated at 700 °C × 1 h. The J_c increases with C contents and reaches a maximum of 1.8×10^4 A/cm^2 (4.2 K, 10 T) for 10% C. This value is about 14 times the J_c for the undoped PIT wire. This value of J_c corresponds to a $J_e = 5.0 \times 10^3$ A/cm^2 (4.2 K, 10 T). With further increase of C concentration, the J_c decreases as seen from the plot for sample with 15% C. Extrapolating the slopes for the wires to low field shows that the undoped and 2% C wires have higher J_c than the 10% doped wire. These results indicate that carbon contents have to be optimized for best J_c as per the field to which the conductor will be put to use. Microstructural studies show that there is hardly any change in the microstructure of MgB_2 with carbon doping. The XRD studies reveal that at 5% C level about half of the added carbon substitute for B. This would mean that coronene is an active source of C. Addition of more than 10 wt% coronene does not seem to influence the C substitution as though the substitution process is saturated at 10% coronene.

Figure 7.6b shows the plots of J_c versus field of the coronene IMD wires 0.6 mm in diameter with different levels of C doping starting from undoped to 2, 5, 10 and

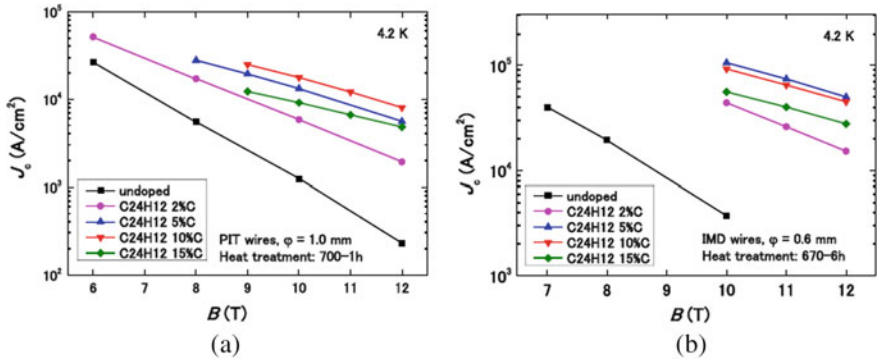

Fig. 7.6 Enhancement of J_c with the addition of coronene ($C_{24}H_{12}$) in PIT and IMD processed MgB_2 wires with different C-contents. J_c–B plots of undoped MgB_2 wires are for comparison **a** J_c–B plots of PIT wires prepared using coarse Mg powder, 1 mm in diameter, Fe clad and reacted 700 °C × 1 h. **b** J–B plots for IMD wires 0.6 mm in diameter, Fe clad and reacted 670 °C × 6 h [25]. With permission from IOP

15% C. Contrary to PIT wires the J_c is found maximum for 5% C instead of the maximum J_c we found for 10% C in PIT-processed wires. It appears likely that with 10% C doping there is more substitution for B but the impurity level due to the release of hydrogen during decomposition goes up which will affect grain connectivity. It is possible that in 10% C in PIT wires hydrogen impurity is taken care of by voids without affecting J_c. The highest value of J_c for IMD wires doped with 5% C is 1.07 × 10^5 A/cm^2 (4.2 K, 10 T) and the corresponding J_e value = 1.12 × 10^4 A/cm^2 (4.2 K, 10 T).

The optical microscope picture of the transverse cross section of an IMD-processed wire drawn to 0.6 mm diameter reveals a uniform and dense MgB_2 layer formed at the inner side of the outer Fe sheath with a hole at the centre. Some very thin reacted layer about 5 μm thick is also observed at the boundary of the MgB_2 layer and the Fe sheath, but this has no effect on J_c.

The irreversibility field B_{irr} determined using a critical current criterion of 100 A/cm^2 comes out to be 25 T which is higher than that for the PIT-processed wire (22.5 T). This high value of B_{irr} in IMD processed wires is related to high-density MgB_2 and better connectivity. The decisive factor, however, is that coronene is an active source of C ensuring substitution of C at the B sites in the MgB_2 lattice. This carbon substitution also leads to an increase of B_{c2} which in turn is responsible for high B_{irr} and J_c. This is observed in both the processes, that is, PIT and IMD.

From the above discussion, it can now safely be concluded that coronene ($C_{24}H_{12}$) is a better source of C and is a superior additive compared to SiC. Carbon content in coronene being 96% there is hardly any probability of impurity getting into the MgB_2 layer. On the other hand, Si impurity, while adding SiC, is a major problem. In coronene-added samples, carbon coating over the B particles is very uniform which is conducive to uniform J_c of MgB_2 layer along the length of the wire. The studies

also confirmed, beyond doubt, that the IMD technique is far superior to PIT technique leading to higher H_{irr} and J_c values.

7.3.5 A Hybrid IMD/PIT Technique

In a quest to raise the J_c and J_e of MgB_2 conductors, attempts continue to find still better techniques and/or to modify the existing successful techniques. The hybrid IMD/PIT technique is one such attempt. This is a modified IMD process [29] and involves a small addition of Mg into B powder packed in the annular space available in an IMD process. The diameter of the central Mg rod has to be reduced suitably to maintain proper stoichiometry of MgB_2. Addition of Mg in B powder reduces the quantity of unreacted B but also causes voids in the MgB_2 layer just like in PIT conductor. These voids enable the Mg infiltration into B, enhancing MgB_2 volume fraction increasing thereby J_c of the IMD processed MgB_2 wires. At the same time, the process results in a smaller hole at the centre of the wire. As the Mg contents increase, J_c continues to rise, attains a maximum value ($J_e = 6 \times 10^3$ A/cm^2 (4.2 K, 10 T) and decreases thereafter. The maximum is observed at an addition of 6 mol% Mg. Using high-quality C-doped nanosized B powder, the maximum J_c in IMD wires comes out to be 1.0×10^5 A/cm^2 (4.2 K, 10 T). The reason for high J_c is the smaller amount of unreacted B left after heat treatment. The problem associated with the use of high-quality B powder in IMD process is that the MgB_2 layer formed in the IMD process is quite dense which prevents infiltration of Mg from the centre towards the outer metal sheath leaving B-rich region close to the metal sheath. It is for this reason that the MgB_2 layer in IMD process is thin < 90 μm leading to smaller MgB_2 area and low J_e.

In the hybrid method, however, the use of a high-quality B nanopowder reduces the Mg infiltration distance which increases MgB_2 layer thickness. This is seen from the optical microscope pictures in Fig. 7.7. Addition of Mg powder also produces many small voids in the MgB_2 layer which facilitates faster Mg infiltration and an increase in the MgB_2 layer thickness. As a result, the MgB_2 area fraction increases and so does the J_e. Therefore, if we use high-quality B nanopowder in hybrid method the addition of Mg powder is likely to cause a decrease in only J_c, due to the formation of voids. The J_e will, however, increase because of the larger MgB_2 area fraction. Therefore, this method can yield MgB_2 wires with high J_e values for practical application, regardless of the B powder used. Shujun and Kumakura [26] fabricated MgB_2 wires following this hybrid method using a nanosized B powder (< 250 nm)) with 10 mol% Mg powder (325 mesh) and 6 mol% C using $C_{24}H_{12}$ as a C source. A value of $J_e = 1.0 \times 10^4$ A/cm^2 (4.2 K, 10 T) was reported. For achieving maximum J_e value, the optimization of Mg and B powder size is very important.

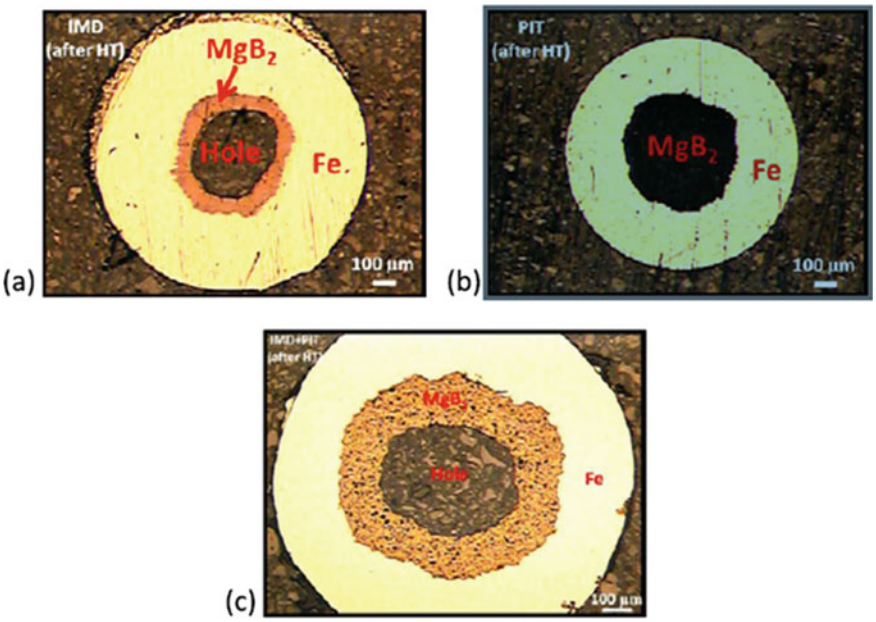

Fig. 7.7 Optical microscope pictures of the transverse cross sections of the **a** IMD, **b** PIT and **c** hybrid IMD + PIT-processed wires after heat treatment. A thin dense MgB_2 layer in IMD wire and a thicker layer in hybrid wire in the lower row are distinctly visible [29]. With permission from IOP

7.4 Low AC Loss MgB_2 Wires/Cables

Low AC loss is a crucial parameter in practical superconductors used for AC applications and in magnets where the current sweep rate is high. It is imperative that MgB_2 MF wires are produced in the form of twisted fine filaments and using cladding and thermal stabilizing materials which cause minimum AC losses. We have already discussed in Chap. 2 that AC losses in multifilamentary superconductors arise because of (i) hysteresis loss in filaments (ii) inter-filamentary coupling and (iii) eddy currents generated in metallic parts/components in the vicinity. In MgB_2 conductors, the outer sheath used is usually ferromagnetic such as Fe, Ni, Monel or Cu-Ni. These materials contribute an additional loss term coming from their magnetization. Attempts are thus being made to replace these outer sheaths with nonmagnetic materials with good mechanical strength and thermal stabilization properties. The hysteresis loss below the penetration field is proportional to B^n where n lies between 2 and 3. Above the penetration field, the hysteresis losses are proportional to B. Optimization of all the process parameters to minimize AC losses in MF superconducting wires and cables thus assumes great importance. Experimental AC loss data at temperature and magnetic field of interest is crucial for the design of an AC application device.

The present MgB_2 conductors involving copper stabilizer and ferromagnetic outer sheath serve well DC applications but pose problems when used for AC applications. Copper causes strong eddy current losses and ferromagnetic component (outer sheath) increases magnetization losses. Coupling current losses become high in untwisted filaments. Ways have been found to circumvent these limitations to minimize AC losses by:

1. Reducing the filament diameter which lowers the hysteresis losses.
2. Using a conducting material for thermal stabilization other than copper to reduce eddy current losses.
3. Reducing inter-filamentary coupling by twisting and using a filament barrier (Nb, Ta, Ti or Nb-Ti) which prevents reaction of MgB_2 with the matrix.
4. Using non-magnetic sheath material with requisite mechanical strength to eliminate extra loss due to the magnetization of the sheath material.

A new sheath material, lightweight Al-Al_2O_3 MMC (metal-matrix composite) with a brand name HITEMA (high-temperature aluminium) has been used by Kovac et al. [30]. This Al-Al_2O_3 MMC is an excellent material for use at low temperature with a RRR ($R_{300\,K}/R_{25\,K}$) = 20 and a room temperature ultimate tensile strength (σ_{UTS}) of 235 MPa. The material also has attractive thermal and electrical properties. Its melting point is 652 °C, quite close to the reaction temperature of MgB_2. The temperature range over which the material can be used is too restrictive.

As a substitute to copper and magnetic sheath material the Kovac group [31] chose Glidcop Al-60, a non-magnetic MMC for the outer casing of the MgB_2 wires and were able to reduce AC losses significantly. Glidcop is a copper-based metal-matrix composite (MMC) alloyed with aluminium oxide (Al_2O_3) ceramic particles. Alloying marginally reduces thermal and electrical conductivity, but greatly increases the copper's resistance to thermal softening, enhances strength at elevated temperature and also increases resistance to radiation damage.

Figure 7.8a is a monofilament wire (1f) square cross section with MgB_2 (22%), Nb barrier (23%) and Glidcop A-60 (55%) as the outer sheath. Figure 7.8b is a 30 filaments wire (30f), non-twisted with MgB_2 (12.4%), Ti barrier (24.3%) with a central core and the stabilizing outer casing of Glidcop (63.3%). This wire has also been twisted with pitch lengths of 2.5 mm, 5 mm and 10 mm designated as 30f–2.5 mm, 30f–5 mm and 30f–10 mm, respectively. Figure 7.8c is a cable having 7 untwisted 30f strands of 0.416 mm diameter and designated as (7 × 30f). Figure 7.8d is another cable fabricated with 7 monofilament wires with Cu as stabilizer and Ti as filament barrier designated as (7 × 1f). Both the cables have one wire at the centre and another 6 transposed around the central wire with 15 mm length of transposition. AC loss measurements [31] were carried out in the temperature range of 15.5–40 K, at two frequencies of 72 and 144 Hz and field up to 26 mT. Some of the important findings of the group are summarized below:

1. For monofilamentary wire (sample 1f) the AC loss at 18 K is very small because of high J_c and hardly any field penetration. Loss rises with the increase of temperature (at fixed field of 26 mT) because of fall in J_c and increased field

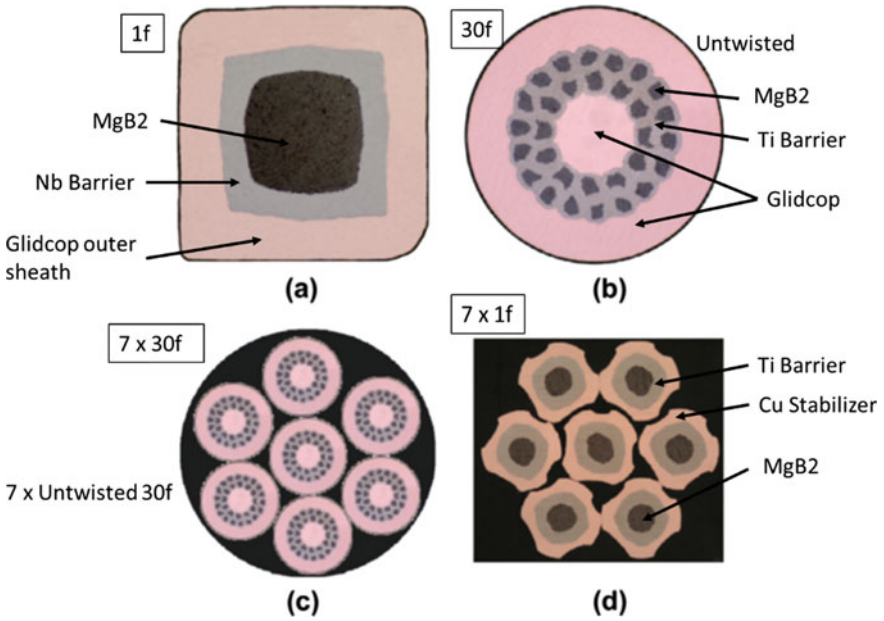

Fig. 7.8 Cross sections of MgB_2 wires with **a** single filament, **b** 30-filaments, **c** 7 × 30 filaments and **d** 7 filaments. Cable 7 × 1f is used for AC loss measurements [31]. Courtesy L. Kopera and P. Kováč, and with permission from Elsevier

penetration. A peak appears close to 28 K where the loss value is 1.5×10^3 J/m^3. The peak corresponds to full-field penetration at this field and temperature. AC loss decreases sharply at higher temperature after the peak as the J_c decreases close to T_c ($\approx$ 35 K). The loss does not change with frequency which confirms the fact that the loss is purely hysteretic and the coupling loss is absent in monofilamentary wire.

2. For 30 filament wire (sample 30f), the AC loss is higher than in monofilamentary wire. This too rises with temperature until a peak appears at a temperature of 27 K with a loss value $Q = 7 \times 10^3$ J/m^3. The loss in this 30 filament wire is found to be frequency dependent confirming the presence of losses due to filament coupling. Changing magnetic field induces a voltage which drives the shielding currents from one filament to another across the non-superconducting matrix. Shielding current loops are formed occupying the whole of the composite instead of confining to individual filaments. As the temperature rises, the hysteresis part of the loss increases, a peak appears at 27 K and drops sharply close to T_c just like in monofilamentary wire (sample 1f). However, if the composite conductor is twisted along its axis cutting effectively the length equal to one fourth of the twist pitch, it behaves as a collection of isolated filaments and coupling loss is eliminated.

3. Experimental data on 30 filament wire (samples 30f) with different twist pitches (pitch lengths 2.5, 5 and 10 mm) confirm the reduction of losses in twisted wires. The loss at the peak in the loss curve of the sample 30f twisted with a pitch of 2.5 mm is $Q \approx 1.1 \times 10^3$ J/m^3 in comparison with the untwisted sample 30f ($Q \approx 7 \times 10^3$ J/m^3). Twisting does bring down the coupling losses, but it is not from the decoupling of the filaments alone but also due to a degradation in critical current caused by mechanical stress during twisting.

In view of the I_c degradation due to twisting, the twist pitch has to be optimized so as to benefit most by twisting. Kovac et al. [31] introduced normalized AC loss $Q_{norm} = (I_{cN}/I_{cT})$ where Q is the ac loss of the wire, I_{cT} is the critical current of the twisted wire and I_{cN} critical current of the wire without twisting. Figure 7.9 shows the plots of Q_{norm} against the temperature at fixed field 26 mT and frequency 72 Hz. Interestingly, the Q_{norm} is found to be lowest for wire with a twist pitch of 10 mm. Wires with twist pitches 2.5 and 5 mm have higher losses than the wire with 10 mm pitch, meaning thereby that shorter twist pitches do not necessarily improve the AC loss performance of the wires. The inset is a plot of Q_{norm} against twist pitch at different temperatures and at a field of 26 mT and 72 Hz frequency. The losses are minimum for 10 mm pitch. This means that the decrease of losses with twisting has a limit and one needs to optimize pitch which leads to minimum loss. The conductor geometry and the fabrication process play a role in this optimization. Q measurements in cables reveal that cabling does not influence the AC loss in untwisted strands. The loss peak of the 7 × 30f cable is found to be shifting to lower temperature compared to the untwisted 30f strand. 7 × 1f cable behaves like a wire with much thinner

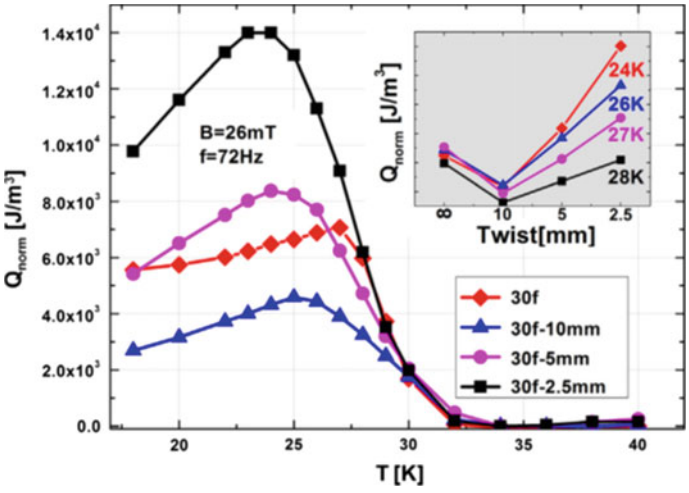

Fig. 7.9 Magnetization losses normalized by a factor of critical current degradation at 26 mT field and 72 Hz frequency plotted against temperature. The inset is a plot of normalized AC losses versus twist pitch at various temperatures [31]. Courtesy L. Kopera and P. Kováč, and with permission from Elsevier

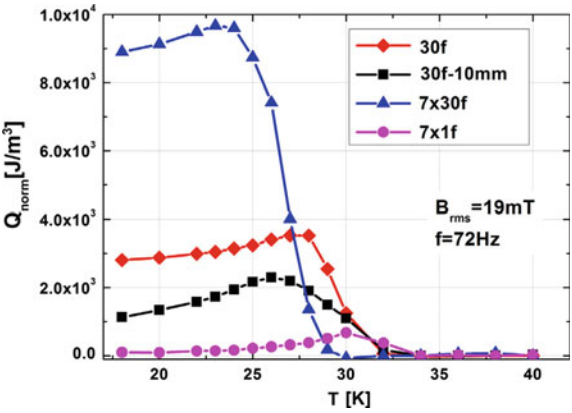

Fig. 7.10 Magnetization loss normalized by a factor of critical current degradation at 19 mT field and 72 Hz frequency. Out of the four samples (7 × 30f, 30f, 30f–10 mm and 7 × 1f), cable 7 × 1f has the minimum AC loss and cable 7 × 30f maximum AC loss [31]. Courtesy L. Kopera and P. Kováč, and with permission from Elsevier)

filaments but without any reduction in coupling loss. Presence of coupling loss is verified from the frequency dependence of the loss and loss behaviour observed at low temperature. Figure 7.10 shows the plots of ac magnetization loss normalized by a factor of critical current degradation, Q_{norm} at 19 mT field and 72 Hz frequency. Out of the four samples (7 × 30f, 30f, 30f-10 mm and 7 × 1f), cable 7 × 1f has the minimum AC loss and cable 7 × 30f maximum AC loss. The loss behaviour of 7 × 1f cable is purely hysteretic, minor variation of loss with frequency is believed to be caused by eddy current generated in the metal matrix. Further, the full penetration in 7 × 1f cable is reached at a higher temperature ≈ 30 K. This behaviour hints at a larger size of superconducting filaments in the cable made from 7 monofilament wires. The authors do not find evidence of appreciable degradation of critical current during the cabling operation either. They concluded that cable 7 × 1f has the lowest normalized magnetization AC losses, Q_{norm} and did not show coupling loss. This cable configuration can thus be considered promising for producing cables for future AC applications.

7.5 Rutherford MgB_2 Cables

The attractive features of MgB_2 especially, the low anisotropy and the ease of manufacturing as compared to high T_c cuprates have fuelled the race to produce this material in the form and shape needed for the application of interest. The Rutherford style cable is the most popular cable configuration used for accelerator magnets. The fill factor of a winding using rectangular wire/cable is higher approximately by a factor of 1.27 than the winding done using cable with circular cross section. Another advantage specific to MgB_2 cable is that the cable flattening die, used for the compression of Rutherford cable, also increases the packing density of the MgB_2 core. High density of MgB_2 leads to higher J_c.

Kopera et al. [32] reported studies on MgB_2 Rutherford cable by transposing 12 monocore wires fabricated using PIT in situ technique. Monocore wires had 8 wt% SiC, Ti barrier, Cu stabilizer and Monel 400 as the outer casing. The composite assembly is cold processed to wire of 0.3 mm diameter. The wire is heat reacted at 800 °C for 30 min under argon atmosphere. Two cables were prepared by twisting 12 and 19 wires helically around a copper stabilizer and around a monocore wire and designated as HC12 and HC19, respectively. The Rutherford cable is fabricated by stranding helically the wires around a specially designed mandrel and finally compacted by roller dies to flat shape of 2 mm × 0.54 mm cross section. During this process, the circular-shaped wires too get deformed and flattened which increases the core packing density and J_c. Relevant parameters of the wires and the cables are given in Table 7.5. The critical current, I_c of the Rutherford cable turns out to be close to 12 times the I_c of a single wire which confirms good homogeneity of the wires and the cable. This is an indication that the cable processing did not degrade the I_c of wires.

Figure 7.11 shows the plots of engineering critical current density, J_e of the MgB_2 cables HC12, HC19 and the 12 wire transposed Rutherford cable at 4.2 K plotted against the magnetic field. The figure shows interesting results. J_e of 19 core cable is higher than the HC12 cable. The reason is that HC12 has large central core of Cu (0.9 mm dia.) which results in low J_e. The Rutherford cable has higher J_e compared to even HC19 which has 19 wires in spite of the fact that the packing factors in both

Table 7.5 Parameters of the MgB_2 mono/MF wires and Rutherford cable (data compiled from [32])

Wire/strand (PIT)		Rutherford cable	
Parameter	Value	Parameter	Value
Monofilament wire dia.	0.3 mm	Width	2 mm
MgB_2 core diameter	93 μm	Thickness	0.54 mm
Volume fraction		No. of wires transposed	12
MgB_2	10%	Cable type	
Ti barrier	18%	SSRC ε_{irr} σ_{irr}	40 μm SS strips Soldered 0.75% 300 MPa
Copper	18%	InRC ε_{irr} σ_{irr}	In-impregnated 0.63% 238 MPa
Monel outer sheath	54%	J_e (4.2 K, 8 T)	1.2×10^3 A/cm^2
SiC	8 wt%		
J_e of HC12[a] (4.2 K, 8 T)	5×10^2 A/cm^2		
J_e of HC19[b] (4.2 K, 8 T)	8×10^2 A/cm^2		

[a]Cable HC12: Helically wound 12 monocore wires around a 0.9-mm-diameter central Cu wire
[b]Cable HC19: Consists of 6 + 12 strands helically wound around a central strand

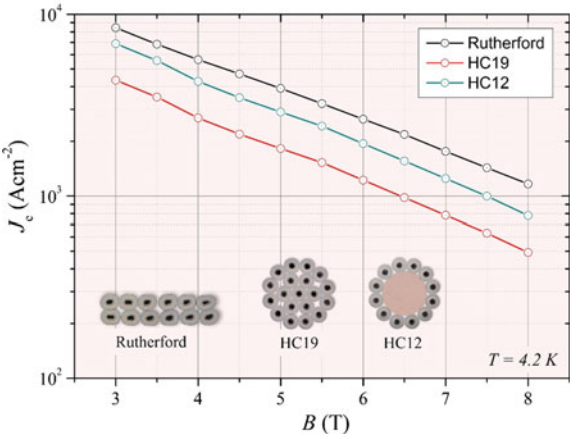

Fig. 7.11 Engineering current density, J_e of the MgB_2 cable HC12, HC19 and the 12 wire Rutherford cable at 4,2 K plotted against the magnetic field [32]. Courtesy L. Kopera and P. Kováč, Institute of Electrical Engineering, SAS, Bratislava

the cables are close within 3%. It appears that the J_e in Rutherford cable is high because of the higher core density due to the flattening by the roller dies. Further, the effective J_e will be higher in the winding of a magnet with flat cable as compared to the winding with round cable. The fill factor of the winding with round cable will only be a maximum of 78.5% of the winding with rectangular cable.

These studies also revealed that the Rutherford cable has a higher tolerance to stress and strain caused by bending over small diameters. Kopera et al. [32] found an enhancement of critical current by about 6.5% with bending diameter from 70 mm to 38 mm with a maximum at 38 mm. I_c starts degrading when bending diameter is reduced to below 34 mm. Enhancement of I_c with bending could be due to a reduction of the residual strain in the cable. The Young's modulus (4.2 K, 6 T) of the Rutherford cable, InRC (indium infiltrated) and SSRC (Rutherford cable SS laminated on both sides), within the elastic range of $\varepsilon = 0.1$–0.3%, is 50 GPa, 52 GPa and 54 GPa, respectively. Thus, the Young's modulus of all the three types of cables is nearly the same. The stiffness of the cable though increases with In-infiltration and with 40 μm SS strips soldered both sides. The irreversible strain and stress measured for InRC cable come out to be $\varepsilon_{irr} = 0.63\%$ and $\sigma_{irr} = 238$ MPa, respectively. Cable with mechanical enforcement by SS strips, SSRC has increased $\varepsilon_{irr} = 0.75\%$ and $\sigma_{irr} = 300$ MPa up by 20% and 26%, respectively. I_c in both cables (InRC and SSRC) increases with strain up to ε_{irr} and decreases thereafter. Increasing the tensile load continuously increases the contact pressure between adjacent strands, which get stretched more uniformly. All of these factors reduce the compressive strain and increase the critical current. This tendency continues up to a strain of 0.65% a value comparable to $\varepsilon_{irr} = 0.65\%$ of the InRC sample. If the tensile strain continues to increase beyond this value crack formation starts in the MgB_2 core which brings down I_c.

7.5.1 *Rutherford Cable with Al-Al_2O_3 Metal-Matrix Composite (MMC) Sheath*

Making a departure from using traditional outer sheath Kováč et al. produced MgB_2 Rutherford cable using a lightweight and high strength outer sheath of Al-Al_2O_3 metal-matrix composite (MMC). The cable has been fabricated with 12 monofilamentary MgB_2 wires prepared by following the IMD process. The motivation for this innovative technique was twofold, one that the IMD wires have been found carrying larger transport current compared to an equivalent PIT wire. The other reason being that high-strength composite used for outer cladding allows higher compaction of the MgB_2 core and thus higher J_c. Similarly, the optimized wire deformation is not possible with soft material like pure Al, but the Al_2O_3-reinforced Al-MMC meets this requirement comfortably. The stress–strain characteristics of the cable also improve. Besides these benefits, the cable is a lightweight conductor which is preferred over the traditional conductors where the weight of the device is an important consideration. The density of aluminium is 2.6 g/cm^3 only compared to 8.9 g/cm^3 of Cu. While producing Rutherford cable one must keep in mind that for good tolerable bending strain the wire diameter should be small. It also favours short transposition length. Since reducing the filament size to a very small value might result in a strong degradation of critical current, it is better to use thin wires with fewer number of filaments.

Kováč et al. [33] produced IMD MgB_2 square wires of 1.04 mm using Mg/B/Ta/Al-1.37 V% Al_2O_3 MMC architecture and following the process of swaging and groove rolling. The wire was further cold drawn to wire of 0.465 mm diameter and 92 m length. Intermediate annealing treatments at 300 °C × 30 min were given during the groove rolling to maintain ductility. The final wire had 11% Mg, 12% B, 27% Ta barrier and 50% Al-MMC. A total of 12 pieces of this wire were stranded and cabled with a transposition length of 20 mm. The cable was flattened and compacted to a final dimensions of 0.85 mm × 2.9 mm. The cable was heat reacted at 630 °C for 10 min. This reaction temperature is just below the melting point of Mg (650 °C) and that of Al-MMC (652 °C). Precaution has to be taken that Mg does not come in contact of Al at the cable edge and form Al–Mg compounds. A resistive transition temperature, $T_c = 36$ K was recorded in the reacted cable.

The comparison of critical current, I_c of a single strand and the 12 wire Rutherford IMD cable (0.85 mm × 2.9 mm) as evaluated by the DC transport and ac transport measurements at 4.2 K plotted against magnetic field show good agreement between the DC and AC transport data and also between the I_c of the IMD Rutherford cable and that of twelve strands at 8 T. This indicates that cabling of the strands does not degrade the I_c of the strands. The in situ 12 strand PIT cable with 19.8% MgB_2 was found to have a $J_e = 10^4$ A/cm^2 (4.2 K) in a field of 3.25 T [33], whereas the 12 strand IMD cable with only 9.6% MgB_2 has this J_e at a higher field, 4.75 T. There is further increase of J_e of this cable by about 36.7% when the cable is compacted to a thickness of 0.80 mm, a reduction of just 5.8%. This is consistent with earlier

studies that B densification by about 10% leads to an increase of J_c in in situ MgB_2 wires by a factor of two. Larger compaction might damage the Ta barrier.

The stress/strain studies reveal that J_c degradation in the cable starts below a bending diameter of 70 mm quite similar to the Rutherford cable (0.72×2.55) using in situ PIT strands of reference [32] with $Cu_{10}Ni$ sheath. Initial J_c enhancement up to a bending diameter of 90 mm observed in PIT cable was not seen in these IMD cables with Al-Al_2O_3 MMC sheath. This difference in behaviour has been attributed to the different residual strain within the sheath material. The bending strain of the IMD cable at the start of J_c degradation is 6% compared to a low value of 0.54% in in situ PIT cable. Undoubtedly the mechanical properties of the outer sheath material play a significant role in controlling the stress/strain tolerance of the cable. A heat treatment of the cable at 640 °C does not reduce the hardness of Al-Al_2O_3 MMC which allows the cable to maintain good strain tolerance.

7.6 Thin Film Route for MgB_2 Conductors

MgB_2 films have been deposited and studied following a variety of techniques such as molecular beam epitaxy (MBE) [34], pulsed laser deposition (PLD) [35], modified reactive method (MRM) [36], hybrid physical–chemical vapour deposition (HPCVD) [37–39] and electron beam evaporation (EBE) [40]. By far the most effective technique, which yielded high quality film with excellent superconducting parameters, turned out to be the HPCVD technique. This technique is a combination of two processes, namely the chemical decomposition of diborane (B_2H_6) and physical vapour deposition of magnesium metal. Alloying Mg and B to realize MgB_2 phase as per the conventional P–T diagram is not feasible because of large mismatch of their melting points. The melting point of Mg is low (650 °C) and that of B is high (2076 °C). Further, the sticking coefficient of Mg being relatively low at higher temperatures, the film growth should proceed at lower temperature to realize high yield of MgB_2 phase. Diborane decomposes at low temperature to hydrogen and other boron hydrides and at high temperature into hydrogen gas and Boron. It decomposes even at room temperature, though slowly, into hydrogen and higher borane. Thus, in HPCVD technique decomposition of diborane leads to high distribution of active B compatible with the high vapour pressure of Mg.

A typical HPCVD coating system used by Ranot and Kang [41] is shown in Fig. 7.12a, b. It has a bell-shaped quartz reactor with pressure and temperature control, gas inlet with flow control system, a SS susceptor with an induction heater outside and a load-lock chamber. The process chamber is connected to the load-lock chamber with a gate valve in between. The gate valve protects the process chamber against contamination during the deposition of MgB_2 films. Unlike the PIT process, where MgO and O impurities obstruct the inter-grain current, the HPCVD grown films are free of such impurities and one gets high-quality MgB_2 films.

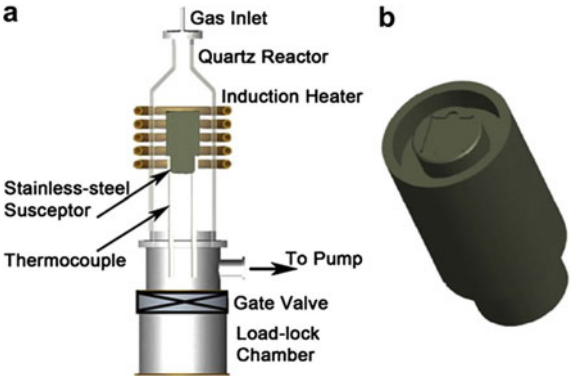

Fig. 7.12 **a** Schematic diagram of the HPCVD coating system consisting of a load-lock chamber, a process chamber, SS susceptor, an induction heater and a bell-shaped quartz reaction chamber. **b** The SS susceptor has a central raised substrate holder and a concentric groove. The substrate is mounted at the centre, and Mg pieces are spread around in the groove enough to maintain high vapour pressure during deposition [41]. With the permission from Elsevier

Ranot and Kang [41] fabricated MgB_2/Cu tapes over a wide temperature range of 460–520 °C by depositing epitaxial film of MgB_2 using HPCVD technique on textured Cu (0 0 1) and polycrystalline Hastelloy tapes. The tapes had a T_c ranging between 36 and 38 K with a transition width (ΔT_c) of about 0.3–0.6 K. The highest critical current density (J_c) of 1.34×10^5 A/cm^2 (5 K, 3 T) was obtained for the MgB_2/Cu tape grown at 460 °C. For increasing the J_c further through C doping, a SiC layer was coated on the Cu tape. These SiC-doped MgB_2/Cu tapes exhibited very high J_c values as compared to undoped MgB_2/Cu tapes. Doped film also showed a trend in the dependence of J_c with growth temperature as compared to that shown by undoped tapes. The significant improvement in J_c has been attributed to strong flux pinning provided by SiC impurity and the grain boundaries.

Scanning electron microscope (SEM) pictures of the surface morphology of the films deposited at different temperatures are shown in Fig. 7.13. These micrographs reveal that the MgB_2 grains are well connected in films deposited at 460 °C (Fig. 7.13a) and 480 °C (Fig. 7.13b). Hexagonal crystallites of 300–500 nm size were also observed in films deposited at 460 °C. The grain size in the films deposited at 500 and 520 °C was irregular, and the grain connectivity too was very poor. Figure 7.13c and d are suggestive of a severe reaction of Mg vapours with Cu tape by way of a eutectic melting or diffusion of Mg vapours in Cu tape.

Figure 7.14 shows the dependence of the critical current density, J_c at 5 K (solid symbols) and at 20 K (open symbols) on magnetic field for HPCVD MgB_2/Hastelloy tapes with film grown at different deposition temperature between 460 and 520 °C. J_c was calculated from the magnetic hysteresis (M-H) loops by using the Bean's critical state model. The J_c was found to be highest for the tape with film deposited at 460 °C. J_c however decreases with the increase of deposition temperature. The J_c of the MgB_2 tape with film grown at 460 °C was about 2.6 times higher than in

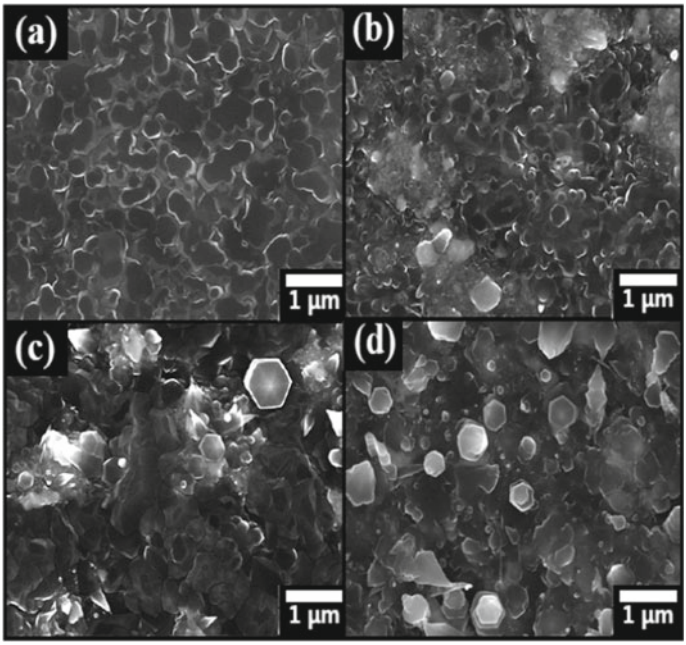

Fig. 7.13 SEM picture of MgB_2/Cu tapes grown at 460° (**a**), 480° (**b**), 500° (**c**) and 520° (**d**) [41]. With the permission from Elsevier

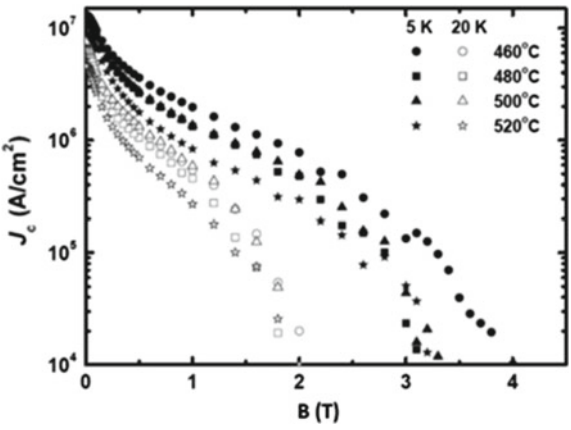

Fig. 7.14 Dependence of the critical current density J_c measured at 5 K (solid symbols) and at 20 K (open symbols) on magnetic field for HPCVD MgB_2/Hastelloy tapes grown at different H_2/B_2H_6 gas mixture flow rates and deposition temperature [41]. With the permission from Elsevier

tape with film grown at 520 °C. High density of grain boundaries obtained in the tape grown at 460 °C might be responsible for an effective flux pining and thus high J_c. The reason for the decrease of J_c at higher deposition temperature could be the formation of $MgCu_2$ phase during the reaction at 520 °C as revealed by the XRD data.

Ranot and Kang [41] also studied thick films of MgB_2 on a 45-μm-thick polycrystalline Hastelloy tapes with different flow rates of hydrogen and diborane H_2:B_2H_6 gas mixture and for different deposition times. All the tapes were deposited at a temperature of 520 °C and a pressure of 200 Torr. The flow rate of B_2H_6 gas was varied from 10 to 30 sccm and that of H_2 from 90 to 70 sccm, respectively, under deposition times of 10 and 30 min. The MgB_2 tapes are polycrystalline because of the polycrystalline nature of the Hastelloy substrate. Long deposition time leads to preferred orientation along the (0 0 l) plane. The observed compression of c-axis lattice parameter due to the increase in MgB_2 layer thickness indicates that the layer is under tensile strain. No impurity or secondary phases were found confirming that MgB_2 does not react with Hastelloy. The SEM pictures of the surface morphology of the MgB_2 films deposited at different H_2/B_2H_6 gas mixture flow rates and for different times are shown in Fig. 7.15. The layer thickness is maximum at 6 μm for a H_2/B_2H_6 flow rate of 70:30 × 30 min and minimum of 0.5 μm for 90:10 for 10 min. The T_c for 6 μm thick film tape was 39 K.

Figure 7.16 shows the dependence of the critical current density J_c measured at 5 K (solid symbols) and at 20 K (open symbols) on magnetic field for HPCVD MgB_2/Hastelloy tapes grown at different temperatures and at different H_2:B_2H_6 gas mixture flow rates. The MgB_2 film grown on Hastelloy tapes at 520 °C with an optimum thickness of 2 μm showed highest $J_c = 5.8 \times 10^6$ A/cm^2 (20 K, 0 T) and $J_e = 2.4 \times 10^5$ A/cm (20 K, 1.5 T). As the film thickness increases beyond 2 μm, J_c starts decreasing. Much thicker MgB_2 films (6 μm) on Hastelloy tape had a $J_c = 1.9 \times 10^6$ A/cm^2 (20 K, 0 T) and $J_e = 2.4 \times 10^5$ A/cm^2 (20 K, 1.5 T). Critical current density, J_c in all the tapes of HPCVD MgB_2 on Hastelloy was found much higher than the J_c in tapes on other metallic substrate, such as Cu, SS and Nb. These results indicate strongly that HPCVD MgB_2-coated conductors can be operated at 20 K and serve as practical superconductor for many applications. Figure 7.17 shows the magnetic field dependence of critical current density in MgB_2 wires/tapes fabricated by various methods in comparison with Nb-Ti and Nb_3Sn conventional superconductors [42]. The figure clearly shows the superiority of J_c in MgB_2/α-Al_2O_3 film compared to conventional Nb-Ti and Nb_3Sn superconductors in field higher than 18 T. The J_c values are bound to rise in near future where MgB_2 could be used in large magnet-based projects.

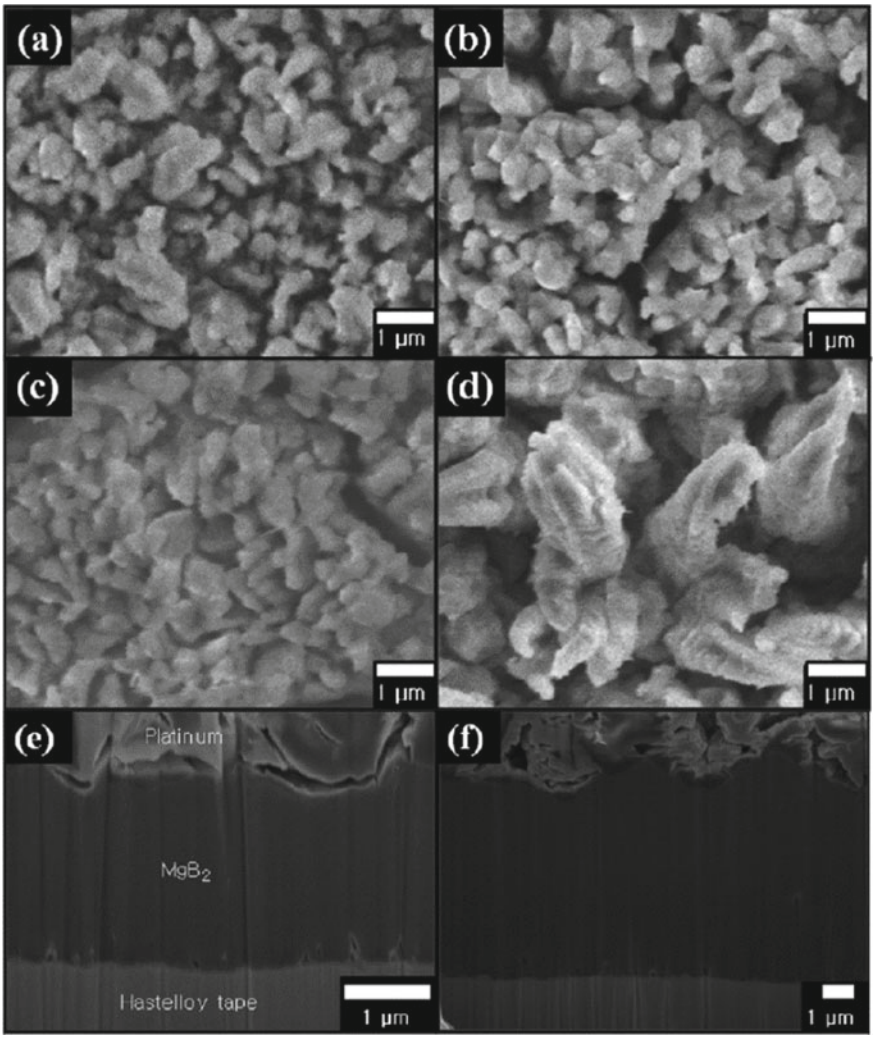

Fig. 7.15 Surface morphology of MgB_2 films deposited on 45-μm-thick polycrystalline Hastelloy tapes at different H_2/B_2H_6 mixture flow rate for different times [41]. **a** H_2/B_2H_6 90:10 sccm gas mixture × 10 min. **b** H_2/B_2H_6 70:30 sccm gas mixture × 10 min. **c** $H_2/B2H_6$ 90:10 sccm gas mixture × 30 min. **d** H_2/B_2H_6 70:30 sccm gas mixture × 30 min. **e** H_2/B_2H_6 70:30 sccm gas mixture × 10 min. **f** H_2/B_2H_6 70:30 sccm gas mixture × 30 min. With permission from Elsevier

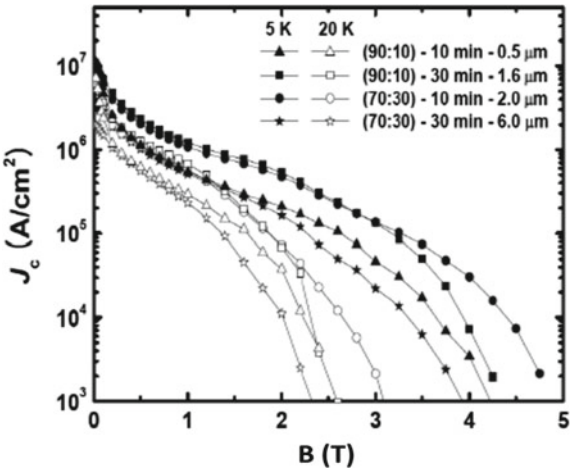

Fig. 7.16 Dependence of critical current density, J_c on magnetic field measured at 5 K (solid symbols) and 20 K (open symbols) for MgB_2/Hastelloy tapes grown at different H_2/B_2H_6 gas mixture flow rates and different deposition times. Best value of J_c is obtained for 2-μm-thick film [41]. With permission from Elsevier

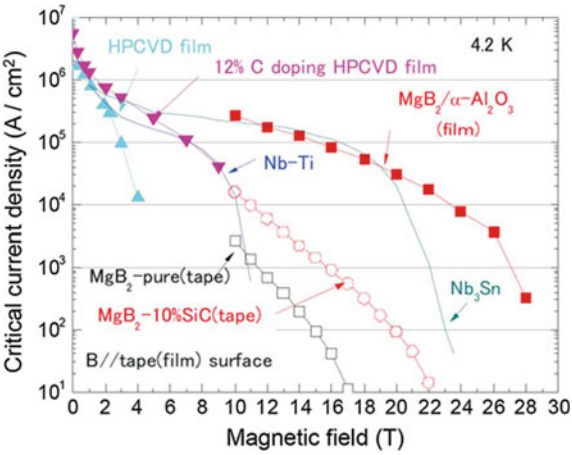

Fig. 7.17 Magnetic field dependence of critical current density, J_c in MgB_2 wires/tapes fabricated by various methods in comparison with Nb-Ti and Nb_3Sn conventional superconductors. Superiority of J_c in MgB_2/α-Al_2O_3 film over conventional Nb-Ti and Nb_3Sn conductors in field higher than 18 T is clearly visible [42]. With the permission from Springer Nature

7.7 An Upswing in the Use of MgB_2 for Applications

Great attraction of MgB_2 as a low-cost superconductor and its ability to operate in the 20–25 K range of temperature, where scarce liquid helium is not required, led to a fast development in the commercial production of this material in the form of wires and cables. MgB_2 wires are already in use for a large number of applications. It has emerged as a superconductor of choice for NMR, MRI, motors, generators, fault current limiters and SMES. Accelerators and nuclear fusion devices might be applications next. At the present time, there are two major manufacturers of this material, Columbus MgB_2 Unit of the ASG Superconductors and the Hyper Tech Research (HTR) LLC.

Figure 7.18a is the cross section of the standard 0.84 mm dia. MgB_2 wire manufactured and marketed by HTR. The wire is Cu-stabilized, has 18 MgB_2 filaments with Nb barrier around and has an outer casing of Monel. The critical current density of the wire at different operating temperature as a function of magnetic field is plotted in Fig. 7.18b. The J_c values of the wire are as: J_c (4.2 K, 4 T) = 2×10^5 A/cm^2 and J_c (20 K, 2 T) = 1.4×10^5 A/cm^2. HTR markets MgB_2 conductors under different brand names with 18, 24, 30 and 36 filaments with fill factors of 8%, 17%, 20% and 15% and copper components of 32%, 16%, 12% and 15%, respectively, for different type of applications. The conductors are being increasingly used for DC and AC applications. Intense efforts are going on for developing technologies for building magnets for a variety of applications. These include:

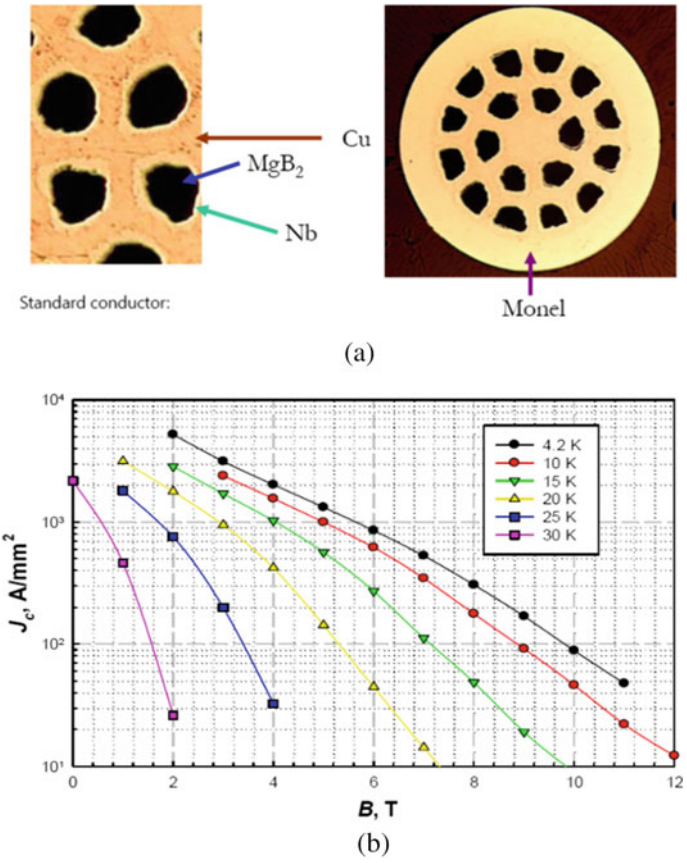

Fig. 7.18 **a** Cross section of the standard 0.84-mm-dia. 18-filament Cu-stabilized MgB_2 wire with Nb barrier marketed by Hyper Tech Research LLC. **b** Magnetic field dependence of the critical current density, J_c of the above MgB_2 wire at different temperatures down to 4.2 K. Copyright Hyper Tech Research, courtesy David Doll

- Whole body 1.5 T, 3.0 T, 5–7 T, and other specialized conduction-cooled magnets which would operate at 10 K. Conceptual designs of such MgB_2 magnets have been made.
- Wholly superconducting wind turbine generators in the range of 8–20 MW are being developed with superconducting stator and rotor operating at 15–20 K.
- Several transport and aviation industries are working on motors and generators technology for building wholly electric aircrafts.
- Many other superconducting components needed for aircraft such as cables, fault current limiters (FCLs) and magnetic energy storage (SMES) too are being built.
- The technology developed for aircraft will surely expand to ships and trains.
- The cable-in-conduit (CIC) conductor cable technology is being developed for use of MgB_2 conductor for low-field poloidal coils and the compensating coils of the fusion reactors.

To conclude, MgB_2 superconductor has come of age and has already established itself as a practical superconductor for low-field applications. Continued research and development will lead to wider acceptability of this material for medium range field in the near future. Its use in conduction-cooled whole-body MRI scanners has great potential and will revolutionize the healthcare sector. MRI scanners then can reach the remotest places the world over, where delivery of liquid helium is just not possible. MRI is indeed the gift of superconductivity to the society.

References

1. J. Nagamatsu, N. Nakagawa, T. Muranaka et al., Nature **410**, 63 (2001)
2. S.L. Budko, P.C. Canfield, Physica C **514**, 142 (2015)
3. A. Gurevich, Phys. Rev. B **67**, 184515 (2003)
4. S.X. Dou, O. Shcherbakova, W.K. Yeoh, J.H. Kim et al., Phys. Rev. Lett. **98**, 097002 (2007)
5. J.K. Kim, Y.-U. Heo, A. Matsumoto, H. Kumakura et al., Supercond. Sci. Technol. **23**, 075014 (2010)
6. J. Kapinski, S.M. Kazakov, J. Jun et al., Phys. C (Supercond.) **385**, 42 (2003)
7. K. Komori, K. Kawagishi, Y. Takano et al., Appl. Phys. Lett. **82**, 1047 (2002)
8. V. Ferrando, P. Orgiani, A.V. Pogrebnyakov et al., Appl. Phys. Lett. **87**, 252509 (2005)
9. G. Glasso, A. Malagoli, C. Ferdeghini et al., arXiv:Cond-Mat/0103563
10. H. Kumakura, A. Matsumoto, H. Fuji, K. Togano, Appl. Phys. Lett. **79**, 2435 (2001)
11. H. Fang, P.T. Putman, S. Padmanabhan et al., Supercond. Sci. Technol. **17**, 717 (2004)
12. M.D. Sumption, M. Bhatia, X. Wu et al., Supercond. Sci. Technol. **18**, 730 (2005)
13. G.Z. Li, Y. Yang, M.A. Susner, M.D. Sumption, E.W. Collings, Supercond. Sci. Technol. **25**, 02500 (2012)
14. A. Malagoli, V. Braccini, in *MgB_2 Superconducting Wire, Basics and Applications*, ed. by R. Flükiger (World Scientific, 2016), pp. 239–270
15. A. Kario, V. Grinenko, A. Kauffmann, W. Haβler et al., Physica C **483**, 222 (2012)
16. G. Giunchi, S. Ceresara, G. Ripamonti, A.D. Zenobio et al., Supercond. Sci. Technol. **16**, 285 (2003)
17. J.M. Hur, K. Togano, A. Matsumoto, H. Kumakura, H. Wada, K. Kimura, Supercond. Sci. Technol. **21**, 032001 (2008)
18. G. Giunchi, G. Ripamonti, E. Perini, T. Cavallin, E. Bassani, IEEE Trans. Appl. Supercond. **17**, 2 (2007)

19. K. Togano, J. Hur, A. Matsumoto, H. Kumakura, Supercond. Sci. Technol. **22**, 015003 (2009)
20. K. Togano, J. Hur, A. Matsumoto, H. Kumakura, Supercond. Sci. Technol. **23**, 085002 (2010)
21. S.J. Ye, A. Matsumoto, K. Togano, H. Kumakura, Physica C **471**, 1133 (2011)
22. G.Z. Li, M.D. Sumption, M.A. Susner, Y. Yang, K.M. Reddy, Supercond. Sci. Technol. **25**, 115023 (2012)
23. G.Z. Li, M.D. Sumption, J.B. Zwayer, M.A. Susner et al., Supercond. Sci. Technol. **26**, 095007 (2013)
24. S.J. Ye, A. Matsumoto, K. Togano, T. Ohmura, H. Kumakura, Supercond. Sci. Technol. **26**, 105027 (2013)
25. S.J. Ye, A. Matsumoto, Y. Zhang, H. Kumakura, Supercond. Sci. Technol. **27**, 085012 (2014)
26. Y.E. Shujun, H. Kumakura, Supercond. Sci. Technol. **29**, 113004 (2016)
27. G. Giunchi, L. Saglientti, A. Figini Albisetti, E. Perini et al., IEEE Trans. Appl. Supercond. **23**, 6200605 (2013)
28. H. Kumakura, J. Hur, K. Togano, A. Matsumoto, H. Wada, K. Kimura, IEEE Trans. Appl. Supercond. **21**, 2643 (2011)
29. S.J. Ye, A. Matsumoto, K. Togano, Y. Zhang, T. Ohmura, H. Kumakura, Supercond. Sci. Technol. **27**, 055017 (2014)
30. P. Kovac, I. Husek, T. Melisek, M. Kulich, A. Rosova et al., Supercond. Sci. Technol. **30**, 105001 (2017)
31. J. Kovac, J. Souc, P. Kovac, I. Husek, F. Gomory, Physica C **495**, 182 (2013)
32. L. Kopera, P. Kováč, I. Hušek, T. Melišek, Supercond. Sci. Technol. **26**, 125007 (2013)
33. P. Kováč, L. Kopera, J. Kováč, M. Hain, T. Melišek et al., Supercond. Sci. Technol. **31**, 015015 (2018)
34. T.H. Kim, J. Korean Phys. Soc. **49**, L1881 (2006)
35. D. Mijatovic, A. Brinkman, G. Rijnders, H. Hilgenkamp et al., Physica C **372**, 1258 (2002)
36. B.H. Moeckly, W. Ruby, Supercond. Sci. Technol. **19**, L21 (2006)
37. W.K. Seong, J.Y. Huh, W.N. Kang, J.-W. Kim et al., Chem. Vapor Depos. **13**, 680 (2007)
38. X.X. Xi, X.H. Zeng, A.V. Pogrebnyakov, A. Soukiassian, S.Y. Xu et al., Nat. Mater. **1**, 35 (2002)
39. T.G. Lee, M. Ranot, W.K. Seong, S.-G. Jung et al., Supercond. Sci. Technol. **22**, 045006 (2009)
40. M. Haruta, T. Fujiyoshi, T. Sueyoshi, K. Miyahara et al., Supercond. Sci. Technol. **18**, 1460 (2005)
41. M. Ranot, W.N. Kang, Curr. Appl. Phys. **12**, 353 (2012)
42. S. Hata, H. Sosiati, Y. Shimada, A. Matsumoto et al., J. Mater. Sci. **48**, 132 (2013)

Chapter 8
Iron-Based Practical Superconductors

Abstract The year 2008 turned out to be a landmark year for the superconductivity community when Hosono discovered superconductivity in iron-based compounds. Iron, which has large magnetic moment, was traditionally considered as an opponent of superconductivity because of the contradiction between the static electron spin ordering in Fe and dynamic formation of electron pairs of opposite spins in superconductors. The discovery opened the floodgate to the emergence of a large variety of iron-based superconductors (IBSCs) popularly known through the acronyms 1111, 111, 122, 11 and more. These IBSCs are characterized by very high H_{c2} (> 70 T at 20 K), low anisotropy γ (< 2), moderate weak link effect and large critical grain misorientation angle 9° compared to the small value of 3°–5° for YBCO. All IBSCs share in common Fe-pnictogen (P or As) or a Fe-chalcogen (Se or Te). A T_c of 26 K was reported in $La(O_{0.89}F_{0.11})FeAs$, the so-called 1111 compound when F^- was substituted for O^{2-}. The substitution leads to a positive charge transfer to insulating La_2O_2 layer and a negative charge transfer to the Fe_2As_2 conduction layer. These are called electron-doped superconductors. T_c as high as 55 K was reached in 1111 $SmFeAsO_{1-x}F_x$ and 1111 $NdFeAsO_{1-x}F_x$ by replacing La by larger ionic radii rare earth in the parent compound $LaO_{1-x}F_xFeAs$. Similar increase in T_c can be achieved by applying high pressure. The common feature of all the 1111-type compounds is that superconductivity appears only when antiferromagnetic ordering (SDW) is fully suppressed at a certain level of doping. Coexistence of SDW and superconductivity has, however, been observed in a number of 122 superconductors of the type $Sr/BaFe_2As_2$. The compound 122 $Ba_{1-x}K_xFe_2As_2$ is a hole-doped superconductor as K^+ is substituted at the Ba^{2+} site. In contrast, the Co-doped 122 $Ba(Fe_{2-x}Co_x)_2As_2$ is electron doped. Compound $(Ba_{0.6}K_{0.4})Fe_2As_2$ has a maximum $T_c = 38$ K. Iron chalcogenides, FeSe (Te, S) also called the 11 phase compounds have the simplest structure with a low $T_c = 8$ K. Pressure studies on IBSCs have shown interesting results. T_c increases with pressure in underdoped IBSC, T_c remains nearly unchanged in optimally doped compounds, and T_c decreases with pressure almost linearly in over-doped compounds. The cost-effective powder-in-tube (PIT) technique has turned out to be the ideal route to wires/tapes. Transport J_c as high as 10^5 A/cm^2 (4.2 K, 10 T) has already been achieved in 122 superconductors which is more than the threshold set for practical superconductors up to a field of 10 T. Recent production of very uniform 122 tape of more than 100 m single length is a

R. G. Sharma, *Superconductivity*, Springer Series in Materials Science 214,
https://doi.org/10.1007/978-3-030-75672-7_8

step forward in scaling-up the production to kms long wires/tapes. This augers well for the use of this IBSC conductor for building high-field magnets in the near future.

8.1 General Features of Iron-Based Superconductors

Bednorz and Muller in 1986 [1] caused big surprise when they discovered superconductivity at 30 K in an insulator, La_2CuO_4 when doped with Ba or Sr and had oxygen as one of the constituents. Still bigger surprise came in 2006 when Kamihara et al. [2] reported superconductivity at 4 K in a new class of materials, the iron-based oxy-pnictides, of the type LaFeOP, a paramagnetic metal containing magnetic materials like Fe, Co and Ni. The crystal structure of the LaFeAsO system is shown in Fig. 8.1. It comprises of alternate stack of an insulating lanthanum oxide ($La^{3+}O^{2-}$) layer and a conduction layer of iron pnictide ($Fe^{2+}P^{3-}$). Impurity doping in the ($La^{3+}O^{2-}$) layer generates carriers which are transferred to the conduction layer ($Fe^{2+}P^{3-}$). Substitution of F at the O-site releases one electron which is transferred to the conduction layer causing carrier flow in the conduction layer [3]. On the other hand, oxy-pnictide LaFeAsO (1111 superconductor) is a Pauli paramagnetic metal at high temperature

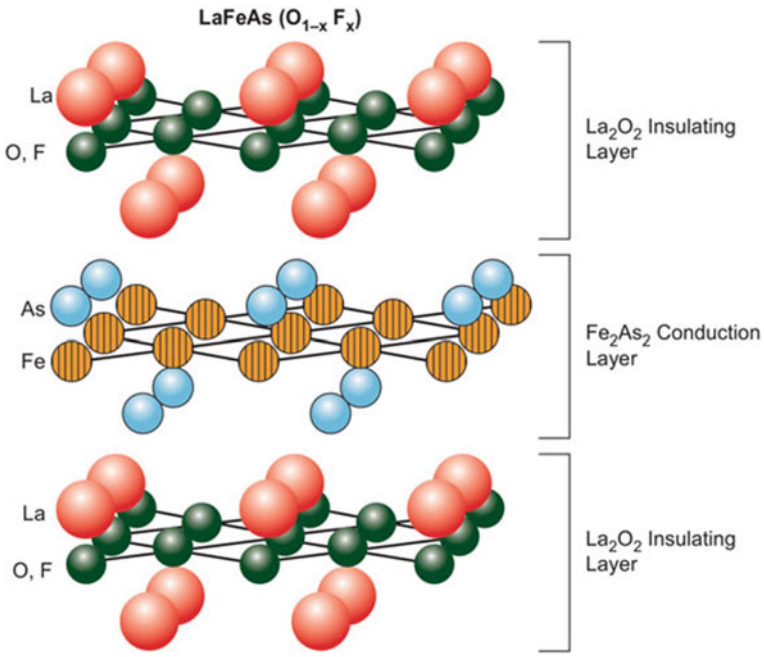

Fig. 8.1 Crystal structure of the oxy-pnictide LaFeAsO (1111) system. The Fe_2As_2 conduction layers are sandwiched between the insulating La_2O_2 layers. The structure is of the type (ZrCuSiAs) [2]. With permission from American Chemical Society

but shows a sudden drop in resistivity and magnetic susceptibility at 160 K, reaches a minimum and rises again. No superconductivity was, however, observed. It has been found that the system of transition metal with odd number of 3d electrons has long-range spin ordering and is not superconducting, whereas the system of transition metal with even number of 3d electron is a Pauli paramagnetic metal and turns superconducting.

Soon, superconductivity was reported by Kamihara et al. [4] at 26 K in a layered Fe-based compound, $La(O_{0.89}F_{0.11})FeAs$ when F^- ion was substituted at O^{2-} site. Replacing O^{2-} with F^- means that a positive charge is transferred to the insulating La_2O_2 layer and a negative charge transferred to the Fe_2As_2 conduction layer. This causes strong electron interaction and its modulation through the density of state. These are also referred to as electron-doped superconductors. Massive efforts were made all around and by 2015 over 10,000 iron-based oxy-pnictides and chalcogenide superconductors were investigated.

These materials had several features quite similar to those of HTSs (cuprates) but have many distinct properties not possessed by HTSs. Both are quasi-two-dimensional-layered compounds in proximity with antiferromagnetism. Both are unconventional, non-BCS-type superconductors where lattice does not seem to play a dominant role in the occurrence of superconductivity. The parent compounds of the HTS are antiferromagnetic Mott insulators due to strong Coulomb repulsion, whereas the parent compounds of IBSC are semimetals. Further, the HTSs are single-band compounds while IBSC has multiband electronic structure. Soon after the online publication of $T_c = 26$ K in $La(O_{1-x}F_x)FeAs$ by Kamihara et al. [4], there was a deluge of research papers on this family of superconductors. Within four months of the discovery in 2008, over 100 papers were published. Great fascination for this material has been its potential for magnet applications, and the overriding reasons for this attraction are its high upper critical field (> 100 T), larger tolerance of grain misalignment angle (9°) and low anisotropy (< 2) of in-field J_c besides high T_c going up to 55 K.

Indeed, critical current density, J_c as high as 1×10^6 A/cm^2 (4.2 K, 10 T) has been reported. Even in a 100-m-long wire, an average $J_c = 1.3 \times 10^4$ A/cm^2 (4.2 K, 10 T) has been achieved. These high critical parameters make these pnictides very promising for future potential applications. In general, IBSCs have several merits over the HTSs and are summarized below:

1. The weak link problem in IBSC is not as severe as in HTS (YBCO).
2. The critical grain misalignment angle that affects supercurrents is ~ 9° for IBSC, substantially larger than 3°–5° in YBCO [5]. This indicates that IBSC wires and tapes can be fabricated in long lengths through normal fabrication techniques such as PIT.
3. IBSCs have low anisotropy 4–5 (for 1111 type), 1–2 (for 122) and 1–2 (for 11 Type) compared to 5–7 in YBCO and 50–90 in Bi-system.
4. The irreversible field, H_{irr} too is high in IBSCs > 50 T (4.2 K) and 15 T (20 K).

To be used as a potential material for magnets, these IBSC wires and tapes have to follow the thumb rule that they should carry an engineering current density, J_e

$\approx 10^4$ A/cm^2 under operating temperature and field conditions. Physics of these materials is interesting which stems from the coexistence of magnetism and superconductivity. As revealed from ARPES studies, all the complex properties of these compounds arise from their multiband electronic structure. A comprehensive review on the development of Fe-based superconductors has been published by Hosono et al. [6].

Application of high pressure has been an effective tool to raise T_c of IBSCs. Hosono et al. were able to increase the T_c of LaFeAs $O_{0.9}F_{0.1}$ to 43 K at a pressure of 4 GPa. Chinese groups mimicked the high pressure effect by substituting large ionic radius elements at the La sites. High-pressure technique also does away with the need to go to high temperature of 1150 °C for the synthesis of the compound as the quartz reaction tube gets softened at this temperature. Electron doping was also found possible via the formation of oxygen vacancy instead of substituting F at the O site. Another route to electron doping was found by Sefat et al. [7] by substituting Co^{2+} ($3d^7$) at Fe^{2+} ($3d^6$) site unlike the replacement of Cu^{2+} in HTS by another transition metal cation. Further, superconductivity has also been observed in IBSCs by hole doping as well. Wen et al. [8] reported superconductivity at 25 K in $La_{1-x}Sr_xFeAsO$, a hole-doped compound.

Rotter et al. [9] soon reported superconductivity at 38 K in $Ba_{1-x}K_xFe_2As_2$. It is pertinent to see that the parent compound $BaFe_2As_2$ has a crystallographic transition from tetragonal (14/mmm) to orthorhombic (Fmmm) phase at 140 K. The ρ-T behaviour and the antiferromagnetic (AF) transition are very similar to the parent compound LaFeAsO. It seems that the parent compound of high T_c IBSC must have a crystallographic transition at high temperature accompanied with an AF ordering. This class of materials is routinely referred to as 122. Other unique feature of IBSC is the bipolarity of the charge doping. Electron doping appears to do better in Fe-oxypnictides 1111 compounds and hole doping doing better in non-oxygen 122 compounds. Both the compounds have, however, one commonality that of a square lattice of Fe. Superconductivity was reported by Hsu et al. [10] in α-FeSe at 8 K. This material, referred to as 11 compound, has the simplest crystal structure consisting of infinite stacking of FeSe layers with Fe forming a square lattice. It has a tetragonal symmetry at room temperature. Subsequently, the T_c was increased to 27 K by Imai et al. [11] by applying a pressure of 1.48 GPa.

8.2 Structure and Phase Diagrams of IBSC Compounds

Even though the IBSC is a large family with several members having different compositions and different structures, yet all share a common Fe-pnictogen (P or As) or a Fe-chalcogen (Se or Te) [12, 13]. The structures of a number of popular compounds are shown in Fig. 8.2. They are abbreviated according to the ratio of their constituent atoms like 11, 111, 122 and 1111. There are many other complicated structures like $(Ae_{n+1}M_nO_y)Fe_2As_2$ and $(Ae_{n+2}M_nO_y)Fe_2As_2$ superconductors. Here A = alkali metal, Ae = alkaline earth, M = transition metal and Ln = lanthanide. All the

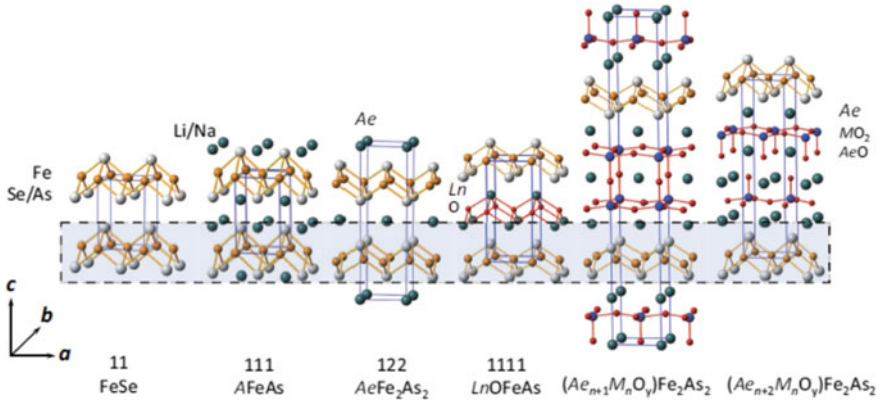

Fig. 8.2 Crystal structures of the most popular IBSC compounds abbreviated as per the ratio of the constituent atoms such as 11, 111, 122 and 1111. There are many other more complicated structures like $(Ae_{n+1}M_nO_y)Fe_2As_2$ and $(Ae_{n+2}\ M_nO_y)Fe_2As_2$ superconductors. Here A = alkali metal, Ae = alkaline earth, M = transition metal and Ln = lanthanide [12]. (Open access Creative Commons CC By license, Xi. Chen et al., National Science Review **1**, 371 (2014), https://doi.org/10.1093/nsr/nwu007)

compounds share the Fe_2X_2 (X = As or Se)-layered structural unit having anti-PbO-type (antilitharge type) arrangement of atoms. We discuss the phase diagram and the structure of the four most popular variants of the IBSCs.

8.3 Electronic and Structural Phase Diagram of LnOFeAs, 1111 Compounds

$LaO_{1-x}F_xFeAs$ was the first compound belonging to (1111) family of IBSC with a respectable $T_c = 26$ K discovered by Kamihara et al. [4]. The record of highest T_c in IBSC is held by this class of compounds. Thus, for example, fluorine-doped $SmO_{1-x}F_xFeAs$ has a $T_c = 55$ K, oxygen-deficient $NdO_{1-y}FeAs$, a $T_c = 54$ K and Th-doped $Gd_{0.8}Th_{0.2}OFeAs$, a $T_c = 56.3$ K. Unfortunately, the studies on these materials have been hampered because it is difficult to grow large single crystals of this compound. The single crystals grown are very small in dimensions, only $200 \times 200 \times 10\ \mu m^3$ and the termination of the crystal reveals a polar surface with distinct surface states restricting the use of surface sensitive probe like Angle-resolved photoemission spectroscopy (ARPES) for the study of electronic structure. The electronic phase diagram of $LaFeAsO_{1-x}F_x$ [14] is shown in Fig. 8.3. Superconductivity appears at 20 K as the long-range antiferromagnetic order (SDW) is suppressed through charge carrier doping $x = 0.045$ and the maximum T_c (26 K) is observed for $x = 0.11$. Luetkens et al. [14] carried out investigations on structural and electronic phase diagram using X-ray scattering, μSR and Mössbauer spectroscopy

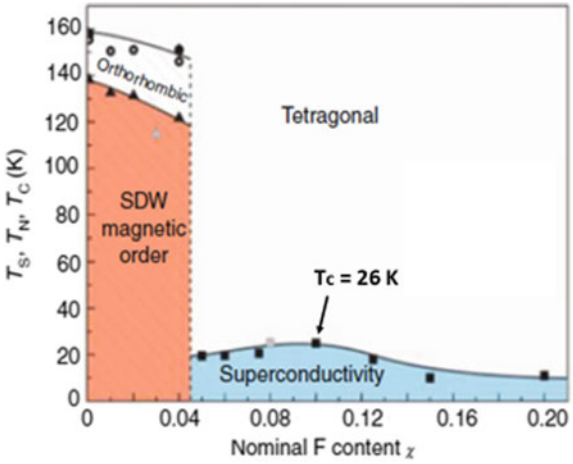

Fig. 8.3 Electronic phase diagram of $LaFeAsO_{1-x}F_x$. Superconductivity appears as long-range antiferromagnetic order is suppressed as a function of charge carrier doping. T_s has been evaluated from XRD and χ(T) data and T_N and T_C have been evaluated from μSR data [14]. With permission from Springer Nature

on a series of $LaO_{1-x}F_xFeAs$ samples. A discontinuous first-order-like change of the Néel temperature, the T_c and respective order parameters have been reported. These results demonstrate a strong coupling of the structural tetragonal to orthorhombic transition and the magnetic order, both disappearing at the phase boundary of the superconducting state at an appropriate doping. Kamihara et al. [4] had earlier given a phase diagram relating the structural, antiferromagnetic and superconducting transitions dependent on F contents. They also observed an anomaly in the resistivity around 150 K in the parent compound LaOFeAs which disappeared at the emergence of superconductivity.

The common feature of all the 1111-type compounds is that there is no coexistence of magnetic (SDW) ordering and superconductivity. Superconductivity appears only when SDW ordering is fully suppressed at a certain level of doping, and these two are connected by a quantum critical point (QCP). The SDW suppression and structural transition can be abrupt or continuous, but there is no coexistence of these transitions and superconductivity. Coexistence of SDW and superconductivity has, however, been observed in a number of 122 superconductors which suggests that complete disappearance of SDW ordering is not a prerequisite for the emergence of superconductivity. As seen from Fig. 8.3, suppression of superconductivity could not be seen for heavily F-doped compounds because of low solubility of fluorine ($x < 0.20$). So the superconductivity dome remains incomplete. As an alternative way to observe superconductivity at high doping content was adopted by Hosono's group by using hydrogen dopant in (Ce, Sm)$FeAsO_{1-x}H_x$ ($0 < x < 0.5$) which has

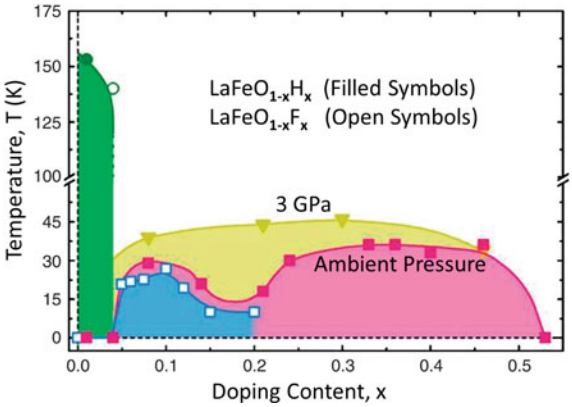

Fig. 8.4 Phase diagrams of $LaFeO_{1-x}H_x$ and LaFe O_{1-x} F_x. Superconducting region of $LaFeAsO_{1-x}H_x$ (filled symbols) has two domes with a minimum of T_c in between. The filled square represents T_c at ambient pressure, and inverted filled triangles represent T_c at a pressure of 3 GPa. At this pressure, the two domes merge in to a single dome. LaFe O_{1-x} F_x (open symbols) has single dome, but data at high F contents are missing [15] (Open access, S. Limura et al., Nature Commun. **3**, 943 (2013), https://doi.org/10.1038/ncomms1913)

a high solubility, up to 0.5. Substitution of O^{2-} by H^- is similar to the substitution by F^- as both release an electron to the FeAs conduction layer. Using H doping [15] up to 0.5, the authors were able to map complete superconductivity dome. A T_c of 47 K was observed in H-doped Ce system and 56 k in H-doped Sm system. As shown in Fig. 8.4 in $LaFeO_{1-x}H_x$ system, one, however, observes two-dome like superconducting region spanning between $x = 0.21$ and $x = 0.53$ with a maximum $T_c = 36$ K at $x = 0.3$. The minimum of T_c between the two domes disappears, and the two domes merge and form a single wide dome if a pressure of 3 GPa is applied to the sample. An optimum $T_c = 46$ K is obtained as represented by inverted filled triangles.

8.4 Superconductivity in LaFeCoAsO Induced by Co Doping

Superconductivity can also be induced by doping Co at Fe site and by applying pressure in 1111 superconductors. Wang et al. [16] established the electronic phase diagrams of $LaFe_{1-x}Co_xAsO$ and $SmFe_{1-x}Co_xAsO$ samples. The phase diagram of $LaFe_{1-x}Co_xAsO$ is shown in Fig. 8.5. The SDW phase region or the incipient SDW is very narrow. At $x = 0.02$ Co doping SDW order is completely destroyed and superconductivity emerges in $LaFe_{1-x}Co_xAsO$ by Co doping at the Fe site at $x = 0.025$ and stays till $x = 0.125$. Superconductivity in $SmFe_{1-x}Co_xAsO$, on the other hand, emerges at $x = 0.05$. The T_c–x curves for both the compounds are dome

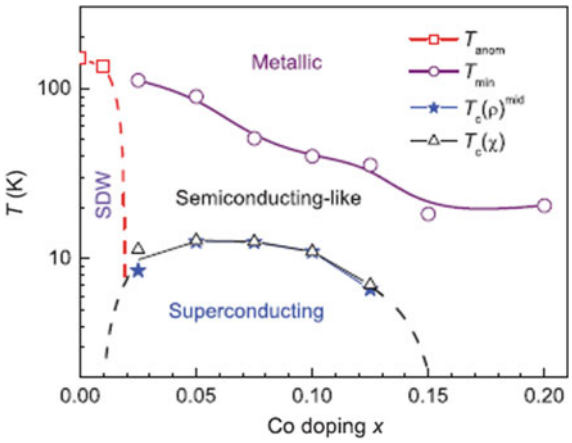

Fig. 8.5 Electronic phase diagram of $LaFe_{1-x}Co_xAsO$. T_{anom} is the temperature of resistivity anomaly, T_{min} divides the metallic region from the semiconducting like regions in the normal state of the superconductors. Note that the T-axis is in logarithmic scale [16]. With permission from American Physical Society

shaped with the maximum T_c of 13 K at $x = 0.075$ in $LaFe_{1-x}Co_xAsO$ and 17.2 K at $x = 0.1$ in $SmFe_{1-x}Co_xAsO$. We also notice from Fig. 8.5 that in $LaFe_{1-x}Co_xAsO$ there is a semiconducting region above T_c followed by the metallic region at still higher temperature. The phase boundary between the semiconducting and metallic regions is not sharp, the sample being polycrystalline. Further, superconductivity is not found to survive beyond $x = 0.15$. TEP measurements confirm that both the compounds show predominantly electron transport behaviour. The emergence of superconductivity caused by Co doping at the Fe site is in sharp contrast with the destruction of superconductivity in high T_c cuprates through substitution of Cu by its neighbours—Co, Ni and Zn.

The phase diagram of the Co-doped $LaFe_{1-x}Co_xAsO$ system and that of F-doped $LaFeAsO_{1-x}F_x$ system have similarities and dissimilarities among them. The maximum T_c in $LaFe_{1-x}Co_xAsO$ system is quite low (13 K) as compared with the $LaFeAsO_{1-x}F_x$ system (26 K). Superconductivity emerges in $LaFe_{1-x}Co_xAsO$ compounds at very low doping level compared with $LaFeAsO_{1-x}F_x$ compounds. Co doping suppresses the SDW transition more strongly. Optimum level of doping in $LaFe_{1-x}Co_xAsO$ is significantly lower and the range of superconductivity narrow. A semiconducting state is observed above T_c in $LaFe_{1-x}Co_xAsO$ compounds.

The electrical resistivity of $LaFe_{1-x}Co_xAsO$ shows an anomalous drop at 150 K. Neutron-diffraction study revealed a structural phase transition at 155 K which was followed by a SDW transition at 137 K in parent LaFeAsO. After the Co doping, T_{anom} drops to 135 K for $x = 0.01$ and appears just like a kink. For $0.025 < x < 0.125$, the anomaly disappears and a resistivity minimum appears at T_{min} which depends upon the level of Co doping. Superconductivity emerges at 7–13 K. The superconducting

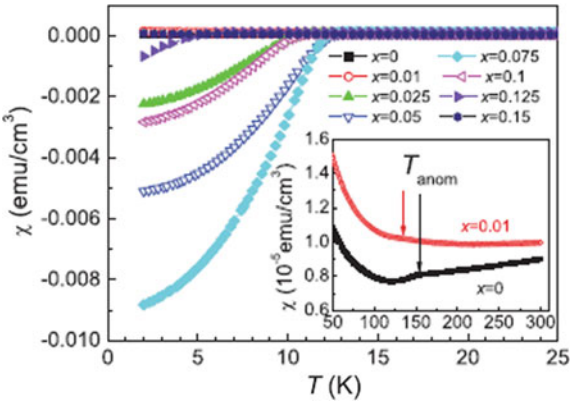

Fig. 8.6 Magnetic susceptibility χ of $LaFe_{1-x}Co_xAsO$ samples in field-cooled (FC) condition and in a field of 10 Oe. Inset shows the χ–T data for the samples with $x = 0$ and 0.01, measured in 1000 Oe field. A drop at 150 K and a kink at 135 K for $x = 0$ and 0.01, respectively, are noticeable [16]. With the permission from American Physical Society

transition width, ΔT_c is 1–2 K. The samples with $x = 0.15$ and 0.2 show no sign of superconducting transition down to 3 K.

Figure 8.6 shows the temperature dependence of magnetic susceptibility in $LaFe_{1-x}Co_xAsO$ samples in field-cooled (FC) condition and in a field of 10 Oe. No superconductivity was observed in sample with $x = 0$ and 0.01 down to 2 K. Samples with $x = 0.025$ to $x = 0.125$ show strong diamagnetic signal. The Meissner effect fraction and magnetic shielding fraction of the sample with $x = 0.075$ turn out to be 11% and 13%, respectively, both confirming the presence of bulk superconductivity. Susceptibility shows a Curie–Weiss-type upturn at below 125 K, as shown in the inset which must have been caused by defects and trace impurities present in the samples.

8.4.1 Superconductivity in Co-Doped Sm(FeCo)AsO Compounds

We now briefly discuss the electronic/structural phase diagram of $SmFe_{1-x}Co_xAsO$, one more member of the 1111 superconductor family. Figure 8.7 shows the electronic phase diagram of $SmFe_{1-x}Co_xAsO$ [16] constituted from the resistivity data. Superconductivity again has a dome-shaped curve in a T_c–x diagram between $x = 0.05$–0.20 with a maximum $T_c = 17.2$ K at the optimum doping level of $x = 0.1$. This T_{cmax} value is higher than the $T_{cmax} = 13$ K for $LaFe_{1-x}Co_xAsO$. The superconductivity window between 0.05 and 0.20 too is bigger than that in $LaFe_{1-x}Co_xAsO$, (0.025–0.125). There is a semiconducting behaviour in resistivity above T_c followed by a metallic behaviour similar to in $LaFe_{1-x}Co_xAsO$. Magnetic susceptibility data

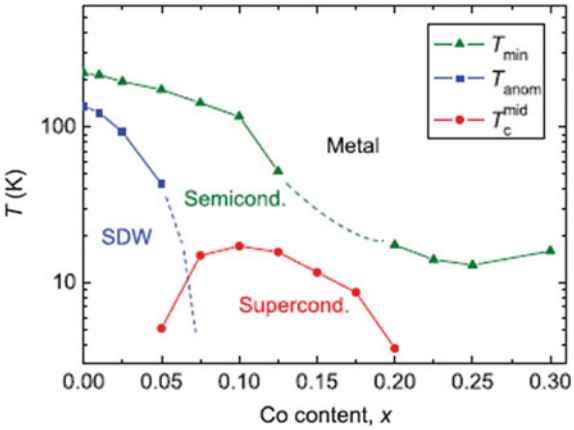

Fig. 8.7 Electronic phase diagram of $SmFe_{1-x}Co_xAsO$. In the dashed line of T_{min}, the resistivity minimum was absent because of the onset of superconductivity. Vertical axis is on a logarithmic scale [16]. With permission from American Physical Society

yield a volume fraction of magnetic shielding of over 60% for the optimally doped sample. The SDW state in this compound too is narrow. At 5% ($x = 0.05$) Co doping SDW almost disappears and superconductivity sets in. A T_c–x curve dome shaped in the range of $0.05 < x < 0.20$ is established similar to in the $LaFe_{1-x}Co_xAsO$ system. The TEP of $LaFe_{1-x}Co_xAsO$ and $SmFe_{1-x}Co_xAsO$ is negative indicating that the conduction in these materials is electron dominated. Thermopower measurements show dominant electron-type transport in Co-doped sample, $LaFe_{1-x}Co_xAsO$ in accordance with itinerant nature of Co 3d electrons. A close correlation between T_c and the abnormally enhanced part of normal-state thermopower have been confirmed.

8.5 Phase Diagram and Characteristic Properties of (Li/Na)FeAs 111 Compounds

Another simple structure IBSC is the compound AFeAs or the so-called the 111 phase. It is, however, very reactive with air and yields interesting results. Here A is the alkali metal, Li or Na. It has a space group of P4/nmm and each unit cell contains 2A, 2Fe and 2 As atoms. The Fe and As constitute anti-PbO-type layers enclosing double Li/Na planes in square-based pyramidal coordination by As. The parent material LiFeAs has a $T_c = 18$ K and lattice parameters $a = 3.775$ Å and $c = 6.353$ Å. High-quality single crystals of LiFeAs cleave between the two Li layers. The material can typically be synthesized [17] by taking the appropriate amounts of the constituent elements and packed in a quartz tube under high purity argon and sealed. The sample is heated to 740 °C and allowed to cool down slowly over a day. The crystal structure of LiFeAs, shown in Fig. 8.8, is different from other

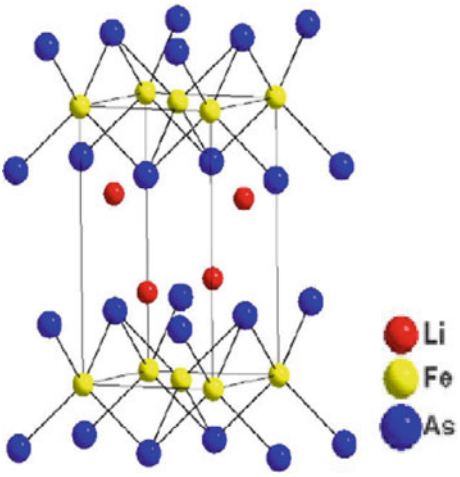

Fig. 8.8 Crystal structure of LiFeAs 111 featured by Fe_2As_2 layers stacked in an alternate fashion along the c-axis with nominal Li double layers [18]. With permission from Elsevier

iron-based superconductors like 122 AFe_2As_2 and $AeFe_2As_2$ (A = K, Rb, Cs and Ae = Sr, Ba), that crystallize in the $ThCr_2Si_2$-type structure. Similar to LaOFeAs 1111, which crystalizes in a (ZrCuSiAs)-type structure, LiFeAs 111 features Fe_2As_2 layers, based on edge-shared tetrahedral $FeAs_4$ units. The Fe_2As_2 layers are stacked in an alternate fashion along the c-axis with nominal Li double layers.

Tapp et al. [17] find superconductivity in stoichiometric Li:Fe:As as 1:1:1, whereas Wang et al. [18] had reported that for the occurrence of superconductivity, Li has to be significantly deficient. They report a T_c = 16–18 K in $Li_{1-x}FeAs$ (x = 0, 0.2 and 0.4). The electrical resistivity has been found significantly reduced in samples with nominal composition $Li_{1-x}FeAs$ hinting at the possibility for hole doping. The superconductivity in LiFeAs occurs due to the incomplete charge transfer from the strongly polarizing Li atoms to the electron-rich $(Fe_2As_2)^{2-}$ conduction layers. This again supports the hole-like behaviour of the carriers. No evidence of a SDW phase transition has been found in LiFeAs compounds, in contrast with 1111 and 122 superconductors, indicating thereby that a SDW transition may not be a prerequisite for the occurrence of superconductivity in 111 compounds.

The LiFeAs sample crystallizes into a structure characterized by alternative [FeAs] layers interlaced with Li. Magnetic susceptibility and resistivity data of LiFeAs samples are plotted in Fig. 8.9a, b, respectively. The complete diamagnetic shielding signal (Fig. 8.9a) confirms that superconductivity in LaFeAs is bulk in nature with a T_c = 18 K. Evidently, LiFeAs is metallic in normal region and has a negative curvature which is an indication of a strong electron–electron correlation, as in KFe_2As_2, or a strong electron–phonon interaction. Resistivity too shows a sharp transition at 18 K. A small finite resistivity observed at lowest temperature might be caused by grain boundary contacts. Resistivity and magnetic susceptibility are consistent with the thermoelectric power which is large and negative indicating that the major

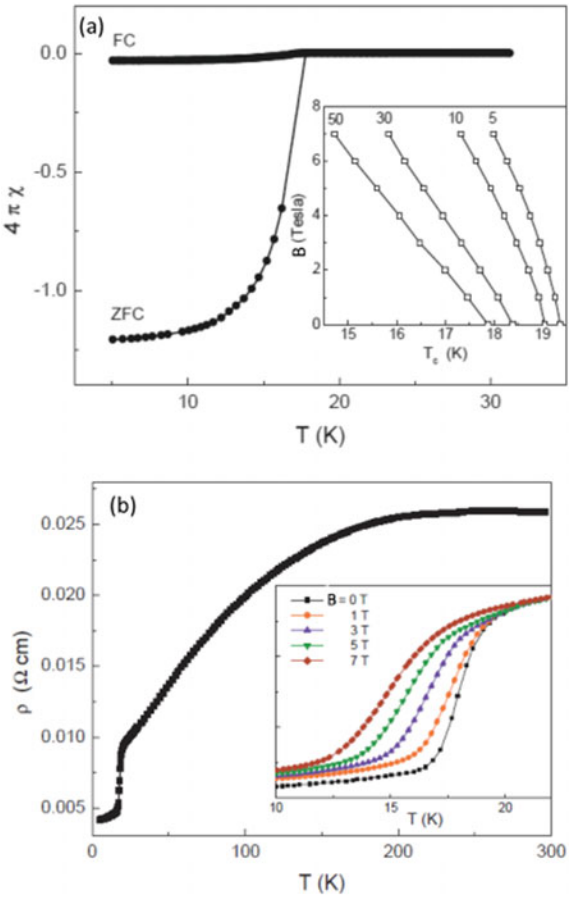

Fig. 8.9 **a** Temperature dependence of the magnetic susceptibility of 111 LiFeAs showing sharp transition at 18 K. Inset is the critical magnetic field extracted from different percentage values of the resistivity drops [17], **b** temperature dependence of the resistivity of LiFeAs in different magnetic field up to 7 T. Inset shows the broadening of the transition with magnetic field [17]. With permission from American Physical Society

carriers in LiFeAs are electron like similar to in $ReFeAsO_{1-x}F_x$ 1111 superconductors and contrasting with 122 KFe_2As_2 superconductors which have majority hole-like carriers. Interestingly, the thermoelectric power is zero at T_c. This anomaly was explained by the author [19, 20] some years ago in bulk $Y_1Ba_2Cu_3O_{7-x}$ and Bi(Pb)SrCaCuO cuprates that the percolation threshold for thermoelectric power (TEP) is much smaller than for electrical conductivity. Consequently, it is possible that the TEP in a superconductor is zero at a smaller superconducting volume fraction than needed for electrical conductivity. Thus even though the resistivity is finite at T_c in a certain superconducting material, yet the TEP may drop to zero.

The inset of Fig. 8.9a shows the plots of critical field B versus T_c with T_c defined at resistivity values corresponding to changes of 5, 10, 30 and 50% in the total drop across T_c. Employing the Ginzburg–Landau formula for the critical field,

$$B_c(t) = B_c(0)\frac{(1-t^2)}{(1+t^2)} \tag{8.1}$$

where $t = (T/T_c)$. From the 5% resistivity drop, the extrapolated upper critical magnetic field at zero-temperature turns out to be > 80 T. It is interesting to find that undoped LiFeAs is superconducting even though it does not show SDW transition. On the other hand, the $AeFe_2As_2$ 122 and La(OF)FeAs 1111 display SDW transitions but do not exhibit superconducting transition in their undoped state and under ambient pressure.

8.5.1 Superconductivity in Co-Doped AFeAs 111 Compounds

As discussed in the previous sections, the parent compounds of 111 AFeAs (A = Na, Li) show interesting characteristics. For example, NaFeAs has only filamentary superconductivity and LiFeAs does not undergo structural and SDW transitions yet exhibits bulk superconductivity. Undoped NaFeAs undergoes structural transition from tetragonal to orthorhombic at 54 K, SDW transition (antiferromagnetically aligned spins along the 'a' and 'c' directions and ferromagnetically aligned spins along the b direction) at 39 K and superconducting transition at 10 K.

Superconductivity in IBSCs is induced by hole doping, electron doping or by applying pressure. Bulk superconductivity in NaFeAs can be achieved by substituting transition metals like Co, Ni and Cu, where the structural and SDW transitions are suppressed and superconductivity is induced. Superconductivity has been observed by Ye et al. [21] in high-quality single crystals of $LiFe_{1-x}Co_xAs$ at 16.4 K, 11 K and at 4.4 K for $x = 0$, 0.03 and 0.09, respectively. In $NaFe_{1-x}Co_xAs$, superconductivity has been observed at 13 K, 20.3 K, 14.8 K and at 6 k for $x = 0$, 0.045, 0.065 and for $x =$ 0.1, respectively. Evidently, T_c in $LiFe_{1-x}Co_xAs$ decreases with Co doping, whereas in $NaFe_{1-x}Co_xAs$ T_c goes up with Co doping and then decreases with higher Co doping. The T_c–x phase diagrams for $LiFe_{1-x}Co_xAs$ and $NaFe_{1-x}Co_xAs$ are shown in Fig. 8.10a, b, respectively. In $NaFe_{1-x}Co_xAs$, the SDW phase and the superconductivity phase overlap for low doping contents. This overlap could be either due to the microscopically coexistence of the two phases or a phase separation. Oh et al. [22] through their ^{23}Na and ^{75}As NMR measurements on $NaFe_{0.983}Co_{0.017}As$ confirmed the microscopic coexistence of an incommensurate SDW and superconductivity.

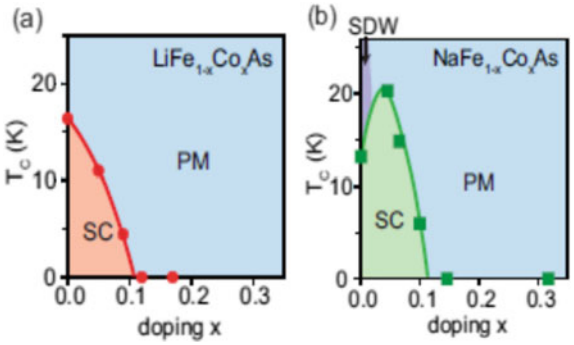

Fig. 8.10 **a** T_c–Co doping (x) phase diagram of $LiFe_{1-x}Co_xAs$. **b** The T_c–Co doping (x) phase diagram of $NaFe_{1-x}Co_xAs$ (Open access under CCA 3.0, Z. R. Ye et al. Phys. Rev. X **4**, 031041 (2014) [21]. https://doi.org/10.1103/PhysRevX.4.031041)

8.6 Phase Diagram and Characteristic Properties of 122 $BaFe_2As_2$ Compound

Soon after the discovery of superconductivity in an iron-based compound 1111 $La(O_{0.89}F_{0.11})FeAs$ at 26 K [4], Rotter et al. [9] reported, first time, superconductivity in an oxygen-free iron pnictide, $BaFe_2As_2$ 122 at 38 K when doped with K. Very high upper critical field of the order of 100 T, high critical current density of the order of 10^6 A/cm^2 in thin films and low-field anisotropy $H_{c2}^{ab}/H_{c2}^{c} = 1.5$–$2.0$ make them very attractive materials for applications and have therefore been studied most. Since high-quality single crystals in large size can be grown easily the material remained popular for electronic structural studies. The K^+ substitution at the Ba^{2+} site leads to hole doping and happened to be the first hole-doped iron-based superconductor. The parent compound $BaFe_2As_2$ has a crystal structure of the type $ThCr_2Si_2$ with space group I4/mmm. The crystal structure of Ba-122 is included in Fig. 8.2. $BaFe_2As_2$ displays a structural phase transition from the room-temperature tetragonal I4/mmm space group to the low-temperature orthorhombic Fmmm space group and magnetic transition to a long-range ordered SDW state at the same temperature of 140 K. The phase diagrams of K-doped $Ba_{1-x}K_xFe_2As_2$ and Co-doped $Ba(Fe_{1-x}Co_x)_2As_2$ are shown in Fig. 8.11a, b respectively [23]. Both the doping suppress the structural and SDW transitions and induce superconductivity. In $Ba(Fe_{1-x}Co_x)_2As_2$ compound the two transitions no longer appear at the same temperature with increasing Co concentration. Instead, the structural transition occurs first and then SDW transition during cooling, as seen in Fig. 8.11b.

Figure 8.11b shows that the line in the T–x phase diagram indicating the transition from tetragonal to orthorhombic phase bends towards low x values while entering the superconducting state. This indicates a strong interaction between superconductivity and the structural transition. Superconductivity appears in electron-doped $Ba(Fe_{1-x}Co_x)_2As_2$ for $x = 0.03$ [23] and a maximum T_c of 23 K is obtained at $x =$

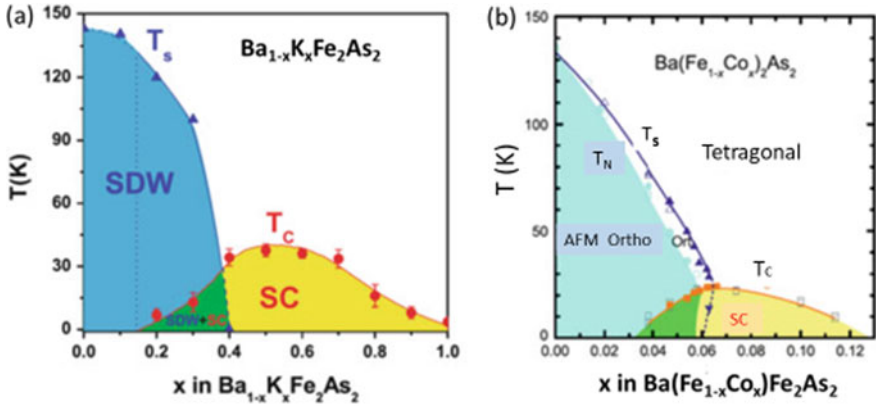

Fig. 8.11 **a** T-x phase diagram of K-doped $Ba_{1-x}K_xFe_2As_2$ compound, **b** T-x phase diagram of Co-doped $Ba(Fe_{1-x}Co_x)_2As_2$ compound [23]. With permission from Springer Nature

0.07. In hole-doped $Ba_{1-x}K_xFe_2As_2$ compound superconductivity first appears at $x = 0.1$ and attains the maximum T_c of 38 K for $x = 0.4$. All the 122 compounds have a unique feature that of SDW ordering and superconductivity coexisting together in these materials. Whether the SDW and superconducting states coexist microscopically or are phase separated had been a subject matter for investigation. It seems that the coexistence of SDW ordering and superconductivity is an intrinsic phenomenon in K-doped $BaFe_2As_2$. This coexistence has been confirmed by Li et al. [24] quite unambiguously through their ^{75}As NMR experiments.

8.6.1 Superconductivity in K-Doped $BaFe_2As_2$ Compound

The phase diagram of K-doped 122 $(Ba_{1-x}K_x)Fe_2As_2$ compound has been shown in Fig. 8.11a. $Ba_{1-x}K_xFe_2As_2$ is a hole-doped superconductor as K^+ is substituted at the Ba^{2+} site. As seen from the figure, the structural and magnetic transition curves coincide and T_s and T_N (Neel temperature) fall on the same curve. This is in contrast with electron-doped $Ba(Fe_{2-x}Co_x)_2As_2$ where the two transition curves split apart. These coinciding temperatures start dropping from 139 K for undoped $BaFe_2As_2$ ($x = 0$) and become zero at $x = 0.4$. Superconductivity sets in at $x = 0.15$ and T_c starts increasing linearly with x until it crosses the SDW/Orthorhombic phase boundary. Between $x = 0.15$ and 0.4, superconductivity coexists microscopically with SDW/Orthorhombic phase although a small suppression of SDW/Ortho is noticed. At higher doping ($x \approx 0.52$) $(Ba_{1-x}K_x)Fe_2As_2$ compound has a maximum T_c of 38 K and falls to near zero value at $x = 1.0$.

Rotter et al. [9], who discovered superconductivity in this hole-doped 122 $(Ba_{1-x}K_x)Fe_2As_2$ compound, prepared the material following the solid-state reaction technique. Appropriate quantities of the constituent elements as per the stoichiometric ratios were thoroughly mixed and heated slowly to 600 °C at a rate of 50 °C/h under high-purity argon, kept at this temperature for 15 h and furnace cooled. After homogenization, the product was annealed at 650 °C for 15 h, homogenized again and pressed in to pellets. These pellets were sintered at 750 °C for 12 h and furnace cooled to room temperature. $BaFe_2As_2$ and KFe_2As_2 too were synthesized by the same technique for comparison.

Temperature dependence of resistivity of $(Ba_{0.6}K_{0.4})Fe_2As_2$ normalized to resistivity at 40 K is shown in Fig. 8.12. The inset is the plot of the slope of resistivity curve against temperature revealing the sharpness of the transition. Emergence of superconductivity at 38 K was further confirmed through susceptibility data plotted in Fig. 8.13. The zero-field-cooled (ZFC) susceptibility plots measured at 1 and 0.5 mT coincide with each other and amount to − 94% shielding at 1.8 K which corresponds to perfect diamagnetism, that is, $4\pi\chi = -1$. The Meissner fraction depends on the applied field, and the measured field cooled (FC) susceptibility values at 1.8 K are – 0.64 at 0.5 mT and – 0.3 at 1 mT.

The aforesaid discussion on the phase diagrams of the doped 122 IBSC compounds has established that microscopic coexistence of the SDW ordering and superconductivity is a characteristic feature of all the 122 compounds. Confirmation of the presence of this coexistence came from Li et al. [25] through their ^{75}As NMR measurements in high-quality single crystals of $(Ba_{1-x}K_x)Fe_2As_2$. Similar measurements carried out on Co-doped $BaFe_{2-x}Co_xAs_2$ compounds and some other isovalent-doped 122 compounds (including P-doped and Ru-doped) too confirmed the microscopic coexistence of the SDW ordering and superconductivity.

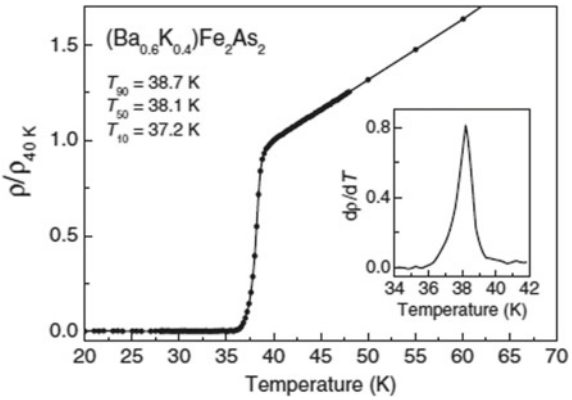

Fig. 8.12 Temperature variation of resistivity of $(Ba_{0.6}K_{0.4})$ Fe_2As_2 normalized to resistivity at 40 K. Inset is the plot of the slope of resistivity curve against temperature [9]. With permission from American Physical Society

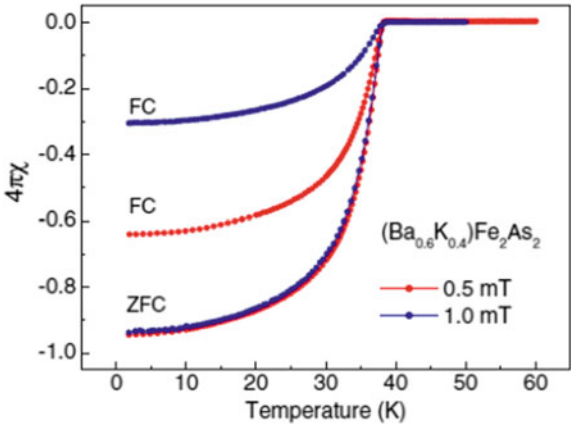

Fig. 8.13 Magnetic susceptibility of $(Ba_{0.6}K_{0.4})Fe_2As_2$ in 0.5 and 1.0 mT field under zero-field-cooled (ZFC) and field-cooled (FC) conditions [9]. With permission from American Physical Society

8.7 Phase Diagram of Iron Chalcogenides 11 Compounds

Hsu et al. [26] discovered superconductivity in a new Fe-based compound of the PbO-type α-FeSe with a T_c of 8 K. These so-called iron chalcogenides, FeSe (Te, S) or just the 11 phase compounds have several types of crystal structures depending upon their composition and the synthesis route. This variety of IBSC has the simplest crystal structure among the large family of IBSCs. Among these chalcogenides, FeTe is a most stable compound and is obtained in phase pure form in the solid-state reaction technique. FeSe does form by solid-state reaction technique but is less stable as it forms at high temperature in a hexagonal phase. For obtaining pure phase FeSe, an additional low-temperature annealing at 300–400 °C is to be carried out. Figure 8.14 shows the T_c dependence of the magnetic susceptibility of FeSe sample subjected to different heat treatments as reported by Mizuguchi and Takano [27]. Sample (a) was reacted at 1100 °C and followed by annealing at 400 °C for 200 h, has a sharp transition and highest T_c. Samples (b) and (c) were reacted at 1100 °C and 680 °C, respectively. These results do confirm that both the high-temperature reaction and low-temperature annealing are required to obtain the high-quality FeSe sample. Further, compound FeS is much unstable and can only be formed by a chemical process in an aqueous solution and not by the solid state reaction.

This iron chalcogenide, FeSe, consists of alternate FeSe (anti-PbO) layers in which the cations and anions occupy the opposite sites of Pb and O atoms of the litharge. For this reason, FeSe is called as anti-PbO or antilitharge structure. It has a space group of P4/nmm. As seen from Fig. 8.2, the Fe_2Se_2 monolayer has a flat Fe_2 square lattice sandwiched by two Se/Te monolayers. Each Fe atom coordinates with four Se atoms to form an edge-shared $FeSe_4$ tetrahedron, thus forming a 2D square-net Fe_2Se_2 monolayer. A $T_c = 8$ K has been reported by Hsu et al. [10] in FeSe. Figure 8.15 shows the variation of resistivity of the compound $FeSe_{0.88}$ with

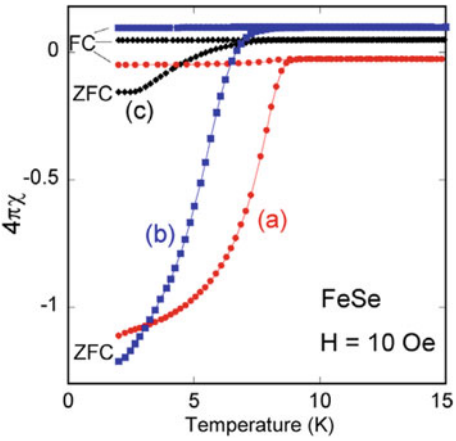

Fig. 8.14 Variation of magnetic susceptibility with temperature for FeSe prepared by following three reaction processes: **a** heat treated at 1100 °C + 400 °C × 200 h anneal, **b** reacted at 1100 °C, **c** reacted at 680 °C [27]. *Courtesy* Yoshihiko Takano and with permission from The Physical Society of Japan (c) (2010)

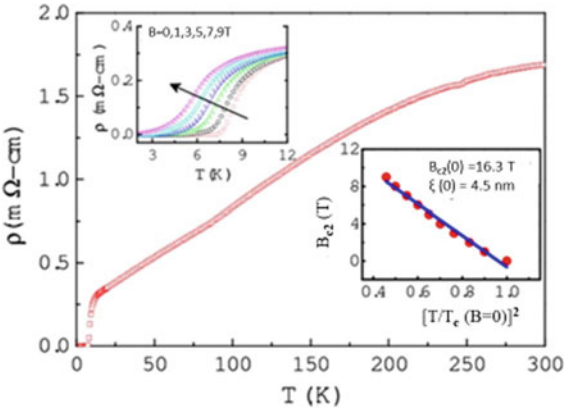

Fig. 8.15 Variation of resistivity with temperature of the Se deficient $FeSe_{0.88}$ compound. The top inset shows the temperature variation of resistivity in magnetic field of 0, 1, 3, 5, 7 and 9 T. Bottom inset is the plot of estimated upper critical field $B_{c2(0)}$ with reduced temperature (T/T_c) [10]. Copyright (2008) National Academy of Sciences, USA, permission from PNAS

temperature. The top inset shows the temperature variation of resistivity in magnetic field of 0, 1, 3, 5, 7 and 9 T. Bottom inset is the plot of estimated upper critical field $B_{c2(0)}$ with normalized temperature (T/T_c). The experimental results were fitted to the expression $B_{c2}/B_{c2(0)} = 1 - (T/T_{c(0)})^2$, which yielded the value of the upper critical field, $B_{c2(0)}$ as 16.3 T and a coherence length $\approx$ 4.5 nm.

Figure 8.16a shows the magnetic susceptibility of the compound $FeSe_{0.88}$ measured in a field of 30 G plotted against temperature [10]. Nearly temperature independent, zero-field-cooled (ZFC) susceptibility indicates that the sample is a Pauli

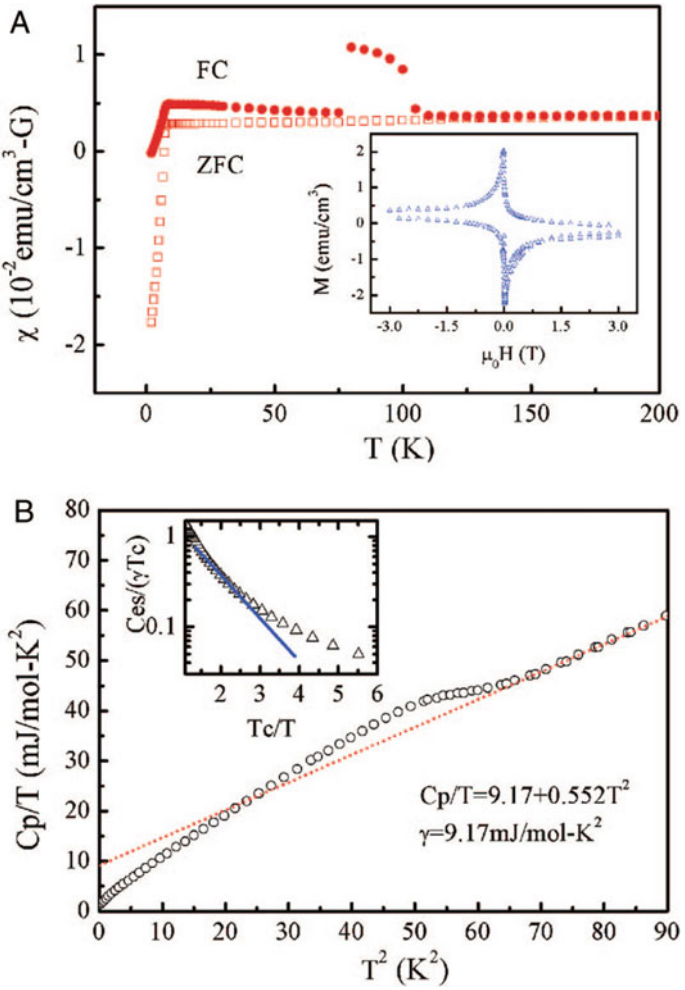

Fig. 8.16 Magnetic susceptibility and specific heat of $FeSe_{0.88}$. **a** Temperature dependence of the magnetic susceptibility, measured in a 30 G field. Note a small anomaly in susceptibility in FC curve at 105 K. The sample also shows a hysteresis in magnetization at 2 k (inset) which is a characteristic feature of superconductivity [10], **b** specific heat data of $FeSe_{0.88}$ below 10 K plotted as C_p/T versus T^2. The red dotted straight line is the fit of the specific heat data to the electronic and phonon components equation ($C_p = \gamma T + \beta T^3$). The intercept 9.17 mJ/mole-K^2 at 0 K is the coefficient of electronic component γ. A jump in specific heat appears at 8 K, which is same as the T_c. The inset is the semilogarithmic plot of Ces/T_c versus T_c/T in the superconducting state. The experimental data show deviation from the linear curve (blue straight line) of the fully gapped Superconductor [10]. Copyright (2008) National Academy of Sciences, USA, permission from PNAS

paramagnet before turning superconducting. A sharp drop occurs at 8 K, the temperature at which the zero resistance has been observed. A small anomaly is observed in field-cooled (FC) magnetic susceptibility at 105 K similar to the anomaly observed in the resistivity curve. The inset is a typical hysteresis curve measured at 2 K, a characteristic behaviour of type II superconductor. Figure 8.16b is the specific heat data of $FeSe_{0.88}$ below 10 K plotted as C_p/T versus T^2. The red dotted straight line is the fit of the specific heat data to the electronic and phonon components equation ($C_p = \gamma T + \beta T^3$). This straight line intercepts C_p/T axis at 0 K which is the value of the coefficient of electronic component of specific heat, $\gamma = 9.17$ mJ/mole-K^2. A jump in specific heat appears at 8 K which coincides with the superconducting transition temperature. The inset shows the plot of semilogarithmic C_{es}/T_c versus T_c/T in the superconducting state. The measured data, however, show deviation from the linear curve (blue straight line) of the fully gapped superconductor.

The T_c of FeSe was increased to 27 K by Imai et al. [11] under a pressure of 1.48 GPa. Its ternary combination $Fe_{1-y}Se_xTe_{1-x}$ has a $T_c = 14$ K at $x = 0.5$ as reported by Fedorchenko [28]. Excess Fe is used to grow single crystals of FeSe wherein after filling the square Fe lattice positions, Fe atoms occupy the interstitials of the Te layers. The effect of pressure on the magnetic and superconducting states of α-$FeSe_x$ for $x = 0.8$ and 0.88 has been studied by Li et al. [29]. The magnetic measurements show a diamagnetic signal below T_c (= 8 K), a rapid rise of magnetization (antiferromagnetization transition) at about 78 K, and a magnetization decrease (ferromagnetization transition) at 106 K. High-resolution X-ray diffraction measurements, however, show that these two phase transitions are also structural transformations associated with changes of the lattice symmetry. All the three phase-transition temperatures shift to higher temperatures under high pressure which hints at the coexistence of superconductivity and magnetism [29].

The parent compounds of IBSC display antiferromagnetic ordering or the SDW ordering, at low temperature. In addition, with decreasing temperature, the parent compounds also show a structural transition at a certain temperature, T_S from high-temperature tetragonal structure to low-temperature orthorhombic structure. The temperature T_S is usually slightly higher than or even equal to the antiferromagnetic transition temperature (T_N). Such structural transitions are found to be followed by the antiferromagnetic transition and strongly coupled to it. The structure transition temperature T_S and antiferromagnetic transition temperature T_N of the different phases of the parent (undoped) IBSC are listed in Table 8.1.

Superconductivity can be achieved through doping with hole carriers or the electron carriers into the parent compound by choosing optimal chemical doping. Both the transitions, structural and antiferromagnetic, are suppressed continuously by electron as well as hole doping. Above a critical doping, superconductivity starts emerging and coexists with suppressed antiferromagnetic ordering in part of the phase diagram. The superconducting transition temperature, T_c increases with doping attaining a maximum value at the 'optimal doping level' quite similar to HTS cuprates. T_c drops from its peak value on either side of doping, that is, in the underdoped or the over-doped regions. Superconducting phase thus has a dome-like structure in the T_c versus doping level plot. A structural transition from high-temperature tetragonal to

Table 8.1 Structural transition temperature T_S and antiferromagnetic transition temperature T_N of the different phases of the parent (undoped) IBSC compounds (data compiled from [23])

Type	Compound	T_S (K)	T_{SDW} (K)	Type	Compound	T_S (K)	T_{SDW} (K)
1111	LaFeAsO	158	134	122	$SrFe_2As_2$	205	205
1111	PrFeAsO	154	135	122	$CaFe_2As_2$	171	171
1111	CeFeAsO	155/151	140/145	122	$EuFe_2As_2$	190	190
1111	NdFeAsO	150/143	141/137	111	$Na_{1-\delta}FeAs$	50	40
1111	SmFeAsO	175	135	11	FeTe	75	75
1111	GdFeAsO	135	128	–	$K_{0.8}Fe_{2-y}Se_2$	578/551	559/540
1111	SrFeAsF	180	133	–	$Rb_{0.8}Fe_{2-y}Se_2$	540	534
1111	CaFeAsF	134	114	–	$Cs_{0.8}Fe_{2-y}Se_2$	525	504
122	$BaFe_2As_2$	142	142				

low-temperature orthorhombic phase occurs in $FeSe_{1-x}$, without being followed by an antiferromagnetic order, a behaviour quite different from other IBSCs. $FeSe_{1-x}$ exhibits superconductivity below 10 K.

8.7.1 *Behaviour of the Mixed Phase, $Fe_{1+x}Te_{1-x}Se_x$*

FeSe and FeTe have the same crystal structure but differ widely in their physical properties. For example, the temperature variation of the resistivity of the FeSe compound shows a metallic behaviour all the way down to 13 K when it goes in to the superconducting state. Mizuguchi and Takano [27] report an increase of T_c (= 37 K) under high pressure. Compound FeTe, on the other hand, does undergo antiferromagnetic ordering around 70 K but does not turn superconducting [30]. The crystal structure of FeSe shows the presence of a structural transition from tetragonal to orthorhombic phase between 70 and 90 K. The properties of FeTe depend on the content of excess Fe at the interlayer site. The compound $Fe_{1.076}Te$, with a small excess Fe, displays a structural transition from tetragonal to monoclinic and an antiferromagnetic ordering. Higher excess Fe suppresses superconductivity. Substitution of Se at Te site in the compound FeTe suppresses the antiferromagnetic ordering and gives rise to superconductivity. The mixed phase, $FeTe_{1-x}Se_x$ has been studied extensively as its large single crystals can be grown easily.

Figure 8.17 shows the temperature dependence of resistivity of the mixed phase $FeSe_{1-x}Te_x$ with different contents of Te and Se. Even though all the samples were phase pure yet the superconducting transition is very broad for primitive polycrystalline samples which indicate the presence of local phase separation. There is evidence from the lattice parameters '*a*' and '*c*', that there is a miscible region, at which the phase separation occurs, around $x = 0.7$–0.95 [30]. The tetragonal to orthorhombic transition in FeSe was suppressed with increasing Te content. At Te

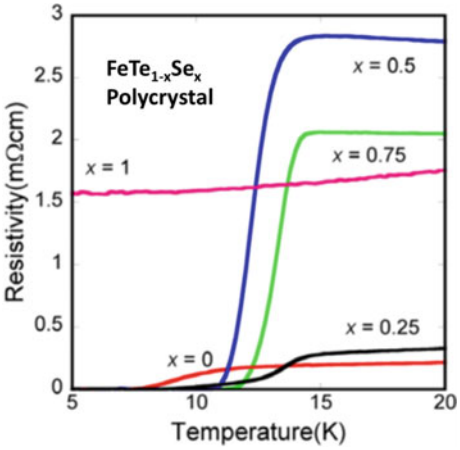

Fig. 8.17 Temperature dependence of resistivity of polycrystalline $FeTe_{1-x}Se_x$ for $x = 0, 0.25, 0.5$ and 0.75 [27]. *Courtesy* Yoshihiko Takano and with permission from The Physical Society of Japan (c) (2010)

$= 0.43$, the tetragonal to orthorhombic structural transition drops to 40 K and disappears all together for Te $= 0.51$. With further increase in Te contents, short-range antiferromagnetic fluctuations grow [31]. A long-range antiferromagnetic ordering and the tetragonal–monoclinic structural transition have, however, been observed for $Fe_{1.06}Te_{0.87}Se_{0.13}$. A superconducting transition temperature (T_c) of 14 K was observed in a high-quality large single crystal of $FeTe_{0.5}Se_{0.5}$ through magnetic susceptibility measurement [27] as shown in Fig. 8.18a. Effect of annealing on superconducting transition in $FeTe_{1-x}Se_x$ has also been evaluated in view of the fact that a 400 °C anneal was found necessary to achieve bulk superconductivity in FeSe. Mizuguchi and Takano [27] synthesized the single crystal of $FeTe_{1-x}Se_x$ by the melting method with 400 °C annealing for $x = 0.13, 0.25$ and 0.35. Figure 8.18b shows the temperature dependence of magnetic susceptibility of these samples at the zero-field cooling (ZFC) and field cooling (FC) at 50 Oe.

Thus, the phase diagram of $FeTe_{1-x}Se_x$ shown in Fig. 8.19 reveals that the orthorhombic–tetragonal structural transition observed in FeSe is suppressed with increasing Te contents. The highest T_c (= 14 K) appears in the tetragonal phase near $x = 0.5$. With the further increase of Te, the T_c decreases and the antiferromagnetic ordering accompanying the tetragonal–monoclinic distortion sets in. Bulk superconductivity ultimately disappears. Table 8.2 gives the highest T_c, stoichiometric composition and parent compound details of some compounds representative of the four popular systems, 1111, 111, 122, 11 of the iron based superconductors.

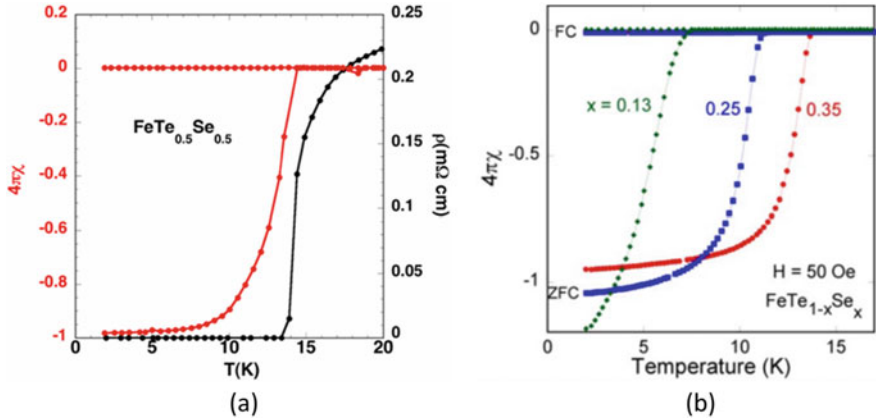

Fig. 8.18 **a** Temperature dependence of magnetic susceptibility and resistivity of $FeTe_{0.5}S_{e0.5}$ single crystal. The compound undergoes superconducting transition at 14 K [27] (*Courtesy* Yoshihiko Takano and Permission from Am. Phys. Soc. © 2009 Am. Phys. Soc., Phys. Rev. **79**, 094,521(2009)). **b** Temperature dependence of magnetic susceptibility of $FeTe_{1-x}S_{ex}$ for $x = 0.13$, 0.25 and 0.35 at 50 Oe [27] (*Courtesy* Yoshihiko Takano and permission from The Physical Society of Japan © 2010)

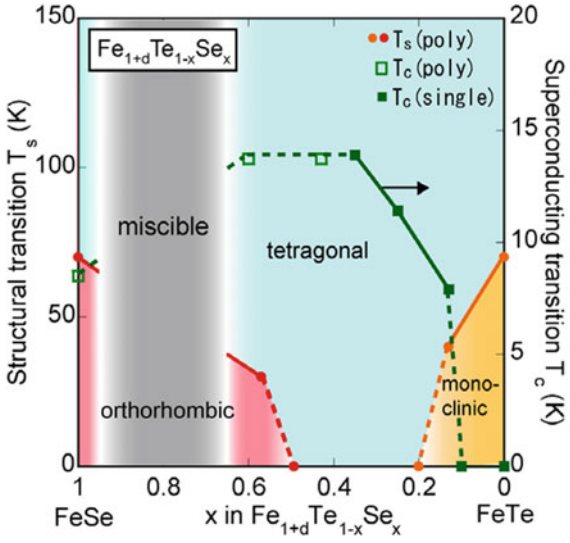

Fig. 8.19 T-x phase diagram of $FeTe_{1-x}Se_x$ with small excess Fe. Te substitution suppresses tetragonal–orthorhombic structural transition. The highest $T_c = 14$ K is observed in the tetragonal phase near $x = 0.5$ [27]. *Courtesy* Yoshihiko Takano and with permission from The Physical Society of Japan © (2010)

Table 8.2 Highest T_c, stoichiometric composition and parent compound details of some compounds representative of four popular systems, 1111, 111, 122, 11 of the iron based superconductors. Data compiled from [23] and other publications. A = alkali metals, RE = rare earth, M = transition metal

S. No	Class/phase	Stoichiometric composition	T_c (K)$_{max}$	Parent compound, name	Comment
Ferro-Oxypnictides—LaOMPn 1111 compounds					
1	1111	$La[O_{1-x}F_x]FeAs$	26	REOMPn	M = Mn, Fe, Co, Ni Pn = P and As RE = Rare earth
2	1111	$NdFeAsO_{1-y}$	54	REFeAsO	Oxygen deficient
3	1111	$SmFeAsO_{1-x}F_x$	55	REFeAsO	Single crystal
4	1111	$Gd_{0.8}Th_{0.2}FeAsO$	56.3	REFeAsO	$200 \times 200 \times 10\ \mu m^3$ thin platelet
111 compounds (highly reactive in air)					
5	111	LiFeAs	18	LiFeAs	Highly reactive with air
6	111	NaFeAs	23	NaFeAs	Less reactive than LiFeAs, enhanced superconductivity in NaNiAs and NaCoAs
Non-Oxypnictide 122 compounds (most studied compounds)					
5	122	$Ba_{1-x}K_xFe_2As_2$	38	$BaFe_2As_2$ (BFA)	Hole doped
6	122	$Ba(Fe_{1-x}Co_x)_2As_2$	22	$BaFe_2As_2$ (BFA) BFA not superconductor	Electron doped
7	122	KFe_2As_2	3	KFe_2As_2 (KFA)	
8	122	$BaFe_2(As_{1-x}P_x)_2$	30	$BaFe_2As_2$ (BFAP)	Hole doped
9	122	Ba_1-xNaxFe$_2$As$_2$	34	$BaFe_2As_2$ (BNFA)	Hole doped
10	122	Ca_{1-x}NaxFe2As2	20	$CaFe_2As_2$ (CNFA)	
11	122	$CaFe_2As_2$	> 10	$CaFe_2As_2$ (CFA)	

(continued)

Table 8.2 (continued)

S. No	Class/phase	Stoichiometric composition	T_c (K)$_{max}$	Parent compound, name	Comment
12	122	$EuFe_2(As_{1-x}P_x)_2$	26	$EuFe_2As_2$ (EFAP)	
Ferro-chalcogenides 11 compounds					
15	11	FeSe	8 37	(Under pressure)	Ferro-chalcogenide
16	11	FeTe	Non-SC ~ 10 K	On S substitution $FeTe_{0.8}S_{0.2}$, $FeTe_{0.9}S_{0.1}$	
17	11	$FeSe_xTe_{(1-x)}$	14	$FeTe_{0.5}Se_{0.5}$	
18	11	$Fe_{(1+y)}Se_xTe_{(1-x)}$	14	$Fe_{1.06}Te_{0.87}Se_{0.13}$	Excess iron
19	245	$A_{0.8}Fe_{1.6}Se_2$	30 (max.)	$A_2Fe_4Se_5$	A = K, Rb, Cs, Tl Insulating up to 100 K then turns superconductor
20	× 22	$A_xFe_2Se_2$			Metallic + Insulating Metal phase turns super

8.8 Pressure Effect in Iron-Based Superconductors

Pressure is one of the critical physical parameters which can modify the electronic and the phonon energy spectra of a solid. Hydrostatic pressure in particular in isotropic materials does not cause any chemical complexity either. The application of pressure changes the inter-atomic distances and modifies the physical states of solids. Several non-superconducting elements were found turning superconducting at high pressure. We also recall that the T_c of cuprate superconductor $HgBa_2Ca_2Cu_3O_{9+\delta}$ (Hg1223) rose from 134 K to a record value of $T_c = 164$ K under an applied pressure of 30 GPa [32]. A good review has been published by Chu and Lorenz [33] on the high pressure studies on Fe-pnictide superconductors. The authors conclude that T_c increases ($dT_c/dP > 0$) with pressure in underdoped IBSC, T_c remains nearly unchanged ($dT_c/dP = 0$) in optimally doped compounds and T_c decreases (($dT_c/dP < 0$) with pressure almost linearly in over-doped compounds. We will now discuss pressure effects in all the most popular four homologous series of IBSC family.

8.8.1 Pressure Effects in 1111 Compounds

The first high T_c IBSC $La(O_{1-x}F_x)FeAs$ 1111 discovered by Hosono in 2008 became the most studied material with the use of all conceivable characterization techniques available with research groups at the time. One such popular study was on the effect of pressure on the T_c of the optimally doped polycrystalline $La(O_{1-x}F_x)FeAs$ with $x = 0.11$. Takahashi et al. [3] studied pressure effect on the superconducting behaviour of $La(O_{0.89}F_{0.11})FeAs$. Onset T_c is highest at 43 K for a pressure of 4 GPa and then drops at higher pressure bringing down T_c to 9 K at $P = 30$ GPa as shown in Fig. 8.20.

Takahashi et al. [34] later extended their studies on this compound with different levels of doping, that is, undoped, ($x = o$), underdoped ($x = 0.05$), optimally doped ($x = 0.11$) and over-doped ($x = 0.14$) $La(O_{1-x}F_x)FeAs$ with $T_c = 0$ K, 24 K, 29 K and 20 K, respectively, at ambient pressure. For all the samples, T_c initially rose with pressure up to a maximum value limited to about 5 GPa and dropped beyond this pressure. The maximum T_c was obtained for the optimum-doped sample (43 K) but dropped rather steeply (8 K/GPa) at higher pressure. For $x = 0$ and 0.05 the corresponding highest values of T_c are 20 K and 29 K, respectively. The undoped LaOFeAs also turns superconducting at a pressure > 2 GPa.

Lorenz et al. [35] chose analogous $Sm(O_{1-x}F_x)FeAs$ compound for pressure studies, which already had $T_c = 43$ K at ambient pressure. A hydrostatic pressure up to 1.7 GPa, using the Be-Cu clamps technique, was applied to samples with $x = 0.05$, 0.13 and 0.30. The measured onset T_c of these samples was 1.2 K, 24.7 K and 43.6 K, respectively. The resistivity anomaly observed in sample with $x = 0.05$ shifts to lower temperature with increasing pressure indicating a suppression of the SDW order favouring superconductivity. T_c in electron over-doped sample (x

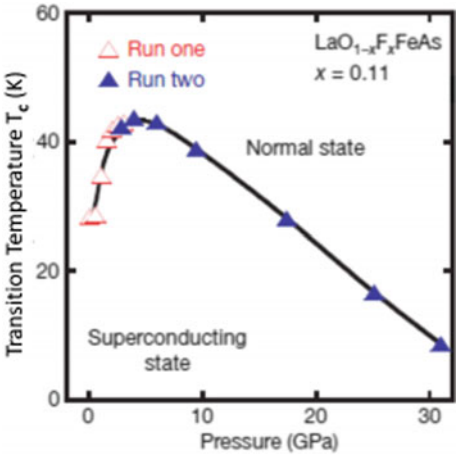

Fig. 8.20 T_c–P phase diagram of $La(O_{0.89}F_{0.11})FeAs$. Onset T_c rises to 43 K at 4 GPa and drops with further increase of pressure down to 9 K at 30 GPa [3]. With permission from Springer Nature

$= 0.3$), however, shows a decrease at the rate of -2.3 K/GPa. For electron underdoped $Sm(O_{0.87}F_{0.13})FeAs$ sample ($x = 0.13$), T_c increases with pressure at the rate of about + 1.3 K/GPa below 0.8 Gpa and saturates or shows a small decrease for higher pressure. It appears that the application of pressure promotes electron doping in $Sm(O_{1-x}F_x)FeAs$. Further, the suppression of the SDW transition observed should also contribute to the increase of T_c with pressure (positive dT_c/dP) of the underdoped $Sm(O_{1-x}F_x)FeAs$.

As discussed earlier in this chapter, electron doping is also accomplished through oxygen deficiency in $RO_{1-y}FeAs$ (R = Sm, Nd, Gd). Ren et al. [36] achieved a $T_c =$ 54 K in these samples. Takeshita et al. [37] reported $T_c = 54$ K, 41 K and 0 K for $1 - y = 0.6$, 0.8 and 0.85, respectively, up to a pressure of 18 GPa. Under applied pressure, the onset T_c of these samples decrease with pressure at the rate of about – 2 K/GPa. Similar decrease in T_c has been reported in oxygen deficient Sm and Nd 1111 compounds. No T_c maximum has been observed in these compounds.

8.8.2 Pressure Effects in 111 Compounds

The undoped NaFeAs shows a slight decrease in T_c with the increase of pressure and then increases quickly with pressure above 1 GPa. The highest offset T_c reached is 11.9 K at 1.79 GPa. The Co-underdoped sample $NaFe_{0.99}Co_{0.01}As$ had an offset $T_c = 16$ K. In optimally doped $NaFe_{0.972}Co_{0.028}As$ single crystal sample, the structural/SDW transition is suppressed completely by Co doping and T_c measured by in-plane resistivity is found [38] increasing from 20.4 to 31.0 K with increasing pressure from 0 to 2.28 GPa. The pressure coefficient 4.67 K/GPa is much larger

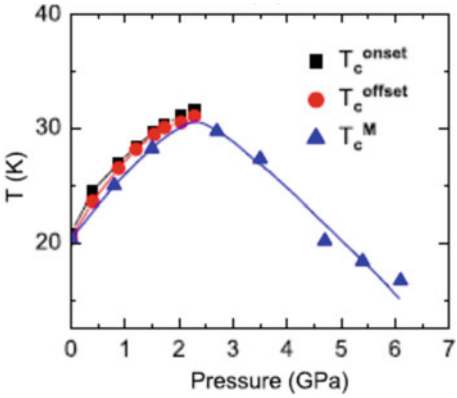

Fig. 8.21 T_c obtained from resistivity and susceptibility measurements as a function of pressure for optimally doped $NaFe_{0.972}Co_{0.028}As$ single crystal sample [38]. Open access article under the terms of Creative Commons, A. F. Wang et al. https://doi.org/10.1088/1367-2630/14/11/113043

than the low value of 1 K/GPa found in optimally doped $Ba(Fe_{1-x}Co_x)_2As_2$ and comparable to 5 K/GPa in optimally doped $LaFeAsO_{1-x}F_x$ [3]. Figure 8.21 shows the T_c^{onset}, T_c^{offset} and T_c^M values plotted against pressure for the optimally doped $NaFe_{0.972}Co_{0.028}As$. Evidently, T_c increases with pressure to a high value of 31 K at $P = 2.3$ GPa. At higher pressures, T_c decreases almost linearly. For over-doped $NaFe_{0.925}Co_{0.075}As$ single crystal sample, the plots of Fig. 8.21 show that T_c^{onset}, T_c^{offset} and T_c^M increase with pressure up to a value of 24.5 K at a pressure of 2.32 GPa and decrease thereafter with increasing pressure.

From the above discussion, we find that the maximum T_c enhancement and the corresponding critical pressure is nearly the same in all the samples which is quite distinct from other IBSC where the pressure effect is different in various regions of the electronic phase diagram. Phosphorous (P) substitution at As site could be thought of as chemical pressure, which changes Fe–Pn distance and causes similar effects on superconductivity as the physical pressure. One possible reason for the lower maximum T_c obtained in over-doped $NaFe_{0.925}Co_{0.075}As$ could be the disorder or additional scattering induced by excess cobalt doping. This differs from the case of over-doped $LaFeAsO_{1-x}F_x$ in which the conduction layer is not affected by F doping. Consequently, the highest T_c reached in optimally and over-doped samples are almost the same. However when pressure is applied to extremely over-doped non-superconducting sample, pressure does not induce superconductivity.

In conclusion, the T_c of $NaFe_{1-x}Co_xAs$ increases strongly in the entire superconducting regime of the phase diagram and pressure effect is quite large and positive unlike other members of the family of IBSCs. Maximum $T_c = 31$ K is uniformly obtained in underdoped and optimally doped $NaFe_{1-x}Co_xAs$ samples. The STM and ARPES measurements also confirm that the similarity of pressure effect in underdoped and optimally doped samples arise from the similarity of electronic structure within the superconducting dome.

8.8.3 *Pressure Effects in 122 Compounds*

The two prominent members of the 122 family of IBSC are $SrFe_2As_2$ and $BaFe_2As_2$ which are semimetals, turn superconducting when hole doped by partially substituting alkali element at the alkaline earth site. Thus, the compound $(Sr_{1-x}K_x)Fe_2As_2$ becomes superconducting with a maximum $T_c = 38$ K for $x = 0.4 - 0.5$. The $T_c - x$ phase diagram in Fig. 8.22 shows an overlapping of SDW and superconductivity for $x = 0.2 - 0.3$. Electrical resistivity and magnetic susceptibility measurements [34] under hydrostatic pressure of up to 1.7 GPa show positive pressure coefficient of T_c for the underdoped ($x = 0.2$) sample, nearly zero for the optimally (0.4) doped sample and negative coefficient for over-doped sample. It appears as though pressure enhances hole doping. It is also revealed from Fig. 8.22 that SDW transition in hole-doped $(Sr_{1-x}K_x)Fe_2As_2$ is suppressed just like in electron-doped 1111 $Sm(O_{1-x}F_x)FeAs$. The studies on isoelectronic 122 sample of $(Ba_{1-x}K_x)Fe_2As_2$ with $x = 0.45$ and $T_c = 30$ K show, under hydrostatic pressure, a negative coefficient of pressure $= -0.21$ K/GPa which suggests the sample to be in over-doped region.

Similar to in hole-doped system, superconductivity is also observed in electron-doped 122 systems by partial substitution of Co at the Fe site. Thus, a maximum $T_c = 22$ K was found in $Ba(Fe_{1-x}Co_x)_2As_2$ for $x = 0.1$ [39]. Its complete T_c and $T_{SDW} - x$ phase diagram is quite similar to the phase diagram of 122 $(Sr_{1-x}K_x)Fe_2As_2$ shown in Fig. 8.22. Ahilan et al. [40] investigated the effect of hydrostatic pressure up to 2.5 GPa on underdoped ($x = 0.04$) and optimally doped ($x = 0.1$) $Ba(Fe_{1-x}Co_x)_2As_2$ samples. Surprisingly, the results are same as observed in hole-doped 122 $(Sr_{1-x}K_x)Fe_2As_2$ superconductors. Underdoped sample suppresses the SDW transition and enhances T_c with pressure, the optimally doped sample, on the other hand, is nearly independent of pressure. This extraordinary similarity of the pressure effects in both hole- and electron-doped 122 Ae-pnictides displays the electron–hole symmetry in IBSC. Undoped $SrFe_2As_2$ turns superconducting at pressures

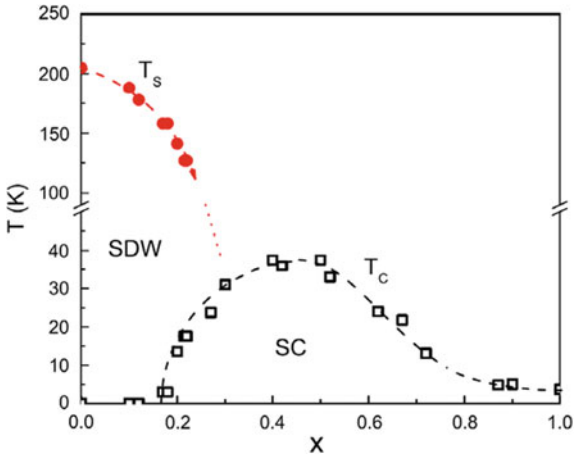

Fig. 8.22 T_c and $T_{SDW} - x$ phase diagram of 122 $(Sr_{1-x}K_x)Fe_2As_2$ [33]. With permission from Elsevier

< 2 GPa, and a maximum $T_c = 34$ K is achieved at 14 GPa. This value of T_c is nearly the same as obtained in hole-doped $(Sr_{1-x}K_x)Fe_2As_2$.

The undoped non-superconducting $BaFe_2As_2$ turns superconducting with the application of pressure above 2 GPa with a maximum $T_c = 29$ K [41] and extends up to 6 GPa. The introduction of electron or hole first reduces the SDW transition temperature and ultimately induces superconductivity above a critical pressure. The pressure suppresses the SDW transition from its ambient pressure value of 140 K like in other members of the Ae-122 family. The T-P phase diagrams of $BaFe_2As_2$ and $SrFe_2As_2$ possess similarity with the $T - x$ phase diagrams of the electron or hole-doped $AeFe_2As_2$. Characteristic signature of the SDW transition is seen in a narrow doping (pressure) range above the T_c. Similar inferences can be drawn for hole-doped $(Ba_{1-x}K_x)Fe_2As_2$ and for the electron-doped $Ba(Fe_{1-x}Co_x)_2As_2$.

8.8.4 *Pressure Effects in 11 $FeSe_x$ Compounds*

Even though superconductivity was discovered in PbO-type α-FeSe compound at 8 K, yet the T_c could be raised to 27 K (onset of resistivity drop) in a Se-deficient $FeSe_x$ compound. Li et al. [25] studied the effect of pressure on the magnetic and superconducting properties of α-$FeSe_x$ for $x = 0.8$ and 0.88. Magnetic measurements show three distinct anomalies at increasing temperature, a diamagnetic signal below the superconducting transition at 8 K, a rapid rise of magnetization at about 78 K and a magnetization decrease at 106 K. The latter two transitions have been ascribed to an antiferromagnetic and a ferromagnetic transition, respectively. High-resolution X-ray diffraction measurements, however, show that these two phase transitions are also structural transformations associated with changes of the lattice symmetry. Under external pressure, all the three phase-transition temperatures shift to higher temperatures. Superconducting transition temperature, T_c goes up to 27 K. This has been interpreted as a sign of coexistence of Superconductivity with magnetism.

8.9 Critical Current in IBSC Wires and Tapes

The basic requirement for a practical superconductor always remains that it has to be produced in the form of a wire or a tape containing a large number of fine superconducting filaments embedded in a high conductivity matrix. Among the IBSCs belonging to four types 1111 SmOFeAs ($T_c = 55$ K), 111 LiFeAs ($T_c = 20$ K), 122 Ba/$SrFe_2As_2$ ($T_c = 38$ K) and 11 FeAs ($T_c = 8$ K), the 122 Ba/$SrFe_2As_2$ superconductor stands out most promising. These IBSCs are characterized by very high H_{c2} (> 70 T at 20 K), low anisotropy γ (< 2) and moderate weak link effect. Other attractive advantage with IBSC is that the critical grain misorientation angle in this system is large (= 9°) compared to the small value of 3°–5° for YBCO. The critical angle is a characteristic value beyond which the misorientation of grains starts

bringing down the critical current in IBSCs. Powder-in-tube (PIT) technique turns out to be the ideal route to produce IBSC wires/tapes being cost effective and offers a practical way to produce long lengths of wires and tapes. Transport J_c as high as 10^5 A/cm^2 (4.2 K, 10 T) has already been achieved [42] which is significantly higher than the threshold set for practical superconductors for use in field up to 10 T. Another significant development taken place is the production of 122 wire in excess of 100 m length which augers well for the use of this wire for building magnets.

8.9.1 Fabrication of Wires/Tapes Through PIT Technique

IBSCs can be produced by the PIT technique either by following the 'in situ route' or the 'ex situ route'. The methodology followed in the two PIT techniques is the same except that in an in situ technique one starts with a mixture of raw precursor filled in a metal tube, whereas in ex situ route powder of reacted superconducting IBSC is packed in the desired metal tube. The schematic of the two processes is shown in Fig. 8.23. Wires produced following the in situ route have rather poor J_c because of the voids, cracks and the presence of impurity phases in the superconducting core. Qi et al. [43] produced $Sr_{0.6}K_{0.4}Fe_2As_2$ (Sr-122) wires, by ex situ PIT method with a dense core. The preformed K-doped superconducting powder was filled in Ag tube which in turn was inserted in a Fe tube for mechanical strength and the composite billet was rolled, swaged, rolled to fine wires and/or flat rolled to tapes. Wires/tapes were heat treated at 900 °C for 20 h. They reported a transport $J_c = 3750$ A/cm^2 (4.2 K, sf). They further reported improvement in J_c by doping the core material with Pb or Ag which improved the grain connectivity. The ex situ PIT technique found

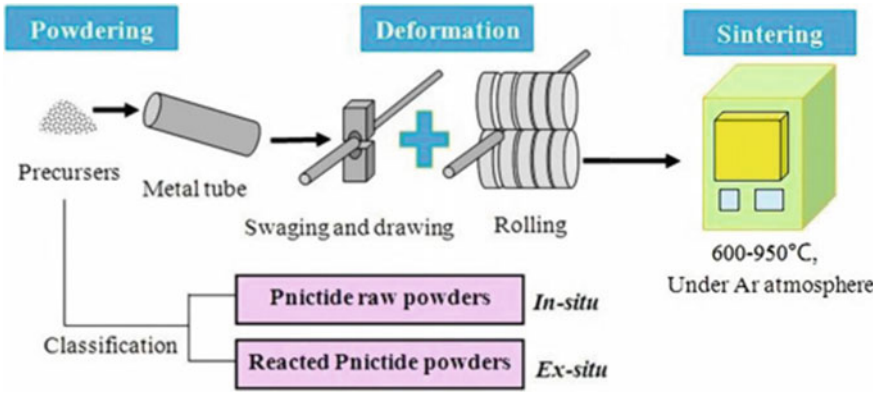

Fig. 8.23 Schematics of 'in situ' and 'ex situ' PIT process for the fabrication of IBSC wires and tapes. In in situ process, one starts with the mixture of raw precursor filled in a metal tube whereas in ex situ process powder of reacted superconducting IBSC is packed in the desired metal tube. Rest of the process to prepare wires and tapes is the same [6]. With permission from Elsevier

widespread acceptability and research groups achieved very impressive values of J_c in 122 wires in the range of 10^4–10^5 A/cm^2 at 4.2 K. The choice of sheath material is restricted to metals which do not react with the pnictides. Cu, Ag, Fe and Nb have been used as sheath material. Ag has proven to be the preferred sheath material showing near negligible reaction with pnictides at the optimized reaction temperature. An additional sheath of Cu/Fe/SS may also be used outside the Ag sheath to enhance the mechanical strength of the wire. This is in contrast with high T_c cuprates Bi-2212 and Bi-2223 where only Ag can be used for cladding as it is non-poisonous to BSCCO and is permeable to oxygen at the sintering temperature. Irrespective of sheath material right amount of Cu has to be introduced within the cross section of the wire for stability. Thus, IBSC wires can be manufactured by PIT method at a much reduced cost.

8.9.2 Achieving High J_c in IBSC 122 Wires/Tapes

Achieving high J_c in 1111 and 11 IBSCs has been very problematic. Control of F stoichiometry in 1111 during sintering and removal of excess Fe from the 11 wires has been found difficult. Another limiting factor in these IBSC wires has been the presence of non-superconducting glassy phase and an amorphous oxygen rich layer around the grains which hinders the current flow across the grain boundaries. It was observed that Ag addition leads to a suppression of formation of glassy phase as well as the amorphous layer and improves the grain connectivity and thus J_c. It also reduces the porosity of the core material. Different additives like Sn, Ag, Pb and Zn have been used by different groups to improve J_c in different types of IBSCs. For example, pre-sintering of Sn-added Sm-1111 powders results in the depletion of the FeAs wetting phase, filling of the voids between grains, yielding better inter-grain connectivity and ultimately enhancing the transport J_c. Critical current density, J_c as much as $= 3.95 \times 10^4$ A/cm^2 (4.2 K, 0 T) was reported by Zhang et al. [44]. The same group later reported still higher $J_c = 2.9 \times 10^4$ A/cm^2 (4.2 K, 10 T) in Sm-1111/Fe tapes through the use of high purity superconducting core.

High J_c also requires high mass density of the core which allows enhanced current flow between the grains. Weiss et al. [45] fabricated Ba-122 round wires by applying high isostatic pressure (HIP) of 192 MPa at 600 °C for 20 h and obtained a highly dense core with a $J_c = 10^5$ A/cm^2 (4.2 K, 0 T) and 8.5×10^3 A/cm^2 (4.2 K, 10 T). Togano et al. [46] at NIMS produced 122 /Ag tapes by following a process of flat rolling and isostatic pressing and obtained a dense filamentary core. They obtained a value of $J_c = 2.1 \times 10^4$ A/cm^2 (4.2 K, 10 T) and still higher $J_c = 8.6 \times 10^4$ A/cm^2 (4.2 K, 10 T) using a repeat process of flat rolling and cold pressing at a pressure of 2 GPa [46]. High J_c obtained by this process is the result of a uniform deformation achieved by pressing than by rolling. Cold rolling, however, causes microcracks which cannot be healed during successive annealing.

Zhang et al. [47] employed hot-pressing technique for the fabrication of Sr-122 PIT wires and achieved an all-time high $J_c = 10^5$ A/cm^2 (4.2 K, 10 T), a value needed

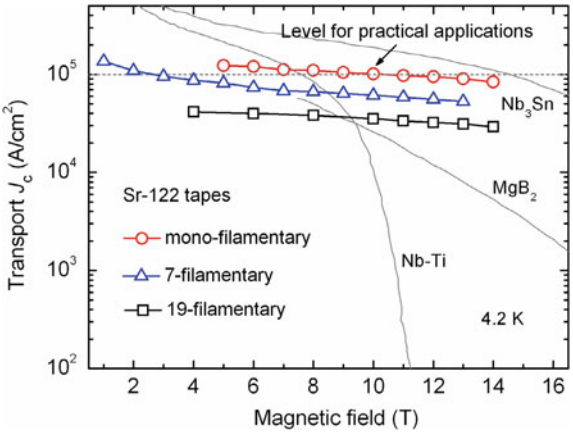

Fig. 8.24 Dependence of transport J_c on magnetic field for hot-pressed mono- and multifilamentary Sr-122 tapes. Values for MgB_2, NbTi and Nb_3Sn wires are shown for comparison [6]. With permission from Elsevier

for practical applications. In fact, 122 samples hot pressed at 900 °C yielded record value of $J_c = 10^5$ A/cm^2 (4.2 K, 14 T) as shown in Fig. 8.24. Microstructural studies revealed that the grains in hot-pressed wires get coupled strongly, reducing voids and cracks drastically. This leads to high mass density and consequently high J_c. There are no impurity phases at the grain boundaries either. Hot-pressed tapes have high texturing and good grain connectivity leading to high J_c. It is seen from Fig. 8.24 that Sr-122 IBSC samples even surpass J_c of Nb-Ti and MgB_2 in field > 10 T. Liu et al. [48] in an attempt to bring down the production cost of long lengths of the Ba-122 conductors used composite sheath of Cu/Ag (copper tube with Ag lining to prevent reaction) for fabricating $Ba_{0.6}K_{0.4}Fe_2As_2$ (Ba122) tapes. A reasonably high $J_c = 5.8 \times 10^4$A/cm^2 (4.2 K, 10 T) has been reported.

Enhancement of vortex pining is yet another tool to increase J_c. Dong et al. [49] carried out studies on vortex pining and dynamics in hot-pressed PIT-processed $Sr_{0.6}K_{0.4}Fe_2As_2$ tapes characterized by high J_c values. Figure 8.25 shows the plots of J_c versus magnetic field for this Sr-122 tape at different temperatures ranging between 5 and 30 K. They found that even though grain boundary vortex pining dominates, yet high density dislocations too may provide effective pining sites. For high J_c it is thus desirable that the grain size be kept small to have high density of grain boundaries which provide strong vortex pining. From the temperature dependence of J_c, the authors conclude that vortices are pinned by the spatial fluctuation of mean free path of the charge carrier. Magnetic relaxation measurements indicate that the relaxation rate in the low and intermediate temperature region is small. Accordingly, it exhibits a weak temperature and field dependence which is an indication of strong pining force. Because of its small size (comparable to coherence length), the point defects may provide more effective pining than surface pining. Introduction of artificial point

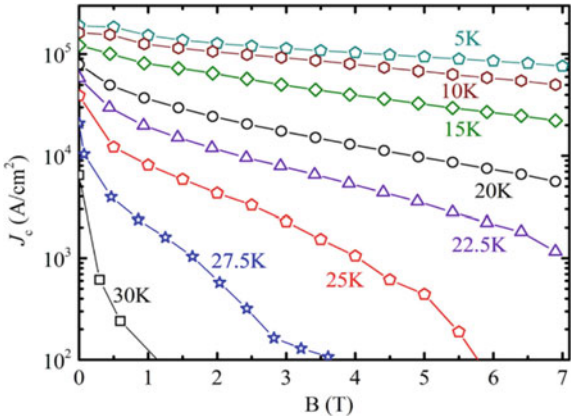

Fig. 8.25 Field dependence of J_c of hot-pressed $Sr_{0.6}K_{0.4}Fe_2As_2$ PIT-processed tape at different temperatures, 5–30 K [49]. Reproduced from J. App. Phys. **119**, 143906 (2016) with the permission of AIP Publishing

defects through radiation or the introduction of nanoparticles may be yet another approach to increase flux pining leading to still higher J_c.

8.9.3 Multifilamentary IBSC Wires/Tapes for Applications

For practical applications, a superconductor, as explained in Chap. 5, needs to be produced in a multifilamentary style contained in a high conductivity matrix for thermal and EM stability. Besides, it should have excellent mechanical strength to take care of very high stresses, large engineering current density, J_e always > 10^4 A/cm^2 at the temperature and field of interest. The conductor should have small anisotropy of critical current with respect to the direction of the field and finally the ability to be produced in long lengths at a reasonable cost. Fine filaments and multifilamentary structure of the superconducting wires and cables are vital to minimize AC losses caused by hysteresis, the eddy currents induced in metallic matrix and inter-filamentary coupling currents. Yao et al. [50] produced 7-, 19- and 114-filament Ag/Fe wires and tapes of $Sr_{0.6}K_{0.4}Fe_2As_2$ (Sr-122) following the ex situ PIT process. The ex situ prepared precursor was packed in a Ag tube and drawn to monofilamentary wires of various diameters. Seven and nineteen wires were then bundled, packed in an iron tube and finally rolled/drawn to wires of 2 mm diameter. Part of the wires was flat rolled in to tapes of different thicknesses. 114-filament wire was fabricated by staking six pieces of the 19-filament wire of dia. 1.58 mm in an iron tube and processed in to wire and tapes. All the wires and tapes were finally heat treated at 900 °C for 30 min. Figure 8.26 shows the optical micrographs of the cross section of 114-filament IBSC 122-type wire and tape fabricated by PIT technique. Figure 8.26a is the cross section of the 2 mm dia. wire, Fig. 8.26b is the cross section

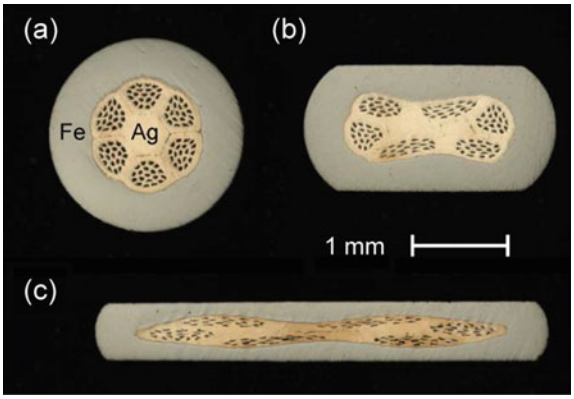

Fig. 8.26 Optical micrographs of the cross section of 114-filament $Sr_{0.6}K_{0.4}Fe_2As_2$ (Sr-122) wire and tapes fabricated by ex situ PIT technique, **a** cross section of the 2 mm dia. wire, **b** cross section of tape of thickness 1 mm, **c** cross section of tape of thickness 0.6 mm [50]. Reproduced from J. App. Phys. **118**, 203,909 (2015) with the permission of AIP Publishing

of tape of thickness 1 mm and Fig. 8.26c is the cross section of tape of thickness 0.6 mm. The 2 mm dia. wire had filaments smaller than 50 μm in size.

Field dependence of the transport J_c of Sr-122/Ag/Fe 114-filament 2 mm dia. wire and tapes of various thicknesses is shown in Fig. 8.27. The transport J_c of the 2 mm dia. wire is only 800 A/cm^2 (4.2 K, 10 T). The J_c in flat rolled tapes, however, is much higher and increases as the thickness keeps reducing. The J_c for 0.6-mm-thick tape comes out to be 6.3 × 10^3 A/cm^2 (4.2 K, 10 T). Flat rolling results in densification

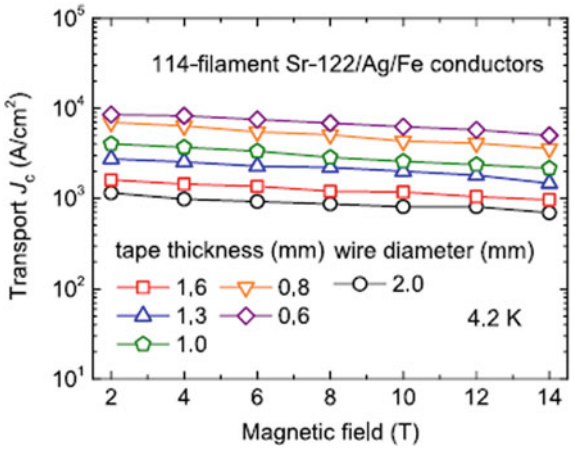

Fig. 8.27 Field dependence of the transport J_c of $Sr_{0.6}K_{0.4}Fe_2As_2$ /Ag/Fe with 114 filaments, 2 mm dia. wires and tapes of various thicknesses [50]. Reproduced from J. App. Phys. **118**, 203909 (2015) with the permission of AIP Publishing

of the Sr-122 core and a significant increase in transport J_c. Most striking feature of the plots in Fig. 8.27 is that J_c in these materials is very weakly dependent on field up to a high field of 14 T. This is a good sign for IBSCs to become potential superconductors for future high-field applications. Another important finding is that the transport J_c decreases with the increase of number of filaments. This may be related to the continuous reduction of filament size in 7-, 19- and 114-filament tapes. The J_c for 114-filament tape is 6.3×10^3 A/cm^2 nearly half of the $J_c = 1.4 \times 10^4$ A/cm^2 for 7-filament tape. Detailed microstructural studies revealed that as the number of filaments increase, the deformation causes sausages and the filaments are no longer of uniform cross section.

In high-field applications, the superconducting wire/cable experience large electromagnetic loads and therefore the conductor should have high mechanical strength and tolerance to large stresses. Kovac et al. [51] reported strain effect in $Sr_{0.6}K_{0.4}Fe_2As_2$/Ag ex situ PIT-processed tapes. J_c increases with strain up to $\varepsilon \sim 0.2\%$ and decreases at higher values of the strain. J_c drops rather rapidly beyond a strain of 0.25%. Liu et al. [52] studied strain effect over a wide range of axial strain from -0.6 to $+ 0.3\%$ in 122 IBSC and demonstrated that the material is less sensitive to compressive strain compared to Nb_3Sn. Similarly, the AC loss and quench behaviour in 122 IBSC tapes are superior to MgB_2 and the conventional superconductors (LTS). An additional sheath of Fe, Cu or SS has been preferred outside the Ag cladding to increase the mechanical strength and reduce the cost. Gao et al. at NIMS [53] used double sheath of Ag and SS for fabricating the 122 tapes. A J_c value of 3×10^4 A/cm^2 (4.2 K, 28 T) was achieved in the rolled and pressed Ba-122 tapes. This was the first such value at a high field of 28 T. The microstructure studies reveal higher mass density of the core and uniform deformation. This resulted in better texturing and must be the reason for high current densities. Short, 12-cm-long-rolled tape samples show very high homogeneity and high $J_c = 7.7 \times 10^4$ A/cm^2 (4.2 K, 10 T) which is better than the low-temperature superconductors (LTSs). Use of Cu as sheath material has been an interesting development; Cu is a cheaper material than Ag and provides excellent thermal stability to the superconductor. It has one drawback that it reacts with the superconducting core at the reaction temperature (~ 900 °C). The problem has been solved by reducing the reaction temperature down to 740 °C. Lin et al. [54] fabricated Cu-sheathed $Sr_{1-x}K_xFe_2As_2$ tapes using hot pressing method and reacting at 740 °C. They report systematic correlation between the sintering time, microstructure, reaction layer thickness and superconducting properties. Samples, hot pressed for one hour have transport $J_c = 3.5 \times 10^4$ A/cm^2 (4.2 K, 10 T) and 1.6×10^4 A/cm^2 (4.2 K, 26 T). Furthermore, the engineering critical current density (J_e) value of the samples is over 1.0×10^4 A/cm^2 (4.2 K, 10 T). This is by far the highest J_e reported for Cu-sheathed IBSC tapes. Cu sheath has also been used to produce Sm-1111 tapes by hot pressing at 400 °C. A $J_c = 2.37 \times 10^4$ A/cm^2 (4.2 K, 0 T) [55] has been obtained which is comparable to J_c in Ag sheathed tapes.

Having achieved impressive J_c in short-length Sr-122 tapes, the next step to realize practical superconductor is to perfect the manufacturing technology to produce kms long wires with uniform critical current across the entire length. First step of scaling up was taken in 2014 by Ma [56] at the Institute of Electrical Engineering, Chinese

Academy of Sciences (IEECAS) producing 11-m-long $Sr_{1-x}K_xFe_2As_2$/Ag tape by rolling with a uniform J_c. The process was soon scaled up at the same institute (IEECAS) and a 7-filament 115 m long single length of $Sr_{0.6}K_{0.4}Fe_2As_2$ (Sr122) tapes was produced following the PIT technique. The tape had an average $J_c = 1.3 \times 10^4$ A/cm^2 (4.2 K, 10 T) with good uniformity over the entire length.

Thus we find that even though IBSCs have T_c lower than the high T_c cuprates, yet they offer many advantages such as high B_{c2}, good grain boundary quality, large critical grain misorientation angle and the ability to be manufactured by a simpler technique, the PIT technique. Another added advantage is the very small field dependence of J_c in high-field region. With the advancement of cryocooler technology, IBSC magnets can be conveniently operated in 20–30 K temperature range without the use of liquid helium. Compact low-cost cryocooled NMR spectrometer and MRI scanners may be on the horizon in not so distant future. Recent success in the production of wires and tapes, more than 100 m long, has been an important landmark development bringing the IBSCs a step closer to become a practical superconductor of future for high-field-based applications.

8.9.4 The Thin Film Route

The thin film studies are important not only from the point of view of attaining high critical parameters like J_c and B_{c2} but are crucial for the fundamental understanding of the occurrence of superconductivity in these materials. This in turn involves detailed studies on many parameters related to the choice of the substrate, the buffer layers, all the parameters of deposition, the thickness, grain structure, maintaining stoichiometry, the deposition temperature and the right choice of deposition technique. The optimized parameters may be different for different members of the IBSC family, that is, 1111, 111, 122 and 11. A comprehensive 40-page review on the present status of the thin film technology in respect of all the members of the IBSC family has been published by Hänisch et al. [57]. Studies on the viability of Fe(Se, Te)-coated conductors on a RABiTS template have been carried out by Sylva et al. [58]. The substrate used was the Ni–5 at% W tapes with an out-of-plane orientation of 7° and an in-plane orientation of 5°. The RABiTS template for Fe(Se, Te)-coated conductor was realized by depositing a CeO_2 thin buffer layer (350 nm) on the Ni-W tape by pulsed laser deposition (PLD). The buffer layer acts as a chemical barrier against Ni diffusion. Fe(Se, Te) thin films yield a $T_c = 16$ K and $J_c = 3 \times 10^4$ A/cm^2(4.2 K, 18 T). The upper critical field B_{c2} (0 K) evaluated by using the Werthamer–Helfand–Hohenberg (WHH) relationship $B_{c2(0)} = -0.693\ T_c\ (dB_{c2}/dT)|T_c$ was found to be 790 T for B//ab and 90 T for B//c [58]. The field anisotropy in both field is very small. $B_{c2(//ab)}/B_{c2(//c)} = 2.3$ at 17 K and the ratio $B_{irr(//ab)}/B_{irr(//c)} = 1.8$ at 15 K. Figure 8.28a shows the dependence of critical current density, J_c of the tape, at 4.2 K and 9 K in both field orientations (B//ab and B//c) on the magnetic field. Figure 8.28b shows the magnetic field dependence of the pinning force density of the tape at 4.2 and 9 K in both orientations (B//ab and B//c) [58].

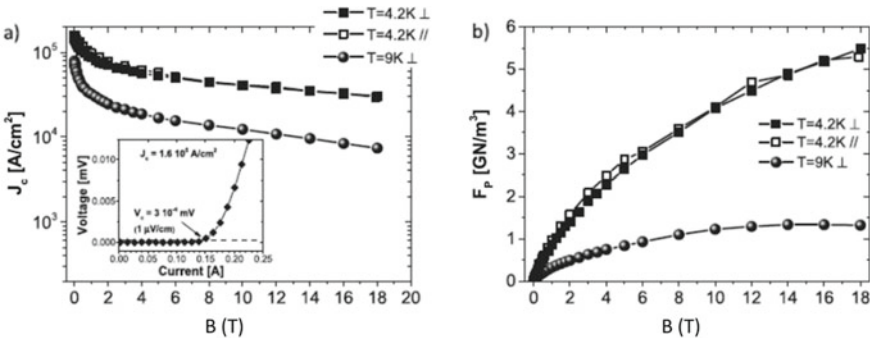

Fig. 8.28 **a** Dependence of critical current density, J_c at 4.2 K in both field orientation (B//ab and B//c) and 9 K measured on the tape. The inset is the I–V plot showing the criterion of I_c determination [58]. **b** Pinning force density of the tape plotted against magnetic field at 4.2 K and 9 K in both orientations (B//ab and B//c) [58]. With permission from IOP

An all-time high $T_c > 100$ K has been reported by Ge et al. [59] in a FeSe single-layer film grown on a Nb-doped $SrTiO_3$ conductive surface has caught the attention of theorists to understand if the interface-enhanced electron phonon coupling causes superconductivity. This will motivate researchers to tailor the interfaces between two different materials to observe high T_c superconductivity in iron-based superconductor family.

More recently, Imai et al. reported [60] a $T_c = 33.7$ K and a transport $J_c = 4 \times 10^4$A/cm^2 (4.2 K, 4 T) in a silver-sheathed $Ba_{0.6}Na_{0.4}Fe_2As_2$ (BaNa-122) superconducting tape fabricated using PIT technique. This reasonable good value of J_c is believed to be due to the enhanced c-axis orientation achieved during the fabrication process. An excellent topical review has just been published by Yao and Ma [61] which covers a whole gamut of the fabrication techniques, AC loss, mechanical properties and thermal and EM stability of the IBSC conductors. Merits of present-day fabrication techniques used to realize high transport J_c in relation with the intergrain connectivity, grain texture and flux pinning in IBSC wires and tapes have been discussed. Table 8.3 reproduces the important parameters like the critical current density and critical magnetic field values of all the practical superconductors which are in use or are likely to be used in the near future for high-field applications.

Even though impressive values of J_c have been achieved by many groups, yet there seems to be room for further improvement in J_c through optimization of process parameters. The important factors to be considered are increase in the mass density, improvement in grain connectivity, grain texturing, more studies on effect of grain size and texturing on J_c vis-à-vis pinning strength, percentage increase in the volume fraction of the core material to increase J_e, deformation process to prevent cracks, increased mechanical strength and finally the heat treatment optimization. IBSCs stand bright chance to compete with Nb-Ti, Nb_3Sn, cuprates and MgB_2 if only it could be produced in km lengths with uniform J_c by the cost-effective PIT technique.

Table 8.3 Important parameters of practical superconductors for applications (data compiled from [61]

Family of superconductor	Type of superconductor	SC acronym	T_c (K)	B_{c2} (T) @ 4.2 K	J_c A/cm^2 @ 4.2 K	Coherence length ξ_{ab} (nm)	Field anisotropy
Conventional	Alloy	Nb-Ti	9	11.5	4×10^5 (5 T)	4	Negligible
Conventional	A-15 Intermetallic	Nb_3Sn	18	25	10^6	3	Negligible
High T_c	Intermetallic	MgB_2	39	18	10^6	6.5	2–2.7
High T_c	Cuprate	REBCO	92	> 100	10^7	1.5	5–7
High T_c	Cuprate	Bi-2223	110	~ 140	10^6	1.5	50–90
High T_c	Cuprate	Bi-2212	90	~ 200	10^6	3.5	1300
High T_c	Iron-based	1111 IBSC	55	> 100	10^6	1.8–2.3	4–5
High T_c	Iron-based	122 IBSC	38	> 80	10^6	1.5–24	1.5–2
	Iron-based	11 IBSC	16	> 40	10^5	1.2	1.1–1.9

High critical field, high T_c, very small anisotropy and their ability of operating at 20–30 K make them potential conductors for high-field applications.

References

1. J.G. Bednorz, K.A. Muller, Z. Phys. B: Condens. Matter **64**, 189 (1986)
2. Y. Kamihara, H. Hiramatsu, M. Hirano, R. Kawamura, et al., J. Am. Chem. Soc., **128**, 10012 (2006)
3. H. Takahashi, K. Igawa, K. Arii, Y. Kamihara, M. Hirano, H. Hosono, Nature **453**, 376 (2008)
4. Y. Kamihara, T. Watanabe, M. Hirano, H. Hosono, J. Am. Chem. Soc. **130**, 3296 (2008)
5. T. Katase, Y. Ishimaru, A. Tsukamoto, H. Hiramatsu et al., Nat. Commun. **2**, 409 (2011)
6. H. Hosono, A. Yamamoto, H. Hiramatsu, Y. Ma, Mater. Today **21**, 278 (2017)
7. A.S. Sefat, A. Huq, M.A. McGuire, R. Jin, et al., Phys. Rev. B **78**, 104505 (2008)
8. H.-H. Wen, G. Mu, L. Fang, H. Yang, X. Zhu, Europhys. Lett. **82**, 17009 (2008)
9. M. Rotter, M. Tegel, D. Johrendt, Phys. Rev. Lett. **101**, 107006 (2008)
10. F.C. Hsu, J.Y. Luo, K.W. Yeh, T.K. Chen, T.W. Huang et al., Proc. Natl. Acad. Sci. U. S. A. **105**, 14262 (2008)
11. T. Imai, K. Ahilan, F.L. Ning, T.M. McQueen, R.J. Cava, Phys. Rev. Lett. **102**, 177005 (2009)
12. X. Chen, P. Dai, D. Feng, T. Xiang, F. Zhang, arXiv:1403.2612v1 [cond-mat.mtrl-sci] 7 Mar 2014, Nat. Sci. Rev. **1**, 371 (2014)
13. A.A. Kordyuk, arXiv:1209.0140v1 [cond-mat.supr-con] 1 Sep 2012
14. H. Luetkens, H.H. Klauss, M. Kraken et al., Nat. Mater. **8**, 305 (2009)
15. S. Limura, S. Matsuishi, H. Sato, T. Hanna, Y. Muraba et al., Nat. Commun. **3**, 943 (2013)
16. C. Wang, Y.K. Li, Z.W. Zhu, S. Jiang, X. Lin, Y.K. Luo, et al., Phy. Rev. B **79**, 054521 (2009)
17. J.H. Tapp, Z. Tang, B. Lv, K. Sasmal, B. Lorenz, P.C.W. Chu, et al., Phys. Rev. B **78**, 060505 (R) (2008)
18. X.C. Wang, Q.Q. Liu, Y.X. Lv, W.B. Gao, L.X. Yang et al., Solid Sate Commun. **148**, 538 (2008)
19. S.R. Jha, Y.S. Reddy, R.G. Sharma, Pramana **33**, L615 (1989)

20. S.R. Jha, R. Rajput, D. Kumar, Y.S. Reddy, R.G. Sharma, Solid State Commun. **81**, 603 (1992)
21. Z.R. Ye, Y. Zhang, M. Xu, Q.Q. Ge, Q. Fan, et al., arXiv: 1303.0682v2[cond-mat-con] 29 April 2014; Phy. Rev. **X 4**, 031041 (2014)
22. S. Oh, A.M. Mounce, J.A. Lee, W.P. Halperin, C.L. Zhang, et al., Phys. Rev. **B 88**, 134518 (2013)
23. P.D. Johnson, G. Xu, W.-G. Yin, *Iron—Based Superconductivity.* Springer Series in Materials Science Vol. 211 (2015)
24. Z. Li, R. Zhou, Y. Liu D. L. Sun, J. Yang, C.T. Yen, et al., Phys. Rev. **B 86**, 180501(R) (2012)
25. L. Li, Z. R. Yang, M. Ge, L. Pi, J.T. Xu et al., arXiv:0809.0128 (2008)
26. F.-C. Hsu, J.-Y. Luo, K.-W. Yeh, T.-K. Chen, et al., arXiv.org > cond-mat > arXiv:0807.2369 (2008)
27. Y. Mizuguchi, Y. Takano, J. Phys. Soc. Japan, **79**, 102001 (2010)
28. A.V. Fedorchenko, G.E. Grechnev, V.A. Desnenko, A.S. Panfilow et al., Low Temp. Phys. **37**, 83 (2011)
29. L. Li, Z.R. Yang, M. Ge, L. Pi, J.T. Xu et al., J. Supercond. Novel Magn. **22**, 667 (2009)
30. Y. Mizuguchi, F. Tomioka, S. Tsuda, T. Yamaguchi, Y. Takano, J. Phys. Soc. Jpn., **78**, 074712 (2009)
31. S. Li, C. de la Cruz, Q. Huang, Y. Chen, J.W. Lynn, et al., Phys. Rev. **B 79**, 054503 (2009)
32. L. Gao, Y.Y. Xue, F. Chen et al., Phys. Rev. B **50**, 4260 (1994)
33. C.W. Chu, B. Lorenz, Physica C **469**, 385 (2009)
34. H. Takahashi, H. Okuda, K. Igawa, K. Arii et al., J. Phys. Soc. Jpn. **77**, C78 (2008)
35. B. Lorenz K. Sasmal, R.P. Chaudhury, X.H. Chen, R.H. Liu, et al., Phys. Rev. **B 78**, 012505 (2008)
36. Z.A. Ren, G.C. Che, X.L. Dong, J. Yang, W. Lu et al., Europhys. Lett. **83**, 17002 (2008)
37. N. Takeshita, A. Iyo, H. Eisaki, H. Kito, T. Ito, et al., J. Phys. Soc. Jpn. **77**, 075003 (2008)
38. A.F. Wang, Z.J. Xiang, J.J. Ying, Y.J. Yan et al., New J. Phys. **14**, 113043 (2012)
39. A.S. Sefat, R. Jin, M.A. McGuire, B.C. Sales, D.J. Singh, et al., Phys. Rev. Lett. **101**, 117004 (2008)
40. K. Ahilan, J. Balasubramaniam, F.L. Ning, T. Imai, A.S. Sefat, et al., J. Phys.: Condens. Matter **20**, 472201 (2008)
41. P.L. Alireza, Y.T. Chris Ko, J. Gillett, C.M. Petrone, J.M. Cole, et al., J. Phys.: Condens. Matter **21**, 012208 (2009)
42. X.P. Zhang, A. Yamamoto, H. Hiramatsu, Y. Ma, IEEE Trans. Appl. Supercond. **27**, 7300705 (2017)
43. Y.P. Qi, L. Wang, D. Wang, Z. Zhang, Z. Gao, et al., Supercond. Sci. Technol., **23**, 055009 (2010)
44. Q. Zhang, H. Lin, P. Yuan, X. Zhang, C. Yao, et al., Supercond. Sci. Technol., **28**, 105005 (2015)
45. J.D. Weiss, C. Tarantini, J. Jiang, F. Kametani, A.A. Polyanskii, et al., Nat., Mater., **11**, 682 (2012)
46. K. Togano, Z. Gao, A. Matsumoto, H. Kumakura, Supercond. Sci. Technol., **26**, 115007 (2013)
47. X. Zhang, et al., Appl. Phys. Lett., **104**, 202601 (2014)
48. S. Liu, Z. Cheng, C. Yao, C. Dong, et al., Supercond. Sci. Technol. **32**, 044007 (2019)
49. C.H. Dong, H. Lin, H. Huang, C. Yao, X. Zhang, et al., J. Appl. Phys., **119**, 143906 (2016)
50. C. Yao, H. Lin, Q. Zhang, X. Zhang, D. Wango, et al., J. Appl. Phys., **118,** 203909 (2015)
51. P. Kovac, L. Kopera, T. Melišek, M. Kulich, I. Hušek, et al., Supercond. Sci. Technol. **28**, 035007 (2015)
52. F. Liu, C. Yao, H. Liu, C. Dai, J. Qin, et al., Supercond. Sci. Technol. **30**, 07LT01 (2017)
53. Z. Gao, K. Togano, A. Matsumoto, H. Kumakura, Supercond. Sci. Technol., **28**, 012001 (2015)
54. K. Lin, C. Yao, X. Zhang, Q. Zhang, H. Huang, et al., Supercond. Sci. Technol., **29**, 095006 (2016)
55. Q.J. Zhang, C. Yao, X. Zhang, D. Wang, C. Dong et al., IEEE Trans. Appl. Supercond. **26**, 7300304 (2016)
56. Y.W. Ma, Physica C **516**, 17 (2015)

57. J. Hänisch, K. Iida, R. Hühne, C. Tarantini, Supercond. Sci. Technol., **32**, 093001 (2019)
58. G. Sylva, A. Augieri, A. Mancini, A. Rufoloni, et al., Supercond. Sci. Technol. **32**, 084006 (2019)
59. J.F. Ge, Z.L. Liu, C. Liu, C.L. Gao, D. Qian, et al., Nat. Mater. **14**, 285 (2015)
60. S. Imai, S. Itou, Y. Ishida, A. Tsuchiya, A. Iyo, et al., Sci. Rep. **9**, 13064 (2019)
61. C. Yao, Y. Ma, Supercond. Sci. Technol. **32**, 023002 (2019)

Chapter 9
Building Laboratory Superconducting Magnets and Present Status of High-Field Magnets

Abstract This chapter gives tips to the researchers how to design, build and operate standard superconducting solenoid magnets in the laboratory and use them for physical property measurements. Broad parameters discussed are the design dimensions, homogeneity, current lead optimization, quench protection and persistent current switches. Multifilamentary Cu/Nb-Ti conductor is the universal choice for building (multi-section) magnets producing field up to 8 T (4.2 K). Additional field is produced by using inserts of A-15 Nb_3Sn conductor, usually of the 'wind and react' type. Specific examples of the design, fabrication and operation of a 7 T Nb-Ti magnet, a 11 T Nb-Ti/Nb_3Sn combination magnet and a 6 T cryo-free magnet, built in author's laboratory, have been discussed. Delicate steps followed during winding, tension adjustment, controlled high temperature reaction, preparation of current contacts and the final impregnation of the Nb_3Sn magnet have been elaborated. The chapter presents all salient features of a superconducting magnet and the latest developments made in achieving record fields in conventional and HTS magnets. Details of high-field magnets all using an insert of Bi-2223, Bi-2212 or REBCO tape (coated) conductors nested inside the Nb-Ti and Nb_3Sn combination magnets have been presented. A 24 T magnet built at TML, Tsukuba Japan, a 32 T magnet built at NHMFL and the latest all time high 45.5 T magnet again built at NHMFL have been discussed in detail. The emergence of REBCO-coated conductor as a high field and mechanically strong superconductor has led us to believe that 50–60 T magnets are on the horizon.

9.1 Introduction

The property of a superconductor that it carries current without dissipation has made it an ideal material for building magnets. A magnet however is a common element to the entire electro-technology. A magnetic field is an essential tool for scientific research in several disciplines like condensed matter physics, material science, atomic and molecular physics, life sciences and chemistry. High magnetic field enabled the observation of Quantized Hall Effect (QHE) and Fractional Quantum Hall Effect (FQHE) in quantized electron energy levels. Unprecedented field stability and very high fields available with superconducting magnets has made high-resolution Nuclear

R. G. Sharma, *Superconductivity*, Springer Series in Materials Science 214,
https://doi.org/10.1007/978-3-030-75672-7_9

Magnetic Resonance (NMR) spectroscopy a powerful tool to study structure of large and complex molecules. 1.2 GHz NMR spectrometers (28.2 T field) are now commercially available. The whole-body Magnetic Resonance Imaging (MRI) based on NMR principle has become an important diagnostic tool with radiologists and has benefited the society at large. In present times, superconducting magnets are playing pivotal role in high energy particle accelerators and fusion reactors. The success of Large Hedron Collider (LHC) can be attributed to a large extent to superconducting magnets. The success of on-going projects like International Thermonuclear Energy Reactor (ITER) and futuristic International Linear Collider (ILC), FCC and EIC too will be equally dependent on the perfection to which the magnets will be built.

9.2 Evolution of Superconducting Magnets

Kamerlingh Onnes realized the importance of superconducting materials for producing high magnetic field soon after the discovery of superconductivity, but his dream of producing high field using Pb wire remained unfulfilled because of the inherent limit of low critical field, B_c of this material. The first superconducting magnet was built at Physics Laboratory in Leiden Uni. by winding Pb wire (Fig. 9.1a), but the results were too disappointing. Magnets became a possibility in mid-1950s after the discovery of type II superconductors with high upper critical field, B_{c2} values. George Yntima [1] built a successful superconducting magnet shown in Fig. 9.1b for producing low temperature by adiabatic demagnetization of a paramagnetic salt. He wound a fine enamelled strained Nb wire (dia. 0.05 mm) over a soft iron core and produced a field of 0.7 T in a pole gap of 2.78 mm. The number of turns of Nb wire was 4296. The Nb layer was covered by another layer, that

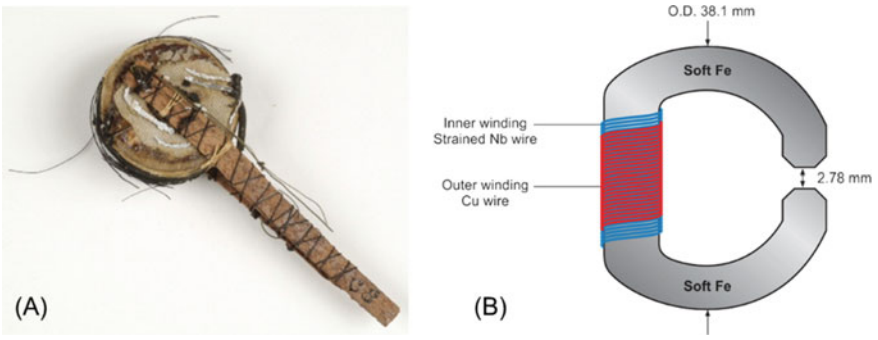

Fig. 9.1 **a** World's first superconducting magnet wound with Pb-wire at Leiden Physics Laboratory in 1912. Image Courtesy of Museum Boerhaave, Leiden, The Netherlands (2011). http://www.aps.org/meetings/march/vpr/2011/imagegallery/supercoil.cfm. **b** World's first successful superconducting magnet wound by Yntima using strained Nb wire at Uni. of Illinois in 1954 producing a field of 0.71 T. (adapted and modified from [1])

of the bare Cu wire of 0.46 mm diameter, having 183 turns. He wound magnets using cold-worked as well as annealed Nb wires and found that cold-worked wires carried larger current compared to annealed wires and produced higher field. This was perhaps the first indication that defects introduced in superconductors enhance the critical current via the mechanism of flux pinning.

An important event was the development of a 9.2 T magnet by Coffey et al. [2] using three sections of Nb-Ti wire in a background field of 5 T provided by two-section Nb–Zr coil. High-field superconducting magnets, however, became possible only after the discovery of A-15 superconductors. The year 1961 proved to be a turning point in the history of superconducting magnet development when Kunzler et al. [3] at Bell Laboratories showed conclusively that field in excess of 10 T were possible using Nb_3Sn conductor. Nb_3Sn Magnets in pancake structure were built using flexible tapes of Nb_3Sn deposited on hastelloy tapes either by Sn-diffusion technique or the chemical vapour deposition (CVD) technique in 1960s. These magnets were, however, not stable against flux jumps. The emergence of Cu-stabilized multifilamentary (Nb-Ti and Nb_3Sn) wires and cables in 1970s laid a strong foundation for real high-field superconducting magnet technology. Continuous improvement in the J_c values of Nb_3Sn conductor through improved mechanical deformation techniques and metallurgical processing has led to an all-time high magnetic fields. Multi-section (Nb-Ti/Nb_3Sn) magnets producing 20 T field are commercially available. The use of HTS (Bi-2223, Bi-2212 or 2G YBCO) inserts has pushed this value to still higher fields in excess of 22 T. A 32 T superconducting magnet was designed, fabricated and operated at NHMFL, Florida State University in 2012 [4]. The magnet uses two sections of Nb–Ti and three sections each of Nb_3Sn and YBCO conductors. Other advances in producing intense field have recently been made at BNL and NHMFL, BNL which produced a field of 16 T by a REBCO stand-alone magnet. NHMFL generated a record field of 35.4 T [5] using a REBCO insert in a background field of 31 T provided by a resistive 20 MW magnet. The insert contributed a field of 4.4 T. More recently, a world record of 45.5 T field has been established by Hahn et al. at NHMFL [6]. The innermost coil wound using ultra-thin REBCO-coated superconducting tape produces a field of 14.4 T in a background field of 31.1 T provided by a resistive magnet.

During last few decades, ‘conduction-cooled’ or ‘cryo-free’ superconducting magnet systems have flooded the research laboratories which do away with the use of liquid helium for magnet cooling. Instead, the magnet system is cooled by closed cycle refrigerators (CCRs). This has been possible for two reasons. One is that CCR of 1.5 W cooling capacity at 4 K is commercially available, and second is that HTS current leads capable of carrying thousands of ampere current have been commercialized. Cryo-cooled magnets capable of generating high field up to 20 T have found their way in research laboratories. These magnets form critical components of a large variety of physical and magnetic measurement systems.

9.3 Unique Features of a Superconducting Magnet

The winding of a superconducting magnet is quite an intricate exercise because of the peculiar behaviour of a superconductor carrying large current in high magnetic field and the large mechanical forces encountered by the conductor. We discuss below some of these peculiarities.

- In a superconducting magnet, the critical current of the conductor is a function of temperature and the magnetic field unlike normal metal like copper. The maximum current that a coil can carry depends upon the maximum field experienced by the superconductor. The operating temperature for most magnets is 4.2 K provided by liquid helium bath. For enhanced fields, the magnet is operated at a reduced temperature of 1.8 K.
- The magnet wire is subjected to mechanical load primarily due to winding tension and the bending strain.
- Differential thermal contraction of the constituent materials of the magnet gives rise to stress when cooled to operating temperature.
- There is stress internal to the conductor because of the sharp change of temperature from reaction temperature (~ 700 °C for Nb_3Sn) to operating temperature (4.2 K).
- Since these magnets generate strong fields, the conductor experiences large radial Lorentz force which gives rise to hoop stress (=BJR) which can be severe in large size magnets. Here B is the magnetic field, J the current density, and R is the radius of the magnet coil.
- The critical current density, J_c, of superconducting wires has a very strong stress–strain characteristic. Strain under load can bring down J_c drastically.
- Any micromovement of the conductor under large Lorentz force can generate heat sufficiently high to drive the conductor to normal state and quench the magnet. To prevent such movement of the conductor the magnet is always impregnated with a suitable low-temperature compatible epoxy or bees wax.
- The magnet is always susceptible to quench for a variety of reasons such as insufficient cooling, exceeding the current beyond J_c, too high-current ramp rate or for any unforeseen thermo-mechanical disturbance. During the quench, the stored energy of the magnet (=½ LI^2) released can burn the magnet. This energy therefore has to be dumped outside of the magnet. A fool-proof quench protection system is therefore integrated with the superconducting magnet to save it from burnout.
- Notwithstanding the extreme care that is needed to build superconducting magnet systems, the magnet industry has seen an unprecedented growth over last six decades. This is because of the distinct advantages these magnets have over the normal copper–iron electromagnets. Superconducting magnets are indispensable when intense magnetic field is required. These magnets are very compact, occupy little space, are light in weight and consume very little energy. No elaborate water cooling system is required either. Superconducting magnets are traditionally operated in liquid helium bath, but small size magnets are increasingly cooled by cryocoolers, purely a mechanical device.

9.4 Design Considerations of a Solenoid Magnet

An excellent paper on the method of optimization of winding parameters of a superconducting solenoid magnet was published by Boom and Livingston [7] as early as in 1962. The calculation method is based upon the classical theory of Fabry [8]. Quite a few good books [9–13] too have been published at different times which have been widely used for designing and constructing laboratory superconducting magnets. Several computer programmes for different applications are available for various aspects of magnet design.

Superconducting magnets extensively used for research are solely solenoids. It will therefore be most appropriate if we describe the design of such a magnet in detail. Let us consider a solenoid as shown in Fig. 9.2 with a working bore $2a_1$, outer winding dia. $2a_2$ and the winding length 2ℓ. The current I produces a central field B_0 and a maximum field, B_M close to the inner winding layer. The axial field of an infinite length solenoid is given by

$$B_0 = J\lambda a_1 F(\alpha, \beta) \tag{9.1}$$

where B_0 is the axial field in the mid-plane, J the current density of the conductor, λ the space factor (total conductor cross section divided by the total winding cross

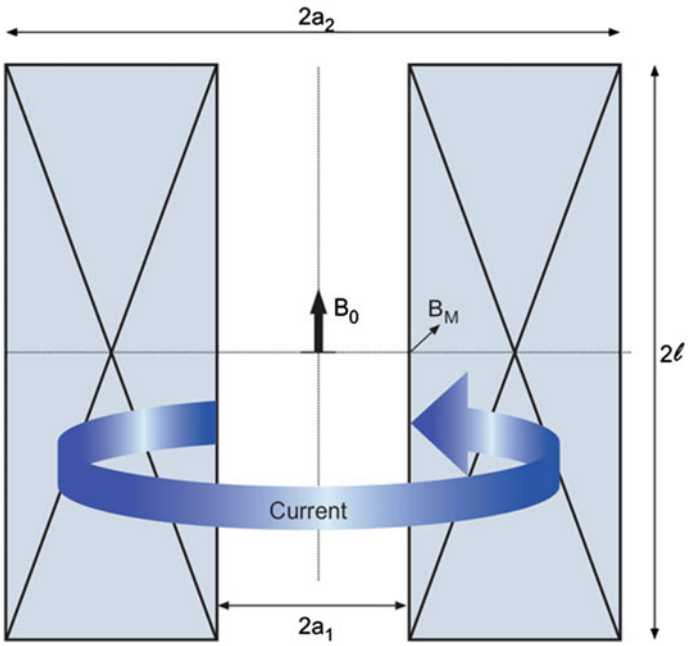

Fig. 9.2 Solenoid magnet of inner dia. $2a_1$, outer dia. $2a_2$ and a winding length 2ℓ. The axial field is B_0 and the maximum field B_M at the innermost winding layer

section), $\alpha = a_2/a_1$, the ratio of the outer winding diameter to inner winding diameter, $\beta = 2\ell/2a_1$, the ratio of the winding length to inner winding diameter and $F(\alpha, \beta)$ is a geometry dependent quantity called field factor, shape factor or Fabry parameter and is given by

$$F(\alpha, \beta) = \mu_0 \beta \ln\left[\frac{\alpha + \left(\alpha^2 + \beta^2\right)^{1/2}}{1 + \left(1 + \beta^2\right)^{1/2}}\right] \tag{9.2}$$

To start designing a solenoid magnet, we select the working bore and then the inner winding dia. $2a_1$, after taking the thickness of the former in to account. We then select the central axial field, B_0. The current density J is found out from the I_c-B plot of the conductor intended to be used. The space factor λ usually varies from 0.7 to 0.9 depending upon the voids in the winding and non-superconducting stuff such as interlayer insulation etc. used. The value of field factor, $F(\alpha, \beta)$, is now determined. Interestingly, for one value of $F(\alpha, \beta)$, several combinations of α and β are possible to yield the same field as shown in Fig. 9.3.

It is possible to choose a combination values of α and β which corresponds to the minimum winding volume. Unfortunately, this geometry leads to a short and fat coil which in turn leads to a poor field homogeneity and consume more conductor. For high-field homogeneity, we must select parameters α and β away from minimum

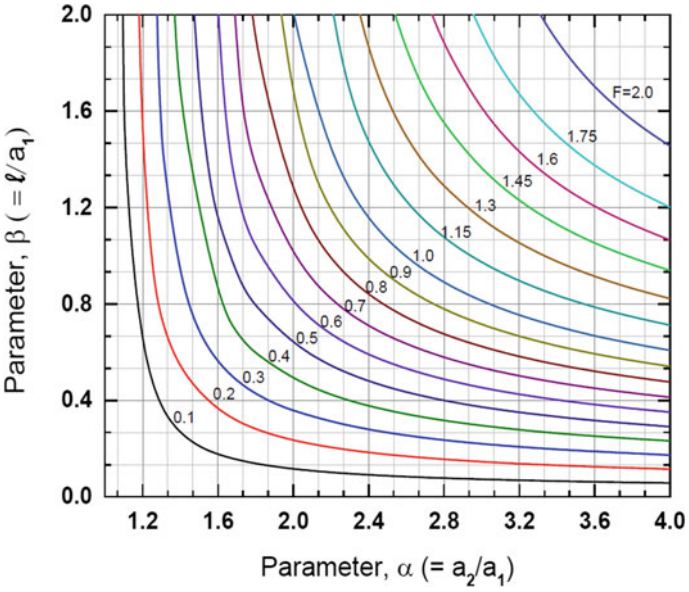

Fig. 9.3 Febry parameter, $F(\alpha, \beta)$, curves plotted as a function of α and β. Several combinations of α and β are possible for a given value of $F(\alpha, \beta)$ and thus for a magnet to produce a particular field (*Courtesy* Soumen and Vijay)

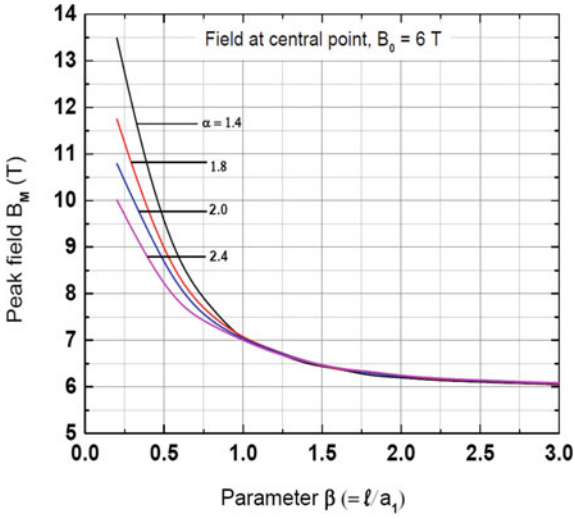

Fig. 9.4 Peak field $B_{\mathbf{M}}$ versus β plots for different values of $\alpha = 1.4$, 1.8, 2.0 and 2.4 for a 6 T magnet. Field homogeneity improves with increasing β and appears to saturate beyond $\beta = 3$ (*Courtesy* Vijay, Phaneendra and Soumen)

volume criterion and choose larger value of β. The maximum axial field is experienced on the innermost layer of the winding. It is this field which ultimately restricts the operating current of the magnet and not the central field. In Fig. 9.4, we have plotted the maximum field experienced by the conductor at the innermost layer, $B_{\mathbf{M}}$, for a central field of 6 T and for different values of α (= 1.4, 1.8. 2.0 and 2.4).

Boom and Livingston [7] have plotted the homogeneity curves represented by the ratio, $k = B_{\mathbf{M}}/B_{\mathbf{0}}$ (ratio of peak field to the central field) as a function of α and β. It is clear from the figure that for high homogeneity one has to choose α and β values such that the $B_{\mathbf{M}}/B_{\mathbf{0}}$ ratio is as close to 1 as possible. This means β has to be much larger than that given by the minimum volume criterion. This is clearly seen from Fig. 9.4 that for a 6 T axial filed the peak field rises sharply for β values less than 1 for all values of α. The peak field is reduced for β greater than 1 and becomes close to the central field $B_{\mathbf{0}}$ close to $\beta = 3$. Such a magnet will consume lesser quantity of conductor and yield high homogeneity. This results from the fact that the maximum field or the peak field is now much reduced and the magnet can be operated at a higher current producing higher field. The central axial field $B_{\mathbf{0}}$ increases as we move away from the centre along the radius, becomes maximum ($B_{\mathbf{M}}$) close to the innermost winding layer and decreases thereafter and even becomes negative close to the outer edge of the winding. This means that a smaller operating magnet current is now chosen corresponding to $B_{\mathbf{M}}$ instead of the central field $B_{\mathbf{0}}$. Since the outer layers of the winding are exposed to decreasing field, the conductor is capable of carrying much larger current than the inner part of the winding. It is therefore advisable to wind the magnet in multi-sections, outer sections operating at larger current densities than the inner ones. Better still, if we use different dia. wires in different sections and run them at the same current, that is, at different current densities as dictated by the J_c-B plots of the conductor. Such a magnet will consume lesser quantity of conductor and yield high homogeneity. This results from the fact that the maximum

field or the peak field is now much reduced and the magnet can be operated at a higher current producing higher field. One should therefore use thicker wire for the inner and thinner wire for the outer sections. We built several 7–8 T Nb–Ti magnets in two sections using 0.75 mm dia. wire for the inner section and a 0.54 mm for the outer section and running them in series using the same power supply.

9.4.1 *Specific Example of a 7 T Superconducting (Nb–Ti) Magnet*

Let us take an example of designing a 7 T Nb–Ti magnet to be used as an insert to a 100 mm neck dia. liquid helium storage vessel [14]**.** To keep the outer diameter of the magnet smaller than 100 mm (LHe-vessel neck dia.), we chose a thicker Cu/Nb-Ti wire (0.75 mm dia.) and a high operating current ~ 210 Amp. We started with a former of clear bore of 46 mm and the inner winding dia. ($2a_1$) of 50 mm. We used a 45 filament Cu/Nb-Ti wire supplied by Vacuumschmelze. This wire had an I_c = 245 A at 7 T field, and we take 85% of this value, that is, 208 A as the operating current. λ, the space factor, is taken to be 0.78, a value we find consistently in many of our magnets wound using a fibre-glass cloth as inter-layer material. J is obtained by dividing 208 by area cross section of the wire (0.4418×10^{-6} m^2) which turns out to be 470×10^6 A/m^2. By putting the appropriate values in (9.1), the function $F(\alpha, \beta)$ comes out to be 0.76255×10^{-6} for a field of 7 T. Using the B_M/B_o plots for different combinations of α and β in Fig. 3.3 of [11], we selected a ratio k (B_M/B_0) to be 1.0112 such that the peak field at the inner winding layer is just 7.078 T low enough to allow a safe operating current of 208 A. We now select from the same figure a combination of $\alpha = 1.665$ and $\beta = 3$ compatible with this field ratio. Thus, the outer winding diameter of the coil, $2a_2$, becomes = 83.25 mm and the winding width = 16.6 mm. Since β is to be 3, a winding length 150 mm has been chosen. One layer will have 200 turns, and there will be 22 layers in all. The total number of turns thus becomes = 4400. The parameter details of the magnet are reproduced in Table 9.1.

The former was made out of SS and a layer of fibre-glass cloth was wrapped on the bare surface of the former before starting winding. Thin G-10 sheets were fixed on the inside of the two SS end flanges. The flanges and the central pipe of the former had perforations to allow LHe to seep and cool the winding. The wire terminals were taken out through the top-end flange at an easy slope. A schematic diagram of the former and the winding is shown in Fig. 9.5. Winding was carried out on a modified lathe with 0.75 mm pitch and rotating at a comfortable speed of 18 rpm. Each layer was very tightly wound and had 200 turns. A tension of 1 kg was uniformly maintained throughout the winding. To prevent possibility of wire movement under Lorentz force during operation of the magnet precaution should be taken not to leave gap in the winding. We always wind an even number of layers so that the second-end terminal of the wire can also be taken out from the top flange.

Table 9.1 Parameters of the 7 T solenoid magnet of insert type

Parameter	Value	Parameter	Value
Working bore	46 mm	Conductor used	Cu/Nb–Ti (MF)
Inner winding dia. $2a_1$	50 mm	Cu: Nb-Ti	1.8: 1
Outer winding dia. $2a_2$	83.25 mm	Conductor dia	0.75 mm
Winding width w	16.6 mm	No. of filaments	45
Winding length, 2ℓ	150 mm	Filament dia	38 μm
Parameter α	1.665	Inductance	0.4 H
Parameter β	3	Field at 208 A	7 T
Function F(α, β)	0.76255×10^{-6}	Field factor	33.65 mT/A
Field homogeneity	0.094% (10 mm DSV)	Quench field at 210 A	7.1 T
No. of layers	22	Stored energy at 210 A	8.8 kJ
Total no. of turns	4400	Impregnating material	Bees wax
Conductor length	0.9 km	Inter-layer material	Fibre-glass cloth

After the winding, the two terminals of the wire were secured in position and the magnet was vacuum-pressure impregnated in bees wax.

The magnet was suspended from a top flange using G-10 supports and radiation shields. Two vapour-cooled optimized current leads also terminate at the top flange for connecting with the power supply. Figure 9.6a shows the bottom part, and Fig. 9.6b shows the top part of the magnet assembly. A relief valve is provided at the top flange for He-gas to escape in the event of a pressure build-up in the LHe vessel. Helium gas flow through the current leads is regulated using a control valve which is connected to the recovery line. A He-gas flowmeter, in the gas recovery line, measures the He-gas evaporation rate. The magnet assembly pre-cooled with liquid nitrogen is gently and slowly lowered in to the LHe-storage vessel, and experiments can be performed rather quickly as compared with conventional magnets operated in dedicated LHe-dewars which need time to be ready for operation.

The axial field variation with the distance from the mid-plane is plotted in Fig. 9.7. The inset shows the axial field homogeneity of 0.098% in a 10 mm diameter spherical volume (DSV). The radial component of the axial field along the axis remains zero.

Figure 9.8 shows the plots of the magnetic field lines using Poisson Superfish computer programme. Three distinct features can be noted from this figure, first is the density of magnetic field lines which increases as one moves away from the

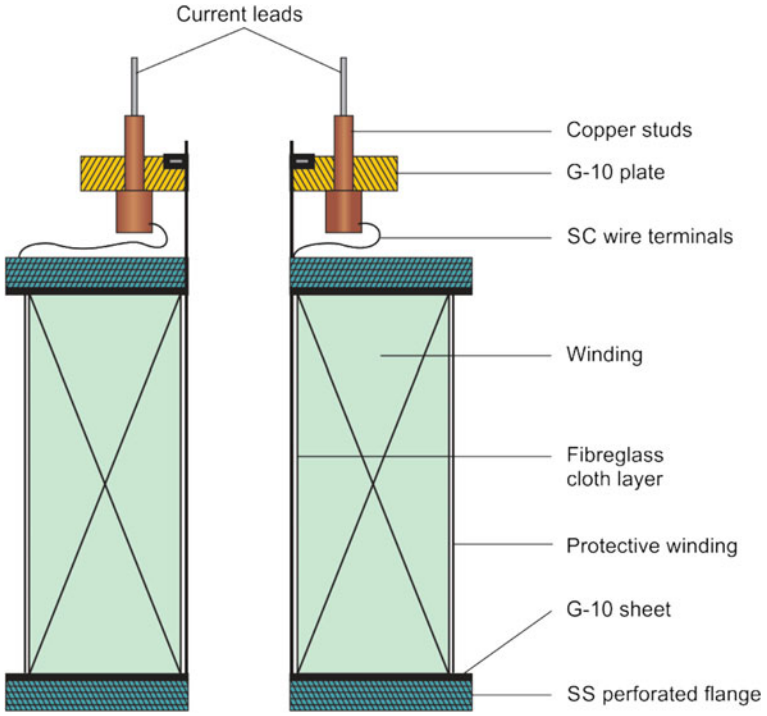

Fig. 9.5 Schematic diagram of the former and the winding of a 7 T magnet of the insert type

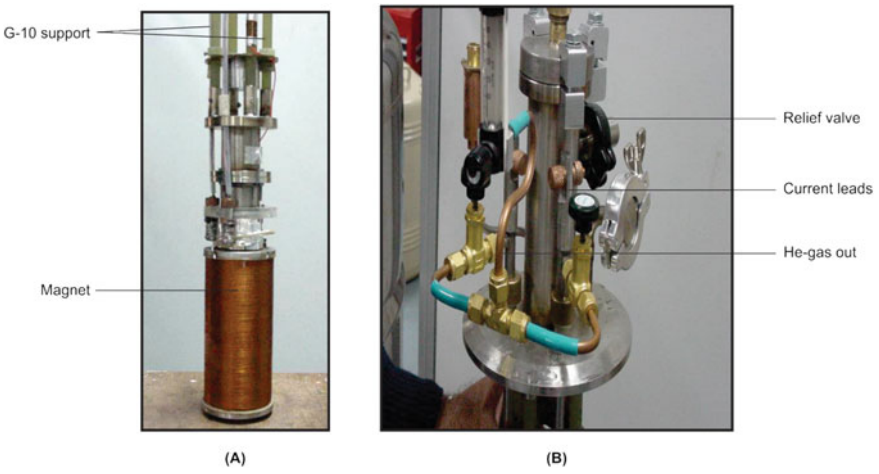

Fig. 9.6 **a** 7 T magnet and the bottom part of its support system. **b** The top view: the flange, seen in the picture fits on to the top of the LHe-vessel neck, He-gas flows through the current leads and is collected via a gas flowmeter [14] (Courtesy photo IUAC Delhi)

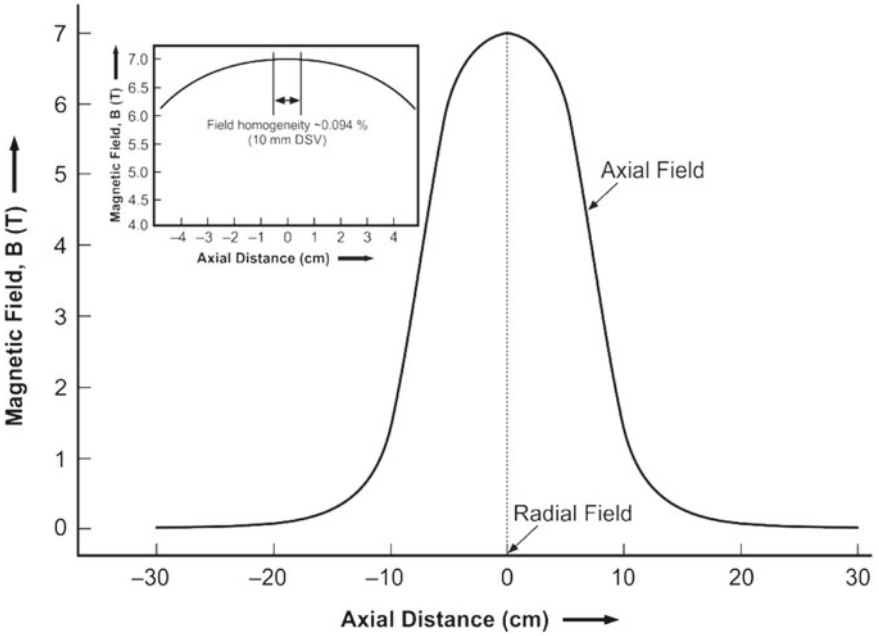

Fig. 9.7 Axial field profile of the magnet at 7 T. The inset shows a field homogeneity of 0.098% in a 10 mm DSV. The radial field along the axis is nearly zero [14]

mid-plane along the radius of the magnet. It becomes maximum at the innermost winding layer. It is for this reason that the axial field peaks at the inner winding layer. Second is the density of lines of force which decreases thereafter and becomes zero close to the outermost layer. The zero-field region is indicated in the figure. Thirdly, the lines of force bend near the ends of the magnet, (this is true for any finite length solenoid as ours) and reverses the field direction beyond the outer most layer. The Lorentz force, generated by the interaction of perpendicular current and magnetic field ($B \times I$), at the outer layer will therefore reverse the direction and will tend to compress the coil from outside. There is already a Lorentz force acting on the innermost layer compressing the coil outwards. As one moves away along the radius, this force decreases and then changes direction. Bending at the ends also introduces a radial component of the field which produces an axial Lorentz force tending to compress the coil axially. A magnet is therefore like a pressure bottle similar to a high-pressure gas cylinder trying to explode. This pressure is $= B^2/2\mu_0$, and for a field value of 10 T, it turns out to be as high as 4×10^7 N/m^2 which is close to the yield strength of copper. Large Lorentz force also gives rise to large hoop stresses tending to explode the magnet. Reinforcement of the magnet winding is thus extremely important. The fact that peak axial field occurs at the innermost layer implies that the critical current density, J_c, of the conductor chosen should be with respect to this peak field and not the field at the centre.

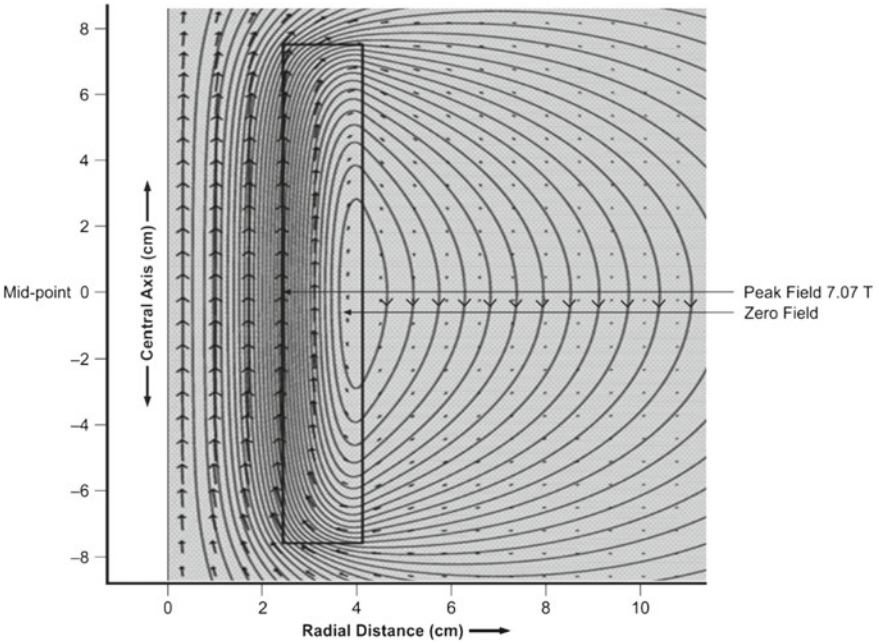

Fig. 9.8 Field profile of the 7 T magnet plotted by using Poisson Superfish computer programme. Note the peak field region and the zero field region [14]

9.4.2 Optimization of Vapour-Cooled Current Leads

The current lead is a critical component of a superconducting magnet system in so far as it is the biggest source of heat leak to the LHe-bath. The current lead carries large current and consequently generates large amount of Joule heat. This heat is transported to He-bath. Heat is also transported from the top plate at room temperature to the bath though the leads via thermal conduction. The dimensions of the current leads can, however, be optimized for a given current such that the heat leak to the bath is minimum. Copper current leads have been universally used because of its being a good electrical conductor. Paradox, however, is that any good electrical conductor also happens to be a good conductor of heat. The thermal conductivity (k) and the electrical resistivity (ρ) of a metal are related through the.

Weidemann–Franz Law, namely $k_{(\mathbf{T})}\ \rho_{(\mathbf{T})} = L_{\mathbf{0}}T$ where $L_{\mathbf{0}}$ is the Lorenz number $= 2.45 \times 10^{-8}$ W Ω K^{-2}. So, it does not matter what material one chooses for current leads, SS or copper. In SS, the Joule heating will be very high but heat conduction to the bath will reduce, SS being a poor conductor of heat. In copper leads, it will be just reverse; that is, Joule heating will be small, but thermal conduction will be very high. The length and cross section of the leads are optimized such that heat leak is reduced to minimum for a given lead current. Once the length of the current lead is chosen, it is the cross section of the leads which is determined through the optimization

procedure. The heat transport to the bath will, however, increase for higher operating current. To reduce the heat leak further, evaporated out-going helium vapours are used to cool the current leads. As shown in Fig. 9.9, the He-vapours from the cryostat are forced to flow spirally past the copper leads encased in a SS tube. The annular space between the leads and tube is packed with fibre-glass roving to create fine multiple channels for efficient heat exchange.

Optimization of the current leads is done using steady-state energy balance equation:

$$\frac{\mathrm{d}}{\mathrm{d}x}\left[k(T)A\frac{\mathrm{d}T}{\mathrm{d}x}\right] - f \cdot m \cdot C_{\mathrm{P}}\frac{\mathrm{d}T}{\mathrm{d}x} + I^2\frac{\rho(T)}{A} = 0 \tag{9.3}$$

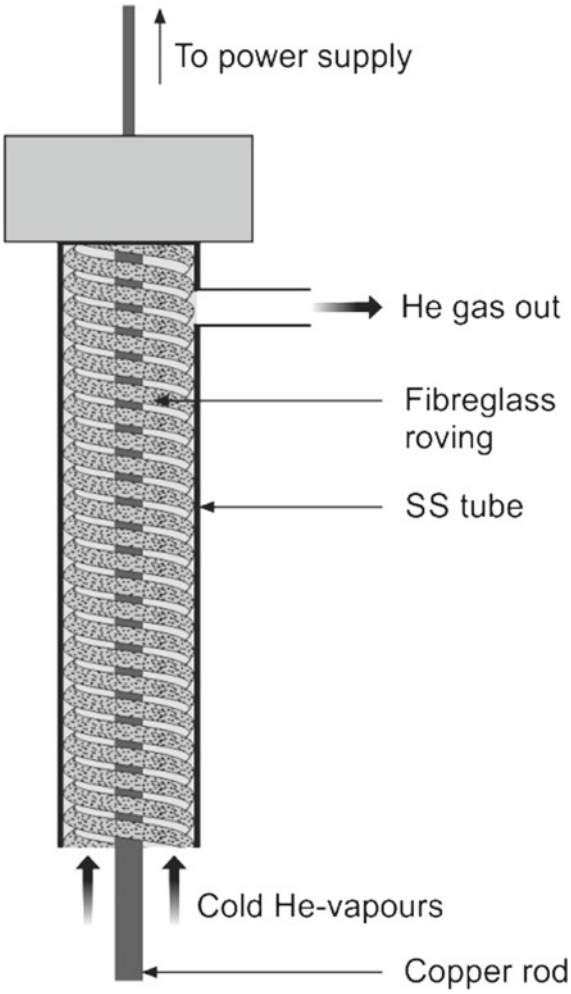

Fig. 9.9 Schematic design of the vapour-cooled current leads [14]

where A is the area cross section of the lead, C_p the specific heat at constant pressure and can be assumed constant, f is the efficiency of the heat transfer between the leads and vapours, I, the operating current and m (kg/s) the mass of liquid helium boil off by the heat leak from the lead. We optimized the leads with cross section 0.3 cm^2 and length 75 cm for a current of 200 A. For our shape factor (IL/A) = 3.5×10^6 A/m, the minimized heat leak through the current lead comes out to be 1.04 mW/A. Thus, the total heat flow to the He-bath by the two current leads at 200 A current turns out to be 0.4 W. The flow rate of the He-gas escaping from the top of the magnet system is regulated through a valve depending upon the lead current. He-gas coming out of the top flange is found to be at room temperature establishing the efficacy of our optimization calculations.

9.4.3 Magnet Quench

Quench is a term used for a superconducting magnet when all of a sudden, it turns normal (resistive) during the operation. This transition from superconducting state to normal state invariably occurs whenever any of the three parameters temperature, magnetic field or current exceed its critical value. This happens even if a minute part of the winding becomes resistive. The Joule heating (I^2R) across this resistive part will spread rather fast to the entire winding turning the magnet normal and dumping the stored energy (1/2 LI^2) in to the LHe-bath. This heat evaporates large amount of liquid helium and raises the temperature of the magnet far above the bath temperature. In extreme cases, this dissipation of energy can burn the magnet. The occurrence of quench can, however, be minimized by stabilizing the magnet through a careful design and winding. The conductor therefore is chosen with appropriate filament size and Cu:SC ratio.

One can comfortably prevent quench caused by excessive current or poor cooling by keeping the current below the critical limit and maintaining LHe-level. The tricky part is the quench caused by the micro-movement of the conductor in the winding under the influence of large Lorentz forces and by the release of strain energy. It will happen even if enough precautions are taken during winding. The quench is quite common due to wire movement during the virgin run. Let us consider a small heat pulse in the conductor in a very small part of the conductor. The heat will travel through a conductor longitudinally in both the directions at a rate determined by its thermal conductivity. We can assume near negligible dissipation in transverse direction because of inter-layer insulation and thermal contact resistance etc. If the heat dissipation from the 'hot spot' is faster than the generation of heat, the normal zone will collapse and the magnet will be stable. If the heat dissipation is slower, the normal zone will grow and spread throughout the winding thus quenching the magnet. Interestingly, the time scale involved in quench are in the range of μs and ms. In fact, there is a critical size of the normal zone, called as minimum propagation zone (MPZ) for a given conductor which will initiate quench. This is discussed in the next section.

9.4.4 The Minimum Propagating Zone

To understand the concept of minimum propagating zone (MPZ) let us consider a superconductor of area cross section A carrying a current at a density J generating heat $Q_{\mathbf{gen}}$ due to some disturbance and raising the temperature locally of a small length ℓ to a value above $T_{\mathbf{c}}$, turning it normal. The MPZ area and the temperature profile are shown in Fig. 9.10. The heat generated over a short length, ℓ, will travel through the superconductor longitudinally in both the directions. The heat generated in this normal region (I^2R) due to Ohmic heating will be

$$Q_{\mathbf{gen}} = J^2 A\, \ell\, \rho \tag{9.4}$$

where ρ is the resistivity of the superconductor in normal state. This heat will travel along both the directions at a rate determined by the thermal conductivity of the superconductor.

Thus, the heat dissipated away $Q_{\mathbf{Diss}}$ will be determined by the thermal conductivity of the superconducting region.

$$Q_{\mathbf{Diss}} = 2kA(T_{\mathbf{c}} - T_{\mathbf{B}})/\ell \tag{9.5}$$

Here k is the thermal conductivity of the superconductor and $T_{\mathbf{B}}$ the bath temperature. The factor of 2 enters because of the heat being dissipated in two directions. Under the equilibrium condition, the two equations can be equated and we get the

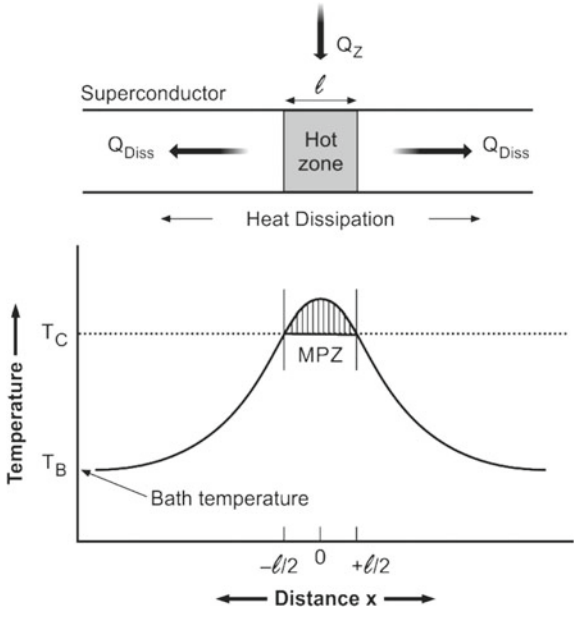

Fig. 9.10 Concept of minimum propagation zone (MPZ) and the temperature profile

expression for ℓ as

$$\ell = \left[\frac{2k(T_c - T_B)}{J^2\rho}\right]^{\frac{1}{2}} \tag{9.6}$$

If the size of the hot zone is less than ℓ, heat generated will dissipate away and the hot spot will disappear but will grow if the size exceeds ℓ.

To have an idea of the magnitude of MPZ in Nb–Ti, let us assume a $J = 4 \times 10^{8}$ A m^{-2}, T_c (6 T) = 6.71 K, T_B = 4.2 K, the electrical resistivity, $\rho = 6.5 \times 10^{-7}$ Ω m and thermal conductivity, $k = 0.1$ W m^{-1} K^{-1}, the MPZ, ℓ turns out to be just 2 μm. A simple calculation will show that for bare Nb-Ti the heat required to trigger quench is tiny, just of the order of 10^{-9} J. The problem has, however, been solved by producing composite superconductors with fine filaments embedded in high conducting copper which has a thermal conductivity of about 400 W m^{-1} K^{-1}. This topic has already been discussed in Chap. 5.

9.4.5 *Quench Voltage and Temperature Rise*

A solenoid magnet, in general, is a pure inductance in its normal operation. Part of the winding, however, turns resistive during a quench. This resistive part is shown in Fig. 9.11 as R_Q. During the normal magnet operation, the power supply voltage is nearly zero. Small voltage develops during ramp-up (charging) and ramp-down

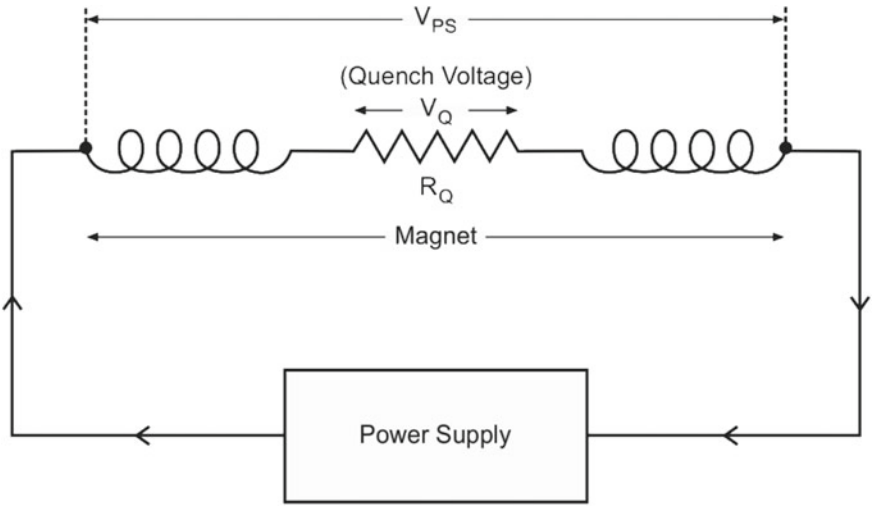

Fig. 9.11 Part of the magnet winding goes resistive (R_Q) and develops huge voltage across this part. Voltage across magnet terminals is restricted to power supply voltage, V_{PS}

(discharging) with opposite polarity. The power supply is turned-off as soon as a quench is detected. Large voltage is generated within the resistive winding which can burn insulation and even lead to arcing within the winding. The expression for quench voltage $V_{\mathbf{Q}}$ can be found out from the following equations.

$$V_{\mathbf{Q}} = I R_{\mathbf{Q}} - M \mathrm{d}I/d\mathrm{t} \tag{9.7}$$

and

$$L \mathrm{d}I/\mathrm{d}t = I R_{\mathbf{Q}} \ (V_{\mathbf{PS}} \text{ being zero}) \tag{9.8}$$

where I is the magnet current at the time of quench, $R_{\mathbf{Q}}$ is the resistance of the quenched part, L is the self inductance of the magnet and M is mutual inductance between the resistive part and the rest of the inductance of the magnet.

From the two equations

$$V_{\mathbf{Q}} = I R_{\mathbf{Q}} \ (1 - M/L) \tag{9.9}$$

$V_{\mathbf{Q}}$ is often of the order of few hundreds or thousands of volts. In the worst scenario, ignoring M, the internal voltage will be

$$V_{\mathbf{Q}} = I R_{\mathbf{Q}} \tag{9.10}$$

With time, $R_{\mathbf{Q}}$ will increase and so will M, but the current will fall. The internal voltage will therefore rise to a peak and then fall. It is extremely important to estimate maximum temperature reached at the point of quench initiation in the winding and keep it restricted, in any case below room temperature. An exact estimate is tedious as the quench process is too fast taking place in a fraction of a second. As the temperature rises, the physical properties like resistivity and specific heat keep changing by orders of magnitude. We may follow Maddock and James [15] for the estimation of the maximum temperature and write heat balance equation of the unit volume of the winding.

$$J^{\mathbf{2}}(\mathrm{t})\mathrm{d}t = C(T)\mathrm{d}T/\rho(T) \tag{9.11}$$

where $J(t)$ is the current density which changes with time t, ρ is electrical resistivity, dt is time duration, d is the density and $C(T)$ is specific heat at temperature T. All the quantities are averaged over the total winding cross section. By integrating the above equation, we find that the maximum temperature, $T_{\mathbf{MAX}}$, is solely dependent on material properties and can thus be worked out by substituting the relevant values in (9.12). $J_{\mathbf{0}}$ is the initial current density and $t_{\mathbf{d}}$ the decay time of the current after the quench. $T_{\mathbf{MAX}}$ should always be kept under safe limit, in any case well below room temperature. After fixing the maximum upper limit of temperature, we can find the decay time of the current and calculate the value of the dump resistance in the protection circuit.

$$\int_0^{\infty} J^2(t)\mathrm{d}t = J_0^2 t_d = \int_{4.2}^{T_{MAX}} \frac{C(T)}{\rho(T)}\mathrm{d}T = F(T_{MAX}) \tag{9.12}$$

9.4.6 *Quench Protection*

We have just seen in the previous section that a quench can lead to very serious consequences and destroy a magnet if not protected intelligently. Suppose a magnet with 10 H inductance and running at a current of 200 A quenches in 1 s, it will induce a voltage of 2 kV. The stored energy equal to 0.2, MJ if released in the winding, will burn the winding and can even melt the conductor. Protection circuits are therefore integrated with the magnet so as to dump the energy stored in unquenched part of the winding in to an external device and save the magnet. Two types of protection circuits are most popular and used by the scientific community and by the manufacturing companies. One is the resistor protection circuit, and the other is resistor-diode protection circuit. We briefly discuss them below.

A. **Resistor Protection Circuit**

This circuit is very simple and cheap. An external low value dump resistance, $R_{\mathbf{D}}$, as shown in Fig. 9.12, is connected across the magnet. The resistance is selected such that the time constant is small for the current to decay and the induced voltage is moderate not exceeding a few kV. Table 9.2 shows the value of time constant, τ ($= L/R_{\mathbf{D}}$) and induced voltage ($= L\ \mathrm{d}I_{\mathbf{0}}/\mathrm{d}t$) corresponding to the dump resistance of 0.5, 1.0, 10 and 100 Ω for the 7 T magnet discussed in Sect. 9.4.1. The magnet

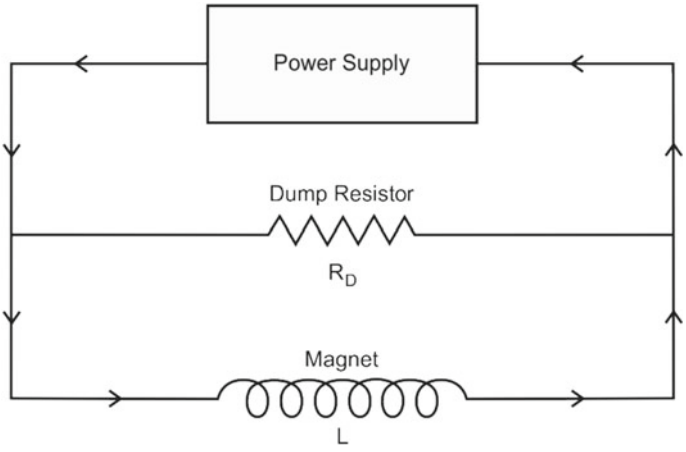

Fig. 9.12 Magnet quench protection by dump resistor, $R_{\mathbf{D}}$

Table 9.2 Induced voltage corresponding to dump resistance value

Dump resistor R_D (Ω)	Time constant τ (s)	Induced voltage V (V)
0.5	0.8	105
1.0	0.4	210
10	0.04	2100
100	0.004	21,000

had an inductance of 0.4 H. I_0 is the magnet current at the start of the quench, 210 A in this case. As soon as a quench appears, the power supply detects an increasing voltage and switches off automatically. The stored energy is rapidly dumped in to $R_{\mathbf{D}}$ according to

$$I = I_0 e^{-(R_D/L)t} = I_0 e^{-(1/\tau)t} \tag{9.13}$$

where t is the time and τ the time constant. The selection of dump resistor value is kept small as dictated by the requirement of low $T_{\mathbf{MAX}}$ and low maximum voltage $V_{\mathbf{MAX}}$, limited to Ohmic voltage across $R_{\mathbf{D}}$. There is, however, one drawback with the use of resistor that during the ramp-up and ramp-down of the current, the induced voltage drives a current through the dump resistor dissipating heat. This heat will evaporate liquid helium and at high ramp rates can lead to dangerous pressure build-up in the cryostat if the resistor is kept under LHe-bath. As an example, suppose we charge our magnet of 0.4 H inductance and having 0.5 Ω dump resistance across it to 210 A in one minute, the induced voltage will be 1.4 V. A current of 2.8 A will flow through the resistor dissipating 3.92 W energy. This energy, if released in to the LHe-bath will evaporate 5 l/h liquid helium. If the magnet is to be ramped repeatedly, this dissipation will add up to very high value and will evaporate large amount of liquid helium. On the other hand, if the same magnet is charged to full current in 10 min, the dissipation will be as low as 0.04 W and will evaporate just 52 ml of LHe. To prevent this dissipation from entering the LHe-bath, the dump resistor should be mounted on a radiation baffle in vapour phase. This arrangement assumes greater importance while dealing with large magnets dumping huge energy in to the LHe-bath during a quench.

When a magnet is wound in multi-sections, each section nested inside the other is protected against quench by incorporating separate dump resistance across each section. The total stored energy of the magnet is thus divided among the sections. In the event of any mishap, only the section affected will be damaged.

B. Diode-Resistance Protection Circuit

A better alternative for quench protection is the diode-resistance technique which prevents current flow through the resistor under the influence of induced voltage during ramping up and ramping down. As shown in Fig. 9.13, a set of special diodes is connected in series with the dump resistor. These diodes should be highly reliable, able to function at 4.2 K and sustain current during quench. The number of diodes in

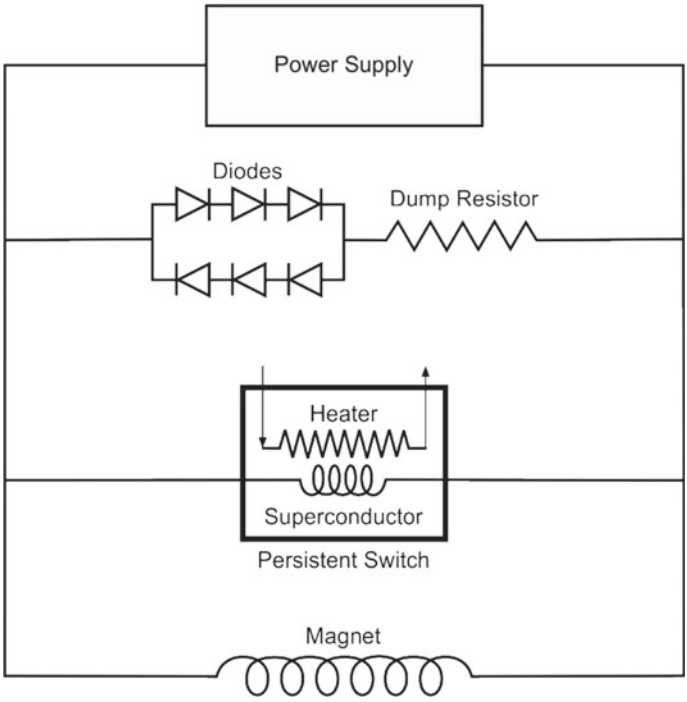

Fig. 9.13 Schematic of a diode-resistor quench protection system for a superconducting magnet. A persistent switch is also shown and connected across the magnet

the circuit should be chosen such that the forward conducting voltage of the diodes is of the order of few volts. They should not switch on and allow the current to flow through the resistor due to the voltage developed during ramping up and ramping down. Since we need both polarities during ramping, we use two sets of back-to-back diodes in an arrangement shown in Fig. 9.13. This arrangement enables the current in either direction during a quench. At the initiation of quench, the voltages starts rising until the diodes 'switch on' allowing the current to flow through the resistor. The peak voltage is then reached in the resistor. Since in normal operation no current flows through the circuit, this protection system can as well be mounted in LHe-bath. This does away with the need of heavy current leads dumping heat in to the bath. Helium evaporation is thus drastically curtailed. In the case of very large magnets, we have to have a re-look if the protection system, with or without diodes, should at all be mounted in LHe-bath. During the quench, the energy dissipated may cause excessive helium vapour build-up to dangerous level. External dump resistors may be a better option for the protection of huge magnets used in accelerators and fusion reactors. This will be discussed in the next two chapters.

9.4.7 The Persistent Switch

Shown in Fig. 9.13 is also a persistent switch used to run the magnet in persistent mode at a fixed field with power supply switched-off. The switch is connected in parallel with the magnet. The switch has a small non-inductive (bifilar) superconducting winding of 10–100 Ω room temperature resistance and a heater wound over it. The switch is encased and impregnated with epoxy. To have the superconducting wire of manageable length, the persistence switch wire is an Nb–Ti wire with a Cu-Ni resistive matrix. During the start-up of the magnet, the heater is 'switched-on' turning the persistent switch normal. The resistance of the switch becomes much higher than the magnet resistance such that the current flows through the magnet only and not through the persistent switch. As the current is ramped up, the voltage $V = Ir + L\,\mathrm{d}I/\mathrm{d}t$ is seen increasing. Here, the first term is the voltage drop across lead resistance 'r' and the second term is induced voltage due to the charging of the magnet. After the required field is achieved, the heater current is 'turned-off'. It is necessary to note down this magnet current. After a pause of 10–20 s, the current from the power supply to magnet is reduced to zero. As current through the leads decreases, current through the switch increases to the magnet current level. The current now flows through the magnet in a close-loop, and the magnet runs in persistent mode. In NMR and MRI magnets, the current leads are de-mountable and are removed once the magnet is put in persistent mode.

A reverse procedure is followed while de-energizing the magnet. Power supply is 'turned-on' and the current raised to the value, at which the magnet was put in persistent mode. The switch heater is now turned-on, and the main current is ramped down to the new value as per the new desired field. The switch can be 'turned-off' again to put the magnet in persistent mode. An auxiliary 50 mA power supply is usually in-built in the main power supply for the operation of the persistent switch heater.

The fabrication of a persistent switch is straightforward and simple, but the functioning of the switch strongly depends upon quality of the superconducting joints. Ideally, the joints should have zero resistance. In fact, the jointing technique is a top-guarded secret of the manufacturers. The usual steps involved are to etch away the copper cladding of the MF wire, de-oxidize the filaments of the two terminals and twist them. Twisted terminals can be encased in a Nb–Ti sleeve and squeezed under high pressure. This sleeve can be electron-beam welded along the length. There are many variants of this procedure followed by individual laboratories and the commercial establishments. Jointing is trickier in case of brittle Nb_3Sn and HTS magnets as joints need controlled post-heat treatments. Some superconducting Pb-Bi-Sn solders are also available now for jointing the filaments to filaments.

The field does decay with time but quite slowly depending upon the inductance, the design of the switch and the number and quality of the joints. A stability of 10 ppm/h is attained quite comfortably. For high-resolution NMR spectroscopy applications, the field stability has to be improved to 0.01 ppm/h.

9.4.8 Training of the Magnet

Training of the magnet is an important part of the magnet operation. Commercial magnets are trained at the factory site before being shipped and need no further training. More often than not, a magnet quenches at a current much below its designed value in the virgin run. The problem is fixed through 'training' the magnet. The specific heat of the superconductor at 4.2 K is small, of the order of 10^{-4} J/g/K, and therefore, any tiny thermo-mechanical disturbance in the magnet can generate heat and form a hot spot which might drive the temperature of the superconductor beyond its T_c. If this hot spot does not subside and propagates, it can lead to quench. Further, a superconducting magnet is a complex composite of several materials like the metallic conductor, the former, inter-layer insulation and epoxy used for impregnation. Their thermal contraction coefficients are widely apart. During cool down, there is a mismatch in thermal contraction and large stresses are frozen-in. Fracture can occur when large Lorentz forces are built up. Cracks in the epoxy can release strain energy sufficient to cause quench.

Once the strain energy is released, the quench will occur during re-energization at the next level of strain and the magnet can be charged to higher current value. Similarly, the winding adjusts itself against micromovements of the conductor during successive energizations. Experimentally, in the first run of the magnet built in the laboratory, one sweeps the current at low rate to a small value say 10 A/min, stays for a few minute at this level, ramp-down the current to zero. Next time, charge the magnet to higher current and ramp-down to zero. This way in a finite number of steps, one goes to the highest designed current. In several of our magnets, we did not observe the quench of the magnet during training phase. This must have been due to a perfect winding and good impregnation. Figure 9.14 is a typical training curve of a magnet where the current was ramped-up and ramped down to a smaller current in steps without inducing quench.

We built several 7–8 T magnets in 1970s using different types of impregnating materials like silicon grease, bees wax and epoxy stycast. We have preferred vacuum impregnation route in some and wet winding in others. Both performed admirably well. We found wet-winding, using wax as well as epoxy to be a superior technique. Wet winding ensures impregnation between each layer and each turn, even though it is a bit messy process. Other advantage is that one can use a filler material with epoxy or wax to reduce the mismatch of the thermal contraction coefficients of the constituents. Filler is not practical in vacuum impregnation technique as the material has to have low viscosity and has to flow through fine channels. We got excellent results using wet-winding technique using stycast (2850 FT from Emerson & Cuming) mixed with 20% Al_2O_3 powder in our cryo-free magnet. As mentioned earlier, in many magnets we used fibre-glass cloth as the inter-layer which allows free flow of impregnating material during vacuum impregnation process.

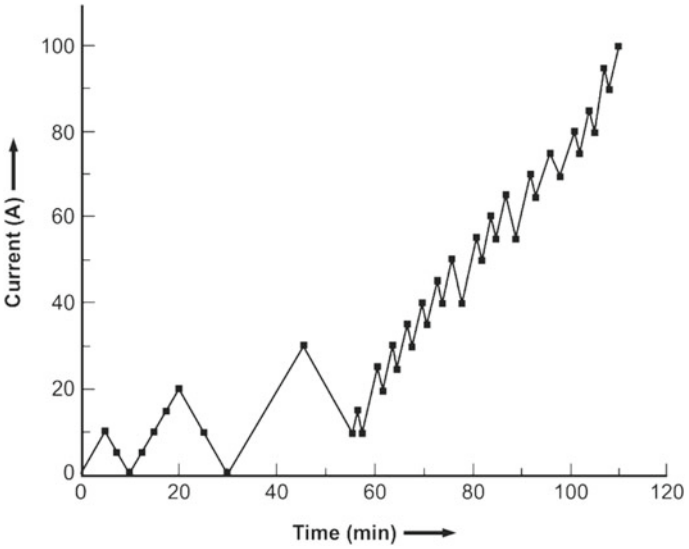

Fig. 9.14 Ramping-up and ramping down the current in steps during 'training' of a magnet [14]

9.5 High Homogeneity Field

We observed in Fig. 9.7 that the field decreases along the magnet axis as we move along the Z-direction away from the centre. The typical field homogeneity obtainable through the judicious selection of the parameters α and β is limited to about 1 in 10^3 in 10 mm DSV. This homogeneity is, however, quite inadequate for a variety of applications. In principle, field homogeneity can be improved by lowering the peak field at the centre of the magnet by missing certain number of turns in the middle part of the magnet or by adding extra coils at the two ends to enhance the field on either side of the centre. Use of these compensating coils can raise the homogeneity to 10^{-5}–10^{-6} level. NMR magnets need still higher homogeneity of the order of 10^{-9} which is provided by a set of a large number of superconducting 'shim coils' to compensate higher-order field expansion terms. We will discuss them in the context of the magnets used in NMR spectrometer in Chap. 12.

Before we discuss the compensating coils to improve the field homogeneity, let us find how the field varies along the axis. To calculate field at point S, a distance Z (Fig. 9.15) away from the centre along the axis, we can make use of (9.1) and (9.2) and divide the solenoid magnet into two parts as shown in Fig. 9.15, each part being half of a solenoid. The field at the end of the solenoid magnet can be taken as half of the field at the centre. The field at the point S can thus be written as:

$$B_z = {}^1/_2 J\lambda a_1[\,\mathrm{F}(\alpha,\ \beta_1) + \mathrm{F}(\alpha,\ \beta_2)] \tag{9.14}$$

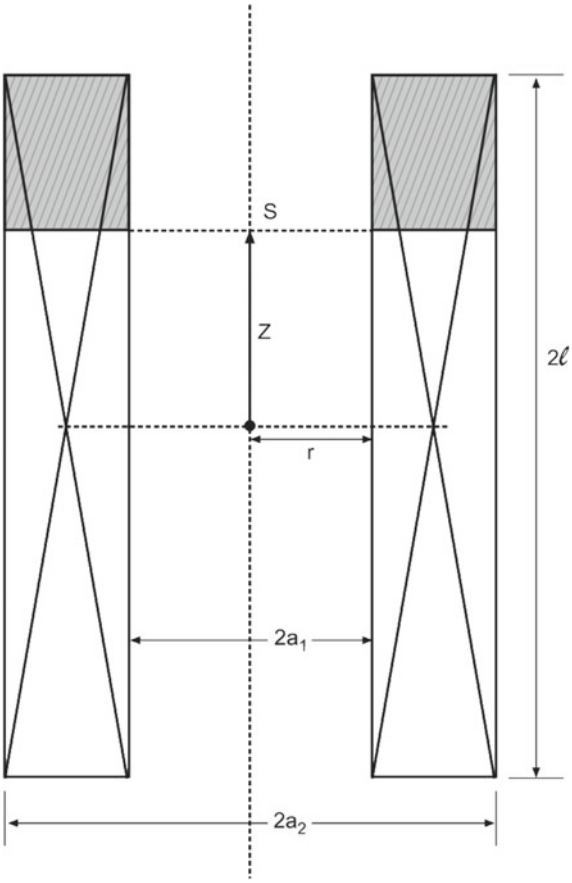

Fig. 9.15 To find field at a distance Z from the centre, magnet is divided in to two parts each one-half of a solenoid. β for the two solenoids will now be $(\ell + Z)/a_1$ and $(\ell - Z)/a_1$

where $\alpha = a_2/a_1$, $\beta_1 = (\ell - Z)/a_1$ and $\beta_2 = (\ell + Z)/a_1$. It is to be noted that β_1 becomes negative for $Z > \ell$, for points outside the end point of the magnet, $F(\alpha, \beta_1)$ should therefore be taken as $F(\alpha, -\beta_1)$, or $= -F(\alpha, \beta_1)$. Following Montgomery [9], the axial and radial components of the axial field in a centrally symmetric solenoid can be written as the expansion series as:

$$B_Z(Z,0) = B_0\left[1 + E_2\left(\frac{Z}{a_1}\right)^2 + E_4\left(\frac{Z}{a_1}\right)^4 + E_6\left(\frac{Z}{a_1}\right)^6 + \cdots\right] \tag{9.15}$$

$$B_Z(0,r) = B_0\left[1 - \frac{1}{2}E_2\left(\frac{r}{a_1}\right)^2 + \frac{3}{8}E_4\left(\frac{r}{a_1}\right)^4 - \frac{5}{16}E_6\left(\frac{r}{a_1}\right)^6 + \cdots\right] \tag{9.16}$$

where the error coefficients E_n are given from the standard formula for the coefficients in a Taylor series:

$$E_{2n} = \frac{1}{B_0}\left[\frac{1}{(2n)!}\right]\frac{\mathrm{d}^{2n}B_Z(Z,0)}{\mathrm{d}^{2n}Z}z = 0 \tag{9.17}$$

The values of these coefficients can be determined by taking the derivative of the field (9.14) with respect to Z, that is, along the axis and evaluating them at $Z = 0$. First few E_{2n}-dominant terms have been given by Montgomery [9] (Table 8.2, p. 236). It is noticed from (9.15) and (9.16) that near the centre where r/a_1 is small, the E_2 term dominates and the deviation of the field in the radial direction is only half of that along the axis. For a simple solenoid, E_2 term is always negative. The field along the axis decreases but increases in the radial direction until $r = a_1$. It decreases thereafter because of certain boundary conditions.

9.5.1 High Homogeneity Field by Compensated Coils

Field expansion (9.15) and (9.16) indicates very clearly that in a solenoid magnet the inhomogeneity in the axial field along longitudinal and radial directions come from the higher-order terms in these equations. To get high homogeneity field, it is therefore imperative to get rid of the successive terms in these equations. Larger the number of terms eliminated, higher is the homogeneity of the field. This can be achieved by subtracting a smaller coil from the main coils. These so-called compensating coils operate at the same current level as the main coil. Compensating coils will look like a gap or will appear as a notch in the main winding. The number of terms to be cancelled depends upon the number of variable geometrical parameters chosen for the compensating coil. For example, with one of the variable parameters α and β keeping same for both the coils and varying the other parameter, we can cancel one term, E_2. The magnet will be compensated to fourth-order similar to a Helmholtz coil. With two variable parameters α and β, one can cancel two terms, E_2 and E_4, compensating the main coil to sixth order. This compensating coil can be incorporated either at the inner winding bore or at the outer winding bore and are referred to as 'inside notch' and 'outside notch', respectively.

The fourth-order compensation geometry is shown in Fig. 9.16, which is just a Helmholtz coil. Here the missing coil is the gap in the middle of the main coil. The main coil as also the gap has the same value of α ($\alpha = \alpha_c = a_2/a_1$) but different values of parameter β. As seen in Fig. 9.16, β for the main coil is ℓ/a_1 while for the correction coil β_c is ℓ_c/a_1. Here the subscript 'c' indicates the parameters for the compensating coil.

For sixth-order compensation (E_2 and $E_4 = 0$), both 'inside notch' and 'outside notch' geometry, is possible and is shown in Fig. 9.17 . Shaded areas are the missing part or the so-called compensation coils. In sixth order (inside notch) again has the same a_1 as for the main coil. The modified field expression for the combined coil can now be written as

$$B_z(Z,0) = J\lambda a_1\left[F_0(\alpha,\beta) - F_c(\alpha_c,\beta_c) + \{F_0E_2(\alpha,\beta) - F_cE_2(\alpha_c,\beta_c)\}(Z/a_1)^2\right.$$

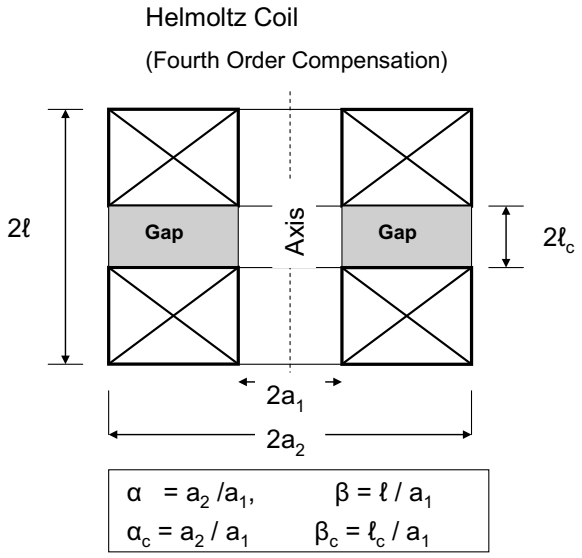

Fig. 9.16 Graphical representation of the fourth-order compensation. Note same value of α for the main coil as well as for the compensating coil but different values of β and β_c

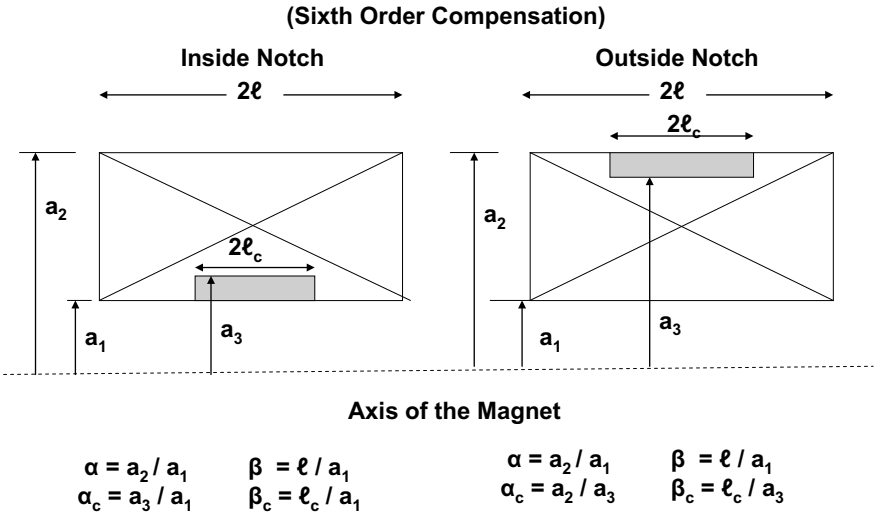

Fig. 9.17 Graphical representation of sixth-order compensation with 'inside notch' (left) and 'outside notch' (right). Missing turns are shown shaded. Values of α, β and α_c, β_c have also been given

$$+\{F_0 E_4(\alpha, \beta) - F_c E_4(\alpha_c, \beta_c)\}(Z/a_1)^4 \ldots] \tag{9.18}$$

For fourth-order compensation, the terms $F_0\, E_2(\alpha, \beta)$ and $F_0\, E_2(\alpha_c, \beta_c)$ are equal and opposite in sign and therefore cancel out. The field uniformity improves. The

functions $F\ E_2\ (\alpha, \beta)$ and $F\ E_4\ (\alpha, \beta)$ when plotted against β for different values of α show a peak which means that there are two values of β for each value of the functions $F_0\ E_2(\alpha, \beta)$ and $F_0\ E_2(\alpha_c, \beta_c)$ for the same value of α. The smaller value of β on the left of the peak yields β_c for the small compensating coil. Since the inner diameter of the compensating coil (both fourth order and sixth order, inside notch) is the same as that of the main coil the corresponding length of the compensating coil can be calculated from β_c.

Figure 9.18 shows the contours of constant FE_2 and FE_4 intersecting at two points. Intersection at $\alpha = 3$ and $\beta = 2$ corresponds to the main magnet, and the second intersection at $\alpha_c = 1.87$ and $\beta_c = 1.33$ corresponds to the sixth-order compensating coil. The cancellation of the first two terms, FE_2 and FE_4, thus leads to higher field homogeneity than the fourth-order Helmholtz coil. It is important to control the dimensions of the compensating coils very precisely, within 2% of the calculated value, homogeneity being extremely sensitive to the errors in choosing the dimensions. This sensitivity is significantly reduced by choosing β much larger than the minimum coil volume criterion. The magnitude of the higher-order terms to be cancelled is significantly reduced.

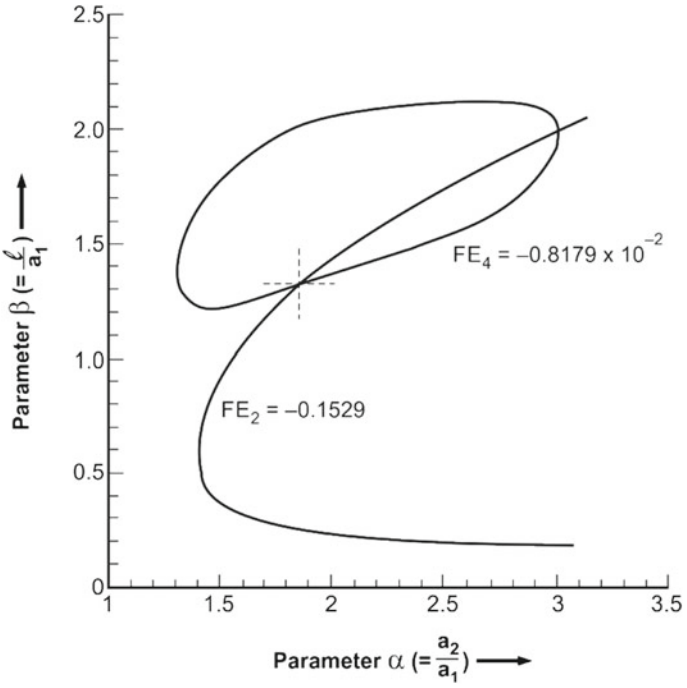

Fig. 9.18 Contours of constant FE_2 and FE_4 intersecting at two points, intersection at $\alpha = 3$ and $\beta = 2$, corresponds to the main magnet and the second intersection at $\alpha_c = 1.87$ and $\beta_c = 1.33$ corresponds to the sixth-order compensating coil [9] (*Courtesy* D. B. Montgomery "Solenoid Magnet design")

Very useful tables for the design of the compensating coils have been given by Montgomery [9] for fourth-order (Table 8.9, p. 255) and for sixth-order compensation inside notch (Table 8.10a and 8.10b, pp. 255–256) and outside notch (Table 8.11, p. 257). We made a few Nb-Ti magnets of the sixth-order compensation using these tables in early 1970s. One, rather long and low field (2.35 T) solenoid magnet with $\alpha = 1.224$ and $\beta = 3.38$, we built [16] using outside notch gave us an homogeneity of 3×10^{-6} in 10 mm SDV.

9.6 An 11 T Nb–Ti/Nb_3Sn Combination Magnet

For field production above 9 T at 4.2 K, traditionally our option has been limited to the A-15 Nb_3Sn superconductor. With the availability of Nb_3Sn conductors produced by improved techniques and with elemental additions (Chap. 5), field higher than 21 T have been produced [17] in 1990s by operating the magnet below 2 K. Standard Nb_3Sn magnets going up to 20 T are now marketed commercially and are usually integrated with various measurement systems. Building Nb_3Sn magnets is quite difficult as compared to Nb-Ti magnets. The main reason is being the extreme brittleness of this material. Commercial multifilamentary cryo-stabilized Nb_3Sn wires and cables are by and large available in pre-reacted form, that is, with Nb-filaments in Cu–Sn bronze matrix. The wire is ductile enough to be wound in to a coil. The coil is then heat reacted at high temperature under controlled conditions whereby Sn from the matrix diffuses in to Nb-filaments to form intermetallic Nb_3Sn. The magnet is then impregnated as usual, but extreme care is required to handle the reacted magnet.

9.6.1 Winding the Background Nb–Ti Magnet

As an example, we take up the construction of an 11 T magnet which we built [18] many years ago as an exercise. The magnet is a combination of an outsert of Nb–Ti coils and an insert of Nb_3Sn coil. The Nb–Ti outsert magnet provides a background field of about 7.2 T and the rest, 3.8 T generated by the insert Nb_3Sn coil. The magnet coils were designed as per the standard procedure described in Sect. 9.4. The magnet had a working bore of 50 mm. The outsert had two concentric Nb–Ti coils and a clear bore of 100 mm to accommodate Nb_3Sn coil. Its winding length was 220 mm. All the actual dimensions of all the coils and other magnet parameters [19] have been listed in Table 9.3. We used a Nb-Ti wire of 0.75 mm diameter for winding the inner coil and 0.54 mm for the outer coil of the Nb–Ti outsert. As Table 9.3 shows, the inner coil of the outsert had 22 layers consisting of 6458 turns and used a total of 2.65 km of 0.75 mm dia. wire. The outer coil was wound using 0.54 mm dia. Nb-Ti wire. It had a total of 26 layers each consisting of 407 turns and thus used a total of 5.6 km of wire. Both the coils were wound one over the other on the same former. The formers for Nb–Ti magnet as well as for Nb_3Sn magnet were made of SS 304.

Table 9.3 Parameters of the 11 T superconducting magnet [19] working bore dia. = 50 mm

S. No.	Parameter	Innermost Coil (Nb_3Sn)	Outer coils (Nb-Ti)	
			Inner section	Outer section
1	Inner winding dia	56.6 mm	110.6 mm	148.8 mm
2	Outer winding dia	100 mm	148.5 mm	180.5 mm
3	Winding length	170 mm	220 mm	220 mm
4	Parameter α	1.766	1.34	1.21
5	Parameter β	3.00	1.99	1.48
6	Parameter F(α, β)	0.873×10^{-6}	0.36828×10^{-6}	0.21149×10^{-6}
7	Conductor used	Nb_3Sn	Nb–Ti	Nb–Ti
8	Conductor dia	0.85 mm	0.75 mm	0.54 mm
0	No. of filaments	6000	54	54
10	No. of layers	20	22	26
11	Total no. of turns	3863	6458	10,584
12	Field at 90.5 A	2.395 (T)	Field by Nb-Ti coils 7.315 (T)	
13	Final field with 90.5 A in Nb-Ti coils and 140 A in Nb_3Sn coil		11.03 (T)	
14	Conductor length (approx.)	1 km	2.65 km	5.6 km
15	Interlayer material	Fibre-glass cloth		
16	Impregnation (vacuum)	Bees wax		
17	Quench protection	Through dump resistor		

The cylindrical part of both the formers was uniformly perforated to allow liquid helium to cool the inner parts of the coil and also to reduce eddy currents induced during ramping up and down. Similarly, the two end flanges of both the magnets had perforation and also curved radial slots enabling again cooling by liquid helium and taking the end terminals of the coils out. For Nb_3Sn coil, we used a bronze-processed 'wind and react' wire of 0.85 mm diameter supplied by Vcuumschmelze, Germany. We had no choice of choosing wire diameters optimized for the same current but had to use the wire available, and we could procure.

The end terminals of the coils were wrapped over the copper studs which had spiral grooves. Sufficient length of the wires was wrapped and soldered with Pb–Sn solder. This was meant to keep the joint resistance low. Vapour-cooled current leads were taken out to the top plate of the cryostat. The three current terminals at the top plate enabled us to operate both the magnets, Nb–Ti and Nb_3Sn, in either series or separately. The magnet was vacuum-pressure-impregnated with bees wax following the standard procedure.

9.6.2 Winding the Nb_3Sn Magnet

Winding the Nb_3Sn magnet is rather tricky**.** This is for several reasons. The first one is that since the wire is finally to be reacted at high temperature, it does not have the usual electrical insulation. The wire is covered with a glass sleeve which is quite fragile. Handling the wire during winding is thus a difficult task. Glass cloth was used as interlayer. The space factor 'λ' in Nb_3Sn coil is smaller than in the case of Nb-Ti coils. As shown in Table 9.3, the magnet had a clear working bore of 50 mm and an inner winding diameter of 56.6 mm. Here again we preferred SS-340 former. The winding length was 170 mm. The Vacuumschmelze supplied bronze-processed Cu-Sn/Nb wire, used for winding, had a diameter of 0.85 mm and glass sleeve as electric insulation. The wire had 6,000 filaments. In all, we had 20 layers and a total of 3836 number of turns.

9.6.3 Preparation of Current Terminals

Before carrying out heat treatment, it is essential to fix the coil terminals on to a pair of copper studs without removing the glass sleeves from the wires. Figure 9.19 shows the Nb_3Sn coil before heat treatment (A) and after the heat treatment (B). It is seen clearly from these figures that the wire terminals of the coil have been taken out through the ceramic bushes fixed in the metal flanges to prevent electrical short. The two long copper studs have a central hole and half-circular cross sections. The coil terminals are tied with the help of a copper wire on to these two studs at a number of places. The precaution to be taken here is that the glass sleeve should be in place along the entire length of the wire. At no place, the superconducting wire should come in contact with the copper studs. If by chance it happens, the Sn from the bronze wire will diffuse in to copper studs during the heat treatment and stoichiometric Nb_3Sn will not form, making the magnet unusable.

9.6.4 Heat Treatment and Impregnation

Now comes the most critical phase of the magnet fabrication. The pure Nb-filaments embedded in Cu–Sn bronze have to be converted in to Nb_3Sn filaments. Before going in for heat treatment of the magnet we kept the magnet under running water to get rid of starch coating on glass sleeve and glass cloth. Earlier through some preliminary study on the heat treatment of the short sample of the bronze wire, we found the glass sleeve to be charred and covered with thick layer of carbon. Significant amount of starch was washed out from the magnet winding by the process we followed. As discussed in detail in Chap. 5, a two-step heat treatment is advisable to get high critical current density in the wire. A long heat treatment at comparatively lower temperature enables the formation of small size grains in the Nb_3Sn compound which is a prerequisite for all A-15 superconductors to have high J_c. This treatment

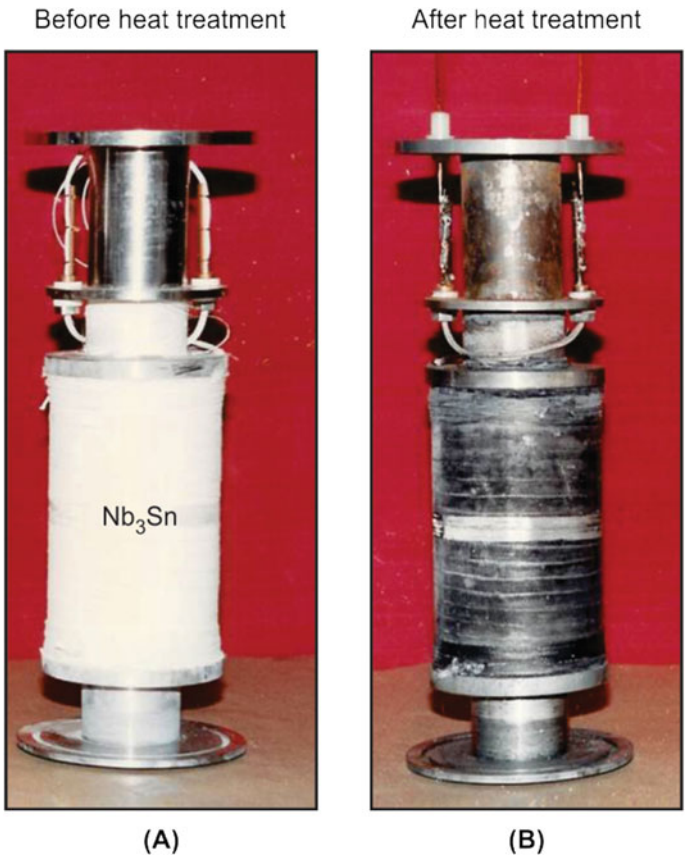

Fig. 9.19 Nb_3Sn coil before heat treatment (**a**) and after heat treatment (**b**). Note how the coil terminals have been taken out through the metallic flanges using ceramic spacers to prevent electrical shorts. [19] (*Photo courtesy* NPL Delhi)

should be followed by a second heat treatment for a shorter period but at higher temperature to improve stoichiometry of the Nb_3Sn which in turn raises the upper critical magnetic field B_{c2} and thus J_c.

Another important step in the heat reaction is that there should be no trace of oxygen in the reactor. The heat treatment must be carried out either in vacuum or under inert gas atmosphere. For all our Nb_3Sn magnets, we carried out heat treatment under flowing high purity argon gas. The reactor chamber was thoroughly pumped and flushed several times with Ar-gas after the magnet was loaded in to the reactor. The magnet was kept at a temperature of 120 °C for many hours to get rid of moisture. Out of a few options of heat treatment schedules given by the supplier of the wire, we chose a two-step process. The magnet was kept at 570 °C for 120 h followed by another heat treatment of keeping the magnet at 700 °C for 80 h after which the magnet was furnace cooled. The real challenge comes at this stage, how to handle the brittle magnet right from the stage of taking it out of the reactor, making current contacts

and carrying out impregnation. To make electrical contacts of the coil terminals with the copper studs, the glass sleeve was very carefully removed and the reacted wire is cleaned. These bare wire terminals are now soldered with the Cu-studs using (Pb–Sn) solder along the full length. The next step is the impregnation of the magnet using either bees wax or the epoxy in a way similar to the Nb–Ti magnets. After the impregnation, handling of the magnet becomes easier.

9.6.5 Assembly of Magnet Coils and Operation

The Nb_3Sn magnet is nested inside the Nb–Ti magnet and rigidly fixed in position. The combined magnet is then suspended from the support structure consisting of radiation baffles, liquid helium-level sensor, LHe-fill line and G-10 support rods. All the three sections of the magnet were protected against quench independently by separate dump resistors which were mounted in the vapour phase inside the cryostat. Separate vapour-cooled current leads were taken out from the two magnets such that they can be energized independently as well as jointly by making series connection outside the cryostat at the top plate. The combined magnet is shown in Fig. 9.20 and the whole magnet assembly along with the support system in Fig. 9.21.

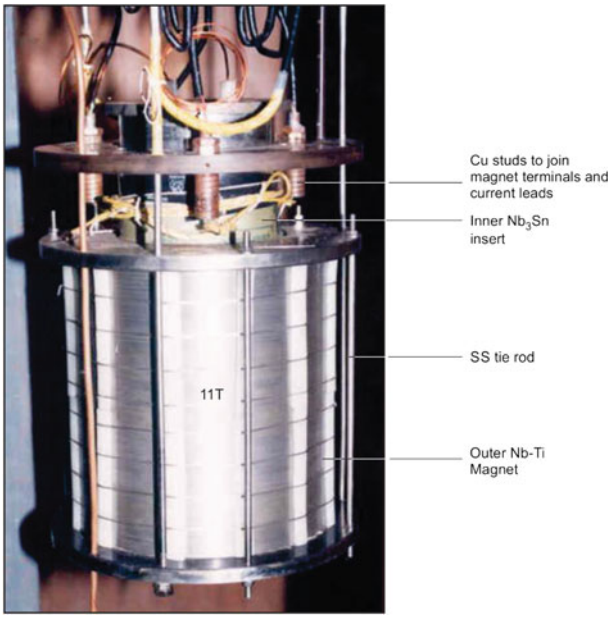

Fig. 9.20 11 T Nb–Ti/Nb_3Sn magnet made in author's laboratory in 1990. The outer coil seen is the Nb–Ti magnet with tie rods. Liquid helium fill line and level metre too are seen on the left. Nb_3Sn insert coil is in the centre. [19] (Photograph courtesy NPL Delhi)

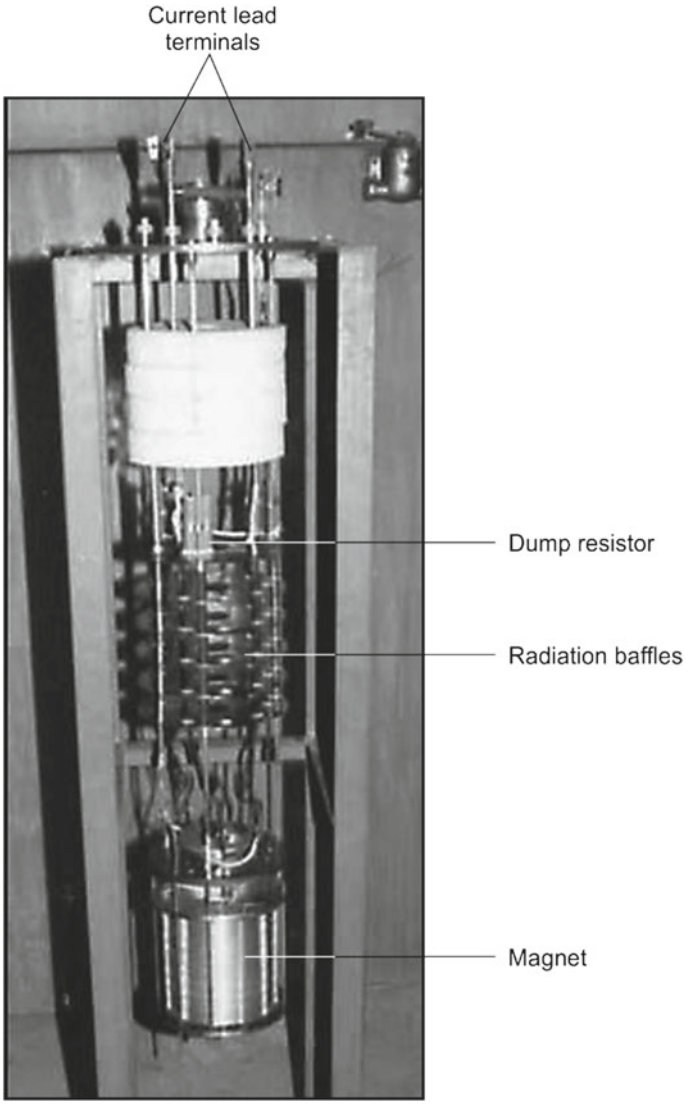

Fig. 9.21 Nb–Ti/Nb_3Sn magnet along with the support system (*Photo*graph*courtesy* NPL Delhi) [19]

Standard procedure for the operation of the magnet can now be followed to cool down the magnet system to 4.2 K and energize. Two power supplies were used because of the mismatch of the currents in the two magnets. The Nb-Ti magnet produced a field of 7.315 T at a current of 90.5 A, whereas the Nb_3Sn magnet generated an additional field of 3.715 T at a current value of 140 A. A total field of 11 T is thus achieved as per the objective of this magnet. During the training, we did

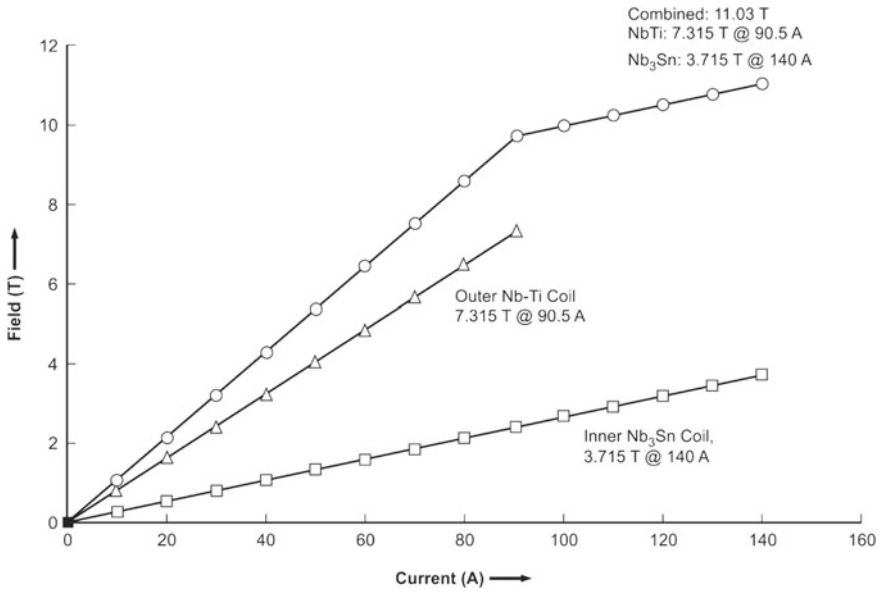

Fig. 9.22 Field versus current relationship for the Nb–Ti (middle curve) and Nb_3Sn magnet (lower curve). The I-B profile of the combined magnet is the top curve producing a field of 11 T [19]

ramped-up and ramped down the field in steps of 10 A, no quench occurred in any of the coils. The current-field profiles of the Nb-Ti magnet, the Nb_3Sn magnet and the two in combination are plotted in Fig. 9.22.

9.7 Intense Field Magnets

The quest to reach highest possible magnetic field has never diminished. After surpassing the threshold of 20 T, the next target set was 30 T. Focus shifted from a combination of Nb-Ti, Nb_3Sn and low temperature (1.8–4.2 K) to yet another combination of Nb–Ti-, Nb_3Sn- and the HTS, REBCO-coated conductors in particular though still operating at 4.2 K. Although YBCO-coated conductor remains superconducting at much higher temperatures (92 K) than niobium-based materials, but superconductivity gets stronger lower the temperature we go. These superconductors perform best at low temperatures (4.2 K). The advantage of using REBCO insert has been that it can withstand very high magnetic field and very high level of mechanical stress. Race has continued without a pause to achieve higher and higher magnetic field in the research laboratories. The scientists and engineers at NHMFL Tallahassee in 2019 broke all previous records and produced a mighty field of 45.5 T [6]. This high field, when opened as users' facility, will help scientists break new ground in several areas like the studies on quantum oscillations in complex metals,

nuclear magnetic resonance, electron magnetic resonance, fractional quantum Hall effect, molecular solids and such other areas. We will discuss these magnets in next sections.

9.7.1 A 21.1 T Superconducting Magnet Built by NIMS

Great strides have been made in the production of fields of the order of 20 T and above using the combinations of these two, so-called, low T_c superconductors (LTS), namely the Nb-Ti and the A-15 Nb_3Sn. Having built world's first highest field 17.5 T wholly superconducting magnet [20], the NRIM, now called National Institute of Material Science (NIMS), has been a forerunner in enhancing this field steadily to higher than 21 T. The 17.5 T superconducting magnet was built by Tachikawa et al. [20] using Nb_3Sn, and an insert coil of V_3Ga tapes, developed by NRIM by diffusion process. With the improvement in J_c of Nb_3Sn through elemental additions, V_3Ga has been pushed to the background by Nb_3Sn which is comparatively cheaper. The field was increased to 21.1 T [21] by NIMS in 1994 by using coils of Nb-Ti, $(Nb,Ti)_3Sn$ and $(Nb,Ta,Ti)_3Sn$ conductors. This magnet was an improvement over the earlier magnet built by NIMS [22] producing a field of 20.33 T in a clear bore of 44 mm. The new magnet replaced the innermost coil by a coil which was wound using $(Nb, Ta, Ti)_3Sn$ conductor and following a 'wind and react process'. This conductor had much lower copper ratio of 0.48 in place of the earlier conductor which had a ratio of 0.8. This meant a much higher engineering current density J_e. Yet another innovation carried out was the removal of the SS former of this innermost coil. This made available a larger working bore of 50 mm and also prevented high stress between the former and the coil. The complete parameters of the magnet are given in Table 9.4.

The total magnet system is housed in a cryostat with two separate chambers in vacuum. The outer chamber houses the two outer coils and the inner chamber remaining two inner coils. The two outer coils were connected in series and jointly produced a field of 15 T. The middle coil generated an additional field of 3.6 T at an operating current of 350 A. The innermost coil was run on an independent power supply and added another 2.5 T. The operating temperature was maintained at 1.8 K. The total field produced was 21.16 T, the highest ever reported using only the metallic superconductors (LTS), that is, without the use of a HTS insert coil. The magnet is huge in size and of a complicated nature [23]. This magnet produced a field of 21.5 T field at 1.8 K in a clear bore of 61 mm good enough to accommodate an inner HTS coil to produce still higher fields. The magnet was built at Tsukubs Magent Laboratory (TML).

The production of very high or ultra-high magnetic field is limited not so much by cost as by the stringent requirement of the superconducting material to carry high current in the presence of intense magnetic field and to withstand very large electromagnetic forces, BJR. Low-temperature superconductors (LTS) based magnets discussed so far seem to have saturated at 21.5 T even when we operate them at superfluid helium temperature (1.8 K). The only hope to raise further this limit appears to

Table 9.4 Parameters of the 21 T magnet built in 1994 at NIMS (data compiled from [21] with permission from Elsevier)

Magnet coil	Inner most (Nb, Ta, $Ti)_3Sn$	Middle (Nb, $Ti)_3Sn$	Outer-1 (Nb, $Ti)_3Sn$	Outer-2 (Nb–Ti)
Inner coil dia	50 mm	180 mm	380 mm	801 mm
Outer coil dia	151.2 mm	291.8 mm	725.6 mm	1175.8 mm
Coil length	220.3 mm	463.5 mm	1230 mm	1293.6 mm
Coil form	solenoid	31 double pancakes	40 double pancakes	41 double pancakes
Total no. of turns	1760	1364	1520	2296
Conductor dimensions	2.42 × 2.0 mm	6.0 × 2.0 mm	13.4 × 8.15 mm 11 strand ract. cable	13.8 × 6.0 mm 19 strand ract. cable
Process	Bronze process Wind and react	Bronze process Wind and react	Bronze process React and wind	Normal commercial process
Operating current	350 A	910 A	4717 A	4717 A
Field produced	2.5 T	3.6 T	Total (both coils) 15 T	
Total field	21.1 T @ 4.2 K			

be the HTS conductors. Even though the dream of producing high magnetic field at 77 K has not been realized so far, yet these materials have shown promise in pushing the field limit well beyond 21.5 T, only if HTS magnets are operated at 4.2 K, their B_{c2} being very high. Their critical current values are very high at large field when operated at 4.2 K. The driving force to produce ultra-high magnetic field using superconducting magnets has come from researchers from solid-state physics, chemistry and the life sciences. Availability of such intense magnetic field will lead to new phenomena, hitherto undiscovered in a variety of solids and also open up possibility of building ultra-high-field NMR spectrometers with unprecedented resolution. It will then be possible to study extremely complex molecular structure of proteins and similar species. The strategy to attain high field has been to generate maximum possible field by the suitable combination of the Nb-Ti and Nb_3Sn coils and using an innermost HTS coil as insert.

9.7.2 A 24 T Magnet Using GdBCO Insert Coil (NIMS)

A team led by S. Matsumoto at Tsukuba Magnet Laboratory, (TML), NIMS, Japan, had produced a record breaking field of 24 T in 2011 [24]. The inner-most coil has been wound using GdBCO thin film wire (coated conductor) produced by Fujikura

Ltd., Japan, and vacuum-impregnated in wax. The beauty of the magnet is that it operates at 4.2 K instead of 1.8 K which is so much simpler to handle than handling a superfluid. The coil generates a field of 6.8 T at a current level of 321 A and an electromagnetic force BJR of 408 MPa. The coil has a clear bore of 40 mm and is nested in a combination magnet of Nb–Ti and Nb_3Sn generating together a background field of 17.2 T. The central field thus becomes 24 T. Some of the parameters of this magnet system are given in Table 9.5.

As mentioned above a background field of 17.2 T is provided by a combination magnet of Nb–Ti and Nb_3Sn. The middle coil is a Nb_3Sn coil with 135.2 mm inner dia., 318.4 mm outer dia. and has a height of 440 mm. It produces a field of 8.2 T at an operating current of 241.1 A. The outermost coil is a Nb–Ti coil with an inner dia. of 330.3 mm, outer dia. 516.8 mm and a height of 710 mm. It produces a field of 9.0 T at an operating current of 241.1 A. The highest central field produced thus turns out to be 24. 8 T at 4.2 K. Figure 9.23 shows the configuration (left) of the magnet coils of Nb-Ti, Nb_3Sn and the innermost coil of GdBCO conductor, each nesting inside the other. The photograph of the magnet is shown on the right side of Fig. 9.23.

Table 9.5 Parameters of the inner-most insert coil of the 24 T magnet coils (data compiled from [24])

Coil parameters	Unit	Innermost Coil	Outsert-1	Outsert-2
Conductor (tape)		(Gd–Ba–Cu–O)	Nb3Sn	Nb–Ti
Coil inner dia	mm	50.27	135.2	330.3
Coil outer dia	mm	112.80	318.4	516.8
Coil height	mm	88.33	440.0	710.0
Conductor dimensions ($w \times t$)	mm × mm	5.00 × 0.15		
Total no. of layers		124		
Total no. of turns		2010		
Total conductor length	m	515		
Operating current	A	360	241.1	241.1
Central field by the inner coil	T	6.8		
Background field by Nb–Ti and Nb_3Sn coils	T	17.2	8.2	9.0
Total central field	T	24.0		
Operating temperature	K	4.2	4.2	4.2

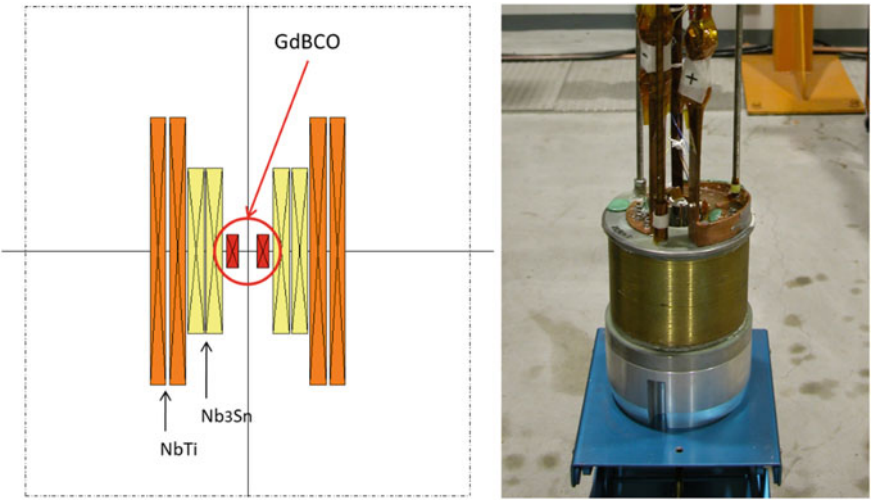

Fig. 9.23 24 T superconducting magnet built at NIMS in 2011, then a world record. Left: Configuration of the magnet coils, the GdBCO insert coil produces a field of 6.8 T and the Nb_3Sn / Nb–Ti outserts produce a field of 17.2 T. Right: A photograph of the 24 T magnet (*Courtesy* Shinji Matsumoto, Press Release 2011 NIMS, Tsukuba, Japan). https://www.nims.go.jp/news/press/2011/09/hdfqf1000000dzr6-att/p201109070.pdf

9.7.3 A 26.8 T YBCO Insert Coil at NHMFL (FSU)

Yet another important development towards the goal of achieving 30 T field and beyond by superconducting magnets took place at FSU. The NHMFL in collaboration with SuperPower produced a coil using coated YBCO tape conductor. The coil produced a record field of 26.8 T in a background field of 19 T generated by a 20 MW, 20 mm bore resistive magnet [25]. The coil had a clear bore of only 9.5 mm, but it did establish the possibility of generating field in excess of 30 T if only the innermost insert coil is made of HTS and operated at liquid helium temperature (4.2 K).

9.7.4 A Record Field of 32 T at NHMFL (FSU)

FSU built a wholly superconducting magnet using inner insert coils of REBCO-coated superconductor to produce a record field of 32 T in a 32 mm bore [4] in a background field of 20 T generated by a resistive magnet. This happened to be a world record of field produced by a combination of superconducting and resistive magnets in 2017. This was a landmark development and deserves to be discussed a bit in detail. These efforts were aimed at technology demonstration and resolving problems related to conductor behaviour under conditions of high-field and high

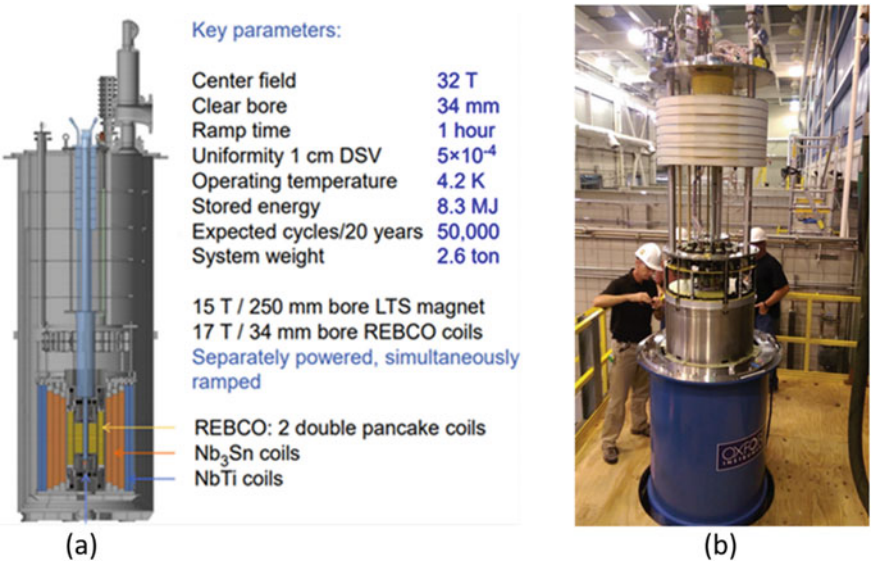

Fig. 9.24 **a** Schematic of the 32 T superconducting magnet system built at NHMFL. The Nb-Ti (2 coils) + Nb_3Sn (3 coils) provides a background field of 15 T, two inner REBCO coils provide a field of 17 T making a total field of 32 T. Key parameters of the magnet are given on the right of the figure [27] (*Courtesy* Huub Weijers and Mark D. Bird, NHMFL). **b** The 32 T magnet with its support system lowered in the cryostat (*Courtesy* Huub Weijers: Credit National High Magnetic Field Laboratory)

mechanical stresses. Magnet's I_c-B behaviour vis-à-vis field orientation and strain effect, the quench protection, the jointing of the conductor crucial to the stability of field required in NMR-type applications were studied thoroughly and data generated for building magnets producing stronger fields. The 32 T superconducting magnet built at NHMFL [26, 27] and shown schematically in Fig. 9.24 consists of a total of 7 concentric superconducting coils nested one inside the other. The outsert is a combination of 5 LTS coils, outermost 2 coils are wound with Nb-Ti conductor and the inner 3 coils with Nb_3Sn conductor. This LTS outsert produces a central field of 15 T in a wide bore of 250 mm. at an operating current of 268 A. An additional field of 17 T is generated by a REBCO insert consisting of a pair of coils, coil-1 (innermost) and coil-2 (outer). The clear working bore of the magnet is 34 mm. The total inductance of the outsert is 294 H and the stored energy 7 MJ. Some key parameters of the magnet are given in Fig. 9.24a. Figure 9.24b on the right shows this 32 T magnet, with its support system, being lowered in to the cryostat. The parameters of the LTS outsert and the insert coils of REBCO have been listed in Table 10.6. The outsert must be able to tolerate the quench of HTS insert coils. Similarly, the quench of the LTS coils must not destroy HTS coils. These stringent conditions make the design of high-field magnets extremely complex. Mutual inductance between the coils has to be understood well and accounted for in the design. Behaviour of LTS

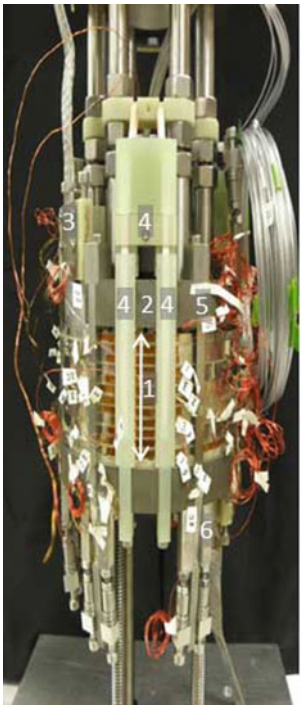

1: Six double pancake modules with spacers between pancakes and heater spacers between modules
2: Top flange
3: Top terminal
4: Protection covers for the quench heater wiring
5: Axial compression strap
6: Tension mechanism for axial strap

Fig. 9.25 Photograph of the 6-module innermost coil 1 of the 34 mm bore multi-section 32 T superconducting magnet showing the support structure and the instrument wiring [26] (*Courtesy* H.W. Weijers, W.D. Markiewicz and D. C. Larbalestier, National High Magnetic Field Laboratory

coils during HTS quench needs to be studied. The HTS coils too have to be protected with quench heaters.

The photograph of the REBCO coils with its support structure is shown in Fig. 9.25. Important parameters of the 32 T magnet consisting of a 15 T outsert and a 17 T insert are given in Table 9.6. The magnet was successfully tested in 2017 at NHMFL. The inner HTS coil has a clear bore of 40 mm and outer dia. 140 mm and consists of 20 modules of double pancakes. The outer HTS coil has an inner dia. 164 mm and an outer dia. of 232 mm and consists of 36 double pancake modules. These dimensions are good enough to accommodate a dilution refrigerator. Availability of such high field and mK temperature range will undoubtedly open new frontiers of research in condensed matter physics.

The HTS conductor is the coated tape of the size about 4.1 mm $\times$ 0.17 mm and uninsulated. The tape conductor is co-wound with an insulated SS tape which provided turn to turn insulation as well as mechanical strength through reinforcement. A double layer of G-10 provides module-to-module insulation and also sandwiches the encapsulated heaters used for quench protection. The inner and the outer HTS coils generate a field of 10.7 T and 6.3 T, respectively, at an operating current of 174 A. The total stored energy in the two coils is 267 kJ, and another 1.06 MJ is added

Table 9.6 Important parameters of the outsert and the insert of the 32 T magnet. The outsert has two Nb-Ti coils and three Nb_3Sn coils generating a field of 15 T. The insert has two REBCO coils which together generate a field of 17 T at an operating current of 174 A (data compiled from [4] & [27])

Specification of the 32 T magnet			
The outsert			
Parameter	Unit	Value	
Bore dia. of the outsert	mm	250	
Field produced by outsert	T	15	
Operating current	A	268	
No. of Nb-Ti coils		2	
No. of Nb3sn coils		3	
Inductance	H	294	
Stored energy	MJ	7	
Quench protection		Passive	
The insert (two REBCO coils)			
Parameter	Unit	coil-1	coil-2
Working cold bore	mm	34	
Inner diameter	mm	40	164
Outer diameter	mm	140	232
Height	mm	178	318
No. of double pancakes		20	36
Dim. of REBCO tape conductor	mm × mm	4.1 × 0.17	
Field by REBCO coils	T	10.7	6.3
Operating current	A	174	174
Average current density J_{av}	A/mm^2	200	170
Outermost dia. of REBCO coil 2	mm		232
Conductor length	km	2.9	6.8
Conductor piece length	m	60	110
Inductance	H	2.6	9.9
Quench protection		Heaters	Heaters
Co-wind thickness	μm	25	50
Outer dia. of the HTS outer coil(2)	mm	232	
Maximum ramp rate (0–180 A)	A/sec	1	1
Impregnation material		Wax	Wax
Maximum hoop stress	MPa	297	

due to the mutual inductance of the HTS coils and the LTS coils. The LTS magnet system along with the cryostat was supplied by Oxford Instruments. The design allows the use of the LTS magnet system in stand-alone mode providing a field of 15 T in 250 mm cold bore. Both the magnet systems, the REBCO and the LTS, run on two separate power supplies and protected independently against quench.

Since no data on the conductor behaviour under such extreme conditions of field, operating current and mechanical stresses were available quench protection to save the magnet at such high fields was a challenge. FSU therefore undertook first time studies on numerous parameters critical to the design of such a high-field magnet. They investigated J_c/B behaviour of HTS at 4.2 K and variation of J_c with field, temperature, strain and field orientation. Crucial and unique to HTS is the variation of J_c with field orientation. At the magnet ends (top and bottom), the field lines curve and make an angle with the direction of the field. J_c decreases with the angle, and this variation has to be found out. It turned out that the limiting operating current of the inner HTS coils is not determined at high-field mid-plane but at the magnet end. In this particular magnet design, the field orientation angle is 18 degrees at the magnet edge. These studies have brought out interesting facts about HTS needed for magnet construction. These are summarized below.

- REBCO tapes have good irreversible strain of 0.6% which stays at the lap joints of the tape if the overlapping length is more than 60 mm. For a given strain value, the stress decreases as the amount of copper layer is kept 40–100 μm thick on a 50 μm thick Hastelloy tape. The tape also becomes soft with the addition of copper.
- The bare HTS tapes and wires supplied by the manufacturers need suitable electrical insulation. Metal oxide, UV-cured epoxy and Kapton have been studied. The SS co-wind with a turn insulation was found to be a good winding technique. Sol–gel and UV-cured epoxy have been found good as turn insulation on the SS strip. SS co-wind not only enhances mechanical strength but makes tape handling far more easier.
- Dry winding in double pancake structure involving number of steps and a large number of joints has been followed successfully. The winding is quite convenient as the REBCO tapes possesses large bending strain tolerance.
- The coils were operated at an average current density of 1.8 to 2×10^4 A/cm^2 (taking in to account conductor thickness, copper fraction, inter pancake spacers and SS co-wind).
- The maximum stress in the winding was 400 MPa and the maximum strain 0.4%.
- Winding lengths of the coils are determined as per the field and field uniformity requirement. Longer winding also cuts down radial component of the field. Inner coil uses a conductor length of 150 m per module and the outer coil 220 m.
- Passive quench protection system, good for LTS magnets, is no good for HTS because of the very low quench propagation velocities, high operating current densities and current sharing temperatures. The quench protection is provided by heaters distributed throughout the coils which have been found to be most

Table 9.7 Ultra-high-field users' facility worldwide (*Courtesy* Mark Bird, NHMFL, Tallahassee)

Year	Field	Conductor	Maker	Location
2017	24.5	Bi-2223 + LTS	Toshiba	Sendai
2019	25.8 (1.1 GHz)	REBCO + LTS	Bruker	Nashville
2020	28.2 (1.2 GHz)	REBCO + LTS	Bruker	Florence
2017–2020	32.1	REBCO + LTS	Maglab	Tallahassee

effective. A quench detector activates the protective heaters the moment a quench is detected. Outer LTS coils have usual passive protection of resistors and diodes.

- The outer LTS coils and the inner HTS coils run on two separate power supplies

After these exhaustive studies, the magnet coils were designed, fabricated and finally tested experimentally. The magnet coils have been successfully operated at current values higher than needed for 32 T field. This 32 T magnet is a popular users' facility which is expected to serve the world community for next 20 years or more. Still higher field of 35.4 T was reported by Trociewitz et al. [5] in a small REBCO coil nested in a background 31 T resistive magnet. A single-tape length of 100 m of the coated REBCO conductor was used for winding the coil. The tape conductor was covered with a thin polyester film which introduces a weak circumferential plane in the coil pack which prevented conductor delamination observed in many epoxy impregnated coils made earlier. Table 9.7 shows the high-field magnet facilities available to users from across the world.

9.7.5 A New World Record of Magnetic Field—45.5 T at NHMFL (FSU)

The National High Magnetic Field Laboratory (NHMFL), Tallahassee, Florida, which held a world record of 45 T produced by a hybrid magnet for more than two decades exploited REBCO-coated conductor for building a magnet producing a record field of 45.5 T [6]. Figure 9.26 shows the principle of no-insulation winding technique and the design of the little big coil (LBC) with double pancake structure. On the right is the innermost and sleek coil of 2G YGdBCO tape with improved J_e supplied by SuperPower. Hahn et al. [6] used this paper thin, 0.043 mm (43 μm) YGdBCO tape without any electrical insulation. The background field of 31.1 T was provided by the resistive coil consuming 31 MW of power. The 2G YGdBCO insert coil produced an additional field of 14.4 T, and thus, a new record of 45.5 T was established in 2019. In fact, this magnet coil was the third coil made with REBCO-coated conductor by the NHMFL team code named LBC-3. The earlier coils LBS-1 had produced a field of 40 T and LBC-2 produced 42.5 T field. The operating current of LBC-3 at 45.5 T field was 245.3 A amounting to a current density of 1260 A/mm^2 which is 5 times higher than the current density in the 32 T magnet discussed in the

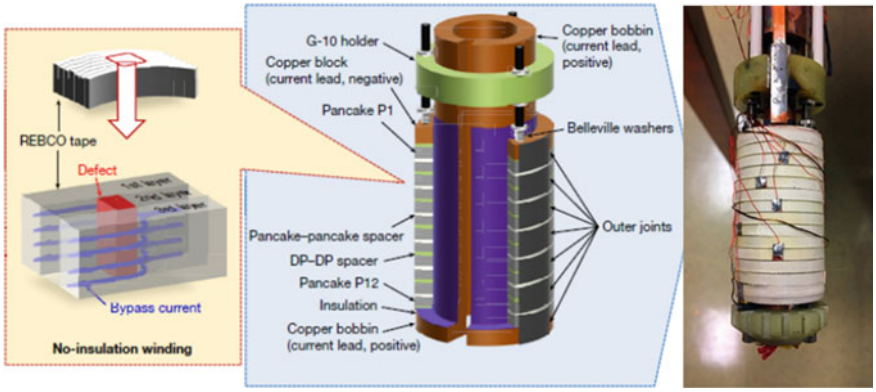

Fig. 9.26 Design and construction of littlie big coils (LBS): Left: principle of no-insulation technique, Centre: construction design of LBC, Right: the small insert REBCO magnet coil which produced highest ever magnetic field of 45.5 T in a background field of 31.1 T field at NHMFL Tallahassee. Ultrathin 0.043 mm thick 2G REBCO SuperPower tape was used for winding. The insert magnet weighs just 390 gms and the field, 45.5 T is a world record [6] (with permission from Springer Nature, Copyright © 2019, Springer Nature)

previous section. Quench occurred at a current density of 1420 A/mm^2. Interestingly, the quench did not lead to burnout and the maximum temperature in the winding did not go beyond 85 K. The 4.02 mm wide and 43 μm thick tape conductor used in the magnet was coated on a 30 μm thick Hastelloy substrate. The Hastelloy substrate was coated by a set of buffer layers, followed by 1.5 μm thick REBCO layer, a thin Ag layer and finally 5 μm thick electroplated Cu layer which provides stability. The coil was operated at a high current density of 1260 A/mm^2 which made the magnet very compact. The LBC-3 was dry-wound free of epoxy. The turns are found self-supporting against a peak hoop stress (BJR) of 691 MPa and a total strain magnetic and bending which turned out to be 0.38%. The winding without insulation made it possible to operate the magnet at high current density. This also allows rapid and safe quenching from the superconducting to the normal state. The key parameters of the magnet and the tape used are given in Table 9.8. The successful operation of this 45.5-T test magnet does confirm the supremacy of the cuprate superconductors over the low-temperature Nb-based superconductors.

Quenching of such high-field magnets with large stored energy may turn disastrous if the quench protection system is not perfect or develops some fault as happened at CERN in Sept. 2008 when 53 dipole magnets of the LHC were damaged. It is essential to prevent such catastrophic quench for operating a superconducting magnet slated to be used as users' facility for long periods. An innovation, that helped in reducing quench, introduced in the development of this magnet was the use of bare REBCO tape for winding. The magnet team found that non-insulated REBCO tape laid layer upon layer behaves a little like a single-layered thick superconductor. We know well that any weak spot in the insulated superconducting tape in a single-layer piece of tape will impede the current flow and heat that segment of the superconductor raising

Table 9.8 Key parameters of the LBC-3, the REBCO-coated conductor and the 31 T resistive background magnet (data compiled from [6])

Insert LBC-3			REBCO tape (SuperPower)		
Parameter	Unit	Value	Parameter	Unit	Value
Inner winding dia	mm	14	Width of tape	mm	4.02
Outer winding dia	mm	34	Thickness of tape	μm	43
Height of the coil	mm	53.1	Substrate thickness	μm	30
No. of pancakes		12	REBCO thickness	μm	1.5
No. of turns/pancake		226.4	Thickness of copper	μm	10
Total no. of turns		2717	31 T resistive background magnet		
Inductance	mH	50.4	Field constant	mT/A	0.843
Field constant	mT/A	59.7	Self-inductance	mH	4.30
Charging time constant	s	1.07	Mutual inductance with LBC-3	mH	1.09

the temperature above T_c. This results in a quench. Avoiding the insulation allows the current to reroute around the weak spot (an impurity in the lattice) and prevent quench. This current sharing by adjacent layer bypasses the dissipative region of the conductor. Another innovation was in the fabrication of the REBCO tape by SuperPower in reducing the thickness of the tape which increased the engineering current density J_e significantly and made the insert magnet very compact. The NHMFL research team is aggressively pursuing the path of invading the 50 T territory by nesting such REBCO coil in a 32 T magnet. In fact, in principle one may even exceed 50 and 60 T if only we find the appropriate structural material which can withstand huge mechanical stresses. The field appears to be open.

9.7.6 First High Current (4 kA) Insert Magnet Wound with CORC® Cable

Large magnets in accelerators and fusion tokamaks are required to have low inductance and operate at currents well over 5 kA at relatively high ramp rates. Rutherford style cables with twisted and transposed strands, containing fine filaments (~ 5 μm), have been used in accelerators quite successfully. HTS cables have been produced in other configurations too, such as Roebel cables, Twisted Stacked Tape Conductor (TSTC) and Conductor on Round Core, CORC® wires and cables discussed in Chap. 6. The advantage of CORC® wires is that the uninsulated tapes are wound in opposite directions between successive layers and are in direct contact. As such, there is significant current sharing between the tapes which prevents single-point burnout. The precise control of the tape I_c needed in single-layer tape is no longer required. CORC® conductors being mechanically as well as electromechanically isotropic conductors are ideally suited for constructing magnets operating at high current.

These magnets will have much higher safety factor with conventional quench protection like using external dump resistor circuits in contrast with anisotropic single-tape REBCO magnets.

The viability of CORC® (REBCO) cables in producing magnetic field under condition of high current (exceeding 4 kA), high current density and high hoop stress has been established by Laan et al. [28] at Advanced Conductors Technologies (ACT) in collaboration with University of Colarado, NHMFL and LBNL. The team has built an insert magnet operating at 4 kA and generating a central field of 15.86 T in a background field of 14 T. The peak field on the conductor was 16.77 T. The magnet operated at a current of 4404 A, equivalent to an engineering current density (J_e) of 282 A/mm^2 and generated a hoop stress (JBR) of 275 MPa. The photograph of the magnet is shown in Fig. 9.27. The ramp rates of 20 - 50 A/s did not induce a quench in the magnet. The magnet had four layers with innermost layer diameter of 100 mm and the outermost diameter of the fourth coil 143 mm. The height of the

Fig. 9.27 CORC® insert magnet with G10 support holding flexible S-bend in the cable ends. The magnet operates at a current of 4404 A and did not quench at a ramp rate of 50 A/s (with permission from IOP)

innermost layer was 46.3 mm and that of the fourth layer 60.2 mm. The magnet was wet wound with stycast epoxy 2850 using the CORC® cable which had 14 REBCO tapes wound in 14 layers with an estimated $I_c = 3$ kA (77 K, sf) and 6 kA (4.2 K, 16 T). The total length of the cable used was 19.5 m. The cable was 4.56 mm thick including two layers of 25 μm polyester heat sink tube outside of the cable and had used nearly 900 m of REBCO SuperPower tape. The tape was 3 mm wide with REBCO film deposited on a 30 μm thick hastelloy substrate and had a 5 μm thick copper plating.

The 100 mm bore insert magnet was nested in a 160 mm bore 14 T LTS magnet and energized by 6 power supplies connected in parallel capable of supply of 7.2 kA. Figure 9.28a is the circuit diagram of the quench protection system consisting of a dump resistor, high-current power diodes, and contactors. The photograph in Fig. 9.28b shows the cryostat top, the current injection hardware, the quench protection system of the magnet, vapour cooled current leads, current shunt, dump resistor, power diodes, contactors and power supplies. Vapour-cooled current leads feed the current to the magnet from the power supplies. The successful operation of the insert magnet in a background field of 14 T clearly establish the fact that the CORC® cables have come to stay as a high-current/high-field practical conductor for future applications in accelerators and fusion machines. The CORC® cables will be the conductor of choice for low inductance high field (> 20 T) magnets.

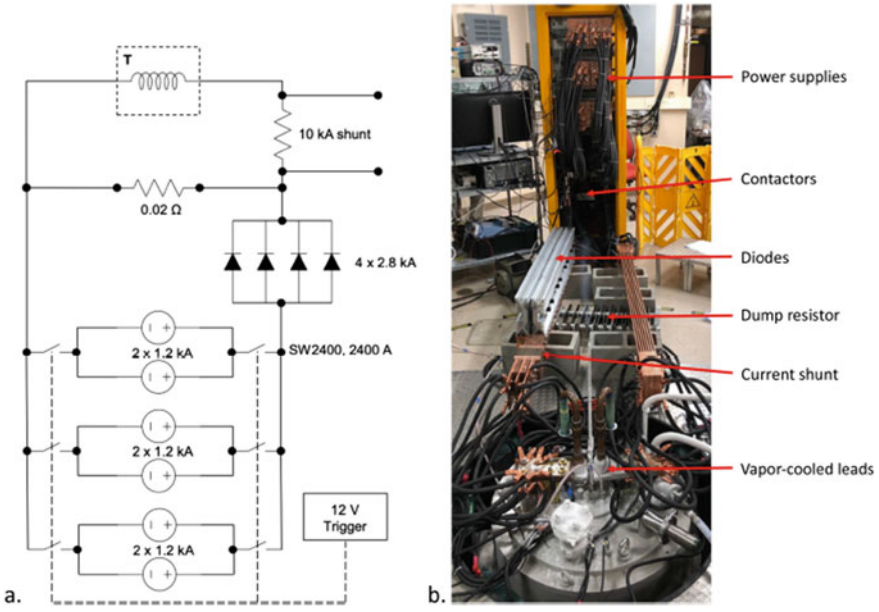

Fig. 9.28 **a** Circuit diagram of the quench protection system consisting of a dump resistor, high-current diodes and contactors for the CORC® insert magnet. **b** The current injection and quench protection system of the CORC® insert magnet consisting of vapour cooled current leads, current shunt, dump resistor, power diodes, contactors and power supplies [28] (with permission from IOP)

9.8 Cryo-Free Superconducting Magnets (CFSM)

The biggest and immediate fall-out of the discovery of HTS was the development of HT current leads capable of transporting large currents without Joule heating when operated below T_c. This development together with the availability of two-stage Gifford–McMahon (GM) closed cycle refrigerator (CCR) of 1.5 W @ 4 K capacity led to the development of Cryo-Free Superconducting Magnets (CFSM) producing high fields. The HTS current leads have two advantages, one that there is no Joule heating across the leads and two that they behave nearly like a thermal insulator as superconductors have poor thermal conductivity, about 500 times smaller than OFHC. Since there is no hassle of producing and transferring liquid helium to the system, these magnets have found wide spread popularity in a short time. The feasibility of a cryo-free magnet was reported by Hoenig [29] in 1983 who produced a field of 3.3 T using Nb_3Sn conductor and a 10 K two stage CTI-1020 CP Cryodyne cryocooler. This 12 kg Nb_3Sn magnet was operated at 14 K and produced a field of 3.3 T at a current density of 6×10^4 A/cm^2. It was, however, during 1990s when the HTS current leads became commercially available, that massive development of CFSM, the world over, took place. There are numerous publications, such as [30, 31] on CFSM. A world record of 27.5 T by a hybrid magnet using a cryo-free outsert and the resistive magnet as an insert was established by IMR, Tohoku University, Sendai years ago. Presently, CFSM-producing field up to 20 T is available in the market.

Of late, pulse tube cryocoolers (PTC) with 1.5 W cooling capacity have become commercially available. PTC has the advantage that there is no moving part in it like the displacer in the GM cryocooler. They are thus free from mechanical vibrations and from electromagnetic noise. These PTCs are preferred for experiments where vibrations are not acceptable and the noise level has to be small. Secondly, the life cycle is going to be much higher than 10,000 h. of free maintenance of the GM cryocoolers. The PTCs do consume large power in so far as about 6.5 kW power is required to produce 1.5 W of cold compared to 0.25 kW to 1 kW power required to produce 1 W of cooling by liquid helium. This cost is, however, more than off-set by net saving in helium cost and heavy investment if one has to install helium liquefaction facility.

A 5 T Nb–Ti magnet with room temperature bore of 50 mm was built by Giebeler et al. [32] in 2004 using a two stage PTC with a cooling capacity of 0.4 W at 4.2 K. It is a compact 12 kg magnet, 190 mm in height and produces a field of 5 T at a charging current of 35 A. The PTC cools down the magnet to 2.7 K in 44 h. The minimum temperature attained is 2.4 K. The stable temperatures at the first and second stage are 5 K and 0.1 K, respectively, over a period of 21 days. The magnet runs in persistent mode. The persistent switch is cooled by the second stage of the PTC.

We would like to take up the design and operation of a CFSM a bit in detail now. As an example, we again take up the construction of our own 6 T, 50 mm room temperature bore magnet which we built at our centre many years ago. Before we do that, let us discuss the crucial issues involved in the design and operation of a

cryo-free magnet and which are generally not reported being a propriety item of the manufacturers.

9.8.1 Important Considerations for CFSM System Design

- The most important and foremost issue is that there is no longer a liquid helium bath which has large capacity to cool the magnet and absorb heat rather quickly. Cryo-free magnets are cooled by the second stage of the CCR through thermal conduction which is a slow process and depends upon the quality of the thermal contacts. A small thermal disturbance, if not dissipated to the CCR fast enough, may raise the temperature locally beyond T_c and quench the magnet.
- A thermal analysis of all heat loads to the two stages of the CCR must be carried out carefully before embarking on the design. Total heat loads should be reasonably below the refrigeration capacity of the two respective stages of the CCR.
- The thermal shield and the magnet, the two heaviest components of the whole system, are cooled by the first stage and the second stage of the CCR respectively by thermal conduction only. Thermal contacts have therefore to be nearly perfect with least thermal resistances.
- Flexible OFHC braids are ideal for thermal connections whether fixed mechanically or through soldering. Flexibility prevents stresses in the system during thermal cycles.
- The magnet should preferably use former made of copper. The former must have perforations and should have a slit along the entire length (including flanges) to minimize the eddy current heating during ramp-up and ramp-down of the magnet.
- The magnet is cooled via the top and bottom flanges of the former in thermal contact with the second stage. Cooling of coil starts from the outer and inner layers. Inter-layer insulating material should be avoided as this will slow down the thermal conduction making the layer-to-layer heat transfer inefficient.
- We recommend wet winding using stycast epoxy mixed with 15–20 wt. % aluminium nitride (ALN) powder. Wet winding ensures fool-proof impregnation and ALN powder improves the thermal conductivity of the stycast. ALN also reduces the mismatch of the thermal contraction coefficients of the epoxy and the conductor, minimizing cracking under Lorentz forces during magnet operation.
- Since there is no bath to keep the magnet temperature constant, operating temperature has to be estimated at the target field. The magnet temperature rises from the zero-current state as the magnet current is ramped-up. A good temperature margin (> 1 K) should be maintained between the operating temperature and the current sharing temperature. Temperature margin is a concern more in LTS and especially in Nb-Ti because of low T_c.
- The maximum heat to the system comes from the current leads. In CFSM, the current leads are hybrid, a combination of copper leads from room temperature to thermal shield and HTS leads from thermal shield to the magnet connected with the second stage of the CCR. Heat input to the thermal shield consists of

heat conducted from the room temperature top plate and also due to Joule heating within the copper leads. The copper current leads therefore should be optimized for the operating current to minimize Joule heating.

- Between the shield and the magnet, the current leads are the HTS leads generating practically no heat. These leads are joined to the copper current leads. These contacts should have very low electrical resistance to minimize Joule heating. These joints should be anchored to the shield through spacers of material like ALN which are not only good electrical insulator but also good thermal conductor. The lower ends of the HTS leads are connected electrically to the magnet terminals and thermally to the second stage of the CCR via the heat transfer plate.
- The performance of the CCR and the HTS leads deteriorate in presence of the magnetic field. A field profile of the magnet should therefore be carried out in advance so that the HTS leads and the CCR heads are positioned in low field areas where the stray field is below 0.1 T.
- An efficient quench protection system similar to one used with the bath-cooled magnets has to be designed such that the magnet temperature does not exceed 40–50 K after the quench. In these systems, there is no helium gas pressure build-up at quench in contrast with the bath-cooled magnets.

9.8.2 The Design and Winding of the Magnet

To discuss the construction details of a CFSM system, we take up the example of a 6 T, 50 mm warm bore Nb-Ti magnet we built [33, 34] in our laboratory. The design considerations for the bore dia., field strength, current and number of turns and layers are the same as for any bath-cooled magnet, discussed in detail in Sect. 9.4. The major consideration here is that the operating temperature of the magnet is to be calculated from heat loads coming to the magnet from different sources for the given field, the three critical parameters of the conductor, T_c, J_c and B_{c2} being inter-dependent. The operating current is then chosen from the conductor I_c-B plots.

To have a warm bore of 50 mm, we chose the inner winding dia. of 104 mm and a winding length of 200 mm on the basis of field homogeneity criterion. The outer winding dia. comes out to be 137 mm. At an operating current of 102 A, the magnet should produce a field of 6 T. This current is 68% of the short sample I_c value supplied by the manufacturer. We emphasize that the J_c and B_{c2} values quoted are at 4.2 k and at zero current. Similarly, T_c value is always quoted in zero field and at zero current. For CFSM, we have to find out the current sharing temperature, T_{cs} which is higher than zero current T_c. The current sharing temperature, T_{cs}, is defined as the temperature at which the current starts flowing partly through copper. As the magnet current rises, T_{cs} too starts rising. The temperature window to operate magnet becomes narrower. Values of T_c and T_{cs} can be estimated at different fields using following equations given by Lubell [35].

$$T_c(B) = T_c(0) - [1 - (B/14.5)]^{0.59} \tag{9.19}$$

Table 9.9 Current transfer temperature T_{cs} at 6 T and different operating currents and the temperature margin, ΔT for Supercon 0.54 mm dia. Nb–Ti wire with different I_c values at 6 T, 4.2 K

Operating current (A)	% of I_c	T_b (K)	T_c (B) at 6 T (K)	T_{cs} (K)	$\Delta T = T_{cs} - T_b$ (K)
50	33.3	4.2	6.71	5.86	1.67
90	60	4.2	6.71	5.204	1.0
102	68	4.2	6.71	5	0.8
135	90	4.2	6.71	4.45	0.25
150	100	4.2	6.71	4.2	0

$$T_{cs}(B) = T_b + [T_c(B) - T_b](1 - J_{op}/J_c) \tag{9.20}$$

where $T_{cs}(B)$ is the current sharing temperature at a field B, T_b is the operating temperature, J_{op} is the operating current and J_c is the critical current. The T_{cs} values and also the temperature margin for operating the magnet at 6 T field have been evaluated for different operating currents and are listed in Table 9.9. For an operating current of 102 A and an operating temperature of 4.2 K, the T_{cs} for this 6 T magnet is 5 K. Thus, the temperature margin ΔT is only 0.8 K. However, if the magnet is operated at 3.3 K the ΔT goes up to 1.7 K. The T_c of Nb–Ti at 6 T is 6.71 K. The operating temperature should therefore be as low as feasible by reducing the heat leaks to the two stages of the CCR to a minimum. T_{cs} thus becomes an important input parameter for the magnet design calculations,

The magnet is wound on an electro-tough pitch (ETP) copper former with a slit along the entire length. The slit reduces heat generation due to eddy current induced in the former during charging and discharging of the magnet. A layer of thin Kapton tape was wrapped on the former surface to make it electrically insulating. Supercon 0.54 mm dia. Cu/Nb-Ti wire was used for coil winding. We preferred wet winding using stycast epoxy mixed with ALN (aluminium nitride) powder as filler to improve its thermal conductivity and reduce mismatch in thermal contraction values of the epoxy and the conductor. Since the cooling of the coil proceeds layer to layer, no inter-layer has been used which would have hampered layer-to-layer conductance. All the parameters of the magnet are given in Table 9.10.

9.8.3 The Current Lead Design

The optimization of the copper part of the hybrid current leads is crucial in so far as it determines the heat input to the top plate of the thermal shield and its temperature. This directly affects the minimum temperature reached at the second stage and hence the operating temperature of the magnet. Please remember that there is no helium vapour cooling available like in bath-cooled magnets. Optimization of conduction-cooled current leads can be done using following equations given by the McFee

Table 9.10 Parameters of a 50 mm warm bore CFSM built at author's laboratory [32, 33]

Magnet parameter	Unit	Value
Inner winding dia	mm	104
Outer winding dia	mm	137
Winding length	mm	200
Inter-layer		None
Impregnation (wet winding)		Stycast with filler
Conductor used		MF Cu / (Nb-Ti)
Wire dia	mm	0.54
No. of filaments		54
Filament dia	μm	38
Cu/Nb-Ti ratio		2.0 ± 0.2: 1
Total conductor length	km	4.1
No. of layers		32
No. of turns/layer		370
Peak field	T	6.2
Current at peak field		105.3
Field factor (T/A)		0.0588
Stored energy at peak field	kJ	31.04
Quench protection (dump resistor)	Ω	0.5

model [36].

$$\frac{Q_{\mathrm{OPT}}}{I} = \sqrt{L_0\left(T_W^2 - T_C^2\right)} \tag{9.21}$$

$$\left(\frac{IL}{A}\right)_{\mathrm{OPT}} = \frac{1}{\sqrt{2}} \int_{T_C}^{T_W} \frac{k(T)dT}{\sqrt{L_0\left(T_W^2 - T_C^2\right)}} \tag{9.22}$$

where $Q_{\mathbf{OPT}}$ is the optimized heat flow, $L_{\mathbf{0}}$ is the Lorenz number, $T_{\mathbf{W}}$ and $T_{\mathbf{C}}$ are the temperatures at the warmer end and the colder end of the copper lead, respectively. I is the lead current, L and A are the length and the area cross section of the lead, respectively. $k(T)$ is the temperature-dependent thermal conductivity of the lead material. Using (9.21) $Q_{\mathbf{OPT}}$ for a lead carrying current between 300 and 33 K comes out to be 47 mW/A. Substituting appropriate values of the different parameters, in (9.22), the lead parameter, IL/A, for copper of RRR 150 purity turns out to be 4.5×10^{6} A/mm^2. Thus, for a current lead of area cross section 15 mm^2 and optimized for 85 A, the length should be 800 mm. Calculations show that for values of RRR 50 to RRR 300 the lead parameter is same at all temperatures from 300 K down to 30 K.

9.8.4 The Cryostat Design

The CFSM system is schematically shown in Fig. 9.29 which basically consists of a wide body SS vacuum chamber. The CCR sits off-the-centre on the top plate of the chamber. The top plate of the cylindrical thermal shield, made out of ETP copper, was suspended from the top plate of the chamber using G-10 strips. This plate is thermally connected to the first stage of the CCR using copper braids. Indium gaskets have been used at all the contact interfaces to reduce thermal resistance. The magnet is mounted on a slotted ETP copper plate which is thermally anchored, mechanically, to the cold head of the second stage of the CCR through sixteen semi-flexible copper strips (20 mm × 2 mm). Apiezon N grease mixed with copper powder is used at the interface to improve thermal conduction. The magnet, weighing about 15 kg, is supported by G-10 strips from the top of the shield as shown in Fig. 9.29. The total thermal mass directly cooled by the second stage cold head is about 17 kg which consists of the former, Nb–Ti coil and the heat transfer plate. A pair of hybrid current leads consisting of pure copper leads in the warmer region (between top plate and the shield) and HTS leads in the colder region (between shield and the magnet) are used to charge the magnet. The copper part of the leads was optimized

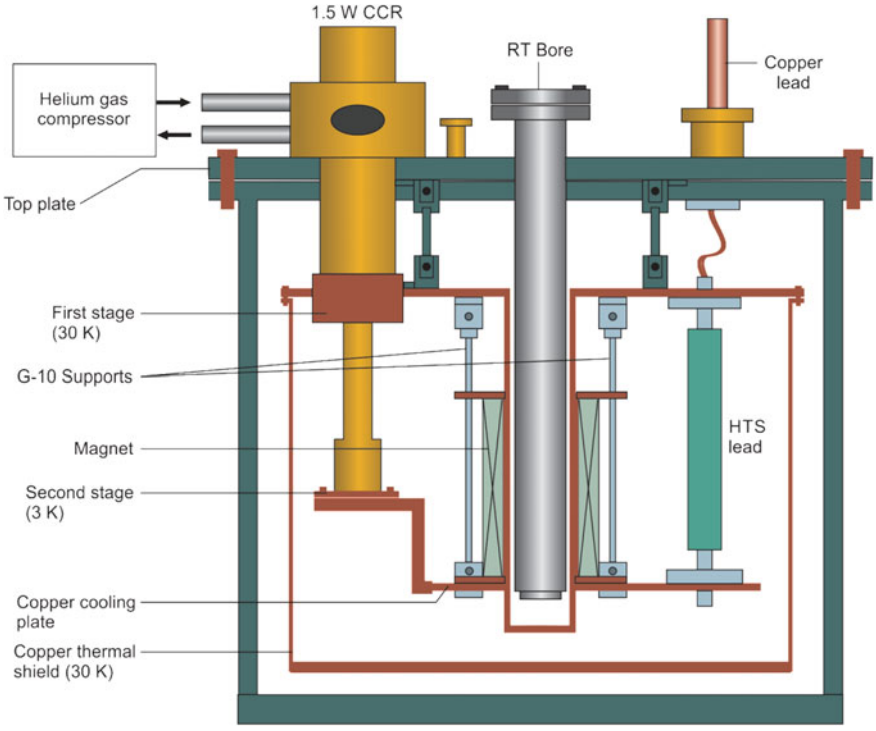

Fig. 9.29 Schematic diagram of a 6 T CFSM system built in author's laboratory at IUAC [32, 33]

for an operating current of 102 A between 300 and 35 K using Mcfee model [36]. The dimensional parameter, (IL/A) for copper of RRR 150 turns out to be 4.4×10^{-6} A/mm^2. For a 15 mm^2 cross-sectional area, the length of the lead has to be 650 mm. The heat load per lead works out to be 4.7 W. It is a good idea to simulate the experiment in advance with a dead mass of weight equal to the magnet and find out the different heat loads static and dynamic with and without the magnet current. This will help to know the temperature of the shield and optimize the copper current leads correctly. We carried out such simulation for this magnet [37]. The complete assembly of the system is shown in Fig. 9.29. The entire system hangs from the top plate of the vacuum chamber. Copper current leads (in braid form) are joined with the copper braid terminals of the HTS inside a copper bush with lead–tin solder. These joints are thermally anchored to the top plate of the thermal shield and electrically insulated through the use of ALN disc spacers. Similarly, the lower ends of the HTS leads (copper braids) are soldered to Nb-Ti wire terminals and anchored to the heat transfer plate using same type of copper block and ALN spacer. This plate is already thermally connected with the second stage of the CCR.

Figure 9.30 shows a clear view of the inner assembly of the magnet. The thermal shield, HTS current leads and shield chamber can be seen in the picture. Figure 9.31 is the photograph of the complete CFSM system with central 50 mm RT bore and all feed-thrus. The Bi-2223 HTS leads, (model CSL-7/120.1) were bought from CAN superconductors. The conductive heat leak through the lead pair between 64 and 4 K is 20 mW. Silicon diode temperature sensors have been mounted at several locations of the system to monitor temperature for carrying out thermal analysis.

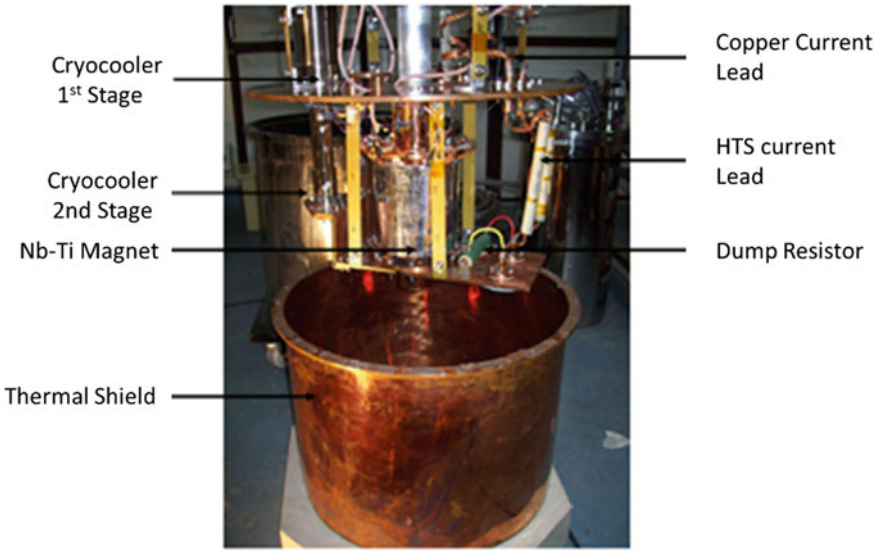

Fig. 9.30 Photograph of the inner assembly of the 6 T CFSM built at IUAC. The thermal shield, HTS current leads and shield chamber can be seen in the picture (Courtesy IUAC, New Delhi)

Fig. 9.31 Photograph of the complete CFSM system with central 50 mm RT bore and all feed-thrus (Courtesy IUAC, New Delhi)

9.8.5 Operating the Magnet

Prior to installing the magnet in to the cryo-cooled cryostat, we decided to test the magnet and the quench system in our liquid helium-cooled test cryostat. The magnet was energized at a slow rate of 3A/min. The first quench occurred at 80.1 A (4.7 T), second at 87.2 A (5.15 T) and third at 99 A (5.85 T). Finally, the magnet produced a field of 6.2 T at a current of 105.2 A without quench. After the training, the magnet was charged at a sweep rate of 30 A/min to 6 T without quench. The B-$I_{\mathbf{op}}$ data obtained and quench positions are plotted in Fig. 9.32. After the magnet was tested and trained up to 6 T, it was dismounted from the test cryostat and was transferred to its new destination within the vacuum chamber. The performance details can be found in [38]. All the components of the system in the final configuration are shown in Fig. 9.30. After ensuring all the lead connections, proper mounting of the thermal transfer plates to the two stages of the CCR, the vacuum chamber was evacuated to 10^{-5} mbar. The magnet cools down to a minimum of 3.3 K in 15 h. The vacuum at this temperature improves to 10^{-9} mbar. The equilibrium temperatures of the cold head, magnet cooling plate and the copper anchor recorded are 2.75 K, 3.1 K and 4.5 K, respectively. The difference between the temperatures of the cold head and

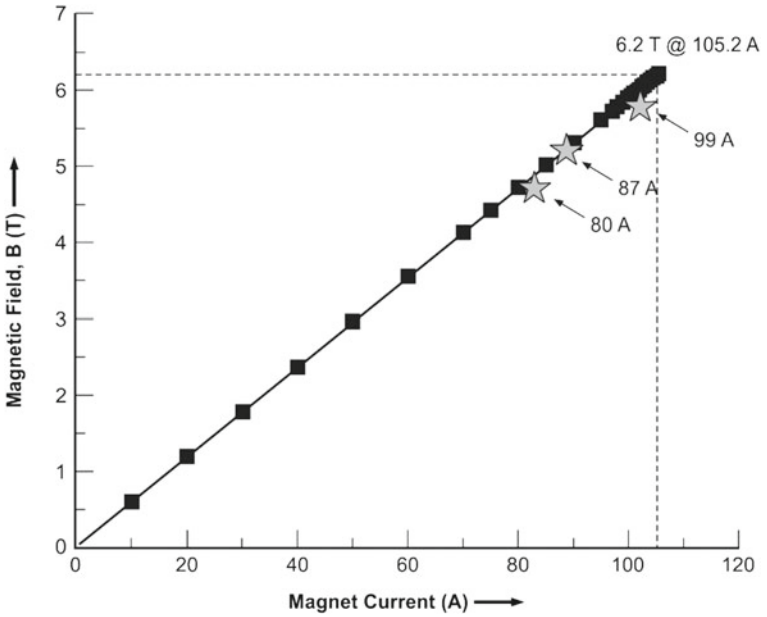

Fig. 9.32 Training of the magnet in liquid helium bath. Maximum field produced 6.2 T at 105.2 A. The magnet quenched at 80, 87 and 99 A during training [38]

the outer layer of the magnet is only 0.6 K. The thermal shield temperature stabilizes at 35.7 K.

The magnet was energized in steps of 10 A at a ramp rate of 3 A/min. up to 102 A corresponding to the field 6 T. Magnet quenched at 87 A and 102 A during the first run of this system. Temperature of the magnet rose to 41.5 and 54 K after the quench at the two current values, respectively. Magnet, however, cooled down to 3.3 K, the operating temperature in just 40 min. We found the maximum workable ramp rate to be 6A/min. Beyond this value, the heat generation caused by the AC losses and the induced eddy currents exceeds the heat extraction rate by the CCR. This is because of the inherent thermal resistances at the current lead joints. At 102 A current, the magnet stabilizes at 4 K and the cold head at 3.13 K. Temperature at the lower end lead joint too goes from 4.5 to 6.6 K at 102 A. This temperature rise is due to the Joule heating of the copper braid which connects the HTS lead with the magnet. With a resistance of 10 $\mu\Omega$, the braid generates 210 mW of heat at 102 A. Estimates show that static heat load at the first stage without lead connection is only 14.6 W and goes up to 19.8 W after lead connections but no current and to 25.3 W at 102 A in the leads. A variable temperature controller 4 K-300 K and a physical property measuring system were built and integrated with the magnet for use by the researchers.

An elegant and systematic electro-thermal analysis of the heat load transferred to the two stages of the CCR by various sources has been carried out by Kar et al.

[39]. The entire magnet system from room temperature to magnet has been reduced to a network of electrical and thermal resistances as detailed in Fig. 9.33. Electrical contact resistances of all the joints were measured experimentally. Thermal resistances were calculated from the measured temperatures at appropriate places and using thermal conductivity of the material. It turns out that the heat input to the first stage comes mainly from the optimized copper current leads followed by warm end cu-braid, Cu–Cu joints and Cu-HTS joints. All these heat inputs show an increase with magnet current. Similarly high heat input to the second stage comes from heating of the lower copper braid, followed by Cu-HTS joints and Cu-Nb-Ti joints, all again going up with the increase of magnet current. Heat generated in HTS leads is less than 5 mW and stays current independent.

Above discussion clearly establishes the fact that it is extremely important to design the hybrid current leads meticulously so that the heat inputs to the two stages of the CCR are well within their cooling powers. All the inter-lead joints should have low contact resistance producing minimum heat. Anchoring to thermal shield and magnet cooling plate has to be perfect. Technology to build cryo-free magnets producing field

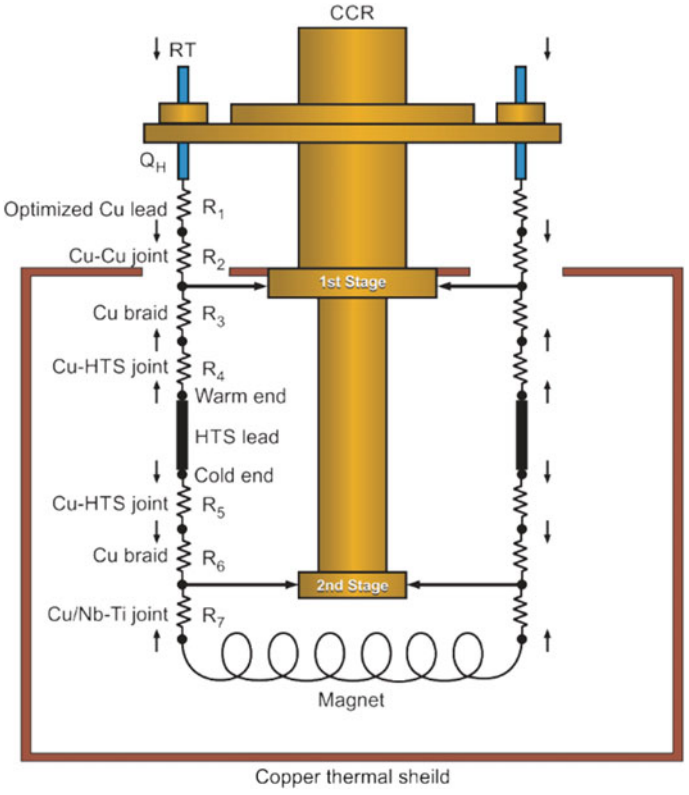

Fig. 9.33 Resistance network model used to calculate heat loads to the first and second stage of the CCR, generated by various resistances and joints [39]

up to 20 T is well established by now. Looking at the great developments that are taking place in the production of superior quality, HTS conductors in long lengths and similar development in high power CCRs, cryo-free magnets producing 30–50 T field will be a reality one day.

References

1. G.B. Yntema, IEEE Trans. Magnetism, **MAG-23**, 390 (1987)
2. H.T. Coffey, J.K. Hulm, W.T. Reynolds et al., J. App. Phys. **36**, 128 (1965)
3. J.E. Kunzler, E. Buehler, F.S.L. Hsu, J.H. Wernick, Phys. Rev. **6**, 89 (1961)
4. W.D. Markiewicz, D.C. Larbalistier, H.W. Weijers et al., Magnet Technology, MT-22, 2CO-8, (2011). IEEE Trans. App. Supercond. **22**, 4300707 (2012)
5. U.P. Trociewitz, M. Dalban-Canassy, M. Hannion, et al., Appl. Phys. Lett. **99**, 202506 (2011)
6. S. Hahn, K. Kim, K. Kim et al., Nature **570**, 496 (2019)
7. R.W. Boom, R.S. Livingston, Proc. IRE **50**, 274–285 (1962)
8. Ch. Fabry, J. Phys. **9**, 129 (1910)
9. D.B. Montgomery, Solenoid Magnet Design (Wiley-Interscience, London, 1969)
10. H. Brechna, Superconducting Magnet System (Springer, Berlin, 1973)
11. M.N. Wilson, Superconducting Magnets (Clarendon Press, Oxford, 1983, 1986, 1989)
12. Y. Iwasa, *Case Studies in Superconducting Magnets—Design and Operational Issues* (Plenum Press, New York, 1994).
13. K.H. Mess, P. Schmüser, S. wolff, Superconducting Accelerator Magnets (World Scientific Hemberg, 1996)
14. S. Kar, R. Kumar, M. Kumar et al., Ind. J. Cryo. **32**, 131 (2007)
15. B.J. Maddock, G.B. James, Proc. IEE **115**, 543 (1968)
16. R.G. Sharma, Y.S. Reddy, R.B. Saxena, et al., A superconducting magnet system for 100 MHz NMR spectrometer, in *Advances in Instrumentation, Proceedings of International Conference on Instrumentation (ICI-1996)*, Bangalore, India, ed. by B.S. Ramprasad et al., 8–10 Aug 1996
17. T. Kiyoshi, M. Kosuge, K. Innoue, H. Maeda, Physica B **216**, 196 (1996)
18. R.G. Sharma, Y.S. Reddy, M.M. Krishna, et al., News item "NPL Develops Nb_3Sn Magnet Technology", NPL (India) Technical Bulletin, April 1992, p 14
19. R.G. Sharma, R.B. Saxena, M.A. Ansari, "*An 11 T Nb-Ti/Nb_3Sn Magnet*" Research Report, NPL (India), June 2003
20. K. Tachikawa, Y. Tanaka, K. Inoue et al., 17.5 Tesla Superconducting Magnet. J. Cryogenic Soc. Japan **11**, 252 (1976). ((in Japanese))
21. M. Oshikiri, K. Inoue, T. kiyoshi et al., Physica **B 201**, 521 (1994)
22. T. Kiyoshi, K. Inoue, K. Itoh et al., IEEE Trans. App. Super. **3**, 78 (1993)
23. T. kiyoshi, M. Kosuge, K. Inoue and H. Maeda, Physica, **B 216**, 196 (1996)
24. S. Matsumoto, T. Kiyoshi, A. Otsuka, et. al, Supercond. Sci. Technol. **25**, 025017 (2012)
25. D. Larbalestier, New Magnet Lab. record promises more to come, News and press releases, August 7, 2007. www.magnet.fsu.edu/mediacenter/news/pressreleases/2007august7.html
26. H.W. Weijers, W.D. Markiewicz, A.J. Voran, et al., IEEE Trans. App. Supercond. **24**, 5 (2013)
27. H.W. Weijers, PPT "The NHMFL 32 T superconducting Magnet", EUCAS 2017. https://indico.cern.ch/event/659554/contributions/2708372/attachments/1525993/2386079/3P1-01_Huub_Weijers_Room_1.pdf
28. D.C. van der Laan, J.D. Weiss, U.P. Trociewitz, et al., Supercond. Sci. Technol. **33**, 05LT03 (2020)
29. M.O. Hoenig, IEEE Trans. Magn., **MAG**-19, 880 (1983)
30. K. Watazawa, J. sakuraba, F. Hata, et al., IEEE Trans. Magn., **MAG-32**, 2594 (1996)
31. K. watanabe, S. Awaji, J, Sakuraba, et al., Cryogenics, **36**, 1019 (1996)

32. F. Giebeler, G. Thummes, K-J Best, Supercond. Sci. Technol. **17**, S-135 (2004)
33. S. Kar, P. Konduru, R. Kumar et al., Adv. Cryo. Eng. **57A**, 597 (2012)
34. S. Kar, P. Konduru, R. Kumar et al., Adv. Cryo. Eng. **57A**, 909 (2012)
35. M.S. Lubell, IEEE Trans. Magn. **19**(3), 754 (1983)
36. R. McFee, Rev. Sci. Instrum. **30**, 98 (1959)
37. S. Kar, A. Chaudhury, P. Konduru et al., Ind. J. Cryog. **35**, 246 (2010)
38. P. Konduru, S. Kar, M. Kumar et al., Ind. J. Cryo. **36**, 81 (2011)
39. S. Kar, P. Konduru, R.G. Sharma et al., IEEE Trans. Appl. Super. **23**, 4800507 (2013)

Chapter 10
Superconducting Magnets in Accelerators

Abstract Particle accelerators and high-field superconducting magnets had been the greatest promoters of each other. In accelerators, RF power is used to boost the beam energy through the use of superconducting (RF) cavities. Bending, focusing and steering of the beam is provided by superconducting magnets. Fundamentally, an accelerator can either be of circular type or linear. Circular accelerators like Large Hadron Collider (LHC) are suitable for heavy ions like protons because the energy loss caused by synchrotron radiation in a circular accelerator varies inversely to the fourth power of the mass of the ion. Brief discussion on the superconducting colliders built and operated, namely Tevatron, HERA, SSC, RHIC prior to LHC have been given in the chapter. LHC magnets have been discussed in greater details. LHC, world's most powerful particle accelerator has, been in operation since 2009 and has yielded vast data and has confirmed the existence of Higgs boson. Parameters of the collider magnet system and the specifications of the conductor used are presented. Innovative magnet designs and development of superior conductors have been included. Linear accelerator is the choice for light particle like electrons and positrons. An international effort has been made to build a 31 km long linear collider named International Linear Collider (ILC) for colliding electrons and positrons with a collision energy of 500 GeV (~1 TeV in future). World's first superconducting cyclotron of the class K-500, world's biggest cyclotron, K-1200 (both at MSU) and the world's biggest ring cyclotron, RIKEN SRC K-2500 have been described. K-1200 can accelerate U to 90 meV and the SRC K-2500 up to 350 meV. The successor of LHC, namely the high-luminosity LHC (HL-LHC), and the Future Circular Collider (FCC) are also discussed towards the end. Nb_3Sn quadrupole and dipole magnets developed for the two projects have been described. The chapter closes with the expectation that LTS capability of producing high magnetic field would be exhausted soon, and reliance will be made on HTS cables which are already being developed for DEMO TF coils.

R. G. Sharma, *Superconductivity*, Springer Series in Materials Science 214,
https://doi.org/10.1007/978-3-030-75672-7_10

10.1 The Accelerators

Particle accelerators and high-field superconducting magnets had been the greatest promoters of each other. Great advancement made in the development of high-field superconducting magnet technology led particle accelerators to acquire higher and higher beam energies. High-energy accelerators, in turn, have been responsible for the unprecedented growth in the design and production of superconducting cables capable of carrying several thousand of ampere current with high stability and low AC losses. It looks, as though, the two technologies have been moving in tandem.

In an accelerator, the beam is accelerated by pumping RF through superconducting radio frequency (SCRF) cavities (mostly Nb) to produce high voltage gradient. High-energy accelerators built are mainly either of circular type or of linear configuration. In both the types of accelerators, the beam is accelerated in an array of SCRF cavities. In a circular accelerator, the beam travels through the SCRF cavities arranged in a nearly circular path. Dipole magnets are used for bending the beam by producing appropriate and very precise field transverse to the beam path. As the beam particles travel through the cavities repeatedly, they gain energy and their velocity increases. The accelerating field in the cavity too is adjusted accordingly. For higher energy, the magnetic field has to be adjusted to keep the particle moving in the same trajectory. Once the velocity approaches relativistic value equal to the speed of light, c, the RF frequency stays constant. This design of accelerator has been followed in colliders in which two energetic beams travelling in opposite directions collide to produce particles that were not seen before. The most famous of such colliders is the Large Hadron Collider (LHC) built and operated at European Organization for Nuclear Research (CERN) to accelerate two protons travelling in counter clock directions to acquire an ultimate energy of 7 TeV and collide to produce a collision energy of 14 TeV. LHC installed in a 27 km long tunnel used earlier by the Large Electron–Proton ColliderLEP) has been successfully operating since Sept. 2009. The first collision between two 3.5 TeV beams was observed in March 2010 and the long sought after Higgs boson was observed in Nov. 2012.

The difficulty with the circular accelerators, however, is that the relativistic particles emit radiation while travelling perpendicular to the field in the bending region. This results in a significant loss of energy as the energy loss is found to be proportional to E^4. The size of the machine is therefore greatly increased. Further, the energy loss also scales with the rest mass of the radiating particle as $1/m^4$. For this reason alone, the energy in LEP never reached beyond 200 GeV even after upgradation till it was retired in Nov. 2000. Circular accelerators are thus suitable to accelerate heavy particles only, like protons in LHC.

Linear accelerators (linac) are preferred to accelerate light particles like electrons and positrons. Here, the beam is accelerated in a straight line trajectory. The energy is proportional to the accelerator length as the beam travels through a cavity only once. In a linear collider, two beams are accelerated in two opposite directions and made to collide at the intersection point (IP) and discarded in to the beam-dump. A new bunch is used each time. The advantage of the linac is that there is no energy loss due

to synchrotron radiation. The energy is proportional to the number of RF cavities and the gradient of each cavity but does not depend on particle mass. Maximum luminosity is obtained by increasing the frequency of collision and reducing the area cross section of the beam.

Cyclotrons are yet another type of accelerators which can accelerate heavy ion like U to high energies up to 350 meV and the superconducting magnets again play a pivotal role in achieving such high energies. The ions circulate spirally under the influence of a vertical magnetic field and an RF across two gaps between two dees. The RF frequency matches with the cyclotron frequency of the charged particle and accelerate it each time it crosses the gap. The beam is finally extracted through an extraction system and used to bombard targets for the production of radioisotopes.

In this chapter, we will focus on the role of superconducting magnets in all these types of accelerators with special reference to LHC, its successors, high luminosity LHC (HL-LHC) and Future Circular Collider (FCC), International Linear Collider (ILC) and also mention about the recently launched electron–ion collider (EIC) at Brookhaven National Laboratory.

10.2 Role of Superconducting Magnets in Accelerators

Superconducting magnets have become the essential part of all types of accelerator designs. Successful operation of LHC owes much to the high-field superconducting magnets used along its 27 km circumference. LHC is using more than 1600 superconducting dipole and quadrupole magnets and many other magnets. The future International Linear Collider (ILC) will have as many as 715 superconducting quadrupole magnets and 1374 correctors. Besides many other types of magnets, the dipole magnets and quadrupole magnets constitute the backbone of any high-energy accelerator. To achieve transverse field, the dipoles are made of long saddle-shaped coils or the simpler racetrack coils and are installed in two halves all along the entire curved part of the ring. Quadrupole superconducting magnets are used to keep the beam well focused. In addition, there are higher-order magnets, the correctors, to compensate for the field errors arising in the main dipoles and quadrupoles. These field errors are caused by the persistent magnetization currents generated in superconducting filaments during field ramping and also by the manufacturing errors/tolerances.

Circular accelerators are built in long underground circular tunnels so that the beam keeps circulating to get repeated acceleration in SRF cavities by the accelerating voltage. The beam energy obtainable in a relativistic accelerator is approximately given by the equation $E = 0.3\, B_{\text{dipole}} \times R$, where E is the energy in TeV, B_{dipole}, the dipole field in tesla and R the effective radius of the tunnel in km. For high energies, therefore it is imperative to have very long tunnels and high magnetic field depending on the budget available. All pervading Nb–Ti/Cu cables have been used in almost all the modern high-energy accelerators. This superconductor has an upper limit of producing field of 9 T when operated below 2 K. For field 10–15 T, attempts are being made to develop Nb_3Sn magnets. Some proto-type Nb_3Sn dipoles and quadrupoles

have already been built and tested primarily at CERN and Fermi Lab. (USA). An excellent and comprehensive book has been written by Mess, Schmuser and Wolff [1] on all aspects of superconducting accelerator magnets. A useful review article had also been published earlier by Schmuser [2].

10.3 High-Energy Accelerators Using Superconducting Magnets

Below, we give a brief account of all the superconducting accelerators built prior to LHC. The experience gained through the operation of these accelerators led to the design and construction of the most powerful accelerator LHC which promises to unravel the mystery of matter.

10.3.1 Tevatron (FNAL, USA)

Tevatron was the first high-energy hadron collider built at Fermi National Accelerator Laboratory (FNAL), near Chicago, USA, using superconducting magnets and commissioned in 1983. It was a proton–antiproton collider which achieved an energy of 1 TeV. It had warm iron yoke putting less low temperature load but high heat input to the cold mass. The entire EM forces are taken by the collars. It accelerated protons and antiprotons in a ring of 6.3 km circumference. By 1987, it attained a beam energy of 0.9 TeV thus a collision energy of 1.8 TeV, the highest energy ever attained till that time. It used 774 dipoles each 6 m long, 224 quadrupoles magnets and several correcting magnets. The dipoles generated a field of 4.4 T at 4.4 K. Cu/Nb–Ti cables had been used for magnet coils. Tevatron has been shut since September, 2011 especially because Large Hadron Collider (LHC) at CERN started operation and producing much higher collision energy (13 TeV). Nevertheless, Tevatron has become a trendsetter for building high-energy beam colliders using high-field superconducting magnets. Over more than two and half decades of operation, this collider yielded profound data of 500 trillion collisions from year 2001 onwards. The analysis of the data led the Fermilab team of researchers to believe strongly the possible existence of all illusive Higgs Boson which has since been confirmed from LHC's data.

10.3.2 Hadron Electron Ring Accelerator (HERA), DESY, Hemberg, Germany

Soon, the technology of building hadron collider using superconducting magnet was adopted by DESY (Deutsches Electronen Synchroton), Hemberg, Germany, to build their electron–proton beam collider, HERA. The accelerator started operations in 1989 and continued until it was shut down in 2007. Unlike the Tevatron, the HERA had a cold iron yoke enclosing the high strength Al-alloy ($AlMg_{4.5}Mn$) collars. It was installed in a tunnel 6.3 km long and up to 25 m deep underground. It had two storage rings mounted one at the top of other. Normal room temperature magnets had been used in the electron storage ring which ran below the proton storage ring. Superconducting magnets have, however, been used in the proton ring only. The proton ring employed 422 main dipole magnets to provide 5.3 T field for beam bending and 244 main quadrupoles for beam focusing. Four dipoles, four quadrupoles, six sextupoles and correction magnets were grouped together as one 47 m long module along the curved path. These magnets had two-layered coils and operated at 4.2 K. The electron ring used conventional magnets, 456 main dipoles providing a field of 0.17 T and 605 main quadrupoles. One dipole, one quadrupole, one sextupole and a few correction dipoles were grouped in to a 12 m long module. Old accelerators were used to pre-accelerate the proton beam. The last accelerator was PETRA which accelerated the electron beam to 14 GeV before injection in to HERA. Sixteen four-cell cavities with an accelerating field of 5 MV/m were used to accelerate the beam to a final energy of 0.92 TeV.

10.3.3 Superconducting Super Collider (SSC), Texas, USA (Abandoned)

The SSC was the most ambitious collider project conceived during mid-1980s in USA and finally sanctioned in 1991. The project was, however, abandoned due to high cost involved, just two years later. It was aimed at accelerating proton to energy 20 TEV thus producing a collision energy of 40 TeV. It was to be a chain of five accelerators pre-accelerating proton to 2 TEV before being finally injected in to the SSC. It was to be a two racetrack like rings with 70 cm separation. More than a total of 9600 superconducting magnets were envisaged to be used. These included 7860 main dipoles, 1360 main quadrupoles, many corrector magnets and 648 special magnets for directing beams to six collision points. The design and development work on dipoles were carried out by Fermilab and BNL (Brookhaven National Lab). The R&D work on quadrupoles was done by Lawrence Berkeley Laboratory (LBL). The dipoles were 16.6 m long to produce a field of 6.6 T at 4.35 K, whereas the quadrupoles were 3.3 m long and to produce a field gradient of 230 T/m at 4.35 K. The dipoles were two-layered Cosine θ coils wound using Cu/Nb–Ti cable with an inner diameter of 4 cm. Coils were collared and closed with a split yoke consisting of lamination of the

arc accurately die-punched sheets of low carbon steel and 1.5 mm thick. Yoke too formed the part of the cold mass cooled by supercritical helium at 4.15 K at 4 atm. pressure. Many full-scale magnets were built and tested successfully for their critical performance as per the quality assurance codes. Many problems related to quench and training were solved. Alas! the project was dropped soon after it was sanctioned for lack of funds.

10.3.4 Relativistic Heavy Ion Collider (RHIC), BNL, Upton, USA

RHIC was built by Brookhaven National Lab, (BNL), Upton, USA. It has been under operation since 1999. Until 2010, it was the highest energy collider in the world, now taken over by LHC at CERN. But it is the only collider which accelerates spin polarized protons. Positively charged heavy ions and/or protons circulate in opposite directions at 99–99.5% of the speed of light, in two independent rings, hexagonal-shaped and 3.8 km in length. A total of 1740 superconducting magnets have been used in the two rings. Dipoles produce a field of 3.46 T at an operating current of 5.1 kA. Out of 1740 magnets, 396 are the main dipoles and 492 quadrupoles. Rest of the magnets are the corrector magnets. The dipole magnet is 9.45 m long, the coil I.D. 80 mm and O.D. 100 mm. The inner and outer diameters of the yoke are 119.4 mm and 266.7 mm, respectively. An important feature of the magnets of RHIC is that there are no separate collars between the coils and the yoke. The yoke itself serves the purpose of collars and provide required pre-stress to the coil. The yoke is the part of the cold mass. The collision between gold ions resulted in a record temperature of more than 4 trillion K creating conditions that might have existed moments after the 'big-bang'. It has six intersection points where the heavy ions up to gold collide and produce an energy of 0.1 TeV per beam. RHIC upgrade will facilitate collisions between positively charged and negatively charged particles.

10.3.5 Large Hadron Collider (LHC), CERN (Switzerland/France)

LHC is the world's largest particle accelerator, built by CERN at Geneva Switzerland. It has a tunnel 27 km long and 50–175 m deep underneath the border between France and Switzerland. LHC attained a collision energy of 13 TeV and produced 3.4×10^{14} collisions till it was shut down on 3 December 2018 for two years for high-luminosity upgrade. It collected over 5 inverse femtobarns (5 fb^{-1}) data till before the shut down. Proton beams are pre-accelerated by old Super Proton Synchrotron (SPS) to 450 GeV before being injected in to the LHC. SPS uses normal magnets. The yearly data some

25 petabytes/year are analysed in 140 computing centres spread over 36 countries and connected by the world's largest computing grid.

The LHC has used about 6000 superconducting magnets, out of which 1232 are the main dipoles along the curved path of the beam pipe. These are 15 m long with 56 mm inner diameter. The number of quadrupole magnets is about 400 and the rest are different types of magnets including multipole corrector magnets. All the magnets are divided in to eight sectors for operation powered by eight power supply systems. Each sector has 154 main dipoles and 45 quadrupoles. The dipoles produce a field of 8.34 T. To produce such high fields using Cu/Nb–Ti cables, the magnets are operated at a reduced temperature of 1.9 K using superfluid ^{4}He. The conductor is a Rutherford cable 15.2 mm wide with 36 strands of 0.825 mm diameter and each strand having 6425 filaments of 6 μm dia. each. One unique feature of LHC is that the main magnets around the two beams are collared together and contained in one yoke. This makes the cold mass a compact system and much economical.

Schematic cross sections of the main dipole magnets of these accelerators are reproduced in Fig. 10.1.

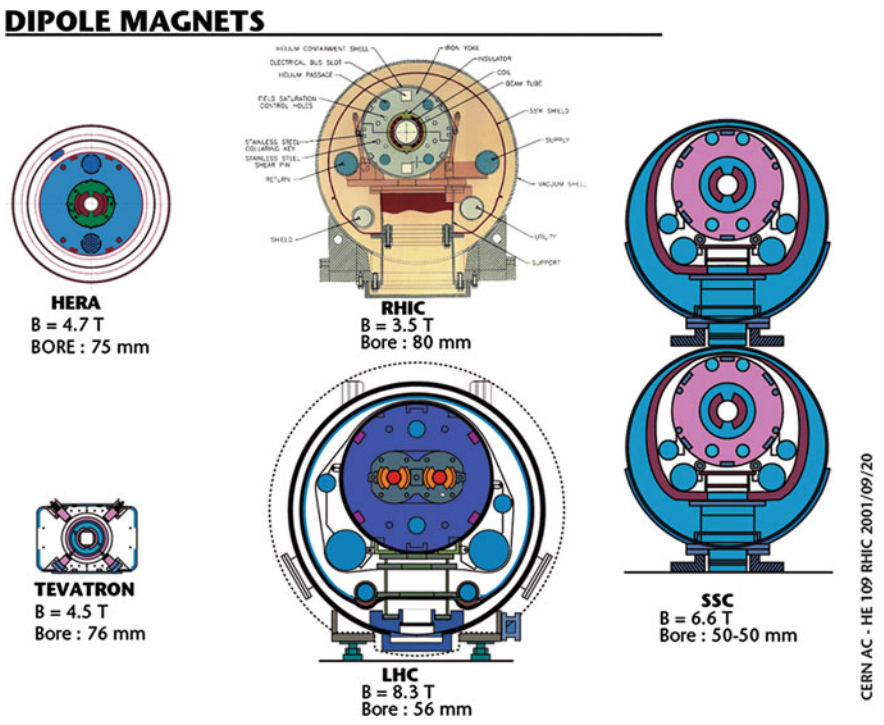

Fig. 10.1 Schematic cross section of the main dipoles of the five accelerators, HERA, RHIC, Tevatron, LHC and SSC [3] (Courtesy Lucio Rossi, CERN Photo Library and with permission from 'CAS')

10.4 Unique Features of the Accelerator Magnets with Special Reference to LHC

In this section, we will discuss important characteristics of the accelerator magnets with a special reference to LHC which has been built with several new features over the past accelerators. A good number of papers have been published by Lucio Rossi of CERN on all aspects of LHC magnets and cryogenic system. I refer to a few of them [3–7]. The magnets are the most critical components of any accelerator. A dipole magnet is far more longer than its aperture; the conductor therefore runs parallel to the beam except a small part which bends at the coil ends. It is built in two halves with current flowing in opposite directions and producing required field in a direction transverse to the beam as shown in Fig. 10.2. Dipole magnets are not straight, instead they follow the curvature of the beam pipe. The deviation from a straight line is, however, so small in comparison with the dipole magnet length that it is hardly noticed. This curvature makes the design of the magnets quite complicated and difficult. Computer codes like TOSCA, ANSYS, POISSON, DXF and ROXIE have been developed and used for magnet designs. ROXIE (**R**outine for the **O**ptimization of magnet **X**-sections, **I**nverse field calculation and coil **E**nd Design software programme) Package was developed by Rossenschuk [8, 9] for LHC magnets and is widely used by many institutions for magnet design. It is a versatile and easy to use programme. It is used to give integrated design of a superconducting magnet, including the conceptual design, optimized field, coil ends design, end spacers, cross sections of the coils, collars and the iron yoke and produces detailed drawings. 'End spacers' design is interfaced with CAD-CAM for the five axes CNC milling machines to produce these pieces. It has the capability of tracing manufacturing errors which affects the field quality.

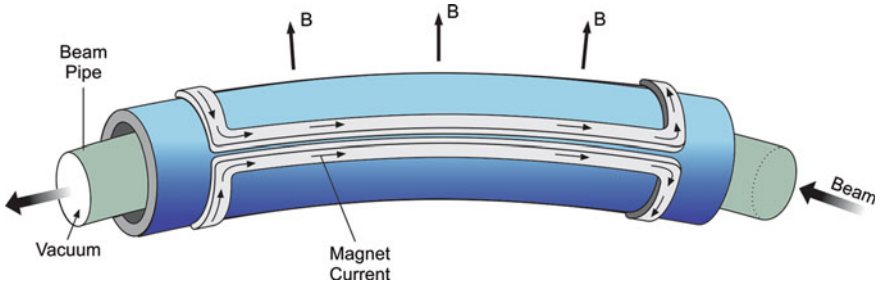

Fig. 10.2 Dipole magnets produce transverse field to bend the beam along the curved path. Current in the two halves of the coil flows mostly longitudinally except short coil ends and in opposite directions

10.4.1 The Coil Geometry

A perfect dipole field can be produced [1] by a current sheet with surface current density distribution of azimuthal-type varying as Cosine ($n\varphi$). One obtains dipole, quadrupole and sextupole field for $n = 1$, 2, and 3 respectively. For perfect dipole field, such a coil geometry is obtained by the intersection of two cylinders [10] and also by the intersection of two ellipses (shaded parts) carrying equal volume current densities but in opposite directions as shown in Fig. 10.3a, b. A perfect quadrupole field can similarly be obtained by the intersection of two crossed ellipses as shown in Fig. 10.3c each quadrant carrying equal current densities but reversing the current polarity in alternate segments. A very common and well-known geometry of the current shell generating dipole field is shown in Fig. 10.4a and the current shell generating quadrupole field is shown in Fig. 10.4b. The value of the limiting angle φ of a dipole is kept 60° which eliminates sextupole ($n = 3$) but higher multipoles

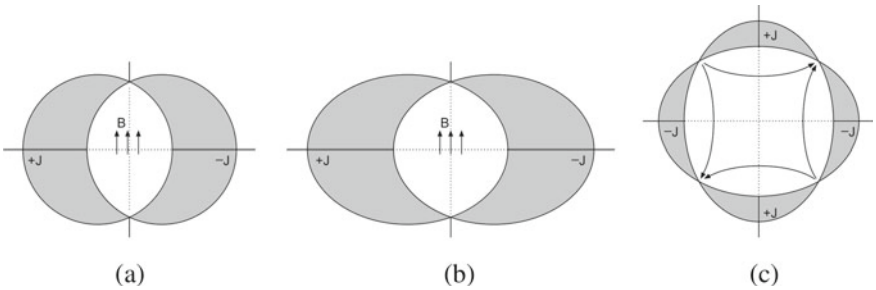

Fig. 10.3 **a** Perfect dipole field by intersecting two cylinders. **b** Perfect dipole field by two intersecting ellipses (both carrying uniform current but in opposite directions). **c** Quadrupole field generated by the intersection of two crossed ellipses

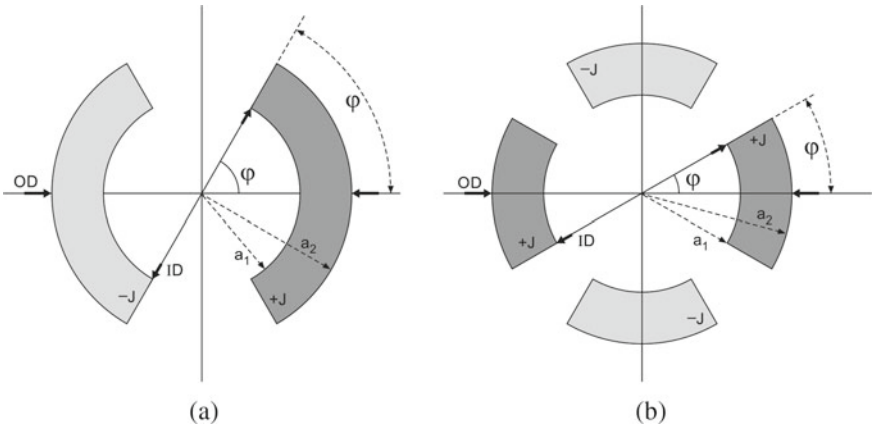

Fig. 10.4 **a** Current shell geometry with dipole symmetry and **b** quadrupole symmetry

like decapole ($n = 5$) and 12-pole do exist. These higher multipoles can only be eliminated by winding the shells in two layers. Similarly, the quadrupole current shells are wound in two layers to eliminate higher-order multipoles (Fig. 10.4b). The limiting angle of the quadrupole shell φ is 30° and for a sextupole 20°. The field homogeneity is further improved by introducing longitudinal wedges in the windings.

In a perfect dipole with a current density of J Cos φ, the field B is proportional to J and ΔR ($B \propto J \times \Delta R$) where ΔR is the coil thickness. To keep the volume of the coils within reasonable limits, we have to look for high J_c conductor for a given beam aperture. Further, these magnets are wound in two layers, and since the outer layer experiences lower field, one can operate the outer coil at much higher current compatible with the field. This reduces the coil volume too. Operating the two coils at different current levels will, however, be complicated because it requires two separate power systems and quench protection/detection systems.

Designing the coil ends is difficult as these are raised above the longitudinal winding. Bending of the conductor at the ends has to be carried out accurately and should be below the permissible strain limit of the conductor. The bends are of the shape of a saddle. To keep the end winding in position, suitable spacers machined from fibreglass–epoxy composites are inserted. Coil ends are impregnated with resin to fill the gaps between spacers and the winding and to obtain good finished surface for collaring.

10.4.2 The Collars

The dipole magnet coils are wound in two halves over the beam tube, both repelling each other. At high J_c and high field, these coils experience huge lateral force ($=J \times B$) with a large horizontal component, which is not self-supported like in a solenoid winding. This force is huge, of the order of several MN at the level of the field produced. The two halves are thus held together mechanically by strong clamps referred to as collars. Collaring is carried out in a large press to compress the coils to 100–120 MPa so that the collars remain compressed to a pressure of 60–90 MPa after the pressure is released. In LHC, the two dipoles around the two beam pipes are housed in a single cold mass system. Both the dipole coils are collared together and called ‘twin’. The collars used in LHC are made of stamped laminations of austenitic steel. HERA at DESY has used collars made of laminations of a strong Al–Mg–Mn alloy. The two halves are held in position together using pins and dowel rods. The collar material has to remain non-magnetic even after thermal cycling to LHe temperatures, cold worked during stamping or after welding. Protection sheets have been used between the coils and the collars which also provide ground insulation. Sometimes, very thin 3–5 mm skin spacers have been used in place of collars and all the compression to the coil is provided by the outside yoke. The field enhancement too increases because of closer proximity of the yoke with the coil. Quadrupole coils are collared individually.

10.4.3 The Yoke

The compression by collars is further enforced by the iron yoke fitted outside the collars. The yoke is used to reduce the fringe field outside the magnet to below 10 mT. At the same time, the yoke also enhances the magnet field. Warm (room temperature) as well as cold (cooled to LHe-magnet temperature) yokes have been used in different accelerators. Enhancement of field is higher when the yoke is part of the cold mass because of the close proximity of the yoke with the coil. Cold yoke only requires more cryogen and the magnet system takes little more time to cool down, which is not very important because accelerator magnets are not warmed-up and cooled-down frequently. Moreover, fast cooling is not desirable to prevent excessive thermal stresses. Enhanced field, however, allows the use of smaller operating current in the coil, which results in the reduction of stored energy and the consequent enhancing protection against quench. One drawback of the cold yoke is that the shrinkage in soft iron yoke is larger than in the coil after cool-down and therefore larger pressure has to be applied while compressing the yoke. Second problem could be the saturation of the yoke which may generate higher-order poles and distort the field. This has to be well accounted for during the design stage itself. RHIC, however, does not use collars at all; instead, the coils are compressed directly by the yoke.

In LHC, the yoke is 600 mm thick and made in two halves and put around the collars. The yoke is of cylindrical shape consisting of 1.5 m long packs of stamped laminations compressed together to a density of 98.5%. A cylindrical shell in two halves and of 10-mm-thick 316 LN steel then surrounds the yoke. Welding is carried out simultaneously on top and bottom parts under a pressure of 400 tons. After mounting electrical systems in place, the two end parts too are welded. All along the length of a dipole a total welding of 16 m is carried out. This 316 LN SS cylinder also forms part of the LHe-cryostat.

10.4.4 The Magnets

The magnets constitute the most critical part of an accelerator and more so the dipoles which produce high field quite close to the limit of Nb–Ti conductor. These magnets operate at high current. To minimize heat input to the cryostat, the number of current leads is cut down to minimum. All the magnets in one sector are therefore connected in series and powered by a single-sector power system using only one pair of current leads. The twin magnets and common collar and the yoke are installed in the same liquid helium cryostat. This whole assembly is commonly referred to as the ‘cold mass’. A schematic cross section of the cold mass is shown in Fig. 10.5. The dipole characteristic parameters are tabulated in Table 10.1. The stringent requirement of all the dipole magnets in the lattice is that they must produce almost identical field in magnitude as well as in quality. The field strength and the harmonic contents of all the dipoles must be same within the range of the order of 10^{-4} (one unit). This

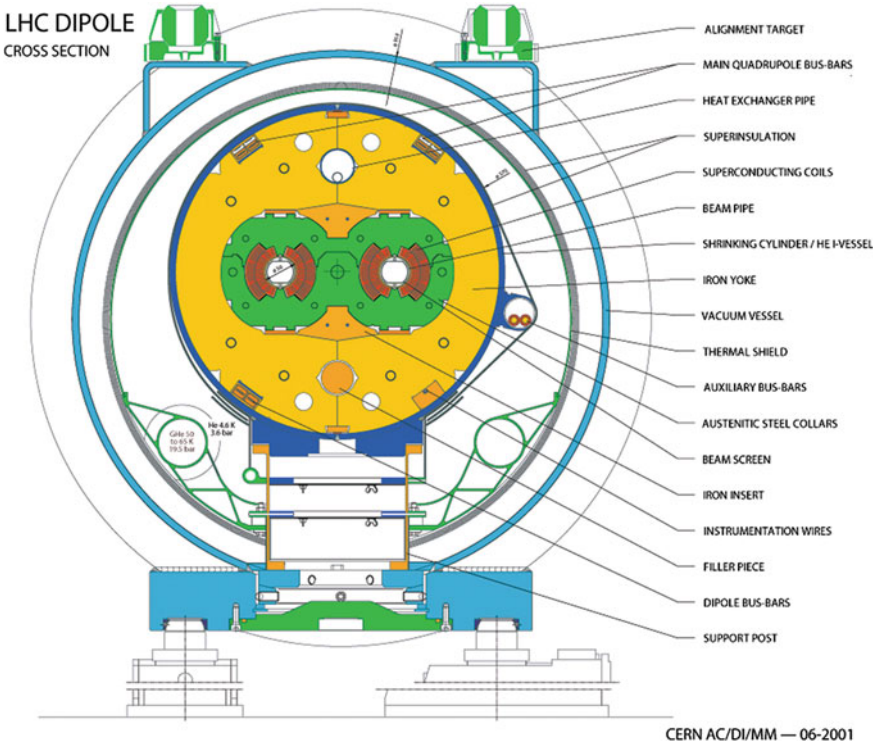

Fig. 10.5 Cross section of the compact cold mass of the main LHC dipole. The two dipoles of the two oppositely circulating beams are coupled together by a single austenitic steel collar and compressed within the same iron yoke [3] (Courtesy Lucio Rossi, CERN Photo Library and with permission from CAS")

Table 10.1 Important parameters of the main LHC dipole

Parameter	Unit	Value
Operating field	T	8.33 (can operate up to a max. 9.00 T)
Operating current	kA	11.85
Operating temperature	K	1.9
Coil aperture	mm	56
Distance between the two aperture axes	mm	194
Stored energy/channel	MJ	3.5 @ 8.33 T
Magnet length	m	14.3
Cold mass length	m	15.18
Cold mass O. D	mm	570

Data compiled from [5, 6]

means that the coils of two poles (top and bottom) of each dipole have to be identical and so should be for all the dipoles built at different locations. Each coil is wound in two layers using two different cables running at different current densities but same operating current. The geometrical dimensions of the two layers of all the magnets have to match within a variation of less than 100 μm. Small variation can cause appreciable change in the main field and the higher harmonics. These requirements call for precision winding and should be perfectly reproducible in all magnets.

The photograph in Fig. 10.6 shows the cutaway cross section of the twin aperture dipole magnet used in LHC. Each dipole is about 15 m long. All the dipole magnet systems (cold mass) alone occupy close to 20 km length of the tunnel.

The stringency of field uniformity equally holds for quadrupoles which too are wound in two layers and using the same cable as used for winding the outer layer of the main dipoles. A small shortfall (<10%) in the focal strength of a magnet can, however, be compensated by successive quadrupoles.

So far, the most favoured superconductor for all the accelerator magnets has been the Cu/Nb–Ti (Rutherford type) cables because of its superior mechanical properties and comparative large tolerance of stresses. The production procedures for manufacturing large quantities of Nb–Ti conductor are well established and standardized since the material is being produced commercially for over six decades. In an accelerator, the quantity of conductor used for winding large number of magnets is huge

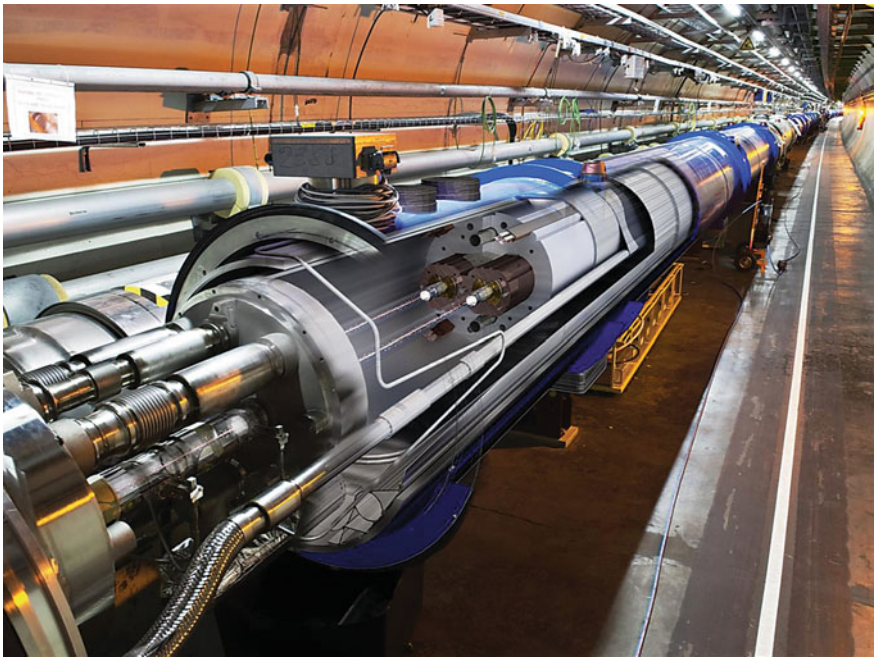

Fig. 10.6 Cutaway cross section of a twin aperture dipole magnet mounted in a 27 km long tunnel. All the dipoles together occupy nearly 20 km length of the tunnel (CERN Photo courtesy Ph. Lebrun)

and cannot be supplied by a single manufacturer. For field uniformity and field reproducibility, the total quantity of conductor produced by all the manufacturers has to be uniform within a small tolerance limit. LHC has used something like 1200 tons of cable, out of which the Nb–Ti is about 400 tons.

The quality control of the conductor starts from the compositional uniformity of the basic material, Nb–Ti, its processing, uniformity of filament size, the strand size and finally the braided cable dimensions. The strand diameter has to be uniform within 1 μm and the cable size to ±6 μm. The uniformity of the size of the cable is crucial to the conductor positioning in the coil and ultimately the field profile. To prevent degradation in the overall I_c of the cable, the strands must be compacted to no less than 90%. Equally crucial is the uniform distribution of current among the strands and the inter-strand resistance of a cable. CERN has devised an ingenious and cost effective technique for the production of Rutherford cable used for LHC. The strands are coated with a Sn–Ag alloy before they are cabled. The cable is then oxidized by heating it under controlled conditions in air. The technique, in fact, has proved a turning point in the successful production of Rutherford cable for LHC. The contact resistance is low also because the coil is pre-stressed to 80–100 MPa.

The most important parameter of the cable is its engineering critical current J_e. The microstructure of Nb–Ti is to be well controlled so as to have effective flux pinning. For stability, a copper to Nb–Ti ratio of 1.5–2 has been used for accelerator magnets. To boost J_e further, the Cu to Nb–Ti ratio has been reduced to 0.7–0.8 for future magnets with no deterrent to conductor stability and/or the quench protection.

To keep the inductance and the stored energy within limits, these magnet coils are optimized for high currents somewhere in the range of 10–13 kA. One has to keep in mind that the transverse field produced by (cosine θ) type coils is smaller than that produced by a simple solenoid coil for the same J_c and same coil thickness. The field in a solenoid is $B = \mu_0 J t$, whereas for a cosine θ coil, it is $B = ½ \mu_0 J t (\cos \theta)$. Here, J is current density and t the winding thickness. Rutherford cables capable of carrying such large current have invariably been used for accelerator magnets. Each cable has few tens of strands with high I_c value, braided together in a rectangular shape (see Fig. 5.10). The cable has a high compaction density of about 90%. The main parameters of the cable and the strand used for LHC dipoles are tabulated in Table 10.2.

Table 10.2 Parameters of the strands and the Cu/Nb–Ti Rutherford cable used for LHC dipoles

Strand			Cable		
Parameter	Unit	Value	Parameter	Unit	Value
Diameter	mm	0.825	Width	mm	15.1
Filament diameter	μm	6	Thickness @ 70 MPa	mm	1.48 ± 0.006
No. of filaments		6425	No. of strand		36
Cu/Nb–Ti ratio		1.9–2.0	Inter-strand resistance	μΩ	20–80
I_c @ 1.9 K	A	380 @ 7 T	I_c @ 1.9 K	kA	12.97 @ 7 T

Data compiled from [5, 6]

Well-microstructured Nb–Ti with effective pinning optimally has been serving well as high I_c conductor for accelerator magnets, nevertheless, suffers from the big problem of persistent (magnetization) current which can distort the field. These superconductors retain magnetization even when the field from its maximum value of 8.33 T is ramped down to the lowest injection value of 0.54 T. Since the critical current density is very high of the order of 10 kA/mm^2, the persistent magnetization current can be significant and can damage the field quality drastically. The magnetization scales as $M \propto J_c\ D_{eff}$, where D_{eff} is the effective diameter of the filament and J_c the critical current density. D_{eff} sometimes can be much more than the geometrical diameter, if the filaments touch each other or are coupled together in metal matrix due to small inter-filament separation. In such cases, the filaments are usually cladded with a barrier like Nb. Since we cannot afford a drop in J_c, we must reduce the filament diameter to the extent possible. For LHC application, a filament diameter of 6–7 μm was found ideal and selected. Still smaller filament diameter leads to much lower J_c values.

10.4.5 Training of Magnets

Training of accelerator dipoles assumes special importance because of the low Cu:Nb–Ti ratio of the conductor used and the coil running at very high-current density. It is almost impossible that the magnet attains its peak field and the peak operating current in the virgin run. The large EM forces may cause some movement of the strands or the cable in the coil winding and quench the magnet at a current which may be much lower than the maximum operating current for which the magnet is designed. In successive runs, the magnet quenches at increasingly high currents. After a few cool-down cycles, the magnet reaches a saturation point where the maximum current and field are achieved. The magnets are therefore 'trained' before being installed at their designated locations. The final quench current and the quench field so attained after training should be reproducible each time the magnet is operated and thermally recycled to room temperature. All the magnets are operated at a level little below the quench current values to make allowance for small variation in the performance of such a large number of magnets.

The training process is most expensive one as it involves huge quantity of liquid helium for such a large number of magnets but cannot be done away with. It is important that the training is irreversible and the magnets do not quench after their installation below the quench current value. A premature quench in a single dipole may cause a chain reaction, of the sort, and affect all the 154 dipoles which are connected in series in one sector. If one magnet quenches, energy from all other magnets in the sector has to be discharged safely. A quench in one magnet may result in the increase of temperature of all other magnets in a sector, above T_c, turning them normal. LHC did face this problem in Sept. 2008 within nine days of its first operation, when one main dipole magnet in sector 3–4 quenched due to a faulty electric connections and consequent mechanical damage and release of LHe.

This resulted in the damage of 50 expensive magnets. It took fourteen months to repair the damage and to bring back LHC to life in Nov. 2009.

At last, LHC succeeded in discovering all evasive Higgs Boson, first predicted by Peter Higgs together with five other physicists in 1964. The first indication came in July 2012 and the final announcement of the confirmation of Higgs particle was made in March 2013. Peter Higgs and Francois Englert were awarded the 2013 Nobel Prize in physics. The particle has a mass of 125 GeV/c^2, zero spin and zero electric charge. Its decay time is found to be 1.56×10^{-22} s.

10.4.6 The Quench Protection

Since quench cannot be ruled out in a superconducting magnet, it is very important to provide a most reliable and fool-proof quench protection system for accelerator magnets especially when the magnets are operating at high field. No sooner the hot spot is detected, the current should decay fast and the stored energy should spread over the entire coil so as not to allow excessive heating at the hot spot. Quench protection in LHC-type magnets is tricky because each magnet has large stored energy and a large number of them, 154, are connected in series and energized by a common source. Normal protection systems were found inadequate. LHC magnets have superconducting bus bars in parallel with magnet coils. In the event of a quench, Joule heat dissipation starts at the hot spot and the voltage increases. As soon as the voltage exceeds the opening voltage of the by-pass diodes, the current gets diverted in to the superconducting bus bars. This prevents excessive heating and rise in temperature beyond acceptable limit of room temperature. The current decays over a time constant ($=L/R$) which in LHC magnets is too large, R being very small. R is kept small because the quench propagation in the LHC conductor is slow at 20 m/s and $dR/dt = 10$ mΩ/s. Large time constant means it will take a long time to stop heat dissipation at the hot stop risking the magnet safety.

Dumping energy in an external resistor will need high resistance (~1 Ω) for LHC magnets which will induce high voltage of the order of 10 kV across the magnet which is too high and well above the prescribed limit of 1 kV. LHC magnets are protected by activating the SS strip heaters mounted between the coil winding and the collars. This helps in spreading the quench to the larger part of the coil and rather fast. The resistance R rises and the time constant decreases. The stored energy thus spreads uniformly across the whole coil without excessively increasing the temperature at the hot spot. This also avoids thermal gradients and consequent unwanted stresses in the coil. Since the resistive voltage and the inductive voltage have opposite polarity, they balance each other to great extent. As a result, the voltage rise in LHC during the quench does not exceed beyond 600 V.

The main parameters of all the superconducting colliders discussed above are summarized in Table 10.3.

Table 10.3 Summery of the specifications of the superconducting colliders discussed in the text

Parameter	Unit	Tevatron FNAL (USA)	HERA[a] DESY (Germany)	SSC TEXAS (USA)	RHIC BNL (USA)	LHC CERN (Europe)
Year of operation		1987	1989	Proposed 1991	1999	2009
Present status		Shut 2011	Shut 2007	Abandoned 1993	Working	Working
Tunnel length	km	6.3	6.3	87.1	3.8	27
Colliding species		$p^+ - p^-$	$e^- - p^+$	$p^+ - p^+$	Ions-proton	$p^+ - p^+$
Collision energy	TeV	1.8	0.92	40	0.2 (Au-p^+)	14
Main dipoles		774	422 proton ring only)	7860	396	1232
Main quadrupoles		224	244 (proton ring only)	1360	492	400
Dipole field	T	4.4	5.3	6.6	3.46	8.34
Operating Temp	K	4.4	4.2	4.35	4.6	1.9
Conductor used		Cu/Nb–Ti	Cu/Nb–Ti	Cu/Nb–Ti	Cu/Nb–Ti	Cu/Nb–Ti
Collar used		Yes	Yes	Yes	No, Yoke only	Yes
Yoke (iron)		Warm	Cold	Cold	Cold	Cold

[a]HERA has proton ring and electron ring one over the above. Proton ring has superconducting magnets and the electron ring normal magnets. The electron ring has 456 normal dipole magnets (1.7 T) and 605 quadrupole magnets

10.5 High-Field Magnets for Future Accelerators

The quest of high-energy community to achieve higher beam energy has never ceased. While world's largest accelerator, LHC at CERN was being built R&D on developing still high-field superconducting magnets had continued at CERN and other places notably in USA. The aim has been to build 15 T magnets in immediate future and 20 T magnets for a distant future. Obviously, in today's scenario, the only conductor available is the brittle A-15 Cu/Nb_3Sn composites. The next candidate for fields higher than 15 T could be Nb_3Al [11] of the same family. Another option is to use high-T_c superconductors like Bi-2223 or 2G YBCO after they are produced in sufficient lengths by cost effective technique and meet the stringent characteristic parameters set for accelerator magnets. Major efforts in this direction have been going on at several places like CERN, FNAL, BNL, LBNL, University of Twente (NZ) and other such individual places as well through mutual collaborations. So far,

these efforts have been directed towards using Nb_3Sn superconductor albeit produced by different techniques.

10.5.1 The Nb_3Sn Conductor for Accelerator Magnets

The biggest challenge to High-Field Accelerator Magnet (HFAM) programme stems from the brittle nature of the Nb_3Sn. The conductor is manufactured in preformed (Nb filaments in a Cu + Sn composite matrix) state. It is only after the coil is wound that the superconducting compound Nb_3Sn is formed in the final stage through a controlled heat treatment, what is generally termed as 'wind-and-react' technique. So far, this reaction temperature is quite high in the range of 650–700 °C which poses several problems related to electrical insulation and application of pre-stress etc. The 'react-and-wind' technique which is feasible for HTS like Bi-2223 and YBCO tape conductors is being pursued at some places. Extensive R&D efforts are being made to study the effect of bending dia. on the J_c of Nb_3Sn. One option being tried is to react the cable under bend position at a certain diameter so that the degradation by final diameter winding is cut significantly.

Nb_3Sn also suffers from poor ultimate tensile strength as compared to Nb–Ti and therefore needs re-enforcement. Cables with SS core have been produced and used for accelerator magnets. Conductors produced by four different techniques, namely the Modified Jelly Roll (MJR), the Internal Tin Diffusion (ITD), Powder In Tube (PIT) and Restack Rod Process (RRP), have been used for making model dipoles and quadrupoles by FNAL or in collaboration with BNL and LBNL [12]. We have discussed these techniques in some detail in Chap. 5. Conductors with $J_c \sim 2500$ A/mm^2 with a filament dia. of less than 50 μm and a Cu/Nb_3Sn ratio between 1 and 1.5 have been used for magnet fabrication. To keep persistent current under control, the filament dia. should be reduced further to ~20 μm or still lower. Further, the Cu/Nb_3Sn ratio needs to be brought down to 50–60% which in turn demands very effective quench protection procedures. Fine filaments seem to be possible with PIT technique. After over a decade of extensive research, it is now feasible to have magnets producing a nominal field of 12 T and the maximum field of 16 T. Advanced R&D studies on Nb_3Sn conductors have generated plethora of useful data on coil design, conductor evaluation, mechanical structure, coil pre-stress, quench performance, field quality and coil performance. These studies will go long way in establishing a reliable Nb_3Sn technology for 15 T and higher accelerator magnets.

10.5.2 Nb_3Sn Accelerator Magnets Development at FNAL

In the context of Nb_3Sn magnet development programme for future high-energy accelerators, it will be appropriate to discuss the high-field programmes pursued at

Fermi Lab. [12] for LHC IR upgrade, Muon Collider Storage Ring and future high-field accelerators. Fermi Lab. while developing this technology also had collaboration with BNL and LBNL. It built approximately 20 dipoles and 35 qudrupole magnets in 1, 2 and 4 m lengths and later another 14 quadrupoles, all 4 m long. Magnets have performed well up to a nominal field of 12 T, and a maximum field of 15 T. vast data with regard to cable parameters, collaring technique, pre-stress, mechanical structure, field quality and quench behaviour has been generated. The data have indeed laid the foundation for future development of Nb_3Sn accelerator magnet programme.

Fermi Lab. built base line dipoles for Very Large Hadron Collider (VLHC), generating 10–11 T field @ 4.5 K, in an aperture of 43.5 mm. The coil was of two-layer shell type with a mechanical structure which had a cold iron yoke 400 mm thick and a SS skin 10 mm thick but had no collars. It also developed Nb_3Sn quadrupoles for the LHC luminosity upgrade under the US-LARP (LHC Accelerator Research Programme) having an aperture of 90 mm and providing a nominal field gradient of 200 T/m. This value is the same as in the 70 mm aperture of the present LHC Nb–Ti quadrupoles. These magnets will also be operated at 1.9 K. These quadrupoles too have a two-layer shell-type coils with a 25-mm-thick SS collar, a 400-mm-thick cold iron yoke and a 12 mm-thick-SS skin.

For dipoles, keystoned Ruherford cable 14.24 mm × 1.8 mm size with 27/28 strands of dia. 1 mm was used. For quadrupoles, similar cable of the dimensions 10.05 mm × 1.26 mm, with 27 strands of 0.7 mm dia. each was used. The keystone angles of the two cables were 0.9 and 1.0 degrees, respectively. The maximum field generated by the dipoles was 12.05 T @ 4.5 K and a peak field of 12.6 T at the coil. The quench current was 21.06 kA. The quadrupoles operated at 1.9 K and provided a field gradient of 233 T/m with a peak field of 12.1 T at the coil. These values were obtained at a quench current of 14.07 kA. The characteristic parameters of the cables used and the performance parameters of the dipoles and quadrupoles [12] are given in Table 10.4. To prevent persistent currents caused by magnetization, the filament

Table 10.4 Characteristic parameters of the Nb_3Sn cables and the performance parameters of the model dipoles and quadrupoles built at FNAL

Parameter	Unit	Dipoles	Quadrupoles
Cable (keystoned Rutherford) size with SS core	mm	14.24 × 1.80	10.05 × 1.26
Keystone angle	degrees	0.9	1.0
Number of strand		27/28	27
Strand diameter	mm	1	0.7
Filament dia.	μm	~20	~20
Maximum field @ 4.5 K	T	12.05	
Field gradient @ 1.9 K	T/m		233
Peak field at the coil	T	12.6 (4.5 K)	12.1 (1.9 K)
Quench current	kA	21.6	14. 07

Cables used are produced by MJR, PIT and RRP techniques. Data compiled from [12]

size should be kept below 20 μm without lowering J_c. The eddy current effects are dependent upon the twist pitch of the strand and of the cable, the matrix resistivity and the inter-strand resistivity. These effects have been suppressed by the insertion of a SS core in the cable which increases the inter-strand resistance and also by having well twisted strands.

The strands used in cables for the magnets were made following three different methods, namely MJR, PIT and RRP. The J_c of the strands produced by the three techniques was in the range of 2–2.8 kA/mm^2 and filament size 50–100 μm. The insulation studied were the ceramic tape, S-2 glass sleeve and E-glass tape. Ceramic insulation proved to be the best from the coil fabrication point of view but it is rather thick and more expensive of the three. Ceramic tapes was used for all the dipoles and S-2 and E-glass sleeve for quadrupole magnets.

To handle the coil processing, FNAL used a ceramic binder which after curing holds rigidly all the components of the coil like wedges, pole blocks etc. and enhances the mechanical strength of the electrical insulation. During heat treatment, this binder turns in to fine ceramic particles serving as filler material during the impregnation of the coil. So far, the magnets have been impregnated with epoxy CID 101 K. Efforts are on to find an epoxy which is more resistant to hard radiation.

Brittle Nb_3Sn coils and the need for pre-stress pose serious challenge to the mechanical structure design. A thick SS shell structure was used for some magnets and a SS collar supported by SS skin for others. Two Al-clamps pre-stress the dipole coils to 20 MPa at room temperature. The final pre-stress of 100–120 MPa at 4 K is provided by the yoke and the skin. In quadrupole magnets, the coils are stressed to 30–35 MPa by the collars and to final pre-stress of 110–150 MPa by the SS skin. Control spacers have been used to prevent over-compression during yoking.

10.5.3 EuCARD Nb_3Sn Dipole Magnets

The European Coordination for Accelerator R&D (EuCARD) project was aimed at developing technologies for future accelerators in Europe with higher energies and higher luminosities. Its Work Package-7 relates to the development of high-field Nb_3Sn magnets for accelerators. One of the key objectives of this work package was the fabrication of a 1.5 m long dipole magnet with a 100 mm aperture and a bore field of 13 T. This will replace the present Nb–Ti based dipole magnet of FRESCA, the Cable Test Facility at CERN, and has been code named as FRESCA-2. The magnet was put under operation in 2013.

The detailed design of the model FRESCA-2 dipole has been given by Milanese et al. [13] and a status report at the end of 2012 has been published by Ferrasin et al. [14]. A block layout has been preferred for the coil design in place of a Cos θ configuration. It has two coils each having two layers. The first coil (inner) consisting of layer 1 and layer 2 has 36 turns and is wound over a Ti pole with 100 mm diameter hole. The second coil (outer) consisting of layer 3 and layer 4 is wound with 42 turns around an iron pole. Each coil has a double pancake structure and wound using

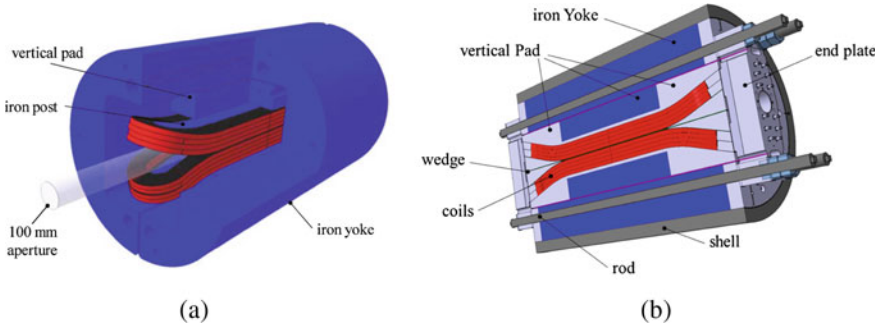

Fig. 10.7 **a** Cutaway sectional view of the FRESCA-2 dipole coils and the beam aperture. The coil ends are bent upwards supported by wedges [13]. **b** Longitudinal cross section of the FRESCA-2 dipole coils (© CEA/IRFU, courtesy P. Manil, J.-F. Millot)

single length of the conductor, reacted and impregnated separately. Insulating inter-layer shims (0.5 mm) and inter-coil shims (1.5 mm) are used. The coil ends are bent upwards at an angle of 17° to make room for the 100 mm aperture as shown in Fig. 10.7. The bent coil ends are supported by steel wedges.

FRESCA-2 design phase has been funded by the European Commission under the framework of EuCARD under the Grant Agreement n° 227,579.

The salient feature of the design of FRESCA-2 is the use of the so-called bladder and key concept developed earlier by LBNL. Horizontal and vertical pads have been used between the coils and the yoke made of 5.8 mm iron laminations compressed by SS end plates. The pads transfer the entire force to the 'split iron yoke. The iron yoke covers the entire coil length and is fitted in to a 65-mm-thick pre-tensioned (with bladders) cylindrical shell made of a 7075 Al-alloy. Ultimately, the entire force is contained by the shell. The shell shrinks more than the other parts of the assembly during cool-down and pre-compresses the coil further. The mechanical support design of FRESCA-2 ensures sufficient pre-compression on the coil to counter Lorentz force effectively as the current keeps rising during the energization of the magnet. It also keeps the peak stress under limit in the cool-down state. In the cool-down state, the maximum horizontal stress observed is 150 MPa at 13 T field.

The presence of iron vertical pads close to the second coil (layer 3 and 4) and the iron yoke makes a significant impact on the field strength inside the bore as well as on the peak field at the coils. The target field of 13 T is achieved at a magnet current of 10.8 kA instead of at 12.8 kA that would have been required without iron. It also reduces the peak field from 13.9 T to 13.2 T. Lorentz force, however, remains unaffected. The fringe field at a distance of 1 m, too, decreases from 150 to 100 mT.

The cable used for winding is a Rutherford cable of the size 20.90 mm × 1.82 mm (pre-reacted) with 40 strands of 1 mm diameter. Each strand contains 192 filaments of ~48 μm diameter and a Cu/Nb_3Sn ratio of 1.3. Strands are produced by PIT method as well as by the RRP technique. The magnet design takes in to account the cable size increase during reaction. The cable size after reaction turns 21.32 × 1.89 mm. The strand reaches a critical current density, $J_c = 2450$ A/mm^2 (4.2 K,

Table 10.5 Parameters of the magnet and strand/cable used for FRESCA-2 dipole produced by PIT technique

Cable/strand parameters	Unit	Value	Magnet parameters	Unit	Value
Cable type		Rutherford	Aperture diameter	mm	100
Cable size (before reaction)	mm	20.9 × 1.82	Outer diameter of the magnet	m	1.03
Cable size (after reaction)	mm	21.32 × 1.89	No. of turns in layer 1 and layer 2		36
No. of strands		40	No. of turns in layer 3 and layer 4		42
Strand diameter	mm	1	Bore field (4.2 K)	T	13
No. of filaments		192	Magnet current at 13 T	kA	10.9
Filament dia.	μm	~45	Stored energy(13 T)	MJ	4.6
Cu:SC ratio		1:3	Quench protection		Resistors + heaters
Strand J_c (4.2 k, 15 T)	A/mm^2	1400	Coil fabrication		Wind and react

Data compiled from [12–14]

12 T) and 1400 A/mm^2 (4.2 K, 15 T). Cabling brings down the J_c by about 5%. The cable is insulated with a 0.2-mm-thick braided S2 glass fibre. The strand and cable parameters are given in Table 10.5.

The stored energy of the FRESCA-2 magnet is extremely high, 4.6 MJ (Table 10.5) and therefore quench protection system becomes a critical part of this project. An efficient protection system, based on dump resistors and quench heaters, has been provided. The external dump resistor is of 95 mΩ so that the voltage at the magnet terminals does not exceed 1 kV. The heaters are SS strips 25 μm thick and 12 mm wide. These heaters are mounted on the outer surface of each layer covering nearly 50% of the surface area available. The response time from the initiation of quench to activating heaters is expected to be less than 40 ms and the maximum temperature to be 150 K.

10.6 Common Coil High-Field Dipole Magnets—A New Approach (LBNL)

An innovative design, the so-called common coil design earlier proposed by Gupta [15, 16] has been pursued actively at LBNL. This design is also sometimes referred to 2-in-1 dipole. The salient feature of the common coil design is that the coils are of simple racetrack type and a single pair of coils provides opposing high field to both the apertures aligned now in vertical direction (one over the other), making it most

cost effective. The bend diameter of the coils is thus much larger than in LHC design as this is now determined by the separation between the two apertures and not by the small aperture diameter. This is extremely crucial for the Nb_3Sn conductor which is very brittle. Use of 'react-and-wind' Nb_3Sn conductor also becomes a possibility. LBNL has already demonstrated [17] successfully a 6 T prototype dipole magnet (RD-2) based on common coil design and using Nb_3Sn conductor. This magnet used a Rutherford cable of the size 12.34 mm × 1.45 mm containing 30 strands of Nb_3Sn 0.808 mm dia. manufactured by Teledyne Wah Chang Albany. The strand J_c was only 610 A/mm^2 (12 T, 4.2 K). This was the precursor to the later 15–16 T racetrack dipole magnets built at LBNL.

LBNL built and tested [18] its first 14 T racetrack common coil dipole (RD-3) using Nb_3Sn conductor with a J_c of 2000 A/mm^2 supplied by Oxford Superconducting Technologies (OST). At 14 T the total horizontal Lorentz force turns out to be ~12 MN over a 780 mm coil length which tries to push the coil windings apart. The mechanical support structure was designed to withstand such large forces. The inflatable bladder and interference key system has been employed for RD-3. The design of the cross section of the RD-3 dipole is shown in Fig. 10.8. The bladders installed between the coil pack and the iron yoke work as an internal press compressing the coil packs to 70 MPa. It also provides a tension of 155 MPa to the surrounding 40-mm-thick aluminium shell. Next, the keys are inserted and the bladders are deflated and removed leaving a tension of 140 MPa on the aluminium shell. This stress rises to 250 after cool-down due to the thermal mismatch between the yoke and the shell. The magnets use 3 modular coils. The two 10 mm aperture beam pipes are inserted between the coils.

During training, first quench occurred at 8.1 T and the field reached 14 T after 35 quenches. No quench occurred up to this field after thermal cycling. Quenches below 13.7 T were found to be caused by conductor movement in the inner coil module

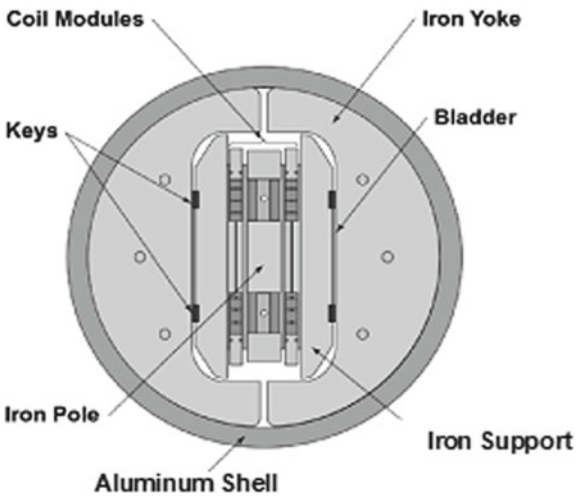

Fig. 10.8 Cross section of the 14 T common coil dipole magnet built at LBNL (RD-3) [18] (Courtesy, 'Lawrence Berkeley Nat'l Lab')

located in high-field region and quenches above this field originated in the outer coil modules. A record field of 14.7 T was achieved which was close to the short sample limit of the conductor in the two coils. No degradation in J_c was thus observed by cabling or due to Lorentz forces. The mechanical structure too withstood the forces as per the prediction made by TOSCA and ANLYS models.

10.7 The 15 T HD-2 Dipole

LBNL continues to carry forward the common coil dipole development programme with the ultimate aim of generating a field of 16 T in a bore of 40 mm dia. LBNL built one racetrack-type dipole, code-named HD-1 which generated 16 T in a bore dia. of 8 mm. The next target was to increase the bore dia. to 35 mm and generate a field of 15 T. Ferracin et al. at LBNL [19, 20] achieved 15 T in a 36 mm dia. bore field in a 1 m long dipole, code-named HD-2. The design is again based on the simple racetrack coil geometry, the block-coil module configuration and the bladder-interference key technology. The cross section of HD-2 is shown in Fig. 10.9. HD-2 has two double-layer coil modules. Each module has two layers. Coil 1 is wound on a Ti-alloy pole having a central cut-out for the bore pipe and has 24 turns. Coil 2 has 30 turns wound on another Ti-alloy pole. The coil ends are flared and supported by Al-bronze wedges with a central cut-out for the beam pipe. The two coils are separated by a SS mid-Plane sheet 1.37 mm thick.

A Rutherford Nb_3Sn cable (22 × 1.4 mm) of 'wind-and-react' type consisting of 51 strands of 0.8 mm dia., Cu/SC ratio 0.94 has been used. Strands were supplied by 'Oxford Superconducting Technologies (OST)' and the cable was fabricated at

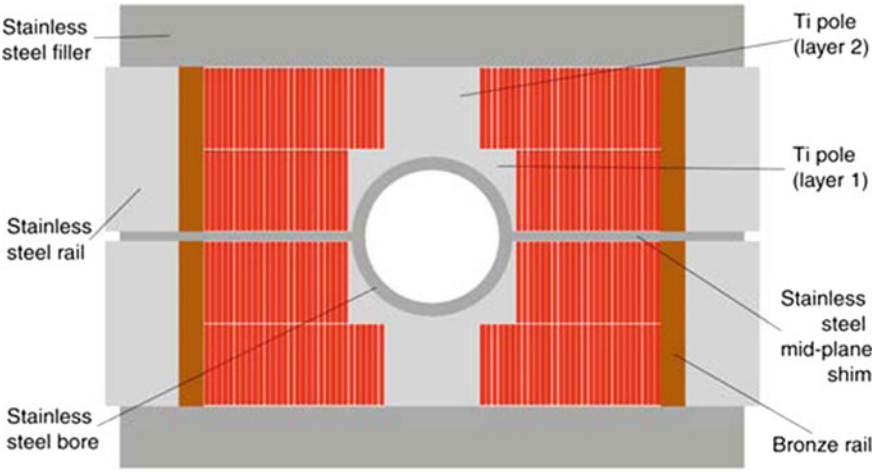

Fig. 10.9 Schematic of the cross section of the HD-2 dipole magnet [20] (Courtesy, 'Lawrence Berkeley Nat'l Lab')

LBNL. The strand with 54/61 sub-elements was produced by RRP technique. Strand J_c was 2800–3000 A/mm^2 (4.2 K, 12 T). The support structure is quite similar to the dipole RD-3 and consists of the outer 41-mm-thick Al-shell pre-tensioned using inflatable bladders and the interference keys. The iron yoke is made in two halves with 50-mm-thick laminations.

HD-2 produced an accelerator quality bore field of 15 T at 4.2 K. Field harmonics have been suppressed to acceptable level. The design could suppress persistent current induced effects quite significantly.

10.8 Work on the Design of 15 T Nb_3Al Dipole

Yet another programme on the design and development of a 15 T dipole based on coil block concept is going on using Nb_3Al superconducting cable. Yamada et al. [21] have been carrying out this work under a collaboration between Fermi National Accelerator Laboratory (FNAL), National Institute for Material Science (NIMS) and High-Energy Accelerator Research Organization (KEK). A Rutherford cable (13.93 mm $\times$ 1.84 mm) containing 28 strands (1 mm Dia.) of Nb_3Al produced by the so called, Rapid Heating Quench and Transformation (RHQT) process is slated to be used for the dipole. The RHQT technique has already been discussed in Chap. 5. The strand has a non-Cu J_c of 1000 A/mm^2 (15 T, 4.2 K). The filament dia. is 50 μm and the Cu:Nb_3Al ratio 0.5. Nb_3Al is known to have much larger B_{c2} and has better stress tolerance than the Nb_3Sn conductor. NIMS has already produced a field of 19.5 T in a background field of 15 T using this material. The dipole has been designed using ROXIE and the stress analysis carried out using ANSYS. The total stress at the mid-plane due to Lorentz force is 85.4 MPa and the horizontal stress at the outer surface of the block coils is 67 MPa at 4.5 K. Both are well within the tolerance limit of the conductor. The biggest fall-out of the accelerator programme has been the emergence of the state-of-the-art technologies for the manufacture of high-current efficient superconductors.

10.9 Linear Colliders with Special Reference to ILC

As discussed in Sect. 10.1, linac is a preferred option for accelerating light particles like electrons and positrons, as the energy loss due to synchrotron radiation is no longer a major problem. In 2004, the International Committee on Future Accelerator (ICFA) had recommended superconducting RF cavity (SCRF) technology for future accelerators. The three large accelerators, namely Next Linear Collider (NL) at SLAC, Global Linear Collider (GLC) in Japan and Terra Electronvolt Energy Superconducting Accelerator (TESLA) in Germany decided to pool their efforts together and build International Linear Collider (ILC). In ILC, electrons and positrons will

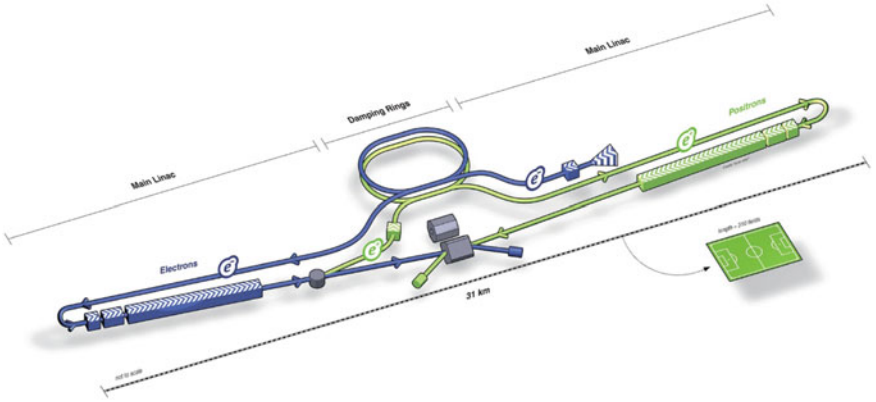

Fig. 10.10 Schematic layout of the ILC [22]. ILC conceptual diagram (© ILC GDE)

be accelerated in linear accelerators in opposite directions and collide with a collision energy of 500 GeV which could be upgraded to 1000 GeV (1 TeV) later. It will be 30 km long to start, with a provision of extending up to 50 km. The site of location of the ILC is expected to be one of the two sites selected in Japan's mountainous regions, Kitakami (Tohoku Prefecture) or Sefuri (Kyushu Prefecture). The ILC will have 13,000 magnetic elements out of which more than 2300 will be superconducting. Tompkins et al. [22] have reported the major superconducting magnets need for the ILC. A schematic diagram of ILC [22] is shown in Fig. 10.10. Electrons are produced by striking a gallium-arsenide photocathode with a nanosecond laser. The electrons are also made to move through a helical undulator to create photons. These photons in turn produce a pair of electron and positron when they strike a titanium target. The positrons proceed to be accelerated in the main linac, whereas the electrons and the remaining photons are dumped. Positrons are accelerated in a separate linac. After acceleration, both the beams collide and the fragments are picked up by two detectors.

Evidently, the collision energy of the ILC, initially at 500 GeV, is much smaller than the collision energy of LHC, but use of smaller particles, electrons and positrons with higher accuracy results in an unprecedented precision. It is expected that the ILC can analyse the data accurately and can verify if the Higgs boson is the same as predicted by the standard model of particle physics.

10.9.1 Superconducting Magnets in ILC

The ILC Reference Design Report (RDR) [23] was presented in 2007. As per the design report, superconducting magnets will be used in ILC to transport beam all along the accelerator length. ILC will use 2333 superconducting magnets out of a total of more than 13,000 magnets which will be used in the entire machine. The main

superconducting magnets are: 715 quadrupoles to focus the beam and 1374 dipole correctors to steer the beam. In addition, there are 12 sextupoles, 14 octupoles, 16 simple solenoids, 160 wigglers and 42 undulators. To a large extent, the success of the collider will depend upon the precision with which the magnets are designed, manufactured and positioned. The field quality for most of the length of the collider should be few parts in 10^4 the beam size being only 6 nm $\times$ 600 nm. In a linear accelerator, the magnets must meet several stringent requirements such as discussed below.

The magnet centre field stability should stay within an accuracy of 5 μm during the operation of the quadrupoles and the beam-based alignment (BBA) process up to a 20% change in the focusing field. Beam alignment is extremely critical in this accelerator to keep on track such a small size beam for collision. Horizontal and vertical dipole correctors are used in the quadrupole magnets to correct all magnet centre deviations caused by field variation and the BBA. The magnetic centre stability is influenced by a number of factors such as the mechanical misalignment of the magnets, the magnetization effects in the magnets, the hysteresis effects in the iron core and its saturation, thermal deformations in magnet on cooling, Lorentz forces and the coupling between the coils of the quadrupole and dipole. The dipole correctors need to be programmed to restore magnet centre under all circumstances. Since the magnets are mounted close to SCRF cavities, they have to be effectively shielded to limit the fringe field on the cavities below 1 μT during cooling. This is required to prevent flux trapping in the cavities. During normal operation, the fringe field should not exceed 10 μT. A cut-view of the cross section of ILC cryomodule can be seen in Fig. 10.11. The cavity and other components of the cryomodule are seen in the picture.

Fig. 10.11 Cut-view of the cross section of ILC cryomodule. Cavity and other components are seen in the picture (© Rey.Hori/KEK)

10.9.2 The ILC Quadrupole and Dipole Correctors

We have just seen in the last section that the quadrupole/dipole corrector magnets play a crucial role in the success of the beam transport in ILC. Superferric quadrupole magnet design has been chosen by RDR for ILC. In this design, the field is substantially enhanced even after the iron core is saturated. The design and fabrication of the model quadrupole magnet have been carried out by Kashikhin et al. [24] at the Fermi Lab. The field in the quadrupole is produced by a set of 4 rectangular racetrack coils. The design optimization has been done using OPERA 2-D and 3-D codes. Since field region of interest is limited to 5 mm radius only, the core and coil positions are not very critical. The conceptual cross section of the Q pole magnet is shown in Fig. 10.12.

The details of the *Q*-pole magnet and the conductor used for winding are given in Table 10.6. The coils wound are of racetrack geometry which have the advantage of showing low superconducting magnetization effect. The coils have been wound using a single strand Nb–Ti wire with a filament size of 3.7 μm. The winding is done on a SS former with channels. Kapton insulation is provided to the winding to prevent ground shorts. The coil of each pole consists of 700 turns. The coil is vacuum-pressure impregnated with epoxy inside a mould. The yoke is made of laminations precisely cut-out of a 1.5-mm-thick sheet of AISI 1006 steel. Two (single lamination) flat iron sheets are fixed at the two ends of the magnet for magnetic shielding to limit the fringe field on the SCRF cavities to 1 μT. The quadrupole magnets will be mounted inside the cryomodules close to the SCRF cavities. As shown in the conceptual design in Fig. 10.13, the quadrupole is mounted below the centre support. Some SRF cavities including one 9-cell cavity and the *Q*-pole magnets are also shown in Fig. 10.13.

The model quadrupole magnet has been tested at Fermi Lab. by Kashikhin et al. [25]. The magnet centre stability shifts by ± 2.5 μm for a current range of 3–10 A. The

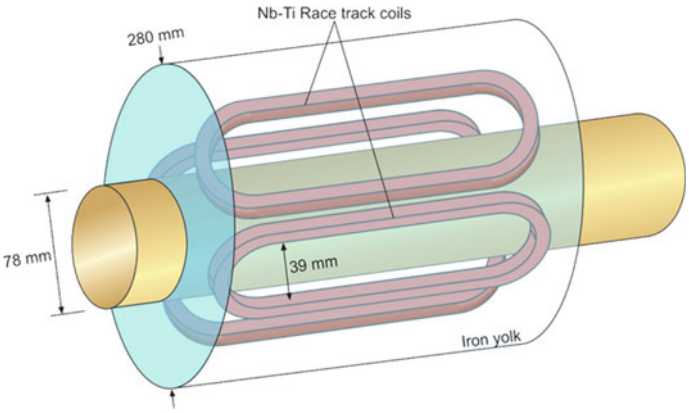

Fig. 10.12 Conceptual design of the quadrupole magnet for ILC consisting of four racetrack coils around the beam pipe (Concept from [24])

Table 10.6 Quadrupole magnet parameters and conductor specifications for a beam energy of 250 GeV

Quadrupole magnet parameters and conductor specifications					
Parameter	Unit	Value	Parameter	Unit	Value
Magnet aperture	mm	78	Conductor used		Nb–Ti
Magnet length	mm	680	SC wire dia.	mm	0.5
Yoke outer diameter	mm	280	Filament dia.	μm	3.7
Integrated field strength	T	36	Cu/Nb–Ti ratio		1.5
Peak gradient	T/m	54	Coil maximum field	T	3.3
Peak current in Q-pole and dipole correctors	A	100	SC wire I_c @ 5 T and 4.2 K	A	200
Magnet stored energy	kJ	40	Operating Temp	(K)	2
Magnet centre stability at BBA	μm	5	No. of turn/pole of Q-pole coil		700
Field nonlinearity at 5 mm radius	%	0.05	No. of turns/pole of dipole corrector		100

Data compiled from [24, 25]

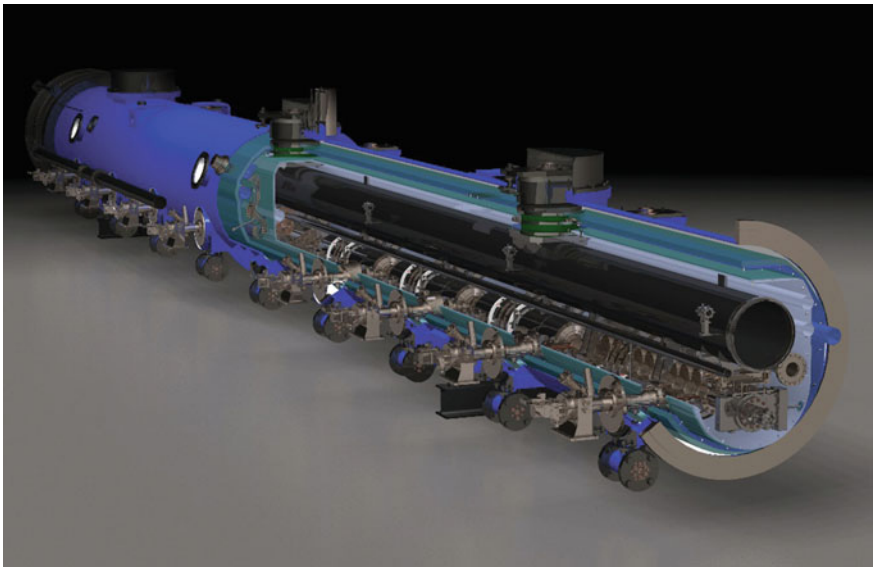

Fig. 10.13 ILC showing the location of SCRF cavities and the quadrupoles focusing magnets inside the cryomodule (Courtesy Fermilab)

studies on the coupling effects between quadrupole and dipole corrector coils have been carried out by connecting them in series. This eliminates current imbalance between the two sets of coils. The magnet needs multiple training because of the multiplicity of various Lorentz forces. The magnet is protected against quench by an external resistor of 10 $\mu\Omega$ and coil heaters. The quench is detected by voltage taps in 50 ms with a heater response time of 100 s. The maximum temperature raise during quench is restricted to safe limit, 74 K. and the induced voltage to below 1 kV.

Kashikhin et al. [26] at Fermi Lab. had come out with an innovative design and fabricated a split-quadrupole magnet with the same dimensions. The need for modifying the design arose from the requirement of assembling the magnet under extremely clean conditions as they are installed between the SCRF cavities inside the cryomodules. In the new design, the magnet is split along the vertical plane and is installed around the beam line without exposing the beam pipe to room temperature contamination. A four racetrack and superferric coil designs were followed. In the new design, the magnet is not cooled in a liquid helium bath but is conduction cooled using cryomodule liquid helium supply and gas return lines. The newly designed quadrupole produced 20% higher field gradient than the rated value. The design was improved further to reduce magnet centre shift.

Kashikhin [27] again came out with an interesting proposal to reduce the number of power supplies needed for operating the ILC quadrupole/corrector magnets. This proposal can improve the magnet centre stability and significantly enhance the operational reliability of the magnets. In the RDR design, each magnet in the accelerator runs on a dedicated power supply and separate sets of bus bars and current leads. In the new approach, suggestion has been made to group a certain number of magnets and power the group with a single power supply. Further, the magnets, qudrupoles and dipole correctors should run in persistent mode using superconducting persistent switches. In this arrangement, each magnet is energized to the required field level by a single power supply by opening the persistent switch and locking after regulating the magnet current by closing the switch. The process is repeated for every individual quadrupole as well as for the dipole corrector and are put in persistent mode of operation one by one. The new design will not only reduce the cost but will also add to the reproducibility and reliability of operation as the field stability in persistent mode is extremely high.

10.9.3 The Wiggler Magnets

The luminosity performance of the ILC requires extremely low emittance e− and e+ beams with high bunch charges. As per the RDR, ILC will use damping rings equipped with superconducting wiggler magnets to damp the beams effectively. A wiggler magnet provides a sequence of transverse fields with alternate polarity and forcing the charge particles (e− and e+) to wiggle up and down emitting EM radiation. Crittenden et al. [28] have developed an OPERA based finite element ILC model for the design of the wiggler magnets. They followed a Cornell Electron Storage

Ring (CESR) wiggler magnet design with a few changes in the parameters. About 54 magnets, each 2.2 m long, with a peak field of 1.51 T for 5 Hz mode and 2.16 T for the 10 Hz mode will be used to provide damping for the required horizontal emittance in each ring. These magnets will operate at 4.5 K. The wiggler magnets are of the superferric type where the coil is wound over an iron pole. There are 14 poles, 30 m period and a pole gap height of 7.62 cm.

10.9.4 The Undulator

The superconducting undulator will be used to generate positron source using the electron beam in the linac itself. The helical undulator will be placed in the main electron accelerator at a point of 150 GeV beam energy. The undulator produces synchrotron radiation and polarized photons which in turn produce positrons by impinging on a Ti target. The model coil is a double helical coil wound on a copper tube of ID 5.85 mm and OD 6.35 mm which produces helical transverse field. The undulator has 42 modules each with two magnet coils. The length of the field is 2 $\times$ 1.74 m. The axial field is 0.86 T at a nominal current of 250 A. The period is 11.5 mm. The tolerances to maintain alignment are very tight because of the small aperture. The winding is done on a SS former with grooves using a 0.4 mm dia. Nb–Ti wire. A SS yoke has been used which enhances the field by 10% and also provide mechanical support.

10.9.5 Other Superconducting Magnets

In addition to the magnets discussed above, the collider will have 12 sextupoles, 14 octupoles and 16 solenoids serving the interaction region (IR), the beam delivery system (BDS), the $e^- - e^+$ source region and the ring to main linac (RTML) region.

The fabrication and installation of such a large number of magnets with great precision is a big challenge. The design details discussed above are as per the RDR which was largely based upon concepts and is subjected to modification. The 'ILC Final Design Report' has been submitted to ICFA on 12 June 2013 simultaneously at Tokyo, Geneva and Chicago, the representative cities of three continents, Asia, Europe and USA. Several modified versions of the focusing magnets are being studied at BNL, Fermilab and SLAC laboratories. The accelerator community is however disappointed that the long-pending ILC project is still hanging fire as the Japanese government has not committed itself to this $ 7.5 billion project.

10.10 Superconducting Magnets in Cyclotron

Superconducting magnets have played equally important role in the development of yet another type of particle accelerators, the cyclotron. Cyclotrons have been very successful in accelerating light to very heavy particles like U to high energies equivalent to K values of 2500 meV. Here, K value represents the energy in MeV of a proton to which it can be accelerated in a cyclotron. Since a nucleus contains many protons and neutrons, the nucleus energy will be much smaller. The beam injection in a cyclotron is done using either a linear accelerator or an ECR source. This class of accelerators has been very popular in the study of nuclear physics, production of radioisotopes used as tracer elements and particle therapy for the treatment of cancer.

A cyclotron uses a pair of hollow electrodes which are of the shape of 'D' (dee) arranged in opposite configuration with a gap as shown in Fig. 10.14. These electrodes are held between the poles of a magnet which produces a uniform vertical field. An alternating voltage, in MHz range, is applied to the electrodes. An ion source kept in the gap at the centre produces ions which get attracted by the first electrode. The ions execute circular motion inside the electrode (in magnetic field) and get attracted across the gap by the second electrode when they emerge from the first electrode because of the opposite polarity of the second electrode. The ions again execute circular motion in the second electrode and get accelerated in the gap by the first electrode. Ions after acceleration gain energy and move in a larger circle. This process of acceleration in gaps continues and the ions continue to travel in circles

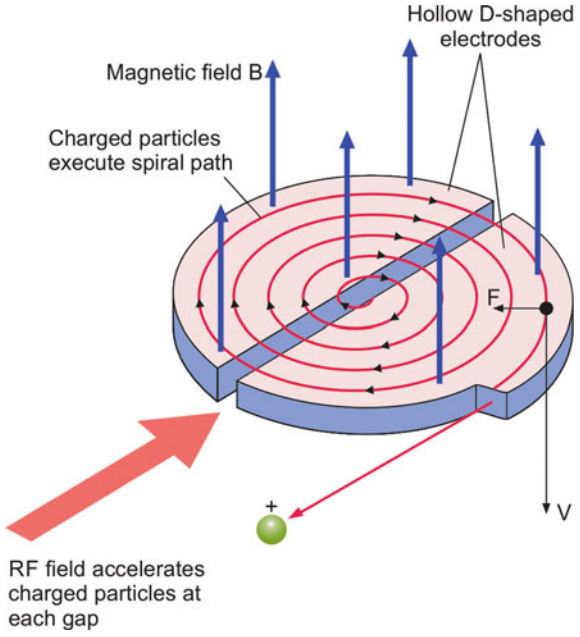

Fig. 10.14 In a cyclotron, a charged particle executes a spiral trajectory under the influence of a RF field and a perpendicular uniform magnetic field. The ions travel in circles of increasing radii till they exit from the dee through an extraction route and hit the target

of increasing radii till they exit from the dee through an extraction route. To achieve this condition the RF frequency must match the cyclotron resonance frequency so that the ions are in phase with the RF to get repeated acceleration. This intense beam can be used to bombard a variety of target materials to produce rare radioisotopes or to conduct nuclear physics experiments. Powerful cyclotrons need high magnetic field which can be provided by a superconducting magnet alone.

The orbital motion to the ions in a magnetic field such as in a cyclotron is provided by the Lorentz force which acts as the centripetal force:

$$qvB = mv^2/r \tag{10.1}$$

$$r = mv/qB \tag{10.2}$$

where r is the radius of the dee, m mass of the particle, v the particle velocity, q the charge of the particle and B the magnetic field. The time taken by the ion to execute half a circle in a dee will be

$$t = \pi r/v = \pi m/qB \tag{10.3}$$

The cyclotron time period thus will be

$$T = 2t = 2\pi m/qB \tag{10.4}$$

and the cyclotron frequency

$$f = qB/2\pi m \tag{10.5}$$

The maximum kinetic energy can be obtained by calculating the maximum velocity at the periphery of the dee, that is, by replacing 'r' by 'R' the radius of the dee:

$$E_{\max} = \frac{1}{2}\left(m\,v^2\right) = \frac{1}{2}(m\,q^2B^2R^2)/m^2 \tag{10.6}$$

$$= q^2B^2R^2/2m \tag{10.7}$$

This cyclotron frequency (10.5) is constant only for low non-relativistic velocity where 'm' is constant. For high velocities, the relativistic mass increases and therefore the cyclotron frequency decreases. For continuous acceleration, either the frequency has to decrease like in a synchrocyclotron or the magnetic field be increased as the particles move towards the perimeter of the dees. So the cyclotron is now isochronous wherein the magnetic field increases with radius to keep the angular frequency of the particle constant.

10.10.1 Cyclotron Magnet

The pioneer work on the design and building of cyclotron has been done by Blosser at MSU [29]. A cyclotron has four major subsystems [29], the injection system, the magnet system, the RF system and the extraction system. Each of these subsystems has to be compatible with others and is designed through a sustained iteration process till the construction stage. Our discussion will be restricted to magnet part which certainly is the most critical subsystem of the cyclotron as a whole. As shown in Fig. 10.15, the magnet is a long solenoid nested in a rather thick iron yoke and having top and bottom iron pole caps and a large gap [29]. In an isochronous cyclotron the magnet provides axial field to the particle for circular motion as well as an axial focusing to the beam which becomes critical as the velocity approaches relativistic values (>0.5 c). For axial focusing, the field should increase azimuthally as the spiral radius increases. This is achieved by creating hills (high field) and valleys (low field) at the pole tips which too are spiralled to improve focusing further. In a superconducting magnet and high-field region the pole tips are fully saturated which results in the enhancement of field at the hills by 1.5 T, higher than the field in the valleys. This saturation or the complete alignment of the magnetic moments is in fact equivalent of a surface current of 450 kA on a 250-mm-thick ordinary steel pole tip and with no cost. The azimuthal width of the valley and the hill is kept same so as to benefit from maximum focusing effect.

The next consideration about the magnet design is the number of hills or the so called 'sectors'. The thumb rule is that good axial focusing at the centre is obtained by a smaller number of sectors but to operate the cyclotron at high beam energies a larger number of sectors are needed. For example, 200 meV/nucleon seems to be the

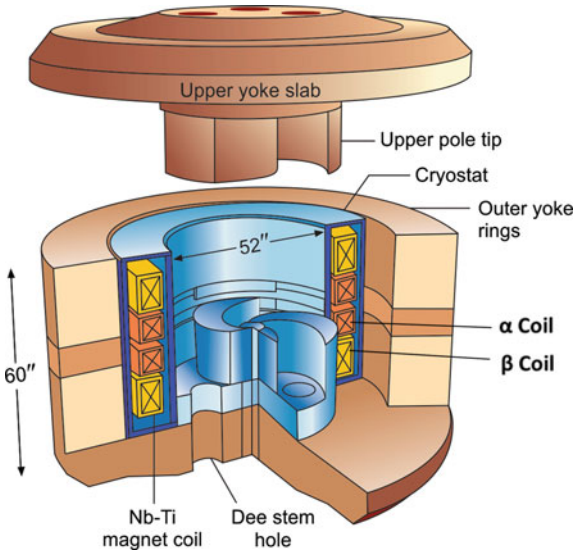

Fig. 10.15 Sketch and dimensions of the MSU cyclotron K-500, world's first superconducting cyclotron [29, 30] (Courtesy Marti Felix and Gelbke Konrad, NSCL, Michigan State University)

upper limit to which the K-800 cyclotron of MSU, with three sectors, can accelerate a beam. For higher energies, one has to use either four sectors or three inner sectors breaking in to six outer sectors. To keep the magnetic field to be isochronous and maintain azimuthal field variation for focusing, trim coils are often used. For variable energy, the magnetic field profile has to remain synchronous so that the beam does not go out of phase with the accelerating voltage. This may need large adjustment in the radial field increase ranging from almost 1% to 20% in K-800 class of cyclotron depending on the beam being accelerated. This is best achieved by dividing the main coil in to two or more no. of coil pairs symmetric to the median plane and exciting them at different currents.

10.10.2 Some Landmark Superconducting Cyclotrons

We list below some of the well-known superconducting cyclotrons built and operated in Europe, Japan and USA.

1. K-500 NSCL, MSU (USA) 1982
2. K-520 Chalk River (Canada) 1985
3. K-500 (TAMU) Texas A&M Uni. (USA) 1985
4. K-1200 NSCL, MSU (USA) 1989
5. K-800 LNS, Catania (Italy) 1994
6. K-600 (AGOR), KVI (Orsey-Groningen,) 1996
7. K-2500 RIKEN Ring Cyclotron, RIKEN (Wako, Japan), 2006
8. K-500 VECC (Kolkata, India) (First beam line acceleration 2009).

Below, we discuss three trendsetting cyclotrons, namely, K-500, K-1200 and K-2500 mentioned above.

10.10.3 K-500 Cyclotron at NSCL (Michigan State University)

World's first superconducting cyclotron K-500 was built and operated at National Superconducting Cyclotron Laboratory, MSU, USA, in Nov. 1981, and the first beam was extracted in August 1982. Since then, many cyclotrons have been built ranging up to very high energies up to K-2500. Some of these cyclotrons have been listed in the previous section. The MSU design of the cyclotron got popularity and was followed by a number of laboratories. The schematic diagram of the cross section of the cyclotron is shown in Fig. 10.16. The cyclotron is 2.184 m tall and 3.048 m wide (dia.). The magnet has two pairs of superconducting coils on either side of the median plane placed symmetrical, namely, α coils close to the centre and β coils away from the centre. The α and β coil sets are energized independently which allows proper adjustment of the isochronous field for all the beam energies and the central field.

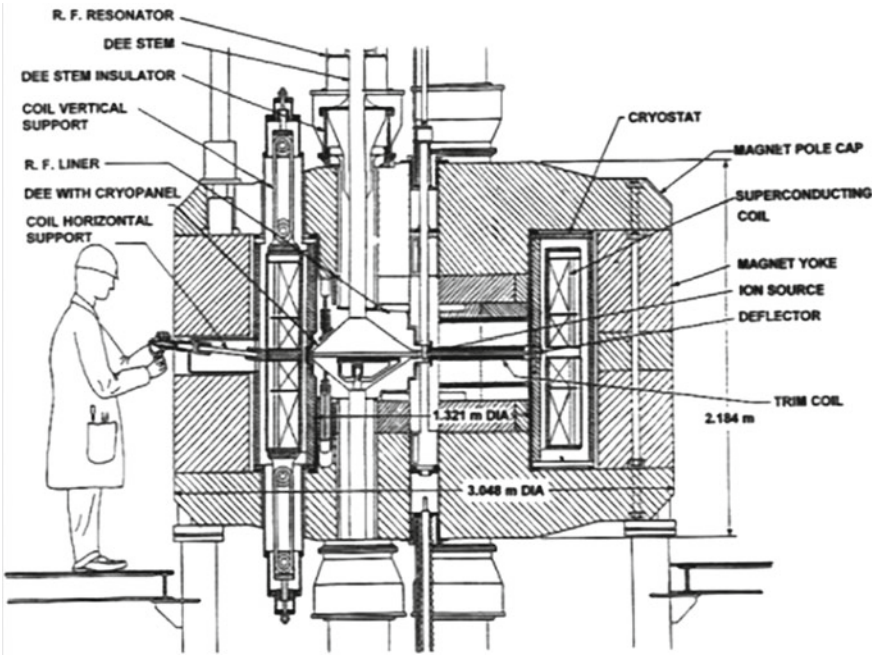

Fig. 10.16 Schematic cross section of the K-500 cyclotron (MSU) [29] (Courtesy Marti Felix and Gelbke Konrad, NSCL, Michigan State University)

The magnet is installed in an annular cryostat with thermal shields and diagnostic tools. After welding, the magnet becomes an integral part of the annular cryostat as a single unit. The magnet operates in a liquid helium bath (4.2 K) and produces a field up to 5 T. The gap between the two coil sets allows different type of radial insertions in the median plane especially the extraction elements.

10.10.4 K-500 Cyclotron (VECC, Kolkata)

The K-500 superconducting cyclotron built at VECC [31], Kolkata is based upon the MSU design already shown in Fig. 10.15. The design parameters of the cyclotron are given in Table 10.7. The main magnet is divided in four coils, two identical pairs of α coils and β coils on either side of the median plane. Both the α coils and β coils are energized by two different power supplies. The α coils are short coils placed closure to the median plane and the larger β coils away from the median plane. All the coils have same inner and outer diameter and wound on a common SS former. The α and β coils are separated by an insulating 10-mm-thick glass epoxy laminate spacer which has six segments of 60° each. The spacer has alternate grooves spaced at 2° pitch for liquid helium flow and for lead entry and exit. The former surface is electrically

Table 10.7 Design parameters of the α and β coils of the main magnet of the K-500 (VECC, Kolkata [31])

Parameters of the α coils			Parameters of the β coils		
Parameter	Unit	Value	Parameter	Unit	Value
No. of α coils		2	No. of coils		2
Inner dia.	mm	1521	Inner dia.	mm	1521
Outer dia.	mm	1793	Outer dia.	mm	1793
Coil height	mm	162	Coil height	mm	327
No. of layers/coil		36	No. of layers/coil		36
No. of turns/coil		1083	No. of turns/coil		2234
Inductance of coils	H	13.8	Inductance of coils	H	27.6
Designed coil current	A	800	Designed coil current		800
Weight of coil	kg	690	Weight of coil	kg	1410
Aluminium banding	mm	2.48 × 5.13	Aluminium banding	mm	2.48 × 5.13
No. of layers		10	No. of layers		10
No. of turns/layer		62	No. turns/layer		32
Total cold mass				ton	8
Main magnet frame dimensions (height)				mm	2184
Main magnet frame dimensions (dia.)				mm	3048
Weight of the main frame				ton	100
Total stored energy				MJ	22

Data compiled from PPT presentations by VECC

insulated with layers of Mylar followed by a layer of 40 mil × 13 mm wide NEMA G-10CR laminate placed at a gap of 13 mm to allow the flow of liquid helium. Flange spacers of G-10 glass epoxy laminate with grooves of 2° pitch and 13 mm wide alternating ducts are used at the two ends of the former. These ducts provide liquid helium cooling channels. For inter-layer insulation also G-10 spacers, (180 in number) have been used, providing axial flow channels. Since during operation, the winding is subjected to large EM forces, to prevent cable movement, the winding is carried out under tension of 2000 psi. The terminal of the magnet coils and the current leads is taken out through the top flange of the former. The two α coils and the β coils are connected in series to form two pairs and are operated using two separate power supplies. After insulating the coils with several layers of Mylar, ten layers of aluminium (5052—H34 grade) banding (2.48 mm × 5.13 mm) were wound on the coils at a high tension of 20,000 psi. This banding increases the compressive stress on the coils significantly. The space between the two pairs of coils in the median plane is used for a variety of horizontal inserts.

The magnet former is welded shut inside the annular helium vessel such that the former itself acts as the inner wall of the helium container. The helium container is surrounded by an annular 80 K thermal shield and finally suspended inside a

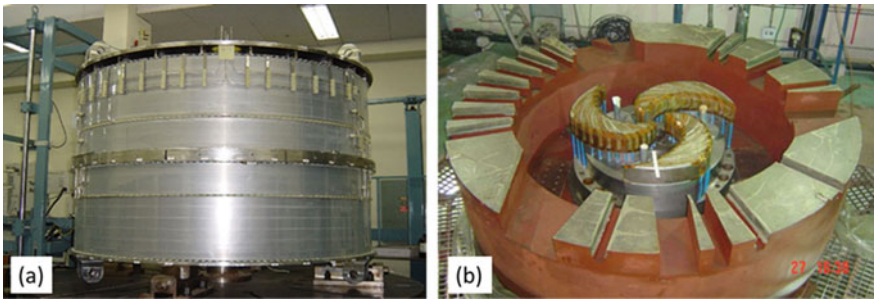

Fig. 10.17 **a** Annular helium vessel housing the magnet coils. **b** Lower half of the yoke with bottom pole caps and three sector shaped pole tips. Each pole tip has 13 trim coils (Courtesy D. Srivastava and S. Saha, VECC, Kolkata)

vacuum tank using G-10 vertical and horizontal support links. Many ports such as vacuum port, refrigeration ports and ports for current leads and other diagnostic tools are provided at the top of the vacuum container. The helium container is shown in Fig. 10.17a. The whole assembly is now positioned in a magnet frame which is one half of the iron yoke and weighs about 100 tons. The yoke carries top and bottom pole caps and three pole tips of sector shape, spaced at 120°. The lower half of the yoke is shown in Fig. 10.17b. Each pole tip has 13 trim coils wound over them for fine-tuning of the field for different radii. A forged steel of AISI 1020 grade has been used for the fabrication of the yoke components including pole caps. All the components have been machined to a precision of 1.6 μm for perfect mating. Cylindrical symmetry around the axis and mirror symmetry of the two halves on either side of the median plane has been achieved using VTB machine.

The conductor used is a 1.2 mm dia. multifilamentary wire of Nb–Ti (46%) composition. The complete specifications of the conductor used are given in Table 10.8. The wire is embedded in the groove of a copper bar of dimensions 2.794 × 4.978 mm and filled with Pb–Sn soft solder. Since the maximum single length of the cable available was limited to 6 km, three joints were made in each β coil and two joints in α coils. Special technique was developed to prepare low resistance joints. A total of 35 tons of cable has been used. The VECC cyclotron machine with beam line system is shown in Fig. 10.18. First beam acceleration took place in August 2009.

The quench protection system uses external dump resistors and consists of two independent circuits one each for α and β coils. The circuit shown in Fig. 10.19 enables the dumping of the stored energy in the resistors either in a slow-dump mode (4 A/min) or in a fast-dump mode (15.3 A/s) in different situations. The slow dump is activated in the event of a power failure. However, whenever some cryostat parameters exceed the acceptable limit such as liquid helium level, current lead voltage or strain related force etc., the energy will dissipate in fast dumping resistors. The magnet system was first operated in 2009. A field of 4.8 T was achieved at the pole tips (hill region) at a radius of 0.55 m by charging α and β coils to 550 A current.

Table 10.8 Specifications of the conductor used for winding coils for K-500 (VECC, Kolkata, [31])

Parameter	Unit	Value
Type of conductor		MF (Nb-46% Ti) wire soldered in a Cu-channel
Cable outer dimensions	mm	2.794 × 4.978
MF—Nb–Ti wire dia.	mm	1.20
No. of filaments		500
Filament dia.	μm	40
Cu/SC ratio in the wire		1.3
Overall Cu/SC ratio in the cable		20
Overall current density	A/mm^2	58
Critical current @ 5.5 T, 4.2 K	A	1030
Conductor yield strength	MPa	117
Max. conductor single length	km	6
Total length of conductor used	km	35

Data compiled from PPT presentations by VECC

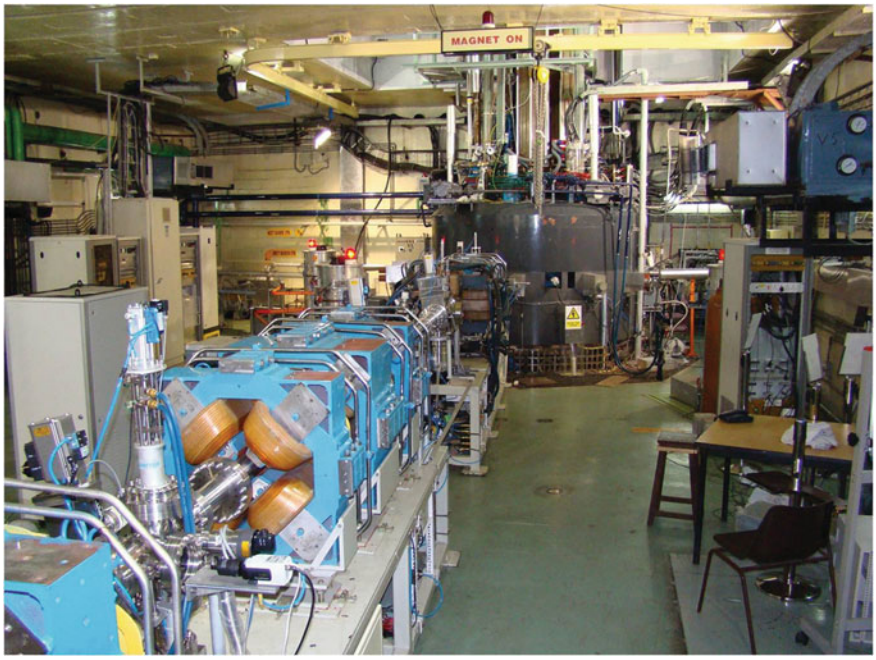

Fig. 10.18 VECC superconducting cyclotron with beam line system (first beam line acceleration in August 2009) (Courtesy D. Srivastava and S. Saha, VECC, Kolkata)

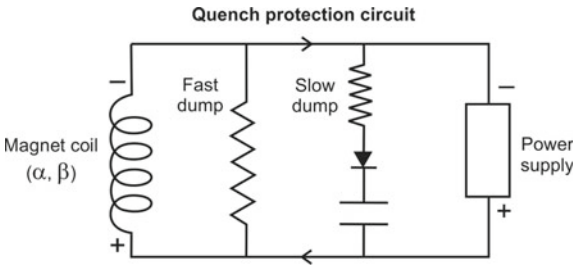

Fig. 10.19 Quench protection circuit provides slow and fast discharge of energy in external dump resistors in different situations

10.10.5 K-1200 Cyclotron (NSCL, MSU)

NSCL built yet another powerful cyclotron, K-800 [32, 33] as a booster to K-500 which went in to operation in 1988. The new cyclotron performed superbly and provided excellent focusing power and was renamed K-1200 a year later in 1989. K-1200 continues to be world's highest energy superconducting cyclotron in its class. The design envisaged a beam energy of 200 meV/nucleon for fully stripped light ions and 30 meV/nucleon heavy ions depending upon the charge state of the ions injected. Even though the design was based upon the use of K-500 as an injector, the option was kept to operate K-1200 in stand-alone mode using ECR ion source injector. All important parameters of the cyclotron and the conductor used in magnet construction are given in Table 10.9.

The design of K-1200 is similar to that of K-500 but differs in respect of several parameters. For example, the pole diameter was increased from 2.05 to 2.1 m, hill gap increased from 62.5 to 75 mm and the hill width from 46° to 51° at the outer radii. The distance between the two α coils increased from 75 to 100 mm making larger space for radial insertions especially for the magnetic channels of the extraction system. The pairs of α and β coils are powered by two independent power supplies like in K-500 to adjust the isochronous field for all ions and the main magnetic field. For most relativistic ions and for energies approaching focusing limit, current in β coils may be negative with respect to α coil and the average field increases by 20% from $R = 0$ to $R = 1$ m. For non-relativistic ions these coils are positive with respect to α coils, and the average field B_{ave} is almost constant with radius. Figure 10.20 is a photograph of K-1200 during the assembly procedure.

The picture shows the lower half of the yoke with several radial penetrations related to the beam extraction system and other diagnostic tools. The coil and lower hills too are visible.

The magnet operated in a range of 3–5 T field with a magnetic rigidity of 5 T m (K-1200). The magnet coils were run at a maximum current density of 3500 A/cm^2. A monolithic Nb–Ti wire of the size 1.1 mm × 1.65 mm embedded in a copper channel (in a groove filled with solder) has been used for winding. The dimensions of the cable are 5.175 mm × 3.75 mm. A set of 21 trim coils have been used to have required B_{ave} versus R slope. These coils have been wound on the pole tips using conventional copper conductor. A set of thick and heavily spiralled steel pole tips

Table 10.9 Important parameters of K-1200, the magnet coils and the conductor

Parameters of K-1200 cyclotron, the magnet and conductor					
Parameter	Unit	Value	Parameter	Unit	Value
Operating field	T	3–5	Number of coil pairs		2 (α and β)
Pole diameter	m	2.1	Inner coil diameter	m	2.275
No. of sectors used		3	Outer coil diameter	m	2.575
Minimum hill gap	mm	75	Height of α coil (closer to median plane)	mm	400
Maximum valley gap	mm	900	Height of β coil (away from median plane)	mm	262.5
Yoke inner diameter	m	2.95	Separation between α coils	mm	100
Yoke outer diameter	m	4.375	Al-alloy banding thickness	mm	50
Yoke height	m	2.875	Inner dia. of vacuum tank	m	2.1125
No. of trim coils		22	Outer dia. of vacuum tank	m	2.925
Max. current in any trim coil	A	400	Total height of cryostat	m	1.725
Max. power in any trim coil	kW	70	Conductor used (embedded in Cu-channel)		Nb–Ti (monolithic)
Peak dee voltage	kV	200	Conductor dimensions	mm	5.175 × 3.75
K value at 5 T		1200	Overall Cu:SC ratio		25: 1
RF frequency range	MHz	9–27	Max. nominal current	A	1,000
Total inductance including mutual inductance at $J_\alpha = 3500$ A/cm^2				H	88.8
Total stored energy				MJ	61
Weight of the magnets				ton	280

Data compiled from [32]

with three-fold symmetry provides vertical focusing. The gap between the valleys is 0.9 m. The sector area has a central hole of 175 mm which increases to 250 mm in the poles. This cyclotron happened to be first to have used a vertical injection and a ECR source for injection. There are 42 holes of dia. 18.75 mm, on the two sides of each of the hills for the leads from the 21 trim coils. Holes have also been provided for feeding RF. The number of trim coil layers has been reduced from two to one and the gap between the hills increased to 75 mm. This enables easy slide of the deflector inwards at lower fields and helps in the extraction system. Nine magnetic channels and two electrostatic deflectors have been used in the extraction system.

The cyclotron went on stream and the first beam of $^{20}Ni_{3+}$ with 18 meV energy was extracted successfully on 6 June 1988. The cyclotron performance was in excellent agreement with design calculations and the beam followed the highly intricate

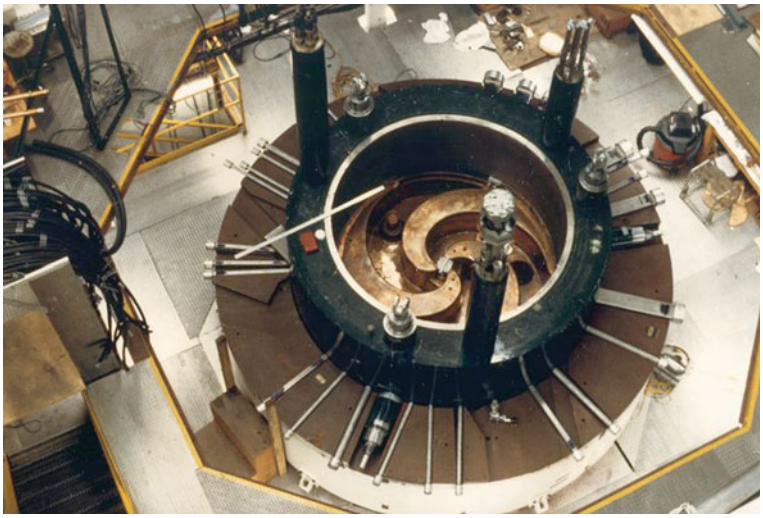

Fig. 10.20 K-1200 during the assembly process, the return yoke, the penetrations associated with the extraction elements (radial tubes) and the coil as well as the lower hills are seen in the picture (Courtesy Marti Felix and Gelbke Konrad, NSCL, Michigan State University)

trajectory accurately. The beam spot was 4 mm well within the calculated value of 5 mm. The construction of the cyclotron was indeed most challenging because of much larger EM forces, a very intricate extraction system, much tighter pole tip spiral and a much larger size isochronous cyclotron with a magnet rigidity of 5 T m.

In 2001, K-1200 was coupled [34] to K-500 at the injection stage through an intermediate coupling line with a magnetic system. An ECR source injects the beam in to K-500 which accelerates the beam to 17 meV/nucleon which in turn is injected in to K-1200. The ions pass through a thin foil stripper which increases the charge state by a factor of 2.5. The beam is finally accelerated to 200 meV/nucleon. It thus became possible to accelerate light ions to high intensities and heavy ions to large energies. This upgraded version can accelerate the U beam to 90 meV/nucleon and in stand-alone mode can accelerate U beam to 25 meV/nucleon. The cyclotron can as well be operated in stand-alone mode using ECR source producing very high charge state. The cyclotron produces radioactive ion beam and is used by a vast community of nuclear scientists from across the globe.

10.10.6 K-2500, RIKEN Superconducting Ring Cyclotron

The RIKEN superconducting ring cyclotron (SRC) is the most important accelerator of the RIKEN radioactive ion beam factory (RIBF) project in Japan. The beam energy from the old ring cyclotron K-540 is boosted using a cascade of ring cyclotrons with K values of 570 meV, 980 meV and the 2500 meV. The final beam energy goes up

to 440 meV/nucleon for light ions like carbon and 350 meV for very heavy ions like U. The high-energy beam of heavy ions are then converted in to high-intensity radioactive ion beam through the fragmentation of stable isotopes. RIBF is world's unique facility which provides most intense radioactive ion beams of all the elements across the periodic table. Figure 10.21 is a complicated picture of Superconducting Ring Cyclotron (SRC) showing the organization of sector magnets and various other components constituting the ring.

The K-2500 SRC [35, 36] is 19 m in diameter and 8 m in height. The main components of the SRC are six sector magnets, one flat-top RF cavity, four main RF cavities, an injection system and an extraction system. The beam from the previous cyclotron is injected in to the SRC at a radius of 3.56 m. Important parameters of

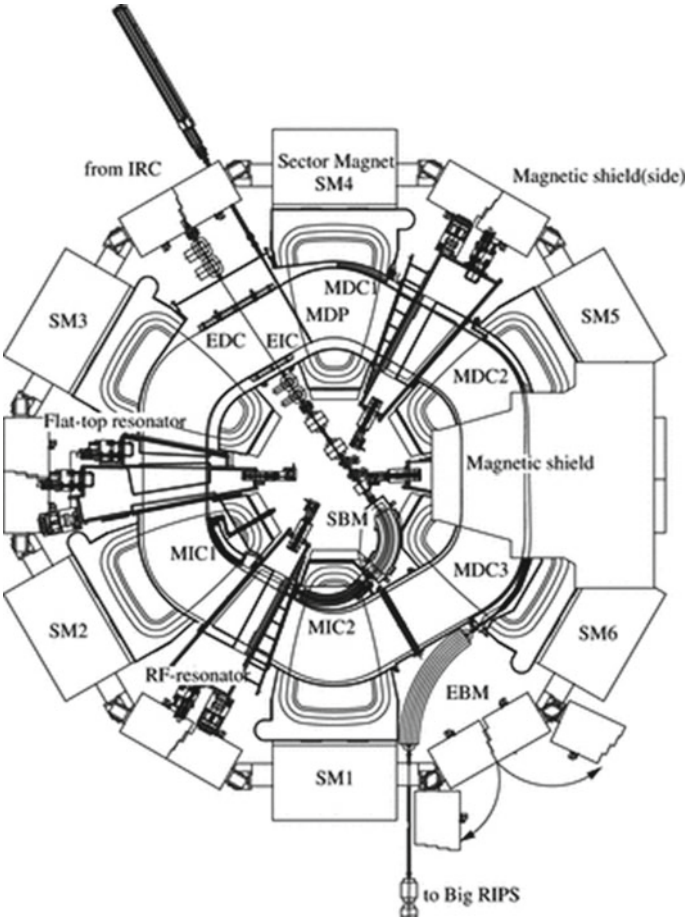

Fig. 10.21 Layout of the six sector magnets of the RIKEN K-2500 Superconducting Ring Cyclotron (SRC) [35] (Courtesy Hiroki Okuno and with permission of Oxford University Press on behalf of Physical Society of Japan)

Table 10.10 Important parameters of RIKEN K-2500 SRC and the magnet

Parameters of RIKEN K-2500 SRC and the magnet					
Parameter	Unit	Value	Parameter	Unit	Value
Outer dia. of SRC	m	19	Max. sector field	T	3.8 @ 5 kA
Height of SRC	m	8	Total stored energy	MJ	235
Injection radius	m	3.56	Length of sector magnet	m	7.2
Extraction radius	m	5.36	Height of sector magnet	m	6
Total weight	ton	8300	Weight of a sector magnet	ton	800
No. of sector magnets		6	Conductor used		Nb–Ti
Sector angle	degree	25°	Type of conductor		Rutherford
Poles and yoke		Warm	Cable outer dimensions	mm	15 × 8
No. of main coils		2	Jacket material		Al-alloy
No. of SC trim coils		4 sets	Yield strength of Al-alloy	MPa	55

Data compiled from [35, 36]

the SRC and the sector magnets are given in Table 10.10. Each sector magnet is 7.2 m long, 6 m in height and has a sector angle of 25°. Each sector magnet module comprises of a pair of main coils, four sets of superconducting trim coils, thermal shield, thermally insulating supports and the cryostat. The magnet is operated at 4.5 K. In addition, there are 22 pairs of normal conducting trim coils, warm poles and warm yoke. Each sector magnet weighs ~800 tons. The total cold mass of all the six sector magnets is 140 tons which needs three weeks to cool to 4.5 K from room temperature. A unique feature of the construction of the SRC is the use of 1-m-thick iron slabs for an effective radiation and magnetic shielding. These slabs cover the valley regions between the two adjacent sector magnets and also vertically along the sides between the top and bottom slabs. This minimizes the inverse-direction stray field which influences beam deflection power in the valley. The decrease in leakage field brings down the magneto-motive force at the peak bending power. In all, the iron slabs weigh around 3000 tons. The SRC itself becomes massive weighing 8300 tons. The beam is finally extracted at a radius of 5.36 m. The maximum field produced is 3.8 T which accelerates U^{+88} to an energy of 350 meV and is a world record.

The cable used for winding the main coils of the sector magnet and the superconducting trim coils is of a Nb–Ti Rutherford type with an outer dimensions of 15 mm × 8 mm. The stabilizing cladding material is an aluminium alloy containing about 1000 ppm Ni which increases the yield strength of this alloy from 44 to 55 MPa. The maximum operating current for the main magnet is 5000 A and for the trim coils 3000 A. The main coil has a solenoid winding with 396 turns and generates a magneto-motive force of 4×10^4 AT (Ampere Turn). Inter-turn and inter-layer fibreglass-reinforced plastic (FRP) spacers have been used in the horizontal and vertical gaps to insulate the conductor electrically as well as to provide cooling channels for the conductor. About 50% area of the cable is left exposed. For trim coils, also the same conductor has been used. Four sets of trim coils, installed in the

beam accelerating area of the sector magnet, are wound in a double pancake structure. The wide and thin trim coil is sandwiched between two Al-alloy plates having grooves. These grooves serve as cooling channels for the forced flow of two-phase helium. A control Dewar mounted at the top of the SRC supplies liquid helium to all the six sector magnets in a closed-loop mode. A refrigerator with a capacity of 620 W at 4.5 K and 400 W at 70 K has been used which is far more than the heat load of the total cold mass (140 tons).

The injector system too has a superconducting bending magnet (SBM) [37] for bending the beam before injection in to K-1200. This magnet generates a field of 3.8 T along the beam trajectory having a curvature of 1.21 m at a current of 363 A. The special features of the magnet are the flat coil geometry, iron poles used as former for coil winding and the iron yoke in two parts, one H-shaped cold yoke and another C-shaped warm yoke. The total cold mass is only 3 tons. A monolithic Nb–Ti conductor of the dimensions of 2.4 mm $\times$ 0.8 mm has been used for winding. The coil is finally vacuum epoxy impregnated. A photograph of RIBF [38] after its assembly in the vault is shown in Fig. 10.22. The control liquid helium vessel is seen at the centre of the cyclotron on the top.

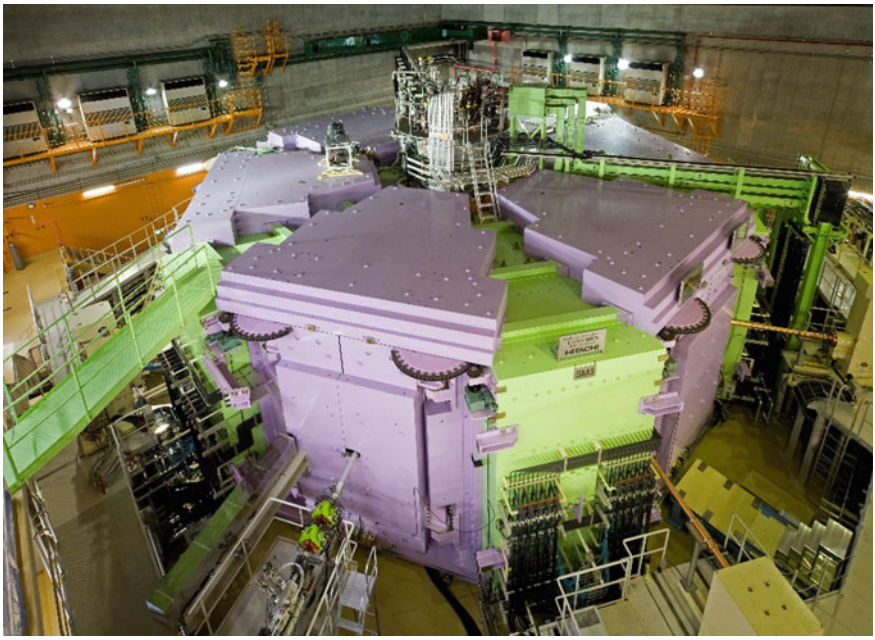

Fig. 10.22 SRC after assembly in the vault. The control liquid helium Dewar is seen on the top in the centre of the cyclotron (Courtesy Hiroyoshi Sakurai and with permission from RIKEN Nishina Centre and iTHEMS Promotion Office) https://ribf.riken.jp/RIBF-TAC05/1_Overview.pdf

10.11 New Developments in Accelerator and Magnet Technology

Human quest for reaching the top, breaking old records and setting new records has never diminished. The most powerful accelerator of the world, LHC went on full stream in September 2010 after a mishap, which happened soon after the start of operation in September 2008. Till end of 2018, LHC produced a collision energy of 13 TeV as the protons circulating in opposite directions smashed. LHC produced 3 million Higgs bosons in a year (2017) and 150 inverse femtobarns (fb^{-1}) data/year, corresponding to a 12 km high stack of about 10 million standard DVDs in a year. Notwithstanding these achievements, the accelerator scientists/engineers decided to shut down the LHC for its upgradation for increasing its luminosity by a factor of ten. The LHC will now appear in its new incarnation to be called high-luminosity LHC (HL-LHC). CERN has also taken up a new project of building an advanced accelerator which will reach an ultimate P-P collision energy of 100 TeV to be installed in a 100 km long underground tunnel named as Future Circular Collider (FCC). We will discuss these new projects in the following sections.

10.11.1 The High-Luminosity–Large Hadron Collider (HL-LHC)

The HL-LHC will produce >15 million Higgs bosons and 250 inverse femtobarns data/year with a capability of collecting 4000 fb^{-1} data (1 inverse femtobarn, fb^{-1} = 100 million million). LHC is supposed to reach an integrated luminosity of 300 fb^{-1} by 2027. This corresponds to about 2.5×10^{16} proton–proton collisions. The number of collisions in a given time is measured in terms of luminosity, higher the number of collisions higher the luminosity, more data the experiments can gather to allow physicists to observe rare processes. The HL-LHC was conceived in 2013, and the technical design report was completed in October 2015. CERN is leading the project in collaboration with 29 institutions in 13 countries, including the USA, Japan and Canada. LHC is presently under long shut down (2019–2021).

One element of LHC upgrade is the development of a test station for characterizing the new high-current cables in a high-field environment. Such a facility, in the form of a dipole magnet, called FRESCA-2, with a large aperture of 100 mm and generating a field of 13.3 T has been set up at CERN as part of collaboration between CERN and CEA-Saclay in the framework of the European *EuCARD programme*. The magnet and conductor details of FRESCA-2 have already been discussed in Sect. 10.5.3. The other important element of the project is the development of 12 T magnet technology using Nb_3Sn cables. The magnets generating fields of almost 12 T are already being manufactured for the HL-LHC. CERN and its partners have already started building 16 T magnets for Future Circular Collider (FCC) project to be discussed in the next

section. The entire programme is run under the LHC Accelerator Research Project (LARP).

In the beginning of August 2017, FRESCA-2 reached its design magnetic field of 13.3 T at the centre of a 100 mm aperture and maintained it for 4 h, a first for such a large aperture [39]. By contrast, the dipole magnets in the LHC generate a field of 8.3 T at the centre of a 50-mm aperture at 1.9 K. Testing of the cables is important not only for J_c but also for all other EM effects under high magnetic field. How precisely the intensity of the magnetic field can be adjusted is a key feature of an accelerator. The magnetic field, that guides the beam, should increase smoothly without sudden spikes as the beam energy is increased otherwise the beams could be lost. The beams circulate for hours at a time in LHC magnets because the field in the LHC magnets can be controlled with precision. The Nb–Ti 8.3 T dipoles of LHC will be replaced by new 11 T Nb_3Sn two-in-one dipoles and the quadrupole magnets will be replaced by Nb_3Sn quadrupoles named Magnet Quadrupole X-interaction region F-version F of the design (MQXF). Successful tests have been carried out on a full-length 4.5-m-long Nb_3Sn coil that produced a nominal field value of 13.4 T at Brookhaven National Laboratory (BNL). The winding of 7.15-m-long coils is being done at CERN. High-performing Nb_3Sn cables have been developed through PIT and RRP techniques and accelerator magnets have been tested up to 16. 5 T field which will be used in the FCC accelerator.

The high rate of collisions is to be achieved (a) by increasing the beam intensity by a factor of 2 through the use of additional collimators, (b) by reducing the size of the beam at the interaction points. One therefore needs larger aperture magnets in the vicinity of detectors, ATLAS and CMS, that is, the triplet involving the separation and the recombination dipole and the associated correctors. The programme involves the replacement of the existing 14.3-m-long dipole with a 11-m-long Nb_3Sn magnet and a room temperature collimator. Four Nb_3Sn triplets are planned to be installed during 2024–25, half of them are being built in the US. Twenty 4.2-m-long magnets have been built in USA and ten 7.15-m-long magnets built at CERN under LARP. This programme of upgrade is now transiting from short model phase to the actual length prototype. High field and long length of the magnets pose severe complications which have to be dealt with ingenuity. We discuss these complications below.

10.11.2 Factors Influencing the Specific Parameters of Dipole and Quadrupole Magnets

Several factors like the winding width, critical current in strand and cables, the coil size, reaction temperature and duration, pre-stress, insulation and protection against quench play vital role in building these magnets and need highest consideration for perfect operation. Let us discuss them briefly. The field in a dipole, based on sector coil of angle ϕ is a function of the current density J and the coil winding width w as given by Todesco et al. [40]. The dipole field can be calculated using the following equation.

$$B = \frac{2\mu_0}{\pi} J w \sin\phi \tag{10.8}$$

The gradient in a quadrupole magnet of aperture r and winding width w is given by:

$$G = \frac{\mu_0}{\pi} J \log\left(1 + \frac{w}{r}\right) \sin 2\phi \tag{10.9}$$

Above equations tell us that the dipole field and the field gradient can be increased by increasing the coil width or the current density or both. Increasing the width w is convenient but it will lead to a larger dimension of the magnet in transverse direction which may not be permissible because of the constraint of the tunnel size. Besides, it will consume larger quantity of superconductor. Increasing the critical current of the conductor is a better option though more difficult with regard to large strains on the conductor induced by EM forces. Issue of stability of the conductor due to self-field and magnetization and the quench protection constraint are some other problems with high J_c conductors. Early accelerators used an engineering current density, J_e between 500 and 600 A/mm^2 and a coil width ranging between 10 and 30 mm. The specification for the critical current of the superconductor for the 2-in-1 dipole and MQXF quadrupole has been set at 2280–2450 A/mm^2 (4.2 K, 12 T) and 1280 A/mm^2 (4.2 K, 15 T) respectively. As already mentioned, high-field Nb_3Sn models with 45 mm coil width were built and tested at BNL producing a field of 13.5 T.

The cable used for MQXF is made from both RRP strands of the configuration 108/127 and PIT strands of 192 configuration. Both cables use 40 strands. The cable for 11 T dipole is made with the RRP 108/127 strands as seen from Table 10.11. Protection requirements put the limit of copper/non-copper fraction at 1.2 for MQXF and 1.15 for the 11 T dipole. The Rutherford cable dimensional parameters (18.094 mm × 1.529 mm) used for winding are optimized through a trade-off between good compaction to prevent strand pop out during winding and low deformation which may cause degradation of critical current. In all, 10 km cable was produced for the MQXF and 14 km for the 11 T dipole (short models and prototypes). Insulation of the cables is yet another problem because the coils are reacted at high temperature. A 66-tex braided S2 fibreglass insulation has been used for the cable. An additional 50-μm-thick C-shaped mica insulation has been used for 11 T dipoles. After the reaction, the insulation thickness for MQXF is 0.145 mm and for the 11 T dipole is 0.100 mm.

The biggest challenge of the Nb_3Sn magnet technology comes from the requirement of high-temperature reaction (650–700 °C) of the coils, which are composite in nature. The differential thermal contraction of the composite materials, encountered when the magnet is operated at 1.9 K, has to be managed very intelligently. The problem gets compounded with the increase of the length of the magnet. LARP earlier has successfully tested 3.4-m-long coils. The extension was consequential, requiring a subdivision of the Al shells to minimize the accumulation of longitudinal stresses. HL-LHC magnets will range between 5 and 7 m and the final target for FCC

Table 10.11 Parameters of the MQXF, 11 T dipole of the HL-LHC along with the parameters of LHC dipole and the FCC dipoles (cos θ)

Parameter	Unit	MQXF *Q*-pole	11 T dipole	LHC dipole	FCC (cos θ)
Aperture	mm	150	60	56	50
Length	m	7.15	5.3	14.3	14.3
Field	T		11.2	8.3	16
Peak field	T	11.4	11.6	8.7	16.5
Field gradient	T/m	132.6			
Operating current/% of short sample current	kA %	16.47 78	11.85 80	11.85 86	11.23 86
Coil winding width	mm	36	30	31	50
Stored energy	MJ	8.37	5.313	7.0	37
Strand diameter	mm	0.85	0.7	1.065/0.825	1.1/0.7
No. of strands		40	40	28/36	22/336
Cu: non Cu	Ratio	1.2	1.15	1.65/1.95	0.9/2.2
Cable (bare) width after heat treatment	mm	18.363			
Cable (bare) thickness after heat treatment	mm	1.594			

Data compiled from [40, 41]

is 15-m-long dipoles similar to the existing ones in LHC. The 11 T dipole magnet initially was planned to be 11 m long but was split in two units of 5.3 m each. CERN is building 7.15-m-long Q2 MQXF and the USA is building Q1/Q3 magnets which are divided in to two 4.2-m-long magnets to alleviate the risks related to long coils. The two segments will however be placed in the same cold mass at a minimal distance of ~500 mm, so that the loss in terms of integrated gradient is limited to 5%.

Collaboration between CERN and three US laboratories, Brookhaven National Laboratory (BNL), Fermi National Accelerator Laboratory (FNAL) and Lawrence Berkeley National Laboratory (LBNL) led to the development and testing of a large number of short model MQXF quadrupoles and dipoles using Nb_3Sn magnets. Figure 10.23 shows the cross sections of the 11 T dipole [39, 40] and MQXF quadrupole [40, 41]. These studies helped the accelerator community to collect critical data on the performance of the conductor and the coils in real operating situation and freeze the design of the prototype magnets. Magnet protection against quench is one single most crucial task for the magnet design. All the magnets have been tested for 12 T, slightly above the peak fields on the conductor, 11.4 T in MQXF and 11.6 T in the dipole. The parameters of the MQXF and the dipole are given in Table 10.11. Some of test results on some 21 magnets (MQXF and dipoles) reported by Todesco et al. [40] are discussed below.

Out of 21 short model magnets tested none quenched up to 50% of the short sample current. The training starts at 70% of the short sample current in MQXF magnets and

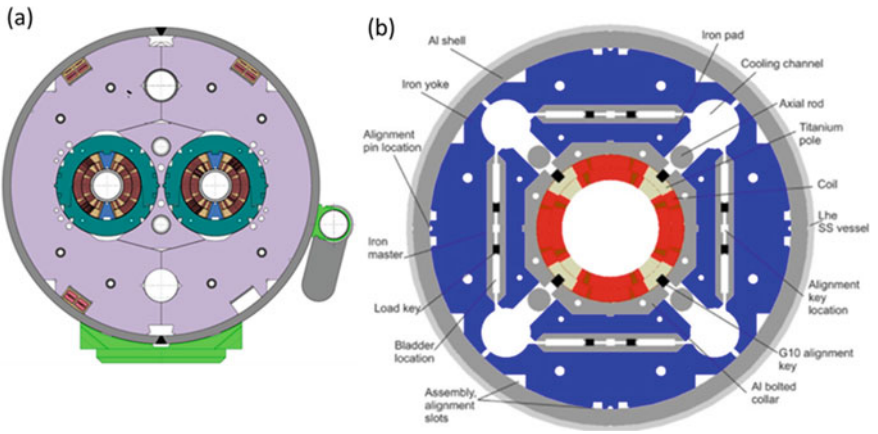

Fig. 10.23 **a** Cross section of the 11 T dipole magnet for HL-LHC [39–41] (Courtesy Frederic Savary, CERN). **b** Cross section of the MQXF quadrupole magnet (Courtesy Ezio Todesco, P. Ferracin (CERN) and G. Ambrosio (FNAL))

at 60% of the short sample current in 11 T dipoles. Five to ten quenches were needed to reach the nominal field in the coils. Interestingly the assembly of double aperture with two coils which have been already trained in single aperture configuration reached the nominal value without quench. Some of the coils which did not perform well, displayed detraining after thermal cycling, were replaced. Development of these magnets motivated a number of institutes and manufacturers to produce Nb_3Sn strands with unprecedented current density of 700–800 A/mm^2. The real challenge had been to manage the thermal contraction problem, from the reaction temperature of ~950 K to the superfluid tempearture of 1.9 K in long magnets. Another challenge is the dimensional tolerances of the coil and the control of pre-stress during the assembly which has been successfully met in short model programme. The prototype coil programme is already on, and several long coils have been produced and tested. Figure 10.24 shows the second prototype 7.15-m-long MQXF-BP2 magnet which has just been assembled in September 2020 and is ready for test.

10.11.3 Testing of Nb_3Sn Quadrupole and Dipole Magnets for High HL-LHC

A 4.2-m-long Nb_3Sn quadrupole magnet with a large aperture of 150 mm has been tested [41] successfully in the USA for the high-luminosity LHC (HL-LHC). It attained a peak field of 11.4 T at the conductor. Several such quadrupoles are being built by US laboratories and CERN for the HL-LHC programme. These magnets will squeeze the proton beams more tightly at the intersection point close to ATLAS and CMS to produce higher luminosity. This will soon be followed by tests of other 7.2

Fig. 10.24 Second prototype 7.15-m-long MQXF-BP2, magnet assembly completed (September 2020) (Courtesy Ezio Todesco, Credit: CERN, high luminosity LHC project and Magnets Superconductors and Cryostat group)

and 4.2 m quadrupole magnets at CERN and the USA. Figure 10.25 shows the 4.2-m-long Nb_3Sn quadrupole magnet with 150 mm aperture which is being readied for test at the BNL. A total of 16 Nb_3Sn quadrupole magnets will be provided by FNAL, BNL and LBNL for the intersection regions of the HL-LHC. The BNL team operated the 8-ton quadrupole magnet in January 2020 at a nominal field gradient of around 130 T/m at a temperature of 1.9 K for five hours continuously. The field gradient produced by the quadrupole magnet in the radial direction focuses the charged-particle beams.

Apart from these strong focusing magnets with 130 T/m gradient, the HL-LHC also needs 11 T Nb_3Sn new dipole magnets to be placed on both sides of a collimator to correct off-momentum protons in the high-intensity beam. These dipoles have shorter length and higher field compared to the present dipoles of the LHC [42]. The new dipoles will enter the magnet lattice of the LHC and replace the old dipoles. The 11 T Nb_3Sn dipole magnets at CERN is shown in Fig. 10.26. In July 2019, CERN tested a Nb_3Sn dipole magnet with a full length of 5.3 m and 60 mm twin aperture. The magnet produced a nominal field of 11.2 T (1.9 K) and a peak field of 11.8 T (1.9 K) on the coil. This is considered to be a major breakthrough in Nb_3Sn magnet technology for accelerators.

In February 2020, the CERN under the FCC project [44] produced a record field of 16.36 T (1.9 K) at the centre of a Nb_3Sn short 'enhanced racetrack model coil' (eRMC). In June 2019, FANL successfully tested a 'cos θ' dipole magnet with an aperture of 60 mm up to a bore field of 14.1 T (4.5 K). For induction of these magnets in the LHC magnet lattice the two magnets, a dipole and a quadrupole, have to be

Fig. 10.25 4.2-m-long Nb_3Sn quadrupole magnet with 150 mm aperture being readied for test at the BNL, USA [42]. *Credit* Brookhaven National Laboratory

Fig. 10.26 Nb_3Sn 11 T dipole magnet for HL-LHC undergoing tests at CERN's SM 18 facility. *Credit* CERN-Photo-202002-5 [43]

joined in pair. This is in contrast with LHC in which the longer magnets were single units. Both the magnets in a pair have the same winding and differ only in their mechanical interfaces and in electrical circuitry. The field regime thus changes from 8 to 12 T, an increase of 50%. These magnets will squeeze the beam and increase the HL-LHC integrated luminosity. The total number of collisions are expected to go up by a factor of 10.

10.12 Future Circular Collider (FCC)

The HL-LHC discussed in the last section is only a springboard to build a more powerful accelerator which will dwarf LHC. Labelled as Future Circular Collider (FCC), it will smash particles finally with an energy of 100 TeV. The concept design of FCC was unveiled by the physicists at CERN in January 2019. It would have a underground tunnel 100 km in circumference that would be excavated around the city of Genova and the surrounding areas [45, 46]. LHC would feed particles into the new collider similar to LEP fed LHC as though enacting an action replay by FCC and LHC. FCC is like several projects in to one. In the first phase, it will collide electrons with their antimatter particles positrons. Both particles, when collide, annihilate each other completely and all their energy is converted in to a new particle. This collision would be very clean compared to in LHC as protons are not fundamental particles like electrons. Protons have several smaller particles including quarks and gluons. Spotting new particles after collisions thus becomes harder because proton–proton collisions spread debris which make measurements inaccurate.

The collision energy will increase in stages to perform different types of experiments. The collider would produce energy of 91 GeV for 4 years, at 160 GeV for two years and then at 240 GeV for three years during which period the FCC-ee would focus on creating a million Higgs bosons. The properties of the Higgs bosons can then be studied an order of magnitude more accurately than it was possible with the LHC. The collider would then be shut down for a year to prepare it to run at around 360 GeV for producing a million top and antitop pairs over five years. After the physics experiments of the FCC-ee are complete, the same tunnel would then be used to house a proton–proton collider (FCC-hh) much in the same way that LEP made way for the LHC. A proton–proton collider with unprecedented energy would offer the best chance to discover new particles. As stated earlier, the FCC-hh would use the LHC and its pre-injector accelerators to feed FCC that could reach a top energy of 100 TeV—seven times greater than the present LHC. In November 2019, Chinese physicists too revealed a plan of building a 100-km-long 100 TeV circular collider with many similarities with the FCC design.

10.12.1 Magnet Technology for FCC-Hh

The Future Circular Collider high-luminosity, high-energy (FCC-hh) projected to produce 100 Tev collision energies would need 16 T dipolar field which will be provided by Nb_3Sn magnets. Important parameters of the FCC dipole magnet [40] are given in Table 10.11. The FCC dipole magnet would be of a Cos θ type 14.3 m long, 50 mm of aperture and would produce a field of 16 T and a peak field of 16.5 T. The magnet will operate at a current of 11.23 kA and will have a stored energy of 37 MJ. The magnet would be wound using Nb_3Sn conductor having 22/326 strands each of dia. of 1.1/0.7 mm and a Cu: non Cu ratio = 1: 2.44. Figure 10.27 is the photograph of the first Racetrack Model Magnets successfully tested for 16 T thus establishing the reliability of 16 T Nb_3Sn dipole magnets for Future Circular Collider (FCC).

In recent times, the Nb_3Sn conductor technology has been developed to a great extent in the context of ITER and HL-LHC projects and would meet the 16 T target of the FCC comfortably. We have already discussed the large aperture (100 mm) dipole, FRESCA-2 built in 2018 under CERN—CEA collaboration attained a field of 14.6 T at 1.9 K using Nb_3Sn conductor. More recently in June 2019, Fermilab under the US Magnet Development Programme (MDP) carried out the successful test of a 'Cos θ' dipole with an aperture of 60 mm US-MDP 'Cos $\theta - 1$' which attained a field of 14.1 T (4.5 K). The magnet is shown in Fig. 10.28. We have also discussed that CERN in February 2020 reported a record central field of 16.36 T (1.9 K) and a peak field 16.5 T in an enhanced racetrack model coil (eRMC). These results assure us that the next-generation collider, the FCC-hh is perfectly achievable.

For a field of 16 T Nb_3Sn conductor thus seems to be just appropriate. For field higher than 16 T, a very large coil and correspondingly a huge quantity of conductor

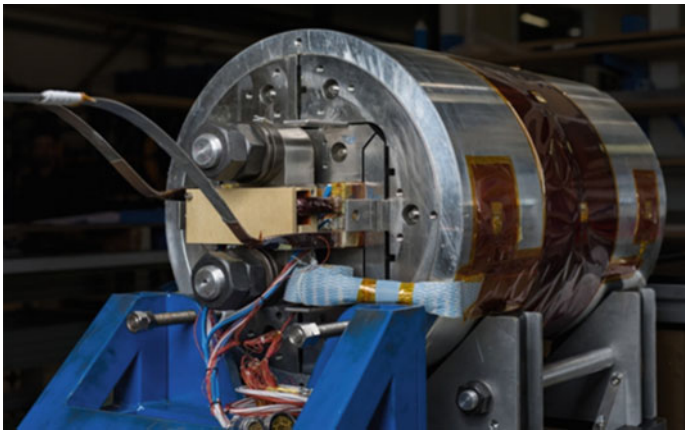

Fig. 10.27 Photograph of the first Racetrack Model Magnets successfully tested for 16 T establishing the reliability of 16 T Nb_3Sn dipole magnets for Future Circular Collider (FCC) (Courtesy Panagiotis Charitos, CERN, Credit: FCC Study/CERN: (Credits FCC Study/CERN: https://cds.cern.ch/record/2653532)

Fig. 10.28 US-MDP 'Cos θ − 1' dipole magnet wound with Nb_3Sn conductor achieved a field of 14.1 T (4.5 K) at Fermilab in 2019 [43]. *Credit* Fermi National Accelerator Lab.

would be needed if Nb_3Sn is to be used. The Nb_3Sn conductor technology needs to be improved further as newer problems are being identified during the ongoing work on the HL-LHC magnets. These problems are aggravated by the high magnetic field, large stored energy and alarmingly large electromagnetic force. CERN, in collaboration with research centres, universities and industries, is pursuing the goal of finding Nb_3Sn innovative production technology which ensures high performance and reasonably low cost. We are however close to the limit of Nb_3Sn, and it is a matter of time that we will have to switch over to HTS.

We have already discussed the development of a variety of 2G REBCO cables, namely Roebel, CORC, CroCo and CroCo-CICC with unprecedented critical currents in Chap. 6. KIT has been engaged in the development of these cables and achieved very encouraging results. Rutherford cables with 11 CroCo strands over a rectangular metallic core and jacketed in a SS casing is expected to have a critical current of 84 kA (4.2 K, 13.5 T) far above the requirement of 50–60 kA for DEMO toroidal field coils. It is thus clear that large critical current for future magnets may not be a problem but management of huge stresses and structural stability of the materials used in magnet will pose challenge of high magnitude. Another big challenge will be the detection of quench and magnet protection in large HTS magnets, the stored energy being enormous. New issues might come up for resolution when

we move from LTS regime to HTS regime. Production cost would certainly be one of them.

10.13 The High-Energy 28 TEV Large Hadron Collider (HE-LHC)

Notwithstanding the ongoing construction of HL-LHC and the FCC colliders, one more proposal has cought the attention of the accelerator community, that of the high-energy LHC (HE-LHC) which would achieve a centre-of-mass energy of 28 TeV. This accelerator will use the LHC tunnel and the FCC magnet technology to achieve significantly higher luminosity than at the HL-LHC. The discovery of the Higgs boson mass at ∼125 GeV hinted that supersymmetry can be observed only in the several TeV region. Aboubrahim and Nath [47] investigated the potential reach of HE-LHC for the discovery of supersymmetry and compared it with the potential reach of the HL-LHC. They concluded that the discovery of supersymmetry would require a HL-LHC run between 5 and 8 years, whereas the same parameter points can be discovered in few weeks to ∼1.5 year at HE-LHC which would run at a luminosity of 2.5×10^{35} cm^{-2} s^{-1}.

10.13.1 Emergence of Supercable-In-Conduit Conductors (SuperCICC) for High-Field Accelerator Magnets

The new accelerators need 16 T dipole magnets for which Nb_3Sn magnets have been developed and tested at a few participating institutions. So far, Rutherford cables have been preferred for winding accelerator magnets of all the designs. Managing Lorentz stress within the winding packs has however been a major problem. Further, to save on the cost, high-field magnets should be wound in hybrid configuration using HTS, Nb_3sn and Nb–Ti conductors in field regions from high field to low field as one moves radially away from the centre. A cable-in-conduit (CIC) conductor can accommodate hybrid winding containing sub-windings of HTS, Nb_3Sn and Nb–Ti which minimizes the amount of most expensive HTS Bi-2212. The conventional cable-in-conduit conductors (CICCs) used in tokamak magnets however have limitation of stress management. In these cables, the Nb_3Sn strands in rope form are wound over a central spiral flexible tube and then compressed inside an armoured sheath. This compression causes severe indents in the cross section of the strand affecting the performance of the strands. Differential thermal contraction during cool-down induces compressive strain in the conductor which further degrades the critical current of the cable because the strand ropes are friction-locked to the armour. Repeated ramping up and down of current in presence of magnetic field also adds to the critical current degradation perhaps because part of strands within the rope may

not be supported. Consequently, the conventional CIC conductors (CICC) perform at less than 50% of the current density calculated on the basis of the critical current of the individual strands. For example, the TF and CS coils of the ITER have J_{WP} of only 20 A/mm^2 even though the average J_e of the Nb_3Sn wire used is 380 A/mm^2 (4.2 K, 12 T).

Texas A&M University (TAMU) in collaboration with Accelerator Technology Corp. (ATC), and HyperTech Research (HTR) has developed [48] a novel technique for producing cable-in-conduit (CIC) conductor nicknamed 'SuperCIC' conductor which accounts well for all the factors affecting the performance of the CICC fabricated by the conventional method. The new CICC winding provide high strength support to the coil as a whole including flared ends. The 'SuperCIC' technology does not cause indentation on the wire cross section and provides uniform support to all the strands in the cable over its full length. It also eliminates friction-lock ends and bypasses the Lorentz stress. As a result, new CICC performance is not degraded in high field. In this technique, the superconducting strands are wound around a perforated thin walled SS 316L tube with a twist pitch equal to the arc length around a 90° bend, that is, $= \pi R/2$ where R is bend radius. This is then wrapped with a thin-foil tape. A second layer of strands is then wrapped over the foil with opposite twist. Instead of inserting the cable in a tube and drawing it as in the conventional CICC technique, HyperTech Research used its proprietary method of continuously tube forming (CTFF) onto the cable over the entire length and weld it to make it helium leak tight. HyperTech developed this technique for the dipole magnets of the recently launched EIC (electron–ion collider) which will be discussed briefly in the next section. EIC needs about 300-m-long SuperCICC cable for its dipole magnets. Using this innovative technique, HTR manufactured CICC cables of HTS Bi-2212, Nb_3Sn and Nb–Ti superconductors and used for winding racetrack coils in hybrid formation to minimize the quantity of expensive Bi-2212 conductor. The perforations in the central tube allow the flow of the cooling fluid in to the voids between the strands of the cable. Direct contact between liquid helium and the strands provides thermal stability against microquenches. A detailed description of the two-layer SuperCIC conductor has been published by Breitschopf et al. recently [49]. Figure 10.29 shows (a) Rutherford cable used in LHC, (b) the CICC used in ITER, (c) the SuperCIC conductor with single layer (d), SuperCIC with double layer and (e) is the cutaway view of the SuperCIC showing the central flexible pipe wound with two layers of strands wound over the tube with opposite twist and with a thin foil as interlayer. We summarize the salient features of the SuperCIC conductors below.

1. All the strands within the SuperCIC are well supported preventing strain degradation even at very high fields.
2. These CIC cables have enabled building of high-field magnets in hybrid formation which minimizes the quantity of HTS, the most expensive part of winding and thus reduces the cost.
3. The robust sheath tube manages the stress well within each sub-winding.
4. SuperCIC can be bent over a radius of 8 × cable radius which qualifies the cable for use in collider dipoles.

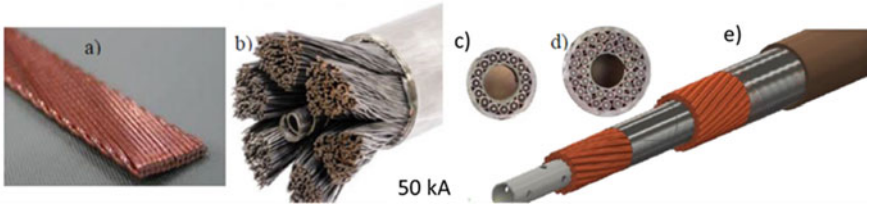

Fig. 10.29 Superconducting cables used in in accelerators and tokamaks [49]. **a** Rutherford cable used in accelerator dipole magnets. **b** Cable-in-conduit conductor (CICC) used in TF coils and central solenoid of ITER tokamak. **c** Single-layer SuperCIC cable developed for arc dipole of JLEIC. **d** Two-layer SuperCIC cable developed for HE-LHC hybrid dipole, TF coils and solenoids. **e** Cutaway view of two-layer SuperCIC cable from HyperTech Open access under CCA 3.0 [49] J. Breitschopf et al. ICMC 2019, IOP Conf. Series: Mat. Sc. and Engineering, **756**, 01203 (2020), IOP Publishing https://doi.org/10.1088/1757-899X/756/1/012031

5. Cable to be used for toroidal coils can be provided with co-wind armour shell for increased strength structure without a degradation of the cable.
6. SuperCIC cables with 50 kA operating current have been designed and prototype produced.
7. The technique has been applied for the manufacture of cables of Nb–Ti, Nb_3Sn and Bi-2212 at HyperTech.

With the development of SuperCIC cables, it appears that hybrid winding of high-field magnets will get wide acceptance by the accelerator and fusion reactor community. It will also reduce the cost significantly as HTS will be used only for the production of the high-field component, the background field being provided by the Nb–Ti and Nb_3Sn combination.

10.13.2 The HE-LHC Dipoles in Hybrid formation—A New Concept

The development of SuperCIC conductor by HyperTech offered an advantageous way of building accelerator magnets in hybrid formation utilizing fully the current carrying capacities of the constituent superconductors in different field regions. McIntyre et al. [50, 51] designed and built 19 and 16 T hybride dual dipoles of block-coil geometry by grouping block-coil sub-windings of Bi-2212, Nb_3Sn and NbTi in regions of increasing distance from the vertical mid-plane and decreasing magnetic field. The field at the boundary of Nb–Ti and Nb_3Sn sub-windings was kept 7 T, the field at the boundary of Nb_3Sn and Bi-2212 sub-windings at 14 T such that all the sub-windings operate at the same fraction of critical current and produce a bore field of 19 T at an operating temperature of 5 K. Figure 10.30 shows the field distribution in the dual dipole at the maximum excitation current of 27 kA. Colour code has been used to indicate field distribution in the range of 0–19 T. The vertical

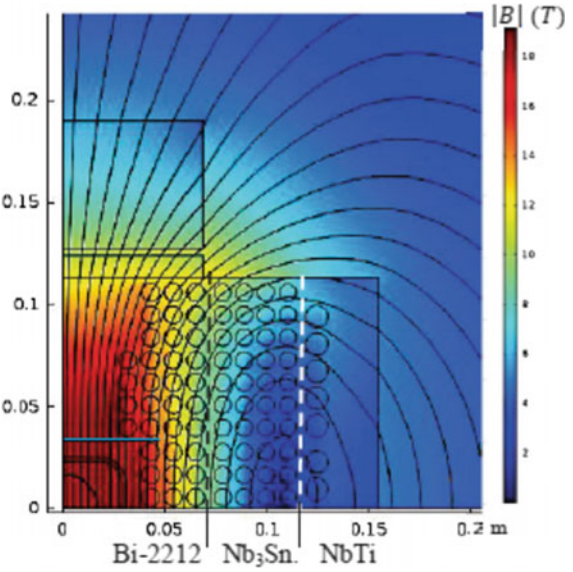

Fig. 10.30 Lines of force in a 19 T hybrid dual dipole operated at a maximum operating current of 27 kA. Colour code has been used to depict field in the range 0–19 T B-2212, Nb_3Sn and Nb–Ti SuperCICC have been used in hybrid formation [50] (Open access, P.M. McIntyre et al., JACoW Publishing under CCA 3.0 Int. licence, https://doi.org/10.18429/JACoW-IPAC2019-MOPMP048)

orientation of the field seen in Fig. 10.30 is unique to block-coil dipoles not seen in any of the Cos θ, Canted Cosine θ or the common coil dipoles. Optimization to partition the sub-windings is necessary so that they can be separately wound, heat treated and finally assembled in to the winding. Main parameters of the 19 T hybrid dual dipole are given in Table 10.12.

The magnetic design ensures collider-quality field distribution over a range of field from 0.5 T at 0.5 GeV injection point to 18 T at the collision point (15 TeV

Table 10.12 Parameters of the 19 T hybrid dual dipole for HE-LHC wound with SuperCIC cables of Bi-2212, Nb_3Sn and Nb–Ti

Parameter	Value		
Bore field @ 5 K	19 T		
Coil current @ 19 T	27 kA		
Operating temperature	4.2–5 K		
Stored energy/bore	6 MJ/m		
Parameter	2-layer SuperCIC sub-windings		
	Nb–Ti	Nb_3Sn	Bi-2212
No. of layers	2	4	4
No. of turns/bore	14	80	68
No. of strands	16 + 22	17 + 23	17 + 23
Wire diameter (mm)	1.2	0.80	0.88
B_{Max} in sub-winding (T)	6.3	11.5	19.8

per beam). In low field the persistent current (PC) in the CICC wires generates multipoles and a snapback when the current is switched from discharging mode to charging mode. Situation is still worse in inner windings of Nb_3Sn and Bi-2212 because of the larger size of the filament in these wires compared with Nb–Ti which has much finer filaments. The salient feature of the CICC dipole is that it suppresses PC multipoles with the use of horizontal steel flux plates mounted above and below the beam tube and shown in light blue in Fig. 10.30. All other dipoles with Bi-2212 or Nb_3Sn windings have PC multipoles, which are at least 20 times larger. The structure material used is G-11 fibre-reinforced polymer but for Nb_3Sn and Bi-2212 sub-windings, one has to use a high-temperature material.

Plymouth Tube, the manufacturer of titanium alloys, has developed a design for the central structural beam and the channel plates of a Ti-alloy. The structure is modelled on the FRP structure developed for the NbTi windings for JLEIC (Jefferson Lab. Electron–Ion Collider). The Ti structure bypasses the stress and permits the heat treatments for Nb_3Sn and Bi-2212.

10.14 The State-of-the-Art Electron–Ion Collider (EIC)—A Discovery Machine

The Nuclear Science Advisory Committee (NSAC) of the US Department of Energy (DOE) Office of Nuclear Physics (NP) [52] recommended highest priority for the construction of electron–ion collider (EIC) in 2017. Two proposals were considered one from the Brookhaven National Laboratory (BNL) and the other by the Thomas Jefferson Laboratory (JLab). The two machines were based upon two different designs. BNL proposed to use the infrastructure of its Relativistic Heavy Ion Collider (RHIC) and the Thomas Jefferson National Accelerator Laboratory (JLab) to use the Continuous Electron Beam Accelerator Facility (CEBAF). The EICs with high-luminosity (high collision rate and large data) and highly polarized beams will act as a high-precision sub-atomic microscope also referred to as ‘Fentoscope’. The EIC will unfold several mysteries of the quarks and gluons, the fundamental building blocks of the atom. The EIC results will reveal how these two fundamental particles are arranged, how they interact and build up the mass of most of the visible matter. EIC will also uncover the secret of the strongest force in nature and reveal how the packed quarks and gluons inside a proton combine their spins to generate the net spin of the proton. It will also throw light on the fact that quarks and gluons are never observed in isolation but are always confined within protons and neutrons. No wonder therefore the EIC is also called a ‘Discovery Machine’. In short, the success of EIC will push the limits of our understanding of inner structure of the nucleus, accelerator science, particle detector design and high-performance computing. Technology fall-out of the project would be enormous. The EIC would have two intersecting accelerators, one accelerator would produce an intense beam of electrons and the other accelerator a beam of protons (or heavier atomic nuclei) [53]. The two beams would then

be steered into head-on collisions at centre-of-mass-energies (E_{CM}) in the range of 20–140 GeV with luminosity more than $10^{33}/cm^2/s$ in 40–140 GeV range, and a top luminosity of $10^{34}/cm^2/s$ at $E_{CM} = 105$ GeV. Both the beams will be more than 70% spin polarized. This means that scientists can alter the alignment and understand the proton spin.

10.14.1 ERHIC—The Electron–Ion Collider at Brookhaven National Laboratory

The Brookhaven National Laboratory (BNL) in Long Island, New York under DOE, USA officially launched [54] the next-generation electron–ion collider (EIC) at BNL on 18 September 2020. The project with a proposed budget of ~$1.6–2.6 billion from the DOE's Office of Science and $100 million from New York State, will involve experts from the DOE institutions, several universities and laboratories around the world. Physicists from Brookhaven Lab and Jefferson Lab will play leading roles.

The BNL proposes [53] to add an electron storage ring to the RHIC complex. Ion beams ranging from deuterium to heavy uranium ions will be available for collision. The BNL machine referred to as eRHIC has been designed jointly by nuclear physicists and accelerator scientists and would enable large-acceptance experiments involving quarks and gluons with unprecedented resolving power. The Preliminary Conceptual Design Report (PCDR) of the eRHIC would guide the construction of this electron–ion collider. A schematic conceptual drawing of the BNL eRHIC [55] is shown in Fig. 10.31.

The RHIC ion storage ring (yellow ring) and the new electron storage ring (blue ring), respectively, provide intense hadron and electron beams stored in two storage rings for collision with required centre-of-mass energy in the range of 20–140 GeV. RHIC needs few modifications but the challenge lies in the accommodation of the electron accelerator in the existing 3.86-km-long tunnel which requires an intelligent planning. Further, the enhancement of the luminosity up to $4.3 \times 10^{33}/cm^2/s$ has to be achieved with strong hadron cooling or using some other innovative technique. The collider will have one or more interaction regions. There is a provision for two large-solid-angle detectors which will utilize the space occupied by the RHIC detectors STAR and PHENIX/sPHENIX. Even though most components needed are based upon the known technologies, yet there are components that are at state-of-the-art level or a little beyond the present technology. The special superconducting magnets with large aperture in the interaction regions fall in this category. The addition of an electron storage ring and its injectors to the RHIC complex appears to be an attractive and a low risk solution, which meets all the requirements of an electron–ion collider at a reasonable cost.

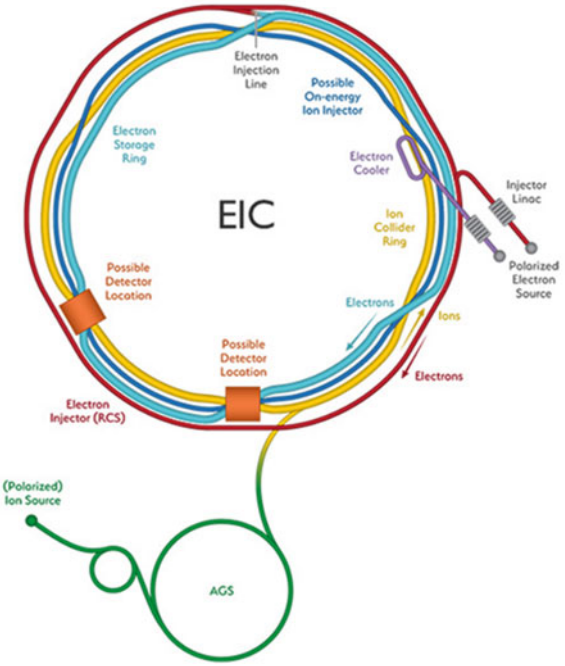

Fig. 10.31 Schematic of the electron–ion collider (EIC) to be built at Brookhaven National Laboratory [55]. *Credit* Brookhaven National Laboratory

10.14.2 The Jefferson Lab Electron–Ion Collider (JLEIC)

The design of the JLab EIC will exploit [56] its existing Continuous Electron Beam Accelerator Facility (CEBAF) upgraded to 12 GeV recently and long experience in building accelerators. JLab will be building an electron storage ring, a new modern ion accelerator and a storage complex. The JLEIC will deliver a centre-of-mass collision energy of 15–65 GeV between electrons and the nuclei. The CEBAF accelerator would inject an intense beam of electrons into a new electron collider ring. JLab will build a new ion accelerator and a collider complex which will deliver up to 100 GeV protons or 40 GeV/nucleon ions. The JLEIC will have a minimum luminosity of 10^{33} cm^{-2} s^{-1} in the entire energy range with a maximum of a few 10^{34} cm^{-2} s^{-1}. The novelty of the JLEIC lies in the figure of 8 design of the two storage rings [57]. Since the figure—8 design for the main rings and booster has never been tested and a large subscale model accelerator is just not possible because of huge cost, the design has to be fully validated theoretically and computationally.

The symmetric figure—8 design however does not need a strong spin-control and thus a relatively weak spin-control technology will work.

A conceptual schematic drawing of the JLEIC is shown in Fig. 10.32. The figure shows two interaction regions (IRs) though there will be only one IR installed in the first phase. The crossing angle in the IR will be 50 mrad. This relatively large crossing angle allows an efficient detection of reacting particles with dipoles in the forward

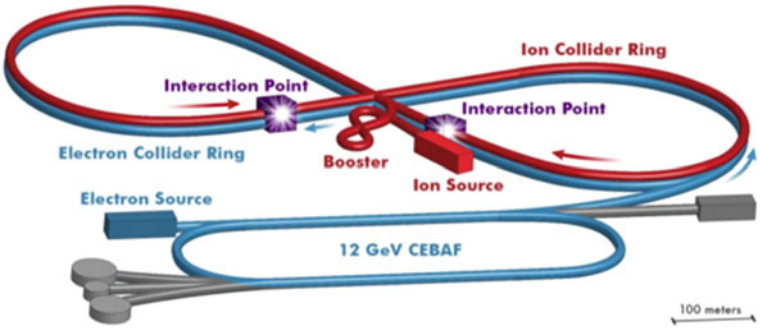

Fig. 10.32 Conceptual design of the Jefferson Laboratory Electron–Ion Collider (JLEIC) (Courtesy Kandice Carter, image credit: Department of Energy's Jefferson Lab)

direction, central solenoid being not very effective. Such a concept of large crossing angle and the forward direction detection will need large aperture final focusing magnets. Electron ring will use normal Cu-magnets only. The upgraded CEBAF will inject 12 GeV electron beam with an average current of 3 A in to the electron storage ring. Both the collider rings have nearly the same circumference of 2.25 km and will be stacked vertically in the same tunnel close to CEBAF.

It is a challenge to design the JLEIC superferric magnets in the interaction region up to 6 T tip field, gradient field 90 T/m and with a large 12 cm radius aperture for a large acceptance. These magnets have to perform in the hostile environment of high heat loads, strong synchrotron radiation, ion losses and the fringe fields of adjacent magnets including the main solenoid. JLab in collaboration with Texas A&M University (TAMU) has come out with various conceptual designs of the magnets [52]. For the ion ring, JLEIC has to develop 3 T dipole magnets with fast ramp rate of 1 T/s in the Booster Ring. A 1.2-m-long prototype 3 T superferric dipole magnet was built by TAMU with a field quality $< 10^{-4}$ over a 6 cm $\times$ 10 cm cross section and over the full dynamic range. Superferric magnet technology has been used by the GSI (Helmholtzzentrum für Schwerionenforschung) for the synchrotron SIS300 of their FAIR (Facility for Antiproton and Ion Research) project. GSI built 2 T dipoles for the SIS-100 ring at FAIR. The field specifications for the JLEIC and GSI magnets are however are not identical and extrapolations from 2 to 3 T may not be realistic.

10.14.3 Magnets in the Interaction Region (IR) of the JLEIC

Renuka et al. at JLab have reported [58] preliminary design of the quadrupoles, skewquadrupole, solenoids and corrector magnets for use in the 32-m-long IR region of the JLEIC. The electron ring and the ion ring will have 6 quadrupole magnets each and all will be of Cos θ design. In addition to the main detector solenoid, there will

be 4 solenoid magnets in the IR region 3 of them will be identical and the fourth will be of a wider diameter. A total of about 37 magnets will be used in the IR. Various computer codes have been used to simulate the performance of the magnets related to stress strain behaviour of the coils and the conductor due to cooling and Lorentz forces. All the electron beam IR quadrupoles will have the same magnetic length but will generate different field gradients ranging between 13.63 and 44.78 T/m for electron energy of 10 GeV. The peak field in the coil will be around 3.5 T. Various options of using an MRI-type wire or a Rutherford-type cable will be considered for winding the magnets. These electron beam quadrupoles will be operated at 4.5–4.7 K.

As stated above, the Ion Beam IR too will have 6 Quadrupoles, 3 upstream and 3 downstream. The upstream quadrupoles will have a relatively smaller aperture but higher field gradients than the downstream quadrupoles. All these quadrupoles will have different magnetic lengths and provide field gradients, varying from 35 to 149 T/m. The first quadrupole on the ion downstream side, QFFB1 will require a beam aperture radius of 8.5 cm and a field gradient of 88 T/m, the middle quadrupole, QFFB2 will require a beam aperture radius of 12.6 cm and a field gradient of 51 T/m. The peak field in QFFB2 turns out to be 10.3 T which means that Nb_3Sn conductor will have to be used for this quadrupole and operate it at 4.5 K. Stress analysis done on this quadrupole QFFB2 gives the value of maximum von Mises stress as 185 MPa after cool-down and 180 MPa due to the Lorentz forces during the operation of the magnet. These values are similar to in LARP and well within the acceptable limits. Similar simulations have been carried out for the skew quadrupole magnets, solenoid magnets and the corrector magnets. These magnets will be built using Cu/Nb–Ti conductor as the peak field is limited to below 5 T. The 32-m-long IR is a crowded region accommodating 30 magnets in close proximity with each other, is a challenge. The fringe field of the magnets will interfere with the electron and ion beams. R&D work on efficient shielding is in progress at BNL under a Small Business Innovative Research (SBIR) project.

10.14.4 Modular Quadrupole Design for EIC

Gupta et al. [59] have proposed a modular design of the quadrupole magnets for EIC which is based upon the racetrack coils. This design does away with costly tooling and enables the use of the same coils in the Nb_3Sn magnets of different apertures. They argue that though the Cos θ design, invariably used for accelerator magnets, is an efficient way to produce high-field gradients, yet the high pole field needed in EIC necessitates the use of Nb_3Sn conductor which is less robust and more sensitive to strain than Nb–Ti. The Nb_3Sn quadrupole magnets wound in a planar racetrack style will perform better than the magnet wound in complex non-planar Cos θ configuration and will be less prone to quench. These racetrack coils are of modular nature, a number of which can be stacked or an individual module can be replaced. Use of modular racetrack coil also permits alteration of the aperture by the set of same coil modules. The authors have carried out design calculations for quadrupole

Q1PF for BNL, which has a field gradient of 140 T/m and an aperture of 96 mm. It has been shown that one racetrack coil cross section can be used in other quadrupoles with different values of field gradient, aperture and other design parameters. Similar calculations will be carried out for the design parameters of the three quadrupoles for JLEIC, namely, QFFB1, QFFB2 and QFFB3. Design calculations have considered a Nb_3Sn cable of the dimensions 15.35 mm × 1.637 mm consisting of 35 strands of 0.8 mm diameter with Cu: SC = 1.17 and a current density of 2087 A/mm^2 (4.4 K, 13.54 T). The authors also carried out simulations by moving the coils of BNL design and creating the aperture for the QFFB1_US, QFFB2_US, QFFB3_US quadrupoles designs and obtained good quality field.

For structural analysis, authors have assumed that the SS 304 collar having a 96 mm aperture hole for the beam holds the coils. Using ANSYS Finite Element programme, the authors found that the peak in the von Mises stress for one of the designs occurs in the collar between the coils. A bending stress also occurs on the inner surface of the aperture.

A value of 44 GPa has been assumed for the Young's modulus of Nb_3Sn for the calculation of strain on the conductor from the Lorentz force. The largest stress is found to be on the collar close to space between the coils. The peak values of displacement, stress and strain are all within the limiting values of the material. For example, in one of the designs, the mechanical displacement is found to be 10.5 μm, peak von Mises stress on collar is 95 MPa against the material limit of 210 MPa, peak von Mises stress on the coil is 46 MPa against the material limit of 210 MPa and the peak coil strain of 0.1% against the material limit of 0.23–0.28%.

10.14.5 Passive Superconducting Shield for Magnets in EIC

One stringent requirement of the EIC is also to provide a field free region for the electron beam near the high-gradient quadrupole for the ion beam in the IR area. Ramesh Gupta et al. [60] under a Small Business Innovation Research (SBIR) project have proposed the use of a passive superconducting shield instead of the presently designed active shield with superconducting coils to meet this requirement. The shielding principle is based upon the simple Lenz's law that current induced in a conductor opposes the change in the field. Such currents already flow in a superconductor persistently limited to a critical value and oppose the field entry. The authors have considered tubes of LTS and HTS, LTS sheets and HTS tapes for the shield. The shielding is further augmented with an iron ring between the beam tube and the superconducting shield. The iron ring will provide shielding against any transient or decay of shielding currents inside the superconductor. This shielding technique will be compatible with magnets in the IR region of the eRHIC as well as of JLEIC and will enable the IR magnets to be operated at reduced current. It will also increase the luminosity of the EIC and will save on radial space, which is a challenge. The shielding of the BNL quadrupole Q1PF closest to IR interaction point with 96 mm aperture and 140 T/m field gradient is most critical.

The shielding test results show that superconducting tubes can provide efficient shielding over a wide range of field distributions and shapes in the IR of the EIC. Nb–Ti tube is robust intrinsically, Bi2223 and ReBCO can be made robust by incorporating a support tube. In fact, we can use multiple concentric tubes or multiple layers across the radius and/or length for increased efficiency. Shielding tests at 77 K with bulk HTS tubes and at 4.2 K for the LTS/HTS tubes have shown promising results for shielding the electron beam from the fringe field of the close-by dipoles and quadrupole magnets of the EIC. This passive system consisting of a superconducting shield with an iron ring inside is far superior to active superconducting shield. Besides being cost effective, it does not need an increase in the magnet current to overcome the opposing field produced by the active superconducting coils. Notwithstanding these promising results, a complete shielding solution has to be worked out once the design of the IR magnets is completed and model magnets are built. Long-term stability of the shielding mechanism too has yet to be established.

The runaway success of the LHC lifted the confidence of the accelerator and superconducting magnet communities to a very high level. This confidence emboldened the physicists and engineers to plan most ambitious future accelerator projects aiming at unprecedented collision energies, which will unravel the secret of nature. The new accelerator projects have also propelled manufacturers of the superconducting wires and cables to focus on the R&D work to achieve highest ever current densities in HTS cables enabling the production of very high magnetic field and the magnets to operate at 20–35 K in the immediate future.

References

1. K.H. Mess, P. Schmuser, S. Wolff, *Superconducting Accelerator Magnets* (World Scientific, 1996)
2. P. Schmuser, Rep. Prog. Phys. **54**, 683 (1991)
3. L. Rossi, Very high field magnets, in *Course Lecture*, *Proceedings CAS* (*CERN Accelerator School*), ed. by S. Russenschuk, G. Vandoni (Erice, Italy, 2002), 8–17 May 2002, pp. 177–195
4. L. Rossi, IEEE Trans. Appl. Supercond. **12**, 219 (2002)
5. L. Rossi, IEEE Trans. Appl. Supercond. **13**, 219 (2003)
6. L. Rossi, Cryogenics **43**, 281 (2003)
7. L. Rossi, IEEE Trans. Appl. Supercond. **14**, 153 (2004)
8. S. Russenschuk, Electromagnetic design of superconducting accelerator magnets, in *Course Lecture*, *Proceedings CAS* (*CERN Accelerator School*), ed. by S. Russenchuk, G. Vandoni (Erice, Italy, 2002), 8–17 May 2002, pp. 71–151
9. S. Russenschuk, ROXIE—a computer code for the integrated design of accelerator magnets. http://accelconf.cern.chg/accelconf/e98/PAPERS/TUP11H.PDF
10. L. Rossi, The role of SC magnets for high energy physics, in *John Adams Lecture* (CERN, 2012), original reference I.I. Rabi, Rev. Sci. Instrum. **5**, 78 (1934)
11. T. Takeuchi, A. Kikuchi, N. Banno et al., Cryogenics **48**, 371 (2008)
12. A.V. Zlobin, arxiv.org/ftp/arxiv/papers/1108/1108.1869.pdf
13. A. Milanese, M. Devaux, M. Durante et al., IEEE Trans. Appl. Supercond. **22**, 4002604 (2012)
14. P. Ferrasin, M. Devaux, M. Durante et al., Report No. CERN-ATS-2013-022, in *Applied Superconductivity Conference* (*ASC 2012*). Portland, Oregon, USA, 7–12 Oct 2012

15. R. Gupta, A common coil design for high field 2-in-1 accelerator magnet, in *Proceedings of the 1997 Particle Accelerator Conference*, vol. 3 (1997), p. 3344
16. R. Gupta, Common coil magnet system for VLHC, in *Proceedings of 1999 Particle Accelerator Conference* (1999) p. 3239. https://accelconf.web.cern.ch/accelconf/p99/PAPERS/THP120.PDF
17. S.A. Gaurlay, K. Chow, D.R. Dietderich et al., Fabrication and test results of a prototype, Nb_3Sn superconducting racetrack dipole magnet. SC MAG 628, LBNL# 41575, in *1999 Particle Accelerator Conference*, NY, Mar 1999
18. R. Benjegerdes, P. Bish, D. Byford et al., Fabrication and test results of a high field, Nb_3Sn superconducting racetrack dipole magnet, in *Proceedings of the 2001 Particle Accelerator Conference* (Chicago, 2001), pp. 208–210. LBNL, 2LC03SC-MAG#764 LBNL-49901. http://escholarship.org/uc/item/76w9q3sg#page-1
19. P. Ferracin, S.E. Bartlett, S. Kaspi et al., IEEE Trans. Appl. Supercond. **16**, 378 (2006)
20. P. Ferracin, S. Caspi, D.W. Cheng et al., *e scholarship* (LBL, Publication 09-29-2008). http://www.escholarship.org/uc/item/4n89827c
21. R. Yamada, G. Ambrosio, E. Barzi et al., Design study of 15-Tesla RHQT Nb_3Al block type dipole magnet. FERMILAB-CONF-05-426 TD (2005)
22. J.C. Thompkins, V. Kashikhin, B. Parker et al., in *Particle Accelerator Conference* (*PAC07*). Albuquerque, 25–29 June 2007
23. N. Phinney et al., International linear collider reference design report. ILC-REPORT-2007-001
24. V.S. Kashikhin, N. Andreev, M.J. Lamm et al., IEEE Trans. Appl. Supercond. **18**, 155 (2008)
25. V.S. Kashikhin, N. Andreev, G. Chlachidze et al., IEEE Trans. Appl. Supercond. **19**, 1176 (2009)
26. V. Kashikhin, N. Andreev, J. Kerby et al., IEEE Trans. Appl. Supercond. **22**, 4002904 (2012)
27. V. Kashikhin, IEEE Trans. Appl. Supercond. **22**, 4003904 (2012)
28. J.A. Crittenden, M.A. Palmer, D.L. Rubin, Wiggler magnet design development for the ILC damping rings, in *Proceedings of the IPAC 2012* (TUPPR, New Orleans, Louisiana, USA, 2012), p. 065 http://accelconf.web.cern.ch/accelconf/IPAC2012/papers/tuppr065.pdf
29. H.G. Blosser, Design, construction and operation of superconducting cyclotron, in *Lecture Notes of 1986 RCNP Kikuchi Summer School on Accelerator Technology*, Osaka, 20–23 Oct 1986, pp. 39–78
30. H.G. Blosser, IEEE Trans. Nucl. Sci. **NS-26**, 2040 (1979)
31. S. Saha, J. Chaudhury, G. Pal et al., Cryogenics **49**, 235 (2009)
32. F.G. Resmini, G. Bellomo, H.G. Blosser et al., IEEE Trans. Nucl. Sci., **NS-28**, 2749 (1981)
33. J.A. Nolen Jr., Nuclear instruments and methods. Phys. Res. B **40/41**, 870 (1989)
34. R.C. York, H.G. Blosser, T.L. Grim et al., The NSCL coupled cyclotron project-overview and status. http://www.nscl.msu.edu/~marti/publications/overview_ganil_98/overview.pdf
35. H. Okuno, N. Fukunishi, O. Komigaito, Prog.Theor. Exp. Phys. 03C002 (2012). https://doi.org/10.1093/ptep/pts046
36. Y. Yano, Nuclear Instruments and Methods. Phys. Res. B **261**, 1009 (2007)
37. H. Okuno, S. Fujishima, T. Tominaka et al., IEEE Trans. Appl. Supercond. **14**, 275 (2004)
38. Overview of the RIBF project. https://ribf.riken.jp/RIBF-TAC05/1_Overview.pdf
39. G. Apollinari et al., *High-Luminosity Large Hadron Collider (HL-LHC) Technical Design Report V. 0.1*, vol. 4 (2017) (Chapter 11). https://doi.org/10.23731/CYRM-2017-004
40. E. Todesco, M. Annarella, G. Ambrosio et al., IEEE Trans. Appl. Supercond. **28**, 4008809 (2018)
41. P. Ferracin, G. Ambrosio, M. Anerella et al., IEEE Trans. Appl. Supercond. **29**, 4001309 (2019)
42. CERN Courier, HL-LHC superconducting quadrupole successfully tested, 23 Mar 2020. https://cerncourier.com/a/hl-lhc-superconducting-quadrupole-sets-record/
43. L. Bottura, Taming the superconductors of tomorrow. CERN Courier, 11 May 2020. https://cerncourier.com/a/taming-the-superconductors-of-tomorrow/
44. CERN News, A demonstrator magnet produces a record magnet field, 25 Mar 2020. https://home.cern/news/news/accelerators/demonstrator-magnet-produces-record-magnet-field

45. News and Analysis (2019) Europe unveils successor to the Large Hadron Collider. Physics World, Feb 2019. https://iopscience.iop.org/article/10.1088/2058-7058/32/2/11/pdf
46. H. Cliff, Large hadron collider replacement plans unveiled—here's what it could discover. Physics ORG, 18 Jan 2019. https://phys.org/news/2019-01-large-hadron-collider-unveiled.html
47. A. Aboubrahim, P. Nath, Phys. Rev. D **98**, 015009 (2018)
48. P.M. McIntyre, J. Breitschopf, T.E. Brown, D. Chavez et al., IEEE Trans. Appl. Supercond. **30**, 4203407 (2020)
49. J. Breitschopf, D. Chavez, T. Elliott, et al., in *IOP Conference Series: Materials Science and Engineering* (*ICMC 2019*), vol. 756 (IOP Publishing, 2020), p. 01203. https://doi.org/10.1088/1757-899X/756/1/012031
50. P.M. McIntyre, D. Chavez, J. Breitschopf, J. Kellams, A. Sattarov, in *10th International Particle Accelerator Conference* (*IPAC 2019*) (JACoW Publishing, Melbourne, Australia, 2019), p. 553. https://doi.org/10.18429/JACoW-IPAC2019-MOPMP048
51. P.M. McIntyre, J. Breitschopf, D. Chavez, J.N. Kellams, A. Sattarov, IEEE Trans. Appl. Supercond. **30**, 4901906 (2020)
52. Report of the community review of EIC accelerator R&D for the office of nuclear physics, 13 Feb 2017. https://www.osti.gov/servlets/purl/1367855
53. An electron-ion collider study. Brookhaven National Laboratory, Aug 2019. https://wiki.bnl.gov/eic/upload/EIC.Design.Study.pdf
54. https://www.bnl.gov/newsroom/news.php?a=117399
55. Electron-ion collider. https://www.flickr.com/photos/brookhavenlab/albums/72157714316624996
56. Electron-ion collider. https://www.jlab.org/eic/#home_section2
57. The electron-ion collider will unravel some of the science's mysteries. Big Think, 27 May 2018. https://bigthink.com/philip-perry/the-electron-ion-collider-will-unravel-some-of-sciences-greatest-mysteries
58. R.R. Ghoshal, R. Fair, P.K. Ghoshal et al., IEEE Trans. Appl. Supercond. **29**, 4100906 (2019)
59. R. Gupta, M. Anerella, J. Cozzolino et al., IEEE Trans. Appl. Supercond. **29**, 4001505 (2019)
60. R. Gupta, S. Joshi, B. Parker et al., IEEE Trans. Appl. Supercond. **29**, 4002104 (2019)

Chapter 11
Superconducting Magnets in Fusion Reactors

Abstract A fusion reactor is an artificial sun created under laboratory environment to produce inexhaustible energy. When two nuclei of hydrogen isotopes are forced to fuse, under condition of high temperature and high pressure, the reaction produces huge amount of energy and the heavier atoms of helium. The tokamak concept for magnetic confinement of plasma in a fusion reactor made the use of superconducting magnets most attractive and a natural choice. This chapter gives an account of the fusion process, the Lawson criterion for realizing 'ignition', different methods of plasma confinement and the superiority of tokamak concept. In a tokamak, plasma is confined in a torus by an axial field generated by a set of toroidal coils distributed around the torus and a poloidal field generated by a set of poloidal coils. A high-field central solenoid induces current in the plasma to heat it to high temperature through ramping of the field. This current, in turn, also produces poloidal field. We discuss the superconducting magnet systems built for most important fusion reactors so far, namely T-7 of Russia, Tore Supra of France, JT-60 SA of Japan, KSTAR of Korea, EAST of China and SST-1 of India. The magnet systems of ITER have been discussed in greater details. Two tokamaks, namely TFTR of USA and JET at Culham UK both using normal magnets have also been included for they had many firsts and the data collected from them contributed significantly to the design of ITER. Two more reactors, the stellarator W7-X built in Germany and IGNITOR an Italian–Russian joint fusion reactor being built in Russia, have also been included towards the end of the chapter. Chinese new tokamaks, HL-2M and CFETR and the design of India's SST-2, have also been discussed.

11.1 The Fusion Reaction

The sun and stars produce their own energy through a hydrogen–hydrogen fusion reaction under conditions of high pressure (high gravitational pull) and high temperature. At high temperature, hydrogen gas converts to plasma and the positively charged nuclei so formed fuse together under high pressure. Under such condition, the attractive nuclear force overcomes the Coulomb repulsion between the positively charged nuclei forcing them to fuse. The fusion reaction produces heavier nuclei of helium

R. G. Sharma, *Superconductivity*, Springer Series in Materials Science 214,
https://doi.org/10.1007/978-3-030-75672-7_11

and releases huge amount of energy. This huge energy is a consequence of the loss of a small mass during the reaction which gets converted into energy ($E = mc^2$). Fusion scientists were keen (since around 1930s) to create the conditions of the sun in the laboratory and use fusion as an inexhaustible source of energy for future. The big challenge is how to create massive gravitational pull, such as available on the sun, inside a laboratory. One option is that we raise the temperature of the plasma to ~10^8 K, about 6 times higher than the sun temperature. The other condition to be met is that the plasma should remain dense enough for long intervals so that the fusion continues and reaches 'ignition' stage as the new fuel is continuously fed. In other words, the re-deposition of fusion energy back into plasma must exceed the energy lost by the plasma to the reactor walls by conduction and radiation. This is referred to as 'self-sustaining plasma' or the so-called ignition and is attained in a laboratory under controlled conditions.

The present efforts are focused on the fusion reaction between the two heavy isotopes of helium, namely deuterium (D) and tritium (T) which yields much higher fusion energy compared to D-D or H-D fusion. Deuterium is most abundant in sea water but tritium is not available in nature. It is radioactive but has a small half-life of 12 years. Tritium, however, can be produced in the fusion reactor itself by reacting lithium with neutrons generated in fusion reaction ($^1n_0 + {}^6Li_3 = {}^3T_1 + {}^4He_2$). The D-T reaction is schematically shown in Fig. 11.1. In a fusion device, the energetic (14.1 MeV) neutrons are absorbed by a thick blanket containing lithium which gets

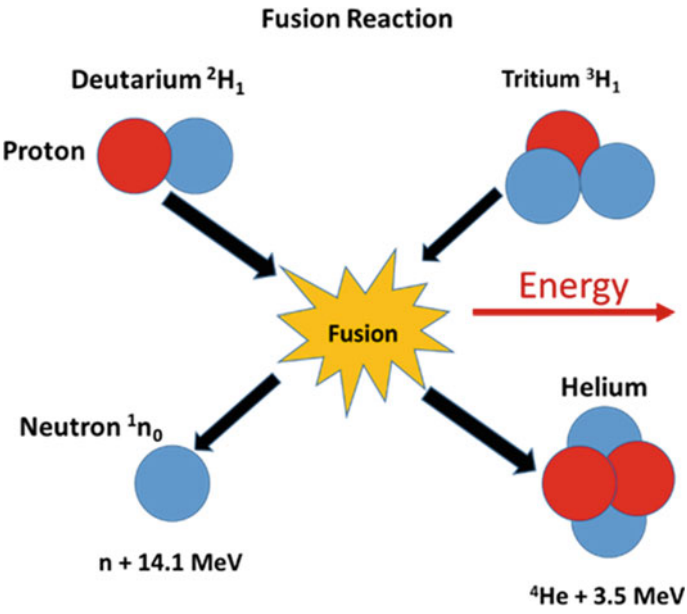

Fig. 11.1 Fusion reaction: two isotopes of hydrogen, deuterium and tritium, fuse under condition of high temperature and high pressure to produce 14.1 MeV neutrons and helium atoms and high energy. Energy will be used to produce steam to rotate turbine and generate power

heated-up. In a power-producing reactor, this heat will be used for the production of steam for rotating turbines in a conventional power plant.

Fusion is attractive because it does not release polluting obnoxious gases like the fossil fuels do. There is no chain reaction either like in fission and no possibility therefore of a 'melt-down' or 'runaway'. Any interruption in the control system in heating of the plasma will automatically terminate fusion. The fusion product is helium which is neither radioactive nor toxic.

11.2 Plasma Ignition

The 'Lawson's criterion' [1] stipulates that the plasma can reach the 'ignition' stage only if the triple product of plasma temperature (T), the plasma (electron) density (n_e) and the energy confinement time (τ_E) fulfils the following condition:

$$n_e T \tau_E \geq \frac{12 k_B}{E_{ch}} \frac{T^2}{\langle \sigma . v \rangle} \tag{11.1}$$

where k_B is the Boltzmann constant, $E_{ch,}$ energy of the charged fusion product, σ, fusion cross section, v, the relative velocity and $\langle \sigma v \rangle$ the average of Maxwellian velocity distribution at temperature T. The above 'triple product' value for a D-T reaction, on a 50:50 basis, turns out to be

$$n_e T \tau_E \geq 10^{21} \text{ keV s/m}^3 \tag{11.2}$$

This condition has not been achieved in any reactor so far, though ITER is designed to attain this triple product value. The energy confinement time, τ_E is defined as the rate at which a system losses energy to its surroundings and is given by

$$\tau_E = \frac{W}{P_{loss}} \tag{11.3}$$

where W is the energy density (per unit volume), and P_{loss} is the power loss density (rate of energy loss per unit volume).

Lawson had assumed that the fusion energy loss is mostly caused by conduction and radiation (Bremsstrahlung). His calculations show that the plasma temperature in a D-T reaction has to reach 30 million degrees, and for a D-D reaction it has to reach 150 million degrees. In practice, plasma is heated by a combination of techniques. Most highly developed techniques are heating by inducing current in electrically conducting plasma by ramping field in a central solenoid, by EM radiation (in radio frequency and microwave frequency range) using ICRH and ECRH techniques and by high-energy neutral beam injection. High temperature causes turbulence in plasma which tends to escape to the walls of the container and thus lowers the plasma temperature. To sustain the plasma, the fusion materials are to be added continuously

and prevent plasma escape to the reactor walls by suitable confinement technique with a long energy confinement time (τ_E). Two types of confinements have been studied in depth: the inertial confinement and the magnetic confinement. We briefly discuss these techniques below.

11.3 Plasma Confinement

Confinement of hot plasma in a fusion reactor has been a big challenge. The purpose of confinement is to sustain the plasma pressure for a long energy confinement time so as to yield high-energy gain ratio Q. Steller plasmas such as in sun are confined by massive gravity which cannot be created in a laboratory. Inertial confinement can be an option in which a deuterium–tritium fuel pellet is compressed to high density, whereby significant fusion burn occurs before the compressed pellet expands. The expansion rate of the internal plasma is limited by the inertia of the pellet. The Lawson criterion would be satisfied at a plasma density, $n = 10^{30}/\text{m}^3$ for a confinement time $\geq 10^{-10}$ s. Laser beam or particle beam can be employed to compress the pellet. Since plasma consists of charged particles (electrons and ions), magnetic confinement has been found to be most promising. The tokamak concept of magnetic confinement has been widely accepted as norm for prolonged confinement of high density plasma. We will discuss briefly these techniques and most famous of the superconducting tokamaks operating and being built in many countries.

11.3.1 The Inertial Confinement

In inertial confinement, the plasma is confined by its own inertia, and the energy confinement time (τ_E) is only about 1 ns, thus limited to pulse operation only. This means that the break-even point (where the fusion energy is equal to the energy spent in fusion reaction) in an inertial confinement will reach only at a very high plasma density, about 10^{30} particles/m^3 (100 times the density of a liquid). Such high densities are achieved by compressing mm size solid fuel pellets by focusing an intense laser or a particle beam onto the pellet. The inertial confinement [2] is schematically shown in Fig. 11.2. These techniques are often referred to as 'laser fusion' and 'particle beam fusion', respectively. Laser fusion became popular during 1970s but has been taken over by the magnetic confinement in the following years. In the rest of the chapter, we will restrict our discussion to 'magnetic confinement' only.

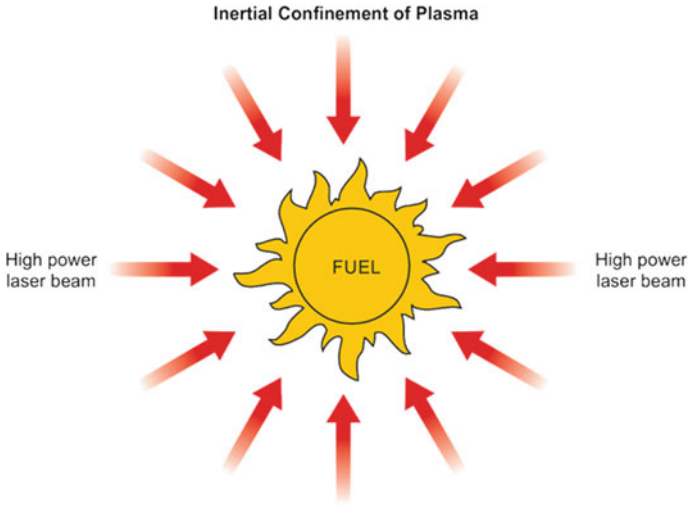

Fig. 11.2 Principle of inertial plasma confinement (dense plasma but short confinement time)

11.3.2 The Magnetic Confinement

In magnetic confinement, the plasma, having a charge, makes helical path along the field direction and is confined for long period of time. Since the plasma has a density of 10^{21} particles/m^3 only, orders of magnitude smaller than the density of air at room temperature, it must have an energy confinement time of at least 1 s. This simply means that the energy of plasma should be replenished every 1 s.

Magnetic confinement together with high temperature (~100,000 °C) stands out to be the best option for stabilizing plasma in the laboratory and a substitute for the gravitational pressure on the sun. Magnetic confinement is based on the principle that the charged particles in the plasma travel in a helical path along the direction of the magnetic field as shown in Fig. 11.3. Several configurations of magnetic confinement were proposed and tried, but three major configurations were pursued and developed over last few decades with varying degree of success. These are 1. magnetic mirror, 2. stellerators and 3. tokamaks and are briefly discussed below.

11.3.3 Magnetic Mirror

The magnetic mirror confinement is a simpler technique. It employs a cylindrical magnet with an axial field. The axial field does prevent plasma escape in the radial direction, but they can escape from the two ends. This escape can be eliminated by plugging the ends magnetically and electrostatically. In this configuration [3], the magnetic field at the ends is increased by placing two coils as shown in Fig. 11.4.

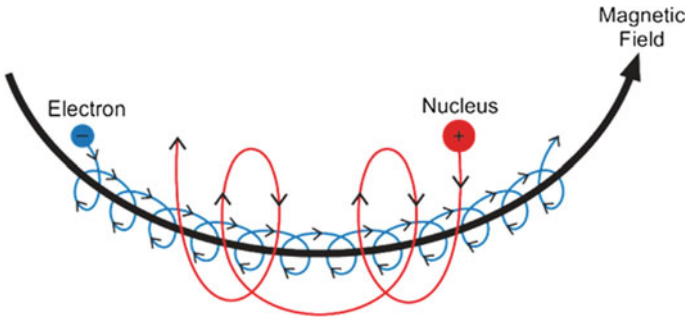

Fig. 11.3 Principle of magnetic confinement. Charged particles of the plasma circulate around the magnetic field and move along the axis (low density plasma but long confinement time)

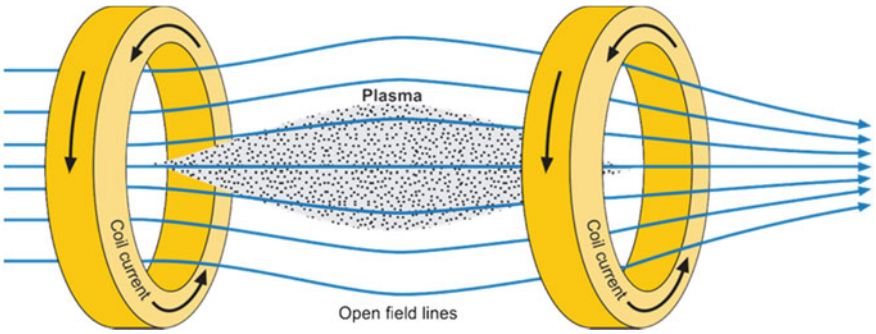

Fig. 11.4 Schematic diagram of a magnetic mirror configuration with magnetic lines. The two end coils with strong field create a 'constriction' for plasma at the ends (Adapted from [3])

Such an arrangement creates a 'constriction' at the ends with stronger field at the two ends and a weaker field in the middle. The plasma with charged particles slows down and gets reflected from the ends or the so-called magnetic mirrors. However, plasma particles possessing very high speed can still escape through the mirrors. Such particles can be stopped by providing electrostatic end plugs. A pair of additional plasma sections are added at the two ends beyond the magnetic mirrors. Plasma in these sections generates a potential barrier which prevents the plasma escape. Such a configuration is termed as 'tandem mirror'. A tandem mirror test facility (TMTF) [4] was built by Lawrence Livermore National Laboratory in 1986 but was closed immediately after.

11.3.4 The Stellarator

The concept of stellarator was proposed by Spitzer [5] in 1950 under a secret project 'Matterhorn' at Princeton, USA, and the device was built the very next year but the project was declassified in 1961 only, under a new name, Princeton Plasma Physics Laboratory (PPPL). Spitzer proposed a new and simpler technique to prevent the escape of plasma from the two ends by bending the solenoid into the form of a torus and closing the two ends. In this configuration, the winding at the inner edge is tight and close to each other but gets farther apart at the outer edge. As a consequence, the magnetic field at the outer edge is weaker than at the inner edge and is thus no longer uniform. Spitzer modified the geometry by stretching out the torus converting it into the shape of a racetrack coil and twisting one end by 180° so as to form a figure of '8'. In such a geometry, the downward drift of the plasma particles in one curved section is counter balanced by the upward drift in the other curved section. The net drift is, thus, greatly reduced but is not 'perfect'. Like magnet mirror confinement, the stellarator too is a low plasma density and high confinement time device. Here the strategy has been to use differing magnetic field such that the net force on the torus is neutralized. It uses helical coils which may be continuous or discrete around the torus. A typical stellarator magnet is shown in Fig. 11.5.

The remarkable advantage that a stellarator offers is that a steady-state operation of the reactor is possible after the ignition has been achieved. The superconducting coils need not be pulsed or the energy be stored. There are no current disruptions either. The design also makes large aspect ratio possible and does not need complicated correction coils for shaping the field and position control coils. It gained popularity in 1950s and 1960s but lost the race to tokamaks in 1970s. Tokamaks were built in many countries independently. Finally, these countries joined hands to pool together with their vast experience and resources in building International Thermonuclear Experimental Reactor (ITER) in France. Interest in stellarator reactors has, however, revived in recent time in view of the complexities involved in building tokamak

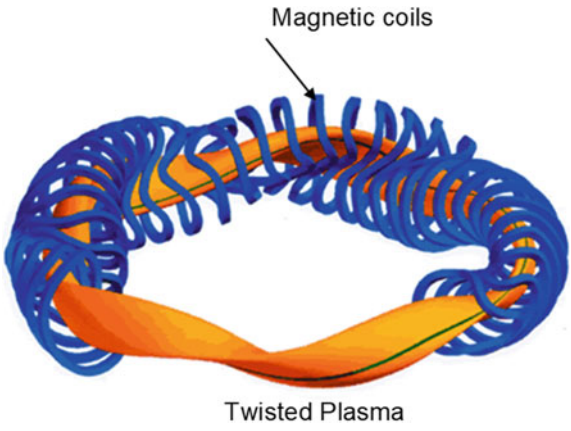

Fig. 11.5 Magnetic coil configuration in a stellarator. *Courtesy* Thomas Klinger, Max Planck Institute for plasma Physics

devices. Some of the important reactors recently built are 1. W 7-X (Wendelstein 7-X), Germany, 2. Helically Symmetric Experiment (HSX), USA, and 3. Large Helical Device (LHD), Japan. A review on stellarators was published by Beidler et al. [6] in 2001.

11.3.5 The Tokamak

The concept of magnetic confinement of high-temperature plasma was given by Soviet scientists (now Russian) Igore E. Tamm and Andrei D. Sakharov of Kurchatov Institute, Moscow, in 1950 (see references 1–3 in [7] of this chapter) while working in a secret project on controlled thermonuclear reactor at 'Arzamas-16 Nuclear Centre'. The abbreviation 'tokamak' has been taken from the Russian term 'Toroidalnaya Komneta s Magnetiymi Katushkami' which in English translates in to 'Toroidal Chamber with Axial Magnetic Field'. Beginning 1951, Sakharov had worked out the tentative parameters of a toroidal thermonuclear D-D fusion reactor of 900 MW power. The dimensions read like, major radius 12 m, minor radius 2 m, field 5 T, plasma density $3 \times 10^{20}/\text{m}^3$ and plasma temperature ~100 keV (1000 million degree Celsius). These values when extrapolated to D-T fusion reaction are close to the modern D-T tokamak dimensions. The confinement was proposed by a combination of a toroidal field and a field produced by a current circulating in the plasma itself. The work on thermonuclear fusion was declassified in 1954. A good account of the contribution of the Russian scientists to tokamak development has been given by Smirnov [7].

11.3.6 Magnetic Field in a Tokamak

High-temperature plasma in a toroid is confined by a combination of two fields: one a poloidal field produced by the current circulating in the plasma and another an axially symmetric strong magnetic field parallel to the current. The axial field is produced by a set of toroidal coils spaced around the torus. The resultant field is a helical field around the circular plasma and close to the surface as shown in Fig. 11.6. It is this helical field which confines the plasma. The toroidal field can be calculated using Ampere's law. A toroidal magnet is a group of coils each carrying same current. The magnetic field inside a torus at any distance from the centre is uniform because of the symmetry. If the number of coils is N each carrying a current I, the magnetic field will be

$$B = \frac{\mu N I}{L} = \frac{\mu N I}{2\pi R} \quad (L \text{ being} = 2\pi R) \tag{11.4}$$

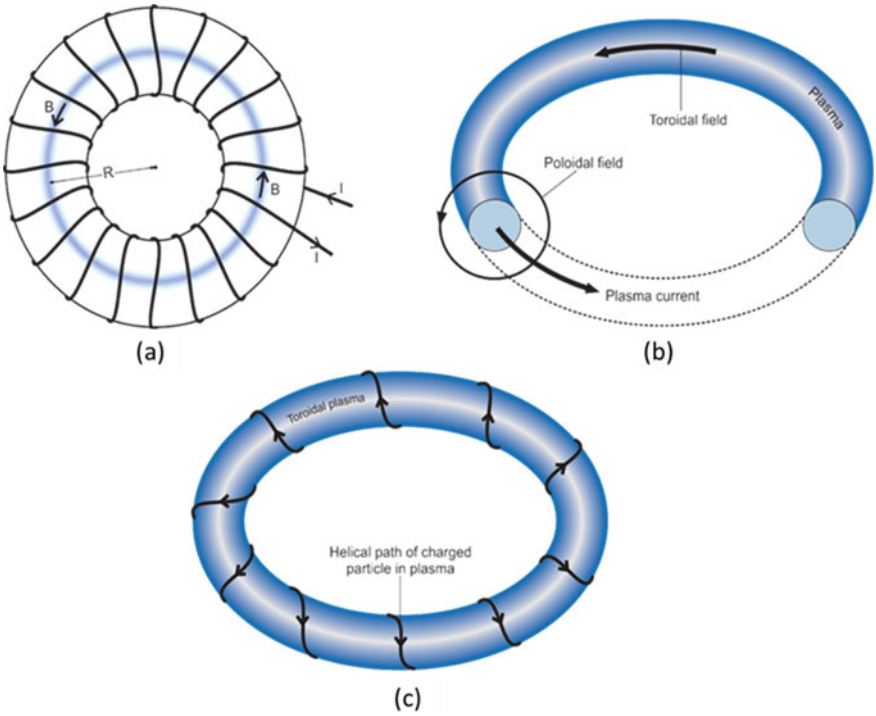

Fig. 11.6 **a** Toroidal field produced by coils wound around the torus. **b** Poloidal field produced by the current flowing in the plasma. **c** The helical path followed by the charged particles in the plasma

where R is the distance of the plasma axis from the centre. Thus, we find that the toroidal field is inversely proportional to the distance from the centre. The field, therefore, at the outer periphery is weaker than at the inner radius. The role of the strong toroidal field is to suppress the main magnetohydrodynamic (MHD) instabilities. The cross section of the magnetic surface in a plane passing through the axis Fig. 11.6b can be considered only approximately circular. Plasma equilibrium analysis shows that at a high toroidal field magnetic surface shape deviates significantly from a circle. Further, the field in a tokamak is also not perfectly symmetric. The toroidal field is produced by a number of coils spaced around the torus. The coils cannot be brought too close because enough space is required for the insertion of a large number of diagnostic instruments and vacuum ports. Still with a larger number of coils, the field symmetry obtained is quite good, and the field oscillations are well within the acceptable limit.

Plasma equilibrium on macroscopic scale is another crucial aspect of a tokamak. Even though the superposition of toroidal field and poloidal field leads to good plasma containment, yet under the influence of electrodynamic forces the plasma current loop tends to expand outwards. The laws of electrodynamics say that a ponderomotive force acts on a current-carrying conductor such that it tends to increase its inductance.

In a circular conductor, it will mean that the radius of the plasma loop will increase. To maintain the equilibrium, this expanding force is to be balanced by applying additional magnetic field parallel to the major axis of the toroid. A perpendicular magnetic field $B_{\perp}$ interacts with I and creates a force $= 2\pi RIB_{\perp}/c$ which acts on the entire length of the plasma loop. This interacting force of the supplementary current-carrying coils producing vertical field will act inwards to counter balance this expanding force with a correct choice of sign. Besides, tokamak devices use a conducting toroidal casing which compensates the internal forces expanding the loop. Eddy currents are produced in the metal casing when the current-carrying loop moves outwards. These eddy currents interact with loop current and give rise to a force which acts inwards. The real breakthrough in fusion research came in 1958 in USSR when they achieved required plasma temperature and confinement time in a doughnut-shaped vessel called tokamak T-1, world's first tokamak. Tokamak T-1 had the major radius of 0.67 m and minor radius of 0.17 m, achieved a temperature of 100 keV and a plasma current of 100 kA. The world's first superconducting tokamak T-7 too was built in USSR in 1978 [8], but it used only toroidal magnets as superconducting. Other magnets were normal magnets.

Present-day tokamaks use all the magnets superconducting to reduce power consumption. Figure 11.7 shows the scheme of different magnets used in present-day tokamak device. Magnetic confinement of plasma is realized by a set of toroidal coils

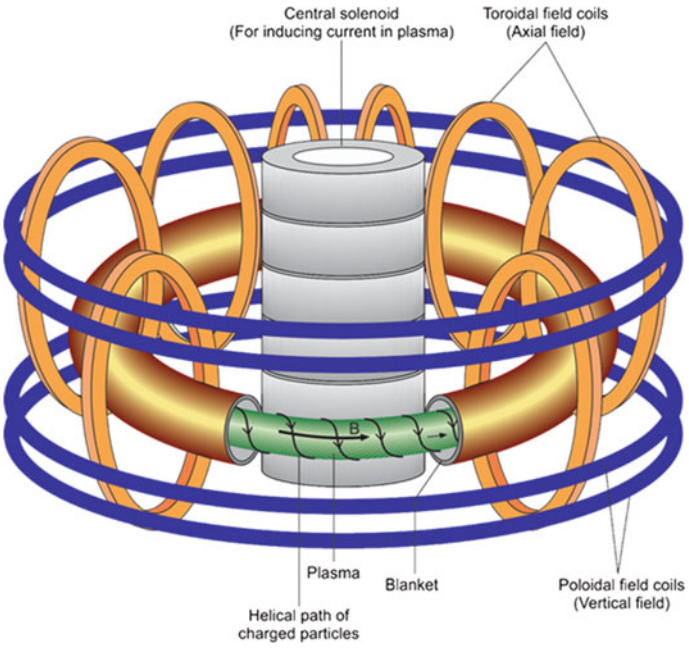

Fig. 11.7 Magnetic confinement of plasma realized by a set of toroidal and poloidal coils. A central solenoid induces current in plasma which, in turn, heats the plasma and generates poloidal field

arranged equidistant around the torus, and a set of poloidal coils mounted around the toroidal coils. A central solenoid (CS) produces high field which induces current in plasma when ramped. This, in turn, heats the plasma and generates poloidal field. The CS, in a way, acts as a primary of a transformer and the plasma as the secondary. This induced current causes Ohmic heating of the plasma. The Ohmic heating is, however, not enough to raise the plasma temperature to the required level. It can raise the plasma temperature to only 20–30 million °C. Additional heating is provided by using EM high-frequency waves like electron cyclotron resonance heating (ECRH), ion cyclotron resonance heating (IRCH) in the 40–55 MHz frequency range and neutral beam injection as shown in Fig. 11.8. A neutral beam has to have a large kinetic energy (~1 MeV) to heat the plasma. Since neutral atoms cannot be accelerated by an electric field, a positively charged ^{2}D beam is first accelerated to high energy and then allowed to pass through a ^{2}D gas cell called 'ion beam neutralizer' where it picks up the lost electron to become neutral again. Neutral beam is injected

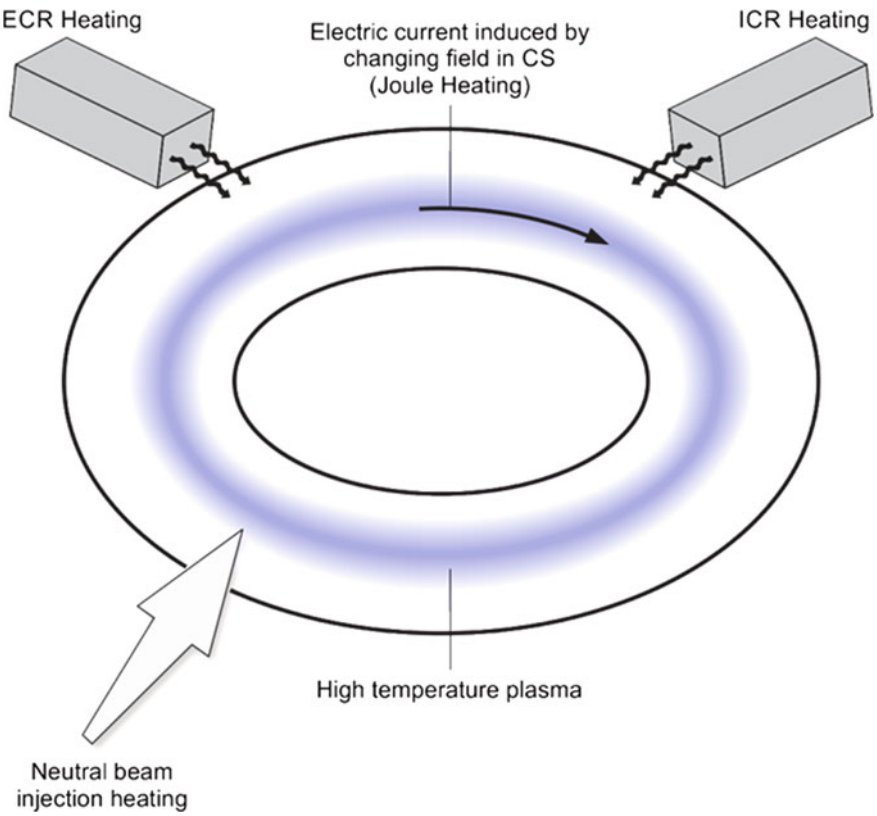

Fig. 11.8 Three different modes of plasma heating. Electric current through plasma is induced by the changing magnetic field in the central solenoid. Additional heating is done by ICR, ECR and neutron beam injection

into the plasma stream where it collides and transfers energy to plasma and heats it up. Till now, more than 200 fusion reactors of different sizes, using magnetic confinement techniques, have been built and operated world over. Some of them are still working. More advanced tokamaks and stellarators are being built in Europe, Asia and USA. In the following sections, we will discuss the magnet systems of some of the important fusion reactors.

11.4 Important Superconducting Tokamaks

High triple fusion product requires large confinement time and thus high magnetic field. Such fields can be generated by superconducting magnets only. Use of these magnets enables operation in continuous mode and also results in a substantial saving of power, an important factor to cross the break-even point. Many superconducting toroidal magnets were built, (T-7 to T-20) in Russia (Moscow), Toresupra (WEST) in France (Cadarache) and JT-60 (Japan Torus) in Japan (Naka). Some of them are operational and others not. HT-7 (Hefei Tokamak) in China (Hefei) was the first fully superconducting tokamak in the world. Fusion reactors, Joint European Torus (JET) at Kulham, UK, and Toroidal Fusion Test Reactor (TFTR) at Princeton Plasma Research Laboratory (PPPL, USA) though non-superconducting, contributed greatly to our present-day understanding of fusion. JET achieved 16 MJ fusion energy first time surpassing the 10.7 MW achieved by TFTR, but remained well below the break-even point, where the fusion energy produced is equal to the power spent in operating the machine. JET used 50:50 deuterium and tritium fuel mixture similar to TFTR and has the distinction of developing the remote handling system for tritium first time. TFTR is no longer in operation. PPPL also built a spherical torus 'NSTX' (Next-Step Spherical torus Experiment) in 1999 with spherical plasma with a central hole but had to stop in 2008 because of the lack of funding. New fusion reactors based on stellarator concepts of magnetic confinement (Wendelstein 7-X) have been built at Greifswald in Germany which started operation in 2015 and is expected to achieve 30 min of continuous plasma discharge in 2021. The experience accumulated over last 55 years on these reactors has finally culminated in building world's biggest tokamak fusion reactor, ITER, an international effort and a precursor to a power plant, DEMO to be built in 2030s. We will discuss very briefly some of the superconducting tokamaks in the following sections.

11.4.1 Tokamak Development in USSR/Russia

As mentioned in the previous section, the concept of tokamak confinement originated in the then Soviet Union (USSR) at the Kurchatov Institute in Moscow. A large number of tokamaks, small and big were built to carry out research on specific

problems related to plasma physics which involve plasma temperature, plasma parametric stability, different modes of heating and conductor selection for magnets. The parameters of some of the important tokamaks built at Kurchatov institute are tabulated in Table 11.1. The first tokamak was built in 1958 designated as tokamak T-1 which used only Ohmic heating. A picture of this historic tokamak is shown in Fig. 11.9a. Other important milestone was the first ever use of superconducting toroidal [8] magnet in tokamak T-7. Complete specifications of tokamak T-7 [9] are given in Table 11.2. T-15 was the largest Russian tokamak built in 1988–95 which was also world's first tokamak which used Nb_3Sn toroidal coils. Plasma heating system consisted of Ohmic heating and NB (9 MW) + ECRH (6 MW) + ICRH (6 MW), pulse 1.5 s heating. The picture of T-15 tokamak is shown in Fig. 11.9b.

Artisimovich and Safranov [10] in 1972 came up with a brilliant idea of an elongated plasma cross section which yielded enhanced plasma stability. This led to the development of a 'D'-shaped toroidal coil first time. A number of reactors, T-8, T-9 and T-12 TBD, were built with 'D'-shaped toroidal coils which established the efficacy of the magnetic field in the formation of an equilibrium plasma in an elongated shape and an efficient use of the magnetic volume. Tokamak T-15 stopped in 1995 because of money crunch, was revived in 2010 and upgraded [11] for a graphite diverter designed to withstand heat loads in the range of 20 MW/m^2, expected in ITER. Upgrades also included improved heating and current drive systems enabling

Table 11.1 Some of the early tokamaks built in USSR/Russia (data compiled from [7])

Tokamak name	Year of start/operation	Major radius (m)	Minor radius (m)	Toroidal field B_{tor} (T)	Plasma current	Salient features
T-1	1958	0.67	0.17	1.5	100 kA	First tokamak of the world, only Ohmic heating
T-7	1978	1.22	0.35	4.0		First-ever superconducting tokamak (toroidal only SC)
T-8	1976	0.28	0.048	0.9	24 kA	World's first 'D'-shaped toroidal coil elongated plasma
T-10	1975	1.5	0.40	5.0	0.65 MA	Ohmic + ECRH (4 MW) 1987
T-15	1988–1995	2.43	0.78	3.5	1.0 MA	World's first Nb_3Sn toroidal coils, heating – Ohmic + NB (9 MW) + ECRH (6 MW) + ICRH (6 MW), Pulse 1.5 s

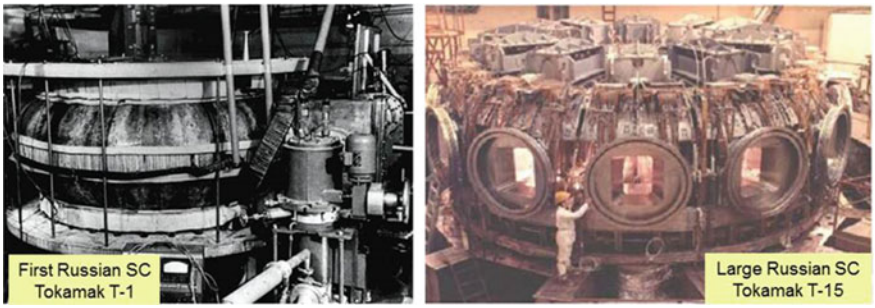

Fig. 11.9 **a** World's first superconducting tokamak, T-1 fusion reactor built at Kurchatov Institute (USSR/Russia) in 1958 [7]. **b** Large Russian superconducting tokamak, T-15 fusion reactor built at Kurchatov Institute (USSR, Russia) in 1988, upgraded to T-15 MD (Modified diverter) in 2010 and finally dismantled to make way for fission–fusion hybrid reactor (both pictures with permission from 'Nuclear Fusion' IAEA)

Table 11.2 Specifications of world's first superconducting tokamak T-7 (data compiled from [7])

Parameter	Unit	Value	Parameter	Unit	Value
Year of operation		1978	SHe mass flow rate	g/s	8
Present status		1992 sold to China	SHe temperature (forced flow of SHe)	(K)	4.5
Major radius	(m)	1.22	Field at torus axis	(T)	3
I.D. of vacuum chamber	(m)	0.175	Peak field on conductor	(T)	5
No. of toroidal DP coils		48	Field volume	(m^3)	6
Average radius of pancake	(m)	0.50	Operating current	(kA)	6
Winding width	(cm)	15	Average Ic at 3 T	(kA/cm^3)	1
No. of turns in a coil		60	Stored energy at 3 T	(MJ)	20
No. of coil modules		24	Quench protection ext. resistor	(Ω)	0.17
Superconductor		Nb-Ti	Total cold mass	(ton)	12
			Refrigerator capacity	(W)	400

a significant increase of heating power (up to 20 MW) and the pulse duration up to 1000 s.

11.4.2 The Russian Hybrid Fusion–Fission Reactor

The upgraded fusion reactor T-15 was finally retired in 2018, and a hybrid fusion–fission reactor (FFR), which combines the principles of thermonuclear and nuclear power, has come up at the site. The reactor [12] is expected to be operational during 2021. In this reactor, the neutrons produced in a small tokamak will be captured in a molten salt blanket located around the torus. Thorium which is cheaper and more abundant than uranium will be used as fuel. Extreme high temperatures needed in a fusion reactor for generating energy would not be required. The neutrons produced in the fusion reactor would be fed into the fission section to sustain the fission process. Thorium is not fissile and can thus be used as a fuel only in conjunction with a fissile material. Thorium can breed fissile uranium-233 in a molten salt blanket of the fusion reactor. The process would be inherently safe because it can be shut down quickly and the high burn up of fissile material would leave few by-products. This hybrid tokamak is now called as T-15 MD (modified divertor).

11.4.3 TFTR (Tokamak Fusion Test Reactor, Non-superconducting), PPPL, USA

TFTR built at Princeton Plasma Physics Laboratory (PPPL) is not a superconducting tokamak but has an important place in the development of fusion reactors insofar as it has many firsts and is an important link to the modern reactors. This was the first fusion reactor which used deuterium and tritium mixture (in 50:50 ratio) as fuel and produced a fusion power of 10.7 MW at a power density of 2.8 MW/m^3. Some of the TFTR parameters are shown in Table 11.3.

Table 11.3 Parameters of TFTR (PPPL, USA) (data compiled from [13, 14])

Parameter	Unit	Value	Parameter	Unit	Value
Start of operation		1982	Coil coolant		Water
Final operation		1997	Toroidal coil current	(kA)	73.3
Plasma major radius	(m)	2.6	Coil winding configuration		Spiral (DP)
Plasma minor radius	(m)	0.9	Plasma current	(MA)	3
Nature of magnets		Normal	Heating pulse duration	(s)	4
No. of TF coils		20	Fusion power (1994)	(MW)	10.7
Field at plasma centre	(T)	6	Auxiliary plasma heating	(MW)	51, RF(11) (NB-40)
			Fuel used		D + T

TFTR used water-cooled normal conductor magnets [13]. The toroidal magnet has 20 coils at 18° interval. Each coil is a double pancake with 44 turns. The magnet generates a field of 6 T at the major radius of 2.6 m (centre of plasma) for a flat-top time of 4 s. The pulse interval is a minimum 300 s, and the magnet has to sustain 300,000 full power pulses. Each coil of the magnet is encased inside Ti cells to transmit the forces to the support structure outside. Coils are cooled by 10 °C chilled water and to protect the electrical insulation, the coil temperature is not allowed to go beyond 65 °C. The whole tokamak is made in ten modules each spaced at 36° angle apart. Each module consists of a 36° segment of the vacuum vessel and two toroidal coils. This configuration allows remotely controlled removal and replacement of coils in a module in the event of a malfunctioning of the coils after the operation with tritium. It produced first time fusion power at a level of 10.7 MW. Figure 11.10 is a photograph of TFTR which operated from 1982 to 1997 at PPPL.

TFTR had its last and final run [14] on 4 April 1997. During its operation (1982–1997), it not only achieved most of its scientific and technical objectives but surpassed them. During this period, TFTR produced a total of 80,000 plasma shots which included more than 1000 shots of D-T plasma. It firmly established the feasibility of a fusion reactor with deuterium and tritium mixture fuel reaching the ignition stage albeit in a pulse mode. It also proved the efficacy of the magnetic confinement of the plasma and made way for more advanced tokamaks inching towards power generation.

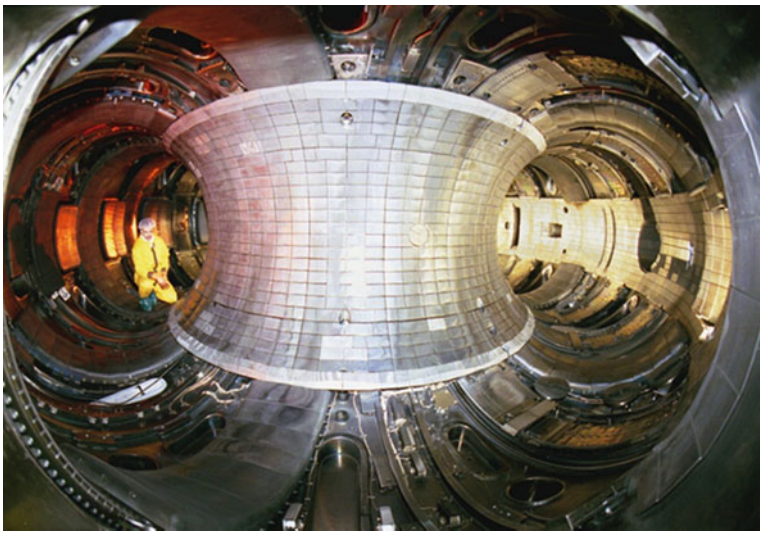

Fig. 11.10 TFTR at Princeton Plasma Physics Laboratory (PPPL, USA). *Courtesy* Mirium Edvardse, Princeton Plasma Physics Laboratory

11.4.4 JET (Joint European Torus), Non-superconducting (Culham, UK)

JET [15, 16] tokamak too has normal copper magnets but is an ongoing large and most powerful tokamak which has a number of landmark achievements to its credit. It has been working under European Fusion Development Agreement (EFDA) and used by over 40 laboratories from EURATOM associations. It may be called as the predecessor of ITER as over the years it has changed to ITER like experimental configuration to provide feedback to ITER in key areas. In 2006, JET changed its magnet to ITER like configuration. During 2009–2011, the carbon-lined plasma container was replaced with beryllium container to prevent neutron retention in carbon. The experience gained and data collected on plasma physics from JET operation have surely given a boost to the international efforts to the ultimate realization of fusion power. Its construction began in 1978, produced first plasma in 1983 and released fusion energy in 1991. It established a world record of generating 16 MW (@ 65% of the input power) fusion power for 1 s in 1997 using deuterium and tritium fuel mixture. JET also has the distinction of having the capability of remote handling of tritium. Table 11.4 gives the main specifications of the JET tokamak. Figure 11.11 shows the interior of the JET tokamak (a) and the cutaway view of the magnet coil structure (b).

Table 11.4 Parameters of JET (Culham Centre for Fusion Energy, UK) (data compiled from [15, 16])

Main parameters	Unit	Value
Year of first plasma		1983
Present status		Ongoing
Plasma major radius	(m)	2.96
Plasma minor radius	(m)	2.1 (vertical) 1.25 (horizontal)
Plasma current	(MA)	3.2 (circular plasma) 4.8 (D-shaped plasma)
Plasma volume	(m^3)	200
Fusion power (upgraded)	(MW)	20
TF field at plasma centre	(T)	4
Plasma sustains for	(s)	5–30
Flat-top pulse length	(s)	20–60
Auxiliary heating	(MW)	NB-34, ICRH-10 LHCD-7
Plasma container walls		Beryllium/Tungsten
Weight of TF coils	(ton)	384
Weight of vacuum vessel	(ton)	100
Fuel used		D + T

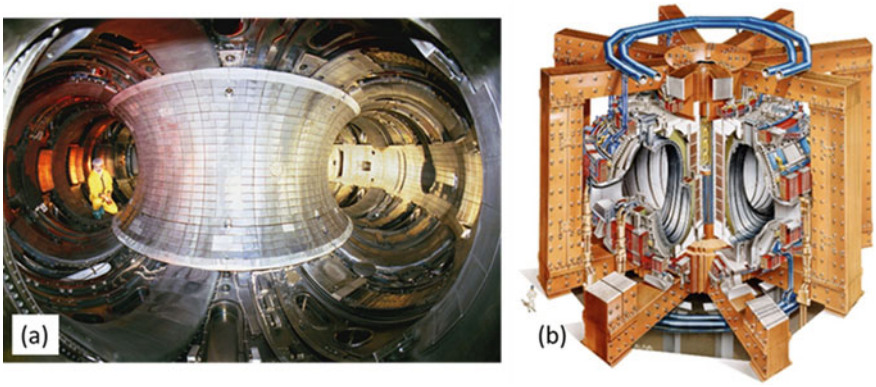

Fig. 11.11 **a** Interior of JET tokamak. **b** A cutaway view of the coil structure of toroidal and poloidal magnets of JET. *Courtesy* Nick Holloway, 'EFDA JET'

Upgraded JET is fully geared to find solution to problems related to plasma physics and engineering expected to be encountered in ITER operation. JET has been very successful in establishing the reliability of remote-controlled handling and replacement of components inside the tritium-infected vacuum vessel.

11.4.5 Mega Ampere Spherical Tokamak (MAST) Upgrade

The MAST upgrade is the new version [17] of the old device which was operational from 2000 to 2013 at Culham Centre. The new device will have higher performance including longer pulses, a stronger magnetic field, increased heating power and an innovative divertor for the new plasma exhaust system. The successor facility called MAST Upgrade began operation in 2020. This work was intended to reduce the size of the tokamak and address physics issues for ITER. The divertor processes spent fuel and heat ejected from the plasma. The exhaust must be cold enough to make sure that any damage to the divertor components is minimal and does not need replacement frequently. MAST Upgrade is the first tokamak to test the 'Super-X divertor'. This is an exhaust system designed to reduce heat and power loads from particles leaving the plasma that means the divertor components will last much longer. MAST Upgrade project was to increase neutral beam power from 5 to 12.5 MW and the energy deposited in plasma from 2.5 to 30 MJ. First plasma was observed in MAST-U in October 2020.

MAST Upgrade will also be able to operate at Culham Centre for Fusion Energy (CCFE) with a variety of other divertor configurations to compare their effectiveness and guide the design choices for future fusion reactors. Data from MAST Upgrade will be used by ITER due for operation in mid 2020s. If successful, Super-X could be used in prototype power plants and produce compact commercial fusion reactors in

2040. This will be implemented under a project called 'STEP' (Spherical Tokamak for Energy Production). STEP is expected to deliver net electricity greater than 100 MW and to ensure tritium self-sufficiency. Other objectives are to identify materials and components compatible with fusion environment and make STEP an affordable life cycle device. In 2019, the UK government approved the conceptual design of the STEP at Culham at a cost of £22 million over four years.

The team at CCFE has announced the beginning of testing of plasma in the upgraded MAST in November 2020. The plasma test has come after seven years of work in upgrading the original MAST. As part of the upgrade, the exhaust system has been upgraded, which will handle very large massive stresses without the need for constant replacements. The system has been named as 'Super-X divertor'. MAST in the near term will focus heavily on testing the new divertor design. Though the MAST is of spherical design as opposed to doughnut shape, yet is controlled by (superconducting) magnetic field. This design will be beneficial for constructing much smaller fusion plants, which will be much less expensive.

11.4.6 Tore Supra (NRC, Cadarache, France)

Tore Supra was a large superconducting tokamak run by Euratom-CEA Association at 'Nuclear Research Centre', Cadarache, France. It started operation in 1988 and since then has carried out extensive research on problems related to plasma physics and technical issues concerning engineering design of the plasma container and other components of the tokamak system. The research has been somewhat complementary to JET. It provided crucial inputs to the final design of the ongoing ITER tokamak programme and continues to play supporting role for the success of ITER and the later versions like the DEMO. A photograph of Tore Supra is shown in Fig. 11.12.

The tokamak has 18 superconducting toroidal coils [18–21] built in six modules of three coils each and is suitably spaced around the vacuum chamber and joined together to complete the torus. The three coils, each insulated electrically, are mechanically interlocked using strong insulated shear keys to make a rigid structure as shown in Fig. 11.13. Each coil is wound in a 26 double pancake structure. Each pancake is separated by electrically insulting spacers which allows large contact area between the winding and the superfluid. The coil becomes rigid after curing and is enclosed in a thin (2 mm) SS casing with perforated glass spacers and ground insulation in between. The casing serves as a superfluid helium (1.8 K) vessel as well. The void volume inside the winding though is filled with superfluid helium, and the individual turns are insulated by pre-impregnated fibre glass tape co-wound with the conductor. This thin casing, in turn, is enclosed in a thick SS mechanically strong casing with the inter-layers of polymic alumina chalk. The thick casing provides mechanical strength against the radial forces caused by the toroidal field. It also acts as a vacuum jacket around each coil and a magnetic shield against the field fluctuations. The thick casing is cooled separately to 4.5 K by pressurized (1.5 MPa)

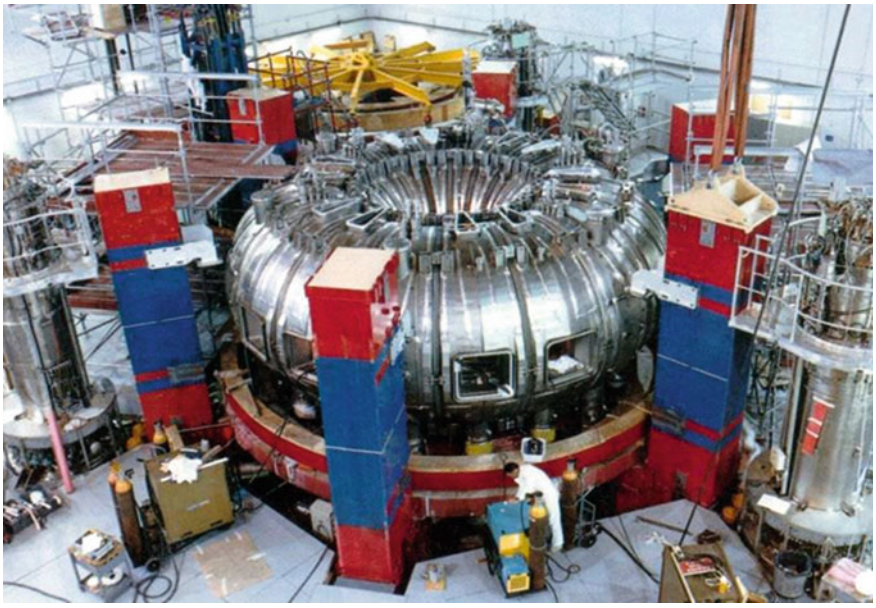

Fig. 11.12 Tore Supra tokamak (Cadarache, France) [18]. *Courtesy* Valerie Lamaison and J-L Duchateau (Copyright CEA-IRFM, Institute for Magnetic Fusion Research)

supercritical helium. Most of the heat dissipation takes place in this casing minimizing heat load on the coils which operate at 1.8 K. A cutaway cross section of the coil [19] is shown in Fig. 11.14. The insulation can withstand a voltage of 5 kV. Complete specifications of plasma, toroidal coils and the conductor are given in Table 11.5.

Each of the six modules is assembled as a complete 1/6th segment of the torus, that is, containing inner vessel, thermal shield, the magnet system, the outer thermal shield and the outer cryostat vessel. All the modules are assembled to make a complete torus. Each module is a rigid entity capable of withstanding the forces experienced during magnet operation.

The tokamak was designed for a toroidal field of 4.5 T at the plasma axis. The peak field at the conductor turned out to be 9 T. Nb_3Sn would, therefore, have been the ideal choice. To avoid the complexity of high-temperature heat reaction involved in Nb_3Sn magnets, a copper-stabilized low-loss Nb-Ti conductor to be operated at 1.8 K was preferred. Full specifications of the Nb-Ti conductor have been given in Table 11.5. The stored energy is 600 MJ. The poloidal coils are the normal non-superconducting water-cooled copper magnets and mounted outside the toroidal magnet and the cryostat. The toroidal coils are protected against quench by 18 dump resistors of 2.5 Ω each in series with as many coils to keep the current equal in each coil. A set of resistances, 5 Ω each, is also connected in parallel with each coil to limit the voltage. The magnet coil discharges in 14 s and limits the voltage across the coil to 3500 V and ±1750 V to ground.

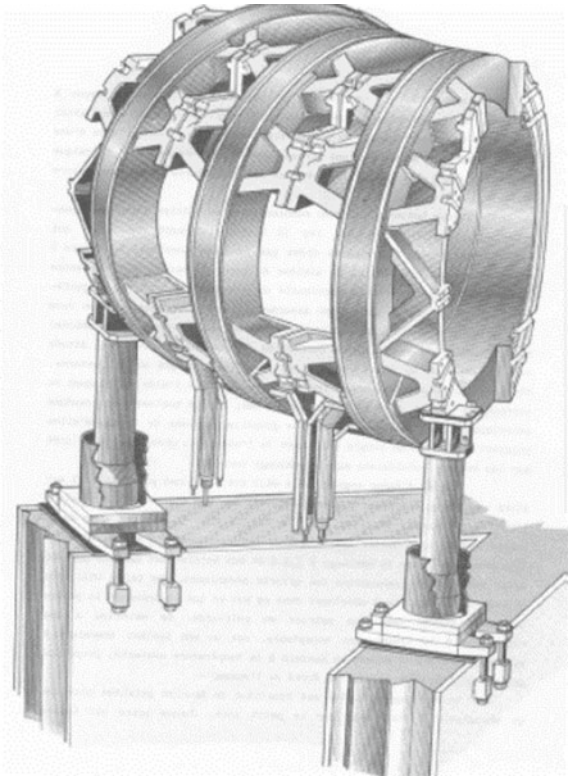

Fig. 11.13 One module of three superconducting coils of the toroidal magnet of Tore Supra joined together rigidly by shear keys. There are six such modules to complete the torus [18]. *Courtesy* Valerie Lamaison (Copyright CEA-IRFM, Institute for Magnetic Fusion Research)

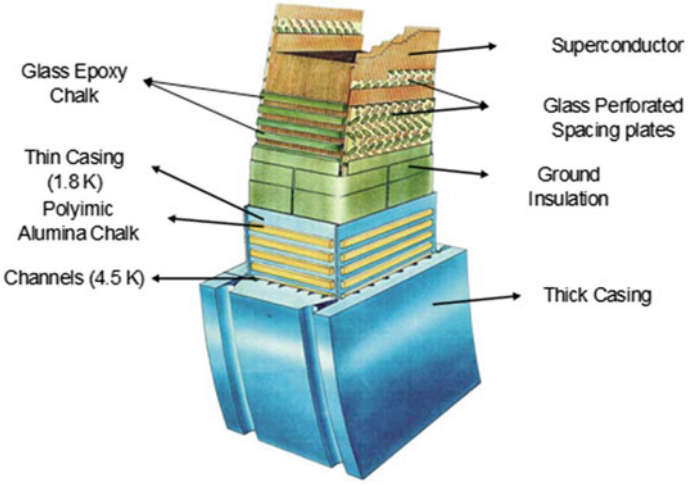

Fig. 11.14 Cutaway view of the toroidal coil of Tore Supra. Note the two cooling channels, one for 1.8 K superfluid, inside the thin case for cooling the winding and the other for 4.5 K supercritical helium, to cool the outer thick casing [18]. *Courtesy* Valerie Lamaison (Copyright CEA-IRFM, Institute for Magnetic Fusion Research)

Table 11.5 Parameters of Tore Supra and toroidal magnet specifications (data compiled from [18, 19])

Parameter	Unit	Value
Year of start of operation		1988
Present status		Operated till 2013 upgraded to WEST
Year of start of WEST		2016
Overall diameter	(m)	11.5
Overall height	(m)	7.2
Plasma major radius	(m)	2.25
Plasma minor radius	(m)	0.70
Plasma current, I_P	(MA)	1.7
Plasma heating	(MW)	Ohmic-2, NBI-10 ICRH-9, LHH-6
Plasma hold time	(min)	Up to 6
Plasma volume	(m^3)	24
No. of toroidal coils		18
No. of modules of toroidal coils		Six with three coils each
Toroidal field at the plasma centre	(T)	4.5
Maximum field on conductor	(T)	9.0
Operating current	(A)	1400
Operating temperature	(K)	1.8
Magnetic structure temperature	(K)	4.5, supercritical He
Total weight of magnet	(ton)	160
Magnet stored energy	(MJ)	600
Conductor specifications		
Conductor used		Nb-Ti (46.5 wt%)
Nb-Ti: Cu: Cu-Ni ratio		0.29: 0.62: 0.09
Conductor dimensions	(mm)	(2.8 × 5.6)
Number of strands		1 with 11,000 filaments
Filament diameter	(μm)	23
Total Nb-Ti conductor used	(m)	622 × 494 lengths
Total weight of superconductor	(ton)	45

11.4.7 WEST (Tungsten (W) Environment in Steady-State Tokamak)

After 25 years of its first plasma discharge (1988), Tore Supra has appeared in 2013 in its new incarnation 'WEST' (Tungsten (W) Environment in Steady -State Tokamak) for testing the efficacy of the tungsten divertor to be used in ITER. WEST [22, 23] will investigate issues related to the operation of actively cooled tungsten divertor components in a fusion reactor and its influence on plasma performance. It will test the technology of high heat flux removal which will be implemented in ITER. The divertor structure will also remove helium produced by fusion reaction or any unwanted atoms from the plasma chamber. All these elements are thrown by the centrifugal force into an absorber generating tremendous heat. WEST has been designed to test prototype components which will be used in ITER. WEST will collect data on the functioning of the divertor and test the durability of tungsten materials used for divertor. Several modifications were carried out to transform Tore Supra into WEST which begun in 2013. New poloidal field magnetic coils were installed in the vacuum vessel to focus energy on the divertor. All plasma-facing components were made metallic, and a new active cooling system for cooling the divertor was provided. Some of the technical parameters of WEST are given in Table 11.6.

A divertor structure is a key feature of tokamaks for removing unwanted atoms including the helium produced by fusion itself and are flung by centrifugal force into an absorber material. This heats up the vacuum vessel tremendously. WEST is involved in testing prototype components and accelerating their development for ITER. The main objective of the WEST is to test tungsten divertor slated to be used in ITER. An extensive refit was carried out between 2013 and 2016 to transform Tore Supra into WEST.

Table 11.6 Parameters of WEST (Former Tore Supra) (data compiled from [23])

Parameter	Unit	Value
Refit started		2013
Year of first plasma		2016 (Dec.)
Major plasma radius	(m)	2.5
Minor plasma radius	(m)	0.50
Field at plasma centre	(T)	3.7
Plasma current	(MA)	1
Longest plasma discharge	(s)	1000
Auxiliary heating (ECRH, ICRH, LHCD)	(MW)	17
Present status		Operating

11.4.8 JT-60 SA (Japan Torus-60 Super Advance), JAERI, Naka, Japan

JT-60 SA is the biggest and wholly superconducting tokamak built at Naka, Japan, under the 'Broader Approach' (BA) agreement between Japan Atomic Energy Agency (JAEA) and the Euratom. This ITER companion is located at the Japanese 'National Institute for Quantum and Radiological Science and Technology (NIQRST)' at Naka. The tokamak is designed in ITER configuration as its satellite facility for a successful start-up of ITER leading to energy production by DEMO. JT-60SA, in fact, is a replacement of JT-60 and its later upgraded version JT-60U at the same site. JT-60 SA may as well be called a real mini replica of ITER.

A cutaway view of the JT-60 SA device is reproduced in Fig. 11.15. The figure shows the locations of the toroidal coils, equilibrium coils, the central solenoid, the vacuum vessel, the plasma and the cryostat. A large number of ports for diagnostic instruments and tools are a common feature of any fusion machine. JT-60 SA [24] has been built with an objective to achieve steady-state plasma for 100 s under condition of high β, flexible low aspect ratio (2.5–3.1) and plasma shape. The plasma current would go up to 5.5 MA for low aspect ratio. The magnet system of JT-60 SA is quite similar to that of ITER. All the magnets are superconducting, to achieve steady state.

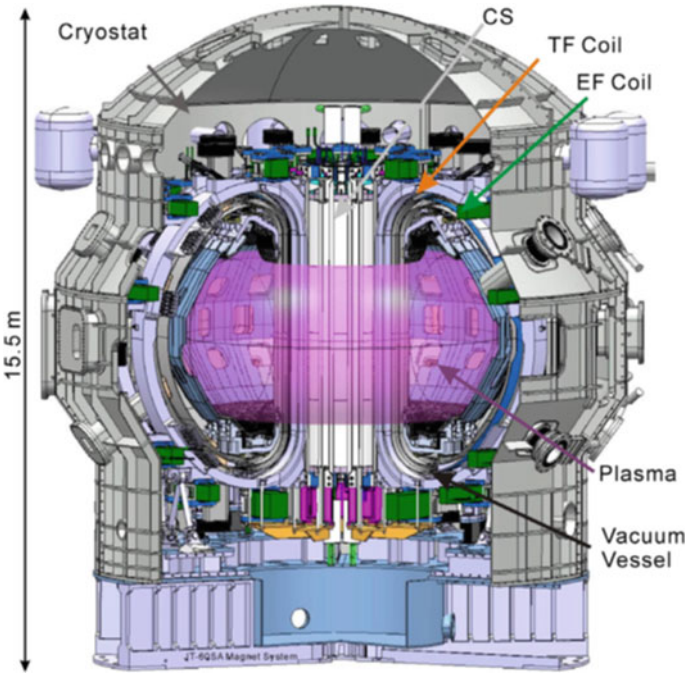

Fig. 11.15 Cutaway view of the JT-60 SA device showing locations of TF, EF, CS, plasma and vacuum vessels, cryostat and the ports [24] (with permission from 'Elsevier')

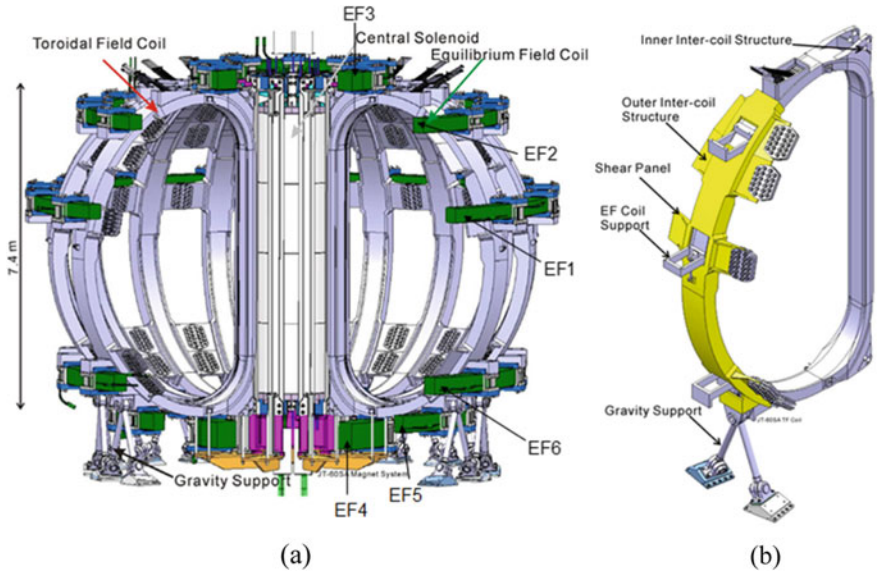

Fig. 11.16 **a** Toroidal coils, equilibrium coils and central solenoid of the JT-60 SA tokamak [24]. **b** The 'D'-shaped toroidal coil with ground supports and inter-coil jointing mechanical pieces [24] (with permission from 'Elsevier')

It consists of 18 toroidal coils to confine the plasma. It has six plasma equilibrium field coils which provide vertical stability to plasma and position equilibrium of the plasma current. A central solenoid consisting of four-stacked solenoid modules controls the plasma shape by increasing the plasma current through the ramping of the field. Figure 11.16a shows the total magnet system and Fig. 11.16b, a typical 'D'-shaped toroidal coil with gravity supports and inter-coil mechanical parts for joining with other coils. The other requirements of the upgradation are the 41 MW heating and current drive system and a divertor which can carry 15 MW/m^2 heat flux. The main parameters of the tokamak are given in Table 11.7.

The toroidal coils have been built by Euratom under the (BA) agreement. The TF coils are wound using a rectangular SS jacketed Nb-Ti cable-in-conduit conductor (CICC) of the dimensions 22 mm $\times$ 26 mm consisting of 324 strands and 162 copper wires without central spiral. To reduce AC losses, either the strands are coated with nickel or the Cu-Ni barriers are used inside the strand matrix which brings down the inter-strand coupling. Each toroidal coil has six double pancakes with six turns each. Every winding package has electrical insulation wrapped around and finally vacuum-pressure impregnated. The dimensions of a winding pack are 345 mm (toroidal) $\times$ 150 mm (radial). This pack is enclosed in an AISI austenitic steel casing which withstands most of the EM forces generated in the magnet system and provides support to the equilibrium coils.

The toroidal magnet produces a field of 2.69 T on the plasma axis at an operating current of 25.7 kA. The coils are cooled to 4.8 K by the forced flow of supercritical

Table 11.7 Main plasma parameters (designed) of JT-60 SA tokamak (data compiled from [24])

Parameters	Unit	Value
Year of start		2014
Major plasma radius, R	(m)	3.06
Minor plasma radius, a	(m)	1.15
Aspect ratio		3.1
Plasma volume	(m^3)	127
Plasma current	(MA)	5.5
Plasma duration	(s)	100
Plasma elongation, (κ)		1.76
Triangularity, (δ)		0.45
Plasma heating power	(MW)	34 (NBI) 7 (ECRH)
Fuel to be used		D + D

helium at a flow rate of 4.8 g/s. The peak field at the conductor turns out to be 6.5 T. The stored energy is 1.06 GJ. Three pairs of current leads are used to energize the magnet. The parameters of the toroidal magnet and the conductor used are given in Table 11.8. The test results on the TF coils match closely with the conceptual design calculations [25, 26].

The central solenoid (CS) consists of four identical coil modules CS1 (top) to CS4 (bottom) stacked together vertically with insulation in between except between central modules CS2 and CS3 which are connected in series. The modules can be energized separately to accomplish the plasma shape. The terminals and bus bars are taken outside the solenoid to the terminal box which is connected to the supply and return lines for helium. The CS produces a field of 8.9 T and is wound using Nb_3Sn (W&R) conductor. The conductor consists of a 21 mm dia. cable inserted in to a 27.9 mm $\times$ 27.9 mm squire-shaped jacket of SS 316LN with a central hole. The parameters of the CS magnet and the conductor used are listed in Table 11.9. The jacket allows the heat treatment of the coils at 650 °C ($\times$100 h). The cable has 216 Nb_3Sn strands produced by a multistage process and 108 copper strands cabled around a central cooling spiral of 7 mm inner diameter and 9 mm outer diameter. The cooling spiral greatly enhances the extraction of excessive heat generated due to AC losses during a break down.

The assembly of the JT-60SA fusion reactor, which started in 2013, was completed at the end of March 2020 [27]. JT-60SA will remain the world's largest and most advanced tokamak until the time ITER starts operation. It will complement ITER. JT-60SA will study quasi-stationary plasma (long-lasting) to enlarge the database for DEMO, a future demonstration power plant. The plasma pulses of JET are not long enough because of its copper magnetic coils. Figure 11.17 is the photograph of the newly completed fusion reactor JT-60 SA.

Table 11.8 Specifications of the toroidal magnet and the conductor to be used in JT-60 SA (data compiled from [24–26])

Parameter	Unit	Value
No. of toroidal coils		18
No. of double pancakes in a coil		6
No. of turns in a pancake		6
No. of turns/coil		72
No. of current lead pairs		3
Toroidal field at plasma axis	(T)	2.69
Peak field on conductor	(T)	6.5
Operating current	(kA)	25.3
Operating temperature	(K)	4.8 (SHe)
Mass flow rate of He	(g/s)	4.8
Stored energy in TF coils	(GJ)	1.06
Total weight of the toroidal magnet (including structure)	(ton)	700
The conductor		
Conductor used		Nb-Ti/Cu/Cu-Ni
No. of strands/copper wires		324/162
Void volume		34%
Cable dimensions	(mm)	22 × 18
Conductor jacket dimensions	(mm)	26 × 22
Jacket material		SS 316LN
Total conductor length	(km)	24.4 (=74 × 0.33)

11.4.8.1 Present Status of the JT-60SA

As mentioned in the beginning of Sect. 11.4.8, JT-60SA is the modified version of the old fusion reactor JT-60U and is built in ITER configuration under the 'Broader Approach' (BA) agreement between Japan Atomic Energy Agency (JAEA) and the Euratom, an agency of the European Union, signed in 2007. Located at the 'National Institutes for Quantum and Radiological Science and Technology (QST)' at Naka, Japan. It is world's biggest and wholly superconducting fusion reactor today and will remain so until ITER starts operation. The assembly of various components of the sub-systems started in 2013 and completed successfully in March 2020 [27]. Figure 11.17 is the picture of the fully assembled JT-60SA at the QST at Naka. Various sub-systems of the JT-60SA are being tested in a sequence, and the first plasma was observed in the autumn of 2020. In March 2021, the JT60SA successfully produced its designed TF field. All the 18 TF coils, six PF coils and the four module CS were fabricated as per the original design. The TF and PF coils used CICC Cu/Nb-Ti conductors of 7 cm × 94 cm and 7 cm × 33 cm cross sections, respectively. The field produced along the plasma axis by the TF magnet is 2.69 T as per the design. The tokamak uses six PF coils the biggest PF coil is PF-1 with a

Table 11.9 Designed parameters of the central solenoid and the Nb_3Sn conductor of JT-60 SA (data compiled from [24])

Parameters	Unit	Value
Overall height	m	9.5
Nominal peak field	T	8.9
Operating current	kA	20
Operating temperature	K	5.1 (SHe)
No. of solenoid modules		4
Total conductor length	km	11.5 (unit length 352 m)
No. of current lead pairs		4
Total weight of CS and structure	ton	92
Conductor used (CICC)		Nb_3Sn (W&R)
No. of Nb_3Sn strands		216
No. of copper strands		108
Void fraction	%	34
Cable diameter	mm	21
Conductor size (after jacketing)	mm	27.9 × 27.9
Central cooling spiral dia.	mm	7 (id) × 9 (od)

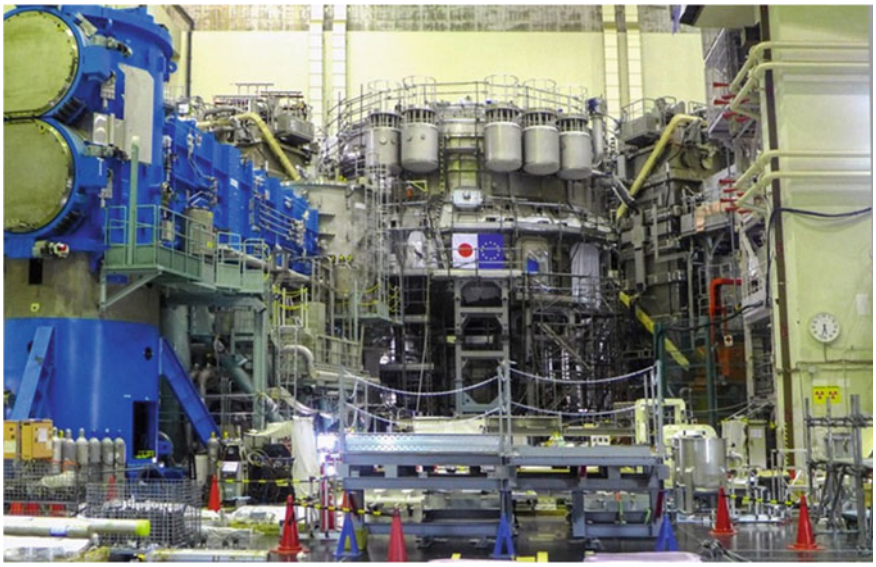

Fig. 11.17 JT-60SA Japanese-European fusion plant at Naka, Japan, fully assembled in March 2020 [27]. *Credit* Courtesy Sakaino Taeko, National Institutes for Quantum and Radiological Science and Technology, (QST)

diameter of 12 m and weighs 27 tons. EF-2 is 9.6 m in diameter and again weighs 27 tons. The PF-3 is the smallest PF coil with a diameter of 9.6 m and weight 21 tons.

The CS has a diameter of 2 m and a height of 6.4 m. The CS consists of four modules and generates a field of 8.9 T at an operating current of 20 kA at 4.5 K. CICC Nb_3Sn conductor has been used for the fabrication of CS coils. All the magnets operate at a temperature of 4.5 K provided by circulating SHe through the cooling channels in the CICC cables. Rich data are expected from the reactor which will be utilized in the operation of ITER and its successor DEMO.

11.4.9 KSTAR (Korean Superconducting Tokamak Reactor), NFRI, Daejeon

KSTAR is an all-superconducting magnet fusion reactor [28], operating at National Fusion Research Institute (NFRI), Daejeon, Republic of Korea, since 2008, and has many similarities with ITER. It is a steady-state fusion reactor with high-performance plasma and with a capability of confining plasma for 300 s. Figure 11.18 is a schematic diagram of the position of toroidal, poloidal and central solenoid together with the

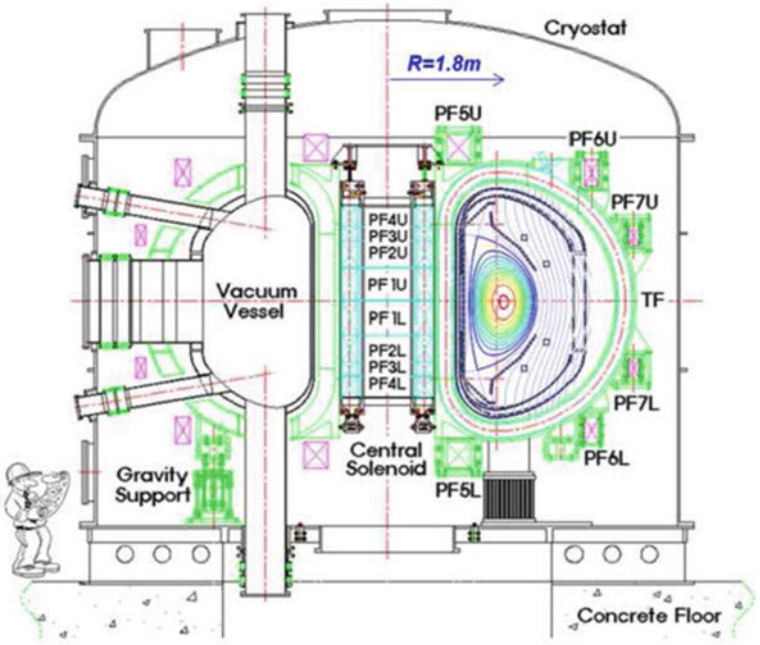

Fig. 11.18 Schematic diagram of KSTAR fusion device indicating the position of the superconducting magnets (toroidal, polloidal and CS) and the vacuum vessel [28]. *Courtesy* Yeong-Kook Oh, NFRI, Daejeon, Korea

vacuum vessel. It has 16 TF coils and 14 PF coils. Four pairs of the PF coils (PF1–PF4) are located in the central solenoid magnet system, and six pairs of PF coils (PF5–PF7) are outside the TF coil system. All the TF coils and smaller dia. PF coils (PF1, PF2, PF3, PF4 and PF5) are wound using CICC Nb_3Sn conductor (wind-and-react type), and the larger PF coils PF6 and PF7 coils are wound using CICC Nb-Ti conductor. The requirement for conductor for TF coils and PF coils is, however, quite different. The TF coils run in static mode and, therefore, the conductor must have high-current density, greater than 750 A/mm^2 (4.2 K, 12 T) (the HP-I criterion). The PF coils, on the other hand, have to operate in pulse mode and should have low hysteresis losses meeting HP-II criterion (loss should be less than 250 mJ/cc at 3 T cycle). NFRI developed Nb_3Sn conductor which meets both the criteria simultaneously (HP-III) and has been used for all the coils except PF6 and PF7.

The conductor has more than 3000 filaments carrying high current and low hysteresis. To have low AC loss performance, the strands are coated with a ~2-μm-thick resistive layer of chromium. This chromium layer remains intact during the long period of heat treatment of the coil. In the first step, two superconducting strands and one OFHC copper wire are cabled together to form a triplet. These triplets are further cabled in $3 \times 3 \times 3 \times 3 \times 6$ and $3 \times 4 \times 5 \times 6$ configurations to 486 strands cable for TF coil and 360 strands cable for PF coils, respectively. Each cable is wrapped with a 30 mm × 0.05 mm SS strip with 20% overlapping and jacketed in an incoloy 908 casing. The cladding material has been chosen to prevent large strain in the conductor due to the mismatch of the thermal contraction during cooling. The main design parameters of the KSTAR and the TF coil are given in Table 11.10.

Most coils have winding in single length of conductor without a joint inside the coil except the large coils PF6 (upper and lower) which have one joint each inside the winding. After the winding, coils are subjected to a three-step heat treatment, (460 °C × 100 h) + (570 °C × 200 h) + (660 °C × 240 h) under inert atmosphere wherein Sn diffuses in to Nb filaments to form Nb_3Sn layer. The final heating is done at 660 °C for the formation of stoichiometric (3:1) Nb_3Sn. Electrical and ground insulation is then provided using Kapton, S2-glass tapes, S2-glass roving and G-10 pieces (shaped to fill the voids). Quench detecting sensors are also mounted at designated places.

The magnet structure is strong enough to withstand large Lorentz forces experienced during the operation. KSTAR used high-strength STS 316LN stainless steel for its 16 TF structures, one CS structure and 80 PF structures. The TF coils are subjected to in-plane force of as much as 15 MN when charged to the nominal current of 35.2 kA. Similarly, the PF coils, the CS and plasma current too exert an out-of-plane force of 2.6 MN/m. The CS structure is designed such that it applies 15 MN (at 5 K) vertical compressive force on the CS coils to nullify the repulsive forces between the coils. The six PF coils are mounted on to the 16 TF coils at 80 locations. The structure is designed to absorb the difference in the thermal contraction of the TF and PF coils during cooling to cryogenic temperature. A bird eye view of the KSTAR reactor is shown in Fig. 11.19. The first phase of the operation of KSTAR has been successfully completed in 2012. In its 2011 campaign [29], KSTAR has already achieved 3.5 T toroidal field at an operating current of 35.2 kA with a temperature rise of only 0.1 K. A plasma-inductive current of 1 MA has already been

Table 11.10 Specifications of the KSTAR, the TF coils and the conductor (data compiled from [28])

Parameter	Unit	Value
Year of start of operation		2008
Major plasma radius	(m)	1.8
Minor plasma radius	(m)	0.5
Plasma current	(MA)	2.0
Plasma volume	(m^3)	17.8
Plasma cross section	(m^2)	1.6
Plasma shape		DN, SN
Plasma elongation (κ)		2.0
Plasma triangularity (δ)		0.8
Plasma hold time	(s)	300
Auxiliary heating	(MW)	28
Plasma fuel		H + D
Specifications of the toroidal coils and the conductor		
Total no. of toroidal coils		16
Overall height of the coil winding	(m)	4.2
Overall width of the coil winding	(m)	3.0
No. of pancakes used in a coil		8
No. of turns/pancake		7
Toroidal field at plasma axis	(T)	3.5
Peak field at the coil	(T)	7.2
Operating temperature	(K)	4.5 SHe-forced flow cooled @ 5 bar
Operating current	(kA)	35.2
Stored energy	(MJ)	470
Superconductor material		Nb_3Sn (W&R)
No. of strands		486
No. of filaments		3000
Maximum single conductor length	(km)	1.8
Cold mass of the toroidal magnets	(ton)	150

achieved by ramping the poloidal field. The data obtained on KSTAR tokamak will go a long way to support the operation of ITER and DEMO.

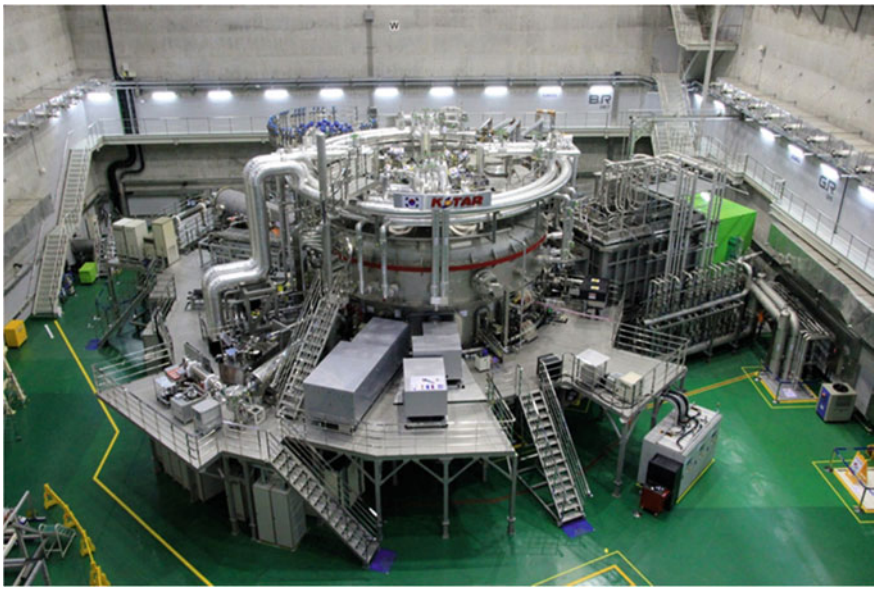

Fig. 11.19 Bird eye view of the of KSTAR [28]. *Courtesy* Yeong-Kook Oh, NFRI, Daejeon, Korea

11.4.10 K-DEMO Being Built by Korea and PPPL

The National Fusion Research Institute (NFRI), Korea, made outstanding achievements during ten years of operation of the fusion reactor KSTAR. It set a world record [30] in December 2016 by sustaining high-performing hydrogen plasma at 50 million degrees for 70 s. In 2019, the plasma temperature was raised to 70 million degrees for 34 s using 9.5 MW heating system and maintained plasma for 8 s at still higher temperature of 100 million degrees in 2020. An important hardware upgrade programme [31] of the KSTAR is the development of a tungsten monoblock divertor for 300 s operation which would replace the present graphite block divertor. Present research programme (phase 3, 2018–2023) is aimed at achieving high-performance steady-state operation of 300 s plasma by overcoming scientific and engineering hurdles. The ultimate objective of a tokamak device is to sustain a permanent plasma current.

NFRI in collaboration with the US Department of Energy's PPPL is building a fusion-based Korean Demonstration Fusion Power Plant to be called 'K-DEMO' that would be rolled out sometime in the 2030s and contribute power to an electric grid. According to PPPL, the plant is expected to generate 'some 1 billion watts of power for several weeks on end', that is, much greater than ITER's expectation of producing 500 million watts for 500 s. K-DEMO will have a 6.65 m diameter major radius tokamak, and a blanket module slated to be used as the DEMO breeding blanket R&D. All the results and data gathered from KSTAR will be utilized in the design of the K-DEMO.

11.4.11 EAST (Experimental Advance Superconducting Tokamak, IPP, China)

EAST is a wholly superconducting experimental fusion reactor built and completed in 2003 at the Institute of Plasma Physics (IPP), Chinese Academy of Sciences, Hefei, Anhui Province in East China. It started operating in September 2006. The reactor is an outcome of the rich experience, the Chinese fusion scientists gained on their earlier fusion reactor HT-7 [32, 33]. Reactor HT-7 was a modified version of Russian tokamak, T-7 bought from Kurchatov Institute, Moscow, by China, and modified with Russian help at Hefei. EAST is focusing on the plasma-facing materials such as multi-element-doped carbon and thick gradient SiC coating on carbon-based materials have also been developed. Other areas on which IPP is focusing is the development of low activation ferritic/martensitic steel, CLAM, the (Chinese Low Activation Martensitic) steel. A special structural material for blanket RAFM (a Chinese version for reduced activation ferritic/martensitic steel) also has been developed. The major parameters of EAST [34] and the TF coils are given in Table 11.11.

A schematic cutaway cross section of EAST depicting the total CS, TF and PF magnet system, thermal shields and the cryostat is shown in Fig. 11.20. EAST has an overall height of 10 m and 8 m diameter and weighs 400 tons. EAST has 16 toroidal coils, three pairs of poloidal coils and three other pairs of the CS system. Both of the biggest poloidal coils outside the TF coils have the diameter of 6.65 m. The PF coil system stores a maximum energy of 50 MJ. Each TF coil is of the size 3.5 m $\times$ 2.6 m and a weight of 10 tons. TF coils operate at 14.5 kA and produces a plasma axis field of 3.5 T. The peak field at the TF coil is 5.8 T. The TF magnet system has a stored energy of 300 MJ. The TF coils are 'D'-shaped with five arcs and one straight leg so as to have a coil free of bending moment. Like any other reactor, EAST has used IPP designed and produced CICC Nb-Ti conductor with high stability, high-current density and low AC losses suitable for pulse operation. For TF coils, the conductor has been made in a configuration (2SC + 2Cu) $\times$ 3 $\times$ 4 $\times$ 5 + 1 central copper cable (CCC). The SC strands were coated with 2–μm-thick Pb-30Sn-2Sb soldering material. For four big PF coils, another CICC configuration, viz (1SC + 2Cu) $\times$ 3 $\times$ 4 $\times$ 5 + 1 CCC was used. In this cable, the SC strands were coated with 3-μm-thick Ni layer. Special CICC Nb-Ti conductors were designed and produced by IPP to fulfil the requirement of TF as well as for PF coil magnet systems.

All the coils have been wound in pancake structure and jacketed in very strong casing of SS 316LN which has a yield stress of 1500 MPa below 80 K. The finite element analysis yields a maximum stress on the TF coil as 350 MPa. The casing of the TF coils has to withstand a centripetal force as large as 1300 tons. The casing is built in a box structure with the case plate is as much as 58 mm thick. Sensors for quench detection are placed at the select places in the winding. Fibre glass 0.5 mm thick is wrapped around the conductor and 1 mm thick on the pancakes for electrical insulation. A 6-mm-thick multilayer glass tape provides ground insulation to the coils which are finally vacuum impregnated. A photograph of EAST along with its all auxiliary systems is shown in Fig. 11.21.

Table 11.11 Major parameters of EAST (data compiled from [33, 34])

Parameter	Unit	Value
Year of start of operation		Sept. 2006
Height of the tokamak	(m)	10
Diameter of the tokamak	(m)	8
Total weight of EAST	(ton)	400
Plasma major radius, R	(m)	1.85
Plasma minor radius, a	(m)	0.45
Plasma elongation, κ		1.6–2
Plasma triangularity, δ		0.6–0.8
Plasma current	(MA)	1.0
Plasma discharge duration	(s)	0–1000
Plasma heating (non-inductive)	(MW)	7.5 (ICRH—3 MW) (LHCD—4 MW) (NBI)—0.5 MW)
Plasma configuration		SN/DN/pump limiter
Plasma fuel		H + D
Specifications of the TF magnet system and conductor		
No. of TF coils		16
Dimension of a TF coil	(m)	3.5 × 2.6
Field at plasma axis	(T)	3.5
Peak field at the coil	(T)	5.8
Operating current	(kA)	14.5
Total stored energy	(MJ)	300
Operating temperature	(K)	4.5 (SHe-forced flow)
Conductor used		Nb-Ti CICC
Conductor size	(mm)	20.4 × 20.4
No. of SC strands		120
Diameter of SC strand	(mm)	0.85–0.87
Diameter of Cu strand	(mm)	0.98
Cable configuration	(2SC + 2Cu) × 3 × 4 × 5 + 1 CCC[a]	
Coating material for strands		Pb-30Sn-2Sb
Temperature margin ($^{b}T_{CS} - T_{OP}$)	(K)	1.88

[a]CCC: central Cu cable, [b]T_{CS}: current sharing temperature

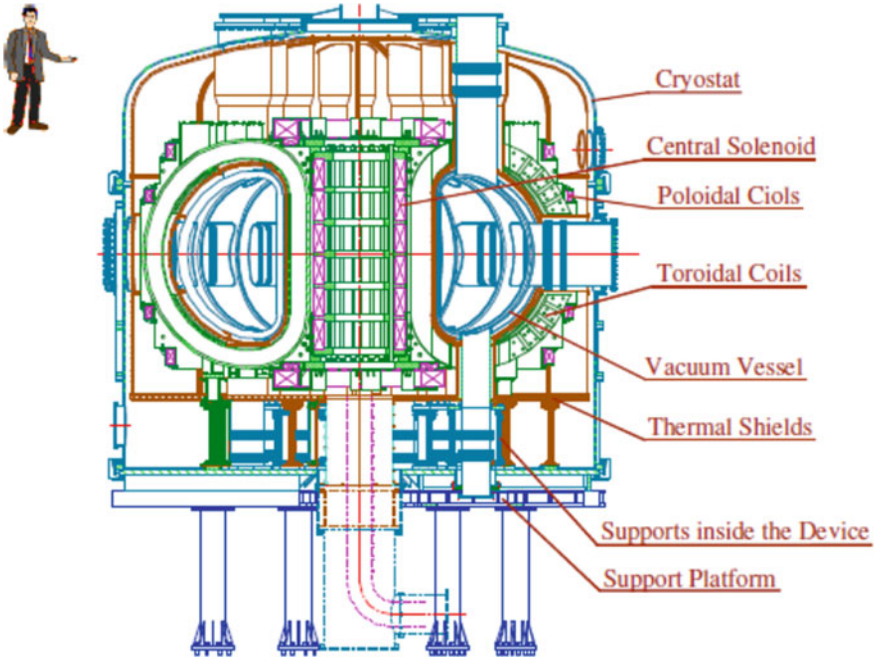

Fig. 11.20 Cutaway cross-sectional view of the EAST machine showing the positions of TF, PF and CS coils [33]. *Courtesy* Jiangang Li, Institute of Plasma Physics, CAS, Hefei, P. R. China

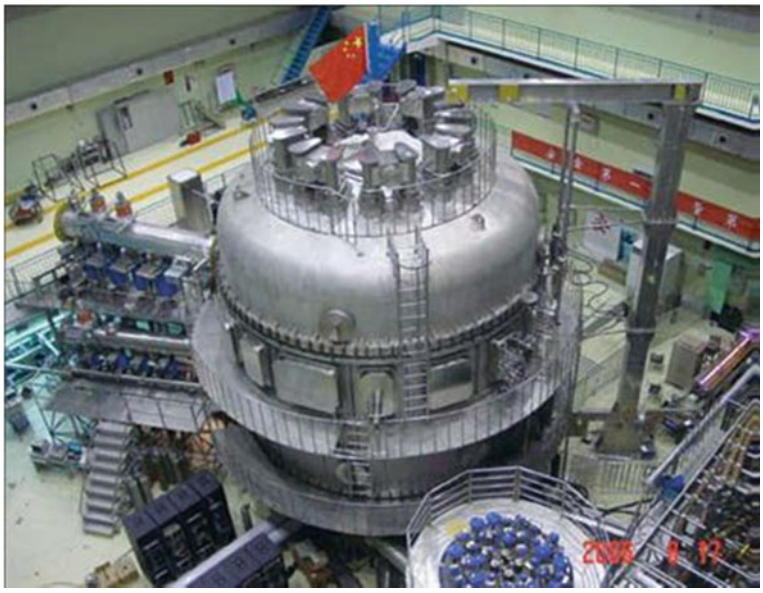

Fig. 11.21 EAST superconducting tokamak built at IPP (Chinese Academy of Sciences), Hefei [32]. *Courtsey* Jiangang Li, Institute of Plasma Physics, CAS, Hefei, P.R. China

11.4.12 HL-2M Tokamak—A New Tokamak Built by China

Other than the HT-7 and EAST, China has invested heavily in building a number of other tokamaks. HL-2M tokamak [35] is an upgrade of the earlier machine HL-2A. This tokamak is different from other tokamaks in so far it has the flexibility of its magnetic field. The magnetic fields stabilize the plasma such that the fusion reactions take place and the energy is released. Plasmas are, however, prone to producing bursts which can damage the reactor wall. When the device operates at high power, the exhaust heat and particles from the fusion-producing core lead to very high heat and particle loads which can damage the surface lining of the wall of the reactor. The flexibility of magnetic field available on HL-2M will allow scientists to find a solution to this problem. HL-2M is expected to yield data on the compatibility of high-performance fusion plasmas with the interior to handle the heat and particles exhaust more effectively.

The data from HL-2M reactor will help in the design development of a commercial fusion reactor. The tokamak has the plasma major radius 1.78 m and minor radius 0.65 m. The device will achieve a temperature of over 200 million degrees Celsius, about 13 times the temperature of the sun's core. The plasma current is expected to reach 3 MA and will be able to address many physics-based issues of a fusion reactor. Several next step facilities like plasma discharge control, plasma heating, fuelling, MHD suppression, etc., will be tested. Study on the particles and heat exhaust using the flexibility of the operation and positioning of the poloidal field coils would enable to freeze the divertor configuration. Various concepts about divertor would be tested to reduce heat load on the target plate. The in-vessel components for plasma discharge control and new high flux resistance materials will be tested and developed further. This tokamak will provide key technical support to ITER and future Chinese tokamak projects.

11.4.13 CFETR (China Fusion Engineering Testing Reactor)—A Power-Producing Tokamak

Buoyed with the successful operation of a number of tokamaks, HT-7 and EAST in particular, the Chinese scientists took to the conceptual design of a large size 'China Fusion Engineering Testing Reactor' (CFETR) in 2015. CFETR [36] will come up at Southwestern Institute of Physics (SWIP) under the China National Nuclear Corporation (CNNC). CFETR will operate in a steady-state mode and produce enough tritium which will be self-sustained, that is, tritium breeding ratio (TBR) will be >1. CFETR will be a conduit between ITER and the DEMO. In phase I, it would produce a fusion power of 200 MW which will ultimately be raised to 1 GW power. The CFETR will be housed in a 73-m-tall building and is expected to generate plasma at temperatures of more than 200 million degrees Celsius. DEMO is expected to be a commercial power-generating station and CFETR will provide DEMO validation.

The main challenge to the design is that CFETR has to generate the steady-state burning plasma (long pulsed) with duty time of about 50% with a fusion gain (Q) of about 20–30. The design has also to ensure that heating by alpha particle (helium atoms), resulting from the fusion reactions, dominates (~80%) over all other forms of heating. The salient parameters of the tokamak and magnets/conductor are given in Table 11.12.

Since the peak field on the coil will be 14.3 T, Nb_3Sn has been chosen for the winding of toroidal magnets. The conductor chosen is of the cable-in-conduit (CICC) type consisting of 900 strands of Nb_3Sn and 522 strands of copper of 1 mm diameter. The round cable of 49 mm diameter will be compacted in a SS 316 L square jacket of (65×65 mm^2) cross section. The jacket has a wall thickness of 8 mm. The T_c of Nb_3Sn is 18 K, and thus the magnets will have a temperature margin of 1.2 K at 14.5 T field. The design of the magnets is based [37] upon the critical parameters

Table 11.12 Salient parameters of the tokamak and magnets of CFETR (China Fusion Testing Reactor) (data compiled from [36, 37])

Parameter	Unit	Value	Parameter	Unit	Value
Major plasma radius	m	7.2	Conductor used for magnets		Nb_3Sn CICC type wind and react
Minor plasma radius	(m)	2.2	Conductor dimensions	(mm)	65×65
Field at plasma centre	(T)	6.5	Cable diameter	(mm)	49
Operating current	(kA)	84.6	Cable pitch	(mm)	30–450 in 5 stages
Peak field on coils	(T)	14.3	Number of Nb_3Sn strands		900
Voltage second	(V s)	480	Number of Cu strands		522
Plasma current	(MA)	13.78	Cable configuration	(2SC + 1Cu) × 3 × 5 × (5 + core) × 6 + spiral	
Fusion power	(GW)	1	Strand diameter	(mm)	1
Power to run the plant	(MW)	238	Void fraction	(%)	32
Gain for whole plant	(MW)	1.98	Conductor configuration		Round cable/squire jacket
Net electric power	(MW)	232	Winding style		Pancake
Neutron power at blanket	(MW/m^{-2})	0.99	Total inductance	(H)	32
Ion/electron temperature	(keV) (K)	24 278×10^6	Maximum stress on coils	(MPa)	303

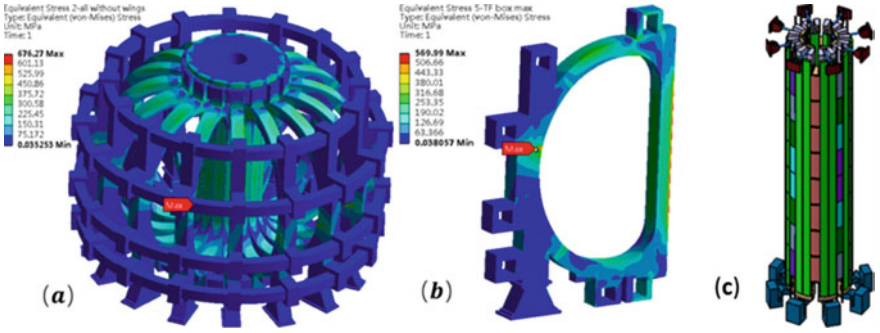

Fig. 11.22 **a** The stress analysis for the complete TF system of CFETR. **b** The stress analysis for one TF coil of the CFETR. **c** The conceptual view of the CS of the CFETR [36]. *Courtesy* Mirium Edvardsen and with permission from IAEA

of a Nb_3Sn conductor sample supplied by Western Superconducting Technologies (WST) which has a critical current of 204 A/mm^2 (4.2 K, 16 T) at a strain level of 0.8%.

CFETR will use 16 toroidal field (TF) coils, a central solenoid (CS) consisting of eight modules, six poloidal field (PF) coils and 18 correction coils (CC) [36]. The 16 D-shaped (six arcs and a straight leg) TF coils have 168 turns and will operate at a maximum current of 84.6 kA to provide a toroidal magnetic field of up to 6.5 T on the plasma axis. The peak field on the coil is expected to be 14.3 T. The stored energy of CFETR TF coils is enormous, 116.34 GJ which is much higher than 40.1 GJ, the stored energy of the ITER TF coils. Stress calculations show that each TF coil will experience a centripetal force in the TF inner leg reaching a maximum of ~570 MPa and a maximum deformation of 14 mm. The force is resisted by the 500-mm-thick coil case. The stress analyses for the TF coil system and of an individual TF coil are shown in Fig. 11.22a, b, respectively. Figure 11.22c shows the conceptual view of the central solenoid (CS) of the CFETR. The CS coils have a maximum radius of 2.25 m. Each module of the CS has 720 turns with the structure of 18 (horizontal) $\times$ 40 (vertical). Each module can be energized independently as per the plasma equilibrium requirement. All the coils are cooled with the forced flow of supercritical helium (SHe) at 4.5 K.

11.4.14 SST-1 (Steady-State Superconducting Tokamak-1), IPR, India

SST-1 is a superconducting tokamak designed and commissioned at the Institute for Plasma Research (IPR), Gandhinagar, India, in the western state of Gujarat. It is a modest size tokamak [38–40] designed to study physics and technology to achieve

Table 11.13 Main parameters of the SST-1 tokamak (data compiled from [38])

Parameter	Unit	Value
Major radius	(m)	1.1
Minor radius	(m)	0.2
Plasma elongation, κ		1.7–2.0
Plasma triangularity, δ		0.4–0.7
Maximum designed field at plasma centre	(T)	3.0
Plasma current	(kA)	220
Plasma hold time	(s)	1000
Plasma configuration		Double null
Plasma temperature	(keV) (K)	1.5 17.4×10^6
Plasma density (average)	(/cm^3)	1×10^{13}
Plasma fuel		H + H
Pre-ionization	(MW)	0.5 (ECRH, 42 GHz)
Plasma heating	(MW)	1.0 (LHCD, 3.7 GHz) 1.0 (ICRH, 22–91 MHz) 0.2 (ECRH, 84 GHz) 0.8 (NBI @ 80 keV)

long duration (1000 s) steady-state hydrogen plasma with significant elongation (1.7–2.0) and triangularity (0.4–0.7) in double null (DN) divertor configuration. SST-1 can sustain a current of 220 kA. The parametric details of the SST-1 tokamak are given in Table 11.13. The auxiliary heating consists of LHCD (1.0 MW), ICRH (1.0 MW), ECRH (0.2 MW) and NBI (0.8 MW). The total heat input, however, would not exceed 1 MW at any given point of time because of the limited heat extraction capability of the first wall of the SST-1.

Superconducting toroidal field (TF) and poloidal field (PF) coils have been used in SST-1 to confine and shape the plasma. SST-1 has sixteen superconducting TF coils and nine superconducting PF coils. Additionally, there are nine resistive coils known as Ohmic transformer coils including compensating coils (TR) to assist in creating the plasma. A pair of vertical field coils (VF) provide the initial equilibrium to the plasma column formed. In addition, two in-vessel PF coils provide the shape and radial control to the initial plasma column. There is also a pair of in-vessel fast feedback coils. The relative positions of these coils can be seen in Fig. 11.23. The 16 TF equally spaced coils are placed around the torus 22.5° apart. The TF coils have been wound using Nb-Ti/Cu cable-in-conduit conductor (CICC) in double pancake configuration. Each TF coil has six double pancakes, and each double pancake has eighteen turns. The details of the TF coil parameters and the conductor specifications are given in Table 11.14. The outer dimensions of the jacketed CICC are 14.8×14.8 mm^2. The jacket is made of non-magnetic SS 304L. The CICC has 135 strands of diameter 0.85 mm each and having Cu: Nb-Ti ratio of 5:1. The strands are twisted in four stages with the pitch of 40, 75, 130 and 290 mm, respectively. The strand has a total

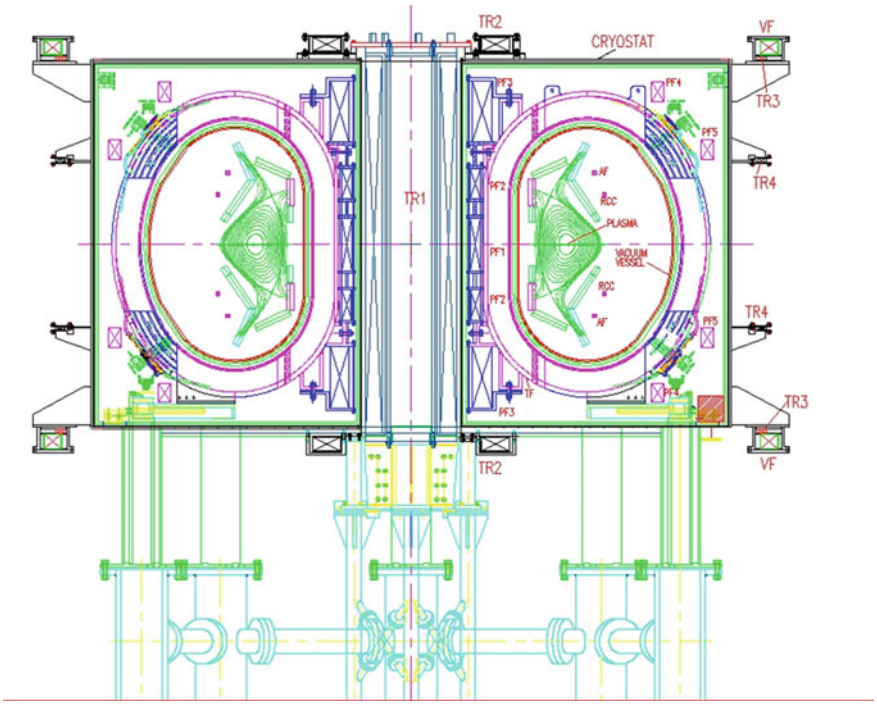

Fig. 11.23 Schematic of the cross section of the SST-1 and the support structure. *Courtesy* SST-1 Team, IPR

no. of 1224 filaments, each of an average diameter of 10 μm. Six double pancakes in the winding pack of each of the TF coil are insulated and then consolidated together after which a ground insulation was put over the consolidated winding pack. The winding pack was finally shrunk fitted into an appropriate casing fabricated from non-magnetic SS 316LN. The SST-1 TF casing comprises of inner and outer rings and side plates, all welded together. All the sixteen TF coil cases in SST-1 machine shell assembly are wedged at the inner legs forming an inner cylindrical vault. At the outer legs of all the TF coils, they are joined together through a mechanical structure known as outer–inter coil structure (OICS). These arrangements in TF coil assembly in SST-1 withstand the centring force as well as the overturning torque acting on the TF coil system resulting from the interaction of the transport current with the magnetic field. The TF coil casings in SST-1 are robust enough to take care of the thermal stresses during the cool-down as well as the entire electromagnetic (EM) forces during the operation. PF coils in SST-1 too have been wound using the same conductor as used for the TF coils. The PF coils are supported on the casing of the TF coils. Liquid nitrogen-cooled thermal shield kept at 80 K has been used between the TF coils and the vessel. Similarly, thermal shield has been placed between the TF coils and the outer cryostat with a vacuum gap. The photograph of SST-1 located at IPR, Gandhinagar, Gujarat State of India, is shown in Fig. 11.24.

Table 11.14 Parameters of the TF coils and the conductor used in SST-1 (data compiled from [38])

Parameter	Unit	Value
No. of TF coils		16
Maximum toroidal field at plasma centre	(T)	3
Max. field at the coil	(T)	5.16
Max. field ripple at the plasma edge	(%)	2.0
TF coil configuration		Six double pancakes
No. of turns/coil		108
Coil current	(kA)	10
Stored energy in TF system	(MJ)	56
Cooling fluid		Supercritical forced flow @ (4.5 K, 4 bar) or two phase flow
Refrigeration capacity	(W)	650 + 200 l/h for the current leads
Energy dump time of TF magnets	(s)	12
Max. dump voltage	(V)	1200
No. of PF coils		9 (8 coils in 4 pairs and one single)
Conductor specifications		
Conductor used		Nb-Ti
Conductor size	(mm)	14.8 × 14.8
No. of strands in the cable		135
Cu: Nb-Ti ratio in a strand		5:1
Strand diameter	(mm)	0.86
No. of filaments/cable		1224
Filament diameter	(μm)	10
Jacket material		SS 304L (1.5 mm thick)
Void fraction	(%)	38

The coils are cooled to 4.5 K using forced flow helium. The helium is fed to the coils from inside of TF coil outer leg region. More than 100 numbers of joints have been made between the double pancakes terminations as well as between the coils and bus bars. Low sub-nano Ohm DC 'handshake'-type joints have been developed in-house using copper termination blocks and low melting Sn-Ag solder as filler. The joint resistance was typically ~0.3–0.4 nΩ at 4.2 K for a current of 10 kA. A large number of sensors have been used in the magnet for quench detection. The coils are protected against quench through dump resistors.

All the SST-1 magnets were tested [39] individually in a dedicated LHe cryostat for its performance during 2010–2011 successfully. The first plasma in SST-1 was observed on 20 June 2013 assisted with ECRH pre-ionization at second harmonic. Since then, several progresses have been made in terms of improvement in magnetic configuration, high field and long pulse operation of TF coils and repeated long pulse plasma [40]. The TF field has been raised to 2.7 T for more than 400 s at the

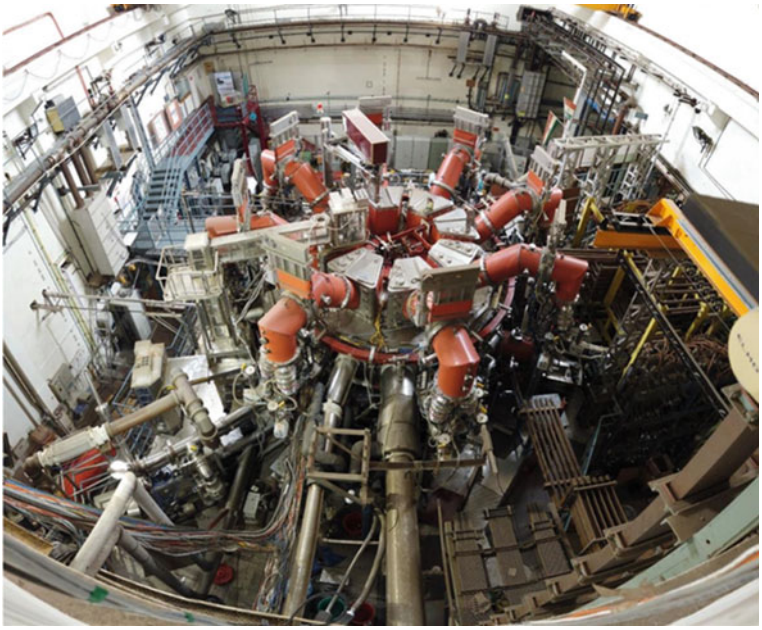

Fig. 11.24 Photograph of Indian tokamak SST-1 under operation since 2013 at the Institute for Plasma Research, Gandhinagar, India. *Courtesy* R Srinivasan, Institute for Plasma Research, India

plasma centre (4.25 T at the TF magnet winding pack) and 1.5–1.6 T for more than 8 h. The plasma current assisted by electron cyclotron resonance (ECR) pulse and loop voltage of 5–6 V driven by Ohmic system for several hundreds of milliseconds followed by the lower hybrid current drive (LHCD) up to 645 ms [41]. The plasma current raised up to 98 kA and sustained for 450 ms by Ohmic system only [41], and this Ohmic duration will allow to transform equilibrium control from copper-based VF to superconducting PF coils and sustain the plasma current by pure LHCD. This is needed for the steady-state operation of SST-1.

11.4.15 SST-2 (Steady-State Tokamak-2) Fusion Reactor, IPR, India

The Institute for Plasma Research (IPR), India, is in the process of designing an intermediate fusion device, the Steady-State Tokamak-2 (SST-2) [41] to realize fusion reactor technology and D-T fuel cycle for an Indian DEMOnstration plant for the production of fusion power. The conceptual design of SST-2 is based upon well-established reactor technologies, materials and various concepts being followed

Table 11.15 Design details of SST-2 tokamak (data compiled from [41, 42])

Plasma parameters			TF and CS magnets parameters		
Parameter	Unit	Value	Parameter	Unit	Value
Major plasma radius	(m)	4.42	Central Solenoid (CS)		
Minor plasma radius	(m)	1.47	Inner radius	(mm)	320
Plasma current	(MA)	11.2	Outer radius	(mm)	940
Plasma volume	(m^3)	323	Height	(mm)	1600
Plasma surface	(m^2)	392	Magnetic field	(T)	13
Total plasma heating	(MW)	30	Operating current	(kA)	45
Plasma elongation (κ)		1.9	Stored flux	(V s)	60.68
Plasma triangularity (δ)		0.36	Conductor to be used		Nb_3Sn
Plasma temperature	(keV)	7.7	TF coils parameters		
TBR for LLCB breeder		0.85	Gap between TF and CS	(mm)	50
TBR for HCCB breeder		0.94	TF coil edge	(m)	2
PF coils parameters			TF field at major radius	(T)	5.42
P1 and P6	(m)	3.45	Peak field on coil	(T)	12
P2 and P5	(m)	9.0	Number of TF coils		18
P3 and P4	(m)	10.55	TF coil thickness	(mm)	800
Flux linkage for 400 s pulse	(V s)	120	Conductor to be used		Nb_3Sn

worldwide. This device will also perform qualification tests on all the reactor components for use in Indian DEMO reactor. Design parameters of SST-2 are given in Table 11.15.

The SST-2 will be a medium-sized fusion machine [41–43], little bigger than JET, and will produce power with a fusion gain, $Q = 5$. It also aims at attaining self-sufficiency in tritium breeding (TBR ~ 1) and authentication of the performance of all the in-vessel components. SST-2 will use existing fusion technology and will generate 100 MW of power. Provision has been made to enhance it to 300 MW by upgrading in-vessel components to withstand higher neutronics and heat loads. The remote handling (RH) aspects during the operation of SST-2 will also be incorporated in the design. For 100 MW fusion power output, the reactor will need an input power of 20 MW. The NBI will provide 12 MW, ICRH 10 MW, LHCD 4 MW and ECRH 4 MW. Present design assumes tritium breeding blankets at the outboard side only and shield blankets at the inboard side. For achieving self-sufficiency in tritium breeding, further evaluation will be done to include breeding blanket at the inboard side as well and its impact on the size of the device and plasma parameters will be quantified. The toroidal coils and poloidal coils dimensions and configuration have been guided by the principle of fusion power varying as $(B_T)^4$ and the plasma shaping being controlled by the poloidal coils. Further, the optimization of the blanket concept not only leads to high TBR but also reduces neutron flux beyond the vacuum vessel to protect TF coils. Figure 11.25 shows the cross section of SST-2 indicating the

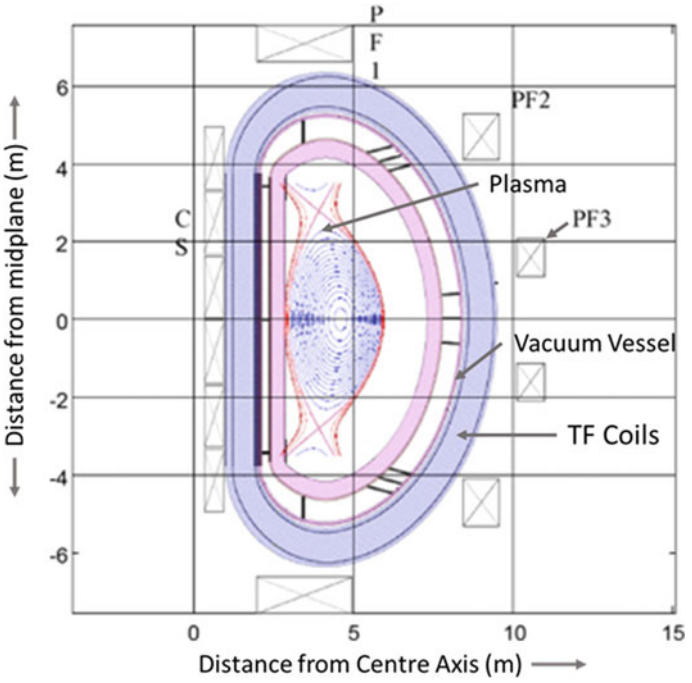

Fig. 11.25 Cross section of SST-2 showing central solenoid (six modules), TF coils, PF coils and the vacuum vessel. *Courtesy* R Srinivasan, Institute for Plasma Research, India

locations of the central solenoid (six modules), TF coils, PF coils and the vacuum vessel. Two schemes, 1. Indian lead–lithium-cooled ceramic breeder (LLCB) and 2. helium-cooled ceramic breeder (HLCB) have been considered in the nuclear design analyses. Nuclear response of SST-2 for one full power year (FPY) has been assessed by calculating one-dimensional radiation transport and tritium breeding response. Shielding requirements have been worked out by calculating various radiation loads to toroidal field (TF) coils. The calculations have been made using the ANISEN code and FENDL 2.1 cross-sectional library which ensure that the radial built-up is quite adequate to protect TF coils for 1 FPY. The TBR values with LLCB and HCCB blankets turn out to be 0.85 and 0.94, respectively.

11.5 The International Thermonuclear Experimental Reactor (ITER)

ITER is an international collaborative project and the culmination of all the efforts that the fusion reactor community around the world has been putting in for well over four decades. ITER is designed to produce fusion power of 500 MW, ten times the

input power ($Q = 10$) and will be the biggest ever tokamak-based fusion reactor built so far. ITER will not produce power but test all the relevant technologies needed for the power-generating reactor, DEMO to be built in 2030s. The objectives include igniting plasma (self-sustaining), verifying tritium breeding concepts from the neutron–lithium reaction and developing efficient technique to extract heat from the fast neutrons generated in the D-T reaction. For this purpose, ITER will evaluate various modules of the blanket designed to slow down and absorb fast neutrons reliably and efficiently. This neutron energy appears as heat which is extracted by the coolant to run the turbines.

ITER means 'way' in Latin and is the result of a broad understanding reached between the two presidents, Reagan of USA and Gorbachev of Soviet Union in 1985 at an IAEA meeting. The design work proceeded between 1988 and 1998, and the project was accepted in 2001. The project is funded by seven countries, European Union (EU), USA, Russia, Japan, China, Korea and India. EU is funding the project to the extent of 45%, and the rest is shared by the other partners (9% each). Figure 11.26 shows the drawing of the ITER tokamak along with the integrated plant systems. The assembly hall was ready in 2017 and by May 2020 cryostat bottom was installed and lower cylinder assembled and welded under India's responsibility. Next, the 9 sector vacuum vessel will be installed and welded. Components of the top lid of the cryostat too have reached the ITER. A large number of reactor components including TF and PF coils are reaching the ITER site. Commissioning phase will begin in 2025. The first plasma is expected in the end of 2025.

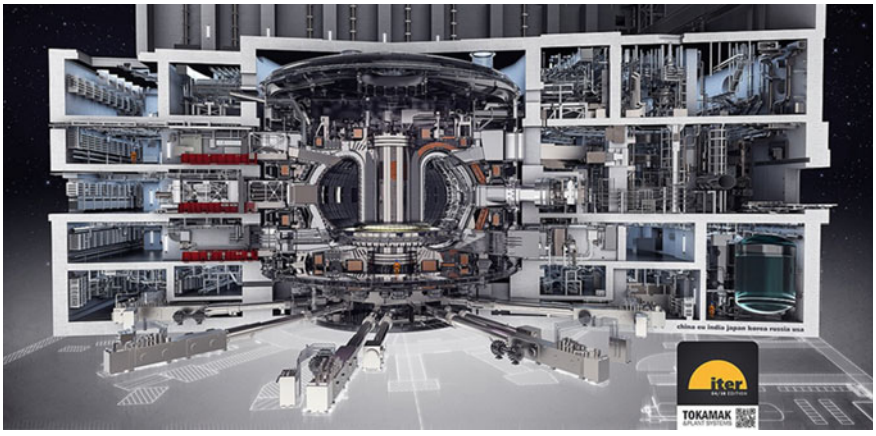

Fig. 11.26 Drawing of the ITER tokamak along with the integrated plant systems. *Credit* © ITER Organization, http://www.iter.org/

11.5.1 The ITER Design

ITER is a fully superconducting tokamak consisting of 18 toroidal coils, six poloidal coils, one central solenoid and nine pairs of correction coils (CC). Correction coils are needed to correct the error fields generated by the imperfections in the manufacturing and/or assembly stages and to stabilize the plasma. All the TF coils are built by EU and Japan, the CS in six identical modules by USA and the poloidal coils by EU, Russia and China. PF 1 and PF6 are built by EU and Russia and PF2 to PF5 being fabricated by China. The nine pairs of CC and 31 feeders too are being supplied by China. These feeders include Nb-Ti CICC bus bars and Bi-2223 HTS current leads. India supplied the cryo-distribution system and 4-km-long cryoline. It also supplied world's biggest cryostat 29.4 m in diameter and 29 m in height. These are now being installed at ITER site. In-wall shielding blocks to protect the magnets from high-energy neutrons were manufactured and transported by Avasarala technologies in Bengaluru, India, to the ITER centre. Figure 11.27 is the cut view of the ITER [44] which shows the 'D'-shaped TF coils and the CS along with several feeders and inserts. The main parameters of the ITER are listed in Table 11.16. The scheme of the PF and CS is shown in Fig. 11.28 [45], and the entire magnet coil system is shown in Fig. 11.29.

Since the peak field in the TF coils is 11.8 T and the field in the CS magnet 13.5 T, Nb_3Sn CICC conductors have been used for these two magnet systems. The

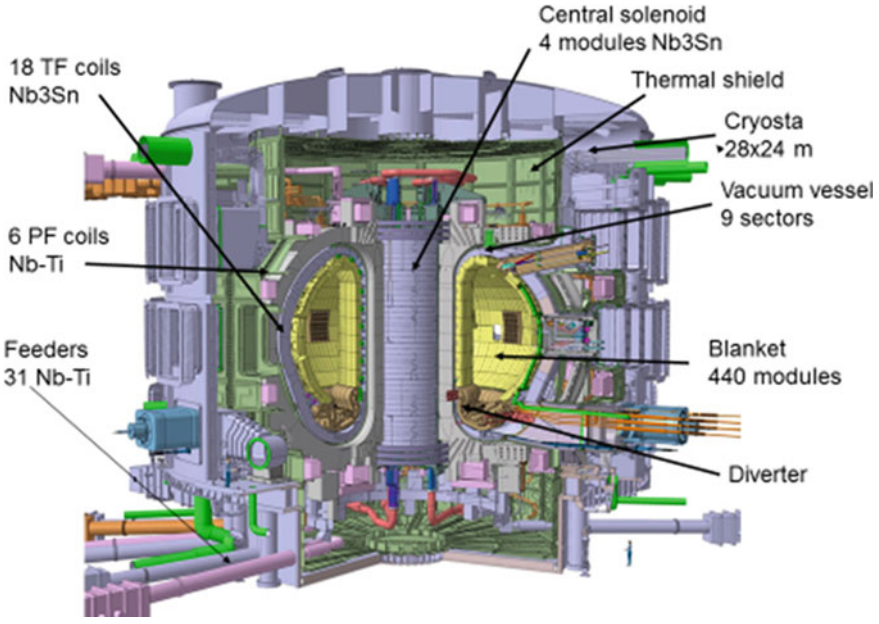

Fig. 11.27 Cut view of the ITER machine [44]. *Credit* © ITER Organization, http://www.iter.org/. *Courtesy* Carlo Sborchia and Amoud Devred

Table 11.16 Main parameters of ITER (data compiled from [46, 47])

Parameter	Unit	Value
Year of start of operation		2025 (expected)
Plasma major radius	(m)	6.2
Plasma minor radius	(m)	2.0
Plasma volume	(m^3)	840
Plasma surface	(m^2)	678
Plasma current	(MA)	15
Plasma average temperature	(keV)	20
Plasma average density	($/m^3$)	10^{20}
Plasma inductive burn time	(s)	300
Average neutron wall loading	(MW/m^2)	0.57
Vertical elongation, κ		1.7–1.85
Triangularity, δ		0.33–0.49
Plasma heating	(MW)	173 (current drive-100, auxiliary-73)
Field at plasma axis	(T)	5.3
Peak field	(T)	11.8
Current leads (Bi-2223 HTS)Ic	(kA)	70
Cryostat height	(m)	29.3
Cryostat diameter	(m)	28.6
Weight of the magnet system	(ton)	10,150
Weight of the cryostat	(ton)	820
Weight of the machine	(ton)	23,350 (magnets + vac. vess. + cryostat)
Fusion power	(MW)	500

peak field in PF coils and CC coils is, however, limited to 6 T at 4.2 T, Nb-Ti CICC conductor has, therefore, been used. All the coils are cooled by the forced flow of supercritical helium (SHe) entering the coil terminals at 4.5 K. Both the conductors have the CICC configuration, and the strands are Cr coated for low AC loss. The general process followed for the manufacture of the CICC conductors used for coil winding for ITER magnets is depicted schematically [44] in Fig. 11.30. About a 1000 multistage superconducting strands, each with a predetermined copper fraction, are twisted around a central cooling spiral tube. SS wraps have been used at the sub-cable stages to reduce AC losses. The cable is then inserted inside SS 316L tubes which are butt welded and extruded as circular jacket for the TF coils and as square

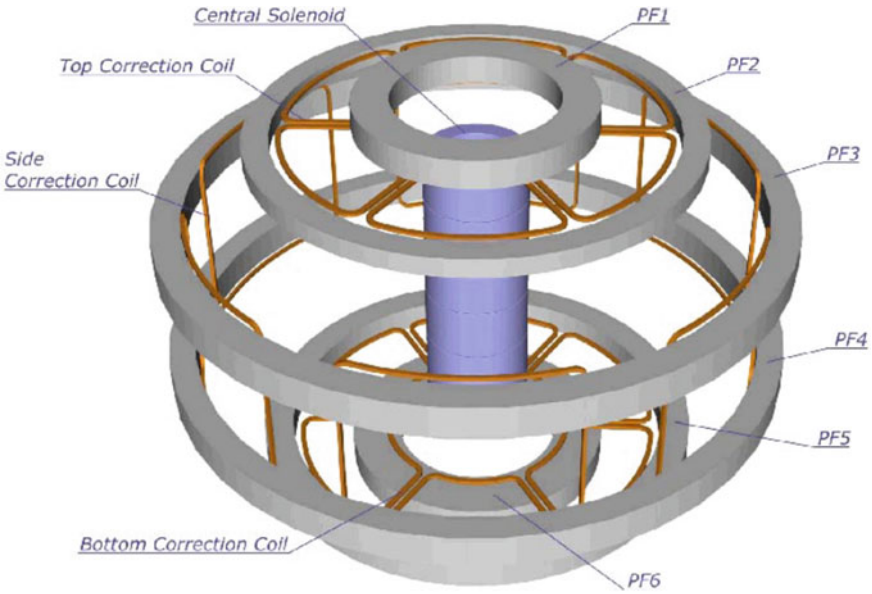

Fig. 11.28 Scheme of PF and CS coils of the ITER [45]. *Credit* © ITER Organization, http://www.iter.org/. *Courtesy* Carlo Sborchia and Amoud Devred

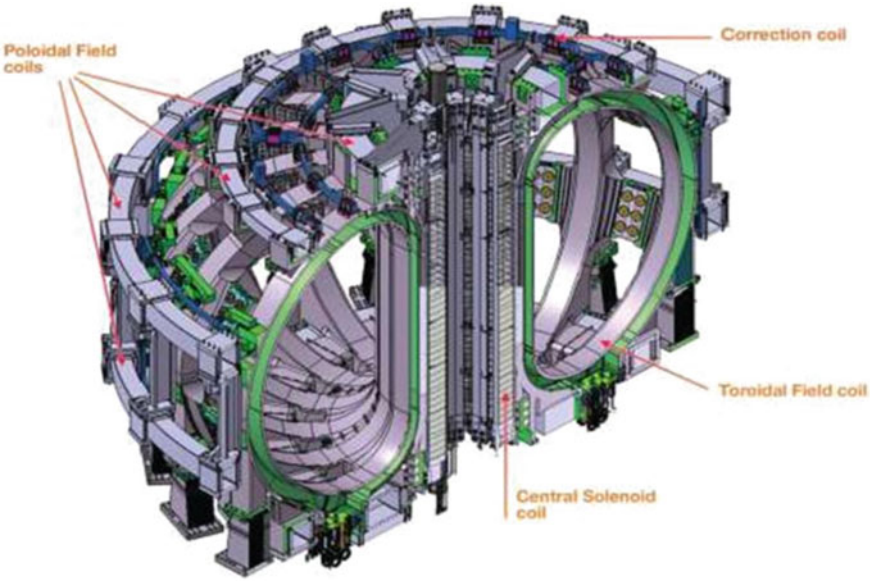

Fig. 11.29 Schematic of the magnet system consisting of CS TF, PF and CC coils of the ITER [46]. *Credit* © ITER Organization, http://www.iter.org/. *Courtesy* Carlo Sborchia and Amoud Devred

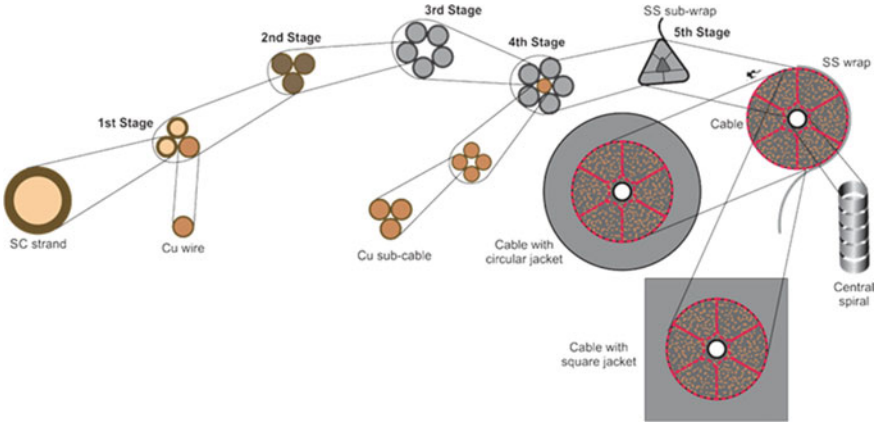

Fig. 11.30 Process through different stages of cabling for CICC cables used for ITER magnet coils. Adapted from [44]. *Credit* © ITER Organization, http://www.iter.org/. *Courtesy* Carlo Sborchia and Amoud Devred

jacket for the other coils. The jacket material for the CICC Nb_3Sn for CS modules is Incoloy Alloy 908. The operating current requirement for the TF coils is 68 kA and for the CS and PF coils 45 kA. The CC coils use a cable with only about 300 strands and without the central channel as they operate at a lower-current level of 16 kA. The conductors have a void volume of about 29%, which facilitates SHe flow for cooling. Table 11.17 gives the specifications of the TF, CS and PF coils [44, 48] and the conductors used. HTS Bi-2223 current leads with a critical current of 70 kA will be used to power the magnets. The use of HTS leads results in a 25% of saving of energy. The total cryogenic power requirement is estimated to be 64 kW.

11.5.2 The TF Coil Winding Pack

Each TF coil consists of seven double pancakes (DPs) wound with Nb_3Sn conductor. The winding of the coils and maintaining the dimensional and geometrical accuracies is a complicated procedure because the winding packs (WPs) are heat treated. The winding has to take into account the conductor elongation (about 0.05%) due to heat treatment. The winding is carried out in a mould to hold the conductor shape during heat treatment. After the winding, the conductor terminations and helium inlets are formed by opening the conductor jackets. Each DP has two terminations, and each winding pack has six DP to DP joints. The coils are now heat treated (650 °C × 200 h) under controlled inert atmosphere. The mould is removed, and radial plates (RP) are inserted between the two single pancakes by creating a gap. The RP is made out of a high-strength thick plate of austenitic steel SS 316LN with finely machined grooves to fit the conductor. This procedure is to be carried out extremely carefully within the conductor strain limit of 0.1%. The conductor is insulated with a thin wrap

Table 11.17 Key parameters of the TF, PF and CS coils of the magnet system of the ITER (data compiled from [44, 48])

Parameter	Unit	TF coil	PF coil	CS coil
No. of coils		18	6	6
Conductor used		Nb_3Sn	Nb-Ti	Nb_3Sn
No. of double pancakes		7	8(PF1,3,4,5) 6(PF2) 9(PF6)	
No. of turns/coil or WP		134	115–459	549
Operating temperature (supercritical helium)	(K)	4.5	4.5	4.5
Max. operating current	(kA)	68	45	45
Nominal peak field	(T)	11.8	6.0	13.0
Total stored energy	(GJ)	41	4	7
Electrical discharge time constant	(s)	15	18	11.5
Total weight of the coils (with case and structure)	(ton)	5364	2163	954
Length of the coil centre line	(m)	34.1	25–27	10.7
WP conductor length	(m)	4570	6009–14,067	6019
Total conductor length	(m)	82,260	63,142	36,114
Conductor unit length	(m)	760/415	387–879	903/601
SC strands/total strands		900/1422	1440, 1152 and 720 (SC)	
Sc: Cu ratio		1	1–2.3	1
Strand plating thickness	(μm)	2	2	2
Strand diameter	(mm)	0.82	0.73	0.83
Cable diameter	(mm)	43.7	35–38	43.7
Jacket		SS 316LN (circular)	SS 316LN (square)	JK2LB (square)
Void fraction	(%)	29		
SHe mass flow rate in conductor	(g/s)	8	8–14	8
SHe mass flow rate in structure	(kg/s)	2.5		

of glass cloth by lifting it gently, and the gap in the groove is filled with glass cloth shims. A perforated cover plate (CP) is fixed by laser welding to lock the conductor in the groove. The perforation in the CP enables the epoxy flow during the vacuum-pressure impregnation. Electrical insulation is provided to the conductor, and ground insulation to the DP. Impregnation of the coil packs is then carried out.

The TF coil casing is the next most critical part of the tokamak as it carries all the support structure for a large number of PF coils, the CS and many other components.

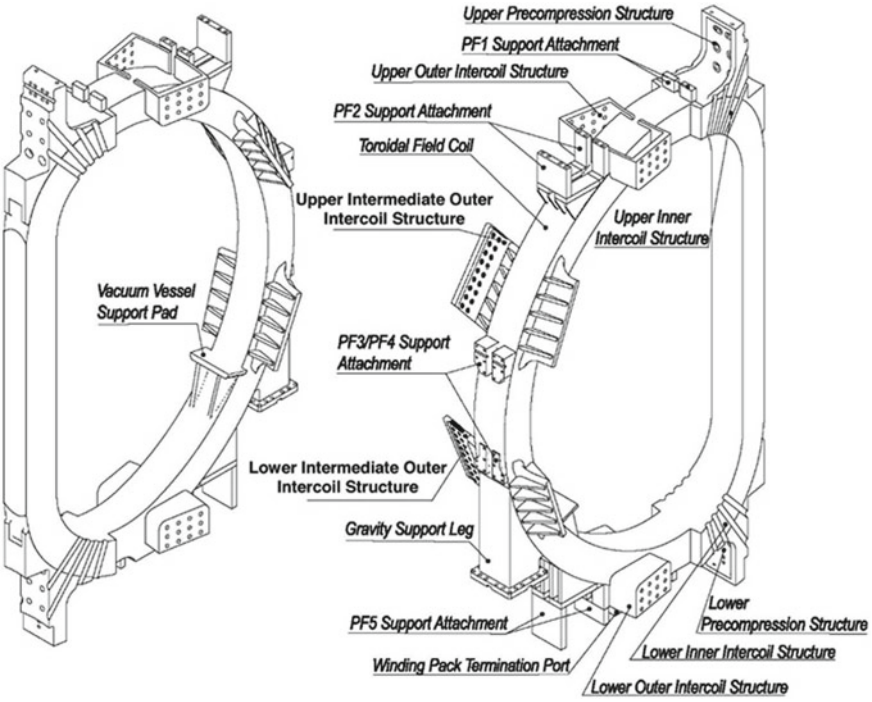

Fig. 11.31 TF coil with casing and various support structures [45]. *Credit* © ITER Organization, http://www.iter.org/. *Courtesy* Carlo Sborchia and Amoud Devred

As shown in Fig. 11.31, the casing carries upper and lower pre-compression structures, upper and lower, inner and outer inter-coil structures, support structure for all the PF coils, gravity support leg structure and terminal port for the WP. The WP is inserted in the casing, and the space between the WP and the casing is filled with epoxy. A two-step process, that is, laser root technique (LRT) followed by submerged arc welding (SAW) technique has been used for welding the casing parts. The casing is finally closed with the plates and welded using the same technique.

11.5.3 The PF Coil Winding Pack

The PF coils too are fabricated in a double pancake (DP) structure. The DPs are wound, electrically insulated and epoxy impregnated. They are stacked together and again impregnated to complete the WP. The winding packs of PF1, PF3, PF4 and PF5 have eight DPs, PF2 has six DPs, and the PF6 has the maximum number, nine DPs. Before a DP is impregnated about 5 m of the conductor, ends are kept unbonded by an antiadhesive wrap. This wrap is removed after the impregnation. These conductor ends are used for making flexible terminations for making joints. A

glass cloth layer is inserted between the DPs to facilitate the resin flow and bonding during impregnation. The inlet and outlet SHe ports are now joined to the cooling pipes which are ground insulated and joined with the cooling system network.

PF coils use Nb-Ti CICC conductors. Since different PFs experience different peak field, the cables with different specifications [48] have been produced and used for winding the PF coils. Coils PF1 and PF6 have the highest peak field than the other PF coils. The conductor for PF1 and PF6 has therefore larger no. of superconducting strands (1440) compared to other coils, 1152 for PF5 and 720 for rest of the PFs. Nb-Ti and Cu strands are cabled like a rope but without a central spiral and jacketed in SS 316LN with a square cross section. The strands in these conductors are coated with Ni. The conductors are manufactured in five cabling stages as indicated in the table. The starting stage is always a triplet (two or three SC strands + one copper strand). The cable in last but one stage is wrapped with a thin SS tape in a helical fashion with gaps. The tape limits the coupling currents, and the gap facilitates SHe flow for cooling. A detailed account of the conductor production has been given by Devred et al. [49].

11.5.4 The CS Coils

The CS magnet is a solenoid consisting of six coil modules stacked vertically one over the above. Each of the six coils is wound using a bare CICC Nb_3Sn conductor in the form of either a quadpancake (QP) or a hexapancake (HP). Spacers are used between the successive turns and between the pancakes for the insertion of insulation. The parameters of the CS coils and the conductor used are given in Table 11.17. The conductor jacket is opened at appropriate locations to make provision for SHe inlet and outlet as well as for the terminations. The hexapancakes/quadpancakes under proper clamping system are then heat treated (650 °C × 200 h), and glass insulation is provided turn to turn and pancake to pancake after removing the spacers extremely carefully. The entire module is now ground insulated. The module is inserted in to a mould and epoxy impregnated keeping the SHe inlet and outlet ports open. The CS with high-strength top hangers, central compression flanges and lower centring system together with the conductor cross section is shown in Fig. 11.32.

The modules with their bus bars extensions are stacked together vertically using a strong and slotted support system. The modules are pre-compressed using a set of super nuts and bolts and by pulling on all the tie plates by tightening the bolts with matching tensile load on every tie plate. The bolts are finally unscrewed to release the load on the thread after the shims are introduced between the tie plates and the key blocks, and the horizontal screws are tightened. The CS is supported on the inboard vault structure of the TF coils.

A very comprehensive review about the status of conductor production for different types of ITER magnets titled ‘Challenges and Status of ITER Conductor Production’ was published by Devred et al. [50] in 2014. The huge amount of conductor required by ITER is being far above the present production capacity of

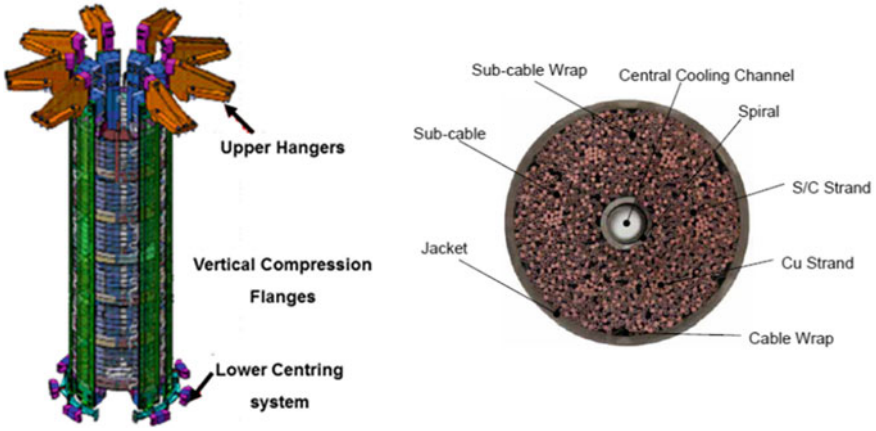

Fig. 11.32 CS (left) and the CICC Nb_3Sn conductor cross-section (right) used for CS coils winding [35]. *Credit* © ITER Organization, http://www.iter.org/. *Courtesy* Carlo Sborchia and Amoud Devred

a single manufacturer, and a large number of suppliers were roped in. It will be first time that Nb_3Sn conductor is used on such a massive scale and exposed to unprecedented large EM forces and high level of stresses during thermal cycling all through its lifetime. All the technical problems envisaged during quality assurance and quality control during production and procurement have been solved.

11.5.5 Final Assembly of ITER

The tokamak is to be assembled in nine sectors each consisting of a pair of TF coils and 1/9th of the cryostat including the vacuum vessel and the thermal shield. Feedthroughs and ports are to be provided in the inter-space between the TF coils. PF5 and PF6 coils will be mounted in position on a temporary structure in the lower part of the cryostat. Gravity support, lower pre-compression rings and various other components of the support structure too will be fixed in position. The nine sectors will then join together to form the torus. Even though all the parts are custom machined within the tolerance limits, yet shimming may have to be used at places during the assembly.

The remaining PF coils and the upper, lower and side correction coils will be installed at appropriate places on the TF coil cases. All the remaining feeders are then to be mounted at this stage through the bottom and the side ports. ITER has a total of 31 feeders, 26 for coils, three for the structure and two for instrumentation. In the final stage of the assembly will be the installation of the CS which is separately assembled and pre-compressed along the central axis of the tokamak. The CS will

finally be lowered in the central bore of the machine and rigidly fixed at the bottom of the TF coils.

11.5.6 HTS Hybrid Current Leads for ITER

HTS current leads technology together with the superconducting magnets is one of the key enabling technologies for reducing the input power requirement for the operation of large fusion power plants. ITER needs about 60 HTS current leads to transport a total current of 2500 kA from room temperature power supplies to magnets at 4.5 K installed in the reactor to reduce heat load and save on the cryogenic cost. This will result in a 25% reduction in the cryogenic power (18 kW @4.5 K). The current leads capable of carrying 70 kA are being procured from the Chinese Domestic Agency through the Institute of Plasma Physics (ASIPP) in Hefei, China. Ding et al. [51] at IPP have already tested a few prototype HTS current leads with different current-carrying capacities, that is, (i) 68 kA for TF coils (ii) 52 kA for PF/CS coils and (iii) 10 kA for CC. The TF leads are the largest ~3 m in length and 600 kg in weight.

A photograph of a pair of HTS current leads developed by ASIPP is shown in Fig. 11.33. These so-called hybrid current leads combine superconducting and resistive sections with many design features similar to the HTS current leads used for the LHC magnets. Gaseous helium (GHe) cools the resistive section between an intermediate temperature (65 K) and room temperature (300 K). The HTS section is cooled indirectly by 5 K SHe. In fact, the key technology included in the design is the forced flow cooling of the resistive section with 50 K helium gas tapped from the appropriate stage of cooling from the He refrigerator and the conduction cooling of the HTS section with SHe from the cold end.

The current leads are made using (HTS) a stack of Bi-2223 tapes clad in Ag-Au alloy sheet. Although 2G REBCO has double the critical current, half as much thermal conductivity, and much higher mechanical strength than the 1G Bi-2223 for

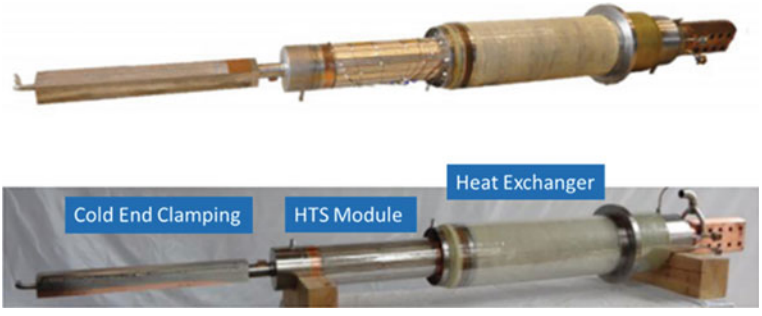

Fig. 11.33 68 kA HTS current leads for TF coils ITER (Upper). 52 kA HTS current lead for PF/CS coils, ITER (Lower) (Ding et al. [51]) (Open access under CC-BY-NC-ND-license, https://doi.org/10.1016/j.phpro.2012.06.232)

analogous quench properties yet ITER decided to go for Bi-2223. The main issue with 2G REBCO has been that the tape has SS support with high resistivity which is no good for efficient current transfer between the tapes. The Bi-2223 tape is 4 mm wide and 0.2 mm thick with superconductor to matrix ratio of 40. The specified critical current of the tape is 100 A (77 K, sf). The tapes are soldered using (Sn-Ag) solder into stacks, which in turn are soldered using Pb–Sn solder in vacuum into Ag-coated grooves of the shunt cylinder. The groove length for the TF coils is 430 mm and for the PF and CC is 410 mm. These current leads have been optimized for 65 K, the temperature at which the thermal shields are cooled by SHe. The current leads have three main components: a copper heat exchanger, an HTS module and the bottom cold end clamping as indicated in Fig. 11.33. Series production of these HTS current leads has already started [52]. For finer details of the design, prototyping and qualifications, readers should go through the 49-page ITER Report no. ITER 18-001 [53] of July 2018 by P. Bauer.

11.6 The Stellarator, W7-X (Wendelstein 7-X) Greifswald, Germany

Notwithstanding the ongoing construction of ITER and the preparation for futuristic DEMO, efforts are going on to build fusion devices at various places to test alternative approaches to produce fusion power. We discuss two such initiatives, namely The Stellarator, W7-X (Wendelstein 7-X) Greifswald, Germany, and IGNITOR, an Italian–Russian collaborative fusion reactor. The W7-X Stellarator fusion device is an alternative to a tokamak system to confine plasma magnetically. W7-X is a steady-state reactor under operation at the Max Planck Institute for Plasmaphysik (IPP), Greifswald, Germany [54–56].

11.6.1 The Magnet System of W7-X

The stellarator is wholly superconducting, consisting of 50 non-planar coils, 20 planar coils, 121 bus bars and 14 current leads. In contrast to tokamak which uses DC and AC fields, the stellarator uses only DC field because PF modulation for plasma positioning and start-up is not needed. It also offers steady-state operational capability and prevents fast plasma disruption which dumps energy on the wall. The main parameters of the machine and the CICC Nb-Ti conductor used for winding magnet coils are given in Table 11.18. All the coils are divided in to five nearly identical modules and together form a toroid. Each module has two mirror symmetric half modules. One half module consists of five non-planar and two planar coils. All the coils in a half module are designed and shaped differently to meet the requirement of a fivefold symmetry of the machine and the flip symmetry installation of the two

Table 11.18 Main parameters of W7-X stellarator and the CICC Nb-Ti conductor used for magnet coils (data compiled from [55, 56])

Parameter	Unit	Value	Parameter	Unit	Value
Year of start		2015	Conductor		Nb-Ti (CICC)
Major radius	(m)	5.5	No. of strands		243
Minor radius	(m)	0.53	Strand dia.	(mm)	0.57
No. non-planar coils		50	No. of filaments/strand		144
No. of planar coils		20	Cabling configuration		$3 \times 3 \times 3 \times 3 \times 3$
Field on the axis	(T)	3	Cu: SC ratio		2.6
Operating current	kA	12	Ground insulation	(kV)	6
Stored energy	(MJ)	600	Void fraction	%	37
Plasma pulse length	(min)	30	Conductor I_c	(kA)	35 (4 K, 6 T)
Plasma volume	(m^3)	30	Temperature margin	(K)	1
Plasma heating	(MW)	14	Total length of strands	(km)	15,000
Plasma temperature	(K)	100×10^6	Total conductor length	(km)	60
Dia. of the cryostat	(m)	16	Max. single length of conductor	(m)	120–130 (PC) 150–170 (NPC)
Height of the device	(m)	4.5	Jacket material		($AlMgSiO_5$)
Weight of the device	(ton)	725	Jacket dimensions	(mm)	16×16
Cold mass	(ton)	425	Cooling media		SHe

identical halves of the module. The coils are rigidly joined together and mounted on to a cast steel central support ring. The magnet system and all the component systems are housed in a 16 m dia. cryostat which has plasma vessel, outer vessel and 254 ports. These ports are used for the installation of diagnostic instruments, heating, water supply to in-vessel components and pumping. All the magnets are grouped in seven electrical circuits each energized by a power supply. Fourteen hybrid current leads are used to power the coils. In addition to the superconducting coils, five water-cooled normal conducting saddle-shaped trim coils are used outside the cryostat to fine-tune the edge magnetic field. Four coils are of the size 3.6 m $\times$ 3.3 m and one coil 2.82 m $\times$ 2 m. The coil assembly is seen in Fig. 11.34.

A Nb-Ti CICC conductor has been used for all the superconducting coils. The cable has 342 strands of 0.57 mm diameter, and each strand has 144 Nb-Ti filaments. The Cu to non-Cu ratio is 2.6. The conductor has a critical current value of 35 kA (4 K, 6 T). The coils are cooled by the forced flow of supercritical helium. The void available for the SHe flow is 37%. In all, 390 double layer lengths of 120–130 m for the planar coils and 150–170 m for the non-planar coils were used for winding.

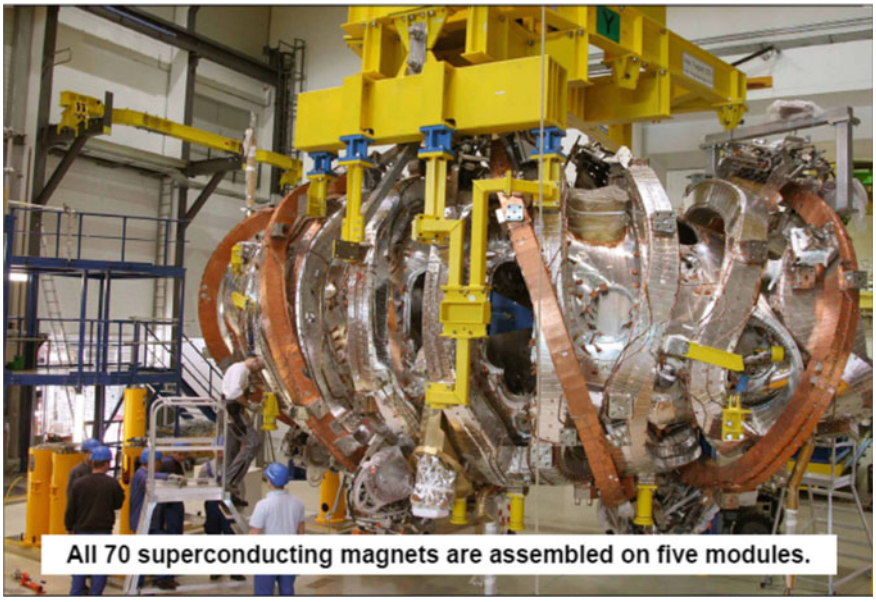

Fig. 11.34 All 70 SC magnets (50 non-planar, 20 planar) of the W7-X stellarator assembled in five modules [55]. *Courtesy* Thomas Klinger, credit Max Planck Institute for plasma Physics

The non-planar coils provide a combination of helical field and the toroidal field and thus play a key role in providing magnetic confinement in stellarators. Each non-planar coil has six double layers consisting of a total number of 108 turns and uses a single length of conductor. All the six double layers are connected in series electrically and in parallel hydraulically for cooling. SHe inlets are connected to the coils on the high-field side (inner most layer). The coil is vacuum-pressure impregnated using fibre glass and hot curing epoxy in a rigid mould. The 5-mm-thick insulation provides a ground insulation of 6 kV. The winding pack, thus, formed is inserted in a strong SS case cast in two halves. The case is strong enough to withstand large EM forces. After the insertion of the coil, the two halves are welded and the gap between the coil pack, and the case is filled with quartz sand and cold curing epoxy. In the final stage, 1100 copper strips are welded around the case, and these are soldered to the four cooling pipes. This arrangement provides an effective cooling shield to the winding pack. The nominal current for the coil operation is 17.6 kA DC. A non-planar coil has the dimensions of about $3.5 \times 2.5 \times 1.5$ m and weighs close to 5.5 tons.

The planar coils are installed around the non-planar coils at an angle of 20° from the vertical axis. These coils are used to move the plasma inwards or outwards and to configure the magnetic field. Coils are fabricated much in the same way as the non-planar ones with some different features.

11.6.2 Bus Bars and HTS Hybrid Current Leads

Superconducting bus bar system has been used for connecting the coils with the current leads. The bus bars (121 nos.) are 4.5–16 m long, made of the same conductor but machined to 17 mm dia. for flexibility, insulated with Kapton tape wrapped with epoxy resin impregnated glass fibre tape. The insulation can withstand a voltage of 13 kV DC. The bus bars are designed to carry current up to 18.2 kA and withstand load up to 17 MPa under extreme quench condition. Hybrid current leads consisting of a copper heat exchanger at the warm end, HTS Ag-Au/Bi-2223 current leads in the middle, and the Cu/Nb_3Sn rods at the lower end were developed and used. The current leads join the room temperature bus bar system to the superconducting parts inside the cryostat. The current leads are mounted at the bottom of the machine with HTS part at the top. Each current lead weighs 260 kg. Current leads were successfully tested up to a current of 20 kA.

11.6.3 Performance Tests on Wendelstein 7-X

After the construction of the stellarator was over in May 2014, the cryostat and magnet system were tested in July 2015. Under the first operational phase (OP1.1) [57], the stellarator produced first helium plasma with a temperatures of 1 million degrees Celsius for 0.1 s in December 2015. In subsequent experiments, plasma electron temperature reached 100 million degree Celsius. Operational phase 1 (OP1.2) continued in 2017 to test the uncooled divertor. In June 2018, a fusion triple product of 6×10^{26} degrees-seconds per cubic metre was recorded with ion temperature reaching 40 million degrees, plasma density 0.8×10^{20} particles/m^3 and confinement time 0.2 s. During the last experiments of 2018, a density of 2×10^{20} particles/m^3, a temperature of 20 million degrees and long discharge times of 100 s were achieved. The highest plasma (electron) temperature reached was 100 million degrees Celsius produced by 4 MW microwave heater pulses lasting one second. More than 2000 pulses were conducted before the reactor was shut for phase 2. The photograph of W7-X stellarator under operation at Max Planck Institute for Plasmaphysik (IPP), Greifswald, Germany, is shown in Fig. 11.35.

In phase 1.2, the vacuum vessel was opened and was lined with protective carbon tiles, and ten uncooled island divertor modules were installed. With hydrogen gas fuelling which is terminated frequently by a radiative collapse, plasma densities of 1–4.5 $\times$ 10^{19} m^{-3} with central electron temperature 50–100 million degrees Celsius were routinely achieved [58]. With hydrogen pellet injection and helium gas fuelling, a plasma density of 1.4×10^{20} m^{-3} was reached. High plasma densities were observed by the boronization of the first wall as the oxygen impurity content was reduced by a factor of 10 and the carbon impurity content by a factor of 5. Since the device is operated without water cooling of the main in-vessel components, the heating energy input is restricted to 200 MJ. The combined effect of the graphite

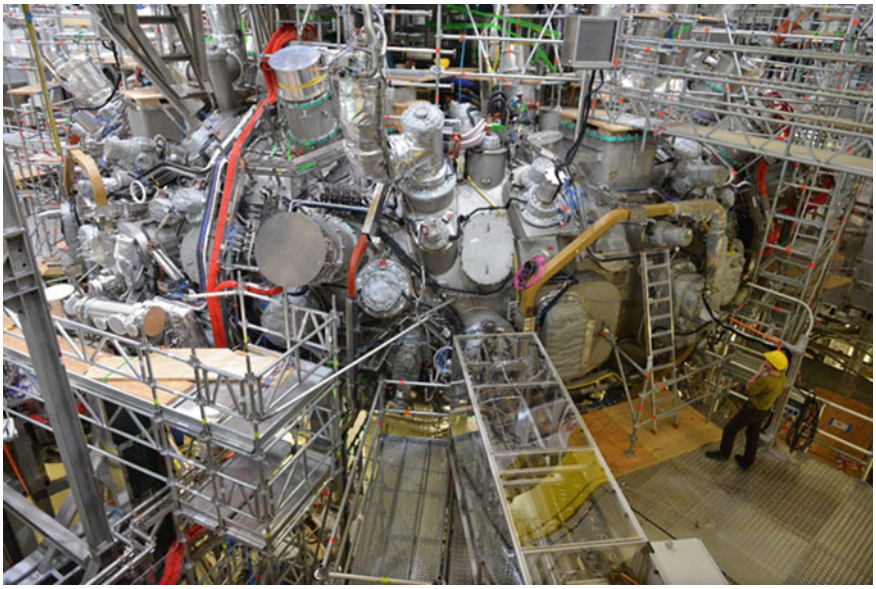

Fig. 11.35 Photograph of the Wendelstein 7-X stellarator, under operation at Max Planck Institute for Plasmaphysik (IPP), Greifswald, Germany. *Courtesy* IPP, Glen Warden

island divertor and the boronized graphite wall elements has resulted [59] in record values of the triple product in stellarators though for short durations. Main limitation to high-performance long pulse plasmas comes from low heating power and non-implementation of water cooling of the in-vessel components.

11.6.4 Wendelstein 7-X Upgrade to Divertor Stage

The upgrade of the Wendelstein 7-X [60, 61] is set to start as the final delivery of components for the so-called divertor has been made. The installation of water-cooled inner cladding of the plasma vessel and water-cooled divertor will facilitate higher heating power and longer plasma pulses lasting up to 30 min. For the confinement of plasma, the reactor will test the optimized magnetic field to be produced by a system of 50 non-planar and 20 planar superconducting coils. The complicated magnet system used in the reactor is, in fact, the critical part of the whole device. Wendelstein 7-X also has the advantage that there is no high plasma current like in a tokamak, and yet the plasma equilibrium and confinement will be of the same quality as in a tokamak of the same size. New water-cooled divertor plates have been designed to withstand a heat load of 10 MW/m^2. The divertor tiles are made of carbon fibre-reinforced carbon and welded on to water-cooled Cu-Cr-Zr (CCZ) plates. To ensure the removal of heat energy, the coolant is supplied by small steel tubes.

All the high-performance components for upgradation are ready for installation, and the reactor is expected to restart operation towards the end of 2021. Testing of all the installations in operation, after the long break, will proceed with low water cooling, low heating power and short plasma pulses. The target of observing longer pulses with plasma energies of up to one GJ will be achieved gradually. It is expected that the new cooled divertors will allow pulses lasting up to 30 min at full heating power, instead of the previous 100 s pulses with heating powers of 2 MW and plasma energies of 200 MJ. The Wendelstein 7-X will not produce energy but would demonstrate whether stellarators are suitable as a power plant, and they have the ability to operate continuously. In contrast, tokomaks can only operate in pulse mode without auxiliary equipment.

11.7 IGNITOR (Italian–Russian Collaboration), ITP, TRINITI, Russia

The Italian company ENEA (New Technologies, Energy and Environment) and the Institute for Tokamak Physics at TRINITI, Russia, entered into an agreement in 2010 to build a tokamak 'IGNITOR' fusion reactor [62, 63]. This tokamak is a revival of the Alcator series of fusion machines built by MIT in USA and Frascati Torus Programme in Italy in 1970s. The IGNITOR will be built in Russia at TRINITI near Moscow, and the core of the machine will be supplied by Italy. IGNITOR relies upon the use of high magnetic field and high plasma energy density in a compact system such that the state of ignition is achieved without external heating. It is a compact machine. It has a major radius of 1.32 m much smaller than ITER. The energy density is, however, twice to that in ITER. This high-energy density is sufficient to heat the D-T plasma to an ignition temperature of 11 keV for a confinement time of 0.6 s. This device will weigh only 700 tons in comparison with ITER which will be 19,000 tons. Main parameters of the tokamak are listed in Table 11.20. The tokamak will have 24 toroidal coils. The ignition is attained at lower fusion power under conditions of high magnetic field and high current in a compact configuration with only Ohmic heating. Figure 11.36a is the conceptual 3D picture of the exterior of the machine [62] and Fig. 11.36b, the cross section showing position of the toroidal, poloidal coils and the central solenoid. Plasma chamber and various other components too can be seen. At present, negotiations between the two partners are going on for the development of the Ignitor Technical Design Project and the preparation of the site of the experimental bench complex [64]. The site is termed as 'Tokamak with Strong Field', complex TSP of the Joint Stock Company 'State Research Centre of Russian Federation, TRINITI' (TRINITI), Moscow, Troitsk (Table 11.19).

One important feature of IGNITOR will be that MgB_2 conductor will be used first time for winding the largest poloidal coil P-14 which has a dia. of 5 m. The coil will operate at 10–15 K cooled by cryocooled He gas and will produce a field of 4–5 T at the coil location. The MgB_2 cable will be a circular conductor of dia. 31.55 mm

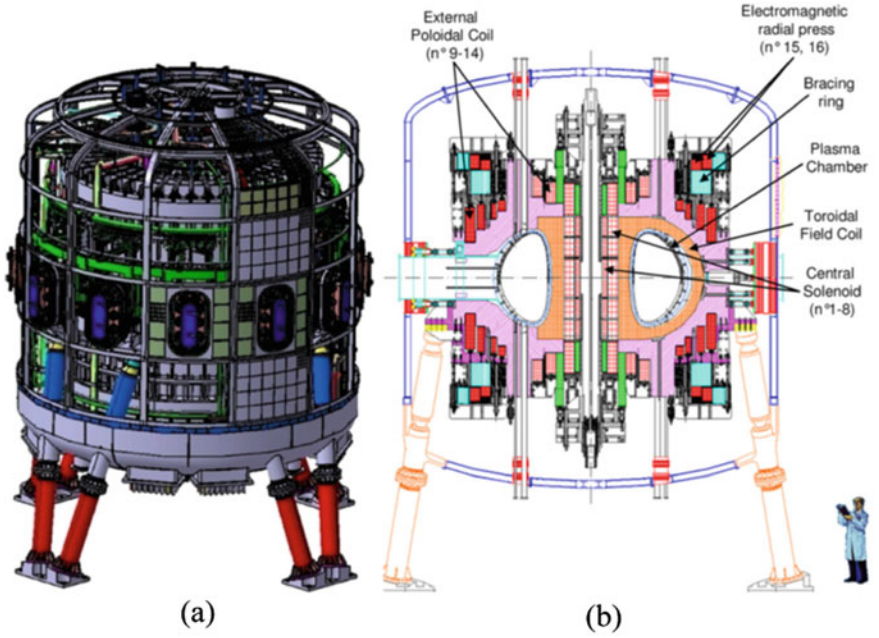

Fig. 11.36 **a** Conceptual 3D picture of the IGNITOR showing its exterior. **b** The cross section of machine showing the locations of magnet coils and ports [63]. *Courtesy* Bruno Coppi and with permission from IAEA

Table 11.19 Some parameters of the IGNITOR fusion device (data compiled from [62, 63])

Parameter	Unit	Value	Parameter	Unit	Value
Plasma major radius	(m)	1.32	Toroidal field	(T)	13
Plasma minor radius	(m)	0.47 × 0.86	No. of TF coils		24
Aspect ratio		2.8	Max. poloidal field	(T)	6.5
Plasma stored energy	(MJ)	11.9	Poloidal current	MA	9
Plasma current	(MA)	11	ICRH power	(MW)	0
Plasma elongation (κ\)		1.83	Ohmic power	(MW)	11.2
Plasma triangularity (δ)		0.4	Toroidal current	(MA)	11
Plasma volume	(m^3)	10	Energy confinement time	(s)	0.62
Plasma temp	(keV)	11	Peak power load on the wall	MW/m^2	1.8
Plasma fuel		D + T	Conductor for PF P-14		MgB_2

having 336 strands of dia. 1.13 mm wrapped around a copper tube facilitating the He flow. Each strand has 37 filaments in a Ni matrix. For enhanced stability, the strand will be coated with a 30 μm Cu layer.

Table 11.20 Comparison of main parameters of some of the important superconducting tokamaks including ITER

Parameter	Unit	T-7 USSR	Tore Supra France	JT-60 SA Japan	K STAR Korea	EAST China	SST-1 India	W 7-X FRG	ITER France
Year of Start		1978	1988	2014	2008	2006	2013	2015	2025
Major radius	(m)	1.22	2.25	3.06	1.8	1.85	1.1	5.5	6.2
Minor radius	(m)	0.35	0.70	1.15	0.5	0.45	0.2	0.53	2.0
No. of TF coils		24 × 2	18	18	16	16	16	50 (NP) 20 (P)	18
Toroidal field	(T)	3.0	4.5	2.69	3.5	3.5	3.0	3.0	5.3
Peak field	(T)	5.0	9.0	6.4	7.0	5.8	5.1		11.8
Operating current	(kA)	6.0	1.40	25.3	35.2	14.5	10.0	12	45
Stored energy	(MJ)	20	0.6	1060	470	300	56	600	5100
Cooling media		SHe	SHe	SHe	SHe	SHe	SHe	SHe	SHe
TF conductor	CICC	Nb-Ti	Nb-Ti	Nb-Ti	Nb_3Sn	Nb-Ti	Nb-Ti	Nb-Ti (CICC)	Nb3Sn
Plasma current	(MA)		1.7	5.5	2.0	1.0	0.22		15,000
Plasma elongation (κ)			1.76	1.76	2.0	1.6–2.0	5.2		1.7–1.85
Plasma triangularity (δ)			0.45	0.45	0.8	0.6–0.8	1.7–2.6		0.33–0.49
Plasma volume	(m^3)		24	127	17.8	840		30	840
Plasma heating	(MW)		27	41	28 (Aux)	7.5 (Aux)	3 (Aux)	14	173
Plasma fuel			D + D	D + D	H + D	D + T ?	H + H		H + D + T

Having discussed a number of fusion machines, it will be worthwhile to present their key parameters in a single table for a quick comparison. Table 11.20 summarizes the key parameters of the important superconducting tokamaks that we discussed in the chapter. All the tokamaks Tore Supra (now WEST), K Star, EAST, JT-60SA, SST-1 and Wendelstein 7-X are already in operation and yielding useful data. Tokamak, JT-60 SA has started operation in March 2020. It is hoped that the experience gained from these reactors will enable ITER to reach its goal as intended.

The dream of realizing power through fusion has always been twenty years away. The ITER, a giant effort being made by the international community and at huge cost might ultimately break this passé and pave the way to build DEMO with high degree of confidence. Next decade is going to be crucial when we get the final answer to the power generation through fusion. Superconductivity will continue to play the leading role in this endeavour. In the wake of these developments, there has been unprecedented growth of production of quality cables with high critical current, high field and low AC losses. This trend is continuing and high-T_c superconductors, such as CORC cables might replace the conventional superconductors and sooner than we expect.

References

1. J.D. Lawson, Some criteria for a power producing thermonuclear reactor. Proc. Phys. Soc. **B70**, 6 (1957)
2. S. Prager, Magnetic Confinement Fusion Science-Status and Challenges. PPT, University of Wisconsin (2005). http://fire.pppl.gov/aaas05_prager_mfe.pdf
3. Magnetic Confinement Fusion, http://library.thinkquest.org/17940/texts/magnetic_confinement/magnetic_confinement.html
4. R.H. Bulmer, Tendam mirror system for the mirror fusion test facility, in *Proceedings of 8th Symposium on Engineering Problems of Fusion Research* (1979), p. 744. http://adsabs.harvard.edu/abs/1979epfr.conf..744B
5. L. Spitzer, D. Grove, W. Johnson et al., USAEC Report NY0-6047 (1954)
6. C.D. Beidler, E. Harrmeyer, F. Herrnegger et al., Stellerator fusion reactor—an overview, in *Toki Conference ITC-12* (2001). http://fire.pppl.gov/itc12_wobig_paper.pdf
7. V.P. Smirnov, Nucl. Fusion **50**, 014003 (2010)
8. A.A. Bagdasarov et al., in *Proceedings of 10th Conference on Controlled Fusion and Plasma Physics*, Moscow, Russia (1981), A-19
9. D.P. Ivanov, V.E. Keilin, B.A. Stavissky et al., IEEE Trans. Magn. **MAG-15**, 550 (1979)
10. L.A. Artsimovich, V.D. Safranov, Soviet Phys. JETP Lett. **13**, 72 (1972)
11. G.S. Kirnev, V.A. Alkhimovich, O.G. Filotov et al., Superconducting Tokamak T-15 Upgrade, FT/P7-3. http://www.naweb.iaea.org/napc/physics/fec/fec2006/paper/ft_p7-3pdf
12. Russia develops a fission-fusion hybrid reactor, 29 May 2018. https://inis.iaea.org/search/search.aspx?orig_q=RN:50012653
13. G.E. Smith, W.F.B. Panchard, TFTR Toroidal Field Coil Design. http://www.osti.gov/bridge/servlets/purl/5154253-mqn8cX/5154253.pdf
14. A. von Halle, The TFTR Group, Final operations of the tokamak fusion test reactor (TFTR), in *Proceedings of 17th IEEE/NPSS Symposium*, 6–10 Oct 1997, vol. 1 (1997), pp. 65–69
15. Joint European Torus, http://en.wikipedia.org/wiki/Joint_European_Torus
16. JET's main features, www.efda.org/jet/jet's-main-features
17. Advancing the spherical tokamak design, https://ccfe.ukaea.uk/research/mast-upgrade/

18. Equipe TORE SUPRA, IEEE Trans. Magn. **25**, 1473 (1989)
19. Jean-Luc Duchateau (CEA Cadarache) PPT "The superconducting TF magnetic system of Tore Supra", http://www-fusion-magnetique.cea.fr/matefu/school_2/Wednesday/duchateau-Toresupra.pdf
20. J.L. Duchateau, J.Y. Jouneaux, B. Gravil, Fusion Sci. Technol. **56**, 1092 (2009)
21. H. Rogalla, P.H. Kes (eds.), *100 Years of Superconductivity* (CRC Press, Boca Raton, 2012)
22. World Nuclear News, First plasma for WEST fusion reactor, 19 Dec 2016. https://www.world-nuclear-news.org/NN-First-plasma-for-WEST-fusion-reactor-1912161.html
23. WEST (formerly Tore Supra), https://en.wikipedia.org/wiki/WEST_(formerly_Tore_Supra)
24. K. Yoshida, K. Tsuchiya, K. Kizu et al., Physica **C 470**, 1727 (2010)
25. K. Kiju, K. Tsuchiya, T. Ando et al., IEEE Trans. Appl. Supercond. **17**, 1348 (2007)
26. A. Pizzuto, L. Semeraro, L. Zani et al., IEEE Trans. Appl. Supercond. **18**, 505 (2008)
27. National Institutes for Quantum Radiological Science and Technology (QRST), Fusion Plasma Research, Update 28 April, 2020—Assembly of JT-60SA Tokamak Main Body Completed (March 2020). https://www.qst.go.jp/site/jt60-english/6599.html
28. Y.K. Oh, K. Kin, K.-R. Park et al., Superconductor application to the magnetic fusion devices for the steady-state plasma confinement achievement, in *Superconductors-Properties, Technology and Applications*, ed. by Y. Grigorashvili (INTECH, 2012). ISBN: 978-953-51-0545-9
29. M. Kwon, Y.K. Oh, H.L. Yang et al., Nucl. Fusion **51**, 094006 (2011)
30. R. Andrews, South Korea just set a nuclear fusion world record. IFLScience (19 Dec 2016)
31. J.-G. Kwak, T. Rhee, H. Han, J.S. Kang et al., IEEE Trans Plasma Sci. **48**, 1388 (2020)
32. Y. Wan, China's Ambitius Path to Fusion Power, an Interview dated Dec 1, 2010, 21st Century Science and Technology (Spring 2011), p. 47
33. Y.N. Pan, P.D. Weng, Z.M. Chen et al., IEEE Trans. Appl. Supercond. **10**, 628 (2000)
34. S. Wu, Q. Huang, J. Chen, Y. Wu, Fusion reactor technologies development in ASIPP, PPCA2-I. http://www-pub.iaea.org/MTCD/publications/PDF/P1250-cd/papers/ppca2-i.pdf
35. L. Qiang, HL-2M Team, The contributions of HL-2M to fusion reactor, in *The International Atomic Energy Agency (IAEA) Third IAEA DEMO Programme Workshop (DPW-3).* https://nucleus.iaea.org/sites/fusionportal/Technical%20Meeting%20Proceedings/3rd%20DEMO/website/abstracts/Li-Qiang.pdf
36. G. Zhuang, G.Q. Li, J. Li, Y.X. Wan et al., Nucl. Fusion **59**, 112010 (2019)
37. J. Zheng, X. Liu, Y. Song et al., IEEE Trans. Appl. Supercond. **29**, 4600104 (2019)
38. Y.C. Saxena, S. Pradhan, PPT, in *20th IAEA Fusion Energy Conference*, 1–6 Nov 2004. http://www.cfn.ist.utl.pt/20IAEAConf/presentations/T5/4T/FT_3_4Ra/talk_FT_3_4Ra.pdf
39. S. Pradhan, IEEE Trans. Appl. Supercond. **22**, 9501804 (2012). https://doi.org/10.1109/TASC.2011.2174951
40. S. Pradhan, K. Doshi, A. Sharma et al., IEEE Trans. Appl. Supercond. **24** (2013). http://doi.org/10.1109/TASC.2013.2290380
41. R. Srinivasan, The Indian DEMO team. Fusion Eng. Des. **112**, 240 (2016)
42. U. Prasad, R. Srinivasan, S. Pradhan et al., IEEE Trans. Appl. Supercond. **26**, 42904 (2016)
43. C. Danani, D. Aggarwal, H.L. Swami et al., Pramana J. Phys. **92**, Article no. 15 (2019)
44. N. Mitchell, A. Devered, P. Libeyre et al., IEEE Trans. Appl. Supercond. **22**, 400809 (2012)
45. Summery of the ITER Final Report, July 2001 by Director ITER (G A0 FDR 4 01-06-28 R 0.2). http://www-pub.iaea.org/MTCD/publications/PDF/ITER-EDA-DS-22pdf
46. C. Sborchia, PPT Lecture on "Fusion Reactor Engineering", Politecnico of Turin (I), 31 Jan 2011. http://staff.polito.it/roberto.zanino/sub1/teach_files/current_topics/lect_sborchia.pdf
47. J.V. Minervini, PPT, "Superconducting Magnets for Fusion and ITER Project" American Nuclear Society-Northeast Region Meeting, Wellesley, MA, 18 April 2002. http://local.ans.org/ne/archives/Superconducting_Magnets%20-%20Joseph_Minervini_April_18_2002.pdf
48. H. Rajainmaki, A. Bonito-Oliva, C. Sborchia et al., The ITER Magnet System: Status of Design and Procurement, PPT, Summer School, Kullaa, 17 June 2008. http://www.prizz.fi/sites/default/files/tiedostot/linkki1ID360.pdf
49. A. Devred, I. Backbier, D. Bessette et al., IEEE Trans. Appl. Supercond. **22**, 4804909 (2012)
50. A, Devred, I. Backbier, D. Bessette et al., Supercond. Sci. Tech. **27**, 044001 (2014)

51. K. Ding, Y. Bi, H. Feng et al., Phys. Procedia **36**, 931 (2012)
52. J. Lorenzo, China launches the series production of HTS current leads for ITER. Fusion Group, 12 July 2019. http://fusion.bsc.es/index.php/2019/07/12/china-launches-the-series-production-of-hts-current-leads-for-iter/
53. P. Bauer, Development of HTS Current Leads for the ITER Project, Report No. ITR-18-001, 18 Feb 2018. http://www.iter.org
54. T. Kupiszewski, O.R. Christianson, Conceptual Design of Superconducting Magnet Coils. http://aries.ucsd.edu/LIB/REPORT/SPPS/FINAL/chap4.pdf
55. T. Klinger, Stellerators Difficult to Build? The Construction of Weldelstein 7-X. PPT. http://www.iter.org/doc/www/content/com/Lists/Stories/Attachments/680/ITER_W7X.pdf
56. T. Rummel, K. Riβe, G. Ehrke et al., IEEE Trans. Plasma Sci. **40**, 769 (2012)
57. 'Wendelstein 7-X', 28 June 2020. https://en.wikipedia.org/wiki/Wendelstein_7-X
58. T. Klinger + many authors from 40 institutions, Nucl. Fusion **59,** 112004 (2019)
59. R. C. Wolf + many authors from 10 Institutions, Phys. Plasmas **26**, 082504 (2019)
60. 'Wendelstein 7-X upgrade moves to divertor stage', World Nuclear News, 17 Mar 2020
61. 'Expansion of the Wendelstein 7-X stellarator underway', Nuclear Engineering International, 19 Mar 2020. https://www.neimagazine.com/news/newsexpansion-of-the-wendelstein-7-x-stellarator-underway-7830324
62. B. Coppi, A. Airoldi, F. Bombarda et al., Critical Physics Issues for Ignition Experiments. MIT (RLE) Report PTP 99/06. http://www.ifp.cnr.it/publications/1999/PTP9906.pdf
63. B. Coppi, A. Airoldi, R. Albanese et al., Nuclear Fusion **53**, 104013 (2013)
64. S.L. Mikhail, A. Gostev, I. Anashkin, A. Belov, I. Levin, Fusion Eng. Des. **146**, 866 (2019)

Chapter 12
Other Applications of Superconducting Magnets

Abstract One area in which superconductivity has directly benefited the society is the health care. Magnetic resonance imaging (MRI), built around a superconducting magnet, is widely used world over for diagnostic purposes like imaging soft tissues of human body. MRI is based on the principle of nuclear magnetic resonance (NMR). High-resolution NMR spectrometers used for studying structure of most complex molecules require high magnetic field with high homogeneity and high temporal stability. Superconducting magnets run in persistent mode with power supply disconnected and produce field with unprecedented stability. High-field homogeneity is provided by the compensating coils and the shim coils. 1.2 GHz (~28.2 T) NMR spectrometers are commercially available with Nb–Ti/Nb_3Sn/HTS combination magnets operating at 1.5–2.2 K. Another potential application is superconducting high-gradient magnetic separator (SHGMS) used to reduce magnetic impurities to ppm level in a variety of minerals. Superconducting magnet energy storage (SMES) is an ideal device to store large amount of energy and releasing it to the grid for load levelling and to balance short duration transient faults. It is used as an attractive pulse power source in strategic applications. Superconducting magnet in persistence mode stores an energy equal to ½ LI^2. Large SMES with stored energy in TJ range for power network system and medium energy 400 MW (70 GJ) SMES for FEL-guided weapons were designed but not built. Micro 5 MVA and 10 MVA SMES have been built and put in use in Japan. All the SMES are designed and built with Nb–Ti superconductors. Attention is now focused on the design of magnets for all the applications based upon 2G REBCO-coated conductor which promises high critical current at elevated temperature, 30–50 K. All these HTS devices will be conduction cooled using cryocoolers and will become commercially competitive. There are many other applications like the Maglev trains largely developed in Japan but not commercialized yet. Superconducting rotating machines like motors and generators have been built for specific applications but not commercialized on cost considerations.

R. G. Sharma, *Superconductivity*, Springer Series in Materials Science 214,
https://doi.org/10.1007/978-3-030-75672-7_12

12.1 Introduction

In the preceding chapters, we have learnt how high-field magnets have been built with the available conventional superconductors such as Nb–Ti and Nb_3Sn in powerful particle accelerators like LHC and are being used in a large number of fusion reactors (tokamaks and stellarators) world over for producing clean energy for the masses. High-T_c cuprates (HTS)—Bi-2223, Bi-2212 and 2G REBCO, have also been used albeit on a limited scale. Bi-2223 leads carrying 80 kA current have been tested and may be used to carry current into TF coils of the ITER. Round wires of Bi-2212 and 2G REBCO-coated conductors have been used in magnets which produced record fields beyond 30 T. More recently, a record magnetic field of 45.5 T has been produced by NHMFL, Florida, using an inner insert of 2G REBCO conductor. Superconducting magnets, however, not only have been used in laboratories and research projects but find wide applications in industry and devices directly benefitting the society. Superconducting magnets are already in use in medical diagnostics (MRI), in pharmaceutical industry (NMR), mineral ore industry (HGMS), for power transmission (low AC loss cables), HTS devices like transformer and fault current limiters for smart grid, electrical machines (motors and generators), superconducting magnet energy storage (SMES) and transportation (levitation of trains). All these applications have been serving the society immensely. We wish to pick up a few specific applications, namely the nuclear magnetic resonance (NMR)/magnetic resonance imaging (MRI), superconducting high-gradient magnetic separator (SHGMS) and superconducting magnet energy storage (SMES) and discuss in this chapter.

12.2 Nuclear Magnetic Resonance (NMR)

NMR spectroscopy, today, is the most powerful technique to study the structure of most complex molecules in all physical, chemical and biological systems and is accepted as an essential tool in a pharmaceuticals R&D laboratory. NMR spectrometer needs intense magnetic field with high homogeneity over the sample volume and high temporal stability. Such stringent requirements can only be met by a superconducting magnet.

Nuclear magnetic resonance (NMR) is a physical phenomenon observed in a nucleus, which has an odd number of protons and/or neutrons and a nuclear spin, $I = 1/2$ or its odd integral multiple. When such a nucleus is placed in a magnetic field (B_0), it absorbs and re-emits electromagnetic radiation. In a constant magnetic field, these nuclear spins get aligned either parallel or antiparallel to the field, thus occupying two energy states, one at higher energy (antiparallel) and another at lower energy (parallel). The lower energy state is slightly more populated than the upper energy state (this difference being of the order of five hydrogen nuclei in a total of two million hydrogen nuclei). If the nuclei are now irradiated with a RF field of frequency matching with the Larmer frequency (resonance condition), the energy is

absorbed and induces a transition from lower energy state to higher energy state. In other words, the nuclear spin flips from parallel to antiparallel state. After the pulse duration, the spin system relaxes back and re-emits the radiation which is recorded as NMR signal. The RF field is applied in a direction perpendicular to the static magnetic field because the signal strength gets maximized. An NMR spectrum is usually acquired in a continuous wave (CW) mode by varying the frequency of the RF radiation but keeping the external magnetic field constant. In an actual experiment, the sample is taken in the form of a solution in a ~5 mm diameter tube held at the centre of the room temperature bore of the magnet Dewar. The sample tube is spun to average out any magnetic field variations and the tube imperfections. The RF antenna and the signal detection coil surround the tube.

In the applied field, the nucleus (like an elementary magnet) precesses around the field, with an angular frequency

$$\omega_I = 2\pi \nu_0 \tag{12.1}$$

called the Larmer frequency. The Larmer frequency depends upon the strength of the static magnetic field as

$$\omega_I = \gamma_I B_0 \tag{12.2}$$

here γ_I is called the gyro-magnetic ratio. Whenever the RF frequency matches the Larmer frequency, the system is in 'resonance', and the interaction is strong yielding a strong NMR signal. We see from (12.2) that higher the static magnetic field higher is the Larmer frequency. In fact, the gyro-magnetic ratio is highest for hydrogen (proton), and a proton frequency of 100 MHz corresponds to a static magnetic field of 2.35 T. The higher the resonant frequency higher is the spectral resolution. It is for this reason that attempts have been continuously made to reach higher and higher magnetic field.

12.2.1 Salient Features of an NMR Magnet and the Present Status

The magnet constitutes the most vital and expensive part of any NMR system. The main requirements of the magnet used in NMR system are as follows:

1. The magnetic field has to be strong enough, compatible with the Larmer frequency of (mostly) proton. Higher the frequency higher is the spectral resolution. NMR spectrometers of 1 GHz frequency with a magnetic field of 23.5 T are commercially available now. Bruker's all-time high-frequency 1.2 GHz (28.2 T) MRI too has entered the market recently.
2. The field homogeneity across the sample volume has to be very high. In NMR, the field inhomogeneity should be restricted to about 1 ppb and in MRI magnets

to about 1 ppm. The sample volume in NMR is few mm^3, but in MRI, it is several litres.

3. The field should have high temporal stability. This is achieved in superconducting magnets by operating them in persistent mode and removing current supply and the leads. This mode of operation also cuts down helium boil-off significantly. Field stability depends strongly on the quality of superconducting joints.
4. The magnet must be shielded so as to reduce the stray field to 0.5 mT level at a distance of about 2 m.
5. To reach highest possible field, the magnet needs to be operated at reduced temperature usually at 1.5–1.8 K.

The technology of magnet construction has evolved considerably over last four decades. The first NMR superconducting magnet was built by Oxford Instruments for a JEOL DELTA-GSX 270 NMR system which was installed by JEOL, USA, in 1979. The magnet used a Nb–Ti conductor and produced a field of 6.3 T compatible with 270 MHz proton frequency. Oxford Instruments also built first magnet which was operated in persistent mode for a 600 MHz spectrometer in 1987. With the availability of high-current conductors, developed in the wake of giant projects in accelerators and fusion reactors, NMR spectrometers have been continuously upgraded to higher frequencies. Thus, a 900 MHz spectrometer was built by Bruker BioSpin [1] and installed at Scrippe research Centre, San Diego, USA, in 2001. A 930 MHz (21.9 T) NMR spectrometer [2] was built at NIMS, Japan, in 2005. World's highest frequency, 1 GHz NMR spectrometer 'AVANCE 1000' was built and installed by Bruker BioSpin [3] at CRMN, Lyon, France, in July 2009. The major players among the manufacturers of NMR spectrometer are Bruker, Varian, JEOL and Hitachi. MRI scanners use wide bore magnets for whole body imaging, but the field is limited to 3 T. Higher field 7 T MRI scanners are in use in the USA and Europe for pre-clinical procedures. Bruker has commissioned a 1.2 GHz NMR spectrometer in 2019 at the University of Florence which started operation in 2020. A 1.3 GHz NMR magnet is being built by Iwasa's group at FBML, MIT.

Like in all other applications, Nb–Ti conductors have been exclusively used for NMR magnets up to 400 MHz (9.4 T) spectrometers. High-frequency spectrometers use the combination of Nb–Ti and Nb_3Sn coils to produce the desired field. Outer coils of Nb–Ti provide the background field, and the inner coils of Nb_3Sn produce additional required field. Such a combination can produce a maximum field of 21.1 T compatible with 900 MHz proton frequency. The design of the magnet is optimized to use full potential of the conductor exposed to a particular field. The magnet therefore consists of a large number of Nb–Ti and Nb_3Sn coils all nested one inside another and each coil operating at maximum current level. To produce highest possible field from such a combination, the magnet is operated at reduced temperature of 1.5–1.8 K. The 1 GHz NMR spectrometer [3, 4] has been built using this option. Yet another record-breaking 1.3 GHz (30 T) NMR spectrometer [5] is nearing completion at the NHMFL. FSU is making use of YBCO-coated superconductor as the innermost coils and operating them at liquid helium temperature. High-T_c superconductors do carry large

current in the presence of high magnetic field at temperatures below 50 K. There are some concerns yet to be resolved with regard to their production in sufficient lengths, uniformity, anisotropy, high-temperature heat treatment, mechanical strength and inter-diffusion of the matrix and the core material.

12.2.2 The Magnet and Shim Coil Design

The outstanding feature of an NMR magnet is to produce required field with homogeneity in ppb range. The dimensions of the magnet are primarily determined by the twin objective of generating required field with high homogeneity and to provide a room temperature standard working bore of 52–54 mm. Errors are, however, introduced often at several stages of fabrication, winding, installing and the presence of magnetic materials in the surrounding building structures. Field homogeneity is restored by providing a number of shim coils which correct the axial and radial field inhomogeneity. The main magnet is wound with large β (length to radius ratio) value which gives a normal homogeneity of the order of 10^{-5}. Use of compensating coils (inner or outer) raises the homogeneity to ppm range. Homogeneity is further improved by a few orders by the use of bipolar axial and radial shim coils. Another set of coils called the shield coils is used to minimize the stray field outside the cryostat. The NMR magnet system thus has a number of coil sets, the main magnet, the compensating coils, the shim coils and the shield coils. Shield coils operate with reverse current so as to cancel out the fringe field outside the magnet cryostat.

The field inhomogeneity is caused by the presence of higher order terms in the field expansion. The magnetic potential on the NMR sample kept at the centre of the magnet can be written as

$$V = \sum_{n=1}^{\infty} \sum_{m=0}^{m=n} r^n P_n^m(\cos\theta)\left[A_n^m \cos m\varphi + B_n^m \sin m\varphi\right] \tag{12.3}$$

where $P_n^m \cos\theta = \sin^m\theta\left(\frac{\partial^m}{\partial^m \cos\theta}\right)[P_n(\cos\theta)]$ is the Legendre polynomial of nth order and degree m.

The axial component of the field B_Z can therefore be written as

$$B_z = \frac{\partial V}{\partial Z} = -\cos\theta\left(\frac{\partial V}{\partial r}\right) + \sin\theta\left(\frac{\partial V}{\partial \theta}\right) \tag{12.4}$$

$$= \sum_{n=1}^{\infty} \sum_{m=0}^{m=n} r^{n-1}\left[(n-m)\cos\theta . P_n^m(\cos\theta) + \sin\theta . P_n^{m+1}(\cos\theta)\right] x [A_n^m \cos m\varphi + B_n^m \sin m\varphi] \tag{12.5}$$

In Cartesian coordinate, the first term in the expansion series of B_Z turns out to be

$$
\begin{aligned}
B_z = {} & A_1^0 + 2A_2^0 z + 3A_2^1 x + 3B_2^1 y + (3/2)A_3^0(2z^2 - x^2 - y^2) \\
& + 12A_3^1 zx + 12B_2^1 zy + 15A_3^2(x^2 - y^2) + 30B_3^2 xy \\
& + 4A_4^0 z[z^2 - (z/3)(x^2 + y^2)] + (15/2)A_4 x(4z^2 - x^2 - y^2) \\
& + (15/2)B_4^1 y(4z^2 - x^2 - y^2) \qquad (12.6)
\end{aligned}
$$

Shim coils are wound to eliminate the first eight terms. Each term is independent of other not affecting the field produced by other coil. Shim coils can be wound inside as well as outside the main solenoid magnet. A bipolar power supply is used to regulate the current in the shim coils in either direction. Axial corrections are provided by eliminating Z and Z^2 terms. Z term is eliminated by using a pair of circular coils placed symmetric about the mid-plane (xoy plane) and fed with opposite current. Z^2 term is eliminated by winding one pair each of circular coils symmetric to the mid-plane (xoy plane) and with reverse currents. The exact position of a shim coil is found by equating the relevant term to zero and calculating the angle of the arc from the centre of the mid-plane. Given the diameter of the shim former, the vertical distance of the shim coil from the mid-point is found out. An experimental 100 MHz NMR magnet system [6, 7] was built for practice in author's group decades ago. For locating the exact positions of the six sets of shim coils, we followed the article published by Sauzade and Kan [8].

The shim coils to provide radial correction are saddle-shaped, wound in the form of arcs to eliminate xy, zx, zy and $x^2 - y^2$ terms. The angle and the location of these arcs are again found out from (12.6). We had used aluminium former for the main solenoid and separate fibreglass epoxy formers for the shim coils. The exterior of this magnet with radial shim coils is seen in Fig. 12.1a. Figure 12.1b shows the radiation shield being wrapped with multilayer insulation (MLI), and Fig. 12.1c shows the NMR cryostat after the integration with the magnet inside [6, 7]. To get rid of zx term, we used eight arcs four on either side of the xoy plane with opposite current polarity at angles (0°–120° and 180°–300°). Similarly, the zy term is eliminated by having eight arcs but shifted by an angle of 45° with respect to the zx coils. So, the new arcs are wound at angles of 45°–165° and 225°–345°. The $x^2 - y^2$ term is eliminated by eight pairs of arcs symmetric to the xoy plane as well as to the $x = y$ and $x = -y$ planes and with current in opposite direction. The angles of the arcs thus are 0°–90°, 90°–180°, 180°–270° and 270°–360°. The xy term also has eight pairs of arcs but rotated by an angle of 45° around the oz axis with respect to the $x^2 - y^2$ coils. Thus, the new arcs are wound at angles 45°–135°, 135°–225°, 225°–315° and 315°–45°. The schematic of the shim coils is shown in Fig. 12.2.

We had cut grooves in the shim formers for winding shim coils. The z and z^2 coils had eight layers, and each layer had 14 turns. Radial shim coils had ten turns each. The shim coils used a 0.279 mm diameter Nb–Ti wire of Supercon make. All the shim coils were connected in series and energized by a single bipolar shim power supply (SPS) of ±25 A as shown schematically in Fig. 12.3. Since the main magnet and all the shim coils have to operate in persistent mode, we developed persistent switches in-house. Two sets of switches were developed, one for high-current main magnet

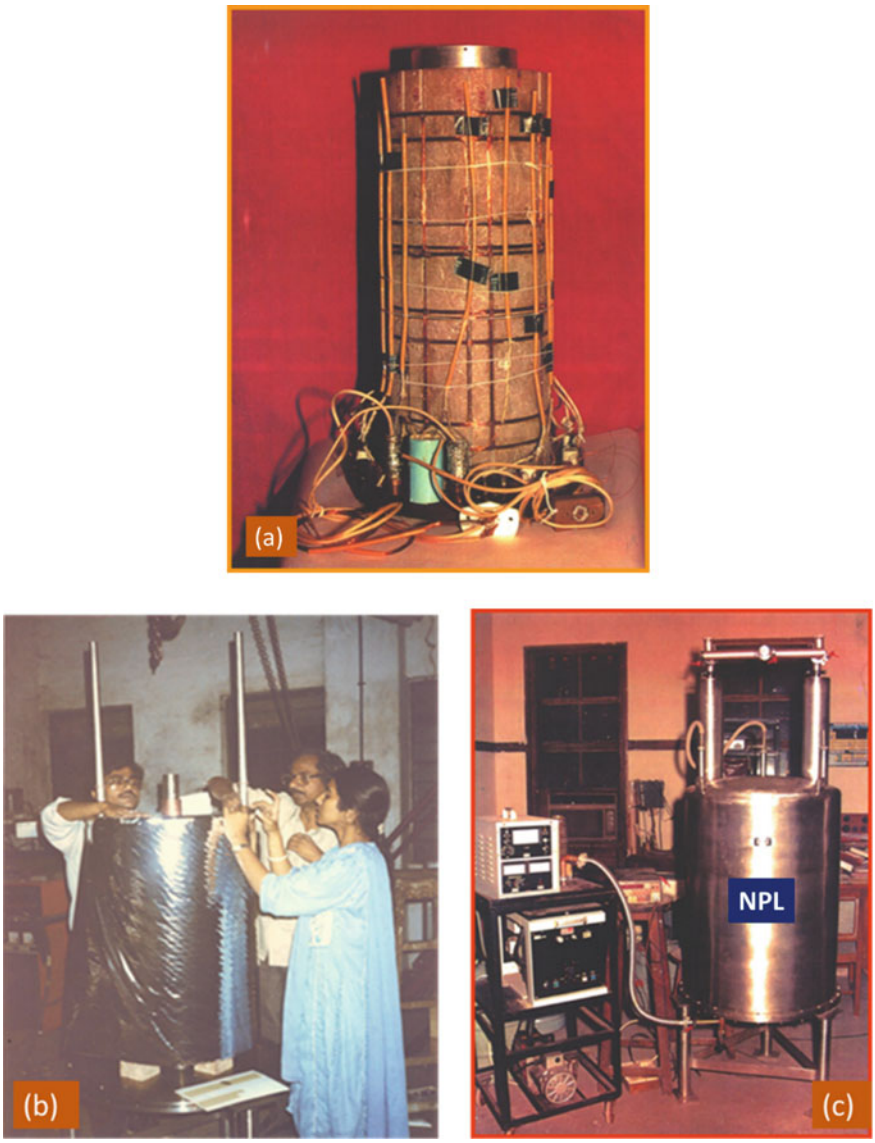

Fig. 12.1 **a** An NMR magnet exterior showing shim coils, superconducting joints and persistent switches for the main magnet and the shim coils. **b** B. Sarkar, Y.S. Reddy and R. Rajput wrapping the superinsulation on the radiation shield. **c** The NMR cryostat after the integration with the magnet inside [6, 7] (Photos courtesy NPL Delhi)

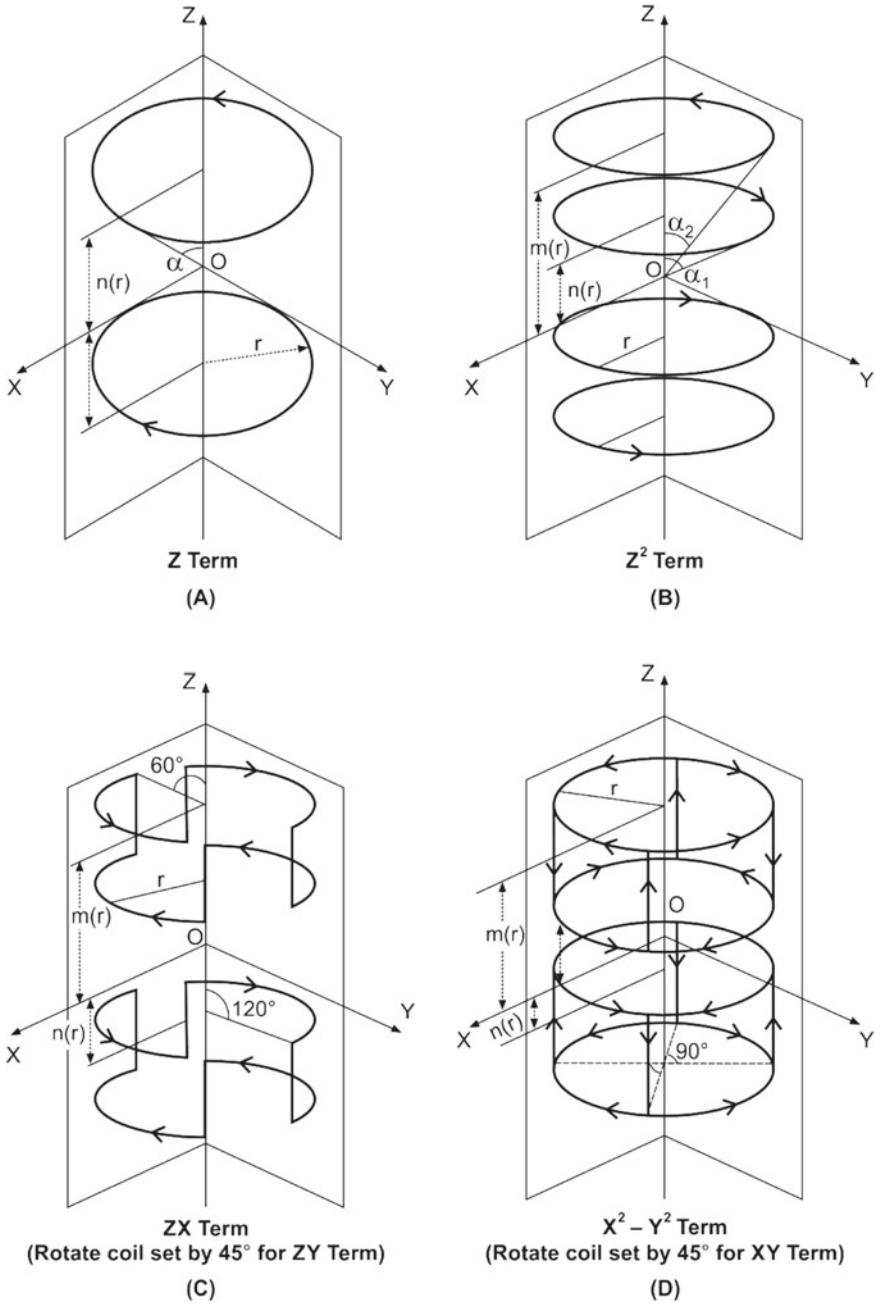

Fig. 12.2 Scheme of circular and saddle shim coils of the NMR magnet [7]

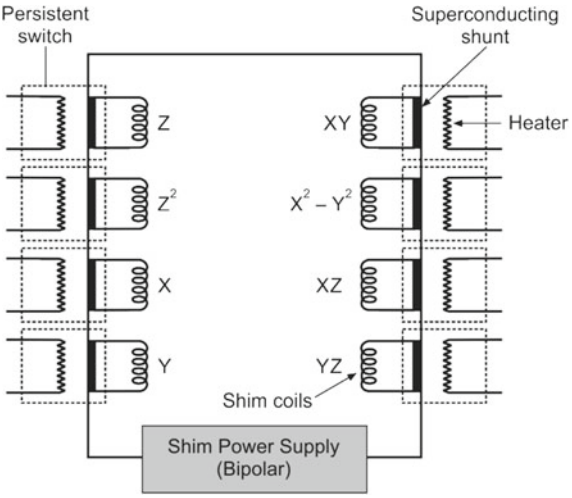

Fig. 12.3 Schematic of the shim coils circuit. All the shims are connected in series and energized by a ±25 A power supply. Each shim coil is provided with a persistent switch

and another for low-current shim coils. We used a Nb–Ti wire in a resistive Cu–Ni matrix Vacry flux 5001 with a diameter of 0.455 mm. It had a room temperature resistance of 2 Ω/m. All the shim switches had an overall dimension of 30 mm × 10 mm. The switch resistance was 7 Ω and the heater resistance 120 Ω. All the switches had bifilar non-inductive winding. All the switches were epoxy moulded and fixed on an insulated platform at the bottom of the magnet.

The main magnet had a winding length of 380 mm and an inner winding diameter of 112.3 mm. The magnet was sixth-order compensated with outer compensating coils. Shims were wound outside. The outermost diameter of the magnet was 137.5 mm. We used a copper-stabilized 0.35 mm diameter Nb–Ti wire of Outokumpu make for winding the main magnet. In all, we used 11 km of wire. Since the operating field was small (2.35 T only) and the magnet had to run in persistent mode, we opted for a monofilamentary wire with the core diameter of 186 μm. The large filament size came handy in making superconducting joints. The magnet had 25 layers each having 1091 turns. Fibreglass cloth was used as inter-layer which allows free flow of the impregnating medium.

12.2.3 Jointing of the Wires

A perfect superconducting joint (non-dissipative) between different coil sections is the key technology needed for achieving high stability of the magnetic field, so essential for any NMR/MRI system. Manufacturers have developed their own techniques which is a proprietary item. Different methods have been used by different groups for fabricating non-dissipative joints between the terminals of a superconductor wire for the persistent mode operation of the magnets. These methods include solder matrix

replacement, ultrasonic welding, diffusion welding, cold-pressing and spot welding. We briefly discuss the technique we followed and quite successfully. The joint has to be made between the superconducting filaments only without the involvement of the matrix. The matrix material, usually copper and/or a cu-alloy, is removed carefully by acid etching. The exposed filaments are now thoroughly cleaned and de-oxidized. The filaments of the terminals are twisted together and wrapped with a thin Nb–Ti thin foil (rolled from a rod) and spot welded all along the length under inert atmosphere. We developed a special vacuum system for carrying out this spot welding process. The joints should be coated with epoxy to prevent oxidation. We did observe deterioration in the performance of the bare joints when exposed to atmosphere. It is important that the critical current at the joint should not be below the I_c value of the conductors. The joints should therefore be evaluated by critical current measurements in magnetic field. All the joints must be located in the cryostat in a region of low magnetic field.

Of late, the solder matrix replacement method using lead–bismuth (Pb–Bi) superconducting solder ($T_c = 8.5$ K) has found wide popularity with the magnet manufacturers because of the reliability of the joints. Dipak Patel et al. [9] fabricated non-dissipative joints of multifilamentary Cu/Nb–Ti wires by matrix replacement method using two types of lead–bismuth (Pb–Bi) solders, namely $Pb_{42}Bi_{58}$ and $Pb_{45.5}Bi_{55.5}$. This process is shown in Fig. 12.4 which is self-explanatory. To begin with, the

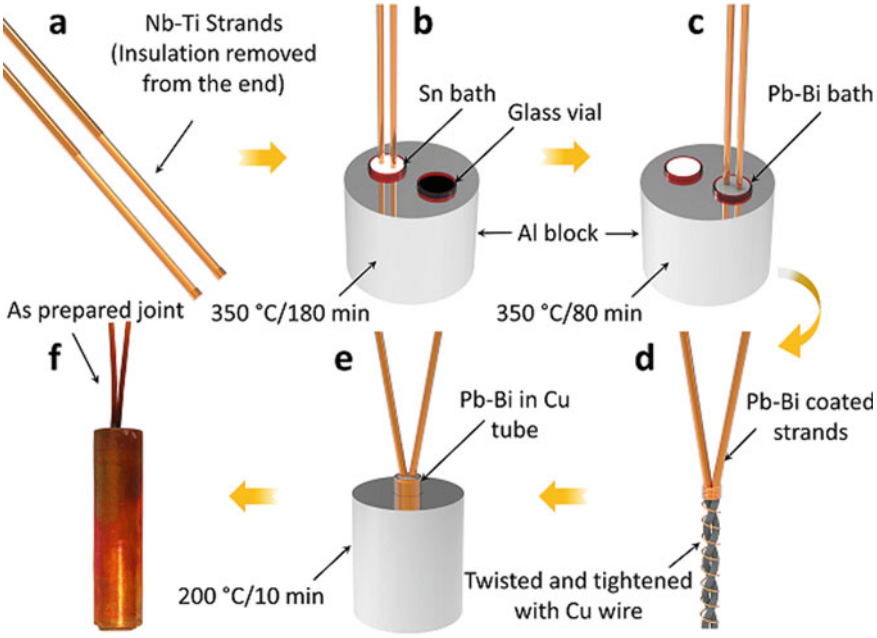

Fig. 12.4 Solder matrix replacement process for making zero-resistance joints of multifilamentary Nb–Ti conductors [9] (Courtesy Jung Ho Kim, AIIM, Uni. Wollongong)

Formvar insulation of the wires is removed, as shown in Fig. 12.4a, cleaned and immersed in a molten Sn bath kept at 350 °C for 180 min (Fig. 12.4b) and transferred to Pb-Bi bath maintained at 350 °C (Fig. 12.4c). After 80 min, the wires are removed from the bath and allowed to cool in open air. The coated wires are then twisted (Fig. 12.4d) together and are again immersed in a Cu tube filled with molten Pb-Bi solder at 200 °C for 10 min (Fig. 12.4e) and allowed to cool down to room temperature. The joint is now ready for characterization as shown in (Fig. 12.4f). Pure argon gas must be flowed continuously on top of the baths to prevent oxidation, while the wires remain inserted and taken out.

The measured onset T_c of both the compositions of the solder was 8.5 K, and the magnetic J_c of $Pb_{44.5}Bi_{55.5}$ and $Pb_{42}Bi_{58}$ was found to be 2.9×10^3 A cm^{-2} and 1.19×10^3 A cm^{-2}, (4.2 K, 1 T), respectively. The authors reported an I_c of 136 A (4.2 K, 1.65 T) for $Pb_{44.5}Bi_{55.5}$. The joint resistance in a single-turn Nb–Ti close-loop measured using the field decay method was estimated to be $= 3.25 \times 10^{-14}$ Ω (4.2 K, sf), thus meeting the technical requirements for persistent-mode magnet operation. Very detailed discussion on the jointing techniques for Nb–Ti persistent current joints can be found in a thesis by Greg Brittles [10].

The jointing, however, becomes complicated when Nb–Ti wires/cables are jointed with other superconductors like Nb_3Sn and HTS conductors commonly used in high-frequency NMR spectrometer magnets. Both these materials need controlled high-temperature heat treatment for conversion to high-T_c phase. During the process of welding, the superconducting phase may get disturbed because of the change in stoichiometry or in the oxygen contents of the HTS. One technique of jointing Nb–Ti and Nb_3Sn conductor has been described by Williams et al. [11]. In this technique, a small hole is drilled in the centre of a compact composite of 90% Nb and 10% of Sn, and the exposed Nb-filaments of the unreacted Nb_3Sn wire are inserted in the composite. After the reaction, the composite surface is polished, and flattened Nb–Ti filaments are spot welded to the surface of the composite through a Nb_3Sn layer of a tape. The welded length is coated with epoxy for protection against oxidation. Most such techniques are in fact developed by the manufacturers, and the details are usually not published.

12.2.4 Bruker's 'UltraStabilized™' Cryostat for 2 K Operation

The magnetic field produced by the combination magnets of Nb–Ti and Nb_3Sn reached an upper limit of 21.1 T (900 MHz) when the magnet was operated at 4.2 K. For higher-frequency NMR spectrometers, HTS conductors are an option, at least for the innermost coil. Iwasa at MIT is building a 30.5 T combination magnet for a 1.3 GHz NMR spectrometer. We will discuss it in detail in a subsequent section. Bruker has been able to build 1 GHz (23.5 T) NMR spectrometer by operating the Nb–Ti/Nb_3Sn magnet system at a reduced temperature of 2 K. More recently, Bruker has

built and installed 1.1 and 1.2 GHz NMR systems at a few locations. These systems have used advanced Nb–Ti/Nb_3Sn/REBCO hybrid magnet technology. The critical current of superconductors at a given field is significantly higher at reduced temperatures. For example, the I_c of a typical Nb–Ti conductor used for 9.4 T (400 MHz) field goes up from 100 A at 4.2 k to 400 A at 1.8 K. In case of Nb_3Sn conductor, the available current density J_c at 17 T is about 76 A/mm^2 at 4.2 K but goes up to about 155 A/mm^2 when operated at 1.8 K. This property of the conductors offers two great advantages. One, that, it is possible to go to higher fields and two, that the quantity of conductor used will be reduced. This will make the whole magnet system very compact and cost-effective.

NMR spectrometers run for years on in a continuous mode and need long-term stability of temperature independent of LHe level and evaporation rate, etc. Bruker developed a new UltraStabilized™ cryostat based on an innovative design [1] and is shown in Fig. 12.5. Most of the features and the exterior appearance of this cryostat are the same as the conventional systems but differ in the design of the LHe vessel. The LHe container is no longer a single vessel but consists of two vessels joined together through a narrow channel to maintain the same pressure. The upper vessel is filled with LHe at 4.2 K, but the lower vessel housing the magnet is cooled to 2 K. The pressure inside both the vessels is kept slightly higher than the ambient pressure to prevent ice formation due to any possible air leak in the vessels. A bath temperature of 2 K corresponds to a He-vapour pressure of 30 mbar, and to prevent such a low pressure over the LHe-bath, the temperature, 2 K and below, is produced by the expansion of LHe into a heat exchanger unit via a *J–T* valve. Thus, only the heat exchanger unit is pumped to pressure below 30 mbar for maintaining a temperature of 2 K and lower in the lower LHe-bath. The LHe flow through the *J–T* valve and the pumping speed is determined by the heat load from the sub-cooled 2 K bath. The bath temperature remains constant because the heat load in the bath due to the operation of the magnet is equal to the heat transfer from the bath to the heat exchanger. The temperature of the bath does no longer depend upon the ambient pressure.

The temperature stability of the lower bath thus depends upon the stabilities of the *J–T* valve and the pumping speed settings both of which determine the amount of helium flowing through the *J–T* valve. The schematic diagram of this UltraStabilized™ cryostat is reproduced in Fig. 12.5. Unprecedented temperature stability of 0.1 mK has been attained in this design. The *J–T* valve can be adjusted over a wide range of flow rates from high cooling power, required during the cool-down and charging of the magnet, to low cooling power sufficient for the normal operation over long periods. The cryostat is highly efficient. It makes full use of the enthalpy of the helium gas escaping from the valve in cooling the insert pipes and the radiation shields. The pumped out gas gives away its entire cold to the sub-cooled system and leaves the cryostat almost at room temperature. The 1000 MHz frequency, 'AVANCE 1000' commercial NMR spectrometer shown in Fig. 12.6a and marketed by Bruker BioSpin used this UltraStabilized™ cryostat.

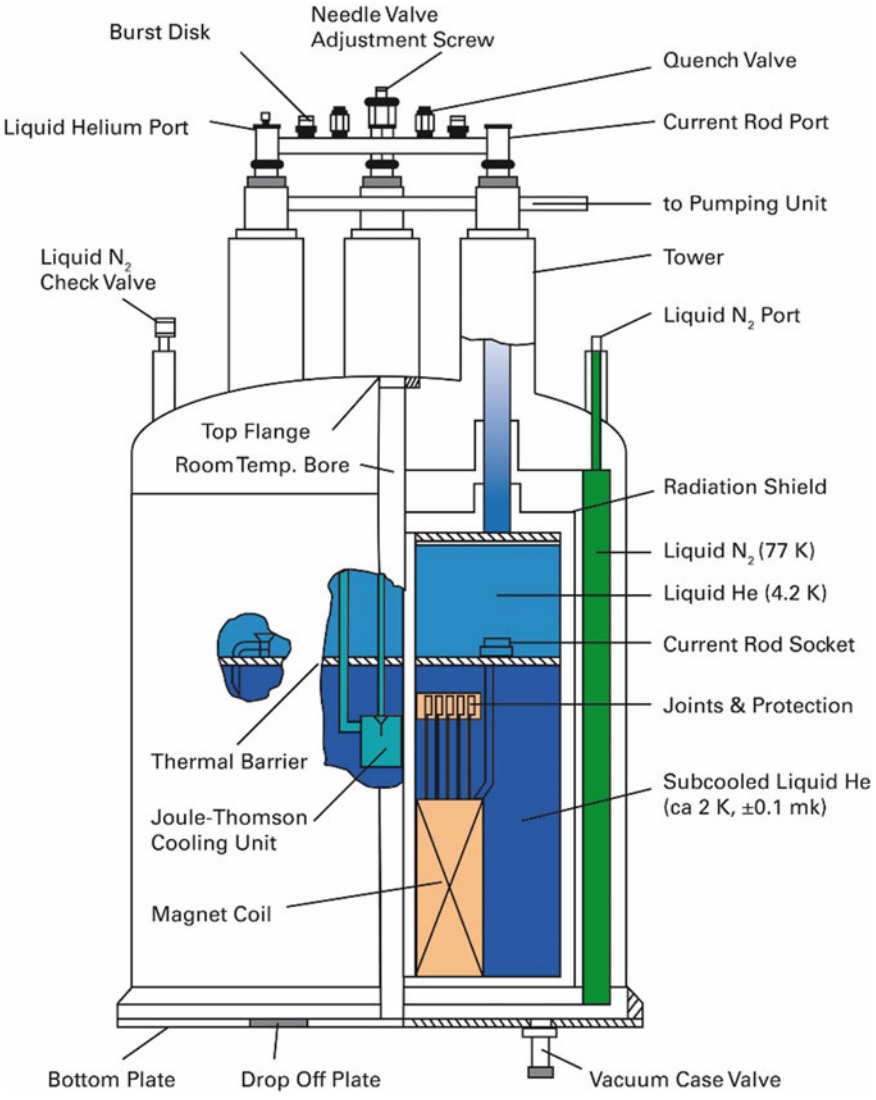

Fig. 12.5 Schematic of the 'UltraStabilized™' Cryostat for 2 K operation of the magnet of high-frequency NMR spectrometer (Courtesy Kuemmerie Rainer, "copyright by Bruker (© Bruker)")

12.2.5 Another World Record in NMR Magnet in 2015

NIMS in collaboration with RIKEN, Kobe Steel and Jeol RESONANCE built yet another record-breaking 24 T magnet for a 1020 MHz (1.02 GHz) NMR spectrometer [12] shown in Fig. 12.6b. The superconducting magnets are about 5 m high and weigh

(a) (b) (c)

Fig. 12.6 Three world records of high-frequency NMR spectrometers. **a** The 1000 MHz 'AVANCE 1000' commercial NMR spectrometer marketed by Bruker BioSpin (2009) (Courtesy Kuemmerie Rainer, "copyright by Bruker (© Bruker)"). **b** The 1.02 GHz NMR magnet system developed by NIMS in 2015 in collaboration with RIKEN, Kobe Steel and Jeol RESONANCE. The superconducting magnets are about 5 m high and weigh about 15 tons. The magnet has coils made of Nb–Ti, Nb_3Sn and HTS Bi-2223HTS. Magnet operates at 1.8 K (2015) [12] (with permission from Elsevier). **c** The 1.2 GHz Ascend™ NMR spectrometer Ascend™ marketed by Bruker Biospin (2020) (courtesy Kuemmerie Rainer, "copyright by Bruker (© Bruker)")

about 15 tons. The magnet has outserts of Nb–Ti and Nb_3Sn and an insert of HTS Bi-2223. The system operates at 1.8 K in a driven mode by an external DC power supply. The stability of the field was initially ±0.8 ppm/10 h without the ^2H lock operation. By using an NMR internal lock operation, the stability improved to better than 1 ppb/10 h. The major problem has been that a superconducting joint technique had not developed sufficiently for stable persistent current operation. Thus, the magnet was designed to operate in a driven mode using an external DC power supply. For a driven-mode operation, an ultra-stabilized DC power supply (Danfysik, MPS 854) was used to energize the magnet using copper bus bars to reduce electric resistance between the power supply and the magnet. Optimized vapour-cooled current leads are used to connect the bus bars to the magnet. A protection circuit for the magnet is installed between the DC power supply and the magnet.

Superconducting (SC) shim coils, room temperature shim coils and the ferromagnetic shims are used for correcting the inhomogeneity of the magnetic field. While the SC shim coils operate in a persistent mode, the main coils of the magnet operate in a driven mode. The spiral winding of the thin Bi-2223 tape and the thicker winding at the coil ends make it difficult to achieve an axisymmetric cylindrical configuration of the field. The field errors thus introduced are much larger in this 1020 MHz magnet than in the earlier 920 MHz NMR magnet. Several types of ferromagnetic shims were therefore installed in the magnet system.

12.2.6 A New World Record of 1.2 GHz NMR Magnet System by Bruker BioSpin (2020)

Bruker announced the development of an ultra-high field (UHF) high-resolution 1.1 GHz NMR spectrometer in 2019 followed by yet another breakthrough in May 2020 announcing the installation of a 1.2 GHz NMR spectrometer Ascend™ [13] at CERM, University of Florence, Italy. Figure 12.6c is the photograph of this two-story 1.2 GHz NMR magnet system generating an axial field of 28.2 T. This is the present world record in high-resolution NMR spectrometry. Study of larger proteins, functional disorder and macromolecular complexes became possible first time. The Ascend™ 1.2 GHz NMR spectrometer has a standard room temperature bore of 54 mm. The magnet utilizes a novel hybrid technology with inner coils of advanced HTS conductors and the outer coils of conventional (LTS) superconductors, that is, Nb–Ti and Nb_3Sn. The magnets of this Ascend™ class of 1.1 and 1.2 GHz NMR systems provide highly stable and homogeneous field perfectly matching the requirements of high-resolution solid-state NMR. The magnet design uses robust quench protection system for the safety of the magnet. The design also provides low drift high-homogeneity field and takes good care of the huge stresses generated by the Lorentz forces during the magnet operation. The successful persistent-mode operation of these ultra-high field magnets shows that Bruker has perfected the technique of jointing superconducting strands of different varieties of superconductors such as

Table 12.1 Key parameters of the 1.2 GHz NMR magnet system Ascend™ from Bruker BioSpin

Parameter	Unit	Value
Proton NMR frequency	GHz	1.2
Magnetic field	T	28.2
Outsert		Nb–Ti
Inserts	Outer / inner	Nb_3Sn / 2G REBCO
Field stability (typical)	Hz/h	<10
Mode of operation		Persistent
RT open bore	mm	54
Operating temperature	K	2.2
Cooling media		LHe-bath
LHe inventory	L	1400
LHe refill/two months	L	360
Height of the magnet system	m	~ 4
Total weight of the magnet system	Ton	9.5

Data compiled from [13]

Nb–Ti and Nb_3Sn and Nb_3Sn and REBCO conductors. The jointing technology is very challenging and remains a top-guarded secret of any company.

The key parameters of the 1.2 GHz magnet system are given in Table 12.1. These ultra-high-field magnets of 1.1 and 1.2 GHz NMR systems, with large stored energy, are housed in LHe-bath cryostats to ensure efficient and reliable cooling of the magnet. In fact, most ultra-high-field NMR centres/laboratories have a number of NMR systems having magnets of different field intensities and are invariably equipped with a Helium recovery and liquefaction facility. At such locations, the bath-cooled magnet solution is more advantageous. The height of the system is about 4 m and weighs about 9.5 tons. The liquid helium (LHe) inventory is 1400 l and needs a refill of 360 l of LHe every two months. Bruker also builds closed-loop Helium reliquefication cryostat called 'Aeon' magnet technology on customer demand.

12.2.7 JEOL's 'Zero Boil-Off Magnet for NMR System'

JEOL USA Inc. introduced [14] in 2013 a magnet system for NMR over a wide range of magnetic field 9.4 T (400 MHz) to 21.8 T (930 MHz) with near negligible boil-off of liquid helium through the use of cryocooler for re-condensing the evaporated He-vapours. It needs maintenance once in two years without disturbing the magnet operation or the NMR signal quality. In the event of a power outage, the LHe reservoir keeps the magnet going for 4 h.

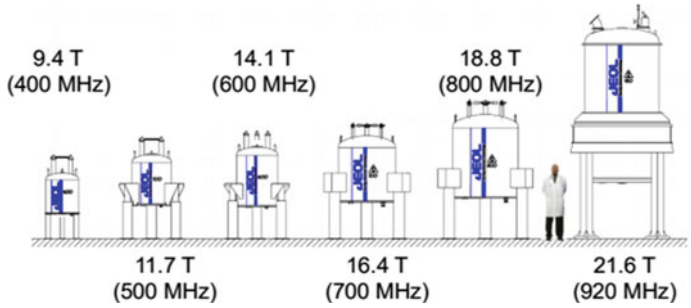

Fig. 12.7 Depiction of increase in size of NMR spectrometers as the magnetic field strength for high-resolution NMR increased over the years. The person in the figure is 175 cm tall [15]. *Credit* NIMS, JASTEC and JSTA. *Source* Press Release NIMS 2011

Figure 12.7 is an interesting figure showing the increase in size of NMR spectrometers as the magnetic field strength for high-resolution NMR increased over the years [15]. The height of the person in the figure is 175 cm.

12.2.8 A Split NMR Magnet System

Hitachi in collaboration with NIMS has introduced [16, 17] a new concept in developing a high-sensitivity solution NMR spectrometer. First option to go to high-sensitivity NMR system is to produce highest possible magnetic field. Further improvement in the sensitivity can be attained by using a cryogenic probe with a solenoid-shaped antenna coil. It is, however, not possible to accommodate this sample probe and the solenoid-shaped antenna detector together in the NMR system of conventional design. Hitachi has come up with a novel idea and designed a split magnet system with two room temperature bores, one bore horizontal, another vertical and the two bores crossing each other at the centre. Figure 12.8 is a schematic diagram [17] of this split magnet. The liquid sample tube is inserted through the vertical bore from the top and the solenoidal antenna coil through the horizontal bore.

The main magnet in this design is divided into two multilayer solenoids separated by a gap which provides the vertical bore. The field produced by the magnet, B_0, is along the horizontal direction. The magnet has several new features as compared with the conventional design. The magnet has shim coils inside as well outside the magnet. The shim coils used have periodically wavy shape. The main magnet has a total of 18 main coils and two self-shielding coils. The six inner pairs are wound using Nb_3Sn conductor and three outer pairs of Nb–Ti conductor. The self-shielding coil too is wound using Nb–Ti conductor. The innermost coil in the present magnet operates at a fixed negative current for improved field homogeneity. The parameters of the magnet and the cryostat are given in Table 12.2.

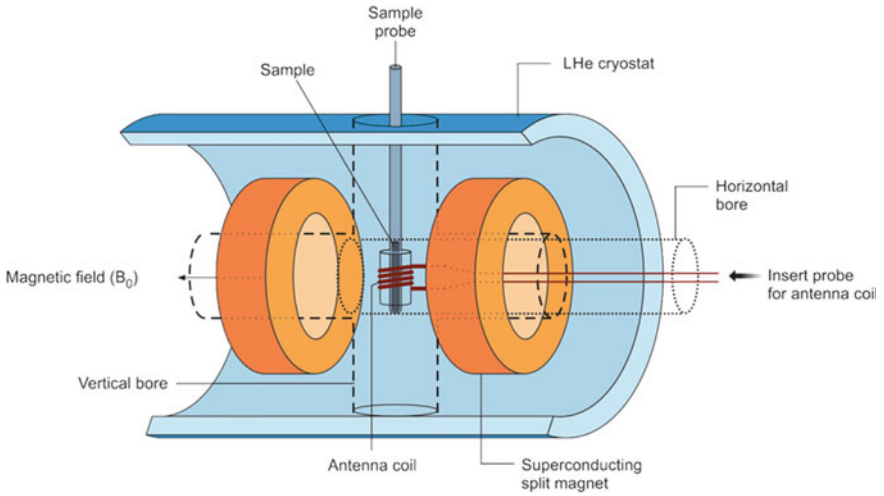

Fig. 12.8 Schematic diagram of a split magnet of an NMR system having a vertical and a horizontal bore (adapted and modified from [16–18])

Table 12.2 Specifications of the Hitachi 600 MHz NMR spectrometer built with split magnet design

Parameter	Unit	Value
Main magnetic field strength	T	14.1
Conductors used		Nb–Ti and Nb_3Sn
Number of inner Nb_3Sn coils		12 (six pairs)
Number of outer Nb–Ti coils		6 (three pairs)
Number of shielding coils		2 (one pair)
Operating current	A	297
Stored energy	MJ	10
Number of inner shim coils		28
Number of outer shim coils		10
Number of Nb_3Sn/Nb–Ti joints		24 (main magnet) 56 (shim coils)
Number of Nb–Ti/Nb–Ti joints		32 (main magnet) 78 (shim coils)
Horizontal bore diameter	mm	54
The cross-bore material		Aluminium

Data compiled from [16–18]

The cross-bore is made of three concentric aluminium pipes. The outer pipe is in contact with the LHe vessel at 4.2 K, the middle one with the thermal radiation shield and the innermost remains at room temperature. The magnet is protected against quench by a passive protection system of resistors and the heaters. The resistance heaters are connected in parallel with each coil close to the next coil.

Once a coil quenches, its heater heats the next coil and raises the temperature of this coil. This coil too quenches and heats up the next coil. This way all the coils of the magnet quench distributing the large stored energy evenly among all the coils. The temperature increase of each coil is thus restricted within safe limits.

As seen from the table, the magnet system has a large number of superconducting joints, 24 between Nb_3Sn and Nb/Ti conductors and 32 between Nb/Ti and Nb/Ti conductors. The shim coil joints are in much larger number 56 and 78, respectively, for the two types of joints. Since the stored energy is very high 10 MJ, extreme precautions are taken for magnetic field stability and the structure to support large hoop stresses. The field homogeneity can be improved to tens of ppm by charging the innermost coil with current of reverse polarity. Homogeneity improves to better than 1 ppm with the shim coils activated. The field drift of the magnet system is less than 1 Hz/h.

12.2.9 Superconducting Magnet (30.5 T) for a 1.3 GHz NMR Spectrometer

Structural studies on very complex molecular systems like proteins require high-resolution (high frequency) NMR spectrometer which in turn requires high magnetic field. Sample examination time and the sample quantity needed, too, are reduced significantly. Experimental data on proteins indicate that the resolution, on the basis of transverse relaxation optimized spectroscopy (TROSY) effect, is optimum in the proton frequency range of 1.2–1.4 GHz. Attempts at a few places are therefore being made to build 30.5 T magnet for the development of a 1.3 GHz NMR spectrometer.

A programme of building this 1.3 GHz magnet is in its advance stage of completion at MIT in the laboratory of Iwasa [19, 20]. It is obvious that such a magnet needs a large number of coils of conventional materials Nb–Ti and Nb_3Sn and the inner coils have to be made out of multicore HTS conductors, BSCCO or REBCO-coated tapes or round wires. HTS do carry current with high densities in the presence of very high magnetic field but only if they are operated at LHe-bath temperature (4.2 K). The 11.74 T high-homogeneity magnet L500 (500 MHz) consisting of coils of LTS Nb–Ti, and Nb_3Sn conductors was bought from Japan Superconductor Technology (JASTEC). The H800 (800 MHz) magnet generating a field of 18.7 T built by MIT team consisted of three nested coils using 2G REBCO tape conductor. All the three coils are stacks of double pancakes (DPs) of no-insulation (NI) REBCO and were completed during 2016–2018. Coil-1 is the innermost coil having 26 DPs and produces a field of 8.7 T. Coil-2 has 32 DPs and generates a field of 5.6 T. The outermost coil of H800 is coil-3 consisting of 38 DPs and produces a field of 4.5 T. All the 96 DPs were wound using 6 mm wide and 120 m long SuperPower advance pinning REBCO tapes coated on a 50 μm thick Hastelloy substrate. Each coil was over-banded with 6 mm wide and 76 μm thick stainless steel tape. The over-band thickness for Coil-1 was 7 mm, for Coil-2, 5 mm, and for Coil-3, it was 3 mm.

Table 12.3 Important parameters of the L500 and H800 magnets. L500 is a background magnet, consisting of LTS coils of Nb–Ti and Nb_3Sn, and provides a field of 11.74 T (500 MHz)

Magnet L500 details (JASTEC) LTS—Nb–Ti and Nb_3Sn conductors			Magnet H800 details (MIT) HTS—sREBCO-coated conductor				
Parameter	Unit	Value	Parameter	Unit	Coil-1	Coil-2	Coil-3
Inner cold bore diameter	mm	273	Number of double pancakes (DP)		26	32	38
Outer diameter	mm	780	Inner winding diameter	mm	91.0	150.8	169.9
Overall length	mm	1422	Outer winding diameter	Mm	119.1	169.2	211.3
Operating temp	K	4.2	Winding length	mm	323.65	393.8	465.8
Operating current	A	245.82	Over-banding thickness	mm	7	5	3
Field contribution	T	11.74	Field contribution	T	8.67	5.64	4.46
Inductance	H	152.4	Total field	T	18.77		
Stored energy	MJ	4.6	Stored energy	kJ	178	233	245
Field homogeneity (17 mm × 30 mm)	ppm	0.45	Total stored energy at maximum field	kJ	653		
Weight	kg	1200	REBCO length/coil	km	3.14	3.84	4.61

H800 is an insert consisting of three nested coils of HTS-2G REBCO-coated tapes and produces a field of 18.7 T (800 MHz). Data compiled from [19, 20]

Thus, the two magnet systems H800 and L500 together produce a magnetic field of 30.5 T corresponding to proton resonance frequency of 1.3 GHz. The core parameters of L500 and H800 magnet systems are given in Table 12.3.

The magnet system of the MIT 1.3 GHz NMR spectrometer consisting of LTS coils (Nb–Ti/Nb_3Sn) producing a field of 11.8 T and an insert H800 of HTS (three nested REBCO coils) adding a field of 18.7 T is shown in Fig. 12.9a. The total field produced adds up to 30.5 T [17] corresponding to a proton resonance frequency of 1.3 GHz. Figure 12.9b is a schematic drawing of the shimming arrangement to improve the field homogeneity suitable for 1.3 GHz NMR magnet. The insert H800 was tested at 4.2 K in March 2018. It was charged to 251.3 A in 7 h (0.01 A/s) to limit the peak power dissipation to below 3 W. Several large voltage spikes were observed during the ramp-up from 235.2 A to 251.3 A. The quench occurred when the central field approached a value of 17.93 T about 96% of the H800's designed value of 18.77 T. Experimental data revealed [21] that coil-2 quenched first about roughly 5 min after the coil current reached the designed value of 251.3 A. Nearly 0.3 s later coil-1 quenched, and the coil-3 quenched another after 0.1 s. The current from the power supply stayed constant until the quench reached coil 3 and then decayed rapidly to zero. The prematured quench caused widespread damage to the H800 insert magnet. The MIT team has revised the design of the new 800 MHz insert named H800N. The new insert will be a single coil solenoid which will eliminate excessive mechanical stresses and unbalance forces due to high induced current. The solenoid magnet will consist of 40 stacked DPs with improved crossover routing. The new design will have improved thermal stability and a reduced excessive current

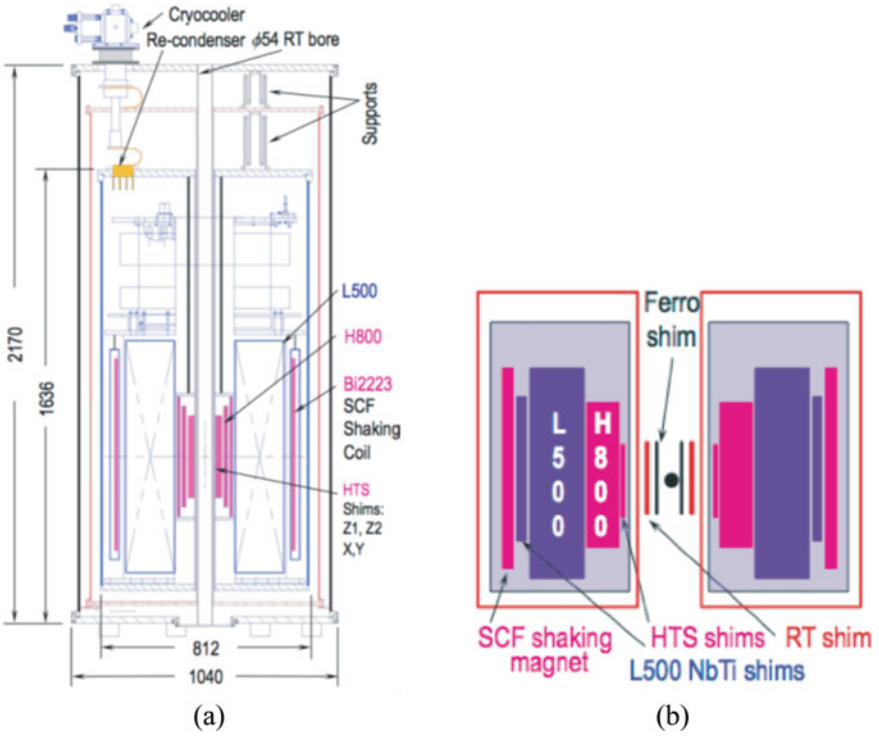

Fig. 12.9 **a** The magnet system of the MIT 1.3 GHz NMR spectrometer consisting of LTS coils (Nb–Ti/Nb_3Sn) producing a field of 11.8 T and an insert of HTS (three nested REBCO coils) adding a field of 18.7 T to make total field 30.5 T. **b** Schematic drawing of the shimming arrangement to improve the field homogeneity suitable for 1.3 GHz NMR magnet (Courtesy Y. Iwasa, FBML, MIT, USA)

margin for quench protection. A non-NMR 30.5 T magnet was to be tested by MIT FBML (Francis Bitter Magnet Laboratory) by combining new H800N with L500 in 2020. The high-resolution 1.3 GHz NMR magnet is expected to be ready for test in 2022.

12.3 Magnets in Magnetic Resonance Imaging (MRI)

MRI is perhaps the best application of superconductivity which directly affected the humanity across the globe. It is a common tool with the radiologist in diagnostic hospitals for imaging various soft tissue parts of the human body and for detecting tumours. The quality of pictures obtained in MRI is far superior to any other technique like X-rays or the computer tomography. The concept of NMR imaging used in present-day MRI systems was proposed by Paul Lauterbur [22] as early as 1973.

MRI exploits the presence of vast amount of hydrogen (protons) in a human body as the water content in a human body is said to be about 80%. When protons in the tissues of the body, aligned in a static magnetic field (B_0), are subjected to resonant RF excitation, they absorb energy. Proton relaxes back and emits resonant signal which is a characteristic of the tissue. The signal is picked up by a receiver located inside the magnet bore and is used to construct the image using Fourier transform. Since the NMR signal frequency is proportional to the magnetic field, the whole tissue can be mapped by assigning different values of the proton frequency to different proton locations in the sample using well-computed field gradient. All MRIs use proton NMR for mapping proton density which is different in different types of tissues. The images show contrast which helps in identifying these tissues and the changes occurring in a sample tissue. MRI turns out to be an ideal technique for soft tissue regions of the body such as brain, eyes and soft tissue part of the head. Since bones have low density of protons, they appear as dark regions.

Under the field gradient along the Z-axis, the (spin-flip) frequency of the emitted NMR signal increases as one moves across the sample tissue from the lower field to a higher field direction. Different frequencies observed from different proton areas are separated using Fourier transform and the location of the target protons identified. To locate the position of protons in other directions (x and y), rotating field gradient coils are used to obtain 2D images.

12.3.1 The Elements of an MRI Scanner

A superconducting magnet is the heart and most expensive part of an MRI scanner. MRI magnets need high homogeneity and high temporal stability similar to NMR spectrometers. Even though the magnetic field requirement in the present-day MRI scanners for clinical use so far has been limited to 3 T, yet more recently, the USA and some European countries have permitted the use of 7 T scanners for pre-clinical use and other investigations. Another major difference with NMR magnet is that sample size in MRI scanners is much larger. The sample now is a human body part, and thus, the magnet needs an homogeneity of < 1 ppm over a SDV (called field of view, FOV) of 50 cm. The magnet assembly is schematically shown in Fig. 12.10. The main magnet is superconducting, cooled to LHe temperature and mounted in an efficient cryostat with a horizontal bore to accommodate the patient. Inside the bore of the main magnet is a set of room temperature gradient coils for changing the field along the X, Y and Z directions required for imaging. Inside the gradient coils are the RF coils producing the field B_1 for rotating the spin by an angle dictated by the pulse sequence. These coils also detect the signal emitted by the spins inside the body. At the centre is a patient table which is computer-controlled.

The typical length of the magnet is 1.6–2.0 m and a clear bore of 0.9–1.0 m. The LHe capacity of the MRI cryostat is typically 1700 l. In the older systems, the LHe vessel was surrounded by a liquid nitrogen (77 K) annular container which worked as a thermal buffer between room temperature and 4.2 K. In modern MRI

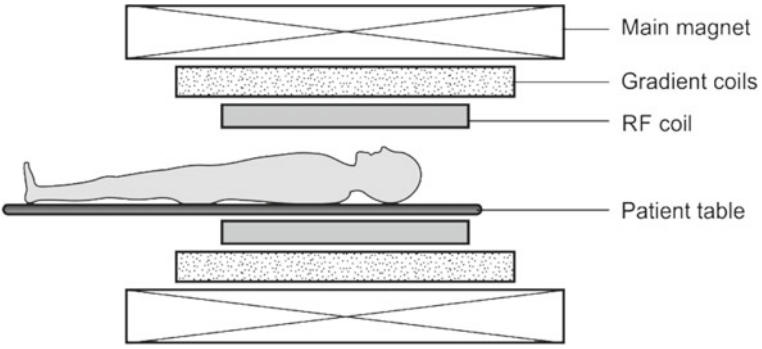

Fig. 12.10 Schematic diagram of a MRI scanner consisting of the main magnet, the gradient coils, the RF coil and the patient table

scanners, the 77 K container has been replaced by a thermal shield cooled by the cryocooler. The LHe cryostat is now fitted with a cryocooler which re-liquefies the evaporated He gas. Refill of LHe is no longer required. These cryostats are called 'zero boil-off' cryostats. Another development that has taken place in recent times is the introduction of active shield coils which reduce the stray field to below 0.5 mT at a distance of 3–4 m, popularly known as 5 gauss line.

The design of an MRI magnet has evolved over the decades to become more friendly to claustrophobic patients. They provide better picture quality and reduce capital and operational cost. We briefly describe the primary requirements of an MRI magnet. The magnet has to produce an axial horizontal magnetic field of desired strength with a homogeneity of $<$ 1 ppm over 50 cm FOV. The stray field inside the scanner room should not be more than 0.5 mT (5 gauss) so that the magnetic field does not interfere with the functioning of the auxiliary equipment or risk the personnel in the room with a pacemaker. The design must be based on an operating current well below the critical current density, I_c, to prevent quench. The threshold for quench therefore should be high, and an efficient fool proof magnet protection system has to be provided. The entire magnet structure consisting of the magnet coils, the former, the cryostat and other components used in the magnet assembly should be able to withstand high stresses produced by the large Lorentz forces and thermal contraction during cooling.

Attention is now focused on designing short magnets producing high field for reducing the perception of claustrophobia. To attain high homogeneity in short magnets however is a challenge.

12.3.2 *Evolution of MRI Magnet design—A Brief Description*

Starting with the cylindrical design, the technology of MRI magnet design has undergone many refinements, and many groups proposed a variety of design procedures and geometries. Garrett [23] proposed a design for a high-homogeneity field based on the compensation of the higher order (6–20th) terms in the spherical harmonic expansion. Figure 12.11 shows the schematic coil configuration of a compensated concentric multisolenoidal MRI magnet. The design was widely followed in early MRI magnets. In later years, quite a few unconventional approaches were made at a number of centres based on hybrid techniques [24, 25]. They combined different aspects of the results of finite element, analytical, variational technique and other numerical methods to obtain optimized design of a high-homogeneity MRI magnet. Crozier and Doddrell [26] proposed compact magnet design based upon stochastic optimization. Zhao et al. [27] proposed a multilayer current density approach to optimize the design. Sinha et al. [28] too have developed a code based on a combination of analytical and numerical methods for a short MRI actively shielded magnet with minimum conductor, inductance and ampere turns. The code is flexible and can be used for a variety of geometries. Lvovsky et al. have published [29] a detailed review on possible novel configurations of the future MRI magnets.

Doddrell and Zhao [30] have a US Patent on an innovative MRI magnet design. In this design, the winding is split into a multilayer coils and also axially separated. Such a geometry results in extra degrees of freedom to optimize the design of short length magnets with high-field homogeneity and minimum conductor volume. The design also minimizes maximum field, excessive stress on the conductor and the stray field outside the magnet. One such design envisages the first layer consisting of four coil pairs, the second layer coil consisting of two pairs and the third and outermost two coil pairs. While the current direction in coils of the first and second layers is positive, that of the third (outer) layer coils is negative. Thus, in a 3 T magnet, the first layer coils generate a field of +2 T, the second layer coils +3 T, and the coil

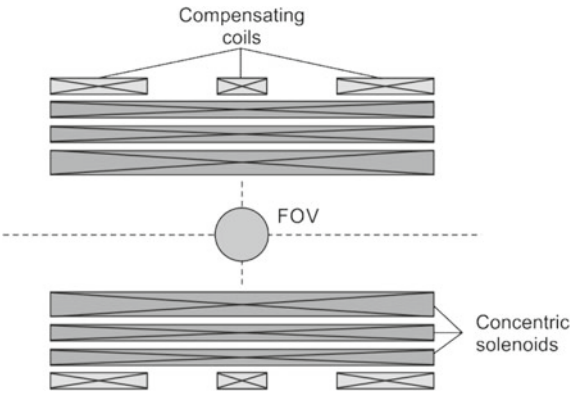

Fig. 12.11 Schematic coil configuration of compensated coaxial multisolenoid MRI magnet

layer 3 generates a field of minus 2 T. One can in fact further split the coils into sub-coils to adjust different parameters of the magnet.

All the attempts to design an MRI magnet have been aimed at attaining high-homogeneity field in a large 'field of view' (FOV), ~50 cm DSV. In general, two distinct magnet designs are followed, a compensated solenoid type and a discrete multicoil type.

12.3.3 Compensated Solenoid Magnet Design

The design has been popular in the first-generation MRI scanners. The coil is wound uniformly across the entire length of the cylindrical former. The winding is divided in a number of sections each wound with optimized graded conductor. This design reduces the peak field to central field (B_{peak}/B_0) ratio and also the stress. The homogeneity of the field is enhanced by winding a number of optimized compensating coils outside the main magnet as shown in Fig. 12.11. Attaining high homogeneity especially in large FOV and short magnets becomes a challenge and so does the stress management. In principle, several multiple coil configurations are possible to yield required field with high homogeneity and low stray field. In practice, a trade-off is made in choosing the design which optimizes the overall dimensions of the machine and keeps the conductor volume and stress level within acceptable limits. In spite of a perfect optimized design, inhomogeneities are often caused by a variety of factors like manufacturing tolerances, winding process, mismatch of thermal contraction of the former and the winding during cooling or the movement of winding due to Lorentz force. To correct these harmonic errors magnetic shimming is mandated to be used in the MRI magnet system. In principle, shim coils can be passive or active (superconducting). In passive shimming shim trays with iron pieces are fitted in slots at predetermined positions either on the magnet bore or in the gradient coil assembly. In addition, there are low field resistive shim coils fitted in gradient coils which are specific to a patient.

Active shimming is provided by a set of superconducting coils wound over the main magnet in the form of circular arcs and racetracks at various azimuthal positions symmetric to the centre along the z-axis. These shim coils are connected in series and energized by a single bipolar power supply through the use of superconducting persistent switches. The main advantage of using active shims is that they can compensate for large tolerances arising during magnet fabrication without adding too much weight. The disadvantage, however, is that the shim coils are located outside the magnet, that is, far away from the FOV, and they are not very effective for high order ($n > 6$) harmonic errors. Some limited passive shimming too is provided together with the active shimming, referred to as 'hybrid shimming'. Different combinations of shimming techniques are employed by the manufacturers to meet the stringent uniformity requirement of the magnetic field.

Use of active shielding coils also adds to the complexity of winding because of large dipole moment of the long solenoid, high stress and the field inhomogeneity

caused by the shielding coil. The design is now restricted to 7 and 9.4 T Nb–Ti high-field research magnets where it is crucial to keep B_{peak}/B_0 ratio low. These magnets are usually long up to 3 m compared to standard 3 T clinical scanner which is about 1.5 m long.

12.3.4 Multicoil Magnet Design

Another popular design of an MRI magnet is in the form of discrete coils centrally symmetric along the z-axis. The number of coils to be used depends on the number of harmonics to be eliminated and the positional angles of the coils. For example, a six-coil magnet can eliminate harmonic errors up to 12th order [23]. The B_{peak}/B_0 ratio and stresses in the coils can be tuned by choosing coil shapes and SC/Cu ratio. Figure 12.12 is a schematic of the modern-day clinical MRI scanners with three symmetric pairs of coils placed along the z-axis constituting the main magnet. The design must also provide effective shielding of the magnet such that the stray field inside the scanning room is reduced to below 0.5 mT. The stray field in MRI magnets tends to be large because of the large dipole moment. Both the types of shielding, passive and active, are possible. For passive shielding iron is used outside the cryostat but has several disadvantages. Passive shielding adds to the magnet

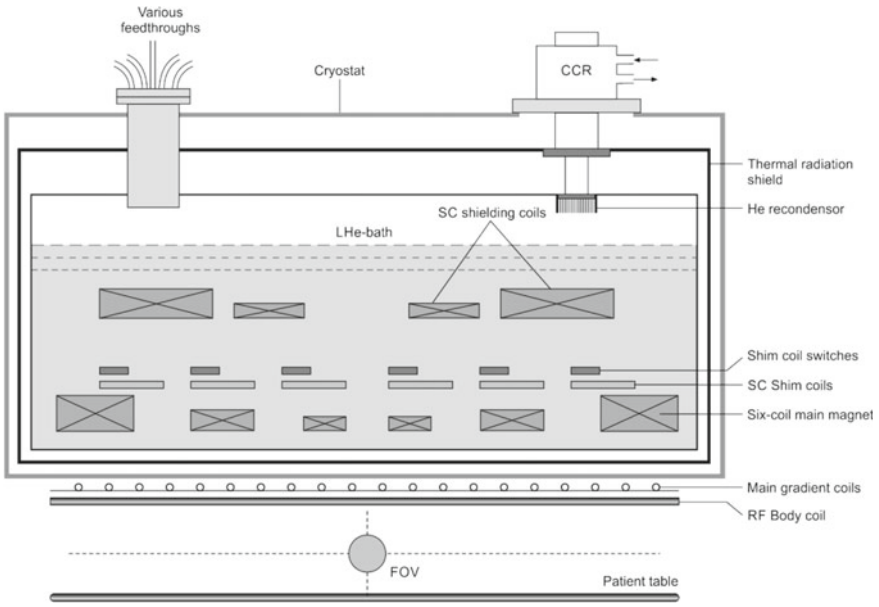

Fig. 12.12 Schematics of a discrete six-coil main magnet with superconducting shims and shielding coils for an MRI scanner (only upper half shown)

weight adversely and is designed for a specific central field. Active shielding is provided by a set of superconducting coils which are coaxial with the main magnet coils but of larger diameter. The current through these coils is in reverse direction which produces a negative field. Active shielding, however, increases the conductor use, the size of the cryostat and the LHe inventory. The advantage is that active shield operates at different central field and does not affect the homogeneity since the coils maintain current-field linearity relationship. The positions of different types of coils are indicated schematically in Fig. 12.12.

Irrespective of the coil designs all the subsystems inside the cryostat are common. All the joints must be superconducting with a joint resistance of less than 10^{-13} Ω (4.2 K, sf) to ensure a drift of less than 0.1 ppm/h. These joints and the persistent switches should be mounted in low field regions. Protection system consists of dump resistors, diodes, quench protection switches and coil heaters. In the event of quench, the switch must open to divert the current through the coil heaters to spread stored energy within the entire magnet to prevent excessive increase in temperature locally. Current leads are normally detachable and are removed after the magnet goes into persistent mode. This cuts down the heat load to the LHe-bath substantially. Most commercial scanners have LHe 4.2 K bath fitted with cryocoolers to re-condense evaporated helium gas. The scanners are now called zero boil-off scanners. These cryostats have a single 40–60 K radiation thermal shield instead of two (10 and 80 K) shields used earlier. This together with improved superinsulation has resulted in reducing the overall dimension of the cryostat.

12.3.5 Design of Cryogen-Free MgB_2 Magnets for MRI

As the popularity of MRI scanners as a diagnostic tool in hospitals grows at a fast pace, the focus of the R&D units of the manufacturers is on

(i) Building magnets which can be cooled by conduction with a cryocooler, without involving the use of liquid helium which is getting scarce and expensive by the day.
(ii) Building magnet wider or in open geometry for patient comfort enabling the scan in claustrophobic-free environment.
(iii) Focusing on MgB_2 superconductor with a T_c of 39 K which has emerged as a potential candidate for MRI magnet as the magnet can now operate at 20 K and be cooled by cryocoolers. GE Global Research has already tested a 3 T MgB_2 magnet of 250 mm bore [31, 32] to study various parameters of the magnet in operation and in quench state.
(iv) ASG superconductors too had brought out a conduction-cooled 0.5 T MgB_2 magnet MRI scanner 'MROpen EVO' [33] which is an enhanced version of their decade old scanner 'OpenSky'.

Baig et al. have presented [34] conceptual designs of conduction-cooled 1.5, 3 and 7 T MgB_2 magnets using improved functional approach [35] based upon inverse

problem solutions. Optimization of the magnet coils is done to achieve the objectives of high homogeneity, small fringe field using set of compact coils and to minimize the quantity of superconducting wire to reduce the cost of such magnets. Optimization has been done using critical parameters of the second generation of MgB_2 wires [36] developed by Hyper Tech Research Inc. (HTRI). The designed magnet operated at 1.5, 3 and 7 T field strengths validated excellent homogeneity and shielding at an operating temperature of 10 K. Attempts have been made to keep the number of coils small which not only makes the construction easier but also reduces the peak magnetic field on individual coils. At the same time, optimization also ensures that the stored energy and the magnetic hoop stress remain within the desired limits.

The positions of the primary coils (1–4) and shield coil (5), field homogeneity over the surface of 45 cm FOV in ppm, field profile in and out of coils and the 0.5 mT stray field contour in one quadrant of the magnet are shown in Fig. 12.13. The current in coils (1–4) is positive and in shield coil (5) is negative. Important parameters of all the three MgB_2 magnets, that is, 1.5 T, 3 T and 7 T are listed in Table 12.4. The maximum peak field in each magnet occurs at outermost primary coils no. 4, and the maximum hoop stress is felt at different coils in different magnet, that is, 76.1 MPa in coil no. 5 in 1.5 T magnet, 129 MPa in coil no. 4 in 3 T magnet and 154.2 MPa

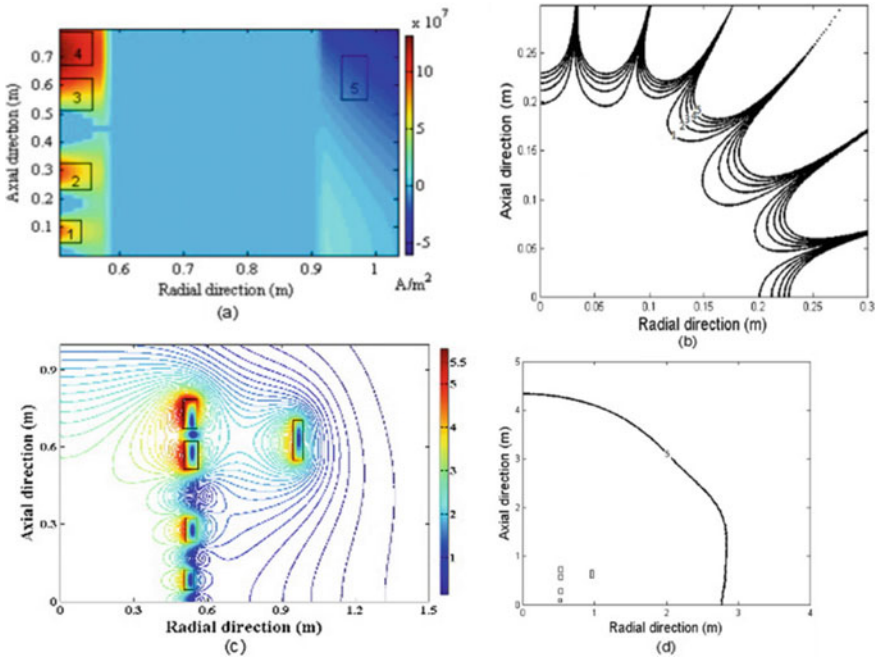

Fig. 12.13 Design of the 3 T MgB_2 magnet consisting of four pairs of primary coils and one pair of shield coils (one quadrant) [34]. **a** The positions of the primary and shield coils. **b** Field inhomogeneity in the DSV in ppm. **c** Field profile in and around coils. **d** 0.5 mT stray field contour (with permission from IOP)

Table 12.4 Salient design parameters of 1.5 T, 3 T and 7 T conduction-cooled MgB_2 magnets for MRI applications

Design parameters of the magnet		1.5 T	3 T	7 T		
		MgB_2	MgB_2	MgB_2	Nb–Ti	Nb_3Sn
Parameter	Unit	Value	Value	Value	Value	Value
Operating temperature	K	10	10	10	4.2	8
Magnet length	m	1.5	1.68	2.3	3.0	2.2
Magnet inner diameter	m	1.0	1.0	1.0	1.0	1.0
Magnet outer diameter	m	1.97	1.98	2.60	>2.5	2.6
Operating current	A/mm^2	175.88	170.5	79.96	<250	99.95
Inductance	kH	0.242	0.804	18.76	–	11.85
Stored energy	MJ	3.74	11.68	59.98	50–90	59.2
Maximum peak field on coils	T	5.4 (coil 4)	5.96 (coil 4)	8.09 (coil 4)	<9 T	9.19 (coil 4)
Field inhomogeneity DSV—45 cm	ppm	3.5	6.98	8.21		4.04
Radial 0.5 mT distance	m	2.7	2.85	4.78	5.0	3.6
Axial 0.5 mT distance	m	3.7	4.35	4.8	7.0	5.81
Maximum hoop stress	MPa	76.10 (coil 5)	129 (coil 4)	154.2 (coil 2)		167.2 (coil 1)
Amp-length	kA-km	18	35.60	90	120–180	86.97

Data compiled from [34]

in coil no. 2 in 7 T magnet. The 0.5 mT stray field spread in all the magnets is well within the guidelines for the MRI magnets.

The peak field on wire in 1.5 T magnet is 5.4 T. At this field, the $J_{c(coil)}$ is 310 A/mm^2 (Fig. 12.14). The operating current density, J_{op} of 175.88 A/mm^2, in 1.5 T magnet is thus only 57% of the $J_{c(coil)}$. For 3 T magnet, the operating current density is 69%, and for 7 T, magnet operating current density is 79.96 A which 66.6% of the $J_{c(coil)}$ at the peak field of 8.09 T. At such high peak field, the *n*-value for multifilament MgB_2 wire drops to about 10. At such low value of n, the MRI magnet will not operate efficiently in persistent mode due to larger current decay rate. The stored energies and the hoop stresses in the design of all the three magnets are within the permissible limits. All the design parameters of the three magnets are reproduced in Table 12.4. For comparison, design parameters have also been calculated for Nb–Ti magnet for 1.5 T, 3 T and 7 T field and for Nb_3Sn magnet for 7 T field and are given in the table.

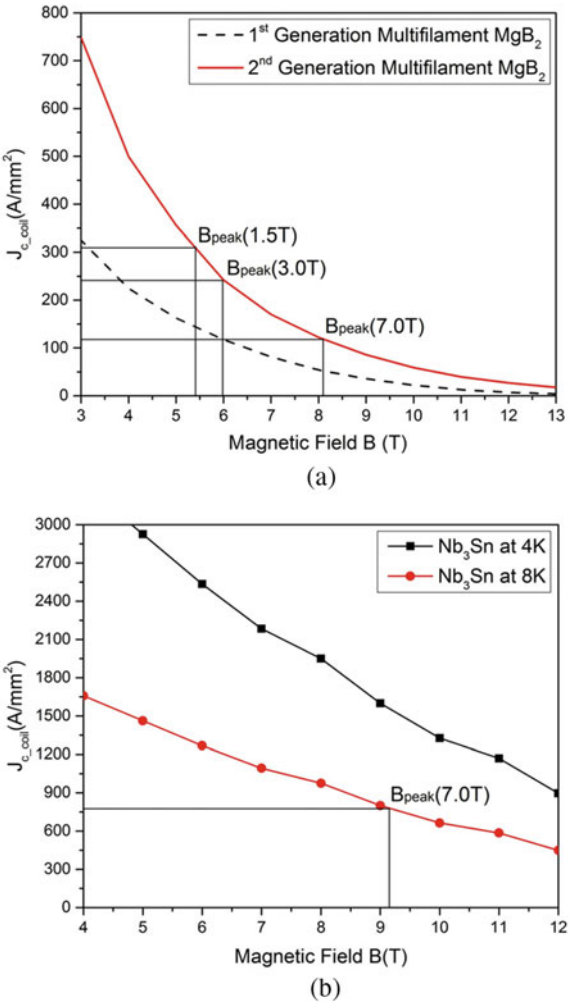

Fig. 12.14 **a** Magnet critical current density versus magnetic field plots for MgB_2 wires of the first and second generation (Hyper Tech Research Inc.) at 10 K. **b** Magnet critical current density versus magnetic field plots for Nb_3Sn at 4 K and 8 K. The peak field on coils, J_c values at B_{peak} are to be used for calculations for magnet design [34] (with permission from IOP)

Parameters like 5 gauss line and field homogeneity in the FOV in MgB_2 and Nb_3Sn magnets meet the guidelines set for the Nb–Ti MRI magnets.

The design parameters of the 7 T MgB_2 magnet given in Table 12.4 show that the operating current density, J_{op}, is 79.9 A/mm^2 which is 66.6% of the critical current density of the second-generation HTRI conductor at the peak field, 8.1 T (Fig. 12.14a). With this low current density, the magnet will be very thick, and the magnet inductance will be high at 18.76 kH as compared to the value of 11.85 kH in Nb_3Sn magnet. From the quench protection perspective, larger amount of copper in the MgB_2 strand may be necessary, and the conductor in 'wire in channel' configuration would be a better option. Most of the parameters of the 7 T MgB_2 magnet are comparable with the parameters of the Nb_3Sn 7 T magnet. We notice

from Table 12.4 that the maximum hoop stress in Nb_3Sn 7 T magnet design is larger than that in the MgB_2 7 T magnet which is due to the larger magnet operating current density, the higher magnetic field and consequently larger Lorentz force. It is also observed from Table 12.4 that 7 T MgB_2 magnet has a higher inductance and larger volume than the Nb_3Sn magnet. The limitation of the operating current density results in larger quantity of the MgB_2 conductor which will not make it as cost-effective as Nb_3Sn unless the J_c of MgB_2 conductors is improved substantially or the price is reduced.

These design studies did show the possibility of designing conduction-cooled MgB_2 magnets which can operate at 10 K but more rigorous studies are needed to construct these magnets. Stress and strain behaviour of coils is vital and needs to be understood for the operation and the safety of the magnet especially during a quench. Optimized design needs an efficient quench protection system. The ratio of superconducting to non-superconducting fractions has to be optimized to prevent overheating at the hot spot by stepping-up heat propagation via copper. Overheating may lead to quench and even burn the coils. The current decay in persistence mode essentially depends upon the n-value of the conductor and the ratio of $J_{op(coil)}/J_{c(coil)}$. Design calculations [34] show that a field decay rate of 0.01 ppm/h is achievable for $n = 30$ and small values of $J_{op(coil)}/J_{c(coil)} = 0.57$ and 0.70, respectively, for 1.5 T and 3 T MgB_2 magnets. However, the 7 T magnet with the $J_{op(coil)}/J_{c(coil)}$ ratio $= 0.67$ cannot meet the current decay threshold for a small value of $n = 10$. MgB_2 wire with higher n values, ideally close to 50, and low $J_{op(coil)}/J_{c(coil)}$ ratio is thus needed to be produced to achieve acceptable current decay rate in a 7 T magnet. At the present moment, Nb_3Sn is a better option to build 7 T MRI magnet with a $J_{op(coil)}/J_{c(coil)}$ ratio of 0.13. This small ratio permits the operation of 7 T magnet in persistent mode even with n-value of 10.

The persistent mode of operation requires near perfect conductor joints with a joint resistance of the order of 10^{-11} Ω. Most R&D centres have been developing the jointing techniques of their own. Iwasa's group [37] has developed jointing technique and tested a small coil in persistent mode. They used HyperTech unreacted monofilamentary MgB_2 wire 0.8 mm diameter consisting of a 0.4 mm diameter MgB_2 core, a layer of niobium, a layer of copper and an uppermost layer of Monel. For making the wire joint, the copper and Monel layers are removed by etching with nitric acid, and the wire terminals are sheared at an acute angle to increase the contact surface area for increasing contact critical current, joined and inserted into a stainless steel billet in well-aligned position. The billet is filled with the stoichiometric mixture of Mg and B powders and sealed with a Cu-plug and ceramic bond. The billet is heated at 700 °C for 90 min. The joint resistance turned out to be 10^{-11} Ω. MgB_2 coil wound with unreacted HyperTech monofilamentary wire, and heat treated was operated in persistent mode, using a persistent current switch which has a superconducting joint in the circuit. The coil was operated in the temperature range of 4.2 and 15 K. The persistent-mode coil reached a persistent current of 100 A corresponding to a self-field of 1 T in the winding for 1 h without a measurable current decay. The coil performed without a quench, and no flux jumping was observed. Monofilamentary superconducting wire is therefore safe to be used for MRI magnet.

12.3.6 A Mini Conduction-Cooled 1.5 T MgB_2 Finger MRI Magnet at MIT

Till such time, the MgB_2 wires are produced in long lengths with good uniformity, the critical current density is improved significantly, and most R&D centres are focusing on the optimized design and the construction of prototype small-sized magnets with all the features of a standard MRI magnet system. Studies are being carried out on the development of persistent current switches (PCSs), very low joint resistance ($<10^{-11}$ Ω) technology, analysis of hoop stress, quench behaviour and the development of an efficient quench protection system for the safety of the magnet. All the studies are aimed at achieving high homogeneity of the field in the FOV and high temporal stability as per the guidelines set for Nb–Ti MRI magnets.

Let us discuss a typical 1.5 T miniature size conduction-cooled MgB_2 MRI magnet ('table top') suitable for finger scan built and operated at MIT in Iwasa's group [37] at MIT. The wire for winding the magnet was supplied by Hitachi which had a MgB_2 core of diameter 0.37 mm with a barrier layer of 75 μm thick Fe and an over-layer of 60 μm thick Cu. The magnet has two coils, coil-1 (L_1) and coil-2 (L_2), wound with a single wire 80 m long designed to produce an axial field of 1.8 T in the centre of coil-2 at an operating current of 108 A. The peak field felt on the innermost layer of coil-2 is 2 T. The ratio $I_{op}/I_{c(B\max)}$ at 0.54 T and 15 K is well within a safe margin of the magnet operation in persistent mode. All the parameters of the two coils are listed in Table 12.5. Figure 12.15 shows the circuit diagram of the two-coil magnet with a joint. Most interesting part of the magnet design is that coil-1 of the magnet has a heater and serves as PCM. Figure 12.15a, b, respectively, shows the PCM in open mode and in the closed mode. Figure 12.15c is the complete circuit having two coils, a superconducting joint of resistance R_{joint} and one of the coils (L_1) working as a PCM. With PCM in open mode (Fig. 12.15a), coil-2 was energized to a current level of 112 A generating a field of 1.8 T in coil-2. As the PCM is closed and the current in the power supply is ramped down, the field started decreasing and settled at 1.75 T when the power supply current is reduced to zero. At this stage, the 112 A current starts flowing through both the coils. When the supply current is reduced to zero, current through the two coils becomes identical. The field decreases marginally due to the index dissipation of the joint and stays at 1.7 T persistently for 35 h corresponding to a joint resistance of 1.2×10^{-11} Ω. Efforts to build MgB_2 magnets with larger bore and improved performance at higher temperature and higher field are in different stages of development. Figure 12.16 shows the photograph of the conduction-cooled mini 'Table Top' MgB_2 Finger MRI magnet (left) and the schematic diagram of the vacuum vessel housing the magnet mounted on the top of the vacuum vessel (right).

12.3.7 Solid-Cryogen Cooling of NMR and MRI Magnets

A solid-cryogen cooling technique for dry magnets has been developed by Iwasa [38] at the FBML, MIT, primarily for NMR and MRI magnets. The technique has proved

Table 12.5 Parameters of the conduction-cooled 1.5 T MgB_2 Finger MRI magnet system

Parameter	Unit	Coil 1 + PCS	Coil 2	Parameter	Unit	Coil 1 + PCS	Coil 2
Inner diameter	mm	12.8	12.8	Operating current	A	108	108
Outer diameter	mm	16.47	25.96	Overall J_c	A/mm^2	180.2	180.2
Axial length from mid-plane z_1	mm	− 43.22	− 14.94	Operating temperature	K	4.2, 10 and 15	4.2, 10 and 15
Axial length from mid-plane z_2	mm	− 29.94	+ 14.94	Peak field B_{max}	T	0.75	2.02
Turns/layer		16	36	Self-inductance	mH	0.18	9.74
Number of layers		5	18	Mutual inductance	mH	0.13	0.13
Total wire length	m	86		Total inductance	mH	10.7	
Wire dia. with *S*-glass insulation	mm	0.79	0.79	Total Mag. energy @ I_{op}	J	59.21	
Conductor used for both the coils: Hitachi MgB_2 wire with a core diameter 0.37 mm with a 75 μm Fe layer and a 60 μm thick Cu layer of 'wind-and-react' type constituting 34% MgB_2, 32% Fe and 34% Cu							

Data compiled from [38]

ideal for cooling the HTS magnets which are characterized by high T_c and thus have a large window of the temperature range of operation. The technique combines the property of high T_c in HTS with large heat capacities of the solid cryogens. Solid cryogens provide exceptionally large thermal mass to the magnet chamber especially in the temperature range of 10–60 K, the most suitable range for the operation of HTS magnets. Figure 12.17 shows the temperature dependence of C_p (T) of solid Neon (SNe), solid nitrogen (SN_2), Pb, Ag and Cu. There is a sharp jump in C_p (T)/T plot at 35.6 K at which SN_2 can absorb an energy density of 8.3 J cm^{-3}. This figure also shows that SNe is an ideal heat capacity enhancer in the temperature range of 4–25 K and SN_2 in the temperature range of 4–60 K. Additional advantage of using SNe and SN_2 solid cryogens is that their respective specific density of 1.25 and 1.0 g/cm^3 is an order of magnitude smaller than the density of the popular heat capacity enhancers like Pb (11 g/cm^3) and Cu (9 g/cm^3) and thus does not add much to the mass of the cryogenic system. In this technique, the magnet chamber filled with liquid nitrogen (LN_2) is further cooled to 10–60 K by circulating compressed helium gas, cooled by the second stage of the cryocooler, around the magnet chamber.

Figure 12.18 shows the drawing of a SN_2-cooled superconducting magnet used by Iwasa et al. [39] for a 800 mm RT bore, 0.5 T MRI magnet submerged in SN_2 and cooled by a cryocirculator. The volume of SN_2 was 15 L. In a cryocirculator

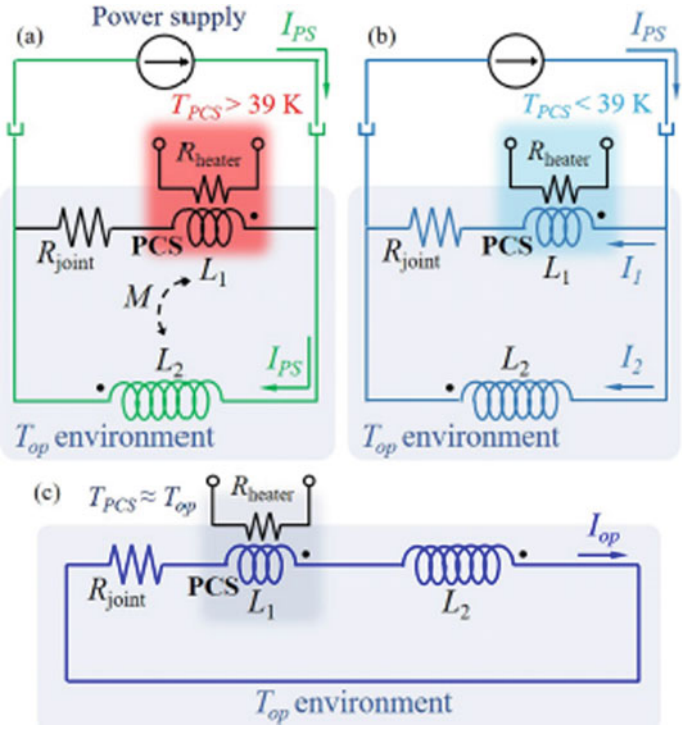

Fig. 12.15 Circuit diagram of the magnet consisting two coils L_1 and L_2 and a joint resistance R_{joint}. Coil L_1 together with a heater constitutes the persistent current switch (PCM). **a** PCM open (heater 'on'). **b** PSM closed (heater 'off'). **c** Complete circuit consisting of coil L_1, L_2 and joint resistance R_{joint} (Courtesy Y. Iwasa, FBML, MIT)

compressed helium gas (20 atm.) cooled by the second stage of the cryocooler circulates at a rate of 0.6 g/s around the magnet chamber. Helium enters the cooling channel at 9.5 K and exits at 10.5 K. The technology developed by Iwasa's group has been successfully used for several LTS and HTS dry magnets for NMR and MRI [40].

The SN_2 cooling technology is ideally suited for operating magnets at constant field such as NMR and MRI magnets running in persistent mode. The large thermal mass of SN_2 helps in maintaining the temperature stable for long period of time even when the cryocooler is stopped or decoupled for replacement or in the event of a power outage. The cryocooler can also be turned off for certain measurements which needs vibration-free ambiance.

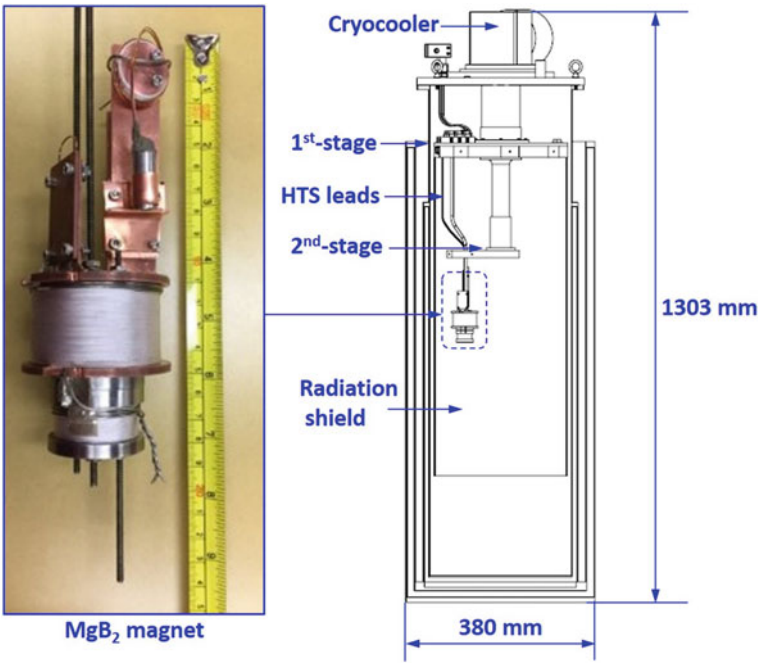

Fig. 12.16 Left: Photograph of the conduction-cooled mini 'Table Top' MgB_2 Finger MRI magnet built at FBML, MIT Right: A schematic diagram of the vacuum vessel housing the MgB_2 Finger MRI magnet conduction cooled by the cryocooler mounted on the top of the vacuum vessel (Courtesy Y. Iwasa, FBML, MIT)

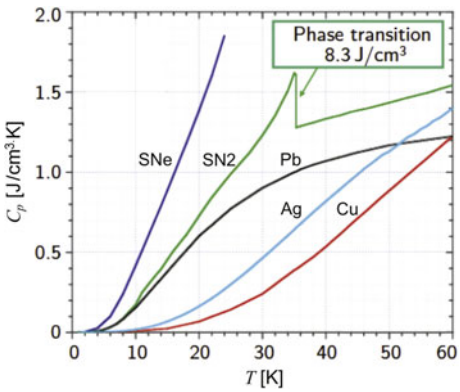

Fig. 12.17 Temperature dependence of C_p (T) of solid Neon (SNe), solid nitrogen (SN_2), Pb, Ag and Cu. There is a jump in C_p (T)/T plot for SN_2 at 35.6 K at which SN_2 can absorb an energy density of 8.3 J cm^{-3} (Courtesy Y. Iwasa, FBML, MIT)

12.3.8 Some Recent Developments in MRI Scanners

Claustrophobia has been a problem with the present-day MRI magnet design where a patient has to lie down in a fully-enclosed tubular magnet bore for imaging. Patient

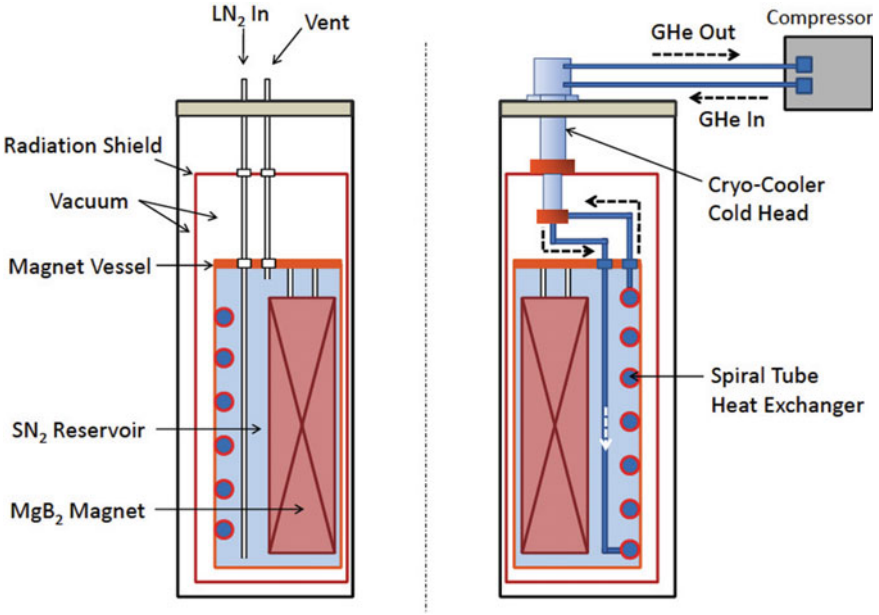

Fig. 12.18 Schematic diagram of a typical magnet cooled by solid nitrogen cooling technique developed by Iwasa at FBML (MIT) for LTS and HTS dry magnets. Cooling is provided by circulating compressed helium gas, cooled (10 K-60 K) by the second stage of the cryocooler, around the magnet chamber. The technique has been used to operate a variety of magnets for NMR and MRI applications (Courtesy Y. Iwasa, FBML, MIT)

comfort has now become a top priority for the manufacturers of the MRI scanners. The present trend is to build wide bore (~70 cm) and short magnet MRI scanners so that the patient head can be kept outside the magnet and the shoulders remaining inside the magnet. Small bore magnets can be more useful for anatomy of body parts like head. Efforts are being made to produce MRI scanners with split-open magnet configuration. The human body in this system is kept in the gap between the two poles of the magnet instead of confining inside a cylindrical coil. The gap can be vertical or horizontal. Some of the open-split MRI scanners in the market are 0.5 T Signa-SP interventional shown in Fig. 12.19, 0.7 T Open Speed both from GE, 1.0 T Panorama from Phillips, 1.2 T Oasis from Hitachi and an MgB_2 0.5 T OpenSky from Paramed. The scanners are patient friendly but expensive because two LHe cryostats are to be built for this configuration. Standard 3 T scanner of the open-split type will not be able to compete with the solenoidal scanner.

Hopes are also pinned on HTS magnets in coming years since they can be conduction cooled by crycoolers and operated at 20–50 K. Most of the issues with the use of HTS for magnet applications have been resolved through rigorous studies carried out at NHFML. However, single length conductor production will have to be stepped up and material cost be reduced to a reasonable level. Siemens and Oxford Instruments have developed proto type 0.2 T MRI system using BSCCO-2223 HTS

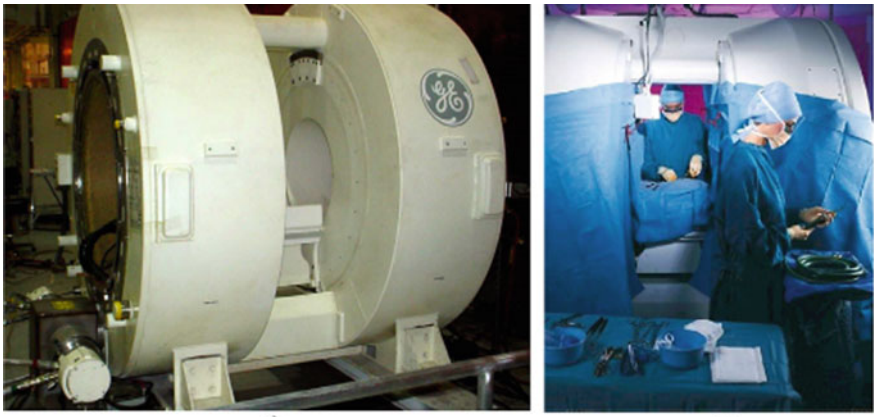

Fig. 12.19 First 0.5 T whole body interventional conduction-cooled MRI using Nb_3Sn magnets [29]. **a** Magnets have access for patient and the surgeons. **b** MRI Scanner 'Signa-SP' during surgery procedure (Courtesy Ernst W. Stautner, GE Global Research)

magnet with a horizontal pole gap. R&D work on a large variant of conventional and non-conventional configurations of magnets has been going on at several places. A detailed account of these efforts has been published in a review by Lvovsky et al. [29]. In the following, we discuss the salient features of a few exotic models of MRI scanners.

12.3.8.1 The MROpen EVO System by ASG Superconductors

It is a cryogen-free MgB_2 magnet MRI scanner with a wide-open design [33] with a lateral gap of 56 cm, which makes it extremely patient friendly. This scanner is the enhanced version of its decade old cryofree OpenSky machine brought out by ASG Superconductors (Ansaldo Superconducttri of Genova). It offers claustrophobic-free environment for scanning and provides high-quality diagnostic images through upgraded digital spectrometer, newly designed coils, new sequences and fast scan. Figure 12.20 is the photograph of the MROpen EVO MRI scanner. The scanner has two magnets housed in two separate vacuum chambers, producing a field of 0.5 T and cooled by two cryocoolers. Since the T_c of MgB_2 conductor is 39 K, it is operated at 20 K instead of at 4.2 K. This means higher stability against quench and low cooling cost. ASG's technology permits the magnetic field to be turned off or on within less than an hour, thus providing greater patient safety and flexibility in maintenance and operation. A patient can be scanned in sitting, standing or lying position as the scanner is open at the top, front and back.

The ASG Paramed has also developed another scanner 'MRJ3300 MRI scanner' which has a 'C' shape for complete musculoskeletal imaging that includes joints of the extremities like Knee, Ankle, Foot, Wrist, Elbow, Hand, shoulder and Hip

Fig. 12.20 ASG Paramed 'MROPen Evo' Upright MRI with many enhancements over its previous version OpenSky. The scanner uses MgB_2 magnet which operates at 20 K. A patient can be scanned in sitting, standing or lying position as the scanner is open at the top, front and back [33] (Courtesy of ASG Superconductors, Paramed MRI Unit)

joints and Spine. The scanner requires very small installation space and minimal site preparation.

12.3.8.2 A Designers' Brain MRI Scanner Under Development at Victoria University Wellington

Scientists and designers of the Victoria University Wellington have come up with an innovative design [41] for brain MRI scan wherein a patient can sit comfortably on a chair during imaging with front, left and right sides open. The magnet system is being developed at the Robinson Research Centre of the university. The scanner is being built in collaboration with researchers from Harvard, Yale, the University of Minnesota, and the University of Sao Paulo. The scanner will make clinical quality head imaging and is going to be more compact. The team faced a challenge of designing the head support as the head should not move more than one millimetre in any direction during imaging period of minimum 20 min. The team ultimately designed a patent-pending inflatable support system that controls the head position without sacrificing the patient comfort. During imaging, the patients will sit in a chair which gently moves their head into the helmet-shaped scanner, leaving the rest of patient's body free. The leg rest, back support, head support, and chair height can be controlled by the patient or the MRI technician. The patient will also be able to see outside through a window provided in the scanner. This way the anxiety and claustrophobic experience of the patient will be reduced drastically.

12.3.8.3 A High-Field Wide-Open MRI 'Panorama HFO' by Philips

Philips has been marketing its 'Panorama HFO' wide-open 1 T field system [42], which offers excellent flexibility for clinical procedures being carried out. The

scanner provides better comfort to the patients and greater accessibility to the clinicians to perform MRI-guided clinical interventions. Design of such C-shaped magnet is however very complicated. These magnets are far less efficient than the solenoidal magnet with axial symmetry. In particular, the mechanical forces which are less symmetric need to be controlled intelligently.

Similarly, the twin cryostat (top and bottom) needed for housing the poles of the magnet is quite complex. Construction of higher field wide-open MRI magnet is therefore very challenging and expensive. The open magnet design however permits superior receiver coils layouts which leads to pictures of high quality comparable with those obtainable with a standard 1.5 T MRI machine. This wide bore magnet attracts anxious, elderly, obese or claustrophobic patients who feel comfortable during scanning. It provides a 360° panoramic viewing angle and offers large space 160 cm-wide and 45 cm pole gap in which the patient feels quite comfortable and relaxing during the scan. The scanner though is of general purpose but is ideal for orthopaedic, paediatric and bariatric imaging. The wide-open patient space allows radiologists to explore new clinical procedures and kinematic joint studies.

12.3.8.4 Siemens' Magnetom Terra 7 T MRI Scanner

We know that proton polarization which is a measure of NMR signal strength increases with the increase of the magnetic field. At high field, therefore, the signal-to-noise ratio (S/N) becomes large, the scan time is reduced, and the image quality improves. The reduction of scan time adds to the comfort of the patient and also increases the patient throughput. Present trend therefore is to develop higher field magnets for MRI scanners. 3 T MRI scanners are already used increasingly for diagnostics in place of 1.5 T scanners. In recent times, 7 T scanners have been launched [43] primarily for pre-clinical research in the USA and Europe. More countries are now allowing the use of this high-field MRI scanners for neurological and musculoskeletal research. 7 T MRI scanners are however awfully costly and will continue to be so. This is because at higher field the critical current density is very low which means that a large quantity of conductor has to be used. This makes the magnet very expensive. In addition, the conductor experiences huge EM forces (Lorentz forces) being proportional to the square of the field. Containment of large Lorentz force poses severe problems. It can cause micromovement of the conductor which will generate frictional heat and raise the temperature locally above T_c causing quenching of the magnet.

Siemens has launched a 7 T MRI Scanner [43, 44] named 'MAGNETOM Terra' for clinical use in the USA and Europe to begin with. Siemens got FDA permission from the USA to use Magnetom Terra for human clinical purposes. The scanner carries the flexibility of operation in two modes. It can switch between the clinical mode operation and the research mode operation in less than 7 min. The magnet has a RT bore of 60 cm and a length of 2.7 m. The overall length of the machine is 2.97 m and the weight 25 tons. With double S/N ratio compared with 3 T MRI scanner, the in-plane resolution of the scanner is now 0.2 mm instead of 1 mm. The scanner is of

'zero boil-off' type and thus has low running cost. The magnet is actively shielded and provides high-field homogeneity. The use of high-field MRI scanners is picking up fast as it provides unique benefits in basics, anatomical and functional imaging. It has opened up an extremely fertile field of research in neurological science.

12.3.8.5 World's Highest Field (11.7 T) MRI Scanner, ISEULT at Neuroscan Centre CEA, Saclay

An all-time high-field (11.7 T) MRI scanner, 'Iseult' has been built and commissioned at the Neuroscan Centre at CEA, Saclay in France under a Franco-Germany collaborative project. This is the present world record in high-field MRI scanners. The Iseult magnet system was installed at Neuroscan Centre in 2017 which attained the designed field of 11.7 T in July 2019 [45]. Auxiliary equipment related to MR imaging has been fitted in the magnet, and the first image is expected during April–May 2021. The innovative design of the magnet was provided by the physicists led by Guy Aubert and physicists specialized in magnets at the Institute of Research into the Fundamental Laws of the Universe (IRFU). A number of MRI industries, Guerbet, Siemens Healthcare, GE—ex-Alsthom/Belfort collaborated to build the magnet. The aim of developing such a high-field (high resolution) system has been to create a human MRI scanner capable of examining the brain more precisely than ever before and diagnose neurodegenerative diseases by pushing the limits of MR Imaging. A conceptual cut-way view of this 11.7 T magnet system [46] is shown in Fig. 12.21.

The magnet system has several unique features. It uses the Cu/Nb–Ti conductor to produce such high field first time by operating the magnet at 1.8 K using superfluid helium for cooling. It has a wide bore of 90 cm to accommodate various substantially sized equipment including the gradient coils. It is preferable to keep the gradient coils away from the main magnet to prevent interference. Iseult employs an active (superconducting) shielding with no iron. It would have taken about 750 tons of iron to shield the magnet passively. The outer diameter of the magnet system is 5 m and the length 5 m. The magnet system weighs 132 tons with a cold mass of 100 tons. The virgin cool-down took 4 months and consumed 250,000 l of liquid nitrogen and 18,500 L of liquid helium. An inventory of 7500 l of superfluid helium is always maintained in the liquid helium vessel backed by a cryogenic system. The magnet generated the field of 11.7 T at an operating current of 1483 A. The peak-to-peak field homogeneity of 0.5 ppm and a field stability of 0.05 ppm/h have been achieved. An external dump resistor of 2.39 Ω has been used for quench protection. The key parameters of the magnet system are given in Table 12.6. The magnet runs in a drive mode and not in persistent mode. It uses an innovative current stabilization system developed through significant R&D efforts. A robust mechanical structure was provided to take care of the dead weight of the magnet. Iseult is expected to achieve a resolution of 0.1 mm as compared with the resolution of 1 mm obtainable with a 3 T MRI.

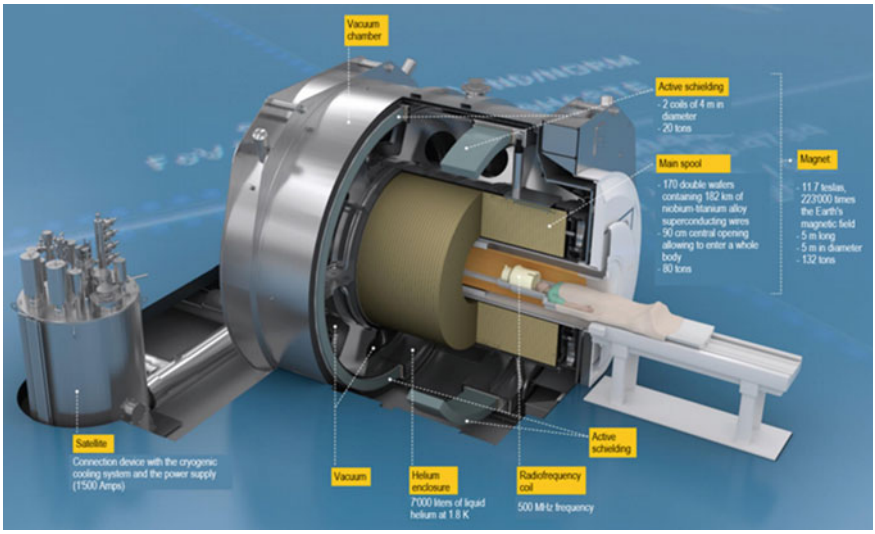

Fig. 12.21 Cutaway view of the conceptual 11.7 T magnet system of the Iseult MRI scanner at Neuroscan Centre, CEA, Saclay. The Iseult magnet system was installed at Neuroscan Centre in 2017 and attained the designated field of 11.7 T in July, 2019, © CEA [46] (courtesy Lionel Quettier, Credits: Animea/F. Durillon/CEA, Frédéric Durillon/Animea)

12.3.8.6 A Compact and Lightweight 3 T MRI Scanner by GE

Even though the 3 T whole body MRI scanner has become the mainstay for brain imaging, yet it is plagued with several limitations. Besides being expensive, it has a weight of 5–8 tons and needs to be installed on ground floor only. The inventory of liquid helium in the conventional 3 T MRI scanner is large at 1500–2000 l which needs an adequate vent system for the huge helium gas pressure build-up during quench. Replenishing liquid helium and re-energization of magnet is costly and time-consuming. To overcome these limitations and other related to low gradient (G_{max}) and low slew rate (SR_{max}), GE in collaboration with some research institutions designed and built a lightweight, compact 3 T conduction-cooled MRI scanner which was installed at the Mayo Clinic at Rochester in March 2016. This compact GE 3 T compact MRI scanner [47] with the overall dimensions and the patient space is illustrated in Fig. 12.22. The locations of the magnet coils, gradient coil, transmit/receive birdcage RF coil, the cold head/cryocooler are also indicated in the figure. The magnets have been wound with Nb–Ti conductor and operated at 4 K. Conduction cooling was provided by a pair of GM cryocoolers which take 6 days to cool the system from warm condition to 4 K. Its imaging performance has been superior to a standard clinical or research whole body 3 T scanner. A 42-cm inner diameter gradient system provides simultaneous high G_{max} (80 mT/m) and high SR_{max} (700 T/m/s) (the maximum slew rate, SR_{max}, is a measure of the speed at which a gradient can be turned on and off and is defined as the maximum gradient

Table 12.6 Key parameters of the magnet system of the Iseult, the 11.7 T MRI scanner operating at Neuroscan Centre CEA, Saclay

Parameter	Unit	Value
Outer diameter of the cryostat	m	5
Overall length of the cryostat	m	5
Open bore diameter	cm	90
Total weight of the system	Tons	132
Total cold mass	Tons	100
Shielding against stray field		Active (superconducting)
Operating temperature	K	1.8 (superfluid helium)
Conductor used		Cu/Nb–Ti
Operating current	A	1483
Liquid helium inventory	l	7,500
Liquid helium for initial cooling	l	18,500
Liquid nitrogen for initial cooling	l	250,000
Field generated	T	11.7
Magnet inductance	H	3.08
Field homogeneity (peak to peak)	ppm	0.5
Field stability	ppm/h	0.05
Mode of operation		Drive mode (non-persistent)

Data compiled from [45, 46]

strength of the gradient divided by the rise time). The key parameters of this scanner and the magnet are given in Table 12.7.

Moving with the prevailing trend of minimizing the use of liquid helium, the compact 3 T scanner uses conduction cooling with a helium gas filled sealed system which liquefies about 12 l helium. This provides a stable 4 K temperature to Nb–Ti magnet for operation, with a temperature margin of 1 K to the T_c of Nb–Ti wire at the operating field. Unlike the conventional liquid helium bath-cooled MRI systems, the new system does not need venting for He gas because in the event of a quench the total gas volume will only be 9.1 m^3 and the stratified helium gas would stay well above the head of a 2 m tall person as the helium vapours can reach down 38 cm only from the ceiling of an MRI room of 24 M^2 area. It will therefore cause no asphyxiation.

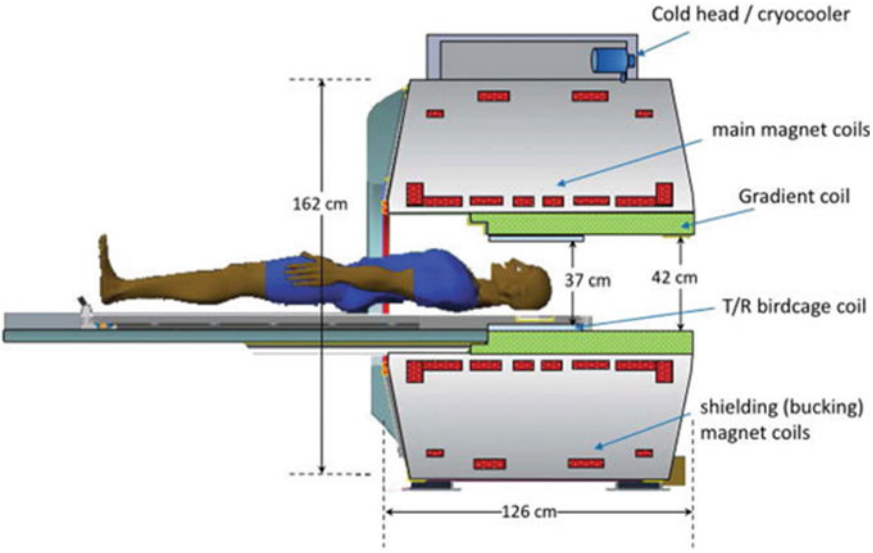

Fig. 12.22 Schematic of the cryocooled compact and lightweight 3 T MRI scanner built by GE showing dimensions in relation to a patient. Locations of all the key components of the system are shown in the figure [47] (with permission from John Wiley and Sons)

Another unique feature of the magnet design is the stoppage of the transmission of vibrations from the cryocooler to the magnet which otherwise would result in the vibration of the central field impacting the image quality adversely. A field homogeneity of less than 2 ppm in a FOV of 26 cm was achieved using passive shims by putting iron chips in shim trays mounted on the inner diameter of the magnet with 54 angular and 46 longitudinal shim positions. The magnet used a total of 35 km of Nb–Ti wire, produced a field of 3 T at an operating current of 300 A and yielded a field stability of <0.01 ppm/h which is within the standard acceptance criteria of 0.04 ppm/h. The peak-to-peak field homogeneity measured at 26 cm FOV was 1.68 ppm. The 5 gauss line is well contained within an area of 6 m $\times$ 4 m area much smaller than the 10 m $\times$ 6 m area for typical 3 T MRI systems. Quench tests performed by switching off the cryocooler showed that no gaseous helium was released from the sealed system. Successive cool-down was done using the cryocooler, and the field was ramped up normally without extra need for helium. This is in contrast to the conventional helium bath magnets which need about 1000–2000 l of liquid helium for re-cooling and energizing the magnet again.

Table 12.7 Key parameters of the GE compact and lightweight 3 T MRI scanner in comparison with the typical standard whole body 3 T MRI scanners

Parameter	Unit	3 T whole body MRI scanner	3 T compact MRI scanner
The scanner specifications			
Imaging FOV	cm	45–50	26 DSV
Length of scanner	m	1.60–1.75	1.26
Outer diameter	m	1.9–2.0	1.62
Warm bore diameter	m	0.88–0.99	0.62
Weight of scanner	Ton	5.5–8.0	<1.9
Liquid helium inventory	l	1500–2000	12
Fringe field 0.5 mT area	m × m	6 × 10	4 × 6
Conductor used		Nb–Ti	Nb–Ti
Cooling provided by		LHe-bath	Pair of cryocoolers
Operating temperature	K	4.2	4.1
Field homogeneity (P-P)	ppm	<1 (40–50 cm FOV)	<1 (26 cm DSV
Gradient specifications			
Inner diameter	cm	65–75	42
Patient bore	Cm	60–70	60
Slew rate	T/m/s	200	700
Gradient amplification	mT/m	50–80	80

Data compiled from [47]

12.4 Superconducting High-Gradient Magnetic Separator (SHGMS)—Principle of Magnetic Separation

Magnetic separation had been a well-established technique for the separation of magnetic materials with differing properties, largely in mineral industry. With the development of superconducting magnet technology in 1970s, magnetic separation found potential application in diverse fields like mining, manufacturing, medicine and pollution control. Magnetic separation is achieved by a combination of a magnetic field B_0 and a field gradient ∇B. The force on a magnetizing particle of volume V_P and susceptibility χ kept in a magnetic flux B_0 and a field gradient ∇B is given by

$$F_m = \frac{\chi V_P}{\mu_0}(B_0.\nabla B) \tag{12.7}$$

where μ_0 is the permeability of air. The magnetic acceleration will be

$$A_m = (F_m/m) = \frac{\chi}{\rho_P}(B_0.\nabla B) \tag{12.8}$$

where ρ_P is the particle density. Since for most of the minerals $\chi = 0.1 - 1.0$ SI units, the product $(B_0.\nabla B)$ should be between 1 and 100 T^2/m to overcome the gravitational force F_g and the fluid drag F_d which oppose the separation. F_g and F_d are given by

$$F_g = \rho_P.V.g \tag{12.9}$$

and

$$F_d = 6.\pi.b.\eta.v_{br} \tag{12.10}$$

where $g = 9.8$ m/s^2 is acceleration due to gravity, v_{br} is the relative velocity of fluid with respect to the particle, and b the radius of the particle assumed to be spherical. η is the viscosity of the medium. For larger particle, especially in air, the gravitational force dominates. For separating small particles, we must use smaller flow velocity and/or higher field and field gradient. The magnetic separators are designed in a way such that it creates a force strong enough to deviate the particles from the fluid flow. The separator can broadly be divided into two categories. In the first category (Fig. 12.23a), the field gradient is produced by the magnet pole faces themselves whereby the magnetic particles get collected in the high-field region. In

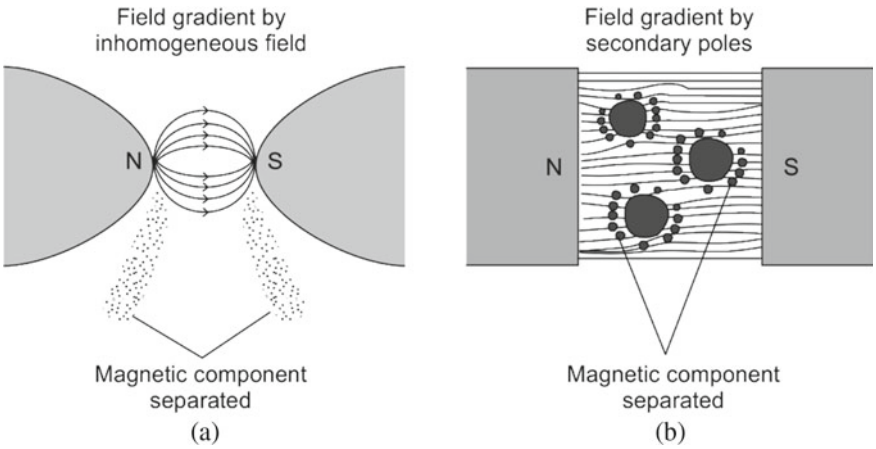

Fig. 12.23 Two principal techniques used for magnetic separation

the second category, the magnet produces a uniform field, and the gradient is created by introducing secondary poles (Fig. 12.23b). The magnetic particles are captured by these secondary poles and the material can be released by switching off the field and recovered. The raw mineral is first crushed or milled to liberation size of the process material and can either be fed directly into the separator for dry separation or in the form of a slurry for wet separation. It is evident from (12.7) that for particle of colloidal size and which are weakly magnetic one needs a high uniform magnetic field and a high magnetic field gradient created by a filter matrix.

Even though the technology of high-gradient magnetic separator (HGMS) was introduced in 1930s, it found popularity in kaolin clay industry to enhance its brightness by the removal of darker magnetic components in 1980s. Like all other magnet applications, the superconducting magnet technology made the HGMS technique economically attractive. State-of-art systems for kaolin clay purification became available in 1989 with almost no 'dead-time' and without operational failures. Superconducting HGMS (SHGMS) only needs periodic refilling of liquid helium. The refill time too has increased drastically with the use of cryocooler re-condensers, and many systems are working in remote locations in the mine areas. SHGMS has been developed [48–52] for a variety of applications built and used for varied applications.

12.4.1 SHGMS Magnet Design

The magnets used in large capacity SHGMS have a room temperature horizontal bore similar to MRI magnets except that it does not require high-field homogeneity. Figure 12.24 is a schematic diagram of a demonstration 5 T SHGMS author's NPL group built in collaboration with BHEL (R&D), a Public Sector Undertaking around 1990 [53]. It has a vertical RT bore of 100 mm housing a 96 mm diameter SS 316 container filled with SS 430 ferromagnetic wool with a fibre diameter of 45 μm at a density of 2–5%. The cryostat was of a tail shape to reduce LHe inventory. The magnet was built in five sections using 0.74 and 0.54 mm Nb–Ti wires and vacuum-pressure-epoxy impregnated. Each section was separately quench protected by dump resistors. The magnet produced a field of 5 T at a current value of 120 A. It had a field uniformity of 5% in a SDV of 150 mm. The parameters of the magnet built for this SHGMS are given in Table 12.8. The cryostat had a LN_2 precooling vessel and a 78 K thermal shield. The tail part of the cryostat had a 25 mm thick ferromagnetic shield to reduce the stray field to < 0.5 mT at a distance of 1 m (at 4.5 T field level). This is to prevent malfunctioning of the process control system and the magnetic operation due to the movement of ferromagnetic material in the vicinity.

Figure 12.25 is a flow diagram of the filtration process using process material in the form of a slurry. The entire process is PLC controlled. Energization and de-energization of the magnet are synchronized with the opening and closing of the relevant solenoid valves. On the extreme left is a 200 l slurry tank with a stirrer. Mineral to be filtered is grounded to about 5 μm size and mixed with water (2–5%) with the addition of a deflaculent such as sodium bicarbonate or hexametaphosphate.

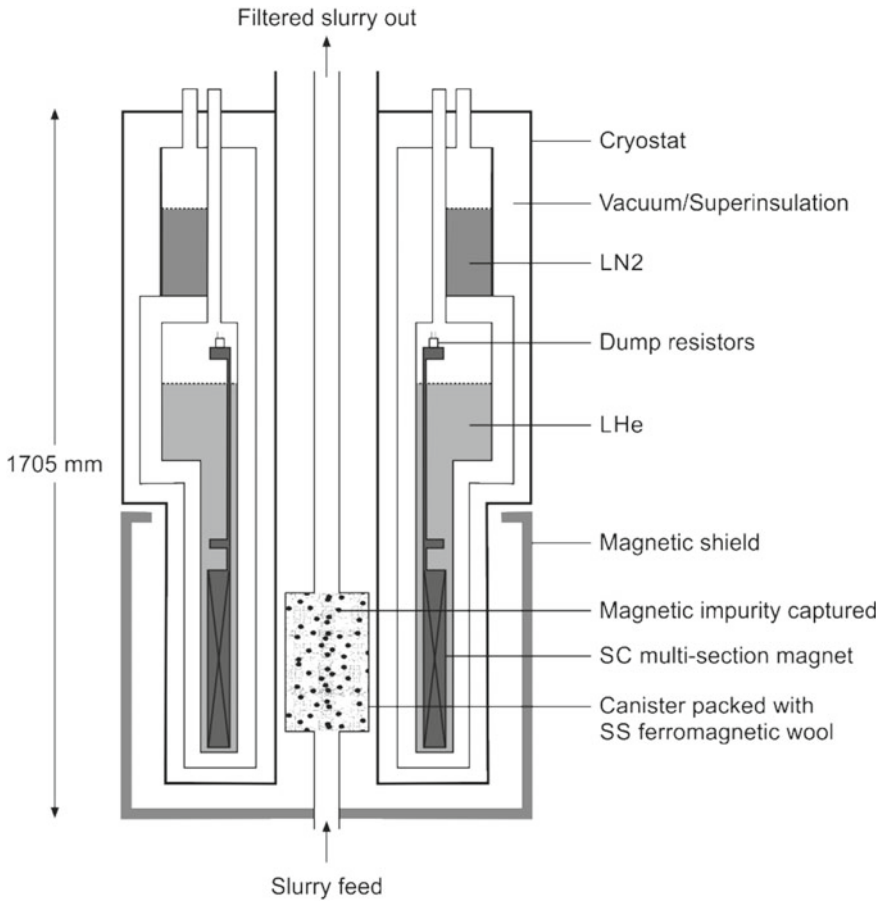

Fig. 12.24 Schematic diagram of a demonstration 5 T SHGMS system built by author's NPL group in collaboration with Bharat Heavy Electricals decades ago [53]

This is done to control pH value and to prevent particles from agglomerating during the slurry process. After the magnet is energized to desired field, the slurry is pumped into the filter matrix through top or bottom distributing header. After filtration, the slurry is collected into three separate containers (not all shown in the fig.), viz (1) the concentrate, the desired material released by rinse water (2) middling which consists of magnetic and non-magnetic components and can be recycled. (3) the tailings, the reject component. System was used extensively for removing magnetic impurities of micron size from a variety of minerals with excellent results [53]. Some of the minerals processed were ball clay, wolframite, magnesite, synthetic rutile and iron ore slime. Optimization was carried out with respect to flow velocities, different magnetic fields, different densities of filter matrix and multiple filtrations for obtaining high grade material. The system was designed for batch processing

Table 12.8 Some parameters of the magnet of the 5 T SHGMS discussed in the text [53]

Parameter	Unit	Value
Central magnetic field	T	5
Inner bore diameter	mm	160
Magnet winding length	mm	320
Warm bore diameter	mm	100
Field homogeneity over 15 mm DSV	%	5
Conductor used		Cu/Nb–Ti
Conductor diameter	mm	0.75 and 0.54
Quench protection		Dump resistors
Stray field at 1 m	mT	<0.5
Shield material		25 mm thick commercial iron

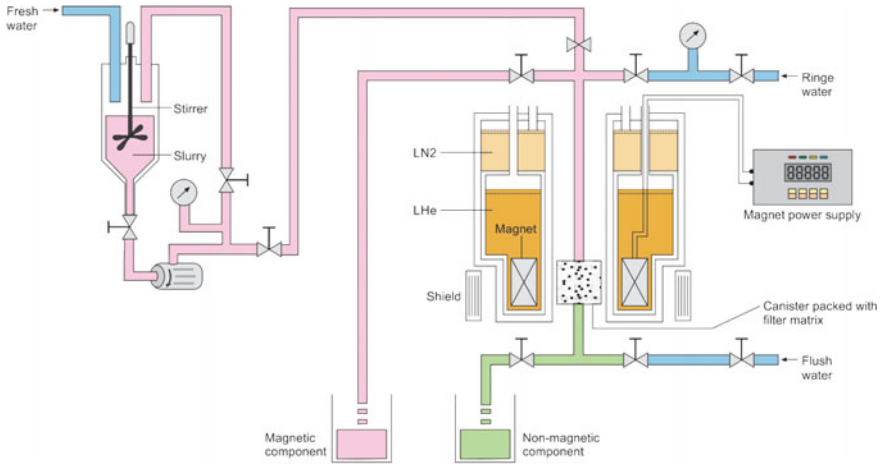

Fig. 12.25 Flow diagram of 5 T SHGMS with slurry handling system [53]

only. Industrial systems use large horizontal RT bore magnets and run in continuous mode on a 24 × 7 basis. In such systems, two reciprocating canisters packed with filter matrix move in and out of the magnetic field on a continuous basis. The magnets are operated in persistent mode consuming little power.

12.4.2 Recent Developments of SHGMS

A 2000 ton/day SHGMS has been developed [54, 55] at Osaka University to recycle wastewater from a paper industry. The wastewater contained suspended solid (SS), glue, colourant, dye and cohesion agents that increase the chemical oxygen demand (COD) to 2000–3000 ppm level and cannot be discharged without being treated.

Table 12.9 Parameters of SHGMS built at Osaka University for recycling paper industry wastewater

Parameter	Unit	Value
Capacity	Ton/day	2000
Magnet field	T	2
Operating current	A	100
RT bore of the magnet	mm	400
Magnet length	mm	680
Conductor used		Cu/Nb–Ti
Reduction in chemical oxygen demand (COD)	ppm	From 2000–3000 to 100
Reduction in turbidity	NTU[a]	From 200–300 to 2–10
Reduction in SS (suspended solid)	Mg/l	From 200–400 to 20–40

Data compiled from [54, 55]
[a]NTU → 'nephalometric turbidity unit'

SHGMS has been found to be most viable technique economically, and treated water is recycled. The magnet has a RT bore of 400 mm, length 680 mm and produces a field of 2 T at a current of 100 A. The magnet uses Nb–Ti conductor. The system has proved to be very successful and reduces the COD to 100 ppm, turbidity from 200–300 NTU (nephalometric turbidity unit) to 2–10 NTU, and suspended solid (SS) from 200–400 mg/l to 20–40 mg/l. The parameters of this SHGMS and the magnet are given in Table 12.9. The system is compact too, occupying just 6 m × 6 m space. The cost of SHGMS is 1/6th to 1/10th of the conventional activated sludge system.

More recently, Ning et al. [56] at the Institute of High Energy Physics (CAS) have built a 300 mm bore, 5.5 T SHGMS for kaolin clay. The magnet used a Nb–Ti conductor of the size 1.28 mm × 0.83 mm, a Cu:Nb–Ti ratio 4:1, filament diameter 80 μm with a tensile strength of 400 MPa and a yield strength of 245 MPa. The magnet coil has an inner diameter of 400 mm, an outer diameter of 474 mm and a length of 815 mm. The coil former is 10 mm thick. The magnet produces a central field of 5.5 T at an operating current of 150 A which is 75% of the short sample value. The maximum field is 5.6 T. An iron octagonal shield has been used which reduces the stray field to below 5 mT at a radial distance of 1 m and an axial distance of 1.2 m (Table 12.10).

Extreme care is taken to control hoop stress due to large Lorentz force. A bandage 14 mm thick consisting of 15 layers of 1 mm diameter SS wire has been used. Stress simulation was carried out by developing a code using 2-D finite element method (FEM) based on ANSYS software. During simulation, the hoop stress has been kept restricted to 150 MPa only, whereas the maximum overall allowable hoop stress of Nb–Ti is 350 MPa. A pre-stress of 70 MPa was applied on the coil and a pre-stress of 100 MPa applied to the bandage. Stress and strain behaviour of the coil during winding, cool-down and charging has been studied in detail. The SHGMS has two canisters with filter matrix reciprocating in the magnet bore. During the time, one canister is being filtered in the magnetic field, and the other canister is cleaned.

Table 12.10 Parameters of SHGMS built at the Institute of High Energy Physics (IHEP), Chinese Academy of Sciences (CAS) for the purification of kaolin clay

Parameter	Unit	Value
Magnet field	T	5.5
Peak field	T	5.6
Operating current	A	150
Magnet bore inner diameter	mm	400
Magnet outer diameter	mm	474
Magnet length	mm	815
Conductor used		Cu/Nb–Ti
Conductor dimensions	mm	1.28 × 0.83
Filament diameter	mm	80 μm
Cu:SC ratio		4:1
Hoop stress	MPa	150
Stray field at 1 m radially	mT	<5
Shield (octagonal) material		Iron
Number of canisters with filter matrix		2

Data compiled from [56]

In recent time, attention has been focused to build conduction-cooled systems which can operate in remote areas where LHe supply is difficult. Quantum Design Inc. has marketed a conduction-cooled 5 T SHGMS system [57] with reciprocating canisters for kaolin clay. The magnet of this system has a bore of 203 mm and produces a field of 5 T with a uniformity of 10% over 406 mm. This long range of uniformity enables the system to process 30–40 tons of material per day depending upon the quality of clay and the desired level of purity. The magnet is cooled by a 1.5 W GM cryocooler and uses a 'energy smart technique' which brings down the operating cost rather dramatically. Virgin cooling of the magnet takes about 45 h. No cryogenic fluid is used. The magnet has non-dissipative HTS current leads which makes the system power efficient. The system has two canisters reciprocating rapidly using a servo drive. An ingenious design of the canister allows to maximize effective filter volume enhancing the processing capacity of the system to 10,000–15,000 tons/year. The system is of modular type such that several modules can be combined together to raise the production capacity to desired level. Routine maintenance of an individual unit can be carried out without any interruption to the clay processing by other units.

The effectiveness of the SHGMS in separating or filtering fine and weakly magnetic particles depends strongly upon the high magnetic field gradient generated by the filter matrix. The matrix also provides surface sites for capturing magnetic particles. Theoretical studies have been made by Ge et al. [58] on the dependence of the field gradient, field distribution and the filtering performance on the material, geometry, size and arrangement of the matrix element. Efforts continue to be made to find micromatrices which can generate higher field gradient for the filtration of superfine magnetic particles needed in several areas of application.

12.4.3 *Superconducting Pulsating High-Gradient Magnetic Separator (SP-HGMS)*

Though the conventional SHGMS is used widely in mineral industry to treat metallic ores, yet it faces problem of retention of non-magnetic particles and matrix clogging when ores contain coarser particles or the particles are weakly magnetic. This results in the lowering of the grade of the magnetic product and makes the maintenance of SHGMS unit difficult. The problem has been largely solved by pulsating the slurry which increases the particle collisions with matrix layers [59]. The pulsating process also increases the probability of capture of magnetic particles on both sides of the matrix wire and also the recovery of magnetic particles. Further, pulsating increases the competing force acting on non-magnetic particles and reduces mechanical trap of the non-magnetic particles. This enhances the grade of the magnetic product with the increase of pulsating velocity. The pulsating frequency and stroke have however to be optimized for each mineral for maximum efficiency. The pulsating SHGMS has now become a new generation industrial equipment for processing hematite, siderite, limonite and other weakly magnetic minerals with high beneficiation ratio.

Xu et al. [60] have integrated superconducting magnet with pulsating high-gradient magnetic separation (SPHGMS) to develop a new technology which improves its separation performance for ultrafine magnetic particles. The authors have discussed the new system abbreviated as SPHGMS theoretically, and a cyclic pilot-scale SLon-CD100 SPHGMS with 9.0 T conduction-cooled superconducting magnet was built. The schematic diagram of superconducting pulsating HGMS (SPHGMS) is shown in Fig. 12.26. The separator was used to purify an ultrafine

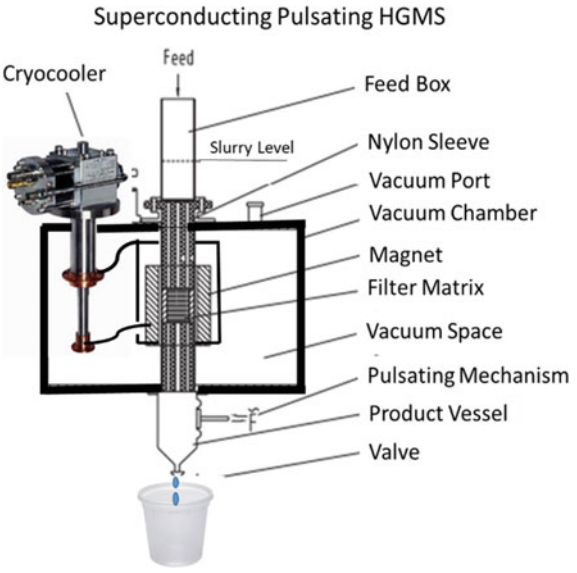

Fig. 12.26 Schematic diagram of superconducting pulsating HGMS (adapted from [60])

kaolin ore and separate a low-grade chalcopyrite ore. The new separator attained an impressive rate of removal of iron impurities from the kaolin ore. It achieved separation for the chalcopyrite ore with Cu recovery reaching higher than 90%. The SPHGMS technique has already been accepted as a sufficiently economical and highly prospective technique for the purification of ultrafine non-metallic ores.

12.5 Superconducting Magnet Energy Storage (SMES)

Superconducting magnet energy storage (SMES) is yet another important application of superconducting magnets. It is a unique device for load levelling and for the stabilization of power utility system which stores and converts electric energy directly with >95% cyclic efficiency. SMES does not convert electric energy into mechanical or chemical energy and vice versa. Compared to other energy storage devices like pumped hydro and compressed air which need large time for the energy conversion from mechanical to electrical, SMES has very small response time and delivers power almost instantaneously and can charge/discharge unlimited number of times. The device does not possess either the highest power density or the highest energy density but has good balance between the two, crucial for certain applications. Further, there is no energy loss in SMES, and the only loss is about 2–3% in the inverter/rectifier system. SMES finds application mainly in uninterrupted power supply (UPS), pulse power system (PPS) and flexible AC transmission system (FACTS). Large number of big [61] and small [62, 63] size SMES have been built since late 1980s and operated mostly in the USA and Japan. Some of them were even abandoned [64] in favour of more economical electrical systems. The status of SMES as in 2008 has been reviewed by Tixador [65]. SMES-based UPS with power rating in MW range is in use in power-sensitive semiconductor chip fabrication and liquid crystal units in the USA and Japan. These industries need ultra clean power and protection against voltage dips to prevent costly shutdowns. Even though high capital cost of SMES has prevented it to become as popular as NMR and MRI, yet they are increasingly used in several dedicated civil and military applications. Recent induction of HTS-based conduction-cooled SMES [66] in power conditioning system by Gesellschaft fur Innovative Energiemwandlung und Speicherung (EUS) for improving power quality locally seems to be very promising.

Two main characteristics of SMES, namely high power density and a fast discharge time, make them attractive for use in metal forming, for EM launchers in weaponry and as a pulse power source. SMES has, however, low energy density of the order of 10 kJ/kg and thus is more useful as a power source. The energy density is limited by mechanical structure needed to counter large EM forces. Other advantages are very large number of charging and discharging possible, high conversion efficiency, and there are no moving parts involved.

One very important element of a SMES system is the power conditioning system (PCS), an interface between the magnet and the power utility system. PCS broadly consists of an AC to DC rectifier and DC to AC inverter which changes the AC

from the power utility to DC and feeds the magnet. A DC to DC chopper, linked to a voltage source inverter, is used to charge and discharge the magnet and for balancing the voltage dip. Conventionally, the power is transmitted at high voltage and low current, and the magnet operates at high current (several kA) and low voltage. A step-down transformer is therefore used in the conventional system for power distribution. Unwanted harmonics are suppressed through the use of passive filters. A digital controller controls various functions of the SMES such as the detection of a voltage dip, voltage balance and the smooth functioning of instrumentation. It also regulates the output voltage and the frequency in stand-alone mode when there is no supply from the utility and SMES is the only source to a strategic application.

12.5.1 Magnet Design in SMES

The energy storage capacity of a SMES solely depends on the size of the magnet and the critical current of the superconductor used. The magnet thus happens to be the heart of a SMES and a most expensive component since it requires large quantity of the conductor, a LHe cryostat, refrigeration system like cryocoolers and the electronic control system for power supply and quench protection. Magnet shielding, passive or active, too is required to reduce stray field below the acceptable level. Other important component is the persistent current switch. The outstanding capability of a superconducting magnet to operate in persistent mode makes it an ideal energy storage device. Since there is no dissipation of energy, the current and the magnetic flux in the magnet remain constant. The energy stored in a magnet is $\frac{1}{2} LI^2$ where L is the inductance of the magnet coil and I, the coil current. When the persistent switch is opened, the stored energy can be transferred to the desired load by lowering the current in the magnet coil. SMES thus serves as a current source in contrast to a capacitor which serves as a voltage source. The energy is the product of mean power and the discharge time. The discharge time is strongly dependent on application. For example, a magnet is designed for short discharge time of ms to s if used for the protection of a sensitive electric load against voltage dips. On the other hand, the magnet must be designed for long discharge time if used for load levelling in a grid. Long discharge time may vary from hours to weeks.

The optimization of magnet design is aimed at achieving maximum possible stored energy for a given amount of conductor with the least probability of a quench. The peak field on the conductor should not exceed 7 T for Nb–Ti conductor. The magnet can either be designed in a solenoid form or in the form of a toroid. A toroid does have the advantage of low stray field because the entire field is contained within the magnet bore itself. This has two benefits, (1) the size of the support structure is reduced, and (2) the toroidal SMES can be installed close to the utility or the load. The design helps in reducing the external magnetic forces and thus the dimensions of the mechanical structure. Further, the toroidal coils always perform under compression by the outer hoop stress and the two discs at the bottom and the top. Mechanical forces start dominating as the SMES size increases and the toroidal design then becomes a

preferred option. A toroidal magnet is realized by using a number of coils wound in pancake structure and distributed along the circumference of the torus. The earlier large SMES had small aspect ratio solenoids with 100 m diameter buried under the earth and supported by rocks. The toroidal SMES, however, stores just 50% of the energy that a solenoid SMES can store using the same amount of conductor volume. Another problem with this design is that the magnet coil experiences a large radial force towards the axis in addition to longitudinal and transverse forces. Quench in such magnets causes imbalance in the force distribution making the protection complicated. The magnet coil must be epoxy impregnated to prevent any movement during ramping. Since the magnet can release energy very fast, the coil should be able to withstand large voltage. The conductor and the inter-layers must have thick insulation layer and spacers, respectively. High power, being the product of the current I and the voltage $V_{\max}$, needs high current as also very good electric isolation for high voltages. Multiple solenoid coil design is yet a third option where the stray field problem is quite small, but it consumes much larger quantity of the conductor for a given energy density.

A solenoidal design of the magnet is ideal for commercial small (micro) SMES which is simpler to fabricate. Mechanical support and quench protection can also be managed easily. The magnet should preferably be built with an even number of solenoids in a modular fashion either in a four solenoid configuration in squire arrangement or in six-coil configuration in an hexagonal arrangement. This design helps in reducing the stray field appreciably. The solenoid design should be optimized for minimum conductor volume when the diameter to height ratio is 5. Passive iron shield as well as active superconducting shield is employed to reduce the stray field. The active shield coils are wound over the main magnet with current in a reverse direction to cancel the field outside.

12.5.2 Factors Affecting SMES

12.5.2.1 The Mechanical Structure

Though the stored energy in a magnet, generating a field B, is proportional to the square of the field strength ($=B^2/2\mu_0$), yet the maximum energy it can store is ultimately limited by the strength of the mechanical structure. A robust structure is required to contain the large Lorentz forces generating high stress. The ratio of the stored energy W to the minimum mass of the structure, M_{m}, for a solenoid magnet as given by virial theorem ($W/M_m = \sigma/d_{\mathrm{sm}}$) turns out to be 12.5 kJ/kg for steel for a working stress of 100 MPa for a finite length solenoid. Here, σ is the working stress, and d_{sm} is the density of structure material. High-strength, low density Al-alloys with density of about 1/3rd of steel can enhance the working stress a bit, but the energy to mass ratio remains largely unaffected. The magnet conductor, chosen for winding, too must be capable of withstanding expected high stresses and deformations without degrading its superconducting critical parameters like the critical current, I_{c}.

To contain large Lorentz forces, two techniques have been followed. In the first technique, the magnet system is buried under ground where the forces are transmitted to rocks and the reinforcement. In the second technique, the cold structure of the magnet itself supports the forces. Support material can be fibreglass reinforced epoxy which is cryogenic compatible. The second technique is more economical and is pursued for SMES systems up to a GJ range of energy.

12.5.2.2 The Conductor

Like in many other applications, the conductor to be used in SMES should have high engineering critical current density, J_e in high magnetic field, should provide safe temperature window for operation, and should be well stabilized in a conducting matrix. The conductor must have sufficient reinforcement to withstand large forces. Since the magnet charges and discharges rapidly, there are AC losses in the coil conductor and eddy current losses in the cryostat. Low AC loss conductors with resistive barrier around the conductor filaments are to be used. Low-loss CICC conductors are ideally suited for use in SMES. Cryostat too is designed to cut the eddy current losses to a minimum. So far most of the SMES have been manufactured with Nb–Ti conductor and operated at 4.2 K (LHe-bath). Operation of the magnet at reduced temperature, 1.8 K, increases J_c and reduces the conductor amount. Use of HTS current leads inside the cryostat cuts down the heat load to the LHe-bath significantly. With the induction of the cryocoolers as re-condensers inside the cryostat, the LHe refill time has increased immensely.

Cryogenic cost can be expected to reduce drastically if the Nb–Ti magnets were to be replaced with HTS magnets which can be operated at much higher temperatures (20–50 K). HTS magnets can be conduction cooled by the cryocoolers, thus doing away with the use of LHe. The second-generation (2G-ReBCO) coated conductors do hold the potential of replacing Nb–Ti in the near future, once the conductors are manufactured in sufficient lengths and with a reasonable cost. The advantage of the 2G conductor is that they can be operated at 50 K instead of at 20 K required for the first-generation BSCCO conductors. Other advantage with the use of HTS is that the magnet is very stable because of the high heat capacity of the conductor, about two orders of magnitude higher at 50 K compared to that at 4.2 K. At such high temperatures, thicker electric insulation can be used which can withstand high voltage. An increase in the operating voltage will increase the power of the SMES system. The insulation thickness has to be optimized such that the temperature gap ΔT between the conductor and the cooling media remains low. Quench protection should take into account the slow propagation velocity of the hot spot (normal zone) in HTS which can raise the local temperature and can even damage the coil. Innovative protection system will have to be designed.

12.5.3 Some Examples of SMES

12.5.3.1 Very Large (1000 MW) SMES.

Why the SMES technology did not find wide acceptability by the power distribution sector for balancing the load in the electricity distribution network was that the scale of power is in range of GW which required gigantic size of superconducting magnets around 1 km in diameter. Building a magnet of this dimension poses severe problems related to mechanical structure, the conductor amount, LHe cooling and the cryostat. Large Lorentz forces have a radial outward component trying to expand the coil and an axial component symmetric to the central vertical line. Strong mechanical structure has to be designed to withstand these forces and the weight of the magnet.

One large SMES system of 1000 MW capacity was designed [59, 63] under the Strategic Defense Initiative (SDI) in the USA in 1987. The specific parameters of this big device are given in Table 12.11. The magnet had a designed diameter 1 km, a height of 19 m and a stored energy of 18.9 TJ. The system was to operate at 1.8 K at a current level of 200 kA producing a working field of 5.18 T. It was planned to be installed inside a trench in mild rock near the surface. Fibreglass reinforced epoxy (G-10CR) struts with graded thickness were to be used as the bottom support to the magnet to take care of the thermal contraction during cool-down. The sequence of fabrication was something like this. The helium outer vessel, the struts and the vacuum vessel were to be fabricated onsite in the trench. The coil was to be wound on the inner side of the helium outer vessel in segments. Helium vessel wall was to be fabricated next, and after winding, each segment of the coil and the helium vessel was to be sealed. The vertical supports between the helium vessel and the inside wall

Table 12.11 Specific parameters of a large SMES of 1000 MW under the strategic defense initiative (SDI), the USA

Parameter	Unit	Value
Peak stored energy	TJ	18.9
Peak power	MW	1000
Magnet diameter	m	1000
Magnet height	m	19
Aspect ratio		0.019
Magnetic field	T	5.18
Peak field	T	6.69
Magnet current	kA	200
Operating temperature	K	1.8
Magnet configuration		Four layers coil
Cool-down hoop stress	MPa	345
Refrigeration load/day	MWh	120
Status		Designed only

Data compiled from [61, 65]

of the vacuum vessel complete the assembly. It was proposed to use CICC conductor with LHe flow through the conductor. Separate LHe vessel was not to be provided for. A network of tubes for carrying LHe for cooling and for heat extraction was, instead, to be fabricated. The device was, however, not constructed and remained confined to design stage only.

12.5.3.2 Medium Scale (400 MW) DNA-SMES

The Defense Nuclear Agency (DNA) of the USA under the SDI initiative took up a 400 MW SMES programme [67] for use as a pulse power (short duration high power) source for free electron laser-directed energy weapons as well as for load levelling and stabilization in power network in 1987. The Electric Power Research Institute (EPRI) proposed [64] an Engineering Test Model (ETM) for this dual use 400 MW SMES. Two teams, Bechtel and Ebasco, came out with two different designs. The key design parameters of the 400 MW SMES as proposed by the two teams are given in Table 12.12. In the Bechtel design, the magnet diameter was 129 m and the height 7.5 m. A 200 kA CICC Nb–Ti conductor, which had very low AC losses, was planned to be used. The critical current of the conductor was 303 kA (1.8 K, 5 T). The CICC conductor with LHe flow channel does not need LHe vessel making the construction of the cryostat less complex. A high-current conductor such as this reduces the total amount of conductor required and also keeps the operating voltage within a safe

Table 12.12 Important design parameters of a medium size 400 ETM-SMES as proposed by Bechtel and Ebasco groups

Parameter	Unit	Bechtel team value	Ebasco/Westinghouse value
Power pulse	MW	400	400
Stored energy	MWhr	20.4 (73 GJ)	20 (70 GJ)
Magnet diameter	m	129	134
Magnet height	m	7.5	4.2
Aspect ratio		0.058	0.00149
Conductor		Nb–Ti	Nb–Ti/Al
Conductor type		CICC	Rutherford cable
Operating current	kA	200	60
Operating temperature	K	1.8 (He-II flow in CICC)	1.8 (He-II bath)
Number of radial layers		2	4
Number of turns		112	32
Power discharge time @ 400 MW	s	100	
Magnet structure material		FRP	G-10CR
Status		Abandoned	Abandoned

Data compiled from [64, 65, 68]

limit of 10–12 kV. Higher operating voltage involves the risk of arcing. Further, the magnet coil was to be operated at a reduced temperature of 1.8 K when the conductor can carry much larger current and save on the conductor cost. He-II (superfluid) ensures uniform temperature of the conductor and faster heat extraction because of its extremely high thermal conductivity. The saving in conductor cost turns out to be orders of magnitude higher than the increased cost of the extra refrigeration need for He-II. A two-layer coil design also allows easy access to inspection and repair of the winding. HTS current leads were to be used because of their poor thermal conductivity and non-dissipative properties. Fibreglass reinforced epoxy (G-10CR) struts were to be used as the bottom support to the magnet to take care of the thermal contraction during cool-down. The magnet was proposed to be built inside a steel lined concrete reinforced trench.

Containing Lorentz forces in such large size magnets is a challenge. Stresses caused by cooling as well by the Lorentz forces are calculated such that the limit of the yield strength of any of the materials used in the coil pack is not reached. The coil pack needs pre-compression radially inward by about 0.15% so that the hoop stresses developed during cool-down in different metal constituents of the conductor (conductor, stabilizer, filament barrier, the central conduit, etc.) remain well below their respective yield strength. Pre-compression also reduces tension across the FRP structure joints. The pre-compression procedure must be carried out by shrinking the coil pack in liquid nitrogen and then locking the outer struts. The vacuum vessel should be fabricated and tested outside and then finally fixed in the trench as liner. No gap or air pocket is to be left between the liner and the trench to rule out possibilities of a structure failure. The coil pack will remain accessible to inspection and repair.

The other design was proposed by the Ebasco/Westinhouse team [68]. This design was based upon a 60 kA Nb–Ti conductor with Al stabilization. The magnet has a solenoid configuration. The coil stack is 134 m in diameter and 4.2 m in height (aspect ratio 0.00149). The coil has four layers, and each layer has eight turns. G-10CR sheets have been used as turn to turn insulation. To counter the stresses, an axial preload is provided by the insulated SS clamping studs with G-10CR clamping plates. Radial mechanical support is provided by G-10CR finger plates between the walls of the Dewar and the outer layers. G-10CR loading bars are used as inter-layer. The G-10CR finger plates and the loading bars also serve as good electrical insulation which is extremely important in these devices as large voltage develops during fast charging/discharging and the quench.

12.5.3.3 Micro SMES (5–10 MW) for Sensitive Industries

Small size micro SMES units have been built and successfully used in semiconductor and liquid crystal sensitive industries in Japan to provide protection against sudden voltage dip at high power level. The performance of the SMES remains unaffected even after charging and discharging of high power. Commercial 5 MVA and 10 MVA SMES systems have been built [62, 63] by Chubu Electric Power Co. and Toshiba Corporation Power System Co. These devices are operational since 2011. The SMES

has a four (even number)-pole solenoid configuration. This design has been chosen to reduce the leakage of the magnetic field. Since the duration of the sudden voltage dip is less than 0.5 s, the SMES has been designed with a compensation time of 1 s. For the 5 MVA SMES, a low AC loss Rutherford Nb–Ti cable with Cu–Ni barrier has been used for coil winding. The coil produces a field of 5.3 T at a current of 2.66 kA and at a temperature of 4.2 K provided by the LHe-bath backed by cryocoolers. The key parameters of the 5 MVA-SMES magnet and the conductor are given in Table 12.13. Since SMES operates at a high-rated voltage (~few kV), for safety, this voltage is reduced to half the value by grounding the coil with a resistor at its neutral point. The current leads used to carry the required current were made by joining together 1 kA class YBCO leads in parallel. The current leads carry a heat load of 3 W to the magnet coils. The leads are capable of withstanding a voltage of 6 kV. The warm ends of the leads were cooled to below 77 K by the use of GM cryocoolers. AIN spacers isolate the leads from the cryocoolers up to a rated DC voltage of 6 kV. A cutaway view of this 5 MVA SMES [62] is shown in Fig. 12.27. The SMES was tested successfully from 2003 to 2006 on site. The sudden voltage

Table 12.13 Key parameters of a small 5 MVA SMES (Chubu Electric Power and Toshiba Corp. Power System Co. Japan)

Parameter	Unit	Value
Rated input and output		3φ, 6600 V, 60 Hz
Peak stored energy	MJ	7.34
Peak power	MW	5.0
Discharge time	s	1
Coil diameter	m	0.53
Coil height	m	0.7
Aspect ratio		1.32
Magnet configuration		Four-pole solenoidal
Maximum field	T	5.3
Rated current	kA	2.657
Operating temperature	K	4.2 (LHe pool boiling)
Rated voltage	kV	2.5
Withstand. voltage	kV	6.0
Conductor/type		Nb–Ti/(Rutherford)
Conductor size	mm	1.67 × 12.0
No. of strands		27
Strand diameter	mm	0.9
Filament diameter	μm	13.5
Cu/CuNi/NbTi		2.25/1.45/1
Critical current	kA	7.9 (5.25 T, 4.2 K)
Present stratus		In use (Japan)

Data compiled from [63, 64]

Fig. 12.27 5 MVA SMES system with four-pole solenoid design, built by Chubu Electric Power and Toshiba Corp. Power System Co. Japan. The inset on the left are the four-pole superconducting magnet coils [63] (with permission from Elsevier)

dips were balanced fast via the power feeding from the SMES without any load on the production line. The same company also marketed 10 MVA SMES units. A number of such commercial units are operating in Japan.

12.5.4 High-T_c Superconductor (HTS) SMES

12.5.4.1 Bi-2223 SMES

Although HTS SMES built so far have been of prototype, yet they hold great potential for future. We have already discussed the main advantages of the HTS conductor over the conventional Nb–Ti conductor. First-generation HTS Bi-2223 tapes/wires have been used to construct small 2–3 kJ SMES devices by Hawley et al. [69, 70] primarily to carry out optimization of the design of the magnet, EM stress analysis, mechanical structure issues, current leads and power control circuit. They built a 2.79 kJ prototype HTS SMES using Bi-2223 coil and operating it at 30 K. Kalsi et al. [71] at American Superconductor Corporation (ASC) built a 5 kJ SMES using the same Bi-2223 material and supplied to EUS (Gesellschaft fur Innovative Energieumwandlung und Speicherung), Germany, after successful tests in 1996. The EUS used the SMES to devise technology to improve poor power quality in plants where a voltage dip or a short interruption can cause long shutdown.

Table 12.14 Design and performance parameters of the AMC 5 KW SMES

Parameter	Unit	Value
Stored energy	kJ	5
Magnet inner diameter	mm	370
Magnet outer diameter	mm	438
Magnet height	mm	98
Peak axial field	T	0.97
Peak radial field	T	0.78
Total ampere turns	kA-turn	140
Effective inductance	H	1
Operating current	A	100
Operating voltage	V	200
Operating temperature	K	20–30
Current leads		Bundle of Bi-2223 wires
Maximum hoop stress	MPa	2.5

Data compiled from [71]

The magnet was built in a solenoid configuration with pancake structure. The pancake structure is ideal for short length conductors and offers an excellent cooling because of large surface exposure. Besides, it is also convenient to replace the conductor in a particular coil. Mechanical support is also superior. The magnetic field direction too is favourable to the critical current under this orientation. The coil inner diameter is 370 mm, the outer diameter 438 mm and the height 98 mm. A pair of bundles of Bi-2223 wires, joined together in parallel, was used as current lead to carry 100 A. The coils were epoxy impregnated. The magnet is housed in a vacuum vessel lined with multilayer insulation (MLI) blanket to minimize radiation heat load. The magnet operates at 20–30 K at 100 A current and stores an energy of 5 kJ. The SMES was fully conduction cooled by using two single-stage GM cryocoolers, a large cryocooler with 25 W @ 20 K cooling capacity and a smaller one with 45 W @ 65 K capacity. The bigger cryocooler takes care of the heat generated in the magnet due to AC losses caused by the frequent and fast ramping of the magnet. The magnet can be ramped from zero to 100 A in 2 s. and back to zero in 2 s. The magnet temperature reaches 35 K, the maximum permissible temperature after 100 such ramps or after 400 s. The smaller cryocooler is used to cool the HTS current leads which are anchored to the cold head maintained at 32 K. Magnet withstands a voltage of 200 V. The maximum hoop stress experienced by the magnet is 2.5 MPa only, and no extra reinforcement was provided. The design and performance parameters of the AMC 5 KW SMES have been compiled and given in Table 12.14. The successful operation of this SMES thus confirms the superiority of the conduction-cooled HTS SMES, and large units seem feasible with continuous improvement in the quality of the HTS materials.

Experimental prototype SMES using Bi-2223 wires have been designed and tested at several places. A detailed investigation on the optimization of magnet design has

Table 12.15 Optimized parameters of a 7.3 kJ (Bi-2223) SMES magnet

Stored energy (kJ)	Number of pancakes	Number of layers	Inner diameter (mm)	Outer diameter (mm)	Height (mm)	Inductance (H)	I_c @ 35 K (A)	B_{max} (T)
7.36	14	104	147.8	360	93.8	0.76	139	0.99

Data compiles from [73]

been carried out by Wojtasiewicz et al. [72] in Poland using a FLUX 2D software. The design parameters were fixed for a single pancake coil-based solenoidal configuration with an outer diameters of the coils of 360 mm and a single length Bi-2223 wire 1500 m long. Various parameters have been evaluated for different number of pancakes. Different coil radii, number of turns, magnet height and two operating temperatures of 35 K and 50 K have been studied. The design selected was a SMES with 14 pancakes, 104 layers, inner diameter 147.8 mm, outer diameter 360 mm and height 93.8 mm. The magnet system has an inductance of 0.76 H, I_c (@35 K) 139 A, B_{max} 0.99 T and stores an energy of 7.36 kJ. A high-strength Bi-2223 wire was planned to be used, and the magnet was to be cooled using a GM two-stage cryocooler. These parameters are given Table 12.15.

A 200 kJ toroidal magnet SMES was designed and optimized by Kim et al. [73] to improve the power quality of a building and to meet strict restriction on stray field. Optimization was done using the so-called 1 + 1 evolution strategy (1 + 1 ES) with line element technique. The toroid consisted of 16 pancake modules, each module having three disc-shaped pancake coils. The coils use a total of 9.6 km Bi-2223 tape of 4.1 mm × 0.2 mm size. The SMES stores 200 kJ energy at an operating current of 200 A. The SMES has a discharge time of 1.5 s and a maximum voltage of 1 kV. The stray field at a distance of 5 m is only 2.84×10^{-9} T. The system will be conduction cooled by a GM cryocooler. Table 12.16 summarizes parameters of the SMES.

A 800 kJ Bi-2212 SMES has been constructed as a pulse power source by Tixador et al. [74] at CNRS, France, for a DGA (Délégation Générale pour l'Armement) project. In the absence of any specification of the stray field, a solenoid design was preferred using a stack of single pancake coils. The inner and outer diameters of the coils are 300 mm and 814 mm, respectively, and the height 222 mm. The magnet has a total of 26 pancakes. The dimensions of the magnet were chosen to minimize the conductor volume and to have a flat magnet. A PIT Bi-2212 Nixan conductor cladded with Ag and then with an Ag-Mg sheath was used for winding. Even with

Table 12.16 Design parameters of a 200 kJ toroidal Bi-2223 SMES

Maximum stored energy (kJ)	Toroid type	Number of modules	Pancakes in a module	Conductor dimension (mm)	Operating current (A)	Discharge time (s)	Maximum voltage (kV)
200	Modular	16	3	4.1 × 0.2	100–200	1.5	1

Data compiled from [73]

Ag-Mg reinforcement, the critical stress remains low at 100 MPa. The conductor is further strengthened with an outer SS sheath raising the allowable stress to 170 MPa. Since the magnet is designed to run at a current of over 300 A and the tape has critical current of 100 A, a number of tapes were joined in parallel to carry this current. The pancakes are wound and bonded with slotted copper plates. Copper plates provide good mechanical support to the coils which are epoxy impregnated. The slots in copper plates reduce eddy current losses during ramping. A Kapton tape wrapped around the conductor provides electrical insulation. Hybrid current leads consist of brass leads between room temperature and an intermediate point and Bi-2212 tubes between this intermediate point and the magnet. The upper ends of the HTS leads together with the thermal shield are kept cooled by a dedicated cryocooler. The quench protection is provided by discharging current in a dump resistor by opening the power supply connection during charging and putting the magnet in persistent mode (during storage mode). The resistor remains connected to the magnet permanently.

The SMES is completely conduction-cooled. Two cryocoolers have been used, one for the magnet coils and the other for the current leads and the thermal shield. The SMES operates at 20 K at a current value of 315 A and stores 814 kJ energy. All characteristic parameters of the SMES are given in Table 12.17. The tests show that the AC losses are mainly due to hysteresis. The eddy current losses in the cryostat are minimal. The magnet discharge causes little loss, and the temperature increase is limited to 2 K.

Table 12.17 Parameters of the 800 kJ HTS SMES constructed by CNRS, France

Parameter	Unit	Value
Stored energy	kJ	814
Magnet type		solenoid
Winding structure		Single pancake
Number of pancakes		26
Coil internal diameter	mm	300
Coil outer diameter	mm	814
Magnet height	mm	222
Conductor used		Bi-2212 (Nexans)
Operating current	A	315
Operating temp	K	20
B_{max} (longitudinal)	T	5.2
B_{max} (transverse)	T	2.5
Maximum hoop stress	MPa	80
Maximum axial stress	MPa	24
Cooling (conduction)		Cryocoolers

Data compiled from [74]

12.5.4.2 2G REBCO Liquid Nitrogen Cooled SMES

Before the arrival of 2G REBCO-coated conductors, only Bi-2223 was commercially available in lengths enough to make coils. The drawback with this material, however, is that it supports magnetic field only up to 0.1 T beyond which the J_c drops sharply with magnetic field. This low field corresponds to an energy density of 4 kJ/m^3 only. The 90 K YBCO superconductor has a superior $J_c - B$ characteristic and can support magnetic field up to 5 T which corresponds to an energy density of 10 MJ/m^3. 2G HTS can be operated at still higher temperature, up to 70 K with good J_c. There has been a continuous improvement in conductor length and the critical current at temperature higher than 40 K. Besides, 2G HTS-coated conductors have high mechanical strength because of the Hastelloy substrate. In recent times, a large number of 2G HTS SMES have been designed and simulated, and some very small models have been laboratory tested. Yuan et al. [75] at Cambridge University have designed a SMES coil and carried out studies on current and magnetic field distribution and AC losses. The design was based on a 100 m length of SuperPower 2G conductor (12 mm × 0.105 mm) with coil inner diameter 80 mm, outer diameter 160 mm, height 12 mm, number of turns 266 and inductance 20 mH.

A 200 kJ SMES has been conceptually designed by Trillaud and Cruz [76] at UNAM, Mexico, using Amperium Cu-stabilized 2G HTS wire for use as UPS for the computer servers to provide power stability during short duration (1–10 s) faults and with long life cycle. A solenoid design of the magnet has been preferred for simplicity and to save on the conductor volume. All the parameters of the SMES and the conductor used are given in Table 12.18. The magnet will have a pancake structure consisting of 31 pancakes and connected in series. The inner diameter of the pancake is kept 0.2 m and the outer diameter 0.676 m.

The inter-coil separation will be 1 mm, and the total height of the magnet 0.418 m. The coils are to be wound using 2G HTS 12 mm wide and 0.2 mm thick conductor having 50 μm thick electrical insulation. Each pancake will have a total of 950 turns. The magnet will operate at a current of 53.8 A (80% of I_c) and at a temperature of 65 K. It will store a total energy of 252 kJ. The SMES is capable of supplying 200 kJ with 52 kJ as spare. It is important to evaluate the operating current from the critical surface (B-T-I) for the operating temperature and for the angle between the magnetic field and the tape (conductor) orientation. The magnet is housed in a MLI insulated liquid nitrogen cryostat fitted with a single-stage pulse tube refrigerator (65 W @ 60 K) to re-condense evaporated liquid nitrogen and to keep a temperature of 65 K. It takes about 56 h to reduce the temperature from 77 to 65 K.

The mechanical structure was designed by performing magnetostatic and mechanical finite element analysis (FEA) for the optimum operating conditions. The maximum stress load due to cooling and the Lorentz force turns out to be at the interface between the former and the coil equal to 33 MPa. This stress load happens to be well below the maximum stress at the I_c degradation, 400 MPa, and the Young's modulus of 2G HTS, 165 GPa.

Serious efforts continue to be made to exploit 2G REBCO-coated conductors for high mass energy density SMES. It is expected that the 13.4 kJ/kg mass energy

Table 12.18 Parameters of a 200 kJ 2G HTS SMES conceptually designed at UNAM, Mexico

Parameter	Unit	Value
Maximum stored energy	kJ	252
Usable energy	kJ	200
Magnet configuration		31 pancakes
Pancake inner and outer diameter	m	0.2 and 0.676
Total height of coil	m	0.418
Number of turns/pancake		950
Magnet inductance	H	174.7
Operating current	A	53.8 (80% I_c)
Operating temperature	K	65
Cooling system		LN2 and CCR re-condenser
Conductor used		Cu/2G HTS
Conductor dimension	mm	12 × 0.2
Conductor I_c (77 K, 0)	A	175
Total conductor length	km	4.2
Insulation thickness	μm	50
Maximum stress	MPa	33

Data compiled from [76]

density limit set by Nb–Ti magnets can be overcome and raised to 20 kJ/kg in 2G HTS SMES through proper optimization of parameters. Vincent et al. [77] have developed an optimization code for a solenoid-based SMES reaching a stored energy range of 5–50 MJ by taking the constraints of the critical current and mechanical strength of the conductor into consideration. Their calculations show that the mass energy density of 20 kJ/kg is achievable with 2G HTS provided it has a current density above 150 MA/m^2 and a stress tolerance higher than 400 MPa. Various solutions are possible for different values of I_e and the inner diameter of the magnet coil. The solution which has low B_{max} is a better option. For high effectiveness and protection, minimum I_e should be selected. The dimensions of the magnets are accordingly determined. The issue of low propagation velocities and increased quench detection time needs careful calculations in this material as well. A list of some superconducting SMES systems in the stored energy range of 1.2 kJ and 30 MJ working in a number of countries is given in Table 12.19.

Table 12.19 List of some superconducting SMES systems in the stored energy range of 1.2 kJ and 30 MJ used in a number of countries

Place of installation	Year	Country	Conductor for magnet	Operating temperature (K)	Stored energy (kJ)
Bonneville power authority	1982	USA	Nb–Ti	4.2	30,000
Superconductivity Inc.	1988	USA	Nb–Ti	4.2	1000
Forschungszentrum Karlsruhe	1995	Germany	Nb–Ti	4.2	188
American Superconductors	1997	USA	BSCCO	25	5
Bar-IIan University	2003	Israel	BSCCO	64–77	1.2
ACCEL Instruments	2003	Germany	BSCCO	20	150
Seoul National University	2005	Korea	BSCCO	20	600
Elettra synchrotron light facility in Trieste-I	2006	Italy	Nb–Ti	4.2	2600
Toshiba	2007	Japan	BSCCO/Nb–Ti	4.2	6500
Chinese Academy of Sciences	2008	China	BSCCO	4.2	1000
CNRS	2008	France	BSCCO	20	814
Chinese Electric Power Research Institute	2010	China	BSCCO YBCO	65–77	
University of Bath	2014	UK	YBCO	77	2

Data compiled from [78, 79]

12.5.4.3 Conceptual Design of MgB_2 Magnet for a 100 MJ SMES

The continuous increase made in the critical current density of MgB_2 conductors and the consequent success of small size MgB_2 magnet-based devices has made the superconductor community feel very confident that MgB_2 will replace Nb–Ti sooner than expected. In anticipation of this belief, many groups are making conceptual designs of several applications including the SMES systems using MgB_2 conductor. In this section, we discuss the conceptual design of a 100 MJ MgB_2 SMES proposed by Atomura et al. [80] as part of an advanced superconducting power conditioning system (ASPCS) meant to stabilize the fluctuating renewable energy, such as wind turbine (WT) and photovoltaic (PV). The power utility network is composed of 5 MW renewable energy resources and 1 MW hybrid storage system. The hybrid storage system is a combination of a fuel cell-H_2-Electrolyzer (FC-H2-EL) and SMES installed adjacent to a liquid hydrogen (LH_2) filing station for vehicles. The ASPCS will need SMES with 100 MJ storage capacity. MgB_2 magnet has been

proposed by the authors because the T_c of MgB_2 is 39 K and the SMES can be operated at 20 K. This temperature can be provided by LH_2.

A toroidal configuration was selected for the magnet design so as to reduce leakage of magnetic field. For design calculations, the authors have selected a Hyper Tech Research Corporation produced MgB_2 strand of 0.84 mm diameter consisting of 18 filaments. The CIC conductor (CICC) is made in a (6SC + 1Cu) × 3 × 4 configuration, and finally, SUS jacketed. The CICC thus has 1296 MgB_2 filaments. Different stages of cabling of the MgB_2 CICC cable used for the design are shown in Fig. 12.28. The CICC cable thus has 72 superconducting strands. After jacketing, the final cable size becomes 11.7 mm × 11.7 mm. Considering the $J_c - B$ behaviour of the CICC at 20 K, the authors have designed the magnet for 2 T field. In a toroidal magnet, the aspect ratio, a_t, is defined as a ratio of minor radius, r_{in}, to major radius, R_c. The quantity of superconductor used is important for cost consideration and is measured in terms of IM, Ampere meter. IM can be expressed in terms of the stored energy E, the maximum magnetic field B_m and aspect ratio a_t according to (12.11).

$$\mathrm{IM} = \left[\frac{16\pi^2 a_t^3}{\mu_0(1-a_t)\left(1-\sqrt{1-a_t^2}\right)^2}\right]^{1/3}\left[\frac{E^2}{B_m}\right]^{1/3} \tag{12.11}$$

where μ_0 is the permeability of vacuum. For a stored energy of 100 MJ and B_{max} = 2 T, the IM factor in Ampere meter becomes a function of the aspect value, a_t only. The minimum value of a_t comes out to be = 0.6. Accordingly, the specifications of the toroidal magnet become R_c = 3.68 m, r_{in} = 2.21 m, and the quantity of CIC conductor IM comes out to be = 204 × 10^6 Am. Thus, we need 10 km of the cable for an operating current of 20.4 kA.

However, because of the low $J_c - B$ profile of MgB_2 wires, the dimensions of the coil, 11.9 × 11.9 × 4.6 m^3, are large compared to that of Nb–Ti coil. Consequently, the conductor length is also larger (3506 km) than the Nb–Ti conductor. With the prospect of significant improvement in $J_c - B$ behaviour in coming years, one can redesign the SMES for higher field, say, 5 T making it more compact and economical, the major radius of the torus being proportional to $B_m^{-2/3}$ and the Ampere meter (IM)

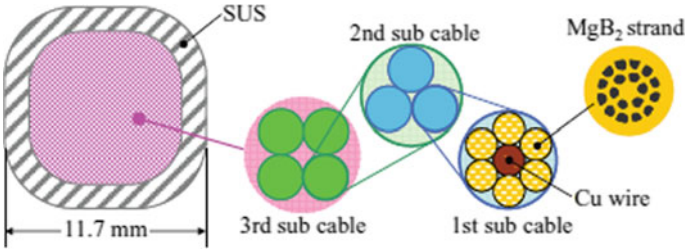

Fig. 12.28 Schematic of different stages of cabling of the MgB_2 CICC cable used for the design of the toroidal SMES of 100 MJ energy storage [80] (with permission from Elsevier)

Table 12.20 Key parameters of MgB_2 CICC cable and the toroid conceptually designed for a 100 MJ SMES

Conductor specifications			Toroid specifications		
Parameter	Unit	Value	Parameter	Unit	Value
Conductor		MgB_2	Magnet configuration		Toroidal
Configuration		CICC	Unit coil configuration		Pancake
Number of SC strands		72	Stored energy	MJ	100
Strand diamater	mm	0.84	Maximum mag. field	T	2
Cable configuration	(6SC + 1Cu) × 3 × 4		Number of unit toroidal coils		18
Cable dimensions	mm	11.7 × 11.7	Inductance	H	12.6
Number of filaments		18	Major radius	m	3.68
Void volume	%	35	Minor radius	m	2.21
Critical current, I_c	kA	8 (20 K, 3.98 T)	Number of turns/unit coil (SP coil × layer)		192 (32 × 6)
Operating current	kA	4	Unit coil width	m	0.41
Stability margin	J/cc	1.128	Centring force	MN	30
Maximum voltage	kV	2	5 gauss line from centre	m	8.25
CICC length	km	48.7	Cooling of coils to 20 K		LH_2
			Aspect ratio, a_t		0.6

Data compiled from [80]

proportional to $B_m^{-1/3}$. Conductor stability, quench protection, leakage of magnetic field, AC loss by the compensation parameters have been studied. Key parameters of MgB_2 CICC cable and the toroid are given in Table 12.20.

12.6 Maglev and Rotating Machines

In this section, we mention very briefly two more applications of the superconducting magnets, though very promising but both remained confined to prototype development level and technology demonstration stage, solely for economic reasons. These

are Maglev and the rotating machines. The technology could be revived in near future with the commercial availability of high-performing HTS conductors.

12.6.1 Magnetic Levitation (Maglev)

Japan had been the leading nation pursuing development of magnetically levitated train using superconducting magnets. The magnets are kept onboard the train and arranged longitudinally in the lower part of the train. Continuous aluminium sheets are embedded inside the concrete track exactly below the magnets. Strong eddy currents are generated in the aluminium sheets due to the magnets moving with the train. These eddy currents produce strong repulsive magnetic field upwards. At a certain speed, the repulsive force exceeds the weight of the train and lifts it off the track by several cms. The friction with the track disappears, and the train moves at high speed. Japan Central Railways has attained a speed of over 600 km/h in 2015. The trains have not been put in regular service for commuting again for the reason of high cost involved in the usage of liquid helium. Maglev for regular passenger travel can be a reality in near future in view of the rapid development in the production technology of the HTS.

12.6.2 Motors and Generators

DC homopolar and AC synchronous machines were built using conventional LTS superconductors in the range of a few kW to several MW and tested between 1970 and 1990s. Super GM of Japan had tested successfully a 70 MW superconducting generator. These machines though not commercialized because of the same reason of the high cost of cryogenic cooling, nevertheless, were built and supplied for specific applications. These machines are still preferred where weight and size are the biggest constraints. Similar to other applications, development of high-performing HTS has revived interest in these devices. HTS-based devices operating at higher temperature (30 K–50 K) are bound to revolutionize the entire electro-technology and will be commercialized in near future. Reputed companies like AMSC, SuperPower, Siemens, GE, Super GM and Relience Electric have been building and supplying high rating motors and generators for specific use to a host of organizations. AMSC has delivered a 36.5 MW 120 rpm motor to ONR for ship propulsion. Weight and volume (space) are at a premium in a ship. Industrial motors of 5000 hp 1800 rpm have been built by Siemens. Most generators use superconductor field winding and a normal copper winding for the armature. The superconducting winding produces high magnetic flux without dissipation. The armature has to have an iron-free structure, that is, an air-gap winding has to be used. This makes it quite compact. The status of superconducting motors and generators as it existed in 2004 has been reviewed by Kalsi et al. [81].

References

1. G. Roth, Ultra high field NMR magnet design. http://www2.warwick.ac.uk/fac/sci/physics/current/teach/module_home/px388/extra_material/bruker_magnets.pdf
2. T. Kiyoshi, S. Matsumoto, A. Satoet et al., IEEE Trans. Appl. Supercond. **15**, 1330 (2005)
3. Overview by Bruker BioSpin on 23.5 T standard-bore, persistent superconducting magnet, the world's first 1 gigahertz NMR. http://www.bruker.com/products/mr/nmr/dnp-nmr/overview.html
4. S.T. Wang, R. Wahrer, F. Anet et al., IEEE Trans. Magn. **30**, 1994 (1994)
5. W.D. Markiewicz, J.R. Miller, J. Schwartz et al., IEEE Trans. Appl. Supercond. **16**, 1523 (2006)
6. R.G. Sharma, Y.S. Reddy, B. Sarkar, R. Rajput, Design and winding of the magnet coils and fabrication of dewar for a 100 MHz NMR system, 1994, NPL, India (unpublished)
7. R.G. Sharma, Y.S. Reddy, R.B. Saxena, M.A. Ansari, A high homogeneity superconducting magnet and a long hold cryostat for NMR application, NPL, (New Delhi). Tech. Bull. 1–17 (1996)
8. M.D. Sauzade, S.K. Kan, *Advances in Electronics and Electron Physics*, vol. 34, ed. by L. Marton (Academic Press, 1973), pp. 1–93 (Chapter 1)
9. D. Patel, Su-Hun Kim 1,3, Wenbin Qiu1, Minoru Maeda4. Sci. Rep. **9**, 14287 (2019). https://doi.org/10.1038/s41598-019-50549-7
10. G. Brittles, Persistent current joints between NbTi superconducting wires. Ph.D. thesis. University of Oxford (2016)
11. J.E.C. Williums, S. Pourrranimi, Y. Iwasa et al., IEEE Trans. Magn. **25**, 1767 (1989)
12. K. Hashi, S. Ohki, S. Matsumoto, G. Nishijim, J. Mag. Reso., **256**, 30 (2015). A Press Release by NIMS http://www.nims.go.jp/eng/news/press/2015/07/201507010.html
13. Successful installation of world's first 1.2 GHz NMR system enables novel functional structural biology research. https://www.bruker.com/news/successful-installation-of-worlds-first-12-ghz-nmr-system.html
14. JEOL Resonance, *JEOL Resonance Introduces New Zero Boil Off Magnet for NMR System.* A Press Release dated 17 Apr 2013
15. Press Release NIMS (2011). https://www.nims.go.jp/news/press/2011/09/hdfqf1000000dzr6-att/p201109070.pdf
16. T. Suzuki, M. Okada, T. Wakuda et al., 8th European conference on applied superconductivity (EUCAS 2007). J. Phys. Conference series **97**, 012133 (2008)
17. K. Saitoh, H. Yamamoto, K. Kawasaki, et al., 8th European conference on applied superconductivity (EUCAS-2007). J. Phys. Conf. Ser. **97**, 012141 (2008)
18. M. Tsuchiya, T. Wakuda, K. Maki et al., IEEE Trans. Appl. Supercond. **18**, 840 (2008)
19. Y. Iwasa, J. Bascuñán, S. Hahn, High-resolution 1.3-GHz/54-mm LTS/HTS NMR magnet. 4LOR2A-03
20. P.C. Michael, D. Park, Y.H. Choi et al., IEEE Trans. Appl. Supercond. **29**, 4300706 (2019)
21. D. Park, J. Bascuñán, P.C. Michael et al., IEEE Trans. Appl. Supercond. **29**, 4300804 (2019)
22. P.C. Lauterbur, Nature (London) **242**, 190 (1973)
23. M.W. Garrett, J. Appl. Phys. **38**, 2563 (1967)
24. S. Pissanetzky, IEEE Trans. Magn. **28**, 1961 (1992)
25. R. Thompson, R.W. Brown, V.C. Srivastava, IEEE Trans. Magn. **30**, 108 (1994)
26. S. Crozier, D.M. Doddrell, J. Magn. Reson. **127**, 233 (1997)
27. H. Zhao, S. Crozier, D.M. Doddrell, Magn. Reson. Med. **45**, 331 (2001)
28. G. Sinha, R. Sundararaman, G. Singh, IEEE Trans. Magn. **44**, 2351 (2008)
29. Y. Lvovsky, E.W. Stautner, T. Zhang, Topical review. Supercond. Sci. Technol. **26**, 0933001 (p 71) (2013)
30. D.M. Doddrell, H. Zhao, Multi-layer magnet. US Patent 7212004 (2007)
31. S. Mine, M. Xu, Y. Bai, S. Buresh, W. Stautner et al., Development of a 3T-10″ bore MgB_2 magnet system. 2LPo2A-07
32. S. Mine, M. Xu, Y. Bai, S. Buresh, W. Stautner et al., IEEE Trans. Appl. Supercond. **25**, 4600604 (2015)

33. H. Mason, The next generation in positional MR imaging. Technical report. MROpen EVO, 29 June 2019. https://www.asgsuperconductors.com/news/mropen-evo-the-next-generation-in-positional-mr-imaging
34. T. Baig, Z. Yao, D. Doll, M. Tomsic, M. Martens, Supercond. Sci. Technol. **27**, 125012 (2014)
35. Y.-C.N. Cheng, T.P. Eagan, R.W. Brown, S.M. Shvartsman, M.R. Thompson, Magn. Reson. Mater. Phys. Biol. Med. **16**, 57 (2003)
36. G.Z. Li, M.D. Sumption, J.B. Zwayer, M.A. Susner et al., Supercond. Sci. Technol. **26**, 095007 (2013)
37. J. Ling, J. Voccio, Y. Kim, S. Hahn et al., IEEE Trans. Appl. Supercond. **23**, 6200304 (2013)
38. Y.H. Choi, Y. Li, D. Park, J. Lee et al., IEEE Trans. Appl. Supercond. **29**, 4400405 (2019)
39. Y. Iwasa, Supercond. Sci. Technol. **30**, 053001 (2017)
40. Y. Iwasa, J. Bascuñán, S. Hahn, D.K. Park, Phys. Proc. **36**, 1348 (2012)
41. https://www.wgtn.ac.nz/wfadi/about/news/university-researchers-create-innovative-mri-technology
42. R. Aarnink, J. Overweg, Europhys. News **43**, 26 (2012). https://doi.org/10.1051/epn/2012404
43. MAGNETOM Terra—Translate 7T research power into clinical care. Siemens Brochure. https://www.siemens-healthineers.com/en-in/magnetic-resonance-imaging/7t-mri-scanner/magnetom-terra
44. Siemens' website. https://www.siemens-healthineers.com/en-in/magnetic-resonance-imaging/7t-mri-scanner/magnetom-terra#CLINICAL_USE
45. L. Quettier, G. Aubert, J. Belorgey, C. Berriaud, G. Billotte et al., IEEE Trans. Appl. Supercond. **28**, 4400604 (2018)
46. How the CEA/Irfu developed Iseult; the gigantic 11.7 T MRI magnet! A discussion with Lionel Quettier 24.02.2020 | Metronews, MFC2046, MRI. https://www.metrolab.com/gigantic-11-7-t-mri-magnet-iseult-a-discussion-with-lionel-quettier/
47. T.K.F. Foo, E. Laskaris, M. Verilyea, M. Xu et al., Magn. Reson. Med. **80**, 22232 (2018)
48. H.H. Kolm, IEEE Trans. Magn. **11**, 1567 (1975)
49. Z.J.J. Steckly, IEEE Trans. Magn. **11**, 1594 (1975)
50. S. Nishijima, K. Takahata, K. Saito et al., IEEE Trans. Magn. **23**, 573 (1987)
51. H. Yamashita, K. Fujita, F. Nakajima et al., Sep. Sci. Technol. **16**, 987 (1981)
52. K. Takahata, S. Nishijima, T. Okada et al., IEEE Trans. Magn. **24**, 878 (1988)
53. R.G. Sharma, Y.S. Reddy, Development of a superconducting high gradient magnetic separator NPL (India). Tech. Bull. 1–8 (1992)
54. Y. Kakihara, T. Fukunishi, S. Takeda et al., IEEE Trans. Appl. Supercond. **14**, 1565 (2004)
55. S. Nishijima, S. Takeda, IEEE Trans. Appl. Supercond. **17**, 2311 (2007)
56. F. Ning, M. Wang, H. Yang et al., IEEE Trans. Appl. Supercond. **22**, 3700104 (2012)
57. D.D. Jackson, P. Beharrel, J. Sloan, *Industrial-Scale Purification of Kaolin Using a Conduction-Cooled Superconducting High-Gradient Magnetic Separator* (Quantum Design Inc., USA). www.qdusa.com/sitedocs/productBrochures/SHGMS_poster_forEUCAS_2013pdf
58. W. Ge, A. Encinas, E. Araujo, S. Song, Results Phys. **7**, 4278 (2017)
59. D. Xiong, S. Liu, J. Chen, Int. J. Miner. Process. **54**, 111 (1998)
60. J. Xu, D. Xiong, S. Song, L. Chenc, Results Phys. **10**, 837 (2018)
61. W. Hassenzhal, IEEE Trans. Magn. **25**, 750 (1989)
62. S. Nagaya, N. Hirano, T. Tanaka et al., IEEE Trans. Appl. Supercond. **14**, 699 (2004)
63. S. Nagaya, N. Hirano, T. Katagiri et al., Cryogenics **52**, 708 (2012)
64. R.J. Loyd, T.E. Walsh, E.R. Kimmy, IEEE Trans. Magn. **27**, 1712 (1991)
65. P. Tixador, Superconducting magnetic energy storage: status and perspective, in *IEEE/CSC and ESAS European Superconductivity News Forum*, vol. 3, Jan 2008. www.ewh.ieee.org/europe/newforum/pdf/CR5_final3_012008.pdf
66. M. Ferrier, Stockage d' energie dans un enroulement supraconducteur, in *Low Temperature and Electric Power* (Pargamon Press, 1970), pp. 425–432
67. G.W. Ullrich, IEEE Trans. Appl. Supercond. **5**, 416 (1995)
68. J.L. Wu, J.F. Roach, D.C. Johnson et al., Adv. Cryog. Eng. **39**, 813 (1994)
69. C.J. Hawley, S.A. Gower, IEEE Trans. Appl. Supercond. **15**, 1899 (2005)

70. C.J. Hawley, D. Cuiuri, C.D. Cook et al., J. Phys. Conf. Ser. **43**, 809 (2006). http://ro.uow.edu.au/cgi/viewcontent.cgi?article=7297&context=engpapers
71. S.S. Kalsi, D. Aized, B. Konnor et al., IEEE Trans. Appl. Supercond. **7**, 971 (1991)
72. G. Wojtasiewicz, T. Janowski, S. Kozak et al., J. Phys. Conf. Ser. **43**, 821 (2006)
73. J.H. Kim, S.Y. Hahn, C. Hwan et al., IEEE Trans. Appl. Supercond. **12**, 774 (2002)
74. P.Tixador, M. Deleglise, A. Badel et al, First tests of 800 kJ HTS SMES. http://arxiv.org/ftp/arxiv/papers/0812/0812.3639.pdf
75. W. Yuan, W. Xian, M. Ainslie et al., IEEE Trans. Appl. Supercond. **20**, 1379 (2010)
76. F. Trillaud, L.S. Cruz, IEEE Trans. Appl. Supercond. **24**, 5700205 (2014)
77. B. Vincent, P. Tixador, T. Lecrevisse et al., IEEE Trans. Appl. Supercond. **23**, 5700805 (2013)
78. W. Yuan, M. Zhang, Superconducting magnet energy storage (SMES) system, in *Handbook of Energy System*, vol. 5, part 4, ed. by J. Yan (Wiley, 2015), p. 2768
79. L. Ottonello, G. Canepa, P. Albertelli, E. Picco et al., IEEE Trans. Appl. Supercond. **16**, 602 (2006)
80. N. Atomura, T. Takahashi, H. Amata, T. Iwasaki et al., Phys. Proc. **27**, 400 (2012)
81. S.S. Kalsi, K. Weeber, H. Takesue et al., Proc. IEEE **92**, 1688 (2004)

Index

R. G. Sharma, *Superconductivity*, Springer Series in Materials Science 214,
https://doi.org/10.1007/978-3-030-75672-7

G

H

T